SCHOLARLY PUBLICATIONS

A CURRENT AWARENESS BULLETIN
OF RESEARCH OUTPUT

@DTU

(143rd Edition)

NOVEMBER 2024

BY: CENTRAL LIBRARY

DELHI TECHNOLOGICAL UNIVERSITY

(FORMERLY *DELHI COLLEGE OF ENGINEERING)*
GOVT. OF N.C.T. OF DELHI
SHAHBAD DAULATPUR, MAIN BAWANA ROAD
DELHI 110042

PREFACE

This is the **One Hundred Forty-Three** Issue of Current Awareness Bulletin started by Delhi Technological University, Central Library. The aim of the bulletin is to compile, preserve and disseminate information published by the faculty, students and alumni for mutual benefits. The bulletin also aims to propagate the intellectual contribution of Delhi Technological University (DTU) as a whole to the academia.

The bulletin contains information resources available in the internet in the form of articles, reports, presentations published in international journals, websites, etc. by the faculty and students of DTU. The publications of faculty and student which are not covered in this bulletin may be because of the reason that the full text either was not accessible or could not be searched by the search engine used by the library for this purpose.

The learned faculty and students are requested to provide their uncovered publications to the library either through email or in CD, etc. to make the bulletin more comprehensive.

This issue contains the information published during **November 2024**. The arrangement of the contents is alphabetical. The full text of the article which is either subscribed by the university or available in the web is provided in this bulletin.

Central Library

CONTENTS

1. A 16–20 GHz Mixer First Receiver Architecture with Active Inductor-Based Low-Pass Elliptic Filter with High OOB-IIP3 in 180 nm CMOS***, 7.1 Gaurav Srivastava*** and Darshak Bhat, ECE, DTU

2. Adaptive Scheduling of Shared Grant-Free Resources for Heterogeneous Massive Machine type Communication in 5G and Beyond Networks, Yukti Kaura , ***8.1 Brejesh Lall*** , Ranjan K. Mallik and Amit Singhal, ECE, DTU

3. AI Based Drive Cycle Prediction for HEV, ***6. Ritul Gehlot***, ***8.1 Shobha Kumari,*** and ***3. Kuldeep Singh***, Electrical, DTU

4. Analysis of Glycyrrhiza Glabra Phytocompounds using Network Pharmacology for Anti-Alzheimer Therapy, ***8.1 Nishtha Jain,8.1 Kunal Dugar, 8.1 Aadya Suri,*** and ***3. Navneeta Bharadvaja***, Biotechnology, DTU

5. APPLICATION OF OPTIMIZATION TECHNIQUES FOR FREQUENCY STABILITY IMPROVEMENT IN MICROGRID, ***6. Philemon Yegon, 3.Mukhtiar Singh***, EE, DTU

6. Artificial intelligence in the workplace- challenges, opportunities and HRM framework: a critical review and research agenda for change, John Mendy, ***6.1 Apoorva Jain*** and ***6.1 Asha Thomas***, Delhi School of Management, DTU

7. Assessment of Mechanical and Slurry Erosive Behavior on Laser-Textured Stainless Steel (SS410), ***6.1 Mohit Vishnoi***, ***3. Qasim Murtaza*** and ***3.Paras Kumar***, Mechanical, DTU

8. An Adaptive Forward Compensation for Enhanced PLL Based Position Estimation of Syn-RL Motor Drive, ***3. Saurabh Mishra***, Bhim Singh, Electrical, DTU

9. A Novel Method for Monitoring Stator Interturn Insulation Degradation of InverterFed Motors Based on Impedance Spectrum Division, Feng Niu , Pengju Zhang , Feng Zhou , Shaopo Huang , Zijun Xu , Lu Zhang , and ***8.1 Anmol Aggarwal,*** Electrical, DTU

10. Application of Paper Mill Lime Sludge Waste in Building Construction Material: State of The Art Report, Arti Chouksey, ***3. Nirendra Dev***, VVL Kantarao, and Manvendra Verma, Civil, DTU

11. BlipGlyphDiff: Glyph-Based Text to Image Generation with Different Styles and Background, ***8.1 Ansh Anurag, 8.1 Bhaskar Anand, 8.1 Ankush Bhagat***, CSE, DTU

12. CMOS compatible TeO2—coated Si3N4 inverse parabolic rib waveguide for on-chip supercontinuum generation and high resolution OCT, ***6. Deepak Garg, 3.Ajeet Kumar***, Applied Physics, DTU

13. Comparative analysis of two novel chaotic systems, and validation of hybrid function projective and complete synchronization using active-adaptive control, D Khattar, ***6. M Sirohi*** and R Bansal, Applied Mathematics, DTU

14. Control of WRIG Based WECS for Grid Integration, ***3. Himanshu Singh, 3. Madhusudan Singh,*** Bhim Singh, Electrical, DTU

15. Comparative Analysis of Carbon Footprint and Environmental Impact of Laptops, ***6. Mohd Tayyab, 3. Ranganath M Singari*** and Peer M Sathikh, Design, DTU

16. Dhivehi Speech Recognition: A Multimodal Approach for Dhivehi Language in Resource-Constrained Settings, ***6. Sunakshi Mehra, 3.Virender Ranga***, and ***3.Ritu Agarwal***, IT, DTU

17. DiabeticChain: a novel blockchain approach for patient-centric diabetic data management***, 6.1 Deepak Kumar Mishra, 3.Pawan Singh Mehra***, CSE, DTU

18. Deep convolutional architectures for optimizing multi-element airfoil systems, 8.1 ***Kartikey Vishnu, 8.1 Devdoot Chatterjee, 3. Anurag Goel*** and ***3. Rajeev Kumar***, ME, CSE, DTU

19. Design & Analysis of Adaptive Noise Equalizer for EV charging infrastructure integrated PV systems***, 6.Anurag Kumar, 3.Ankita Arora*** and ***3.Madhushudan Singh,*** Electrical, DTU

20. Dressing the Imagination: A Dataset for AI-Powered Translation of Text into Fashion Outfits and A Novel KAN Adapter for Enhanced Feature Adaptation, Gayatri Deshmukh, Somsubhra De, ***8.1 Chirag Sehgal***, Jishu Sen Gupta, Sparsh Mittal, CSE.

21. Degradable pH-Sensitive Calcium-Crosslinked Tragacanth Gum/βCyclodextrin/ Sodium Alginate Hydrogel Microspheres Prepared via Ionotropic Gelation Technique for Hydrophobic Drug Delivery, ***6. Priyanka Meena, 3. Poonam Singh*** and ***3.Sudhir G. Warkar,*** Applied Chemistry, DTU

22. Design and optimization of a terahertz photonic crystal fber based biosensor to detect malaria disease, ***6.Vishal Chaudhary, 3.Sonal Singh***, ECE, DTU

23. Developing novel spectral indices for precise estimation of soil pH and organic carbon with hyperspectral data and machine learning, ***6. Shagun Jain, 3.Divyashikha Sethia*** and ***3. Kailash Chandra Tiwari***, Software Engg., Civil, DTU

24. Estimation of tropical cyclone's radius of maximum wind using ensemble machine learning approach, ***6.MONU YADAV, 3.LAXMINARAYAN DAS*** and ***6.SHASHI KANT***, Applied Mathematics, DTU

25. Existence of dual topological phases in Sn-based ternary chalcogenides, ***6.Ramesh Kumar, 3. Mukhtiyar Singh,*** Applied Physics, DTU

26. EMH or AMH? Evidence from the emerging Indian equity market, ***6. Reema Monga, 3.Deepti Aggrawal*** and Jagvinder Singh, DSM, DTU

27. Phenomenology of (3+1) Four Flavour Neutrino Oscillations in Dense Matter, ***6. Ashish Shrivastava***, Bipin Singh Koranga and Seema Rawat, Applied Physics, DTU

28. Potential application of p-type diamane as back surface field layer in silicon-based heterojunction solar cells, ***6. Naima, 3. Pawan K Tyagi and 3. Vinod Singh***, Applied Physics, DTU

29. Highly Sensitive Graded Index PCF-Based Refractometric SPR Sensor Ofering Enhanced FOM, ***6. Akash Khamaru, 3.Ajeet Kumar***, Applied Physics, DTU

30. Identification of Allium cepa L.-Derived Flavonoids as Potential Inhibitors of Human Serum Albumin Glycation in Diabetic Nephropathy: An In-Silico Analysis**,** ***8.1 Kanjam Manocha, 8.1 Shivam Bilandi*** and ***3. Navneeta Bharadvaja***, Biotechnology, DTU

31. IMPACT OF SUPPLY CHAIN DISRUPTIONS ON ENERGY SECURITY IN ZAMBIA: CHALLENGES AND MITIGATION STRATEGIES, ***7. Fredrick Kabwe, 3. Dr. Krovvidi Srinivas*** and ***7.Nakuti Sharon***, Mechanical, Accounting and Finance (MBA), DTU

32. Impact of Temperature and Noise on Gallium Nitride Junctionless Accumulation Mode Nanowire FET (GaN-JAMNWFET), ***6. Anupama, 3. Sonam Rewari,*** and ***3. Neeta Pandey***, ECE, DTU

33. Influence of local meteorology and gaseous pollutant emissions on atmospheric nanoparticle 2 concentrations in a pedestrian way in urban region, ***6.Kanagaraj Rajagopal,*** S. Ramachandran, and ***3. Rajeev Kumar Mishra***, ENVT and Civil, DTU

34. Infuence of samarium ions doping on electrical and optical properties of bismuth antimony fuoroborate glasses, Gunjan Mahajan, M. V. V. K. Srinivas Prasad, K. Swapna1, K. Seshulatha, M. Venkateswarulu, Sk. Mahamuda and ***3. A. S. Rao,*** Applied Physics, DTU

35. International Journal of Future Engineering Innovations***, 3.JP Kesari***, Mechanical, DTU

36. Metaheuristics Approaches Towards Secure and Optimized Routing in IoT: A Systematic Literature Review, ***3. Rohit Beniwal, 3. Vinod Kumar*** and ***8. Vishal Sharma***, ECE, DTU

37. Mathematical Analysis and Topology Derivation for a Family of Novel Dual Output High-Voltage Gain Z-Source Converter for Renewable Energy Application, ***3.A. Gupta 6.D. Joshi***, Electrical, DTU

38. Molecularly imprinted polypyrrole decorated Ti3C2Tx electrochemical sensor for highly selective and sensitive detection of levofloxacin, 6***. Divya Hudda, 3. Devendra Kumar****,* Applied Chemistry, DTU

39. Modelling and TCAD Analysis of Plasma-Assisted Graphene Field Effect Transistor, ***3. Suresh C. Sharma , 6.Monika Verma*** and ***3.Sonam Rewari***, Physics, ECE, DTU

40. Optical temperature sensing and upconversion luminescence in Er3+/ Yb3+ co-doped BNT ferroelectric ceramic, ***6. Megha Narwan, 3. Richa Sharma*** and ***3. Renuka Bokolia,*** Applied Physics, DTU

41. Organisational Clusters Concept—Adding Value to Surveys and Effectiveness to OD Interventions, ***2.1 Anu Singh Lather***, Shilpa Jain and Yogesh Chandra Verma, DTU

42. Performance Analysis of Multiple Delayed Signal Cancellation (MDSC) for Power Quality Improvement for Fixed Speed SEIG-Based Distributed Generation, ***6.Divyansh Shailly , 3.Prakash Chittora*** and ***3. Madhusudan Singh***, Electrical, DTU

43. Passive Islanding Detection Approach for grid integrated SPV System, ***6. Shruti Prajapati, 3. Rachana Garg*** and ***3. Priya Mahajan***, Electrical, DTU

44. Performance analysis of Input Parallel Output Series Full Bridge Converter considering parasitic effect, ***6. Mugdha Goel, 3. Dheeraj Joshi*** and ***8.1 John Mulenga,*** Electrical, DTU

45. Piezo-Ionic Actuator for Haptic Feedback, Antonio ´ Diogo Andr´e, ***6.1 Indrani Coondoo,*** Igor Bdikin, Vinaya Kumar K.B., Rui M.R. Pinto, Pedro Martins and Majid Taghavi, Physics, DTU

46. Performance evaluation of indirect solar drying system for potato slices: Comparative analysis with open-sun drying method, Ankit Srivastava , Atul Sharma and ***3. Anil Kumar***, Mechanical, DTU

47. Recent Developments, Reliability Issues, Challenges and Applications of GaN HEMT Technology***, 6.Tanvika Garg***, ***3.Sumit Kale***, ECE, DTU

48. Rethinking Security Paradigms in the Face of External Backlash: A Case Study in Private Security,***8.1 Soumendra Narain Bagchi***, Rajeev Sharma, Civil, DTU

49. Secure Novel Hybrid PUF Design For Key Generation and Authentication Applications Of IoT, ***6. Bhagyalakshmi Narayanapuram, 3. Jeebananda Panda,*** ECE, DTU

50. Sustainable biodiesel from used cooking oil: a comparative life cycle, energy, and uncertainty analysis, ***6. Kulvendra Patel, 3. S. K. Singh***, Environmental, DTU

51. Unveiling Enhanced Model Predictive Control for Power Regulation in Single Phase AC/DC Converter, ***6.Philemon Yegon, 3. Mukhtiar Singh***, Electrical, DTU

52. Use of butanol, pentanol and diesel in a compression ignition engine: A review, ***7.1 Deepak Kumar, 3. Naveen Kumar*** and ***3. Rajiv Chaudhary***, Mechanical, DTU

53. YAR-Net: Yoga Asanas Recognition Network Based on Variational Autoencoder, ***6. Roli Kushwaha, 6.Manjeet Kumar*** and ***3. Dinesh Kumar***, ECE, DTU

54. Zirili map-based image encryption method for healthcare, military, and personal data security, ***6. Puneet Kumar Pal, 3. Dhirendra Kumar***, Applied Mathematics, DTU

1. *Vice Chancellor*
2. *Pro Vice Chancellor*
3. *Faculty*
4. *Teaching-cum-Research Fellow*
5. *Asst. Librarian*
6. *Research Scholar*
7. *PG Scholar*
8. *Undergraduate Student*

1.1. *Ex Vice chancellor*
2.1. *Ex Pro Vice Chancellor*
3.1. *Ex Faculty*
4.1. *Alumni*
5.1 *Others*
6.1. *Ex Research Scholar*
7.1. *Ex PG Scholar*
8.1. *Ex Undergraduate Student*

This article has been accepted for inclusion in a future issue of this journal. Content is final as presented, with the exception of pagination.

A 16–20 GHz Mixer First Receiver Architecture With Active Inductor-Based Low-Pass Elliptic Filter With High OOB-IIP3 in 180 nm CMOS

Gaurav Srivastava, *Graduate Student Member, IEEE*, and Darshak Bhatt, *Member, IEEE*

***Abstract*— This article introduces an innovative approach to realize a mixer-first receiver architecture, which comprises an N-path differential architecture realized through a passive-switching network, followed by a novel self-biased active inductor-based filter. This combination allows the circuit to achieve high pass-band to stop-band attenuation and the capability to adjust and achieve the desired bandwidth and occupy less area on-chip while maintaining a high selectivity level and rejecting unwanted signals. A noise-cancelling amplifier is placed between the N-path and active inductor-based low-pass elliptic filter to reduce the noise figure of the receiver. In addition to the filter, a novel self-biased baseband amplifier with a wide bandwidth is realized, followed by a buffer to derive a 50 ohms load. The LO signal generation for the proposed receiver is obtained by implementing a passive balun circuit that operates over a wideband followed by an on-chip polyphase filter and buffer. The proof of concept is validated by implementing a designed receiver with an N-path differential architecture followed by a novel active inductor-based low-pass third-order elliptic filter, which occupies less area and achieves high selectivity compared to a passive inductor based filter on 180-nm CMOS technology. The receiver operates within the frequency range of 16-20 GHz and achieves an instantaneous single sideband (SSB) bandwidth of 160 MHz. The proposed filter achieves a pass-band to stop-band attenuation of 47 dB with a Q of 140. Additionally, the receiver exhibits an in-band compression point at -5 dBm and in-band IIP3 of 4–6 dBm with out-of-band signal linearity greater than 10 dBm.**

***Index Terms*— CMOS integrated circuit, active inductor(AI)-based filter, elliptic filter, mixers, receivers.**

I. Introduction

As 5G standards evolve, transitioning to higher frequencies is crucial for alleviating congestion in traditional cellular bands and enabling broader bandwidths for high data rates. In applications like MIMO and beamforming, reducing per-element complexity and power consumption is essential. Thus, flexible, interference-tolerant receiver front ends that meet stringent performance, reliability, and power efficiency requirements are preferred for optimal operation in challenging environments. The K-band [1] is favored in satellite communication, radio navigation, and remote sensing for its power adjustment capabilities and efficiency, offering reduced congestion compared to other bands. Moreover, both the International Telecommunication Union (ITU) and the Space Frequency Coordination Group (SFCG) recommend the K-band for high data rate communication, leveraging the availability of high-performance integrated circuits (ICs) tailored for cellular and base-station communication needs. Furthermore, the forthcoming 3GPP standards for 6G (FR) are considering a transition to the K-band, as architectures designed for these frequencies offer wider bandwidth and cost efficiency. Several project [2] have emerged to provide global-scale broadband internet connectivity through the deployment of large constellations in Low Earth Orbit (LEO) and Medium Earth Orbit (MEO). These constellations primarily operate in the Ku and Ka bands to optimize throughput and may utilize higher frequencies, such as the V and Q bands, for feeder links to ground station networks. Receivers designed for low-frequency applications often encounter limitations related to sub-optimal linearity performance. In space communication, where these frequency bands are highly congested, the demand for such receivers is restricted due to the necessity for high bandwidth to support upgraded software architectures that enhance algorithms and communication standards. Therefore, the paper proposes a receiver architecture designed for high-frequency applications with the aim of achieving high bandwidth with less on-chip area and low cost. Moreover, the frequency application of the implemented architecture is limited by f_T of the 180-nm CMOS technology.

In an RF transceiver system, the mixer-first receiver architecture and N-path filtering offer the advantage of achieving high linearity by utilizing the bilateral nature of the band-pass response to enhance out-of-band linearity. Additionally, a tuneable local oscillator (LO) mitigates parasitic effects from inductors and capacitors, providing wideband tunability and robustness against out-of-band interference at millimeter-wave frequencies.

As illustrated in Fig. 1(a), the mixer-first receiver architecture, as detailed in references [3], [4], [5], [6], [7], [8], [9], and [10] is implemented with a transimpedance amplifier (TIA) based filter utilizing a shunt-notch or positive capacitive feedback topology to achieve high out-of-band (OOB) linearity and enhanced selectivity. This design enables a low noise

Received 31 May 2024; revised 26 July 2024, 29 August 2024, and 7 October 2024; accepted 23 October 2024. This work was supported by the Science and Engineering Research Board (SERB), Government of India, under Start-up Research under Grant SRG/2019/000844. This article was recommended by Associate Editor X. Zhu. *(Corresponding author: Darshak Bhatt.)*

The authors are with the Department of Electronics and Communication Engineering, Indian Institute of Technology at Roorkee, Roorkee 247667, India (e-mail: darshak.bhatt@ece.iitr.ac.in).

Color versions of one or more figures in this article are available at https://doi.org/10.1109/TCSI.2024.3488892.

Digital Object Identifier 10.1109/TCSI.2024.3488892

1549-8328 © 2024 IEEE. Personal use is permitted, but republication/redistribution requires IEEE permission.
See https://www.ieee.org/publications/rights/index.html for more information.

Authorized licensed use limited to: DELHI TECHNICAL UNIV. Downloaded on November 18,2024 at 05:07:46 UTC from IEEE Xplore. Restrictions apply.

This article has been accepted for inclusion in a future issue of this journal. Content is final as presented, with the exception of pagination.

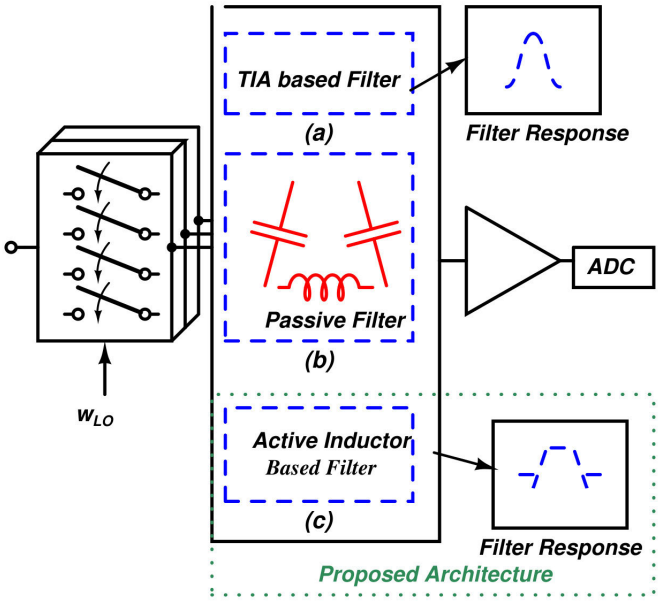

Fig. 1. (a) Mixer-first receiver architecture TIA-based Filter [3], [4], [5], [6], [7], [8], [9], [10]. (b) Mixer first receiver architecture with passive-elliptic or RC filter [11], [12], [13], [14], [15], [16], [17]. (c) The proposed mixer-first receiver architecture.

figure, high gain, and elevated OOB-IIP_3. However, the complexity of this receiver architecture results in increased power consumption and a larger occupied area. Additionally, these architectures are primarily suited for sub-6 GHz applications, where the demand for RF bandwidth is relatively low. Therefore, in Fig. 1(b), mixer first receiver architecture [11], [12], [13], [14], [15], [16], [17] is implemented with a passive-filter configuration so that wideband tunability along with high bandwidth can be attained for mm-wave applications. In [11], a 20-30 GHz mixer-first receiver with a passive N-path and a baseband amplifier with feedback resistor R_F achieves high conversion gain, low noise figure, and moderate pass-band to stop-band rejection. In [12], a 9-31 GHz N-path mixer-first receiver with a differential hybrid-coupler LO and RF using a 1:1 transformer attains wideband transparency with low insertion loss but suffers from high LO power consumption and poor pass-band to stop-band attenuation. In [13], a passive 10-35 GHz mixer-first design with RC load for overlapping/non-overlapping phases is followed by a baseband amplifier, achieving high linearity (both in-band and out-of-band) but with noise degradation.

In [14], a passive mixer with a wideband matching network, featuring a doubly terminated passive ladder filter followed by a baseband amplifier, is implemented. The circuit's wideband performance is influenced by its finite Q and the variation in R_{sw} of the N-path, resulting in a low noise figure and high linearity, though LO power consumption remains high. In-band interference of the down-converted signal can be mitigated using analog or digital filters, but both approaches require significant power, typical for mm-wave systems with large channel bandwidths. In [15], a mm-wave mixer-first receiver with a higher-order passive elliptic filter achieves high bandwidth and strong passband-to-stopband attenuation. However, the large passive inductance occupies significant chip area and has a low Q-factor.

The proposed mixer first receiver architecture is designed with an idea of attaining wideband tunability along with active low-pass filter having high passband to stopband attenuation with a large Q-factor and high in-band and out-of-band linearity. Moreover, the large passive component is replaced with an active element so that the area on-chip can be minimised. Therefore, the proposed receiver is implemented with an N-path differential architecture followed by an active inductor(AI)-based third order elliptic filter.

The proposed mixer first receiver architecture is shown in Fig. 2, and the key highlights includes:

1) The third-order low pass elliptic filter is implemented with an active-inductor based or Gm-C based configuration as it provides the advantages such as:

- Large and tunable self-resonant frequency.
- Large and tunable inductance and Quality factor.
- The area occupied is comparatively less than that of the passive inductor.

2) The active inductor is implemented with a self-bias configuration creating a negative-feedback loop which stabilises the bias-voltage for all the transistors.

3) As shown in Fig. 3(a) third-order low-pass elliptic filter is implemented with a passive inductor and it can be observed that in order to achieve high selectivity high value of inductance is needed. However, the Q-factor attained for the filter is low. Additionally, the area occupied by the on-chip passive inductor is large. Therefore, in the proposed circuit, as shown in Fig. 3(b) passive inductor of an elliptic filter is replaced by a novel self-biased active inductor. The obtained inductance value for the proposed low-pass elliptic filter configuration is low, with high Q-factor and high pass-band to stop-band attenuation.

4) The LO signal for the proposed receiver is generated on-chip using a passive balun circuit followed by a poly-phase filter designed for a centre frequency of 18 GHz. The passive balun circuit is designed with an LC combination, providing wide-band tunability. The proposed receiver architecture is designed in 180-nm CMOS technology and is tested and measured over a frequency range of 16-20 GHz. In order to improve the noise performance of the circuit a noise cancelling stage is embedded between the N-path and low-pass elliptic filter to reduce the noise figure and provide optimum gain for the circuit. The filter is followed by a self-biased baseband amplifier, which amplifies the quadrature signals. The baseband amplifier is designed with the same self-biased configuration, and the required gain along with -3dB bandwidth can be achieved by varying MOS parameters and feedback resistors. The I/Q signal obtained at the O/P of the baseband amplifier is retrieved using a buffer designed by using a differential amplifier.

The content of this article is organized as Section II describes the differential N-path architecture with active filter implementation. Section III describes baseband impedance and its analysis, along with a discussion on LO generation and the parameters of the receiver, such as conversion gain, noise figure and linearity. Section IV briefly discusses CMOS implementation. Section V describes measurement results along

Authorized licensed use limited to: DELHI TECHNICAL UNIV. Downloaded on November 18,2024 at 05:07:46 UTC from IEEE Xplore. Restrictions apply.

This article has been accepted for inclusion in a future issue of this journal. Content is final as presented, with the exception of pagination.

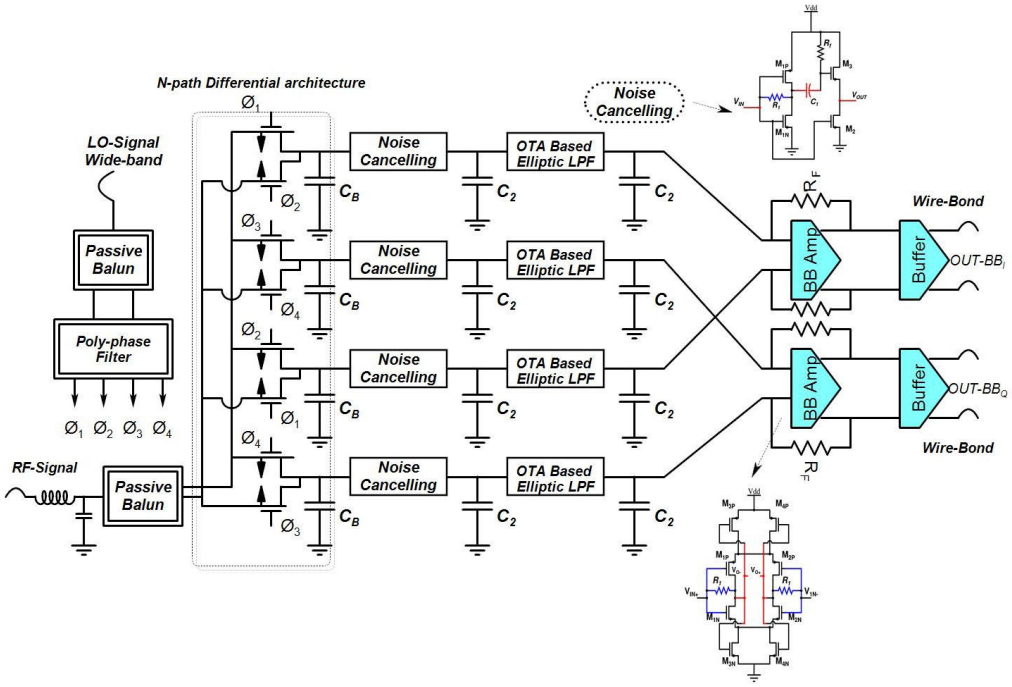

Fig. 2. The proposed receiver architecture.

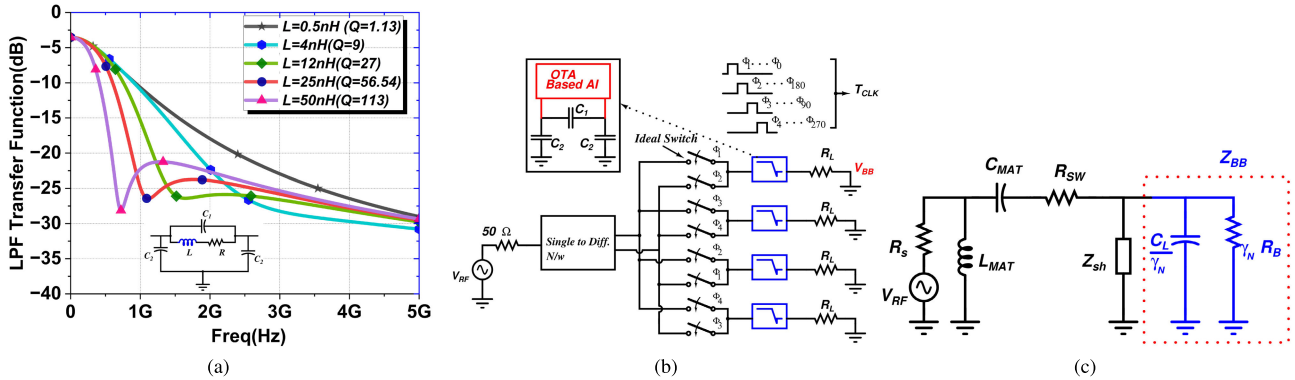

(a) (b) (c)

Fig. 3. (a) The frequency response of third-order elliptic filter for different values of L. (b) The proposed N-path with third-order AI-based low-pass elliptic filter. (c) The proposed N-path Differential architecture.

with the setup and compares them with the other proposed receiver architectures. Finally, in Section VI, the conclusion is summarized and presented. Further, the detailed description of each sub-block, such as differential N-path architecture, noise-cancelling amplifier, and the proposed self-biased-based active inductor are described in the following sub-sections.

II. N-Path Architecture With Proposed Active-Inductor Configuration

A. Proposed N-Path Differential Architecture

In our proposed receiver, a differential N-path architecture is implemented, as it provides potential advantages like cancelling the even order harmonics and switching the capacitor on odd harmonics. The rejection factor of an N-path differential architecture (α) is given by [18], along with its dependence on the output resistance. In order to achieve a high attenuation factor to suppress third-harmonic component and to achieve a high filter rejection, a high output resistance is required which results in reduced bandwidth and a high Q factor. In addition, differential architecture prevents power leakages from switching the clock to the RF I/P. The expression for the input impedance of the proposed N-path architecture is calculated from the LTI equivalent model, as shown in Fig. 3(c) and is given by:

$$Z_T = Z_S + Z_{in} = Z_s + R_{sw} + Z_{sh} \,||\, (\gamma_N Z_{BB}) \tag{1}$$

where, the value of γ is given by:

$$\gamma_N = \frac{sinc(\frac{\pi}{N})^2}{N} \tag{2}$$

$$Z_{sh} = (R_s + R_{sw}) K_{N0} \tag{3}$$

Z_{sh} is modelled as shunt impedance for calculating harmonic losses. where K_{N0} approximately is given by,

$$K_{N0} = \frac{sinc(\frac{\pi}{N})^2}{1 - sinc(\frac{\pi}{N})^2} \tag{4}$$

At high frequencies, the effect of input capacitance and harmonic losses becomes significant; mainly, the K_N denotes harmonic loss factor [18] which becomes more effective

Authorized licensed use limited to: DELHI TECHNICAL UNIV. Downloaded on November 18,2024 at 05:07:46 UTC from IEEE Xplore. Restrictions apply.

This article has been accepted for inclusion in a future issue of this journal. Content is final as presented, with the exception of pagination.

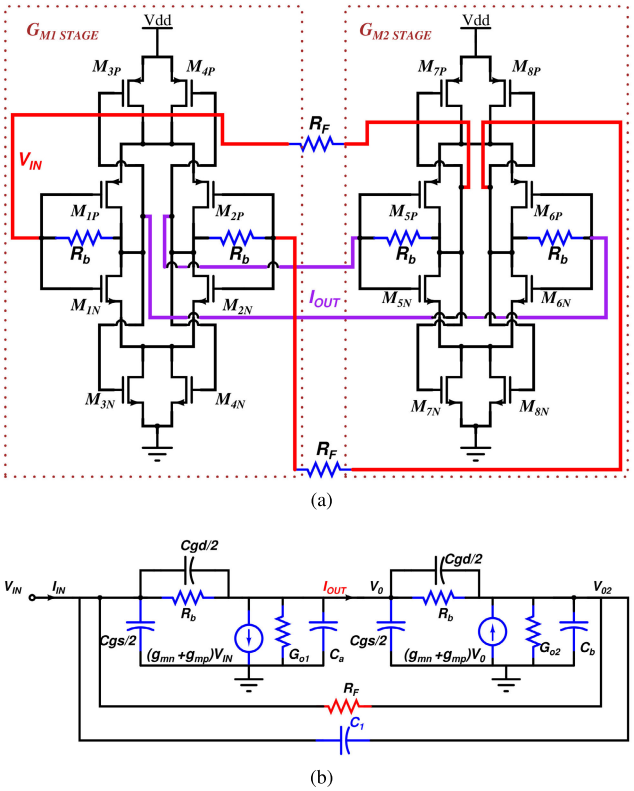

Fig. 4. (a) The proposed AI, and (b) A small-signal model of the proposed AI.

when higher harmonics are considered. The input capacitance of the N-path network shunts the in-band signal and influences the gain at lower frequencies. This shunting effect of the input capacitance can be reduced by resonating it with an impedance-matching network. Moreover Z_{sh}, which represents the images around higher harmonics of the LO, is optimized(with impedance matching network) by minimizing the imaginary component of the shunt impedance as described in [19]. Additionally, the RF input impedance can be resonated relative to the baseband impedance, which is varied within a range defined by R_{sw} and Z_{sh} with an impedance matching circuit. This provides the frequency range over which baseband impedance can be modelled with noise cancelling amplifier which absorbs maximum RF power resulting in comparatively reduced noise figure as explained in [18].

B. Proposed Active Inductor Configuration

The presented receiver architecture proposes a novel AI circuit implemented with a self-biased differential amplifier shown in Fig. 4(a), which is connected in a cross-coupled or feedback structure. The first half of the OTA or AI consists of two differential amplifiers in which one stage acts as a load for the other stage. The biasing for the transistor M_{1N} and M_{1P} is achieved from the output of the drain of M_{5N} and M_{5P} including the effect of R_b, which stabilizes the dc-biasing and turns on transistor M_{3P}, which drives a large amount of current to the other half of the circuit consisting of M_{2P} and M_{2N} which acts as a load to obtain the G_{M1} for the first stage. Similarly, the biasing for the transistor M_{5N} and M_{5P} is obtained from the output of the drains of M_{2P} and M_{2N}

TABLE I
THE TRANSISTOR SIZE OF ACTIVE-INDUCTOR

Transistors	Width
$M_{1N}, M_{2N}, M_{5N}, M_{6N}$	40 um
$M_{1P}, M_{2P}, M_{5P}, M_{6P}$	80 um
$M_{3N}, M_{4N}, M_{7N}, M_{8N}$	40 um
$M_{3P}, M_{4P}, M_{7P}, M_{8P}$	80 um

(including the effect of R_b), which turns on the transistor M_{7P} and driving a large amount of current to the other half of the circuit to obtain the G_{M2} for the second stage. The expression for the transconductance(G_m) of the proposed AI is derived by considering the first half of the small signal model of Fig. 4(b), and the equation of the (G_m) is given by:

$$G_m = [(gm_n + gm_p) + \frac{[G_B + sCgd/2 - (gm_n + gm_p)]}{[G_B + G_{eff} + s(Cgd/2 + C_1)]}] \tag{5}$$

where, $G_{eff} = 1/(rds_{1,n}||rds_{1,p}||rds||_{2,n}||rds_{2,p}||rds_{3,p})$

$G_B = 1/R_b$, *and* $C_1 = Cds_n + Cds_p$. The entire structure of the second half of AI forms the negative feedback for the first half of AI, providing stability. Adding resistance R_F provides the negative resistance necessary to control the Q of the inductor, and adjusting the bias, in conjunction with varying R_b, leads to distinct values for G_{M1} and G_{M2}. The added capacitance C_1 and C_2 (refer Fig. 3(b)) for the proposed active inductor shunt the signal at clock frequency and maintain low input impedance over the range of frequency preserving IIP_2 and IIP_3 with strong OOB interference [20]. On analyzing the small signal model (Fig. 4(b)), $Zin_{diff.}$ of the proposed AI is given by:

$$Zin_{diff.} = \frac{[Go_1 + sC_a][Go_2 + sC_b]}{s^3A + s^2B + sC + D} where, \tag{6}$$

$A = C_aC_bC_{gd}/2 + C_aC_bC_{gs}/2 + C_aC_bC_1$

$B = C_aC_b(G_B + G_F) + (C_{gd}/2)C_b(gm_n + gm_p) + C_1(C_aGo_2 + C_bGo_1)$

$C = G_BC_aGo_2 + G_BC_bGo_1 + G_BC_b(gm_n + gm_p) + Go_1Go_2C_{gs}/2 + G_F(Go_2C_a + Go_1C_b) + (gm_n + gm_p)^2C_1$

$D = Go_1Go_2(G_B + G_F) + (gm_p + gm_n)[Go_2G_B + \$gm_n + gm_p)G_F]$

where,$C_a = Cds_n + Cds_p + C_2$ and $Go_1 = 1/(rds_1 \parallel rds_2)$, $G_B = 1/R_b$ and $G_F = 1/R_F$ for the first half of the OTA. Similarly, $C_b = Cds_n + Cds_p + C_2$,$Go_2 = 1/(rds_1 \parallel rds_2)$ for the second half of the OTA. Table I represents the sizing of the proposed self-biased AI. The post-layout simulation of Zin_{diff} of the proposed (G_m-C) based low-pass filter is obtained by varying R_b, as shown in Fig. 5(a). The inductance L (an imaginary component of Zin_{diff}) and Q of the proposed active inductor are post-layout simulated by varying R_b as shown in Fig. 5(b) and Fig. 5(c). By analyzing, Fig. 5(a), Fig. 5(b) and Fig. 5(c) the maximum pass-band to stop-band rejection of 50 dB is achieved for inductance L of 8.5 nH, Q of 140 at $R_b = 3.6$ K ohms. After, (Zin_{diff}) is also analytically realized by keeping the same width (as stated in Table I) and the values of the small signal parameter(as stated in Table II)

Authorized licensed use limited to: DELHI TECHNICAL UNIV. Downloaded on November 18,2024 at 05:07:46 UTC from IEEE Xplore. Restrictions apply.

This article has been accepted for inclusion in a future issue of this journal. Content is final as presented, with the exception of pagination.

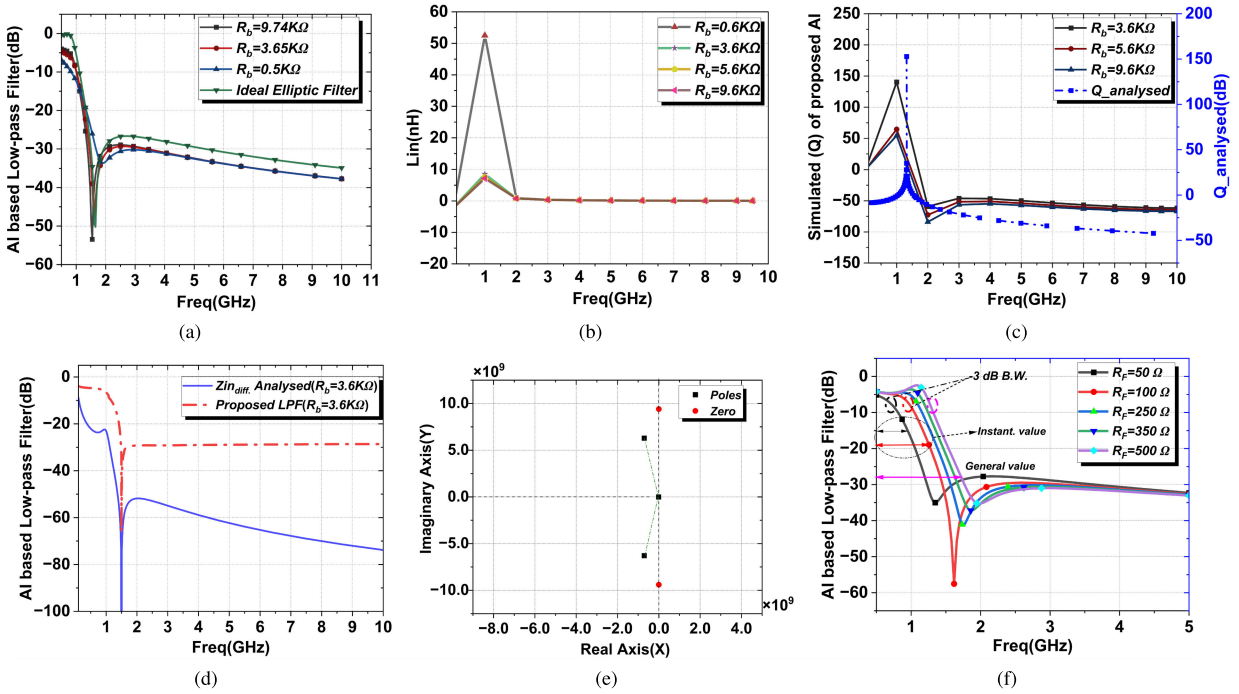

Fig. 5. (a) An Elliptic filter response for varying R_b. (b) An Inductance(L) for varying R_b. (c) The Q-variation over R_b and Q-analysed for R_b=3.6 Kohms. (d) Analytically realised Zin_{diff}. (e) The poles and zero plot for the proposed AI. (f) The variation in the bandwidth obtained for different values of feedback resistor R_F.

TABLE II

THE SMALL SIGNAL PARAMETERS OF THE PROPOSED ACTIVE-INDUCTOR

Parameters	Values
R_b	3.6K ohms
$gm_n + gm_p$	15.55 mS
R_F	100 ohms
$Go_1 = 1/(rds_1 \| rds_2)$	1/(3||3.25)K ohms
$C_a = Cds_n + Cds_p$	21.556fF
$Cgs/2$	36.49fF
$Go_2 = 1/(rds_1 \| rds_2)$	1/(4||2.52)K ohms
$C_b = Cds_n + Cds_p$	21.451fF
C_1, C_2	1.84pF,7.57pF

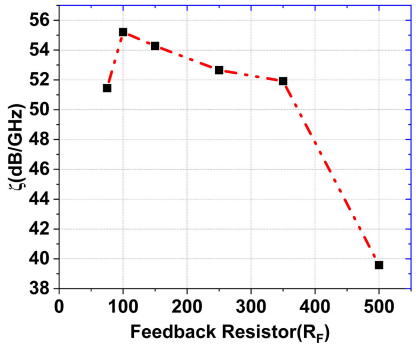

Fig. 6. The roll-off factor variation for different values of R_F.

as shown in Fig. 5(d). After, solving (6) and on replacing $s^3 = -w_p^2 s$ [21] the pole frequency (w_p), the zero frequency (w_z), and (Q_p) are given by (7)–(9), as shown at the bottom of the next page.

Fig. 5(e) represents the stability analysis of the proposed AI; since the resistive feedback R_F forms the negative feedback system so, the values of the capacitor are chosen such that the poles lie in the negative half of the plane and for stability, the damping factor of the proposed AI is optimized by the transconductance of the AI as explained in [19] to limit the oscillation.

In order to achieve high bandwidth for an active inductor feedback resistor R_F can be varied along with the MOS parameters resulting in different value of inductance. Moreover, it results in poor selectivity and low Q factor. Fig. 5(f) represents the variation in feedback resistor R_F resulting in different values of -3 dB bandwidth. Therefore, the R_F of 100 ohms is selected with a -3 dB instantaneous bandwidth of 0.75 GHz, as the purpose of the implemented architecture is to achieve both high rejection and a high Q-factor.

The other important characteristics is the transition band defined as a frequency range when a filter makes transition from pass-band to stop-band. The quantitative analysis of the proposed active inductor-based low-pass elliptic filter is done by calculating the transition band roll-off factor denoted by ζ (dB/GHz) given by [22] as shown in Fig. 6 for a different value of R_F (refer Fig. 5(f)):

$$\zeta_{roll-off} = \frac{\alpha_{-40dB} - \alpha_{-3dB}}{f_s - f_c} \tag{10}$$

where in (10), α_{-40dB} and α_{-3dB} represents the amplitude level at -40 dB and -3 dB of the active inductor based filter, and f_s and f_c denotes stop-band and -3 dB cut-off frequency of the filter.

III. PROPOSED RECEIVER ARCHITECTURE PARAMETERS AND ITS ANALYSIS

A. Baseband Impedance Z_{BB}

As previously mentioned, the proposed mixer first receiver architecture is implemented with an OTA-based elliptic

Authorized licensed use limited to: DELHI TECHNICAL UNIV. Downloaded on November 18,2024 at 05:07:46 UTC from IEEE Xplore. Restrictions apply.

This article has been accepted for inclusion in a future issue of this journal. Content is final as presented, with the exception of pagination.

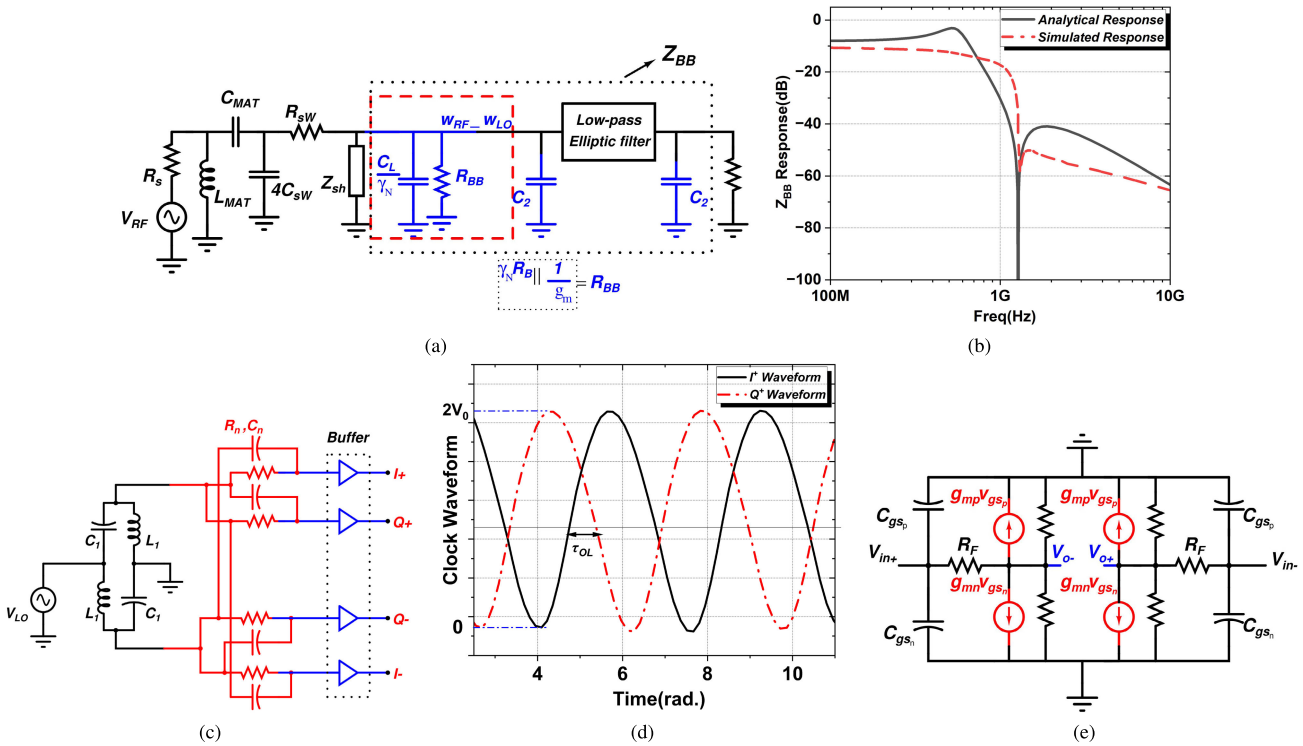

Fig. 7. (a) The LTI equivalent model for realising Z_{BB}(baseband response),and (b) The simulated Z_{BB} response and analytical analysed Z_{BB} response. (c) A Proposed LO signal generation on-chip. (d) A Quadrature sinusoidal LO waveform. (e) The small-signal model of the proposed amplifier.

filter. Initially, the obtained noise figure is high. Therefore, the noise-cancelling amplifier is placed between the N-path architecture and the AI-based elliptic filter to reduce the noise figure. The output of the N-path is given by Z_{BB}(baseband impedance), which consists of R_B and C_L generating a low-pass impedance network(considering the noise cancelling amplifier realized in the form of impedance) at the baseband and AI-based low pass elliptic filter as shown in Fig. 7(a). The transfer function of Z_{BB} is derived by integrating equations (6) and (11) (which correspond to the low-pass impedance network equation extracted from (refer to Fig. 3(c) previously discussed)). The expression for Z_{BB} is given by (12), which is derived, simulated, and analytically realized as shown in Fig. 7(b).

$$TF_1(s) = \frac{\alpha_1 * R_{BB}}{1 + w_{IF}(R_{BB}C_L)} \tag{11}$$

$$Z_{BB}(s) = Zin_{diff.} * TF_1(s) \tag{12}$$

where, α_1 is a gain of the noise-cancelling amplifier. It can be observed from Fig. 5(d) and Fig. 7(b) that it contributes a gain of around 10 dB.

B. LO Signal Generation for the Proposed Receiver

As mentioned in [13], it is difficult to have a 25% duty cycled non-overlapping LO waveform at mm-wave. However, it is possible to generate an overlapping LO waveform with a 50% duty cycle. In addition, it is difficult to generate LO waveform for high frequency using conventional digital circuitry due to limitation of (f_T) in 180-nm CMOS technology. Therefore, for the proposed receiver architecture, LO signal generation is obtained over a frequency range of (16)-(20) GHz using a passive balun circuit consisting of LC connected in a differential form. The values of (L = 0.6 nH) and (C = 0.125 pF) are chosen for single to differential conversion and providing wideband tunability. The balun circuit generates 0 and 180 phases, which are further fed to a single-stage poly-phase filter consisting of four path-balanced R_n and C_n, where the values of (R_n = 50 ohms and C_n = 200 fF) are obtained using a calculation to attain the quadrature phase for a given range of LO frequency with a 50% duty cycle. The simulation indicates that the passive-balun, along with single stage polyphase filter induces a 9 dB loss in a LO signal amplitude level. Therefore, the degraded signal is passed through a two-stage self-biased inverter combination which

$$w_p = \sqrt{\frac{Go_1Go_2(G_B + G_F) + (gm_n + gm_p)[Go_2G_B + (gm_n + gm_p)G_F]}{C_aC_b(G_B + G_F) + C_b(C_{gd}/2)(gm_n + gm_p) + C_1(C_aGo_2 + C_bGo_1)}} \tag{7}$$

$$w_z = \sqrt{\frac{Go_1Go_2}{C_aC_b}} \tag{8}$$

$$Q_p = \frac{\sqrt{[Go_1Go_2(G_B + G_F) + (gm_n + gm_p)(Go_2G_B + (gm_n + gm_p)G_F)]}B}{[C - w_p^2A]} \tag{9}$$

Authorized licensed use limited to: DELHI TECHNICAL UNIV. Downloaded on November 18,2024 at 05:07:46 UTC from IEEE Xplore. Restrictions apply.

This article has been accepted for inclusion in a future issue of this journal. Content is final as presented, with the exception of pagination.

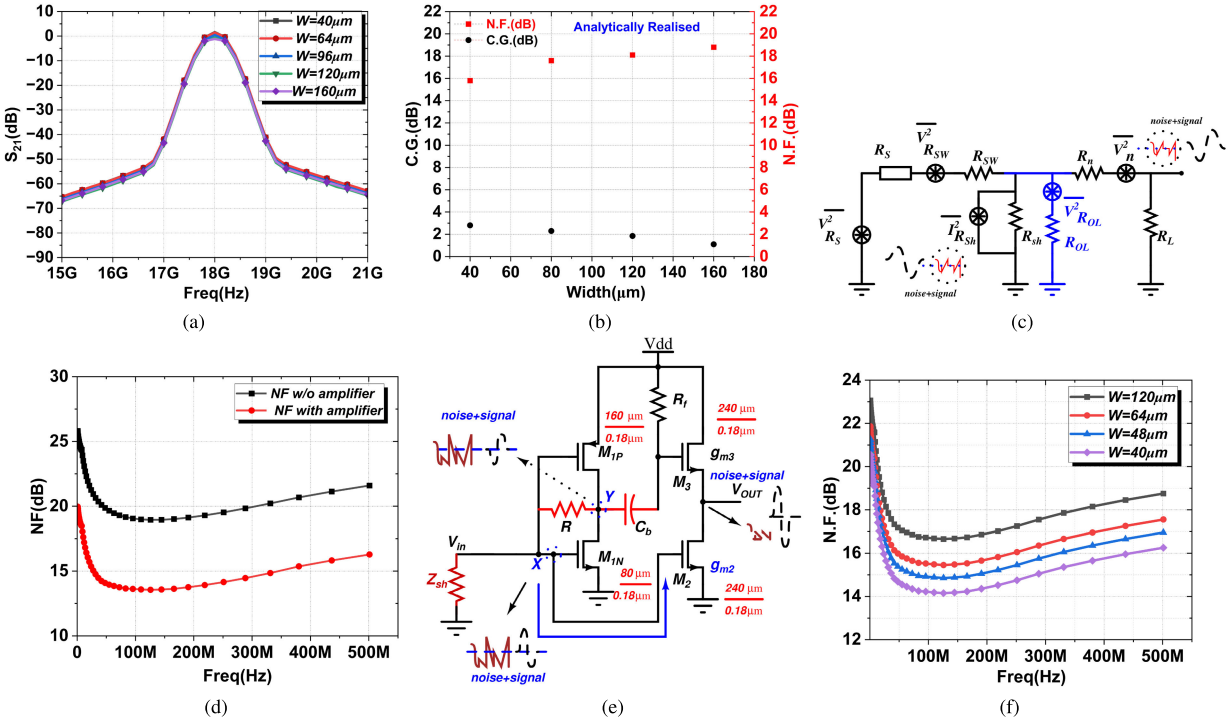

Fig. 8. (a) The simulated CG variation over switch resistance. (b) Analytical analysis over varying widths for switch resistance. (c) The small-signal noise model of the proposed receiver architecture. (d) The simulated NF with and without noise-cancelling amplifier. (e) The proposed noise-cancelling amplifier. (f) The simulated NF variation over switch resistance.

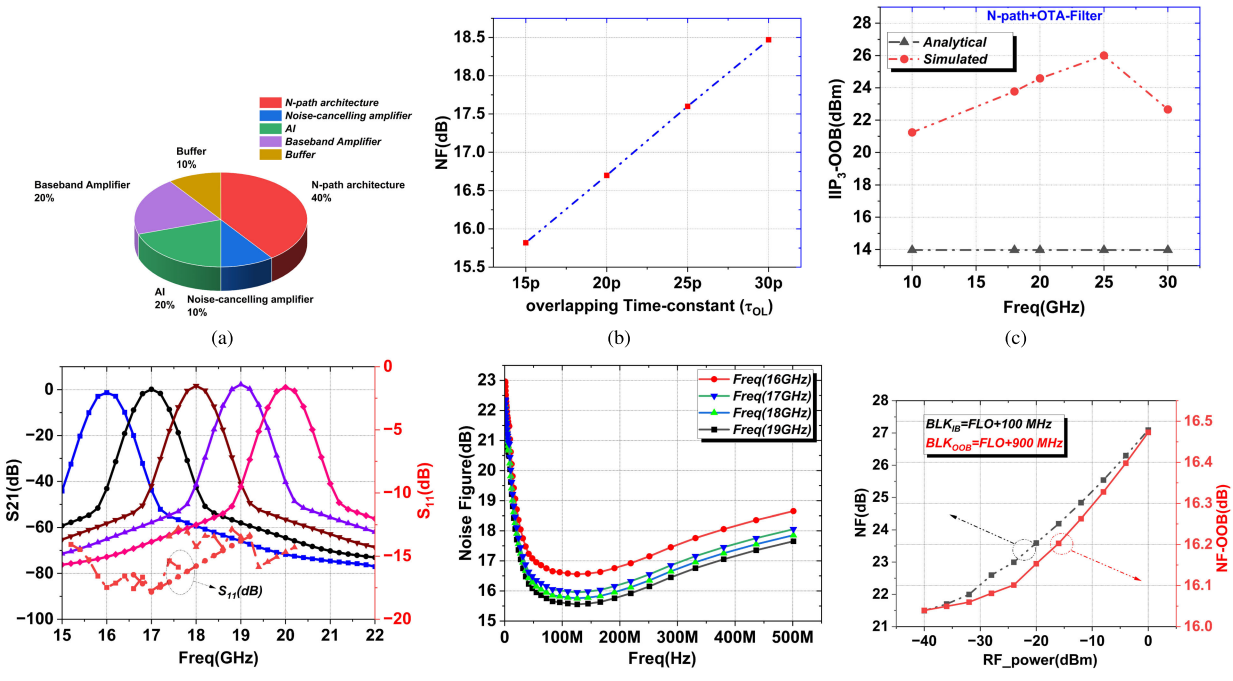

Fig. 9. (a) The contribution of noise figure for various blocks of the proposed receiver architecture. (b) A NF variation for different values of τ_{OL} (c) IIP_3 OOB Plot. (d) The post-layout S_{21}(dB) and S_{11}(dB). (e) The post-layout Noise figure(dB). (f) The post-layout NF with in-band and OOB blocker power level.

acts as a buffer to boost the signal level and drive a high capacitive load at the gate of the N-MOS switch. To maintain a consistent amplitude level with a 50% duty cycle, the clock signals are level-shifted via DC-biasing using resistors at the N-MOS switch. This ensures the NMOS switch retains its ON and OFF timing accurately, even in the presence of source and drain connections from subsequent stages. The LO signal generation circuit for the proposed receiver is shown in Fig. 7(c). Since, the LO signal generation is obtained with quadrature phase having 50% duty cycle. Therefore, τ_{OL}, which denotes overlapping time constant, is ensured to maintain $\tau_{OL} < T_{LO}/N$ (where T_{LO} denotes the length of the individual LO pulse) as shown in Fig. 7(d), ensuring active switching of the N-MOS.

Authorized licensed use limited to: DELHI TECHNICAL UNIV. Downloaded on November 18,2024 at 05:07:46 UTC from IEEE Xplore. Restrictions apply.

This article has been accepted for inclusion in a future issue of this journal. Content is final as presented, with the exception of pagination.

C. Conversion Gain

The conversion gain for the proposed receiver is achieved by including the effect of a self-biased baseband amplifier with a gain of 17 dB. The small signal model of the proposed baseband amplifier is shown in Fig. 7(e), and its equation for the gain is given by:

$$Av = 2[Go_1 + sC_1][\frac{1-(gm_n+gm_p)[G_F+sCgd/2]}{(Go_1+G_F)+s(C_1+C_{gd/2})}] \tag{13}$$

where, $G_{o1} = r_{dsn}\,||\,r_{dsp}$, $C_1 = Cds_n + Cds_p$, $G_F = 1/R_F$. The equation of the conversion gain of the receiver architecture is given by:

$$VBB_N = Acos[\phi + 2\pi n/N]sinc(\pi/N)\frac{Z_{BB} * Av}{Z_{BB} - N(Z_s + R_{sw})} \tag{14}$$

In the equation, the switch resistance(R_{sw}) of an N-path differential architecture is varied from 40 μm to 160 μm, resulting in different values of conversion gain for a frequency of 18 GHz as shown in Fig. 8(a). Similarly, the (14) is analytically realized for a frequency of 18 GHz by considering (N = 4) and ZBB = −9 dB (approx. considering the loss of N-path, active inductor and gain of noise-cancelling amplifier)(calculated from Fig. 7(b)) and varying switch resistance of the N-path. An approximated value of conversion gain is obtained by (neglecting the parasitic effects of the baseband amplifier) as shown in Fig. 8(b). Based on the analytical and simulated result N-MOS with a width of 40 μm is selected.

D. Noise Figure

The noise performance of the proposed receiver is estimated by considering the small signal model, as shown in Fig. 8(c). Initially, the attained noise figure is high due to proposed passive N-path differential architecture and active inductor based filter. Therefore, the noise-cancelling stage is embedded between the N-path and AI-based elliptic filter, as depicted in Fig. 8(d). Based on the simulation result it can be observed that the noise figure reduces by approx. 6 dB. For the present architecture, an improved noise figure is achieved by an effective LC matching network at the RF port which reduces the shunting effect due to harmonics (as explained in section-II). Secondly, the noise cancelling amplifier is realized as shown in Fig. 8(e).The noise cancellation is attained by optimizing the impedance mismatch due to N-path differential architecture(by reducing the impedance mismatch due to switch resistance(R_{sw})). The feedback resistor R of the noise-cancelling amplifier detects the output voltage and returns a current to the input, which constructively enhances the signal at nodes X and Y (refer Fig. 8(e)). Due to the opposite signs of the noise and signal, the noise is cancelled out while the signal is constructively amplified, as described in [23]. The noise figure equation for the proposed amplifier is given by (15), showing that increasing gm_2 by increasing(W/L ratio) can further reduce the noise figure. The input

TABLE III
THE NOISE FIGURE CALCULATION FOR THE RECEIVER

Parameters	Values
R_{sw}	68 ohms
R_S	75 ohms
R_{sh}	615 ohms
R_{OL}	153 ohms
K	$1.38 * (10)^{-23}$ J/K
V_n	$5.90nV/\sqrt{Hz}$

referred noise equation for the noise-canceling stage ($\overline{V^2_{n,Ac}}$), AI ($\overline{V^2_{n,AI}}$) and due to baseband amplifier($\overline{V^2_{n,A}}$) given by:

$$\overline{V^2_{n,Ac}} = 4KT\gamma[g_{m1,n}+g_{m1,p}]\frac{(R+Z_{sh})^2}{4} + 4KTR_f + \frac{4KT\gamma}{g_{m2}}[ro_2||1/g_{m3}]^2 \tag{15}$$

$$\overline{V^2_{n,AI}} = 2\left[\frac{4KT\gamma}{gm_{1,n}+gm_{1,p}} + 8KTR_b + 4KTR_F + \frac{4KT\gamma}{gm_{2,n}+gm_{2,p}}\right] \tag{16}$$

$$\overline{V^2_{n,A}} = 2[\frac{4KT\gamma}{g_{m1,n}+g_{m1,p}} + 4KTR_F] \tag{17}$$

The parameter γ refers to the (device parameters) of the MOS. The complete equation of the input referred noise voltage after combining above stage is given by $\overline{V^2_n}$:

$$\overline{V^2_n} = \overline{V^2_{n,Ac}} + \overline{V^2_{n,AI}} + \overline{V^2_{n,A}} \tag{18}$$

Thirdly, to account for the harmonic losses and additional current flowing through mixer switches due to overlapping phase shunt resistance (R_{OL}) is considered as shown in Fig. 8(c), and is given by(19). For analyzing the value (R_{OL}), τ_{OL}(overlapping phase time constant) of 15 psec is considered and its value for varying switch resistance is calculated from (refer [18]). The equation of the noise figure for our proposed receiver is given by:

$$NF = 1 + \frac{R_{sw}}{R_S} + \frac{R_{sh}}{R_S}(\frac{R_S+R_{sw}}{R_{sh}})^2 + \frac{R_{OL}}{R_S}(\frac{R_S+R_{sw}}{R_{OL}})^2 + \frac{sinc(\pi/N)^2}{N}\frac{\overline{(V^2_n)}}{4KTR_S}[\frac{R_S+R_{sw}}{R_{OL}} + \frac{R_S+R_{sw}+R_{sh}}{R_{sh}}]^2 \tag{19}$$

$$R_{OL} = \frac{NR_{sw}}{w_{LO}\tau_{OL}} \tag{20}$$

NF given by (19) is analyzed by varying the switch resistance (R_{sw}) of the N-path as shown in Fig. 8(b) for a frequency of 18 GHz and the simulated response of NF for varying (R_{sw}) is given by Fig. 8(f). Table III represents the values of the parameters for calculating noise figure analytically. The NF of around (15.8 dB) is obtained for a frequency of 18 GHz and a switch resistance is calculated for 40 μm width.

Since the obtained NF is high for the proposed mixer first receiver architecture. The major noise contribution is obtained due to N-path differential architecture, which contributes around 40% of the total noise figure as shown in Fig. 9(a).

Authorized licensed use limited to: DELHI TECHNICAL UNIV. Downloaded on November 18,2024 at 05:07:46 UTC from IEEE Xplore. Restrictions apply.

This article has been accepted for inclusion in a future issue of this journal. Content is final as presented, with the exception of pagination.

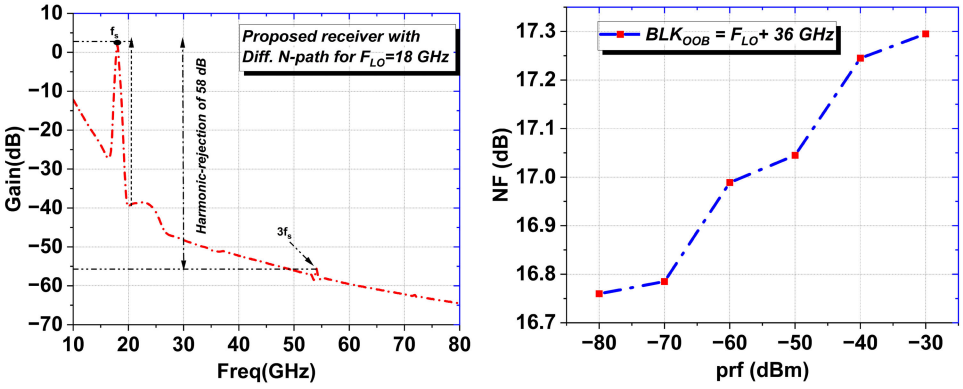

(a) (b)

Fig. 10. (a) The Harmonic rejection plot for $F_{LO} = 18$ GHz (b) The OOB-NF plot for $F_{LO} = 18$ GHz.

To minimize the NF, τ_{OL}(overlapping phase time constant) can be minimised by reducing the overlapping phase between the adjacent pulses as shown in Fig. 9(b). The figure demonstrates that decreasing τ_{OL} leads to achieving the lowest possible NF. Moreover, generating LO pulse with a non-overlapping phase or τ_{OL} poses significant challenges, especially at high frequency in 180-nm CMOS technology.

E. Linearity

Passive mixers are preferred at mm-wave frequency as they provide high linearity and are power efficient. In order to obtain high linearity it is ensured that the MOS of the proposed AI are suitably biased and are made to operate in saturation and linear mode. The equation for in-band linearity is given by:

$$\frac{1}{V_{IIP3}^2} = \frac{1}{V_{IIP3,mix}^2} + \frac{\alpha_1^2}{V_{IIP3,OTA}^2} + \frac{\alpha_1^2\beta_1^2}{V_{IIP3,BB}^2} \tag{21}$$

where the coefficient α_1 refers to gain due noise-cancelling amplifier and β_1 refers the loss due to AI.

The N-path designed along with an AI-based elliptic filter is analyzed using (21) for a width of 40 μm along with coefficients ρ and g_n (velocity saturation voltage parameter). Fig. 9(c) shows that out-of-band $IIP_3 > 20$ dBm can be achieved by varying R_{sw} and bias resulting in different value of g_n. The RF i/p capacitance shunts the in-band signal and enhances rejection by reducing the amplitude level of the OOB-harmonic signal. After analysis, the equation for OOB-IIP_3 is given by:

$$IIP_{3OOB} = \sqrt{\frac{4}{3}\frac{(1+\rho)^4}{\rho^3(2g_2^2 - g_3(1+\rho))}} \tag{22}$$

where, ρ denotes the ratio of Rs/Rsw which is tuned using (W/L) and g_n depends on device parasitics.

IV. CMOS Implementation

The proposed mm-wave Rx prototype, as shown in Fig. 2 is implemented using N-path differential architecture, followed by a self-biased active inductor-based low-pass elliptic filter. On the RF front end, an on-chip LC matching network is realized for impedance matching providing wideband matching over the frequency of 16-20 GHz. After the post-layout simulation S_{11} of around -15 dB is obtained, as shown in Fig. 9(d). Further, after the matching network passive balun network using L and C is realized, which converts the single-ended signal to a differential form directed to the source of the N-path switching network. On the LO front end, the same wideband passive balun network is followed by a poly-phase (RC network) responsible for generating 4 phases with a 50% duty cycle. The post–layout simulation indicates that the passive balun circuit along with a polyphase filter, exhibits a loss of -9 dB in an LO signal amplitude level for a frequency of 18 GHz. Therefore, to compensate for the loss, an LO power of 9 dBm is applied at the LO port. Based on the simulation, to improve the linearity and gain of the system after the filter stage, the baseband amplifier is designed to have optimum gain with high linearity. The post-layout results, as mentioned in Fig. 9(d), show the circuit attains a maximum gain(S_{21}) of around 3 dB with a noise figure of around 16 dB as represented in Fig. 9(e). Additionally, to calculate the blocker noise figure for the in-band signal is introduced at 18.1 GHz for an F_{LO} of 18 GHz. The variation of 5 to 8.5 dB in the attained noise figure for an IF of 100 MHz is observed over the variation of blocker power, as shown in Fig. 9(f). Similarly, for OOB noise figure signal at 18.9 GHz is introduced, and its variation with respect to RF power is shown in Fig. 9(f). In order to consider the harmonic effect for the proposed receiver architecture, which dominates at high frequency as the shunt impedance(Z_{sh}) depends upon the RF input capacitance, which not only shunts the in-band signal but also reduces the signal power that gets re-upconverted to harmonic images of the original signal. Additionally, the shunting effect of the input capacitance can be optimised by series inductance, as described in [19]. Moreover, as shown in Fig. 10(a), the first and third harmonics component are obtained for $f_{LO} = 18$ GHz, and it can be observed that for a proposed receiver architecture 58 dB of harmonic rejection for third-order is achieved. Similarly, the post-layout simulation for the OOB-blocker noise figure with respect to RF-power, considering $f_{LO} = 18$ GHz and blocker signal at 54 GHz, is made as shown in blue Fig. 10(b), and it can be observed that the noise figure increases by

Authorized licensed use limited to: DELHI TECHNICAL UNIV. Downloaded on November 18,2024 at 05:07:46 UTC from IEEE Xplore. Restrictions apply.

This article has been accepted for inclusion in a future issue of this journal. Content is final as presented, with the exception of pagination.

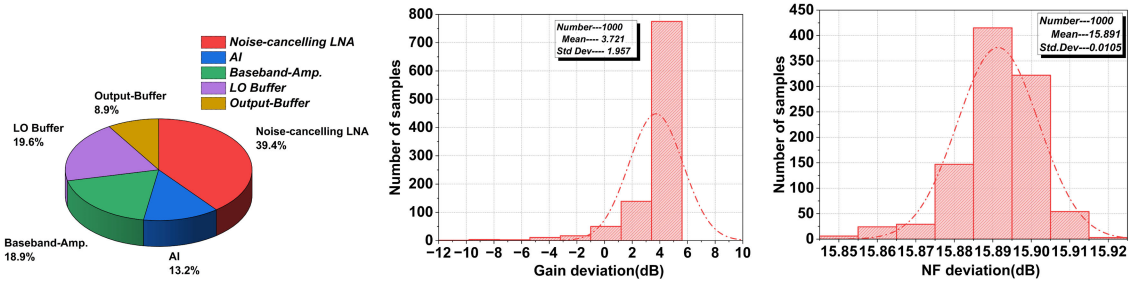

(a) (b) (c)

Fig. 11. (a) The distribution of power consumption for each block of the proposed receiver architecture. (b) Monte-Carlo simulation for CG of entire receiver. (c) Monte-Carlo simulation for the NF of entire receiver.

approx. 0.7 dB to 1 dB from the obtained NF of the proposed receiver architecture. Therefore, the performance parameter of the proposed receiver is not severely affected by the third-order blocker.

On realising the receiver with a passive elliptic filter the component values and inductance value obtained for the passive low-pass elliptic filter is very high with fixed finite pass-band to stop-band attenuation. Thus, the area occupied on-chip is large. Therefore, an AI-based low pass elliptic filter is realised, which provides the potential benefit of tunability of pass-band to stop-band attenuation with high value of Q, the required inductance can also be obtained by tuning and varying the transconductance of AI. The implemented AI is self-biased with negative feedback configuration. The parameters such as feedback resistance R_F and R_b with parasitics capacitance of the filter are varied and optimised to attain the required filter as proposed. The inductance of around 8.5 nH with Q of around 140 with high pass-band to stop-band attenuation of around 50 dB is obtained for R_b of 3.6K ohms and capacitance of 7.5 pF. After, the post layout and fabrication, any change in g_m causes a change in the frequency parameters, high attenuation and losses incurred in AI are a result of phase error due to variation in g_m and output conductance resulting in finite notch depth. Therefore, changing the parameters is critical at the passband corners to attain the Q-factor.

Since, the RF and LO ports of the circuit are driven by a passive network, the major power consumption into the circuit is obtained due to active elements in the circuitry such as the noise-cancelling stage which consumes around 39.4% of the total power consumption is shown in Fig. 11(a). The noise-cancelling stage draws a significant current to bias the second stage of the CS amplifier. Secondly, the LO driving circuit which consumes 19.6% of the total power consumption as it draws a large amount of current to drive the N-path differential architecture. The attained DC-power consumption for the circuitry is found to be 150 mW, excluding the external balun which can be reduced by designing noise-cancelling amplifier which consumes less current and obtaining differential to single ended conversion on-chip. Moreover, it increases the area on-chip. The dynamic power consumption for the proposed receiver architecture is calculated by using (23) for LO signal generation with 50% duty cycle overlapping phase is considered, which is defined as portion of each LO pulse spent overlapping with the adjacent pulse [19](refer Fig. 7(d)). The total power for driving the mixer and buffer when overlapping time constant τ_{OL} is considered is given by [19]:

$$P = \frac{V_{DD}^2}{R_S}\frac{w_{LO}}{2\pi w_g}\frac{N}{\rho}[1+\frac{1+w_p/w_n+w_g\tau_{min}}{(\tau_{OL}-\tau_{min})w_g}] \quad (23)$$

For, the implemented mixer first receiver architecture with f_{LO} of 18 GHz and considering τ_{OL} of 15 psec. The attained dynamic power consumption is approximately 0.26 mW.

In the proposed mixer first receiver architecture, Monte-Carlo simulation is performed to analyze two important parameters such as CG and NF across 1000 samples. The result indicates that the maximum CG is 3.71 dB with a minimal standard deviation of 1.957, which signifies that for most of the samples CG is almost constant as shown in Fig. 11(b). Similarly, NF of 15.8 dB is obtained for a minimum deviation of 0.0105, suggesting consistent NF across the majority of the samples, as shown in Fig. 11(c).

V. Measurement Results and Comparison

The fabricated chip micrograph is shown in Fig. 12(a), and it occupies $0.8mm^2$ active area on the chip. As shown in Fig. 12(b), the chip is mounted with the conductive epoxy on the PCB. The RF, LO and, BB O/P pads are wire-bonded and routed through the K-type SMA connector(HK-R-SR2-SA) for measurement. The PCB designing is performed on Kicad and the designed CPWG is modelled in Keysight ADS by creating a stack of PCB material (Rogers 4003-C). The differential baseband (I/Q) output conversion to single-ended conversion is achieved with an external balun(TCM2-43 X +). The equivalent bond wire circuit is considered in the analysis of the impedance matching of the circuit. The losses due to PCB parasitics, SMA, and balun are calibrated in the measurement results.

Fig. 12(c) represents the block diagram of the complete measurement setup, which consists of a Keysight PNA-X network analyzer(N5247A) acting as a signal generator with a frequency range of (10 MHz–67 GHz) for RF and the LO port. The down-converted quadrature signal(I and Q) are further processed to balun (TCM2-43-X+) for differential-to-single-ended conversion. The measurement for the conversion gain and linearity is further performed in the Keysight PNA-X network analyzer(N5247A), as shown in Fig. 12(d). The RF-to-BB conversion gain reduces by −4 dB on comparison with post layout simulation results. The measured S_{21}(dB) of −1.95 to −6.5 dB is achieved for a frequency of 16-20 GHz

Authorized licensed use limited to: DELHI TECHNICAL UNIV. Downloaded on November 18,2024 at 05:07:46 UTC from IEEE Xplore. Restrictions apply.

This article has been accepted for inclusion in a future issue of this journal. Content is final as presented, with the exception of pagination.

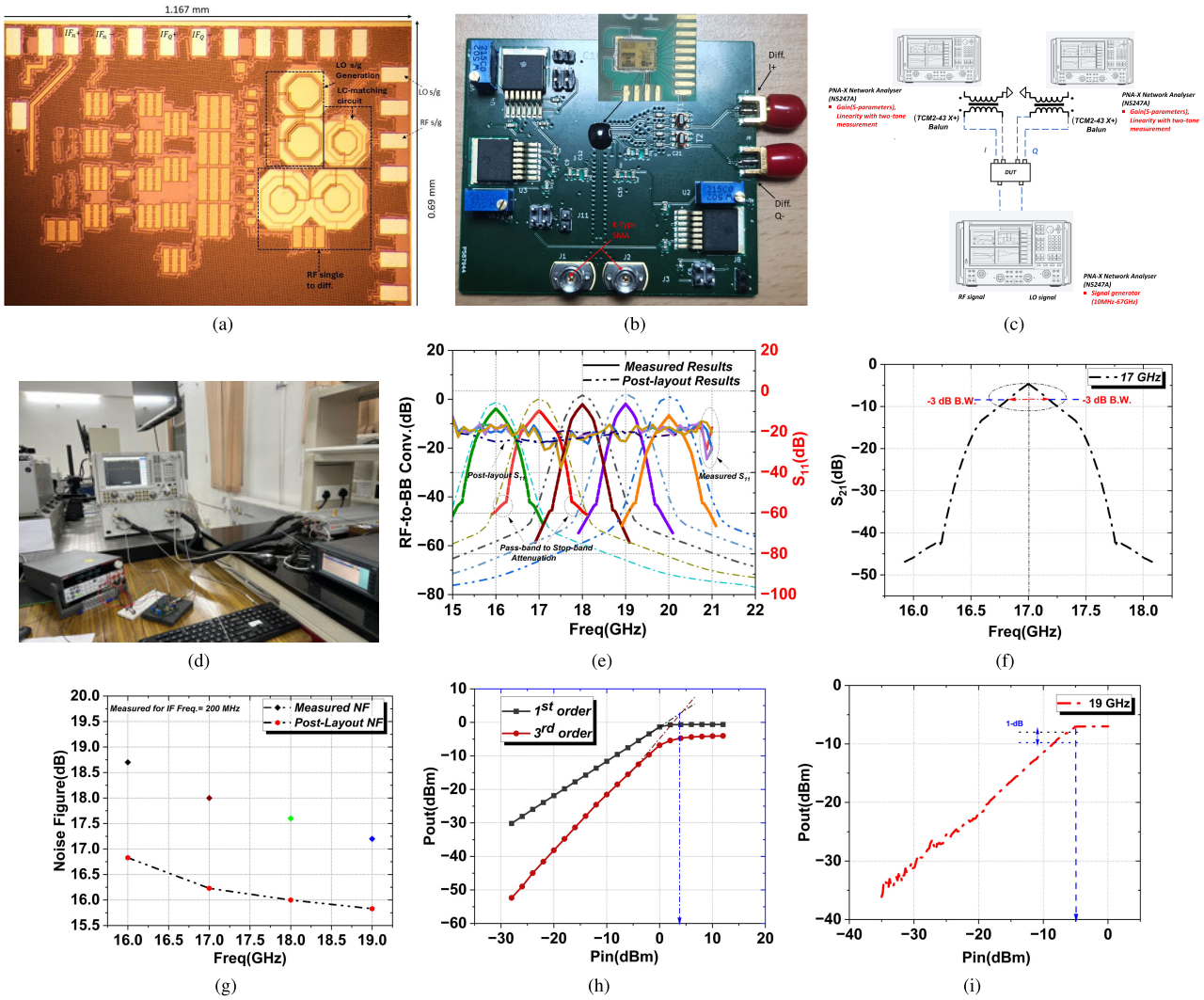

Fig. 12. (a) The die photograph of the fabricated chip. (b) A wire-bonded die PCB. (c) The block-diagram of measurement setup (d) A Measurement-setup. (e) The measured S_{21}(dB) and S_{11}(dB). (f) The measured -3-dB Bandwidth. (g) The measured Noise Figure(dB). (h) The measured IIP3 of the proposed receiver architecture(dB). (i) The measured P-1dB compression point at 19 GHz.

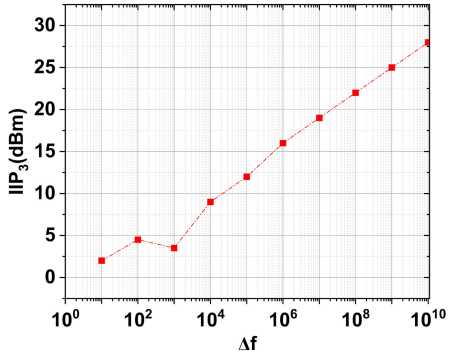

Fig. 13. The measured IIP3-OOB(dBm) at freq. 19 GHz.

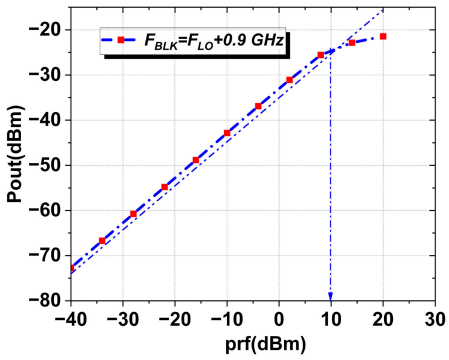

Fig. 14. The measured B_{1-dB} OOB(dBm) at freq. 19 GHz.

with an S_{11} of -15 dB as shown in the Fig. 12(e). Additionally, during measurement and on comparison with post layout -3-dB bandwidth reduces by 160 MHz for a centre frequency of 17 GHz as shown in the Fig. 12(f). The measured noise figure shows an increase of 1.6 dB, reaching 17.6 dB at an IF frequency of 200 MHz as shown in the Fig. 12(g) which is comparatively high due to post-fabrication process and losses due to parasitic and PCB. For F_{LO} centred around 17 GHz, the maximum passband to stopband attenuation of around -45 dB is attained. Note that the receiver is implemented with a Gm-C-based (OTA) low pass elliptic filter where the transconductance shows the dependency on parasitics and output conductance, which is varied, resulting in a finite notch depth. For in-band linearity, a measurement result for the receiver is calculated for $F_{LO} = 19.4$ GHz, RF tones close to 19.5 and 19.51 GHz are placed, and IIP_3 of 4 dBm is achieved, as shown in Fig. 12(h).

Authorized licensed use limited to: DELHI TECHNICAL UNIV. Downloaded on November 18,2024 at 05:07:46 UTC from IEEE Xplore. Restrictions apply.

This article has been accepted for inclusion in a future issue of this journal. Content is final as presented, with the exception of pagination.

TABLE IV
PERFORMANCE SUMMARY AND COMPARISON TO THE STATE-OF-THE-ART

References	[8] JSSC'2020	[11] RFIC'2016	[12] RFIC'2020	[13] JSSC'2021	[15] JSSC'2021	[17] MWCL'2023	[24] JSSC'2023	**This work**
Architecture	Passive-Mixer-First Rx with pos.FB cap.+notch	Passive-Mixer-First Rx with RC-load	Passive-Mixer-First Rx with RC -Load	Passive-Mixer-First Rx with RC-load	Mixer-First Rx with Passive-Elliptic Filter	Passive-Mixer First-Receiver	Passive-Mixer-First Receiver with NU-TAF	**Passive-Mixer First Receiver with Active-Filter**
Tuning Range(GHz)	2∼ 11	20∼ 30	9∼ 31	10∼ 35	21∼ 29	24∼ 29	31∼ 37	**16∼20**
Instantaneous SSB-BW$_{3dB}$(MHz)	40∼ 130	145	NA	NA	500	900	550∼ 660	**160**
DSB-NF(dB)	>10	8	12.5∼ 17.5	12.5∼ 19.2	12∼ 14.5	8.4∼ 9.6	12∼ 17	**17.2∼19**
RF-to-BB Gain(dB)	10∼ 24	20.6	>40	11.5∼ 14.5	3∼ 6	18.2∼ 19.6	4∼ 6	**-1.95 ∼(-6.5)**
ICP$_{-1dBm}$	NA	-13	NA	-2 ∼ 0	-6	-12.6∼ (−14.3)	-6	**-5**
B$_{-1dBm}$(dBm)	1.8	NA	4	NA	6.5	NA	-5.8 ∼ (3.8)	**10**
Stop-Band to Pass-band Rejection(dB)	NA	>15	NA	NA	49	NA	45	**47**
Transition Band BW(GHz)	NA	>0.4	NA	NA	1.2	NA	NA	**0.75**
Power(mW)	2100	41	162	19-37	22.8	12.6	67	**150**
Supply Voltage(V)	4/2.5	0.9/1.8	1	1.2	1.2	NA	0.9/1.1	**1.8**
Active Area(mm)^(2)	0.48	0.75	NA	NA	0.63	0.20	0.46	**0.55*** **0.8****
IIP3-OOB(dBm)	20	NA	21	NA	NA	NA	NA	**>10**
IIP3(dBm)	0∼ 10	-9.3	NA	10 ∼ 14.1	-	-2.2	-	**4∼6**
FOM$_{IB}$[dB/J]	144	151.56	NA	160.87	158.52	162.99	150.67	**149.13**
Technology	130 nm SiGe BiCMOS	45 nm SOI CMOS	65 nm CMOS	28 nm CMOS	65 nm CMOS	28 nm CMOS	28 nm CMOS	**180 nm CMOS**

***w/o LO gen. on-chip** ****with LO gen. on-chip**

The P1-dB of −5 dBm is achieved for an RF frequency of 19 GHz, as shown in Fig. 12(i). The limitation of compression is obtained due to the voltage swing limit and variation in dc-bias at the gates of the N-path. For the OOB-IIP_3 calculation frequency offset (Δf) of 10 MHz is added to the in-band frequency deviation, which increases due to high pass-band to stop-band attenuation, as represented in Fig. 13. Similarly, the calculation of B_{1-dB} is made by introducing two blocker signals at 19.9 GHz and 19.91 GHz(for fair comparison, the ratio of($\Delta f/B.W.$) is normalised). The B_{1-dB} of 10 dBm is achieved, as shown in Fig. 14. For comparative analysis, the author extends the analysis by considering FOM_{IB} of analog-filters for mixer first receiver architecture. For the proposed mixer first receiver architecture Figure of merit(FOM) analysis is performed. Similarly, for the other mixer first receiver architecture mentioned in Table IV. The FOM is given by [4]:

$$FOM_{IB} = IMFDR_3 + 10log[\frac{N*(BW)}{P_{diss.}}] \quad (24)$$

where, $IMFDR_3$ is given by [25]:

$$IMFDR_3 = \frac{2}{3}[P_{IIP3} + 174dBm - NF - 10log(BW)] \quad (25)$$

The performance summary and comparison of the proposed receiver architecture with the state-of-the-art integrated mm-wave mixer first receiver architectures is represented in Table IV. In comparison, the proposed mixer first receiver architecture attains a high-pass band to stop-band attenuation with high-quality factor along with optimal noise figure and superior OOB-IIP_3 with less on-chip area.

VI. CONCLUSION

This paper presents a novel method of implementing a mixer first receiver architecture that consists of differential N-path architecture realized by using a passive switching network. Additionally, mixer first receiver architecture implemented with a third-order elliptic filter realized with novel self-biased active inductor. The LO front end of the proposed receiver is implemented by a passive balun network followed by a polyphase filter, which provides wideband tunability to the circuit in 180 nm CMOS technology. In comparison, the receiver achieves high pass-band to stop-band attenuation of 47 dB with a single sideband of 160 MHz. In order to maintain a high dynamic range, the circuit attains an optimum noise figure of around (17.2-19 dB) with in-band linearity(IIP_3) of around 5 dBm and P_{-1dB} compression point of −5 dBm which is comparatively high when compared to other proposed receiver architectures. Further, the circuit achieves FOM_{IB} of 149.13 dB/J. The Q obtained for the proposed self-biased AI is around 140 for an inductance(L) of 8.5 nH, which is high compared to other passive circuits with wideband tunability. The active on-chip area occupied by the receiver is 0.55 mm^2 (without LO on-chip) which is comparatively less. In addition, the total area including LO on-chip(including passive balun) is 0.8 mm^2. Based on the achieved performance at 16–20 GHz,

Authorized licensed use limited to: DELHI TECHNICAL UNIV. Downloaded on November 18,2024 at 05:07:46 UTC from IEEE Xplore. Restrictions apply.

This article has been accepted for inclusion in a future issue of this journal. Content is final as presented, with the exception of pagination.

the proposed mixer first receiver architecture is one of the best solutions for commercially viable upcoming 5G advanced and 6G applications designed in 180-nm CMOS technology.

REFERENCES

[1] F. Alimenti et al., "K/Ka-band very high data-rate receivers: A viable solution for future Moon exploration missions," *Electronics*, vol. 8, no. 3, p. 349, Mar. 2019. [Online]. Available: https://api.semanticscholar.org/CorpusID:85512453

[2] F. A. Dicandia, N. J. G. Fonseca, M. Bacco, S. Mugnaini, and S. Genovesi, "Space-air-ground integrated 6G wireless communication networks: A review of antenna technologies and application scenarios," *Sensors*, vol. 22, no. 9, p. 3136, Apr. 2022. [Online]. Available: https://www.mdpi.com/1424-8220/22/9/3136

[3] J. Dean, S. Hari, A. Bhat, and B. A. Floyd, "A 4–31 GHz direct-conversion receiver employing frequency-translated feedback," in *Proc. IEEE 47th Eur. Solid State Circuits Conf. (ESSCIRC)*, Sep. 2021, pp. 187–190.

[4] G. Pini, D. Manstretta, and R. Castello, "Analysis and design of a 260-MHz RF bandwidth +22-dBm OOB-IIP3 mixer-first receiver with third-order current-mode filtering TIA," *IEEE J. Solid-State Circuits*, vol. 55, no. 7, pp. 1819–1829, Jul. 2020.

[5] Y.-C. Lien, E. A. M. Klumperink, B. Tenbroek, J. Strange, and B. Nauta, "Enhanced-selectivity high-linearity low-noise mixer-first receiver with complex pole pair due to capacitive positive feedback," *IEEE J. Solid-State Circuits*, vol. 53, no. 5, pp. 1348–1360, May 2018.

[6] Y. Lien, E. Klumperink, B. Tenbroek, J. Strange, and B. Nauta, "A high-linearity CMOS receiver achieving +44 dbm IIP3 and +13 dBm B1dB for SAW-less LTE radio," in *IEEE Int. Solid-State Circuits Conf. (ISSCC) Dig. Tech. Papers*, Feb. 2017, pp. 412–413.

[7] E. C. Szoka and A. Molnar, "Circuit techniques for enhanced channel selectivity in passive mixer-first receivers," in *Proc. IEEE Radio Freq. Integr. Circuits Symp. (RFIC)*, Jun. 2018, pp. 292–295.

[8] Y.-C. Lien, E. A. M. Klumperink, B. Tenbroek, J. Strange, and B. Nauta, "High-linearity bottom-plate mixing technique with switch sharing for N-path filters/mixers," *IEEE J. Solid-State Circuits*, vol. 54, no. 2, pp. 323–335, Feb. 2019.

[9] A. Kumari and D. Bhatt, "A 0.5–2.5 GHz mixer first receiver with 200 MHz RF bandwidth and +18.5 dBm OB-IIP3 in 180 nm CMOS for 5G NR band," *IEEE Trans. Circuits Syst. I, Reg. Papers*, vol. 71, no. 6, pp. 2576–2589, Jun. 2024.

[10] J. Harrison and N. Weste, "A 500 MHz CMOS anti-alias filter using feed-forward op-amps with local common-mode feedback," in *IEEE Int. Solid-State Circuits Conf. (ISSCC) Dig. Tech. Papers*, vol. 1, Feb. 2003, pp. 132–483.

[11] C. Wilson and B. Floyd, "20–30 GHz mixer-first receiver in 45-nm SOI CMOS," in *Proc. IEEE Radio Freq. Integr. Circuits Symp. (RFIC)*, May 2016, pp. 344–347.

[12] Z. G. Boynton and A. Molnar, "RTu1B-3 A 9–31GHz 65 nm CMOS down-converter with >4 dBm OOB B1dB," in *Proc. IEEE Radio Freq. Integr. Circuits Symp. (RFIC)*, Aug. 2020, pp. 279–282.

[13] S. Krishnamurthy, L. Iotti, and A. M. Niknejad, "Design of high-linearity mixer-first receivers for mm-wave digital MIMO arrays," *IEEE J. Solid-State Circuits*, vol. 56, no. 11, pp. 3375–3387, Nov. 2021.

[14] A. Moroni and D. Manstretta, "A broadband millimeter-wave passive CMOS down-converter," in *Proc. IEEE Radio Freq. Integr. Circuits Symp.*, Jun. 2012, pp. 507–510.

[15] P. Song and H. Hashemi, "Mm-wave mixer-first receiver with selective passive wideband low-pass filtering," *IEEE J. Solid-State Circuits*, vol. 56, no. 5, pp. 1454–1463, May 2021.

[16] M.-Y. Huang, T. Chi, S. Li, T.-Y. Huang, and H. Wang, "A 24.5–43.5-GHz ultra-compact CMOS receiver front end with calibration-free instantaneous full-band image rejection for multiband 5G massive MIMO," *IEEE J. Solid-State Circuits*, vol. 55, no. 5, pp. 1177–1186, May 2020.

[17] J. Yoo and S. Hong, "A millimeter-wave mixer-first receiver with LO waveform shaping using varactors," *IEEE Microw. Wireless Technol. Lett.*, vol. 33, no. 9, pp. 1353–1356, Sep. 2023.

[18] A. Molnar and C. Andrews, "Impedance, filtering and noise in N-phase passive CMOS mixers," in *Proc. IEEE Custom Integr. Circuits Conf.*, Sep. 2012, pp. 1–8.

[19] D. Yang, C. Andrews, and A. Molnar, "Optimized design of N-phase passive mixer-first receivers in wideband operation," *IEEE Trans. Circuits Syst. I, Reg. Papers*, vol. 62, no. 11, pp. 2759–2770, Nov. 2015.

[20] F. Yuan, "CMOS active inductors," in *CMOS Active Inductors and Transformers*. New York, NY, USA: Springer, 2008, doi: 10.1007/978-0-387-76479-5. [Online]. Available: https://api.semanticscholar.org/CorpusID

[21] H. Xiao and R. Schaumann, "Very-high-frequency lowpass filter based on a CMOS active inductor," in *Proc. IEEE Int. Symp. Circuits Syst.*, vol. 2, May 2002, p. 2.

[22] S. Soroush and E. Abdi, "A lowpass filter implementation with an ultra sharp transition band and extended stopband bandwidth based on even-mode and odd-mode analysis of lumped circuits," *AEU-Int. J. Electron. Commun.*, vol. 149, May 2022, Art. no. 154192. https://www.sciencedirect.com/science/article/pii/S1434841122000899

[23] F. Bruccoleri, E. A. M. Klumperink, and B. Nauta, "Wide-band CMOS low-noise amplifier exploiting thermal noise canceling," *IEEE J. Solid-State Circuits*, vol. 39, no. 2, pp. 275–282, Feb. 2004.

[24] C. Yang, S. Su, and M. S. Chen, "Millimeter-wave receiver with non-uniform time-approximation filter," *IEEE J. Solid-State Circuits*, vol. 58, no. 5, pp. 1201–1211, May 2023.

[25] B. Razavi, *Fundamentals of Microelectronics*. Hoboken, NJ, USA: Wiley, 2013. [Online]. Available: https://books.google.co.in/books?id=zpMYAgAAQBAJ

Gaurav Srivastava (Graduate Student Member, IEEE) received the B.Tech. degree in electronics and communication engineering from Uttar Pradesh Technical University in 2015 and the M.Tech. degree in microwave and optical communication from Delhi Technological University in 2019. He is currently pursuing the Ph.D. degree in electronics and communication engineering with Indian Institute of Technology (IIT) Roorkee, India. He has published international conferences and journals on the design of low noise amplifiers (LNA) for industrial, scientific, and medical (ISM) band applications. His research interests include analog and RF circuit design for millimeter-wave (mm-wave) applications.

Darshak Bhatt (Member, IEEE) received the B.Eng. degree in electronics from Sardar Patel University, Gujarat, India, in 2004, the M.Eng. degree in communication from the Birla Institute of Technology and Science, Rajasthan, India, in 2011, and the Ph.D. degree from IIT Bombay, IITB-Monash Research Academy, India, in 2018.

He was a Research Intern with Indian Space Research Organization Satellite Centre, Bengaluru, India. In 2017, he was a Post-Doctoral Scholar at FH-Kaernten, Villach, Austria. He is currently an Assistant Professor with the Department of Electronics and Communication Engineering, IIT Roorkee, India. His current research interests include monolithic microwave integrated circuits and analog circuit design for wireless applications.

Dr. Bhatt was a Prime Minister's Fellow for the Ph.D. degree research. He was a recipient of the Gold Medal for Outstanding Academic Performance from Sardar Patel University. He actively contributes to the academic community by reviewing for IEEE journals, such as IEEE TRANSACTIONS ON CIRCUITS AND SYSTEMS—I: REGULAR PAPERS IEEE TRANSACTIONS ON CIRCUITS AND SYSTEMS—II: EXPRESS BRIEFS, IEEE TRANSACTIONS ON COMPONENTS, PACKAGING AND MANUFACTURING TECHNOLOGY, and IEEE TRANSACTIONS ON MICROWAVE THEORY AND TECHNIQUES. In addition, he serves on program committees and is a reviewer for various IEEE conferences, including VLSID, VDAT, ATS, and MAPCON.

Authorized licensed use limited to: DELHI TECHNICAL UNIV. Downloaded on November 18,2024 at 05:07:46 UTC from IEEE Xplore. Restrictions apply.

This article has been accepted for inclusion in a future issue of this journal. Content is final as presented, with the exception of pagination.

A Novel Method for Monitoring Stator Interturn Insulation Degradation of Inverter-Fed Motors Based on Impedance Spectrum Division

Feng Niu, *Member, IEEE*, Pengju Zhang, Feng Zhou, *Member, IEEE*, Shaopo Huang, Zijun Xu, Lu Zhang, and Anmol Aggarwal, *Member, IEEE*

***Abstract*—The switching transient response method has become popular in recent years for monitoring of stator insulation in inverter-fed motors (IFMs). It can detect early insulation degradation and thus prevent serious insulation failures. However, for interturn insulation monitoring, the relationship between the transient response in phase current and interturn insulation degradation is not clear. In this article, a novel method for monitoring stator interturn insulation in IFMs based on switching transient current response is proposed. A lumped-parameter model of stator winding is established, and the division of winding impedance spectrum for insulation condition monitoring based on this model is analyzed. Then, the effect of interturn insulation degradation on the different regions of winding impedance spectrum is verified, and an interturn insulation monitoring indicator (IIMI) extracted from the transient current response based on the impedance spectrum division is proposed. The determination of qualified PWM excitation is also analyzed. Finally, the proposed method was verified using a 3 kW PMSM under field oriented control, and the experimental results show that the proposed IIMI is highly sensitive to the interturn insulation degradation.**

***Index Terms*—Condition monitoring, interturn insulation, inverter-fed motors (IFMs), switching transient current.**

Received 9 June 2024; revised 23 August 2024 and 22 October 2024; accepted 2 November 2024. This work was supported in part by the National Natural Science Foundation of China under Grant 52322702, Grant 52377168, Grant 52077054, Grant 52477035, and Grant 52305048, in part by the Natural Science Foundation of Tianjin Municipality under Grant 23JCZDJC00350, and in part by the Beijing Municipal Education Commission under Grant KM202310017005. *(Corresponding author: Zijun Xu.)*

Feng Niu and Pengju Zhang are with the State Key Laboratory of Reliability and Intelligence of Electrical Equipment, Hebei University of Technology, Tianjin 300401, China (e-mail: niufeng@hebut.edu.cn; 202121401092@stu.hebut.edu.cn).

Feng Zhou is with the College of Electronic Information and Electrical Engineering, Changsha University, Changsha 410022, China (e-mail: zhoufeng@ccsu.edu.cn).

Shaopo Huang and Lu Zhang are with the College of Information Engineering, Beijing Institute of Petrochemical Technology, Beijing 102627, China (e-mail: huangshaopo@bipt.edu.cn; zhangl@bipt.edu.cn).

Zijun Xu is with the Electrical and Information Engineering, Tianjin University, Tianjin 300072, China (e-mail: x_zealjumping@tju.edu.cn).

Anmol Aggarwal is with General Motors Inc., Detroit, MI 48232 USA (e-mail: aggarw43@msu.edu).

Digital Object Identifier 10.1109/TIE.2024.3497310

I. Introduction

INVERTER-FED motors (IFMs) have been widely used in wind power generation, rail transportation, ship electric propulsion, and other important fields, its reliability is crucial to the safe operation of the whole system [1], [2]. The insulation system of motors is continuously subjected to various aging stresses and gradually aging during the operation of the motor, especially with the popularity of wide-bandgap devices in inverters, the higher *dv/dt* and switching frequency greatly accelerate this process. Stator insulation faults account for 30%–40% of low-voltage motor failures and 60%–70% of high-voltage motor failures [3], [4]. A localized interturn short-circuit fault can generate a large circulating short-circuit current, producing significant heat that can damage the insulation between adjacent windings. This rapid deterioration can quickly escalate to a phase-to-phase (PP) or ground-wall (GW) insulation failure [1]. Abrupt motor failure will bring a lot of downtime and economic losses [5]. Therefore, it is necessary to study reliable methods for monitoring motor insulation conditions for early warning of potential failures and preventive maintenance.

Recently, several offline techniques using the inverter have been reported to detect the insulation conditions based on indicators such as partial discharge (PD), insulation capacitance (IC), dissipation factor (DF), and insulation resistance (IR) [6], [7], [8], [9], [10]. Methods utilizing PD detection are particularly prominent [6], [7], [8], where inverters generate high-frequency pulse voltages to excite PD activity, enabling early detection and classification of insulation defects such as interturn, PP, and GW insulation faults. In [7], the PD detection was further optimized by using an Archimedes spiral antenna to enhance signal sensitivity in high-frequency environments. The inverter-based high *dv/dt* pulse was used to detect early PD and monitor PD inception voltage [8]. The IC and DF were analyzed to assess the insulation degradation trends in high-resistance grounding systems [9], and the leakage current induced by the inverter-generated common-mode (CM) voltage was measured to evaluate the dielectric loss and capacitive behavior under different aging conditions. Through the oscillation frequency analysis of the switching transient voltage response generated by the inverter, the IC and dielectric properties were evaluated [10]. Additionally, IR was evaluated using the offline measured CM

0278-0046 © 2024 IEEE. Personal use is permitted, but republication/redistribution requires IEEE permission.
See https://www.ieee.org/publications/rights/index.html for more information.

Authorized licensed use limited to: DELHI TECHNICAL UNIV. Downloaded on December 02,2024 at 05:09:41 UTC from IEEE Xplore. Restrictions apply.

This article has been accepted for inclusion in a future issue of this journal. Content is final as presented, with the exception of pagination.

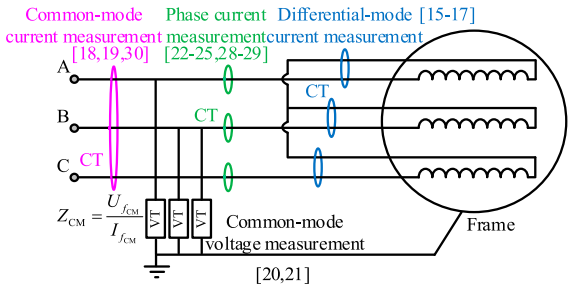

Fig. 1. Electrical signal measurement for insulation monitoring.

voltage to detect GW insulation deterioration [9], highlighting the effectiveness of inverter-based testing for comprehensive ground fault diagnosis. Overall, these methods provide a robust framework for inverter-based offline early insulation degradation testing. However, limitations such as sensitivity to pulse characteristics, precise tuning requirements, and strict electromagnetic environment for PD detection still exist.

Many stator insulation online monitoring techniques have also been proposed. PD online measurement, based on the principle of offline PD test, is commonly used [11]. However, its biggest challenge is the interference of various noises in the motor operating environment [12]. In recent years, the broadband impedance and the switching transient monitoring methods are popular, both of which are based on the principle that insulation degradation changes the impedance of the motor windings. Fig. 1 shows the principle of electrical signal measurement used for insulation monitoring.

For the broadband impedance monitoring, several online methods for stator insulation monitoring have been proposed [13], [14], [15], [16], [17], [18], [19], [20], [21]. Literature [13], [14] proposed online measurement methods of phase-to-neutral and phase-to-ground impedance spectra, based on high-frequency signal injection, to detect changes in the resonant frequency of the windings due to insulation degradation, but both required additional signal injection equipment. In [15], the IC and DF were calculated by measuring the differential-mode (DM) leakage current in each phase to evaluate the overall insulation status of GW and PP of mains-fed motors. Further study [16] can monitor the PP and GW insulation separately and measure the IC of different parts based on the multifrequency information of DM leakage current of the IFMs. However, the above methods can only be applied to six-lead motors. In [17], CM leakage current used to calculate IC/DF was measured to monitor the GW insulation of a three-lead motors. CM voltage and current measurement-based technique had been further proposed, and CM impedance spectrum can be calculated online to evaluate the GW insulation [18] or distinguish between GW insulation and interturn insulation [19]. In [20], a numerical modeling method for the early prediction of high-frequency impedance response in permanent magnet synchronous motor (PMSM) was proposed, but no practical online monitoring method for interturn insulation is mentioned. A broadband stator winding insulation model was established [21], and by analyzing the relationship between interturn insulation and impedance spectrum, the high-frequency parallel capacitance can be estimated to detect interturn aging. The CM phase-to-ground voltage needed to be measured.

For the switching transient monitoring, it is proposed [22], [23], [24], [25], [26], [27], [28], [29] that the time-frequency characteristics of transient current response are used to detect insulation degradation of motor windings. In [22], a noninvasive quasi-online monitoring method for interturn insulation based on the switching transient response of motor phase current was first presented. The transient phase current response was excited by the inverter step voltage when the motor is stationary or before start-up, and the root mean square deviation (RMSD) of transient phase current was used to assess stator winding insulation. The effects of sampling rate [23] and pulse width modulation (PWM) voltage rise time [24] on RMSD were further discussed. According to [25], the different absorbed switching transient current components propagate in different paths within the winding, which is known as multimode propagation. The low-frequency CM component of transient current leaks through the winding to ground and is sensitive to interturn insulation. The high-frequency CM component flows through the parasitic capacitance at the terminal to ground and is sensitive to the line-end coil insulation. According to the multimode propagation theory, the low-frequency CM component was extracted from the phase current oscillations for interturn insulation condition monitoring [26]. Similarly, the high-frequency CM component 7 was used to monitor the GW insulation [27]. In [28], a mathematical model of leakage current was developed, and the time-domain characteristics of the switching transient current were utilized to identify the severity, position, and phase of GW insulation degradation. In [29], a method based on the Fourier transform with a Mel filter (FrFT-Mel) was proposed to detect the turn insulation condition by analyzing the sensitivity of high-frequency switching oscillation currents to turn insulation variations in the fractional domain.

In general, more studies have been conducted on monitoring the GW insulation than on the interturn insulation. Monitoring incipient degradation of interturn insulation is difficult due to its weak degradation features and is recognized as one of the main research gaps for both low- and medium-voltage motors [30]. Although the change of amplitude in the frequency band centered on the parallel resonance point of the transient current transient response was used to detect the interturn insulation condition in the existing method, the different trends in different ranges in the spectra of winding impedance and switching transient current response that is sensitive to the interturn insulation degradation are not analytically specified in detail. On the other hand, the switching transient response is directly affected by the patterns of inverter PWM voltage excitation, which may dynamically change with the operating conditions of IFMs.

This article proposes a novel interturn insulation monitoring method based on impedance spectrum division. First, using a high-frequency model of motor stator windings, the different impedance spectrum regions sensitive to interturn insulation degradation are theoretically determined, which establishes an analytical connection between interturn insulation degradation and the corresponding sensitive regions in the spectra of winding impedance and switching transient current response. Second,

Authorized licensed use limited to: DELHI TECHNICAL UNIV. Downloaded on December 02,2024 at 05:09:41 UTC from IEEE Xplore. Restrictions apply.

This article has been accepted for inclusion in a future issue of this journal. Content is final as presented, with the exception of pagination.

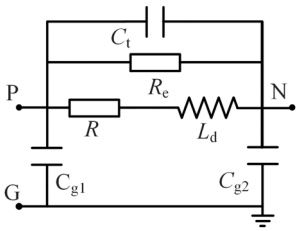

Fig. 2. High-frequency model of stator single-phase winding.

the qualified PWM voltage excitation during normal operation of IFMs is determined, which largely improves the reliability of the monitoring results. The proposed method does not require additional signal injection equipment, is noninvasive, and is easy to be applied industrially. An experimental setup consisting of a 3 kW PMSM controlled by field oriented control (FOC) is established to verify the proposed method.

II. Analysis and Division of Stator Winding Impedance Spectrum for Monitoring Interturn Insulation

Degradation of the stator interturn insulation affects the winding impedance, and thus the switching transient response of motor current [22]. The winding impedance spectrum is obtained first through an analytical stator winding model. Then, the effect of insulation degradation on the impedance spectrum and the impedance spectrum division for degradation monitoring are investigated.

A. High-Frequency Stator Winding Model

Switching transient characteristic studies mainly focuses on the frequency range of several hundred kHz to several MHz, so the modeling of the stator winding considers only its high-frequency characteristics [26], [27], [28]. In high-frequency range, the iron core acts as a winding flux barrier, when the coupling between the stator and rotor can be neglected [31]. A single-phase high-frequency winding model with lumped parameters of a PMSM is shown in Fig. 2 [32], where C_{g1} and C_{g2} are the equivalent capacitances between the coil at the winding terminal and stator core and between the neutral and stator core, respectively; the sum of C_{g1} and C_{g2} is the equivalent capacitance between the stator winding and the stator core at low frequencies, which is mainly determined by the winding GW insulating capacitance; C_t denotes the capacitive coupling effect within the stator winding; R_e is the loss-equivalent resistance; R is the winding resistance; and L_d is the winding inductance. R can be neglected because it is much smaller than the winding inductance (ωL_d) in high-frequency bands.

The parameters in the above model can be obtained through the CM and DM impedance measurements [33], [34], as shown in Fig. 3. The CM impedance is measured between the three-phase terminals shorted together and the stator frame, while the DM impedance is measured between any two shorted phases and the other phase. Both are extracted from an impedance analyzer IM3570, which allows a frequency range between 1 and 4 MHz.

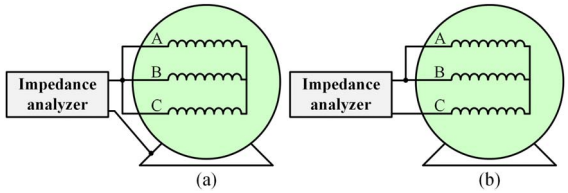

Fig. 3. (a) CM impedance measurement. (b) DM impedance measurement.

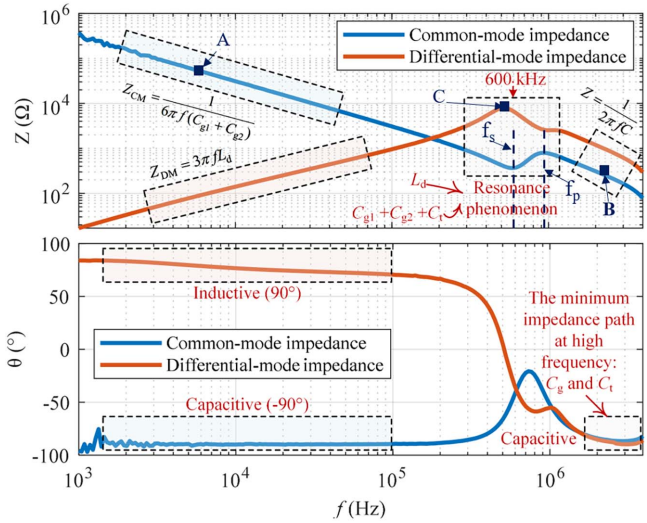

Fig. 4. Measurement results of CM and DM impedance of the tested PMSM.

The measurement results of the CM and DM impedance of the tested PMSM are shown in Fig. 4.

For the CM impedance measurement, the GW insulation is connected in series in the test loop. At low frequencies, the CM impedance is highly capacitive (the phase is near −90°) and has a large amplitude, a property that is mainly influenced by the insulation that impedes the flow of test current from the windings to the motor frame. According to [33], [34] and within this frequency band, the point A in Fig. 4 can be selected to calculate the sum of C_{g1} and C_{g2}. As the frequency increases, the CM impedance amplitude decreases rapidly. Around 600 kHz, the resonance phenomenon occurs, the amplitude and phase angle of this region is determined by the winding inductance (L_d) and insulation capacitance (C_{g1}, C_{g2}, and C_t). Within this frequency band, the series resonance frequency f_s and the parallel resonance frequency f_p can be obtained. As the frequency continues to rise, the parasitic capacitance between the turn-to-turn and the turn-to-frame becomes the minimum impedance path for the high-frequency currents, and thus the CM impedance is again capacitive at high frequencies. The point B can be selected within this frequency band to calculate C_{g1}. On the contrary, the DM impedance is always inductive (the phase is near 90°) at low frequency. As the frequency rises, it becomes capacitive after resonance, and the turn-to-turn parasitic capacitances become the minimum impedance path for the test current. Select resonance point C in the DM impedance, and then combine it with f_s and f_p, the remaining parameters in Fig. 2 can be calculated.

Authorized licensed use limited to: DELHI TECHNICAL UNIV. Downloaded on December 02,2024 at 05:09:41 UTC from IEEE Xplore. Restrictions apply.

This article has been accepted for inclusion in a future issue of this journal. Content is final as presented, with the exception of pagination.

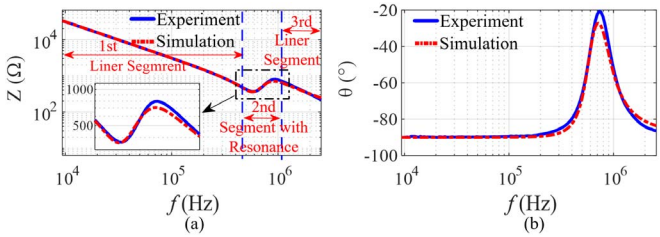

Fig. 5. Experimental and simulation results. (a) Amplitude. (b) Phase angle of CM impedance.

The simulation impedance spectrum of the model in Fig. 2 and the offline measured spectrum of the tested PMSM are compared in Fig. 5, which shows that the simulation is basically consistent with the experimentally measured. Therefore, the established model in Fig. 2 can be used to study the relationship between the interturn insulation degradation and the winding impedance spectrum.

It is shown in Fig. 5(a) that the impedance spectrum is divided into three bands [35]. The impedance in the first frequency band is mainly determined by the GW insulating equivalent capacitance between the stator windings and stator core. In the second frequency band, the effect of inductive coupling among coils becomes significant [33], and the resonance phenomenon due to the interaction of the winding inductance and insulation capacitance occurs in this band. In the third frequency band, the inductive reactance of the coils becomes extremely large, which restricts the test current flow. The impedance response is determined by the turn-to-turn and the turn-to-frame insulation capacitances. Therefore, only in the relatively high frequency range, the second and third bands, the interturn capacitances start to affect the impedance.

B. Impedance Spectrum Division for Monitoring Interturn Insulation Degradation

To obtain accurate monitoring indicators, it is necessary to identify the different regions of winding impedance spectrum sensitive to interturn insulation degradation. From the model shown in Fig. 2, the single-phase winding-to-ground impedance, Z_{PG}, is obtained as

$$Z_{PG}=\frac{s^2L_d(C_t+C_{g2})+s\dfrac{L_d}{R_e}+1}{s(C_{g1}+C_{g2})\left[s^2L_d\left(C_t+\dfrac{C_{g1}C_{g2}}{C_{g1}+C_{g2}}\right)+s\frac{L_d}{R_e}+1\right]}. \tag{1}$$

Z_{PG} is determined by the test frequency and model parameters. The capacitance of interturn insulation C_t depends on the configuration, shape and material of the insulation system, and it changes when the interturn insulation deteriorates [22]. According to [13], [14], [26], C_t increases with the severity of interturn insulation degradation. The partial derivatives of the Z_{PG} amplitude with respect to C_t are derived to clarify the effect of C_t on $|Z_{PG}|$, shown as

$$\frac{\partial|Z_{PG}|}{\partial C_t}=K\begin{bmatrix}(\beta_1+{\beta_2}^2+\beta_3)\cdot(2\pi f)^2\\-\beta_1\beta_3(2\pi f)^4-1\end{bmatrix}(K>0) \tag{2}$$

where

$$K=\frac{(2\pi f)^3L_d{C_{g2}}^2[{\beta_3}^2(2\pi f)^4+({\beta_2}^2-2\beta_3)\cdot(2\pi f)^2+1]^{\frac{1}{2}}}{(C_{g1}+C_{g2})^2[{\beta_1}^2(2\pi f)^4+({\beta_2}^2-2\beta_1)\cdot(2\pi f)^2+1]^{\frac{5}{2}}} \tag{3}$$

$$\begin{cases}\beta_1=L_d(C_t+C_{g2})\\ \beta_2=\dfrac{L_d}{R_e}\quad \beta_3=L_d\left(C_t+\dfrac{C_{g1}C_{g2}}{C_{g1}+C_{g2}}\right).\end{cases} \tag{4}$$

K is always positive, and the positive or negative of the above partial derivative determines the trend of $|Z_{PG}|$ when C_t varies. Solving (2), the positive and negative of partial derivatives in different frequency bands are further deduced as

$$\begin{cases}\dfrac{\partial|Z_{PG}|}{\partial C_t}<0 & f<f_1\cup f>f_2\\ \dfrac{\partial|Z_{PG}|}{\partial C_t}>0 & f_1<f<f_2\end{cases} \tag{5}$$

$$f_1=\sqrt{\frac{\beta_1+{\beta_2}^2+\beta_3-\sqrt{(\beta_1+{\beta_2}^2+\beta_3)^2-4\beta_1\beta_3}}{8\beta_1\beta_3\pi^2}}$$

$$f_2=\sqrt{\frac{\beta_1+{\beta_2}^2+\beta_3+\sqrt{(\beta_1+{\beta_2}^2+\beta_3)^2-4\beta_1\beta_3}}{8\beta_1\beta_3\pi^2}}. \tag{6}$$

The boundary frequencies f_1 and f_2 can be calculated based on (4) to (6) and combined with the model parameters. Thus, the single-phase winding-to-ground impedance can be divided into three regions, and the interturn insulation degradation has different effects on the impedance amplitude in different regions. At frequencies below f_1 in region 1 and above f_2 in region 3, the impedance amplitude will decrease with interturn insulation degradation because the partial derivatives of $|Z_{PG}|$ to C_t are negative. However, according to the discussion in Fig. 5, the interturn capacitances start to affect the winding impedance only in the relatively high-frequency range. Therefore, in region 1, the affect of interturn insulation on the impedance can be ignored since the impedance in this region is mainly determined by the GW insulation. On the other hand, at frequencies between f_1 and f_2 in region 2, the impedance amplitude increases as the degradation severity increases.

C. Verification of Impedance Spectrum Division Under Interturn Insulation Degradation

The relationship between the interturn insulation degradation and the winding impedance spectrum is investigated in simulation by changing the interturn capacitance C_t to simulate different degradation severities. In experiment, the impedance of the single-phase winding to ground with a disconnecting neutral point is measured. To introduce insulation degradation, an additional capacitor C_f is connected over a range of 10% of total turns of phase B. By connecting different numbers of capacitors in parallel, the capacitance can be increased, thereby increasing the degradation severity. The simulated and measured winding

Authorized licensed use limited to: DELHI TECHNICAL UNIV. Downloaded on December 02,2024 at 05:09:41 UTC from IEEE Xplore. Restrictions apply.

This article has been accepted for inclusion in a future issue of this journal. Content is final as presented, with the exception of pagination.

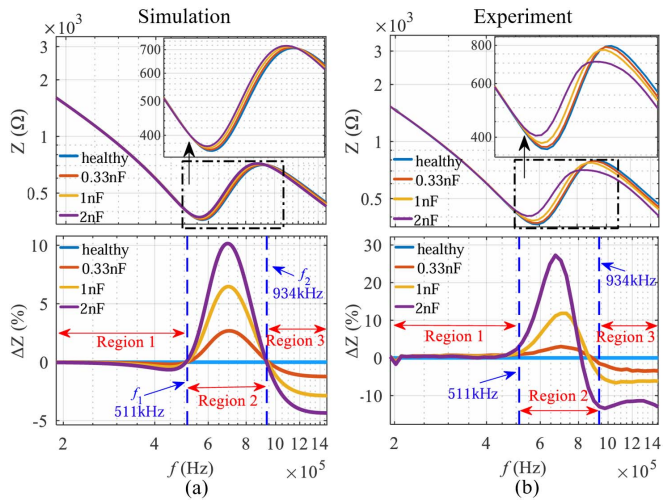

Fig. 6. Changes in different regions of impedance spectrum due to interturn insulation degradation. (a) Simulation. (b) Experiment.

spectra under different degradation severities, and their variations in the different regions of the spectrum divided based on boundary frequencies, normalized by the values in healthy state and denoted as ΔZ, are shown in Fig. 6.

Consistent with the above theoretical analysis, the effects of interturn insulation degradation on the winding impedance spectrum in different frequency bands are different. In the low-frequency band less than about 500 kHz in region 1, the effect of interturn insulation degradation is small and can be ignored. From 500 to 900 kHz approximately in region 2, the impedance amplitude increases with the deterioration of interturn insulation. When the frequency is higher than 900 kHz in region 3, the impedance amplitude decreases. The experimental and simulation results show the same trend, and the impedance spectrum division under interturn insulation degradation is verified.

In addition, the experimental results also show that the upper frequency of region 2, f_2, decreases with the increase in degradation severity. As the degradation severity increases, in region 2, the negative ΔZ of the impedance spectrum increases, but the positive ΔZ increases more, so ΔZ increases overall. However, if region 2 is used for insulation monitoring, the weakening effect of increasing degradation severity on the monitoring indicator becomes significant. In region 3, the impedance amplitude keeps decreasing as degradation severity increase. Therefore, the indicator established in region 3 can more accurately monitor insulation degradation of different severity levels.

III. Proposed Interturn Insulation Monitoring Method for IFMs

For installed motors, using current is more convenient than measuring winding impedance from a condition monitoring perspective. The switching transient current response is determined by the PWM voltage as high-frequency excitation and the stator winding as load, and the winding impedance change due to interturn insulation degradation can be extracted from the transient current response. Thus, the corresponding frequency components in the transient current response can be extracted based on the impedance spectrum division to evaluate the interturn insulation condition.

A. Proposed Interturn Insulation Monitoring Indicator

According to the analysis in Section II, as the degradation severity increases, the winding impedance amplitude increases for frequencies between f_1 and f_2 in region 2, and thus, the amplitude of the corresponding frequency component in the current response will decrease; for frequencies above f_2 in region 3, the winding impedance amplitude decreases, and the amplitude of the corresponding frequency component in the current response increases. Denote the spectrum of the transient current response as $I(g)$, where g represents the discrete frequency order, and the corresponding frequency f_g is calculated using the sampling rate F_s and the number of samples N_s as

$$f_g = g\frac{F_s}{N_s}. \tag{7}$$

Two interturn insulation monitoring indicators based on region 2 and region 3, denoted as $\mathrm{IIMI1}_{p,k}$ and $\mathrm{IIMI2}_{p,k}$, respectively, are defined first as

$$\begin{cases} \mathrm{IIMI1}_{p,k} = \sum_{g=g_1}^{g_2} |I(g)| & \left(g_1\frac{F_s}{N_s} \geq f_1, g_2\frac{F_s}{N_s} \leq f_2\right) \\ \mathrm{IIMI2}_{p,k} = \sum_{g=g_3}^{g_3+\Delta g} |I(g)| & \left(g_3\frac{F_s}{N_s} \geq f_2\right) \end{cases} \tag{8}$$

where p represents the p-phase winding, p = A, B, C; k means the kth switching event; f_1 and f_2 are the boundary frequencies of the impedance spectrum division calculated in Section II-B. $\mathrm{IIMI1}_{p,k}$ and $\mathrm{IIMI2}_{p,k}$ are the superposition of the amplitudes of the corresponding frequency components of the current response in regions 2 and 3, respectively. As the degradation severity increases, $\mathrm{IIMI1}_{p,k}$ decreases and $\mathrm{IIMI2}_{p,k}$ increases.

However, according to the discussion in Fig. 6, the degradation severity has a weakening effect on the monitoring indicator based on region 2. Therefore, the change of $\mathrm{IIMI1}_{B,k}$ will be smaller than that of $\mathrm{IIMI2}_{B,k}$, which implies that $\mathrm{IIMI2}_{B,k}$ is more sensitive to interturn insulation degradation. Therefore, in this article, the proposed interturn insulation monitoring indicator IIMI_p is obtained based on $\mathrm{IIMI2}_{p,k}$, shown as

$$\mathrm{IIMI}_p = \frac{\sum_{k=1}^{m} \mathrm{IIMI2}_{p,k}}{m} \tag{9}$$

where m is the number of switching events. The switching frequency of the inverter is usually above several kHz, so a large amount of transient current responses can be obtained within a few ms. In (9), this averaging effectively reduces the impact of noise and system uncertainties.

B. Determination of Qualified PWM Voltage Excitation

The switching transient current response is directly affected by the patterns of PWM voltage excitation of the inverter. Therefore, to ensure the validity of the monitoring results, the qualified PWM voltage excitation should be determined.

Authorized licensed use limited to: DELHI TECHNICAL UNIV. Downloaded on December 02,2024 at 05:09:41 UTC from IEEE Xplore. Restrictions apply.

This article has been accepted for inclusion in a future issue of this journal. Content is final as presented, with the exception of pagination.

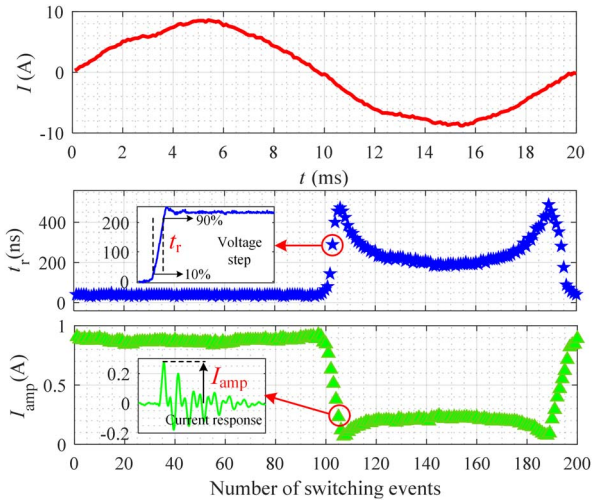

Fig. 7. Statistics of PWM voltage rise time (t_r) and amplitude of switching transient current response (I_{amp}) under different switching events within a fundamental period.

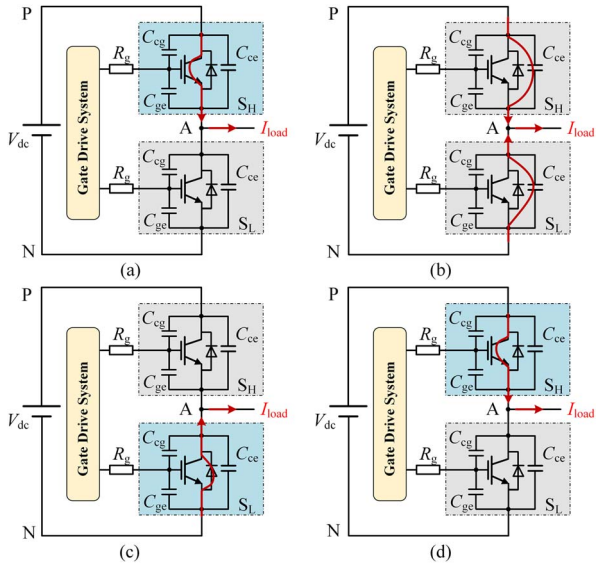

Fig. 8. Switching transitions of half-bridge inverter with positive current polarity. (a) $t < t_1$. (b) $t_1 < t < t_2$. (c) $t_2 < t < t_3$. (d) $t > t_3$.

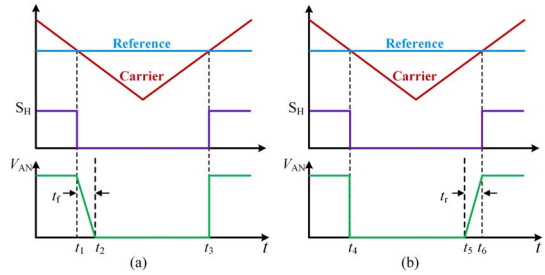

Fig. 9. Output voltage of half-bridge inverter when the load current. (a) Positive. (b) Negative.

The high-frequency characteristics of PWM voltage is mainly depends on its rise time. The statistics of PWM voltage rise time (t_r) and the corresponding amplitude of switching transient current response (I_{amp}) under different switching events within a fundamental period is shown in Fig. 7, where t_r is the time that the PWM voltage rises from 10% to 90% of dc voltage. It can be observed that, the smaller the t_r, the larger the I_{amp}, because the smaller rise time leads to higher voltage excitation [26]. In the positive half-cycle of load current, t_r has the minimum value and I_{amp} has the maximum value. More importantly, they are almost constant, which is important for the winding insulation condition monitoring based on switching transient current.

To illustrate the above phenomena in detail, the circuit schematic of a half-bridge inverter including two IGBTs (S_H and S_L), shown in Fig. 8, is investigated. The main parasitic elements are the gate-emitter capacitance (C_{ge}), collector-gate capacitance (C_{cg}), and collector-emitter capacitance (C_{ce}) [24]. The output current polarity is defined as positive when the current flows out from the midpoint (A) of the half bridge. In Fig. 8 the detailed switching transitions when the output current is positive are presented, and Fig. 8(a)–8(c) show the conduction phase change from the upper switch S_H to the lower switch S_L, and Fig. 8(c) and 8(d) show the opposite case.

The output voltage corresponding to Fig. 8 is shown in Fig. 9, where V_{AN} is the voltage between the midpoint A and the negative point N of the dc-link. When S_H is on, the load current flows through S_H, and V_{AN} is $+V_{dc}$. At t_1, a turn-off signal is applied to S_H, and the antiparallel diode of S_L is subjected to the reverse voltage. V_{AN} does not decrease rapidly because the load current charges the output capacitance ($C_{oss} = C_{cg} + C_{ce}$) of S_H while discharges that of S_L [3]. The fall time depends on the instantaneous value of the load current and the output capacitance C_{oss}, as shown in (10). When the current completely discharges the output capacitance of S_L, the voltage V_{AN} drops to 0 V and current flows through the antiparallel diode of S_L at t_2, as shown in Fig. 8(c). When a turn-on signal is applied to S_H, the current will be transferred directly from the antiparallel diode of S_L to S_H, and the V_{AN} will rise immediately from 0 V to $+V_{dc}$. In this case, the rise time of V_{AN} from 0 V to $+V_{dc}$ is controlled only by the gate resistor (R_g) of the gate driver. Since the voltage rises extremely fast, the rising edge of V_{AN} is denoted as a step edge, as shown at t_3 in Fig. 9(a)

$$t_f = \frac{2C_{oss}V_{dc}}{I_{load}}. \tag{10}$$

When the load current is negative, the switching transition is shown in Fig. 9(b) can be obtained according to a similar mechanism, where the rising edge t_r is a ramp, and the falling edge t_f is a step. In summary, when the load current is positive, the falling edge of V_{AN} is affected by the load current and parasitic capacitance. On the contrary, when the current is negative, the rising edge of V_{AN} is influenced by the load current and parasitic capacitance.

The statistics of PWM voltage rise time (t_r) and fall time (t_f) under different switching events within a fundamental period at different load currents are shown in Fig. 10, where t_f is the time that the PWM voltage falls from 90% to 10% of dc voltage. It can be seen that when the current is positive, t_r is short and not affected by the load current; when the current is negative, t_r is greater than that under positive current, and the larger the

Authorized licensed use limited to: DELHI TECHNICAL UNIV. Downloaded on December 02,2024 at 05:09:41 UTC from IEEE Xplore. Restrictions apply.

This article has been accepted for inclusion in a future issue of this journal. Content is final as presented, with the exception of pagination.

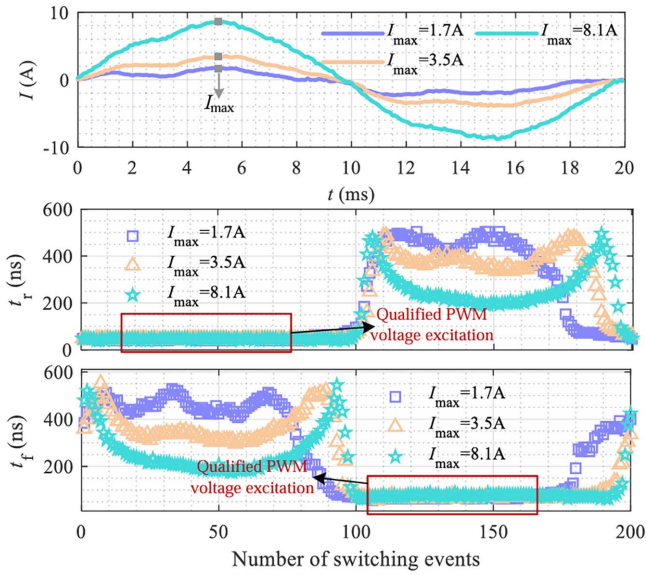

Fig. 10. Statistics of PWM voltage rise time (t_r) and fall time (t_f) under different switching events within a fundamental period at different load currents.

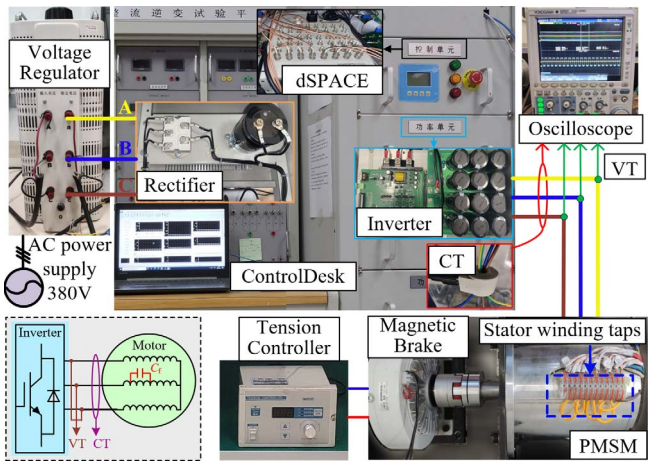

Fig. 11. Overall setup for experimental validation of the proposed scheme.

absolute value of negative current, the smaller t_r. The t_f shows an opposite trend. Therefore, to ensure that the PWM excitation characteristics are consistent, the rising edge of the PWM voltage under positive load current or the falling edge under negative load current can be selected as the qualified PWM voltage excitation. In this way, the influence of load current on the switching transient response can be minimized.

IV. Experimental Verification

A. Experimental Setup

An experimental setup consisting of a 3 kW PMSM controlled by FOC is established to validate the proposed method, and the scheme diagram of the test platform is shown in Fig. 11. The inverter is controlled by dSPACE, and an oscilloscope was used for signal acquisition, with a sampling frequency of 125 MHz and a bandwidth of 50 MHz for the voltage and current probes. The PWM voltages are collected from the inverter terminals, and the distance between the motor and the inverter is 1 m. It is found that the cable mainly affects the resonance in the extremely high-frequency range, while in the motor's inherent series- and parallel-resonance frequency range (f_s and f_p), i.e., the sensitive frequency range related to interturn insulation, the effect of this 1 m cable is not significant.

TABLE I
Motor Parameters And Test Conditions

Parameters	Value
Rated power (kW)	3
Rated current (A)	17
Rated torque (N·m)	19
External capacitor (nF)	0.05–2
Switching frequency (kHz)	10
Fundamental frequency (Hz)	50
DC bus voltage (V)	240

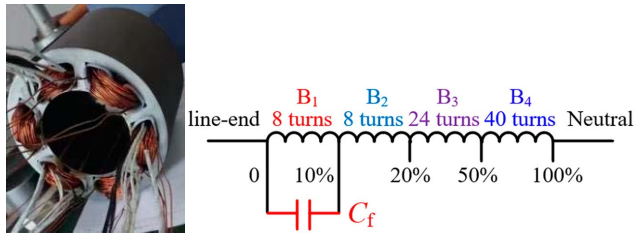

Fig. 12. Windings configuration and taps for connecting external capacitor.

TABLE II
Degradation Severity

C_f / nF	ΔC_t / pF	Severity (ΔC_t / C_t)
0.05	0.54	1.83%
0.1	1.15	3.89%
0.2	1.45	4.83%
0.3	3.56	11.97%
0.5	5.09	16.93%
1	6.51	21.86%
2	13.24	44.41%

The motor parameters and test conditions are presented in Table I. The stator winding is specially designed as shown in Fig. 12, where the winding consists of four coils with different numbers of turns. The taps of each coil are drawn out and connected to an interconnection box, so different numbers of external capacitors C_f can be connected in parallel between the two taps to simulate interturn insulation degradation with different severities, which is a commonly used method in existing research work [13], [14], [33].

The interturn insulation failure usually occurs at the first coil at the terminal end [19]. Therefore, the interturn insulation degradation was introduced in the first coil B_1 of phase B near the line end, which has 10% of the turns of the whole phase winding. To evaluate the degradation severity, the change of C_t in the stator winding model due to external C_f are determined by the offline tests [26], and the degradation severities with different C_f are presented in Table II. The relative change of C_t reaches

Authorized licensed use limited to: DELHI TECHNICAL UNIV. Downloaded on December 02,2024 at 05:09:41 UTC from IEEE Xplore. Restrictions apply.

This article has been accepted for inclusion in a future issue of this journal. Content is final as presented, with the exception of pagination.

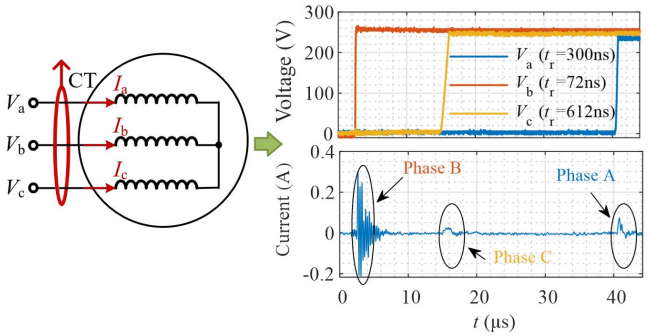

Fig. 13. Measurement of switching transient current responses.

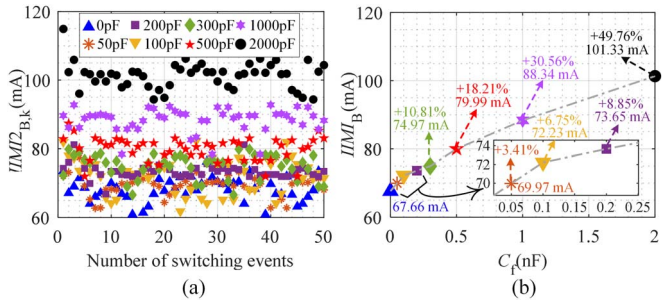

Fig. 15. Experimental results. (a) $IIMI2_{B,k}$. (b) $IIMI_B$ under different degradation severities.

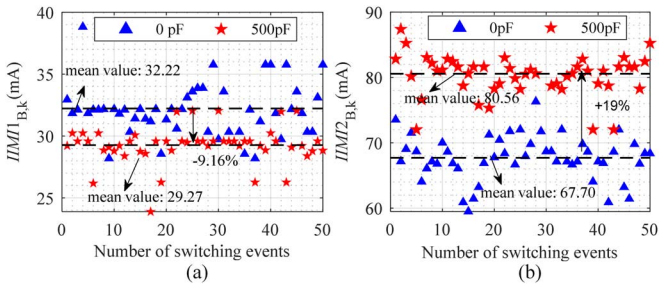

Fig. 14. Changes. (a) $IIMI1_{B,k}$. and (b) $IIMI2_{B,k}$ under interturn insulation degradation.

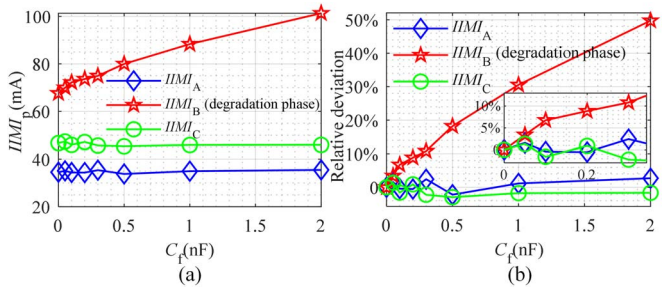

Fig. 16. Experimental results. (a) $IIMI_P$. (b) Relative changes of three phases under different degradation severities.

21.86% when $C_f = 1$ nF, and this level is described as a typical incipient interturn insulation degradation [26], [27], [28].

The amplitude of the transient current response is usually small and can be easily overwhelmed in the load current. Therefore, the current response is measured using a CM approach, as shown in Fig. 11. In this case, the three phase load currents erase each other, and the relatively small transient response in the phase currents can be effectively obtained. The transient current response of each phase can be determined based on the voltage step edge of the corresponding phase, as shown in Fig. 13.

According to the qualified PWM voltage excitation in different phases, the corresponding transient current response is extracted, and the degradation indicator is obtained by combining with f_1 and f_2 to realize the evaluation of stator interturn insulation condition. If not specified, the insulation degradation is introduced in phase B in the experiment.

B. Verification of Indicators Based on Regions 2 and 3

According to the measurement method presented above, 50 sets of transient current response of phase B are obtained within 5 ms at a switching frequency of 10 kHz, and they are all under qualified PWM voltage excitations. The results of $IIMI1_{B,k}$ and $IIMI2_{B,k}$ are shown in Fig. 14. Consistent with the theoretical analysis and discussion in Section III-A, it can be seen that when a 500 pF capacitor is connected, the indicator $IIMI1_{B,k}$ based on region 2 decreases, and the indicator $IIMI2_{B,k}$ based on region 3 increases. In addition, the average of $IIMI1_{B,k}$ decreases by 9.16%, while the average of $IIMI2_{B,k}$ increases by 19%, verifying that $IIMI2_{B,k}$ is more sensitive to interturn insulation degradation. Thus, the corresponding frequency components in the transient current response can be used to monitor the motor impedance variation due to interturn insulation degradation.

C. Validation of Proposed Insulation Monitoring Indicator

Experiments under different degradation severities were conducted to evaluate the proposed monitoring indicator, and the results of $IIMI2_{B,k}$ and $IIMI_B$ under different severities from 1.83% to 44.41% are shown in Fig. 15(a) and 15(b), respectively. It is shown that $IIMI2_{B,k}$ under different degradation levels may fluctuate and overlap, especially at the weak degradation levels, but the proposed indicator $IIMI_B$ obtained by averaging $IIMI2_{B,k}$ under multiple switching events increases with the increasing severity. $IIMI_B$ increases by 30.56% under the typical incipient interturn insulation degradation (severity of 21.86%, connected $C_f = 1$ nF). Even under a weak severity of 1.83% (connected $C_f = 50$ pF), it increases by 3.41%, which means that the proposed indicator has a high monitoring sensitivity.

In addition, it is feasible to determine in which phase the insulation degradation occurs based on the relative changes in $IIMI_p$ of different phases. Under the qualified PWM voltage excitation, the transient current response of each phase is almost independent and is only determined by the impedance of the corresponding phase windings. The absolute value of $IIMI_p$ and its relative change compared with the value in healthy state are shown in Fig. 16(a) and 16(b), respectively. As the degradation severity increases, $IIMI_B$ of the degradation phase increases significantly, and $IIMI_A$ and $IIMI_C$ of the healthy phases remain nearly unchanged.

Authorized licensed use limited to: DELHI TECHNICAL UNIV. Downloaded on December 02,2024 at 05:09:41 UTC from IEEE Xplore. Restrictions apply.

This article has been accepted for inclusion in a future issue of this journal. Content is final as presented, with the exception of pagination.

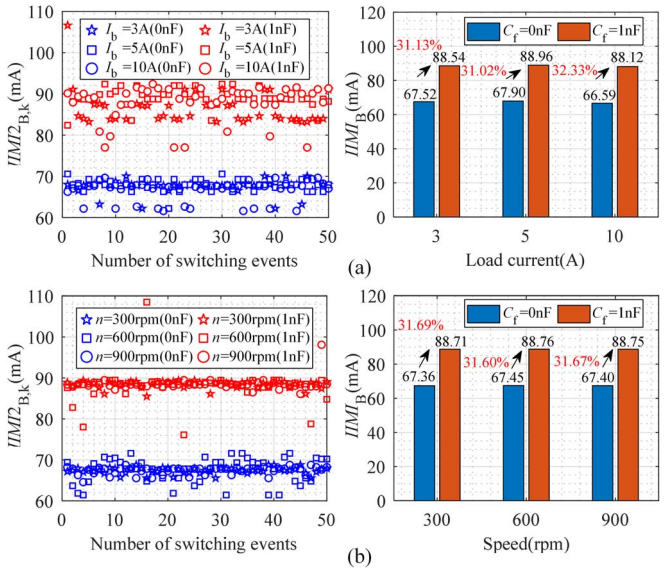

Fig. 17. Experimental results of $IIMI2_{B,k}$ and $IIMI_B$ under: (a) Different load currents (motor speed = 600 rpm); and (b) Different speeds (load current = 5 A).

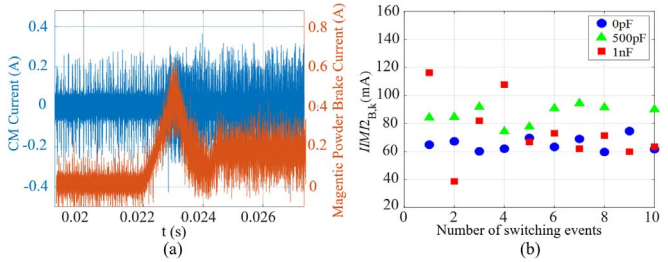

Fig. 18. Experimental results. (a) CM current. (b) $IIMI2_{B,k}$ under sudden torque change.

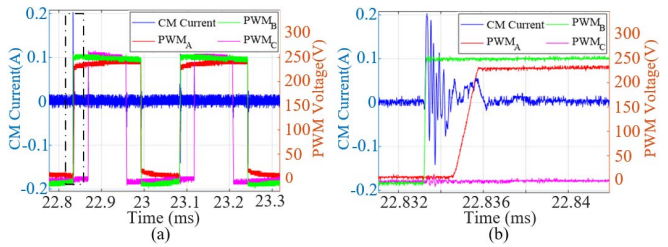

Fig. 19. Transient current response and PWM voltage during transient load. (a) Two switching cycles. (b) Zoomed view of PWM rising edge.

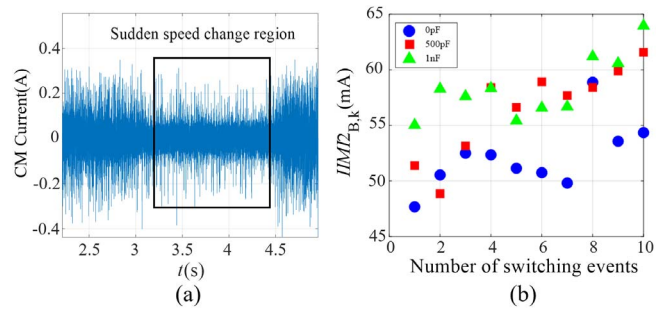

Fig. 20. Experimental results. (a) CM current. (b) $IIMI2_{B,k}$ under sudden speed change.

D. Verification Under Different Operating Conditions

1) Stable Operating Conditions: The experimental results of $IIMI2_{B,k}$ and $IIMI_B$ under different load currents and motor speeds are shown in Fig. 17. It can be seen that for the same degradation severity ($C_f = 1$ nF), the $IIMI2_{B,k}$ extracted from a single switching event has individual singular points, but the increase of $IIMI_B$ remains relatively stable under different load currents and speeds, increasing by 31%–32%. Therefore, the robustness of the proposed monitoring indicator to motor operating conditions can be guaranteed. The reason is that the extracted frequency components in the transient current response are located in a frequency band much higher than the motor fundamental frequency and the inverter switching frequency, and the changes of operating conditions have little impact on these components. On the other hand, the indicator $IIMI_p$ is obtained by averaging multiple switching events within a short time window, and thus, the stability of the proposed monitoring method can be effectively improved.

2) Transient Operating Conditions: Experiments under transient operating conditions were conducted. First, the load was changed from no-load to full-load (the current of magnetic brake changing from 0 to 0.2 A), and the corresponding CM current is shown in Fig. 18(a). The indicator ($IIMI2_{B,k}$) extracted from the switching transient current during the load variation (0.022–0.023 s) cannot accurately monitor the degradation severity, as shown in Fig. 18(b).

During load transients, since the inverter needs to quickly adjust the output voltage to generate the required load current, it is found that most of the PWM switching intervals between different phases are too short, introducing new oscillations before the previous current oscillation has fully decayed, resulting in incomplete transient currents, as shown in the zoomed view of CM current and PWM voltage in Fig. 19. The interval between PWMB and PWMA is about 2.55 μs, while the typical duration of transient current response is about 4 to 5 μs. Therefore, the insulation condition under transient load cannot be detected accurately based on the indicator extracted from the incomplete transient current response.

Then, the speed was increased from 120 to 600 rpm to test the monitoring performance under transient speed condition. The CM current is shown in Fig. 20(a), and the $IIMI2_{B,k}$ extracted from the switching transient current during the transient speed variation (3.3–4.3 s) also cannot accurately monitor the degradation severity, as shown in Fig. 20(b). The reason is similar to the transient load case that most of the PWM switching intervals between different phases become very short due to the change of PWM duty cycle caused by the transient speed, resulting in incomplete transient currents.

However, there are two possible approaches to address this issue. The first one is to calculate the indicator at regular intervals, such as every 1 s, and perform continuous monitoring 3 to 5 times. Degradation can only be determined if all monitoring results indicate degradation. The second one is to monitor the insulation degradation only under stable operating conditions, which can also meet the monitoring requirements.

Authorized licensed use limited to: DELHI TECHNICAL UNIV. Downloaded on December 02,2024 at 05:09:41 UTC from IEEE Xplore. Restrictions apply.

This article has been accepted for inclusion in a future issue of this journal. Content is final as presented, with the exception of pagination.

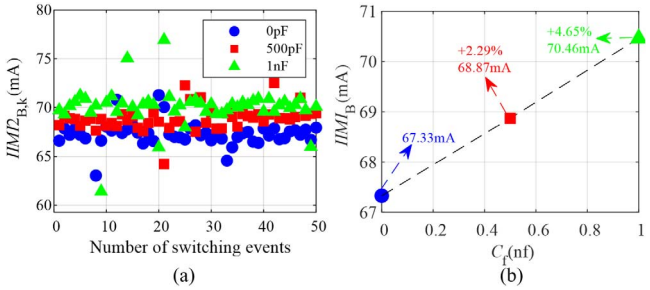

Fig. 21. Experimental results. (a) $IIMI2_{B,k}$. (b) $IIMI_B$ for single turn degradation under different degradation severities.

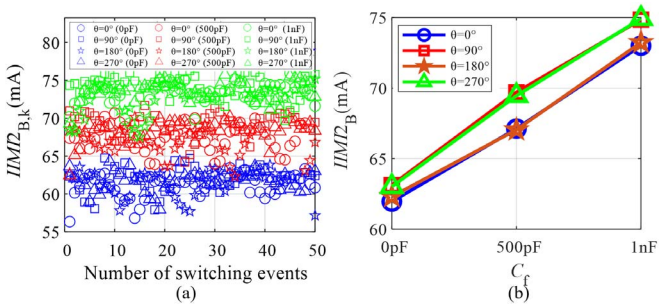

Fig. 22. Experimental results. (a) $IIMI2_{B,k}$. (b) $IIMI2_B$ under different rotor positions.

E. Verification With One Turn Insulation Degradation

The fewer turns involved in degradation, the more challenging it becomes to monitor. To further validate the monitoring performance of the proposed method, more experiments were conducted with different degradation severities for a single turn, and the results are shown in Fig. 21. It shows that the healthy state and degraded states can be distinguished by the proposed indicator $IIMI_B$. However, because the increase of $IIMI_B$ is relatively small, for degradation with lower severity, the degradation might not be detected. Overall, monitoring the degradation of a single turn is challenging, but as the degradation severity increases, it is possible to distinguish it from healthy condition.

V. Discussions

A. Influence of Rotor Position

The measurement of winding impedance is affected by the rotor position. To further investigate the impact of rotor position, experiments were conducted at rotor electrical angles of 0°, 90°, 180°, and 270°. The motor is standstill and the PWM voltage excitation was only connected to B-phase. The results under different degradation conditions and different rotor positions are shown in Fig. 22, and it shows that the insulation degradation with $C_f = 500$ pF and 1 nF can be detected. However, from Fig. 22(b), for the same insulation condition, the indicator values at electrical angles of 90° and 270° are higher than those of 0° and 180°. This shows that due to the influence of the rotor angle, insulation conditions with little difference cannot be distinguished.

B. Influence of Temperature

The measurement of winding impedance is also affected by temperature. More experiments were conducted under four temperatures: 30 °C, 60 °C, 90 °C, and 120 °C. Due to the size limitation of the constant temperature chamber, a 550 W small PMSM was tested. Additional capacitors $C_f = 500$ pF and 1 nF are connected in parallel at 10% turns ratio tap of phase B. The impedance spectrum shifts to the lower left as the temperature increases, as can be seen from Fig. 23. The results of $IIMI2_{B,k}$ and $IIMI2_B$ for different degradation severities at different temperatures are shown in Figs. 24 and 25, respectively.

It can be seen from Fig. 24 that at the same temperature, the indicator increases due to the severity increase. However, increased temperature can cause misdiagnosis because the

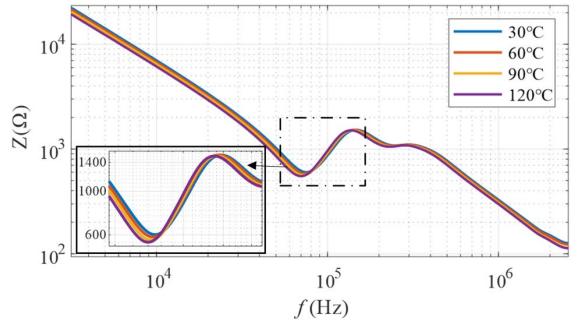

Fig. 23. Impedance spectrum of healthy phase B winding at different temperatures.

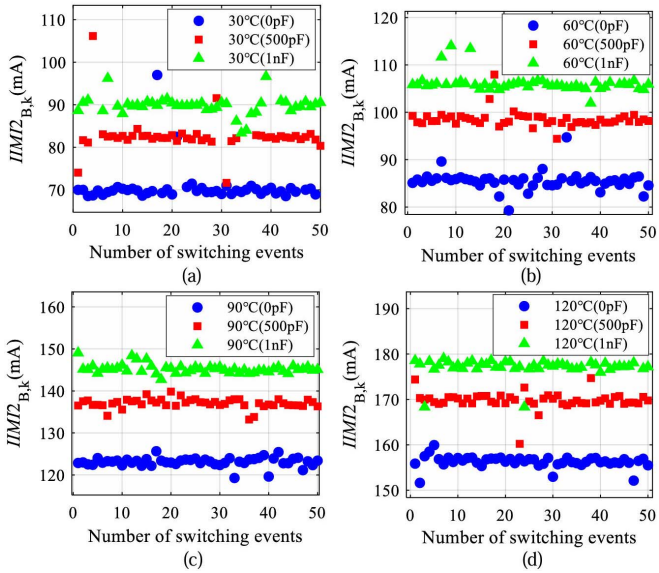

Fig. 24. Experimental results of $IIMI2_{B,K}$ under. (a) 30 °C. (b) 60 °C. (c) 90 °C. (d) 120 °C.

indicator also increases with increasing temperature. As shown in Fig. 25, for example, if the monitoring reference is selected at 30 °C (69.3, $C_f = 0$), when the temperature rises to 60 °C, the indicator increases to 85.5, higher than the 83.1 under degradation condition ($C_f = 500$ pF) at 30 °C, and causing a misdiagnosis. Therefore, in practice, it is necessary to calibrate and fit the indicator values under healthy conditions at different temperatures, collect the motor temperature in real time, and set the corresponding reference value for insulation monitoring.

Authorized licensed use limited to: DELHI TECHNICAL UNIV. Downloaded on December 02,2024 at 05:09:41 UTC from IEEE Xplore. Restrictions apply.

This article has been accepted for inclusion in a future issue of this journal. Content is final as presented, with the exception of pagination.

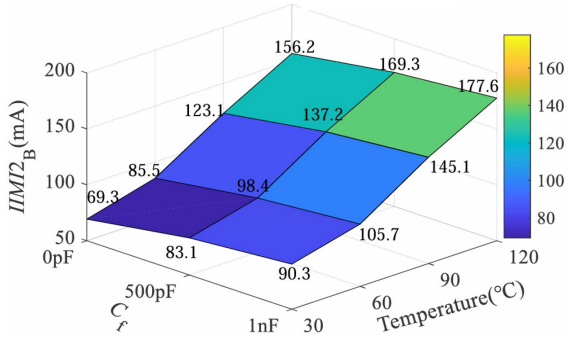

Fig. 25. Experimental results of $IIMI2_B$ under different temperatures.

C. Cost Reduction

The proposed method requires both current and voltage sensors, which dose increase the cost. However, from an engineering standpoint, the cost can be controlled to a certain extent. First, it is found in this article that the PWM voltage rising edge when the current polarity is positive, or the falling edge when the current polarity is negative, can be selected as the qualified excitation. Therefore, a high sampling rate for the PWM voltage is no longer necessary. In practical applications, it is feasible to use the PWM voltage control signal instead of the actual PWM voltage measurement to extract transient current response and corresponding phase information, as demonstrated in the example [36], which means that the voltage sensors are not necessary.

Then, as the motor power increases, the primary spectral peaks of the current response decrease significantly [22], which in turn leads to a substantial reduction in the required sampling frequency. Consequently, in high-power motor scenarios where insulation monitoring is more needed, the frequency range of the transient current response decreases significantly, leading to a reduced performance requirement for the current sensor, thereby lowering the hardware costs.

D. Limitations and Advantages

From the above analysis, the proposed method does have some limitations. First, for single turn early degradation, the monitoring performance needs to be further improved. Second, the indicator is affected by rotor position and temperature. Third, during transient operating conditions, the indicator cannot accurately monitor the degradation severity. However, if the proposed method is implemented to a stationary motor at the same ambient temperature, by forcing aligned the rotor to a certain position, the effects of transient operating condition, temperature and rotor position can be eliminated. The cost can also be much lower since it would not occupy computation time as the processor is at rest.

Another limitation is that although small-value capacitors are usually inserted in existing methods to simulate turn insulation [19], [26], this is indeed a limitation when compared with the turn insulation degradation in real scenarios. Because the insulation degradation is affected by many factors such as heat, electricity, humidity, and mechanics. In engineering practice, there are several types of insulation degradation, and the changes in insulation equivalent capacitance are different. As discussed [27], the insulation capacitance decreases when degradation occurs. More detailed discussion about the change of insulation capacitance can be found [37]. Insulation degradation leading to increased capacitance is more common in certain high-humidity applications. However, more comprehensive research on different insulation degradation types in real scenarios should be conducted in the future.

For the main advantages of this method, first, it clarifies in which frequency region the amplitude of the switching transient current response decreases and in which frequency region it increases as the turn insulation deteriorates. Therefore, an indicator of high monitoring sensitivity is obtained, which can detect degradation of tens of pF (50 pF, 1.83%), as shown in Fig. 15. Second, the qualified PWM voltage excitation is determined in this article to ensure the validity of monitoring results. Third, the proposed method can be used offline, and potentially, online if limitations such as temperature and transient operating conditions can be addressed. In addition, the combination of offline and online turn insulation monitoring based on the proposed method would be robust, accurate, and meaning for future research.

VI. Conclusion

Accurate monitoring of interturn insulation conditions is critical for the security and reliability of IFMs. This article proposes a novel interturn insulation degradation monitoring method using the witching transient current response based on winding impedance spectrum division. Some conclusions are drawn as follows.

1) According to the division of winding impedance spectrum, as the degradation severity increases, in region 2, the impedance amplitude increases and the current response amplitude decreases; in region 3, the impedance amplitude decreases and the current response amplitude increases. Due to the weakening effect of degradation severity on the monitoring indicator based on region 2, the indicator based on region 3 is more suitable for interturn insulation degradation monitoring.
2) Experiment results show that the proposed method can detect about 1.83% of the insulation capacitance change and has high monitoring sensitivity. On the other hand, the monitoring result is robust to different stable motor operating conditions.
3) The monitoring performance is affected by the rotor position, temperature and transient motor operating conditions. For online implementation, some possible approaches to address these limitations have been mentioned in Section IV-D-2 and Section V-B. However, if the proposed method is used offline, the above limitations can be eliminated, as discussed in Section V-D.

In the future, the effects of temperature on monitoring performance will be stressed first, and temperature acquisition or online estimation will be integrated into the diagnosis algorithm to improve its robustness. Importantly, carry out accelerated insulation degradation tests under various stresses to study the

Authorized licensed use limited to: DELHI TECHNICAL UNIV. Downloaded on December 02,2024 at 05:09:41 UTC from IEEE Xplore. Restrictions apply.

This article has been accepted for inclusion in a future issue of this journal. Content is final as presented, with the exception of pagination.

physical relationship between different degradation types and motor impedance spectrum and switching transient current. In this way, the monitoring of different insulation degradation types can be expected to be realized.

REFERENCES

[1] S. Huang, A. Aggarwal, E. G. Strangas, B. Khoshoo, K. Li, and F. Niu, "Mitigation of interturn short-circuits in IPMSM by using MTPCC control adaptive to fault severity," *IEEE Trans. Power Electron.*, vol. 37, no. 4, pp. 4685–4696, Apr. 2022.

[2] N. Lahoud, J. Faucher, D. Malec, and P. Maussion, "Electrical aging of the insulation of low-voltage machines: model definition and test with the design of experiments," *IEEE Trans. Ind. Electron.*, vol. 60, no. 9, pp. 4147–4155, Sep. 2013.

[3] W. Zhou, M. Diab, and X. Yuan, "Impact of parasitic and load current on the attenuation of motor terminal overvoltage in SiC-based drives," *IEEE Trans. Ind. Appl.*, vol. 58, no. 2, pp. 2229–2241, Mar./Apr. 2022.

[4] J. He, C. Somogyi, A. Strandt, and N. A. O. Demerdash, "Diagnosis of stator winding short-circuit faults in an interior permanent magnet synchronous machine," in *Proc. IEEE Energy Convers. Congr. Expo*., Sep. 2014, pp. 3125–3130.

[5] S. Huang, A. Aggarwal, E. G. Strangas, K. Li, F. Niu, and X. Huang, "Robust stator winding fault detection in PMSMs with respect to current controller bandwidth," *IEEE Trans. Power Electron.*, vol. 36, no. 5, pp. 5032–5042, May 2021.

[6] H. Ch. Park et al., "Automated testing for early identification of PD in the stator insulation of low voltage VFD motors," *IEEE Trans. Ind. Appl.*, vol. 59, no. 4, pp. 3910–3919, Jul./Aug. 2023.

[7] P. Wang, S. Ma, S. Akram, K. Zhou, Y. Chen, and M. T. Nazir, "Design of archimedes spiral antenna to optimize for partial discharge detection of inverter fed motor insulation," *IEEE Access*, vol. 8, pp. 193202–193213, 2020.

[8] H. Lee, H. Kim, J. Jeong, K. Lee, S. B. Lee, and G. C. Stone, "Inverter-embedded partial discharge testing for reliability enhancement of stator winding insulation in low voltage machines," *IEEE Trans. Ind. Appl.*, vol. 58, no. 2, pp. 2088–2096, Mar. 2022.

[9] M. F. Shaikh, H. Lee, B. Battulga, S. B. Lee, and G. C. Stone, "Detection of severe ground insulation deterioration before failure in VFD-fed motors using off-line common-mode voltage," *IEEE Trans. Ind. Appl.*, vol. 60, no. 1, pp. 144–152, Jan./Feb. 2024.

[10] D. Zheng, G. Lu, G. Li, M. Yao, and P. Zhang, "Quasi-online technique for health monitoring of stator winding insulation in inverter-fed motor using switching transient voltage response," in *Proc. 26th Int. Conf. Elect. Mach. Syst. (ICEMS)*, Zhuhai, China, 2023, pp. 2444–2449.

[11] K. X. Lai, B. T. Phung, and T. R. Blackburn, "Application of data mining on partial discharge part I: predictive modelling classification," *IEEE Trans. Dielectr. Electr. Insul.*, vol. 17, no. 3, pp. 846–854, Jun. 2010.

[12] G. C. Stone, H. G. Sedding, and C. Chan, "Experience with online partial-discharge measurement in high-voltage inverter-fed motors," *IEEE Trans. Ind. Appl.*, vol. 54, no. 1, pp. 866–872, Jan./Feb. 2018.

[13] F. Perisse, P. Werynski, and D. Roger, "A new method for ac machine turn insulation diagnostic based on high frequency resonances," *IEEE Trans. Dielectr. Electr. Insul.*, vol. 14, no. 5, pp. 1308–1315, Oct. 2007.

[14] P. Neti and S. Grubic, "Online broadband insulation spectroscopy of induction machines using signal injection," *IEEE Trans. Ind. Appl.*, vol. 53, no. 2, pp. 1054–1062, Mar./Apr. 2017.

[15] S. B. Lee, K. Younsi, and G. B. Kliman, "An online technique for monitoring the insulation condition of AC machine stator windings," *IEEE Trans. Energy Convers.*, vol. 20, no. 4, pp. 737–745, Dec. 2005.

[16] D. Zheng and P. Zhang, "An online groundwall and phase-to-phase stator insulation monitoring method for inverter-fed machine," *IEEE Trans. Ind. Electron.*, vol. 68, no. 6, pp. 5303–5313, Jun. 2021.

[17] P. Zhang, K. Younsi, and P. Neti, "A novel online stator ground-wall insulation monitoring scheme for inverter-fed AC motors," *IEEE Trans. Ind. Appl.*, vol. 51, no. 3, pp. 2201–2207, May/Jun. 2015.

[18] I. Tsyokhla, A. Griffo, and J. Wang, "Online condition monitoring for diagnosis and prognosis of insulation degradation of inverter-fed machines" *IEEE Trans. Ind. Electron.*, vol. 66, no. 10, pp. 8126–8135, Oct. 2019.

[19] D. Zheng, G. Lu, Y. Wu, Q. Zhang, and P. Zhang, "Online detection and classification of interturn and groundwall insulation aging based on broadband common-mode impedance spectrum," *IEEE Trans. Ind. Electron.*, vol. 71, no. 3, pp. 3142–3153, Mar. 2024.

[20] J. E. Ruiz-Sarrio, F. Chauvicourt, J. Gyselinck, and C. Martis, "Impedance modeling oriented toward the early prediction of high-frequency response for permanent magnet synchronous machines," *IEEE Trans. Ind. Electron.*, vol. 70, no. 5, pp. 4548–4557, May 2023.

[21] D. Zheng, G. Lu, and P. Zhang, "A noninvasive interturn insulation condition monitoring method based on the common-mode impedance spectrum of inverter-fed machines," *IEEE Trans. Ind. Appl.*, vol. 57, no. 5, pp. 4786–4795, Sep./Oct. 2021.

[22] P. Nussbaumer, M. A. Vogelsberger, and T. M. Wolbank, "Induction machine insulation health state monitoring based on online switching transient exploitation," *IEEE Trans. Ind. Electron.*, vol. 62, no. 3, pp. 1835–1845, Mar. 2015.

[23] C. Zoeller, T. M. Wolbank, and M. A. Vogelsberger, "Inverter-fed drive stator insulation monitoring based on reflection phenomena stimulated by voltage step excitation," in *Proc. IEEE Energy Convers. Congr. Expo.,* 2016, pp. 1–8.

[24] C. Zoeller, M. A. Vogelsberger, and T. M. Wolbank, "Influence of parasitic capacitances of IGBT inverter on insulation condition monitoring of traction machines based on current signal transients analysis," in *Proc. 18th Eur. Conf. Power Electron. Appl.*, 2016, pp. 1–9.

[25] L. Ran, S. Gokani, J. Clare, K. J. Bradley, and C. Christopoulos, "Conducted electromagnetic emissions in induction motor drive systems. I. time domain analysis and identification of dominant modes," *IEEE Trans. Ind. Electron.*, vol. 13, no. 4, pp. 757–767, Jul. 1998.

[26] D. Xiang, H. Li, H. Yan, Y. Zheng, N. Zhao, and B. Liu, "Online monitoring of incipient turn insulation degradation for inverter-fed machine using sensitive tail component in PWM switching oscillations," *IEEE Tans. Power Electron.*, vol. 36, no. 8, pp. 8730–8742, Aug. 2021.

[27] H. Li, Y. Gu, D. Xiang, P. Zhang, P. Yue, and Y. Cui, "Online condition monitoring of line-end coil insulation for inverter-fed machine by switching oscillation mode decomposition," *IEEE Trans. Ind. Electron.*, vol. 69, no. 11, pp. 11697–11708, Nov. 2022.

[28] F. Niu et al., "An online groundwall insulation monitoring method based on transient characteristics of leakage current for inverter-fed motors," *IEEE Trans. Power Electron.*, vol. 37, no. 8, pp. 9745–9753, Aug. 2022.

[29] R. Fan, X. Lei, T. Jia, M. Qin, H. Li, and D. Xiang, "High-sensitive state perception method for inverter-fed machine turn insulation based on FrFT-Mel," *Global Energy Interconnection*, vol. 7, no. 2, pp. 155–165, 2024.

[30] J. E. Ruiz-Sarrio, J. A. Antonino-Daviu, A. Navarro-Navarro, and V. Biot-Monterde, "Broadband technique analysis for insulation fault detection and condition monitoring in rotating electrical machines," in *Proc. IEEE 14th Int. Symp. Diag. Elect. Mach., Power Electron. Drives*, 2023, pp. 574–580.

[31] S. Sundeep, J. Wang, A. Griffo, and F. Alvarez-Gonzalez, "Antiresonance phenomenon and peak voltage stress within PWM inverter-fed stator winding," *IEEE Trans. Ind. Electron.*, vol. 68, no. 12, pp. 11826–11836, Dec. 2021.

[32] A. Boglietti and E. Carpaneto, "Induction motor high frequency model," in *Proc. Conf. Rec. IEEE Ind. Appl. Conf. 34th IAS Annu. Meeting,* 1999, pp. 1551–1558.

[33] M. Schinkel, S. Weber, S. Guttowski, W. John, and H. Reichl, "Efficient HF modeling and model parameterization of induction machines for time and frequency domain simulations," in *Proc. 2lst Annu. IEEE Appl. Power Electron. Conf. Expo*., 2006, pp. 1–6.

[34] O. Magdun and A. Binder, "High-frequency induction machine modeling for common mode current and bearing voltage calculation," *IEEE Trans. Ind. Appl.*, vol. 50, no. 3, pp. 1780–1790, May/Jun. 2014.

[35] G. Lu, D. Zheng, and P. Zhang, "An advanced wideband model and a novel multitype insulation monitoring strategy for VSC-connected transformers based on common-mode impedance response," *IEEE Trans. Ind. Electron.*, vol. 69, no. 1, pp. 879–889, Jan. 2022.

[36] G. Lu, Q. Zhang, D. Zheng, and P. Zhang, "A novel online monitoring strategy for the localized grounding insulation defect of converter transformers based on converter switching states control," *IEEE Trans. Power Electron.*, vol. 37, no. 9, pp. 11 124–11 134, Sep. 2022.

[37] G. C. Stone, I. Culbert, E. A. Boulter, and H. Dhirani, "Off-line rotor and stator winding tests," in *Electrical Insulation for Rotating Machines: Design Evaluation Aging Testing and Repair*, Hoboken, NJ, USA: Wiley, 2014, pp. 317–388.

Authorized licensed use limited to: DELHI TECHNICAL UNIV. Downloaded on December 02,2024 at 05:09:41 UTC from IEEE Xplore. Restrictions apply.

This article has been accepted for inclusion in a future issue of this journal. Content is final as presented, with the exception of pagination.

Feng Niu (Member, IEEE) received the B.S. and Ph.D. degrees in electrical engineering from Hebei University of Technology, Tianjin, China, in 2009 and 2015, respectively.

From 2016 to 2018, he was a Postdoctoral Research Fellow with the College of Electrical Engineering, Zhejiang University, Hangzhou, China. Currently, he is a Professor with the School of Electrical Engineering, Hebei University of Technology. He has authored or co-authored more than 80 technical articles. His research interests include motor system and intelligent electrical equipment.

Pengju Zhang received the B.S. degree in electrical engineering and automation from Hebei University of Engineering, Handan, China, in 2021. He is currently working toward the M.S. degree in electrical engineering with the School of Electrical Engineering, Hebei University of Technology, Tianjin, China.

His research interests include fault diagnosis and condition monitoring of electrical machines.

Feng Zhou (Member, IEEE) received the B.Eng., M.Eng., and Ph.D. degrees in control science and engineering from the Central South University, Changsha, China, in 2009, 2012, and 2017, respectively.

Currently, he is a Lecturer with the College of Electronic Information and Electrical Engineering, Changsha University, Changsha. His research interests include complex systems modeling, and optimization, and industrial process control.

Shaopo Huang received the B.S., M.S., and Ph.D. degrees in electrical engineering from Hebei University of Technology, Tianjin, China, in 2009, 2012, and 2021, respectively.

From 2012 to 2015, he was an Engineer with ABB LV Installation Materials Company Ltd., Beijing, China. From 2017 to 2019, he was a Research Fellow with the Electrical Machines and Drives Laboratory, Michigan State University, East Lansing, MI, USA. Currently, he is with the College of Information Engineering, Beijing Institute of Petrochemical Technology, Beijing, China. His research interests include fault diagnosis and mitigation of electrical machines and drives, and reliability testing of electrical apparatus.

Zijun Xu received the B.S. degree in automation engineering and the M.S. degree in control science and engineering from Hebei University of Technology, Tianjin, China, in 2015 and 2019, respectively. She is currently working toward the Ph.D. degree in electrical and information engineering with Tianjin University, Tianjin, China.

Her research interest includes the motion planning of UAVs and USVs.

Lu Zhang received the Ph.D. degree in mechatronics from Beihang University, Beijing, China, in 2020.

She completed Postdoctoral Research with Beihang University, in 2023. Currently, she is an Assistant Professor with Beijing Institute of Petrochemical Technology, Beijing, China. Her research interests include actuators, sensors, robotics, and navigation systems.

Anmol Aggarwal (Member, IEEE) received the B.E. degree from Delhi Technological University, Delhi, India, in 2013, and the Ph.D. degree from Michigan State University, East Lansing, MI, USA, in 2020, both in electrical engineering.

Currently, he is working as an Electric Motor Controls Engineer with General Motors Inc., Detroit, MI, USA. His research interests include control and design in electric machines and fault diagnosis, etc.

Authorized licensed use limited to: DELHI TECHNICAL UNIV. Downloaded on December 02,2024 at 05:09:41 UTC from IEEE Xplore. Restrictions apply.

This article has been accepted for publication in IEEE Transactions on Network and Service Management. This is the author's version which has not been fully edited and content may change prior to final publication. Citation information: DOI 10.1109/TNSM.2024.3493015

Adaptive Scheduling of Shared Grant-Free Resources for Heterogeneous Massive Machine type Communication in 5G and Beyond Networks

Yukti Kaura, Brejesh Lall, *Senior Member, IEEE*, Ranjan K. Mallik, *Fellow, IEEE*, and Amit Singhal, *Senior Member, IEEE*

***Abstract*—Massive machine-type communication (mMTC) has been identified as a key service type in fifth-generation new radio (5G NR) communication systems. The third-generation partnership (3GPP) project, starting with 5G, has introduced grant-free (GF) or configured grant (CG) scheduling for uplink traffic with small data packets to reduce signaling and latency overheads as compared to prevalent grant-based (GB) schemes. However, when heterogeneous MTC devices compete for pre-configured, shared GF resources, the access results in collisions. No standardized methods exist for ensuring priority-based access in the shared GF scheduling scheme. In this work, we introduce novel methods which utilize both heuristic and multi-objective deep reinforcement learning (DRL) techniques for priority-enabled GF access. The proposed methods adaptively partition GF bandwidth resources per allocation interval for scheduling configured grants to heterogeneous MTC device groups in a way which improves their probability of successful transmission, thereby resulting in a lower average age of information and packet drop rate and simultaneously ensuring fairness. Through extensive simulations set in the context of cyber-physical systems (CPS) with diverse quality-of-service (QoS) requirements across various 5G NR numerology schemes, we exemplify that our proposed approach provides significantly better performance and resource utilization than conventional schemes.**

***Index Terms*—Adaptive resource partitioning, fifth-generation (5G) new radio (NR), grant-free (GF) access, massive machine-type communication (mMTC), reinforcement learning (RL), traffic prioritization.**

I. Introduction

MASSIVE machine-type communication (MTC) refers to machine-initiated autonomous communication. Massive MTC (mMTC) applications often include a massive number of devices with high connection density, limited processing capabilities, low energy utilization, and low mobility. These devices generally execute sporadically and transmit small data [1]. Heterogeneous QoS requirements arising from mMTC in fifth-generation (5G) and advanced systems necessitate an eminent shift in design objectives. Moreover, 5G-Advanced starting with 3GPP Release 18 will enable next-generation radio access networks through standardized support for artificial intelligence/machine learning.

Devices in the grant-based (GB) random access (RA) scheme contend to obtain a grant to transmit the data. The RA procedure used to grant initial access to an MTC device to the network consists of a four-message exchange and significant signaling overhead. This is inefficient for small data packets. Grant-free (GF) scheduling can periodically pre-configure resources to MTC devices [2]. These can be used when devices have data to transmit. Pre-allocating *dedicated* resources can be inefficient if the uplink traffic is sparse, as many of them may go unused. *Sharing* radio resources among MTC devices can increase their usage [3]. However, it can result in packet collisions when two or more devices contend for the same resources, refer Fig. 1. These collisions may result in increasing load on the network due to re-transmissions [4].

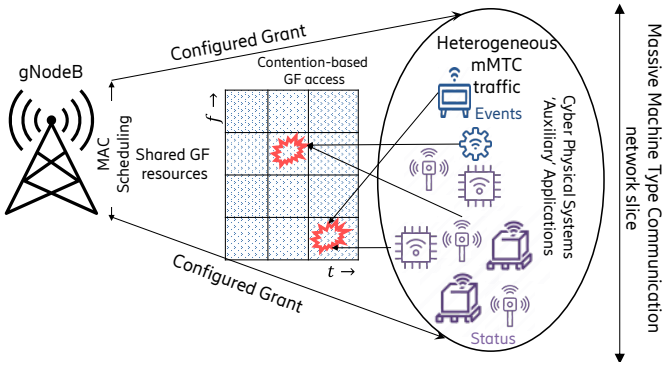

Fig. 1. Heterogeneous uplink mMTC traffic contend on the *shared* GF resources.

There are currently no standardized methods to ensure priority differentiation of shared configured grants (CG) in GF RA, within the 5G service categories such as mMTC. Addressing this issue also becomes important since third-generation partnership project (3GPP) mandates at least one GF uplink transmission mechanism for mMTC [2] and has decided to remove non-orthogonal multiple access (NOMA) from the work items for 5G new radio (NR).

Although timeliness and reliability constraints in the context of mMTC will always be less strict as compared to URLLC,

The work of Ranjan K. Mallik was supported in part by the Science and Engineering Research Board, a Statutory Body of the Department of Science and Technology, Government of India, under the J. C. Bose Fellowship.

Y. Kaura is with the Bharti School of Telecommunication Technology and Management, Indian Institute of Technology Delhi, Hauz Khas, New Delhi 110016, India (e-mail: yukti.kaura@dbst.iitd.ac.in).

B. Lall and R. K. Mallik are with the Department of Electrical Engineering, Indian Institute of Technology Delhi, Hauz Khas, New Delhi 110016, India (e-mail: brejesh@ee.iitd.ac.in, rkmallik@ee.iitd.ac.in).

A. Singhal is with the Department of Electronics and Communication Engineering, Netaji Subhas University of Technology, Sector 3 Dwarka, New Delhi 110078, India (e-mail: amit@nsut.ac.in).

Authorized licensed use limited to: DELHI TECHNICAL UNIV. Downloaded on November 11,2024 at 04:24:50 UTC from IEEE Xplore. Restrictions apply.
© 2024 IEEE. Personal use is permitted, but republication/redistribution requires IEEE permission. See https://www.ieee.org/publications/rights/index.html for more information.

This article has been accepted for publication in IEEE Transactions on Network and Service Management. This is the author's version which has not been fully edited and content may change prior to final publication. Citation information: DOI 10.1109/TNSM.2024.3493015

such constraints do exist. Communication services that support cyber-physical systems (CPS) 'control' applications need to have low latency and high reliability, which is why they can be classified under the 5G service category URLLC. On the other hand, communication services that cater to CPS 'auxiliary' applications can be categorized under the 5G service category mMTC [5]. Examples of auxiliary applications include asset monitoring in Industry 4.0 process automation. This is the focus of our work.

A. Related Work

1) On Existing and Proposed GF Schemes: The authors in [6] detail the approaches and challenges of GF access. The existing GF based approaches are detailed in [7]. They can be classified as standard GF schemes, which are supported in existing 5G releases and proposed GF schemes, which may be included in future 3GPP releases. Standard GF schemes are as follows: (i) ***Reactive GF***: Here a device must transmit GF data and await confirmation from the gNodeB before re-transmission; this is supported in 3GPP Release 15; (ii) ***K-repetitions GF without feedback*** [8]: Here GF transmission is blindly repeated K times. When K replicas are transmitted per packet, there is a possibility that packets may get queued up while the K replicas of the previous packet are being transmitted. This phenomenon is known as self-collision. According to authors in [8], queuing delays caused by self-collisions can significantly affect the capacity of K-repetitions. Numerous studies have suggested ways to enhance the effectiveness of existing GF schemes by combining them with other approaches. One such method, as proposed in [9], is to use an initial transmission on dedicated resource and blind re-transmission on a shared GF resource pool. The performance analysis of GF access schemes in the context of URLLC traffic with latency constraints and with multiple configured grants is done in [10] and [11] respectively. Recent research [12] proposes an enhanced GF scheme such that multi-packet reception can be enabled by leveraging sophisticated technologies with GF transmissions, such as non-orthogonal multiple access (NOMA) [13] and multiple-input multiple-output (MIMO) [14] with joint decoding. Authors in [15] and [16] describe mechanisms to allocate the appropriate number of GF radio resources based on the anticipated traffic load. However, the work described in [15] focuses on URLLC traffic, as the authors contend that the URLLC traffic displays strong correlation across adjacent time slots, and differs significantly from mMTC traffic. The research in [16] deals with the Markov decision process-based slot allocation for GB and GF transmission.

2) On QoS Based Scheduling in 5G NR: QoS-based schedulers have been investigated for 5G NR usage scenarios. A recent study has been published in [17], providing an analysis of scheduling algorithms for 5G use cases, including performance metrics and application suitability. In [18], the authors introduce 5MART, a scheduling framework for mixed traffic scenarios that employs RL to optimize *downlink* scheduling decisions. The study in [19] presents an RL-based resource allocation scheme designed for heterogeneous traffic, which balances QoS provisioning between low latency, high-reliability traffic such as URLLC, and high data rate traffic such as enhanced mobile broadband (eMBB). Most of these algorithms do not focus on mMTC nor consider the contention-based uplink for scheduling configured grants with QoS-based prioritization. Therefore, related work is quite limited.

3) On Priority-Enabled GF Schemes: Existing approaches dealing with priority-based differentiation of heterogeneous mMTC traffic in GFRA are rather nascent. In [20], an algorithm has been proposed for performing time slot-wise allocation to heterogeneous device traffic. Traffic priority-based resource partitioning in time domain seems to be counter-intuitive with the 'arrive and go' semantics of the GF access scheme. Therefore, we consider resource partitioning in frequency domain. In [21], a reservation system per device is developed to improve determinism in an NR unlicensed environment. The authors propose giving intra-group priority to devices for resolving conflicts, but the criteria for forming these groups has not been specified.

B. Motivation

In summary, the existing literature related to GF access either discusses the performance of standardized GF schemes or proposes new schemes attuned towards collision detection/reduction methods or discusses them in conjunction with URLLC and physical layer (PHY) technologies [4], [6]-[10], [12]-[14]. The literature related to 5G NR QoS-based medium access control (MAC) scheduling focuses mainly on scheduling of URLLC, eMBB traffic, or GB schemes [17]-[19]. The literature discussing priority-enabled GF access scheme with shared resources within the 5G service category mMTC establishes little with respect to QoS constraints or fairness [20]-[21], to the best of our knowledge.

The traffic generated by the mMTC devices is mostly uplink. Ideally, heterogeneous devices should not be scheduled on the same shared uplink grant resources which are contention-based. Re-transmissions and packet drops due to collisions may result in a snowball effect and impact the spectral efficiency of the network and energy budget of the devices. The MAC scheduler algorithms are implementation-specific functions and are not defined by the standards [22] and [23]. Therefore, the research question we address in this paper is the following: What algorithms can be applied for scheduling *shared configured grants* at the gNodeB MAC layer for heterogeneous device groups that can provide priority differentiation and improve the probability of successful transmission, and in doing so, lower the average age of information and packet drop rate? Our objective is to balance QoS constraints and fairness among the devices within an mMTC network slice which contend for shared resources. Our work considers the CPS and 5G setting for demonstrating the efficacy of the proposed approaches.

C. Main Contributions

The following are the main contributions of this work:

Authorized licensed use limited to: DELHI TECHNICAL UNIV. Downloaded on November 11,2024 at 04:24:50 UTC from IEEE Xplore. Restrictions apply.
© 2024 IEEE. Personal use is permitted, but republication/redistribution requires IEEE permission. See https://www.ieee.org/publications/rights/index.html for more information.

This article has been accepted for publication in IEEE Transactions on Network and Service Management. This is the author's version which has not been fully edited and content may change prior to final publication. Citation information: DOI 10.1109/TNSM.2024.3493015

- The uniqueness and novelty of this paper stem from its focus on algorithms for the gNodeB MAC layer to schedule *shared* GF resource within mMTC slice in order to enable priority-based GF access. The proposed methods are set in the backdrop of CPS and 5G and beyond networks.
- We derive an expression for the probability of successful transmission under various GF schemes, both with and without collision reduction.
- We introduce novel methods to adaptively partition and schedule GF bandwidth resources across heterogeneous device groups per allocation interval considering various aspects, such as joint maximization of expected transmission success rate, priority-weighting, and joint minimization of drop rate and average age of information.
- We propose a multi-objective RL based CG scheduling algorithm. In this method, two RL agents are trained with competing objectives. They are auto-switched to realize an *equability window*. This mechanism balances simultaneous fairness and QoS-based prioritization within heterogeneous traffic.
- We have conducted extensive simulations using various 5G NR numerologies to verify the accuracy of our proposed methods, and compared our results with existing GF schemes to demonstrate the effectiveness of our proposed approaches.
- Furthermore, integration of the proposed MAC layer scheduling approach with the 3GPP physical downlink control channel (PDCCH) has also been briefly discussed. The PDCCH is primarily used to carry scheduling information to individual UEs, i.e., resource assignments for uplink data transmission and other instructions.

D. Organization

The rest of this paper is organized as follows, Section II presents the system model. In Section III, we conduct an analysis of the probability of successful transmission. We then introduce AAoI and drop rate metrics based on the probability of successful transmission and detail the methodology for approximate arrival estimation. Next, in Section IV, we discuss our proposed algorithms. In Section V, numerical results are presented. The conclusion is provided in Section VI.

Notations: Boldface lower and upper case symbols represent vectors and matrices, respectively. The transpose operator is denoted by $(\cdot)^{\mathrm{T}}$. $\mathbb{E}[\cdot]$ denotes the expectation operator. $|\mathcal{X}|$ denotes the cardinality of set $\mathcal{X}$. We use $\mathbb{N}$ to denote the set of natural numbers and $\lfloor\cdot\rceil$ is the rounding operator.

II. System Model

Fig. 3 depicts the system model overview. Table I presents a summary of model notations. We consider a scenario in which heterogeneous mMTC devices connect with a single 5G base station gNodeB. Bandwidths $W_1, W_2, \ldots$ ($\hat{W}_k$ is for device group k) and $k = |\mathcal{Z}|$ are periodically decided by gNodeB at the beginning of each allocation interval T_A, and they stay unchanged during the entire T_A. There are two types of configured grants standardized by 3GPP [24]: Type 1 and Type 2. Type 1 provides an uplink grant via higher layer signaling, whereas Type 2 provides an uplink grant through PDCCH using physical layer signaling. In our work, we assume CG Type 2 because it allows for faster modification of configured grants. Our system model is at the stage where the Access class barring and random backoff procedures for the arriving devices has been completed and the devices are ready to transmit their packets, which is consistent with GF access models in literature [12]. Each device group would transmit data in the uplink direction. Immediate-first-transmission policy is adopted, i.e., a device will transmit in time $\tau + 1$, τ being the instant when data is received in the buffer. The priority of a given MTC device is known by gNodeB at the time of connection establishment and is utilized for *grouping* devices. We consider a one-hop wireless network where all devices are within communication range. A small packet size is considered with an assumption that each packet (and preamble) may require a resource block in the frequency domain and one transmission time interval (TTI)/ time slot in the time domain even with the lowest modulation and coding scheme. A resource block includes 12 consecutive sub-carriers in 5G NR systems. The GF bandwidth is divided into M resource blocks in one TTI. The base station gNodeB sends acknowledgements (ACK/NACK) over a separate narrow-band channel. These transmissions are considered to be both instantaneous and error-free. We focus on the probability of successful transmission as a baseline metric to determine the efficacy of our approach. However, other than collisions, there may be other errors, such as decoding failure and other channel impacts. Since we consider a relatively static positioning of devices and inorder to present the main idea, these errors are being omitted in the model.

We consider *symmetric* sources for a given device group. That is, when the state updates of all nodes are equally important, it is desirable for all nodes to achieve the same probability of successful transmission [25].

A. 5G NR Frame Structure and Numerology

5G NR offers a flexible numerology which allows for the configuration of scalable transmission time interval (TTI) per subframe. A shorter TTI is used for low latency and high reliability, while a longer TTI is used for high spectral

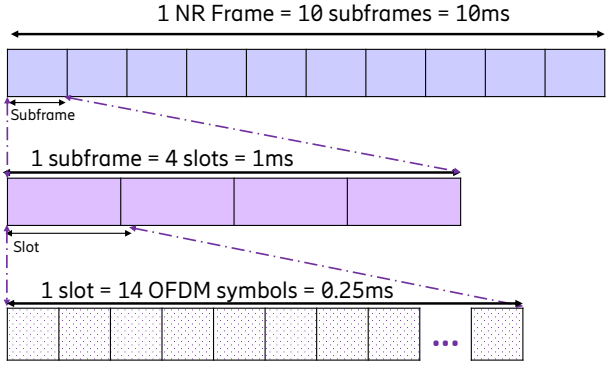

Fig. 2. 5G NR Frame structure with numerology $\beta = 2$.

Authorized licensed use limited to: DELHI TECHNICAL UNIV. Downloaded on November 11,2024 at 04:24:50 UTC from IEEE Xplore. Restrictions apply.
© 2024 IEEE. Personal use is permitted, but republication/redistribution requires IEEE permission. See https://www.ieee.org/publications/rights/index.html for more information.

This article has been accepted for publication in IEEE Transactions on Network and Service Management. This is the author's version which has not been fully edited and content may change prior to final publication. Citation information: DOI 10.1109/TNSM.2024.3493015

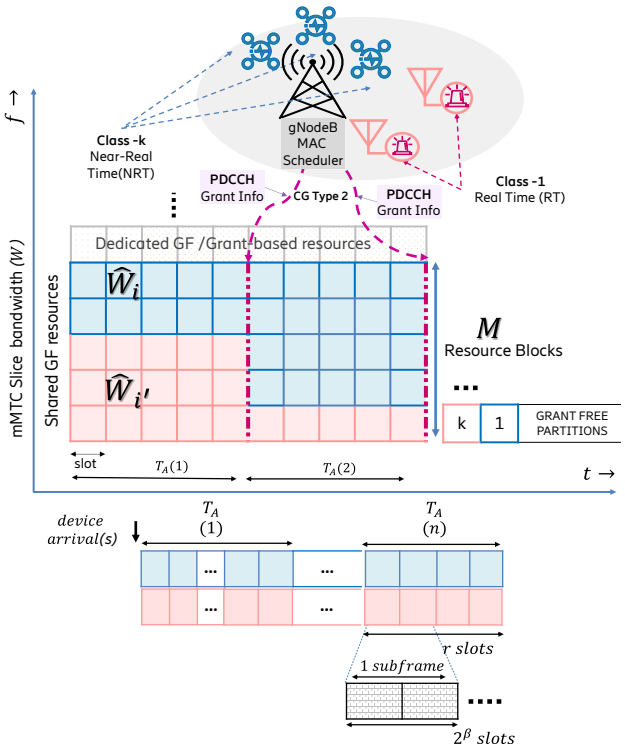

Fig. 3. System model overview.

efficiency. The NR numerology indicator, for this work is taken as β (instead of the default symbol μ as that represents inter-arrival time in our work). The per-frame duration in NR is 10 ms. A frame comprises 10 subframes, each with a duration of 1 ms refer Fig. 2. Furthermore, depending on the value of the numerology index β, one NR subframe may have one (for β = 0) or up to 16 slots (for β =1, 2, 3, 4) i.e., $N_{slot}^{subframe} = 2^\beta$. The number of subframes per allocation interval T_A are $r/2^\beta$ where r is the number of TTIs/slots in an allocation interval. Note that $r \geq 2^\beta$, and r is taken to be a multiple of 2^β. 14 Orthogonal Frequency Division Multiplexing (OFDM) symbols are being considered per slot. Consistent NR numerology is assumed across the available mMTC GF bandwidth.

B. Traffic Model

Table II, enlists traffic models used in 5G CPS standards research. We will be referencing this for our work. *Aperiodic model* refers to data transmission without a preset sending time. Typical activity patterns for which this kind of communication is suitable are event-driven actions. Diagnostic and maintenance events are example of aperiodic traffic. This assumes fixed packet size with *Poisson* arrivals, resulting in exponentially-distributed packet inter-arrival times. These constitute real-time (RT) device group in our work. The *periodic model* uses a fixed packet size and fixed packet inter-arrival time. However, different flows may have phase or time offset differences. These constitute near-real-time (NRT) device group for this study. In a realistic scenario it is reasonable to assume that different periodic mMTC traffic sources are asynchronous. A superposition of the asynchronous periodic traffic processes, from a large number of sources, can be approximated by a *Poisson* process, as studied in [26].

The nomenclature for device groups RT and NRT is chosen to establish their relative priority in terms of timeliness in 5G service category mMTC. RT device group has delay-constrained traffic, while NRT device has age of information (AoI) oriented traffic. AoI measures how recent the information is at the destination.

Let N_i be the number of *active* RT or NRT MTC devices, where $i \in \mathcal{Z}$ and $\mathcal{Z} = \{RT,\ NRT\}$, such that $N_{NRT} \neq N_{RT}$. The current problem scenario derived from [5] considers stationary devices; therefore the value of N_i can be determined in a given environment.

The probability mass function of the Poisson random variable X corresponding to the number of arrivals in an MTC device is given by

$$P\left(X = x\right) = \frac{\lambda_i^x e^{-\lambda_i}}{x!}, \quad x = 0, 1, 2, \ldots, \tag{1}$$

Average number of arrivals, $\lambda_i = T/\mu_i$, in an interval T. The average number of arrivals for a given allocation interval T_A is assumed to be constant but may vary across allocation intervals. Also, without loss of generality, re-transmissions are factored into the aggregate arrival rate to simplify analysis. (Please refer Subsection III-E for further details.)

III. Performance Analysis

We now derive the probability of successful transmission for different partitioning schemes. The analysis is extended further for formulating the algorithm for resource partitioning.

A. Probability of Successful Transmission

The probability of one or more than one transmissions in a given TTI (or time-slot) is given by

$$P_{1_i} = P(X > 0) = 1 - e^{-\lambda_i}. \tag{2}$$

It is assumed that only a single transmission is possible per device in a TTI . Considering one MTC device of interest belonging to device group i, the probability that no other device has transmission in the same TTI from the device group $N_i - 1$ is given by

$$P_{0_i} = (1 - P_{1_i})^{N_i - 1}. \tag{3}$$

The probabilities that c_i, $c_{i'}$ MTC devices from device groups $i, i' \in \mathcal{Z}$ and $i \neq i'$ have transmission occasions in the same time slot are given using the binomial distribution by

$$P_{f_i} = \binom{N_i - 1}{c_i} (P_{1_i})^{c_i} (1 - P_{1_i})^{N_i - c_i - 1}, \tag{4}$$

$$P_{f_{i'}} = \binom{N_{i'}}{c_{i'}} (P_{1_{i'}})^{c_{i'}} (1 - P_{1_{i'}})^{N_{i'} - c_{i'}}, \tag{5}$$

where the device of interest is in device group i. Let the probabilities that c_i , $c_{i'}$ MTC devices do not access the same resource block as the device of interest be P_{g_i}, $P_{g_i'}$ .... Note that the probability of accessing a given resource block *without*

Authorized licensed use limited to: DELHI TECHNICAL UNIV. Downloaded on November 11,2024 at 04:24:50 UTC from IEEE Xplore. Restrictions apply.
© 2024 IEEE. Personal use is permitted, but republication/redistribution requires IEEE permission. See https://www.ieee.org/publications/rights/index.html for more information.

This article has been accepted for publication in IEEE Transactions on Network and Service Management. This is the author's version which has not been fully edited and content may change prior to final publication. Citation information: DOI 10.1109/TNSM.2024.3493015

TABLE I
SUMMARY OF MODEL NOTATIONS

Notation	Description
i	Device group, $i \in \mathcal{Z}$ and $\mathcal{Z} = \{RT, NRT\}$
β	Numerology indicator in the NR frame structure $0 \leq \beta \leq 4$
N_i	Number of *active* MTC devices in device group i
T_A	Allocation interval. An allocation interval consists of d subframes and r time slots with $r = d \times 2^{\beta}$
μ_i	Average packet inter-arrival time for device group i
λ_i	Average number of arrivals for a device in group i (including both new & backlogged arrivals) in a time interval
n_i	$N_i\lambda_i$ total average number of arrivals for all devices in a device group i in a given time interval due to Poisson processes.
ρ	The partitioning factor $\rho \in (0, 1)$ represents the fraction of resources allocated to RT device group.
M	Total number of radio resource blocks in *shared* GF bandwidth in one TTI.
M_i	Resources allocated to a device group i.
P_{S_i}	Probability of successful transmission for device group i.
W	Bandwidth allocated to GF transmission in mMTC slice
$\hat{W}_k$	Partitioned bandwidth for index k, $k = \lvert\mathcal{Z}\rvert$
L	Threshold for number of devices that can be successfully decoded in the event of collision.
$\bar{\Delta}_i$	Average age of information for device group i
δ_i	Packet drop rate for device group i
$\mathcal{F}$	Re-transmission limit of packets, $\mathcal{F} \in \mathbb{N}$
$[\![V]\!]$	Iversion bracket representing variation in arrival rate.
Γ	Threshold number of allocation intervals beyond which NRT fairness mechanism i.e., equability window can be activated.
Θ	Threshold breach indicator

TABLE II
TRAFFIC MODELS USED IN 5G AND CPS STANDARDS RESEARCH [5]

Characteristic	**Periodic model**	**Aperiodic model**
Packet size	Fixed	Fixed
Inter-arrival time	Fixed	Statistical
Transmission	Unicast	Unicast

partitioning is $1/M$, where M is the total number of resource blocks. The event that there is no collision between the MTC device of interest and other MTC devices is either that the devices other than the device of interest do not transmit on the same resource block in a given time slot or do not transmit in a given time slot. This is captured as having a joint probability of all device groups transmitting in the same bandwidth resource, as

$$P_{S_i} = \left(\sum_{c_i=1}^{N_i-1} P_{f_i}\, P_{g_i} + P_{0_i}\right) \times \left(\sum_{c_{i'}=1}^{N_{i'}} P_{f_i'}\, P_{g_i'} + P_{0_i'}\right) \ \ldots\ , \tag{6}$$

where P_{S_i} corresponds to the probability of successful transmission of one MTC device in a given device group i. In (6), **[...]** represents that the expression would extend if there are more device groups.

1) **Case 1: Grant-Free Resource Sharing (GFRS)**
This is the default GF access scheme. Here, the entire bandwidth is *shared* between the devices. There is no partition specific to any device group.
The probability P_S can be derived from (6), where P_{g_i}, $P_{g_i'}$ are obtained as

$$P_{g_{RT}} = (1 - 1/M)^{c_{RT}}, \quad P_{g_{NRT}} = (1 - 1/M)^{c_{NRT}}. \tag{7}$$

GF Reactive : This scheme has been included in 3GPP, Release 15. It entails one GF initial transmission and re-transmission on NACK. The expression for the GFR scheme, considering one re-transmission attempt, can be formulated as

$$P_{S_{GFR}} = P_S + (1 - P_S)P_{S_1}P_{S_2}\,, \tag{8}$$

where P_S is the probability of success and is derived from (6), P_{S_1} is the probability of successful re-transmission and is assumed to be equal to P_S for the derivation, P_{S_2} is the error probability in the re-transmission. The expression in (8) is has been derived in [9].

2) **Case 2: Grant-Free Resource Partitioning (GFRP)**
Here the transmission bandwidth is partitioned into dedicated partitions for specific device groups. The partitioning factor $\rho \in (0, 1)$ determines the fraction of resources allocated to the RT device group and the open interval indicates an allocation lesser than maximum resources available. Since only one device group transmits in given bandwidth resources, the probability expression in (6) becomes

$$P_{S_i} = P_S \ = \sum_{c_i=1}^{N_i-1} P_{f_i}\, P_{g_i} + P_{0_i}\,. \tag{9}$$

Note that $P_{S_{RT}}$ and $P_{S_{NRT}}$ are derived from (9), where the expression for P_{g_i} is evaluated as

$$P_{g_{RT}} \ = \ (1 - 1/\lceil \rho M \rceil)^{c_{RT}}\,, \tag{10}$$

$$P_{g_{NRT}} \ = \ (1 - 1/\lceil (1-\rho) M \rceil)^{c_{NRT}}\ . \tag{11}$$

We can simplify (9) as

$$P_{S_i} = \sum_{c_i=0}^{N_i-1} \binom{N_i - 1}{c_i} (e^{-\lambda_i})^{N-c_i-1} \left((1 - e^{-\lambda_i}) \left(\frac{M_i - 1}{M_i}\right)\right)^{c_i}, \tag{12}$$

Authorized licensed use limited to: DELHI TECHNICAL UNIV. Downloaded on November 11,2024 at 04:24:50 UTC from IEEE Xplore. Restrictions apply.
© 2024 IEEE. Personal use is permitted, but republication/redistribution requires IEEE permission. See https://www.ieee.org/publications/rights/index.html for more information.

This article has been accepted for publication in IEEE Transactions on Network and Service Management. This is the author's version which has not been fully edited and content may change prior to final publication. Citation information: DOI 10.1109/TNSM.2024.3493015

where M_i is the number of resource blocks allocated to the device group i: $M_i = \rho M$ for RT device group and $(1-\rho)M$ for NRT device group. Simplifying equation (12) using the binomial theorem, we obtain
Thus, for an allocation interval T_A we have

$$P_{S_i} = \left(\frac{e^{-r \times \lambda_i} + r \times M_i - 1}{r \times M_i} \right)^{N_i - 1}. \quad (13)$$

1) Constraint on Probability of Successful Transmission: To support a minimal constraint for the probability of successful transmission by a given device group, we arrive at a value for $\hat{M}_i$ bandwidth resources using (13) as

$$\hat{M}_i = \left\lfloor \frac{1 - e^{-\lambda_i}}{1 - (P_{S_i,\,\theta_x})^{(1/(N_i-1))}} \right\rceil, \quad (14)$$

where $P_{S_i,\,\theta_x}$ is the constraint on the probability of successful transmission for given latency targets, $P_{S_i,\,\theta_x} < 1$ and $x \in \{1, 2\}$. The expressions $P_{S_i,\,\theta_1}$ and $P_{S_i,\,\theta_2}$ represent upper and lower transmission success probability thresholds, respectively. It is assumed that $\theta_1 > \theta_2$. We can calculate the minimum required bandwidth resources $\hat{M}_{RT}$, $\hat{M}_{NRT}$ from (14). It can be observed that $\min \hat{M}_{NRT}$ is 1 because of the rounding function $\lfloor . \rceil$.

B. Probability of Successful Transmission With Collision Reduction

This scheme operates on the premise that the gNodeB can reliably decode multiple transmissions from devices sharing the same resource block, provided the number of devices does not exceed a specified threshold, represented by L. This threshold is influenced by several physical layer (PHY) factors, such as transmission power and receiver performance. Accordingly, in (9), the probability that the device of interest collides with other devices $(l \leq L-1)$ but the packet is still decodable and can be written as

$$P_{S_i} = \sum_{c_i=1}^{N_i-1} P_{f_i} \sum_{l=0}^{L-1} P_{g_i} + P_{0_i}, \quad (15)$$

where P_{g_i}, the probability that l devices in c_i devices access the same block as the device of interest, is given by

$$P_{g_i} = \binom{c_i}{l} \left(\frac{1}{M_i} \right)^l \left(1 - \frac{1}{M_i} \right)^{c_i - l}. \quad (16)$$

C. Proportionally Fair Partitioning Factor

Lemma 1. *There exists a proportionally fair partitioning factor $\widetilde{\rho}$ which jointly maximizes the expected successful transmission rate for both device groups such that $\forall \lambda_i, \lambda_{i'} > 0$ and for $N_i, N_{i'} >> 1$,*

$$\widetilde{\rho} = \frac{N_i \sqrt{(1 - e^{-\lambda_i})}}{N_i \sqrt{(1 - e^{-\lambda_i})} + N_{i'} \sqrt{(1 - e^{-\lambda_{i'}})}}, \quad (17)$$

where $i \neq i'$.

Proof. Please see Appendix A for the proof. ■

We now proceed to derive average age of information and packet drop rate in terms of probability of successful transmission.

D. Average Age of Information (AAoI)

The age of information (AoI), denoted as Δ_i for device group i represents how "fresh" the information is from the perspective of the receiver. Consider a source-destination communication dyad. The AoI quantifies the freshness at any given time as the elapsed time since the last received status update was generated by the source [27]. Timely updating a destination about a remote system is not the same as maximizing the utilization of the communication system or ensuring that generated status updates are received with the smallest possible latency [28]. We assume that the system employs the standard automatic repeat request (ARQ) protocol, which discards failed transmissions at the destination. The device would update its status at next transmission.

1) Average Age of Information (AAoI) and Probability of Successful Transmission: We provide here the analysis for the AAoI with standard ARQ. As the AoI state of the receiver only depends on the state in the previous time slot, it can be modeled as a discrete-time Markov chain (DTMC). Let $A_i(t) \in \mathbb{N}$ depict the AoI at time instant t for device group i. At each time slot, the AoI with standard ARQ drops to one in the case of successful status update, implying $A_i(t+1) = 1$; otherwise it increases to $A_i(t) + 1$.

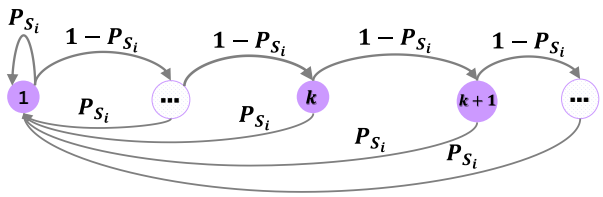

Fig. 4. Discrete Time Markov Chain for AoI with standard ARQ.

The corresponding DTMC is shown in Fig. 4, where P_{S_i} represents probability of successful transmission for device group i as described in Sec. III-A.

The row-stochastic transition probability matrix $\mathbf{P}_i$ of the Markov chain is given by (initial states are indexed by rows and final states are indexed by columns)

$$\mathbf{P}_i = \begin{bmatrix} P_{S_i} & 1 - P_{S_i} & & \\ P_{S_i} & & 1 - P_{S_i} & \\ \vdots & & & \ddots \end{bmatrix}. \quad (18)$$

We denote the steady state distribution of the Markov chain by $\pi(i) = [\pi_1(i), \pi_2(i), \cdots]$, with the equilibrium equation $\pi(i)\mathbf{P}_i = \pi(i)$. Also, the following conditions should hold: $\sum_{k=1}^{\infty} \pi_k(i) = 1$ and $\pi_k(i) \geq 0 \ \forall k$. On solving the steady state equations, the state probabilities are obtained as

$$\pi_k(i) = \begin{cases} P_{S_i}, & k = 1, \\ (1 - P_{S_i})^{(k-1)} P_{S_i}, & k > 1. \end{cases} \quad (19)$$

where $\pi_k(i)$ represents the probability for the AoI to have the value of k. We can now obtain the expression for the AAoI. The AAoI $\bar{\Delta}_i$ is calculated as

Authorized licensed use limited to: DELHI TECHNICAL UNIV. Downloaded on November 11,2024 at 04:24:50 UTC from IEEE Xplore. Restrictions apply.
© 2024 IEEE. Personal use is permitted, but republication/redistribution requires IEEE permission. See https://www.ieee.org/publications/rights/index.html for more information.

This article has been accepted for publication in IEEE Transactions on Network and Service Management. This is the author's version which has not been fully edited and content may change prior to final publication. Citation information: DOI 10.1109/TNSM.2024.3493015

$$\bar{\Delta}_i = \sum_{k=1}^{\infty} k\pi_k(i) = \sum_{k=1}^{\infty} k(1-P_{S_i})^{(k-1)}P_{S_i} = \frac{1}{P_{S_i}}. \quad (20)$$

Note that $\bar{\Delta}_i$ of a single user equipment is the reciprocal of the probability of successful transmission. Considering the symmetry between sources in a device group, the AAoI of the device group is also the reciprocal of the probability of successful transmission.

E. Packet Drop Rate

The packet drop rate, denoted as δ_i for device group i, is the ratio of the number of requests that did not succeed in any of the transmission attempts to the total number of initial requests transmitted. In other words, δ denotes the probability that a user equipment request is unsuccessful in all its transmission attempts and, as a result, drops its request.

1) Drop Rate and Probability of Successful Transmission: Here we provide the expression for the drop rate of a device. We consider that if a packet from a device is not successfully transmitted because of collisions, we have the option to re-transmit it. In particular, we re-transmit the packet until its successful transmission limit after which the packet would be dropped. Due to the presence of delay constraints (albeit relaxed in the context of mMTC) and a GF scheme, we are considering "fast retrials" as described in [29]. This method utilizes multiple channels to re-transmit data in a 1-persistent type manner, without the use of exponential backoff. The arriving packets are stored in a buffer.

More specifically, we consider the traffic with a delay bound $\mathcal{D}$ and a re-transmission limit $\mathcal{F}$. The maximum number of transmissions that can take place is $\mathcal{F}+1=\mathcal{D}$ subframes in time.

The probability that d subframes are required to successfully make a transmission in an allocation interval is expressed as

$$P\{\text{delay} = d+1\} = P_{S_i}(1-P_{S_i})^d,\ 0 \le d \le T_A, \quad (21)$$

where each subframe d is composed of 2^β time slots and P_{S_i} represents the probability of successful transmission for device group i. The probability that the delay is smaller than or equal to $\mathcal{D}$ is given by

$$\begin{aligned} P\{\text{delay } \le \mathcal{D}\} &= P_{S_i}\sum_{d=0}^{\mathcal{D}-1}(1-P_{S_i})^d \\ &= 1-(1-P_{S_i})^{\mathcal{D}}. \end{aligned} \quad (22)$$

Accordingly, the drop rate or probability that a packet will be dropped after $\mathcal{D}=\mathcal{F}+1$ transmission attempts is $P\{\text{delay } > \mathcal{D}\} = 1 - P\{\text{delay } \le \mathcal{D}\}$ and is given by

$$\delta_i = (1-P_{S_i})^{\mathcal{D}}. \quad (23)$$

The probability of the device being successful in one of its (at most $\mathcal{F}$+1) transmission attempts is $1-\delta_i$.

Recall that our system model considers that the total arrivals consists of both re-transmissions and new arrivals. The backlogged arrival rate due to collisions is reduced at each subframe, by a factor φ which is the ratio of actual number of re-transmissions in current subframe d to the number of collisions that happened at previous subframe $d-1$. This is because of the packet drops which exhaust their re-transmission attempts. This can be expressed as

$$\lambda_i(d) = \lambda_a + \varphi\lambda_i(d-1)(1-P_{S_i}).$$

Since the maximum number of re-transmissions is bounded by $\mathcal{F}$, the added arrival rate is reduced by a factor φ, where φ is the ratio of re-transmissions to the number of collisions in the previous interval and λ_a represents new arrivals. We express φ as

$$\varphi = \frac{\sum_{d=0}^{\mathcal{F}-1}(1-P_S)^d}{\sum_{d=0}^{\mathcal{F}}(1-P_S)^d}.$$

F. Arrival Estimation

The number of device arrivals varies over time and gNodeB can monitor the transmission states of resource blocks (success, collision, and empty) to make an arrival estimation. Few approaches pertaining to mMTC traffic are detailed in [30]-[31]. Reference [31] derived the joint distribution function of the number of successful and collided transmission attempts (A detailed arrival estimator is out of the scope of this paper).

Let the estimated number of total arrivals for a device group in a given allocation interval be denoted as $\hat{n_i}(T_A) = N_i\hat{\lambda}_i(T_A)$. The base station gNodeB needs to be able to detect changes in the arrival rate. For this, gNodeB can maintain a moving average on the average number of estimated arrivals for device group i, which is $\mathbb{E}[\hat{n}_i(T_A)]$, with a sliding window of x configurable allocation intervals, as outlined in [16]. If $\mathbb{E}[\hat{n}_i(T_A)]$ is beyond the range of $\mathbb{E}[\hat{n}_i(T_A-1)] \pm \Phi$, where Φ is the change threshold, then it indicates that a change in arrival rate has happened.

Let V be the condition that variation in arrival rate is detected. Then the indicator function in terms of the Iversion bracket is given by

$$[\![V]\!] = \begin{cases} 1, & \text{if } V \text{ is true;} \\ 0, & \text{otherwise.} \end{cases} \quad (24)$$

If the indicator is set, then the decided time-frequency resource allocation (CG scheduling) would be transmitted to all devices through a downlink control. If no downlink control message is received, the devices continue transmitting with the same resource allocation information value used in the previous allocation interval. To further define our methodology, we will utilize the expression provided in (24).

IV. Proposed Method

We introduce adaptive GF resource partitioning (AGFRP) that determines the partitioning of GF bandwidth resources across device groups at each allocation interval based upon estimated arrivals. At each T_A, gNodeB MAC Scheduler can utilize AGFRP to schedule configured grants to heterogeneous device groups. The grant information (time-frequency resource allocation) for uplink is relayed by gNodeB to MTC devices through PDCCH via the downlink control information [32]. The MTC device performs uplink transmission based upon this grant information.

We introduce the following three scheduling algorithms:

Authorized licensed use limited to: DELHI TECHNICAL UNIV. Downloaded on November 11,2024 at 04:24:50 UTC from IEEE Xplore. Restrictions apply.
© 2024 IEEE. Personal use is permitted, but republication/redistribution requires IEEE permission. See https://www.ieee.org/publications/rights/index.html for more information.

This article has been accepted for publication in IEEE Transactions on Network and Service Management. This is the author's version which has not been fully edited and content may change prior to final publication. Citation information: DOI 10.1109/TNSM.2024.3493015

1) Proportionally Fair-AGFRP;
2) Priority-Based-AGFRP;
3) Multi-Objective RL-AGFRP.

A. Proportionally Fair-AGFRP (PF-AGFRP)

The proportionally fair partitioning scheme is dependent on the calculation of the optimal partitioning factor $\widetilde{\rho}$, which has been derived in (17). Once $\widetilde{\rho}$ is obtained, it is straightforward to calculate P_{S_i} for device groups RT and NRT from (13) with $\rho = \widetilde{\rho}$. It is a straightforward and computationally efficient method which performs unbiased resource partitioning in each allocation interval to jointly maximize the transmission success rate for both device groups. PF-AGFRP helps to gather insights into the performance of other scheduling algorithms with respect to fairness. Since this scheme does not favor any one device group over the other, which is required as per our problem statement, we further propose a priority-based method to provide preferential access to device group RT.

Algorithm 1: Proportionally Fair-AGFRP

Input: Estimated request arrival rate: $\hat{n}_i(T_A)$ for device group i, where $i \in \{RT, NRT\}$, $T_A = r\times$TTI
Resources: M resource blocks in GF bandwidth W
for $T_A = 1, 2, \cdots$ **do**
  Set $n_i(T_A) = \hat{n}_i(T_A)$;
  if $[\![V]\!]$ **then**
    $\widetilde{\rho} = \frac{N_{RT}\sqrt{(1-e^{-\lambda_{RT}})}}{N_{RT}\sqrt{(1-e^{-\lambda_{RT}})}+N_{NRT}\sqrt{(1-e^{-\lambda_{NRT}})}}$;
    $M_{RT} \leftarrow \lfloor \widetilde{\rho} M \rfloor$;
    $M_{NRT} \leftarrow \lfloor (1-\widetilde{\rho}) M \rfloor$;
    $\hat{W}_i = r \times \ M_i$
    Broadcast configured grants as time-frequency resource allocation information $\hat{W}_i$ to all devices, using downlink signaling;
  end
end

B. Priority-Based-AGFRP (PB-AGFRP)

The algorithm 1 delineates the mechanism of PB-AGFRP. When adequate resources are available, i.e., under *normal traffic load*, both RT and NRT device groups are allocated required resources and remaining bandwidth resources are allocated proportionally based on the estimated arrival rate of a device group. When adequate resources are unavailable, i.e., in *heavy traffic load*, bandwidth resource allocation is done by scaling the normalized allocation for the RT device group with prioritization factor α, the remaining resources are allocated to device group NRT. The prioritization factor $\alpha \in [0, 1)$ controls the bandwidth scaling provided to device group RT and α only plays a role if the overall bandwidth is insufficient to satisfy the traffic load of both device groups. If $\alpha = 0$, then bandwidth resources are allocated proportionally; if $\alpha \approx 1$, then device group RT gets nearly complete bandwidth and corresponds to strict prioritization. If $0 < \alpha < 1$, then device group RT obtains a weighted portion of the bandwidth. The open boundary in α's upper range ensures that some resources are always available to device group NRT for transmission.

Algorithm 2: Priority-Based-AGFRP

Input: Estimated request arrival rate: $\hat{n}_i(T_A)$ for device group i, where $i \in \{RT, NRT\}$, $T_A = r\times$TTI
Constraints: P_{S_{RT},θ_1}, P_{S_{NRT},θ_2}
Resources: M resource blocks in GF bandwidth W
Prioritization factor: α, $\alpha \in [0, 1)$
for $T_A = 1, 2, \cdots$ **do**
  Set $n_i(T_A) = \hat{n}_i(T_A)$;
  if $[\![V]\!]$ **then**
    Calculate $\hat{M}_i$ from (14), $\forall i \in \{RT, NRT\}$;
    if $M > (\hat{M}_{RT} + \hat{M}_{NRT})$ **then**
      $M_{RT} \leftarrow \lfloor \hat{M}_{RT} + \widetilde{\rho}(M - \hat{M}_{RT}) \rceil$;
    end
    else if $M \leq (\hat{M}_{RT} + \hat{M}_{NRT})$ **then**
      $M_{RT} \leftarrow \left\lfloor (M - min\ \hat{M}_{NRT}) \left(\frac{\hat{M}_{RT}}{\hat{M}_{RT} + \hat{M}_{NRT}} \right)^{(1-\alpha)} \right\rfloor$;
    end
    $\rho = M_{RT}/M$;
    $M_{NRT} \leftarrow \lfloor (1-\rho) M \rfloor$;
    $\hat{W}_i = r \times \ M_i$
    Broadcast configured grants as time-frequency resource allocation information $\hat{W}_i$ to all devices, using downlink signaling;
  end
end
End Procedure

C. Multi-Objective RL-AGFRP (MORL-AGFRP)

PB-AGFRP becomes biased as α increases, which prioritizes successful transmission of device group RT over device group NRT. This could lead to starvation of NRT device group. Therefore, an RL-based AGFRP scheme is further proposed as a multi-objective optimization problem to jointly minimize the drop rate and AAoI of RT and NRT device groups, respectively.

1) Optimization Problem Formulation: Weighted multi-objective optimization includes scalarizing a set of objectives into a single objective by adding each objective pre-multiplied by a weight. The weight of an objective is chosen in proportion to the relative importance of the objective. To achieve the optimal performance of both device groups in terms of timeliness (which are relatively less strict for mMTC), we present the optimization problem of simultaneously minimizing the drop rate of RT device group δ_{RT} and the AAoI of NRT device group $\bar{\Delta}_{NRT}$. This can be done by adjusting the transmission success probabilities $P_{S_{RT}}$ and $P_{S_{NRT}}$ which are in turn dependent on the value of the partitioning factor ρ. The general optimization formulation is given by

$$\min_{\rho} \ F(\rho) = w_1 f_1(\delta_{RT}(\rho)) + w_2 f_2(\bar{\Delta}_{NRT}(\rho))$$
$$\text{subject to } \ \delta_{RT} \approx 0, \ \bar{\Delta}_{NRT} \approx \bar{\bar{\Delta}},$$
$$\bar{\bar{\Delta}} = 1, \ \rho \in \ (0, 1),$$

where w_1 and w_2 are the weights of the objective functions f_1 and f_2 and $\bar{\bar{\Delta}}$ is the ideal average staleness the NRT device group can tolerate. To solve this optimization problem, we present an RL based solution.

2) Markov Decision Process (MDP) and Online Reinforcement Learning (RL): An MDP is a discrete-time stochastic

Authorized licensed use limited to: DELHI TECHNICAL UNIV. Downloaded on November 11,2024 at 04:24:50 UTC from IEEE Xplore. Restrictions apply.
© 2024 IEEE. Personal use is permitted, but republication/redistribution requires IEEE permission. See https://www.ieee.org/publications/rights/index.html for more information.

This article has been accepted for publication in IEEE Transactions on Network and Service Management. This is the author's version which has not been fully edited and content may change prior to final publication. Citation information: DOI 10.1109/TNSM.2024.3493015

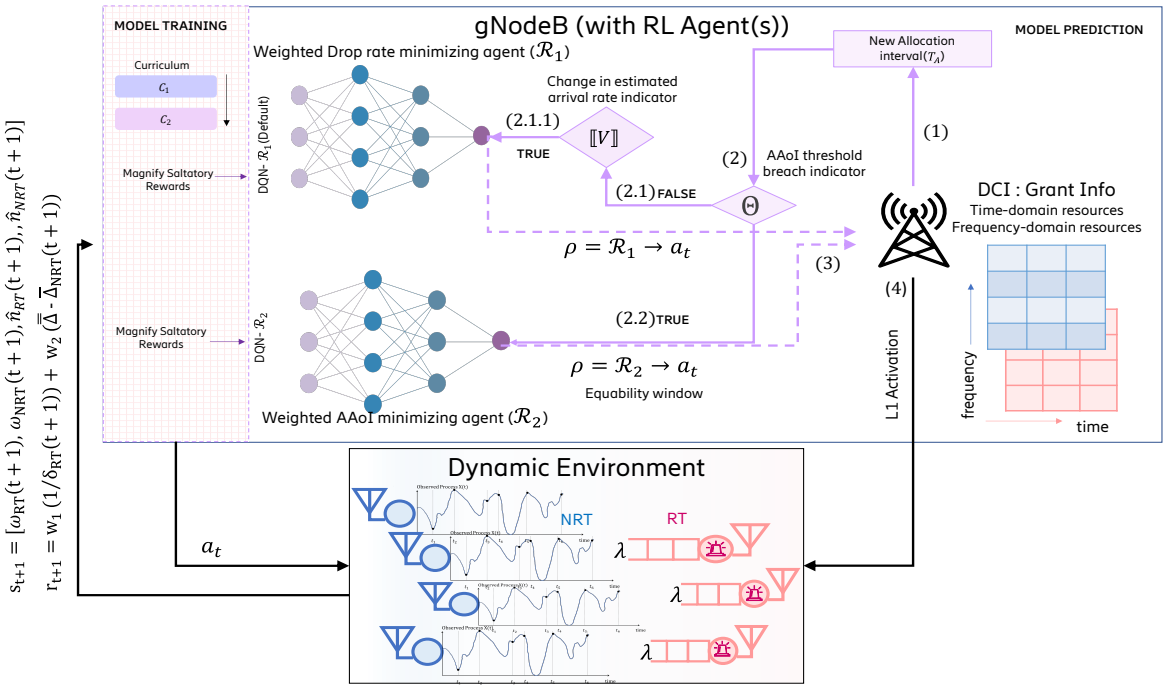

Fig. 5. MORL-AGFRP overall flow: Training and inference.

control process in which agent and environment interact at discrete time steps $t = 0, 1, 2, \ldots$. Let $\mathcal{S}$ and $\mathcal{A}(s)$ denote, respectively, the set of finite states and the set of finite actions available at state s for a given finite MDP. At time step t, an agent receives the representation of the environment's state $s_t \in \mathcal{S}$. It then selects an action $a_t \in \mathcal{A}(s)$. As a consequence of the action, the agent moves to a new state s_{t+1} and receives a reward $r_{t+1} \in R$, where R denotes the set of rewards. The core task for MDP based decision making is to find a policy, i.e., a function $\pi(s)$, that leads to an optimal decision for a given criterion. RL uses the formal framework of the MDP to define the interaction between a learning agent and its environment in terms of states, actions, and rewards as summarized in [33].

3) Q-Learning and Deep Q-Network (DQN): Q-Learning and DQN [34] are core methods in RL. Q-Learning is best suited for RL agents with discrete action spaces. Q-Learning is an *off-policy* algorithm which is based on the notion of a Q-function (the state-action value function) of a policy π, and $Q_\pi(s,a) = \mathbb{E}_\pi[G_t | \mathcal{S}_t = s, \mathcal{A}_t = a]$, with $\mathbb{E}$ denoting the expectation operator, measures the expected return or discounted sum of rewards obtained from state s by taking action a first and following policy π thereafter. Note that $G_t = \sum_{k=0}^{\infty} \gamma^k R_{t+k+1}$, with R_{t+k+1} denoting the reward at time index $t+k+1$, is the expected return and γ is the discount factor. The optimal Q-function follows the Bellman optimality equation $Q^*(s,a) = \mathbb{E}\left[R_{t+1} + \gamma \max_{a'} Q^*(s', a')\right]$.

A DQN learns the action value function Q^* by minimizing the loss function $\mathcal{L}(\theta) = \mathbb{E}_{s,a,r,s'}[(y - Q^*(s,a;\theta))^2]$, where $y = r + \gamma \max_{a'} \hat{Q}^*(s', a')$. Here y is the TD (temporal difference) target and $\hat{Q}$ is a target Q-function whose parameters are periodically updated with set of weights θ. The DQN for $\hat{Q}$ is called the *target network*. This method helps to stabilize learning. Another component for stabilizing DQN learning is an *experience replay buffer* ($\mathcal{B}$) containing transition tuples (s, a, r, s'), for better stability. Epsilon (ϵ)-greedy is a policy used to balance exploration and exploitation, ϵ refers to the probability of choosing to explore, i.e., take a random action, and $1 - \epsilon$ is the probability to exploit, i.e., take greedy action which fetches the maximum value.

4) RL States, Actions, and Reward:

i) *State Space:* In a physical environment, the state in terms of successful transmission can be observed as the *transmission success rate*. Transmission success rate is the ratio between the total number of successfully transmitted devices and the total number of devices in device group i, which arrived during an allocation interval T_A. The transmission success rate for a device group i in an allocation interval T_A, denoted by $\omega_i(T_A)$, is calculated as

$$\omega_i(T_A) = \frac{\sum_{t=1}^{r} succ_i(t)}{\hat{n}_i(T_A)}, \tag{25}$$

where $\hat{n}_i(T_A)$ denotes the estimated number of arrivals for device group i, the allocation interval consists of r time slots, and $succ_i(t)$ represents the number of successful transmissions in time slot t.

The transmission success rate of RT and NRT device groups and the estimated arrivals at time t constitute the state at time t, i.e., $s_t = [\omega_{RT}(t), \omega_{NRT}(t), \hat{n}_{RT}(t), \hat{n}_{NRT}(t)]$ where $s_t \in \mathcal{S}$. The physical environment will determine the estimated device arrivals at time t, i.e., $\hat{n}_{RT}(t)$, $\hat{n}_{NRT}(t)$, whereas the action a_t at time instant t will result in transmission success rates $\omega_{NRT}(t+1)$ and $\omega_{RT}(t+1)$

Authorized licensed use limited to: DELHI TECHNICAL UNIV. Downloaded on November 11,2024 at 04:24:50 UTC from IEEE Xplore. Restrictions apply.
© 2024 IEEE. Personal use is permitted, but republication/redistribution requires IEEE permission. See https://www.ieee.org/publications/rights/index.html for more information.

This article has been accepted for publication in IEEE Transactions on Network and Service Management. This is the author's version which has not been fully edited and content may change prior to final publication. Citation information: DOI 10.1109/TNSM.2024.3493015

at time $t+1$. Hence the state transition satisfies the Markov property. The transmission success rate further determines $\delta_{RT}(t+1)$ and $\bar{\Delta}_{NRT}(t+1)$.

ii) *Action Space:* The action space is defined by $\mathcal{A} \in \{1, \ldots, M_{RT}\}$, where M_{RT} is the maximum number of resources that can be allocated to the RT device group at a given time and $M_{RT} < M$. The fraction of resources to be allocated to RT at any given time t is denoted by $\rho(t)$ and the allocation to NRT is denoted by $1-\rho(t)$. The agent can adjust $\rho(t)$ by choosing an action a_t from a discrete action space $\mathcal{A}$ such that $\rho(t) = \{a_t/M \mid a_t \in \mathcal{A}\}$ and $\rho(t) \in (0,1)$. The agent thus chooses actions with the goal to maximize its expected return.

iii) *Reward Function:* Let $\boldsymbol{w} = [w_1, w_2]^T$, with $(\cdot)^T$ denoting the transpose operator, represent the weight vector corresponding to the relative importance of the two objectives. The reward function $f_r(s_t; \mathbf{w})$ quantifies the objective to achieve the lowest possible drop rate for RT device group with lowest possible AAoI for NRT device group which is aligned to our optimization problem definition in Subsection IV-C1. A weighted linear reward function which determines r_{t+1} is given by

$$f_r(s_{t+1}; \boldsymbol{w}) = w_1 \left(\frac{1}{\delta_{RT}(t+1)} \right) + w_2 \Big(\bar{\bar{\Delta}} - \bar{\Delta}_{NRT}(t+1) \Big), \tag{26}$$

where r_{t+1} is the reward obtained by taking action a_t at time t and transitioning to state s_{t+1}. For minimizing the objective function with $\bar{\Delta}_{NRT}$, the distance to the ideal AAoI is penalized, i.e., greater the distance less the reward. For minimizing the objective function with δ_{RT} we take its inverse. The reward components are calculated on the same scale to rank each component's importance appropriately. We use a scalarized reward function in our multi-objective RL formulation because, in comparison to a time complexity $O(\mathcal{T})$ for the algorithm using the scalar reward function, the algorithm employing an n-dimensional reward function imbibes a time complexity of $O(\mathcal{T}^n)$! as described in [35].

5) RL Agent Training: The training for RL agents (model) is performed as detailed in Algorithm 3. Two agents $\mathcal{R}_1$ and $\mathcal{R}_2$ are trained with different weights: one prioritizing minimization of the drop rate and the other the AAoI. The training comprises of two phases: an offline model training phase and a online reinforcement learning phase.

i) *Magnify Saltatory Reward (MSR)* MSR is an optimization approach for the reward function, it modifies rewards before storing the experience in $\mathcal{B}$. It magnifies the current reward value for a positive saltation and reduces the current reward for a negative saltation to improve the network convergence speed of DRL [36]. In our case, we take an exponentiation of the reward for its magnification.

ii) *Curriculum Learning* We train our agents with curriculum learning. Our curriculum scheme is designed to give the agent step-wise exposure to the environment. The curriculum criterion at level l, denoted as C_l, is increased as the agent improves. The levels correspond to varying traffic arrivals at different configurations of NR numerology indicator β.

Algorithm 3: Multi-Objective RL-AGFRP | Training

Input:
T: Total number of time steps
$\mathcal{R}_1$: Weighted drop rate minimizing agent
$\mathcal{R}_2$: Weighted AAoI minimizing agent
w_1: Reward weight for drop rate
w_2: Reward weight for AAoI
ϕ: Reward saltation function
C_l: Curriculum criterion, at level l
Env: Environment for training the RL agents
Initialization:
Initialize reward weights of $\mathcal{R}_1$ such that, $w_1 > w_2$
Initialize reward weights of $\mathcal{R}_2$ such that, $w_1 \ll w_2$
$w_1, w_2 > 1$
$Env \leftarrow Env\ (C_l)$
Training:
for *RL agents* $\in \mathcal{R}_1, \mathcal{R}_2$ **do**
  for *episode* $= 1, ..., M$ **do**
    for $t = 1, ..., T$ **do**
      Determine a_t using $\epsilon-$greedy policy;
      Take action and observe the environment; the environment steps into a new state s_{t+1};
      Compute the reward r_{t+1};
      Magnify saltatory rewards $r^*_{t+1} = r^{\phi}_{t+1}$;
      Store the transition $(s_t, a_t, r^*_{t+1}, s_{t+1})$ into replay buffer $\mathcal{B}$;
    end
    Randomly sample a mini-batch of the transitions $(s_j, a_j, r_{j+1}, s_{j+1})$ from $\mathcal{B}$;
    Compute $\nabla_\theta \mathcal{L}(\theta) = \nabla_\theta \sum_i (r(s_j, a_j) + \gamma \max_{a_{j+1}} Q(s_{j+1}, a_{j+1}; \theta) - Q(s_{j+1}, a_{j+1}; \theta))^2$;
    Perform gradient descent $\theta^{(j+1)} = \theta^{(j)} - \eta \nabla_\theta \mathcal{L}(\theta)$;
  end
end

The algorithm 4 delineates our proposed approach for MORL-AGFRP inference. The scheme attempts joint minimization of both drop rate and AAoI. The multi-agent learning system consists of two trained RL agents $\mathcal{R}_1$, $\mathcal{R}_2$ which take decisions under different environmental conditions. Agent $\mathcal{R}_1$ is the weighted drop rate minimizing agent and is the default agent. It takes the partitioning decision on every allocation whenever the expected arrival rate changes beyond a certain defined range. Agent $\mathcal{R}_2$, which is the weighted AAoI minimizing agent, takes the partitioning decision whenever the AAoI of device group NRT goes below a defined threshold $\widetilde{\Delta}$ for Γ consequent allocation intervals. This leads to the setting of Θ which is the AAoI threshold breach indicator. The algorithm realizes an $equability$ window, which allows NRT devices to preferentially transmit status updates in order to facilitate maintaining freshness of information at the destination. The approach is depicted in Fig. 5.

i) *Computational Complexity* The complexity of an algorithm can be described in terms of the Big-O notation. Big-O notation is a mathematical notation used to describe and compare the asymptotic behavior or complexity of an algorithm. Here the focus is on how the number of operations scales with the problem size rather than the exact number of operations.We utilize Big-O notation for

Authorized licensed use limited to: DELHI TECHNICAL UNIV. Downloaded on November 11,2024 at 04:24:50 UTC from IEEE Xplore. Restrictions apply.
© 2024 IEEE. Personal use is permitted, but republication/redistribution requires IEEE permission. See https://www.ieee.org/publications/rights/index.html for more information.

This article has been accepted for publication in IEEE Transactions on Network and Service Management. This is the author's version which has not been fully edited and content may change prior to final publication. Citation information: DOI 10.1109/TNSM.2024.3493015

Algorithm 4: Multi-Objective RL-AGFRP | Inference

Input: Estimated request arrival rate: $\hat{n}_i(T_A)$ for device group i, where $i \in \{RT, NRT\}$, $T_A = r\times$ TTI
Resources: M resource blocks in GF bandwidth W
Initialize:
$\mathcal{R}_1$: Trained weighted drop rate minimizing RL agent
$\mathcal{R}_2$: Trained weighted AAoI minimizing RL agent
Θ: AAoI threshold breach indicator
$\widetilde{\Delta}$: AAOI threshold
for $T_A = 1, 2, \cdots$ **do**
  Set $n_i(T_A) = \hat{n_i}(T_A)$;
  Compute Θ // $(\Delta_{NRT}(t) - \widetilde{\Delta}) > 0, \forall\, t \in \{T_A - 1, T_A - 2, \cdots, T_A - \Gamma\}$;
  if (Θ ***is*** *False*) **then**
    if $[\![V]\!]$ **then**
      ρ = $\mathcal{R}_1 \rightarrow a_t$;
    end
  end
  else if *(*Θ ***is*** *True)* **then**
    ρ = $\mathcal{R}_2 \rightarrow a_t$; // Equability window;
  end
  $M_{RT} \leftarrow \lfloor \rho M \rfloor$;
  $M_{NRT} \leftarrow \lfloor (1-\rho) M \rfloor$;
  $\hat{W}_i = r \times\ M_i$
  Broadcast configured grants as time-frequency resource allocation information $\hat{W}_i$ to all devices, using downlink signaling;
end

the purpose of comparison. The resulting expressions are detailed in Table III.

In Algorithm 1 (PF-AGFRP), the dominant operation is the calculation of partitioning factor derived from eq. (17). However, the calculation can be performed in constant time, as the expression requires fixed number of operations independent of the input size. Therefore, computational complexity for execution of PF-AGFRP is $\tilde{\mathcal{O}}(1)$. With a similar reasoning the computational complexity for Algorithm 2 (PB-AGFRP) is also $\tilde{\mathcal{O}}(1)$ since it is dominated by eq. (14).

In comparison, the MORL-AGFRP method involves training costs. It can be observed from Algorithm 3 (MORL-AGFRP Training), that the RL agent is trained for T time steps and M epochs, i.e., the total number of time-steps is MT. In a feed-forward neural network [37] with L layers, where each layer i has u_i neurons, the time complexity for a single forward pass is $\sum_{i=1}^{L} u_i u_{i+1}$. Since the forward and backward passes have similar computational complexity, the factor of 2 can be omitted as it does not affect the asymptotic complexity. Furthermore, the complexity for performing action selection with $\epsilon-$greedy policy in the training phase is $\tilde{\mathcal{O}}|\mathcal{A}|$. The overall computational complexity (ignoring the complexity for training updates and batch size) is captured in Table III corresponding to MORL-AGFRP. Here $|\mathcal{A}|$ is the number of actions, and the value of c depends on the discount factor and the target error in estimating the optimal action-value function. The inference cost for MORL-AGFRP can be approximated to $\tilde{\mathcal{O}}(1)$. Although the training process takes some time to achieve convergence, it only necessitates occasional execution. The capacities of gNodeB are rapidly improving with the development of processors engineered for intelligent computation. Therefore, the computational complexity should not impede the adoption of the MORL-AGFRP scheme.

V. Results and Discussion

A. Simulation Settings and Scenarios

For our simulations, we have chosen the mMTC scenario as detailed in Sec.II-B and [5]. As per the traffic model defined for industrial process automation, the *aperiodic* traffic (RT) has inter-arrival time (μ) between $10 - 30s$ and number of devices ranging with $10 - 10000$, and devices are typically stationary having packet size < 100 bytes. On the other hand, the *periodic* traffic has periodicity between $10ms - 60s$ and number of devices between $10000 - 100000$ with packet size between $20 - 255$ bytes, and the devices are stationary.

The simulation environment is created with Python and related add-ons for plotting and calculations. The Monte-Carlo simulation method is adopted with averaging count of 30000. The distribution of devices is taken as fixed and uniform with 1 gNodeB/cell. The 5G numerology indicator $\beta = 2$ is used as a default. This has a duration $= 25\mu s$. Schemes with $\beta = 1$ and $\beta = 3$ are also employed for comparison.

In a given allocation interval, the arrival rate for both device groups is assumed to be constant. The number of resource blocks M in an mMTC slice is assumed to be $\sim 35\%$ of the total 100 MHz bandwidth which has 135 resource blocks [38]. The remaining resource blocks are assumed to be allocated to other 5G service categories. The transmission limit $\mathcal{F} + 1$ is taken to be 2. The total number of TTIs per subframe is $2^{\beta} = 4$ for $\beta = 2$.

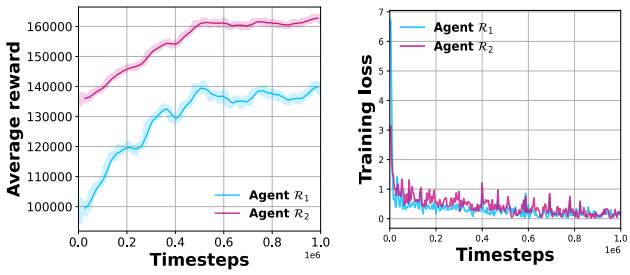

(a) Reward mean (b) Training loss

Fig. 6. RL agent training $\mathcal{R}_1(w_1 > w_2)$ and $\mathcal{R}_2(w_2 >> w_1)$.

MORL-AGFRP utilizes the DQN RL algorithm for training the agents. Stable Baselines is a set of improved implementations of core RL algorithms which includes DQN. It is based on OpenAI Baselines [39]. The values of the hyper-parameters for the RL model are as listed in Table IV. These are tuned with Optuna [40]. A custom gym environment for emulating the defined system model is built atop OpenAI Gym API [41]. OpenAI Gym is an open source Python library for developing RL algorithms by providing a standard API to communicate between learning algorithms and environments. Extensive simulations are performed for an observation time with 10^6 allocation intervals. The other system parameters for

Authorized licensed use limited to: DELHI TECHNICAL UNIV. Downloaded on November 11,2024 at 04:24:50 UTC from IEEE Xplore. Restrictions apply.
© 2024 IEEE. Personal use is permitted, but republication/redistribution requires IEEE permission. See https://www.ieee.org/publications/rights/index.html for more information.

This article has been accepted for publication in IEEE Transactions on Network and Service Management. This is the author's version which has not been fully edited and content may change prior to final publication. Citation information: DOI 10.1109/TNSM.2024.3493015

TABLE III
COMPUTATIONAL COMPLEXITY OF THE PROPOSED AGFRP SCHEMES

Algorithm	Phase	Big-O
PF - AGFRP	Execution	$\tilde{\mathcal{O}}(1)$
PB - AGFRP	Execution	$\tilde{\mathcal{O}}(1)$
MORL - AGFRP	Execution (Inference)	$\tilde{\mathcal{O}}\left(\sum_{i=1}^{L} u_i u_{i+1}\right) \sim \tilde{\mathcal{O}}(1)$
MORL - AGFRP	Training	$\tilde{\mathcal{O}}\left(MT\left(\sum_{i=1}^{L} u_i u_{i+1} + c\lvert\mathcal{A}\rvert\right)\right)$

TABLE IV
MORL-AGFRP TRAINING AND SIMULATION PARAMETERS

Parameter	**Value**
Learning rate	.001
Minibatch size	32
Replay buffer size	20000
Exploration final epsilon (ϵ)	0.05
Exploration fraction	0.5
Number of slots per episode	1000
Number of episodes for training	1000
Γ in allocation intervals	3

MORL-AGFRP are configured as enlisted in Table IV. Fig. 6 depicts the training process of the RL Agents in MORL-AGFRP. As can be seen from Fig. 6(a), with increase in the number of training episodes, the average reward for both agents $\mathcal{R}_1$ and $\mathcal{R}_2$ converge to a constant value, indicating that the learning has stabilized. The RL agents perform multi-objective optimization to minimize the defined objectives based on scalar rewards. For $\mathcal{R}_1$, $w_1 > w_2$, implying that it prioritizes reducing drop rate over AAoI with weight vector $\boldsymbol{w} = [4, 2]^T$, and for $\mathcal{R}_2$, $w_2 \gg w_1$, implying that it prioritizes reducing AAoI over drop rate with weight vector $\boldsymbol{w} = [1, 5]^T$. Accordingly, the average rewards for $\mathcal{R}_2$ are greater than $\mathcal{R}_1$.

Also, the accrued average losses $\rightarrow 0$ with increase in the number of training episodes in Fig. 6(b), thereby confirming that the agents have been trained for the defined objective.

B. Results

It can be observed from Fig. 7 that the analytical model closely follows the simulation model. Furthermore, a higher partitioning factor leads to an increase in transmission success probability for the RT group as depicted in Fig. 7(a). However, a high arrival rate has an inverse impact on the metrics drop rate and AAoI as can be observed from Fig. 7(b) and 7(c), respectively.

The probability of successful transmission is shown for GFRS in Table V and for GFRP in Table VI. For the same set of traffic parameters GFRP consistently performs better than GFRS. It can also be observed that probability of successful transmission is proportional to the partitioning factor ρ and is inversely proportional to the number of devices and the inter-arrival time.

Fig. 8 compares the required resources for the considered GF schemes for achieving the same target probability of success of 0.9 ($P_{S_i} = 0.9$) for both device groups. As illustrated, compared to the conventional counterpart, i.e., GFRS or no partitioning, the GFRP scheme can substantially reduce the required number of resources for a given reliability constraint, thereby leading to better spectral efficiency. The GFRP scheme offers around 49% (for $\mu = 1s$) reduction in the required bandwidth resources as compared to the conventional scheme-GFRS. Note that this difference is distinctly observable because the defined CPS traffic model considers aperiodic traffic arrival rate lower than periodic traffic arrivals. The results are reasonable from the standpoint that more the number of competing devices, more the resources that would be required to ensure a given level of transmission success rate.

It can be observed from Fig. 9(a) and 9(b) that all proposed partitioning schemes, PF-AGFRP, PB-AGFRP ($\alpha = 0, 0.6$), and MORL-AGFRP ($\mathcal{R}_1$) outperform conventional schemes, i.e., GFRS and GF Reactive to achieve drop rate and AAoI

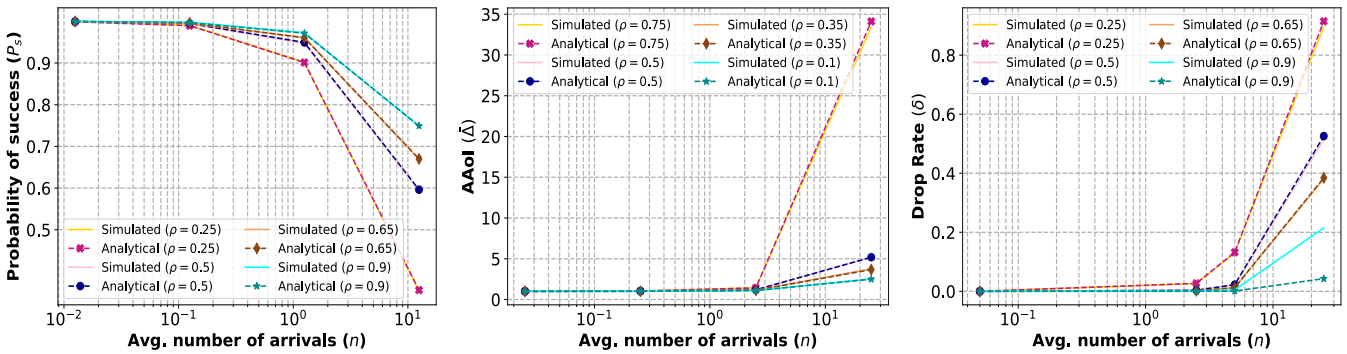

(a) (b) (c)

Fig. 7. Simulation results, GFRP: (a) P_S, (b) $\bar{\Delta}$, and (c) δ with varying ρ.

Authorized licensed use limited to: DELHI TECHNICAL UNIV. Downloaded on November 11,2024 at 04:24:50 UTC from IEEE Xplore. Restrictions apply.
© 2024 IEEE. Personal use is permitted, but republication/redistribution requires IEEE permission. See https://www.ieee.org/publications/rights/index.html for more information.

This article has been accepted for publication in IEEE Transactions on Network and Service Management. This is the author's version which has not been fully edited and content may change prior to final publication. Citation information: DOI 10.1109/TNSM.2024.3493015

TABLE V
GFRS - PROBABILITY OF SUCCESSFUL TRANSMISSION ($P_{S_{RT}}$) WITH $L = 1, \beta = 2$

	$N_{NRT} = 100000$, $\mu_{NRT} = 1s$			$N_{NRT} = 50000$, $\mu_{NRT} = 1s$			$N_{NRT} = 10000$, $\mu_{NRT} = 1s$		
$\mu_{RT}(s)$	N_{RT}=10000	N_{RT}=5000	N_{RT}=1000	N_{RT}=10000	N_{RT}=5000	N_{RT}=1000	N_{RT}=10000	N_{RT}=5000	N_{RT}=1000
30	0.5533	0.5683	0.5807	0.7241	0.7438	0.7600	0.8980	0.9225	0.9425
20	0.5480	0.5632	0.5756	0.7203	0.7403	0.7566	0.8964	0.9213	0.9416
10	0.5325	0.5480	0.5607	0.7091	0.7297	0.7467	0.8917	0.9177	0.9389
1‡	0.5353	0.5640	0.5880	0.5353	0.5640	0.5880	0.8120	0.8554	0.8918

TABLE VI
GFRP - PROBABILITY OF SUCCESSFUL TRANSMISSION ($P_{S_{RT}}$) WITH $L = 1, \beta = 2$

$N_{NRT} = 100000$, $\mu_{NRT} = 1s$									
	$\rho = 0.2$			$\rho = 0.5$			$\rho = 0.9$		
$\mu_{RT}(s)$	N_{RT}=10000	N_{RT}=5000	N_{RT}=1000	N_{RT}=10000	N_{RT}=5000	N_{RT}=1000	N_{RT}=10000	N_{RT}=5000	N_{RT}=1000
30	0.9917	0.9958	0.9992	0.9965	0.9983	0.9997	0.9981	0.9990	0.9998
20	0.9876	0.9938	0.9988	0.9948	0.9974	0.9995	0.9971	0.9985	0.9997
10	0.9753	0.9876	0.9975	0.9896	0.9948	0.9990	0.9942	0.9971	0.9994
1‡	0.7788	0.8825	0.9753	0.9011	0.9493	0.9896	0.9435	0.9714	0.9942

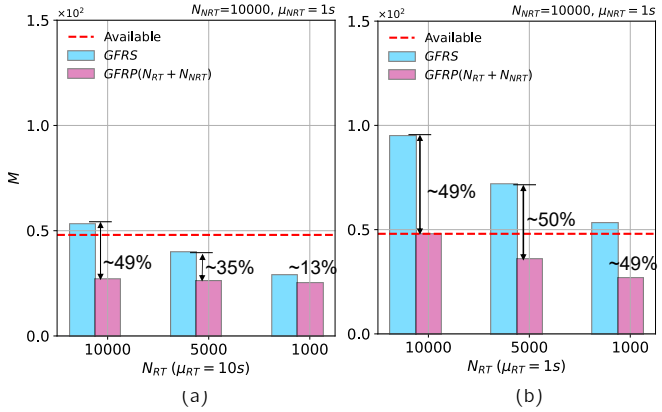

Fig. 8. Resource requirement with constraint on successful transmission: P_{S_{RT},θ_1}, $P_{S_{NRT},\theta_1} = 0.9$, $L = 1$, $\beta = 2$; (a) $\mu_{RT} = 10s$, (b) $\mu_{RT} = 1s$.

reduction.

Furthermore, Fig. 9(a) depicts that relatively low drop rate can be guaranteed for device group RT by the RL agent $\mathcal{R}_1$. Agent $\mathcal{R}_1$ can also be considered a relatively optimal agent as its plot is proximal to the plot of PF-AGFRP. On the other hand, $\mathcal{R}_2$ is an RT traffic de-prioritizing agent; therefore, the drop rate for $\mathcal{R}_2$ shows a steep curve. PB-AGFRP exhibits behavioral variation according to α. The drop rate with $\alpha = 0$ overlaps with PF-AGFRP because in the scenario with heavy load and no prioritization, i.e., $\alpha = 0$, the PB-AGFRP scheme reduces to a proportionally fair/optimal scheme when the targeted success probability is same for both groups of devices. Both $\alpha = 0.6$ and and $\alpha = 0.9$ exhibit expected trends for a drop rate reduction for the RT device population as the prioritization increases at the expense of penalizing the NRT traffic. Thus, α also helps to control fairness in PB-AGFRP. Fig. 9(b) illustrates the AAoI gradation for the NRT device group. The AAoI is kept strictly low by agent $\mathcal{R}_2$, aligned to its defined objective. The behavior of agent $\mathcal{R}_1$ is not a strict NRT de-prioritizing one but is somewhat more balanced, which is again observed by its proximity to the PF-AGFRP. PB-AGFRP, owing to its strict de-prioritization of the NRT device group at $\alpha = 0.9$, shows a steep incline, far greater than all other schemes. Despite N_{NRT} being constant, with higher RT arrivals, the proposed algorithms adaptively increase the partitioning factor and therefore, $\bar{\Delta}_{NRT}$ increases commensurately.

As is depicted in Fig. 10, MORL-AGFRP optimally prioritizes both device groups and autonomously switches to agent $\mathcal{R}_2$ when the threshold is breached successively for $\Gamma = 3$ (configurable) consecutive allocation intervals and the probability of successful transmission (in turn, AAoI) of the NRT device group falls below a configured threshold in T_A index $= 5, 8$ and 12. Agent $\mathcal{R}_2$ emulates an equability window, to allow NRT devices to clear their backlog. Note that agent $\mathcal{R}_2$ would see a high number of arrivals due to the built-up backlog which results in a high partitioning factor $1 - \rho$ for the NRT device group. The NRT devices which follow standard ARQ are able to reset the AoI on making a successful transmission. On the other hand, the RT device group can re-transmit if failed, as in the next allocation interval they will be prioritized again. PB-AGFRP adaptively adjusts the partitioning factor to ensure a threshold probability of success for the RT device group. When the RT traffic burst is encountered for T_A index $= 7$, PB-AGFRP adapts the bandwidth resource allocation based upon the RT prioritization factor and secures its transmission reliability while deprioritizing the NRT traffic.

C. MORL-AGFRP and NR Numerology

The NR subframe duration is fixed for all numerologies as 1 ms. The RL agent behaviour is observed for $\beta = 1, 2, 3$ as depicted in Fig. 11(a) and 11(b). Recall that a T_A consists of d subframes and r time slots with $r = d \times 2^{\beta}$. For the purpose of

‡The value $\mu_{RT} = 1s$ is included to exemplify the bounds of the proposed approach, if traffic burst is encountered.

Authorized licensed use limited to: DELHI TECHNICAL UNIV. Downloaded on November 11,2024 at 04:24:50 UTC from IEEE Xplore. Restrictions apply.
© 2024 IEEE. Personal use is permitted, but republication/redistribution requires IEEE permission. See https://www.ieee.org/publications/rights/index.html for more information.

This article has been accepted for publication in IEEE Transactions on Network and Service Management. This is the author's version which has not been fully edited and content may change prior to final publication. Citation information: DOI 10.1109/TNSM.2024.3493015

simulations we consider $d = 2$. We keep the offered traffic per subframe constant but with varying device inter-arrival time $\mu_i \in \{0.5x,\ x,\ 2x\}$, where $x \in [10, 15]$. The drop rate and AAoI per subframe decrease when a higher-level numerology is adopted, albeit it increases with increase in arrival rate. This is due to the fact that more time slots and hence more resources per subframe are available with a higher-level numerology. The drop rate for the RT device group decreases with a higher-level numerology whereas higher drop rates are experienced by NRT, albeit they too decrease with higher numerology, as can be seen in Fig.11(a). The reverse trend applies to the AAoI performance as is illustrated in Fig.11(b); herein the decrease in AAoI for the NRT device group is greater than that of the RT device group. These observations are aligned to the behavior objectives defined for agent $\mathcal{R}_1$ and $\mathcal{R}_2$. We see that the variation in AAoI appears to be less pronounced as compared to the drop rate; however, it is pertinent to observe that the two quantities are measured on different scales.

VI. Conclusion

We have proposed novel methods for the gNodeB MAC scheduler which enables priority-based allocation of configured grants for heterogeneous mMTC traffic in 5G-Advanced networks. At each allocation interval, a decision is taken to partition and allocate GF resources based upon estimated arrivals of diverse device groups. Through extensive simulations, we demonstrate that the proposed schemes are more reliable as compared to the conventional schemes and offer significant improvement for the metrics under purview, namely drop rate and AAoI. In particular, the MORL-AGFRP offers a near optimal resource allocation with equability mechanism so that QoS constraints and fairness for both device populations can be met as far as possible, which is important in CPS use cases such as wireless industrial automation and smart grid.

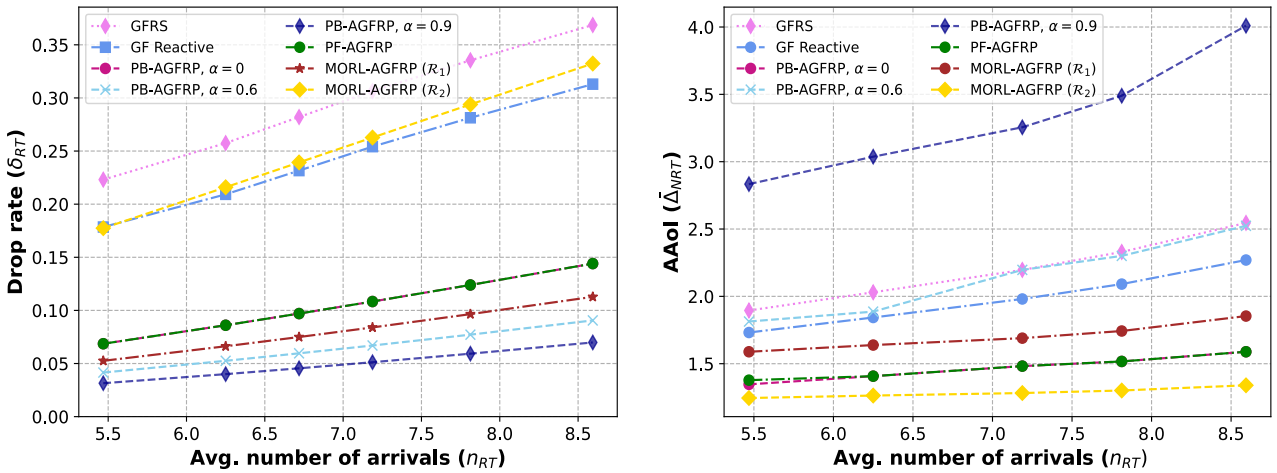

(a) (b)

Fig. 9. Comparison of drop rate and AAoI for various configured GF scheduling schemes (conventional and proposed). $N_{NRT} \approx 10000$, $\mu_{NRT} = 1s$.

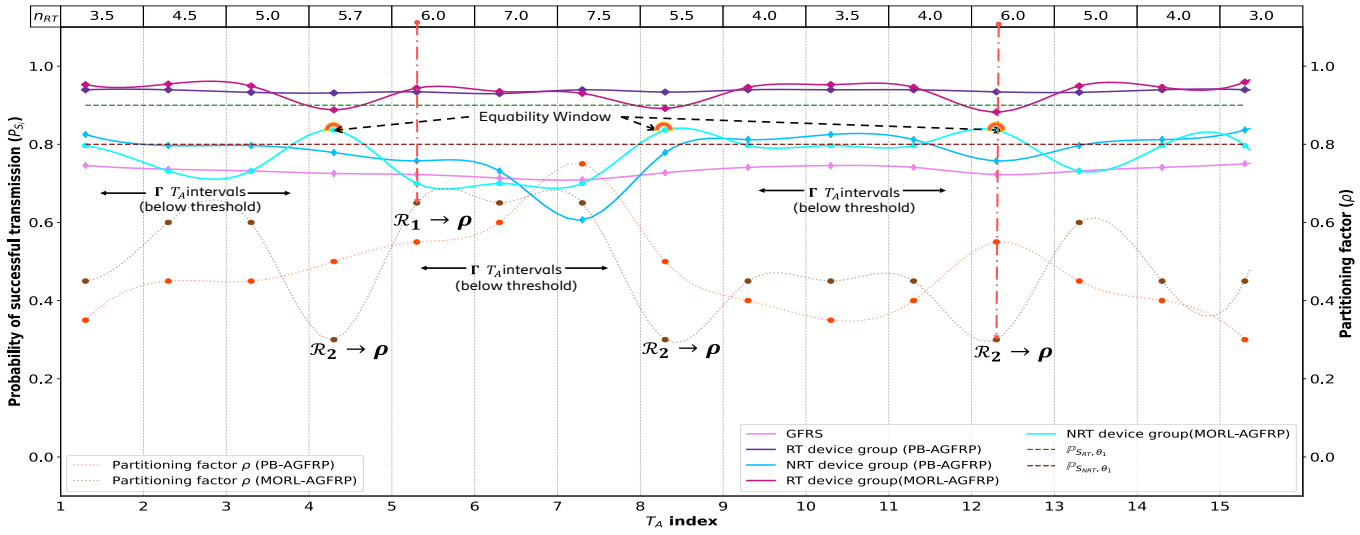

Fig. 10. Probability of success (P_S) and Equability window. $N_{NRT} = 20000$, $\mu_{NRT} = 1s$, $\alpha = 0.6$, $\beta = 2$, $\Gamma = 3$, $T_A : r = 1$ NR subframe $\times\ 2^{\beta}$ TTI .

Authorized licensed use limited to: DELHI TECHNICAL UNIV. Downloaded on November 11,2024 at 04:24:50 UTC from IEEE Xplore. Restrictions apply.
© 2024 IEEE. Personal use is permitted, but republication/redistribution requires IEEE permission. See https://www.ieee.org/publications/rights/index.html for more information.

This article has been accepted for publication in IEEE Transactions on Network and Service Management. This is the author's version which has not been fully edited and content may change prior to final publication. Citation information: DOI 10.1109/TNSM.2024.3493015

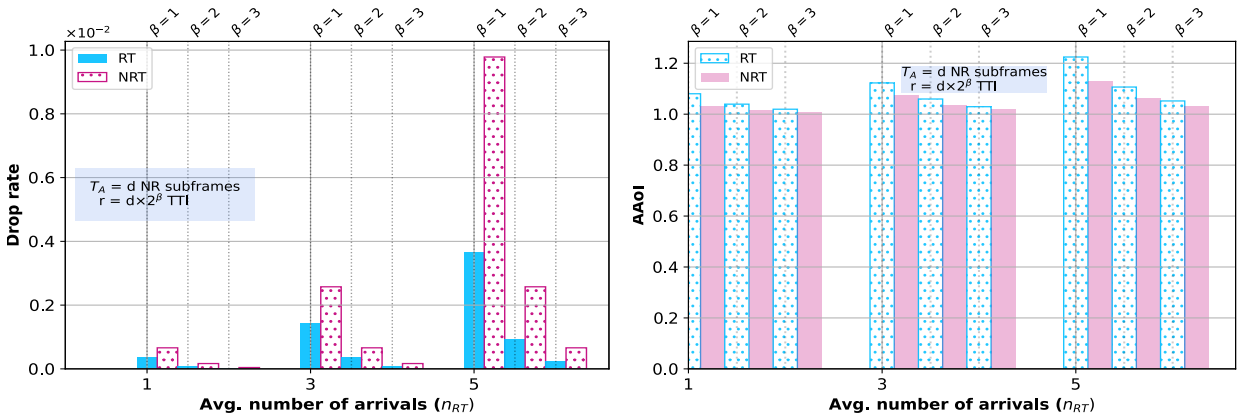

(a) (b)

Fig. 11. MORL-AGFRP agent behaviour for NR numerologies with $\beta = 1, 2, 3$, $T_A : r = 2$ NR subframe $\times$ 2^{β} TTI, $N_{NRT} \approx 10000$, $\mu_{NRT} = 1s$: (a) Drop rate (agent $\mathcal{R}_1$) and (b) AAoI (agent $\mathcal{R}_2$).

Importantly, partitioning GF bandwidth inherently excludes any cross impact between the device groups. This approach can lend itself helpful in an intelligent radio access network for radio resource management. Furthermore, our work can also help with uplink scheduling in NR-Light or reduced capacity (RedCap) service category which was introduced in 3GPP Release 17 and also in private 5G networks (NR-unlicensed) with GF uplink. The analysis in this work has primarily focused on two device groups: RT and NRT. Extension to more classes is a relevant problem to address, but is beyond the scope of this paper.

Appendix A
Proof of Lemma 1

Define ψ_t as the difference of the expected GF access success of i and $i^{'}$ device groups between the GFRP and GFRS schemes From (13) we get

$$\begin{aligned}\psi_t &= N_i \left(\frac{e^{-\lambda_i} + \rho M - 1}{\rho M}\right)^{N_i - 1} \\ &+ N_{i'} \left(\frac{e^{-\lambda_{i'}} + (1-\rho)M - 1}{(1-\rho)M}\right)^{N_{i'}-1} \\ &- (N_i + N_{i'}) \left(\frac{e^{-(\lambda_i+\lambda_{i'})} + M - 1}{M}\right)^{N_i+N_{i'}-1}. \quad (27)\end{aligned}$$

Using $(1+a)^n \geq 1+na$ for $n \geq 0$ and $a \geq -1$ (follows from Bernoulli's inequality), we get $\psi_t \geq \hat{\psi}_t$, where

$$\begin{aligned}\hat{\psi}_t &= N_i \left(1 + (N_i - 1)\left(\frac{e^{-\lambda_i} - 1}{\rho M}\right)\right) \\ &+ N_{i'} \left(1 + (N_{i'} - 1)\left(\frac{e^{-\lambda_{i'}} - 1}{(1-\rho)M}\right)\right) \\ &- (N_i + N_{i'}) \\ &\times \left(1 + (N_i + N_{i'} - 1)\left(\frac{e^{-(\lambda_i+\lambda_{i'})} - 1}{M}\right)\right). \quad (28)\end{aligned}$$

Simplifying further we obtain

$$\begin{aligned}\hat{\psi}_t &= N_i(N_i - 1)\left(\frac{e^{-\lambda_i} - 1}{\rho M}\right) \\ &+ N_{i'}(N_{i'} - 1)\left(\frac{e^{-\lambda_{i'}} - 1}{(1-\rho)M}\right) \\ &- (N_i + N_{i'})(N_i + N_{i'} - 1)\left(\frac{e^{-(\lambda_i+\lambda_{i'})} - 1}{M}\right). \quad (29)\end{aligned}$$

Taking the first derivative of (29), rearranging the terms with respect to ρ, and setting it to 0, it is found that $\hat{\psi}_t$ achieves its maximum $\hat{\psi}_t^{max}$ when $\rho = \widetilde{\rho}$, where

$$\widetilde{\rho} = \frac{\sqrt{N_i(N_i-1)(1-e^{-\lambda_i})}}{\sqrt{N_i(N_i-1)(1-e^{-\lambda_i})} + \sqrt{N_{i'}(N_{i'}-1)(1-e^{-\lambda_{i'}})}}. \quad (30)$$

The expression (30) holds $\forall \lambda_i, \lambda_{i'} > 0$. For $N_i, N_{i'} >> 1$, it becomes

$$\widetilde{\rho} = \frac{N_i\sqrt{(1-e^{-\lambda_i})}}{N_i\sqrt{(1-e^{-\lambda_i})} + N_{i'}\sqrt{(1-e^{-\lambda_{i'}})}}. \quad (31)$$

This completes the proof.

References

[1] I. Leyva-Mayorga, C. Stefanovic, P. Popovski, V. Pla, and J. Martinez-Bauset, *Random Access for Machine-Type Communications* In *Wiley 5G Ref: The Essential 5G Reference Online*, pp. 1–21, John Wiley & Sons, 2019.

[2] 3GPP, "Study on new radio (NR) access technology," 3rd Generation Partnership Project (3GPP), Technical Report (TR) 38.912, Apr. 2022.

[3] Z. Zhou, R. Ratasuk, N. Mangalvedhe, and A. Ghosh, "Resource allocation for uplink grant-free ultra-reliable and low latency communications," in *Proc. IEEE Veh. Technol. Conf. (VTC) Spring*, Porto, Portugal, Jun. 3–6, 2018, pp. 1–5.

[4] H. Grama Srinath, M. Rana, and N. M. Balasubramanya, "Grant-free access for mMTC: A performance analysis based on number of preambles, repetitions, and retransmissions," *IEEE Internet of Things J.*, vol. 9, no. 16, pp. 15169–15183, Aug. 15, 2022.

[5] 3GPP, "NR; Service requirements for cyber-physical control applications in vertical domains," 3rd Generation Partnership Project (3GPP), Technical Specification (TS) 22.104, Mar. 2023.

Authorized licensed use limited to: DELHI TECHNICAL UNIV. Downloaded on November 11,2024 at 04:24:50 UTC from IEEE Xplore. Restrictions apply.
© 2024 IEEE. Personal use is permitted, but republication/redistribution requires IEEE permission. See https://www.ieee.org/publications/rights/index.html for more information.

This article has been accepted for publication in IEEE Transactions on Network and Service Management. This is the author's version which has not been fully edited and content may change prior to final publication. Citation information: DOI 10.1109/TNSM.2024.3493015

[6] J. Choi, J. Ding, N.-P. Le, and Z. Ding, "Grant-free random access in machine-type communication: Approaches and challenges," *IEEE Wireless Commun.*, vol. 29, no. 1, pp. 151–158, 2022.

[7] G. Berardinelli, N. Huda Mahmood, R. Abreu, T. Jacobsen, K. Pedersen, I. Z. Kovacs, and P. Mogensen, "Reliability analysis of uplink grant-free transmission over shared resources," *IEEE Access*, vol. 6, pp. 23602–23611, 2018.

[8] M. C. Lucas-Estan, J. Gozalvez, and M. Sepulcre, "On the capacity of 5G NR grant-free scheduling with shared radio resources to support ultra-reliable and low-latency communications," *Sensors (Basel)*, vol. 19, no. 16, pp. 1–18, Aug. 2019.

[9] R. Abreu, G. Berardinelli, T. Jacobsen, K. Pedersen, and P. Mogensen, "A blind retransmission scheme for ultra-reliable and low latency communications," in *Proc. IEEE Veh. Technol. Conf. (VTC) Spring*, Porto, Portugal, Jun. 3–6, 2018, pp. 1–5.

[10] Y. Liu, Y. Deng, M. Elkashlan, A. Nallanathan, and G. K. Karagiannidis, "Optimization of grant-free NOMA with multiple configured-grants for mURLLC," *IEEE J. Sel. Areas Commun.*, vol. 40, no. 4, pp. 1222–1236, Apr. 2022.

[11] Y. Liu, Y. Deng, M. Elkashlan, A. Nallanathan, and G. K. Karagiannidis, "Analyzing grant-free access for URLLC service," *IEEE J. Sel. Areas Commun.*, vol. 39, no. 3, pp. 741–755, Mar. 2021.

[12] C. Bockelmann, N. K. Pratas, G. Wunder, S. Saur, M. Navarro, D. Gregoratti, G. Vivier, E. De Carvalho, Y. Ji, C. Stefanovic, P. Popovski, Q. Wang, M. Schellmann, E. Kosmatos, P. Demestichas, M. Raceala-Motoc, P. Jung, S. Stanczak, and A. Dekorsy, "Towards massive connectivity support for scalable mMTC communications in 5G networks," *IEEE Access*, vol. 6, pp. 28969–28992, 2018.

[13] A. C. Cirik, N. M. Balasubramanya, L. Lampe, G. Vos, and S. Bennett, "Toward the standardization of grant-free operation and the associated NOMA strategies in 3GPP," *IEEE Commun. Standards Mag.*, vol. 3, no. 4, pp. 60–66, 2019.

[14] A.-S. Bana, E. De Carvalho, B. Soret, T. Abrao, J. C. Marinello, E. G. Larsson, and P. Popovski, "Massive MIMO for internet of things (IoT) connectivity," *Physical Commun.*, vol. 37, article no. 100859, pp. 1–17, 2019.

[15] Z. Zhao, Q. Du, and L. Sun, "Network-load estimation for K-repetition grant-free access enabling adaptive resource allocation towards QoS enhancement," in *Proc. IEEE Pers., Indoor and Mobile Radio Commun. (PIMRC)*, Helsinki, Finland, Sep. 13–16, 2021, pp. 1073–1078.

[16] T. N. Weerasinghe, A. M. I. Balapuwaduge, F. Y. Li, and V. C. Giner, "MDP-based resource allocation for uplink grant-free transmissions in 5G new radio," in *Proc. IEEE Wireless Commun. Netw. Conf. (WCNC)*, Seoul, Korea (South), May 25–28, 2020, pp. 1–6.

[17] A. Mamane, M. Fattah, M. E. Ghazi, M. E. Bekkali, Y. Balboul, and S. Mazer, "Scheduling algorithms for 5G networks and beyond: Classification and survey," *IEEE Access*, vol. 10, pp. 51643–51661, 2022.

[18] I.-S. Comsa, R. Trestian, G.-M. Muntean, and G. Ghinea, "5MART: A 5G SMART scheduling framework for optimizing QoS through reinforcement learning," *IEEE Trans. Netw. Serv. Manag.*, vol. 17, no. 2, pp. 1110–1124, Jun. 2020.

[19] A. Kaur and K. Kumar, "A reinforcement learning-based green resource allocation for heterogeneous services in cooperative cognitive radio networks," *IEEE Trans. Netw. Serv. Manag.*, vol. 19, no. 2, pp. 1554–1566, Jun. 2022.

[20] T. N. Weerasinghe, V. Casares-Giner, I. A. M. Balapuwaduge, and F. Y. Li, "Priority enabled grant-free access with dynamic slot allocation for heterogeneous mMTC traffic in 5G NR networks," *IEEE Trans. Commun.*, vol. 69, no. 5, pp. 3192–3206, May 2021.

[21] M. C. Lucas-Estan and J. Gozalvez, "Sensing-based grant-free scheduling for ultra reliable low latency and deterministic beyond 5G networks," *IEEE Trans. Veh. Technol.*, vol. 71, no. 4, pp. 4171–4183, Apr. 2022.

[22] J. Korhonen, "Scheduling," May 2023. [Online]. Available: https://www.3gpp.org/technologies/scheduling

[23] E. Dahlman, S. Parkvall, and J. Skold, *5G NR: The Next Generation Wireless Access Technology*, USA: Academic Press, 2018.

[24] 3GPP, "NR; medium access control (MAC) protocol specification," 3rd Generation Partnership Project (3GPP), Technical Specification (TS) 38.321, Apr. 2024.

[25] R. D. Yates and S. K. Kaul, "Status updates over unreliable multiaccess channels," in *Proc. IEEE Int. Symp. Inf. Theory (ISIT)*, Aachen, Germany, Jun. 25–30, 2017, pp. 331–335.

[26] F. Metzger, T. Hobfeld, A. Bauer, S. Kounev, and P. E. Heegaard, "Modeling of aggregated IoT traffic and its application to an IoT cloud," *Proc. IEEE*, vol. 107, no. 4, pp. 679–694, Apr. 2019.

[27] A. Kosta, N. Pappas, and V. Angelakis, "Age of information: A new concept, metric, and tool," *Foundations and Trends in Networking*, vol. 12, pp. 162–259, 2017.

[28] A. M. Bedewy, Y. Sun, and N. B. Shroff, "Optimizing data freshness, throughput, and delay in multi-server information-update systems," in *Proc. IEEE Int. Symp. Inf. Theory (ISIT)*, Barcelona, Spain, Jul. 10–15, 2016, pp. 2569–2573.

[29] Y.-J. Choi, S. Park, and S. Bahk, "Multichannel random access in OFDMA wireless networks," *IEEE J. Sel. Areas Commun.*, vol. 24, no. 3, pp. 603–613, 2006.

[30] E. Eldeeb, M. Shehab, A. E. Kalor, P. Popovski, and H. Alves, "Traffic prediction and fast uplink for hidden Markov IoT models," *IEEE Internet Things J.*, vol. 9, no. 18, pp. 17172–17184, Sep. 15, 2022.

[31] L. Tello-Oquendo, V. Pla, I. Leyva-Mayorga, J. Martinez-Bauset, V. Casares-Giner, and L. Guijarro, "Efficient random access channel evaluation and load estimation in LTE-A with massive MTC," *IEEE Trans. Veh. Technol.*, vol. 68, no. 2, pp. 1998–2002, Feb. 2019.

[32] 3GPP, "NR; multiplexing and channel coding," 3rd Generation Partnership Project (3GPP), Technical Specification (TS) 38.212, Apr. 2022.

[33] R. S. Sutton and A. G. Barto, *Reinforcement Learning: An Introduction*, Cambridge, MA, USA: A Bradford Book, 2018.

[34] V. Mnih, K. Kavukcuoglu, D. Silver, A. Graves, I. Antonoglou, D. Wierstra, and M. A. Riedmiller, "Playing Atari with deep reinforcement learning," *Nature*, vol. 518, pp. 529–533, 2015.

[35] S. Srinivasa, "Multi-objective reinforcement learning," Dec. 2016. [Online]. Available: https://sunil-s.github.io/2016/12/10/Multi-objective-Reinforcement-Learning.html

[36] Z. Hu, K. Wan, X.-G. Gao, and Y. Zhai, "A dynamic adjusting reward function method for deep reinforcement learning with adjustable parameters," *Math. Probl. Eng.*, vol. 2019, pp. 1–10, 2019.

[37] S. Haykin, *Neural Networks and Learning Machines*, NJ, USA: Pearson Education, Inc., 2009.

[38] 3GPP, "NR; user equipment (UE) radio transmission and reception," 3rd Generation Partnership Project (3GPP), Technical Specification (TS), Mar. 2023.

[39] A. Raffin, A. Hill, A. Gleave, A. Kanervisto, M. Ernestus, and N. Dormann, "Stable-baselines3: Reliable reinforcement learning implementations," *J. Mach. Learn. Res.*, vol. 22, no. 268, pp. 1–8, 2021.

[40] T. Akiba, S. Sano, T. Yanase, T. Ohta, and M. Koyama, "Optuna: A next-generation hyperparameter optimization framework," in *Proc. 25th ACM SIGKDD Int. Conf. Knowl. Discovery Data Mining*. New York, NY, USA: ACM, 2019, pp. 2623–2631.

[41] G. Brockman, V. Cheung, L. Pettersson, J. Schneider, J. Schulman, J. Tang, and W. Zaremba, "OpenAI Gym," *ArXiv*, 2016.

Yukti Kaura graduated as a Gold Medalist in Computer Science and Engineering and received her Master's degree in Software Systems from the Birla Institute of Technology and Science (BITS), Pilani, Rajasthan, India, in 2009. She currently serves as a Senior Architect at Ericsson, specializing in core networks, cloud computing, and large-scale distributed systems, with extensive experience in designing and architecting advanced telecommunications solutions. She is pursuing her Ph.D. at the Bharti School of Telecommunication Technology and Management at the Indian Institute of Technology Delhi. Her primary research interests include machine-type access in 5G and beyond networks, advancing innovations in connected technologies.

Authorized licensed use limited to: DELHI TECHNICAL UNIV. Downloaded on November 11,2024 at 04:24:50 UTC from IEEE Xplore. Restrictions apply.
© 2024 IEEE. Personal use is permitted, but republication/redistribution requires IEEE permission. See https://www.ieee.org/publications/rights/index.html for more information.

This article has been accepted for publication in IEEE Transactions on Network and Service Management. This is the author's version which has not been fully edited and content may change prior to final publication. Citation information: DOI 10.1109/TNSM.2024.3493015

Brejesh Lall (Senior Member, IEEE) received the B.E. degree in electronics and communication engineering and the M.E. degree in signal processing from the Delhi College of Engineering, New Delhi, in 1991 and 1992, respectively, and the Ph.D. degree in signal processing from the Indian Institute of Technology (IIT) Delhi, New Delhi, in 1999. From 1997 to 2005, he was with Hughes Software Systems, where he worked in the signal processing group on source coding and PHY layer solutions for many communication technologies, such as terrestrial wireless, GEO and LEO satellite communication systems, and satellite broadband. He joined the Department of Electrical Engineering, IIT Delhi as a faculty member in 2005, where he is currently a Professor. He has served as the Head of the Bharti School of Telecommunication Technology and Management, IIT Delhi, and the Coordinator of the National Cadet Corps, IIT Delhi. His research interests are broadly in signal processing, image processing, and communications, including the areas of object representation, tracking, and classification, odometry, depth map generation, representation, and rendering, vector sensor-based underwater acoustic communications, and performance issues in molecular communications.

Ranjan K. Mallik (S'88–M'93–SM'02–F'12) received the B.Tech. degree from the Indian Institute of Technology Kanpur, Kanpur, in 1987 and the M.S. and Ph.D. degrees from the University of Southern California, Los Angeles, in 1988 and 1992, respectively, all in electrical engineering. From August 1992 to November 1994, he was a scientist with the Defence Electronics Research Laboratory, Hyderabad, India, working on missile and EW projects. From November 1994 to January 1996, he was a faculty member with the Department of Electronics and Electrical Communication Engineering, Indian Institute of Technology Kharagpur, Kharagpur. From January 1996 to December 1998, he was with the faculty of the Department of Electronics and Communication Engineering, Indian Institute of Technology Guwahati, Guwahati. Since December 1998, he has been with the faculty of the Department of Electrical Engineering, Indian Institute of Technology Delhi, New Delhi, where he is currently a Professor. His research interests are in diversity combining and channel modeling for wireless communications, space-time systems, cooperative communications, multiple-access systems, power line communications, molecular communications, difference equations, and linear algebra.

Dr. Mallik is a member of Eta Kappa Nu, the IEEE Communications, Information Theory, and Vehicular Technology Societies, the American Mathematical Society, the International Linear Algebra Society, and the Association for Computing Machinery; a fellow of the Indian National Academy of Engineering, the Indian National Science Academy, The National Academy of Sciences, India, Prayagraj, the Indian Academy of Sciences, Bengaluru, The World Academy of Sciences-for the advancement of science in developing countries (TWAS), The Institution of Engineering and Technology, U.K., The Institution of Electronics and Telecommunication Engineers, India, The Institution of Engineers (India) [IEI], the Asia-Pacific Artificial Intelligence Association, and the Artificial Intelligence Industry Academy; and a life member of the Indian Society for Technical Education. He is a recipient of the Hari Om Ashram Prerit Dr. Vikram Sarabhai Research Award in the field of electronics, telematics, informatics, and automation, the Shanti Swarup Bhatnagar Prize in engineering sciences, the Khosla National Award, the IEI-IEEE Award for Engineering Excellence, and the J. C. Bose Fellowship. He has served as an Area Editor and an Editor for the IEEE TRANSACTIONS ON WIRELESS COMMUNICATIONS, and as an Editor for the IEEE TRANSACTIONS ON COMMUNICATIONS.

Amit Singhal (S'14–M'18–SM'23) received the dual degree with B.Tech. in electrical engineering and M.Tech. in information and communication technology from the Indian Institute of Technology (IIT) Delhi in 2009, and the Ph.D. degree in molecular communications from IIT Delhi in 2016. He is currently an Assistant Professor with the Department of Electronics and Communication Engineering, Netaji Subhas University of Technology (NSUT), New Delhi, India. He has a total teaching experience of more than 14 years. Before joining NSUT in June 2021, he worked with JIIT, Noida, and Bennett University, Greater Noida. His areas of interest include next-generation communication systems, theory and applications of Fourier methods, biomedical engineering, image processing, and molecular communications.

Authorized licensed use limited to: DELHI TECHNICAL UNIV. Downloaded on November 11,2024 at 04:24:50 UTC from IEEE Xplore. Restrictions apply.
© 2024 IEEE. Personal use is permitted, but republication/redistribution requires IEEE permission. See https://www.ieee.org/publications/rights/index.html for more information.

AI Based Drive Cycle Prediction for HEV

2024 International Conference on Electrical Electronics and Computing Technologies (ICEECT) | 979-8-3503-7809-2/24/$31.00 ©2024 IEEE | DOI: 10.1109/ICEECT61758.2024.10738952

Ritul Gehlot
Electrical Engineering Department
Delhi Technological University
Delhi, India
gehlotritul01@gmail.com

Shobha Kumari
Electrical Engineering Department
Delhi Technological University
Delhi, India
shobha0502dtu@gmail.com

Kuldeep Singh
Electrical Engineering Department
Delhi Technological University
Delhi, India
kuldeepsingh@dtu.ac.in

***Abstract*—HEVs (Hybrid Electrical Vehicles) is regarded as one of the most effective solutions in the context of environmental pollution and fuel consumption. Nevertheless, formulating the sustainable Energy Management Strategies (EMSs) for HEVs is not an easy task while at the same time one has to meet different design objectives and achieve maximum fuel economy. Among numerous EMSs, the present paper highlights the new system of AI-powered Driving Cycle Prediction. Using the Machine Learning Algorithms and Time Series Forecasting, we apply Dynamometer Drive Schedules data for EVs, meanwhile, Mean Squared Error (MSE) helps to evaluate the model quality. XGBoost and NBeats algorithms comparison shows that the last one has much higher forecasting accuracy; however, it is computationally heavier. Such study is focused on the development of HEV technology and hence the availability of sustainable transport solutions through the process of providing detailed information on the algorithmic outputs.**

***Keywords*— HEVs (hybrid electrical vehicles), energy management strategies (EMSs), mean squared error (MSE)**

I. INTRODUCTION

EVs - Battery and electric motors-based vehicles epitomize a breakthrough in transport and signify a departure from a fossil fuel era to a cleaner, greener and more sustainable automobile age[1]. These EVs proved to be a prototype of transition towards sustainability with zero tailpipe emissions and higher energy efficiency when compared to conventional vehicles even. EVs as a global phenomenon may be conducted because of the mixture of many factors especially battery technology boom which takes the forefront. These developments have significantly boosted EVs' performance and pricing, with falling battery price and increasing energy densities making electric vehicles more worthy competitors on the automotive market, catalyzing customer interest and adoption rates.

Alongside the tremendous growth of EVs, hybrid electric vehicles (HEVs) became a sensible choice since they use the traditional internal combustion engine coupled with the electric drive trains [2]. As a result, the hybrid vehicles create a good blending of the two technologies.

As opposed to EVs, HEVs may seamlessly switch between electric and gasoline and, therefore, have the inherent advantage of "range extension" which itself addresses the anxiety among EV owners regarding "range anxiety". The adaptability of HEVs means that they are suitable for various types of trips, such as the family vacation as well as places which have little or no charging networks. Moreover, HEVs are a tool buffer during the corresponding of electric vehicles protest a smooth transition. Despite EVs being superior in terms of less pollution and fuel efficiency, HEV technology is still perfect for better fuel efficiency and less emission compared to normal IC engine vehicles. EVs are changing the horizons of automotive industry by giving the consumers options between various designs that could satisfy environmental and practical needs.

EVs in particular are developing as a decent compromise for those who still have some reservations abandoning gasoline-powered vehicles completely for battery-powered electric alternatives [1][2]. Through a hybrid system consisting of conventional internal combustion engines and electric motors, HEVs serve as a good example of a combination between two power sources while still solving the issue of a limited range.

Electric electric vehicles' effectiveness depends on the energy management strategy (EMS) which ensures that energy is transferred among the internal combustion engines, electric motors, and batteries as smartly as possible. Through the wavering of power allocation depending on the driving modes, the EMS increases the fuel effectiveness while decreasing the emission rates, at the end the EMS enhances the overall performance of a HEV [3].

The integral part of Hybrid Electric Vehicles is the energy management strategy (EMS) that is a complicated control system designed to obtain the maximum from energy utilization and vehicle performance. The EMS uses the best energy distribution amongst the internal combustion engine, electric motor(s), and battery, which are adjustable to specific driving conditions [4]. The EMS with electric power modulation or the internal combustion engine control boosts fuel efficiency and helps in lowering emissions, in turn, optimizing the performance of the Hybrid Electric Vehicles.

Electric vehicles are seen as a new way of moving from one place to another, a cleaner and more sustainable alternative to the traditional engine. And while EVs may have helped in this regard, it is still most important that energy be well utilized in such cars [1]. This begins as an influential element in system functions of all elements and actuator subsystems since only it takes into account system efficiency and related task requirements.

Predictive Maintenance and AI: An artificial intelligence system used to predict driving cycles can similarly be

979-8-3503-7809-2/24/$31.00 ©2024 IEEE

Authorized licensed use limited to: DELHI TECHNICAL UNIV. Downloaded on November 09,2024 at 04:47:40 UTC from IEEE Xplore. Restrictions apply.

employed for predictive maintenance. Through scrutinizing the real-time data from a variety of automobile parts, the AI algorithms can detect latent breakdowns in advance and thus prevent them from becoming serious faults [3]. This proactive approach minimizes downtime and optimizes overall vehicle performance.

The application of AI to the area of charging infrastructure has the potential to bring about a revolution through Optimal station placements, determination of usage patterns, and management of the charging process in order to create a seamless user experience. Moreover, AI may also contribute to improving battery technology by maximizing its performance, increasing its lifespan, and ensuring safety through careful supervision and degradation forecast [4].

Making EVs More User-Friendly Using AI: Artificial intel-license allows for personalization of EV features so that they respond intuitively and make use of voice control systems. One of the most profound areas where AI exceeds self-driving cars lies in these spheres. The machine learning algorithms can modify vehicle settings using data about users' preferences, and the AI-based infotainment systems ensure that passengers receive relevant information, access entertainment, and enjoy all the advanced driving assistance functionalities, contributing to an even more enhanced user experience, offering a holistic approach to improving electric vehicle technology and paving the way for a cleaner and more sustainable transportation future [1].

Optimizing performance on the road: Predictive energy management for electric vehicles Traditional energy man-agreement systems (EMS) in electric vehicles (EVs) rely on real-time data to optimize power distribution. However, with predictive EMS, a new wave of innovation is emerging. This forward-looking approach aims to improve energy efficiency by incorporating predictions of future driving conditions into the decision-making process.

The main goal of predictive EMS in this paper is to optimize power allocation by predicting upcoming driving scenarios. These include factors such as future speed, road conditions and traffic patterns. Predicting EMS performance depends heavily on the accuracy of these predictions, especially when it comes to future vehicle speeds. Predicting the entire driving cycle with perfect accuracy remains a challenge, but short-term predictions can bring significant benefits.

II. Predictive Power: Next-Generation EVS

A. Types of Predictive EMS: A Focus on Driving Cycle Prediction using Artificial Intelligence

Real-time data is used by the EMSs of Traditional Electric Vehicles (EVs) to optimize power distribution. However, a new wave of innovation has emerged with predictive EMS. This proactive approach seeks to include future driving predictions in optimizing energy efficiency [5].

The key objective of Predictive Energy Management System (EMS) is to allocate power effectively by predicting driving scenes that are forthcoming. These may encompass future rates, traffic patterns or road conditions amongst other things. The quality of these predictions has a lot to do with how well it predicts EMS performance particularly with respect to speed of the vehicle going forward. Being able to predict the rest of the journey cycle absolutely accurately still remains a challenge, however there can be significant gains from short term predictions [6].

Several aspects such as driver behavior, road conditions and traffic patterns as well as presence of vehicles ahead can influence their accuracy. To increase prediction accuracy Predictive EMS draws on an increasing number surrounding information which enables it make more informed decisions about directing power in future [2].

Many ways could be used to implement Predictive EMS. Nevertheless, this article concentrates on one certain and very prospective method of driving cycle predictions such as applying AI to guarantee better fuel economy.

Commonly, conventional EMSs use standard driving cycle in their power split calculation. This can be interpreted that when real-world situations involving random phenomena like traffic jams are considered, it will lead to poor fuel efficiency. Predictive EMS founded on driving cycle predictions thus aims at using different prediction techniques which forecast the future velocity/direction of movement, and optimizes the power split toward having a strong relationship with fuel economy.

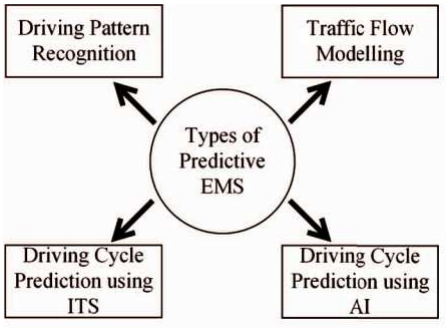

Fig. 1. Types of predictive EMS.

Various methods have been discovered for predicting driving cycles referring to Fig 1. Types of Predictive EMS, but AI-based ones are especially useful due to their benefits and prospects. Here is a summary of some popular forecasting techniques that are common and why AI is so unique [6]:

A. Driving Pattern Recognition: Historical database of "Driving Patterns" created by this method collects past data, while the similar pattern to the current situation is identified using patterns recognition techniques like fuzzy logic or neural networks. Although it may be effective in predesigned routes, it may lack the ability to cope with real world variations [2].

B. Traffic Flow Modeling: The velocity of vehicles is esti-mated using traffic flow models in this approach. Nevertheless, these models often extrapolate general principles and may not take into account individual driving behavior or unexpected events [2].

C. Predicting the driving cycle using an Intelligent Trans-portation System (ITS): Real time traffic information collected through GPS, GIS and V2V communication among cars can predict future driving scenarios. However,

Authorized licensed use limited to: DELHI TECHNICAL UNIV. Downloaded on November 09,2024 at 04:47:40 UTC from IEEE Xplore. Restrictions apply.

even if it incorpo-rates real time data, presence of errors in predictions can still limit accuracy of such data [2].

D. AI based Driving Cycle Prediction This is why we are focusing on driving cycle predictions using AI in this study [2].

Machine Learning and Artificial Neural Networks (ANNs): We employ Machine learning algorithms such as ANNs to scrutinize huge data sets about driving patterns, traffic volume and historical information [4]. ANNs are useful since they can handle intricate dynamics well and also address the indirect relationships that exists within the data [6].

Outstanding Performance: Furthermore, other research has shown that ANNS have a better ability of predicting vehicle velocities associated with HEV energy management. Therefore, it brings out more precise forecasts leading to much improved energy optimization.

Continuous Improvement: Continuous learning and im-provident is possible through AI techniques. By utilizing V2V/V2I communication data along with advanced method-ologies such as Bayesian networks, we can create more comprehensive models that handle uncertainties and enhance predictability further.

While there are various methods of driving cycle prediction for Predictive EMS, traditional approaches often struggle in the face of real-world complexities. AI methods thrive here. In addition, another advantage is seen with artificial neural networks (ANNs) which are machine learning algorithms [6]. Their competency in dealing with intricate data, reaching more precise predictions on vehicle velocity and updating their knowledge bases from time to time make them a strong enabler of energy efficiency enhancement in electric vehicles.

In addition, building upon previous work this study investigates the use of AI-based driving cycle prediction methods in Predictive EMS for EVs. Specifically, we exploit the merged power of N-Beats and XGBoost algorithms, two well-known machine learning models, to design a better performing model one. This concentration on AI and some algorithms' specifics underscores how this research is innovative when it comes to improving energy utilization by Electric Vehicles.

III. METHODOLOGY

Adaptive control systems can include machine learning models that change vehicle parameters according to the present state of driving for an overall better vehicle performance and quicker reactions. Adaptive control and machine learning have related primitive concepts, update laws thus one may use results obtained from both areas to find solutions to new problems more effectively. Whereas adaptive control tackles the problem of regulating critical variables in engineering systems with uncertain dynamics, machine learning improves performance through experience and parametric model-based function approximations. This integration provides a basis for realtime control and learning in the presence of parametric un-certainties in dynamic systems. In addition, understanding how these fields relate can foster development of new approaches toward intricate issues and enhance system operation.

Data Set:

The data used in the study consists of Dynamometer Drive Schedules for Electric Vehicle (EV) specifically presenting speed values in mph at every cycle step [7]. Some specific samples have been taken from 1800 cycle steps and are only concerned with dynamometer readings related to EVs, starting at zero mph [7]. For Time Series Forecasting, two lists were developed using a systematic approach of preparing this type of data: Backcast and Forecast [4]. Backcast list had speed in mph for the first fifteen samples while forecast had five consecutive sample appended to it at each index of the dataset. This process aligned the data for utilization in machine learning algorithms [4]. The dataset was carefully checked without finding any missing values within it [7].

This is further refined by taking window size around 5 on the dataset [7]. Thereafter, line plots were extensively analyzed that provided insights into different aspects of EV performance as shown in Dynamometer Drive Schedules[7].

Metrics:

Mean Squared Error (MSE) is a common metric used to evaluate the performance of a predictive model, particularly in regression analysis [8]. It quantifies the average squared difference between the actual and predicted values of a dataset. The formula for Mean Squared Error is [8]:

$$MSE = \frac{1}{n} \sum_{i=1}^{n} (y_i - \hat{y}_i)^2$$

A. XGBoost

XGBoost has been credited for being one of the most efficient and effective methods in both regression and classification among others while popular machine learning algorithms are available today. It is based on gradient boosting framework using decision trees as weak learners [9]. This involves some major features like regularization, par-allelism tree-pruning along with hardware optimization for rapid scaling during trainings. Its customizable parameters along with being able to identify feature importances widely applicable makes it suitable for a range dataset characteristics amongst other aspects.

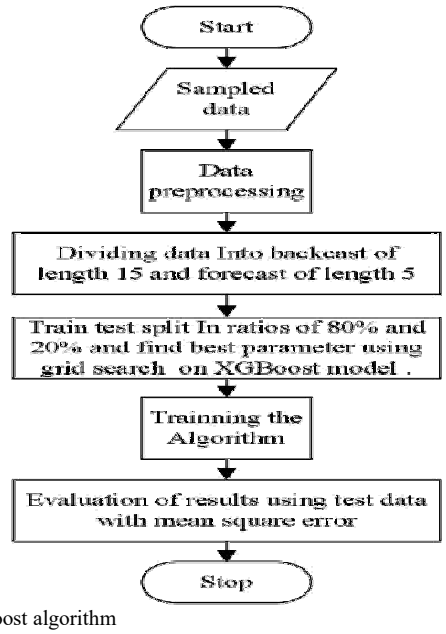

Fig. 2.XGBoost algorithm

Authorized licensed use limited to: DELHI TECHNICAL UNIV. Downloaded on November 09,2024 at 04:47:40 UTC from IEEE Xplore. Restrictions apply.

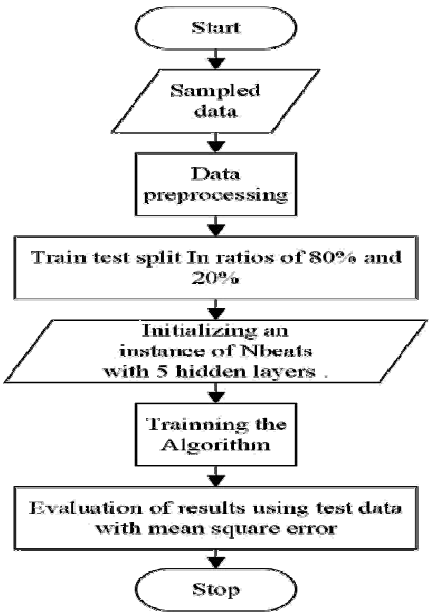

Fig. 3.Nbeats Algorithm

We have taken an approach where in the modelling process; all inputs are based on a backcast of 15 and outputs represent forecast of 5. Our modeling efforts were primarily facilitated using the powerful library known as XGBoost. To build the model successfully, major parameters including regression learning rate (0.3), maximum depth (around 13), tree method (auto) and other parameters left at default values were vital [9]. The reasoning as to why the choice of these particular shapes were made is drawn from insights extracted from NBeats paper [10]. To ensure that optimal performance was obtained, XGBoost parameters were fine-tuned.

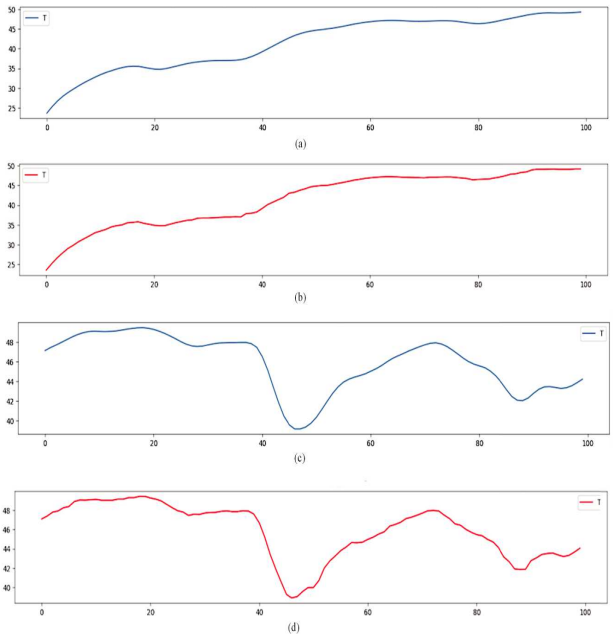

Fig. 4. XGBoost expected and predicted velocity values

MSE (Mean Squared Error) has been used to measure loss and this helps in gauging how effective the training process was. The algorithm had an average MSE of 0.067 which indicates its strong ability to capture and learn patterns from the underlying data. For visual evaluation of the results, plot "Speed In mph" on Y-axis versus relative cycle steps from initial cycle step on X-axis. Thus, in Fig 4. XGBoost Expected and Predicted Velocity Values, we can see that blue line represents true speed (mph) while red line is for predicted

speed (mph). The flowchart of driving cycle prediction using XGBoost algorithm as shown in Fig. 2. XGboost Algorithm.

B. NBeats

N-BEATS is an efficient deep learning algorithm that out-performs when dealing with wide-ranging datasets. It lever-ages a set of fully connected neural networks in order to make predictions on subseries with temporal operations to capture short-term and long-term patterns [10].

Table I

Parameters	XGBoost	Nbeats
MSE Value	MSE=0.06	MSE=0.006
Performance	Inferior	Superior
Execution Time	10 min	1.5 hrs

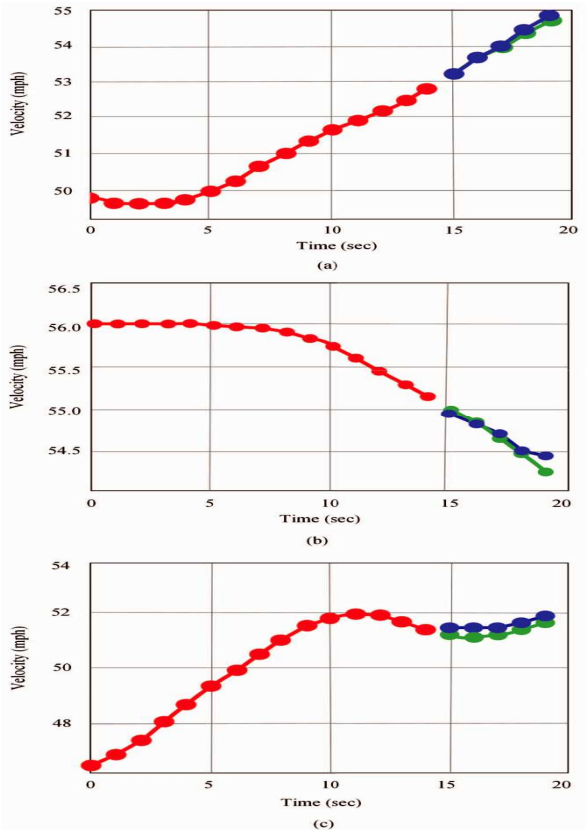

Fig. 5.NBeats expected and predicted velocity values

One of the main features of N-BEATS is its flexibility in processing different types of time data and its scalability to large datasets. N-BEATS has been successful in the financial, energy and retail markets and is popular for its ability to deliver results and solve many forecasting problems.

NBeats tackles the univariate times series point forecasting problem using deep learning [10]. We adopt a deep neural architecture with backward and forward residual links together with a very deep stack of fully-connected

Authorized licensed use limited to: DELHI TECHNICAL UNIV. Downloaded on November 09,2024 at 04:47:40 UTC from IEEE Xplore. Restrictions apply.

layers [10]. It is interpretable, domain-independent, and can be trained quickly among other features [10].

"NeuralBeats" model was developed using "NBeats" Library. Then, we reshaped the data so it could meet requirements for dataset. After this, training started with a (n,1) format. The forecast length of around 5 accompanied by backcast length approximated at about 15. The algorithm went through three epochs.

The Mean Squared Error metric was used and a significant loss of about 0.006 was realized. Visual evaluation of the results in Fig 5.NBeats Expected and Predicted Velocity Values, involves plotting "Speed In mph" on the Y-axis and the relative cycle steps from initial cycle step on the X-axis. The blue line is a Backcast, green line indicates real forecast while red line shows predicted forecast. The flowchart of driving cycle prediction using NeuralBeats algorithm as shown in Fig. 3. Nbeats Algorithm.

IV. RESULTS

This study investigates Neural Beats algorithm which outperformed XGBoost in terms of Mean Squared Error (MSE) but having longer runtime. XGBoost finished execution within 10 minutes with an MSE of 0.06 while NeuralBeats took 1.5 hours on two x T4 GPU to achieve lower MSE at 0.006, demonstrating its efficiency in capturing and predicting patterns in data set. As mentioned in Table 1 (Comparison Table).

XGBoost predicts values based on features and historical data while NBeats utilizes back cast, real forecast, and predicted forecast components. Nbeats does representation by showing actuals, predictions in different colors for analysis over time while for Xgboost only it compares between real and predicted values over several timestamps.

The two models offer diverse viewpoints on forecast and determining errands: XGBoost emphasizes feature-based mod-eling, whereas NBeats gives structure to past and anticipated information. Being mindful of the subtle elements in each model's yield can help in elucidation and enhancement of figure exactness.

XGBoost Model Analysis:

In evaluating the XGBoost model shown in Fig. 4. XGBoost Expected and Predicted Velocity Value ,actual(expected) values (represented by blue color) are compared with the model's predicted values (represented by red color) across a range of time stamps. The graphs are subdivided into subgraphs each covering 100 time steps totaling to 199 as the overall range. This particular representation allows for clear contrast between real values and forecasts that were made by XGBoost model.

NBeats Model Analysis:

In the NBeats model graph shown in Fig. 5. XGBoost Ex-pected and Predicted Velocity Value, Back Cast is represented by red depicting historical data leading up to forecast period, Real Expected velocity value Forecast is indicated by green showing actual values for this period and Predicted velocity value Forecast is shown in blue which represents forecasted values from the model. NBeats Model Analysis: In the NBeats model graph shown in Fig. 5. XGBoost Ex-pected and Predicted Velocity Value, Back Cast is represented by red depicting historical data leading up to forecast period, Real Expected velocity value Forecast is indicated by green showing actual values for this period and Predicted velocity value Forecast is shown in blue which represents forecasted values from the model.

V. CONCLUSION

In the conclusion, analysis of XGBoost and NBeats algorithms as applied to driving cycle prediction in Hybrid Electric Vehicles (HEVs) demonstrated the following. The XGBoost algorithm took approximately 10 minutes to perform the task with a MSE of 0.06. The NBeats algorithm, in contrast, attained a substantially lower MSE of 0.006 in 1.5 hours using two x T4 GPU. NBeats' advantage of capturing more delicate patterns with high precision shows its suitability for forecasting with better precision. In spite of resulting in a longer overall runtime, NBeats has many advantages, namely its systematic representation of past and future data and its visual illustration of actual and forecasted data over time. On the other hand, XGBoost methodology is based on feature-based modeling, by comparing the real and predicted values. Recognizing the specific outputs of each algorithm is the most crucial thing for determining the effectiveness levels of the forecast. Specifically, the study of this arises from a suggestion of more efficient Energy Management Strategies for HEVs as a step toward advanced sustainable transportation alternatives. For future research of this topic, the focus could be to enrich the efficiency of NBeats so as to include in the real-world settings.

REFERENCES

[1] J. Van Mierlo, M. Berecibar, M. El Baghdadi, C. De Cauwer, M. Messagie, T. Coosemans, V. A. Jacobs, and O. Hegazy, "Beyond the State of the Art of Electric Vehicles: A Fact-Based Paper of the Current and Prospective Electric Vehicle Technologies," *World Electric Vehicle Journal*, vol. 12, no. 1, p. 20, 2021.

[2] S. Onori, L. Serrao, and G. Rizzoni, *Hybrid Electric Vehicles: Energy Management Strategies*, London: Springer, 2016.

[3] J. Yang *et al.*, "Designing a Car Price Prediction Model in the Metaverse with Machine Learning," in *Proc. 2023 IEEE Int. Conf. on Metaverse Computing, Networking and Applications (MetaCom)*, June 2023.

[4] M. A. Ozer, O. Aydogdu, and B. Guven, "Predictive Energy Management for Electric Vehicles," *IEEE Transactions on Vehicular Technology*, vol. 71, no. 8, pp. 1-12, Aug. 2022.

[5] S. Kutter and B. Baker, "Predictive Online Control for Hybrids: Resolving the Conflict Between Global Optimality, Robustness, and Real-Time Capability," in *Proceedings of the 2010 IEEE Vehicle Power and Propulsion Conference*, Lille, France, Sep. 2010, pp. 1–3.

[6] F. Jiang, Y. Wang, J. Tang, and W. He, "Energy Management Strategies for Hybrid Electric Vehicles: Review, Classification, Comparison, and Outlook," *MDPI*, vol. 13, no. 13, p. 3352, 2020.

[7] "The Dynamometer Drive Schedules Used in the Study Were Based on Guidelines Provided by the Environmental Protection Agency (EPA)," [Online].

[8] E. Orellana, "Not Nice Square Error," *Medium*, 2023. [Blog post].

[9] T. Chen and C. Guestrin, *XGBoost: A Scalable Tree Boosting System* (3rd ed., vol. 2), 2016.

[10] B. N. Oreshkin, D. Carpov, N. Chapados, and Y. Bengio, "N-BEATS: Neural Basis Expansion Analysis for Interpretable Time Series Forecasting," 2019.

Authorized licensed use limited to: DELHI TECHNICAL UNIV. Downloaded on November 09,2024 at 04:47:40 UTC from IEEE Xplore. Restrictions apply.

An Adaptive Forward Compensation for Enhanced PLL Based Position Estimation of Syn-RL Motor Drive

Saurabh Mishra[1,2], *Senior Member, IEEE* and Bhim Singh[1], *Fellow, IEEE*
1,Department of Electrical Engineering, Indian Institute of Technology Delhi, Hauz Khas, New Delhi-110016, India
2,Department of Electrical Engineering, Delhi Technological University, New Delhi-110042, India
(saurabhmishra@dtu.ac.in, bsingh@ee.iitd.ac.in)

***Abstract*— Electric vehicle (EV) drive systems that don't rely on speed sensors are more dependable, affordable, and stable. However, achieving precise control without sensors throughout whole speed spectrum is quite challenging. This paper presents an improved position and speed estimation using speed adaptive forward compensation based enhanced quadrature phase locked loop (AFCE-QPLL) technique. Syn-RL motor's active flux (AF) notion is used in proposed method to eradicate variations in estimated flux from cross-coupling. High-frequency noise and DC bias insensitivity of explained system improve its robustness. The presented method has less speed and position inaccuracy than traditional and methods. The presented system is integrated with solar PV array for augmenting battery performance. The battery performance and driving range of EV are enhanced by utilizing a roof-mounted solar panel while vehicle is in motion or stationery. The system is examined and verified using MATLAB for a 22-kW electric vehicle propulsion system based on a Syn-RL motor. It provides a thorough portrayal of EV dynamics, as well as motor battery's improved performance.**

Keywords—Synchronous Reluctance (Syn-RL) Motor, Disturbance Observer (DO), Active Flux (AF), Vector Control (VEC).

I. INTRODUCTION

The electrification of vehicles has emerged as most effective way for automotive industry, which is one of major producers of carbon dioxide (CO2) emissions, to satisfy environmental regulations and modify automobile market. One of most significant contributors to carbon dioxide emissions is automotive sector. Plug-in hybrid electric vehicles and electric vehicles that are powered only by batteries are two categories that can be used to categorize electric vehicles (EVs). Because they do not contribute to air pollution, battery electric vehicles (BEVs) are most environmentally friendly and sustainable solution to reduce CO2 emissions over time. Despite fact that battery electric vehicles (BEVs) represent a viable transportation solution for achieving low carbon emissions, they continue to face two key obstacles in market for passenger automobiles: limited range and lengthy charging periods. BEVs predominantly employ electric motors that are based on permanent magnet (PM) technology. These motors include PM-BLDCM, surface-mounted PMSM, and saliency-based PMSM. PM electric motors have several disadvantages, including potential for demagnetization, a restricted temperature range, and significant cogging torque. EV drives are increasingly adopting synchronous-reluctance (Syn-RL) motors. Syn-RL motors employ a straightforward rotor configuration consisting of laminated steel with clearly defined poles or slots. Syn-RL rotors do not contain permanent magnets, windings, or rotor cages, which sets them apart from permanent magnet motors or induction motors. The design's minimalism reduces production complexity and costs. Syn-RL motor is controlled by vector control (VEC), which requires information about both speed and position. The drive frequently depends on encoders to provide speed and position data, which could potentially undermine mechanical robustness and reliability. The concept of encoder-less control has attracted considerable interest due to its capacity to improve both reliability and performance. Encoder-less control solutions can be divided into two primary categories: high-frequency injection approaches and model-based methods. In order to determine rotor's position, high-frequency injection technique takes advantage of Syn-RL rotor's special properties to identify inductance variations. Still, controlling system can detect audible sound from this method. But model-based approach can function without the injected signal. One method uses back electromotive force (back EMF), and other uses flux estimation. To get estimated flux, it is common practice to use an open loop observer derived from voltage equation. However, a large DC error may occur since the integral is sensitive to starting value. For accurate flux estimation for IPMSM motor, active flux based technique using various feedforward methods to enhance dynamic performance of IPMSM drive is presented in [1]. The authors in [2] have presented a hybrid model of flux observer with both voltage and current model used for accurate flux estimation of Syn-RL motor. Higher order generalized integrator (GI) based flux estimation is also becoming popular in Syn-RL motor with simple structure and implementation. Multiple second order GI (SOGI) based flux estimation is thoroughly investigated in [3] for solar water pumping application. An improved adaptive flux based speed sensorless control is presented in [4] for light EVs with conventional arc tangent method based speed and position estimation. To improve accuracy and precision of rotor position and speed, PLL based rotor position and speed estimation is current research area for speed sensorless control. Different PLL techniques for power application is outlined in [5]. Type-I, II and III PLLs with focus on position and speed estimation is investigated in [6, 7]. As the order of PLL increases complexity increases. The authors in [8] have presented a system with compensation for position estimation error. A complex band pass filter with different PLLs is presented in [9] with improved back-EMF estimation and corresponding speed and position estimation. Other improved flux estimation technique is presented in [10] for Syn-RL motor drive for high power rating uses AFCE-QPLL technique to implement a robust speed and position

2024 IEEE Region 10 Symposium (TENSYMP) | 979-8-3503-6486-6/24/$31.00 ©2024 IEEE | DOI: 10.1109/TENSYMP61132.2024.10752228

979-8-3503-6486-6/24/$31.00 ©2024 IEEE

Authorized licensed use limited to: DELHI TECHNICAL UNIV. Downloaded on November 25,2024 at 04:49:24 UTC from IEEE Xplore. Restrictions apply.

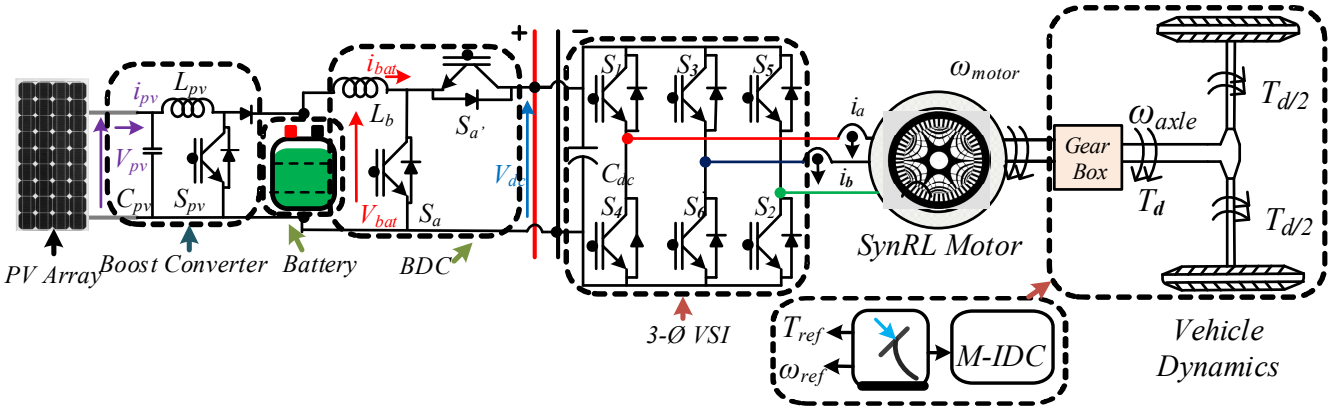

Fig.1 EV power train with Syn-RL motor.

estimation along with disturbance observer (DO) for active flux estimation. The EV drive presented produces negligible speed and position deviations across entire driving spectrum. Harnessing photovoltaic solar energy improves battery's performance.

Six distinct sections organize provided work, with second section providing a detailed explanation of overall system configuration. Third section of research delves into design and modelling of EV drive under discussion. Section IV examines control of individual converters and Syn-RL motors through utilization of speed and position estimation. Section V contains detailed simulation results, whereas Section VI provides related conclusions.

II. System Configuration

An EV powertrain utilizing a Syn-RL motor, a battery and solar PV panel is depicted in Fig. 1. Syn-RL motor is primarily energized by a battery, and its operation is regulated by field-oriented control (FOC) via a voltage source inverter (VSI). Solar photovoltaic (PV) array is employed to enhance battery performance by deploying a boost converter.

III. Design And Modeling Of EV PowerTrain

This section delves with design and modeling of drivetrains for electric vehicles, including mathematical modeling of tractive forces, selection of solar photovoltaic array, and bi-directional DC-DC (BDC) converter. In addition, mathematical modeling of Syn-RL motor in a stationary reference frame is also included in this section.

A. Modeling of Electric Vehicle Dynamics

Modeling of vehicle dynamics involves employing of tractive force concept, which takes into consideration several forces that impact vehicle, including propulsion force, aerodynamic drag, rolling resistance, and gravitational forces expressed as,

$$F_t = F_d + F_r + F_g + F_\omega \tag{1}$$

where, F_d = aerodynamic drag, F_r= rolling resistance, F_g= gradient , F_ω=angular rotation

B. Design of Bi-directional DC-DC Converter (BDC)

By utilizing a half-bridge design, voltage source inverter (VSI) DC link and battery are linked together. This is done in conjunction with a bidirectional DC converter (BDC). BDC operates in boost mode during cruising and acceleration, switching to buck mode during deceleration. When modeling boost mode of BDC, DC link voltage is represented by V_{dc}, and battery voltage is represented by V_{bat},

$$V_{dc} = \frac{V_{bat}}{1-d_a} \tag{2}$$

where, d_a is the duty cycle of BDC during acceleration.

In EV dynamics, BDC duty cycle is determined as,

$$d_a = \frac{V_{dc}-V_{bat}}{V_{dc}} = \frac{600-400}{600} = 0.33 \tag{3}$$

The inductance L_1 of BDC is calculated for maximum current ripple (ΔI) of 20% with switching frequency (f_{sw}) of 15 kHz,

$$L_1 = \frac{V_{bat}\times d_a}{f_{sw}\times \Delta I_{bat}} = \frac{400\times 0.33}{15k\times 7.33} = 1.2mH \tag{4}$$

BDC output capacitance (C_{dc}) is estimated while motor is working at minimum speed (ω_{min}), and DC voltage output fluctuation (ΔV) is 10%,

$$C_{dc} = \frac{I_{dc,pk}}{6\omega_{\min}\times \Delta V_{dc}} = \frac{36}{6\times 52.33\times 40} = 2800\mu F \tag{5}$$

C. Design of Solar PV Array for EV System

The vehicle's structure and total size restrict available space for installing a solar photovoltaic (PV) array. Given constraints of vehicle and motor, a solar panel with a maximum output of 600 W is selected. The open circuit voltage (V_{oc}) is set at 400V, and the short circuit current (I_{sc}) is set at 2A. Typically, for maximum power point tracking (MPPT), the voltage at maximum power (V_{mp}) and current at maximum power (I_{mp}) is determined as,

$$V_{mp} = 0.85 * V_{oc} = 0.85 * 400 = 340V \tag{6}$$

$$I_{mp} = \frac{P_{mp}}{V_{mp}} = \frac{600}{340} = 1.76A \tag{7}$$

Authorized licensed use limited to: DELHI TECHNICAL UNIV. Downloaded on November 25,2024 at 04:49:24 UTC from IEEE Xplore. Restrictions apply.

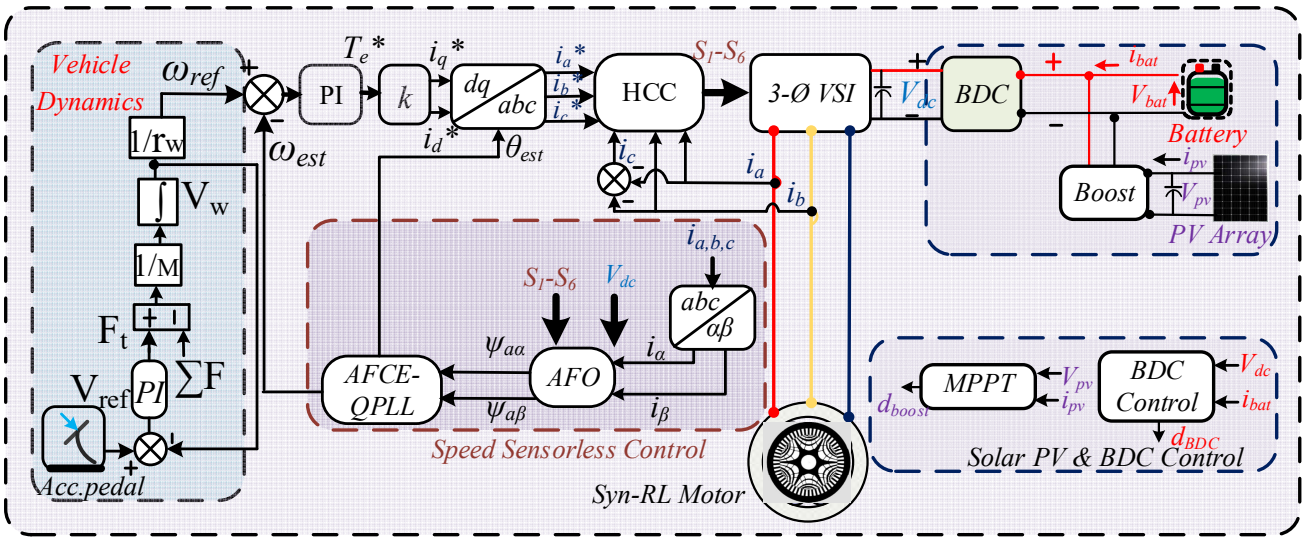

Fig.2. Control Schematic

D. Modelling of Syn-RL Motor with Active Fluxes (AF)

The active flux model of Syn-RL motor is less influenced by variations in motor configurations and loads. The modeling in α-β frame is expressed as [3],

$$v_\alpha = \{R_s + pL_q\} i_\alpha + p(\psi_d^a \cos\theta_r) \quad (8)$$

$$v_\beta = \{R_s + pL_q\} i_\beta + p(\psi_d^a \sin\theta_r) \quad (9)$$

$$p(\psi_d^a \cos\theta_r) = p\psi_d^a \cos\theta_r - \omega_r \psi_d^a \sin\theta_r \quad (10)$$

$$p(\psi_d^a \sin\theta_r) = p\psi_d^a \sin\theta_r + \omega_r \psi_d^a \cos\theta_r \quad (11)$$

where, ψ_d^a is active flux and is expressed as, $\psi_d^a = (L_d - L_q) i_d$. $v_{\alpha\beta}, i_{\alpha\beta}$ are stator voltages and currents in α-β axes. R_s denotes stator resistance. L_d and L_q denote d-q axes inductances ω_r is rotor speed and θ_r represents rotor position. i_d and i_q represent d-q axes component of currents.

IV. Control Schematic

This section presents EV system control, with an emphasis on Syn-RL motor's speed and position estimation outlined in Fig. 2. A vector control (VEC) approach is used to regulate speed and torque of Syn-RL motor. This system estimates motor's speed and position using AFCE-QPLL technique and disturbance observer based active flux estimation. The reference values of current along d-q axes are provided by VEC so that voltage source inverter (VSI) can create switching pulses. When vehicle is not in motion, battery is charged using a rooftop PV array.

A. . Syn-Rel Motor Control

Vector control (VEC) encompasses a speed proportional-integral regulator that produces necessary torque expressed as,

$$T_e^* = T^*_{e(z-1)} + K_{p\omega}\{\omega_{est(z)} - \omega_{est(z-1)}\} + K_{i\omega}\omega_{est(z)} \quad (12)$$

The electromagnetic torque of Syn-RL motor is expressed in terms of d-q axes current as,

$$T_e^* = \frac{3}{2} * \frac{P}{2}(L_d - L_q) i_d^* i_q^* \quad (13)$$

The currents (i_d*, i_q*) in d-q frame follow reference torque as,

$$i_d^* = \sqrt{\frac{4|T_e^*|k}{3P(L_d - L_q)}} \quad (14)$$

$$i_q^* = \frac{i_d^*}{k} * \operatorname{sgn} T_e^* \quad (15)$$

where, ω_{est} is estimated speed , $k = \sqrt{L_d / L_q}$, inductances are L_d , L_q and no of poles as P.

B. Control of Bi-directional DC-DC Converter(BDC)

With dual loop control structure (inside current loop and outside voltage loop) shown in Fig. 3, BDC controls primary power source, battery. A voltage-proportional-integral (PI) controller generates reference battery current. Conversely, a current PI controller generates reference control voltage for switching pulses. BDC is in boost mode while electric car accelerates or cruises; it is in buck mode when it slows down.

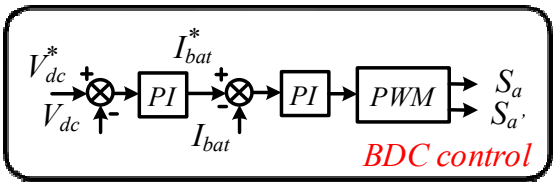

Fig.3 BDC Control

C. MPPT Control for Solar PV Array

Maximum power point tracking (MPPT), which is necessary to maximize performance of solar photovoltaic (PV) array, requires monitoring of V_{pv} and I_{pv}. The incremental conductance (InC) approach is widely used for solar PV array control because of its rapid convergence. To achieve MPPT, an InC control algorithm controls switching pulses of a boost converter.

D. Active Flux Estimation Disturbance Observer (DO)

Syn-RL motor with active flux model is expressed as,

Authorized licensed use limited to: DELHI TECHNICAL UNIV. Downloaded on November 25,2024 at 04:49:24 UTC from IEEE Xplore. Restrictions apply.

$$V_{\alpha,\beta} = \left(R_s + sL_q\right) i_{\alpha,\beta} + \psi^a_{\alpha,\beta} \tag{16}$$

$$\hat{\psi}^a_{d,\alpha\beta} = g_1\left\{\hat{i_{\alpha,\beta}} - i_{\alpha,\beta}\right\} + g_2\left\{i_{\alpha,\beta}\right\} + g_3\left\{V_{\alpha,\beta}\right\} \tag{17}$$

where, $\hat{\psi}^a_{d,\alpha\beta}$ and $\hat{i_{\alpha,\beta}}$ are estimated active flux and current respectively. g_1 is the PI controller, g_2 is the feedforward gain due to current and g_3 is the function of g_2.

The estimated current [1, 2] and g_3 can be expressed as,

$$\hat{i_{\alpha,\beta}} = \frac{V_{\alpha,\beta} - \hat{\psi}^a_{d,\alpha\beta}}{R_s + sL_q} \tag{18}$$

$$g_3 = -\left[\frac{g_2}{R_s + sL_q}\right] \tag{19}$$

Transfer function of DO technique is expressed as,

$$\frac{\hat{\psi}^a_{d,\alpha\beta}}{\psi^a_{d,\alpha\beta}} = \left\{\frac{g_2 - g_1}{R_s + L_q + g_2 - g_1}\right\} \tag{20}$$

The disturbance observer is modelled using stationary axes voltage and current as presented in Fig. 4(a).

E. Speed and Position Estimation using Adaptive Forward Compensated Enhanced QPLL (AFCE-QPLL) technique

In Syn-RL motor drive, speed and position is achieved using open loop conventional arc tangent technique which suffers from tracking problem. With PLL based estimation, tracking problem is mitigated but problem for ramp inputs still remains. For EV, acceleration and deceleration are always associated with ramp inputs. A speed adaptive with forward compensation is presented in Fig. 4(b), which focuses on forward compensation for zero steady state error for ramp inputs. Moreover, reference speed obtained from modified Indian driving cycle (M-IDC) is added to estimated speed for better tracking of speed. Conventional PLL technique has speed and position transfer function modelled as,

$$\frac{\Delta\theta}{\theta} = \frac{K_p s + K_i}{s^2 + K_p s + K_i} \tag{21}$$

where, $K_i = \omega_n^2$ and $K_p = 2\xi\sqrt{K_i}$ represents gains of PLL.

For AFCE-QPLL technique, small signal model is presented in Fig.4 (c) and transfer function is modelled as,

$$\frac{\Delta\theta}{\theta} = \left[\frac{(1 - G_{FC}(s))s}{s + L(s)}\right] \tag{22}$$

$$G_{FC}(s) = \frac{1}{sT + 1} \tag{23}$$

where, L(s) is proportional and integral controller, $G_{FC}(s)$ is forward compensation block modelled as first order transfer function with T as time constant. For obtaining steady state error for presented AFCE-QPLL technique in terms of position, transfer function is expanded as,

$$\frac{\Delta\theta}{\theta} = \left[\frac{\left(1 - \frac{1}{sT+1}\right)s}{s + \left(K_p + \frac{K_i}{s}\right)}\right] = \frac{s^3 T}{s^3 T + s^2(TK_p + 1) + s(TK_i + K_p) + K_i} \tag{24}$$

where, K_p and K_i are gains of the PI controller.

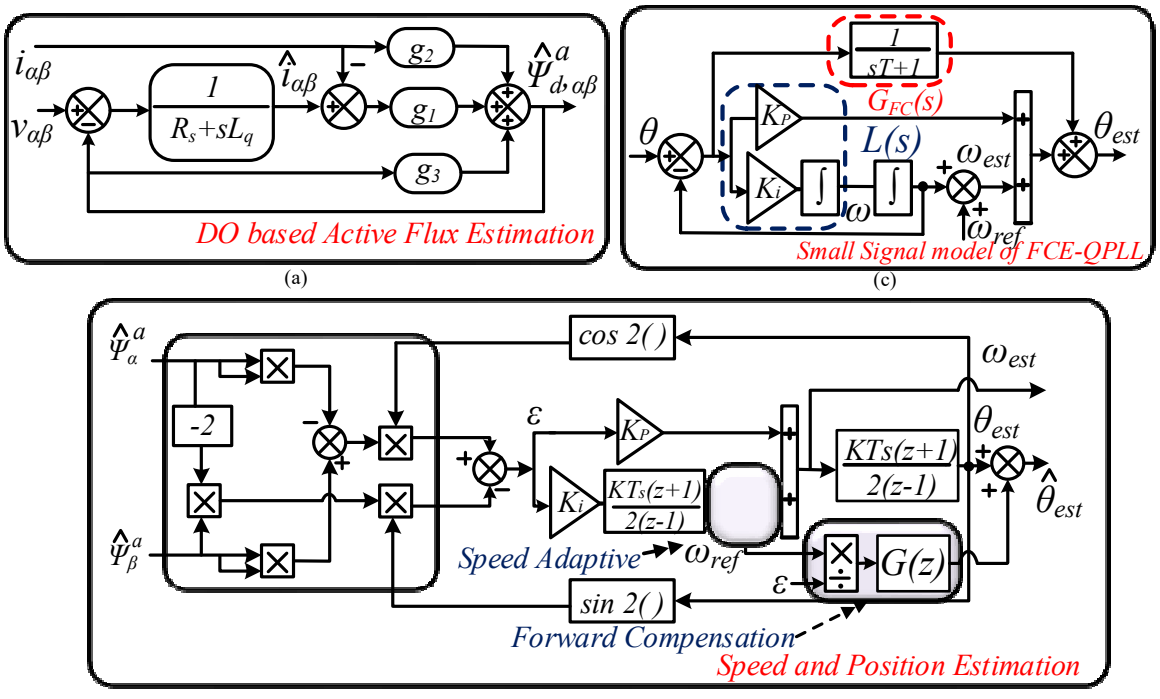

Fig.4.Control structure (a) DO based active flux (AF) estimation (b) Speed and position estimation using speed adaptive FCE-QPLL technique (c) Small Signal model of speed adaptive FCE-QPLL.

Authorized licensed use limited to: DELHI TECHNICAL UNIV. Downloaded on November 25,2024 at 04:49:24 UTC from IEEE Xplore. Restrictions apply.

Presented transfer function of AFCE-QPLL resembles third order system, for which steady state error is zero for ramp inputs. But for QPLL technique, steady state error is a non-zero value.

$$\Delta\theta_{ss} = \lim_{s\to 0}\{s\Delta\theta(s)\} * \frac{1}{s^3} = 0 \tag{25}$$

The speed transfer function is also modelled as,

$$\frac{\Delta\omega}{\omega} = \left[\frac{s}{s+L(s)}\right] \tag{26}$$

V. Results And Discussion

An analysis of vehicular propulsion utilizing Syn-RL motor is conducted in MATLAB Simulink, incorporating a precise estimation of active flux (AF). AF is employed in speed and position estimation using AFCE-QPLL technique to minimize position (Δθ) errors for EV dynamics. In order to conduct a thorough analysis, a 22kW Syn-RL motor [10] is used for the EV system, which has precise speed and position estimation capabilities. A gear ratio of 9:1 is selected based on maximum acceleration of EV drive according to modified Indian driving cycle (M-IDC) and machine ratings. Dynamic performance of presented EV drive is illustrated in Fig.5 for a portion of driving cycle. The speed dynamics with estimated position and error is outlined in Fig.5 (a) considering active flux (AF) estimation by disturbance observer (DO) and speed and position estimation by AFCE-QPLL technique. Active flux (AF) with estimated speed and position is presented in Fig.5 (b). Fig.5 (c) presents estimated torque, d-q axes current and stator currents for said duration emulating 4-wheeler performance. For understanding accuracy of presented AF technique, locus of estimated AFs is illustrated in Fig.5 (d). The locus is smooth circular curve with minimal error. The locus is plotted for cruising stage of vehicle with minimum loading. Presented AF technique is compared to conventional flux observer which utilizes a low pass filter (LPF) for flux estimation. Fig.5 (e) represents flux estimation locus with LPF flux

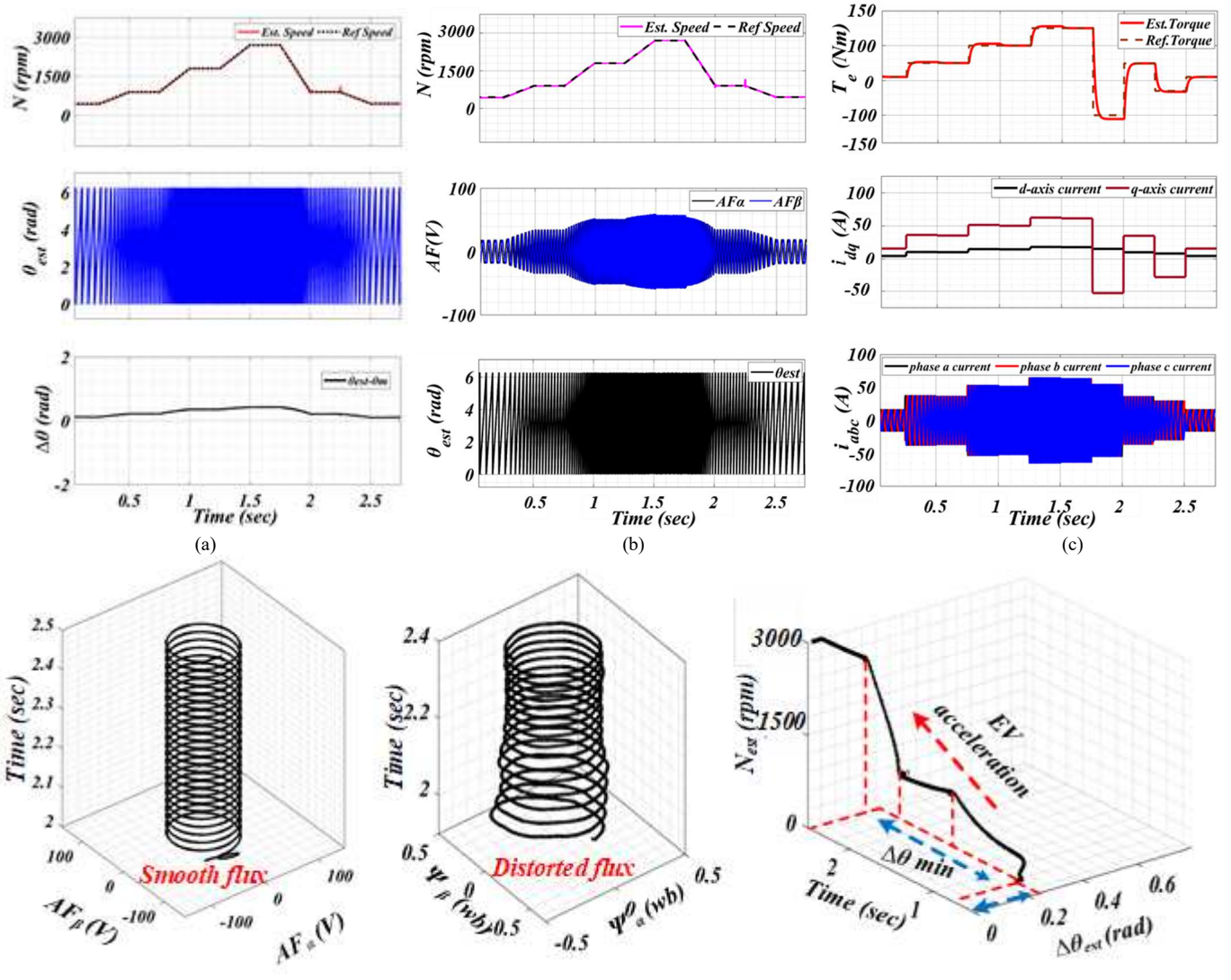

Fig.5 System Performance (a) Estimated and Reference speed (rpm), estimated rotor angle (rad) and rotor position error (rad) (b) Estimated and Reference speed (rpm), estimated active fluxes (AF) (V) and estimated rotor angle (rad) (c) Estimated motor torque and reference motor torque (Nm), reference d-q axes currents and stator phase currents (A) (d)Estimated active fluxes (AF) plot w.r.t time with DO technique (e) Estimated fluxes (wb) plot w.r.t time with conventional LPF base flux estimation (f) Plot of estimated speed (rpm) and estimated position error (rad) for AFCE-QPLL technique.

Authorized licensed use limited to: DELHI TECHNICAL UNIV. Downloaded on November 25,2024 at 04:49:24 UTC from IEEE Xplore. Restrictions apply.

observer. As per locus distortion in estimated fluxes are more as compared to AF technique for same loading scenario. With AF technique, position error (Δθ) of maximum 0.1 rad is achieved for acceleration period as presented in Fig.5 (f), same can be predicted for deceleration period. Comparison of position error for AFCE-QPLL and E-QPLL technique is presented in Fig.6. Fig.7 presents battery performance during dynamics and battery charging through regenerative braking and solar PV array from t=2s to 3s.

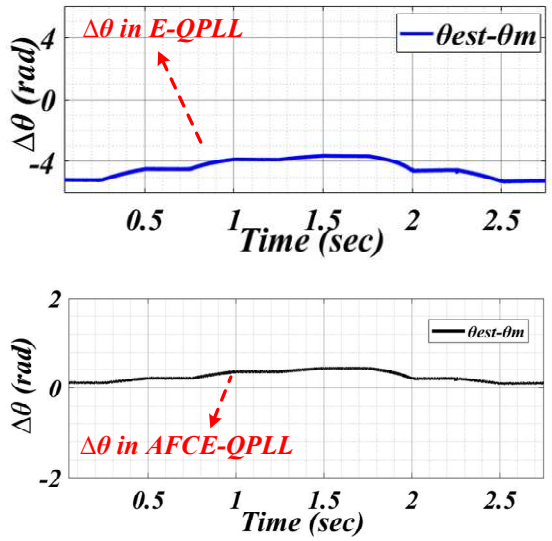

Fig.6 Comparison of Δθ in E-QPLL and AFCE-QPLL technique.

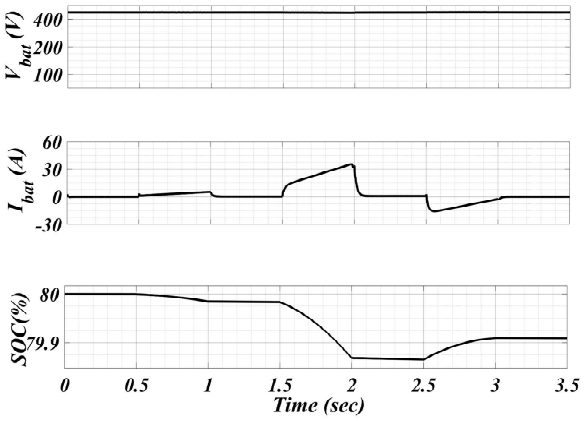

Fig.7 Battery performance during EV dynamics

VI. Conclusion

Presented work has introduced a Syn-RL motor with electric vehicle (EV) dynamics. A disturbance observer (DO) based active flux estimation is presented. The estimation of active flux mitigates cross-coupling effect and improves estimation of speed and position. The incorporation of AFCE-QPLL technique for speed and position estimation also enhances predictability and robustness of system in relation to overall dynamics of vehicle. Presented Syn-RL motor-based electric vehicle (EV) drive also improves battery performance with roof top solar PV integration.

Appendices

Syn-RL Motor Ratings: P_{rated}=22 kW, N_{rated}=3000 rpm, N_{max}=4500rpm, T_{rated}=140Nm, V_{rated}=380 V, R_s=0.1 Ω, L_d =35.64 mH, L_q=6.12 mH, I_{rated}=49 A, pole pair=2.

Boost Converter Parameters: V_{in}= V_{mpp}, V_{out}=V_{bat}, d=0.17, L=4mH, Converter frequency (f_s) =15 kHz.

BDC parameters: V_{in}= V_{bat}, V_{out}=V_{dc}, d=0.33, L=1.2mH, C_{dc}=2800uF, Switching frequency (f_s) =15 kHz

Solar PV Parameters: P_{mpp}-600 Wp, V_{mpp}-340 V, I_{mpp}-1.76A, V_{oc}-400 V, I_{sc}-2 A.

Acknowledgment

The authors are very grateful to Science and Engineering Research Board (SERB) National Science Chair Fellowship for supporting this work.

References

[1] A. T. Woldegiorgis, X. Ge, H. Wang and Y. Zuo, "An Active Flux Estimation in the Estimated Reference Frame for Sensorless Control of IPMSM,"*IEEE Transactions on Power Electronics*, vol. 37, no. 8, pp. 9047-9060, Aug. 2022.

[2] A. Varatharajan, G. Pellegrino, E. Armando and M. Hinkkanen, "Sensorless Synchronous Motor Drives: A Review of Flux Observer-Based Position Estimation Schemes Using the Projection Vector Framework," *IEEE Transactions on Power Electronics*, vol. 36, no. 7, pp. 8171-8180, July 2021.

[3] H. Parveen and B. Singh, "PV Array Fed Synchronous Reluctance Motor Driven Water Pumping System with Grid Integration and Seamless Operability," *IEEE Transactions on Industry Applications*, vol. 60, no. 2, pp. 3724-3733, March-April 2024.

[4] S. Mishra, B. Singh and A. Varshney, "Adaptive Flux Based Speed Estimation of Syn-Rel Motor Drive for Electric Vehicle with Solar-PV Assistance," *IEEE Transactions on Industry Applications*, early access, May 2, 2024, doi: 10.1109/TIA.2024.3396120.

[5] M. Karimi Ghartemani, Enhanced Phase-Locked Loop Structures for Power and Energy Applications. Hoboken, NJ, USA: Wiley, 2014.

[6] Y. Wang, H. Ahmed, H. Zhang and W. Hua, "Feedforward PLLs for Motor Position Estimation Using Embedded Magnetic Encoder," *IEEE Sensors Journal*, vol. 24, no. 7, pp. 10307-10315, April 2024.

[7] Y. Wang , H. Zhnag, K. Lui, M.Hu, Z.Wu, C. Zhang, W.Hua, "A Forward Compensation Method to Eliminate DC Phase Error in SRF-PLL," *IEEE Transactions on Power Electronics*, vol. 37, no. 6, pp. 6280-6284, June 2022.

[8] Y. Wang, H. Zhang, and W. Hua, "A robust forward compensated Type-2 PLL without DC phase error during frequency ramp for embedded magnetic encoder," *IEEE Transactions on Power Electronics*., vol. 38, no. 5, pp. 5649–5654, May 2023.

[9] Z. -Z. Xin, J. -J. Wang and H. -J. Zhao, "Rotor Position Estimation Using Harmonic-Decomposition Complex-Coefficient Filter-Based PLL for PMSM With Switch Hall-Effect Sensors," *IEEE Journal of Emerging and Selected Topics in Power Electronics*, vol. 12, no. 2, pp. 2249-2259, April 2024.

[10] P. Sun, D. Zhang, Z. Bai, Q. Xiao, B. Chen and Z. Yu, "Comparison Study of MRAS and EEMF-based Sensorless Control for Synchronous Reluctance Motor," *2019 22nd International Conference on Electrical Machines and Systems* (ICEMS), pp. 1-5, Harbin, China, Dec. 2019.

Authorized licensed use limited to: DELHI TECHNICAL UNIV. Downloaded on November 25,2024 at 04:49:24 UTC from IEEE Xplore. Restrictions apply.

Analysis of Glycyrrhiza Glabra Phytocompounds using Network Pharmacology for Anti-Alzheimer Therapy

Nishtha Jain
Department of Biotechnology
Delhi Technological University
Rohini, Delhi, India
nishthajn27@gmail.com

Kunal Dugar
Department of Biotechnology
Delhi Technological University
Rohini, Delhi, India
kunal.dugar115@gmail.com

Aadya Suri
Department of Biotechnology
Delhi Technological University
Rohini, Delhi, India
aadyasuri.01@gmail.com

Navneeta Bharadvaja
Department of Biotechnology
Delhi Technological University
Rohini, Delhi, India
navneetab@dce.ac.in

2024 International Conference on Electrical Electronics and Computing Technologies (ICEECT) | 979-8-3503-7809-2/24/$31.00 ©2024 IEEE | DOI: 10.1109/ICEECT61758.2024.10739190

***Abstract*— Alzheimer's disease (AD) is a highly complex and neurodegenerative disease that has clinical symptoms like memory loss along with degrading cognitive functioning. The rise in the prevalence of this diseases in recent years attributed to modern lifestyle by various studies has created a crucial requirement to comprehend AD pathophysiology and create effective treatment plans. The intricacy and difficulty of both the disease and its underlying causes are demonstrated by the fact that over 200 viable medication candidates have failed clinical trials and that the advancement of AD is unaffected by the pharmaceutical techniques produced to date. The central pathophysiology of the disease has shown that AD is characterized by amyloid plaques of β-amyloid peptide. To overcome the complexities associated with AD, scientific investigations have shifted their focus towards the plant compounds resent in the ecosystem. Many plants and their compounds have shown efficacy for treating AD. In this paper we have studied all the phytocompounds of plant Glycyrrhiza glabra, known to contain potential anti- Alzheimers phyto compounds for therapeutic purposes. By utilizing the techniques of network pharmacology combined with molecular docking analysis, this paper provides a potential pathway to find new drugs and modify existing drugs based upon observations made by studying multiple compounds-target interactions.**

Keywords—Alzheimer's disease, network pharmacology, molecular docking

I. INTRODUCTION

Alzheimer's disease now affects tens of millions of people globally and is a serious public health concern. It is an irreversible, progressive neurodegenerative disease. About 29 million people worldwide live with this type of dementia, making it the most common type. 5% of people between the age group 65 and 74 and approximately 3% people in the age group of 75 to 84 live with this (Sheokand et al., 2024). Alzheimer's disease is characterized by an intraindividual pattern of loss in thinking and memory that affects at least two cognitive areas (Long & Holtzman, 2019). At cellular level, two key pathways characterize accumulation of extracellular amyloid beta (Aβ) peptide plaques and formation of intracellular neurofibrillary tau tangles (DeTure & Dickson, 2019). The amyloid cascade theory states that aberrant processing of APP that is Amyloid Precursor protein results in soluble Aβ, which in turn causes neuronal death and dysfunction in the pathophysiology of AD (Tanzi & Bertram, 2005). 2 competing pathways are generally involved in the processing of APP wherein fragments which are non-amyloidogenic in nature are produced by the cleavage of α-secretase enzyme and production of peptide chains of Aβ by lead cleavage of β-secretase which is the target BACE-1 protein, which could form toxic oligomeric species through misfolding and aggregation. BACE-1 is a transmembrane aspartyl protease, which is the key enzyme for initiating APP processing (Cheignon et al., 2018). Therefore, therapeutic inhibition of the genes responsible for accumulation of AD proteins holds promise for reducing Aβ production and alleviating amyloid- induced toxicity (Murphy & LeVine, 2010). Many believe that past research efforts have been insufficient because they focused solely on one aspect or mechanism of the disease, overlooking the intricate interplay of various factors. Thus, given the complexity of Alzheimer's disease development, creating drugs with multifunctional capabilities targeting multiple factors may offer more promising outcomes for AD treatment (Ma et al., 2022). Researchers are shifting their focus towards plants present in our ecosystem having potential compounds for countering AD.

A novel field known as network pharmacology (NP) has arisen, aiming to comprehend how drugs affect and interact with various targets. NP utilizes computational resources to methodically document the molecular interactions of a drug within a living cell. NP endeavors to uncover fresh opportunities for drug development and identify novel targets, as well as repurpose existing drug compounds for alternative therapeutic applications, by facilitating an impartial exploration of potential target domains (Chandran et al., 2017). NP combined with another computational method called "molecular docking" which forecasts the binding pose and affinity between a ligand and the structure of a target protein (Van Drie, 2007) operates as a virtual screening environment in the structure-based drug discovery pipeline in the

979-8-3503-7809-2/24/$31.00 ©2024 IEEE

Authorized licensed use limited to: DELHI TECHNICAL UNIV. Downloaded on November 09,2024 at 04:47:09 UTC from IEEE Xplore. Restrictions apply.

biotechnological and pharmaceutical industries (Aplin et al., 2022) These have become irreplaceable tools in the early- stage drug discovery and design, e.g., to discover drugs in silico and to manage hits as lead compounds. When using molecular docking techniques, having knowledge about the specific region on the target protein where the ligand binds is crucial (Koukos et al., 2019).

II. METHODOLOGY

A. Extraction of plant chemical compounds and their corresponding protein receptors

On performing secondary research, the plant *Glycyrrhiza glabra* was identified for extraction of phytochemicals that are potent of treating AD. Roots of this plant are enriched with such phytochemicals and are under the radar of researchers for their therapeutic properties against AD. All the phytochemicals were extracted from publicly available Dr Duke's Phytochemical and Ethnobotanical Databases (https://phytochem.nal.usda.gov/). 12 compounds from the root region of *Glycyrrhiza glabra* were shortlisted based on their anti Alzheimer's characteristics.

B. Screening for Drug Likeliness and Pharmacokinetic Properties

SwissADME, an online tool (https://www.swissadme.ch/) was employed to do initial screening of compounds and eliminate the ones violating Lipinski's rule of five. Here, the 5 conditions considered are that the phytochemical has less than 5 H-bond acceptors and the H-bond donors should also be less than 5, higher lipophilicity (LogP <5), ligand's molecular weight (<500Da) and molar refractivity (between 40 to 130) are considered for screening. More than two violations lead to disqualifications of those molecules from any further investigation. The attributes for each variable excluding molar refractivity were procured from PubChem. After screening, all 12 ligands were further processed for network pharmacological study.

C. Target Prediction

The shortlisted phyto compounds were screened for the binding targets. Super Pred (https://prediction.charite.de/) was employed and the known strong binders having binding probability of 75% and above were selected.

D. GIFt Score Calculation

Gene Annotation is a crucial part of computational genomics, therefore quantitative assessment of the annotation landscape is required. GeneCards Inferred Functionality Score (GIFtS) (https://www.genecards.org/) is a metric to predict the degree of functionality of a gene of a disease. It provides objective number to display the level of knowledge about the gene functionality in humans. We shortlisted targets having GIFtS greater than 50.

E. Finding target combination between phytocompounds and AD genes

The concept of Venn diagrams was utilized to find the gene combination between that of phytocompounds and Alzheimer's disease. Venny 2.1 tool helps to make accurate venn diagrams between the disease and compounds genes. Fig 1 displays the venn diagram obtained using Venny 2.1 tool.

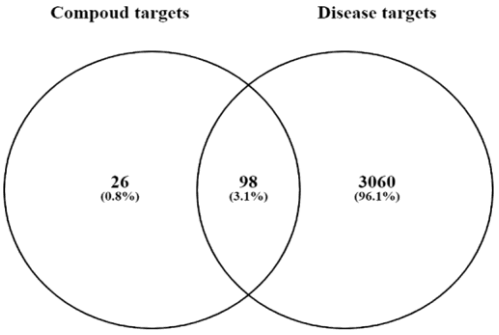

FIG 1 – Venn diagram showcasing the overlap of 98 genes between the compound gene targets and AD gene targets

F. Protein-Protein Interaction study and Pathways Selection

Using the String Database, all the genes were mapped to study the protein-protein interactions between the shortlisted genes. A list of all associated pathways with those genes obtained from Kegg analysis was further refined to select only the pathways of the genes directly related to Alzheimer's to obtain an accurate map for the desired result.

G. Cytoscape

All the protein-protein interaction networks and the biological pathways were visualized using an open-source software called Cytoscape. It yields a web diagram as shown in Fig 2, making it easy to study the interactions and the conjunction between the networks. Top 10 gene targets were chosen from cytoscape and the 2 best active phyto nutrients. The combination of these were further taken for molecular docking analysis.

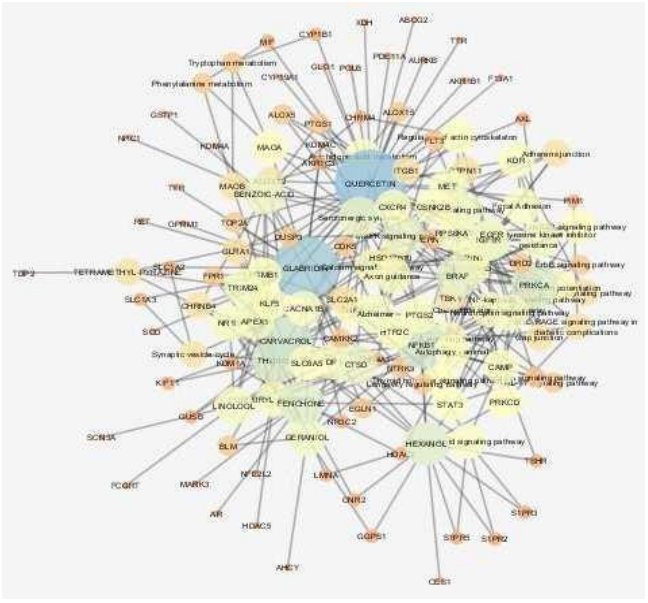

Fig 2 – Network cluster analysis from Cytoscape

H. Molecular Docking Studies

The docking of top 10 gene targets against the phyto nutrients using the software AUTODOCK version 4.2.6 was performed with Lamarckian Genetic Algorithm. Water was removed from both the receptor as well as the ligand after which polar hydrogen ions were added to the main target

Authorized licensed use limited to: DELHI TECHNICAL UNIV. Downloaded on November 09,2024 at 04:47:09 UTC from IEEE Xplore. Restrictions apply.

protein and the required charges consisting Kollman and Gasteiger were added to the molecule. Subsequently, ligand and the protein were completely prepared by removing the H-atoms from the macromolecule. The docking process involves preparing the ligand and receptor by converting the pdb file to a pdbqt format, which serves as the input for Autodocking. The search grid box encompasses the entire protein, and the active site amino acids for each target are chosen during docking.

Docking research provided the Lamarckian GA output. For each ligand, the procedure was repeated, and the final optimal conformation with the lowest binding energy was carefully considered out of the ten conformations obtained for each operation. To forecast how the binding energy (kcal/mol) would change during binding, the scoring function was examined. The energy of the unbound system (kcal/mol), torsional energy (kcal/mol), total int energy (kcal/mol), and intermolecular energy (vdW + H-bond + desolv Energy) (kcal/mol) were recorded.

TABLE 1: ADME ANALYSIS OF THE SELECTED 12 PHYTOCOMPOUNDS SHORTLISTED FROM THE PLANT GLYCYRRHIZA GLABRA

CHEMICALS	PUBCHEM ID	MOL WT (g/mol)	H BOND ACCEPTORS	H BOND DONORS	MOLAR REFRACTIVITY	LIPINSKI RULE
BENZOIC-ACID	243	122.12	2	1	33.4	Yes; 0 violation
CARVACROL	10364	150.22	1	1	48.01	Yes; 0 violation
FENCHONE	14525	152.33	1	0	45.64	Yes; 0 violation
FURFURYL-ALCOHOL	7361	98.1	2	1	24.84	Yes; 0 violation
GERANIOL	637566	154.25	1	1	50.4	Yes; 0 violation
GLABRIDIN	124052	324.37	4	2	93.25	Yes; 0 violation
GLYCYRRHIZIN	14982	822.93	16	8	202.84	No; 3 violations
HEXANOL	8103	102.17	1	1	32.12	Yes; 0 violation
LINALOOL	6549	154.25	1	1	50.44	Yes; 0 violation
QUERCETIN	5280343	302.24	7	5	78.03	Yes; 0 violation
TETRAMETHYL-PYRAZINE	14296	136.19	2	0	41.9	Yes; 0 violation
THYMOL	6989	150.22	1	1	48.01	Yes; 0 violation

III. RESULT AND DISCUSSION

A. *ADME (Absorption, distributiom, metabolism, excretion) Analysis*

An essential step in determining the safety and efficacy of a drug includes the analysis of its pharmacokinetic properties that involves ADME analysis of that drug in our body. This helps in ensuring that the drug has a therapeutic effect when used in certain doses as medicines for the patients. Initially, we took 12 phyto compounds to perform their analysis but 1 violated the Lipinski Rule and thus 11 phyto nutrients (Table I) were taken for further analysis.

B. *Target prediction*

Using Super Pred, 224 targets were identified for the 11 drug likely phytonutrients and using the GIFt score calculation, a total of 3159 gene targets of Alzheimer's disease were obtained. Through Venn diagram (Fig I), 98 non duplicate genes were found that were perfectly overlapping i.e. these genes we suitable to be combined for the purpose of therapeutics. These were the genes that are the targets of the phyto compounds and are involved in the functionality of Alzheimer's disease and a protein-protein interaction network was examined using STRING which had 98 nodes and 394 edges

C. *Kegg Analysis*

Extensive literature review was performed on the 95 pathways obtained via Kegg analysis to obtain 32 major pathways that are directly associated with the onset of Alzheimer's disease along with the 171 genes responsible for those.

D. *Identification of active phytonutrients and gene targets*

Using Cytoscape software, a network was made and the interactions between the target genes and phytonutrients of the plant *Glycyrrhiza glabra* were analyzed. Then using CytoHubba plugins, the top 10 hub gene targets (Fig 3) were identified- MET, KDR, SRC, ABCG2, STAT3, NFKB1, CXCR4, ITGB1, IGF1R, PTPN11 through its maximum clique centrality (MCC) and degree analysis. The two active phytonutrients identified were Quercetin and Glabridin.

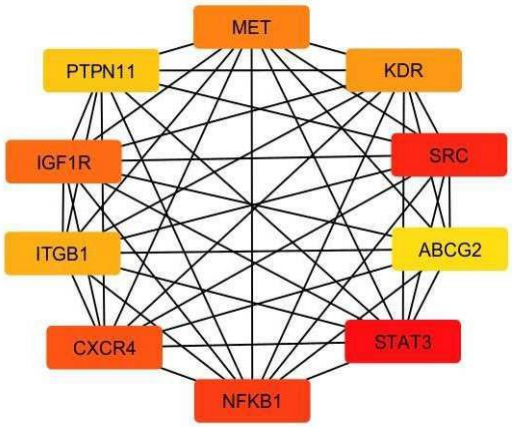

Fig 3 – 10 gene targets identified from Cytoscape pluggins used for docking studies

Authorized licensed use limited to: DELHI TECHNICAL UNIV. Downloaded on November 09,2024 at 04:47:09 UTC from IEEE Xplore. Restrictions apply.

E. Molecular Docking

The top 10 anti-Alzheimer's core targets with PDB IDs 1FYR, 1Y6A, 1A07, 6ETI, 6TLC, 8TQD, 3OE0, 3GRW, 1P4O, were molecularly docked with Quercetin and Glabridin and the binding energies were calculated (Table II). The higher binding capacity of the phytonutrients and targets is shown by the decreased binding affinity. The best interaction was seen between Quercetin and the gene MET, having binding affinity of -9.55 Kcal/mol, which is involved in various important pathways concerned with the onset of Alzheimer's disease. MET also showed good binding affinity with Glabridin with -8.92 Kcal/mol as its binding energy. ABCG2 is another gene with high binding capacity with these 2 compounds presenting energies of -8.07 Kcal/mol with Glabridin and -7.58 Kcal/mol with Quercetin. Thus, these 2 gene targets can be used as main inhibitors for Quercetin and Glabridin to be used as drugs for the therapeutics of Alzheimer's disease.

TABLE 2: MOLECULAR DOCKING ANALYSIS PRESENT BINDING ENERGY (KCAL/MOL) OF GENE TARGETS WITH 2 ACTIVE PHYTO NUTRIENTS

	GLABRIDIN	QUERCETIN
MET	-8.92	-9.55
ABCG2	-8.07	-7.58
KDR	-7.87	-7.03
SRC	-6.96	-6.24
STAT3	-6.73	-5.18
NFKB1	-7.65	-7.03
CXCR4	-6.79	-5.65
ITGB1	-5.33	-5.51
IGF1R	-7.55	-6.66
PTPN11	-7.25	-5.62

IV. Conclusion

To conclude, this paper highlights that *Glycyrrhiza glabra* can be useful for the therapeutics of AD. The study found active phytonutrients in G. glabra root and clarified their interactions with the key targets implicated in AD development using a network pharmacological approach. The findings presented that these compounds significantly inhibit the pathways that lead to onset of AD. This also signifies the importance of looking for therapeutics in natural plant nutrients along with the other types of therapies currently used and are in study for different neurological disorders. Applying network pharmacological technique leads to an in-depth knowledge of the biochemical pathway behind *G. glabra's* anti-AD effects, which in turn makes development of precision treatment easier.

The future scope of these treatments can only be increased when proper methods and techniques are developed to effectively form and deliver them. This has a good prospect in improving the mechanisms and the end result of curative measure of Alzheimer's.

References

1. Aplin, C., Milano, S. K., Zielinski, K. A., Pollack, L., and Cerione, R. A. Evolving Experimental Techniques for Structure-Based Drug Design. The Journal of Physical Chemistry B, 126(35), 6599–6607, 2022.
2. Chandran, U., Mehendale, N., Patil, S., Chaguturu, R., and Patwardhan, B. Network Pharmacology. In Innovative Approaches in Drug Discovery (pp. 127– 164) Elsevier, 2017
3. Cheignon, C., Tomas, M., Bonnefont-Rousselot, D., Faller, P., Hureau, C., & Collin, F. (2018). Oxidative stress and the amyloid beta peptide in Alzheimer's disease. Redox Biology, 14, 450–464, 2018.
4. DeTure, M. A., & Dickson, D. W. The neuropathological diagnosis of Alzheimer's disease. Molecular Neurodegeneration, 14(1), 2019.
5. Koukos, P. I., Xue, L. C., & Bonvin, A. M. J. J. Protein–ligand pose and affinity prediction: Lessons from D3R Grand Challenge 3. Journal of Computer- Aided Molecular Design, 33(1), 83–91, 2019.
6. Long, J. M., & Holtzman, D. M. Alzheimer Disease: An Update on Pathobiology and Treatment Strategies.Cell 179(2),312–339, 2019.
7. Ma, X., Zhao, Y., Yang, T., Gong, N., Chen, X., Liu, G., & Xiao, J. Integration of network pharmacology and molecular docking to explore the molecular mechanism of Cordycepin in the treatment of Alzheimer's disease. Frontiers in Aging Neuroscience, 14, 2022.
8. Murphy, M. P., & LeVine, H. Alzheimer's Disease and the Amyloid-β Peptide. Journal of Alzheimer's Disease, 19(1), 311–323, 2010.
9. Sheokand, D., Grewal, A., Kumar, P., Chauhan, R., Saini, V., & Kumar, A. Molecular docking analysis of marine phytochemicals with BACE-1. Bioinformation, 20(2), 151–155, 2024.
10. Tanzi, R. E., & Bertram, L. Twenty Years of the Alzheimer's Disease Amyloid Hypothesis: A Genetic Perspective. Cell, 120(4), 545–555, 2005.
11. Van Drie, J. H. Computer-aided drug design: the next 20 years. Journal of Computer-Aided Molecular Design, 21(10–11), 591–601, 2007.

Authorized licensed use limited to: DELHI TECHNICAL UNIV. Downloaded on November 09,2024 at 04:47:09 UTC from IEEE Xplore. Restrictions apply.

2024 International Conference on Electrical Electronics and Computing Technologies (ICEECT) | 979-8-3503-7809-2/24/$31.00 ©2024 IEEE | DOI: 10.1109/ICEECT61758.2024.10739301

APPLICATION OF OPTIMIZATION TECHNIQUES FOR FREQUENCY STABILITY IMPROVEMENT IN MICROGRID

Philemon Yegon
Electrical Engineering Department
Delhi Technological University
Delhi, India
pkuruiphilemon@gmail.com

Mukhtiar Singh
Electrical Engineering Department
Delhi Technological University
Delhi, India
smukhtiar_79@yahoo.co.in

***Abstract*—The paper presents adaptive virtual control strategy for inertia support in the present power network with increased penetration of RES. Owing to low inertia response capabilities of RES frequency degradation manifested. To address abovementioned challenge, modified PSO based PID controller is used to make the HESS participates in inertia support to enhance frequency response. Comparison between conventional PSO and modified PSO was carried out. Frequency is measured at PCC to achieve frequency nadir, settling time and ROCOF after each disturbance.**

Finaly, simulation of microgrid was carried out in MATLAB to verified control strategy effectiveness.

keywords—rate of change of frequency , frequency nadir, modified pso , microgrid

I. INTRODUCTION

With the increase penetration of renewable energy sources in the modern power system network, frequency deterioration in the system occurs due to lack of rotational mass in intermittent RES[1]. RES are integrated to power system network by means of power electronics devices (converters inverters). Because of the intermittent nature of the RES and lack of inherent inertial response, rising RES in the microgrid causes stability difficulties [2], particularly.

When the system fully utilized maximum power. Furthermore, the vulnerability of microgrids to power disruptions rises[3]. Due to frequency deterioration, some technical techniques and researches has been proposed to solve low inertia in microgrid. Energy storage system Has been used in virtual synchronous generator (VSG) for frequency stability [4]. ESS helps to optimize effectiveness during operation to avoid abrupt load shedding or system blackout. The VSG enhances the low-inertia isolated microgrid in [5] by integrating with the traditional PI to control a superconducting magnetic energy storage (SMES). A supercapacitor (SC) is incorporated into a PV system's DC connection in [6]to sustain the microgrid frequency and enable virtual inertia control. In [7], HESS consumption is lower due improved frequency and faster restoration of steady- state frequency.

The microgrid's frequency responsiveness would be impacted by the inertia constant in addition to load frequency controllers and the frequency droop coefficient of power sources. It is possible to lower the maximum frequency deviation and hasten the frequency's restoration to its normal value by fine-tuning the load frequency controllers. Using evolutionary algorithms to optimise the conventional PI/PID controllers has been the attention of several studies. An MG with generation rate constraint (GRC) has its load frequency controllers tuned using the bacterial foraging optimisation technique in [8]. To enhance the quality of frequency control, a fuzzy logic-based hierarchical technique has been presented in [9], [10].

Moreover, has implemented electrical vehicles for the purpose of controlling frequency [11]. For LFC in a multi-area power system, fractional order PID controllers have been presented in [12].

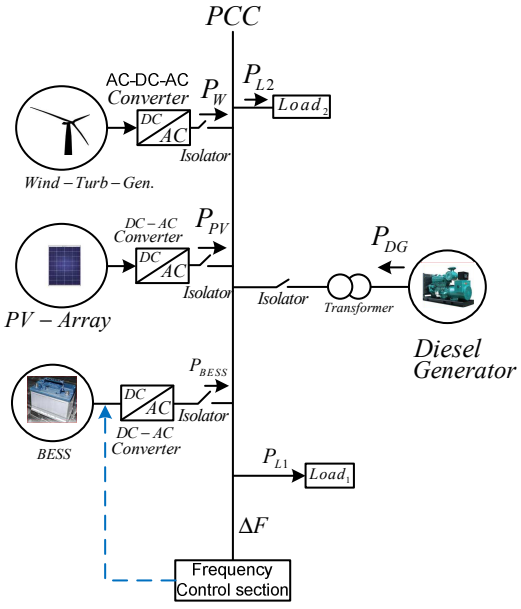

Fig. 1 schematic of the considered microgrid

In this paper, for the purpose of frequency response and damping features enhancement, PID controller is optimized based on modified PSO for inertia support in microgrid. For improved PSO performance (LDIW-PSO), a linear dynamic inertia weight update equation is typically used [13] . Nevertheless, it suffers local optima during space exploration.

In [14], the weight updating equation now includes a natural exponential with a squared power component. This method can avoid the local minima

979-8-3503-7809-2/24/$31.00 ©2024 IEEE

Authorized licensed use limited to: DELHI TECHNICAL UNIV. Downloaded on November 09,2024 at 04:52:56 UTC from IEEE Xplore. Restrictions apply.

problem, but it suffers from an inherent increase in the number of repetitions, which lengthens the time it takes for convergence. Furthermore, as the search procedure is analogous to the movement of a fluid, the lower values of ω (0.6 & 0.1) start and end respectively signify a decrease in viscosity. This work intentionally avoided squaring the natural exponential component in order to minimise the number of iterations. The values of ω start and end have also been raised to 0.9 and 0.2 respectively in order to reduce the convergence time.

II. SYSTEM DESCRIPTION

In Fig. 1, a 15 MW solar plant PV, 200 MVA DG and 25 MW wind turbine power plant are combined in the proposed system to form a microgrid. As seen in Fig. 1, two loads of utilised the microgrid supply. Energy storage system (ESS) is connected to improve the stability of the microgrid [15]. The major power supply is DG, with which contains governor and turbine with valve which control frequency. The governor control turbine speed with delay hence which triggers utilization of dead band section under disturbances for frequency control. The dead band of this turbine get saturated at governor constant of ± 0.12 p.u. MW/min.

To regulate the frequency deviation beyond allowable threshold during any given disturbances, Fig. 2 shows a microgrid under imbalance consumption and supply of power. Frequency deviate from the normal, the lowest part of deviation is called nadir. When this happened, three control schemes are applied; inertia control, primary and secondary controls. The hierarchical control system in which the imbalance between load and generation is stabilised for frequency restoration and control.

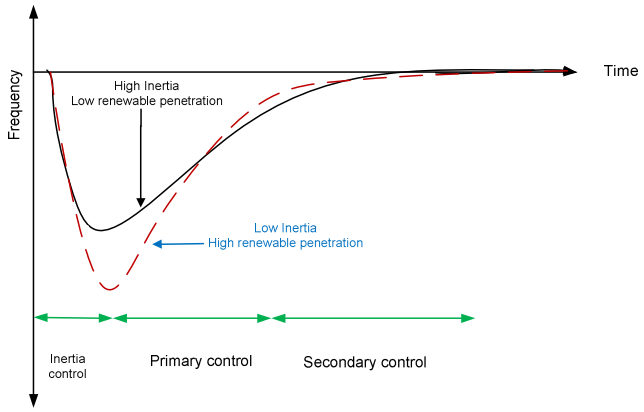

Fig. 2. Frequency deviation under disturbance

The mathematical modelling are as follows;

$$\Delta P_G(t) - \Delta P_C(t) = \frac{2Hd\Delta f(t)}{dt} + D\Delta f(t) \quad (1)$$

Where ΔP_G DG power change
ΔP_C change in power consumed
Δf frequency change
H Inertia coefficient
D Damping coefficient

The frequency deviation in a model form;

$$\Delta f = \frac{\Delta P_m + \Delta P_W + \Delta P_{PV} + \Delta P_{VI} - \Delta P_L}{2Hs + D} \quad (2)$$

Where

$$\Delta P_m(S) = \frac{1}{1+sT_t}\Delta P_g(S) \quad (3)$$

$$\Delta P_g(S) = \frac{1}{1+sT_g}(\Delta P_C(S) - \frac{1}{R}\Delta f(S)) \quad (4)$$

$$\Delta P_C(S) = \frac{Ks}{S}(\beta.\Delta f(S)) \quad (5)$$

$$\Delta P_W(S) = \frac{1}{1+sT_{WT}}\Delta P_{Wind}(S) \quad (6)$$

$$\Delta P_{PV}(S) = \frac{1}{1+sT_{PV}}\Delta P_{Solar}(S) \quad (7)$$

Where
ΔP_C system power change (signal)
ΔP_P primary control power change
ΔP_{Wind} wind power change.
ΔP_g DG power change
ΔP_{PV} Solar system power change
ΔP_L Load change in the system
ΔP_{VI} Power Change in virtual inertia

Fig. 3, depicts control block configuration.

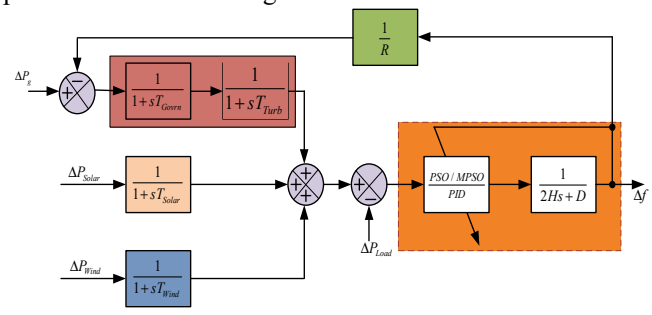

Fig. 3. System control block diagram

III. MODIFIED PARTICLE SWARM OPTIMIZATION (PSO)

The traditional Particle Swarm Optimisation model is designed to mimic the actions of a flock of birds searching for food[16]. The subsequent equation calculates the location and velocity of every particle: p_i best local position and g_i global position.

$$d_i^{t+1} = d_i^t + u_i^{t+1} \quad (8)$$

Authorized licensed use limited to: DELHI TECHNICAL UNIV. Downloaded on November 09,2024 at 04:52:56 UTC from IEEE Xplore. Restrictions apply.

$$u_i^{t+1} = wu_i^t + c_1 r_1 (p_i^t - d_i^t) + c_2 r_2 (g_i^t - d_i^t) \quad (9)$$

Where r_1 and r_2 are random constants that vary from 0 to 1

c_1 and c_2 social constant and cognitive constant,
ω inertia weight
ωu_i^t inertia
$c_1 r_1 (p_i^t - d_i^t)$ cognitive component
$c_2 r_2 (g_i^t - d_i^t)$ social component

The inertia weight, denoted by ω, plays a crucial role in both exploitation and exploration within the search area. An efficiently optimized value decreases the time it takes to achieve convergence. A technique for dynamically modifying the inertia weight in a PSO algorithm was proposed in [17]. [17]This approach, known as linearly decreasing inertia weight PSO, is represented by equation (10).

$$w = (w_{start} - w_{end}) \times (\frac{T_{\max} - t}{T_{\max}}) + w_{end} \quad (10)$$

Where, ω_{start} beginning value of inertia weight
ω_{end} final value of inertia
T_{max} maxiters

The modified equation is as given below:

$$w = (w_{start} - w_{end}) \times (\frac{T_{\max} - t}{T_{\max}}) + w_{end} \times e^{-t/(\frac{T_{\max}}{10})} \quad (11)$$

Where $\omega_{start} = 0.9$ and $\omega_{end} = 0.2$

IV. Results Simulation and Discussion

The load fluctuation either decreasing or increasing, solar variation and wind speed variation are the microgrid disturbances. Frequency is measured at the PCC after the disturbances and the following parameters; RoCoF, frequency zenith and nadir, ITAE are obtained to assess the performance of the microgrid. Furthermore, the mentioned parameters give a note on the capacity of HESS energy needed. The MATLAB Simulink tool is used to simulate the microgrid, i.e, photovoltaic system, wind turbine, ultracapacitor, battery and DG blocks are obtained from the MATLAB.

The optimal goal function is frequency deviation Δf;

$$ITAE = \int_0^{T_{Sim}} |\Delta f| . t dt \quad (12)$$

Where;

$ITAE$ - Integral of Time-weighted Absolute Error
T_{Sim} -simulation time range

Both optimisation techniques are applied in (12), and the results were tabulated as indicated in TABLE 1.

TABLE 1. PSO & MODIFIED PSO OPTIMIZED PARAMETERS

Optimal Parameters	PSO	Modified PSO
K_P	1000	1000
K_I	39.0995	0.6893
K_D	0	0

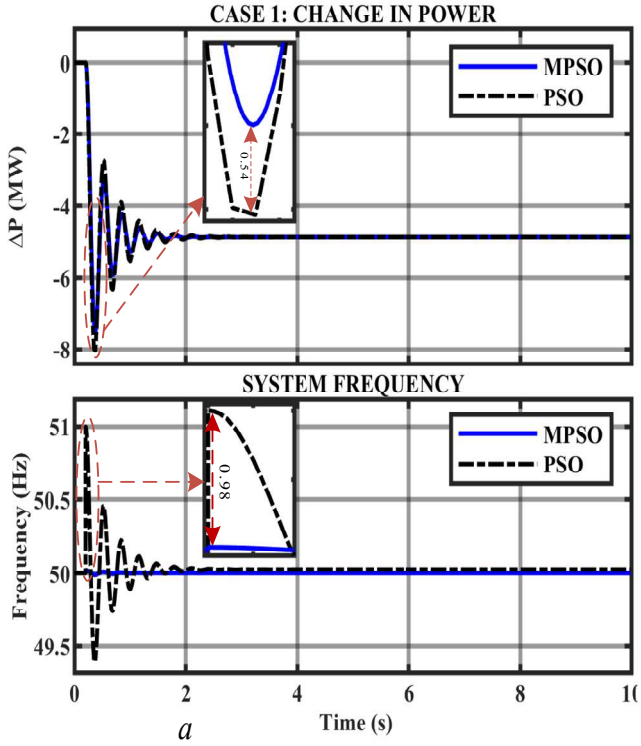

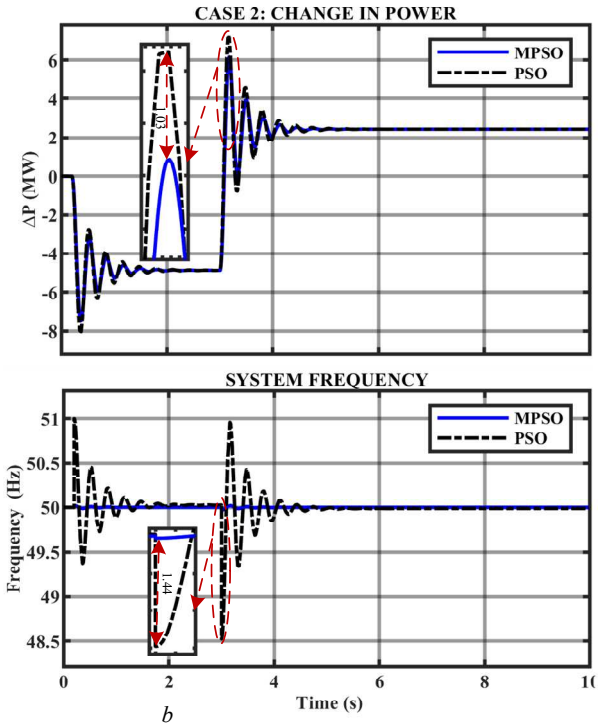

Authorized licensed use limited to: DELHI TECHNICAL UNIV. Downloaded on November 09,2024 at 04:52:56 UTC from IEEE Xplore. Restrictions apply.

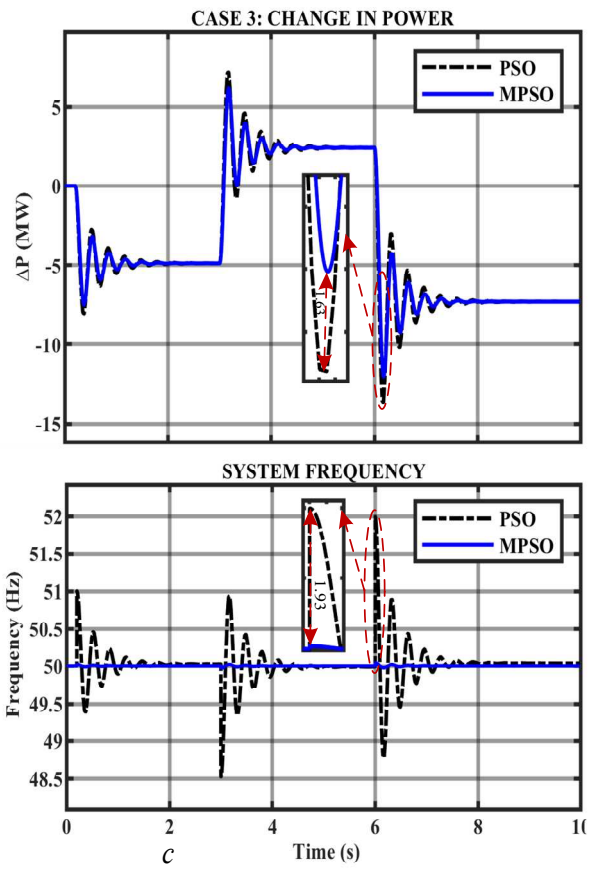

Fig. 4. a.b.c Combination of frequency deviation and power variation

A. *Scenario 1: 2% disturbance, decrease in load demand:*

For the first 0.2 seconds, the system operates steadily at a frequency of 50 Hz. However, a sudden decreased of 5 MW load demand, causing a frequency increase seen in Fig. 4 a. The system returns to steady operation at a 50 Hz frequency in both techniques as witnessed. Moreover, the deviation in modified PSO is 0.0199 while in PSO is 0.997.

B. *Scenario 2: 3% disturbance, increase in demand:*

After three seconds, an increase in demand occurred of 7.5 MW of power, causing fluctuations in both frequency and power. Eventually, the frequency is once more brought back to its nominal value as shown in Fig. 4 b.

C. *Scenario 3: 4% disturbance, decrease in load demand:*

Another disruption with a sudden load demand reduction of 10 MW happened in the sixth second. Frequency nadir and high-power oscillation amplitude occurred. Once more, the frequency settles down to its rated value as witness in Fig. 4 c.

Table 2.Frequency Δf (Hz) and power ΔP (MW) variations in microgrids

CASE	PSO		Modified PSO	
	Δf	ΔP	Δf	ΔP
1	0.997	3.1133	0.0199	2.4939
2	1.4752	4.7006	0.0295	3.6494
3	1.9886	6.1704	0.0398	4.5479

As evidence in Fig. 4 a.b.c modified PSO has better results than traditional PSO. Frequency and power changes in each case is used to evaluate the capacity of HESS needed. The differences brought about by the PID controller when optimization techniques are applied in each case is utilise to evaluate the capacity of HESS reduced hence the overall cost reduction.

V. Conclusion

Adaptive virtual control strategy-based optimisation technique was implemented to tune PID controller's parameters. The primary goal of this control strategy is to boost the microgrid's inertia support with the aim of increase frequency responsiveness. ESS required capacity reduced therefore the overall system is economical.

As evidence in the results, frequency performance parameters such as ROCOF and frequency nadir has been improved, and settling time is reduced. The optimisation techniques minimise the objective function to obtain optimal performance hence validate the effectiveness of this control strategy.

REFERENCES

[1] B. K. Poolla, D. Groß, and F. Dörfler, "Placement and Implementation of Grid-Forming and Grid-Following Virtual Inertia and Fast Frequency Response," *IEEE Trans. Power Syst.*, vol. 34, no. 4, pp. 3035–3046, 2019, doi: 10.1109/TPWRS.2019.2892290.

[2] M. Elshenawy, A. Fahmy, A. Elsamahy, S. A. Kandil, and H. M. El Zoghby, "Optimal Power Management of Interconnected Microgrids Using Virtual Inertia Control Technique," *Energies*, vol. 15, no. 19, pp. 1–30, 2022, doi: 10.3390/en15197026.

[3] H. S. Hlaing, J. Liu, Y. Miura, H. Bevrani, and T. Ise, "Enhanced Performance of a Stand-Alone Gas-Engine Generator Using Virtual Synchronous Generator and Energy Storage System," *IEEE Access*, vol. 7, pp. 176960–176970, 2019, doi: 10.1109/ACCESS.2019.2957890.

[4] C. L. Bhattar and M. A. Chaudhari, "Centralized Energy Management Scheme for Grid Connected DC Microgrid," *IEEE Syst. J.*, vol. 17, no. 3, pp. 3741–3751, 2023, doi: 10.1109/JSYST.2022.3231898.

[5] G. Magdy, A. Bakeer, and M. Alhasheem, "Superconducting energy storage technology-based synthetic inertia system control to enhance frequency dynamic performance in microgrids with high renewable penetration," *Prot. Control Mod. Power Syst.*, vol. 6, no. 1, 2021, doi: 10.1186/s41601-021-00212-z.

[6] M. A. Mosa, M. Y. Yousef, S. M. El Masry, A. M. Abdel Ghany, and A. A. Ali, "Frequency support of AC microgrid with high penetration of photovoltaic using super-capacitor," *Sustain. Energy Technol. Assessments*, 2022, doi: 10.1016/j.seta.2022.102364.

Authorized licensed use limited to: DELHI TECHNICAL UNIV. Downloaded on November 09,2024 at 04:52:56 UTC from IEEE Xplore. Restrictions apply.

[7] M. M. Elwakil, H. M. E. Zoghaby, S. M. Sharaf, and M. A. Mosa, "'Adaptive virtual synchronous generator control using optimized bang-bang for Islanded microgrid stability improvement,'" *Prot. Control Mod. Power Syst.*, vol. 8, no. 1, 2023, doi: 10.1186/s41601-023-00333-7.

[8] S. K. Singh, R. Singh, H. Ashfaq, and R. Kumar, "Virtual Inertia Emulation of Inverter Interfaced Distributed Generation (IIDG) for Dynamic Frequency Stability & Damping Enhancement Through BFOA Tuned Optimal Controller," *Arab. J. Sci. Eng.*, 2021, doi: 10.1007/s13369-021-06121-5.

[9] Z. A. Obaid, L. M. Cipcigan, and M. T. Muhssin, "Fuzzy hierarchal approach-based optimal frequency control in the Great Britain power system," *Electr. Power Syst. Res.*, vol. 141, pp. 529–537, 2016, doi: 10.1016/j.epsr.2016.08.032.

[10] T. Kerdphol, M. Watanabe, K. Hongesombut, and Y. Mitani, "Self-Adaptive Virtual Inertia Control-Based Fuzzy Logic to Improve Frequency Stability of Microgrid with High Renewable Penetration," *IEEE Access*, vol. 7, pp. 76071–76083, 2019, doi: 10.1109/ACCESS.2019.2920886.

[11] S. Ke *et al.*, "A Frequency Control Strategy for EV Stations Based on MPC-VSG in Islanded Microgrids," *IEEE Trans. Ind. Informatics*, vol. 20, no. 2, pp. 1819–1831, 2024, doi: 10.1109/TII.2023.3281658.

[12] E. A. Mohamed, E. M. Ahmed, A. Elmelegi, M. Aly, O. Elbaksawi, and A. A. A. Mohamed, "An Optimized Hybrid Fractional Order Controller for Frequency Regulation in Multi-Area Power Systems," *IEEE Access*, vol. 8, pp. 213899–213915, 2020, doi: 10.1109/ACCESS.2020.3040620.

[13] M. A. Arasomwan and A. O. Adewumi, "On the performance of linear decreasing inertia weight particle swarm optimization for global optimization," *Sci. World J.*, vol. 2013, pp. 5–16, 2013, doi: 10.1155/2013/860289.

[14] S. Oladipo, Y. Sun, and O. Adeleke, "An Improved Particle Swarm Optimization and Adaptive Neuro-Fuzzy Inference System for Predicting the Energy Consumption of University Residence," *Int. Trans. Electr. Energy Syst.*, vol. 2023, 2023, doi: 10.1155/2023/8508800.

[15] P. Yegon and M. Singh, "Frequency Stability Enhancement of Microgrid Using Optimization Techniques-Based Adaptive Virtual Inertia Control," *Int. Trans. Electr. Energy Syst.*, vol. 2023, 2023, doi: 10.1155/2023/2121721.

[16] A. Slowik, "Particle Swarm Optimization," in *The Industrial Electronics Handbook - Five Volume Set*, 2011, pp. 1942–1948. doi: 10.1007/978-3-319-46173-1_2.

[17] Y. Ma, W. Cao, L. Yang, F. F. Wang, and L. M. Tolbert, "Virtual Synchronous Generator Control of Full Converter Wind Turbines with Short-Term Energy Storage," *IEEE Trans. Ind. Electron.*, vol. 64, no. 11, pp. 8821–8831, 2017, doi: 10.1109/TIE.2017.2694347.

Appendix

Parameters	Symbol	value
Source voltage	v_s	415V rms
Frequency	f_{grid}	50 Hz
Source inductance	L_S	1 μH
Source resistance	R_S	$10^5\Omega$
DC link capacitnce	C_{dc}	2200 μH
DC link voltage	V_{dc}	600 V
Damping constant	D	0.8
Turbine constant	T_{Turb}	0.5 s
Governor revolution	Rev. per min	0.05
Gen Inertia Constant	H	5 s
Governor Time Constant	T_{Gorvn}	0.2 s

Authorized licensed use limited to: DELHI TECHNICAL UNIV. Downloaded on November 09,2024 at 04:52:56 UTC from IEEE Xplore. Restrictions apply.

ResearchGate

See discussions, stats, and author profiles for this publication at: https://www.researchgate.net/publication/385598049

Application of Paper Mill Lime Sludge Waste in Building Construction Material: State of The Art Report

Article · November 2024

CITATIONS
0

READS
8

4 authors, including:

Arti Chouksey
Deenbandhu Chhotu Ram University of Science and Technology, Murthal
14 PUBLICATIONS **52** CITATIONS
SEE PROFILE

Nirendra Dev
Delhi Technological University
50 PUBLICATIONS **801** CITATIONS
SEE PROFILE

Manvendra Verma
GLA University
52 PUBLICATIONS **936** CITATIONS
SEE PROFILE

All content following this page was uploaded by Manvendra Verma on 07 November 2024.

The user has requested enhancement of the downloaded file.

STM JOURNALS

Journal of
Polymer & Composites

ISSN: 2321-2810 (Online)
ISSN: 2321-8525 (Print)
Volume 12, Special Issue 7, 2024
DOI (Journal): 10.37591/JoPC

https://journals.stmjournals.com/jopc

Research JoPC

Application of Paper Mill Lime Sludge Waste in Building Construction Material: State of The Art Report

Arti Chouksey [1], Nirendra Dev [2] , VVL Kantarao [3], Manvendra Verma [4,*]

Abstract

A Comprehensive Literature review is done to find various areas of application of Lime Sludge. Temperature-treated Lime sludge proves to be highly beneficial to be used as Building material. Lime Sludge has an application area in all types of Building materials such as bricks, Tiles, Cement etc. especially, in Cement it is highly beneficial in all the phases of cement from Clinker to, mortar and as a replacement in Concrete. As per the literature review, the application of Lime Sludge is limited to 10-20 % replacement when used alone, with a high replacement level of up to 30% observed in case of use with other SCMs such as Fly Ash, and Metakaolin. Lime Sludge is waste from the paper industry and can be effectively used in different building materials to reduce the depletion of natural resources and to reduce the carbon footprint of the product. There is a need to further investigate and enhance the utilization potential of Lime Sludge for Higher %ages for Sustainable construction practices.

Keywords: Sustainable construction material; Supplementary cementitious materials; Mechanical properties; Compressive strength; concrete composites

INTRODUCTION

Urbanization and rapid population growth especially in developing countries, escalate, housing, and infrastructure demand. It is at a much faster rate than is ever experienced. Global cement output has reached 2.8 billion tonnes annually and is anticipated to reach 4 billion tonnes annually by 2050. The epicentre of these growths is mainly China and India., with other developing regions like the Middle East and Northern Africa. [1, 2,3]

The process of cement manufacturing is highly carbon and energy-intensive. It is projected that the production of 1 ton of Portland cement generates 730-990 kg of CO_2, which is responsible for about 8% of total CO_2 Production. [4,5]. So, in recent years, the focus of the researcher shifted towards the production of new binders, which are less energy-intensive. Reduction in Co2 emission can be accomplished by partial replacement in a binder by Supplementary Cementitious Materials called as SCMs, mostly derived as unwanted by-products from other industries. This byproduct is viable only if it performs similarly to or better than concretes manufactured from OPC since these products are industrial waste so skillful utilization of this product reduces the cost of production significantly and also performance can be enhanced in case of some SCM.[6, 7] In recent years, there have been several attempts to use different types of industrial waste as substitute materials, but there is still room for improvement. Due to the limited supply of materials used to make typical cement constituents. Widely used alternate Materials, such as fly ash,

***Author for Correspondence**
Manvendra Verma

[1]Assistant Professor, Department of Civil Engineering, DeenBandhu Chhotu Ram University Science and Technology, Murthal, Haryana, India.
[2]Professor, Department of Civil Engineering, Delhi Technological University, Delhi, India.
[3] Ex. Principal Scientist, CRRI, Delhi, India.
[4]Assistant Professor, Department of Civil Engineering, GLA University, Mathura, Uttar Pradesh, India

Received Date: April 23, 2024
Accepted Date: August 08, 2024
Published Date: October 16, 2024

Citation: Arti Chouksey, Nirendra Dev, VVL Kantarao, Manvendra Verma. Application Of Paper Mill Lime Sludge Waste in Building Construction Material: State of The Art Report. Journal of Polymer & Composites. 2024; 12(Special Issue 7): S172–S187p.

© STM Journals 2024. All Rights Reserved

blast furnace slags, and other natural pozzolans, are available in much smaller quantities compared to the worldwide demand for ordinary Portland cement (OPC). [8,9] So, research interest has been shifted towards readily available sources of SCMs such as clays and Sludge from various industries such as paper mills, textile, water treatment, and sewage sludge [10,11].

The pulp and paper industries produced a huge amount of lime sludge. In India, During the white liquor recovery process, the paper companies produce about 4.9 million tonnes of lime sludge annually.[12,13], Because it is frequently dumped straight into landfills, lime sludge contributes to both anthropogenic and natural environmental impacts. this causes issues with the environment such as carbon breakdown, microbial activity, leaching, and ion exchange processes. This led to the contamination of the surface, groundwater, and soil.to reduce the risk of landfilling It is essential to use this waste material in applications like building materials such as cement and Aggregate [14](7). The major component in Lime sludge is Calcium Carbonate, while Silica and Alumina also present a small proportion [15]. The two primary crystalline phases in lime sludge are kaolinite ($Al_2O_3.2SiO_2.2H_2O$, 10–20%) and calcite ($CaCO_3$, 60–90%). Reactive lime (CaO) and Metakaolin ($Al_2O_3.2SiO_2$) were produced during the thermal treatment of lime sludge, which accounts for their high reactivity when used as additional materials in cement [16,17,18]. Figure 1. shows the composition of cement at the global level.

Materials & Methods

Lime sludge is made up of very small precipitated CaC03 particles and leftover, unsettled green liquor clarifier dregs. Table 1 displays the typical Physicochemical characteristics of waste Lime Sludge. The Main mineralogical component of Lime Sludge is Calcite, Quartz, Hemihydrate [19,20]. Table 1 represents the main oxide components of raw lime sludge [21].

An estimated 13 million tonnes of paper, paperboard, and newsprint are produced in India annually, making up 3.18 % of the overall production (408 million tonnes annually) [22]. Paper production produces waste products. For every tonne of paper produced, a pulp and paper mill generate 1.63 tonnes of lime sludge. The pulp and paper industries are among the most polluting due to the enormous amounts of lime sludge they produce [23]. In the paper industries' chemical recovery division, lime sludge is produced. Chemical recovery systems are installed in every integrated large-scale paper manufacturing facility in India [24]. Chemicals are dissolved in water while they are still molten during the chemical recovery process to green liquor, make it. Through the causticization process, this green liquor is transformed into white liquor. The majority of the smelt, soda ash (Na_2CO_3), is converted to calcium carbonate ($CaCO_3$), or lime sludge, during the causticization process by combining with calcium oxide (CaO) to produce caustic soda (NaOH). Lime sludge can be recycled in the lime kiln and used once more as lime (CaO) during the causticization process. On the other hand, paper mills' lime recovery processes require a lot of energy (1530–1830 kcal/kg of lime). One problem brought on by high silica concentration (5–10% in lime sludge) is scaling in the lime kiln (22). This is the rationale behind why paper businesses typically prefer to landfills instead of recycling lime sludge. Landfilling and land Rectification are the preliminary measures taken to get rid of lime waste from paper mills [6 [25)]. However, as landfill sites become more expensive and limited due to taxes, strict regulations, and declining potential, the cost of land-filling is rising. Due to its high quality, lime sludge is therefore extremely important for usage in building construction materials [26]. The potential uses of lime sludge in different building applications are shown in Figure 2.

Table 1. %Weight of different components in Raw Lime Sludge

Element	O	Al	Si	S	Ca	Fe
Weight %	58.79	1.71	9.72	2.98	25.35	1.45
Atomic weight%	75.99	1.31	7.16	1.92	13.08	0.54

© STM Journals 2024. All Rights Reserved

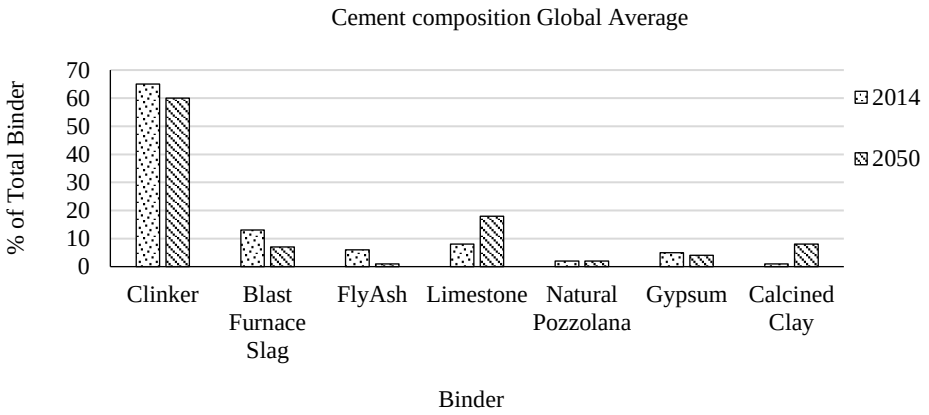

Figure 1. Global average of cement composition.

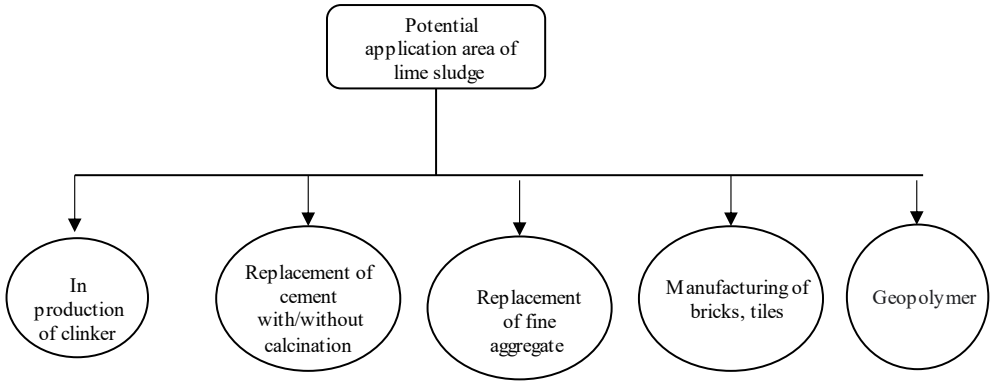

Figure 2. Potential application areas of lime sludge.

The demand for building materials is rising along with the global population. Therefore, the construction industry is now concerned about the imbalance between supply and demand for building materials [27]. Therefore, researchers are creating suitable alternative options for construction materials in order to close this gap and ensure the ongoing supply of building materials (21). Utilizing waste products from various sectors may be the way to close the supply-demand gap in the construction sector. Lime sludge, among other waste products, has excellent potential for use as building materials. Additionally, it is a successful strategy for reducing solid waste. Lime sludge has recently been combined with other wastes to produce a variety of materials used in construction. There have been numerous review papers and books written about paper mill waste [28–31], but none specifically discuss the use of lime sludge as a Binder in Construction and other building materials such as Bricks, Ceramics etc. cementitious binders, concrete, and ceramics. As a result, the current review paper has enormous potential for understanding how lime sludge consumption trends have evolved. Fig 3 depicts the process of manufacturing of lime sludge.

Cement Fabrication Uses

The demand for building materials is expanding exponentially, and cement remains the key component to meet these demands. As a result, it is crucial to address the expanding issues facing the cement business, such as resource conservation, CO_2 emissions, and energy use. The utilization of alternative materials mainly industrial waste and energy-efficient processes are the primary levers for the cement industries, according to the International Energy Agency. Although there have been recent efforts to promote the use of alternative materials, there is still room for growth in this area. There are consequently restrictions on the availability of the materials used to make typical cement constituents. As a result, in the upcoming years, new alternative materials might take the place of cement's component parts. Burnt clay pozzolanic cement blends with and without silica fume were examined by Amin et al. [19]. The 10% bunt clay with OPC exhibits improved compressive strength. The synthesis of CSH and

© STM Journals 2024. All Rights Reserved

CASH with CH products was shown in the DSC and XRD tests. For the creation of blended cement paste, both silica fume and electric arc furnace slag were shown to be useful [20]. A similar strategy was also tested for making cement using lime sludge. The calcium carbonate, together with some silica and alumina, makes up the majority of the lime sludge. The calcium carbonate, together with some silica and alumina, makes up the majority of the lime sludge. Calcite and kaolinite are the two primary crystalline phases Table 1 found in lime sludge. While kaolinite is comprised of hydrous aluminium silicate ($2H_2OAl_2O_32SiO_2$), Metakaolin ($Al_2O_{3\ 2SiO2}$), a highly reactive byproduct of the calcination of lime sludge, can be employed as a cement ingredient. Reusing lime sludge demonstrates its potential as a source of pozzolanic activity for the creation of cementitious binders. The cementitious binder is thus the best material for utilizing lime waste.

A study on the utilisation of dried lime sludge in cement production was conducted by Wei et al. The result indicates that the addition of lime sludge enhanced the clinker's capacity to burn,[32] which in turn decreased the temperatures required for calcium carbonate decomposition and liquid phase production. Tricalcium silicate (C_3S) formation in cement clinker was also made possible by the presence of phosphorus and other trace elements, which enhanced the liquid phase and decreased the viscosity. [33] investigation into the manufacture of belite using nano-silica and paper mill lime waste. Alite is the primary component that makes up 80% of cement clinker, whereas belite, also known as b-dicalcium silicate (b-C2S, Ca2SiO4), makes up 20% of Portland cement clinker.

But in this case, the elite was created via a solid-state reaction with lime sludge and nano-silica at a comparatively modest temperature of 850 °C. Additionally, the ratio of lime sludge to nano silica employed for the clinker preparation was 2 to 1. Lime sludge and silica fume were combined in[34] further study to create belite. The belite synthesis was carried out using the same experimental protocol but at a higher temperature. A study on the manufacturing of the binder from paper mill waste was conducted by [35]. To create belitic and Portland clinkers, various mixtures of lime sludge, biological sludge, and fly ash were made and then sintered at a temperature that was slightly lower than usual—1350 °C—for clinker synthesis. Additionally, it was determined that the mixture of 49 % lime sludge The largest quantity of belite synthesis was created using, 20% fly ash, and 30% biological sludge, which was also utilised to create the belite cement-based mortar, which provided adequate mechanical strength and exhibited no evidence of deterioration or durability flaws. (17) attempt to make eco-clinkers, lime sludge, coal biomass ash, and wastewater treatment process sludge were all utilised. In different quantities and configurations, the three fundamental materials were created and then burned at temperatures between 1350 and 1450 °C. According to the study, an eco-clinker formulation consisting of 69 % lime sludge, 29 % biomass ash, and 2 % wastewater process sludge at 1450 °C displayed the principal crystalline phases often present in commercial cement.

Additionally, the eco-cement was made with this eco-clinker (95 wt % of eco-clinker and 5 wt. % of gypsum). [36] Additionally, eco mortar was made using the eco-cement that was generated. It was found that the functionalization of eco-cement in mortar demonstrated a compressive strength of 21 MPa after 28 days of curing. Researchers also studied the function of lime sludge in geopolymer concrete in light of recent developments. In an experimental investigation, [37,38] employed lime sludge as an activator in the manufacturing of geopolymer cement CEM IIIC and type 32.5 N class in accordance with European Standards EN-197. To manufacture one part of geopolymer cement, the lime sludge was combined with blast furnace slag after being prepared with sodium hydroxide. In the mortar preparation, more lime sludge that hadn't yet reacted served as filler. By adding more lime sludge, cement demonstrated greater compressive strength. It was found that an application of 18 % lime sludge produced the highest compressive strength (42 MPa)[39]. the strength characteristics of the mortars are examined taking into account the heat of hydration and setting time of cement. The cumulative heat release from the lime sludge cement is found to be equal to the OPC cement in terms of the heat of hydration. (27) The industries' disposal issues may be resolved by using lime sludge in cement production in an environmentally and economically responsible way. When lime sludge is used in the process of making cement, less naturally natural resources are consumed, which also reduces carbon emissions because less energy is used. [35,40] Table 2 describes the lime sludge use in preparation of clinker.

© STM Journals 2024. All Rights Reserved

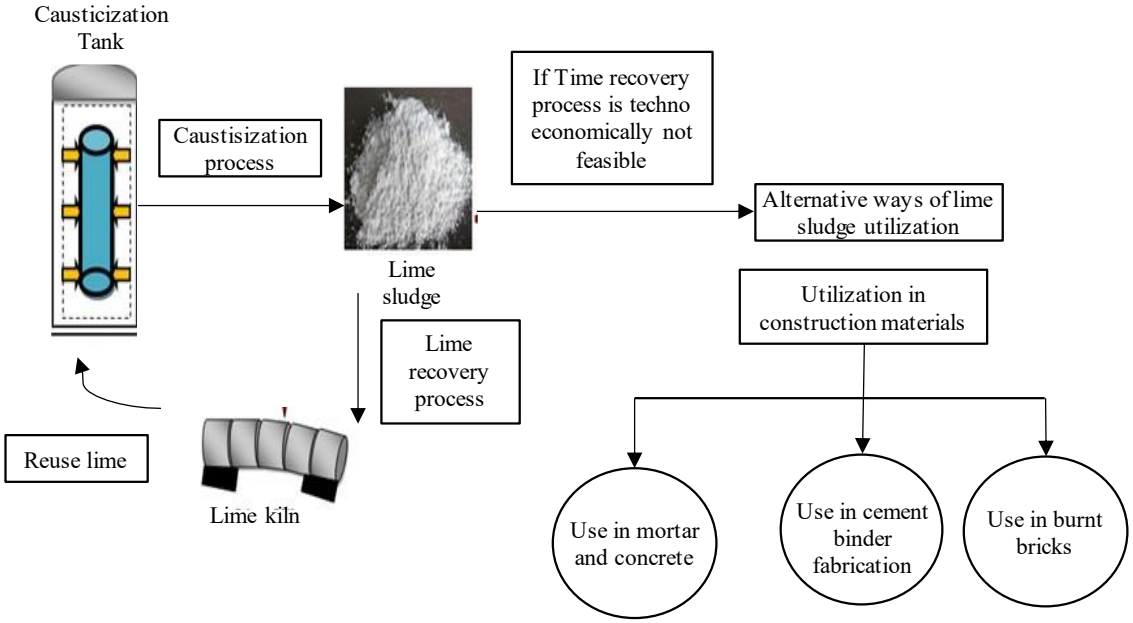

Figure 3. Manufacturing of lime sludge.

Table 2. Lime Sludge Use in Preparation of Clinker.

S.no.	Author	Parameter studies	Material used	Product
1	(33)	Mineralogical studies	Nano silica	Clinker
2	(34)	Mineralogical studies	Silica Fume	Clinker
3	(35)	Mineralogical, hydration and compressive strength	Fly ash and biological sludge	Clinker
4	(41)	The cement kiln's inclusion of lime sludge increased sintering.	Cement	Cement
5.	(35)	Density and Compressive Strength	LM and gypsum	Clinker
6	(37)	Ground granulated blast furnace slag and sodium hydroxide	Compressive strength, heat of hydration, and mineralogy	Geopolymerbinder

RESULTS & DISCUSSION

Application in cement mortar

Masonry work involves the use of mortar, a malleable mixture made of cement and sand. As a substitute for cement and fine aggregates, lime sludge has been used in mortars. It is used in mortars in various configurations calcined and as received and mixtures with other substances. The research of many researchers on the impact of lime sludge in mortars is summarised in Table 3. The reactivity of lime sludge is increased by calcining it between 650 and 800 degrees Celsius[42]. The lime produced by the breakdown of $CaCO_3$ is hydraulically reactive and stable for use in the production of binders. Additionally, to create secondary CASH products, active CaO reacts with the SiO_2 that is present in matrices. However, an excessive amount of CaO may harm durability. For the preparation of mortar, [43] employed burned lime sludge. In the preparation of mortars, 25% of the cement was replaced by lime sludge that had been heated to various degrees. The mortars' compressive strength was evaluated after 90 days with 25 % lime sludge, and it was found to be higher than that of regular concrete[19,44–46]. The conversion of calcium carbonate from the lime sludge calcium carbonate into calcium oxide during the heat treatment process may be the cause of the subsequent development of compressive strength. When lime is used in mortar, it aids in the creation of additional calcium silicate hydrate, which leads to a late-stage enhancement in the strength qualities of the mortars.

The calcination of the lime sludge uses a tremendous amount of energy, which is wasteful. Lime sludge should be used exactly as it was received from an economic standpoint. In line with the

© STM Journals 2024. All Rights Reserved

aforementioned rationale, [47]Modolo et al. focused on the usage of received lime sludge. To compare mortars made with normal filler (commercial filler) application to those made using lime sludge as a filler material, the results were obtained. Following ball milling with a smaller particle size, lime sludge was employed. Mortars were created by substituting lime sludge for 6, 12, and 18% of the total aggregates, respectively, increasing the compressive strength by 10%, 17%, and 23% compared to the reference mortar. Due to the presence of small, ball-milled particles in the concrete matrix, this effect may be linked to the filler and binder effects of lime sludge. Following this conclusion, some research has also concentrated on substituting fine aggregates with lime sludge. (23) investigated two different mortar types with four different combinations of lime sludge binders. Binder 1 was created using lime sludge (30%) and fly ash (70%) while Binder 2 was created using the same proportions but with 1% gypsum. Due to an increased pozzolanic reaction, the inclusion of gypsum had a favourable influence on the compressive strength of mortars. By using fly ash and lime sludge from paper mills that had already been received. [48] research focused on creating environmentally friendly materials for construction purposes. Both lime sludge and fly ash were used to prepare the mortars. Maximum compressive and flexural strengths were attained by substituting lime sludge for 10% of the total cement; however, strength was reduced if the %age of lime sludge replacement exceeded 10%. Experimental research by [49]. focused on the usage of fly ash and paper mill lime sludge in a mortar. The mortars with a 12.5 % lime sludge and 12.5 % fly ash replacement of the cement had the highest compressive strength of 25 KPa. The compressive strength of mortar made with more lime sludge and fly ash was significantly reduced. Lime sludge, fly ash, and Portland cement were used to create a cement adhesive by. The mortars were grounded using cement pastes that contained a maximum of 20% lime sludge and fly ash(19). In the preparation of the mortar, fluidized bed reactor sand was utilised in place of the fine aggregates. The study found that adding fly ash to lime sludge increased the cement paste's yield stress and viscosity. Mortars with a 10% fly ash and 10% lime sludge addition to cement paste demonstrated the highest compressive strength. According to the study, lime sludge has a significant chance of taking the place of cement or fine aggregates in concrete and mortar. Researchers studied various concrete grades; however, it was found that the compressive strength of concrete and mortars satisfy the requirement of strength up to replacement of 30% of total cement and then starts to drop with an exponential rate beyond that[50,51]. a rise in the use of lime sludge in place of cement. This application limit for lime sludge has been increased in several studies to 10–20 %. Up to a 25 to 30 % application of lime sludge, replacing fine aggregates with it had no appreciable impact on the compressive strength of mortars and concrete. Other industrial by-products were applied along with lime sludge, and this improved the strength properties

Table 3. Lime Sludge Application in Mortar.

S. no.	Material replaced	Material added	% replacement	Optimum replacement	Parameters studies	Impact	Reference
1	Cement	Fly Ash, Gypsum	89-100	80	Compressive Strength	+2.7% (increase)	(23)
2	Cement		10-30	25	Compressive Strength	+3.1% Increase	(48)
3	Fine Aggregate		10-30	30	Compressive Strength	+1.34% (Increase)	(47)
4	Cement and Fine Aggregate	FlyAsh	10	10	Compressive strength	-37% (Decrease	(19)
5	Cement	FlyAsh	10-20	10	Compressive Strength	-6% Decrease	43
6	Cement	FlyAsh	12.5	12.5	Flexural and Compressive Strength	-4.1% Decrease	(49)
7	Cement	Flyash, Silica Fume	30-70				(27)
8	CementFine aggregate		0-20	15	Compressive and Flexural strength,	-7% decrease	(50)

© STM Journals 2024. All Rights Reserved

Application In Concretes

Concrete is a composite material that consists of cementitious binders holding fine and coarse particles together. Researchers from all over the world are attempting to use a variety of wastes from various industries, including fly ash, recycled aggregates, sugarcane bagasse ash, rubber waste, silica fume, ground granulated blast furnace slag, waste glass sludge, ceramic waste, hydrated lime and agro waste, to produce concrete that is both affordable and sustainable. These components were used in the cement-based concrete either as filler or as pozzolanic ingredients [51–57] The manufacturing of cement-based building materials also uses wastes from the pulp and paper industries, such as lime sludge, deinking sludge, primary sludge, and waste paper fibre sludge. Different application techniques for lime sludge in the creation of concrete are shown in Table 4. Fig 4 demonstrates the work of various researchers for different grades of concrete and it demonstrates that the influence of Lime Sludge is more at lower strengths but for higher strengths the capability of lime sludge is limited[49,58–60]

Table 4. Lime sludge application in concrete.

S.no.	Replaced by	% replaced	Optimum % obtained	Parameter studies	Effect	Reference	Grade
1.	Cement	10-70	30	Compressive Strength	Decrease 4%	Srinivasan et al. 2010	M30
2	Cement	10-30	30	Modulus of Elasticity, Viscosity Cohesion	Decrease 1.34	Modolo et al 2011	M30
3.	Cement	10-40	10	Fluidity, Compressive strength	Increase	Pitroda et. *al. 2013*	M40
4.	Cement	10-40	15	Compressive strength, Modulus of elasticity	Increase16	*Yousuf et al. 2014*	M15
5	Cement	10-20	30	Compressive Strength	Increases 8%	*Manchriyal et al. 2016*	M20
6	Cement	10-40	30	Compressive strength	Increase 6%	*Abhishek et al2017*	M20
7	Cement	10-30	30	Compressive Strength	Decrease 6.2%	*Alam et. al. 2015*	M20
8	Fine Aggregate	10-25	25	Compressive Strength	Decrease 5%	*Soni et. al. 2015*	M25
9	Fine Aggregate	10-40	20	Compressive strength	Increase 3.7	*Shermale et al. 2015*	M30

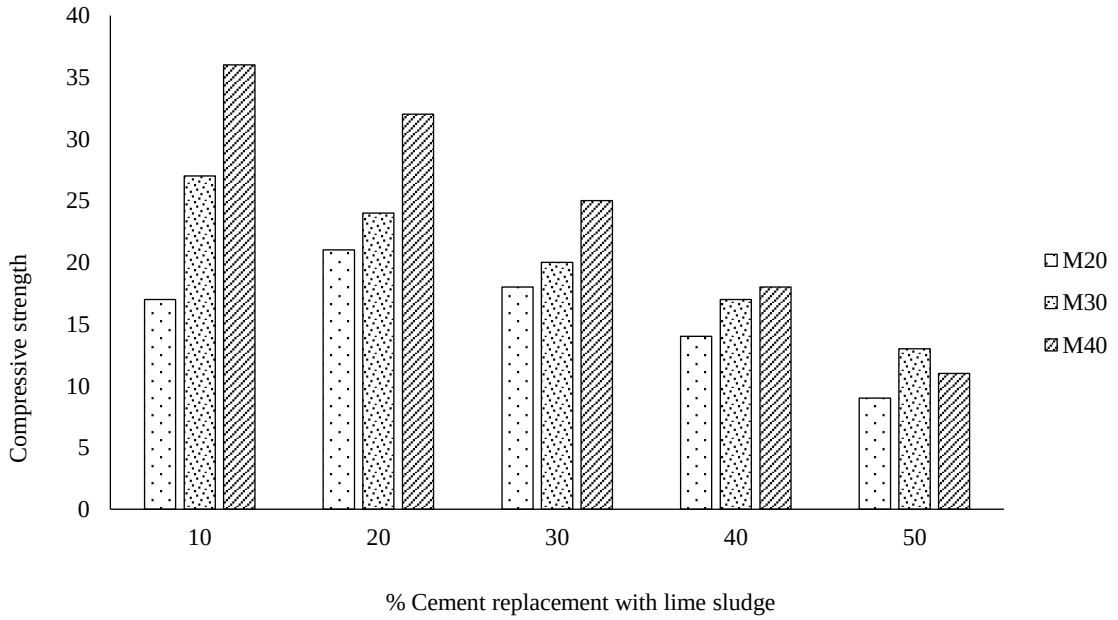

Figure 4. Variation of compressive strength with various design mixes.

© STM Journals 2024. All Rights Reserved

Effect on compressive strength of concrete

The impact of lime sludge on concrete has been the subject of numerous investigations. Table 5 summarises the findings of numerous studies on the effects of applying lime sludge to different concrete grades after 28 days of curing. Researchers have used lime sludge to prepare various concrete grades. According to research on the concrete of the M20 grade, lime sludge replaced cement 10–20 % of the time, slightly increasing compressive strength compared to reference concrete. However, the compressive strength was reduced as a replacement was further increased. Furthermore, lime sludge demonstrates comparable compressive strength to conventional M20 grade concrete at a 30 % cement substitution level[59,61,62]. It's possible that the saturation of lime sludge binding in the matrix is what is having a detrimental effect on the larger %age of lime sludge. This limits the use of lime sludge in concrete in large quantities. The researchers used lime sludge in the higher grade of concrete since it was necessary to use lime sludge in large quantities. Numerous researchers attempted to increase the use of lime sludge in concrete blocks of the M30 grade. However, no researcher has identified a pattern akin to the one identified in the instance of M20 concrete. According to (61), lime sludge reduced compressive strength and only allowed a 30 % replacement of total cement. Since the compressive strength substantially reduced below the M30 grade of concrete beyond this limit of replacement. Similarly, [63] noted a decline in compressive strength. According to the study, lime sludge acts as a filler and only 20% of cement replacement is permissible in concrete of the M30 grade. There is no literature discussing the root cause and mechanism of these discrepant compressive strengths of M20 and M30 grade concrete. [64] advised replacing up to 10% of the cement with lime sludge without reducing the strength of the concrete in terms of the impact of lime sludge on the compressive strength of M40-grade concrete. Some investigations have concentrated on replacing fine aggregates with lime sludge in addition to replacing cement with the substance. In a study that contributed to the novelties in lime sludge utilisation, (49) found that concrete strength decreases when fine aggregate is replaced with lime sludge, but that this decrease is not equal to a 25 per cent replacement of fine aggregate. The claimed decline in compressive strength may be caused by the concrete's decreased workability. When lime sludge replaces fine aggregate with equivalently smaller particle size, the workability of the concrete matrix is maintained thanks to the coarser fine aggregate. The concrete matrix's reduced compressive strength is ultimately caused by the extra water present.

The presence of lime sludge affects the rheological characteristics of concrete, including fluidity, yield stress, plastic viscosity and cohesion between particles. (25,47,64). While raising the yield stress and cohesion between particles in the fresh state, adding more lime sludge decreased the matrix's fluidity and plastic viscosity. As lime sludge application increased, the apparent porosity of concrete decreased; at around 30%, compared to the reference concrete, the apparent porosity was reduced by 6%. The study recommended up to 30% replacement of the lime sludge based on the results of rheological experiments. In a study, [65]. found that, as the proportion of lime sludge grew, the yield stress of mortar increased and the plastic viscosity dropped. Additionally, it was found that applying lime sludge reduced the fluidity of mortar and increased the cohesiveness between particles and water.

After this point, the concrete's elasticity significantly decreased. The M40 grade of concrete provided the same modulus of elasticity as regular concrete. This influence on the rheology of concrete is generally attributed to the small particle size of the lime sludge, which lowers the free water content. As a result, the concrete loses workability and elastic modulus while increasing cohesiveness, viscosity, and yield stress.

Application With Other Waste Materials

To keep the concrete's desirable quality, lime sludge has also been used in conjunction with other pozzolanic supplementary cementitious materials. When combined with calcium hydroxide, pozzolanic materials—which are either siliceous or siliceous and aluminous—form cement. Pozzolanic elements were successfully included in lime sludge-based binders, greatly improving their resistance to deterioration in harsh environments and increasing their durability. In both conventional curing and air curing, binary blended cement concrete with pulverised fly ash and metakaolin and various

© STM Journals 2024. All Rights Reserved

combinations of cementitious systems demonstrated increased strength and durability. According to reports, the reduction in chloride ions intrusion resulted in the reinforcement of safety measures. In comparison to the control mix, the ternary mixed concrete with cement, fly ash, and silica fume offers increased strength and greater durability. For ternary blended concrete, long-term resistance to sulphate attack revealed very strong chemical resistance. [20,66–68]

One of the most important characteristics of lime sludge-based concrete and mortar is durability. Numerous studies show that using fly ash and silica fume in particular ratios with lime sludge as a partial replacement improves the durability of concrete. Numerous supplementary cementitious materials (SCMs) are utilised widely, such as fly ash, slag cement, rice husk ash, metakaolin, palm oil fuel ash, and silica fume [49,69–71]. [. In order to study the chemical resistance of lime sludge-based cement concrete, (49) subjected it to 5% HCl and 5% H_2SO_4. The acid mass loss factor for H_2SO_4 was higher than for HCl, indicating that concretes are more vulnerable to sulphate attack.

Due to the similar effects of quarry dust and fly ash on concrete, the application of lime sludge along with fly ash and quarry dust had a favourable impact on compressive strength (60). In their study of the mechanical characteristics of concrete with a strength of 30 MPa, substituted lime sludge for fine aggregates and silica fumes for cement, respectively. (33)The investigations were also conducted using a mixture of silica fume and lime sludge. At 28 days, it was found that replacing 20% of the fine aggregate with lime sludge and 20% of the cement with silica fume produced concrete with a similar compressive strength to the control concrete. (68) replaced cement with nano-silica and paper mill lime sludge and found that the compressive strength remained the same as that of traditional concrete of M30 grade at 4% nano-silica and 30% dried and crushed lime sludge. The boiler ash employed in the procedure was used to create the nano silica, which had a specific surface area of 450 m2/g with particle sizes ranging from 10 to 25 nm.

The strength of the concrete was increased by adding silica fume and nano-silica to lime sludge, but this procedure also has to be evaluated for its economic viability. Jute and glass fibres were used by(49) in addition to drinking and repulping generated paper mill lime sludge. For the M30 grade of concrete, lime sludge and sludge were combined in place of cement. Concrete only attained a modest amount of compressive strength, and only a 10% application of sludge was suitable when combined with jute and glass fibre. [72] Lime sludge and wood ash were applied together for the manufacture of concrete, this study recommended using lime sludge in concrete to minimize sludge disposal and to cut back on carbon dioxide and other greenhouse gases[73–77].

Table 5. Other materials used with Lime Sludge.

S.no.	Added material	Material replaced	Optimum % replacement	Grade	Parameter studies	Chang in strength	Reference
1	Jute and Glass Fibers	Cement	30%	M30	Compressive Strength	Increase	(49)
2	Nano Silica	Cement	30%	M20		Decrease 1.37%	(68)
3	Quarry Sand	Cement	20%	M20		Decrease 12.5%	(60)
4	Silica Fume	Fine aggregate	20%	M30		Decrease 6.09%	(63)
5	Fly Ash	Cement	10%	M20	Flexural Strength, Workability	Increase 8.91%	(58)

Application In Bricks and Ceramics

In India, burned clay bricks are widely used. Due to its great plasticity and appropriateness for moulding, river basins, ponds, and coastal locations are where the clay scrap is typically found when

© STM Journals 2024. All Rights Reserved

creating high-quality burnt clay bricks. Due to the nation's expanding need for clay-based bricks, alluvial soil supplies that are ideal for building bricks are being used up more quickly than they can be replenished. It also raises more issues because alluvial soil accounts for the majority of India's agricultural production.

There have been several studies on the use of recycled paper mill waste, craft pulp residue, sludge from the marble business, trash from the rice industry, waste from the sugarcane industry, waste glass sludge, sawdust, and urban garbage in the manufacturing of burnt bricks [28,78–81].

The completed work of the Researcher on the impact of lime sludge in burnt clay bricks and ceramics is compiled in Table 6. The mechanism of the reaction between the calcium and silicate phases during brick firing was put out by [82]. Furthermore, XRD (X-ray diffraction spectroscopy) investigations came to the conclusion that the most important aspect in brick creation and the development of strength in the bricks is the firing temperature. Better brick manufacture results from significant phase shifts caused by temperatures more than 1000 °C. A technique for producing burnt clay bricks using textile mill effluent that contains red, white, and black soil was devised by (79). Additionally, sludge was combined with soils for brick manufacture to get superior physical and mechanical characteristics while still meeting the requisite amount of silica and other minerals in the soils. For the best compressive strength of the bricks, a firing temperature of 800 °C and a firing time of 24 hours were determined to be ideal. Compressive strength of 4.5 N/mm2 was acceptable for bricks containing 15% lime sludge, while bricks containing more than 15% lime sludge were found to have a compressive strength that was less than the minimal permissible level of 3.5 N/mm2 for burnt clay bricks [83]

Studies on the utilisation of lime sludge also demonstrate its application in the creation of pottery. According to a study by [84], lime sludge and fly ash from the paper industry can be used to create anorthite ceramic through the process of solid-state reaction. Additionally, studies were conducted to test various mixtures of lime sludge and fly ash under various sintering temperatures. The anorthite phase was found to be primarily synthesised in the sample containing 36% lime sludge, however, it was mostly present in all samples at 1100 °C. Further research on the synthesis of ceramic material by direct mixing of already-received lime mud, fly ash, and other additives (sawdust, shale, diatomite, and perlite) was done by the author.

Table 6. Lime sludge application in bricks.

S.no.	Material	% replacement	Prepared material	Parameter studied	Effect on strength	Reference
1	Clay, Fly ash	40	Bricks	Compressive strength	Decrease 4.1%	(85)
2	Fly Ash	36	Artistic Ceramic	Compressive Strength and Mineralogy	Decrease 5.1%	(40)
3	Fly Ash	60	Bricks	Compressive strength and Mineralogy	Decrease 2.3%	(86)
4	Flay Ash	20	Tiles	Compressive strength		(45)
5	Fly Ash	40	Bricks	Compressive strength		(87)

ENVIRONMENTAL ADVANTAGES OF LIME SLUDGE UTILIZATION AS A BUILDING MATERIAL

Due to the need for vast amounts of primary and non-renewable resources and the flexibility/variety of products available, the building materials are an ideal target for the usage of lime sludge (cement, concrete, aggregates, ceramics, etc.). The desire for. The supply of raw materials in appropriate quantities and quality, as well as cost increases related to energy supply, are some of the issues the cement industry is currently dealing with. By lowering the amount of cement used in the concrete, the use of lime sludge in cement-based construction can address these difficulties.

© STM Journals 2024. All Rights Reserved

Sludge from paper mills is often disposed of in landfills. Natural and man-made environmental changes have a big impact on how metallic contaminants, if any, behave in sludge because they can modify how they appear. The redox potential, pH, temperature, leaching, ion exchange procedures, and microbiological activity are a few examples of such external influences [88]. Paper mill sludge when compacted has very low hydraulic conductivity. it can serve as a natural hydraulic barrier having permeability value in the range of 4.00 10—6 and 6.00 10—10 m/s. As a result, paper mill sludge can replace the use of natural clay as a natural hydraulic binder in the construction of the landfill hydraulic barrier layer, which can save disposal costs and also be a great alternative in locations without access to clay resources locally. The finding by [89]. demonstrated that the %age of leachable trace elements was extremely low, which was advantageous for the utilization of lime sludge.

CONCLUSIONS

The replacement of cementitious binder or fine aggregates in concrete and mortar with lime sludge has substantial potential. According to several published works, the compressive strength of concrete and mortars doesn't change until 30 % of the cement is replaced by lime sludge, after which the compressive strength starts to decline. Nevertheless, some studies have improved this cap on lime sludge use to 10- 20 %. Up to a 25–30% application, there was no discernible difference in the compressive strength of mortars and concrete when fine particles were replaced with lime sludge. Better strength properties were obtained in mortar and concrete when lime sludge and fly ash or metakaolin were combined. Lime sludge, however, alters the rheological characteristics of mortar and concrete, causing a drop in plastic viscosity and an increase in yield stress.

The issue of topsoil being used extensively in the manufacturing of burnt bricks and ceramics could be resolved by using lime sludge instead. Up to 20% of lime sludge can be used to make bricks, and 40% can be used to make ceramics. Utilizing lime sludge in the manufacture of bricks and ceramics can save energy because it requires a lower sintering temperature than the standard procedure while maintaining the same compressive strength. Since lime sludge produces eco-clinker at relatively lower temperatures and with substance usage of lime sludge, lime sludge has enormous potential as a raw material for the manufacture of cement (up to 70 %). Since calcium carbonate serves as the calcium phase during clinker synthesis it can be used directly in the production of cement clinker. In cement industries, its synthesis can be increased to large-scale production. Therefore, the tonnes of uncontrolled waste created by the pulp and paper sector each year might be replaced by using lime sludge in construction materials. Use of Lime Sludge in the production of Clinker also Limits the overusing the lime’s natural resource.

Application of lime sludge in concrete may yield more significant benefits if it is chemically activated before being applied to various grades of concrete. Future opportunities for the researchers may lie in their efforts to better understand the process of lime sludge in concrete.

The study is beneficial to a lot of resource persons who are involved in using used lime sludge to make sustainable building materials.

REFERENCES

1. Vashistha P, Kumar V, Singh SK, Dutt D, Tomar G, Yadav P. Valorization of paper mill lime sludge via application in building construction materials: A review. Constr Build Mater. 2019;211:371–82.
2. Sahu V, Gayathri V. The Use of Fly Ash and Lime Sludge as Partial Replacement of Cement in Mortar. International Journal of Engineering and Technology Innovation. 2014;4(1):30–7.
3. Priya AK, Nithya M, Rajeswari M, Priyanka PM, Vanitha R. Experimental investigation on developing low cost concrete by partial replacement of waste sludge. Int J Chemtech Res. 2016;9(1):240–7.
4. Ferreira V, Labrincha JA, La T. Lime-mud from pulp and paper mills effects in cement based materials. 2011.

© STM Journals 2024. All Rights Reserved

5. Abishek GL. Experimental Study on Behaviour of Paper Sludge Concrete. Iioabj. 2017;8:73–8.
6. Simão L, Jiusti J, Lóh NJ, Hotza D, Raupp-Pereira F, Labrincha JA, et al. Waste-containing clinkers: Valorization of alternative mineral sources from pulp and paper mills. Process Safety and Environmental Protection. 2017;109:106–16.
7. Bajpai P. Generation of Waste in Pulp and Paper Mills. Management of Pulp and Paper Mill Waste. 2015. 9–17 p.
8. Rafique A. Sustainable Use Of Paper Wastes (Hypo Sludge) In Concrete Mix Design. First International Conference on Emerging Trends in Engineering, Management and Scineces. 2014;2014(December).
9. Solanki JV, Pitroda J. Investigation of Low Cost Concrete Using Industrial Waste as Supplementary Cementitious Materials. International Journal of Engineering Science and Innovative Technology (IJESIT). 2013;2(1):81–8.
10. Bullard JW, Jennings HM, Livingston RA, Nonat A, Scherer GW, Schweitzer JS, et al. Mechanisms of cement hydration. Cem Concr Res. 2011;41(12):1208–23.
11. Kumar S, Amit S, Islam MR. Application of Paper Sludge Ash in Construction Industry – a. 2016;(February):978–84.
12. Ochoa de Alda JAG. Feasibility of recycling pulp and paper mill sludge in the paper and board industries. Resour Conserv Recycl. 2008;52(7):965–72.
13. Raut SP, Ralegaonkar R V., Mandavgane SA. Development of sustainable construction material using industrial and agricultural solid waste: A review of waste-create bricks. Constr Build Mater. 2011;25(10):4037–42.
14. Shakir AA, Naganathan S, Mustapha KN. Development Of Bricks From Waste Material : A Review Paper. In 2013.
15. Govind Karada A, Awchat GD. International Journal of Computer Science and Mobile Computing A Review on Partial Replacement of Fine Aggregate by Waste Paper Sludge in Concrete. International Journal of Computer Science and Mobile Computing [Internet]. 2017;6(6):369–76. Available from: www.ijcsmc.com
16. de Azevedo ARG, Alexandre J, Xavier G de C, Pedroti LG. Recycling paper industry effluent sludge for use in mortars: A sustainability perspective. J Clean Prod [Internet]. 2018;192:335–46. Available from: https://doi.org/10.1016/j.jclepro.2018.05.011
17. Simão L, Jiusti J, Lóh NJ, Hotza D, Raupp-Pereira F, Labrincha JA, et al. Waste-containing clinkers: Valorization of alternative mineral sources from pulp and paper mills. Process Safety and Environmental Protection [Internet]. 2017;109:106–16. Available from: http://dx.doi.org/10.1016/j.psep.2017.03.038
18. Pitroda J, Zala LB, Umrigar FS. Durability of concrete with Partial Replacement of Cement by Paper Industry Waste (Hypo Sludge). International Journal of Innovative Technology and Exploring Engineering (IJITEE). 2013;(3):2278–3075.
19. Oliveira KA, Nazário BI, De Oliveira APN, Hotza D, Raupp-Pereira F. Industrial wastes as alternative mineral addition in Portland cement and as aggregate in coating mortars. Materials Research. 2017;20:358–64.
20. Simão L, Jiusti J, Lóh NJ, Hotza D, Raupp-Pereira F, Labrincha JA, et al. Waste-containing clinkers: Valorization of alternative mineral sources from pulp and paper mills. Process Safety and Environmental Protection [Internet]. 2017;109:106–16. Available from: http://dx.doi.org/10.1016/j.psep.2017.03.038
21. de Azevedo ARG, Alexandre J, Pessanha LSP, Manhães R da ST, de Brito J, Marvila MT. Characterizing the paper industry sludge for environmentally-safe disposal. Waste Management [Internet]. 2019;95:43–52. Available from: https://doi.org/10.1016/j.wasman.2019.06.001
22. Sahoo BB, K D, V L, S K G, S K C, B N M, et al. Characterizations of Lime Sludge from Indian Paper Industry: A Step towards Sustainable Growth for Indian Cement Industry. International Journal of Science, Engineering and Management. 2022;9(1):1–5.
23. Sahu V, Gayathri V. The Use of Fly Ash and Lime Sludge as Partial Replacement of Cement in Mortar. International Journal of Engineering and Technology Innovation. 2014;4(1):30–7.

© STM Journals 2024. All Rights Reserved

24. Bajpai P. Generation of Waste in Pulp and Paper Mills. Management of Pulp and Paper Mill Waste. 2015. 9–17 p.
25. Ferreira V, Labrincha JA, La T. Lime-mud from pulp and paper mills effects in cement based materials. 2011.
26. Suriyanarayanan S, Mailappa AS, Jayakumar D, Nanthakumar K, Karthikeyan K, Balasubramanian S. Studies on the characterization and possibilities of reutilization of solid wastes from a waste paper based paper industry. Global Journal of Environmental Research. 2010;4(1):18–22.
27. Dong B, Chen C, Fang G, Wu K, Wang Y. Positive roles of lime mud in blended Portland cement. Constr Build Mater [Internet]. 2022;328(December 2021):127067. Available from: https://doi.org/10.1016/j.conbuildmat.2022.127067
28. Shakir AA, Naganathan S, Mustapha KN. Development Of Bricks From Waste Material : A Review Paper. In 2013.
29. Frías M, Rodríguez O, Sánchez De Rojas MI. Paper sludge, an environmentally sound alternative source of MK-based cementitious materials. A review. Constr Build Mater. 2015;74:37–48.
30. Zhang J, Zheng P, Wang Q. Lime mud from papermaking process as a potential ameliorant for pollutants at ambient conditions: A review. J Clean Prod [Internet]. 2015;103:828–36. Available from: http://dx.doi.org/10.1016/j.jclepro.2014.06.052
31. Raut SP, Ralegaonkar R V., Mandavgane SA. Development of sustainable construction material using industrial and agricultural solid waste: A review of waste-create bricks. Constr Build Mater [Internet]. 2011;25(10):4037–42. Available from: http://dx.doi.org/10.1016/j.conbuildmat.2011.04.038
32. Husillos Rodríguez N, Martínez-Ramírez S, Blanco-Varela MT, Donatello S, Guillem M, Puig J, et al. The effect of using thermally dried sewage sludge as an alternative fuel on Portland cement clinker production. J Clean Prod [Internet]. 2013;52:94–102. Available from: http://dx.doi.org/10.1016/j.jclepro.2013.02.026
33. Maheswaran S, Kalaiselvam S, Saravana Karthikeyan SKS, Kokila C, Palani GS. β-Belite cements (β-dicalcium silicate) obtained from calcined lime sludge and silica fume [Internet]. Vol. 66, Cement and Concrete Composites. Elsevier Ltd; 2016. 57–65 p. Available from: http://dx.doi.org/10.1016/j.cemconcomp.2015.11.008
34. Maheswaran S, Kalaiselvam S, Arunbalaji S, Palani GS, Iyer NR. Low-temperature preparation of belite from lime sludge and nanosilica through solid-state reaction. J Therm Anal Calorim. 2015;119(3):1845–52.
35. Buruberri LH, Seabra MP, Labrincha JA. Preparation of clinker from paper pulp industry wastes. J Hazard Mater [Internet]. 2015;286:252–60. Available from: http://dx.doi.org/10.1016/j.jhazmat.2014.12.053
36. Simão L, Hotza D, Raupp-Pereira F, Labrincha JA, Montedo ORK. Characterization of pulp and paper mill waste for the production of waste-based cement. Revista Internacional de Contaminacion Ambiental. 2019;35(1):237–46.
37. Adesanya E, Ohenoja K, Luukkonen T, Kinnunen P, Illikainen M. One-part geopolymer cement from slag and pretreated paper sludge. J Clean Prod [Internet]. 2018;185:168–75. Available from: https://doi.org/10.1016/j.jclepro.2018.03.007
38. Vashistha P, Moges KA, Pyo S. Alkali activation of paper industry lime mud and assessment of its application in cementless binder. Developments in the Built Environment [Internet]. 2023;14(March):100146. Available from: https://doi.org/10.1016/j.dibe.2023.100146
39. Singh SK, Singh A, Singh B, Vashistha P. Application of thermo-chemically activated lime sludge in production of sustainable low clinker cementitious binders. J Clean Prod [Internet]. 2020;264:121570. Available from: https://doi.org/10.1016/j.jclepro.2020.121570
40. Qin J, Cui C, Cui XY, Hussain A, Yang CM. Preparation and characterization of ceramsite from lime mud and coal fly ash. Constr Build Mater [Internet]. 2015;95:10–7. Available from: http://dx.doi.org/10.1016/j.conbuildmat.2015.07.106
41. Xu W, Xu J, Liu J, Li H, Cao B, Huang X, et al. The utilization of lime-dried sludge as resource for producing cement. J Clean Prod [Internet]. 2014;83:286–93. Available from: http://dx.doi.org/10.1016/j.jclepro.2014.07.070

© STM Journals 2024. All Rights Reserved

42. Elouazzani DC, Bouamrane A, Mansouri K, Fokam C. Valorization of paper mill sludge in construction: Mineralogical analysis of the impact of incineration conditions. Journal of Materials and Environmental Science. 2012 Jan 1;3:628–35.
43. Bouamrane A, Tiruta-Barna L, Mansouri K. Valorization of paper mill sludge as a partial replacement of Portland cement in mortar: The impact of incineration conditions on the strength of mortars. 2014;(May 2016):605–14. Available from: https://www.researchgate.net/publication/286807432
44. de Azevedo ARG, Alexandre J, Xavier G de C, Pedroti LG. Recycling paper industry effluent sludge for use in mortars: A sustainability perspective. J Clean Prod [Internet]. 2018;192:335–46. Available from: https://doi.org/10.1016/j.jclepro.2018.05.011
45. Singh M, Garg M. Reactive pozzolana from Indian clays-their use in cement mortars. Cem Concr Res. 2006;36(10):1903–7.
46. Kumar KA, Rajasekhar K, Sashidhar C. Experimental Investigation on Fly Ash and Lime Sludge in Cement Mortar. Ijltemas. 2016;V(II):47–50.
47. Modolo R, Senff L, Ferreira VM, Labrincha JA, Tarelho LA. Use of Lime-Mud From Pulp Mill Plant in Cement-Mortars. 1St International Conference of Wastes: Solutions, Treatments and Oportunities. 2011;(Lm):1–6.
48. Brás I, Almeida R, Silva PC, Marques L. Industrial Waste Valorization to Produce Eco-materials for Construction Applications. International Journal of Environmental Science and Development. 2016;7(8):559–62.
49. Kumar VVP, Prasad DR. Study on strength and durability characteristics of lime sludge based blended cement concrete. Journal of Building Pathology and Rehabilitation [Internet]. 2019;4(1):1–13. Available from: https://doi.org/10.1007/s41024-018-0041-5
50. Malaiskiene J, Kizinievic O, Kizinievic V, Boris R. The impact of primary sludge from paper industry on the properties of hardened cement paste and mortar. Constr Build Mater [Internet]. 2018;172:553–61. Available from: https://doi.org/10.1016/j.conbuildmat.2018.04.011
51. Malagavelli V. Strength Characteristics of Concrete using Solid Waste an Experimental Investigation Strength Characteristics of Concrete using Solid Waste an Experimental Investigation. 2020;04(September):937–40.
52. Sgobba S, Marano GC, Borsa M, Molfetta M. Use of rubber particles from recycled tires as concrete aggregate for engineering applications. 2nd International Conference on Sustainable Construction Materials and Technologies. 2010;i:465–75.
53. Cordeiro GC, Toledo Filho RD, Tavares LM, Fairbairn EMR. Pozzolanic activity and filler effect of sugar cane bagasse ash in Portland cement and lime mortars. Cem Concr Compos. 2008;30(5):410–8.
54. Martirena F, Favier A, Scrivener K. Calcined Clays for Sustainable Concrete. RILEM Bookseries. 2018.
55. Nithya M, Priya AK, Muthukumaran R, Arunvivek GK. Properties of concrete containing waste foundry sand for partial replacement of fine aggregate in concrete. Indian Journal of Engineering and Materials Sciences. 2017;24(2):162–6.
56. Abishek GL. Experimental Study on Behaviour of Paper Sludge Concrete. Iioabj [Internet]. 2017;8:73–8. Available from: www.iioab.org
57. Joshaghani A, Moeini A, Balapour M. Evaluation of incorporating metakaolin to evaluate durability and mechanical properties of concrete. Advances in Concrete Construction. 2017 Jun 1;5:183–99.
58. Solanki JV, Pitroda J. Investigation of Low Cost Concrete Using Industrial Waste as Supplementary Cementitious Materials. International Journal of Engineering Science and Innovative Technology (IJESIT). 2013;2(1):81–8.
59. Priya AK, Nithya M, Rajeswari M, Priyanka PM, Vanitha R. Experimental investigation on developing low cost concrete by partial replacement of waste sludge. Int J Chemtech Res. 2016;9(1):240–7.
60. Dhananjaya HR. Cost Effective Composite Concrete Using Lime Sludge , Fly Ash and Quarry Sand. 2017;4(1):195–202.

© STM Journals 2024. All Rights Reserved

61. Srinivasan M, Kumar VR, Balasubramaniam B, Palani G, Iyer N. Studies on Lime Sludge for Partial Replacement of Cement. Applied Mechanics and Materials. 2011 Jul 1;71–78.
62. Pitroda JR. Evaluation of Modulus of Elasticity of Concrete with Partial Replacement of Cement by Thermal Industry Waste (Fly Ash) and Paper Industry Waste (Hypo Sludge). Certified International Journal of Engineering Science and Innovative Technology (IJESIT). 2008;9001(1):2319–5967.
63. Maheswaran S, Ramesh Kumar V, Bhuvaneshwari B, Palani GS, Iyer NR. Studies on lime sludge for partial replacement of cement. Applied Mechanics and Materials. 2011;71–78:1015–9.
64. Pitroda J. Assessment of Sorptivity and Water Absorption of Concrete With Partial Replacement of. 2015;(August):1–8.
65. Pitroda J, Zala LB, Umrigar FS. Durability of concrete with Partial Replacement of Cement by Paper Industry Waste (Hypo Sludge). International Journal of Innovative Technology and Exploring Engineering (IJITEE). 2013;(3):2278–3075.
66. Moges KA, Pyo S. Effect of high replacement ratio of lime mud as a filler on mechanical and hydration properties of high-strength mortar. Constr Build Mater [Internet]. 2023;392(May):131974. Available from: https://doi.org/10.1016/j.conbuildmat.2023.131974
67. Sadrmomtazi A, Tahmouresi B, Amooie M. Permeability and mechanical properties of binary and ternary cementitious mixtures. In 2017.
68. Vashistha P, Singh SK, Kumar V. Sustainable Utilization of Paper-Industry Lime Sludge through Development of Metakaolinite-Based Cementitious Binder. Journal of Materials in Civil Engineering. 2021;33(3).
69. Samaras P, Papadimitriou CA, Haritou I, Zouboulis AI. Investigation of sewage sludge stabilization potential by the addition of fly ash and lime. J Hazard Mater. 2008;154(1–3):1052–9.
70. Ganesan K, Rajagopal K, Thangavel K. Rice husk ash blended cement: Assessment of optimal level of replacement for strength and permeability properties of concrete. Constr Build Mater. 2008;22(8):1675–83.
71. Ghrici M, Kenai S, Said-Mansour M. Mechanical properties and durability of mortar and concrete containing natural pozzolana and limestone blended cements. Cem Concr Compos. 2007;29(7):542–9.
72. Rudrawar M, Ghale S. EXPERIMENTAL STUDY OF CONCRETE MADE WITH HYPO SLUDGE AND WOOD ASH: A REVIEW. In 2017.
73. Verma M, Nigam M. Investigation on the Effect of Curing Time on the Mechanical Properties of Geopolymer Concrete. AIP Conf Proc. 2023;2721(1):020031.
74. Verma M, Nigam M. Experimental Investigation on the Properties of Geopolymer Concrete after Replacement of River Sand with the M-Sand. AIP Conf Proc. 2023;2721(1):020029.
75. Verma M, Meena RK, Singh I, Gupta N, Saxena KK, Reddy MM, et al. Investigation on the impact of elevated temperature on sustainable geopolymer composite. Advances in Mechanical Engineering. 2023;15(9):1–16.
76. Verma M, Nigam M. Effect of FRP on the Strength of Geopolymer Concrete. AIP Conf Proc. 2023;2721(1):020030.
77. Sharma U, Gupta N, Bahrami A, Özkılıç YO, Verma M. Behavior of Fibers in Geopolymer Concrete : A Comprehensive Review. Buildings [Internet]. 2024;14(136):1–28. Available from: https://doi.org/10.3390/buildings14010136
78. Kazmi SMS, Abbas S, Saleem MA, Munir MJ, Khitab A. Manufacturing of sustainable clay bricks: Utilization of waste sugarcane bagasse and rice husk ashes. Constr Build Mater [Internet]. 2016;120:29–41. Available from: http://dx.doi.org/10.1016/j.conbuildmat.2016.05.084
79. JAHAGIRDAR SS, SHRIHARI S, MANU B. Reuse of Textile Mill Sludge in Burnt Clay Bricks. International Journal of Advanced Technology in Civil Engineering. 2013;3:43–6.
80. Abbas S, Saleem MA, Kazmi SMS, Munir MJ. Production of sustainable clay bricks using waste fly ash: Mechanical and durability properties. Journal of Building Engineering [Internet]. 2017;14:7–14. Available from: http://dx.doi.org/10.1016/j.jobe.2017.09.008
81. Singh SK, Kulkarni S, Kumar V, Vashistha P. Sustainable utilization of deinking paper mill sludge for the manufacture of building bricks. J Clean Prod [Internet]. 2018;204:321–33. Available from: https://doi.org/10.1016/j.jclepro.2018.09.028

© STM Journals 2024. All Rights Reserved

82. Cultrone G, Rodriguez-Navarro C, Sebastian E, Cazalla O, De La Torre MJ. Carbonate and silicate phase reactions during ceramic firing. European Journal of Mineralogy. 2001;13(3):621–34.
83. IS: 2117. Indian standard guide for manufacture of hand-made common burnt clay building bricks. Indian standards institution, New Delhi, India. 2002;
84. Qin J, Cui C, Cui XY, Hussain A, Yang CM. Preparation and characterization of ceramsite from lime mud and coal fly ash. Constr Build Mater [Internet]. 2015;95:10–7. Available from: http://dx.doi.org/10.1016/j.conbuildmat.2015.07.106
85. Sarkar R, Kurar R, Gupta AK, Mudgal A, Gupta V. Use of paper mill waste for brick making. Cogent Eng [Internet]. 2017;4(1). Available from: http://doi.org/10.1080/23311916.2017.1405768
86. Qin J, Cui C, Cui X, Hussain A, Yang C, Yang S. Recycling of lime mud and fly ash for fabrication of anorthite ceramic at low sintering temperature. Ceram Int [Internet]. 2015;41(4):5648–55. Available from: http://dx.doi.org/10.1016/j.ceramint.2014.12.149
87. Munir MJ, Kazmi SMS, Wu YF, Hanif A, Khan MUA. Thermally efficient fired clay bricks incorporating waste marble sludge: An industrial-scale study. J Clean Prod. 2018;174:1122–35.
88. Kazi TG, Jamali MK, Kazi GH, Arain MB, Afridi HI, Siddiqui A. Evaluating the mobility of toxic metals in untreated industrial wastewater sludge using a BCR sequential extraction procedure and a leaching test. Anal Bioanal Chem. 2005;383(2):297–304.
89. Kuokkanen T, Nurmesniemi H, Pöykiö R, Kujala K, Kaakinen J, Kuokkanen M. Chemical and leaching properties of paper mill sludge. Chemical Speciation and Bioavailability. 2008;20(2):111–22.

© STM Journals 2024. All Rights Reserved

View publication stats

ResearchGate

See discussions, stats, and author profiles for this publication at: https://www.researchgate.net/publication/385655140

Artificial intelligence in the workplace -challenges, opportunities and HRM framework: a critical review and research agenda for change

Article *in* Journal of Managerial Psychology · November 2024

DOI: 10.1108/JMP-05-2024-0388

CITATIONS
0

READS
30

3 authors:

John Mendy
University of Lincoln
172 PUBLICATIONS **882** CITATIONS
SEE PROFILE

Apoorva Jain
Vivekananda Institute Of Professional Studies
1 PUBLICATION **0** CITATIONS
SEE PROFILE

Asha Thomas
Wroclaw University of Science and Technology
36 PUBLICATIONS **1,561** CITATIONS
SEE PROFILE

All content following this page was uploaded by John Mendy on 08 November 2024.

The user has requested enhancement of the downloaded file.

The current issue and full text archive of this journal is available on Emerald Insight at:
https://www.emerald.com/insight/0268-3946.htm

Journal of Managerial Psychology

Artificial intelligence in the workplace – challenges, opportunities and HRM framework: a critical review and research agenda for change

John Mendy
Department of People, Leadership, Organisations and Management, Lincoln International Business School, University of Lincoln, Lincoln, UK
Apoorva Jain
Vivekananda School of Business Studies, Vivekananda Institute of Professional Studies, New Delhi, India, and
Asha Thomas
Department of Operations Research and Business Intelligence, Faculty of Management, Wrocław University of Science and Technology, Wrocław, Poland

Received 30 May 2024
Revised 19 September 2024
Accepted 6 October 2024

Abstract

Purpose – This paper specifically aims to examine how (via which activities, methods and capabilities) organizations' management deploy Artificial Intelligence (AI) systems to address underperformance. Five mitigation strategies/recommendations are introduced to manage the challenges and facilitate greater efficacies in changing organizations.

Design/methodology/approach – This paper conceptually synthesizes 47 articles, thematically reports and critically analyzes the AI–HRM–managerial decision-making relationship in changing organizations and discusses the impacts.

Findings – The results highlight three significant challenges and opportunities for changing organizations: (1) job performance challenges, (2) organizational performance challenges and HR and (3) collaborative intelligence opportunities.

Originality/value – The paper's originality lies in addressing the current lack of a theoretical framework guiding HRM and AI experts on the managerial and strategic capabilities needed to address underperformance and their impacts in facilitating collective efficacies in human–AI collaboration in changing organizations. By further capturing an innovative HR Framework's (1) human, (2) AI, (3) employees' well-being, (4) jobs and (5) organizational performance, and its five key managerial recommendations/strategies, this paper develops two concepts: "technological servitization" and "re-ontological in-securitization" to advance theory in Managerial Psychology regarding the unintended/paradoxical consequences of managements' AI-driven organizational performance interventions, including meaninglessness in organizations.

Keywords AI, Challenges, Opportunities, Capabilities, Change, Literature review, Framework

Paper type Conceptual paper

1. Introduction

Artificial Intelligence (AI) is an increasingly significant topic, with great potential to transform organizations (Zuboff, 1991, 2023) and resolve the chronic underperformance problem faced by individuals, teams and organizations (Mendy and Rahman, 2019; Peter *et al*., 2020). While AI tools and systems (e.g. robotics, algorithms, machine learning, etc.) have the potential to boost organizational competitiveness (He *et al*., 2024), the current predominant focus in AI–HRM scholarship is on resolving organizational-level underperformance (Wennberg *et al*., 2011). Despite management resorting to the use of more creative/advanced AI tools in the hope that a more efficacious use of resources (human and material) will increase human capabilities development and thereby resolve organizational underperformance (Andrieux *et al*., 2024; Baporikar and Shikokola, 2020), the scholarship remains polarized and management's capacities to tackle underperformance and complexly engrained organizational

Journal of Managerial Psychology
© Emerald Publishing Limited
0268-3946
DOI 10.1108/JMP-05-2024-0388

cultural issues remain unresolved (Simpson *et al.*, 2022). Research on whether to initiate organizational strategies (Narver *et al.*, 2000), HRM team-based practices (Singh *et al.*, 2017) or develop technical-structural-human configuration frameworks to boost organizations' higher performance (Guest, 2011; Kalleberg *et al.*, 2006) remains inconclusive. Consequently, such inconclusiveness in current studies has highlighted key aspects in the AI–HRM literature, including, but not restricted to, managements' in-effective resource reorganization (Pavlov *et al.*, 2017; Katzenbach and Smith, 2015), the paradoxical, unintended and non-homogenous adverse consequences of AI deployment on people, jobs and, overall, collective performance. We also do not know whether adopting a more multi-level framework (Prikshat *et al.*, 2023) as opposed to the ongoing management-centric and homogenous focus on the positive aspects of AI–HRM (Pereira *et al.*, 2023) will ultimately provide the panacea to employee, team-level and/or firm-level underperformance (Arslan *et al.*, 2022).

While generative AI (Gen AI – henceforth AI) tools such as ChatGPT, Google's PaLM (including audio, text, video and images) have highlighted the importance of management's increased influence particularly via automation or "informating" (Zuboff, 1991) of business operations, the purported revolutionization of work processes and management actions' impacts on employee and organizational (collective) level underperformance continues unresolved (Banal-Estañol and Seldeslachts, 2011; Sverdrup and Stensaker, 2014). Additionally, while the emerging literature has highlighted the need for humanizing AI use (Manresa *et al.*, 2023; Marimon *et al.*, 2024) via management's greater ethical engagement with staff (Wijayati *et al.*, 2022), the anticipated increase in job engagement has not been materially transformed into organizational-level performance effectively (He *et al.*, 2024). Therefore, underperformance remains a significant problem at multiple organizational levels (Aguinis *et al.*, 2024; Wamba *et al.*, 2023). This is partly noticeable especially in the streamlining of business processes and tasks (Wijayati *et al.*, 2022; Shaikh *et al.*, 2023), as well as in the overall impact of such measures on attempts to reorganize business efficacy (e.g. toward change readiness, cultural reorientation and greater firm security and individual and collective teams' skills' orientations – Zuboff, 2023; Suseno *et al.*, 2022).

Additionally, there is a paradoxical unintended set of consequences/impacts referred to in this study as homogenous vs non-homogenous aspects when management adopts AI-driven tools to resolve underperformance at various individual, team and organizational levels (Nazareno and Schiff, 2021). The unattended focus on the multi-dimensional and complex nature of the underperformance problem in AI–HRM discourse has partly led to its under theorization (Wamba *et al.*, 2023). This has consequently produced this paper's aim: to systematically explore, systematize and insightfully critique the scientific knowledge on AI opportunities (the homogenous aspects/capabilities) and challenges (the non-homogenous elements) posed to address multi-level individual, team and organizational underperformance (Bankins *et al.*, 2024; Aguinis *et al.*, 2024) and the development of two novel concepts: (1) "technological servitization" and (2) "re-ontological in-securitization" to advance Managerial Psychology theorizing in this fundamental field. Therefore, the rationale (justification) for this present study is to go beyond the current, siloed approach to addressing individual and/or organizational and/or team performance (Muridzi *et al.*, 2024; Abulsaoud Ahmed Younis and Adel, 2020) by (1) undertaking a systematic literature review on AI–HRM and the impacts of such technological deployment on employee, team and organizational-level's effective performance; (2) highlighting challenges (non-homogenous) and opportunities (homogenous aspects) at multi-dimensional levels and (3) outlining future research directions to help advance both theoretical and practical knowledge and understanding on the impacts of managements' AI-driven interventions in changing organizations.

To this end, the study systematically reviews 47 research articles published in the past 5 years (2020–2024) and through Paul and Criado's (2020) thematic analysis procedure surfaces three major themes. These broadly highlight challenges (referred to as non-homogenous aspects) and opportunities (homogenous aspects) faced by management when implementing AI measures in changing organizations, namely: (1) job performance challenges; (2) organizational

productivity challenges and HR and (3) collaborative intelligence opportunity. We advance Managerial Psychology and AI theorizing (Carvalho *et al*., 2022; Suseno *et al*., 2022) by highlighting the nature, scale, complexity and contingencies of the multi-dimensional aspects and their impacts (Aguinis *et al*., 2024; Budhwar *et al*., 2024) on individual, team and organizational level performance in changing organizations (Wamba *et al*., 2023). We also examine the range of HR-related activities to highlight the impacts of managerial actions on people's job satisfaction, on management–individual–team-level collaborations, and on the ethicality of HR-related activities taken to remedy underperformance, namely recruitment and governance (He *et al*., 2024). We also develop two novel concepts to further advance Managerial Psychology theory in this increasingly evolving field.

Structurally, this paper proceeds with an explication of the systematic steps used for the review, including (1) a PRISMA article selection procedure and (2) a systematic organization, analysis and synthesis of the thematic categorizations following Paul and Criado's (2020) frame. The implications of our theoretical contributions of (1) HRM Framework, (2) "technological servitization" and (3) "re-ontological in-securitization" are discussed (1) theoretically, (2) practically/functionally and (3) contextually. Future research directions are charted.

2. Methodology

We conducted a systematic literature review on contemporaneous and emerging research findings on AI–HRM, and the impact of managements' role on jobs and organizational performance (Wamba *et al*., 2023). The study adopted Paul and Criado's (2020) seminal procedure highlighting two sequential steps to ascertain the thematic categories of this study and to help highlight managements' impacts at multiple (complex) levels of individual, organizational and team levels of performance. We did so by (1) systemically and systematically reviewing the literature in these areas and (2) providing the state-of-the-art advancements on the extent of the homogenous (opportunities) and non-homogenous (challenging and divergent) impacts of managements' activities in AI deployment in contemporary changing organizations. The reviewing part relates to the article selection process through PRISMA while the more complex procedure focuses on progressing/advancing theory and knowledge on both the traditionally dominant homogenous aspects and the lagging non-homogenous aspects of how management's actions in AI deployment sought to tackle underperformance at multiple levels. Key aspects of the second stage include systematically organizing, critically analyzing and synthesizing findings from the literature to produce three key results on multi-level (individual, organizational and team) challenges and opportunities as the foundation for the development of two new concepts for Managerial Psychology, Human Resource, AI and Change Management research.

2.1 Article selection procedure

Systematic article selection is conducted using the PRISMA (Preferred Reporting Items for Systematic Reviews and Meta-Analysis) guidelines (Moher *et al*., 2009), as recommended in the Social and Natural Sciences, including Managerial Psychology (Shahid and Alarifi, 2021; Thukral and Jain, 2021; Carvalho *et al*., 2022 – see PRISMA flow diagram in Figure 1). The *Identification* stage included the selection of a combination of keywords and the search in the Web of Science (WOS) database (Paul and Criado, 2020; Alayo *et al*., 2021). Given its high quality for article selection, our WOS database search yielded 434 research articles. We proceeded with the *Screening* stage, in which we examined article abstracts, titles and keywords. In total, 199 relevant articles were originally obtained from the AI field (11 were subsequently added after the first round of reviews). We then text-screened the remaining articles in the next stage: *Eligibility*. 111 research articles were eliminated based on their lack of relevance/appropriateness to AI and managements' impacts. We finally identified 47 published articles in total in a 5-year period at the last *Included* stage (see Figure 1).

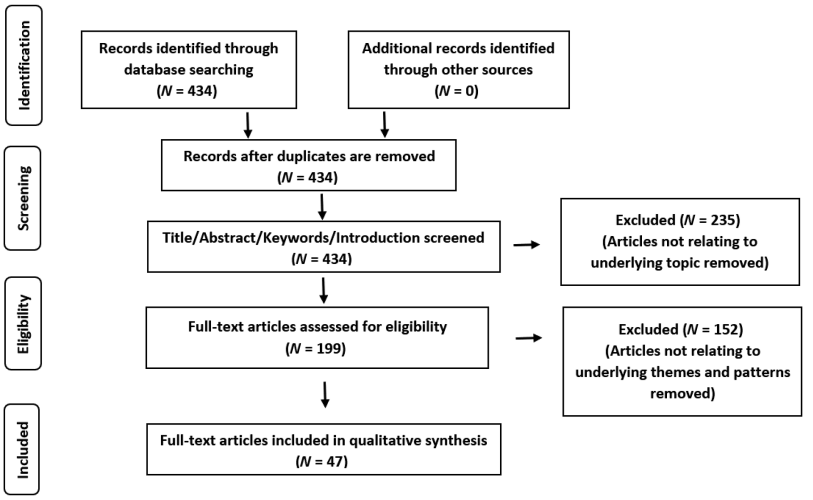

Source(s): Authors' own creation

Figure 1. Research data collection following PRISMA guidelines

2.1.1 Inclusion criteria. To ascertain which articles should be included in the analysis of the range of complexities and contingencies in AI–HRM and underperforming individuals, teams and organizations, we adopted the following WOS criteria:

(1) The researchers' search for the combination of keywords in the "*Topic*" which includes title, abstract, author keywords and keywords plus. The following keywords' combinations were searched – ("Artificial Intelligence" OR "AI" OR "Generative Artificial Intelligence" OR "Generative AI" OR "Chat GPT") AND ("Workforce Productivity" OR "Employee Productivity" OR "Workforce Performance" OR "Employee Performance" OR "Human Resource Management").

(2) Article searches in the following four WOS Index – Social Science Citation Index (SSCI), Science Citation Index Expanded (SCI-E), Emerging Sources Citation Index (ESCI) and Arts and Humanities Citation Index (A&HCI) given their popularity in Management and the Social Sciences in general.

(3) Article searches included: Management, Business, Industrial Relations Labour, Social Science Interdisciplinary, Business Finance, Ethics and Computer Science Information Systems.

(4) Time period criterion was kept open-ended to enhance a high yield of AI articles covering a substantial period (5 years emerged for this study).

(5) Articles published only in the English language and

(6) Exclusion of non-AI–HRM and performance-related articles.

2.2 Thematic analysis procedure

To ascertain managements' role in AI deployment and impacts on people's and organizational underperformance and to progress knowledge in Management, including Managerial Psychology, we conducted an in-depth review of publications and additionally provided a summary chart to highlight how we critically analyzed the core arguments and made novel propositions. First, we carried out a thematic analysis using the famous classification method

(Paul and Criado, 2020). Second, we organized the ideas by adopting homogeneity (i.e. converging all the homogenous factors) to demonstrate opportunities arising from managements' AI deployment. Our analysis went a step further. Third, we organized the emerging ideas from a non-homogenous (divergent) perspective to highlight the factors/ideas showing challenges for AI–HRM. The three procedures produced three critically emerging themes: (1) job performance challenges; (2) organizational performance challenges and HR and (3) collaborative intelligence opportunities. These themes fitted two categorizations: "non-homogenous" (i.e. divergent from current AI–HRM logics) for the challenges and "homogenous" (i.e. convergent with current AI–HRM narratives) for the opportunities. We present and critically discuss these next and demonstrate three key propositions that help in advancing theory, enriching the understanding and practice of Managerial Psychology, AI and HRM. These are (1) HR Framework, (2) "technological servitization" and (3) "re-ontological in-securitization."

3. Results

This section presents a clear, accurate and appropriate account of the literature review results in terms of the non-homogenous (challenges) and homogenous (opportunities) aspects of managements' AI deployment. By showcasing the impacts, complexities and contingencies of AI–HRM at organizational, team-level and/or individual levels of underperformance, this study extends knowledge and understanding of the theoretical, managerial and practical aspects in each of the three ensuing areas and their two ensuing affiliated implications. The homogenous and non-homogenous categories of AI–HRM are then combined to develop a novel HRM Framework with its complex aspects highlighting what is needed by Managerial Psychologists, HRM and AI experts to resolve the ongoing organizational underperformance crisis.

3.1 Non-homogenous impacts: job performance challenges

The use of AI in organizations has increased dramatically over the years in different sectors globally (Bankins *et al.*, 2024; Madancian and Taherdoost, 2023). The literature highlights how managements deploy AI as a game changer to resolve employee job performance (Chukwuka and Dibie, 2024), job-engagementand expertise challenges (Wamba *et al*., 2023). Although the current dominant logic is that managerial-level intervention has had positive impacts on employee performance and led to the acquisition of new, updated skills, job engagement (Manresa *et al.*, 2023; Shaikh *et al*., 2023), these tend to focus on employee-level service quality delivery and the collection, dissemination and communication of reliable, accurate and prompt customer service (Prentice *et al*. (2023). However, organizational underperformance (Wamba *et al*., 2023) and the capturing of the more complex human capabilities needed for adaptation to change (Suseno *et al*., 2022) remain inconclusive. This study's framework helps in resolving this complexity.

Wang *et al*. (2023), among others (Arslan *et al*., 2022), had attempted to address this problem by observing the way new generation employees' ease-of-use impact online networking technologies. While they highlighted how AI has become a social media marketing and customer satisfaction tool, thereby adding to the current positive portrayal of AI deployment on performance, the negative impact on employees' sense of team and job responsibility and a feeling of being "surveillanced" (Zuboff, 2023) by robots/gadgets have been surfaced such that the positive aspects are downplayed. This emerging stream of literature elucidates the (un)ethicality of HR's existence at work and questions around how artificially intelligent robots could replace people (Ho and Kuvaas, 2020). The fuelling of a longer hours' working culture in contemporary organizations whereby individuals', teams and the collective's professional well-being has also come under scrutiny as management's use of AI to streamline and optimize large amounts of business information at lower costs has come

to the fore (Wijayati *et al*., 2022). Such activities have engendered counter impacts such as the reduction of long-term relationships between employees and machines, and the duty of care between team members and their propensity to boost organizational-level performance (Suseno *et al*., 2023; Wang *et al*., 2023). While such a lag could signal a lack of good managerial oversight of change (He *et al*., 2024; Zhao *et al*., 2023), more recent claims that employees could be replaced in more efficient ways (Budhwar *et al*., 2023), highlight not only the multi-dimensional factors needed to be synergized in AI–HRM to facilitate effective change (e.g. structural, financial, market and entrepreneurial – Mendy and Rahman, 2019) but to do so in a way that addresses the contingencies of deploying such interventions as staff fight to save their jobs, as individual and team level competition render some human competences more valuable than others, and as employees try to outperform others within increasingly performance-metrics-driven workplace environments (Aguinis *et al*., 2024). Therefore, the positive impacts of AI–HRM activities on underperformance also have adverse impacts on staffs and managements' mental, psychological and emotional well-being (e.g. job related stress, dissatisfaction and anxiety – Nazareno and Schiff, 2021), disengagement from training opportunities that HR may initiate (Suseno *et al*., 2022), job in-securitization and a "surveillanced," uncertain future (Zuboff, 2023) have led to our consideration of this study's additional complexities and contingencies within AI–HRM and its additional non-homogenous impacts at other levels.

3.2 Non-homogenous impacts: organizational performance challenges and HR

Managements' attempts at transforming business organizations via AI include operational workflow streamlining, enhancing staff–customer interactions and redesigning how HR utilizes resources (Halid *et al*., 2024; Chukwuka and Dibie, 2024). Such new ways of resource utilization have purportedly enhanced employer-level reputation and enhanced new organizational change processes (also Singh *et al*., 2017; Ates *et al*., 2013; Trocin *et al*., 2021 despite Kot *et al*., 2021; Singh *et al*., 2017; Ates *et al*., 2013; Trocin *et al*., 2021). These AI benefits on HR's operational capabilities, including the reduction in biases in data analysis have also partly warranted Floridi's (2010) proposition for additional managerial capabilities (also Hayes, 2022; Peter *et al*., 2020) to address market fluctuations that management-level interventions had not earlier been resourcefully aligned to. While Floridi's introduction of management "reontologizing" highlights the need for enhanced decision-making capabilities at the organizational leadership level, it also signals the hidden complexities involved when AI is being utilized to facilitate change in organizations. "Reontologizing" has been conceptualized as a radical change in organizations' structures, designs and entire systems to help address the apparent elusiveness of achieving higher levels of performance at individual, team and organizational levels (Guest, 2011). Yet, the recommended mechanisms such as performance appraisals and (re)training and development (Katzenbach and Smith, 2015) have served to reorientate organizational-level survival in some South Asian contexts with acquiescing firm cultures (Kshetri, 2021; Sithambaram and Tajudeen, 2023) but their application has raised concerns of unethical (non-homogenous) conduct in how employee-level data are utilized and the general well-being of staff is compromised (Aguinis *et al*., 2024).

To resolve such an AI–HR – underperformance conundrum, Rodgers *et al*. (2023) developed a throughput model to analyze managements' decision-making processes using algorithmic HRM. While new strategy development during change seems to offer a way out for HR, managements' short-term gains, the desire for tangible results (including Kulkov, 2021) from deploying Internet of Things and cloud computing in recruitment processes has inadvertently ushered additional layers of complexities in AI–HRM. This includes the tendency to sidestep others' priorities/needs for selfish, individualistic goals' achievement (He *et al*., 2024) and organizational-level cost-saving mechanisms dampening collective and team-level performance outcomes (also see Malik *et al*., 2022).

The set of organizational performance challenges are therefore not only complex in the nature and dynamics within which management, staff (humans) and non-human aspects at

work (e.g. bots) relate with each other (Wang *et al*., 2020) but also how managements' impacts on relationships and resource utilization during change provides contingency measures that may alleviate the complex levels of underperformance but may also hinder them. While their study of enterprises in Eastern and Southern China highlights the importance of developing a Human Resources Client Relationship Management (HR–CRM) framework was anticipated to positively impact on the sustainability of organizational-level performance, implementing such an idea via strategic HR practices, change and sustainability has been problematic at the combined individual, team and organizational levels as multiple values, autonomies, effort expectations and HR professionals' adaptations and capabilities in different situations come under scrutiny (Tanantong and Wongras, 2024). To see what could be added to this increasing set of complexities and contingencies in AI–HRM, we examine our third finding, which now focuses on the homogenous aspects of the current topic.

3.3 Homogenous impacts: collaborative intelligence opportunity: AI–humans

Our third thematic category: "collaborative intelligence" highlights a convergence of various complex AI streams such as emotional intelligence and human judgment. Defined as complementarity between human and AI decision-making capabilities (He *et al*., 2024; Abbas *et al*., 2023), the concept highlights a fundamentally new shift (change) that combines two concepts from AI–HRM: human reasoning and machine processing. Although seen as a potential resolution of the organizational underperformance problem (Wamba *et al*., 2023) and a harmonization of the strengths of *both* human (management and employee level) intelligence and AI systems (Aguinis *et al*., 2024; Arslan *et al*., 2022; Sutherland *et al*., 2020), such a novel concept does not address the social intelligence dimension of change (i.e. the ability to comprehend and respond to one's own behaviors, feelings and emotions in relation to those of others and in the midst of non-homogeneity). Although Song and Wu attempted to highlight the extent to which human behaviors may converge within their HRM–AI model using 251 responses from Spain, they did not examine additional factors beyond managerial engagement, attitudes and trust. Given the wider social dimensions that could influence collaboration and performance (e.g. the ability to self-regulate and self-motivate), such elements may mitigate against the adverse implications of managements' AI deployment (e.g. human–AI distrust, lack of due care and emotional disengagement with change) and therefore provide a welcome panacea for organizational-level underperformance. While Abbas *et al*. (2023) noted the benefits of social intelligence as a crucial moderator in enhancing team-level relations (Prentice *et al*., 2020), our third finding denotes something special: the importance of management and staff's abilities to augment their analytic reasoning and intuitive thinking when the ethical, moral, employment security threats and technology "surveillance" in AI–HRM (i.e. the non-homogenous elements) present themselves (Zuboff, 2023). We also include this aspect not only as a new theorization in AI–HRM but also as an extension of the dominant managerial and technological capabilities required at management, team and organizational levels when management attempts to address organization-wide underperformance via AI tools.

Homogenous impacts have been observed to have greater effects on resolving organizational-level underperformance when socio-technical synergies between AI and HRM professionals are harnessed via research and development (Venumuddala and Kamath, 2023; Peter *et al*., 2020). However, while this may have the potential to re-shape the way jobs are performed and mitigate against AI deployment costs, such benefits are questionable in roles involving data engineering, remote and distributed work where trust could be an issue. We suggest the inclusion of culture-sensitive utilization of language particularly at team level as a new set of strategic capabilities in resolving team, organizational- and individual-level underperformance in the context of implementing AI in changing organizations and society. We identify a more detailed set of mechanisms for tackling multi-level underperformance and their implications for AI–HRM theory and practice next.

3.3.1 AI as a symbol of job performance optimization. One context in which AI–human collaboration is increasingly providing significant opportunities is in customer service organizations (Venumuddala and Kamath, 2023). While the literature has reported an increase in employee skills, greater levels of employee engagement and better job performances in this sector (Wang *et al*., 2023; Libert *et al*., 2020), the misuse of AI systems and lower service delivery quality at organizational and team levels jeopardize such performance optimization claims (Prentice *et al*., 2023). Recent suggestions for the adoption of more strategic digital advertisement mechanisms in marketing and education, for example, El Hana *et al*. have not fully tackled the wider organizational level underperformance concerns. To advance the scholarship in Managerial Psychology, we propose "contextual opportunity," which recognizes the complex (non-homogenous) challenges and contingencies of tackling chronic underperformance simultaneously at multiple individual, team *and* organizational levels using AI–HRM systems. Within our proposition, we highlight the identification and use of innovative capabilities at management, staff and organizational operational levels to enhance firm, team and employee-level readiness-for-change in more effective ways that earlier suggested by Suseno *et al*. (2022), among others.

Kohtamäki *et al*. (2020) and Hsuan *et al*. (2021) earlier noted the potential in-securitization of staff data and the servitization of people as digitalization mechanisms take hold in firm-level performance. We argue for greater recognition and inclusion within emerging AI–HRM debates of the enhancement of organizational and employee-level engagement, and the value and creativity they bring as counter measures against HRM's unrestricted, unregulated use of large amounts of people's personal data/information and AI's tendency to provide management with such unrestricted "surveillance" (Zuboff, 2023). Adding to such calls in the literature is how greater product market competition and additional structural, human, technological and social complexities of change have exacerbated the individual, team and organizational-level underperformance problem around AI–HRM (Chowdhury *et al*., 2024; Budhwar *et al*., 2024; Watson *et al*., 2020). The extent to which these complexities and contingencies around underperformance have been resolved via the traditional adoption of HRM plans and AI systems remains problematic (see Singh *et al*., 2017). It is to this unresolved issue that we turn our attention to see how best we can help advance Managerial Psychology theorizing. We propose our second concept: "technological servitization" (the use of AI-driven technologies as tools for the optimization of performance while paradoxically recognizing its potential for employee servitude if applied unrestrictedly to boost multi-level performances).

3.3.2 AI as a symbol of functional utility (and propensity to functional stupidity): recruitment. The use of one of such tools includes AI-enabled Video Interviews (AIVs) in recruitment. While HR professionals may see the need to boost employees' skillsets within pressurized market environments and other management-level staff may resort to conventional CV screenings via AIV methods to enhance their selection of candidates for high-performing and diverse teams, Olajide and Sposato's (2022) findings demonstrate how AI tools have significantly increased prejudices at organizational and team levels. These have had the unintended consequence of hampering management-level decision-making in selection processes and in the training and development of staff for key performance roles.

Hofeditz *et al*.'s (2022) study, which observed 194 participants/candidates being selected via an AI custom online platform found a greater tendency to select older and female candidates. While this may suggest the racial profiling of such candidates, it also shows the complexities involved when technological tools are deployed to resolve the inadequacies within human judgment unguardedly. We advance Managerial Psychology theorizing by proposing the inclusion of the notion of paradoxicality in the homogenous aspects of AI–HRM's functional utilitarianism (i.e. the positive functional impacts of AI deployment in the hiring of high individual and team performers) and the non-homogenous functional stupidity of such applications and understandings (the unintended adverse managerial impacts of utilizing AI without due emotional, social and cultural intelligence and care of individuals

within teams). The recent theoretical advancements made by Explainable AI (XAI – Guidotti *et al*., 2018; Miller, 2019) as a notion that helps us to understand management's cognitive processes/logics in AI–HRM and the complexities of dealing with the homogenous and non-homogenous intricacies of AI–HRM decision-making processes involved in individual and team selection have not deepened our knowledge and understanding of how HR professionals' decision-making capabilities could positively augment individual- and team-level engagement and organizational-level performance. To advance theorizing, knowledge and understanding in this field, we propose an additional extension for AI–HRM and underperformance, which is an HRM framework consisting of a comprehensive set of aspects, mediating variables and recommendations to help address the complexities and contingencies of individual, organizational and team levels of underperformance. To date, something of this nature and scale has not existed in Managerial Psychology.

3.3.3 HRM framework. The afore thematic analysis highlighting the homogenous and non-homogenous complexities of AI–HRM has been used to create this study's additional contribution, which is an HRM framework. Its multi-dimensional aspects highlight the human (employee, management), non-human (AI, HR processual and procedural) and mediating aspects showing the complexities and nuances of managing individual, team and organizational performance. These serve as theoretical extensions in the form of two novel concepts for Managerial Psychology and HRM, which are (1) "technological servitization" and (2) "re-ontological in-securitization." These help in deepening understanding and knowledge of the scale, nature and complexities of tackling underperformance and ways of resolving them at individual, organizational and team levels (see Figure 2).

3.3.4 Recommendation 1: job performance via human intelligence. The first aspect of our framework focuses on the use of AI methods ranging from data mining to data extraction in hiring and training and development (Baporikar and Shikokola, 2020; Malik *et al*., 2021) to address jobs-in-securitization and human–machine mistrust (Dwivedi *et al*., 2023) with devastating personal consequences on employees' job engagement (Marimon *et al*., 2024) and managements' psychological propensity to manage individuals' employees' job demands and

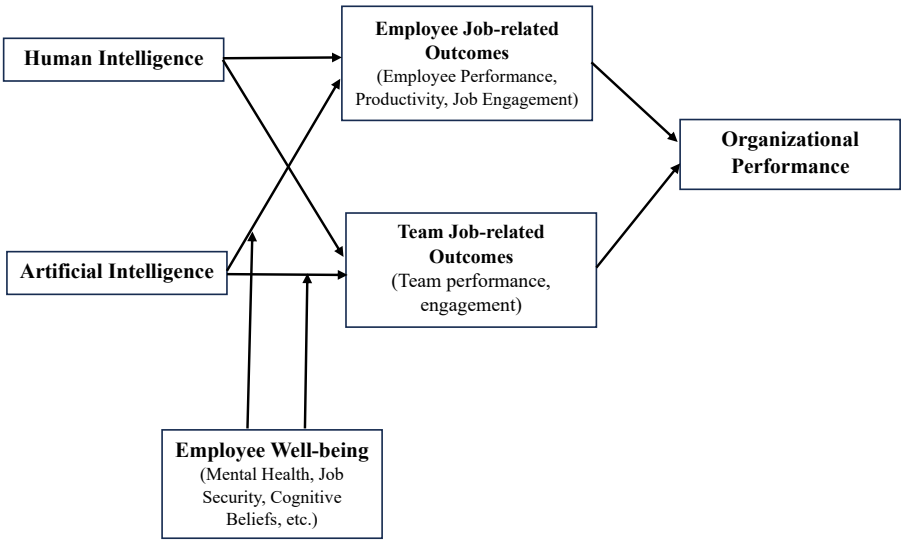

Source(s): Authors' own creation

Figure 2. HRM framework

engagement (Marimon *et al*., 2024), performance and well-being (Nazareno and Schiff, 2021). We therefore recommend that HR professionals should be adequately trained in identifying bias and stress-inducing AI activities from the homogenous AI–HRM sets of activities such as recruitment, performance evaluations, remuneration and career progression and helping to minimize these.

3.3.5 Recommendation 2: organizational performance via AI intelligence support. The second aspect highlights how challenges faced in operational workflows are framed around the streamlining of workplace – external interactions and the redesigning of resources (Chukwuka and Dibie, 2024). While Floridi captures such organizational-level AI–HRM restructuring as "reontologization" (2010) and Rodgers *et al*. (2023) conceptualizes it as decision-making algorithmic HRM at a cognitive level of adaptation (Tanantong and Wongras, 2024), such efficiency systems (Kar *et al*., 2023) continue to pose problems on employee-level engagement and performance. We therefore conceptualize and recommend that management develop not only technological (ontological) know-how (Ivanov and Webster, 2019) but also the non-technological (non-homogenous) "know-what" and "know-when" to address individual and team level in-securitization in the context of change.

3.3.6 Recommendation 3: employees' job satisfaction via job securitization. AI–HRM combination is currently framed as *the* panacea of organizational underperformance (Sampson *et al*., 2020; Peter *et al*., 2020; Bitkina *et al*., 2020), particularly when implemented strategically (He *et al*., 2024; Abbas *et al*., 2023). However, such theoretical framing also denotes a paucity in how jobs are performed and employees derive satisfaction from their performance. This is partly explicable in Glickson and Woolley's (2020) and Webster and Ivanov's (2020) relational mistrust and employees' job displacement and replacement idea. To resolve this theorization deficit, we propose a reframing, which includes a mix of qualitative, quantitative and empathetic evaluation capabilities to optimize employees' satisfaction at work (e.g. creating a culture of trust, developing congenial machine – people working strategies, etc.). Doing so will help theoretically enrich and help current thinking in HR and Managerial Psychology on which critical bits of the non-homogenous parts of individual job-related underperformance should be addressed.

3.3.7 Recommendation 4: collective performance via ethical resource utilization. Current AI–HRM debates are increasingly being framed around ethical concerns about how staff and technological systems are managed (Aguinis *et al*., 2024; Dwivedi *et al*., 2023). This has particularly come to the fore amidst increasing attention to cost and efficiency-based arguments and the need for organizations' management to demonstrate returns-on-investments on AI performance-driven tools (Malik *et al*., 2022) and standardized operational systems. Such framing also highlights a paucity of more complex forms of theorizing. To advance theory in Managerial Psychology, we propose a more integrated framing that considers the collective performance of individuals, firms and teams in a more ethical and culturally sensitive adoption and adaptation of homogenous and non-homogenous components of AI–HRM.

3.3.8 Recommendation 5: readiness-for-change via employee well-being programs. While the academic attention on employees' mental and psychological well-being in the context of AI systems' deployment and changing organizations is currently framed around resource optimization, profit and cost (Malik *et al*., 2022), the extent to which employee level readiness for change and HR professionals' role in this is lagging (Wamba *et al*., 2023). The additional theoretical paucity is reflected in how employees' fear, frustration and anxiety of job losses have been patchily addressed (Suseno *et al*., 2022; Ivanov and Webster, 2019) despite repeated calls (Aguinis *et al*., 2024; Budhwar *et al*., 2024) to do so via appropriate use of communication (Sampson *et al*., 2020). While this may not necessarily resolve job losses (Suseno *et al*., 2022), a more collective conceptualization of what it takes to be collectively ready for change within an AI–HRM changing organizational context constitutes our framework's fifth aspect/dimension.

4. Discussions and implications

We discuss the framework's implications for HRM in general and Managerial Psychology in particular and introduce two novel concepts that help in advancing theory in these fields: (1) "technological servitization" and (2) "re-ontological in-securitization."

4.1 Framework's theoretical legitimacy

Theoretically, "technological servitization" (see Vendrell-Herrero *et al.*, 2017; Kohtamäki *et al.*, 2020) or servitization via digitalization) alludes here to the systematic and systemic utilization of AI systems within organizations' structures, work processes and procedures rendering employees less autonomous. While such a form of organizing and managing is associated with large-scale organizational change (e.g. AI introduction at work – Klumpp and Ruiner, 2022) based on its promises of effective and efficient task functioning (Puhovichova and Jankelova, 2020), it is also increasingly being interpreted as a mechanism of managerial control and monitoring of workers' performance (Wamba *et al.*, 2023; Budhwar *et al.*, 2024). This perception/interpretation sparks a sense of irrationality (purposelessness) and paradoxicality (irony) – i.e. the originally intended purpose of performance optimization is unachieved because of the standardization processes used which eventually render employees as "serfs" to AI systems. In such a context, the technical and functional opportunities/benefits of AI (i.e. hiring and performance optimization - Dwivedi *et al.*, 2023) are lost while meaningful functionality is gradually replaced by a sense of missed opportunities and management – staff – technological systems disconnect/non-alignment.

This paper's HRM framework highlights multi-dimensional aspects regarding the range of human and non-human conceptualizations of the homogenous and non-homogenous opportunities, difficulties and resolution mechanisms. By extrapolating literature from AI, HRM and Managerial Psychology and individual-, organizational- and team-level interventions in managing underperformance, the multiple perspectives highlight the current state of play on how technological initiatives are either helping or hindering organizational change processes in different settings. By adopting a more multi-dimensional/perspective outlook to AI–HRM instead of focusing solely on a homogenous or non-homogenous perspective or a technological or competence-based approach, our paper has shown the utilitarian value of the AI – HRM interface, and how its cost-efficiency, market competitiveness and individual, team and organizational performance-centric logics can be theoretically extended when a combination of homogenous and non-homogenous, ethical, socio-cultural and emotional nuances are considered. This, we argue, provides not only a significant contribution to the current AI–HRM focus on efficiencies and performance, but also a way of highlighting the unintended consequences of doing so at individual, organizational and team levels of underperformance.

Consequently, "technological servitization" is proposed to highlight an alternative framing, one that is characterized by surfacing managements' overemphasis on job designs and performance evaluation ("surveillance?") to the point where such control and monitoring measures on where, how and why jobs are being done in AI–HRM (Wirtky *et al.*, 2016) only serve to perpetuate a managerial hegemony (Levy *et al.*, 2003) as its medium (or guise?). Such "technological servitization" (and possible "surveillance"?) is also characterized by the introduction of and reliance on new work procedures and employment, performance and productivity policies standardizing work outcomes, with an expectation of strict compliance "or else." "Technological servitization" engenders loss of employee engagement, mistrust of management and apprehensive of AI systems, the very aspects that had adversely impacted on individual-, organizational- and team-level performance. Such a theoretical enrichment surfaces earlier, unattended issues regarding the constraining, rather than unleashing opportunities of AI, and the resultant loss of the human freedom to create, innovate and experiment with new technologies at work. This paradoxically sparks a sense of meaninglessness/lack of purpose/lag in organizations and management deployment of a range of strategies to enhance workplaces' transition to AI systems. Consequently, this paper calls for a more critical, multi-dimensional

and nuanced examination of theories underpinning AI and their impacts (intended and unintended) on people, processes and procedures beyond the current organizational performance anchor of AI scholarship (Hemmati and Rahmani, 2022; Peng *et al*., 2022; Kar *et al*., 2023).

4.2 Framework's practical/functional legitimacy

The second set of implications should also recognize and tackle the adverse, unintended consequences of an organizationally centric transformation agenda (Suseno *et al*., 2022; Carvalho *et al*., 2022) based purely on monitoring and control systems via AI systems as these lead to jobs in-securitization, disengagement and dissatisfaction.

Our paper's practical implications for AI and HRM practitioners and Managerial Psychologists are equally as multi-dimensional as are our theoretical extensions and implications. For example, we demonstrate how the numerous functional methods (e.g. recruitment and selection, rewards and incentivization schemes) in AI–HRM can ought to be applied to resolve organizational underperformance in various aspects such as Key Performance Indicator(s) (KPIs), target setting and performance evaluations (Aguinis *et al*., 2024). Although "surveillance" fears and anxieties could persist when such measures are deployed, as part of the unintended consequences of focusing on organizational-level underperformance (Suseno *et al*., 2022; Carvalho *et al*., 2022), the propensity of mitigating against chronic multi-dimensional underperformance and the promotion of greater synergy between the challenging forces of non-homogeneity and the beneficial impact of homogeneity injects a less authoritarian discourse than what currently abounds in the AI-cost-and-efficiencies driven rhetoric and practice.

To enrich the AI literature and advance Managerial Psychology theorizing, our paper's second concept: "re-ontological in-securitization" serves to highlight and extend key aspects in the current debates on theoretical advancements and the practice gap in implementation. On the one hand, while utopian expectations of resolving underperformance via AI introductions persist in the literature, Floridi's (2010) "re-ontologization" and Croft's (2012) and Ejdus and Tijana's (2021) "ontological insecurities" highlight some of the potential unintended results of AI systems' use in the hope that using an in-loop HR model could play a role in wholesomely addressing chronic underperformance and internal organizational data insecurity issues at different levels of the performance crises (Tooze, 2021). Our introduction of the notion of "re-ontological in-securitization" heightens staff – AI – managements' misalignment of intentions, preferences and commitments to change and the need for current AI–HRM practices to be conscious of such a reality and to critically re-conceptualize AI–HRM systems and practices in an era of increasing change.

4.3 Framework's contextualized legitimacy

Our framework's application is contextually dependent (geographic, workplaces deploying AI systems, the nature and scale of the technological transformations and management and staff's cognitive, and moral beliefs regarding technological systems in workplaces). While previous scholars have framed AI systems' deployment using ethical, legal and policy frameworks (Ashok *et al*., 2022) and others have called for business adaptability to facilitate AI's applications, the AI–human collaboration (Budhwar *et al*., 2023; Chowdhury *et al*., 2023) needed in today's fast-evolving organizational spaces (Dwivedi *et al*., 2021) could also be enriched from additional critique and contextualization beyond the existing performance rhetoric in firms (Kar *et al*., 2023). By highlighting HR's policy adoption and ethical, procedural oversight role in AI deployment, we anticipate a more meaningful collaboration and adoption of AI in contemporary organizations than is currently the case. We consider future research directions next.

This paper's framework is drawn primarily from a range of AI, HRM, Managerial Psychology and other theoretical discourses highlighting homogenous and non-homogenous tendencies toward AI–HRM. Consequently, the success of applying such a framework and the

parameters for evaluating what that outcome could look like is contextually dependent (geographic, workplaces deploying AI systems, the nature and scale of the technological transformations and how and when management may decide to implement AI measures in workplaces). While we have considered the range of AI systems' deployment aspects from ethics to legal policy issues (Ashok *et al*., 2022) in framing our current HRM framework, we have made a special addition/extension. This is the introduction of why it is critical for AI, HRM and Managerial Psychologists to combine homogenous and non-homogenous perspectives as part of a novel socio-cultural and ideological re-orientation toward tackling the perennial individual, organizational and team-level underperformance in changing businesses to enhance their sustainability.

5. Future research

This section provides a particular set of directions for future research on AI in changing workplaces and managerial impact. First, there is a need for future research into how relationships between human and artificial intelligence evolve over time, impacts on people, jobs and organizational performance, personal and collective well-being and which managerial transformation initiatives could work more effectively. A question to consider here is how cost-minimization strategies/changes (Malik *et al*., 2022) could be addressed more positively and how managements adopt a dual operational and strategic role: (1) deploying AI initiatives/activities/tools to boost organizational performance and (2) strategically enhancing employee well-being interventions via job crafting. Second, a combination of conceptual, longitudinal, cross-industry, functional and contextual studies beyond the current emphasis on organizational underperformance in changing organizations (Aguinis *et al*., 2024; Wamba *et al*., 2023) is required. Third, while the range of HR recommendations provided by our framework could be used in extending He *et al*.'s (2024) judgements, intentions and Singh *et al*.'s (2017) focus on specific HR practices and Baporikar and Shikokola's (2020) managements' digital technological dependence, we proposition that management develop self-regulating, self-motivating capabilities to help tackle employees' propensities of apprehension and mistrust of changing interventions in organizations. Finally, we proposition a renewed need to embed managerial self-restraint, empathy and regulation, as key capabilities when organizations are being "reontologized" as Floridi (2010) conceptualized earlier. We also add personal and collective well-being as part of the "reontologization" that could deal with Zuboff's (1991, 2023) "surveillance" ideology to help facilitate mental, cognitive and psychological securitization of workers in changing organizations. Future research should consider additional challenges, opportunities and HR capabilities, and how to further advance new theories, methodologies and practices that add to the HRM framework, and the two concepts we developed: (1) "technological servitization" and (2) "re-ontological in-securitization" for Managerial Psychology literature and research.

6. Conclusion

This paper was aimed at conducting a critical, systematic literature review of the literature on AI–HRM in contemporary changing organizations. It highlighted the non-homogenous (challenges) and homogenous managerial impacts (opportunities) on individual, team and organizational performance, particularly in terms of the factors impacting on jobs' performance in changing organizations. Having fully fulfilled the study's aims, we additionally propositioned an HRM framework consisting of five aspects/recommendations to advance Managerial Psychology theorization on the conceptualization and operationalization of effective performance when AI tools are used (Malik, 2024; Aguinis *et al*., 2024). We also highlighted how a set of nuanced (and important) emphasis on the strategic, empathy and decision-making capabilities for effective AI deployment in changing organizations (see five recommendations) is needed for the practical, managerial resolution of

underperformance at multiple levels of the organization. We also introduced two key concepts: (1) "technological servitization" and (2) "re-ontological in-securitization" to further enrich Managerial Psychology's theorization paucity in explicating and extending knowledge on the non-technical, non-financial, non-measurable aspects of performance in this emerging field and highlight the multi-dimensional and complex factors that could help to explain why organizational, individual and team underperformance in changing organizations is still a problem. By doing so, we provide organizations' management with a holistic set of AI, human and other tools to resolve non-performance, non-costs, and non-efficiencies related problems in contemporary changing organizations. However, we also recognize that such recommendations and critical discussions currently focus on an examination of the current state-of-play of the literature in this emerging area and combining both a conceptual evaluation with an empirical study on AI–HRM could be developed as a more holistic and more comprehensive program of support (both operationally and strategically (i.e. in the longer-term) for Managerial Psychologists, AI and HRM professionals and enthusiasts in future studies. Doing so is anticipated to add to emerging theoretical insights in this impactful study on the impacts of AI–HRM on the resolution of underperformance and further enhance the meaningfulness of any practical capacity development programs for management and staff alike.

References

Abbas, S.M., Liu, Z. and Khushnood, M. (2023), "When human meets technology: unlocking hybrid intelligence role in breakthrough innovation engagement via self-extension and social intelligence", *Journal of Computer Information Systems*, Vol. 63 No. 5, pp. 1183-1200, doi: 10.1080/08874417.2022.2139781.

Abulsaoud Ahmed Younis, R. and Adel, H.M. (2020), "Artificial intelligence strategy, creativity-oriented HRM and knowledge-sharing quality: empirical analysis of individual and organisational performance of AI-powered businesses", *The Annual International Conference of The British Academy of Management (BAM)*.

Aguinis, H., Beltran, J.R. and Cope, A. (2024), "How to use generative AI as a human resource management assistant", *Organizational Dynamics*, Vol. 53 No. 1, 101029, doi: 10.1016/j.orgdyn.2024.101029.

Alayo, M., Iturralde, T., Maseda, A. and Aparicio, G. (2021), "Mapping family firm internationalization research: bibliometric and literature review", *Review of Managerial Science*, Vol. 15 No. 6, pp. 1517-1560, doi: 10.1007/s11846-020-00404-1.

Andrieux, M., Henrio, L. and Radanne, G. (2024), "Active objects based on algebraic effects", in *Active Object Languages: Current Research Trends*, Springer Nature Switzerland, Cham, pp. 3-36.

Arslan, A., Ahokangas, P., Haapanen, L., Golgeci, I., Tarba, S.Y. and Bazel-Shoham, O. (2022), "Generational differences in organizational leaders: an interpretive phenomenological analysis of work meaningfulness in the Nordic high-tech organizations", *Technological Forecasting and Social Change*, Vol. 180, 121717, doi: 10.1016/j.techfore.2022.121717.

Ashok, M., Madan, R., Joha, A. and Sivarajah, U. (2022), "Ethical framework for artificial intelligence and digital technologies", *International Journal of Information Management*, Vol. 62, 102433, doi: 10.1016/j.ijinfomgt.2021.102433.

Ates, A., Garengo, P., Cocca, P. and Bititci, U. (2013), "The development of SME managerial practice for effective performance management", *Journal of Small Business and Enterprise Development*, Vol. 20 No. 1, pp. 28-54, doi: 10.1108/14626001311298402.

Banal-Estañol, A. and Seldeslachts, J. (2011), "Merger failures", *Journal of Economics and Management Strategy*, Vol. 20 No. 2, pp. 589-624, doi: 10.1111/j.1530-9134.2011.00298.x.

Bankins, S., Ocampo, A.C., Marrone, M., Restubog, S.L.D. and Woo, S.E. (2024), "A multilevel review of artificial intelligence in organizations: implications for organizational behavior research and practice", *Journal of Organizational Behavior*, Vol. 45 No. 2, pp. 159-182, doi: 10.1002/job.2735.

Baporikar, N. and Shikokola, S. (2020), "Information technology adoption dynamics for SMEs in the manufacturing sector of Namibia", *International Journal of ICT Research in Africa and the Middle East (IJICTRAME)*, Vol. 9 No. 2, pp. 60-77, doi: 10.4018/ijictrame.2020070104.

Bitkina, O.V., Jeong, H., Lee, B.C., Park, J., Park, J. and Kim, H.K. (2020), "Perceived trust in artificial intelligence technologies: a preliminary study", *Human Factors and Ergonomics in Manufacturing and Service Industries*, Vol. 30 No. 4, pp. 282-290, doi: 10.1002/hfm.20839.

Budhwar, P., Chowdhury, S., Wood, G., Aguinis, H., Bamber, G.J., Beltran, J.R., Boselie, P., Lee Cooke, F., Decker, S., DeNisi, A., Dey, P.K., Guest, D., Knoblich, A.J., Malik, A., Paauwe, J., Papagiannidis, S., Patel, C., Pereira, V., Ren, S., Rogelberg, S., Saunders, M.N.K., Tung, R.L. and Varma, A. (2023), "Human resource management in the age of generative artificial intelligence: perspectives and research directions on ChatGPT", *Human Resource Management Journal*, Vol. 33 No. 3, pp. 606-659, doi: 10.1111/1748-8583.12524.

Budhwar, P., Wood, G., Chowdhury, S., Aguinis, H., Breslin, D., Collings, D.G., Cooke, F.L., Darabi, F., Eby, L.T., Martin, U.M., Morley, M.J., Morris, S., Ren, S., Saunders, M.N.K. and Suddaby, R. (2024), "Articulating scholarship in human resource management: guidance for researchers", *Human Resource Management Journal*, Vol. 34 No. 3, pp. 830-863, doi: 10.1111/1748-8583.12567.

Carvalho, L., Martinez-Maldonado, R., Tsai, Y.S., Markauskaite, L. and De Laat, M. (2022), "How can we design for learning in an AI world?", *Computers and Education: Artificial Intelligence*, Vol. 3, 100053, doi: 10.1016/j.caeai.2022.100053.

Chowdhury, S., Dey, P., Joel-Edgar, S., Bhattacharya, S., Rodriguez-Espindola, O., Abadie, A. and Truong, L. (2023), "Unlocking the value of artificial intelligence in human resource management through AI capability framework", *Human Resource Management Review*, Vol. 33 No. 1, 100899, doi: 10.1016/j.hrmr.2022.100899.

Chowdhury, S., Budhwar, P. and Wood, G. (2024), "Generative artificial intelligence in business: towards a strategic human resource management framework", *British Journal of Management*, Vol. 35 No. 4, pp. 1680-1691, doi: 10.1111/1467-8551.12824.

Chukwuka, E.J. and Dibie, K.E. (2024), "Strategic role of artificial intelligence (AI) on human resource management (HR) employee performance evaluation function", *International Journal of Entrepreneurship and Business Innovation*, Vol. 7 No. 2, pp. 269-282, doi: 10.52589/ijebi-het5styk.

Croft, S. (2012), "Constructing ontological insecurity: the insecuritization of Britain's Muslims", *Contemporary Security Policy*, Vol. 33 No. 2, pp. 219-235, doi: 10.1080/13523260.2012.693776.

Dwivedi, Y.K., Hughes, L., Ismagilova, E., Aarts, G., Coombs, C., Crick, T., Duan, Y., Dwivedi, R., Edwards, J., Eirug, A., Galanos, V., Ilavarasan, P.V., Janssen, M., Jones, P., Kar, A.K., Kizgin, H., Kronemann, B., Lal, B., Lucini, B., Medaglia, R., Le Meunier-FitzHugh, K., Le Meunier-FitzHugh, L.C., Misra, S., Mogaji, E., Sharma, S.K., Singh, J.B., Raghavan, V., Raman, R., Rana, N.P., Samothrakis, S., Spencer, J., Tamilmani, K., Tubadji, A., Walton, P. and Williams, M.D. (2021), "Artificial Intelligence (AI): multidisciplinary perspectives on emerging challenges, opportunities, and agenda for research, practice and policy", *International Journal of Information Management*, Vol. 57, 101994, doi: 10.1016/j.ijinfomgt.2019.08.002.

Dwivedi, Y.K., Kshetri, N., Hughes, L., Slade, E.L., Jeyaraj, A., Kar, A.K., Baabdullah, A.M., Koohang, A., Raghavan, V., Ahuja, M., Albanna, H., Albashrawi, M.A., Al-Busaidi, A.S., Balakrishnan, J., Barlette, Y., Basu, S., Bose, I., Brooks, L., Buhalis, D., Carter, L., Chowdhury, S., Crick, T., Cunningham, S.W., Davies, G.H., Davison, R.M., Dé, R., Dennehy, D., Duan, Y., Dubey, R., Dwivedi, R., Edwards, J.S., Flavián, C., Gauld, R., Grover, V., Hu, M.C., Janssen, M., Jones, P., Junglas, I., Khorana, S., Kraus, S., Larsen, K.R., Latreille, P., Laumer, S., Malik, F. T., Mardani, A., Mariani, M., Mithas, S., Mogaji, E., Nord, J.H., O'Connor, S., Okumus, F., Pagani, M., Pandey, N., Papagiannidis, S., Pappas, I.O., Pathak, N., Pries-Heje, J., Raman, R., Rana, N.P., Rehm, S.V., Ribeiro-Navarrete, S., Richter, A., Rowe, F., Sarker, S., Stahl, B.C., Tiwari, M.K., van der Aalst, W., Venkatesh, V., Viglia, G., Wade, M., Walton, P., Wirtz, J. and Wright, R. (2023), "Opinion Paper:"So what if ChatGPT wrote it?" Multidisciplinary perspectives on opportunities, challenges and implications of generative conversational AI for research, practice and policy", *International Journal of Information Management*, Vol. 71, 102642, doi: 10.1016/j.ijinfomgt.2023.102642.

Ejdus, F. and Rečević, T. (2021), "Ontological insecurity as an emergent phenomenon", *European Psychologist*, Vol. 26 No. 1, pp. 29-44, doi: 10.1027/1016-9040/a000419.

Floridi, L. (2010), "Ethics after the information revolution", in *The Cambridge Handbook of Information and Computer Ethics*, pp. 3-19.

Glikson, E. and Woolley, A.W. (2020), "Human trust in artificial intelligence: review of empirical research", *The Academy of Management Annals*, Vol. 14 No. 2, pp. 627-660, doi: 10.5465/annals.2018.0057.

Guest, D.E. (2011), "Human resource management and performance: still searching for some answers", *Human Resource Management Journal*, Vol. 21 No. 1, pp. 3-13, doi: 10.1111/j.1748-8583.2010.00164.x.

Guidotti, R., Monreale, A., Ruggieri, S., Turini, F., Giannotti, F. and Pedreschi, D. (2018), "A survey of methods for explaining black box models", *ACM Computing Surveys*, Vol. 51 No. 5, pp. 1-42, doi: 10.1145/3236009.

Halid, H., Ravesangar, K., Mahadzir, S.L. and Halim, S.N.A. (2024), "Artificial intelligence (AI) in human resource management (HRM)", in *Building the Future with Human Resource Management*, Springer International Publishing, Cham, pp. 37-70.

Hayes, J. (2022), *The Theory and Practice of Change Management*, Bloomsbury Publishing, pp. 153-155.

He, G., Zheng, X., Li, W., Tan, L., Chen, S. and He, Y. (2024), "The mixed blessing of leaders' artificial intelligence (AI)-oriented change behavior: implications for employee job performance and unethical behavior", *Applied Research in Quality of Life*, Vol. 19 No. 2, pp. 469-497, doi: 10.1007/s11482-023-10250-4.

Hemmati, A. and Rahmani, A.M. (2022), "The Internet of Autonomous Things applications: a taxonomy, technologies, and future directions", *Internet of Things*, Vol. 20, 100635, doi: 10.1016/j.iot.2022.100635.

Ho, H. and Kuvaas, B. (2020), "Human resource management systems, employee well-being, and firm performance from the mutual gains and critical perspectives: the well-being paradox", *Human Resource Management*, Vol. 59 No. 3, pp. 235-253, doi: 10.1002/hrm.21990.

Hofeditz, L., Clausen, S., Rieß, A., Mirbabaie, M. and Stieglitz, S. (2022), "Applying XAI to an AI-based system for candidate management to mitigate bias and discrimination in hiring", *Electronic Markets*, Vol. 32 No. 4, pp. 2207-2233, doi: 10.1007/s12525-022-00600-9.

Hsuan, J., Jovanovic, M. and Clemente, D.H. (2021), "Exploring digital servitization trajectories within product–service–software space", *International Journal of Operations and Production Management*, Vol. 41 No. 5, pp. 598-621, doi: 10.1108/ijopm-08-2020-0525.

Ivanov, S. and Webster, C. (2019), "Conceptual framework of the use of robots, artificial intelligence and service automation in travel, tourism, and hospitality companies", in *Robots, Artificial Intelligence, and Service Automation in Travel, Tourism and Hospitality*, pp. 7-37, doi: 10.1108/978-1-78756-687-320191001.

Kalleberg, A.L., Marsden, P.V., Reynolds, J. and Knoke, D. (2006), "Beyond profit? Sectoral differences in high-performance work practices", *Work and Occupations*, Vol. 33 No. 3, pp. 271-302, doi: 10.1177/0730888406290049.

Kar, A.K., Varsha, P.S. and Rajan, S. (2023), "Unravelling the impact of generative artificial intelligence (GAI) in industrial applications: a review of scientific and grey literature", *Global Journal of Flexible Systems Management*, Vol. 24 No. 4, pp. 659-689, doi: 10.1007/s40171-023-00356-x.

Katzenbach, J.R. and Smith, D.K. (2015), *The Wisdom of Teams: Creating the High-Performance Organization*, Harvard Business Review Press, pp. 177-245.

Klumpp, M. and Ruiner, C. (2022), "Artificial intelligence, robotics, and logistics employment: the human factor in digital logistics", *Journal of Business Logistics*, Vol. 43 No. 3, pp. 297-301, doi: 10.1111/jbl.12314.

Kohtamäki, M., Parida, V., Patel, P.C. and Gebauer, H. (2020), "The relationship between digitalization and servitization: the role of servitization in capturing the financial potential of digitalization",

Technological Forecasting and Social Change, Vol. 151, 119804, doi: 10.1016/j.techfore.2019.119804.

Kot, S., Hussain, H.I., Bilan, S., Haseeb, M. and Mihardjo, L.W. (2021), "The role of artificial intelligence recruitment and quality to explain the phenomenon of employer reputation", *Journal of Business Economics and Management*, Vol. 22 No. 4, pp. 867-883, doi: 10.3846/jbem.2021.14606.

Kshetri, N. (2021), "Evolving uses of artificial intelligence in human resource management in emerging economies in the global South: some preliminary evidence", *Management Research Review*, Vol. 44 No. 7, pp. 970-990, doi: 10.1108/mrr-03-2020-0168.

Kulkov, I. (2021), "The role of artificial intelligence in business transformation: a case of pharmaceutical companies", *Technology in Society*, Vol. 66, 101629, doi: 10.1016/j.techsoc.2021.101629.

Levy, D.L., Alvesson, M. and Willmott, H. (2003), "Critical approaches to strategic management", *Studying management critically*, Vol. 1, pp. 92-110, doi: 10.4135/9781446220030.n5.

Libert, K., Mosconi, E. and Cadieux, N. (2020), "Human-machine interaction and human resource management perspective for collaborative robotics implementation and adoption", *Conference: HICSS-53At: Maui, Hawaï*.

Madancian, M. and Taherdoost, H. (2023), "The impact of artificial intelligence on human resource management: opportunities and challenges", *International Conference Interdisciplinarity in Engineering*, Cham, Springer Nature Switzerland, pp. 406-424.

Malik, N., Tripathi, S.N., Kar, A.K. and Gupta, S. (2021), "Impact of artificial intelligence on employees working in industry 4.0 led organizations", *International Journal of Manpower*, Vol. 43 No. 2, pp. 334-354, doi: 10.1108/ijm-03-2021-0173.

Malik, S. (2024), "From traditional to humane security challenges-analysing Pakistan's response to the poly crisis of covid 19", *Strategic Studies*, Vol. 44 No. 1, pp. 1-25, doi: 10.53532/ss.044.01.00353.

Malik, A., Budhwar, P., Patel, C. and Srikanth, N.R. (2022), "May the bots be with you! Delivering HR cost-effectiveness and individualised employee experiences in an MNE", *International Journal of Human Resource Management*, Vol. 33 No. 6, pp. 1148-1178, doi: 10.1080/09585192.2020.1859582.

Manresa, A., Sammour, A., Mas-Machuca, M., Chen, W. and Botchie, D. (2023), "Humanizing GenAI at work: bridging the gap between technological innovation and employee engagement", *Journal of Managerial Psychology*.

Marimon, F., Mas-Machuca, M. and Akhmedova, A. (2024), "Remote assessment in higher education: insights from Southern Europe", *10th International Conference on Higher Education Advances (HEAd'24)*, Editorial Universitat Politècnica de València, pp. 1-8.

Mendy, J. and Rahman, M. (2019), "Supporting SMEs' internationalisation through a deeper understanding of human and technology barriers: applying effective HRM processes from a developing country", *Journal of Organizational Effectiveness: People and Performance*, Vol. 6 No. 4, pp. 205-226, doi: 10.1108/joepp-12-2018-0121.

Miller, T. (2019), "Explanation in artificial intelligence: insights from the social sciences", *Artificial Intelligence*, Vol. 267, pp. 1-38, doi: 10.1016/j.artint.2018.07.007.

Moher, D., Liberati, A., Tetzlaff, J., Altman, D.G. and PRISMA Group*, T. (2009), "Preferred reporting items for systematic reviews and meta-analyses: the PRISMA statement", *Annals of Internal Medicine*, Vol. 151 No. 4, pp. 264-269, doi: 10.7326/0003-4819-151-4-200908180-00135.

Muridzi, G., Dhliwayo, S. and Isabelle, D.A. (2024), "Artificial intelligence in transforming HRM processes by organisations", *ISPIM Innovation Symposium*, The International Society for Professional Innovation Management (ISPIM), pp. 1-15.

Narver, J.C., Slater, S.F. and MacLachlan, D.L. (2000), *Total Market Orientation, Business Performance, and Innovation*, Vol. 116, Marketing Science Institute, Cambridge, MA.

Nazareno, L. and Schiff, D.S. (2021), "The impact of automation and artificial intelligence on worker well-being", *Technology in Society*, Vol. 67, 101679, doi: 10.1016/j.techsoc.2021.101679.

Olajide, O. and Sposato, M. (2022), "Opportunities and risks of artificial intelligence in recruitment and selection", *International Journal of Organizational Analysis*, Vol. 30 No. 6, pp. 1771-1782, doi: 10.1108/ijoa-07-2020-2291.

Paul, J. and Criado, A.R. (2020), "The art of writing literature review: what do we know and what do we need to know?", *International Business Review*, Vol. 29 No. 4, 101717, doi: 10.1016/j.ibusrev.2020.101717.

Pavlov, A., Mura, M., Franco-Santos, M. and Bourne, M. (2017), "Modelling the impact of performance management practices on firm performance: interaction with human resource management practices", *Production Planning and Control*, Vol. 28 No. 5, pp. 431-443, doi: 10.1080/09537287.2017.1302614.

Peng, C., van Doorn, J., Eggers, F. and Wieringa, J.E. (2022), "The effect of required warmth on consumer acceptance of artificial intelligence in service: the moderating role of AI-human collaboration", *International Journal of Information Management*, Vol. 66, 102533, doi: 10.1016/j.ijinfomgt.2022.102533.

Pereira, V., Hadjielias, E., Christofi, M. and Vrontis, D. (2023), "A systematic literature review on the impact of artificial intelligence on workplace outcomes: a multi-process perspective", *Human Resource Management Review*, Vol. 33 No. 1, 100857, doi: 10.1016/j.hrmr.2021.100857.

Peter, K.A., Schols, J.M., Halfens, R.J. and Hahn, S. (2020), "Investigating work-related stress among health professionals at different hierarchical levels: a cross-sectional study", *Nursing open*, Vol. 7 No. 4, pp. 969-979, doi: 10.1002/nop2.469.

Prentice, C., Dominique Lopes, S. and Wang, X. (2020), "Emotional intelligence or artificial intelligence–an employee perspective", *Journal of Hospitality Marketing and Management*, Vol. 29 No. 4, pp. 377-403, doi: 10.1080/19368623.2019.1647124.

Prentice, C., Wong, I.A. and Lin, Z.C. (2023), "Artificial intelligence as a boundary-crossing object for employee engagement and performance", *Journal of Retailing and Consumer Services*, Vol. 73, 103376, doi: 10.1016/j.jretconser.2023.103376.

Prikshat, V., Islam, M., Patel, P., Malik, A., Budhwar, P. and Gupta, S. (2023), "AI-Augmented HRM: literature review and a proposed multilevel framework for future research", *Technological Forecasting and Social Change*, Vol. 193, 122645, doi: 10.1016/j.techfore.2023.122645.

Puhovichova, D. and Jankelova, N. (2020), "Changes of human resource management in the context of impact of the fourth industrial revolution", *Industry 4.0*, Vol. 5 No. 3, pp. 138-141.

Rodgers, W., Murray, J.M., Stefanidis, A., Degbey, W.Y. and Tarba, S.Y. (2023), "An artificial intelligence algorithmic approach to ethical decision-making in human resource management processes", *Human Resource Management Review*, Vol. 33 No. 1, 100925, doi: 10.1016/j.hrmr.2022.100925.

Sampson, J.P., Kettunen, J. and Vuorinen, R. (2020), "The role of practitioners in helping persons make effective use of information and communication technology in career interventions", *International Journal for Educational and Vocational Guidance*, Vol. 20 No. 1, pp. 191-208, doi: 10.1007/s10775-019-09399-y.

Shahid, S.M. and Alarifi, G. (2021), "Social entrepreneurship education: a conceptual framework and review", *International Journal of Management in Education*, Vol. 19 No. 3, 100533, doi: 10.1016/j.ijme.2021.100533.

Shaikh, F., Afshan, G., Anwar, R.S., Abbas, Z. and Chana, K.A. (2023), "Analyzing the impact of artificial intelligence on employee productivity: the mediating effect of knowledge sharing and well-being", *Asia Pacific Journal of Human Resources*, Vol. 61 No. 4, pp. 794-820, doi: 10.1111/1744-7941.12385.

Simpson, A., Day, C., Goulding, J. and Asha, J. (2022), "Australian teachers' perceptions of effectiveness in a performative culture", *Teaching and Teacher Education*, Vol. 109, 103542, doi: 10.1016/j.tate.2021.103542.

Singh, S., Darwish, T.K., Wood, G. and Mohamed, A.F. (2017), "Institutions, complementarity, human resource management and performance in a South-East Asian Petrostate: the case of Brunei", *International Journal of Human Resource Management*, Vol. 28 No. 18, pp. 2538-2569, doi: 10.1080/09585192.2016.1170713.

Sithambaram, R.A. and Tajudeen, F.P. (2023), "Impact of artificial intelligence in human resource management: a qualitative study in the Malaysian context", *Asia Pacific Journal of Human Resources*, Vol. 61 No. 4, pp. 821-844, doi: 10.1111/1744-7941.12356.

Suseno, Y., Chang, C., Hudik, M. and Fang, E.S. (2022), "Beliefs, anxiety and change readiness for artificial intelligence adoption among human resource managers: the moderating role of high-performance work systems", *International Journal of Human Resource Management*, Vol. 33 No. 6, pp. 1209-1236, doi: 10.1080/09585192.2021.1931408.

Suseno, Y., Chang, C., Hudik, M. and Fang, E.S. (2023), "Beliefs, anxiety and change readiness for artificial intelligence adoption among human resource managers: the moderating role of high-performance work systems", in *Artificial Intelligence and International HRM*, Routledge, pp. 144-171.

Sutherland, W., Jarrahi, M.H., Dunn, M. and Nelson, S.B. (2020), "Work precarity and gig literacies in online freelancing", *Work, Employment and Society*, Vol. 34 No. 3, pp. 457-475, doi: 10.1177/0950017019886511.

Sverdrup, T.E. and Stensaker, I.G. (2014), "Restoring trust and renegotiating psychological contracts in the context of strategic change", *Academy of Management Proceedings*, Vol. 2014 No. 1, 16164, Briarcliff Manor, NY, Academy of Management, doi: 10.5465/ambpp.2014.16164abstract.

Tanantong, T. and Wongras, P. (2024), "A UTAUT-based framework for analyzing users' intention to adopt artificial intelligence in human resource recruitment: a case study of Thailand", *Systems*, Vol. 12 No. 1, 28, doi: 10.3390/systems12010028.

Thukral, S. and Jain, A. (2021), "Unveiling contemporary dimensions in the internationalisation of family firms through bibliometric analysis and thematic analysis", *Review of International Business and Strategy*, Vol. 31 No. 4, pp. 507-539, doi: 10.1108/ribs-09-2020-0121.

Tooze, A. (2021), *Shutdown: How Covid Shook the World's Economy*, Part II, Chapters 5-8, Penguin UK.

Trocin, C., Hovland, I.V., Mikalef, P. and Dremel, C. (2021), "How Artificial Intelligence affords digital innovation: a cross-case analysis of Scandinavian companies", *Technological Forecasting and Social Change*, Vol. 173, 121081, doi: 10.1016/j.techfore.2021.121081.

Vendrell-Herrero, F., Bustinza, O.F., Parry, G. and Georgantzis, N. (2017), "Servitization, digitization and supply chain interdependency", *Industrial Marketing Management*, Vol. 60, pp. 69-81, doi: 10.1016/j.indmarman.2016.06.013.

Venumuddala, V.R. and Kamath, R. (2023), "Work systems in the Indian information technology (IT) industry delivering artificial intelligence (AI) solutions and the challenges of work from home", *Information Systems Frontiers*, Vol. 25 No. 4, pp. 1375-1399, doi: 10.1007/s10796-022-10259-4.

Wamba, S.F., Queiroz, M.M., Jabbour, C.J.C. and Shi, C.V. (2023), "Are both generative AI and ChatGPT game changers for 21st-century operations and supply chain excellence?", *International Journal of Production Economics*, Vol. 265, 109015, doi: 10.1016/j.ijpe.2023.109015.

Wang, X.L., Lei, N. and Hou, Y.Z. (2020), "How does human resource department's client relationship management affect sustainable enterprise performance-in the context of artificial intelligence?", *International Journal of Technology Management*, Vol. 84 Nos 1-2, pp. 50-69, doi: 10.1504/ijtm.2020.112139.

Wang, J., Xing, Z. and Zhang, R. (2023), "AI technology application and employee responsibility", *Humanities and Social Sciences Communications*, Vol. 10 No. 1, pp. 1-17, doi: 10.1057/s41599-023-01843-3.

Watson, D., Womack, J. and Papadakos, S. (2020), "Rise of the robots: is artificial intelligence a friend or foe to nursing practice?", *Critical Care Nursing Quarterly*, Vol. 43 No. 3, pp. 303-311, doi: 10.1097/cnq.0000000000000315.

Webster, C. and Ivanov, S. (2020), *Robotics, Artificial Intelligence, and the Evolving Nature of Work*, Springer International Publishing, pp. 127-143.

Wennberg, K., Wiklund, J. and Wright, M. (2011), "The effectiveness of university knowledge spillovers: performance differences between university spinoffs and corporate spinoffs", *Research Policy*, Vol. 40 No. 8, pp. 1128-1143, doi: 10.1016/j.respol.2011.05.014.

Wijayati, D.T., Rahman, Z., Rahman, M.F., Arifah, I.D. and Kautsar, A. (2022), "A study of artificial intelligence on employee performance and work engagement: the moderating role of change leadership", *International Journal of Manpower*, Vol. 43 No. 2, pp. 486-512, doi: 10.1108/ijm-07-2021-0423.

Wirtky, T., Laumer, S., Eckhardt, A. and Weitzel, T. (2016), "On the untapped value of e-HRM: a literature review", *Communications of the Association for Information Systems*, Vol. 38 No. 1, pp. 2-83, doi: 10.17705/1cais.03802.

Zhao, F., Barratt-Pugh, L., Suseno, Y., Standen, P. and Redmond, J. (2023), "A framework for exploring digital entrepreneurship development from a social interaction perspective", *Journal of General Management*, Vol. 48 No. 2, pp. 115-126, doi: 10.1177/03063070211044578.

Zuboff, S. (1991), "Informate the enterprise: an agenda for the twenty-first century", in *National Forum*, Honor Society of Phi Kappa Phi, Vol. 71 No. 3, p. 3.

Zuboff, S. (2023), "The age of surveillance capitalism", in *Social Theory Re-wired*, Routledge, pp. 203-213.

Further reading

Bankins, S., Formosa, P., Griep, Y. and Richards, D. (2022), "AI decision making with dignity? Contrasting workers' justice perceptions of human and AI decision making in a human resource management context", *Information Systems Frontiers*, Vol. 24 No. 3, pp. 857-875, doi: 10.1007/s10796-021-10223-8.

Bartosiak, M.L. and Modlinski, A. (2022), "Fired by an algorithm? Exploration of conformism with biased intelligent decision support systems in the context of workplace discipline", *Career Development International*, Vol. 27 Nos 6/7, pp. 601-615, doi: 10.1108/cdi-06-2022-0170.

Chuang, S. (2024), "Indispensable skills for human employees in the age of robots and AI", *European Journal of Training and Development*, Vol. 48 Nos 1/2, pp. 179-195, doi: 10.1108/ejtd-06-2022-0062.

Dutta, D., Mishra, S.K. and Tyagi, D. (2023), "Augmented employee voice and employee engagement using artificial intelligence-enabled chatbots: a field study", *International Journal of Human Resource Management*, Vol. 34 No. 12, pp. 2451-2480, doi: 10.1080/09585192.2022.2085525.

Elmadag, A.B., Okan, M. and Kurtuldu, E. (2023), "Improving self-regulated learning competencies of service employees: roles of regulatory appraisals and supportive resources", *Journal of Organizational Change Management*, Vol. 36 No. 2, pp. 290-304, doi: 10.1108/jocm-04-2022-0122.

Islam, M., Mamun, A.A., Afrin, S., Ali Quaosar, G.A. and Uddin, M.A. (2022), "Technology adoption and human resource management practices: the use of artificial intelligence for recruitment in Bangladesh", *South Asian Journal of Human Resources Management*, Vol. 9 No. 2, pp. 324-349, doi: 10.1177/23220937221122329.

Kambur, E. and Akar, C. (2022), "Human resource developments with the touch of artificial intelligence: a scale development study", *International Journal of Manpower*, Vol. 43 No. 1, pp. 168-205, doi: 10.1108/ijm-04-2021-0216.

Kong, H., Yuan, Y., Baruch, Y., Bu, N., Jiang, X. and Wang, K. (2021), "Influences of artificial intelligence (AI) awareness on career competency and job burnout", *International Journal of Contemporary Hospitality Management*, Vol. 33 No. 2, pp. 717-734, doi: 10.1108/ijchm-07-2020-0789.

Kong, H., Yin, Z., Chon, K., Yuan, Y. and Yu, J. (2024), "How does artificial intelligence (AI) enhance hospitality employee innovation? The roles of exploration, AI trust, and proactive personality", *Journal of Hospitality Marketing and Management*, Vol. 33 No. 3, pp. 261-287, doi: 10.1080/19368623.2023.2258116.

Li, P., Bastone, A., Mohamad, T.A. and Schiavone, F. (2023), "How does artificial intelligence impact human resources performance. Evidence from a healthcare institution in the United Arab Emirates", *Journal of Innovation and Knowledge*, Vol. 8 No. 2, 100340, doi: 10.1016/j.jik.2023.100340.

Mihai, F., Aleca, O.E. and Gheorghe, M. (2023), "Digital transformation based on AI technologies in European union organizations", *Electronics*, Vol. 12 No. 11, 2386, doi: 10.3390/electronics12112386.

Pan, Y., Froese, F., Liu, N., Hu, Y. and Ye, M. (2022), "The adoption of artificial intelligence in employee recruitment: the influence of contextual factors", *International Journal of Human Resource Management*, Vol. 33 No. 6, pp. 1125-1147, doi: 10.1080/09585192.2021.1879206.

Pessach, D., Singer, G., Avrahami, D., Ben-Gal, H.C., Shmueli, E. and Ben-Gal, I. (2020), "Employees recruitment: a prescriptive analytics approach via machine learning and mathematical programming", *Decision Support Systems*, Vol. 134, 113290, doi: 10.1016/j.dss.2020.113290.

Qahtani, E.H.A. and Alsmairat, M.A. (2023), "Assisting artificial intelligence adoption drivers in human resources management: a mediation model", *Acta logistica*, Vol. 10 No. 1, pp. 141-150, doi: 10.22306/al.v10i1.371.

Qin, S., Jia, N., Luo, X., Liao, C. and Huang, Z. (2023), "Perceived fairness of human managers compared with artificial intelligence in employee performance evaluation", *Journal of Management Information Systems*, Vol. 40 No. 4, pp. 1039-1070, doi: 10.1080/07421222.2023.2267316.

Rožman, M., Tominc, P. and Milfelner, B. (2023), "Maximizing employee engagement through artificial intelligent organizational culture in the context of leadership and training of employees: testing linear and non-linear relationships", *Cogent Business and Management*, Vol. 10 No. 2, 2248732, doi: 10.1080/23311975.2023.2248732.

Soleimani, M., Intezari, A. and Pauleen, D.J. (2022), "Mitigating cognitive biases in developing AI-assisted recruitment systems: a knowledge-sharing approach", *International Journal of Knowledge Management*, Vol. 18 No. 1, pp. 1-18, doi: 10.4018/ijkm.290022.

Tian, X., Pavur, R., Han, H. and Zhang, L. (2023), "A machine learning-based human resources recruitment system for business process management: using LSA, BERT and SVM", *Business Process Management Journal*, Vol. 29 No. 1, pp. 202-222, doi: 10.1108/bpmj-08-2022-0389.

Tong, S., Jia, N., Luo, X. and Fang, Z. (2021), "The Janus face of artificial intelligence feedback: deployment versus disclosure effects on employee performance", *Strategic Management Journal*, Vol. 42 No. 9, pp. 1600-1631, doi: 10.1002/smj.3322.

Vedapradhan, R. and Ravi, H. (2021), "Innovation in banking: fusion of artificial intelligence and blockchain", *Asia Pacific Journal of Innovation and Entrepreneurship*, Vol. 15 No. 1, pp. 51-61, doi: 10.1108/apjie-09-2020-0142.

Wijayati, H. and Haqqi, H. (2022), "The Indonesian global cocoa chain's position in the pandemic era", *International Journal on Social Science, Economics and Art*, Vol. 12 No. 1, pp. 10-21, doi: 10.35335/ijosea.v12i1.75.

Xu, S., Stienmetz, J. and Ashton, M. (2020), "How will service robots redefine leadership in hotel management? A Delphi approach", *International Journal of Contemporary Hospitality Management*, Vol. 32 No. 6, pp. 2217-2237, doi: 10.1108/ijchm-05-2019-0505.

About the authors

Dr John Mendy, Associate Editor, Senior Lecturer in HRM, co-Chair of the Organisational Transformation, Change and Development Special Interest Group, British Academy of Management and Associate Editor, MCIPD and SFHEA, UK. I am interested in resilience research, the intersection between big data, International HRM and International Business, Organisational Studies, Strategy, labour/employment relationships, autism and employment/HRM policies and practices in a range of organizations in developed and emerging economies. I have published in a respected range of peer-reviewed journals and wrote books on HRM, Organizational Behaviour, Business Research Methods and Absurdity in the Workplace. John Mendy is the corresponding author and can be contacted at: jmendy@lincoln.ac.uk

Dr Apoorva Jain is currently serving as an Assistant Professor at Vivekananda Institute of Professional Studies, Guru Gobind Singh Indraprastha University. Her teaching interest lies in Finance, Accountancy and International Business. She completed her Doctor of Philosophy (Ph.D.) from Delhi School of Management, Delhi Technological University (DTU) in Family Business Management and International Business. She completed her master's in commerce (M. Com) from the Department of Commerce,

University of Delhi and her bachelor's in commerce [B. Com (Hons.)] from Shri Ram College of Commerce, University of Delhi. Her research interest lies in International Business, Strategy and Family Business Management.

Dr Asha Thomas, Assistant Professor at Wroclaw University of Science and Technology, Wroclaw, Poland, completed her PhD in management and quality sciences with a specialization in knowledge management and innovation from Delhi Technological University. Her areas of research interest include big data, grassroots innovation, knowledge management, open innovation and SMEs. With more than 10 years' teaching and industry experience, she has published in the *European Journal of Innovation*, *Journal of Intellectual Capital*, *Journal of Knowledge Management*, *Knowledge Management Research and Practice*, *Kybernetes* and *Management Decision*. She has published 15 books, book chapters and policy for G20 (T20).

For instructions on how to order reprints of this article, please visit our website:
www.emeraldgrouppublishing.com/licensing/reprints.htm
Or contact us for further details: **permissions@emeraldinsight.com**

View publication stats

JMEPEG
https://doi.org/10.1007/s11665-024-10351-7

©ASM International
1059-9495/$19.00

ORIGINAL RESEARCH ARTICLE

Assessment of Mechanical and Slurry Erosive Behavior on Laser-Textured Stainless Steel (SS410)

Mohit Vishnoi, Qasim Murtaza, and Paras Kumar

Submitted: 16 February 2024 / Revised: 15 July 2024 / Accepted: 14 September 2024

In this paper, laser surface texturing (LST) has been used to create the circular and diamond shape texturing pattern on martensitic steel of grade SS410 to alter the various mechanical, surface, and tribological properties. The mechanical and surface characterizations have done on various shape-textured surfaces on SS410. Moreover, the slurry jet erosion test has performed on textured surfaces using a slurry erosion test rig. The hardness value of the various textured shape surface is higher than the others because mechanism of material removal for pattern is melting and evaporation, after applying an intense heat sudden cooling takes place. This might be altering the microstructure and enhances the hardness of the textured steel. The hardness value was the highest for circular-inward-textured case (HV0.3≈206) among all texturing. The tensile and flexural yield strength has marginally increased after texturing. The value of percentage elongation has marginally decreased after texturing. The modulus values for all the textured samples have enhanced as compared to untextured sample. Moreover, the modulus value of diamond-in textured samples are observed to be the highest i.e., ≈265GPa. The contact angles for all shapes of texturing patterns have greater values than untextured samples. All the textured surfaces show the hydrophobic and untextured surface as hydrophilic behavior. The outward textured surface has greater contact angle value (≈110°) as compared to others. The erosion resistance for the untextured samples have lesser among all textured samples, and the circular-in pattern has the highest erosion resistance. Because the erosion resistance is primarily depend on the hardness of the material, the plowing, microcutting lips, crater, and carbide pull-out type of wear mechanism has been identified using a scanning electron microscope.

Keywords laser surface texturing, mechanical characterization, slurry jet erosion, SS410, wettability

1. Introduction

Laser surface texturing (LST) has emerged as a promising technique for enhancing the performance of materials and components across diverse fields, including tribology, energy systems, and biomedical engineering (Ref 1). The continuous evolution of technology has led to an escalating demand for high-quality materials that can cater to the specific requirements of various industries. To address this demand, scientists and engineers are actively involved in the development of innovative coating and texturing methods aimed at augmenting material properties and overall performance. These advanced techniques are not only instrumental in improving material properties but also in tailoring materials to meet specific application needs, spanning industries such as aerospace, automotive, biomedical, and electronics (Ref 2). The versatility of laser surface texturing has contributed to the creation of materials with unique and advantageous properties. Examples include self-healing coatings, superhydrophobic surfaces, and materials designed for enhanced biocompatibility (Ref 3). In the realm of manufacturing processes, the quest for well-textured stainless-steel components remains imperative. Achieving the desired machinery or structural characteristics, encompassing superior tribological behavior and erosion resistance, is a crucial consideration (Ref 4). Laser surface texturing plays a pivotal role in meeting these requirements, allowing for precise modification of surfaces to enhance their functional and performance attributes. The surface texturing is one of the most intrinsic measures which might be followed even before the application of coatings as it ameliorates the longevity of coats (Ref 5). One such illustration is to overcome the low wear resistance of stainless steel-substrates, the Hilbert pattern curve was laser textured improving it 29 times over non-textured one (Ref 6). Surface texturing encompasses surface alteration via the formation of microgrooving, dimples, and channels as well. The machinability of steel is enhanced significantly by simply texturing it in either a positive or negative manner. An internal combustion engine is one prime example where well-textured parts are essential to reduce friction and promote efficiency

The invited article is part of a special topical issue of the *Journal of Materials Engineering and Performance* on Advanced Materials Manufacturing. The issue was organized by Antonello Astarita, University of Naples Federico II; Glenn S. Daehn, The Ohio State University; Emily Kinser, ARPA-E; Govindarajan Muralidharan, Oak Ridge National Laboratory; John Shingledecker, Electric Power Research Institute, Le Zhou, Marquette University, and William Frazier, Pilgrim Consulting, LLC, and Editor, *JMEP*; on behalf of the ASM International Advanced Manufacturing Technical Committee.

Mohit Vishnoi, Department of Mechanical Engineering, Delhi Technological University, Delhi 110042, India; and Department of Mechanical Engineering, JSS Academy of Technical Education, Noida 201301, India; and **Qasim Murtaza** and **Paras Kumar**, Department of Mechanical Engineering, Delhi Technological University, Delhi 110042, India. Contact e-mails: vishnoi.mohit06@gmail.com, qasimmurtaza@dce.ac.in, and paraskumar@dtu.ac.in.

Published online: 12 November 2024

(Ref 7). To achieve the reduction in friction and promoting the efficiency, there are various machining techniques out of which, laser surface texturing is the most widely used (Ref 8). In the case of stainless steel and engineering materials, laser surface texturing stands out as an impervious technique that promises better tribological performance and enhanced erosion resistance (Ref 9). Laser micropatterning of thermal spray coatings avoids issues like embedded grit particles, large affected zones, and surface embrittlement seen in conventional grit blasting pre-treatment. It produces better quality coatings without severe surface deformation or crack initiation sites (Ref 10). Textured Ti-6Al-4 V surfaces with 23% density exhibited lower friction at low loads/speeds due to wear debris trapping in dimples; MoS2 lubricant particles alongside texturing showed excellent friction reduction and anti-wear properties at low speeds for all loads (Ref 11). Friction reduction of up to 80% was discovered in steel sliding pairs at 50 °C oil temperature, with dimple diameters 40-200 μm and 10% texturing density (Ref 12). Laser-textured microdimples were fabricated on nitride steel surfaces, reducing average friction coefficient by half compared to untextured surfaces, improving hydrodynamic lift (Ref 13). Microdimpled diamond-like carbon films were established on titanium alloy using magnetron sputtering and LST. Forty-four percent dimple density reduced friction by trapping wear particles, while 24% density exhibited excellent wear resistance (Ref 14). Up to 70% friction and wear reduction on laser-textured AISI 52100 steel was observed, with increasing textured pocket volume corresponding to increasing reciprocating strokes during wear testing (Ref 15). Picoseconds laser texturing was performed upon aluminum alloy with dimples (5-50% density), cross-grooves (64%), and concentric rings (70%), evaluating wettability and corrosion. Dimples exhibited hydrophilicity, while cross/ring patterns showed hydrophobicity due to roughness variations (Ref 16, 17). Nanosecond laser texturing with 50% overlap ratio was used on aluminum, creating super hydrophobic and ice-repellent surfaces with 170° water contact angle, opposed to hydrophilic untextured surfaces (Ref 18). Sintered steel with irregularly shaped pores was compared to laser-textured steel surfaces. The porous-sintered steel disrupted formation of lubricant film and thus resulted in an increase in friction. Moreover, the regular laser-textured microcavities have reduced friction effectively between mating surfaces (Ref 19). Linear and semicircular microchannels were fabricated on Ti6Al4V with 90% laser pulse overlap, 30 μm width, 10 μm depth, and 13 μm height. At 200% packing density, textured samples exhibited up to 160 times lower friction coefficient compared to untextured specimens (Ref 20). There are various widely used texturing techniques such as: Laser surface texturing, abrasive jet machining, chemical etching, electro spark process, and ultrasonic-assisted grinding. One of the authors has conducted their research on SS410 by deploying rare earth doped carbide coatings and comparison of characterization of coating with substrate has been made (Ref 21). Recently various researchers have conducted their experimentation by considering the laser texturing on different materials such as pure aluminum and commercially used titanium and measured the various mechanical and tribological properties (Ref 22-24). After exhaustive literature survey, it is evident that the comparative analysis of textured shapes on SS410 remains an understudied area. This research is focused on investigating the impact of different texturing shapes on steel, with a primary objective of augmenting the mechanical and tribological (specifically slurry erosive) characteristics of the material. Moreover, a key aim is to render the material surface to be hydrophobic. Because the hydrophobicity enhances the water repelling tendency of the material and hardness enhances the erosion resistance, this leads to explore the applications where the environments around the steels are wet of the surface texturing using LST.

1.1 Laser Surface Texturing (LST) Method

LST allows for precise control over the size, shape, and orientation of the surface textures, which can be tailored to specific applications. It is also a non-contact process, which means that it does not damage the material being processed and can be done without the need for harsh chemicals or high temperatures. A schematic diagram of the laser surface texturing is shown in Fig. 1.

LST can be performed on a variety of materials, including metals, ceramics, polymers, and composites, and can produce textures with high reproducibility and consistency (Ref 25). This technique involves the use of a high-energy laser beam to selectively melt or vaporize material from the surface of a substrate. The laser beam is usually directed through an optical system to focus it onto the surface, creating a localized melting or vaporization effect that forms the desired texture. Contamination can also be minimized with LST, as there is no physical contact between the processing equipment and the substrate being textured. This reduces the risk of introducing impurities or contaminants onto the surface, which can be important in applications where surface cleanliness is critical, such as in biomedical or microelectronics applications (Ref 26). The most used laser beam is Nd: YAG because of its narrow focus areas and high-energy density (Ref 27). The most recent uses of LST include the development of wettability (Ref 28), superhydrophobic coatings (Ref 29), enhanced prosthetics, and an improved bone-implant interface (Ref 27). To improve the texturing performance of existing LST, the ultrafast-pulsed technique has first introduced by Srinivasan et al. (Ref 30) and Stuke (Ref 31). Recently, ultrafast-pulsed laser technology has gained increasing attention in the tribological community due to its ability to create high-quality surface textures with minimal thermal damage to the surrounding material. One industrial application of ultrafast-pulsed laser technology is in the manufacture of silicon wafers, which are used in a variety of electronic and optical devices. For example, ultrafast-pulsed lasers can be used to create precise patterns and structures on silicon wafers for use in solar cells, micro-optical devices, inkjet printer nozzles, and plasma display panels (Ref 32).

2. Experimental Details

2.1 Material Used

Bhagirath Steel and Alloys Delhi provided the annealed and pickled martensitic stainless (SS410) steel of dimensions (305 mm × 254 mm × 5 mm). The SS410 consists of major elements such as Iron, chromium (≈12 wt. %), manganese (≈0.63 wt. %), silicon, nickel, carbon, phosphorus, and Sulfur. The chemical composition of the received material is given in Table 1.

The SS410 plates have been used as a texturing of various shapes as shown in Fig. 2 and compared with untextured samples.

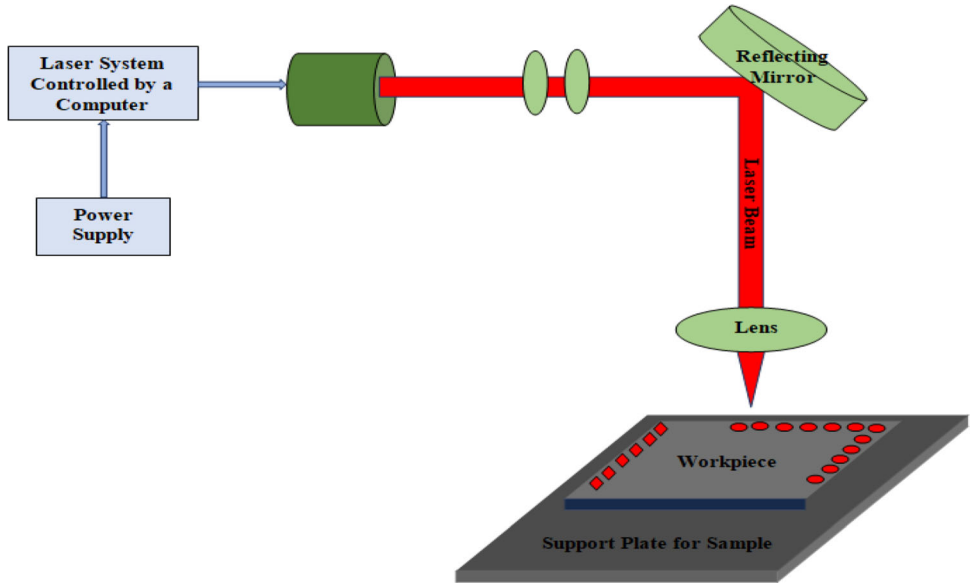

Fig. 1 A schematic diagram of the laser surface texturing

Table 1 Chemical composition of martensitic (SS410) stainless steel

Element	C	Si	Mn	P	S	Cr	Ni
Wt.%	0.12	0.52	0.63	0.03	0.004	12.35	0.18

As shown in Fig. 2(a)-(d), the different shapes of texturing such as diamond and circular having micropits and bump, respectively, were done on stainless steel (SS410) sample surface by LST. The processing parameters like average power (P_{avg}): 50 W, frequency: 40 kHz, dimple depth; 40 μm, and scanning speed: 500 mm/sec have considered with various texturing shapes such as diamond and circular on stainless steel (SS410).

2.2 Characterization of Samples

2.2.1 Hardness Test. The Vickers microhardness tester (up to 1600 HV maximum hardness) the model, Matrix DVS 1AT8, and the maximum load of 1 kg are used to determine the specimens' hardness value in accordance with the ASTM-A270 standard. The Vickers hardness (HV0.3) test is used to determine the hardness values of different shape-textured and untextured samples.

2.2.2 Tensile and Flexural Test. The tensile test and three-point bend test (flexural test) were performed on the Universal Testing Machine (maximum capacity: 100 kN, crosshead speed: 0.005-40 mm/min, maximum crosshead displacement: 700 mm, and model: Instron-1195) in order to determine the various mechanical properties of samples before and after different shapes texturing in accordance with ASTM-E8 (samples as shown in Fig. 3) and ASTM-D790 (samples as shown in Fig. 4) standards, respectively.

2.2.3 Slurry Jet Erosion Test Rig. A slurry jet erosion test apparatus (Model: TR-41, Make: DUCOM-Bangalore, India) is used to conduct the slurry erosion test on both textured and untextured stainless steel (SS410), as illustrated in Fig. 5.

In accordance with ASTM G-136 standard, samples with dimensions of 25 × 25 × 5 mm^3 were employed for the slurry jet erosion test. Sand, which is naturally occurring silica with an irregular shape, is used as an erodent and combined with water to create slurry. The slurry jet erosion test was carried out on different textured shape stainless-steel samples (SS410). The erodent size (≈ 300 μm), impact velocity (≈30 m/sec), and time duration (120 min) were considered parameters during the erosion test.

2.2.4 Scanning Electron microscope. Surface characterization of specimens at 500X is carried out using a scanning electron microscope (JSM-6010 LA) (W-SEM). The scanning electron microscope was used to know the morphology of textured and untextured surfaces; which were represented as micrographs of the considered surface. Furthermore, compositional analysis of the samples was conducted with the assistance of an energy dispersive x-ray (EDX) detector integrated into the SEM. Moreover, the working parameters of EDS are given in Table 2 in which live time indicates that the actual time spent collecting useful data, dead time is the time when the detector is inactive and unable to record new events, and real time is the total duration from the start to the end of the data acquisition, including both live and dead times.

2.2.5 Wettability Test. The measurement of wettability over the surface was carried out using a sessile droplet test per ASTM D7334-08 standard. The contact angle meter having model (DMe−211 plus) was used to measure the static water contact angle.

3. Results and Discussions

3.1 Surface Characterization:

The surface characterizations of stainless steel (SS410) were investigated using different techniques as follows:

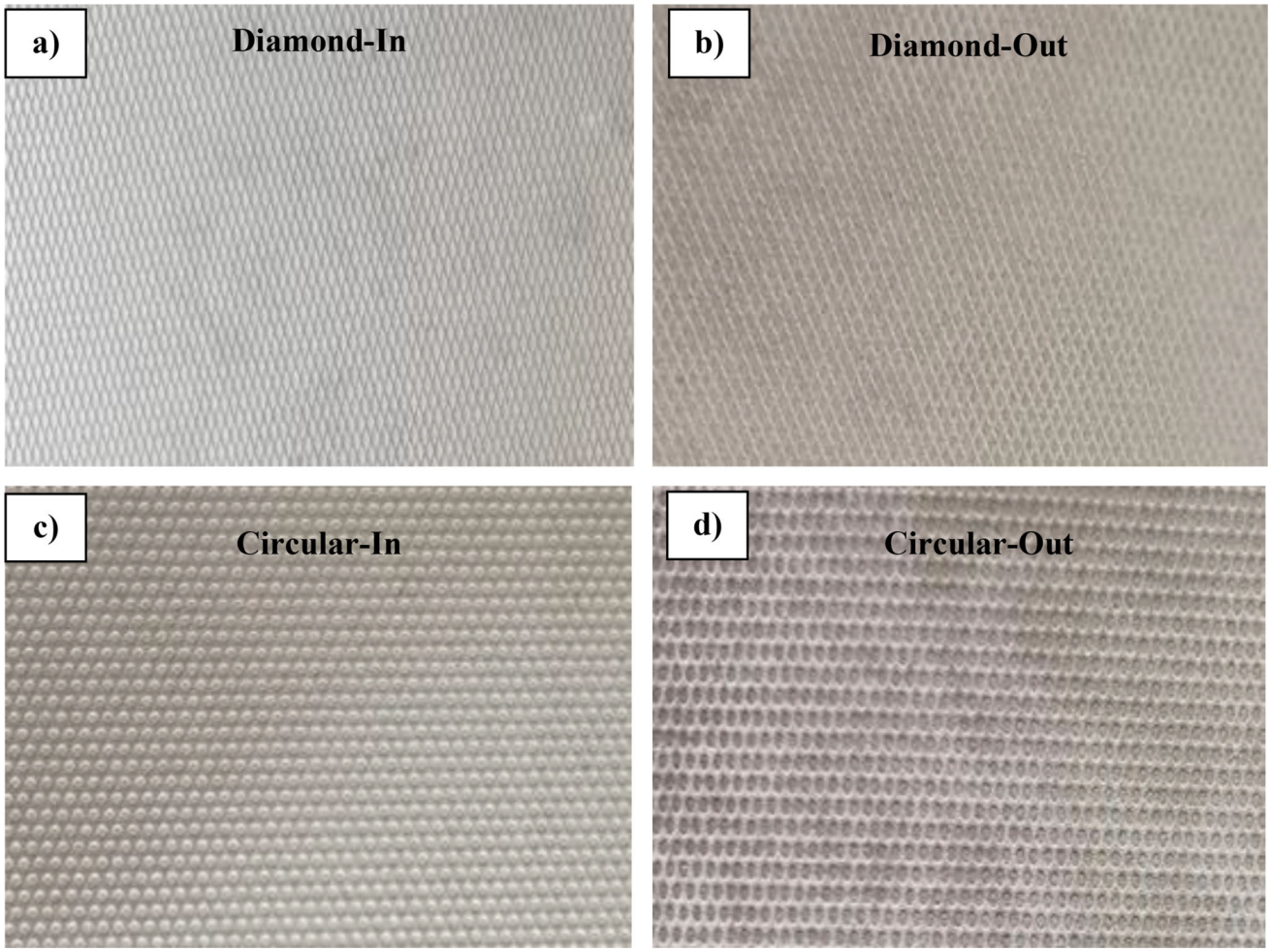

Fig. 2 Laser surface texturing (a) diamond-In (b) diamond-out (c) circular-In and (d) circular-out on SS410, respectively

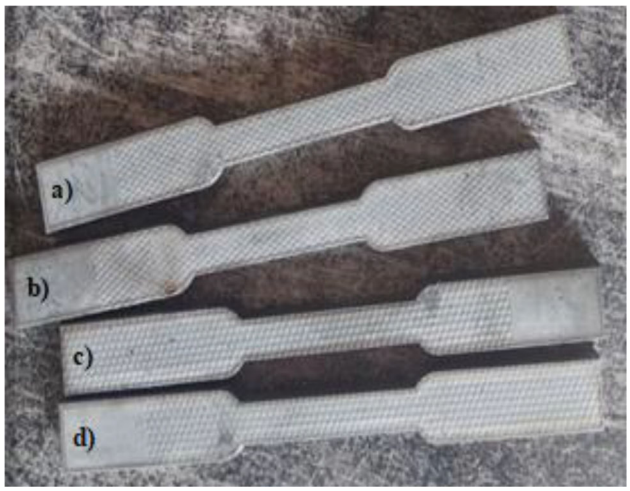

Fig. 3 Tensile test specimen with different texturing shapes: (a) diamond-inward, (b) diamond-outward, (c) circular-inward, and (d) circular-outward

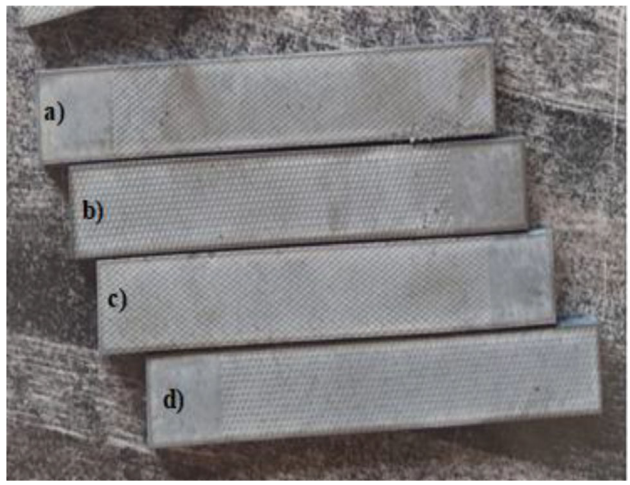

Fig. 4 Flexural test specimen with different texturing shapes: (a) diamond-outward, (b) circular-inward, (c) diamond-inward, and (d) circular-outward

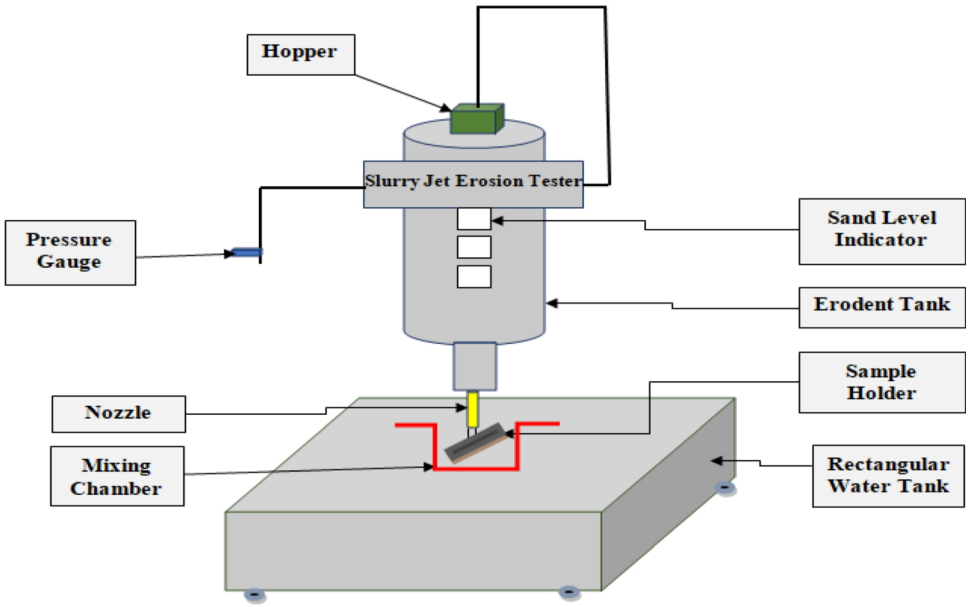

Fig. 5 Slurry jet erosion tester (Ref 36)

Table 2 Working parameters

Acquisition condition of EDS	
Volt	20.00kV
Live time	196.60 sec.
Real time	202.27 sec.
Dead time	4.00%
Count rate	1754.00 CPS

3.1.1 Energy-Dispersive x-ray Spectroscopy (EDS) of Stainless Steel (SS410). The identification and mapping of various elements have done using EDS as shown in Fig. 6.

The element identification was carried out through energy-dispersive x-ray spectroscopy analysis, as depicted in Fig. 6g. Fig. 6(a)-(f) showcases the distinct identification of individual elements, including C, Si, Cr, Mn, Fe, and Ni, with each element represented by a unique color.

3.1.2 X-ray Diffraction and Surface Morphology Examination. The x-ray diffraction analysis was carried out on the martensitic stainless steel (SS410) as shown in Fig. 7.

The x-ray diffraction analysis reveals that the different phases available with crystallographic planes. Among various allotropes of iron such as alpha (α-ferrite), gamma (γ-ferrite), and delta (δ-ferrite) but the peaks of alpha (α-ferrite) phases of iron at different crystallographic planes have been identified using JCPDS files. The crystallographic planes (110) and (200) of alpha iron have been identified as shown in Fig. 7.

3.2 Mechanical Characterization

The various types of mechanical testing were carried out to know the mechanical behavior of textured and untextured samples as follows:

3.2.1 Hardness Test. The Vickers hardness test has been performed on different textured shapes of stainless steel. The test was conducted as per the ASTM-A270 standard.

The test has done under a load of 300 gm with 10 s as a dwell time. The averages of three readings were considered with a deviation of approximate ± 5%. The hardness values of each sample are shown in Fig. 8. The highest hardness has been achieved in the case of circular shape inward texturing among all considered texturing. The hardness values of textured samples are considerably high as compared to untextured or base samples as shown in Fig. 8. When a laser beam is directed toward the surface of a workpiece, the energy of the laser is absorbed by the material at the surface. This energy is converted into heat, causing the temperature of the material to rise rapidly. As the temperature of the material at the surface rises, it can reach the melting or vaporization point of the material. This results in the formation of a plasma plume or vapor cloud above the surface of the material. The plasma plume or vapor cloud above the surface of the material absorbs some of the laser energy, causing it to expand and cool rapidly. This expansion and cooling create a shockwave that propagates into the material, causing some of the material to be removed from the surface. The heating and sudden cooling may be one of the causes of increasing the hardness value after laser texturing on stainless steel. The hardness of inward textured is observed to be more as compared to the outward textured samples. The mechanism of material removal in laser texturing is due to melting and evaporation. So, the inward textures expose to more surface area toward heat than outward-textured samples. So, sudden cooling happens more in case of inward texturing, this leads to enhanced hardness value in inward-textured samples as compared to outward-textured samples.

3.2.2 Tensile Test. The test was conducted as per the ASTM-E8 standard. The averages of three readings were considered with a deviation of approximate ± 5%.

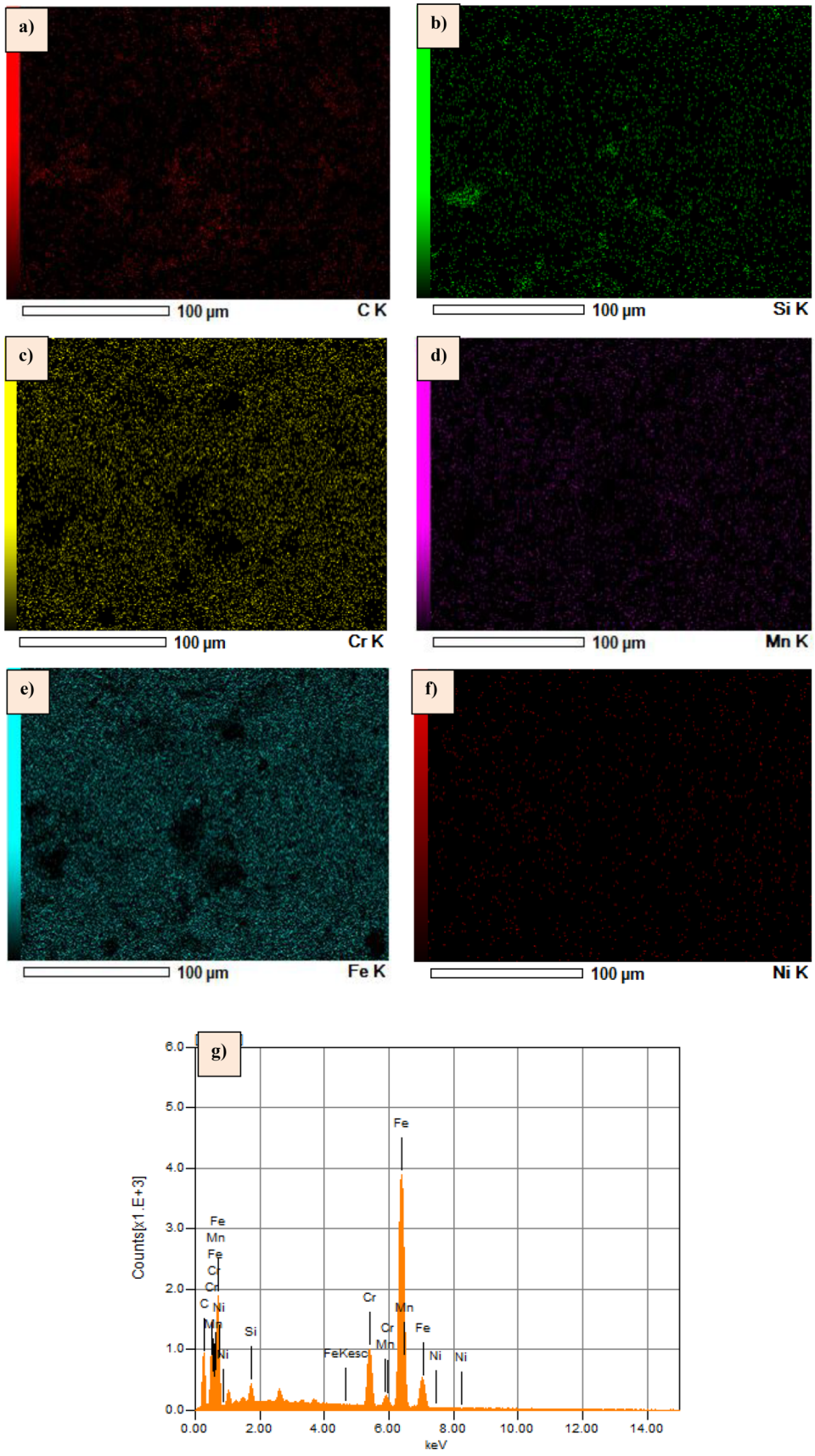

Fig. 6 The elements identification using energy-dispersive x-ray analysis: (a) carbon (C), (b) silicon (Si), (c) chromium (Cr), (d) manganese (Mn), (e) iron (Fe), (f) nickel (Ni), and (g) EDX peaks of elements

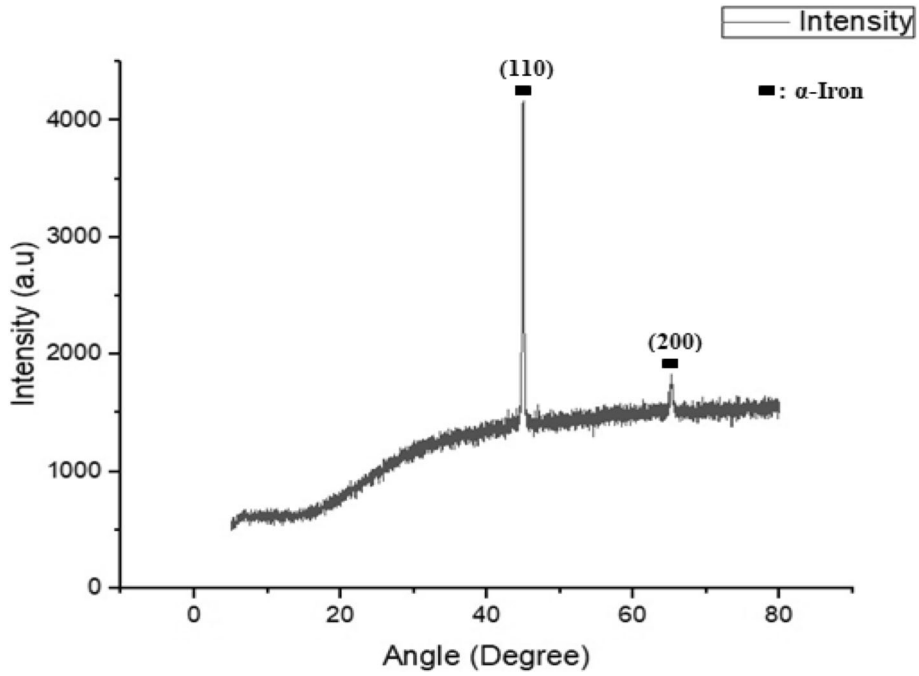

Fig. 7 X-ray diffraction spectra of stainless steel (SS410) (Ref 33)

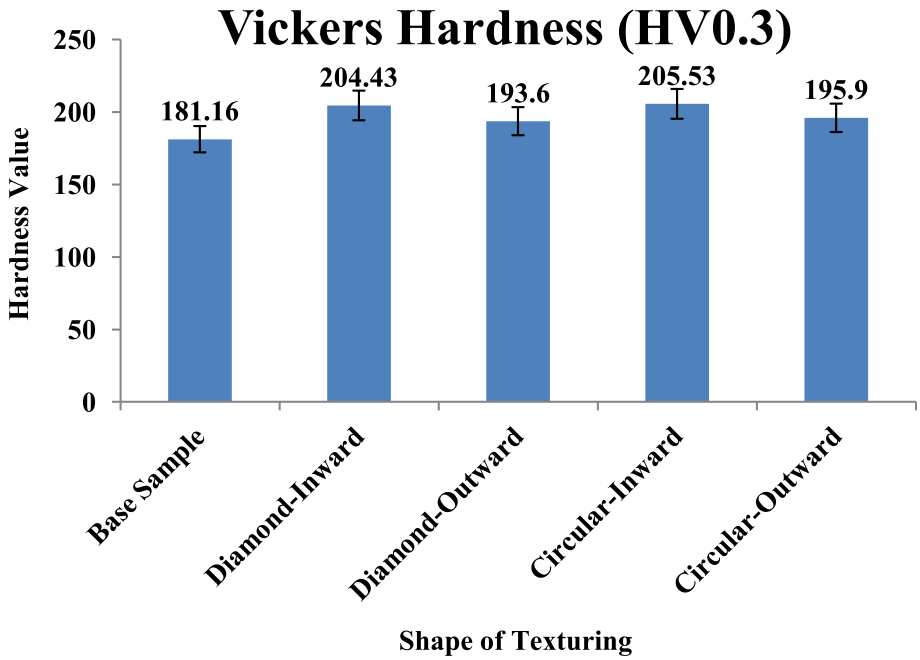

Fig. 8 Vicker's hardness test (HV0.3) on various textured and untextured samples

The stress versus strain curve has obtained by conducting the tensile test for untextured and different textured stainless-steel samples using the universal tensile testing machine as shown in Fig. 9(a)-(e).

The values of various properties were obtained from stress versus strain curve as shown in Fig. 9(a)-(e). The values such as percentage elongation and elastic modulus are shown in Fig. 10(a) and (b), respectively. Moreover, the value of 0.2% offset yield stress (Yield strength) and ultimate tensile strength is shown in Fig. 11. The percentage elongation for the untextured specimen was the highest among all considered samples. This shows that the untextured sample has more ductility as compared to others. The value of yield and tensile strength is the highest for circular-inward-textured as compared

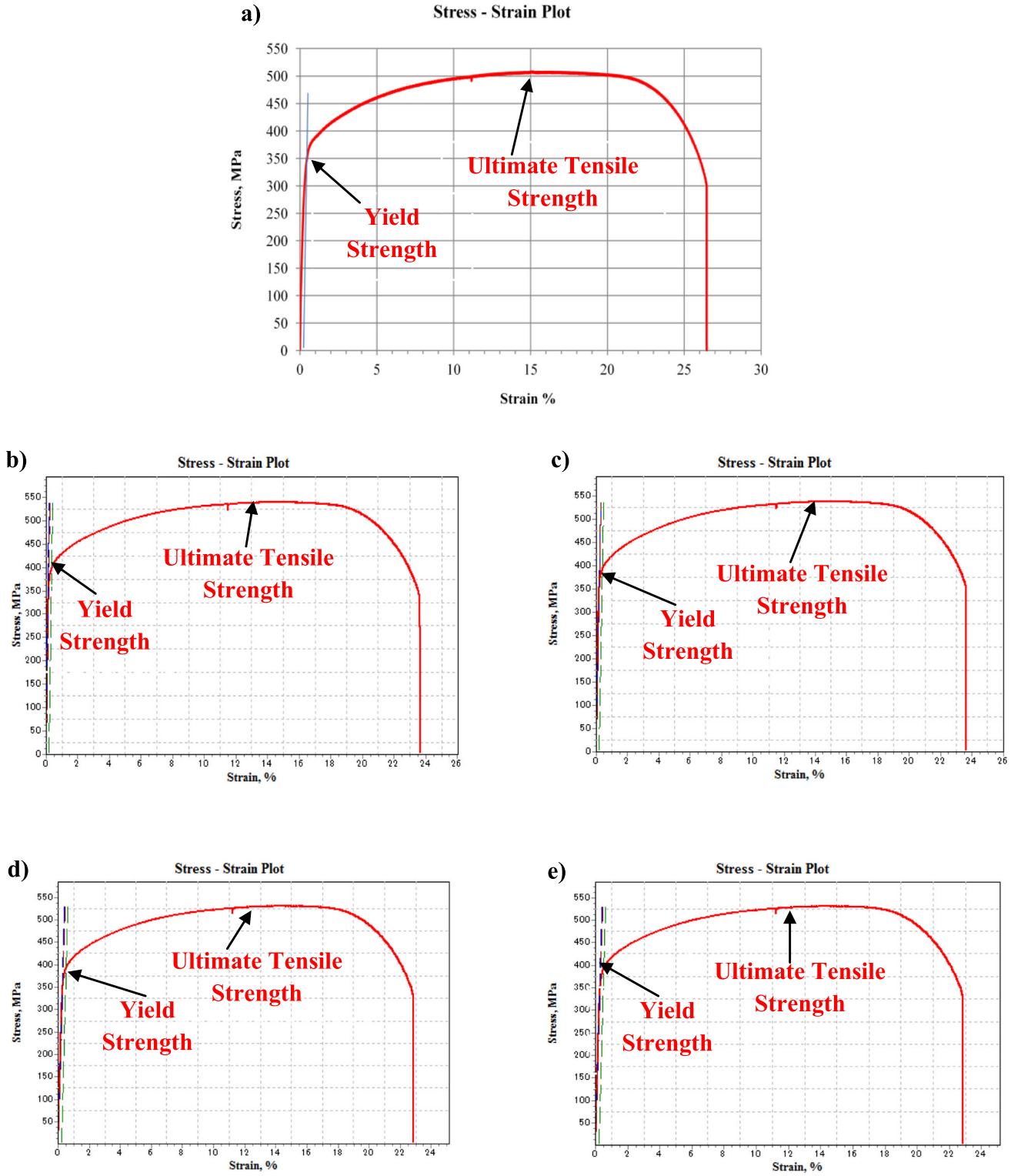

Fig. 9 Stress-strain curve obtained from the tensile test of: (a) untextured, (b) diamond-inward, (c) diamond-outward, (d) circular-inward, and (e) circular-outward shape texturing

to other textured and untextured samples. Laser surface texturing can lead to an increase in tensile and yield strength due to the creation of a rougher surface texture that enhances the frictional resistance between the material and its surroundings. This can increase the strength and toughness of the material. Additionally, laser surface texturing can improve the surface area-to-volume ratio of the material, which can lead to an increase in tensile strength. Particularly, when the laser parameters are not properly optimized then there is a decrease in tensile and yield strength after laser surface texturing, this

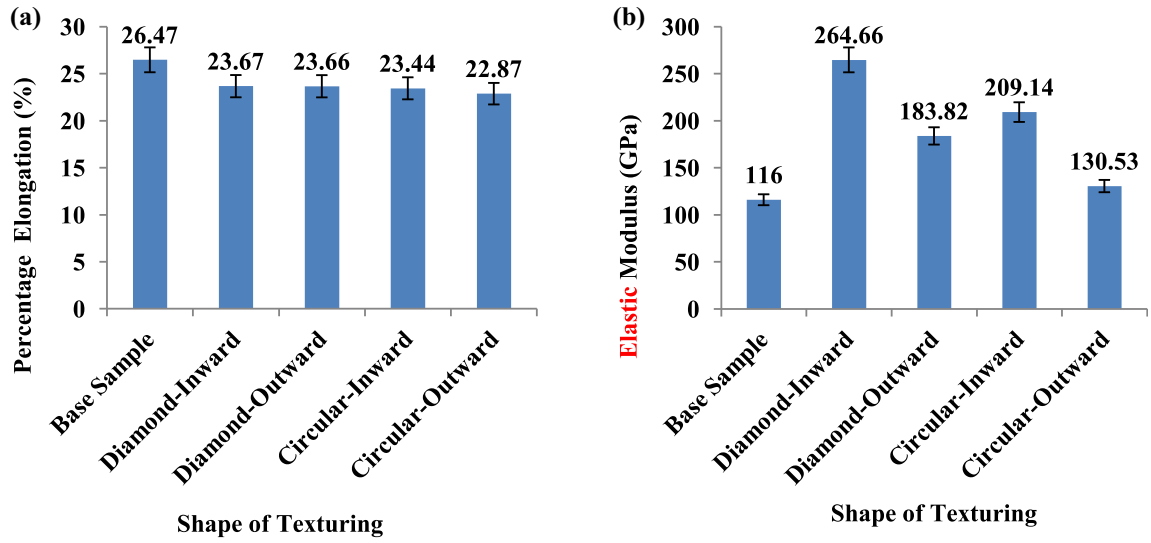

Fig. 10 (a) Percentage elongation and (b) modulus values of various textured and untextured samples

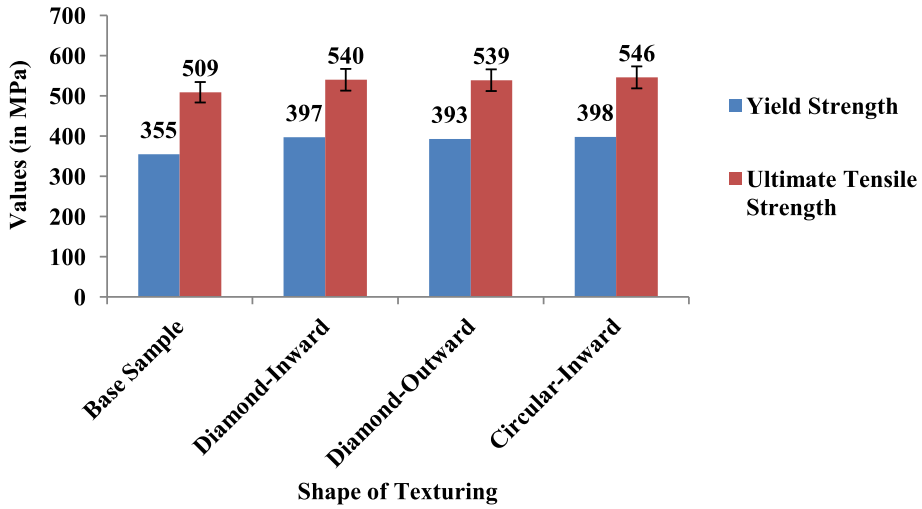

Fig. 11 The yield and ultimate tensile strength values of various textured and untextured samples

can be due to the creation of microcracks or other defects on the surface of the material during the laser surface texturing process, which can weaken the material and reduce its tensile strength. The modulus of elasticity is the measure of stiffness or resistance to deformation when subjected to an applied force. Fig. 9(b) shows that the young's modulus or elastic modulus values have enhanced for all the textured samples as compared to the untextured samples. The elastic modulus values of the diamond-inward textured has to be observed as the highest value among all textured and untextured samples. The enhancement in the resistance to deformation of textured samples is due to the increase in the value of hardness i.e., HV (0.3) 204.43 which is almost close to the highest value i.e., HV (0.3) 205.53. Moreover, the diamond-inward texture likely increases the effective density of these bonds per unit volume by introducing more surfaces and edges within the material. This can lead to more bond interactions and constraint, thereby increasing the overall rigidity and stiffness, reflected in a higher Young's modulus.

3.2.3 Flexural Test. The test was conducted as per the ASTM- D790 standard. The averages of three readings were considered with a deviation of approximate ± 5%.

The values of various properties were obtained from stress versus strain curve as shown in Fig. 12(a-e). The values of properties such as flexural strength and yield strength are shown in Fig. 13 and 14, respectively.

Laser surface texturing has an effect on flexural strength which is the material's resistance to bending and breaking under

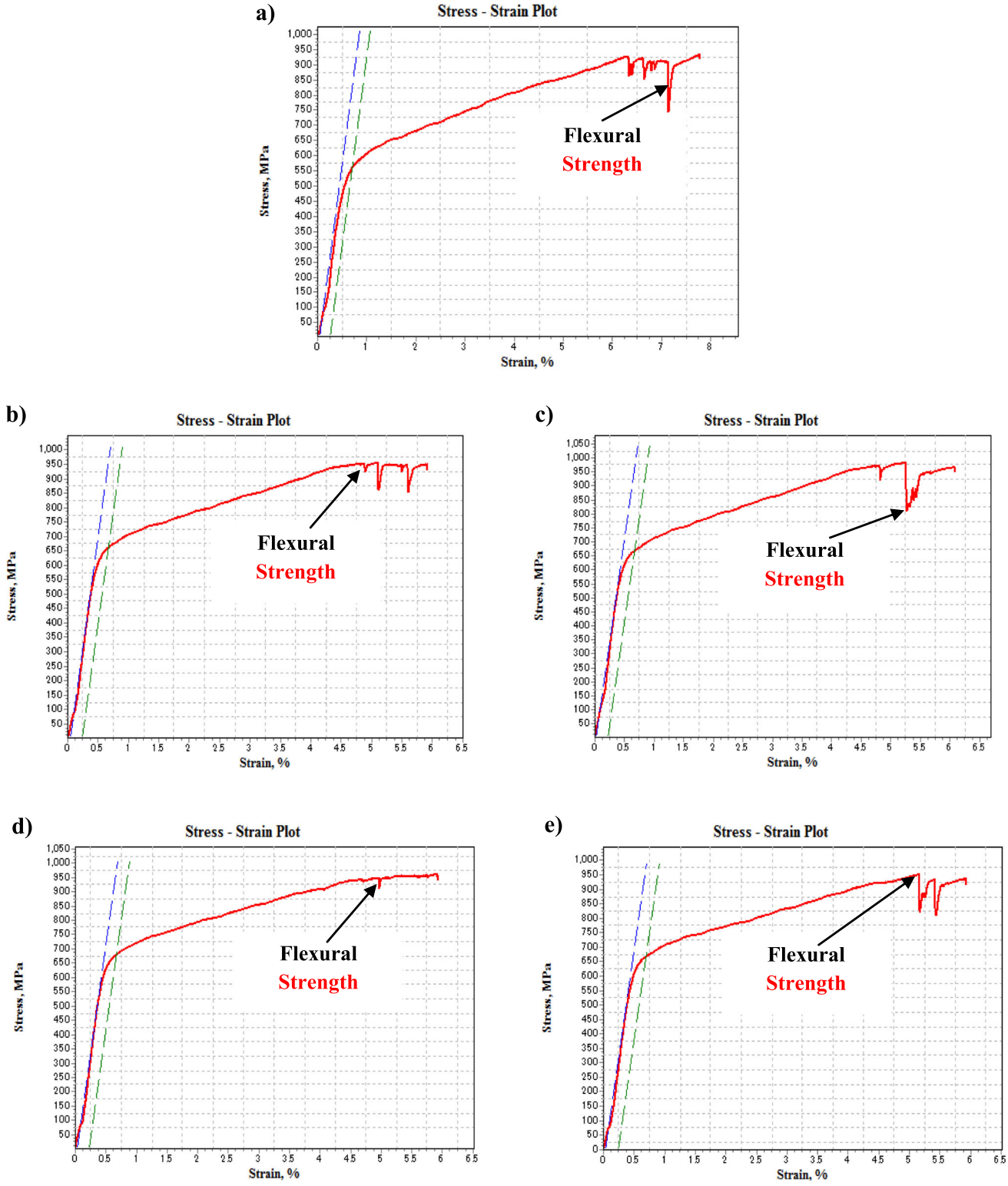

Fig. 12 Stress-strain curve obtained from the flextural test of (a) un-textured, (b) diamond-inward, (c) diamond-outward, (d) circular-inward and (e) circular-outward shape texturing

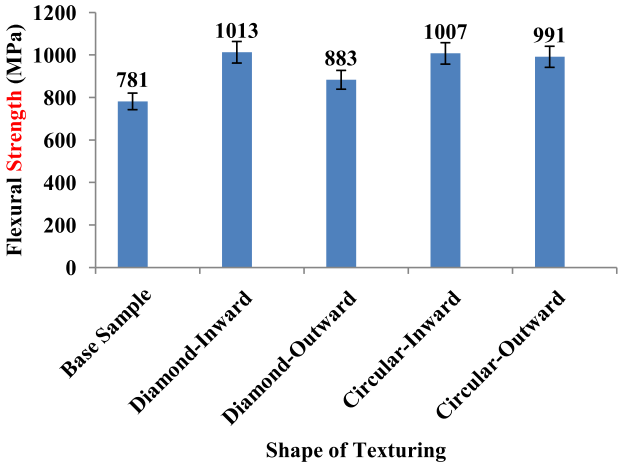

Fig. 13 The flexural strength values of various textured and untextured samples

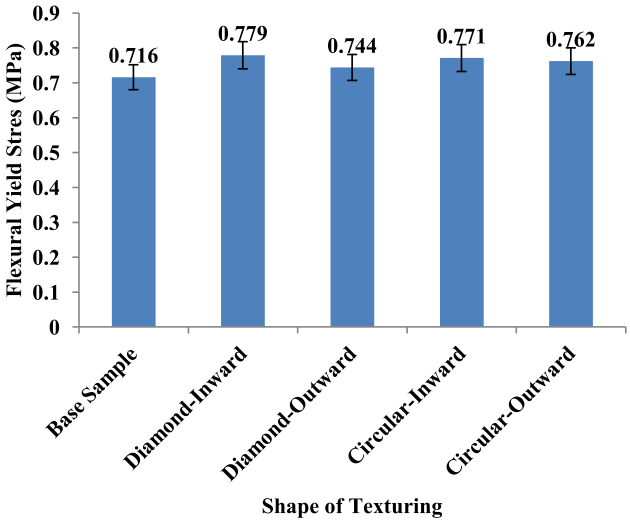

Fig. 14 The flexural yield stress values of various textured and untextured samples

a load. By altering the surface texture, laser surface texturing has increased the material's flexural strength as shown in Fig. 13; this is because the microcavities or grooves can create a rougher surface that provides more friction and surface area for the material to resist deformation. Additionally, the texture can help distribute the load more evenly across the surface, reducing the risk of localized stress concentrations that can lead to failure. The value of flexural strength is more for diamond-inward as compared to other untextured and textured samples. The flexural strength is the highest i.e., 1013 MPa for diamond-inward samples due to its high hardness value also.

Moreover, laser surface texturing affects flexural yield strength, which is the maximum stress a material can withstand before it starts to deform permanently. By altering the surface texture, laser surface texturing has increased the material's yield strength as shown in Fig. 14, by creating more surface area for stress to be distributed across, as well as reducing the risk of stress concentration. The value of flexural yield strength is more for diamond-inward as compared to other untextured and textured samples.

3.3 Slurry Jet Erosion Test

The test was conducted as per the ASTM G-136 standard (34). The averages of three readings were considered with a deviation of approximate ± 5%. The variation of erosion rate with impingement angle (15°, 30°, 45°, 60°, 75°, and 90°) is shown in Fig. 15. The circular-inward-textured shape samples show high erosion resistance as compared to other untextured and textured samples. The untextured samples show less erosion resistance as compared to other textured samples. In general, the erosion behavior of the untextured material is primarily depended on the hardness value. The shape of texturing is enhanced the erosion resistance behavior. The hardness value of diamond- and circular-inward was the highest and almost comparable as compared to others. The slurry erosion rate was observed to be very less in these textured shapes.

The authors reviewed various kinds of literature and conclude an important fact that the rotation of fluid flow over the textured dimples, which leads to the air cushion effect, enhances the fluid flow, and decreases the impact of abrasives on the surface (5). The mechanism of erosion in circular and diamond in shape textured is shown in Fig. 16. In Fig. 16(a), impinges slurry showed circular or swirl motion at the textured area, this swirl motion enhances the erosion resistance. In Fig. 16(b), the circular or swirl motion is not so effective due to diamond in shape texturing having sharp corners which creates obstacles in the swirling motion. This ineffective effect of swirling enhances the erosion rate compared to the circular in shape texturing dimples.

The surface is like a hill and valley in the case of circular-out and diamond-out as shown in Fig. 17(a) and (b), respectively, the bumpy place reduces the distance between the nozzle tip and impact surface, which reduces the erosion rate but in diamond-out, the erosion rate was little higher due to sharp edges or stress concentration at the top of the tip. The gaps between the two bumpy surfaces create little circulation which also reduces the erosion rate as compared to untextured surfaces as shown in Fig. 17(c).

3.3.1 Scanning Electron Micrographs (SEM). As shown in Fig. 18(a)-(e), the major mechanism of material removal at 45° impingement angle (such as microcutting lips, plowing, crater formation, and carbide pull-out) has been observed using scanning electron micrographs.

The micrograph 18a (untextured sample) has shown; the majority of the material has worn out in the form of a larger carbide particle pull-out mechanism. The textured surface such as diamond-out, circular-out, diamond-in, and circular-in micrographs is shown in Fig. 18(b)-(e), respectively. The

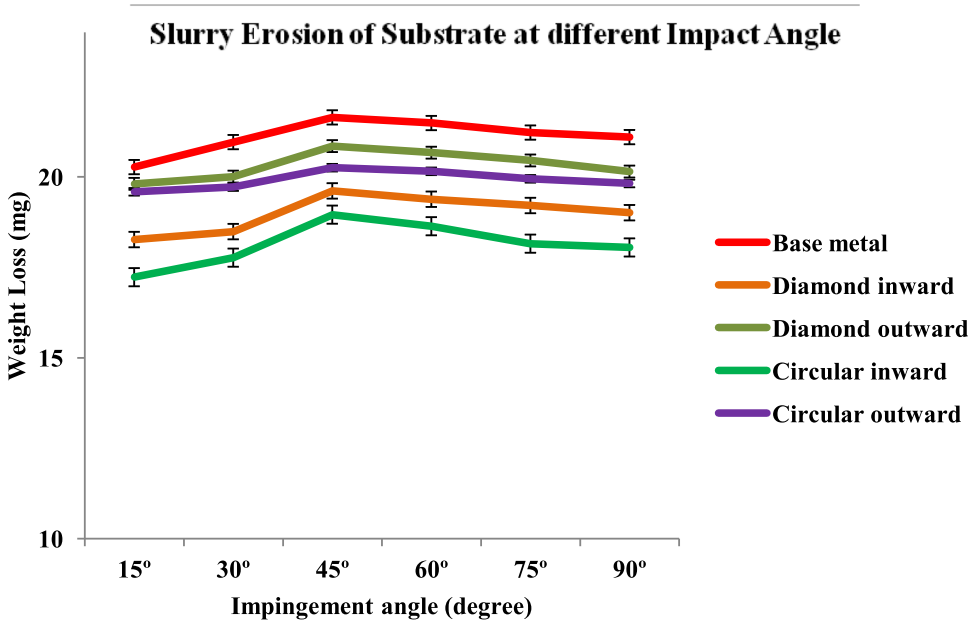

Fig. 15 The erosion rate versus impingement angle of various textured and untextured samples

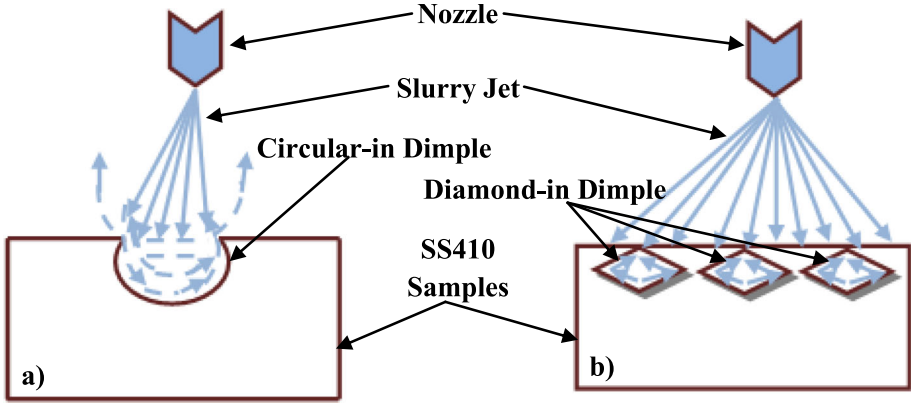

Fig. 16 The mechanism of erosion in (a) circular-in and (b) diamond-in

circular-in textured surface showed considerably good erosion resistance among all the considered samples for the experiment.

3.4 Contact Angle Measurement

As shown in Fig. 19(a)-(e), the wettability behavior of the surface has been analyzed using a sessile droplet test by measuring the contact angle on the textured and untextured surfaces. The test was carried out according to the ASTM D7334-08(2013) standard.

The wettability behavior of any surface is majorly dependent on the roughness of that surface. The effect of surface roughness on wettability behavior has been justified using Wenzel and Cassie Baxter's model as shown in Fig. 20(a) and (b) respectively (Ref 35, 36). Introducing the roughness on any surface increases the trapping of air in the roughened area, which enhances the hydrophobic behavior of the surface (Ref 37, 38).

It is familiar that the categorization of wettability behavior is based on the value of contact angle, if the contact angle of any surface is less than 90°, then the surface is categorized as hydrophilic; otherwise, the surface is hydrophobic in nature (Ref 39–41). As shown in Fig. 19(b)-(e), the textured sample shows a higher water contact angle as compared to the

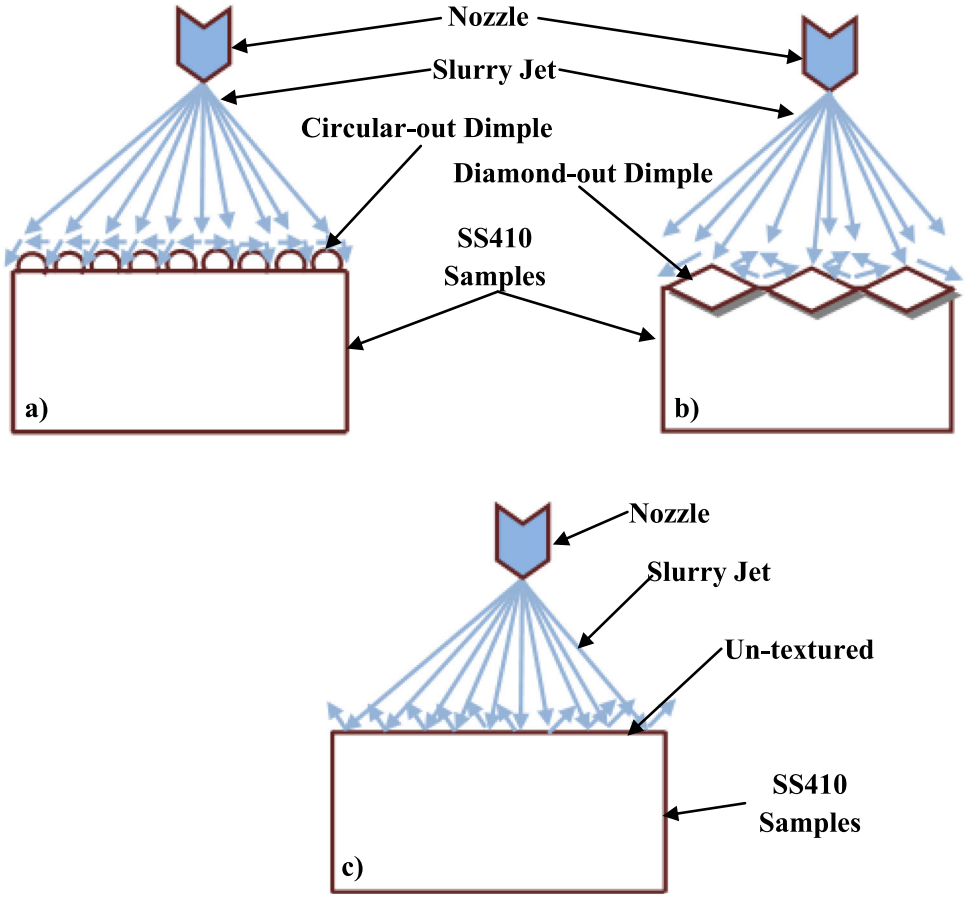

Fig. 17 The erosion mechanism of (a) circular-out, (b) diamond-out, and (c) untextured

untextured sample. The value of the contact angle for textured surfaces was greater than 90 degrees which turns out the textured surface to be hydrophobic in nature compared to untextured having a contact angle of 62.6 ± 2 degrees as shown in Fig. 19(a), which leads the surface to be hydrophilic. The surface having microbumps as shown in Fig. 19(c) and (e) has more contact angle compared to the micropits in Fig. 19(b) and (d). Moreover, surface texturing of any kind has enhanced the hydrophobicity compared to untextured surfaces.

4. Conclusions

The following conclusion has been made from the above experiments:

1. The hardness values for various shape of a textured surface on stainless steel is estimated using the Vickers hardness test are in the increasing order of untextured < diamond-out < circular-out < diamond-in < circular-in.
2. The tensile and flexural strength of all types of textured surfaces is considerably higher than the untextured surface.
3. The modulus of elasticity has been enhanced for all the textured samples than untextured samples. Moreover, the modulus value for diamond-in textured sample has the highest i.e., ≈265GPa.
4. From the slurry erosion test, the erosion resistance is remarkably improved for all types of considered texturing; moreover, the highest erosion resistance is obtained in the case of a circular-in pattern.
5. From SEM micrographs; plowing, microcutting, crater wear, and carbide pull-out are wear mechanisms observed.
6. The wettability behavior of surfaces is anticipated from contact angle measurements in the increasing order untextured < diamond-in < circular-in < circular-out < diamond-out. After texturing the obtained surface showed hydrophobicity behavior and the contact angle is merely the same for all textured patterns.

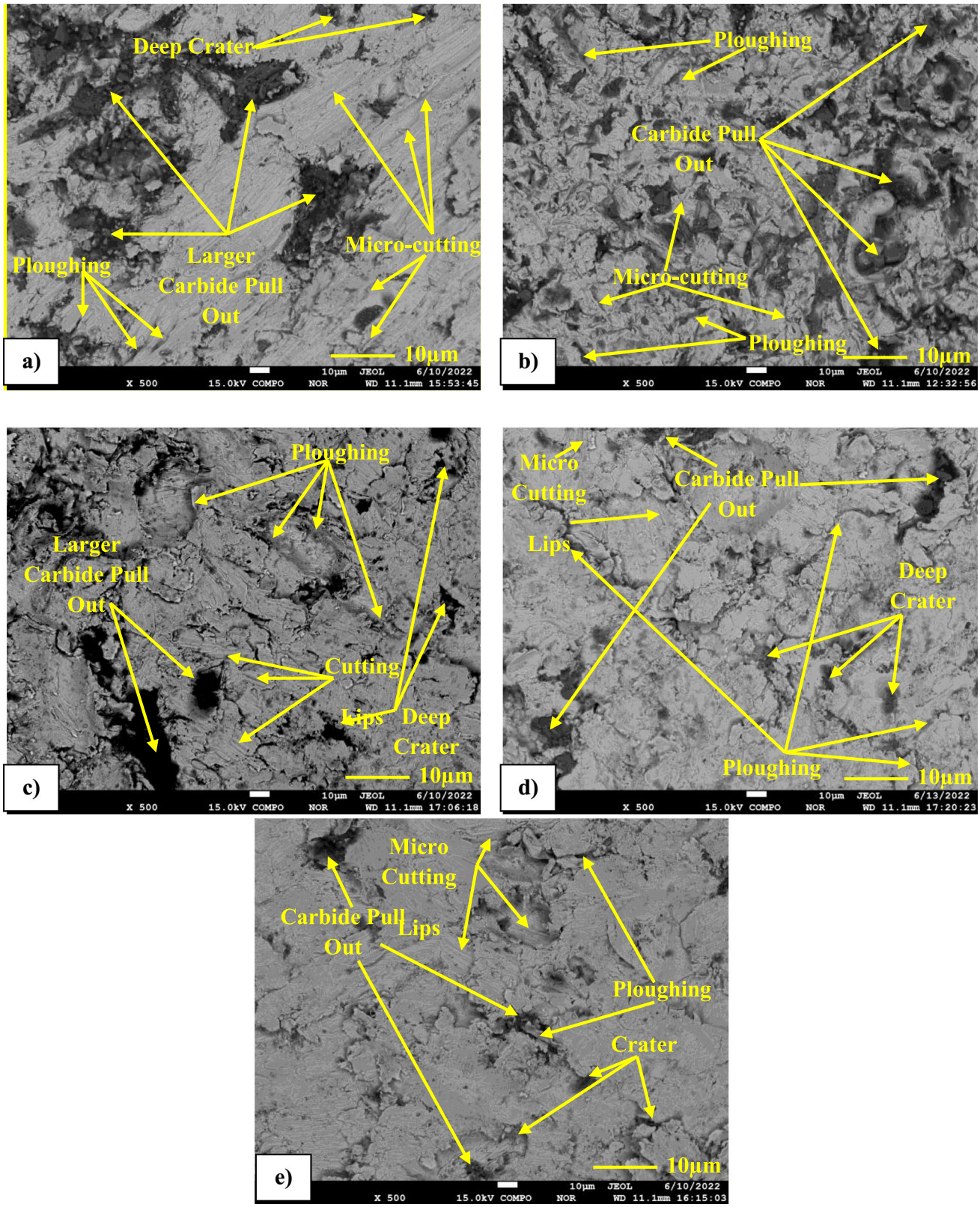

Fig. 18 Few micrographs of (a) untextured, (b) diamond-out, (c) circular-out, (d) diamond-in, and (e) circular-in textured stainless steel (SS410) at 45° impingement angle, respectively

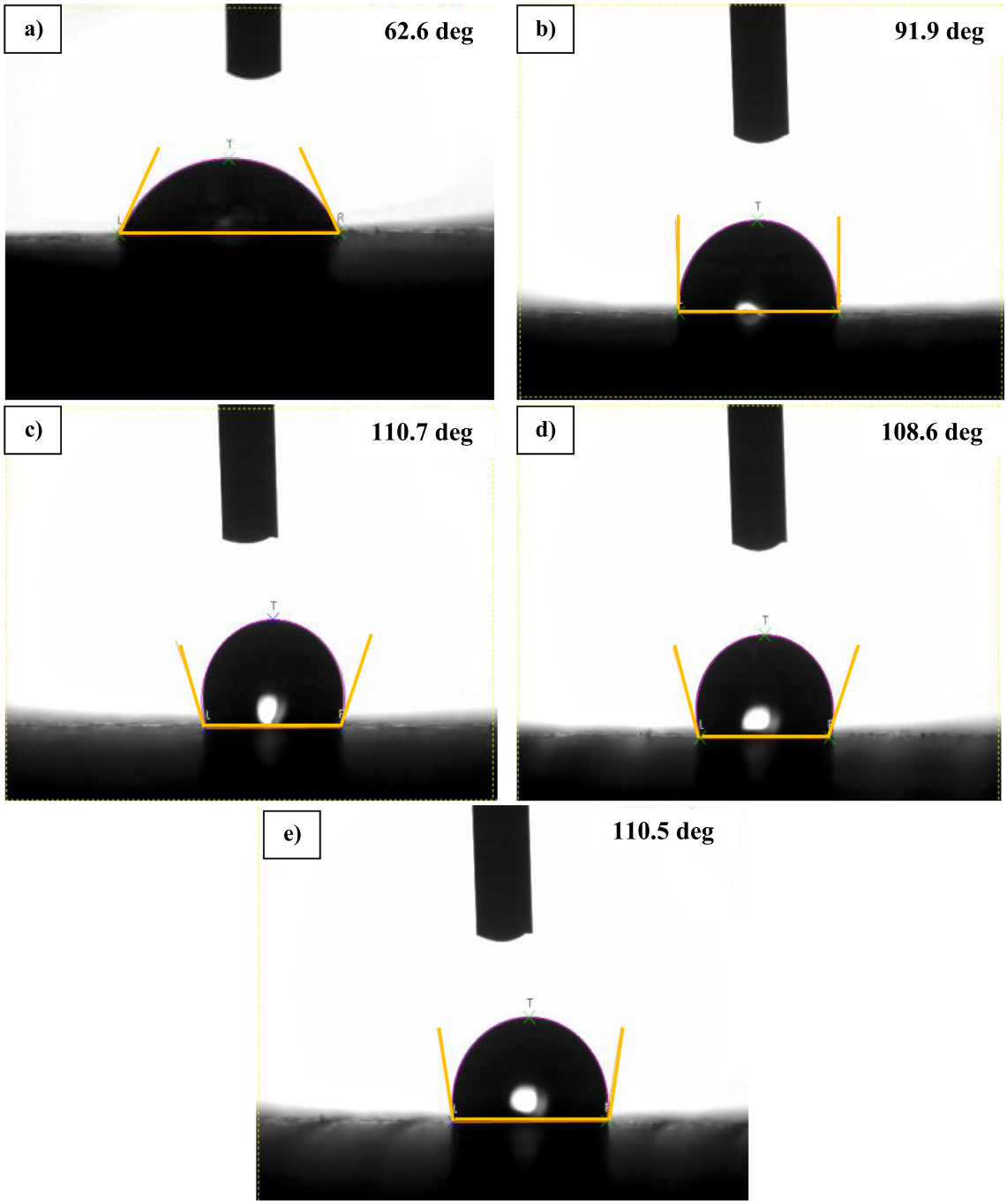

Fig. 19 Contact angle measurement of (a) untextured, (b) diamond-in, (c) diamond-out, (d) circular-in, and (e) circular-out SS410

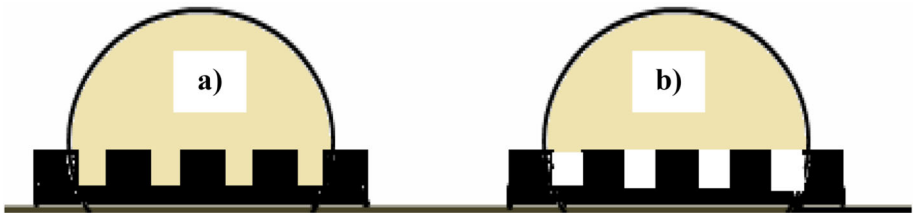

Fig. 20 Possibilities of the interaction of drop with the pattern (a) Wenzel and; (b) Cassie state model (Ref 35, 36)

4.1 Future Scope

This work further can be carried out for tribological characterization on pin on disk/ball test to know the coefficient of friction with and without lubrication. Moreover, different existing coating methods can also be applied to coat the textured surface.

Acknowledgment

The author would like to thank Precision Manufacturing Lab at Delhi Technological University, Delhi, and the Indian Institute of Technology, Kanpur for helping us in the Characterization (Mechanical and Surface) of the textured and untextured SS410.

Author Contribution

Mohit Vishnoi was contributed conceptualization, investigation, data curation, and writing–original draft. Qasim Murtaza was involved in conceptualization, review and editing, and supervision. Paras Kumar was performed review and editing and supervision.

Funding

No funding was received to assist with the preparation of this manuscript.

Conflict of interest

The authors declare that they have no known competing financial interests or personal relationships that could have appeared to influence the work reported in this paper.

Ethics Approval and Consent to Participate

This chapter does not contain any studies with human participants or animals performed by any of the authors. Informed consent was obtained from all authors included in the study.

Consent to Publish

Consent was obtained from all authors to publish in the journal.

References

1. T. Hu, L. Hu and Q. Ding, The Effect of Laser Surface Texturing on the Tribological Behavior of Ti-6Al-4V, *Proc. Inst. Mech. Eng. Part J: J. Eng. Tribol.*, 2012, **226**(10), p 854–863.
2. J. Bonse, S. Höhm, S.V. Kirner, A. Rosenfeld and J. Krüger, Laser-Induced Periodic Surface Structures—A Scientific Evergreen. *IEEE J. Sel. Top. Quantum. Electron.,* 2016, **23**(3)
3. E. Kostal, S. Stroj, S. Kasemann, V. Matylitsky and M. Domke, Fabrication of Biomimetic Fog-Collecting Superhydrophilic–Superhydrophobic Surface Micropatterns using Femtosecond Lasers, *Langmuir*, 2018, **34**(9), p 2933–2941.
4. H. Yamakiri, S. Sasaki, T. Kurita and N. Kasashima, Effects of Laser Surface Texturing on Friction Behavior of Silicon Nitride under Lubrication with Water, *Tribol. Int.*, 2011, **44**(5), p 579–584.
5. M. Vishnoi, P. Kumar and Q. Murtaza, Surface Texturing Techniques to Enhance Tribological Performance: A Review, *Surf. Interfaces*, 2021, **27**, 101463
6. F. Soltani-Kordshuli, C. Miller, N. Harris and M. Zou, Laser Surface Texturing of Both Thin Polytetrafluoroethylene Coatings and Stainless Steel Substrates for Improving Tribological Properties, *Polym. Test.*, 2023, **117**, 107852
7. A. Borghi, E. Gualtieri, D. Marchetto, L. Moretti and S. Valeri, Tribological Effects of Surface Texturing on Nitriding Steel for High-Performance Engine Applications, *Wear*, 2008, **265**(7–8), p 1046–1051.
8. I. Etsion, State of the Art in Laser Surface Texturing, *Eng. Syst. Des. Anal.*, 2004, **41731**, p 585–593.
9. B. Mao, A. Siddaiah, Y. Liao and P.L. Menezes, Laser Surface Texturing and Related Techniques for Enhancing Tribological Performance of Engineering Materials: A Review, *J. Manuf. Process*, 2020, **53**, p 153–173.
10. I. Šulák, K. Obrtlík and L. Čelko, High Temperature Low Cycle Fatigue Characteristics of Grit Blasted Polycrystalline Ni-Base Superalloy, *Key Eng. Mater.*, 2016, **665**, p 73–76.
11. T. Hu, L. Hu and Q. Ding, Effective Solution for the Tribological Problems of Ti-6Al-4V: Combination of Laser Surface Texturing and Solid Lubricant Film, *Surf. Coat. Technol.*, 2012, **206**(24), p 5060–5066.
12. D. Braun, C. Greiner, J. Schneider and P. Gumbsch, Efficiency of Laser Surface Texturing in the Reduction of Friction Under Mixed Lubrication, *Tribol. Int.*, 2014, **77**, p 142–147.
13. E. Gualtieri, A. Borghi, L. Calabri, N. Pugno and S. Valeri, Increasing Nanohardness and Reducing Friction of Nitride Steel by Laser Surface Texturing, *Tribol. Int.*, 2009, **42**(5), p 699–705.
14. D. He, S. Zheng, J. Pu, G. Zhang and L. Hu, Improving Tribological Properties of Titanium Alloys by Combining Laser Surface Texturing and Diamond-Like Carbon Film, *Tribol. Int.*, 2015, **82**, p 20–27.
15. S.C. Vlădescu, A.V. Olver, I.G. Pegg and T. Reddyhoff, Combined Friction and Wear Reduction in a Reciprocating Contact Through Laser Surface Texturing, *Wear*, 2016, **358**, p 51–61.
16. J.I. Ahuir-Torres, M.A. Arenas, W. Perrie, G. Dearden and J. De Damborenea, Surface Texturing of Aluminium Alloy AA2024-T3 by Picosecond Laser: Effect on Wettability and Corrosion Properties, *Surf. Coat. Technol.*, 2017, **321**, p 279–291.
17. V. Singh, A.K. Singla and A. Bansal, Influence of Laser Texturing on Hydrophobicity and Slurry Erosion Behaviour of VC-CuNiCr Based HVOF Coatings, *Surf. Topogr. Metrol. Prop.*, 2023, **11**(3), 035005
18. Y. Liu, Z. Zhang, H. Hu, H. Hu, A. Samanta, Q. Wang and H. Ding, An Experimental Study to Characterize a Surface Treated with a Novel Laser Surface Texturing Technique: Water Repellency and Reduced Ice Adhesion, *Surf. Coat. Technol.*, 2019, **374**, p 634–644.
19. G. Boidi, I.S. Tertuliano, L.G.B.S. Lima, F.J. Profito and I.F. Machado, Porosity Effect of Sintered Steel on the Frictional Performance of Conformal and Nonconformal Lubricated Contacts, *Tribol. Trans.*, 2019, **62**(6), p 1029–1040.
20. D. Kümmel, M. Hamann-Schroer, H. Hetzner and J. Schneider, Tribological Behavior of Nanosecond-Laser Surface Textured Ti6Al4V, *Wear*, 2019, **422**, p 261–268.
21. M. Vishnoi, Q. Murtaza and P. Kumar, Mechanical and Surface Wettability Analysis of Rare Earth Modified Composite Coating Developed using Metal Spraying, *Arab. J. Sci. Eng.*, 2024, **49**(2), p 2065–2076.
22. X. Lei, N. Lin, S. Yuan, C. Lei, M. Nouri, Z. Liu and Y. Wu, Combining Laser Surface Texturing and Double Glow Plasma Surface Chromizing to Improve Tribological Performance of Ti6Al4V Alloy, *Surf. Coat. Technol.*, 2024, **478**, p 130418.
23. J.I. Ahuir-Torres, H.R. Kotadia, T.T. Öpoz and M.C. Sharp, A Study on the Corrosion Behaviour of Laser Textured Pure Aluminium in Saltwater, *Processes*, 2023, **11**(3), p 721.
24. S. Velayuthaperumal and R. Radhakrishnan, A Novel Nanosecond Pulsed Laser Textured Moat Configurations for Enhancing Surface Wettability, Corrosion and Tribology Behaviour of Ti6Al4V Implant Material, *Mater. Today Commun.*, 2024, **39**, 108701
25. L. Calabrese, A. Khaskhoussi, S. Patane and E. Proverbio, Assessment of Super-Hydrophobic Textured Coatings on AA6082 Aluminum Alloy, *Coatings*, 2019, **9**(6), p 352.
26. S. Chen, G. Qian and L. Yang, Precise Control of Surface Texture on Carbon Film by Ion Etching through Filter: Optimization of Texture Size for Improving Tribological Behavior, *Surf. Coat. Technol.*, 2019, **362**, p 105–112.
27. W. Zhou, J. Tang and W. Shao, Modelling of Surface Texture and Parameters Matching Considering the Interaction of Multiple Rotation

Cycles in Ultrasonic Assisted Grinding, *Int. J. Mech. Sci.*, 2020, **166**, 105246
28. M. Conradi, T. Sever, P. Gregorčič and A. Kocijan, Short-and Long-Term Wettability Evolution and Corrosion Resistance of Uncoated and Polymer-Coated Laser-Textured Steel Surface, *Coatings*, 2019, **9**(9), p 592.
29. H. Fan, Y. Su, J. Song, H. Wan, L. Hu and Y. Zhang, Design of "Double Layer" Texture to Obtain Superhydrophobic and High Wear-Resistant PTFE Coatings on the Surface of Al_2O_3/Ni Layered Ceramics, *Tribol. Int.*, 2019, **136**, p 455–461.
30. Y. Yu, S. Bai, S. Wang and A. Hu, Ultra-Short Pulsed Laser Manufacturing and Surface Processing of Microdevices, *Engineering*, 2018, **4**(6), p 779–786.
31. R. Srinivasan, E. Sutcliffe and B. Braren, Ablation and Etching of Polymethylmethacrylate by Very Short (160 fs) Ultraviolet (308 nm) Laser Pulses, *Appl. Phys. Lett.*, 1987, **51**(16), p 1285–1287.
32. H.J. Booth, Recent Applications of Pulsed Lasers in Advanced Materials Processing, *Thin Solid Films*, 2004, **453**, p 450–457.
33. M. Vishnoi, Q. Murtaza and P. Kumar, Mechanical and Erosion Characterization of Untreated and Solution-Treated Nitrogen-Alloyed (23–8N) Austenitic Stainless Steel, *J. Mater. Eng. Perform.*, 2023, **32**(24), p 11107–11117.
34. M. Vishnoi, Q. Murtaza and P. Kumar, Mechanical and Surface Characterization of $Er_2O_3/La_2O_3/CeO_2$ Doped Carbide Coating Developed using High Velocity Oxy Fuel (HVOF), *Phys. Scr.*, 2023, **98**(11), 115618
35. R.N. Wenzel, Resistance of Solid Surfaces to Wetting by Water, *Ind. Eng. Chem.*, 1936, **28**(8), p 988–994.
36. A.B.D. Cassie and S. Baxter, Wettability of Porous Surfaces, *Trans. Faraday Soc.*, 1944, **40**, p 546–551.
37. C.C. De Foggi, A.L. Machado, C.A. Zamperini, D. Fernandes, A.F. Wady and C.E. Vergani, Effect of Surface Roughness on the Hydrophobicity of a Denture-Base Acrylic Resin and C Andida Albicans Colonization, *J. Investig. Clin. Dent.*, 2016, **7**(2), p 141–148.
38. A.T. Kittu, R. Bulut and J. Puckette, Effects of Surface Roughness on Contact Angle Measurements on a Limestone Aggregate. In: Recent Developments in Evaluation of Pavements and Paving Materials p 1–8 2014
39. M. Vishnoi, V. Muthupandi and S.S. Murugan, Characterization of Hydrophobic Coating Developed by Micro Arc Oxidation on AA2014 Alloy 2017
40. W. Liu, Y. Luo, L. Sun, R. Wu, H. Jiang and Y. Liu, Fabrication of the Superhydrophobic Surface on Aluminum Alloy by Anodizing and Polymeric Coating, *Appl. Surf. Sci.*, 2013, **264**, p 872–878.
41. M. Vishnoi, Q. Murtaza and P. Kumar, Characterization of Erbium Oxide Doped HP-HVOF Deposited Carbide Ceramic Coating on Martensitic Steel, *Proc. Inst. Mech. Eng. Part C J. Mech. Eng. Sci.*, 2023, **237**(23), p 5743–5754.

Publisher's Note Springer Nature remains neutral with regard to jurisdictional claims in published maps and institutional affiliations.

Springer Nature or its licensor (e.g. a society or other partner) holds exclusive rights to this article under a publishing agreement with the author(s) or other rightsholder(s); author self-archiving of the accepted manuscript version of this article is solely governed by the terms of such publishing agreement and applicable law.

BlipGlyphDiff: Glyph-Based Text to Image Generation with Different Styles and Background

Ansh Anurag, CSE Dept., Delhi Technological University, New Delhi, India (anshanurag@ieee.org)

Bhaskar Anand, CSE Dept., Delhi Technological University, New Delhi, India (bhaskaranand025@gmail.com)

Ankush Bhagat, CSE Dept., Delhi Technological University, New Delhi, India (ankushbhagat14@gmail.com)

***Abstract*—The creation of text-to-image generative models that use diffusion-based methods to generate logical and aesthetically pleasing textual content has attracted increasing attention in recent times. To address this goal, a new and effective technique called BlipGlyphDiff is presented in this study. In contrast to previous methods that rely on character-sensitive text encoders like ByT5 and necessitate retraining and fine-tuning of text-to-image models, our approach makes use of extra glyph conditional information to improve the performance of the readily available Stable-Diffusion model for producing accurate visual text. Users can adjust the generated text's content, layout, and size to suit their needs by integrating glyph instructions. This research project, titled "BlipGlyphDiff: Glyph-Based Text to Image Generation with Different Styles and Background" utilizes a pre-trained benchmark dataset called LAION-Glyph[1]. Our experimental assessments highlight the efficacy of our approach by showing that our model outperforms contemporary methods incorporated in DALL·E 2, Midjourney, and Ideogram in terms of Fréchet Inception Distance score, similarity score in text embeddings, and Optical Character Recognition accuracy.**

Keywords: Text-to-image generation, Diffusion, BlipGlyphDiff, Glyph conditional information, Stable-Diffusion model, Visual text generation, LAION-Glyph dataset, Fréchet Inception Distance (FID) score, CLIP score, Optical Character Recognition (OCR) accuracy.

I. INTRODUCTION

The growth of universal text-to-image production has progressed manifolds by the development of noising-denoising based diffusion probabilistic models[5], which demonstrate the capability of producing exceptionally high-resolution images with great relevance to the prompt used. Even though there are a lot of diffusion-based techniques that can create a lot of beautiful and realistic images, most of them still lack in the production of specific text that is clear and readable in the generated images [29, 30]. The complex structure that visual language has by nature presents this difficulty alongside the customized styles utilized to present text in an image. Studies show that most popular text-to-image generation model text encoders do not have enough character-level information to spell words correctly, mostly because they use a BPE tokenizer[39]. As such, it has been noted that switching to character-aware models can result in significant improvements. Additionally, problems like errors in layout—such as missing or combined glyphs—remain in the output images even after efforts to improve text encoders inside generation models have been made [20]. This implies that accurate visual text rendering might not be possible with only textual input prompts. To address this problem, we suggest incorporation of text glyph data into the robust text-to-image generation models that we currently use for the production of visual text in an image. We formulate the challenge of creating visual text as a glyph-conditional control task. More specifically, we propose to use an extra glyph picture to manage the visual text production. This glyph, in turn acts as a clear spatial layout guide, directing the diffusion models[5] to produce visually structured and cohesive text. In addition, our method uses the ControlNet[37] encoder. The ControlNet is robust even when trained on small datasets since it learns task-specific circumstances in an end-to-end manner.

In the project **"BlipGlyphDiff: Glyph-Based Text to Image Generation with Different Styles and Background"**, we present a major breakthrough in our implementation: the BlipGlyphDiff framework that we created, which is intended to improve the pre-made text-to-image generation model by using a ControlNet[37] branch to extract shape information from the glyph image. Specifically, we used the 5 billion text-image pairs in the LAION-5B Training Dataset and the 50 million text-image pairs in the LAION-Glyph benchmark [1] for this purpose. Furthermore, we created two assessment benchmarks, EasyBench and HardBench, to compare our model's performance to other reliable, already-in-use methodologies. We carried out extensive studies to demonstrate the effectiveness of our strategy, and we discovered that, in comparison to DeepFloyd IF[40], our method consistently produced much greater OCR[1] accuracy and similarity score. We provide empirical evidence that users can modify the generated visual text's content, placement, and size.

II. MOTIVATION

Present-day text-to-image tools are able to produce fantastic visuals from descriptions, but they have difficulty rendering text understandable within such images. This is a significant task. Diffusion models[5] are excellent at producing images, but they frequently struggle with accurately representing text. We offer a new approach, BlipGlyphDiff, to solve this, which enhances the current text-to-image models[41]. It gives the user far greater control over the created image's text, including size, content, and arrangement. This is made possible by a unique part known as ControlNet[37], which makes use of data from pre-prepared text pictures.

Our model seeks to provide greater customization in order to address the shortcomings of the existing text-to-image generating technology. Users can provide the text precise directions, which produces more distinctive and eye-catching outcomes. Based on our tests, our model effectively provides users with fine-grained control over the generated text. This makes it an effective tool for producing text inside of photos in an excellent manner and being highly configurable.

2024 IEEE Region 10 Symposium (TENSYMP) | 979-8-3503-6486-6/24/$31.00 ©2024 IEEE | DOI: 10.1109/TENSYMP61132.2024.10752310

979-8-3503-6486-6/24/$31.00 ©2024 IEEE

Authorized licensed use limited to: DELHI TECHNICAL UNIV. Downloaded on November 25,2024 at 04:43:41 UTC from IEEE Xplore. Restrictions apply.

III. OBJECTIVE

A. *Develop a Robust Representation Learning Framework:*

The BlipGlyphDiff framework elevates existing text-to-image generation models by incorporating a dedicated ControlNet branch that leverages the rich shape information within glyph images. This approach establishes a powerful representation learning mechanism specifically tailored to the intricacies of visual text generation.

B. *Incorporate Variated Style and Background Generation Techniques:*

Implement techniques inspired by GLIDE and Imagen to incorporate varied style and background generation capabilities into our model. This entails leveraging cascaded diffusion models and generic large language models to ensure comparable or superior image quality while accommodating diverse visual styles and backgrounds.

C. *Accommodate Glyph Conditional Text Inputs:*

Propose integrating glyph-based text inputs into the text-to-image generation process to empower users with fine-grained control over text in generated images. This approach leverages ControlNet [37] as the foundation. By providing glyph instructions through the user interface, users can specify the content, placement, and size of the visual text within the generated image. Essentially, ControlNet [37] would be adapted to manage the local structure of the image using these additional glyphs, ensuring the generated text aligns with the user's specifications. In order to encode the text information, the BLIP [17] model is utilized.

D. *Benchmark Against Existing Methods:*

Conduct comprehensive benchmarking against existing methods such as unCLIP, Stable Diffusion, Imagen, eDiff-I, DeepFloyd IF, DALL·E 3, and GlyphDraw to evaluate the performance of the BlipGlyphDiff framework. This includes assessing the flexibility, customization, and overall effectiveness of the proposed approach in comparison to state-of-the-art techniques.

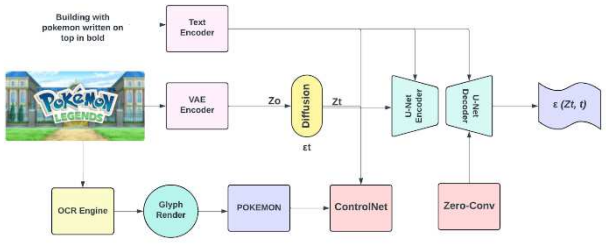

Fig. 1: *The Figure shows the Training Pipeline of BlipGlyphDiff.*

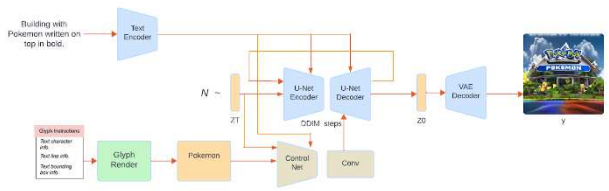

Fig. 2: *The Figure shows the Inference Pipeline of BlipGlyphDiff.*

IV. THEORY

A. *Stable Diffusion*

Stable Diffusion Base 2 (SD 2.0-base4) significantly improves text-to-image generation by building on the core concepts of Stable Diffusion. This advanced model leverages cutting-edge techniques to produce exceptional image quality, surpassing its predecessor. The foundation of SD 2.0-base4 lies in a robust training framework that incorporates a powerful CLIP text encoder and additional training data. This ensures better outcomes for generating high-quality visuals.

To achieve this leap in quality, SD 2.0-base4 utilizes several innovative methods, including a secondary text encoder and a significantly larger U-Net architecture. The creators specifically chose "stable-diffusion-2-base" as the base model. This meticulously trained model undergoes an intensive training process, requiring hundreds of hours on powerful GPUs. The training focuses on a curated subset of the LAION-5B dataset known for its aesthetic quality.

B. *ControlNet Encoder*

Neural network designs have advanced significantly with the ControlNet encoder, especially in the area of conditional input learning. This novel model learns end-to-end task-specific conditions and shows impressive robustness even when trained on short datasets, typically fewer than 50,000 samples. The ControlNet encoder's effectiveness in training is one of its most notable qualities. ControlNet is incredibly accessible, even on personal devices, as it can be trained as quickly as a diffusion model, in contrast to many other intricate neural network architectures. Furthermore, the ControlNet model scales easily to handle big datasets with millions to billions of data points for users with access to strong computation clusters. One key benefit of the ControlNet encoder is its ability to enhance large diffusion models, such as Stable Diffusion, by incorporating various conditional inputs. These inputs can include edge maps, segmentation maps, and key points, allowing for more control over the image generation process. By improving large diffusion model control techniques, this integration creates new opportunities for creative applications in a variety of fields. All things considered, the ControlNet encoder, with its efficiency, scalability, and diversity, is a significant breakthrough in conditional input learning. The amalgamation of huge diffusion models with it has great potential to enhance the functionalities of neural networks and enable an extensive array of uses in domains like computer vision, natural language processing, and more.

C. *BLIP-2*

BLIP-2 generates text embeddings that are used in the training and inference pipeline while encoding the media. It acts as a benchmark engine to generate text embeddings from

Authorized licensed use limited to: DELHI TECHNICAL UNIV. Downloaded on November 25,2024 at 04:43:41 UTC from IEEE Xplore. Restrictions apply.

the resulting image and compare the similarity with the embedding of the prompt used to generate the resulting image.

V. Approach

A. BlipGlyphDiff

The model is a recent advancement in text-to-image generation that grants users significant control over the text appearing in the final image. This method utilizes predefined symbols, known as glyphs, to provide conditional information that influences the image generation process through a specialized network called ControlNet [37]. Our model offers several advantages. It improves the accuracy of the generated text by reducing spelling errors and enhancing character formation. Additionally, it empowers users to customize the text within the image by allowing them to specify the content, placement, size and style, and even line breaks. This level of control opens up exciting possibilities. Imagine generating images with precise signage, customized logos, or even artistic text layouts within a scene. By incorporating BlipGlyphDiff, text-to-image generation takes a significant step towards creating truly artistic and informative visuals.

1) Framework:

• *Text Preprocessing:* Using a text encoder BLIP-2, majority of the input text is preprocessed. This stage guarantees that the textual data is successfully parsed and comprehended.

• *Glyph Information:* Each character in the input text has a pre-rendered glyph image associated with it. The created visual text's layout and appearance are entirely controlled by these glyph pictures, which act as the text's visual representation.

• *ControlNet:* Integrating seamlessly with existing text-to-image generation models, the framework introduces a key element: the ControlNet. This specialized network plays a critical role by analyzing and interpreting the provided glyph images. Unlike the standard ControlNet which handles various conditional inputs, our ControlNet focuses specifically on the precise geometric structures encoded within the glyphs as generated using the Glyph Instruction in the form of a PNG image with text styled and positioned as per configuration.

• *Image Generation:* To create the final image, the primary text-to-image generation models, including Stable Diffusion, make use of the encoded text and the control map as per our model. With exact layout control, the model may produce clear and comprehensible visual text by combining the textual data and the glyph-based control map.

2) Implementation:

We adhere to the same architecture and starting weights for the U-Net and Variational Autoencoder as they are utilized in the Stable Diffusion 2.0 [1] model in our implementation. Furthermore, we follow the approach of using classifier-free guiding, as previously shown in similar research. EasyOCR[1], the optical character recognition engine that is essential for identifying and interpreting text contained in photos, is integrated into our training process. This guarantees that during the training phase, the model gets accurate textual input. Users must supply glyph instructions during the inference phase in order to personalize the resulting graphics to their liking. This module provides a flexible range of drawing and image manipulation capabilities that enable accurate and effective glyph rendering onto the created images. By including these components in our solution, we guarantee a smooth and intuitive experience while creating personalized visual text.

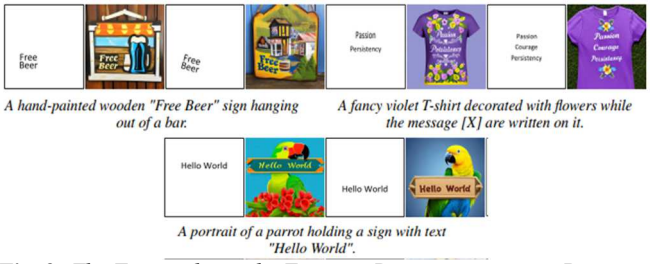

Fig. 3: *The Figure shows the Training Dataset containing Prompts, Glyphs and their expected images.*

B. LAION-Glyph Benchmark

1) Overview

While large datasets like LAION-5B exist for training AI models, there's a lack of specific datasets focused on creating images with text. To address this, we introduce LAION-Glyph, a new benchmark built from LAION-2B-en (a subset of LAION-5B). We carefully selected images rich in visual text information using the easyOCR engine.

Our two-step data creation process ensured high quality. First, we removed low-text images using an aesthetic scoring model. Next, easyOCR helped with text recognition and detection. To further ensure quality, we excluded images where text boxes were solely on borders, had excessive bounding boxes, or small text areas. Finally, we used the BLIP-2 model to correct captions from the original LAION dataset. This resulted in LAION-Glyph, a 50 million image dataset with accurate captions and comprehensive OCR data.

VI. Result, Evaluation & Conclusion

A. Training Dataset

Three datasets with varied sizes (500k, 5M, and 50M pictures) and different training periods (80, 40, and 12 epochs, respectively) were used to train our system.
Weights from a pre-trained text-to-image model (Stable Diffusion 2.0) were used for the initialization of our system's GlyphDiff and main image creation.

In order to maximize the BlipGlyphDiff segment's training speed, we adjusted a variable called the learning rate to a precise value (0.00001). To retain its learned capabilities, we kept the U-Net component unaltered in the meantime. We gave the GlyphDiff portion more weight in order to counterbalance the effect of text descriptions on the two system components. This lessened the effect of text guiding and prevented an excessive reliance on textual input. Prior to the photos being processed by the system, they were all

Authorized licensed use limited to: DELHI TECHNICAL UNIV. Downloaded on November 25,2024 at 04:43:41 UTC from IEEE Xplore. Restrictions apply.

downsized to 512x512 pixels in order to maintain uniformity throughout the training process.

B. Evaluation

- **Text Recognition Accuracy:** We examined the degree to which the created text in the photos could be read by specialized software (Optical Character Recognition). We examined two methods for quantifying this:
  - **Word-level accuracy (Acc):** This ignores case (upper vs. lower letters) and compares each word the OCR reads to the actual text in the prompt.
  - **Character-level accuracy (LD)** counts the number of adjustments (replacements, insertions, and deletions) that the OCR must perform to produce exactly the proper text.
- **Text Alignment with Prompt:** To determine how closely the generated text adhered to the original text prompt, we employed similarity scores between text embeddings.
- **Image Quality:** To assess the overall realism and excellence of the generated photos, we employed an alternative technique (FID score).

We employed two sets of text prompts that were previously utilized by other researchers for comparable tasks in order to ensure test fairness.

EasyBench: These were easy to understand and implement.
HardBench: These required substitutions within quotes and were more imaginative and difficult.

Our goal in employing these many tests and situations was to have a comprehensive understanding of the framework's performance.

C. Result

In both test settings, our model fared better than alternative approaches in terms of OCR accuracy. Text that was readable was difficult for Stable Diffusion to produce, and even improved versions did not live up to expectations. While DeepFloyd techniques performed better with more complicated components, our solution performed better with fewer components. Our model's ability to handle text in different letter cases sets it apart from certain competitors and increases its practicality. Training on a larger dataset specifically designed for text in photos significantly increased text recognition accuracy, demonstrating the significance of specialized data for further improvement. This demonstrated the importance of training data size.

Text recognition is just one aspect of BlipGlyphDiff. Using similarity scores for text embeddings, we evaluated the degree to which the generated images matched the original text descriptions. Our system either outperformed generic text-to-image models or produced results that were equivalent, proving its capacity to accurately incorporate text descriptions into photos. Most remarkably, the FID score showed that our system generated the highest caliber and most lifelike photos.

Inference 1*: The figure 1 is the glyph that is input with the prompt "Green colored signboard in a forest with PETS NOT ALLOWED written on it" and the result generated is shown in the figure 2.*

Inference 2*: The figure 1 is the glyph that is input with the prompt "Piggy holding a sign that says "brussels" and the result generated is shown in the figure 2 & figure 3.*

Inference 3*: The figure 1 is the glyph that is input with the prompt "A newspaper headline read "provoke" and a photo showed a half-eaten pumpkin" and the result generated is shown in the figure 2.*

Method	No. Params	Text Encoder	Training Dataset	Acc(%)t	Acc(%)t	LD t
Stable Diffusion v2.0	865M	CLIP(354M)	LAION 1.2B	0/0	3/2	4.25/5.01
SDXL 1.0	5.8B	CLIP & OpenCLIP(817M)	Internal Dataset (>100M)	0.3/0.53	12/8	6.16/6.30
DeepFloyd (IF-I-M)	2.1B	T5-XXL(4.8B)	LAION 1.2B	0.3/0.1	19/11	2.40/3.86
DeepFloyd (IF-I-L)	2.6B	T5-XXL(4.8B)	LAION 1.2B	0.3/0.72	22/17	1.77/3.37
DeepFloyd (IF-1-XL)	6.0B	T5-XXL(4.8B)	LAION 1.2B	0.6/1	33/21	1.63/3.09
BlipGlyphDiff	1.3B	BLIP2(2.7B)	LAION-Glyph-500K	22/19	30/24	1.57/2.58
BlipGlyphDiff	1.3B	BLIP2(2.7B)	LAION-Glyph-5M	32/26	39/30	1.39/2.47
BlipGlyphDiff	1.3B	BLIP2(2.7B)	LAION-Glyph-50M	35/28	42/34	1.23/2.40

Table I:

The table displays comparison results between previous approaches in the realm of visual text generation and metrics linked to OCR. The findings have been averaged using four buckets of word frequency. The above slash shows the results from EasyBench (left) and HardBench (right), respectively.

Method	#Params	Text Encoder	Limitations
Stable Diffusion v2.0	865M	CLIP(354M)	Limited parameters, poor accuracy, weak generalization.
SDXL 1.0	5.8B	CLIP & OpenCLIP (817M)	High complexity, potential overfitting, opaque dataset
DeepFloyd (IF-I-M)	2.1B	T5-XXL(4.8B)	Large model, weak accuracy, poor task generalization.
DeepFloyd (IF-I-L)	2.6B	T5-XXL(4.8B)	Moderate improvement, limited by dataset scope.
DeepFloyd (IF-1-XL)	6.0B	T5-XXL(4.8B)	Size-performance trade-off, marginal accuracy gain.
BlipGlyphDiff	1.3B	BLIP2(2.7B)	Small dataset, scalability limits.
BlipGlyphDiff	1.3B	BLIP2(2.7B)	Improved, but dataset-model balance may limit growth.
BlipGlyphDiff	1.3B	BLIP2(2.7B)	High performance, diminishing returns with dataset size.

Table II:

Comparison of visual text generation models highlighting their parameter sizes, text encoders, and key limitations.

Authorized licensed use limited to: DELHI TECHNICAL UNIV. Downloaded on November 25,2024 at 04:43:41 UTC from IEEE Xplore. Restrictions apply.

D. Qualitative Analysis

We conducted a thorough analysis of images produced by several systems, such as BlipGlyphDiff, DALL·E 2, Midjourney, Ideogram, enhanced SD (SDXL), and stable diffusion (SD). This is what we discovered:

- **Text is a problem for many methods:** SD, SDXL, IF, and DALL·E 2 frequently produced photos with incorrect text. Some letters were misplaced, mixed up, or otherwise incorrect. Sometimes they were unable to produce any text at all.
- **BlipGlyphDiff assumes charge:** Our Model regularly produced understandable text that precisely matched the description because it employs different instructions for every letter (glyph).
- **Long text puts others to the test:** Sentences and longer content were problematic with SDXL, IF, and Midjourney. While Ideogram performed better, our model remained the most precise.
- **Multiple text areas:** Midjourney has trouble placing text in different locations within the same image, despite its ability to produce stunning graphics. With ease, our model completed this task.

VII. CONCLUSIONS, LIMITATIONS & FUTURE WORK

In conclusion, our BlipGlyphDiff system represents a significant advancement in text-to-image creation. It gives you complete control over the text's size and placement. Although we're working on adding those functions, it can't currently modify the color or style of the font. Additionally, we are investigating how to work with extremely small text and how to use the model for even better-quality graphics. A few areas for improvement were identified by our investigation, including small text rendering and improved caption models. However, Model's overall effectiveness can be attributed to two main factors: a large dataset of text-in-image samples (LAION-Glyph) and a specialized text control network (ControlNet). Our system outperforms other previous techniques by utilizing BlipGlyphDiff with LAION-Glyph in terms of text reading accuracy (OCR), image quality (FID), and image matching accuracy (CLIP score). This demonstrates how effective our model is at producing legible and precise text within images. Our approach sets the foundation for future improvements in text-in-image production. We can't wait to address the remaining issues with BlipGlyphDiff and enable font style and color customization

VIII. REFERENCES

[1] Y. Yang, D. Gui, Y. Yuan, W. Liang, H. Ding, H. Hu, and K. Chen, "GlyphControl: Glyph Conditional Control for Visual Text Generation," arXiv:2305.18259v2, 2023.

[2] Midjourney v5.2. https://www.midjourney.com/, 2023. Accessed: 2023-10-10.

[3] Y. Balaji, S. Nah, X. Huang, A. Vahdat, J. Song, K. Kreis, M. Aittala, T. Aila, S. Laine, B. Catanzaro, et al., "ediffi: Text-to-image diffusion models with an ensemble of expert denoisers," arXiv preprint arXiv:2211.01324, 2022.

[4] J. Betker, G. Goh, L. Jing, T. Brooks, J. Wang, L. Li, L. Ouyang, J. Zhuang, J. Lee, Y. Guo, W. Manassra, P. Dhariwal, C. Chu, Y. Jiao, and A. Ramesh, "Improving image generation with better captions," 2023.

[5] P. Dhariwal and A. Nichol, "Diffusion models beat gans on image synthesis," Adv. Neural Inf. Process. Syst., vol. 34, pp. 8780–8794, 2021.

[6] Y. Du, C. Li, R. Guo, C. Cui, W. Liu, J. Zhou, B. Lu, Y. Yang, Q. Liu, X. Hu, et al., "easyOCRv2: Bag of tricks for ultra lightweight ocr system," arXiv preprint arXiv:2109.03144, 2021.

[7] Y. Du, C. Li, R. Guo, X. Yin, W. Liu, J. Zhou, Y. Bai, Z. Yu, Y. Yang, Q. Dang, et al., "easyOCR: A practical ultra lightweight ocr system," arXiv preprint arXiv:2009.09941, 2020.

[8] R. Gal, Y. Alaluf, Y. Atzmon, O. Patashnik, A. H. Bermano, G. Chechik, and D. Cohen-or, "An image is worth one word: Personalizing text-to-image generation using textual inversion," in Proc. Eleventh Int. Conf. Learning Representations, 2022.

[9] D. Gui, K. Chen, H. Ding, and Q. Huo, "Zero-shot generation of training data with denoising diffusion probabilistic model for handwritten chinese character recognition," arXiv preprint arXiv:2305.15660, 2023.

[10] H. He, X. Chen, C. Wang, J. Liu, B. Du, D. Tao, and Y. Qiao, "Diff-font: Diffusion model for robust one-shot font generation," arXiv preprint arXiv:2212.05895, 2022.

[11] J. Ho, A. Jain, and P. Abbeel, "Denoising diffusion probabilistic models," Adv. Neural Inf. Process. Syst., vol. 33, pp. 6840–6851, 2020.

[12] J. Ho, C. Saharia, W. Chan, D. J. Fleet, M. Norouzi, and T. Salimans, "Cascaded diffusion models for high fidelity image generation," J. Mach. Learn. Res., vol. 23, no. 1, pp. 2249–2281, 2022.

[13] J. Ho and T. Salimans, "Classifier-free diffusion guidance," in NeurIPS 2021 Workshop on Deep Generative Models and Downstream Applications, 2021.

[14] L. Huang, D. Chen, Y. Liu, Y. Shen, D. Zhao, and J. Zhou, "Composer: Creative and controllable image synthesis with composable conditions," in Int. Conf. Mach. Learn., 2023.

[15] B. Kawar, S. Zada, O. Lang, O. Tov, H. Chang, T. Dekel, I. Mosseri, and M. Irani, "Imagic: Text-based real image editing with diffusion models," in Proc. IEEE/CVF Conf. Comput. Vis. Pattern Recognit., pp. 6007–6017, 2023.

[16] DeepFloyd Lab. Deepfloyd if. https://github.com/deep-floyd/IF, 2023.

[17] J. Li, D. Li, S. Savarese, and S. Hoi, "Blip-2: Bootstrapping language image pre-training with frozen image encoders and large language models," arXiv preprint arXiv:2301.12597, 2023.

[18] H. Liu, C. Li, Y. Li, and Y. J. Lee, "Improved baselines with visual instruction tuning," arXiv preprint arXiv:2310.03744, 2023.

[19] H. Liu, C. Li, Q. Wu, and Y. J. Lee, "Visual instruction tuning," arXiv preprint arXiv:2304.08485, 2023.

[20] R. Liu, D. H. Garrette, C. Saharia, W. Chan, A. Roberts, S. Narang, I. Blok, R. J. Mical, M. Norouzi, and N. Constant, "Character-aware models improve visual text rendering," in Proc. Annu. Meet. Assoc. Comput. Linguistics, 2022.

[21] Ideogram. https://ideogram.ai, 2023. Accessed: 2023-10-10.

[22] C. Meng, Y. He, Y. Song, J. Song, J. Wu, J.-Y. Zhu, and S. Ermon, "Sdedit: Guided image synthesis and editing with stochastic differential equations," in Int. Conf. Learning Representations, 2021.

[23] C. Mou, X. Wang, L. Xie, J. Zhang, Z. Qi, Y. Shan, and X. Qie, "T2i-adapter: Learning adapters to dig out more controllable ability for text-to-image diffusion models," arXiv preprint arXiv:2302.08453, 2023.

[24] A. Q. Nichol, P. Dhariwal, A. Ramesh, P. Shyam, P. Mishkin, B. Mcgrew, I. Sutskever, and M. Chen, "Glide: Towards photorealistic image generation and editing with text-guided diffusion models," in Int. Conf. Mach. Learn., pp. 16784–16804, 2022.

[25] Y. Nikankin, N. Haim, and M. Irani, "Sinfusion: Training diffusion models on a single image or video," in Int. Conf. Mach. Learn., 2022.

[26] OpenAI, "Dall·e 3 system card," 2023.

[27] D. Podell, Z. English, K. Lacey, A. Blattmann, T. Dockhorn, J. Müller, J. Penna, and R. Rombach, "Sdxl: Improving latent diffusion models for high-resolution image synthesis," arXiv preprint arXiv:2307.01952, 2023.

[28] C. Raffel, N. Shazeer, A. Roberts, K. Lee, S. Narang, M. Matena, Y. Zhou, W. Li, and P. J. Liu, "Exploring the limits of transfer learning

Authorized licensed use limited to: DELHI TECHNICAL UNIV. Downloaded on November 25,2024 at 04:43:41 UTC from IEEE Xplore. Restrictions apply.

with a unified text-to-text transformer," J. Mach. Learn. Res., vol. 21, no. 1, pp. 5485–5551, 2020.

[29] A. Ramesh, P. Dhariwal, A. Nichol, C. Chu, and M. Chen, "Hierarchical text-conditional image generation with clip latents," arXiv preprint arXiv:2204.06125, 2022.

[30] R. Rombach, A. Blattmann, D. Lorenz, P. Esser, and B. Ommer, "High resolution image synthesis with latent diffusion models," in Proc. IEEE/CVF Conf. Comput. Vis. Pattern Recognit., pp. 10684–10695, 2022.

[31] C. Saharia, W. Chan, S. Saxena, L. Li, J. Whang, E. L. Denton, K. Ghasemipour, R. Gontijo Lopes, B. Karagol Ayan, T. Salimans, et al., "Photorealistic text-to-image diffusion models with deep language understanding," Adv. Neural Inf. Process. Syst., vol. 35, pp. 36479–36494, 2022.

[32] C. Schuhmann, R. Vencu, R. Beaumont, R. Kaczmarczyk, C. Mullis, A. Katta, T. Coombes, J. Jitsev, and A. Komatsuzaki, "Laion-400m: Open dataset of clip-filtered 400 million image-text pairs," arXiv preprint arXiv:2111.02114, 2021.

[33] O. Sidorov, R. Hu, M. Rohrbach, and A. Singh, "Textcaps: a dataset for image captioning with reading comprehension," in Comput. Vis.–ECCV 2020: 16th Eur. Conf., Glasgow, UK, Aug. 23–28, 2020, Proc., Part II 16, pp. 742–758. Springer, 2020.

[34] J. Sohl-Dickstein, E. Weiss, N. Maheswaranathan, and S. Ganguli, "Deep unsupervised learning using nonequilibrium thermodynamics," in Int. Conf. Mach. Learn., pp. 2256–2265, 2015.

[35] J. Song, C. Meng, and S. Ermon, "Denoising diffusion implicit models," in Int. Conf. Learning Representations, 2020.

[36] L. Xue, A. Barua, N. Constant, R. Al-Rfou, S. Narang, M. Kale, A. Roberts, and C. Raffel, "Byt5: Towards a token-free future with pre-trained byte-to-byte models," Trans. Assoc. Comput. Linguistics, vol. 10, pp. 291–306, 2022.

[37] L. Zhang, A. Rao, and M. Agrawala, "Adding conditional control to text-to-image diffusion models," in Proc. IEEE/CVF Int. Conf. Comput. Vis., pp. 3836–3847, 2023.

[38] M. Liao, Z. Zou, Z. Wan, C. Yao, and X. Bai, "Real-Time Scene Text Detection with Differentiable Binarization and Adaptive Scale Fusion," arXiv:2202.10304, 2022

[39] Rico Sennrich, Barry Haddow and Alexandra Birch, " Neural Machine Translation of Rare Words with Subword Units," arXiv:1508.07909v5, 2016

[40] Chen, Junhao, Xiang Li, Xiaojun Ye, Chao Li, Zhaoxin Fan, and Hao Zhao. "Idea-2-3D: Collaborative LMM Agents Enable 3D Model Generation from Interleaved Multimodal Inputs." arXiv preprint arXiv:2404.04363 (2024).

[41] Bird, Charlotte, Eddie Ungless, and Atoosa Kasirzadeh. "Typology of risks of generative text-to-image models." In Proceedings of the 2023 AAAI/ACM Conference on AI, Ethics, and Society, pp. 396-410. 2023.

Authorized licensed use limited to: DELHI TECHNICAL UNIV. Downloaded on November 25,2024 at 04:43:41 UTC from IEEE Xplore. Restrictions apply.

Optical and Quantum Electronics (2024) 56:1904
https://doi.org/10.1007/s11082-024-07759-9

CMOS compatible TeO_2—coated Si_3N_4 inverse parabolic rib waveguide for on-chip supercontinuum generation and high resolution OCT

Deepak Garg[1] · **Ajeet Kumar**[1]

Received: 9 September 2024 / Accepted: 16 October 2024
© The Author(s), under exclusive licence to Springer Science+Business Media, LLC, part of Springer Nature 2024

Abstract
We present the design and theoretical analysis of CMOS compatible Tellurium oxide (TeO_2)-coated- Si_3N_4 inverse parabolic rib waveguide having upper and lower cladding of barium fluoride (BaF_2) for the generation of highly coherent supercontinuum generation having potential applications in the field of non-linear optics. The proposed design is dispersion engineered by tailoring various geometrical parameters and analyzing their effect on the dispersion profile. The proposed design offers a Zero Dispersion Wavelength (ZDW) near 1.7 μm. The design offers a low value of effective mode area 1.65 μm^2 and correspondingly high value of non-linear coefficient 2475.68 W^{-1} km^{-1} at pump wavelength of 2 μm. Our simulation reports a highly coherent supercontinuum broadening from 1–5 μm spanning over 2.32 octaves in only 1 mm long waveguide when pumped with hyperbolic secant pulses having pulse width 45 fs and peak power 6.1 kW. Additionally, operation at 1.3 μm yields a high axial resolution of 1.007 μm, enhancing its potential for optical coherence tomography. The proposed waveguide can help in various applications ranging from non-linear spectroscopy to optical coherence tomography and from medical imaging to high-bit rate telecommunication. Since the proposed design is CMOS compatible, it can be positioned as an excellent platform for low-loss and high performance future photonic integrated circuits.

Keywords Supercontinuum generation · Dispersion · Non-Linearity · Coherence

1 Introduction

Over the span of recent years, optical waveguide based light sources, with spectral domain varying from ultra-violet to mid-infrared region of electromagnetic spectrum have gained considerable attention as these light sources can be used for the various potential applications like optical coherence tomography (Ji et al. 2021; Wen et al. 2015), frequency meteorology, spectroscopy (Ke et al. 2009) and biosesning (Markos

✉ Ajeet Kumar
ajeetdph@dtu.ac.in

[1] Department of Applied Physics, Advanced Photonics Simulation Research Laboratory, Delhi Technological University, Bawana Road, Shahabad Daulatpur, Delhi 110042, India

and Bang 2015) etc. Among these, on-chip supercontinuum (SC) sources and integrated waveguides have emerged as particularly promising due to their high power efficiency, cost-effectiveness, and robust nature, making them preferable over photonic crystal fiber (PCF) counterparts. The spectrum range from ultraviolet to visible region can be used for environmental monitoring and absorption spectroscopy. Moreover, the spectral region between 2 to 5 μm is considered as atmospheric transparent window helping in free-space communication and remote sensing (Saini and Sinha 2021). A lot of work has been reported on the broadband supercontinuum generation using conventional optical fibers, photonic crystal fibers and waveguides geometries using different materials including silica, tellurite (Klimczak et al. 2019), ZBLAN (Jiang et al. 2016), chalcogenide glasses (Tomer and Kumar 2024) etc. Silica has traditionally been the material of choice for SC sources due to its well understood optical properties. However, its utility is constrained by the spectral broadening limit of 2.5 μm, caused by the presence of multiphonon transmission edge phenomena (Sharma et al. 2020). Additionally, while strong mode confinement and desired dispersion characteristics can be achieved in silica based fibers or waveguide structures, their low non-linear kerr coefficient necessitates high pump power to generate an efficient SC. To overcome these limitations and to generate an efficient broadband spectrum materials like tellurite and chalcogenides offers a promising alternate. Their wide transparency window and high non-linearity enables them to produce more efficient supercontinuum spectra. However, since their ZDW lies in the mid-IR region, pumping near ZDW is challenging due to the lack of available pump sources at longer wavelengths (Saini and Supradeepa 2021).

Recently, complementary metal-oxide semiconductor (CMOS) compatible silicon nitride has emerged as a go-to platform for linear and non-linear integrated photonics due to low loss, cost effectiveness and high performance photonic integrated circuits (PICs). The transparency window for silicon nitride extends from visible to mid-infrared region making it suitable material for optical coherence tomography and many sensing applications. The Si_3N_4 waveguides exhibit low bend loss and are well suited for large scale chip production with nanoscale precision using subsisting established processing techniques. Silicon nitride (Si_3N_4) is employed not only in passive devices like switches, filters, multiplexers, and routers for communication applications, but also as a medium for nonlinear optical devices, quantum microsystems, and on-chip lasers (Saini and Supradeepa 2021). Moreover, the thermal and chemical stability of silicon nitride makes it a promising material for supercontinuum generation sources. It has been previously proposed that multifunctionality can be integrated into the Si_3N_4 waveguide platform through subsequent post-processing techniques. TriPlex, a photonic integrated circuit (PIC) that combines Si_3N_4 with silicon dioxide (SiO_2) has been introduced for various applications (Roeloffzen et al. 2018). Further, tellurium oxide (TeO_2)is an oxide glass with exceptional non-linear optical properties i.e. possesses kerr refractive index (n_2) ~ 1.3×10^{-18} m^2/W which is 20 times greater than that of silica and has a wide transparency range extending from 0.4 -5 μm (Bres et al. 2023). Due to low loss and high Raman gain coefficient it can be used in optical fibers or PICs for SC sources, lasers or broadband-Raman amplification. Additionally, tellurium oxide is also considered a strong candidate for seamlessly integrating optical sources with both linear and non-linear functionalities in silicon photonics, without causing non-linear absorption loss (Singh et al. 2020). Furthermore, the use of BaF_2 as upper and lower cladding material has its own advantages in terms of wide transparency window extending from ultra-violet to far-infrared region and low dispersion values (Kanika et al. 2024) Since, a low dispersion profile is necessary to minimize any temporal walk-off during the spectral broadening, BaF_2 as cladding material provides us with such profile.

There have been a lot of research work done for on-ship SC sources and integrated hybrid waveguide geometries exploring TeO_2 and SiN. A hybrid TeO_2 coated SiN waveguide was proposed for SC generation in near to mid-infrared region with zero dispersion wavelength at 3.5 μm wavelength (Kanika et al. 2024). However, this is not ideal for supercontinuum generation and four wave mixing using common pump sources at 1.55 μm and 2 μm. An octave supercontinuum spectrum pumped at 795 nm covering 488–978 nm has been reported using Si_3N_4 waveguide (Zhao et al. 2015). An all normal dispersion engineered waveguide using Si_3N_4 has also been reported capable of producing SC broadening from 950–2100 nm (Ahmed et al. 2019). Further, a hybrid TeO_2 coated SiN waveguide was also proposed which is capable of producing SC broadening from 0.95–5.50 μm when pumped at 2 μm central wavelength having pulse width 200 fs and peak power 10 kW (Saini and Supradeepa 2021). Recently, a group of researchers reported a channel waveguide based on Si_3N_4 capable of producing SC ranging from 0.8–6 μm at 1.55 μm pump wavelength with pulses having peak power 20 kW and pulse width 50 fs (Faisal et al. 2024). Again, a group reported an inverse tapered waveguide using Si_3N_4 as a core material which is capable of generating an SC spectra ranging from 0.76–6.6 μm with pulses having peak power 10 kW (Al Kayed et al. 2021). These advancements are not only crucial for broadening SC spectra but also for enabling non-linear applications such as optical coherence tomography (OCT). In fact, several studies have demonstrated the utility of SC sources in OCT systems, where broad bandwidth especially in near to mid-infrared region is essential for achieving high axial resolution. For instance, a silica photonic crystal fiber has been proposed for optical coherence tomography capable of generation broadband spectra of 600 nm offering axial resolution of 1.24 μm at 1.3 μm central wavelength (Ferhat et al. 2018). Again a silica based PCF has been proposed for ophthalmic OCT having axial resolution of 2.6 μm at 800 nm central wavelength (Pakarzadeh et al. 2023). Furthermore, attempt has been made by a group of researchers reporting a Magnesium fluoride PCF having central wavelengths of 532 nm and 640 nm having pulse width of 50 fs and peak power of 5 kW for optical coherence tomography (Ghanbari et al. 2017).

In this study, we report design and theoretical study of CMOS compatible TeO_2 -coated-silicon nitride (Si_3N_4) inverse parabolic rib waveguide for highly coherent supercontinuum generation and further analysis reveals significant broadening of the spectrum when operated at 1300 nm, indicating the waveguide's potential for optical coherence tomography. We have simulated the dispersion engineered design using Comsol Multiphysics software and optimized the geometrical parameters to obtain low values of dispersion. Finally, we have proposed the optimized design which is capable of producing a highly coherent supercontinuum spectra ranging from 1–5 μm in only 1 mm long waveguide when pumped at 2 μm wavelength having pulse width 45 fs and peak power 6.1 kW. Further, when operated at 1300 nm, the waveguide shows the axial resolution of 1.007 μm in air. Finally, we have compared our proposed design with the previously reported waveguides and PCF geometries for supercontinuum generations and optical coherence tomography.

2 Proposed design and fabrication method

The cross sectional representation of the proposed inverse waveguide is shown in Fig. 1. The hybrid waveguide structure consists of a rectangular strip of silica nitride (Si_3N_4) having dimension $w(\mu m) \times h(\mu m)$. The etch thickness of the tellurium oxide (TeO_2) layer deposited on the Si_3N_4 strip waveguide is denoted by 'b' and the total height of

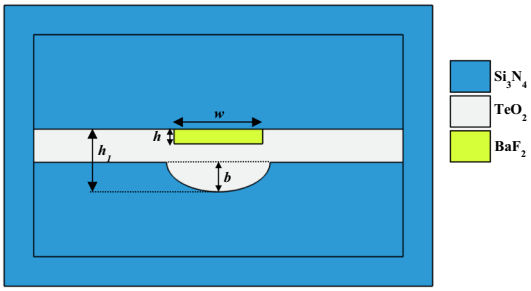

Fig. 1 Transverse profile of proposed design

the TeO_2 layer is denoted as 'h_1'. The optimized waveguide parameters obtained from dispersion engineering are tabulated in Table 1. The thickness (h) of the Si_3N_4 strip is 400 nm and can be deposited by low pressure chemical vapour deposition (LPCVD) method without involving the formation of cracks due to tensile nature of silica nitride. We have considered near seventy percent deposition of TeO_2 layer on both side of silica nitride films. The proposed waveguide also consists of upper and lower cladding layer of BaF_2 ensuring the proper confinement of fundamental mode in the core region with minimum losses. It is worth mentioning that the core region of our waveguide structure supports few modes but the effective indices of propagating modes satisfies the mode suppression condition, preventing inter-modal coupling. This led to selection of fundamental TE mode for simulation and all calculations. The modal profile of fundamental propagating mode at 2 μm is shown in Fig. 1b. From the fabrication perspective, inverse rib waveguides are comparatively easier to fabricate and confines light more efficiently (Hitaishi and Ashok 2023). A high quality Si_3N_4 film can be deposited using subsisting techniques like, LPCVD or reactive sputtering techniques (Heideman et al. 2005; Frigg et al. 2019). Further, the Si_3N_4 strip can be produced using reactive ion etching processes and stepper lithography. After the deposition of Si_3N_4 strip, the wafer annealing can be performed in the presence of N_2 to reduce absorptive losses caused by N–H and Si–H bonds (Saini and Supradeepa 2021). TeO_2 layer can be deposited on both sides of Si_3N_4 strip using reactive sputtering technique followed by the deposition of final BaF_2 cover layer using the spin-coating method.

Table 1 Sellmeier fitting constants for different materials under consideration

Sellmeier Coefficient	TeO_2	Si_3N_4	BaF_2
A_0	3.5483034	1	1.3397
A_1	0.9783726	3.0249	0.8107
A_2	6.6510879	40,314	0.19652
A_3	–	–	4.52469
B_1	0.287522973	135.3406	0.10065
B_2	15	1,239,842	29.87
B_3	–	–	53.82

3 Numerical analysis

To explore our proposed hybrid waveguide design, the fundamental TE modes propagating in waveguide core region were simulated and calculation of effective mode indices is done using Finite element method (FEM) based Comsol Multiphysics software. The linear refractive index of the materials under consideration varies with the variation in the wavelength of input laser pulse which can be calculated using an empirical Sellmeier equation which in general form can be written as (Sharma et al. 2020):

$$n^2(\lambda) = A_0 + \sum_{n=1}^{3} \frac{A_n \lambda^2}{\lambda^2 - B_n^2} \tag{1}$$

where A_0, A_n and B_n are the fitting constants for empirical relation. The values of these constant for different materials under consideration is summarized in Table 1. The variation of refractive index with wavelength for all materials under consideration is shown in in Fig. 2.

When it comes to optical fibers and waveguide sources, understanding and controlling the group velocity dispersion (GVD) parameter becomes very important as it influences the non-linear optical properties. GVD leads to pulse broadening as the various components of input ultrashort pulse travels with different phase velocity. In anomalous dispersion region, nonlinear phenomena can sometimes act against group velocity dispersion leading to formation of solitons. The dispersion profile can be simulated using the wavelength dependency of refractive indices as (Khamaru and Kumar 2024):

$$D(\lambda) = \frac{-\lambda}{c} \frac{d^2 \mathrm{Re}\left(n_{eff}\right)}{d\lambda^2} \tag{2}$$

Another important optical parameter is Effective mode area (A_{eff}) of the fundamental transverse electric mode. (A_{eff}) can be calculated using the equation given below (Garg et al. 2024):

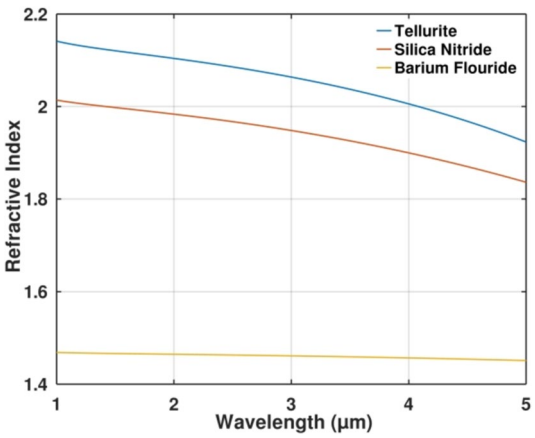

Fig. 2 Refractive index v/s Wavelength for different materials

$$A_{eff} = \frac{\left(\iint_{-\infty}^{\infty} |E|^2 dxdy\right)^2}{\iint_{-\infty}^{\infty} |E|^4 dxdy} \tag{3}$$

where, E is the amplitude of electric field intensity obtained by solving the eigenvalue problem derived from Maxwell's equations.

Material non-linearity serves as one of the main factors in efficient broadening of SC spectra. It can be calculated using the equation given below (Wen et al. 2024):

$$\gamma = \frac{2\pi n_2}{\lambda A_{eff}(\lambda)} \tag{4}$$

where, n_2 is nonlinear refractive index of the material in which the fundamental mode is confined which in our case is TeO_2. To enhance the broadening of SC spectra, the nonlinearity should be maximized while keeping the effective mode area to be minimum. This can be achieved by adjusting waveguide parameters to ensure that the effective mode area gets reduced.

To model supercontinuum (SC) generation, we solve the generalized nonlinear Schrödinger equation (GNLSE) using the split-step Fourier transform method. The GNLSE is given by (Khamaru and Kumar 2024):

$$\frac{\partial A}{\partial Z} + \frac{\alpha}{2}A - \left(\sum_{n\geq 2} \frac{i^{n+1}}{n!}\beta_n \frac{\partial^n A}{\partial T^n}\right) = i\gamma\left(1 + \frac{i}{\omega_0}\frac{\partial}{\partial \mathrm{T}}\right)\left(A(z,t)\int_{-\infty}^{\infty} R(T)\left|A\left(z, T-T'\right)\right|^2 dT + i\hbar_{\mathrm{R}}(z,T)\right) \tag{5}$$

In this equation, the left-hand side (L.H.S.) accounts for all linear optical effects within the waveguide structure, while the right-hand side (R.H.S.) deals with nonlinear effects. Here, β_n denotes the dispersion coefficients, 'A' represents the slowly varying optical wave envelope, α is the waveguide's loss coefficient, 'z' is the spatial coordinate along the waveguide, and 't' is the time variable (Wen et al. 2019). The Raman term $\hbar_{\mathrm{R}}$ is considered negligible due to the short waveguide length used in our study.

The nonlinear response function $R(T)$ combines both instantaneous electronic and delayed Raman response and is given as (Sharma et al. 2020):

$$R(t) = \left(1 - f_R\right)\delta(t) + f_R h_R(t) \tag{6}$$

where the value of f_R for TeO_2 is given as 0.0064. The Raman response function $h_R(t)$ is given by the following formulae (Saini et al. 2015):

$$h_R(t) = \frac{{\tau_1}^2 + {\tau_2}^2}{\tau_1 {\tau_2}^2}\exp\left[\frac{-t}{\tau_2}\right]\sin\left(\frac{t}{\tau_1}\right) \tag{7}$$

In this equation, τ_1 and τ_2 are related to the non-oscillatory photon frequency and the damping time of the vibrating molecules, respectively. For, TeO_2 values of τ_1 and τ_2 are 7.4413 fs and 46.932 fs (Li et al. 2017; Zhang et al. 2009), respectively.

To simulate SC generation, we employed a tunable hyperbolic secant pulse, defined as (Chauhan et al. 2018):

$$A(z=0,t) = \sqrt{P_0}\,\mathrm{sech}\left(\frac{T}{T_0}\right) \tag{8}$$

where P_0 represents the peak power of the input pulse, $T_0 = T_{FWHM}/1.7627$ and T is the co-propagating frame at the group velocity of the envelope and sech represents the secant hyperbolic nature of the pump pulse.

We have employed a single-photon-per-mode noise model, which is a semi-classical approach, to study the coherent properties of mid-infrared supercontinuum generation. In this analysis, the degree of coherence is evaluated using the magnitude of the first-order coherence function g_{12} which varies between 0 and 1 (Khamis et al. 2024).

$$\left|g_{12}^{(1)}(\lambda, t_1 - t_2)\right| = \left| \frac{\left\langle E_1^*(\lambda, t_1) E_2(\lambda, t_1) \right\rangle}{\sqrt{\left\langle \left|E_1(\lambda, t_1)\right|^2 \right\rangle \left\langle \left|E_2(\lambda, t_2)\right|^2 \right\rangle}} \right| \tag{9}$$

The dispersive length (L_D) is the characteristic length over which the dispersion significantly affects the pulse broadening. It can be given as, here our simulated results shows the value of $|\beta_2| = 1.1534 \times 10^{-10}$ ps^2/nm.

$$L_D = \frac{T_0^2}{|\beta_2|} \tag{10}$$

The non-linear length (L_{NL}) is characteristic length of SPM i.e. non linearity and can be qualitatively defined as the propagation distance needed for a pulse with an input peak power P_0 to accumulate a nonlinear phase shift of 1 rad in a waveguide characterized by a nonlinear coefficient γ. It can be given as:

$$L_{NL} = \frac{1}{\gamma P_0} \tag{11}$$

While pumping is anomalous dispersion region, SC can be generated by leveraging the opposite effects of self-phase modulation (SPM) (Dudley et al. 2006) and GVD leading to the generation of solitons (self-stabilized wave packets that arise from the gentle balance between dispersive and non-linear effects). The pulses in soliton regime are characterized by a certain number called soliton number which can be calculated using (Bres et al. 2023):

$$N^2 = \frac{L_D}{L_{NL}} \tag{12}$$

To explore the proposed waveguide design for potential application like optical coherence tomography an important parameter namely, axial resolution (l_c) that determines the level of detail that can be resolved in depth profile of tissue or material and is given by (Ferhat et al. 2018):

$$l_c = \frac{2ln2}{\pi} \frac{\lambda_0^2}{\Delta\lambda} \tag{13}$$

where, λ_0 is the central wavelength and $\Delta\lambda$ is the SC spectrum broadening at 10 dB power level (Pakarzadeh et al. 2023).

Finally, for the performance of waveguide i.e. to indicate the non-linear potential of the platform for SC generation, we define a figure of merit (FOM) which compares the output

SC spectra broadening ($\Delta\vartheta$) with the input peak power and length of waveguide and given as (Bres et al. 2023):

$$FOM = \frac{\Delta\vartheta}{L_{fiber}P} \tag{14}$$

4 Results and Discussion:

We began exploring our design through dispersion engineering by studying the influence of geometric parameters, such as the width (w), height (h) of the silica nitride strip, and the etch thickness (b) of the TeO_2 layer, on the dispersion characteristics of the waveguide. By adjusting these parameters, we aim to achieve an optimal low-dispersion profile suited to our application. In Fig. 3, we illustrate the effect of varying the dimensions of the silicon nitride strip ($w \times h$) while keeping the TeO_2 layer thickness constant. We varied the strip dimensions from 2.2 µm × 0.2 µm to 2.6 µm × 0.6 µm, and observed minimal impact on the positioning of the zero-dispersion wavelength (ZDW). Importantly, the dispersion curves for all three dimensions converge near the pump wavelength of 2 µm, where no significant difference is observed in their behaviour. Since, the dispersion profile remains nearly identical in the critical pump wavelength region, and factoring in the practical considerations of fabrication, we have selected the intermediate dimensions of 2.4 µm × 0.4 µm as the optimized size for the Si_3N_4 strip. The variation of dispersion values along with the variation in the etch thickness of TeO_2 layer is shown in Fig. 4. The variation in the etch thickness is made in steps of 100 nm i.e. etch thickness is varied from 0.8 µm to 1.0 µm. It is observed that the dispersion values at pump wavelength of 2 µm, changes from 57.7236 ps/nm/km to 57.1816 ps/nm/km, which is not a significant change. It can also be seen from the figure that with the increase in the value of b, there is increase in dispersion values in both normal and anomalous dispersion regime. Thus, by considering the minimum dispersion values, alongside fabrication efficiency and overall device stability, we have selected 0.8 µm as the optimal etch thickness for the TeO_2 layer. This choice balances performance, practical manufacturability, and the robustness required for reliable waveguide operation.

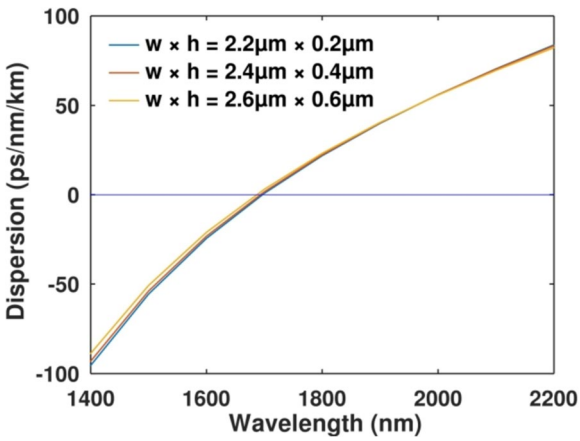

Fig. 3 Dispersion characteristics with variation in Si_3N_4 strip dimensions

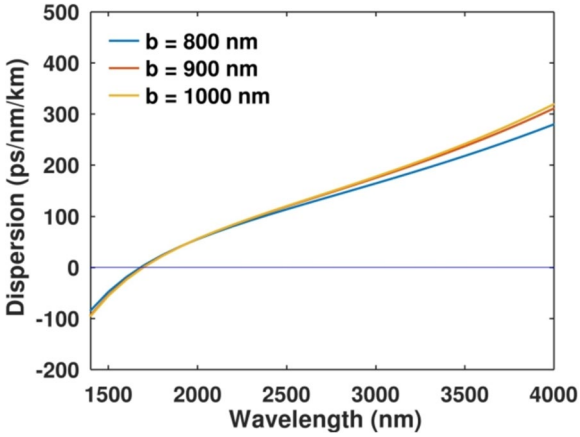

Fig. 4 Dispersion characteristics with variation in etch thickness of TeO_2 layer while keeping other parameter constant

The optimised parameters for the proposed waveguide design is tabulated in Table 2. From the above analysis it can be concluded that for the optimized parameters $w \times h = 2.4\ \mu m \times 0.4\ \mu m$ and etch thickness $b = 0.8\ \mu m$, the dispersion value at pump wavelength gets minimized and the overall dispersion curve attains low values of dispersion. The dispersion characteristics offered by the hybrid waveguide structure is shown in Fig. 5. It can be seen that the proposed design offers zero dispersion wavelength near 1.7 µm and the dispersion value at the pump wavelength of 2 µm is 52.16 ps/nm/km. On considering practical errors during the fabrication processes, we have simulated our proposed optimised structure design with the uncertainty of $\pm 2\%$ in the chosen parameters and observed no significant change in dispersion values.

Table 2 Optimized Parameters of the proposed waveguide structure

Geometrical Parameters	Si_3N_4 Width (w)	Si_3N_4 height (h)	TeO_2 etch thickness (b)
Values	2.4 µm	0.4 µm	0.8 µm

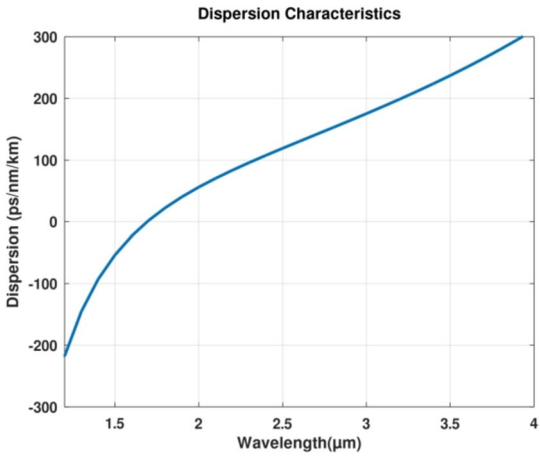

Fig. 5 Dispersion characteristics offered by the final optimized structure

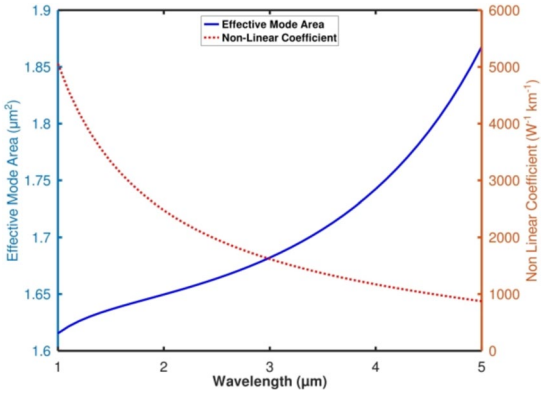

Fig. 6 Spectral variation of Effective mode area and Non-linearity

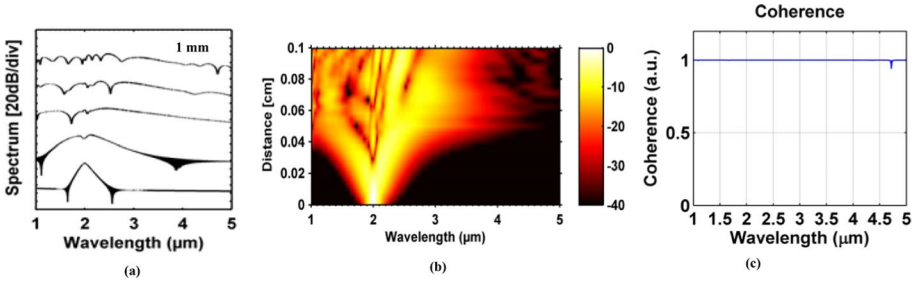

Fig. 7 **a** Line plot of SC spectra with variation in length (from 0.25 mm to 1 mm), **b** Spectral evolution and **c** coherence at 1 mm length

The spectral variation of the effective mode area (A_{eff}) and non-linearity is shown in Fig. 6. It can be seen and observed from the figure that the value of effective mode area and non-linearity at pump wavelength of 2 μm is 1.65 μm^2 and 2475.68 W^{-1} km^{-1}, respectively. With the uncertainty of 2% in the optimized parameters, there is only 0.58% change in effective mode area and 0.40% change in non-linearity at pump wavelength. With these minor variations it can be concluded that our proposed design is robust and stable with minor fabrication errors.

Broadband supercontinuum generation is studied by solving the GNLSE i.e. Equation (5) by employing split step Fourier transform method. The supercontinuum generation is simulated with different laser operating conditions like waveguide length, pulse width and peak power of input laser pulse. The effect of these parameters on SC spectrum broadening and coherency of the output spectra is observed. As the pump wavelength of 2 μm lies in the anomalous region, hence the SC spectrum broadening is guided by the soliton dynamics. The interaction between non-linear chirp, influenced by self-phase modulation, and linear chirp, caused by second-order dispersion, contributes to stable spectrum broadening. The variation in SC spectra with the variation in length of the waveguide is shown in Fig. 7. It can be seen from the figure that with the increase in the length of waveguide from 0.25 mm to 1 mm, the SC broadening increases till it reaches the maximum limit of transmission window of TeO_2. The spectral evolution and coherence is also shown in Fig. 7b and c respectively. The characteristic nonlinear length (L_{NL}) as calculated using Eq. (11) comes out to be 6.6×10^{-2} mm, which is obviously less than the proposed

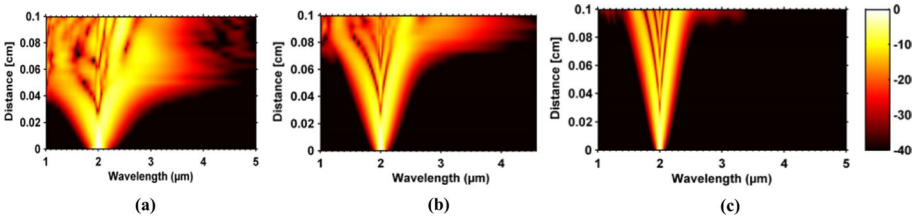

Fig. 8 Spectral evolution with the change in pulse width of input pulse **a** 45 fs**, b** 85 fs and, **c** 125 fs

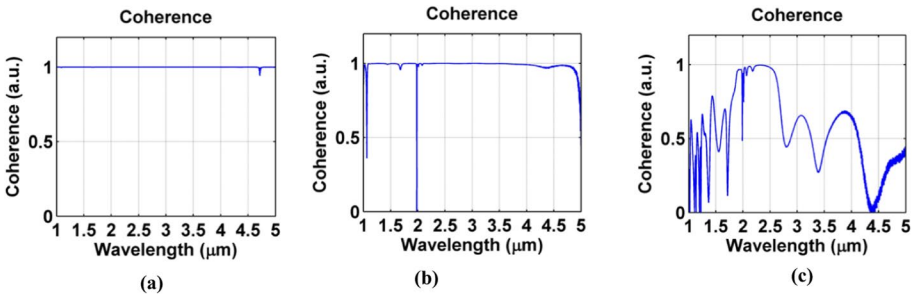

Fig. 9 Coherence with the change in pulse width of input pulse **a** 45 fs**, b** 85 fs and, **c** 125 fs

waveguide length of 1 mm. Further, the dispersion length (L_D) calculated using Eq. (10) comes out to be 5.65 mm which fulfils the condition for pumping and generating SC in soliton regime i.e. $L_D > L_{NL}$ and the corresponding soliton number ($N = \sqrt{L_D/L_{NL}}$) comes out to be ~ 9. Other characteristics lengths like soliton fission length ($L_f = L_D/N$) and modulation instability length ($L_{MI} \approx 16L_{NL}$) comes out to be 0.62 mm and 1.056 mm which means $L_f < L_{MI}$ i.e. soliton fission occurs earlier than modulation instability. The high degree of coherence is attributed to the no. so solitons i.e. since the no. of solitons are less than 16, hence the degree of coherence is high (Bres et al. 2023). When pumped with 2 μm wavelength having pulse width 45 fs and peak power 6.1 kW our proposed structure is able to produce an SC broadening from 1–5 μm i.e. covering almost 2.32 octaves in only 1 mm long waveguide.

Another important laser condition that can be varied is pulse width. The variation of SC spectra with the pulse width is shown in Fig. 8. It can be seen from the spectral evolution 8(a), 8(b) and 8(c) that with the increase in the pulse width of the input laser pulse, the SC spectra broadening reduces. It can be attributed to the fact that with the decrease in temporal width from 125 to 45 fs in steps of 40 fs, the SPM effect becomes more dominant resulting in broader spectra. A decrease in coherence is also observed with the increase in pulse width and is depicted in Fig. 9a, b and c. A simple conclusion can be drawn from the above analysis that the narrower pulse widths favor the SC spectrum broadening if the length of the waveguide structure is short.

Furthermore, peak power of the input ultra-short pulse is also varied and the variation of SC spectra with peak power is shown in Fig. 10. We have varied the peak power from 4.1 kW to 8.1 kW and it can be seen in the Fig. 10 that the spectral evolution and coherence increases first upto 6.1 kW but after further increase in the peak power to 8.1 kW,

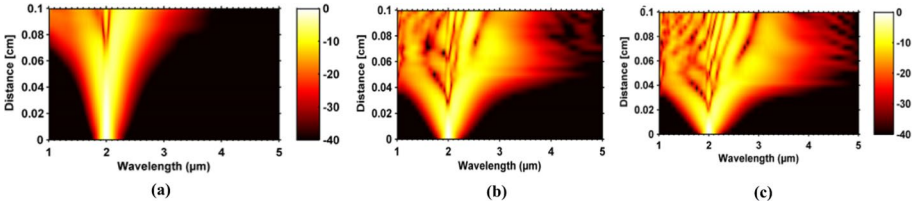

Fig. 10 Spectral evolution with the change in peak power of input pulse **a** 4.1 kW**, b** 6.1 kW and, **c** 8.1 kW

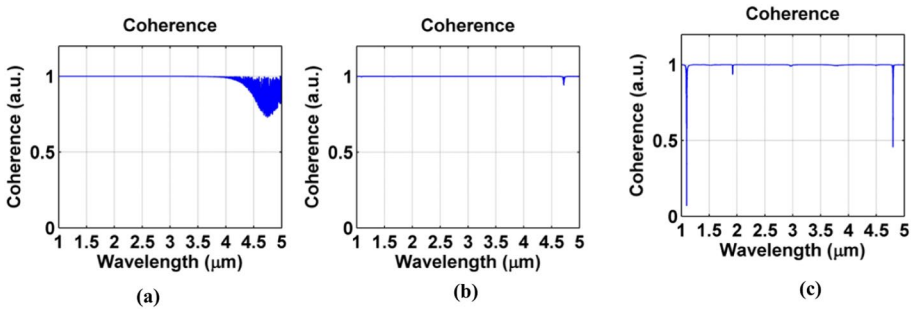

Fig. 11 Coherence with the change in peak power of input pulse **a** 4.1 kW**, b** 6.1 kW and, **c** 8.1 kW

there is possible introduction of noise and hence reducing the coherence which is depicted in Fig. 11.

To assess the performance of our proposed waveguide, we calculated the Figure of Merit (FOM) using Eq. (14), resulting in a value of approximately $\sim 3.93 \times 10^2$ $[THz/(cm.kW)]$. This value surpasses those reported in previous studies on waveguide designs. In comparison to the FOM values reported in a comprehensive review paper (Bres et al. 2023), which calculated FOM based on similar formulae from earlier works, our result demonstrates a significant improvement, indicating the superior performance of our waveguide in terms of nonlinear optical efficiency and power handling.

After thoroughly evaluating our design for efficient and coherent supercontinuum (SC) generation, we now extend its application to optical coherence tomography (OCT). Operating at a central wavelength of 1300 nm, the proposed design achieves SC broadening of

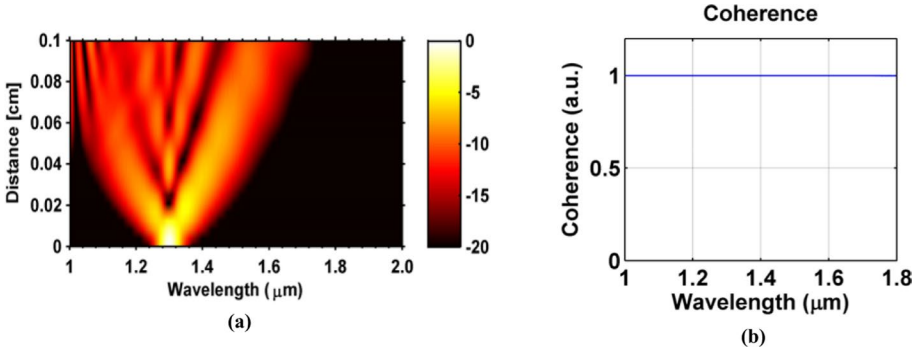

Fig. 12 **a** Spectral evolution at 1300 nm pump wavelength and **b** Coherence

Table 3 Comparison between simulated waveguide results and previous works

Core Material	Purpose	SC Broadening (μm)	Axial Resolution (μm)	Peak Power (kW)	Reference
Si_3N_4 and TeO_2	SC generation	0.95–5.50	–	10	(Saini et al. 2021)
Si_3N_4	SC generation	0.8–6	–	20	(Faisal et al. 2024)
Si_3N_4	SC generation	0.76–6.6	–	10	(Al Kayed et al. 2021)
Si_3N_4	SC generation	1.5–3.9		6.8	(Tagkoudi et al. 2021)
Si	OCT	–	1.24	10	(Ferhat et al. 2018)
Si	OCT	–	2.6	0.77	(Pakarzadeh et al. 2023)
Si_3N_4 and TeO_2	SC generation	1–5	–	6.1	This work
Si_3N_4 and TeO_2	OCT		1.007	4.6	This work

$\Delta\lambda = 740$ nm, covering the spectral range from 1 μm to 1.740 μm at the -10 dB level. The ultrashort pulse driving this broadening has a pulse width of 45 fs and a peak power of 4.6 kW. Using Eq. (13), the calculated axial resolution (l_c) is 1.007 μm (in air) at 1.3 μm. The axial resolution is expected to improve further when applied to biological tissues for imaging. The spectral evolution and coherence is shown in Fig. 12. The axial resolution offered by our structure is 1.007 μm at 1.3 μm which is better than 1.24 μm at 1.3 μm (Ferhat et al. 2018) and 2.8 μm at 1.3 μm wavelength (Ferhat and Cherbi 2016).

After examining our waveguide structure with different laser operating conditions and for optical coherence tomography, we finally confirm our decision to propose the CMOS compatible hybrid inverse parabolic waveguide for on-chip supercontinuum generation and optical coherence tomography. Our simulation results in highly coherent SC spectra ranging from 1–5 μm when pumped with 2 μm pulses having 45 fs pulse width and 6.1 kW peak power in only 1 mm long waveguide. The calculated values of FOM and axial resolution also comes out to be superior to the previously reported results. Additionally, we have compared our results of SC broadening with previously reported results for SC generation in waveguides and found that an efficient, broad and highly coherent supercontinuum spectra can be generated by our proposed waveguide design along with the application specific OCT at lower peak powers. The comparison is tabulated in Table 3.

5 Conclusion

In conclusion, we have proposed and investigated via computational simulation, an inverse hybrid parabolic rib waveguide consisting of CMOS compatible TeO_2 and Si_3N_4 for on chip-mid infrared supercontinuum generation and high resolution optical coherence tomography. We analysed the effect of geometrical parameters on dispersion characteristics to finalise the optimised structure and discussed the fabrication possibility. The optimised design offers zero dispersion wavelength near 1.7 μm and the when pumped at 2 μm wavelength our proposed design structure is able to produce a highly coherent SC spectrum broadening covering 1-5 μm (2.32 octaves), with pulses having temporal width 45 fs and peak power 6.1 kW in only 1 mm long waveguide. Further, we also simulated our proposed design for application specific purpose i.e. for optical coherence tomography. When operated at 1.3 μm, axial resolution of 1.007 μm is achieved using 4.6 kW peak power. Finally, the robustness of the waveguide is studied with the fabrication tolerance having uncertainty of 2% and from the results we can conclude the stability and robustness of

our proposed design. The proposed waveguide can help in various applications ranging from non-linear spectroscopy to optical coherence tomography and from medical imaging to high-bit rate telecommunication. Since the proposed design is CMOS compatible, it can be positioned as an excellent platform for low-loss and high performance future photonic integrated circuits.

Author Contributions D Garg has done writing – original draft, Validation, Methodology, Investigation and A Kumar has done writing – review & editing, Supervision, Software, and Formal analysis.

Funding The authors have not disclosed any funding.

Data availability No datasets were generated or analysed during the current study.

Declarations

Conflict of interest The authors declare no competing interests.

References

Ahmad, H., Karim, M.R., Rahman, B.M.A.: Dispersion-engineered silicon nitride waveguides for mid-infrared supercontinuum generation covering the wavelength range 0.8–6.5 μm. Laser Phys. **29**(2), 025301 (2019)

Al Kayed, N., Karim, M.R., Hussain, A., Jahan, N., and Rahman, B.M.A. Wideband mid-infrared supercontinuum generation using inverse tapered silicon nitride waveguide. In: IEEE International Conference on Telecommunications and Photonics (ICTP) 1–5. IEEE (2021).

Brès, C.S., Della Torre, A., Grassani, D., Brasch, V., Grillet, C., Monat, C.: Supercontinuum in integrated photonics: generation, applications, challenges, and perspectives. Nanophotonics **12**, 1199–1244 (2023)

Chauhan, P., Kumar, A., Kalra, Y.: Mid-infrared broadband supercontinuum generation in a highly nonlinear rectangular core chalcogenide photonic crystal fiber. Opt. Fiber Technol.Fiber Technol. **46**, 174–178 (2018)

Dudley, J.M., Genty, G., Coen, S.: Supercontinuum generation in photonic crystal fiber. Rev. Mod. Phys. **78**, 1135 (2006)

Faisal, M., Karim, M.R., Shafiq, T., Rahman, B.M.A.: Dispersion tailored suspended core SiN channel waveguide for broadband supercontinuum generation. Opt. Quant. Electron. **56**, 351 (2024)

Ferhat, M.L., Cherbi, L.: Self-steepening and intra-pulse Raman scattering for supercontinuum generation in optimized photonic crystal fiber at 1.3 μm. Micro-Struct. Special. Opt. Fibres IV, SPIE **9886**, 29–35 (2016)

Ferhat, M.L., Cherbi, L., Haddouche, I.: Supercontinuum generation in silica photonic crystal fiber at 1.3 μm and 1.65 μm wavelengths for optical coherence tomography. Optik **152**, 106–115 (2018). https://doi.org/10.1016/j.ijleo.2017.09.111

Frigg, A., Boes, A., Ren, G., Abdo, I., Choi, D.Y., Gees, S., Mitchell, A.: Low loss CMOS-compatible silicon nitride photonics utilizing reactive sputtered thin films. Opt. Express **27**, 37795–37805 (2019)

Garg, D., Singh, J., Kumar, A.: Design and theoretical study of rectangular photonic crystal fiber based sensor for chemical sensing in terahertz regime. Indian J. Phys. (2024). https://doi.org/10.1007/s12648-024-03343-9

Ghanbari, A., Kashaninia, A., Sadr, A., Saghaei, H.: Supercontinuum generation for optical coherence tomography using magnesium fluoride photonic crystal fiber. Optik **140**, 545–554 (2017)

Heideman, R. G., Melloni, A., Hoekman, M., Borreman, A., Leinse, A., and Morichetti, F. Low loss, high contrast optical waveguides based on CMOS compatible LPCVD processing: technology and experimental results. In: Proc. of the 9th IEEE/LEOS Symp. in the Benelux, 71–74 (2005).

Hitaishi, V., Ashok, N.: Broadband Supercontinuum Generation Using Dispersion Engineered As_2Se_3-GeAsSe-GeAsS Waveguide at 6 μm. IEEE Access **11**, 12294–12302 (2023)

Ji, X., Mojahed, D., Okawachi, Y., Gaeta, A.L., Hendon, C.P., Lipson, M.: Millimeter-scale chip–based supercontinuum generation for optical coherence tomography. Sci. Adv. (2021). https://doi.org/10.1126/sciadv.abg8869

Jiang, X., Joly, N.Y., Finger, M.A., Babic, F., Pang, M., Sopalla, R., Frosz, M.H., et al.: Supercontinuum generation in ZBLAN glass photonic crystal fiber with six nanobore cores. Opt. Lett. **41**, 4245–4248 (2016)

Kanika, N.J., Saini, T.S.: Dispersion-engineered SiN-Coated TeO_2 hybrid waveguide for nonlinear applications. J. Electr. Mater. **53**(9), 5212–5221 (2024). https://doi.org/10.1007/s11664-024-11228-0

Ke, K., Xia, C., Islam, M.N., Welsh, M.J., Freeman, M.J.: Mid-infrared absorption spectroscopy and differential damage in vitro between lipids and proteins by an all-fiber-integrated supercontinuum laser. Opt. Express **17**, 12627–12640 (2009)

Khamaru, A., Kumar, A.: As38Se62 based segmented clad-graded index photonic crystal fiber for supercontinuum generation covering 3–9.5 µm with moderate peak power. Opt. Quant. Electron. **56**, 1246 (2024)

Khamaru, A., Kumar, A.: Ge-Se-Te based penrose photonic quasi-crystal fiber for SCG covering 2–21 µm MIR regime. Opt. Mater. **155**, 115849 (2024)

Khamis, M.A., Abbasi, Z.Q.: Design of ultra-broadband and highly coherent MIR supercontinuum generation using a photonic crystal fiber. Opt. Quant. Electron. **56**, 1–11 (2024)

Klimczak, M., Michalik, D., Stępniewski, G., Karpate, T., Cimek, J., Forestier, X., Pysz, D., Stępień, R., Buczyński, R.: Coherent supercontinuum generation in tellurite glass regular lattice photonic crystal fibers. JOSA B **36**, A112–A124 (2019)

Li, Q., Liu, L., Jia, Z., Qin, G., Ohishi, Y., Qin, W.: Increased red frequency shift in coherent mid-infrared supercontinuum generation from tellurite micro-structured fibers. J. Lightwave Technol. **35**, 4740–4746 (2017)

Markos, C., Bang, O.: Nonlinear label-free biosensing with high sensitivity using As_2S_3 chalcogenide tapered fiber. J. Lightwave Technol. **33**, 2892–2898 (2015)

Pakarzadeh, H., Fatemipanah, Z., Kumar, U.A.: Supercontinuum generation in silica-based photonic crystal fibers for high-resolution ophthalmic optical coherence tomography. SILICON **15**, 6655–6661 (2023)

Roeloffzen, C.G.H., Hoekman, M., Klein, E.J., et al.: Low-loss Si_3N_4 TriPleX optical waveguides: technology and applications overview. IEEE J. Sel. Top. Quantum Electron. **24**, 4400321 (2018)

Saini, T.S., Sinha, R.K.: Mid-infrared supercontinuum generation in soft-glass specialty optical fibers: A review. Prog. Quantum Electron.. Quantum Electron. **78**, 100342 (2021)

Saini, T.S., Supradeepa, V.R.: Tellurium-oxide coated silicon-nitride hybrid waveguide for near-to-mid-IR supercontinuum generation: design and analysis. J. Mod. Opt. **68**, 29–36 (2021)

Saini, T.S., Kumar, A., Sinha, R.K.: Broadband mid-infrared supercontinuum spectra spanning 2–15 µm using As_2Se_3 chalcogenide glass triangular-core graded-index photonic crystal fiber. J. Lightwave Technol. **33**, 3914–3920 (2015)

Sharma, R., Kaur, S., Chauhan, P., Kumar, A.: Computational design and analysis of $GeSe_2$-As_2Se_3-PbSe based rib waveguide for mid-infrared supercontinuum generation. Optik **220**, 165032 (2020)

Singh, N., Mbonde, H.M., Frankis, H.C., Ippen, E., Bradley, J.D., Kärtner, F.X.: Nonlinear silicon photonics on CMOS-compatible tellurium oxide. Photonics Research **8**, 1904–1909 (2020)

Tagkoudi, E., Amiot, C.G., Genty, G., Brès, C.S.: Extreme polarization-dependent supercontinuum generation in an uncladded silicon nitride waveguide. Opt. Express **29**, 21348–21357 (2021)

Tomer, D.S., Kumar, A.: Design and numerical modeling of chalcogenide parabolic-core waveguide for on-chip supercontinuum generation extending from near-IR region to mid-IR region. Microw. Opt. Technol. Lett.. Opt. Technol. Lett. **66**, e34105 (2024)

Wen, J., Ma, C., Fan, W., Fu, H.: Spectral–temporal description of dispersive wave emission and soliton trapping in micro-nano silicon-on-insulator waveguides. Opt. Laser Technol. **71**, 50–54 (2015)

Wen, J., Duan, L., Ma, C., Fan, W.: Numerical simulation and analysis of femtosecond pulse evolution in liquid-core photonic crystal fiber based on adaptive step-size methods. Opt. Quant. Electron. **51**, 1–14 (2019)

Wen, J., Liang, B., Sun, W., He, C., Xiong, K., Yu, H., Wang, Q.: Coherence analysis of supercontinuum generation in nitrobenzene liquid-core photonic crystal fiber based on adaptive step-size methods. Opt. Quant. Electron. **56**, 619 (2024)

Zhang, W.Q., Shahraam, A.V., Monro, T.M.: A genetic algorithm based approach to fiber design for high coherence and large bandwidth supercontinuum generation. Opt. Express **17**(21), 19311 (2009). https://doi.org/10.1364/OE.17.019311

Zhao, H., Kuyken, B., Clemmen, S., et al.: Visible-to-near-infrared octave spanning supercontinuum generation in a silicon nitride waveguide. Opt. Lett. **40**, 2177–2180 (2015)

Publisher's Note Springer Nature remains neutral with regard to jurisdictional claims in published maps and institutional affiliations.

Springer Nature or its licensor (e.g. a society or other partner) holds exclusive rights to this article under a publishing agreement with the author(s) or other rightsholder(s); author self-archiving of the accepted manuscript version of this article is solely governed by the terms of such publishing agreement and applicable law.

Nanotechnology Perceptions
ISSN 1660-6795
www.nano-ntp.com

Comparative Analysis of Carbon Footprint and Environmental Impact of Laptops

Mohd Tayyab[1], Ranganath M Singari[1], Peer M Sathikh[2]

[1]Department of Design, Delhi Technological University, India.
[2]School of Art, Design & Media, Nanyang Technological University, Singapore.
Email: mdtayyab7809@gmail.com

The widespread use and mass production of desktop and laptop computers contributes to global warming. Due to the demand for increased performance and faster processing capabilities, new models of laptop computers become outdated rather quickly: a laptop's typical lifespan is between three and four years. To understand the environmental impact of different laptops from major brands, A comparative analysis is done by taking same categories (size, weight and type) laptops from different brands (Apple, HP, Dell , Microsoft, Acer, Lenovo and Asus) and compared the amount of carbon release throughout their life cycle. All the data are taken from the respective brands carbon footprint report.
Keywords: Life cycle assessment, Laptops, Carbon Footprint, Environmental impact.

1. Introduction

Background and Motivation

The use of computers, smartphones, and other consumer electronic devices (CEDs) has revolutionised communication, entertainment, and personal productivity in daily life over the past 40 years. According to estimates from the US EPA (2011), more than 900 million desktop and laptop computers as well as 700 million cathode ray tube (CRT) and flat-screen monitors have been sold in the country since 1980.

Between 2013 and 2015, the global market for personal computing devices is anticipated to grow 11%, with tablets, smartphones, and other ultramobile accounting for the majority of that growth (Gartner, 2014). Consumer electronics have many negative environmental effects, ranging from the risk of adverse effects on human and ecological health that may result from the release of toxic materials (heavy metals, flame retardants, etc.) during end-of-

life management (Wager et al., 2011) to the climate change impacts resulting from the significant embodied energy related to manufacturing and use (Teehan and Kandlikar, 2013). Given the rise in popularity of these products, manufacturers, policymakers, and consumers are searching for ways to reduce the environmental impact of electronics over their entire life cycle by promoting greener design, the use of safer materials, and increased recycling and reusing. The term "environmentally preferable" refers to "products or services that have a lesser or reduced effect on human health and the environment when compared with competing products or services that serve the same purpose." Institutional buyers in the public and private sectors are attempting to allocate their purchasing budgets towards "environmentally preferable" electronics goods. The use of raw materials, production, packaging, distribution, use, reuse, operation, maintenance, and disposal are all included in this comparison (Dodd and Wolf, 2013).

According to Moraga et al., (2022) materials should be kept in use for as long as possible to reduce waste and its effects on the environment.

The emergence of environmental standards and eco-labels for personal computers and other electronics globally reflects the demand for environmentally preferable (US EPA, 2014a) electronics. More than 16 private or public standards and eco-labels are found in a database maintained by the Global Eco-labelling Network (Global Ecolabelling Network, 2014) with regard to common CEDs like computers, printers, copiers, televisions, and cell phones. The Energy Star program, which is implemented in the US and 34 other countries, is one example of an additional standard that applies to specific CED features, such as energy use.

A laptop computer requires a lot of time and materials to construct. According to a study by the United Nations University, an average desktop computer with a monitor requires about 1.8 tons of raw materials and other natural resources to produce. A desktop computer and a 17-inch CRT monitor require 240 kilograms of fossil fuels, 22 kilograms of chemicals, and 1,500 kilograms of water to produce (Hoang, A et al., 2009). This is comparable to a mid-size car (Wilson 2004).

In order to obtain data to help the selection of environmentally friendly consumer electronics items, the objective of this study is to carry out a screening-level life cycle evaluation of a laptop. It attempts to improve knowledge of potential environmental trade-offs during the lifespans of well-known laptops from various brands, including Apple, HP, Dell, Microsoft, Acer, Lenovo, and Asus.

2. Literature Review

According to Canalys research (2021), the PC market in India is predicted to grow by 45% in 2021, with shipments of desktop, notebook, and tablet computers reaching 18.6 million units. This makes 2021 the Indian PC market's best year for growth since 2013, when shipment growth was 29%. Most of the market growth was driven by notebook PCs (Laptops), which accounted for 63% of all shipments with 11.8 million units, up 49% year over year (Tech Desk, 2022).

The second pandemic wave and the lockdowns hampered company operations, but they also raised demand for PCs because professionals and students were compelled to spend more

time working and studying at home. The majority of the market growth was driven by notebook PC shipments, which accounted for 63% of all shipments and increased by 49% year over year to 11.8 million units(Tech Desk, 2022).

Lenovo shipped 4.2 million units with a market share of 23% (Lenovo, 2023), trailing HP in the market (including tablets), which it led with 4.6 million units shipped in 2021(HP, 2023). After shipping 2.5 million units with a 14% market share, Dell placed a far-off third (Dell, 2023). Samsung and Acer placed fourth and fifth, respectively, with 7.2 and 6.8 percent of the market (Tech Desk, 2022).

With market shares of 25,1%, 23%, and 14%, respectively, for just notebook and desktop computers (as opposed to laptops), HP Lenovo and Dell are still in the lead. Acer comes in at fourth place with an 8.4% market share, while Apple trails in distant fifth place with a 4.7% market share due to Samsung's protracted absence from the Indian PC market (Tech Desk, 2022).

Desktop, laptop, and netbook computers are all included in the annual worldwide market share of personal computer vendors, but mobile devices, such as tablet computers that do not fit into the category of 2-in-1 PCs, are not (Rimol & Howley, 2023).

Table 1: Ranking of different laptop brands on the basis of Market Share (Q1 2022)

Ranking	Laptop Brands	Share
1	Lenovo	23.8%
2	HP	20.4%
3	Dell	17.7%
4	Apple	9.0%
5	Acer	7.2%
6	Asus	7.1%
	Others	14.8%

How do laptops effect the environments?

A laptop's estimated average carbon footprint is 422.5 kg, which takes into account emissions from manufacturing, shipping, and the first four years of use (Haughton, 2021).

The amount of CO2 released by a laptop varies considerably depending on the maker, the size of the device, and the frequency of usage, which should be noted. Due to the uncertainty of their calculations, all manufacturers' estimates suggest that the CO2 could vary by +/- 15 to 20% (Haughton, 2021).

What is a carbon footprint?

A carbon footprint is the total amount of greenhouse gases—like carbon dioxide and methane—that are produced as a result of our actions.

Usually, the first thing we look at when calculating a laptop's carbon footprint is how much energy it consumes. According to Lars Meiritz, vice-president of Gartner, just 20% of the environmental impact of a laptop is attributable to its use, even if a laptop used for 8 hours a day generates between 44 and 88 kg of CO2 yearly. Then what about the other 80%? (Meiritz, 2021).

The carbon footprint of laptops has become a significant concern, and researchers are exploring ways to reduce their environmental impact. For example, Li et al. (2020) propose a

circular economy framework for laptop design and manufacturing, which considers the entire lifecycle of the device and aims to reduce resource consumption, waste generation, and carbon emissions. The framework includes three phases: design for durability and repair, design for disassembly and recycling, and design for circularity.

Furthermore, there is a growing trend towards sustainable laptops made from recycled materials. Dell, for example, has developed a laptop made from recycled ocean plastic, while HP has launched a laptop made from recycled aluminum (Hsu, 2021). However, sustainable laptops are currently more expensive than traditional laptops, which may limit their widespread adoption.

In conclusion, the increased demand for laptops has a negative impact on the environment, and it is essential to consider the entire lifecycle of the device when analyzing its environmental impact. Researchers are exploring ways to reduce the carbon footprint of laptops, such as circular economy frameworks and sustainable materials. However, these solutions are currently more expensive than traditional laptops, which may limit their adoption. It is crucial to continue research and innovation to reduce the environmental impact of laptops while also meeting the growing demand for these devices.

3. Methodology

In this study, carbon emission was calculated on the basis of carbon footprint reports of different brands of similar specification laptop models which is collected from their respective official website and after that a comparison of these details is performed so that one can easily understand and differentiate between them on the basis of their carbon emission.

These are the models of the laptops of respective brands are taken for comparisons:

1. Apple MacBook Air Laptop with M2 chip: 13.6-inch Liquid Retina Display, 8GB RAM, 256GB SSD, 1.2 Kg.

2. HP Envy 11th Gen Intel Core i5: 14-inch, 16GB RAM, 1TB SSD, 1.59Kg.

3. Dell XPS 13 9370 Core i5: 13.3-inch, 8GB RAM, 128GB SSD, 1.27 Kg.

4. Microsoft Surface Laptop 5: 13.5" Intel® Evo™12th Gen Core™ i7, 16GB RAM, 256GB SSD, 1.288Kg.

5. Acer TravelMate TMP614-52-73EJ 14-inch, Intel Core i7, 16 GB RAM, 512GB SSD, 1.1Kg.

6. Lenovo ThinkBook 13s G3 ACN: 13.3-inch, AMD Ryzen 7, 16 GB RAM, 512 GB SSD, 1.26Kg.

7. Asus ZenBook 14X OLED (UX5401Z): 14-inch, Intel Core i5, 16GB, 512GB SSD, 1.4Kg.

And their carbon footprint are show below which is extracted from their respective official website and percentage contribution of all phases during whole life cycle of laptops are also shown with the help of pie chart respectively as show below:

1. Apple **MacBook Air** Laptop with **M2** chip: According to Carbon Footprint report of Apple MacBook Air, its produce total 147 kg carbon emissions, which is classified as (Apple, 2022):
    - 69% Production
    - 8% Transport
    - 22% Use
    - <1% End-of-life processing

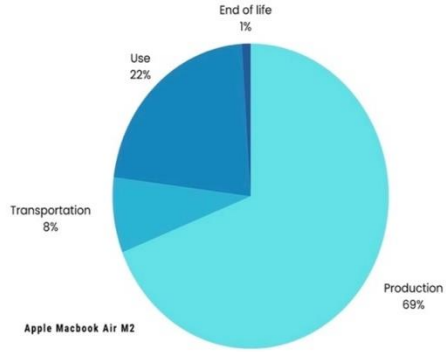

2. **HP Envy** 11th Gen Intel Core i5: **14-inch**: According to Carbon Footprint report, its produce total 206 kg carbon emissions, which is classified as (HP, 2021):
    - 76% Production
    - 5% Transport
    - 19% Use
    - 0% End-of-life processing

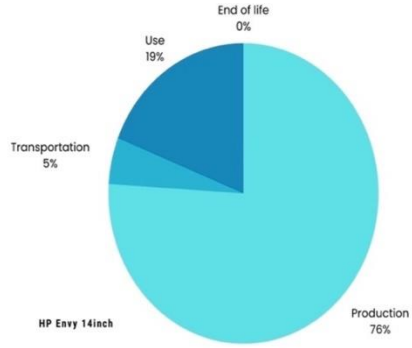

3. **Dell** XPS 13 9370 Core i5: **13.3-inch**: According to Carbon Footprint report, its produce total 297 kg carbon emissions, which is classified as (Dell, 2018):
    - 83% Production
    - 4.3% Transport
    - 12.4% Use
    - 0.3% End-of-life processing

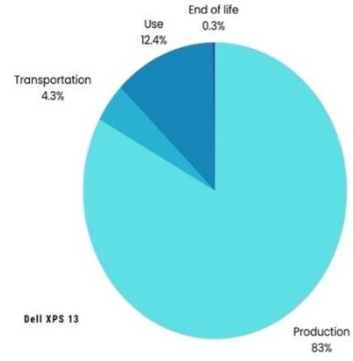

4. **Microsoft Surface Laptop 5: 13.5 inch**: According to Carbon Footprint report, its produce total 255 kg carbon emissions, which is classified as (Microsoft, 2022):
    - 84.7% Production
    - 3.1% Transport
    - 12.1% Use
    - 0.1% End-of-life processing

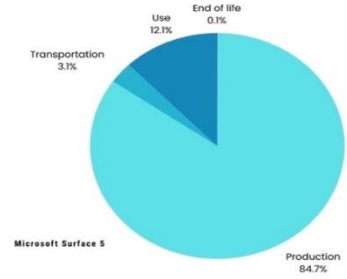

7. **Asus ZenBook 14X OLED (UX5401Z): 14-inch**:
According to Carbon Footprint report, produce total 281 kg carbon emissions, which is classified as (Asus, 2022):
    - 70.3% Production
    - 2.7% Transport
    - 26.9% Use
    - 0.1% End-of-life processing

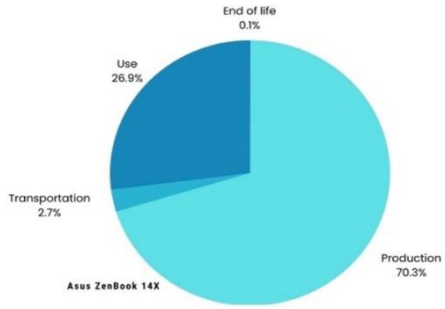

Figure 1, demonstrates the system boundary of LCA study of laptops, in which manufacturing stages includes raw material acquisition, production, packaging, and transportation. At the phase of use it includes the energy consumption and part replacements for maintenance. Lastly during end of life phase in includes waste management such as landfill or incineration, reuse, recycling.

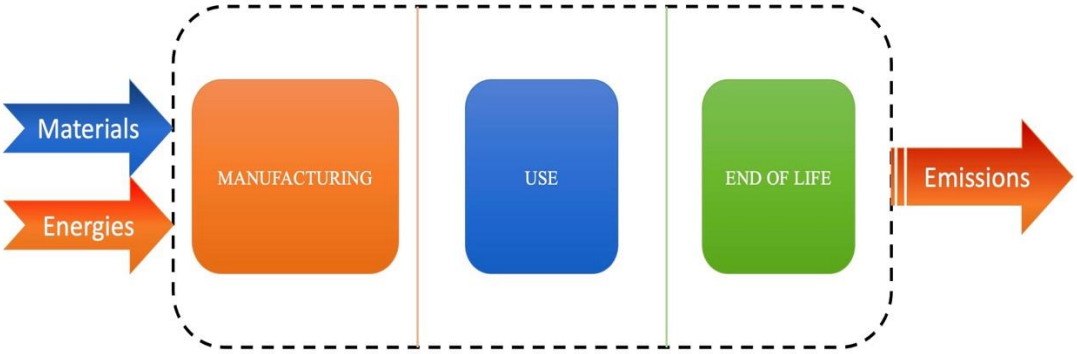

Fig. 1: System boundary of LCA study of Laptops

4. Results and Discussion

The study compared the carbon emissions of seven similar categories laptop models from different brands, based on their carbon footprint reports. The laptops included in the study were: Apple MacBook Air M2, HP Envy, Dell XPS 13, Microsoft Surface 5 Laptop, Acer TravelMate, Lenovo ThinkBook 13s G3, and Asus ZenBook 14X OLED.

Table 2: Product's estimated Carbon Footprint for whole Life Cycle:

Carbon Footprint	Apple MacBook Air M2 (Kg CO2)	HP ENVY Laptop 14-eb0020TX (Kg CO2)	Dell XPS 13 9370 (Kg CO2)	Microsoft Surface Laptop 5 (Kg CO2)	Acer TMP614-52 Business Notebook (Kg CO2)	Lenovo ThinkBook 13s G3 ACN (Kg CO2)	Asus ZenBook 14X OLED (Kg CO2)
Manufacturing	101.43	156.56	246.51	215.5	46.50	379.68	197.54
Transportation	11.76	10.30	12.77	8	2.31	13.56	7.58
Product Use	32.34	39.14	36.83	30.5	92.18	58.76	75.58
End of Life	1.47	0	0.89	1	0.01	0	0.3

Total	147	206	297	255	141	452	281

The results show in Table 2 that the carbon emissions produced by the laptops vary significantly, with the lowest carbon emissions of 141 kg produced by Acer TravelMate and the highest carbon emissions of 452 kg produced by Lenovo ThinkBook. The breakdown of carbon emissions by production, transport, use, and end-of-life processing also varies among the laptop models. For example, the carbon emissions from production ranged from 46.50kg for Acer TravelMate to 379.68kg for Lenovo ThinkBook. The carbon emissions from use ranged from 30.5kg for Microsoft Surface Laptop to 92.18kg for Acer TravelMate. This variation in different phases are shown in Figure 2.

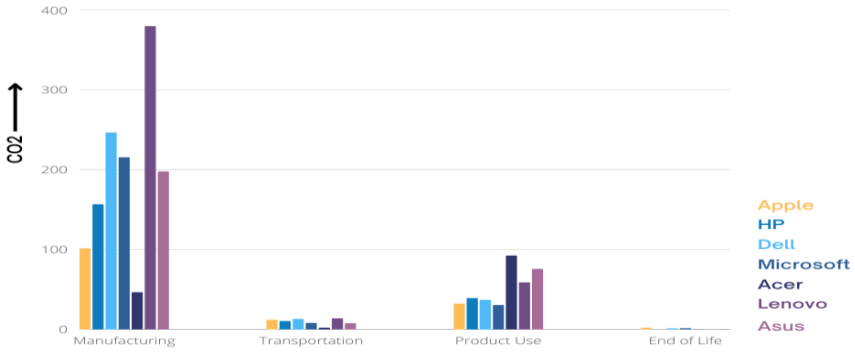

Fig 2. Variation of carbon emission at different phases of life cycle.

The results indicate that the carbon emissions of a laptop are influenced by various factors, such as the materials used in production, the manufacturing process, energy efficiency during use, and waste management practices. The findings of this study can help consumers make more informed decisions about the environmental impact of their purchasing choices and also encourage manufacturers to adopt more sustainable practices in their production processes.

If we calculate carbon emission of these selected laptops on the scale of 0 to 500 Kg CO_2 emission, the environmental performance percentage of these laptops can easily become more understandable as show below in Table 3 and a graphical represented also show below for ease of visualisation in Figure 3:

Table 3: On scale from 0 to 500 kg CO_2 emission

Laptops	Percentage
Acer	28.2%
Apple	29.4%
HP	41.2%
Dell	59.4%
Asus	56.2%
Microsoft	51%
lenovo	90.4%

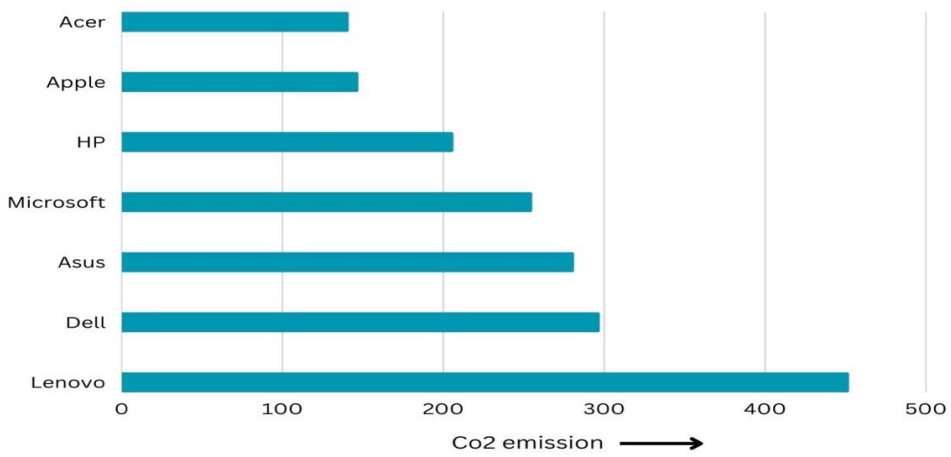

Fig 3. Graphical representation of carbon emission of selected brands on the scale of 0 to 500 kg CO_2 emission

5. Conclusion

In this study, the carbon emissions of seven laptop models were compared based on their carbon footprint reports.

The laptops included in the study were Apple MacBook Air, HP Envy, Dell XPS, Microsoft Surface Laptop, Acer TravelMate, Lenovo ThinkBook, and Asus ZenBook.

The results show that the carbon emissions produced by the laptops vary significantly, with the lowest carbon emissions of 141 kg produced by Acer TravelMate and the highest carbon emissions of 452 kg produced by Lenovo ThinkBook.

The breakdown of carbon emissions by production, transport, use, and end-of-life processing also varies among the laptop models.

The results indicate that the carbon emissions of a laptop are influenced by various factors, such as the materials used in production, the manufacturing process, energy efficiency during use, and waste management practices.

The findings of this study can help consumers make more informed decisions about the environmental impact of their purchasing choices and also encourage manufacturers to adopt more sustainable practices in their production processes.

References

1. Hoang, A., Tseng, W., Viswanathan, S., & Evans, H. (2009). Life cycle assessment of a laptop computer and its contribution to greenhouse gas emissions (Doctoral dissertation, National University, San Diego).
2. Williams E. (2004). Energy Intensity of Computer Manufacturing: Hybrid Assessment Combining Process and Economic Input-Output Methods. United Nation University.

Environmental Science Technology, Volume 38. Tokyo, Japan.
3. Canalys Newsroom - India's PC market grows at its fastest rate in a decade as shipments jump 45% in 2021. (2021, November 30). Canalys Newsroom - India's PC Market Grows at Its Fastest Rate in a Decade as Shipments Jump 45% in 2021. https://www.canalys.com/newsroom/pc-sales-in-india-Q4-2021
4. Tech Desk. (2022, March 25). Indian PC market grew 45 per cent in 2021; HP, Lenovo and Dell lead: Canalys. The Indian Express. Retrieved April 12, 2023, from https://indianexpress.com/article/technology/laptops/indian-pc-market-grew-45-per-cent-in-2021-hp-lenovo-and-dell-lead-canalys-7835937/
5. Lenovo. (2023, April 12). The Indian Express. https://indianexpress.com/about/lenovo/
6. Asus. (2022, August). ASUS Corporate Social Responsibility. ASUS Corporate Social Responsibility. Retrieved April 12, 2023, from https://csr.asus.com/english/article.aspx?id=1827
7. Lenovo. (2021, April). Regulatory Compliance | ECO Declarations | Lenovo US. Regulatory Compliance | ECO Declarations | Lenovo US. Retrieved April 12, 2023, from https://www.lenovo.com/us/en/compliance/eco-declaration/?orgRef=https%253A%252F%252Fwww.google.com%252F
8. Acer. (2021, December). ACER CSR. ACER CSR. Retrieved April 12, 2023, from https://www.acer-group.com/sustainability/en/circular-economy-and-product-life-cycle.html?keyword=PCF
9. Microsoft. (2022). Download Eco Profiles from Official Microsoft Download Center. Download Eco Profiles From Official Microsoft Download Center. Retrieved April 12, 2023, from https://www.microsoft.com/en-us/download/details.aspx?id=55974
10. Dell. (2018, December). Product Carbon Footprints | Dell India. Product Carbon Footprints | Dell India. Retrieved April 12, 2023, from https://www.dell.com/en-in/dt/corporate/social-impact/advancing-sustainability/climate-action/product-carbon-footprints.htm
11. HP. (2021). Sustainable Impact. Sustainable Impact | HP® United Kingdom. Retrieved April 12, 2023, from https://www.hp.com/gb-en/hp-information/sustainable-impact.html
12. Apple. (2022). Environment. Apple (India). Retrieved April 12, 2023, from https://www.apple.com/in/environment/
13. Meiritz. (2021). Financial Times. Financial Times. Retrieved April 12, 2023, from https://www.ft.com/content/49b7eb30-15d6-11dc-a7ce-000b5df10621
14. Energuide. (n.d.). How much power does a computer use? And how much CO2 does that represent? Retrieved April 12, 2023, from https://www.energuide.be/en/questions-answers/how-much-power-does-a-computer-use-and-how-much-co2-does-that-represent/54/
15. Haughton, N. (2021, August 9). What Is The Carbon Footprint Of A Laptop? Circular ComputingTM. https://circularcomputing.com/news/carbon-footprint-laptop/
16. Rimol, & Howley. (2023, January 11). PC Demand Collapses Due to Economic Uncertainty. Gartner. Retrieved April 12, 2023, from https://www.gartner.com/en/newsroom/press-releases/2023-01-11-gartner-says-worldwide-pc-shipments-declined-28-percent-in-fourth-quarter-of-2022-and-16-percent-for-the-year
17. HP. (2023, April 12). The Indian Express. https://indianexpress.com/about/hp/
18. Dell. (2023, April 12). The Indian Express. https://indianexpress.com/about/dell/

Physica Scripta

INCLUSIVE PUBLISHING
TRUSTED SCIENCE

PURPOSE-LED
PUBLISHING™

PAPER

Comparative analysis of two novel chaotic systems, and validation of hybrid function projective and complete synchronization using active-adaptive control

To cite this article: D Khattar *et al* 2024 *Phys. Scr.* **99** 125244

View the article online for updates and enhancements.

You may also like

- Mixed *H* and Passive Projective Synchronization for Fractional Order Memristor-Based Neural Networks with Time-Delay and Parameter Uncertainty
Xiao-Na Song, , Shuai Song et al.
- A New Scheme to Projective Synchronization of Fractional-Order Chaotic Systems
Jun-Wei Wang and Ai-Min Chen
- Image encryption algorithm based on matrix projective combination-combination synchronization of an 11-dimensional time delayed hyperchaotic system
Jyotsna Kumari Bharti, P Balasubramaniam and K Murugesan

This content was downloaded from IP address 14.139.251.98 on 18/11/2024 at 04:59

Physica Scripta

PAPER

Comparative analysis of two novel chaotic systems, and validation of hybrid function projective and complete synchronization using active-adaptive control

RECEIVED
9 August 2024

REVISED
29 October 2024

ACCEPTED FOR PUBLICATION
4 November 2024

PUBLISHED
15 November 2024

D Khattar[1], M Sirohi[2] and R Bansal[3,*]

[1] Department of Mathematics, Kirori Mal College, University of Delhi, Delhi-110007, India
[2] Department of Applied Mathematics, Delhi Technological University, Delhi-110042, India
[3] Department of Mathematics, Ramjas College, University of Delhi, Delhi-110007, India
[*] Author to whom any correspondence should be addressed.

E-mail: rohitbansal97@gmail.com

Keywords: Chaos, novel system, nonlinear control, hybrid function projective synchronization, Lyapunov stability, bifurcation, Poincaré map

Abstract

This study investigates the nonlinear characteristics of two novel 3D-chaotic models using phase portraits, bifurcation diagrams, Lyapunov exponents, time series analysis, and Poincaré maps. Here, we have examined hybrid-function projective and complete synchronization schemes via adaptive and active control methods. Moreover, the performance of hybrid-function projective synchronization, utilizing sine, cosine, and exponential terms, is compared to complete synchronization through two control strategies. Our designed controllers ensure asymptotic global chaotic synchronization based on Lyapunov stability principles. We have also compared our results with other competitive schemes and validated the theoretical findings through simulations on the MATLAB platform.

1. Introduction

Chaos theory is a multidisciplinary field and the applications of this groundbreaking theory encompasses brain activity [1], robotic motion [2], recognizing patterns [3], image encryption [4], economics and finance [5], biological sciences [6], chemical sciences [7], secure communication [8], computer science [9], power converters [10], traffic forecasting [11] and physics [12] and so on. Observing the rich and varied dynamics in chaotic systems with the simplest structure is also fascinating. These systems are distinguished by their beautiful structures, which consist of cylindrical attractors, two-wing attractors, three-wing attractors, etc. Chaos theory governs and influences all aspects of human existence, and therefore it is currently recognized as one of the most fundamental theories. The idea that 'chaos' exists everywhere connects several different fields. During numerical simulations of his model, Lorenz was also the first to observe the essential characteristic of chaos, 'sensitive dependency on initial conditions.' Later, chaos theory became an independent field of research and study.

Chaos synchronization is a procedure where one chaotic system is forced to adjust the properties of another chaotic system for all future states. Pecora and Carroll adopted a drive-response system in 1990 to align identical chaotic structures under distinct initial conditions [13]. There are presently countless synchronization techniques being used, ranging from complete synchronization [14] to various kinds of innovative synchronization like identical synchronization [15], lag synchronization [16], hybrid synchronization [17], phase and anti-phase synchronization [18], projective synchronization [19], compound anti-synchronization [20], hybrid projective synchronization [21], hybrid function projective synchronization and parallel synchronization [22]. In pursuit of better ways for chaos control and synchronization, various types of methods have been developed for dealing with chaos and synchronization of non-identical and identical systems [23–28]. Chaotic systems have been synchronized using a variety of control strategies, such as sliding mode control [29], adaptive control [30], back-stepping strategy [31], active control [32], and linear/nonlinear feedback control [33], etc [34]. The basic theory driving synchronization is to compel or combine two or more chaotic systems to

© 2024 IOP Publishing Ltd. All rights, including for text and data mining, AI training, and similar technologies, are reserved.

adhere to a specific motion feature. Experts from various fields have synchronized novel chaotic and hyper-chaotic systems using the techniques that are already existing in the literature [35, 36], relying on the groundbreaking findings of Lorenz. This theory challenges conventional notions of predictability and also uncovers complex activities within chaotic systems. At its core, chaos theory studies nonlinear dynamical models in which small initial condition alterations result in disproportionately final outcomes.

The primary benefit of employing adaptive control technique is that controllers may be built to achieve drive and response system synchronization without the need to know parameter values. Thus, less information is needed to synchronize the drive and response systems when utilizing this technique. In view of the active control technique, synchronization and anti-synchronization between the drive and response systems are given in [37, 38]. Although the active control theory is simple to use, it has limitations such as fixed and excessively large control signals. As it is understood, signal amplification and reduction are always related to the actual transmission of the signals. Thus, by adjusting the signal's magnitude, the active control can be made better. These days, secure communication is a big concern. Also, as described above, hybrid function projective synchronization (HFPS) offers more complexity to the controller, and the message cannot be readily interpreted by the intruder. Thus, we have utilized the HFPS methodology to define error and the adaptive control technique to regulate the controller. For the purpose of secure communication, their combination will be more beneficial. Additionally, most published papers on HFPS achieve a state where both chaotic systems are integrated into a single chaotic system. However, the Pehlivan chaotic system and the Bhalekar–Gejji chaotic system do not belong in a single chaotic system. The present document is one of the very few that have been described that performs HFPS between two novel chaotic systems in which none of the chaotic systems is a component of the unified chaotic system. Later, in 2016, by using adaptive control technique, the hybrid function projective synchronization of Bhalekar–Gejji and Pehlivan chaotic systems was established where the parameters involved in the system were unknown [30].

In this work, we have presented two new chaotic structures, which are designated as the $\mathcal{R}$-system and the $\mathcal{N}$-system. The Wolf methodology [39] in MATLAB software is applied to determine the Lyapunov Exponents (LEs) of these systems, and the LEs spectrum is displayed to illustrate their chaotic behavior. Systems analysis is done by examining the dynamical qualities through phase visuals, Poincaré sections, and time series. The stability of these systems estimated equilibrium points is addressed. These novel system bifurcation diagrams are carefully studied. With the help of adaptive control, we have implemented hybrid function projective synchronization (HFPS) between these systems and then compared them with the classic approach of active control. The key advantage of adaptive control over active control is that it coordinates responses and driving systems even in the absence of exact parametric knowledge. Furthermore, the response and drive systems' signals are merged in HFPS with multiple and distinct functions, which adds complexity and boosts the confidentiality of the data being transmitted. Owing to the Lyapunov stability theory, we constructed appropriate controllers that enabled us to achieve different synchronizations across these novel systems. In specific scenarios, the following methods are also discussed: hybrid synchronization (HS), anti-synchronization (AS), hybrid projective synchronization (HPS), complete synchronization (CS), and projective synchronization (PS). To validate each theoretical approach, MATLAB is implemented to run numerical simulations that describe the state vectors both before and after the active-adaptive control.

Here we have made the following contribution in this research:

- Two novel chaotic systems are proposed, compared, and studied using various dynamical characteristics such as Poincaré maps, bifurcation charts, etc.
- Complete synchronization is achieved between two novel chaotic models using classical active control.
- We provide important remarks and proofs backing each theoretical finding with the theory of Lyapunov stability.
- We compare the results of active method with adaptive control; keeping the same systems as drive and response model.
- Hybrid function projective synchronization is also implemented using rigor adaptive control.
- We use sine, cosine, and exponential functions to achieve a hybrid function projective scheme; in order to add complexity in the signal.
- Particular cases of synchronization through hybrid function projective schemes such as hybrid synchronization (HS), anti-synchronization (AS), hybrid projective synchronization (HPS), complete synchronization (CS), and projective synchronization (PS) are also discussed.
- All the presented analytical results in the manuscript are then proved using MATLAB simulations.

- A systematic table comparing the outcomes of this research with competing research is also presented.

The outline of the manuscript is as follows: section 2 discusses the general problem of the HFPS synchronization strategy. We have introduced and examined the chaotic features of two novel systems in section 3. The application of the CS using traditional active control is covered in section 4. The use of adaptive control to implement the HFPS and CS is covered in section 5. MATLAB simulations are used in section 6 to validate the presented results. A comparison examination between the HFPS and CS is presented in section 7. Lastly, section 8 presents the research conclusions.

2. Problem formulation

In this section, we explore the challenges in achieving hybrid function projective synchronization (HFPS) between two distinct $n-$ dimensional chaotic models. Let us consider a model for drive described by the following differential equations:

$$\dot{D}(t) = MD + F(D). \tag{1}$$

Here, $D(t) = (d_1(t),\ d_2(t),\ldots,d_n(t))^T \in \mathbb{R}^n$ are states of the drive model, $M \in \mathbb{R}^{n\times n}$ represents some coefficient matrix, and $F(D)$: $\mathbb{R}^n \to \mathbb{R}^n$ is the non-linear portion of the model (1). Further, consider another response model given by:

$$\dot{R}(t) = NR + G(R) + \Psi(D,\ R). \tag{2}$$

In this equation, $R(t) = (r_1(t),\ r_2(t),\ldots,r_n(t))^T \in \mathbb{R}^n$ represents states of the response model, and $N \in \mathbb{R}^{n\times n}$ is again some coefficient matrix with $G(R)$: $\mathbb{R}^n \to \mathbb{R}^n$ being the non-linear portion of the response model (2). The term $\Psi(D, R)$ denotes the adaptive or active controllers to be determined for the purpose of HFPS.

Definition 2.1. The hybrid function projective synchronization (HFPS) is attained between the drive and the response model if:

$$\lim_{t\to\infty} \|e(t)\| = \lim_{t\to\infty} \|R(t) - \Upsilon(t)D(t)\| = 0.$$

Here, $\|.\|$ represents the vector norm, $e(t)$ is the HFPS error, and $\Upsilon(t) = \mathrm{diag}(\Upsilon_1(t), \Upsilon_2(t), \ldots, \Upsilon_n(t))$ is the matrix with $\Upsilon_i(t)$: $\mathbb{R}^n \to \mathbb{R}$ as smooth and bounded functions with $\Upsilon_i(t) \neq 0$ for all t.

Remark 2.2. If $\Upsilon(t) = \mathrm{diag}(\Upsilon_1(t), \Upsilon_2(t), \ldots, \Upsilon_n(t))$ is selected such that each $\Upsilon_i(t) = \Upsilon$(constant), the HFPS reduces to projective synchronization (PS).

Remark 2.3. If $\Upsilon(t) = \mathrm{diag}(\Upsilon_1(t), \Upsilon_2(t), \ldots, \Upsilon_n(t))$ is opted with each $\Upsilon_i(t)$ being an alternative sign constant, then HFPS converts to hybrid projective synchronization (HPS).

Remark 2.4. If $\Upsilon_i(t)$'s are replaced alternatively by ± 1, then HFPS becomes merely a problem of hybrid synchronization (HS).

Remark 2.5. If $\Upsilon(t) = \mathrm{diag}(\Upsilon_1(t), \Upsilon_2(t), \ldots, \Upsilon_n(t))$ is fixed with $\Upsilon_i(t)$ being unity, then HFPS converts to complete (CS) or identical-synchronization (IS).

Remark 2.6. If $\Upsilon(t) = \mathrm{diag}(\Upsilon_1(t), \Upsilon_2(t), \ldots, \Upsilon_n(t))$ is fixed with $\Upsilon_i(t) = -1$, then HFPS converts to anti-synchronization (AS).

3. Systems' description and their systematic analysis

3.1. Chaotic analysis of the $\mathcal{R}$-system

Consider a new three-dimensional $\mathcal{R}$-system given by

$$\begin{cases} \dot{x}_1 &= x_2x_3 - ax_1, \\ \dot{x}_2 &= bx_1 + x_2 - x_1x_3, \\ \dot{x}_3 &= x_2^2 - cx_3 + x_1x_2. \end{cases} \tag{3}$$

where a, b, and c represent certain real parameters, and x_1, x_2, and x_3 are the state elements. The Lyapunov exponents (LEs) pertaining to the aforementioned $\mathcal{R}$-system are $\lambda_1 \approx 5.2682$, $\lambda_2 \approx 0.01497$, and $\lambda_3 \approx -32.6831$, with the system parameters held at $a = 25$, $b = 80$, and $c = \frac{17}{5}$ for $t = 100$. Figure 1 visually represents these exponents spectrum. The dynamical behavior of the $\mathcal{R}$-system is inherently chaotic, as

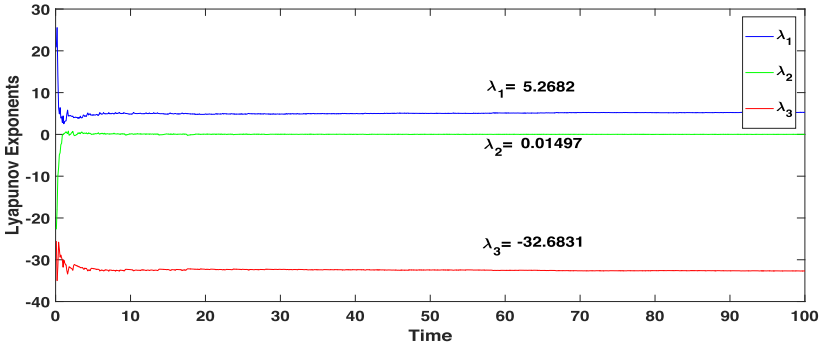

Figure 1. Lyapunov spectrum of the $\mathcal{R}$-system.

evidenced by the presence of one strictly positive, one negative, and one zero LE. Notably, the sum of these exponents, i.e., $\lambda_1 + \lambda_2 + \lambda_3 \approx -27.399$, indicates the dissipative nature of this system. The Kaplan-Yorke dimension of the $\mathcal{R}$-system is $D_1 = 2 + \frac{\lambda_1 + \lambda_2}{|\lambda_3|} \approx 2.16164$ reflecting its fractional dimensionality. The maximum LE for the $\mathcal{R}$-system is identified as 5.2682.

The equilibrium positions of the $\mathcal{R}$-system are nothing but the solutions of

$$\begin{cases} x_2 x_3 - a x_1 = 0, \\ b x_1 + x_2 - x_1 x_3 = 0, \\ {x_2}^2 - c x_3 + x_1 x_2 = 0. \end{cases}$$

and they are $E_1 = (0, 0, 0)$, $E_2 = (-25.86, -8.05, 80.31)$, and $E_3 = (25.86, 8.05, 80.31)$. The Jacobi matrix J_1 for the $\mathcal{R}$-system is:

$$J_1 = \begin{bmatrix} -a & x_3 & x_2 \\ b - x_3 & 1 & -x_1 \\ x_2 & 2x_2 + x_1 & -c \end{bmatrix}.$$

The matrix $J_1(E_1)$ has eigenvalues $\lambda_{11} = -25$, $\lambda_{12} = -3.4$, and $\lambda_{13} = 1.0$. The matrix $J_1(E_2)$ has eigenvalues $\lambda_{21} = -1.55 + 2.14\iota$, $\lambda_{22} = -1.55 - 2.14\iota$, and $\lambda_{23} = -24.28$. The matrix $J_1(E_3)$ has eigenvalues $\lambda_{31} = 3.09 + 36.06\iota$, $\lambda_{32} = 3.09 - 36.06\iota$, and $\lambda_{33} = -33.59$. Therefore, E_1, E_2, and E_3 are all unstable equilibrium points of the new $\mathcal{R}$-system. The two-dimensional phase portraits and the time series of the $\mathcal{R}$-system are depicted in figures 2 and 3, respectively.

3.2. Chaotic analysis of the $\mathcal{N}$-system

Another novel system named as the $\mathcal{N}$-system is given by

$$\begin{cases} \dot{y}_1 &= -y_2 + \delta(y_2 - y_1) - y_3, \\ \dot{y}_2 &= y_1 + 20 y_1 y_3 - \alpha y_2, \\ \dot{y}_3 &= \beta + (y_3 - \gamma) y_1 - y_3 - 15 y_1 y_2. \end{cases} \tag{4}$$

where y_1, y_2, and y_3 represent the $\mathcal{N}$-system's state and α, β, γ, and δ are the parameters of this system. The dynamics of LEs in the $\mathcal{N}$-system are depicted in figure 4 for parameter values $\alpha = 0.75$, $\beta = 16.2$, $\gamma = 5.7$, and $\delta = 5$ at time $t = 100$. The computed LEs are $\beta_1 \approx 0.60956$, $\beta_2 \approx -0.00243$, and $\beta_3 \approx -7.9579$. As evidenced by one zero, one negative, and one positive LE with combined sum being negative, the $\mathcal{N}$-system also exhibits chaos. The phase projections of the $\mathcal{N}$-system are presented in figure 5. The summation $\beta_1 + \beta_2 + \beta_3 \approx -7.35077$, establishes the dissipative nature of the $\mathcal{N}$-system. The Kaplan-Yorke dimension of the $\mathcal{N}$-system is $D_2 = 2 + \frac{\beta_1 + \beta_2}{|\beta_3|} \approx 2.0762$, indicating its fractional dimensionality. The maximum LE of the $\mathcal{N}$-system is identified as 0.60956.

The equilibrium positions in the $\mathcal{N}$-system are the solutions of:

$$\begin{cases} -y_2 - y_3 + \delta(y_2 - y_1) = 0, \\ y_1 - \alpha y_2 + 20 y_1 y_3 = 0, \\ \beta + (y_3 - \gamma) y_1 - 15 y_1 y_2 - y_3 = 0. \end{cases}$$

and they are $E'_1 = (-1.09, -1.36, -0.00)$, $E'_2 = (0.79, 0.98, -0.00)$, $E'_3 = (0.00, 3.94, 15.73)$. The Jacobi matrix J_2 of the $\mathcal{N}$-system is:

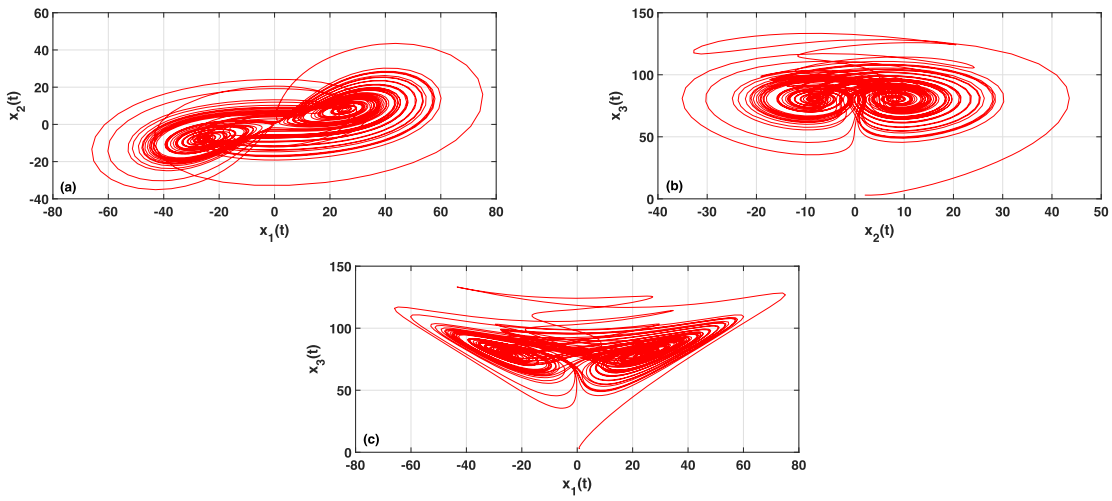

Figure 2. Projections of the $\mathcal{R}$-system in planes: (**a**) x_1-x_2, (**b**) x_2-x_3, and (**c**) x_1-x_3.

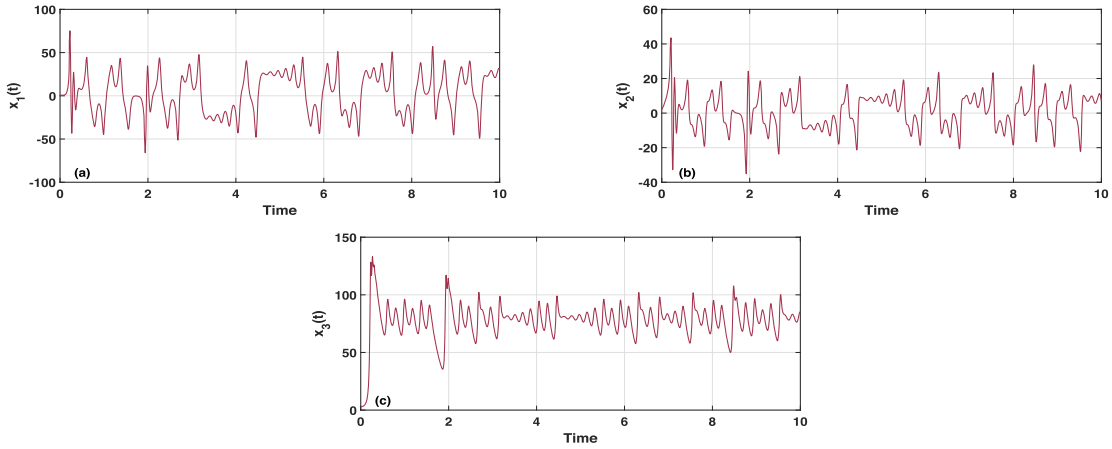

Figure 3. Time series of the $\mathcal{R}$-system: (**a**) x_1 with t, (**b**) x_2 with t, and (**c**) x_3 with t.

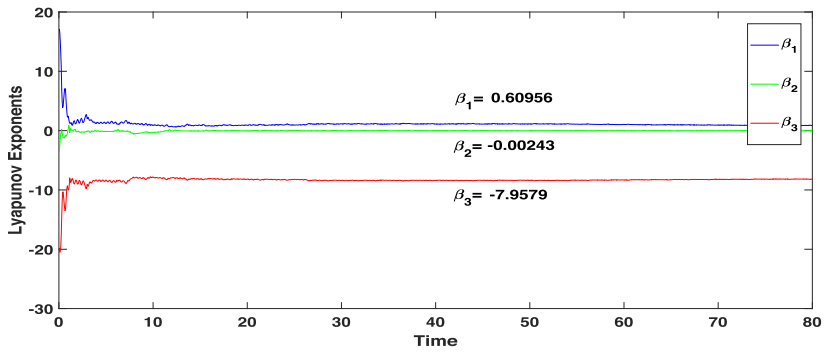

Figure 4. Lyapunov spectrum of the $\mathcal{N}$-system.

$$J_2 = \begin{bmatrix} -\delta & -1+\delta & -1 \\ 1+20y_3 & -\alpha & 20y_1 \\ y_3-\gamma-15y_2 & -15y_1 & y_1-1 \end{bmatrix}.$$

The matrix $J_2(E'_1)$ has eigenvalues $\lambda'_{11} = 0.10 - 19.68\iota$, $\lambda'_{12} = 0.10 + 19.68\iota$, $\lambda'_{13} = -8.04$. The matrix $J_2(E'_2)$ has eigenvalues $\lambda'_{21} = 2.19 + 14.44\iota$, $\lambda'_{22} = 2.19 - 14.44\iota$, $\lambda'_{23} = -10.34$. The matrix $J_2(E'_3)$ has

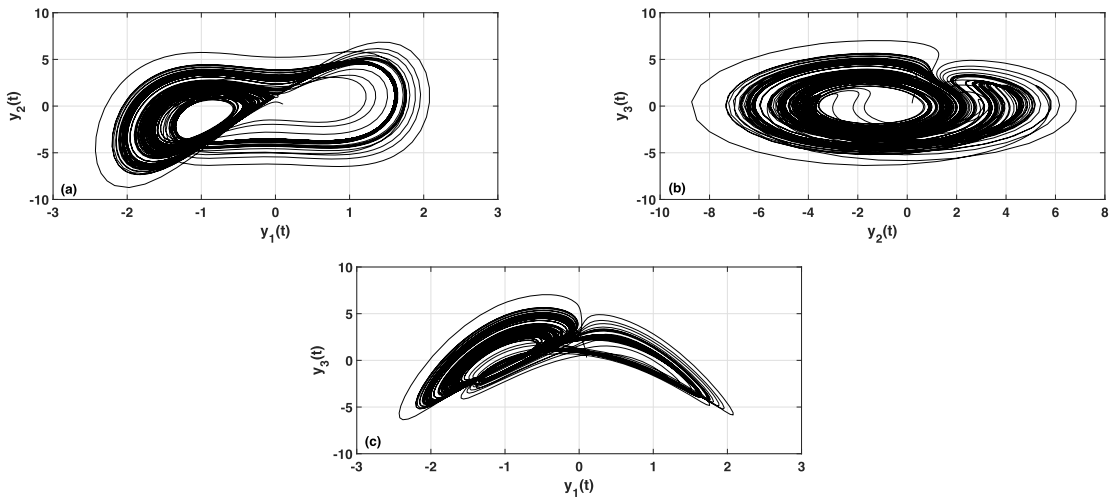

Figure 5. Phase-portraits of the $\mathcal{N}$-system in planes: (**a**) y_1-y_2, (**b**) y_2-y_3, and (**c**) y_1-y_3.

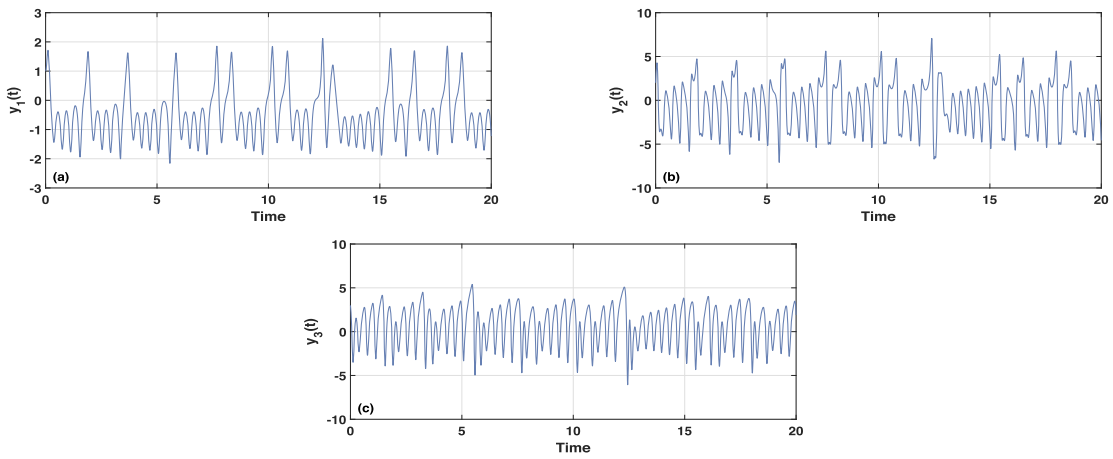

Figure 6. Time series of the $\mathcal{N}$-system: (**a**) y_1 with t, (**b**) y_2 with t, and (**c**) y_3 with t.

eigenvalues $\lambda'_{31} = 33.41$, $\lambda'_{32} = -0.98$, $\lambda'_{33} = -39.16$. Therefore, E'_1, E'_2, and E'_3 are in fact unstable equilibrium positions in phase-space. The two-dimensional projections and the time series analysis of the $\mathcal{N}$-system are added in figures 5 and 6, respectively.

3.3. Poincaré section

The Poincaré map is another approach that is used to study chaotic systems. It involves tracing a dynamical system's trajectory onto the section, also known as the Poincaré surface. System dynamics can be more easily analyzed due to these projections, which reveal significant aspects of the system's conduct, such as its periodic orbits. These maps convert the difficult closed orbit problems to much more approachable fixed point problems. Figure 7 depicts the Poincaré map of the $\mathcal{R}$-system and the $\mathcal{N}$-system.

3.4. Bifurcation plots

A bifurcation diagram displays how a chaotic system responds as one of the system parameters is varied. It illustrates how the dynamics of a model can significantly change as the parameter exceeds certain threshold values, referred to as bifurcation points. To prove the conduct of the $\mathcal{R}$-system when parameter a on [2.5, 30] is added in figure 8. It can be concluded that $\mathcal{R}$-system remains chaotic on the whole domain except on interval [10.6, 11.5], which describes the periodic window of the $\mathcal{R}$-system. While that of the $\mathcal{N}$-system when the parameter δ is varied on [20, 50] is placed in figure 9 and its variation in LEs on the same interval is illustrated in figure 10.

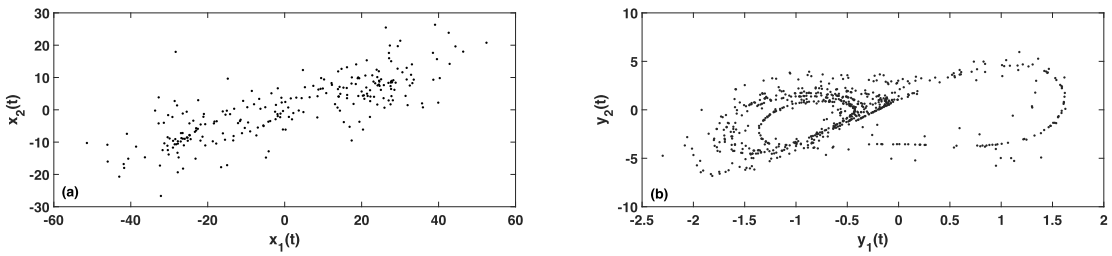

Figure 7. Poincaré map of: (**a**) $\mathcal{R}$-system in x_1-x_2 plane and (**b**) $\mathcal{N}$-system in y_1-y_2 plane.

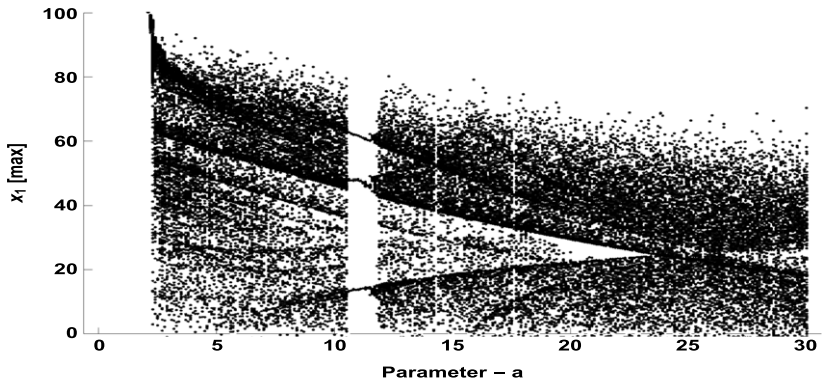

Figure 8. Bifurcation diagram of $\mathcal{R}$-system with $2.5 \leqslant a \leqslant 30$.

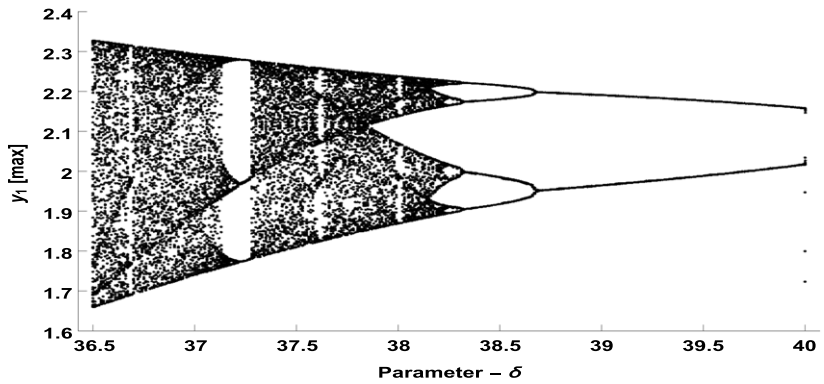

Figure 9. Bifurcation diagram of $\mathcal{N}$-system with $20 \leqslant \delta \leqslant 50$.

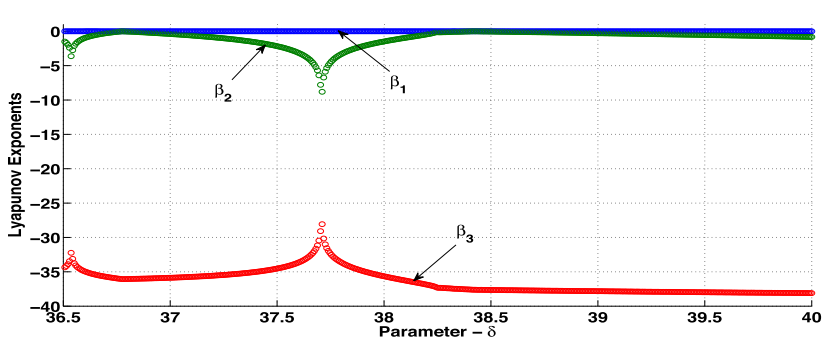

Figure 10. Lyapunov spectrum of $\mathcal{N}$-system varying $20 \leqslant \delta \leqslant 50$.

4. Synchronization via classical active control

To accomplish the complete synchronization between the $\mathcal{R}$-system and the $\mathcal{N}$-system. We define the drive by the $\mathcal{R}$-system:

$$\begin{cases} \dot{x}_1 &= x_2x_3 - ax_1, \\ \dot{x}_2 &= bx_1 + x_2 - x_1x_3, \\ \dot{x}_3 &= x_2^2 - cx_3 + x_1x_2. \end{cases} \tag{5}$$

and the response model by $\mathcal{N}$-system:

$$\begin{cases} \dot{y}_1 &= -y_2 - y_3 + \delta(y_2 - y_1) + u_1(t), \\ \dot{y}_2 &= y_1 - \alpha y_2 + 20y_1y_3 + u_2(t), \\ \dot{y}_3 &= \beta + (y_3 - \gamma)y_1 - y_3 - 15y_1y_2 + u_3(t). \end{cases} \tag{6}$$

where $u_1(t)$, $u_2(t)$, and $u_3(t)$ are some optimal active controllers in equation (6). The main task is to compute these controls in order to identically synchronize the $\mathcal{N}$-system with the driving $\mathcal{R}$-system. The error derivative between the drive and response is defined as:

$$\dot{e_3} = \dot{y}_3 - \dot{x_3}, \qquad \dot{e_2} = \dot{y}_2 - \dot{x_2}, \qquad \dot{e_1} = \dot{y}_1 - \dot{x_1}. \tag{7}$$

Utilizing equations (5)–(7), we get the error system as:

$$\begin{cases} \dot{e_1} &= -(\delta + a)e_1 + (\delta - 1)e_2 - e_3 + \delta(x_2 - x_1) + ay_1 - x_2 - x_3 \\ &\quad - (e_2e_3 - y_2e_3 + x_2y_3) + u_1(t), \\ \dot{e_2} &= (1 + b)e_1 + (1 - \alpha)e_2 - \alpha x_2 + x_1 - y_2 - by_1 + 20(e_1e_3 + x_1e_3 + y_1x_3) \\ &\quad + e_1e_3 - y_1e_3 + x_1y_3 + u_2(t), \\ \dot{e_3} &= -x_2^2 + cy_3 - x_3 + e_1e_3 + x_1e_3 + y_1x_3 - \gamma e_1 - \gamma x_1 - 16e_1e_2 - 15x_1e_2 \\ &\quad + y_1e_2 - 15y_1x_2 - x_1y_2 + u_3(t). \end{cases} \tag{8}$$

Let us define the control $u_1(t)$, $u_2(t)$, and $u_3(t)$ as:

$$\begin{cases} u_1(t) &= -\delta(x_2 - x_1) - ay_1 + x_2 + x_3 + e_2e_3 - y_2e_3 + x_2y_3 + V_1(t), \\ u_2(t) &= \alpha x_2 - x_1 + y_2 + by_1 - 20(e_1e_3 + x_1e_3 + y_1x_3) - e_1e_3 + y_1e_3 - x_1y_3 + V_2(t), \\ u_3(t) &= x_2^2 + e_1e_2 - y_1e_2 + x_1y_2 - cy_3 + x_3 + 15(e_1e_2 + x_1e_2 + y_1x_2) - e_1e_3 \\ &\quad - x_1e_3 - y_1x_3 - \beta + \gamma x_1 + V_3(t). \end{cases} \tag{9}$$

Thus, the error system (8) further converts to

$$\begin{cases} \dot{e_1} = -(a + \delta)e_1 + (\delta - 1)e_2 - e_3 + V_1, \\ \dot{e_2} = (1 + b)e_1 + (1 - \alpha)e_2 + V_2, \\ \dot{e_3} = -\gamma e_1 - (1 + c)e_3 + V_3. \end{cases} \tag{10}$$

The error system given by (10) is essentially a linear system with some functions of errors $V_1(t)$, $V_2(t)$, and $V_3(t)$. The convergence of each e_j to 0, as $t \to \infty$ will indicate the complete synchronization of the $\mathcal{R}$-system with the $\mathcal{N}$-system. So, let

$$\begin{bmatrix} V_1(t) \\ V_2(t) \\ V_3(t) \end{bmatrix} = B \begin{bmatrix} e_1 \\ e_2 \\ e_3 \end{bmatrix}. \tag{11}$$

Numerous choices of $V_1(t)$, $V_2(t)$, and $V_3(t)$ are possible depending on B, where B is a constant 3×3 matrix; for this purpose, a specific selection is made as expressed in (11). To ensure stability in the closed-loop system, the elements of matrix B need to be chosen carefully, such that all eigenvalues of the feedback system must have negative real parts. In our case, the matrix B takes the form:

$$B = \begin{bmatrix} a + \delta - 1 & 1 - \delta & 1 \\ -b - 1 & \alpha - 1 & 0 \\ \gamma & 0 & c \end{bmatrix}.$$

This choice of matrix B ensures that the closed-loop system described by (11) has all eigenvalues with negative unity. Consequently, this selection facilitates the convergence of each $e_j \to 0$, as $t \to \infty$, providing the theoretical proof for the complete synchronization for the $\mathcal{R}$-system and the $\mathcal{N}$-system.

5. Hybrid function projective synchronization via adaptive control

To proceed with HFPS in two newly proposed chaotic dynamical models using the adaptive control strategy. Consider the $\mathcal{R}$-system as our drive model and the $\mathcal{N}$ system as our response model. Once adaptive controllers ϕ_j, ($j=1, 2, 3$) are added to the system of response, we get

$$\begin{cases} \dot{y}_1 &= -y_2 - y_3 + \delta(y_2 - y_1) + \phi_1(t), \\ \dot{y}_2 &= y_1 - \alpha y_2 + 20 y_1 y_3 + \phi_2(t), \\ \dot{y}_3 &= \beta + (y_3 - \gamma) y_1 - 15 y_1 y_2 - y_3 + \phi_3(t). \end{cases} \tag{12}$$

The HFPS error $e = (e_1, e_2, e_3)^T \in \mathbb{R}^3$ is defined by

$$e_j = y_j - \eta_j(t) x_j, \quad \text{with} \quad j = 1, 2, 3. \tag{13}$$

where each $\eta_j(t)$ is a smooth but non-zero, and bounded function. The time-derivative of state errors (13) is given by

$$\begin{cases} \dot{e_1} = \dot{y}_1 - \eta_1(t)\dot{x_1} - \dot{\eta_1}(t) x_1, \\ \dot{e_2} = \dot{y}_2 - \eta_2(t)\dot{x_2} - \dot{\eta_2}(t) x_2, \\ \dot{e_3} = \dot{y}_3 - \eta_3(t)\dot{x_3} - \dot{\eta_3}(t) x_3. \end{cases} \tag{14}$$

Substituting (5) and (12) into (14), we get

$$\begin{cases} \dot{e_1} &= -y_2 - y_3 - \dot{\eta_1}(t) x_1 + \delta(y_2 - y_1) + a\eta_1(t) x_1 - \eta_1(t) x_2 x_3 + \phi_1(t), \\ \dot{e_2} &= y_1 - \alpha y_2 + 20 y_1 y_3 - b\eta_2(t) x_1 - \dot{\eta_2}(t) x_2 - \eta_2(t) x_2 + \eta_2(t) x_1 x_3 + \phi_2(t), \\ \dot{e_3} &= \beta + (y_3 - \gamma) y_1 - 15 y_1 y_2 - y_3 - \dot{\eta_3}(t) x_3 - \eta_3(t) x_2^2 + c\eta_3(t) x_3 \\ &\quad - \eta_3(t) x_1 x_2 + \phi_3(t). \end{cases} \tag{15}$$

To realize Hybrid Function Projective Synchronization (HFPS) between two recently introduced chaotic systems characterized by fully uncertain parameters and arbitrary initial conditions, it is imperative to formulate appropriate controllers denoted as $\phi_j(t)$, ($j=1, 2, 3$). Additionally, a corresponding updated parametric law needs to be designed. These controllers and update rules should be made in such a way that they guarantee the asymptotic stability of the error dynamical system (15). Achieving this ensures HFPS between the $\mathcal{R}$-system and $\mathcal{N}$-system, allowing for the simultaneous estimation of unknown parameters. To theoretically formalize these concepts, the following main theorem is presented:

Theorem 5.1 *To initiate HFPS among the $\mathcal{R}$-system and the $\mathcal{N}$-system, as well as to identify the uncertain parameters $\hat{c}$, $\hat{b}$, $\hat{a}$, $\hat{\gamma}$, $\hat{\alpha}$, $\hat{\beta}$, and $\hat{\delta}$, it is essential to design $\phi_j(t)$ controllers. This above-mentioned synchronization is realized by employing a given scaling function matrix, $\eta(t)$. The controllers are designed in the following manner:*

$$\begin{cases} \phi_1(t) &= y_2 + y_3 - \hat{\delta}(y_2 - y_1) - \hat{a}\eta_1(t) x_1 + \dot{\eta_1}(t) x_1 + \eta_1(t) x_2 x_3 - k_1 e_1, \\ \phi_2(t) &= -y_1 + \hat{\alpha} y_2 - 20 y_1 y_3 + \hat{b}\eta_2(t) x_1 + \dot{\eta_2}(t) x_2 - \eta_2(t) x_1 x_3 + \eta_2(t) x_2 - k_2 e_2, \\ \phi_3(t) &= -\hat{\beta} - (y_3 - \hat{\gamma}) y_1 + 15 y_1 y_2 + y_3 + \dot{\eta_3}(t) x_3 + \eta_3(t) x_2^2 - \hat{c}\eta_3(t) x_3 - k_3 e_3 \\ &\quad + \eta_3(t) x_1 x_2. \end{cases} \tag{16}$$

and the updated parameters law is designed as:

$$\begin{cases} \dot{\hat{a}} = \eta_1 e_1 x_1 - k_4 e_a, \\ \dot{\hat{b}} = -\eta_2 e_2 x_1 - k_5 e_b, \\ \dot{\hat{c}} = \eta_3 e_3 x_3 - k_6 e_c, \\ \dot{\hat{\alpha}} = -e_2 y_2 - k_7 e_\alpha, \\ \dot{\hat{\beta}} = e_3 - k_8 e_\beta, \\ \dot{\hat{\gamma}} = -e_3 y_1 - k_9 e_\gamma, \\ \dot{\hat{\delta}} = e_1(y_2 - y_1) - k_{10} e_\delta. \end{cases} \tag{17}$$

In the specified law, the gains $k_j > 0$, where ($j = 1, 2, \ldots, 10$) are crucial. Furthermore, the variables $\hat{\beta}$, $\hat{\delta}$, $\hat{c}$, $\hat{\alpha}$, $\hat{b}$, $\hat{a}$, and $\hat{\gamma}$ depict the estimated values of unknown parameters. The parameter errors are denoted by $e_\beta = \hat{\beta} - \beta$, $e_\delta = \hat{\delta} - \delta$, $e_c = \hat{c} - c$, $e_\alpha = \hat{\alpha} - \alpha$, $e_a = \hat{a} - a$, $e_\gamma = \hat{\gamma} - \gamma$, and $e_b = \hat{b} - b$. These parameter errors reflect the difference between the estimated and actual values of the respective parameters.

Proof. We strategically select a Lyapunov function to satisfy the prerequisites outlined in stability theory for the updated parameter law. This careful selection gives certainty for the stability of the error dynamical model and, ultimately, the attainment of HFPS. The Lyapunov function is chosen as:

$$V(t) = \frac{1}{2}(e_1^2 + e_2^2 + e_3^2 + e_a^2 + e_b^2 + e_c^2 + e_\alpha^2 + e_\beta^2 + e_\gamma^2 + e_\delta^2).$$

Clearly, $V(t) > 0$ and

$$\begin{aligned}\dot{V}(t) &= e_1(-y_2 - y_3 + \delta(y_2 - y_1) - \eta_1(t)x_2x_3 - \dot{\eta_1}(t)x_1 + a\eta_1(t)x_1 + \phi_1(t)) \\ &\quad + e_2(y_1 - \alpha y_2 + 20y_1y_3 - b\eta_2(t)x_1 - \dot{\eta_2}(t)x_2 - \eta_2(t)x_2 + \eta_2(t)x_1x_3 + \phi_2) \\ &\quad + e_3(\beta + (y_3 - \gamma)y_1 - 15y_1y_2 - y_3 - \dot{\eta_3}(t)x_3 - \eta_3(t)x_2^2 + c\eta_3(t)x_3 - \eta_3(t)x_1x_2 + \phi_3) \\ &\quad + e_a\dot{e_a} + e_b\dot{e_b} + e_c\dot{e_c} + e_\alpha\dot{e_\alpha} + e_\beta\dot{e_\beta} + e_\gamma\dot{e_\gamma} + e_\delta\dot{e_\delta} \\ &= e_1(-e_\delta(y_2 - y_1) - e_a\eta_1x_1) + e_2(e_\alpha y_2 + e_b\eta_2x_1) + e_3(-e_\beta + e_\gamma y_1 - e_c\eta_3x_3) \\ &\quad + e_a\dot{e_a} + e_b\dot{e_b} + e_c\dot{e_c} + e_\alpha\dot{e_\alpha} + e_\beta\dot{e_\beta} + e_\gamma\dot{e_\gamma} + e_\delta\dot{e_\delta}. \end{aligned} \tag{18}$$

On substituting (16) and (17) in (18), we obtain

$$\begin{aligned}\dot{V}(t) &= e_1(-e_\delta(y_2 - y_1) - e_a\eta_1x_1 - k_1e_1) + e_2(e_\alpha y_2 + e_b\eta_2x_1 - k_2e_2) \\ &\quad + e_3(-e_\beta + e_\gamma y_1 - e_c\eta_3x_3 - k_3e_3) + e_a(\eta_1e_1x_1 - k_4e_a) \\ &\quad + e_b(-\eta_2e_2x_1 - k_5e_b) + e_c(\eta_3e_3x_3 - k_6e_c) + e_\alpha(-e_2y_2 - k_7e_\alpha) \\ &\quad + e_\beta(e_3 - k_8e_\beta) + e_\gamma(-e_3y_1 - k_9e_\gamma) + e_\delta(e_1(y_2 - y_1) - k_{10}e_\delta) \\ &= -k_1e_1^2 - k_2e_2^2 - k_3e_3^2 - k_4e_a^2 - k_5e_b^2 - k_6e_c^2 - k_7e_\alpha^2 - k_8e_\beta^2 \\ &\quad - k_9e_\gamma^2 - k_{10}e_\delta^2 \\ &= -e^TKe < 0. \end{aligned} \tag{19}$$

in context, $K = \text{diagonal}(k_1, k_2, \ldots, k_{10})$ and $e = (e_1, e_2, e_3, e_a, e_b, e_c, e_\alpha, e_\beta, e_\gamma, e_\delta)$. The direct method in Lyapunov stability asserts that $\lim_{t\to\infty} ||e(t)|| = 0$, i.e., the error system must asymptotically approach zero [40]. This convergence proves the asymptotic and global attainment of HFPS among the $\mathcal{R}$-system and the $\mathcal{N}$-system, concurrently with the estimation of unknown parameters. □

6. Simulation results on MATLAB

To numerically verify the effectiveness of our obtained analytical results, we perform simulations on mathematical model of these two novel systems. Not only will this assure us of the validity of our desired synchronization schemes but it will also help us to visually verify the obtained results. It is evident that both these novel systems exhibits chaotic behavior if one choose parametric value as defined in sections (3.1) and (3.2). The starting or the initial states of the $\mathcal{N}$-system are taken as $(y_3(0), y_2(0), y_1(0)) = (6, 5, 4)$ while for the $\mathcal{R}$-system is chosen as $(x_3(0), x_2(0), x_1(0)) = (7, 4, 1)$. The dynamics of state vectors of response and the drive system for complete synchronization with the active controllers $u(t)$ are described in figure 11, and their corresponding errors are represented in figure 12.

7. Comparative analysis

The starting states of the $\mathcal{N}$-system are chosen arbitrarily as $(y_3(0), y_2(0), y_1(0)) = (6, 5, 4)$, while for the $\mathcal{R}$-system is chosen as $(x_3(0), x_2(0), x_1(0)) = (3, 2, 1)$. When $k_i = 1$ for all $(i = 1, 2, \ldots, 10)$ is chosen as the control gain and the scaling functions are picked as $\eta_3(t) = 1$, $\eta_2(t) = 1$, and $\eta_1(t) = 1$. Figure 13 represents the simulation findings, and figure 14 depicts the error dynamics for this case. The HFPS does, in fact, achieve complete synchronization under adaptive control. Each error transits to zero as t shoots towards infinity, and the estimated parametric values likewise move from $\hat{\beta} \to \beta$, $\hat{a} \to a$, $\hat{\gamma} \to \gamma$, $\hat{c} \to c$, $\hat{\delta} \to \delta$, $\hat{\alpha} \to \alpha$, and $\hat{b} \to b$, is illustrated in figure 15. The simulation outcomes suggest that when scaling functions are defined as $\eta_3(t) = \sin(t)$, $\eta_2(t) = e^{-t}$, and $\eta_1(t) = \cos(t)$, with control gains set at $k_i = 5$ for all i within the range $(1, 2, \ldots, 10)$, the errors tend to zero as time progresses towards infinity, as depicted in figure 16. Simultaneously, the estimated values of the unknown parameters $\hat{\beta}$, $\hat{a}$, $\hat{\gamma}$, $\hat{c}$, $\hat{\delta}$, $\hat{\alpha}$, and $\hat{b}$ shift towards the actual values $\beta, a, \gamma, c, \delta, \alpha,$ and b, respectively, as shown in figure 17. The comparative table with competing schemes and with first synchronized state time is added in table 1.

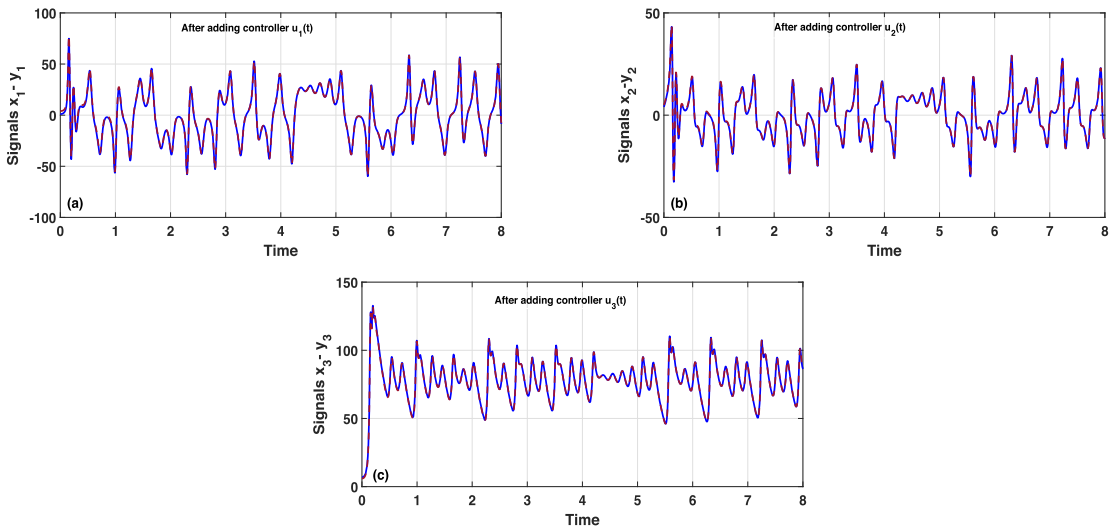

Figure 11. Complete-synchronization of $\mathcal{R}$-system and $\mathcal{N}$-system using active control $u(t)$ i.e., (**a**) signals x_1-y_1, (**b**) signals x_2-y_2, and (**c**) signals x_3-y_3.

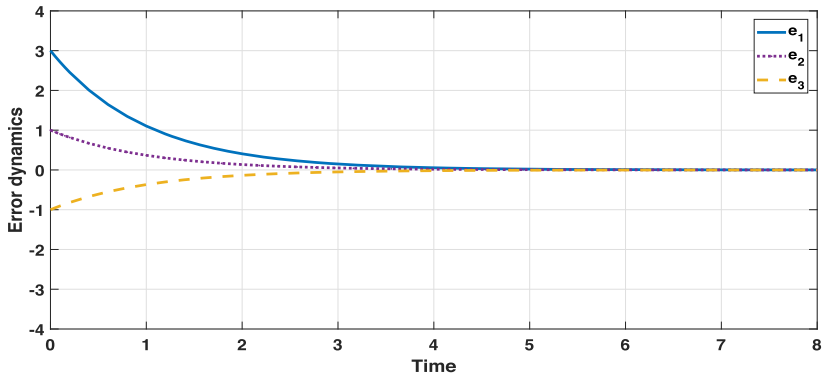

Figure 12. Error dynamics for complete-synchronization using active control $u(t)$.

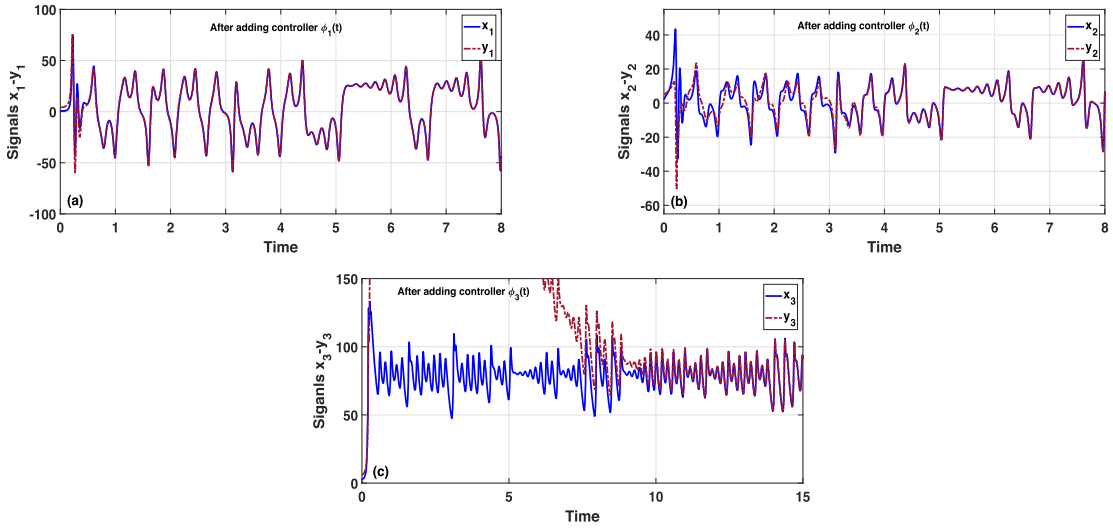

Figure 13. Complete-synchronization of $\mathcal{R}$-system and $\mathcal{N}$-system using adaptive control $\phi(t)$ i.e., (**a**) signals x_1-y_1, (**b**) signals x_2-y_2, and (**c**) signals x_3-y_3.

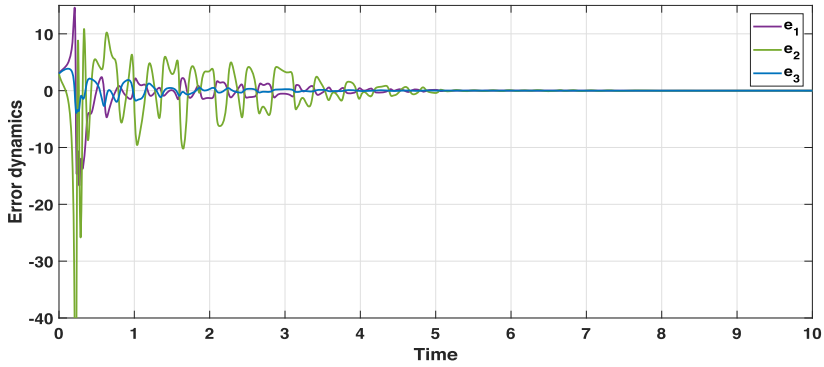

Figure 14. Error dynamics for complete-synchronization using adaptive control $\phi(t)$.

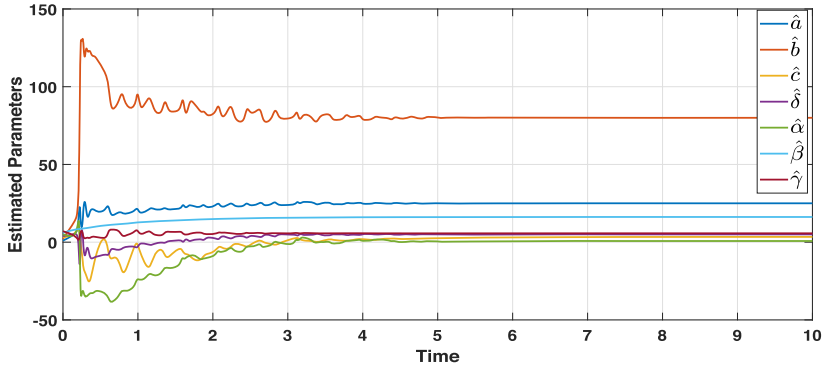

Figure 15. Evolution of the estimated parameters for complete-synchronization via adaptive control $\phi(t)$.

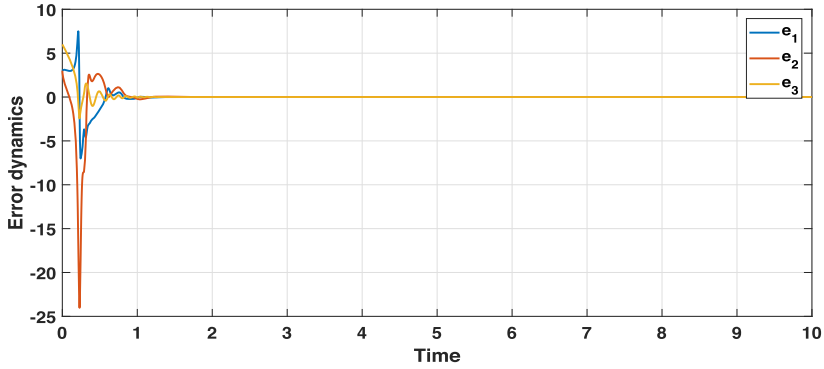

Figure 16. Error dynamics for HFPS using adaptive control $\phi(t)$.

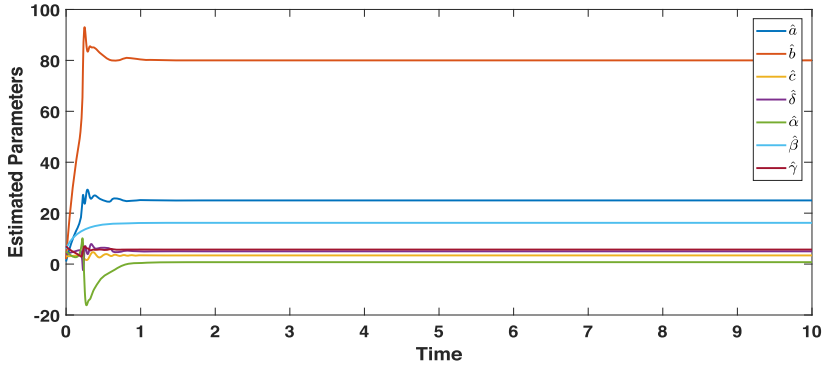

Figure 17. Evolution of the estimated parameters for HFPS via adaptive control $\phi(t)$.

Table 1. Quantitative and comparative analysis with other related schemes.

S. no.	Type of synchronization	Control strategy	Systems	Approximate time in seconds	References
1.	Complete	Adaptive and Back-stepping	Identical	6.5	[41]
2.	Complete	Active	Distinct	7	[42]
3.	Complete	Active and Back-stepping	Identical	22 and 6	[43]
4.	Complete	Back-stepping	Identical	6	[44]
5.	Hybrid Function Projective	Nonlinear	Identical	6	[45]
6.	Complete	Active	Distinct	5	This work
7.	Complete	Adaptive	Distinct	4	This work
8.	Hybrid Function Projective	Adaptive	Distinct	1.8	This work

8. Conclusion

In conclusion, examining phase portraits, bifurcation analysis, time series, and Poincaré maps helped to understand the intricate and complex dynamics of two novel chaotic models. The phase portraits and time series visually represented each system's behavior, showcasing the evolution of trajectories over time. Bifurcation analysis uncovered some critical extremities where the behavior of systems undergoes qualitative changes, shedding light on their erratic nature. Poincaré maps further refined the understanding of the system's periodic behavior and critical patterns. These analyses collectively contributed to a comprehensive characterization of these models, laying the foundation for synchronization using Lyapunov function-based controls. The comparative analysis of HFPS and CS via adaptive control, with the conventional active control strategy, is attempted, and the fact that HFPS and CS with adaptive methods are better than general CS via active control is proved. Further, these findings enhance our theoretical understanding of these chaotic systems and highlight the efficacy of adaptive controls with HFPS synchronizing, showcasing their adaptability for practical applications in various scientific and engineering domains. More generally, it has been demonstrated that the controllers developed with the adaptive control paradigm are more effective than the active control method. Synchronization by the adaptive strategy can be implemented even in an environment or settings with unknown parameters. The signal complexity is further enhanced using functions like sine, cosine, and exponential than traditional constants for signal transfer. The intricacy caused by the system's unknown elements could render it challenging for intruder parties to comprehend the information transferred within chaotic signals. The main drawback of the investigated hybrid function projective scheme is the inherent futility for discontinuous and unbounded functions on the interval $[0, \infty)$. Furthermore, as established controllers are very nonlinear, they can sometimes be quite challenging to execute.

Data availability statement

Not applicable. The data that support the findings of this study are available upon reasonable request from the authors.

Declarations

Conflicts of interests

The author(s) declare the absence of any recognized or potential conflicts of interest pertaining to the conception, execution, or dissemination of this research. Furthermore, the author(s) also declares the absence of any financial or personal affiliations that could reasonably be perceived as an influence on the content or findings presented in this article. These declarations is proffered with the utmost transparency to uphold the integrity and impartiality of the research and its publication.

ORCID iDs

R Bansal https://orcid.org/0000-0001-7005-0079

References

[1] Piccinini J, Ipina I P, Laufs H, Kringelbach M, Deco G, Sanz Perl Y and Tagliazucchi E 2021 Noise-driven multistability vs deterministic chaos in phenomenological semi-empirical models of whole-brain activity *Chaos: An Interdisciplinary J. Nonlinear Sci.* **31**

[2] Grassi G 2021 Chaos in the real world: recent applications to communications, computing, distributed sensing, robotic motion, bio-impedance modelling and encryption systems *Symmetry* **13** 2151

[3] Paolanti M and Frontoni E 2020 Multidisciplinary pattern recognition applications: a review *Computer Science Review* **37** 100276

[4] Zolfaghari B and Koshiba T 2022 Chaotic image encryption: state-of-the-art, ecosystem, and future roadmap *Applied System Innovation* **5** 57

[5] Guegan D 2009 Chaos in economics and finance *Annual Reviews in Control* **33** 89–93

[6] Heltberg M L, Krishna S, Kadanoff L P and Jensen M H 2021 A tale of two rhythms: Locked clocks and chaos in biology *Cell Systems* **12** 291–303

[7] Vaidyanathan S 2015 Adaptive control of a chemical chaotic reactor *Int. J. Pharmtech Res.* **8** 377–82

[8] Aliabadi F, Majidi M H and Khorashadizadeh S 2022 Chaos synchronization using adaptive quantum neural networks and its application in secure communication and cryptography *Neural Computing and Applications* **34** 6521–33

[9] Talatahari S and Azizi M 2021 Chaos game optimization: a novel metaheuristic algorithm *Artificial Intelligence Review* **54** 917–1004

[10] Yang Z, Li H, Ding Y and Wang J 2020 Continuous multi-scroll chaotic PWM and its chaotic signal selection method for EMI suppression of power converters *IEEE Access* **8** 168910–22

[11] Ma Q, Huang G H and Ullah S 2020 A multi-parameter chaotic fusion approach for traffic flow forecasting *IEEE Access* **8** 222774–81

[12] Reichl L E 2021 *Transition to Chaos* (Springer)

[13] Pecora L M and Carroll T L 1990 Synchronization in chaotic systems *Physical Review Letters* **64** 821–4

[14] Mahmoud G M and Mahmoud E E 2010 Complete synchronization of chaotic complex nonlinear systems with uncertain parameters *Nonlinear Dynamics* **62** 875–82

[15] Hammouch Z, Yavuz M and zdemir N 2021 Numerical solutions and synchronization of a variable-order fractional chaotic system *Mathematical Modelling and Numerical Simulation with Applications* **1** 11–23

[16] Wu H, Li C, He Z, Wang Y and He Y 2021 Lag synchronization of nonlinear dynamical systems via asymmetric saturated impulsive control *Chaos, Solitons and Fractals* **152** 111290

[17] Ouannas A, Azar A T and Abu-Saris R 2017 A new type of hybrid synchronization between arbitrary hyperchaotic maps *International Journal of Machine Learning and Cybernetics* **8** 1887–94

[18] Yadav V K, Kumar R, Leung A Y T and Das S 2019 Dual phase and dual anti-phase synchronization of fractional order chaotic systems in real and complex variables with uncertainties *Chinese Journal of Physics* **57** 282–308

[19] Srivastava M, Agrawal S K and Das S 2013 Adaptive projective synchronization between different chaotic systems with parametric uncertainties and external disturbances *Pramana - Journal of Physics* **81** 417437

[20] Khan A, Khattar D and Prajapati N 2017 Multiswitching compound antisynchronization of four chaotic systems *Pramana - J Phys* **89** 90

[21] Velmurugan G and Rakkiyappan R 2016 Hybrid projective synchronization of fractional-order memristor-based neural networks with time delays *Nonlinear Dynamics* **83** 419–32

[22] Khattar D, Agrawal N and Sirohi M 2023 Dynamical analysis of a 5D novel system based on Lorenz system and its hybrid function projective synchronisation using adaptive control *Pramana* **97** 76

[23] Antonik P, Gulina M, Pauwels J and Massar S 2018 Using a reservoir computer to learn chaotic attractors, with applications to chaos synchronization and cryptography *Physical Review* E **98** 012215

[24] Khan A, Khattar D and Agrawal N 2018 Synchronization of a new fractional order chaotic system *Int. J. Dyn. Contr.* **6** 15851591

[25] Li K, Cao J and He J-M 2020 Hidden hyperchaotic attractors in a new 4D fractional order system and its synchronization *Chaos: An Interdisciplinary Journal of Nonlinear Science* **30**

[26] Khattar D, Agrawal N and Sirohi M 2024 Qualitative analysis of a new 6D hyper-chaotic system via bifurcation, the Poincar notion, and its circuit implementation *Indian Journal of Physics* **98** 259273

[27] Shoreh A A and Mahmoud G M 2024 A novel adaptive synchronization algorithm for a general class of fractional-order complex-valued systems with unknown parameters, and applications to circuit realization and color image encryption *Physica Scripta* **99** 025212

[28] Yousefpour A, Jahanshahi H, Munoz-Pacheco J M, Bekiros S and Wei Z 2020 A fractional-order hyper-chaotic economic system with transient chaos *Chaos, Solitons and Fractals* **130** 109400

[29] Vaseghi B, Pourmina M A and Mobayen S 2017 Secure communication in wireless sensor networks based on chaos synchronization using adaptive sliding mode control *Nonlinear Dynamics* **89** 1689–704

[30] Khan A and Shikha 2017 Hybrid function projective synchronization of chaotic systems via adaptive control *International Journal of Dynamics and Control* **5** 1114–21

[31] Vaidyanathan S 2013 Anti-synchronizing backstepping control design for Arneodo chaotic system *International Journal of Bioinformatics and Biosciences* **3** 21–33

[32] Feng C F, Yang H J and Zhou C 2019 Combined projective synchronization for a class of time-delayed hyperchaotic systems via active control *Physica Scripta* **94** 105204

[33] Mobayen S and Ma J 2018 Robust finite-time composite nonlinear feedback control for synchronization of uncertain chaotic systems with nonlinearity and time-delay *Chaos, Solitons and Fractals* **114** 46–54

[34] Karimi S, Effati S and Ghane F H 2019 The synchronization of chaotic systems applying the parallel synchronization method *Physica Scripta* **94** 105215

[35] Sundarapandian V and Pehlivan I 2012 Analysis, control, synchronization, and circuit design of a novel chaotic system *Mathematical and Computer Modelling* **55** 1904–15

[36] Wang X and Zhang H L 2016 A novel image encryption algorithm based on genetic recombination and hyper-chaotic systems *Nonlinear Dynamics* **83** 333–46

[37] Sundarapandian V 2013 Analysis and anti-synchronization of a novel chaotic system via active and adaptive controllers *Journal of Engineering Science and Technology Review* **6** 45–52

[38] Singh P P, Singh J P and Roy B K 2014 Synchronization and anti-synchronization of Lu and BhalekarGejji chaotic systems using nonlinear active control *Chaos, Solitons and Fractals* **69** 31–9

[39] Wolf A, Swift J B, Swinney H L and Vastano J A 1985 Determining Lyapunov exponents from a time series *Physica D: Nonlinear Phenomena* **16** 285–317

[40] Boyce W E, DiPrima R C and Haines C W 1969 *Elementary Differential Equations and Boundary Value Problems* vol 9 (Wiley)

[41] Vaidyanathan S, Kingni S T, Sambas A, Mohamed M A and Mamat M 2018 A new chaotic jerk system with three nonlinearities and synchronization via adaptive backstepping control *Int. J. Eng. Technol.* 1936–43
[42] Agrawal S K, Srivastava M and Das S 2012 Synchronization of fractional order chaotic systems using active control method *Chaos, Solitons and Fractals* **45** 737–52
[43] Tarammim A and Akter M T 2022 A comparative study of synchronization methods of rucklidge chaotic systems with design of active control and backstepping methods *IJMNTA* **11** 31–51
[44] Johansyah M D, Vaidyanathan S, Hannachi F, Sambas A, Foster B, Aruna C, Ramesh R and Rusyaman E 2024 Chaos in chains: Exploring a novel supply chain model through bifurcation analysis, multi-stability and complete synchronization via backstepping control *Partial Differential Equations in Applied Mathematics* **11** 100866
[45] Al-Talib Z S and Al-Azzawi S F 2022 Hybrid function projective synchronization via a nonlinear control. In 2022 *International Conference on Computer Science and Software Engineering (CSASE)* (IEEE) pp 13–8

Control of WRIG Based WECS for Grid Integration

Himanshu Singh, *Member IEEE*
Dept. of Electrical Engineering
Delhi Technological University
Delhi, India
himanshusingh@dtu.ac.in

Madhusudan Singh, *Senior Member*, *IEEE*
Dept. of Electrical Engineering
Delhi Technological University
Delhi, India
madhusudan@dce.ac.in

Bhim Singh, *Fellow*, *IEEE*
Dept. of Electrical Engineering
Indian Institute of Technology
New Delhi, India
bsingh@ee.iitd.ac.in

***Abstract*—This paper presents a transformer-less back to back connected voltage source converter(VSC) configuration of wound rotor induction generator(WRIG) for wind energy conversion system(WECS). The delivery of power to grid from rotor side at same voltage as that of grid is ensured usually by the transformer. A bidirectional DC-DC converter(BDC) is used to replace transformer by providing sufficient magnitude of DC link voltage to the grid side converter(GSC) for grid synchronisation. Simulation results supplement implementation of BDC in between rotor side converter(RSC) an GSC.**

***Index Terms*—Wound Rotor Induction Generator(WRIG), wind energy conversion system(WECS), maximum power point tracking(MPPT), vector control.**

I. Introduction

Wind energy conversion systems (WECS) have several environmental impacts, including reduction of carbon emissions, energy independence, and a diverse, secure power grid.Wind energy doesn't require water for cooling and doesn't emit any pollutants into air or water. On other hand, there may be detrimental effects on the ecosystem and species. Latest research in wind energy conversion systems (WECS) focuses on improving efficiency, reliability, and cost-effectiveness of wind power generation. Various aspects of WECS, including turbine control, power electronics converters (PECs), grid integration and grid synchronism are explored in recent studies [1] [2] [3]. Power swings due to abrupt wind fluctuation could be compensated by optimum control thereby helping to improve consistency of wind turbine energy output, boost efficiency, and extend lifespan of turbine, also power supplied to grid could be supplemented with solar PV system at the DC link.

Regarding power electronics converters (PECs), extensive research is being conducted to enhance complex structural design and optimize commercial cost of wind energy harvesting technology. Prevalence of WRIG and PMSG based system in wind power related technologies along with high voltage power electronics converter(PEC), has opened wide area of research for its applicability in multi megawatt wind power generating system [4] [5].The transformer with its limitation such as incomplete flux linkage, losses due to eddy current, resistive heat production in coil winding could be compensated with usage of PECs especially in area of renewable energy systems. In addition to above limtations of transformer, they may also have limitations in terms of their representational power like, they may have complexity that scales polynomially with the input size for certain tasks, while other architectures may have complexity that scales more favorably.

A bidirectional DC-DC converter(BDC) is a crucial component in various applications such as automotive, server, and renewable energy systems. They play a significant role in addressing power demands in modern automotive designs, especially in micro-hybrid electric vehicles and start-stop cars, where power requirements are increasing. By utilizing bidirectional DC-DC converters, systems can efficiently manage power distribution, reduced cost associated with high-power components, and enhance overall system efficiency. These converters are essential for seamless power delivery in systems like data center servers, motor drive systems, and energy storage devices. In particularily for WECS, with variation of wind speed corresponding to sub synchronous and super synchronous speed of WRIG, power flow in rotor side changes. BDC employed between GSC and RSC ensures smooth and rapid transition between stepping up and stepping down of voltage along with generation of optimum DC link voltage for grid synchronism.

The crucial contribution of this study are as follows.

- Transformer required for voltage matching is replaced with BDC. BDC is used in between RSC and GSC for operation below and above base speed of WRIG.
- BDC ensures extraction of maximum power form solar PV panel when integrated with WECS without usage of boost converter independently for solar PV system.
- Two DC links are created to accomodate/integrate low and high rated DC application system such as charging/discharging of batteries employed for electric vehicle.

II. System Configuration

The system configuration is shown in Fig. 1 and Fig. 2. Fig.1 is conventional topology of back to back connected converter with star delta transformer, Fig. 2 outlines presented system with bidirectional converter and without transformer for grid connection and synchronism.

979-8-3503-6486-6/24/$31.00 ©2024 IEEE

2024 IEEE Region 10 Symposium (TENSYMP) | 979-8-3503-6486-6/24/$31.00 ©2024 IEEE | DOI: 10.1109/TENSYMP61132.2024.10752199

Authorized licensed use limited to: DELHI TECHNICAL UNIV. Downloaded on November 25,2024 at 04:42:01 UTC from IEEE Xplore. Restrictions apply.

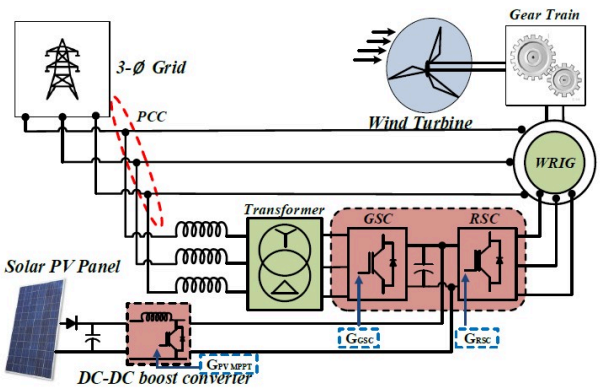

Fig. 1. Schematic of conventional system.

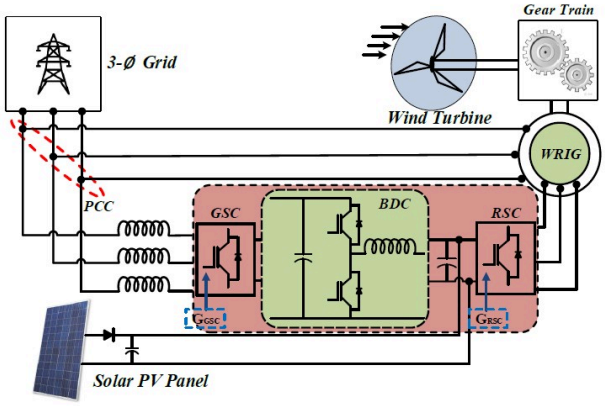

Fig. 2. Schematic of presented system.

A. Design of Wind Turbine

The shaft power developed by the wind turbine in terms of stator power is represented by the following expression:

$$P_t = P_s + P_r = P_s(1+s) \tag{1}$$

For a 2.6kW, 415V, 5.9A, 50Hz delta connected WRIG from (1), a wind turbine of 3.38kW is selected assuming a slip variation of +0.3 to -0.3. The turbine power in terms of energy extracted from the wind [6] can be represented as follows:

$$P_t = (1/2)\rho\pi r^2 v_w^3 C_p \tag{2}$$

where ρ is air density, r is radius, v_w is wind speed and C_p is coefficient of performance of wind turbine. Using (2) for a 3.38kW wind turbine at a base speed of 12m/sec and C_p=0.48 radius(r) of turbine is calculated as 1.455m. Using tip speed ratio as

$$\lambda = \frac{w_T r}{v_w} \tag{3}$$

For λ=λ_{opt}=8.1 the gear ratio(η) of the turbine is calculated as η = 2.024.

B. Modelling of Wound Rotor Induction Generator(WRIG)

Per phase equivalent circuit of WRIG is developed below, with stator measurements at synchronous frequency and rotor measurements at slip frequency.

$$\begin{bmatrix} \frac{d\psi_s}{dt} \\ \frac{d\psi_r}{dt} \end{bmatrix} = \begin{bmatrix} -R_s/\sigma L_s & jw_s R_s/\sigma L_s L_r \\ R_r L_m/\sigma L_s L_r & -jw_{slip} - R_r/\sigma L_r \end{bmatrix} \begin{bmatrix} \psi_s \\ \psi_r \end{bmatrix} + \begin{bmatrix} v_s \\ v_r \end{bmatrix} \tag{4}$$

The d-q model of WRIG can be further developed using (4) to investigate dependence of active and reactive components of power [7].

$$v_{sd} = r_s i_{sd} + \frac{d\psi_{sd}}{dt} - w_s\psi_{sq}, v_{sq} = r_s i_{sq} + \frac{d\psi_{dq}}{dt} + w_s\psi_{sd} \tag{5}$$

$$v_{rd} = r_r i_{rd} + \frac{d\psi_{rd}}{dt} - w_{slip}\psi_{rq}, v_{rq} = r_r i_{rq} + \frac{d\psi_{rq}}{dt} + w_{slip}\psi_{rd} \tag{6}$$

The parameters of WRIG is further illustrated in Appendix.

C. Selection of Photo-Voltaic(PV) Panel

A two stage 2kW solar PV panel is connected at low voltage side of BDC. Maximum power from solar panel is extracted using incremental conductance algorithm to generate desired duty ratio for buck-boost DC-DC converter. Inductor and capacitor of buck-boost DC-DC converter are designed [8] for delivery of voltage at the reference DC link voltages of 700V at output from a 306V input. Boost mode of BDC is utilised for extracting maximum power from solar PV panel using buck-boost DC- DC converter. Parameters of selected solar PV panel is illustrated in Appendix.

III. Control Approach

The system control consists of RSC, GSC and BDC for operation of WRIG in sub synchronous, synchronous and super synchronous modes of operation.

A. Back to Back Connected Converter Control of WRIG

1) Rotor Side Converter(RSC) Control : Using rotor measurement in sysnchronously rotating reference frame [9] [10], reactive power is proportionate to direct rotor current, whereas active power is proportional to quadrature rotor current as,

$$T_{em} = \frac{-3}{2} p \frac{L_m}{L_s}(\psi_s i_{rq}) \tag{7}$$

$$T_{em} = K i_{rq} \tag{8}$$

$$Q_s = \frac{3}{2} w_s \frac{L_m}{L_s} |\psi_s| (i_{rd} - \frac{|\psi_s|}{L_m}) \tag{9}$$

For generation of reference active component of power, reference speed is generated using tip speed ratio MPPT method [11] as follows:

$$w_T = \frac{w_m}{\eta} \tag{10}$$

$$\lambda = \frac{w_T r}{v_w} = \frac{\frac{w_m}{\eta} r}{v_w} \tag{11}$$

Authorized licensed use limited to: DELHI TECHNICAL UNIV. Downloaded on November 25,2024 at 04:42:01 UTC from IEEE Xplore. Restrictions apply.

For λ = 8.1 and η = 2.024 from 3 and radius(r) = 1.455m one gets

$$w_{mref} = 11.268 * v_w \tag{12}$$

Using (7), (8) and (12), reference component of quadrature rotor current is generated using speed PI controller, which in turn is compared with sensed quadrature rotor current and by using current PI controller reference quadrature voltage component is expressed as follows:

$$I_{rq}(n) = I_{rq}(n-1) + k_{pw}[w_{merr}(n) - w_{merr}(n-1)] + k_{iw} w_{merr}(n) \tag{13}$$

$$v_{rq}(n) = v_{rq}(n-1) + k_{pi}[I_{rqerr}(n) - I_{rqerr}(n-1)] + k_{ii} I_{rqerr}(n) \tag{14}$$

Reactive component of power is controlled by direct axis rotor current using (9), and by assuming all reactive power required by WRIG is supplied through RSC to maintain unity power factor operation at stator side, the reference direct axis rotor current is expressed as.

$$I_{rdref} = \frac{\sqrt{2} V_{pcc}}{\sqrt{3} X_m} \tag{15}$$

Where, V_{pcc} is the voltage at the point of common coupling and X_m is the magnetising reactance of the machine, using (15), reference reactive current is processed by current PI controller to generate reference direct axis rotor voltage as.

$$v_{rd}(n) = v_{rd}(n-1) + k_{pi}[I_{rderr}(n) - I_{rderr}(n-1)] + k_{ii} I_{rderr}(n) \tag{16}$$

The inner current loop is thought to be optimal when taking in to account the speed control loop. The proportional and integral gains of speed controller are designed for an underdamped system achieving faster transient and steady state response. Fig. 3 depicts RSC control.

2) Grid Side Converter(GSC) Control: Grid Side Converter(GSC) is controlled in stator voltage oriented reference frame. GSC maintains constant DC link voltage at high voltage side of BDC and zero reactive power flow at stator side of WRIG. Fig. 3 also shows control of GSC.

The reference DC link Voltage is represented as

$$V_{dchighref} = \frac{2\sqrt{2} * V_s}{k\sqrt{3}} \tag{17}$$

where, k is the modulation index and V_s is the stator voltage.

Using PI controller reference direct axis grid current is generated, which in turn is compared with sensed direct axis grid current and processed through current PI controller to generate reference direct axis grid voltage component as follows:

$$I_{gd}(n) = I_{gd}(n-1) + k_{pv}[V_{dcerr}(n) - V_{dcerr}(n-1)] + k_{iv} V_{dcerr}(n) \tag{18}$$

$$V_{gd}(n) = V_{gd}(n-1) + k_{pi}[I_{gderr}(n) - I_{gderr}(n-1)] + k_{iv} I_{gderr}(n) \tag{19}$$

For unity power factor operation at stator side, quadrature axis grid reference current is maintained at zero and is processed through PI controller to generate quadrature axis reference grid voltage as.

$$V_{gq}(n) = V_{gq}(n-1) + k_{pi}[I_{gqerr}(n) - I_{gqerr}(n-1)] + k_{iv} I_{gqerr}(n) \tag{20}$$

B. Control of Bidirectional DC-DC Converter(BDC)

The buck and boost modes of the DC-DC BDC are activated by independent control of upper and lower IGBT. Upper IGBT duty ratio is generated by pulse width modulation(PWM) with carrier frequency of 20kHz during wind speed lower than corresponding to synchronous speed of WRIG, while lower IGBT duty ratio is generated using PV panel MPPT algorithm during wind speed corresponding to synchronous and super sysnchronous speed of WRIG, Fig. 4 shows control of DC-DC BDC converter.

IV. Results And Discussion

Simulation results are analysed for changes in wind speed and irradiance using MATLAB. Embedded MATLAB function is used to simulate solar PV panel. For WRIG, negative power indicates power delivered to the grid and positive power indicates power taken from the grid, for both stator and rotor.

A. Wind Turbine for Variable Wind Speed

WRIG is subjected to wind speed corresponding to sub sysnchronous, synchronous and super sysnchronous modes of operation and voltage at the point of common coupling(V_{pcc}) and DC link voltage($V_{DChigh}$and V_{DClow}) are observed. The solar PV panel is operated at an irradiance(G) of $1000W/m^2$ during all modes of operation.

1) Results for Sub-Synchronous Operation: Sub-synchronous operation is shown in Fig. 5. WRIG is operating approximately at a speed of 90rad/sec corresponding to a wind speed of 8m/sec with an approximate 500W and 850W power being delivered to grid from stator and rotor, respectively.

2) Results for Synchronous Operation: Fig. 6 shows the WRIG operating at 104.7rad/sec(Synhronous speed) corresponding to a wind speed of 9.29m/sec, with constant DC current in rotor circuit resembling synchronous generator. An approximate 750W power form stator side and 900W from rotor side is delivered to the grid.

3) Results for Super-Synchronous Operation: For a wind speed of 11.5m/s, WRIG is operating approximately at a speed of 130rad/sec with 1.1kW power delivered to the grid from stator and an approximate 1kW power from rotor side as seen from Fig. 7.

In all three modes of operation it can be seen that the $V_{DChigh}$and V_{DClow} are continuously tracking repective reference DC link voltages without any perturbation. Moreover V_{pcc} is in synchronism to stator voltage(V_{sa}) in all the modes

Authorized licensed use limited to: DELHI TECHNICAL UNIV. Downloaded on November 25,2024 at 04:42:01 UTC from IEEE Xplore. Restrictions apply.

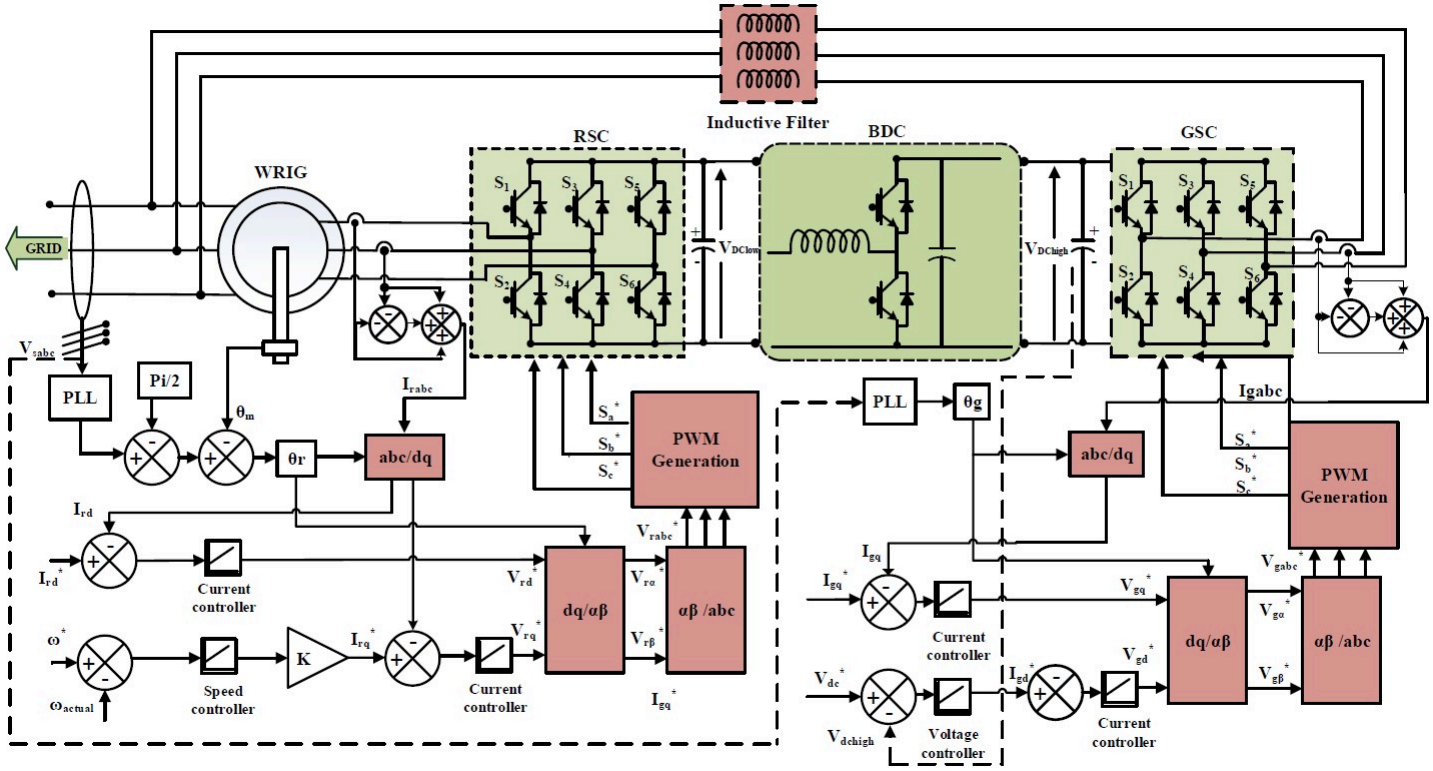

Fig. 3. Control of RSC and GSC.

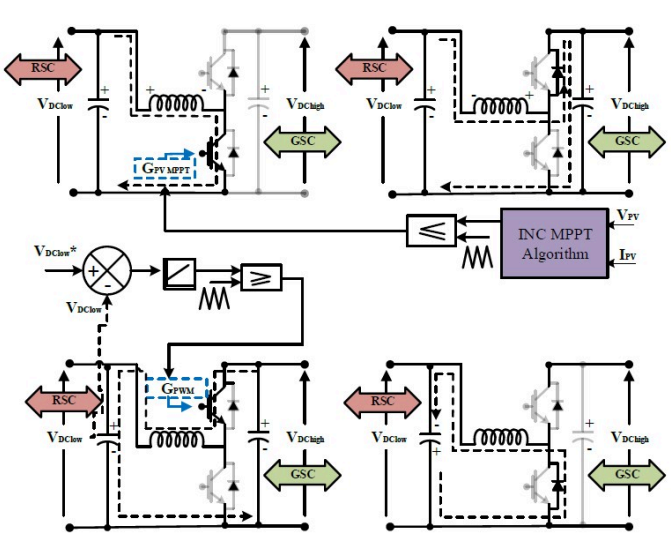

Fig. 4. Control of BDC.

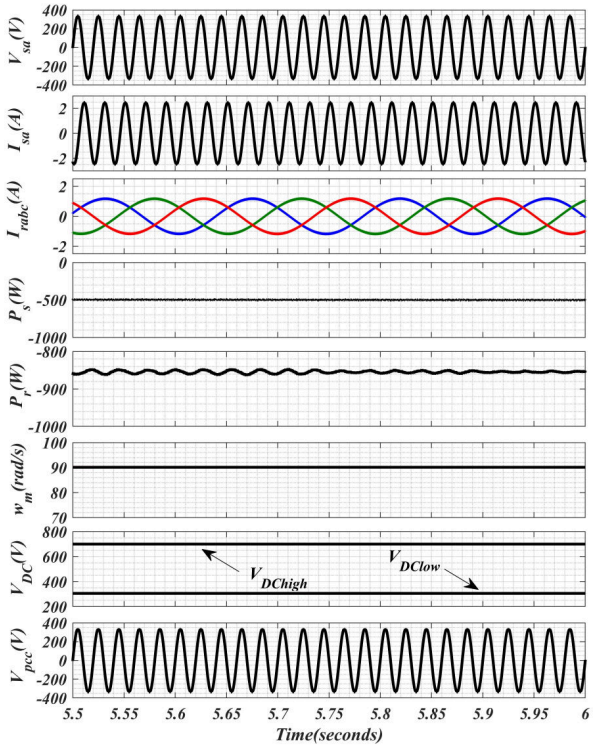

Fig. 5. System performance at constant wind speed of 8m/s (Sub-Synchronous operation of WRIG:$v_{sa}, i_{sa}, i_{rabc}, P_s, P_r, w_m, V_{DC}, V_{pcc}$

and within limits as per the IEEE 519-2014 standard for voltage distortion limits for voltage at the point of common coupling(V_{pcc}).

4) Continuously Varying Wind Speed: The dynamic performance of the system can be seen in Fig. 8 for continuous variation of wind speed. The wind speed is gradually changed from $8m/sec$ to $11.25m/sec$ till $3sec$ after which it is kept

Authorized licensed use limited to: DELHI TECHNICAL UNIV. Downloaded on November 25,2024 at 04:42:01 UTC from IEEE Xplore. Restrictions apply.

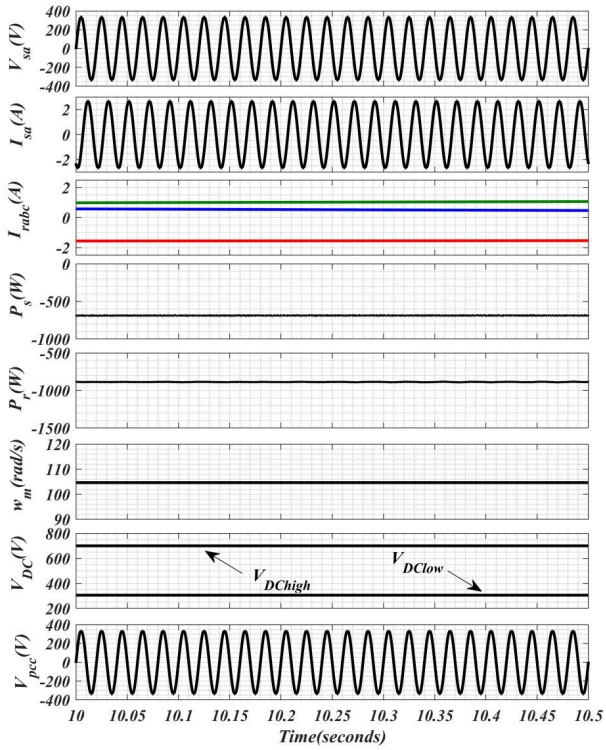

Fig. 6. System performance at constant wind speed of 9.29m/s (Synchronous operation of WRIG: $v_{sa}, i_{sa}, i_{rabc}, P_s, P_r, w_m, V_{DC}, V_{pcc}$

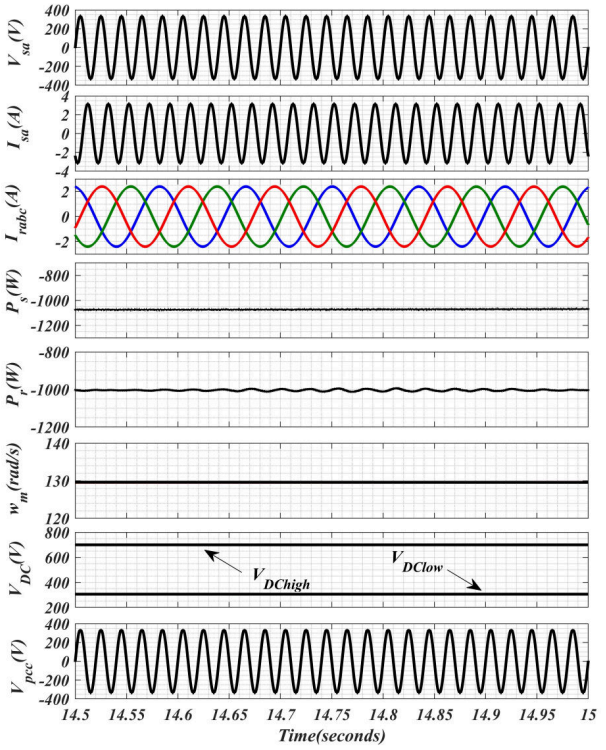

Fig. 7. System performance at constant wind speed of 11.5m/s (Super-Synchronous operation of WRIG:$v_{sa}, i_{sa}, i_{rabc}, P_s, P_r, w_m, V_{DC}, V_{pcc}$

constant at $11.25m/sec$ till $7sec$ and then again gradually changed from $11.25m/sec$ to $8.75m/sec$ till $12sec$, accordingly using tip speed ratio method of wind maximum power extraction the reference generator speed is generated, also in Fig. 8, the shaft speed is continuously tracking the reference speed thereto delivering power to grid. During the variation of wind speed, the DC link voltages are continuously tracking the reference values with slight perturbation during transient period.

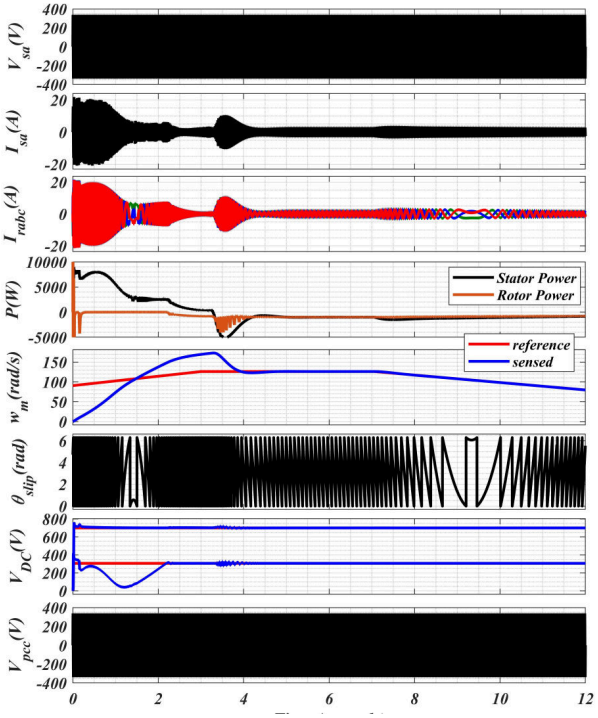

Fig. 8. Dynamic performance of the Proposed system at varying wind speed:$v_{sa}, i_{sa}, i_{rabc}, P_s\&P_r, w_m, \theta_{slip}, V_{DC}, V_{pcc}$

B. Results for Variable Irradiance

WRIG is rotated at a wind speed of 11m/sec and the irradiance of solar PV panel is changed. Fig. 9 and 10 show performance for wide variation of irradiance. At 10sec irradiance is changed from $1000W/m^2$ to $800W/m^2$ and then from $800W/m^2$ to $600W/m^2$ at 13secs and again from $600W/m^2$ to $900W/m^2$ at 16secs. For variation of irradiance the DC link at input and output of BDC is maintained at 306V and 700V, respectively along with synchronised voltage at V_{pcc} and V_{sa}. Moreover corresponding to change in irradiance, the maximum power from the solar array(P_{PV}) changes along with change in power delivery to the grid from the rotor side. As the wind speed is constant throughout variation of irradiance, the stator power to the grid is at a constant value of $1000W$.

VI. Conclusion

This paper has presented for synchronous power delivery to/from the grid along with integration of solar PV panel. The

Authorized licensed use limited to: DELHI TECHNICAL UNIV. Downloaded on November 25,2024 at 04:42:01 UTC from IEEE Xplore. Restrictions apply.

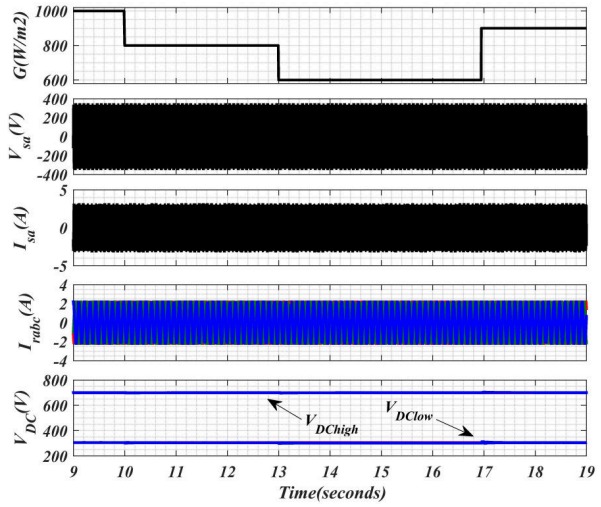

Fig. 9. Dynamic System performance for variable irradiance:$G, v_{sa}, i_{sa}, i_{rabc}, V_{DC}$

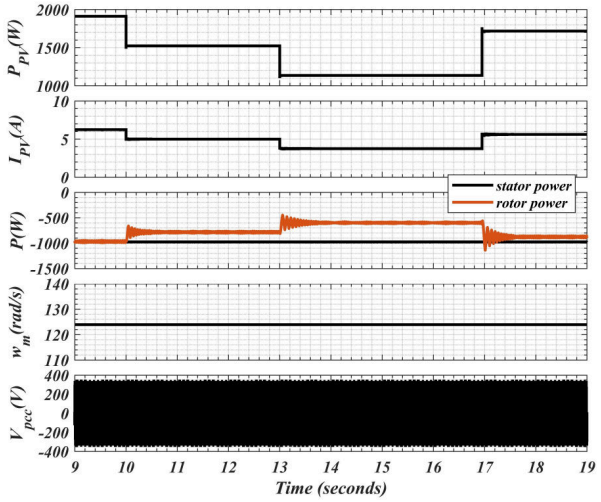

Fig. 10. Dynamic System performance for variable irradiance:$P_{PV}, I_{PV}, P_s\&P_r, w_m, V_{pcc}$

transformer in conventional DFIG based WECS is replaced with BDC. BDC has ensured generation of desired DC link voltage along with extraction of maximum power from the solar PV panel. Simulation results acknowledges continuous delivery of power to the grid.

ACKNOWLEDGMENT

The authors are grateful to National Science Chair Fellowship, Science and Engineering Research Board (SERB), Govt. of India for supporting this work.

APPENDIX

Parameters of simulated model are as follows:

WRIG

2.6kW, 415V, 6 pole, 50 Hz, $L_m = 0.457H$, $L_s = 0.0346H$, $L_r = 0.0346H$, $r_s = 4.605\Omega$, $r_r = 4.6118\Omega$,$J = 0.25Kg - m^2$, $B = 1e^{-3}$

Wind Turbine

3.38kW, $v_w = 12m/sec$, blade radius = 1.455m, gear-box ratio = 2.024, tip speed ratio = 8.1, $Cp_{opt} = 0.48$

Solar PV Panel

$V_{oc} = 360V$, $I_{sc} = 6.94A$, MPPT operating point at standard test conditions is $P_{mp} = 1.91kW$, $V_{mp} = 306V$, $I_{mp} = 6.25A$

REFERENCES

[1] S. Tyagi, B. Singh and S. Das, "Small Hydro Based Grid Forming Converter Having Power Sharing and Synchronization Capability With DFIG Based WECS," *IEEE Transactions on Industry Applications*, vol. 59, no. 4, pp. 5048-5058, July-Aug. 2023.

[2] S. Puchalapalli, B. Singh and S. Das, "Synchronizing Control of Wind Turbine Driven Doubly Fed Induction Generator System With DG in Remote Area Involving Solar PV-Battery Energy Storage," *IEEE Transactions on Industry Applications*, vol. 59, no. 5, pp. 5774-5783, Sept.-Oct. 2023.

[3] S. Das and B. Singh, "Islanding Operation and Seamless Resynchronization in DFIG–SPV System Equipped With Functional Enhancements Through ATLLAD Control Framework," *IEEE Transactions on Power Electronics*, vol. 38, no. 6, pp. 7634-7643, June 2023.

[4] F. Blaabjerg, M. Liserre and K. Ma, "Power Electronics Converters for Wind Turbine Systems," *IEEE Transactions on Industry Applications*, vol. 48, no. 2, pp. 708-719, March-April 2012.

[5] Z. Chen, J. M. Guerrero and F. Blaabjerg, "A Review of the State of the Art of Power Electronics for Wind Turbines," *IEEE Transactions on Power Electronics*, vol. 24, no. 8, pp. 1859-1875, Aug. 2009.

[6] Gonzalo Abad, Jesus Lopez, Miguel Rodriguez, Luis Marriyo, Grzegorz Iwanski, '*Doubly Fed Induction machine: Modelling and control for wind energy generation*' John Wiley and sons Inc. Publication, IEEE press, New Jersey, 2011.

[7] Haitham Abu-Rub, Marius Malinowski, kamal Al-Haddad, '*Power Electronics for renewable energy systems, transportation and industrial applications*' John Wiley and sons Inc. Publication, United Kingdom, 2014.

[8] Razman Ayop, Chee Wei Tan, Design of boost converter based on maximum power point resistance for photovoltaic applications, Solar Energy, Volume 160, 2018,Pages 322-335, ISSN 0038-092X.

[9] R. Pena, J. C. Clare and G. M. Asher, "Doubly fed induction generator using back-to-back PWM converters and its application to variable-speed wind-energy generation," *IEE Proceedings - Electric Power Applications*, vol. 143, no. 3, pp. 231-241, May 1996.

[10] S. Puchalapalli and B. Singh, "A Novel Control Scheme for Wind Turbine Driven DFIG Interfaced to Utility Grid," *IEEE Transactions on Industry Applications*, vol. 56, no. 3, pp. 2925-2937, May-June 2020.

[11] L. Gevaert, J. D. M. De Kooning, T. L. Vandoorn, J. Van de Vyver and L. Vandevelde, "Evaluation of the MPPT performance in small wind turbines by estimating the tip-speed ratio," *2013 48th International Universities' Power Engineering Conference (UPEC)*, Dublin, Ireland, 2013, pp. 1-5.

Authorized licensed use limited to: DELHI TECHNICAL UNIV. Downloaded on November 25,2024 at 04:42:01 UTC from IEEE Xplore. Restrictions apply.

Physics of Fluids

RESEARCH ARTICLE | NOVEMBER 20 2024

Deep convolutional architectures for optimizing multi-element airfoil systems FREE

Kartikey Vishnu (कार्तिकेय विष्णु) ; Devdoot Chatterjee (देवदूत चटर्जी); Anurag Goel (अनुराग गोयल); Rajeev Kumar (राजीव कुमार)

Check for updates

Physics of Fluids 36, 113622 (2024)
https://doi.org/10.1063/5.0234254

View Online Export Citation

Articles You May Be Interested In

A novel deep learning approach for flow field prediction around airfoils leveraging computational space representation

Physics of Fluids (October 2024)

A multi-task learning framework for aerodynamic computation of two-dimensional airfoils

Physics of Fluids (November 2024)

Fast Spatiotemporal Sequence Graph Convolutional Network-based transient flow prediction around different airfoils

Physics of Fluids (October 2024)

25 November 2024 04:46:08

AIP Publishing

Physics of Fluids

Special Topics Open for Submissions

Learn More

AIP Publishing

Physics of Fluids ARTICLE pubs.aip.org/aip/pof

Deep convolutional architectures for optimizing multi-element airfoil systems

Cite as: Phys. Fluids **36**, 113622 (2024); doi: 10.1063/5.0234254
Submitted: 20 August 2024 · Accepted: 31 October 2024 ·
Published Online: 20 November 2024

View Online Export Citation CrossMark

Kartikey Vishnu (कार्तिकेय विष्णु),[a] Devdoot Chatterjee (देवदूत चटर्जी), Anurag Goel (अनुराग गोयल),[b] and Rajeev Kumar (राजीव कुमार)[c]

AFFILIATIONS

Delhi Technological University, Shahbad Daulatpur, New Delhi 110042, India

[a]Author to whom correspondence should be addressed: kartikeyvishnu@gmail.com
[b]Electronic mail: anurag@dtu.ac.in. URL: https://www.dtu.ac.in/Web/Departments/CSE/faculty/anuraggoel.php
[c]URL: https://www.dtu.ac.in/Web/Departments/CSE/faculty/rajeevkr.php

ABSTRACT

The investigation of aerodynamic properties in multi-element airfoils is historically challenging and impractical for real-time applications. Predicting specific angles to achieve predetermined lift and drag forces has been elusive. Advances in machine learning (ML) and deep learning (DL) offer new possibilities, but their application to multi-wing system (multi-element airfoils) is limited by scarce datasets. This study explores development, design, and comparative analysis of ML and novel DL algorithms to predict the aerodynamic coefficients generated by multi-element airfoils given airfoil shape, angle of orientation of each airfoil, and their velocity, a previously unexplored area. Using datasets generated via ANSYS Fluent, the proposed models predict aerodynamic coefficients based on variables such as velocity, airfoil angle, and images of the airfoil system with high accuracy, achieving a mean squared error of 0.0049. The proposed approach also significantly reduces the computational time for predicting the aerodynamic coefficients from 10 to 15 min in a traditional computational fluid dynamics simulation to 1–6 ms using our approach. This real-time prediction capability allows for assessing various angle combinations to find optimal orientations for specific drag and lift forces.

Published under an exclusive license by AIP Publishing. https://doi.org/10.1063/5.0234254

25 November 2024 04:46:08

I. INTRODUCTION

Multi-element airfoils are a cornerstone of modern aerodynamic design, playing a vital role in optimizing the performance of aircraft and race cars. These systems, consisting of multiple interacting airfoil elements, enable superior aerodynamic efficiency by enhancing lift (Cl) and minimizing drag (Cd). The ability to predict and optimize these aerodynamic coefficients is crucial, particularly for applications where efficiency and precision are paramount, such as in high-speed aircraft and competitive motorsports. However, the flow physics around multi-element airfoils is significantly more complex than single-element airfoils, involving intricate phenomena such as flow separation, reattachment, and wake interactions between airfoil components. As a result, their aerodynamic behavior is much harder to predict accurately, especially when compared to simpler airfoil configurations.

Historically, researchers have relied on computational fluid dynamics (CFD) and empirical methods to analyze multi-element airfoil systems.[1,2] These approaches, while powerful, are resource-intensive and time-consuming due to the complex interactions between airfoil elements. Early work, such as that by Drela,[3] employed zonal Euler/boundary layer flow solvers to design and optimize multi-element airfoils. Similarly, Valarezo *et al.*[4] used wind tunnel testing to maximize lift at high Reynolds numbers. Despite significant advances in computational resources and methods, CFD simulations remain the dominant approach for multi-element airfoil studies. Recent work such as that by Qu *et al.*[5] employed CFD to investigate the flow physics of multi-element airfoils in ground effect, while further studies[6–9] explored the use of numerical methods in multi-element airfoil systems. Other notable studies, such as Refs. 10–14, emphasized the broad applicability of CFD in analyzing complex aerodynamic phenomena across various configurations.

Although these methods provide detailed insights into the aerodynamics of multi-element airfoils, they are computationally demanding and often require substantial time to produce results. This limitation becomes especially pronounced when designing and optimizing multi-element airfoil systems, where iterative testing and analysis can further exacerbate the computational burden. To address the challenges of CFD, researchers have begun exploring machine learning (ML) and deep learning (DL) approaches as viable alternatives. Recently, neural networks have also been employed in finite element problems, such as stress analysis,[15] as well as in fluid flow and heat and

Published under an exclusive license by AIP Publishing

mass transfer simulations, as demonstrated by Shilpa *et al.*[16–18] In the context of fluids and airfoils, Moin *et al.*[19] developed a neural network using a backpropagation algorithm to estimate the lift and drag coefficients for NACA single-element airfoils. Similarly, Santos *et al.*[20] and Wallach *et al.*[21] have leveraged ML and DL techniques to predict the aerodynamic properties of airfoil systems. Additionally, more advanced methods, such as those discussed by Wang *et al.*[22] and Tao *et al.*,[23] have optimized aerodynamic shapes by integrating neural networks with multi-fidelity data, further reducing computational costs while enhancing accuracy. Even though these studies show the potential of ML/DL methods in aerodynamic analysis, their focus has largely been confined to single-element airfoils, and relatively little attention has been given to multi-element airfoil systems.

The application of ML and DL to multi-element airfoil systems remains a largely unexplored area. Given the complexity and importance of these systems, there is a clear opportunity to leverage advanced ML/DL methodologies to reduce computational costs while maintaining or even improving predictive accuracy. In this study, we seek to address this gap by developing a novel approach that combines machine learning algorithms with custom-designed deep learning models to predict the aerodynamic coefficients (Cl and Cd) for multi-element airfoils. Unlike previous studies focused on single-element systems, our research extends the application of ML/DL to multi-element configurations, thereby opening up new possibilities for rapid and accurate aerodynamic analysis of complex airfoil systems.

Our approach begins by generating a comprehensive dataset through CFD simulations of a three-element airfoil system, with particular emphasis on the uppermost and central airfoils due to their significant impact on aerodynamic forces. We used ANSYS Fluent to simulate the aerodynamic behavior across various angles of attack and velocities, thereby creating a diverse dataset suited for training machine learning and deep learning models. For the ML part of the study, we employed existing models to establish a baseline for performance. However, for the deep learning component, we developed four different neural network architectures and conducted a comparative study to identify the most effective approach for predicting Cl and Cd. In addition to reducing computational costs, our methodology ensures real-time prediction accuracy, which is crucial for applications requiring swift analysis and decision-making. Our research makes the following important contributions:

- **Comprehensive Dataset:** We address the gap in research on deep learning models for predicting aerodynamic coefficients of multi-wing systems. A new dataset of 1500 CFD simulations is developed, leveraging aerodynamics and CFD domain knowledge to generate specialized images that encode critical features for neural network training, facilitating more accurate prediction of aerodynamic coefficients for multi-wing systems.
- **Efficient Neural Network Design:** We propose a lean convolutional neural network (CNN)-based deep learning model with 2.9 $\times$ 10^6 parameters, 10$\times$ fewer than state-of-the-art models. It achieves an MSE of 0.0049, trains in 100 epochs, and predicts aerodynamic coefficients in under 6 ms, offering substantially faster training and inference times.
- **Comparative Performance Analysis:** Through a comprehensive comparative analysis and evaluation of various deep learning and machine learning models, the lightweight model M4 was found superior in terms of both accuracy and computational efficiency. Despite its lean architecture and fast inference speed, M4 effectively captures the state of multi-element airfoils before and after interaction with velocity, contributing to its enhanced predictive accuracy.
- **Optimal Airfoil Configuration:** Given the fast rate of prediction, the proposed deep learning models can compute aerodynamic coefficients for various combinations of angles of attack and fluid velocities, helping to determine the optimal configuration (orientation) of the multi-element airfoil to achieve the desired lift and drag forces.

This study not only demonstrates the feasibility of applying ML/DL to complex airfoil configurations but also provides a foundation for future work aimed at further enhancing predictive accuracy and generalization across broader aerodynamic scenarios.

II. METHODOLOGY

For testing and validation of our proposed algorithm, the initial setup and the structure of multi-element airfoil were motivated by the fabrication of an actual rear wing of a Formula SAE vehicle (Society of Automotive Engineers).

A. Design and dimensions of the multi-element airfoil

The adoption of the Eppler 423 airfoil[24] for the rear wing of a sports car was based on its excellent performance, including a high lift-to-drag ratio and reliable stall characteristics at elevated angles of attack. The multi-element airfoil was designed with specific dimensions: the lowermost airfoil had a chord length of 0.35 m at an 8° angle, while the middle and upper airfoils had chord lengths of 0.16 and 0.14 m with variable angles α_1 and α_2 ranging from 0° to 32° and 0° to 56°, respectively, based on Simon McBeath's recommendations (Fig. 1).[25] Positioned 0.5 m from the ground, this configuration is expected to significantly enhance downforce and stability, particularly advantageous for high-speed driving and racing.

B. Computational domain and geometry setup

A two-dimensional (2D) analysis was adopted for the wings to simplify the CFD simulations, despite the actual airfoil being three-dimensional (3D) and exhibiting corresponding airflow characteristics.[26] While this simplification neglects the formation of vortices at the airfoil's tip, which persist downstream in reality,[27] it offers advantages in terms of computational time and resource requirements. Although a 2D analysis may underestimate few aspects, it can still provide valuable insights into flow behavior and approximate aerodynamic performance. Using ANSYS Splaceclaim software, a 2D

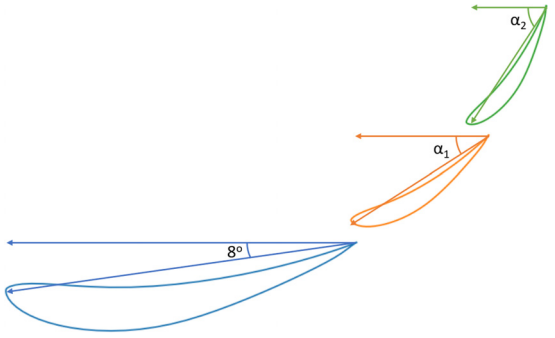

FIG. 1. Multi-element airfoil geometry (inverse E423).

25 November 2024 04:46:08

Published under an exclusive license by AIP Publishing

geometry for the airfoil wing system was constructed (Fig. 2). Input parameters such as angles α_1 and α_2 were defined to characterize the configuration, and a rectangular fluid domain positioned at a height of 0.5 m was created to account for the ground effect. This approach balances computational efficiency and meaningful results, providing insights into flow behavior and aerodynamic performance while acknowledging limitations. The outer rectangular domain had dimensions of 40 times the chord length, ensuring that the far-field boundaries did not interfere with the airflow around the airfoil system. Additionally, an inner rectangular domain with a length of 20 times the chord length was used to refine the near-wall region and capture detailed flow characteristics near the airfoils.

C. Mesh generation

The mesh generation process is crucial in CFD simulations, directly impacting accuracy and reliability. In this study, a second-order triangular unstructured mesh was used to construct the fluid domain around the flow field. The unstructured mesh was chosen over a structured mesh due to the need for effective parameterization and automation of the CFD process. Structured meshes, while potentially more accurate, require a fixed and predetermined configuration, unsuitable for the numerous CFD simulations needed for different airfoil angles.

Specific considerations during the mesh design phase ensured the quality of the mesh and accurate CFD results. The mesh was meticulously crafted to have well-shaped cells with good aspect ratios, avoiding overly stretched or distorted cells (Fig. 3). This approach minimized numerical errors and ensured reliable predictions of flow behavior.[28] Multiple inflation layers were introduced to accurately capture the boundary layer and flow features near the airfoil surface [Fig. 3(b)]. The finer mesh resolution near the airfoil surface allowed for better resolution of the boundary layer and more accurate representation of flow physics (Fig. 4).

A mesh independence study using Richardson extrapolation was conducted to ensure the accuracy of the CFD simulations, confirming that results were not significantly affected by mesh resolution (details in Sec. II F).

D. Boundary conditions and solver parameters

In our CFD simulations using ANSYS Fluent, we assumed a constant flow with an absolute velocity formulation in a two-dimensional space to focus on key aerodynamic phenomena without the complexities of three-dimensional effects. The SST k-Omega turbulence model was chosen over the k-Epsilon model due to its superior near-wall accuracy.[29] The k-Epsilon model often over-predicts turbulence kinetic energy (k) and under-predicts dissipation rate (epsilon) near walls, leading to inaccuracies in skin friction and heat transfer. The SST k-Omega model, combining strengths of both k-Epsilon and k-Omega models, provides a more accurate and robust prediction of near-wall turbulence.

FIG. 2. Computational domain in ANSYS Splaceclaim.

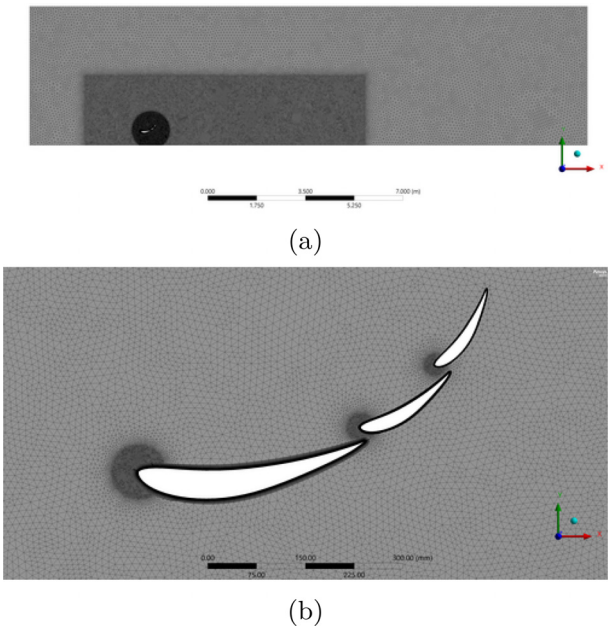

FIG. 3. Mesh of the computational domain: (a) zoomed-out and (b) close-up.

In the SST k-Omega model, the k-Epsilon model is used near the wall where the flow is highly turbulent, while the k-Omega model is applied in the free stream. This captures the complex interactions between turbulence and the boundary layer, improving predictions of turbulent flows near walls. Extensive validation against experimental data has demonstrated its superior performance. Given the presence of multiple airfoils and the importance of near-wall behavior, the SST k-Omega model was ideal for our simulations. It effectively handles near-wall phenomena and resolves adverse pressure gradients better than the k-Epsilon model. The inlet velocity which varied between 14 and 27 m/s was motivated by Formula SAE guidelines, which allowed us to explore a range of flow conditions and assess their impact on the aerodynamic performance of the multi-element wing. A pressure outlet boundary condition was applied at the outlet to allow flow to exit the domain freely, while no-slip boundary conditions were imposed on both the airfoil surface and the ground to accurately represent near-wall flow behavior. Key parameters for the simulations are summarized in Table I.

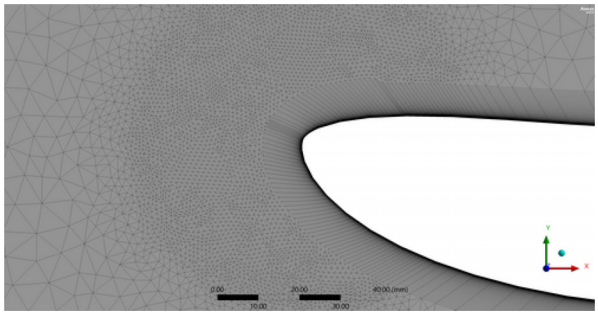

FIG. 4. Mesh near the leading edge of the bottommost airfoil.

25 November 2024 04:46:08

Published under an exclusive license by AIP Publishing

TABLE I. CFD simulation parameters.

Parameters	Values
Fluid properties	Air (density = 1.225 kg/m^3)
Viscosity	1.7894×10^{-05} kg/(ms)
Specific heat ratio	1.4
Operating conditions	Pressure: 101.36 Pa (1 atm) Temperature: 288.16 K
Boundary conditions	Inlet: Velocity range = 14–27 m/s Outlet: Pressure outlet Wall: No-slip condition for airfoil and ground
Initialization method	Hybrid initialization
Turbulence model	SST k-Omega

E. CFD simulation results

In the analysis of the majority of wing systems, the convergence solution typically stabilized within the range of 1×10^{-7} to 1×10^{-8} utilizing the SST k-Omega viscous model, accomplished within approximately 500 iterations, as shown in Figs. 5(c) and 6(c). In our specific case, the wall Y+ value was maintained at approximately 1. A Y+ value of 1 typically indicates that the first cell next to the surface is within the viscous sublayer. This means that the turbulent flow near the wall is resolved by the mesh, rather than being modeled. In general, a low Y+ value (close to 1) is preferred for accurate CFD simulations because it provides better resolution of the near-wall region. The static pressure, velocity distributions, and convergence of residuals for two different orientations are illustrated in Figs. 5 and 6.

F. Mesh independence study

Richardson extrapolation is a numerical method used to improve the accuracy of approximations by using multiple levels of discretization. In CFD, it can be used to reduce numerical error and perform mesh independence studies. The goal is to determine the minimum grid resolution required to achieve the desired level of accuracy. By computing the solution on multiple grids with varying levels of resolution and extrapolating to the limit of zero grid size, the accuracy of the solution can be improved.

To estimate the exact solution using Richardson extrapolation, simulations are performed with at least three different mesh sizes,[30] denoted by h_1, h_2, and h_3, where h_1 is the coarsest mesh and h_3 is the finest mesh, with h_2 being intermediate. Let the grid refinement ratio r be 2 in both cases, i.e., $h_3/h_2 = h_2/h_1 = 2$. The solutions on the coarse, medium, and finest meshes are s_1, s_2, and s_3 respectively. The order of convergence p can be estimated using the following equation:

$$p = \frac{\ln\left(\frac{s_1 - s_2}{s_2 - s_3}\right)}{\ln(r)}. \quad (1)$$

The exact solution can then be approximated using the following equation:

$$s_{\text{exact}} \approx s_3 + \frac{s_3 - s_2}{r^p - 1}. \quad (2)$$

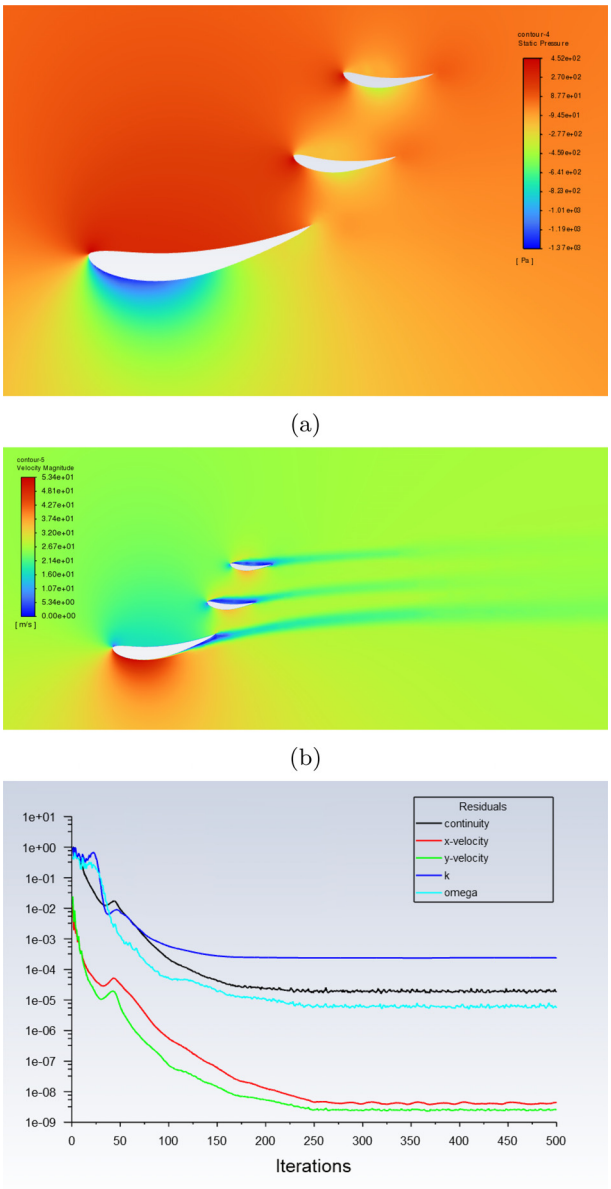

FIG. 5. (a) Static pressure distribution, (b) velocity distribution, and (c) convergence of residuals for $\alpha_1 = 0^o$, $\alpha_2 = 0^o$, and velocity = 27 m/s.

A comprehensive mesh independence study was conducted to evaluate the suitability of different mesh sizes for the CFD simulations of the multi-element airfoil system. Coarse, medium, and fine meshes with 85k, 170k, and 340k elements, respectively, were used to evaluate the convergence and reliability of downforce and drag values across varying angles of attack (α_1 and α_2) and velocity range. The study aimed to ensure the solutions converged to a single value as the mesh size was refined.

Using Richardson extrapolation, the medium mesh solution was compared to the extrapolated solution, revealing a negligible deviation

25 November 2024 04:46:08

Published under an exclusive license by AIP Publishing

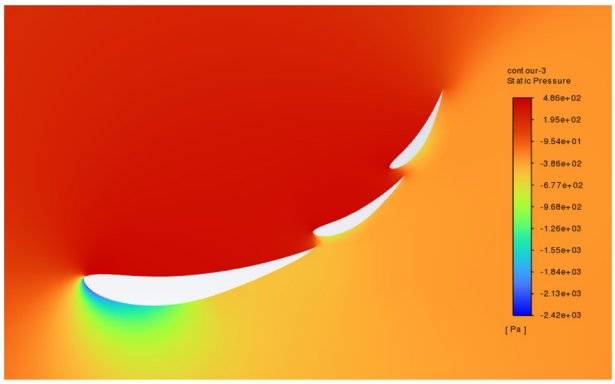

(a)

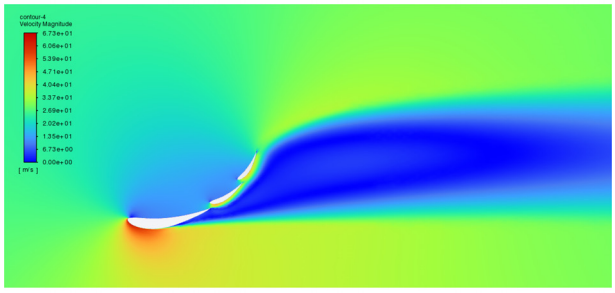

(b)

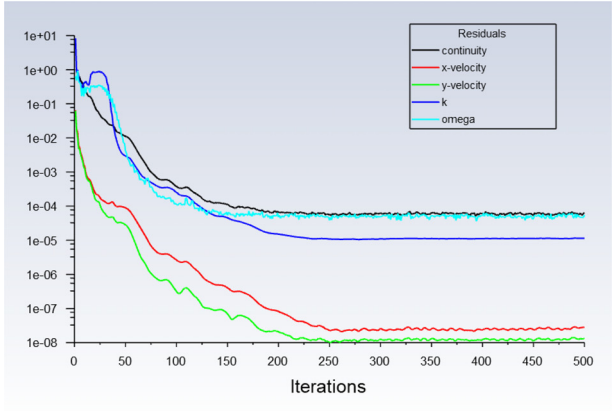

(c)

FIG. 6. (a) Static pressure distribution, (b) velocity distribution, and (c) convergence of residuals for $\alpha_1 = 32^o$, $\alpha_2 = 56^o$, and velocity = 27 m/s.

averaging less than 1.5%. Figures 7 and 8 present the CFD results for drag and downforce, respectively, showing the influence of various velocities and orientations on drag and downforce across different mesh resolutions. This analysis confirmed the accuracy and convergence of the medium mesh, which provided a good balance between computational efficiency and solution accuracy.

Based on these findings, the medium mesh was selected as the optimal choice for generating the dataset. This resolution allowed for expedited CFD simulations while maintaining accuracy in aerodynamic force predictions for the multi-element airfoil system.

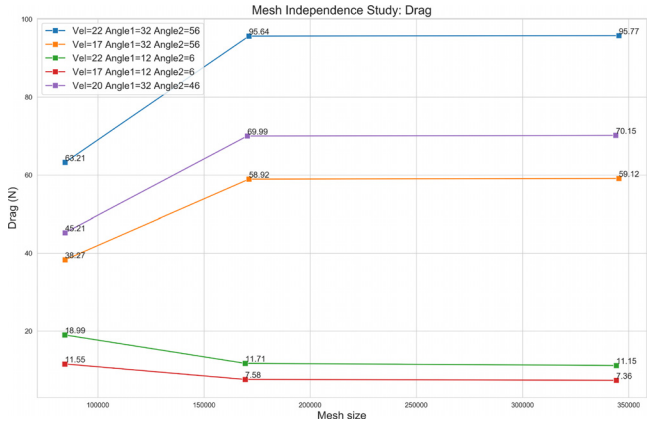

FIG. 7. Mesh independence study analyzing drag for different velocities and orientations.

G. Coefficient calculation

To accurately compute the coefficients of drag (Cd) and lift (Cl) for each angle and velocity configuration, the necessary frontal areas of the airfoil system were calculated. The frontal area in the direction of motion (A_x) and vertically in the y-direction (A_y) were determined using an in-house method, as the direct parameterization of the frontal area was not feasible in ANSYS Fluent.

The frontal area in the direction of motion (A_x) was computed by summing the vertical extents of all airfoils in the system. This approach ensured an accurate representation of the system's frontal area as perceived by the oncoming airflow. Overlaps between adjacent airfoils were carefully accounted for by subtracting the overlapping regions from the total area. For instance, if one airfoil extended into the vertical range of another, the overlapped portion was subtracted from the overall frontal area calculation. Similarly, the frontal area in the vertical direction (A_y) was determined by summing the horizontal extents of all airfoils, with overlapping regions being subtracted in the same manner. This method provided a precise calculation of the effective frontal areas used for determining the coefficients of drag (Cd) and lift (Cl).

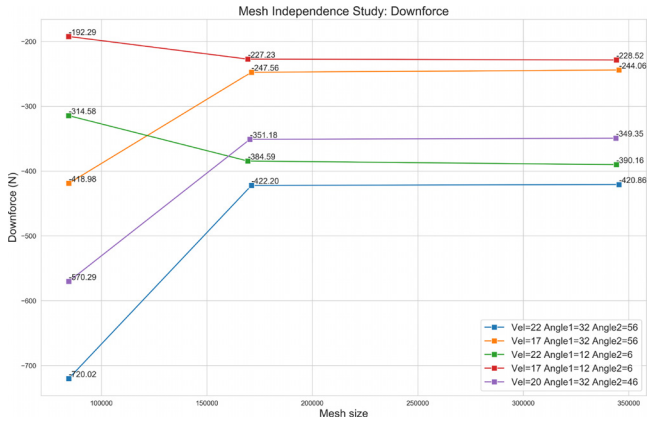

FIG. 8. Mesh independence study analyzing downforce for different velocities and orientations.

25 November 2024 04:46:08

Published under an exclusive license by AIP Publishing

Given that the width of the airfoil system was assumed to be 1 m, this width acted as a constant scaling factor across all configurations. The choice of width does not influence the relative comparison of coefficients because any chosen width would uniformly scale the calculated values of Cd and Cl. Thus, while the absolute values of Cd and Cl might vary depending on the width, their ratios and trends across different configurations remain consistent.

The coefficients of drag and lift were subsequently determined using the standard equations:

$$C_d = \frac{D}{\left(\rho V_\infty^2 A_x/2\right)}, \tag{3}$$

$$C_l = \frac{L}{\left(\rho V_\infty^2 A_y/2\right)}, \tag{4}$$

where

- ρ represents the fluid density,
- V_∞ denotes the free stream velocity,
- D corresponds to the drag force,
- L is the lift force.

H. Dataset creation

The coefficients of lift (Cl) and drag (Cd) were assessed across a spectrum of α_1 and α_2 angles, spanning from 0° to 32° and 0° to 56°, respectively, across a velocity range from 14 to 27 m/s, culminating in a comprehensive collection of 1500 data points.

Notably, while conventional machine learning models can directly utilize this set of parameters for aerodynamic coefficient prediction, the application of deep learning models like convolutional neural networks necessitates the transformation of the input data into a unified representation, such as an image format, to be effectively processed.

In addition to computing the downforce and drag values, we broadened our data generation process to encompass the creation of images that vividly represent the multi-element airfoil system. This involved recreating the entire scenario, including the airfoil boundaries and the ground. Specifically, we designed images against a black background with a distinct white border, capturing the essence of each of the three airfoils in the system. These crafted images were then employed as input for the convolutional neural network (CNN) model, which played a pivotal role in predicting the coefficients of lift (Cl) and drag (Cd).

1. Dataset manipulation

From our study, we observed that CNN-based deep learning architectures are significantly useful in predicting aerodynamic coefficients. So, we merged all the necessary information in an image and used it in our model architectures.

- Coordinates of airfoil boundaries was used to create each and every image. Here, a system comprising of three airfoils was chosen. All three airfoils were stacked on top of each other as shown in Fig. 10. The position of each airfoil was shifted slightly toward the right as we move upwards. Measurement and position of each airfoil in the multi-element airfoil system was motivated by the fabrication of an actual rear wing of a Formula SAE.
- Each image represents a combination of airfoils where all these moves at a certain velocity. So, to impart velocity information into an image, we multiply each pixel of an image with a velocity times modulating factor $V \times \mu$. The direct use of velocity instead of velocity times modulating factor will change the range of lower and upper bound of an image (i.e.,0,255 in non-normalized image) and reduce prediction accuracy of any deep learning model. This modulating factor μ is the inverse of speed of sound; thus, it normalizes velocity when multiplying it with the image.
- It is noted that major fluid interaction takes place with the outer boundary of a 2D airfoil; hence, it was important to mention in the first point that an airfoil is represented with its boundary coordinates because multiplying velocity times modulation factor with an inner solid body of an airfoil would not carry much useful information to the deep learning model. To incorporate this in our dataset, we have created images in such a way that boundary coordinates of airfoils and the line representing ground is shown by white color which is denoted by 1 in a normalized image while inner body is depicted by black color which is denoted by 0. Now when we multiply normalized velocity with the image, only boundary coordinates of a airfoil and the line representing ground gets affected while other parts of the image remains in their previous state (Fig. 9).
- Formula student racing cars uses multi-element airfoil as a rear wing to manipulate downforce for the purpose of maximizing speed. As it is used as a rear wing, it is close to the ground; thus, it is important for our CFD analysis to keep airfoil close to the surface/ground. To replicate same scenario here, we manipulated the images with a white horizontal straight line on the bottom of the image, thus representing ground in the image as shown in Fig. 10.
- A single image of a multi-element airfoil denotes its shape and may be able to identify geometric features/other valuable information associated with it when fed into a deep learning model. But when the velocity times modulating factor is multiplied with the outer boundary of the airfoil, we provide information not only regarding the geometric shape but also regarding the interaction between velocity and outer surface of the airfoil. Thus, a deep learning model now knows the difference between the velocity of fluids interacting with boundary of 2D multi-element airfoil to predict coefficient of lift and drag accurately.
- From our experiments, we also observed that if we stack two images (one is an image of boundary of a multi-element airfoil while other is element wise multiplication of same image with

FIG. 9. State of airfoil with and without interaction with velocity.

25 November 2024 04:46:08

Published under an exclusive license by AIP Publishing

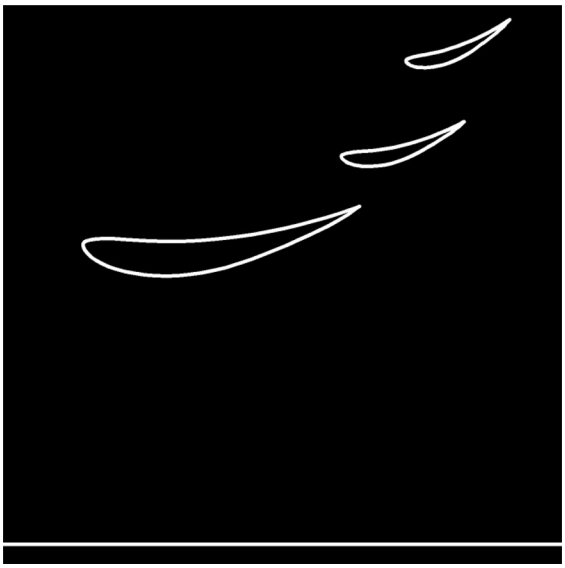

FIG. 10. Sample image from the dataset.

velocity and a modulating factor) on top of each other such that number of channel increases (an image has three channels, so two images stacked on channel will have six channels), we see increase in the accuracy of the prediction of aerodynamic coefficients. The reason behind this is that now the input captures two states, i.e., state of multi-element airfoil with and without velocity interaction.

2. Dataset preparation

Dataset underwent min–max scaler normalization due to exhibited variations in types, scales, and ranges. It is worth noting that due to the inverted airfoil configuration, the coefficient of lift (Cl) yielded negative values. Consequently, in the training of the machine learning and deep learning models, the Cl values were multiplied by −1 to render them positive, whereas no such modification was required for the drag coefficient (Cd). The input parameters for our deep learning or machine learning model architectures were selected from images generated using an in-house code, velocity, Angle 1 (top airfoil angle), and Angle 2 (mid airfoil angle) obtained from CFD simulations. Image generated using our in-house code depicts state of multi-element airfoil. There are two types of images in our dataset that depicts state of multi-element airfoil with and without interaction with velocity at which the car is driving currently. To estimate this, we multiplied velocity and a modulating factor with the entire image, thus feeding velocity information in the input image. The dataset was split into two groups: 80% for training and 20% for testing. The training set, comprising 80% of the dataset, was utilized for model training, while the remaining 20% served as an independent test set for evaluating the model's performance.

I. Loss function

We employed the mean squared error (MSE) as our loss function shown in Eq. (5), which is a commonly used metric in regression tasks. The MSE measures the average squared difference between the predicted and actual values, providing a measure of the model's accuracy. By minimizing the MSE during the training process, the models aim to optimize their parameter values to better fit the training data and generalize well to unseen data.

$$MSE(y, \hat{y}) = \sum_{i}^{n} \frac{(y_i - \hat{y}_i)^2}{n}. \tag{5}$$

J. Machine learning algorithm

In this section, we will discuss all the machine learning algorithms that will be trained and tested on data generated as mentioned in Sec. III.

1. Support vector regression

Support vector regression (SVR) was introduced by Drucker *et al.*[31] in the year 1996. SVR's primary goal is to delineate a hyperplane that optimally aligns with the distribution of data points, leveraging support vectors (data points proximal to the hyperplane) to minimize prediction error.

During our research, an exploration of various kernel functions revealed the polynomial kernel as particularly efficacious for our specific research query with polynomial degrees of 9 and 7 to be most effective for accurately predicting the coefficients of lift and drag, respectively.

2. Random Forest

In Random Forest regression, introduced in Ref. 32, an ensemble of decision trees is generated from random subsets of the training data and features. Each tree predicts the target variable, with the model's final output being the average of these predictions. The optimal number of trees was determined to be 5000 for our analysis.

3. Gradient Boosting

The methodology delineated by Friedman[33] introduces a Gradient Boosting framework that iteratively combines decision trees to enhance predictive accuracy from a collection of weak learners to a strong learner specifically by augmenting the emphasis on weaker learners and diminishing it for stronger ones. In our application, a configuration of 10 000 trees was selected for estimating the lift coefficient and 15 000 trees for the drag coefficient. Unlike traditional methods that adjust weights of individual data points, this model iteratively refines its predictions by focusing on residual errors from previous iterations, with each successive tree building upon the insights acquired from the errors of its predecessors. Foundational model used here is given by the following equation:

$$F_0(x) = arg_\gamma \min \sum_{i=1}^{n} L(y_i, \gamma). \tag{6}$$

The minimization criterion, denoted as argmin, seeks to ascertain a predictive value, or gamma, that ensures the least value of the loss function.

25 November 2024 04:46:08

Published under an exclusive license by AIP Publishing

4. AdaBoost

AdaBoost[34] for regression problems, known as AdaBoost.R, functions by iteratively refining weak regression models to enhance predictive accuracy. Initially, each data point is assigned an equal weight. A weak learner, such as a decision tree, is then trained on this weighted dataset. The learner's prediction errors are quantified, and higher weights are assigned to instances with greater prediction errors. Subsequent weak learners are trained on these re-weighted data points. This is a iterative process with final regression model is an aggregation of these weighted learners

5. Extreme Gradient Boosting or XGBoost

XGBoost stands as a distributed Gradient Boosting framework, amalgamates the forecasts generated by numerous weak models to yield a potent predictive outcome as elucidated by Chen *et al.*[35] XGBoost iteratively generates decision trees. Optimal number of trees tuned for our application is 10 000 and 15 000 for predicting lift and drag coefficients, respectively. The final prediction is computed by aggregating the prediction scores yielded by each individual decision tree given by the following equation:

$$\hat{y}_i = \sum_{k=1}^{K} f_k(x_i), \quad f_k \varepsilon F(x_i), \tag{7}$$

where K is the number of trees, f is the functional space of F, and F is the set of possible CARTs (classification and regression trees). CARTS are decision trees used to iteratively minimize residual errors through Gradient Boosting.

K. Artificial neural network

In artificial neural networks (ANNs),[36] the fundamental building block is the perceptron, and a large neural network is essentially a network of interconnected perceptrons forming layers. The process by which input data propagates through the network to generate an output is known as forward propagation or feedforward computation. In a neural network with L layers, including input (layer 0) and output (layer L), layer l is associated with a weight matrix $W^{(l)}$ and a bias vector $b^{(l)}$, and the activation values of neurons in each layer are denoted as $a^{(l)}$. The forward propagation begins with input data entering the input layer $[a^{(0)}]$, and subsequent layers' activation values are computed iteratively using a weighted sum followed by the application of an activation function $g(\cdot)$ as shown in the following equations:

$$z^{(l)} = W^{(l)} a^{(l-1)} + b^{(l)}, \tag{8}$$

$$a^{(l)} = g\left(z^{(l)}\right). \tag{9}$$

The activation functions, such as sigmoid, tanh, or ReLU (rectified linear unit), introduce non-linearity and enable the modeling of complex relationships in the network.

Backpropagation is a method that allows the network to learn from data by iteratively adjusting its weights and biases based on the discrepancy between predicted and actual outputs.

L. Convolution neural network

In a convolutional neural network (CNN),[37] the input data, such as an image of a multi-element airfoil in this case, undergo a series of convolutional layers that employ learnable filters capable of detecting various features such as edges, curves, and textures within the input image. CNNs, like other deep neural networks, involve two processes: forward propagation and backward propagation. During forward propagation, the input data are processed through convolutional layers, pooling layers, and fully connected layers, ultimately generating output predictions. Backward propagation is then employed to update the learnable parameters based on the error between predicted and actual outputs.

Given an input image I, the convolutional layer applies a set of filters or kernels W to the input. The output of the convolutional layer is obtained by convolving the input with the filters and applying an activation function $g(\cdot)$. The output of a single neuron in the convolutional layer, denoted by (c), can be computed as shown in the following equations:

$$O_c = W_c * I + b_c, \tag{10}$$

$$A_c = g(O_c). \tag{11}$$

An element at (a,b) for channel c of the output matrix O, represented by $O_{a,b,c}$ can be computed using the following equation:

$$O_{a,b,c} = \sum_{a'=1}^{K_1} \sum_{b'=1}^{K_2} \sum_{c'=1}^{C_I} W_{a',b',c',c} \cdot I_{a-a',b-b',c'} + b_c. \tag{12}$$

Here, K_1 and K_2 represent the height and width of the filters, respectively. The depth of the filter would be the same as the number of channels in the input, represented by C_I. b_c is the bias term associated with neuron c. The resulting feature map O_c {c = 1,2,…C_O}, where C_O represents the number of channels in the output as well as the number of filters, captures local patterns, and features present in the input image.

During the backpropagation phase of convolutional neural networks (CNNs), the gradients are systematically propagated from the output layer toward the input layer, facilitating the iterative updating of parameters throughout the network. These gradients are meticulously computed through the application of the chain rule of calculus. Consideration of a loss function L gauging the deviation between predicted and actual outputs allows for the derivation of crucial equations governing the gradient calculations for both the convolutional kernel, W and the input image, I.

M. Deep learning model architectures

In this section, we will discuss in detail all the deep learning model architectures and their performance on the dataset created as well as compare them on the basis of their accuracy. All the models described below were trained using the Adam optimizer[38] with a learning rate of 5×10^{-5}, a batch size of 32, and the mean squared error as the loss function. Hyperparameter tuning was performed using the grid search method. Table II displays common hyperparameters used for all the deep learning models.

1. Model architecture 1: M_1

Model M1 is a deep neural network based on an artificial neural network (ANN) architecture. It takes as input the velocity of the

25 November 2024 04:46:08

Published under an exclusive license by AIP Publishing

TABLE II. Hyper parameters used in deep learning models.

Hyper parameters	Values
Optimizer	Adam optimizer
Batch size	32
Loss function	Mean squared error
Learning rate	5×10^{-5}

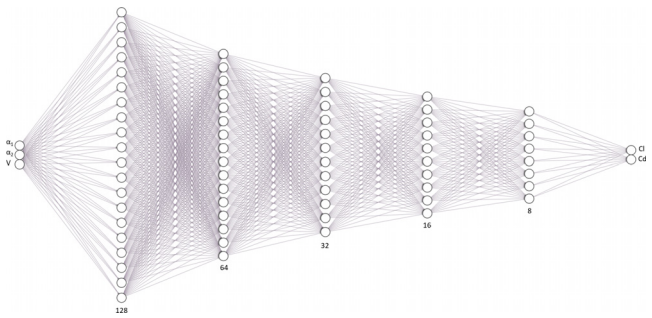

FIG. 11. M_1 model architecture.

airflow and the angles of the top and mid airfoils to predict aerodynamic coefficients, specifically the coefficient of lift (Cl) and coefficient of drag (Cd). The architecture of Model M1 shown in Fig. 11 is as follows:

- The input parameters, velocity, angle 1, and angle 2, form a three-dimensional vector that serves as the input to a series of dense layers in the neural network. The first dense layer contains 128 neurons, followed by a rectified linear unit (ReLU) activation function, which is then connected to successive layers with 64, 32, 16, and 8 neurons, each followed by a ReLU activation function.
- Finally, the output is passed through a dense layer containing two neurons, representing the coefficients of lift and drag, respectively.

These neurons provide the final predictions for the aerodynamic coefficients based on the input parameters. Figure 12 represents training and testing loss vs the number of epochs M_1 was trained on.

2. Model architecture 2: M_2

As shown in Fig. 13, our proposed model, Model M2, is a deep neural network based on a convolutional neural network (CNN) architecture, structured in a "Y" shape. The CNN layers serve as a feature encoder, extracting relevant features from the input image. The velocity and angle information corresponding to each airfoil are concatenated with a flattened vector of the feature map obtained from the image. This concatenated vector is then passed through dense layers to predict the aerodynamic coefficients. The architecture of Model M2 is defined as follows, with the input image dimension being (400, 700).

- The input image is fed into the first convolutional layer with a filter size of (5, 5) and 20 channels. The output is then passed through a max pooling layer of size (2, 2) and a rectified linear unit (ReLU) activation function. The resulting feature map has dimensions of (200, 350, 20).
- The output from the previous layer is then fed into another convolutional layer with a filter size of (5, 5) and 40 channels, followed by a max pooling layer of size (2, 2) and a ReLU activation function, generating a feature map of size (100, 175, 40).
- The next layer in the architecture is a convolutional layer with 60 channels and a filter size of (5, 5), followed by a max pooling layer of size (2, 2) and a ReLU activation function. This results in a feature map of size (50, 87, 60).
- Previous layer's output is flattened and passed to a dense layer with 32 neurons, generating a 32-dimensional feature vector.
- Additionally, from the dataset obtained through CFD simulations, the velocity and angle of the top and mid airfoils corresponding to the input image are extracted as a small three-dimensional feature vector. This auxiliary input is passed through a hidden layer with six neurons.
- The output from the previous step is concatenated with the output from step 4, resulting in a 38-dimensional feature vector.
- This concatenated vector is then fed into a dense hidden layer with 16 neurons, followed by a ReLU activation function.
- Finally, the last layer of the network produces the desired output, with two neurons representing the values of the coefficient of lift and drag, respectively.

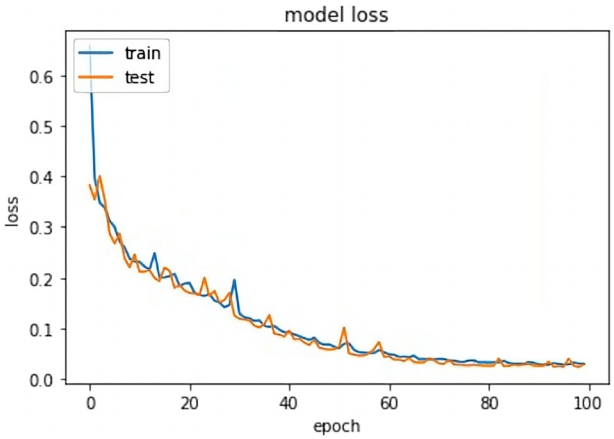

FIG. 12. Training and testing loss graph for M_1 model.

These neurons provide the final predictions for the aerodynamic coefficients based on the input image, velocity, and angle information. Figure 14 represents training and testing loss vs the number of epochs model M_2 was trained on.

3. Model architecture 3: M_3

As shown in Fig. 15, our proposed model, Model M3, is a deep neural network based on a convolutional neural network (CNN) architecture, designed to process a single input image representing the state of a multi-element airfoil after interaction with velocity. The input image is resized to dimensions (200, 350) for efficient processing.

25 November 2024 04:46:08

Published under an exclusive license by AIP Publishing

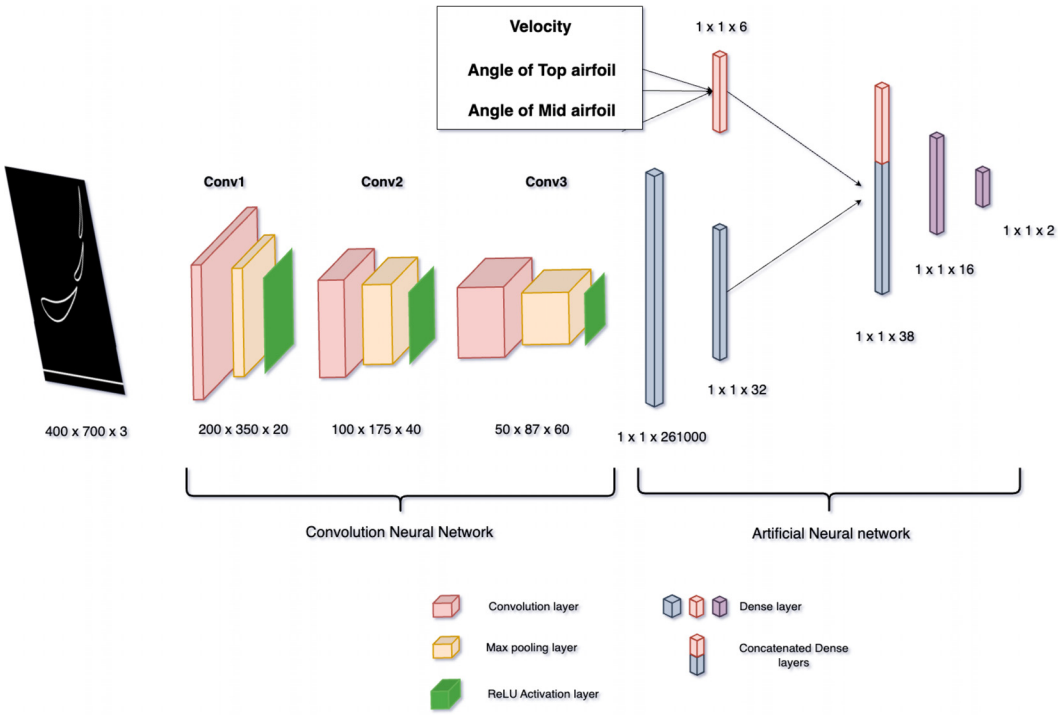

FIG. 13. M_2 model architecture.

- The input image is passed through the first convolutional layer with a filter size of (5, 5) and 20 channels. The resulting feature map is subjected to a max pooling layer of size (2, 2) and a rectified linear unit (ReLU) activation function. The output feature map has dimensions of (100, 175, 20).
- The output from the previous layer is then fed into another convolutional layer with a filter size of (5, 5) and 40 channels. This is followed by a max pooling layer of size (2, 2) and a ReLU activation function, generating a feature map of size (50, 87, 40).

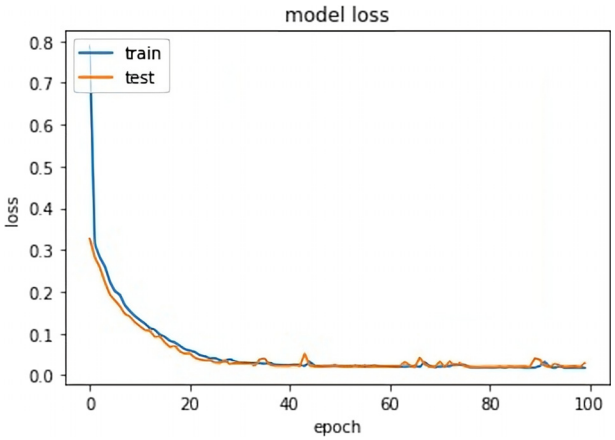

FIG. 14. Training and testing loss graph for M_2 model.

- Subsequently, a convolutional layer with 60 channels and a filter size of (5, 5) is applied, followed by a max pooling layer of size (2, 2) and a ReLU activation function. This yields an output feature map with dimensions of (25, 43, 60).
- The feature map generated from the convolutional layer is flattened and fed into a dense hidden layer with 32 neurons and a ReLU activation function.
- The output from the previous dense layer is then passed through another dense hidden layer with 16 neurons, which is further activated using the ReLU function.
- Another dense hidden layer with eight neurons and a ReLU activation function is applied, resulting in an eight-dimensional feature vector.
- Finally, we have two neurons, each representing the values of the coefficient of lift and drag, respectively.

These neurons produce the final output, predicting the aerodynamic coefficients based on the processed input image. Figure 16 represents training and testing loss vs the number of epochs model M_3 was trained on.

4. *Model architecture 4:* M_4

As shown in Fig. 17, our proposed model, Model M4, is a deep neural network based on a convolutional neural network (CNN) architecture, designed to process a composite input image consisting of two images such that dimension of the composite image will have its channel size doubled. These images represent

25 November 2024 04:46:08

Published under an exclusive license by AIP Publishing

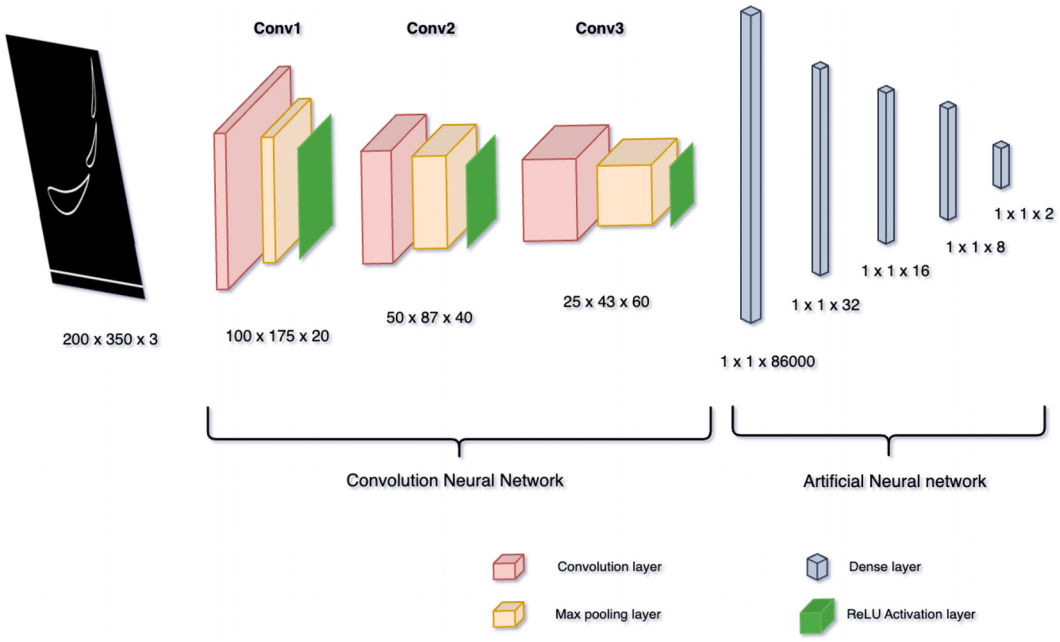

FIG. 15. M_3 model architecture.

the state of a multi-element airfoil before and after interaction with velocity. The input image is resized to dimensions (200, 350, 6) for effective processing.

- The composite image is fed into the first convolutional layer with a filter size of (5, 5) and 40 channels. The resulting feature map is then passed through a max pooling layer of size (2, 2) and a rectified linear unit (ReLU) activation function. The output feature map has dimensions of (100, 175, 40).
- The output from the previous layer is further processed by another convolutional layer with a filter size of (5, 5) and 60 channels. This is followed by a max pooling layer of size (2, 2) and a ReLU activation function, generating a feature map of size (50, 87, 60).

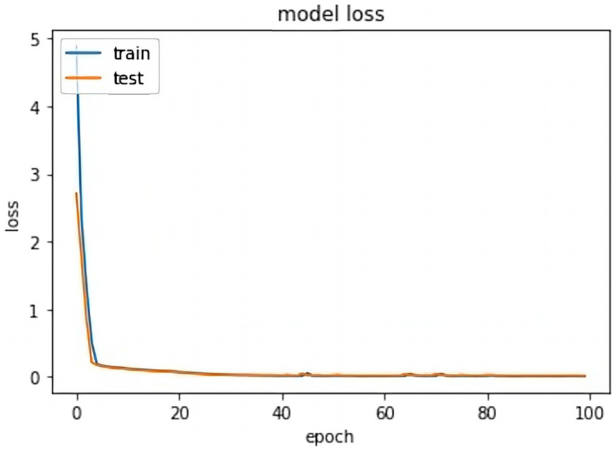

FIG. 16. Training and testing loss graph for M_3 model.

- Subsequently, a convolutional layer with 80 channels and a filter size of (5, 5) is applied, followed by a max pooling layer of size (2, 2) and a ReLU activation function. This produces an output feature map with dimensions of (25, 43, 80).
- The feature map generated from the convolutional layer is flattened and fed into a dense hidden layer with 32 neurons, further activated using the ReLU function.
- Next we apply a dense layer with 16 neurons, and a ReLU activation function, resulting in a 16-dimensional feature vector.
- Last layer consists of two neurons, each representing the values of the coefficient of lift and drag, respectively.

These neurons produce the final output, predicting the aerodynamic coefficients based on the processed composite input image. Figure 18 represents training and testing loss vs the number of epochs model M_4 was trained on. Model M4 designed for input images that contains state of multi-element airfoil before and after interaction with velocity.

III. RESULTS AND DISCUSSION

A. Experimental setup and hardware configuration

All experiments and the corresponding results presented in this paper were conducted on a system equipped with an Intel i7 10th generation processor, 32 GB of RAM, and an NVIDIA Quadro RTX 4000 GPU. Consequently, the time and accuracy analyses discussed in Sec. III B are specific to this hardware configuration.

B. Observation and impact

Upon comparing the outcomes produced by various machine learning and deep learning models, it was noted that the deep learning model exhibited superior performance in prediction accuracy compared to the machine learning models. The predictions made by the

25 November 2024 04:46:08

Published under an exclusive license by AIP Publishing

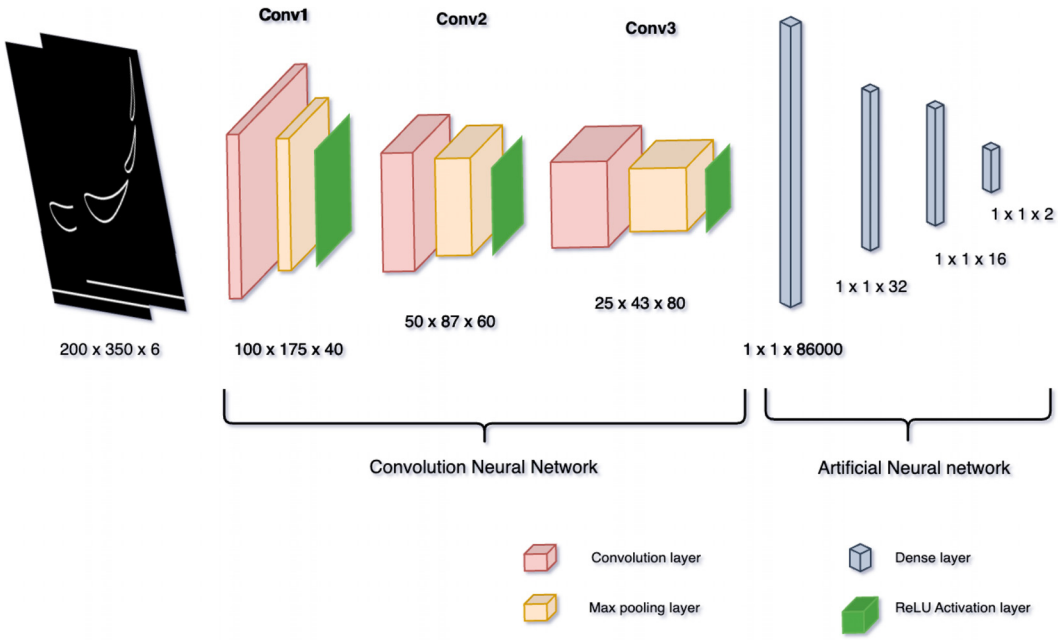

FIG. 17. M_4 model architecture.

machine learning models as shown in Table III, displayed relatively low accuracy and higher mean squared error compared to prediction made by deep learning model as shown in Table IV. Specifically, algorithms such as Random Forest, Gradient Boosting, and Extreme Gradient Boosting (XGBoost) showcased notable efficacy on the given dataset, whereas other machine learning models demonstrated inadequate accuracy. Consequently, this section will primarily concentrate on the comparative analysis of deep learning models. Investigations utilizing four distinct models based on the deep learning paradigm, model 1, model 2, model 3, and model 4, revealed significant disparities in accuracy levels. Analytical representations were crafted, illustrating the predictions rendered by these four deep learning models.

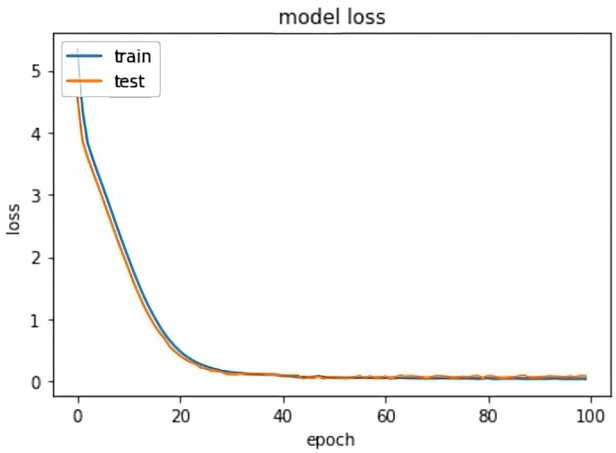

FIG. 18. Training and testing loss graph for M_4 model.

Two categories of graphical representations were devised to elucidate the coefficients of lift and drag:

- One depicting the frequency distribution of the difference between actual and predicted aerodynamic coefficients;
- Second comparing predicted vs actual aerodynamic coefficients for multiple samples.

1. Model M1

Upon examination of the frequency distribution graphs detailing the difference between predicted and actual coefficients of lift (Cl) and drag (Cd) across all models, it became apparent that model 1 exhibited

TABLE III. Metric score for ML algorithms.

Machine learning model	MSE
Support vector regression	0.082 02
Random Forest	0.008 03
Gradient boost	0.009 40
AdaBoost	0.072 53
XGBoost	0.007 45

TABLE IV. Metric score for DL algorithms.

Deep learning model	MSE
Model M_1	0.0064
Model M_2	0.0280
Model M_3	0.0055
Model M_4	0.0049

25 November 2024 04:46:08

Published under an exclusive license by AIP Publishing

notable deviations between predicted and actual values of Cl and Cd, as shown in Figs. 19(a) and 19(c) which demonstrates multiple peaks in both the graphs which are far from zero. This shows that there are multiple samples in our dataset where differences in predicted and actual Cl, Cd is non zero. Here, an ideal graph would have looked like a Gaussian curve with mean at zero (achieving single highest peak at zero) and standard deviation as low as possible. Figures 19(b) and 19(d) further elucidated that the predicted coefficients of lift and drag diverged significantly from their true values, where an ideal representation would approximate a $y = x$ line, indicative of a close alignment between predicted and actual outcomes.

2. Model M2

In the case of model 2, modifications to the architecture yielded minimal enhancements in performance. The frequency distribution of the deviations between predicted and actual coefficients of lift and drag as shown in Figs. 20(a) and 20(c) presented a curve, which is roughly similar to a Gaussian curve, with mean and standard deviations of 0.47, 0.109, and 0.15, 0.14, respectively. These results clearly indicate that average delta of predicted and actual Cl or Cd is significantly more than expected, with comparatively higher standard deviation. This indicates an average prediction error of 0.15 ± 0.42 for Cl and 0.47 ± 0.32 for Cd. Figures 20(b) and 20(d) further highlighted substantial discrepancies in the predicted and actual values for the coefficients of lift and drag.

3. Model M3

Model 3's analysis revealed a stark contrast, particularly in the frequency distribution plot for the deviation in predicted and actual Cd, which showed a mean of −0.009 and a considerably lower standard deviation of 0.02, whereas the frequency distribution plot for the deviation in predicted and actual Cl demonstrated a mean of 0.017 with a standard deviation of 0.3 as shown in Figs. 21(a) and 21(c). These findings highlight a significant improvement in the accuracy of drag coefficient predictions and a notable enhancement for the lift coefficient when compared to prediction accuracy of models 1 and 2. This is attributed to the utilization of model 3, which incorporates the state of multi-element airfoil after interaction with velocity, thus demonstrating its importance. The disparities in predicted vs actual Cl, Cd, as depicted in Figs. 21(b) and 21(d), show that even though there was a substantial increase in the accuracy, there are still a lot of samples in the dataset which needs improvement.

4. Model M4

Conversely, model 4 demonstrated a remarkable uptick in predictive accuracy for both aerodynamic coefficients. The frequency plots for the deviations in predicted and actual values of Cl and Cd formed refined Gaussian distributions, with the Cl predicted at a mean of −0.0016 and a standard deviation of 0.0277, and the Cd at a mean of −0.012 and a standard deviation of 0.0125 as shown in Figs. 22(a) and 22(c). These metrics clearly indicate that mean and standard deviation of delta between actual and predicted aerodynamic coefficients by model 4 is the lowest when compared to the rest of the deep learning models. A subsequent analysis of graphs showcasing the actual vs predicted coefficients of lift and drag as shown in Figs. 22(b) and 22(d)

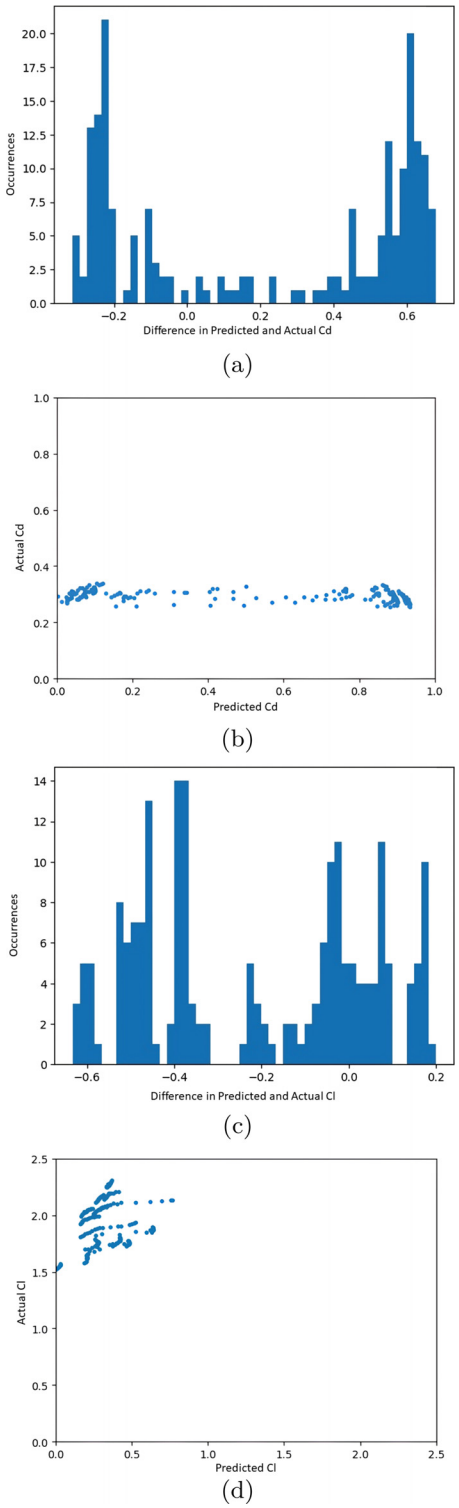

FIG. 19. (a) Frequency plot of difference in actual and predicted Cd by model 1, (b) plot of actual vs predicted Cd by model 1, (c) frequency plot of difference in actual and predicted Cl by model 1, and (d) plot of actual vs predicted Cl by model 1.

25 November 2024 04:46:08

Published under an exclusive license by AIP Publishing

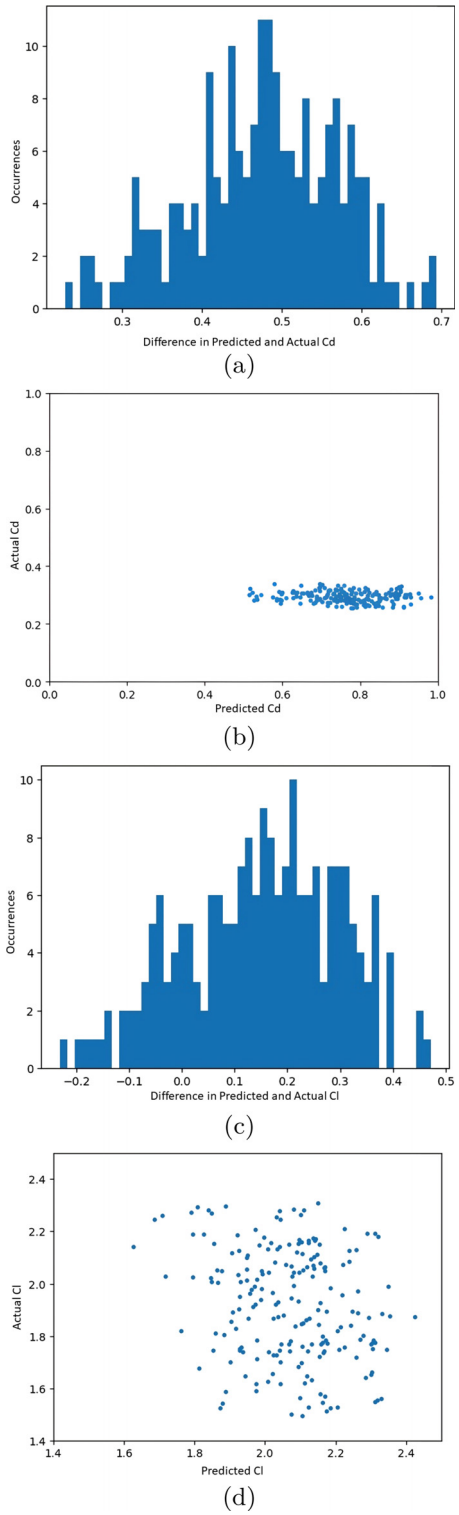

FIG. 20. (a) Frequency plot of difference in actual and predicted Cd by model 2, (b) plot of actual vs predicted Cd by model 2, (c) frequency plot of difference in actual and predicted Cl by model 2, and (d) plot of actual vs predicted Cl for model 2.

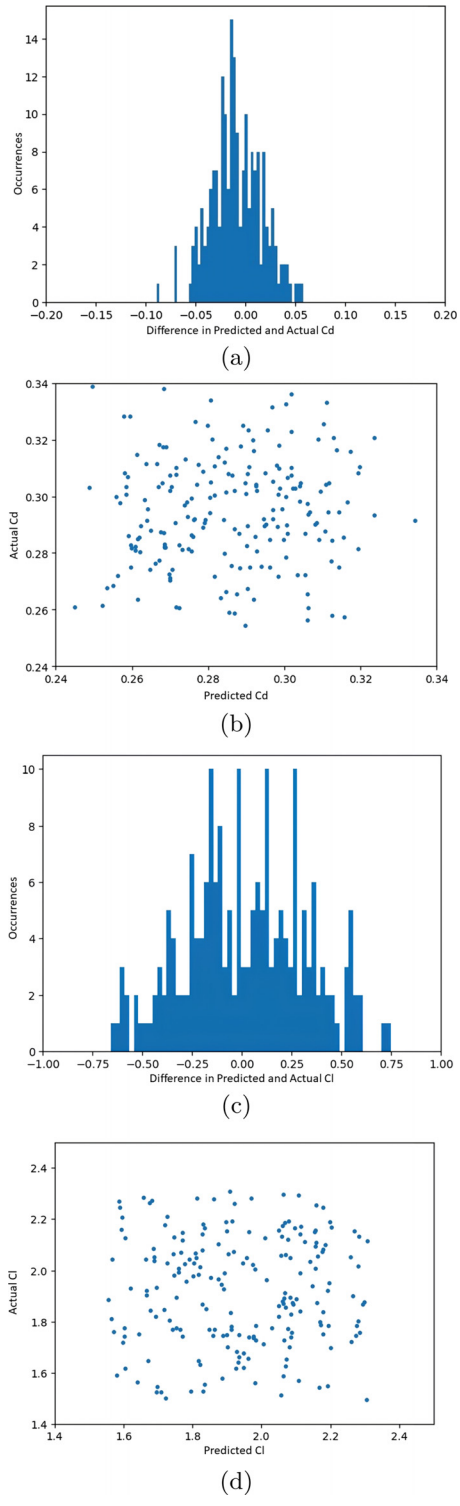

FIG. 21. (a) Frequency plot of difference in actual and predicted Cd by model 3, (b) Plot of actual vs predicted Cd by model 3, (c) Frequency plot of difference in actual and predicted Cl by model 3, and (d) plot of actual vs predicted Cl for model 3.

25 November 2024 04:46:08

Published under an exclusive license by AIP Publishing

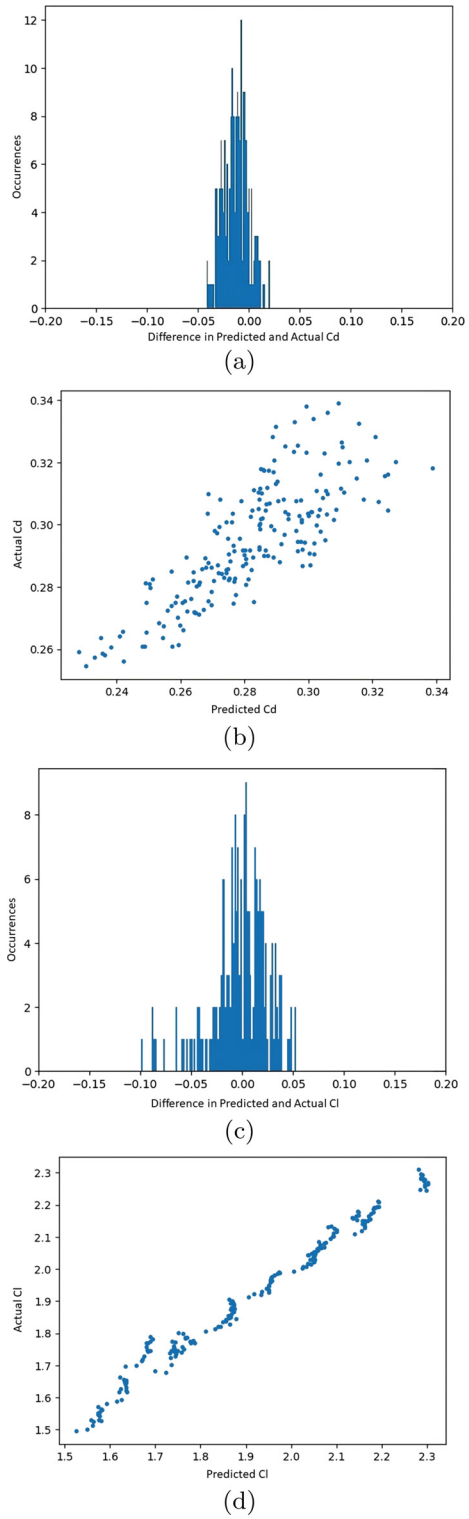

FIG. 22. (a) Frequency plot of difference in predicted and actual Cd, (b) plot of predicted vs actual Cd, (c) frequency plot of difference in predicted and actual Cl, and (d) plot of predicted vs actual Cl for model M_4.

revealed a correlation closely mirroring the ideal y = x line, suggesting a high degree of accuracy in predictions. High jump in the accuracy of the results is due to incorporating the state of the multi-element airfoil pre- and post-interaction with velocity. Therefore, this provides a clear understanding of the differences that occur when the outer boundary of the airfoil interacts with high or low levels of velocity. A comprehensive review of the outcomes from all models and the generated plots clearly indicates that the inclusion of the multi-element airfoil's state information before and after interaction with the velocity enables model 4 to forecast the coefficients of lift and drag with superior precision.

C. Time and parameter analysis

In the literature, there is a dearth of articles and papers on using deep learning to accurately predict aerodynamic coefficients for multi-wing systems (multi-element airfoil) as shown in Fig. 1, at every instant of time given its shape, velocity, and angles of attack. There are many articles and papers doing the same for single element airfoil but not for multi-wing systems (multi-element airfoils).

Given the scarcity of research on using deep learning models on multi-element airfoils, we have benchmarked our approach against CNN-based deep learning models trained on single-element airfoils, evaluating factors such as model parameters, prediction time, and training epochs. We developed lean convolutional neural network (CNN) models, including our model M4 described in Sec. III B 4, which requires training only 2.9×10^6 parameters to predict the aerodynamic coefficients of a multi-element airfoil. In contrast, state-of-the-art CNN based models such as the one described in Ref. 39 require 21.8×10^6 parameters, while another model in Ref. 40 uses 33.6×10^6 parameters to predict the aerodynamic coefficients for a single-element airfoil. Our model is approximately 10 times lighter than existing state-of-the-art CNN models and demonstrates highly accurate predictions of the coefficients of lift and drag, with an MSE score as low as 0.0049.

The entire training process for model M4 required just 100 epochs, compared to state-of-the-art CNN models such as Ref. 40, which took 200 epochs, and Ref. 39, which required 50 000 epochs to train on a single-element airfoil. This demonstrates that our model, even though it is trained on multi-element airfoil, is not only lightweight but also requires fewer epochs for training, resulting in faster model training.

Model M4 can predict aerodynamic coefficients for a multi-element airfoil system in less than 6 ms, given the airfoils' shapes, fluid velocity, and angles of attack at a specific moment. In comparison, the state-of-the-art model[40] takes approximately 27 ms, due to its large number of parameters and large input image size. However, Ref. 39 achieves a similar prediction time of 5–6 ms; this is primarily because of its smaller input image dimensions, which reduce the computational time despite having more parameters.

Given the fast rate of prediction, model M4 can compute aerodynamic coefficients for various combinations of angles of attack and fluid velocities, helping to determine the optimal configuration (orientation) of the multi-element airfoil to achieve the desired lift and drag forces. This allows for optimization of the multi-element airfoil's configuration to meet specific aerodynamic requirements (e.g., lift and drag forces). A detailed explanation of this application is provided in Sec. IV.

25 November 2024 04:46:08

Published under an exclusive license by AIP Publishing

D. Results

All the machine learning algorithms presented in Table III, as well as the deep learning algorithm described in Table IV, were utilized to predict the coefficients of lift and drag (Cl and Cd). These predictions were based on either the input image or the velocity and angle information associated with each airfoil. The performance of the proposed architectures was assessed using the statistical metrics discussed in Sec. II I, and the results are summarized in Tables III and IV. Notably, the deep learning models generally outperformed the machine learning models. There are two major reasons behind this behavior:

- Machine learning models are unable to use geometric data of airfoil; therefore, they only use absolute values of velocity and angles associated with each airfoil within a multi-element airfoil system to predict aerodynamic coefficients.
- On the other hand, deep learning models utilized geometric data from the multi-element airfoil system in addition to the absolute values of velocity and angles corresponding to each airfoil within the multi-element airfoil system to predict aerodynamic coefficients.
- The deep learning algorithms are mathematically and intuitively much more complex than traditional machine learning models. Consequently, they have the capability to capture a broader array of detailed information and features, which are instrumental in making accurate predictions.

Within the spectrum of machine learning techniques, algorithms such as Random Forest, Gradient Boosting, and Extreme Gradient Boosting (XGBoost) demonstrated superior efficacy on the investigated dataset. These methods achieved comparably high performance metrics, accurately forecasting the lift and drag coefficients with mean squared error (MSE) values ranging between 0.0075 and 0.0095. Notably, XGBoost distinguished itself as the most proficient model, securing the minimal MSE value among the evaluated algorithms.

While deep learning models outperformed machine learning models overall, it is noteworthy that among the applied deep learning algorithms, the model architecture M4 exhibited superior performance compared to the others. Model M4 differed from the other architectures in several aspects.

- It adopted a CNN-based model architecture with two images as input.
- It incorporated the interaction between velocity and the airfoil's outer boundary as additional input apart from geometric information, velocity, and angle of each airfoil in a multi-element airfoil system for the prediction of aerodynamic coefficients.
- Furthermore, it utilized the state of the multi-element airfoil before and after the velocity interaction (velocity at which the system is moving), thus giving a clear idea of variations that can be seen when high or low magnitude of velocity interacts with outer boundary of airfoil.

Thus, the proposed model architecture demonstrated highly accurate predictions of the coefficients of lift and drag, with an MSE score as low as 0.0049.

These findings highlight the efficacy of the deep learning approach, particularly Model M4, in accurately predicting the aerodynamic coefficients. The incorporation of comprehensive input features and the utilization of a CNN-based architecture contribute to the superior performance observed in terms of MSE scores.

Our findings demonstrate that the analysis of multi-element airfoil system using computational fluid dynamics (CFD) demands a duration of 10–15 min per assessment, in stark contrast to the machine learning/deep learning algorithm's capability to execute an analysis within the millisecond range, specifically 1–6 ms. Both the experiments were performed on the hardware specification mentioned in Sec. III A. This evidence that the methodology we advocate offers a speed enhancement of approximately 1.5×10^5 times over traditional CFD analyses. This can open avenues for various real-time practical applications. The proposed deep learning algorithms are sensitive to hyperparameters, and significant effort was spent tuning them. Furthermore, Table V presents a comparative analysis of the actual vs predicted coefficients of lift and drag as determined by our Model architecture M4, including the differences between predicted and actual values. These results clearly demonstrate that our deep learning model yields not only fast but also highly accurate predictions.

IV. APPLICATION

A promising application of the insights garnered from this study is the conceptualization of a dynamically adjustable multi-element wing system of a vehicle using an onboard computer or integrated computing unit. Leveraging the current velocity data, an integrated computing unit or an onboard computer could ascertain the most favorable angle of attack corresponding to the prevailing operational parameters, circumventing the necessity for further computational fluid dynamics (CFD) analyses. The deep learning and machine learning models can compute aerodynamic coefficients for a range of velocities and angles combinations in real-time, enabling multi-element system to adjust its angles and optimize the aerodynamic performance.

The architecture of the proposed algorithm is illustrated in Fig. 23. At each timestamp, parameters are extracted from a multi-element airfoil system, encompassing various combinations of velocity,

TABLE V. Predicted values of Cl and Cd using model M_4.

Coefficient of lift (Cl) (Actual)	Coefficient of lift (Cl) (Predicted)	Error in prediction (Cl)	Coefficient of drag (Cd) (Actual)	Coefficient of drag (Cd) (Predicted)	Error in prediction (Cd)
3.629 23	3.629 58	0.000 35	0.269 40	0.269 58	0.000 180
2.757 20	2.757 68	0.000 47	0.312 64	0.312 83	0.000 194
4.156 25	4.155 41	0.000 84	0.287 96	0.288 20	0.000 240
1.712 93	1.711 92	0.001 00	0.247 70	0.247 41	0.000 285
2.770 03	2.771 30	0.001 26	0.334 97	0.334 64	0.000 325

25 November 2024 04:46:08

Published under an exclusive license by AIP Publishing

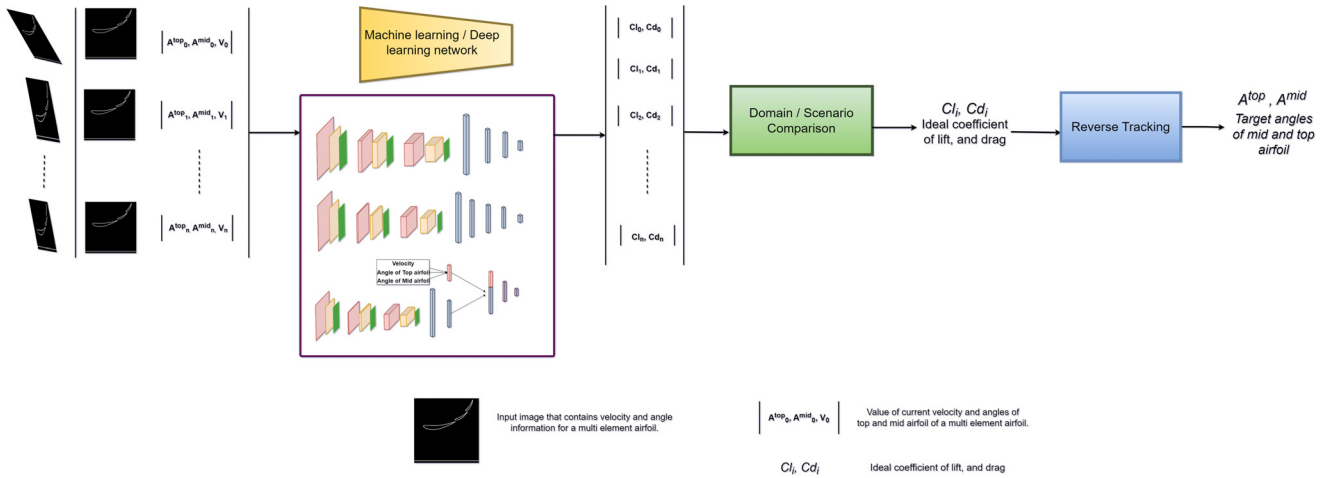

FIG. 23. Complete algorithm: various combination of velocity, top and mid airfoil angles of multi-element airfoil along with an image representing this system are fed into a deep learning algorithm (which can be models 1, 2, 3, and 4). For each combination, model will predict coefficient of lift and drag. The combination that yields the optimal aerodynamic coefficients is identified as the target orientation for the multi-element airfoil system.

airfoil angles it can achieve. Subsequently, these parameters are subjected to multiple machine learning (ML) and deep learning (DL) models, aiming to predict the coefficients of lift and drag for every conceivable combination of angle and velocity within the multi-element airfoil system. Once coefficient for all possible combinations of angles, velocity is achieved. The desired coefficients of lift and drag are determined based on scenario requirements or specific metrics such as maximizing lift or minimizing drag. The reverse tracking process is then employed to deduce the optimal airfoil orientation (angles of multi-element airfoils and velocity) that fulfills these requirements (finalized Cl, Cd based on specific requirements/metrics), facilitating the projection of airfoils at corresponding angles. This approach serves to optimize and enhance efficiency in comparison to static aerodynamic systems. This application has the potential to significantly enhance the performance of high-speed vehicles/aircrafts and may be of interest to researchers and engineers involved in aerodynamics. Our work demonstrates superior performance compared to existing ML and deep learning algorithms. Notably, our approach also exhibits faster computational speeds compared to conventional CFD simulations, offering a compelling alternative for analyzing Cl and Cd. Our approach will foster further research and advancements in this field.

V. CONCLUSION

In this paper, we developed an automated script for CFD analysis of multi-element airfoils, predicting aerodynamic coefficients across various angles and velocities. This dataset was used to train multiple machine learning and deep learning architectures, simulating configurations with and without velocity interactions. Our comparisons show that deep learning models generally outperformed traditional machine learning algorithms, with model M_4's sensitivity to velocity interaction proving critical for accurate predictions. A comprehensive statistical analysis of prediction accuracy is provided in Sec. III. Notably, computational tasks that typically take 15–20 min with conventional CFD simulations can now be completed in just 1–6 ms using ML and DL algorithms. This advancement paves the way for practical applications in real-time optimization of airfoil orientations and angle configurations to achieve desired aerodynamic coefficients. Our research lays the groundwork for further exploration of machine learning and deep learning techniques in the analysis of multi-element airfoils.

VI. LIMITATIONS AND FUTURE WORK

One area for future enhancement lies in expanding the scope of the dataset used for training and evaluation. In this study, we focused on a three-element airfoil system composed of Eppler 423 airfoils, and the models demonstrated strong performance within this configuration. However, to further enhance the model's robustness and versatility, we plan to broaden the dataset by incorporating additional airfoil types and varying the number of elements. This expansion will allow the model to generalize more effectively across a wider range of multi-element airfoil systems, enhancing its adaptability to even more diverse and complex aerodynamic scenarios. In addition, integrating physics-informed machine learning (PIML) methods, such as physics-informed neural networks (PINNs), could further enhance our model by embedding fluid dynamics equations, improving its accuracy and reliability for predicting aerodynamic behavior across a broader range of conditions.

AUTHOR DECLARATIONS

Conflict of Interest

The authors have no conflicts to disclose.

Author Contributions

Kartikey Vishnu: Conceptualization (equal); Data curation (equal); Formal analysis (equal); Methodology (equal); Software (equal); Supervision (equal); Validation (equal); Visualization (equal); Writing – original draft (equal); Writing – review & editing (equal). **Devdoot Chatterjee:** Conceptualization (equal); Data curation (equal); Formal analysis (equal); Methodology (equal); Software (equal); Supervision (equal); Validation (equal); Visualization (equal); Writing – original draft (equal); Writing – review & editing (equal). **Anurag Goel:** Supervision

25 November 2024 04:46:08

Published under an exclusive license by AIP Publishing

(equal); Writing – review & editing (equal). **Rajeev Kumar:** Supervision (equal); Writing – review & editing (equal).

DATA AVAILABILITY

The data that support the findings of this study are available from the corresponding author upon reasonable request.

REFERENCES

[1]A. Gabbasa, B. Jawad, L. Liu, and S. Arslan, "Numerical study of the aerodynamic characteristics of a multi-element airfoil NACA 23012," SAE Int. J. Aerosp. **6**, 8–16 (2013).

[2]E. Benini, R. Ponza, and A. Massaro, "High-lift multi-element airfoil shape and setting optimization using multi-objective evolutionary algorithms," J. Aircr. **48**, 683–696 (2011).

[3]M. Drela, "Design and optimization method for multi-element airfoils," AIAA Paper No. 93-969, 1993.

[4]W. Valarezo, C. Dominik, R. Mcghee, W. Goodman, and K. Paschal, "Multi-element airfoil optimization for maximum lift at high Reynolds numbers," AIAA Paper No. 91-3332, 1991.

[5]Q. Qu, B. Ju, L. Huang, P. Liu, and R. K. Agarwal, "Flow physics of a multi-element airfoil in ground effect," AIAA Paper No. 2016-0856, 2016.

[6]X. Qin, P. Liu, and Q. Qu, "Aerodynamics of a multi-element airfoil near ground," Tinshhua Sci. Technol. **14**, 94–99 (2009).

[7]O. Eisele and G. Pechlivanoglou, "Single and multi-element airfoil performance simulation study and wind tunnel validation," in *Wind Energy - Impact of Turbulence*, edited by M. Hölling, J. Peinke, and S. Ivanell (Springer, 2014), pp. 17–22.

[8]R. Satti, Y. Li, R. Shock, and S. Noelting, "Unsteady flow analysis of a multi-element airfoil using lattice Boltzmann method," AIAA J. **50**, 1805–1816 (2012).

[9]D. Drikakis, P. Tsoutsanis, and A. F. Antoniadis, "Numerical accuracy in RANS computations of high-lift multi-element airfoil and aircraft configurations," AIAA Paper No. 2015-0317, 2015.

[10]H. Nakayama, H.-J. Kim, K. Matsushima, K. Nakahashi, and K. Takenaka, "Aerodynamic optimization of multi-element airfoil," AIAA Paper No. 2006-1051, 2006.

[11]S. Gupta, R. Naveen, B. V. Prathik, and S. Spurthy, "CFD simulation of turbulent flow around multi-element airfoil," AIP Conf. Proc. **2204**, 030008 (2020).

[12]S. Narsipur, B. Pomeroy, and M. Selig, "CFD analysis of multielement airfoils for wind turbines," AIAA Paper No. 2012-2781, 2012.

[13]S. Klausmeyer, "Comparative results from a CFD challenge over a 2D three-element high-lift airfoil," Report No. NASA-TM-112858, 1997.

[14]H. Khormi and S. Alfifi, "Multi-element airfoil analysis for NACA 0012 using computational fluid dynamics," AIAA Paper No. 2022-1528, 2022.

[15]H. Bolandi, X. Li, T. Salem, V. N. Boddeti, and N. Lajnef, "Deep learning paradigm for prediction of stress distribution in damaged structural components with stress concentrations," Adv. Eng. Software **173**, 103240 (2022).

[16]B. Shilpa and V. Leela, "An artificial intelligence model for heat and mass transfer in an inclined cylindrical annulus with heat generation/absorption and chemical reaction," Int. Commun. Heat Mass Transfer **147**, 106956 (2023).

[17]B. Shilpa, V. Leela, I. A. Badruddin, S. Kamangar, M. N. Bashir, and M. M. Ali, "Integrated neural network based simulation of thermo solutal radiative double-diffusive convection of ternary hybrid nanofluid flow in an inclined annulus with thermophoretic particle deposition," Case Stud. Therm. Eng. **62**, 105158 (2024).

[18]V. L. B. Shilpa and M. D. Alsulami, "Artificial neural network approach for MHD mixed convection and entropy generation in a vertical annulus with time periodic thermal boundary conditions in the presence of radial and induced magnetic field," Numer. Heat Transfer, Part B **85**, 1072–1098 (2024).

[19]H. Moin, H. Zeeshan Iqbal Khan, S. Mobeen, and J. Riaz, "Airfoil's aerodynamic coefficients prediction using artificial neural network," in 19th International Bhurban Conference on Applied Sciences and Technology (IBCAST) (2022).

[20]M. Santos, B. Mattos, and R. Girardi, "Aerodynamic coefficient prediction of airfoils using neural networks," AIAA Paper No. 2008-887, 2008.

[21]R. Wallach, B. Mattos, R. Girardi, and M. Curvo, "Aerodynamic coefficient prediction of transport aircraft using neural network," AIAA Paper No. 2006-658, 2006.

[22]L. Wang, H. Zhang, C. Wang, J. Tao, X. Lan, G. Sun, and J. Feng, "A review of intelligent airfoil aerodynamic optimization methods based on data-driven advanced models," Mathematics **12**, 1417 (2024).

[23]G. Tao, C. Fan, W. Wang, W. Guo, and J. Cui, "Multi-fidelity deep learning for aerodynamic shape optimization using convolutional neural network," Phys. Fluids **36**, 056116 (2024).

[24]R. Eppler, "Airfoil data," in *Airfoil Design and Data* (Springer, Berlin, Heidelberg, 1990), pp. 163–512.

[25]S. McBeath, *Competition Car Aerodynamics* (Haynes Pub., 2006).

[26]K. Koay and W. C. Tan, "Computational fluid dynamics study for aerofoil," in Second National Conference in Mechanical Engineering for Research and Postgraduate Studies (2010).

[27]J. Katz, *Race Car Aerodynamics* (Robert Bentley, 1995).

[28]J. Ferziger and M. Peric, *Computational Methods for Fluid Dynamics* (Springer, 2002), Vol. 3.

[29]M. Darbandi, M. Zakyani, and G. Schneider, "Evaluation of different k-omega and k-epsilon turbulence models in a new curvilinear formulation," AIAA Paper No. 2005-5101, 2005.

[30]T. S. Phillips and C. J. Roy, "Richardson extrapolation-based discretization uncertainty estimation for computational fluid dynamics," J. Fluids Eng. **136**, 121401 (2014).

[31]H. Drucker, C. J. C. Burges, L. Kaufman, A. Smola, and V. Vapnik, "Support vector regression machines," in *Advances in* Neural Information Processing Systems 9, edited by M. Mozer, M. Jordan, and T. Petsche (1996).

[32]L. Breiman, "Random forests," Mach. Learn. **45**, 5–32 (2001).

[33]J. H. Friedman, "Greedy function approximation: A gradient boosting machine," Ann. Stat. **29**, 1189–1232 (2001).

[34]Y. Freund and R. E. Schapire, "A decision-theoretic generalization of on-line learning and an application to boosting," J. Comput. Syst. Sci. **55**, 119–139 (1997).

[35]T. Chen and C. Guestrin, "XGBoost: A scalable tree boosting system," arXiv:1603.02754 (2016).

[36]W. S. McCulloch and W. Pitts, "A logical calculus of the ideas immanent in nervous activity," Bull. Math. Biophys. **5**, 115–133 (1943).

[37]Y. Lecun, B. Boser, J. Denker, D. Henderson, R. Howard, W. Hubbard, and L. Jackel, "Handwritten digit recognition with a back-propagation network," in Advances in Neural Information Processing Systems (NIPS 1989), Denver, CO, edited by D. Touretzky (1990), Vol. 2.

[38]D. P. Kingma and J. Ba, "Adam: A method for stochastic optimization," arXiv:1412.6980 (2017).

[39]A. Kasman, A. Zikri, F. Fariduzzaman, and W. Srigutomo, "Convolutional neural networks-based for predicting aerodynamic coefficient of airfoils at ultra-low Reynolds number," JOIV: Int. J. Inf. Visualization **8**, 309–317 (2024).

[40]K. Zhu, X. Liu, and F. Cao, "Prediction of lift and drag coefficients for aircrafts based on CNN-ATT," in *China Automation Congress* (IEEE, 2023), pp. 792–798.

25 November 2024 04:46:08

Published under an exclusive license by AIP Publishing

Journal of Polymers and the Environment
https://doi.org/10.1007/s10924-024-03449-5

ORIGINAL PAPER

Degradable pH-Sensitive Calcium-Crosslinked Tragacanth Gum/β-Cyclodextrin/Sodium Alginate Hydrogel Microspheres Prepared via Ionotropic Gelation Technique for Hydrophobic Drug Delivery

Priyanka Meena[1] · Poonam Singh[1] · Sudhir G. Warkar[1]

Accepted: 11 November 2024
© The Author(s), under exclusive licence to Springer Science+Business Media, LLC, part of Springer Nature 2024

Abstract
Sodium alginate (SA) hydrogel microspheres are attracting interest in biomedical applications due to their easy degradation and non-toxic nature. However, their high swelling capacity and limited loading efficiency for hydrophobic drugs hinder their application in controlled drug release. The objective of the work is to develop smart vehicles that show effective loading and controlled release of hydrophobic drug. In this study, a series of tragacanth gum/β-cyclodextrin/sodium alginate (TG/β-CD/SA) hydrogel microspheres were designed via the ionotropic gelation method for delivery of hydrophobic drug aspirin. The effect of variation in TG, SA, and β-CD concentration on hydrogel microspheres swelling (%) was examined. The hydrogel microspheres were analyzed using Powder X-ray Diffraction (PXRD), Attenuated Total Reflection-Fourier Transform Infrared spectroscopy (ATR-FTIR), and Scanning Electron Microscopy (SEM) techniques. ATR-FTIR confirmed the successful synthesis of crosslinked TG/β-CD/SA hydrogel microspheres. PXRD showed that the microspheres are amorphous and that the drug is uniformly dispersed within the hydrogel. SEM revealed that the polymeric network has a porous and spherical surface morphology. The drug loading (%), sol–gel fraction (%), degradation (%), and rheological studies were investigated. The in vitro analysis shows a controlled release pattern at pH 1.2 and 7.4 in the TG/β-CD/SA hydrogel. The rheological analysis revealed that the elastic nature is dominant over the viscous one (G' > G") in synthesized TG/β-CD/SA hydrogel microspheres. The cytotoxicity evaluations conducted on the HCT-116 cell line indicate the excellent biocompatibility (87.9%) of the hydrogel. The degradation profile of the hydrogel microsphere in pH 7.4 demonstrates complete degradation (100%). Hence, the TG/β-CD/SA hydrogel microsphere reflects its potential as a non-toxic, degradable, and pH-dependent drug delivery system.

✉ Poonam Singh
poonam@dtu.ac.in

✉ Sudhir G. Warkar
sudhirwarkar@gmail.com

[1] Delhi Technological University, New Delhi, India

Published online: 26 November 2024

Graphical abstract

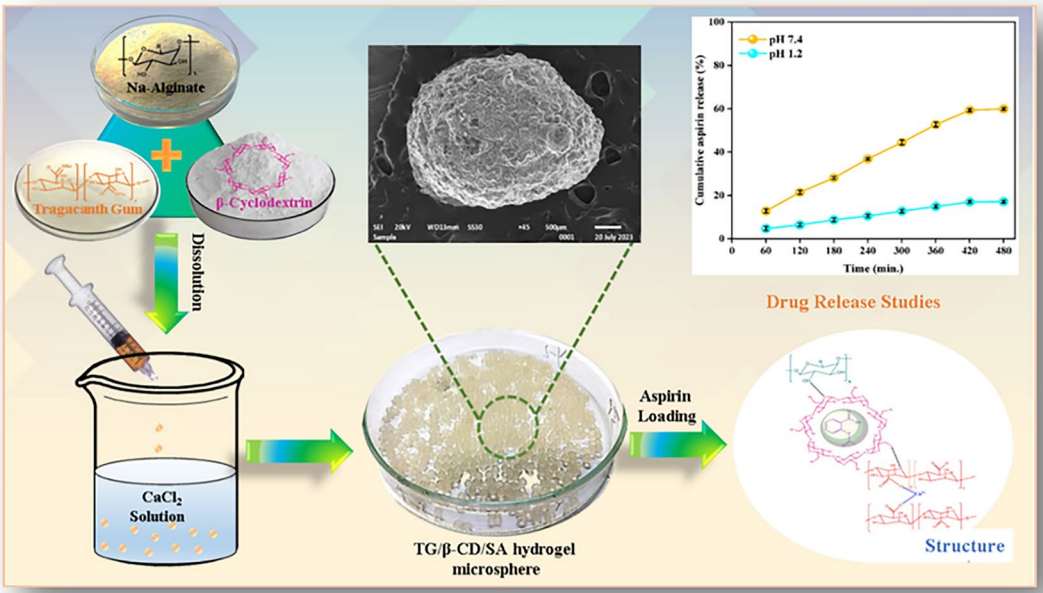

Keywords Biopolymer · Controlled drug release · Degradation · Microspheres · Rheology

Introduction

In recent years, hydrogels have become a versatile candidate in drug delivery due to their vast advantages, i.e., controlled drug delivery, biocompatibility, and ease of administration [1]. These hydrogels are comprised of a crosslinked network of hydrophilic polymers that possess the capability to absorb large amounts of bio-fluids [2]. The hydrogel structure can be tailored to respond to external stimuli, such as pH, light, temperature, magnetic field, etc., allowing the drug to be released at targeted sites within the human body [3].

Nowadays, extensive research has been directed toward the formulation of a controlled oral drug delivery system using hydrogel microspheres [6]. Hydrogel microspheres are sphere-shaped, with sizes ranging from 1 to 1000 µm, and offer several benefits, i.e., adjustable shape, high surface area, drug loading efficiency, biocompatibility, and structure modification. These features make microspheres promising candidates for biomedical engineering [4, 5].

For drug delivery, one can make use of hydrogel, which can be based on natural or synthetic, or semi-synthetic polymers. Several synthetic polymer-based hydrogels exhibit toxicity, poor biocompatibility, and low biodegradability [2]. However, hydrogel materials based on biopolymers like sodium alginate [6], β-cyclodextrin [7], chitosan [8] etc., are naturally occurring, non-toxic, and biodegradable [9]. These features make them better alternatives over synthetic or semi-synthetic hydrogel, as their excellent biodegradability lowers the risk of adverse effects after hydrogel administration and enhances patient safety.

Sodium alginate (SA) is a biopolymer found in the cell walls of various classes of brown algae [10–12]. SA comprises repetitive units of two monosaccharides: D-mannuronic acid and L-guluronic acid. The physical crosslinking technique (ionotropic gelation) was commonly used for the preparation of alginate-based hydrogel [13–16]. The ionotropic gelation method involves the crosslinking of polyelectrolytes (alginate, pectin, etc.) and oppositely charged ions (Ca^{2+}, Mg^{2+}, etc.). An advantage of this method is its preference for the utilization of natural, biocompatible, and biodegradable polymers. Moreover, opting for physical crosslinkers over chemical ones such as glutaraldehyde, eliminates potential toxicity and unwanted effects [17]. However, SA stands out as an excellent biopolymer for drug delivery due to its non-toxic, pH-sensitive, and biodegradable nature. It possesses limitations such as low mechanical strength, leading to burst drug release. To address this issue, our study explored the blend of SA with β-cyclodextrin and another biopolymer tragacanth gum. Tragacanth gum (TG) is a highly branched biopolymer obtained from the sap of the Astragalus plant [18]. TG has gained attention as a promising material in drug delivery due to its excellent

hydrophilicity, biocompatibility, biodegradability, non-toxicity, and cost-effectiveness [19].

β-cyclodextrin is a cyclic oligosaccharide composed of seven glucose units joined together through α-1,4-glycosidic linkage. It has a truncated cone-like structure with a hydrophobic inner cavity and a hydrophilic exterior [7]. The host–guest interaction occurs between the hydrophobic cavity of the host β-CD and the guest molecule (drug). This interaction enables β-CD to increase the loading of hydrophobic drugs such as aspirin as well as control and prolong their release [20]. Aspirin, also called acetylsalicylic acid, is a non-steroidal anti-inflammatory drug (NSAID) mainly utilized to treat pain, arthritis, and fever and decrease heart attacks and stroke risk [21, 22]. Due to its shorter half-life, frequent dosing is required, which ultimately leads to several side effects [10, 23]. Moreover, available research on aspirin often lacks targeted delivery, leading to serious health issues like gastric ulcers, stomach pain, vomiting, etc. For instance, Sethi et al. fabricated Xanthan Gum/starch/poly (acrylic acid) hydrogel for the delivery of aspirin. However, the result demonstrated almost 50% drug was released at pH 1.2, this non-targeted delivery in the stomach can cause gastric irritation and other problems [24]. Therefore, our study aims to solve this problem by fabricating a hydrogel microsphere-based pH-dependent targeted delivery system.

Moreover, to the best of our knowledge, this is the first time TG has been combined with β-CD and SA to develop a novel hydrogel microsphere specifically designed for the release of aspirin drug. Hence, to fill this research gap, in this current study, attempts have been made toward the fabrication of novel hydrogel microspheres based on TG, SA, and β-CD for the controlled release of aspirin using the ionotropic gelation technique. The synthesized microspheres were characterized using ATR-FTIR, PXRD, and SEM techniques. The swelling behavior of all TG-based microspheres was examined at pH values of 1.2 and 7.4. The impact of β-CD on aspirin loading capacity within the microsphere was also investigated and found to be more efficient in TG/β-CD/SA compared to TG/SA microspheres. A sol–gel fraction, degradation, and cytotoxicity analysis was conducted for the hydrogel microspheres. Furthermore, the drug release mechanism was studied by employing mathematical release models such as Hixson-Crowell, Korsmeyer-Peppas, First-Order, Zero-Order, and Higuchi.

Table 1 Different formulations of TG-based hydrogels with required reagent amounts

Sample Code	TG (g)	SA (g)	β-CD (g)
Y-1	0.4	1.0	00
Y-2	0.1	1.0	0.06
Y-3	0.2	1.0	0.06
Y-4	0.3	1.0	0.06
Y-5	0.4	1.0	0.06
Y-6	0.4	0.7	0.06
Y-7	0.4	0.8	0.06
Y-8	0.4	0.9	0.06
Y-9	0.4	1.0	0.03
Y-10	0.4	1.0	0.04
Y-11	0.4	1.0	0.05

Materials and Methods

Materials

β-Cyclodextrin (MW = 1134.98 g/mol, CDH, New Delhi, India), Calcium chloride (MW = 110.98 g/mol, Fischer Scientific, Mumbai, India), Sodium alginate (MW = 1.65×10^5 g/mol, Qualikems Lifesciences Pvt. Ltd., Gujarat, India), Tragacanth Gum (MW = 8.4×10^5 g/mol, CDH, New Delhi, India), phosphate buffer saline pH 7.4, hydrochloric acid pH 1.2 buffer and absolute ethanol (Thermo Fisher Scientific, Mumbai, India) were used as purchased.

Synthesis of TG/SA and TG/β-CD/SA Hydrogel

The TG/SA microsphere (Y-1) and various series of TG/β-CD/SA hydrogels (Y-2 to Y-11) with varying amounts of the SA (0.7–1 g), TG (0.1–0.4 g) and β-CD (0.03–0.06 g) were synthesized through an ionotropic-gelation technique using $CaCl_2$ as a crosslinker, as detailed in Table 1. For the synthesis of the TG/SA hydrogel (Y-1), firstly, a predetermined amount of TG and SA were dissolved in distilled water with continuous stirring for 1 h. The solution of TG and SA was then added dropwise, using a syringe, in an aqueous solution containing $CaCl_2$ (2% w/v). The resulting solution was left undisturbed overnight, after which the obtained microspheres were filtered and oven-dried at 40 °C for 48 h [16]. For fabricating a series of TG/β-CD/SA hydrogel microspheres (Y-2 to Y-11), the desired amount of β-CD was incorporated during the addition of TG and SA, as depicted in Fig. 1. The remaining steps followed the same protocol as outlined above [16].

Characterization

PXRD analysis was done using a Bruker D8 Discover Diffractometer with Cu Kα radiation (λ = 1.5418 Å) in the 2θ from 5–70°. ATR-FTIR spectra were recorded using a Nicolet iS50 FTIR Tri-detector spectrometer in the wavenumber range of 450–4000 cm^{-1}. The surface morphology was analysed through SEM (Model: JEOL Japan Mode: JSM 6610LV).

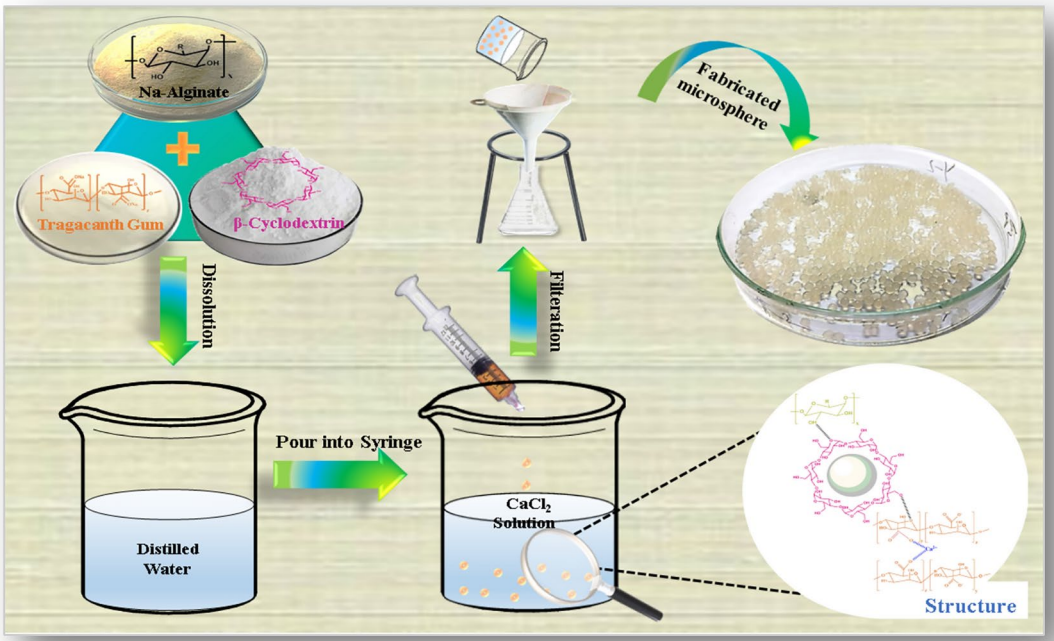

Fig. 1 Illustration of the TG/β-CD/SA hydrogel microsphere synthesis

Swelling Studies

Swelling experiments were performed for all fabricated microspheres in simulated gastric fluid (pH 1.2) and intestinal fluid (pH 7.4). A 0.1 g (W_{DH}) of pre-dried microspheres was dipped in the respective buffer solution. After a predetermined period (1 h), the microspheres were taken out from the buffer solutions, dried with filter paper, and then weighed (W_{SH}) again. This process was repeated constantly for 8 h, and the complete study was implemented in triplicate [1]. The swelling (%) was determined using the equation given below [25].

$$\text{Swelling } (\%) = \frac{W_{SH} - W_{DH}}{W_{DH}} \times 100 \quad (1)$$

Moreover, W_{SH} is replaced with W_{EH} for the calculation of equilibrium swelling, which corresponds to the weight of the hydrogel at equilibrium (maximum swelling).

Sol–Gel Analysis

For calculating the non-crosslinked portion (sol part) and crosslinked portion (gel part) for the formulated microspheres, a sol–gel analysis was performed. Initially, the dried microsphere was weighed (W_i) and swelled in distilled water for 8 h. Afterward, the swollen hydrogel microsphere was dried at 40 °C in the oven till a stable weight (W_e) was achieved [26]. The complete analysis was executed three times, and the given equation was used to analyze the sol–gel fraction [27]:

$$\text{Sol Fraction } (\%) = \frac{W_i - W_e}{W_e} \times 100 \quad (2)$$

$$\text{Gel fraction } (\%) = 100 - \text{ Sol fraction} \quad (3)$$

Rheological Analysis

Rheological measurements were performed using a stress-controlled Anton Paar Modular Compact Rheometer 302 (MCR) equipped with parallel plates of 25 mm diameter and 1 mm gap. The mechanical spectra were recorded over a frequency range of 0.01–100 rad/s at a temperature of 25 °C. The storage (G') and loss (G") moduli, along with the complex viscosity, were determined as functions of frequency.

Aspirin Loading and Entrapment Efficiency

Among all the formulations synthesized, the hydrogel microsphere (Y-5) offers a higher degree of swelling and, therefore, the formulation Y-5 is considered suitable for drug loading. The drug loading behavior of microspheres with β-CD (TG/β-CD/SA) and without β-CD (TG/SA) was compared. The drug loading was carried out through the

swelling equilibrium method. The pre-determined amount of hydrogel microspheres (W_{UH}) was placed into a 100 ml drug solution comprised of a mixture of ethanol and pH 7.4 buffer solution (40:60), containing a specific amount (W_D) of aspirin and left for 8 h. Thereafter, a hydrogel microsphere was taken out and oven-dried at 40ºC, and weight (W_{LH}) was noted. The given equations were employed to calculate the amount of drug loaded, drug loading (DL%) and drug entrapment efficiency (DEE%) [16].

$$\text{Amount of drug loaded} = W_{LH-}W_{UH} \tag{4}$$

$$\text{DL } (\%) = \frac{W_{LH-}W_{UH}}{W_{UH}} \times 100 \tag{5}$$

$$\text{DEE } (\%) = \frac{W_{LH-}W_{UH}}{W_D} \times 100 \tag{6}$$

In Vitro Aspirin Release Studies

To examine the aspirin release from the hydrogel microspheres, a specific quantity of the aspirin-loaded microspheres was dipped in 100 mL buffer solutions of pH 7.4 and 1.2. These solutions were then kept within an orbital incubator shaker at 37 °C. To ensure the volume of the medium remained constant throughout the measurements, 3 mL of the released medium was extracted every 1 h up to 8 h and replaced with 3 mL fresh buffer solutions. The withdrawn solution was diluted with ethanol and the quantification of the released drug in the medium was accomplished using a UV–visible spectrophotometer (Model: Cary 300 UV–Vis), measuring absorbance at λ_{max} 228 nm for pH 7.4 and λ_{max} 226 nm for pH 1.2. The drug amount was found using the calibration curve of aspirin. For measuring drug release in pH 7.4 buffer, the 1:1 (v/v%) mixture of ethanol & pH 7.4 buffer was used as the blank solution, while for drug release measurement in pH 1.2 buffer, the ethanol & pH 1.2 buffer mixture served as the blank solution. Moreover, to verify the stability of the blank solutions, the UV–vis spectra of both fresh blank solution and blank solution kept in incubator at 37 °C for 8 h was also recorded, simulating the conditions of the drug release experiment.

Kinetic Modelling

Various mathematical models (i.e., Hixson-Crowell, Korsmeyer-Peppas, First-Order, Zero-Order, and Higuchi models) were applied to drug release data to gain insights into the drug release mechanism. The regression coefficient (R^2) values were examined corresponding to each model. The model that demonstrated a R^2 value closest to 1 was deemed the best model for describing the release mechanism effectively [1, 28].

Cytotoxicity Analysis

The cytotoxicity of aspirin-loaded TG/β-CD/SA hydrogel microspheres on the HCT 116 human colon cell line, sourced from NCCS Pune, was evaluated via MTT Assay. Cells were seeded at 10,000 cells per well in a 96-well plate and cultured in DMEM medium supplemented with 10% FBS and 1% antibiotic solution at 37 °C with 5% CO_2 for 24 h. Then, cells were exposed to varying concentrations (0.78, 1.56, 3.125, 6.25 µg/ml) of the hydrogel microsphere, while wells without hydrogel serve as control. After further 24-h incubation, MTT Solution was added and incubated for an additional 2 h. Subsequently, the supernatant was discarded, and the cell layer was dissolved in 100 µl of Dimethyl Sulfoxide. Absorbance readings at 540 and 660 nm were taken using an Elisa plate reader (iMark, Biorad, USA) to assess cell viability. Images were also captured under an inverted microscope (Olympus ek2) using a 10 MP Aptima CMOS digital camera (AmScope).

Degradation Studies

Degradation experiments were carried out using a phosphate buffer solution (PBS) with a pH of 7.4 (simulated intestinal fluid) in an orbital incubator shaker (80 rpm) at 37 °C. Initially, the dried hydrogel disc was soaked in PBS until fully swollen and then weighed (W_i). Thereafter, the hydrogel discs were removed every hour, blotted with filter paper, weighed (W_d), and then immersed again in the buffer. The process continued until the discs were completely degraded, and the degradation (%) was calculated using the following equation [29, 30].

$$\text{Degradation } (\%) = \frac{W_i - W_d}{W_i} \times 100 \tag{7}$$

Statistical Analysis

All the experiments were conducted in triplicate (n = 3), and the data are expressed as mean ± standard deviation. All the data were analysed using ANOVA (One-way analysis of variance), and $p < 0.05$ was considered significant for all the experiments.

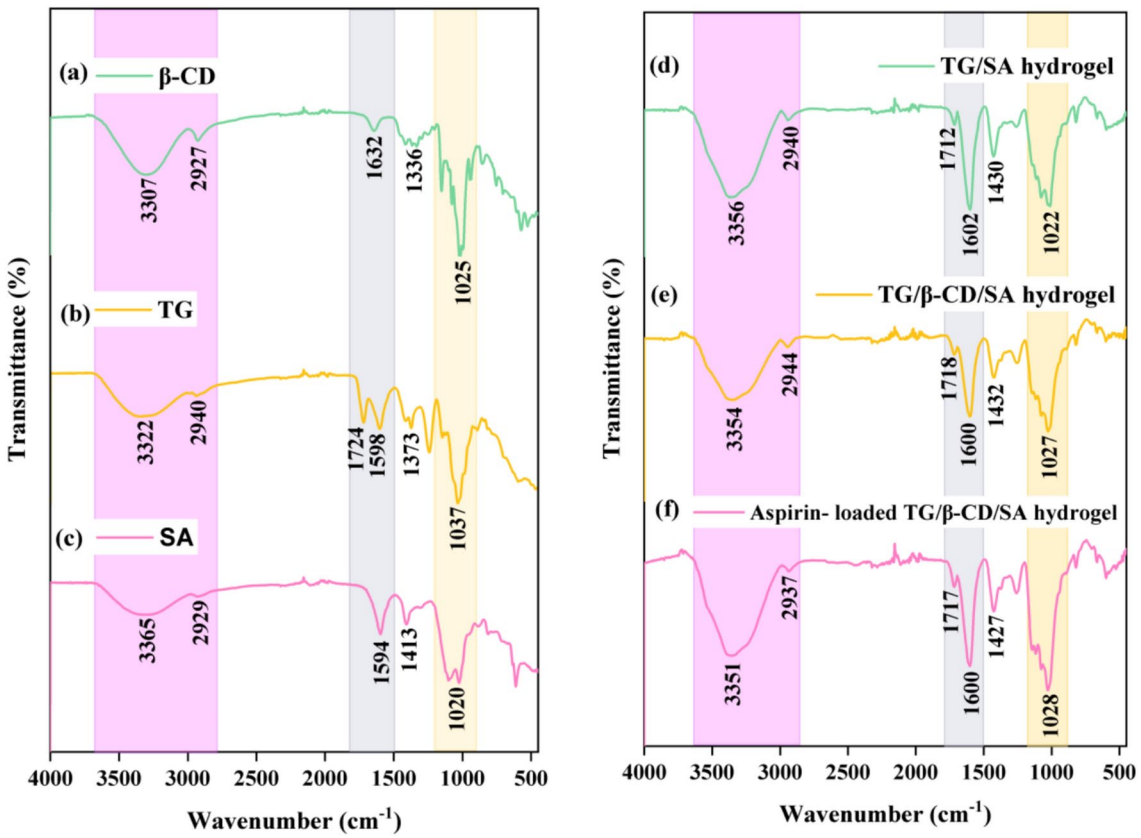

Fig. 2 ATR-FTIR spectrum of β-CD, TG, SA, TG/SA hydrogel microsphere, TG/β-CD/SA hydrogel microsphere, and Aspirin-loaded TG/β-CD/SA hydrogel microsphere

Table 2 ATR-FTIR values of β-CD, TG, SA, TG/SA hydrogel microsphere, TG/β-CD/SA hydrogel microsphere, and Aspirin-loaded TG/β-CD/SA hydrogel microsphere

Functionality	Wavenumber (cm^{-1})						Ref.
	β-CD	TG	SA	TG/SA hydrogel	TG/β-CD/SA hydrogel microsphere	Aspirin-loaded TG/β-CD/SA hydrogel microsphere	
C=O	–	1724	1594	1712	1718	1717	[31], [20]
OH stretching	3307	3322	3365	3356	3354	3351	[31], [33]
COO^- symmetric stretching	1336	1373	1413	1430	1432	1427	[31], [34]
COO^- asymmetric stretching	–	1598	–	1602	1600	1600	[35]
C-H stretching	2927	2940	2929	2940	2944	2937	[9]
C–O–C	1025	1037	1020	1024	1027	1028	[9], [34]
OH bending	1632	–	–	–	–	–	[36]

Result and Discussion

Characterization

The ATR-FTIR spectrum of TG/SA hydrogel (Y-1), TG/β-CD/SA (Y-5) hydrogel, and aspirin-loaded TG/β-CD/SA hydrogel are represented in Fig. 2. The details of the band observed in ATR-FTIR spectra are provided in Table 2. The -OH band at 3365 cm^{-1} of SA shifted to lower wavenumbers of 3356 cm^{-1}, 3354 cm^{-1}, and 3351 cm^{-1} in TG/SA hydrogel, TG/β-CD/SA hydrogel, and aspirin-loaded TG/β-CD/SA hydrogel respectively. This noticeable shift is attributed to the hydrogen bonding among the hydroxyl groups (-OH) of TG and SA with those present on β-CD [31]. This shift

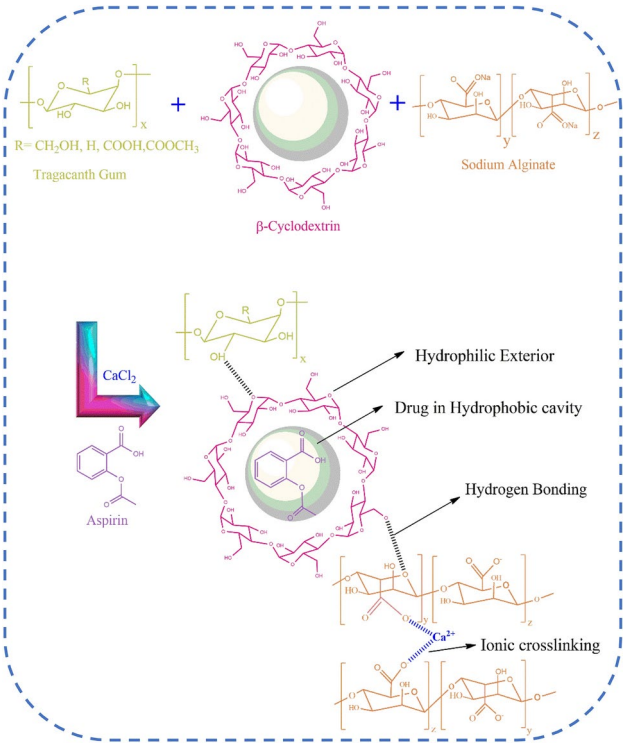

Scheme 1. Mechanism for aspirin-loaded TG/ β-CD/SA hydrogel microsphere

confirmed the occurrence of physical crosslinking (hydrogen bonding) between polymeric chains within the microsphere. Furthermore, the band at 1594 cm^{-1}, due to the presence of the C = O peak of SA, shifted towards higher wavenumbers of 1712 cm^{-1}, 1718 cm^{-1}, and 1717 cm^{-1} in the microspheres. This shift revealed a strong interaction between calcium ions (Ca^{2+}) and the C = O group of SA. The interaction among the C = O group of SA and Ca^{2+}, as well as the H-bonding interaction, results in the development of a hydrogel network [31]. The TG/β-CD/SA hydrogel displayed nearly identical spectrum to the TG/SA hydrogel, primarily because the characteristic peaks (O–H, C-H) of β-CD overlapped with those of TG and SA. Consequently, no discernible new peaks emerged upon the introduction of β-CD. The observed differences were mainly in peak intensity and slight shifts in wave numbers, reflecting the interactions between the β-CD and the existing components.

On comparing FTIR spectra of aspirin-loaded TG/β-CD/SA hydrogel and TG/β-CD/SA hydrogel, the shifting in wavenumber and increase in intensity of –OH, C = O, C-H, COO^- and C–O–C peak confirm the successful loading of drug into the hydrogel matrix [12]. Moreover, the FTIR spectrum of the aspirin loaded TG/β-CD/SA hydrogel and TG/β-CD/SA hydrogel is almost similar. There is no new characteristic peak of drug was observed in the FTIR spectrum of aspirin-loaded TG/β-CD/SA hydrogel microspheres. This confirmed that the aspirin is encapsulated

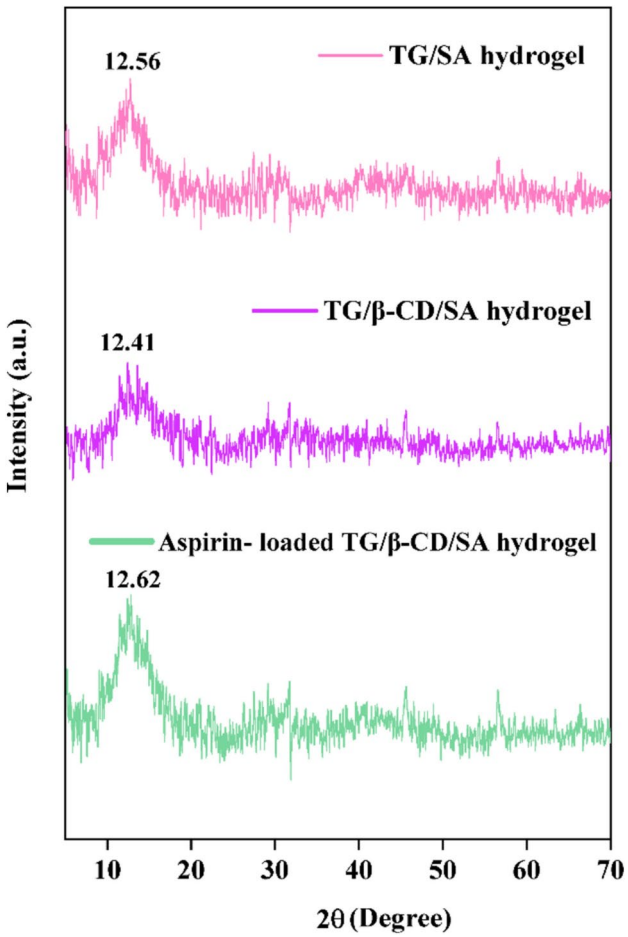

Fig.3 PXRD of TG/SA hydrogel, TG/β-CD/SA hydrogel microsphere, and aspirin-loaded TG/β-CD/SA hydrogel microsphere

within the hydrophobic cavity of β-CD. A similar result was reported by Hao et al. [32], where the FTIR spectrum of curcumin-loaded β-CD/chitosan/αβ-glycerophosphate hydrogel closely resembled that of the β-CD/chitosan/αβ-glycerophosphate hydrogel. The characteristic peaks of curcumin were not observed leading to the conclusion that curcumin was encapsulated within the β-CD cavity and dispersed throughout the hydrogel matrix. Scheme 1 shows the probable mechanism of the aspirin-loaded hydrogel microsphere.

PXRD was carried out to examine the crystalline nature and verify the drug distribution within the hydrogel network, as illustrated in Fig. 3. The broad nature of peak at 2Θ values of 12.56º, 12.41º and 12.62º in the TG/SA (Y-1), TG/β-CD/SA (Y-5) and aspirin-loaded TG/β-CD/SA hydrogel microspheres indicates that the hydrogel microspheres possess an amorphous structure. Furthermore, in the aspirin-loaded TG/β-CD/SA hydrogel, no additional sharp peaks due to the presence of aspirin were observed. This suggested that aspirin was uniformly dispersed within the microsphere [7, 37]. Similar results were reported by Li et al. [10], where

the peaks of aspirin disappeared upon its incorporation into the hydrogel matrix.

The surface morphology of TG/β-CD/SA (Y-5) and aspirin-loaded TG/β-CD/SA hydrogel were observed in Fig. 4. The TG/β-CD/SA hydrogel possesses a rough surface with a spherical and micro-porous structure, highlighting the hydrogel swelling and drug loading efficiency [9]. Furthermore, the SEM image of the aspirin-loaded TG/β-CD/SA microsphere reveals a little smoother, spherical surface with no visible pores. This result indicates that the aspirin has been effectively entrapped within the polymeric matrix, leading to a reduction in the void within the microsphere. Additionally, the diameter of hydrogel microspheres was determined using SEM with Image J software, which was found to be 901 µm for the TG/β-CD/SA hydrogel and 928 µm for the aspirin-loaded TG/β-CD/SA hydrogel. These measurements confirm that the synthesized beads are indeed microspheres. Notably, the larger size of the loaded microsphere implies that the presence of the drug leads to an enlargement in microsphere size, likely due to the surface being covered with aspirin crystals [38].

Swelling Studies

The swelling of the microspheres was found to be highly dependent on the quantities of the TG, SA, and β-CD present in the microspheres, as visualized in Fig. 5. The equilibrium swelling (%) for series of the hydrogels at pH 1.2 and 7.4 are documented in Table 3

Effect of TG, SA, and β-CD on Equilibrium Swelling

The effect of varying the TG (Y-2 to Y-5), SA (Y-6 to Y-8), and β-CD (Y-9 to Y-11) on the equilibrium swelling behaviour of microspheres are shown in Fig. 5a–c, respectively. The equilibrium swelling of microspheres tends to increase ($p < 0.05$), with an increase in the concentration of TG (0.1 g–0.4 g), SA (0.7 g–1 g), and β-CD (0.03 g–0.06 g), reaching maxima at pH 7.4 ($1709.63 \pm 0.92\%$) and pH 1.2 ($158.96 \pm 0.96\%$). This increase is assigned to the hydrophilic nature of the hydrogels since more hydrophilic groups (–OH, COOH) become available with an increase in polymer content [7, 39]. However, this behaviour was observed only to a certain concentration, since a further increase in polymer content results in high viscosity, making stirring tedious and hindering attempts to form microspheres. For all the formulations attempted, a noticeable difference in swelling was observed at pH 7.4 and 1.2. This is related to the deprotonation of the COOH group within TG at pH 7.4. At pH 7.4, electrostatic repulsion occurred between the deprotonated COO^- ions, leading to expansion of the network, hence swelling increases ($p < 0.05$). However, at pH 1.2, the COOH groups of TG bind to the oxygen atom of β-CD through hydrogen bonding interactions, causing the hydrogel to contract and resulting in reduced swelling compared to pH 7.4 [31]. Similar results were observed by Suhail et al. [39], where sodium alginate-co-poly(2-acrylamido-2-methyl propane sulphonic acid) hydrogel demonstrates higher swelling at pH 7.4 compared to pH 1.2. On comparing the swelling behaviour of TG/β-CD/SA (Y-5) with the TG/SA (Y-1) hydrogel, it was evident that the TG/β-CD/SA (Y-5) microsphere exhibits

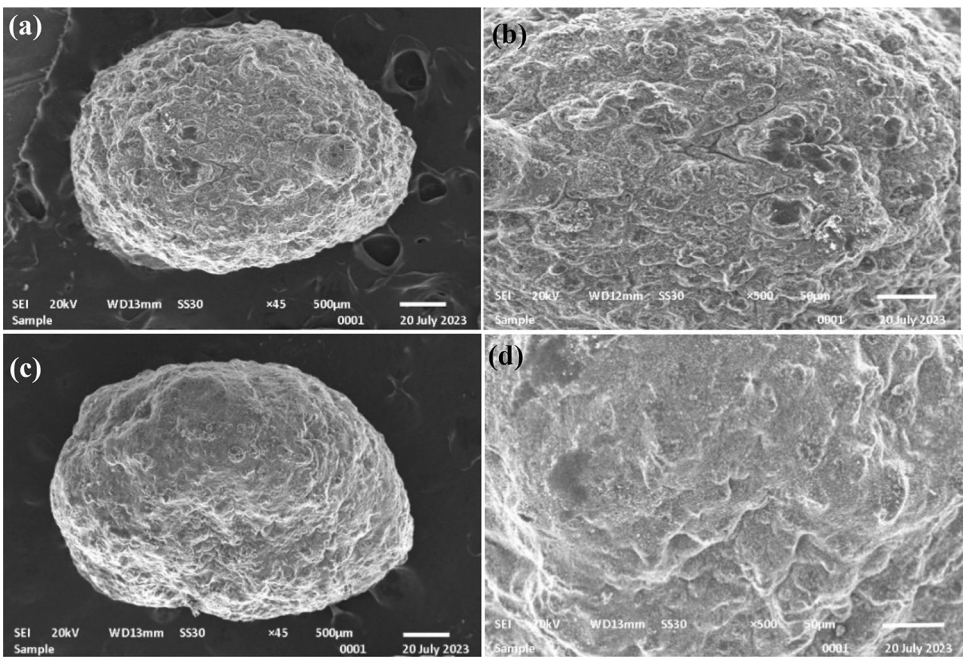

Fig. 4 SEM images of (**a**, **b**) TG/β-CD/SA and (**c**, **d**) Aspirin-loaded TG/β-CD/SA hydrogel microsphere

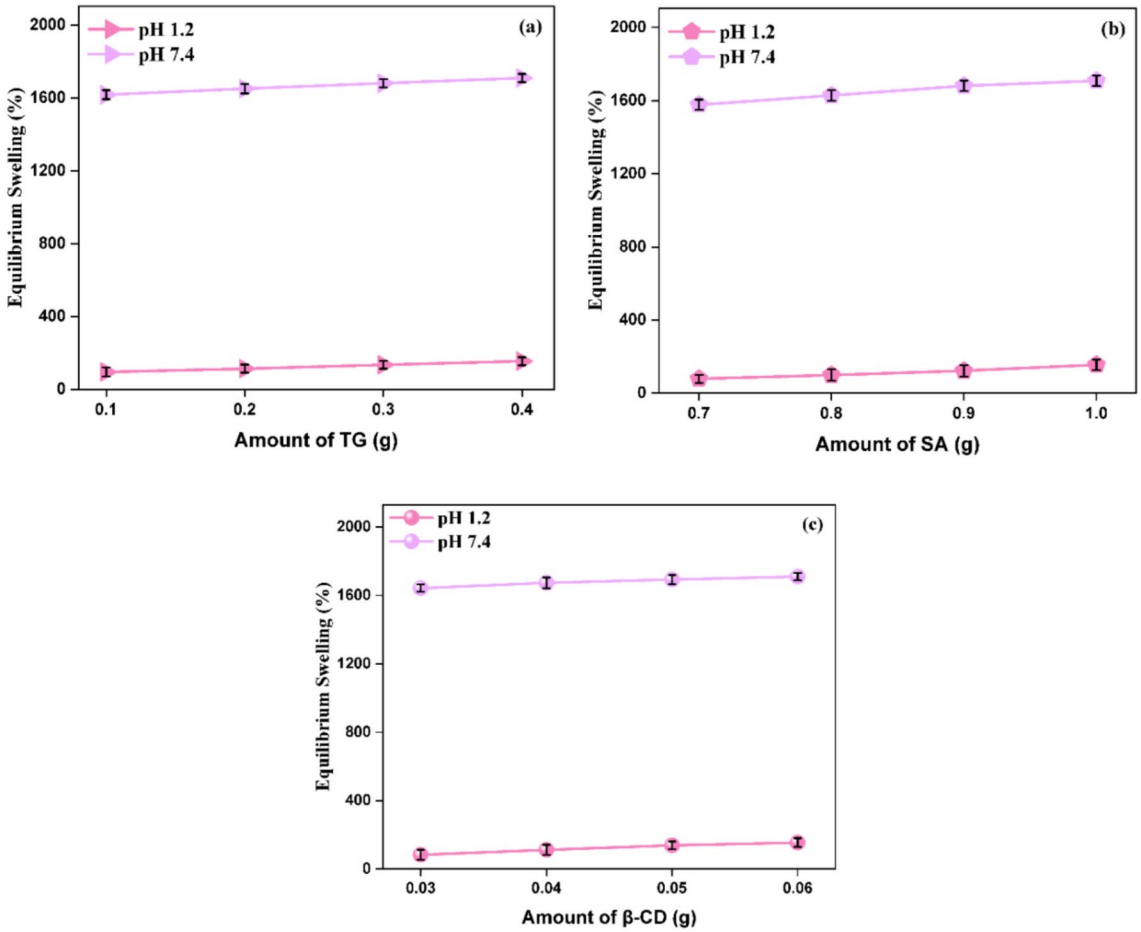

Fig. 5 Effect of the **(a)** TG, **(b)** SA, and **(c)** β-CD on the equilibrium swelling of the hydrogel microspheres

Table 3 Different formulations of TG-based hydrogels with their equilibrium swelling and gel fraction

Sample Code	Equilibrium Swelling (%)		Gel fraction (%)
	pH 1.2	pH 7.4	
Y-1	128.73 ± 0.63	1603.16 ± 0.78	78.52 ± 0.57
Y-2	95.90 ± 0.98	1617.96 ± 0.90	72.12 ± 0.64
Y-3	113.92 ± 0.70	1651.05 ± 0.85	74.34 ± 0.63
Y-4	135.22 ± 0.84	1680.75 ± 0.78	78.25 ± 0.89
Y-5	158.96 ± 0.96	1709.63 ± 0.92	82.67 ± 0.67
Y-6	78.8 ± 0.95	1577.94 ± 0.66	72.44 ± 0.71
Y-7	99.61 ± 0.79	1629.13 ± 0.72	74.48 ± 0.51
Y-8	122.63 ± 0.81	1681.10 ± 0.77	77.85 ± 0.60
Y-9	83.40 ± 0.91	1641.97 ± 0.75	75.06 ± 0.82
Y-10	112.60 ± 0.83	1673.66 ± 0.72	76.73 ± 0.80
Y-11	139.22 ± 0.86	1692.87 ± 0.66	79.85 ± 0.50

The data are expressed as mean ± standard deviation ($p < 0.05$, n = 3)

higher swelling capacity ($p < 0.05$), as depicted in Fig. 6. This pronounced swelling behaviour is ascribed to the introduction of an amphiphilic polymer (β-CD) with hydrophilic moieties (-OH), which enhances the swelling capacity [33]. The TG/β-CD/SA hydrogel microsphere displays a swelling of 1709.63 ± 0.92% and 158.96 ± 0.96% at pH 7.4 and 1.2. Meanwhile, the TG/SA microsphere demonstrates a swelling ratio of 1603.16% and 128.73% at pH 7.4 and 1.2, respectively.

Sol–Gel Analysis

The sol–gel analysis for the prepared microspheres is presented in Fig. 7, with their gel fraction data provided in Table 3. It was noticeable that, as the quantities of TG (Y-2 to Y-5), SA (Y-6 to Y-8), and β-CD (Y-9 to Y-11) increased ($p < 0.05$), there was a considerable increase in the gel fraction as well. This increase in gel fraction is correlated with the presence of a more significant number of free radical-containing polymeric chains, resulting in an increased number of active sites available for cross-linking. Subsequently, the crosslinking density within the microsphere is raised, resulting in an increase in the gel fraction. Moreover, the comparison of gel fractions between the TG/β-CD/SA (Y-5) hydrogel and the TG/β-CD hydrogel microsphere, reveals an increased gel fraction ($p < 0.05$), owing to the addition of β-CD. This increase is primarily associated with the more

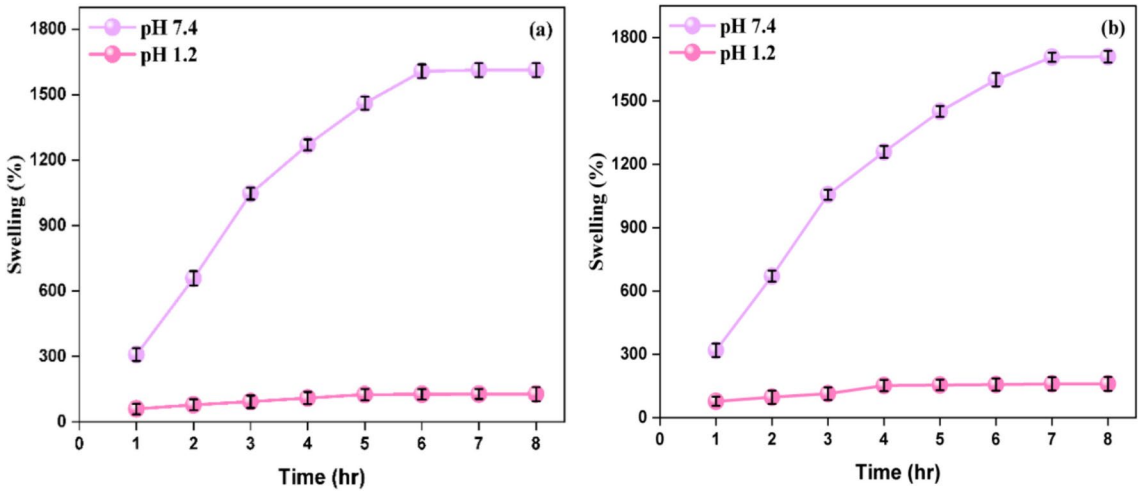

Fig. 6 Swelling analysis of **(a)** TG/SA, and **(b)** TG/β-CD/SA hydrogel microsphere

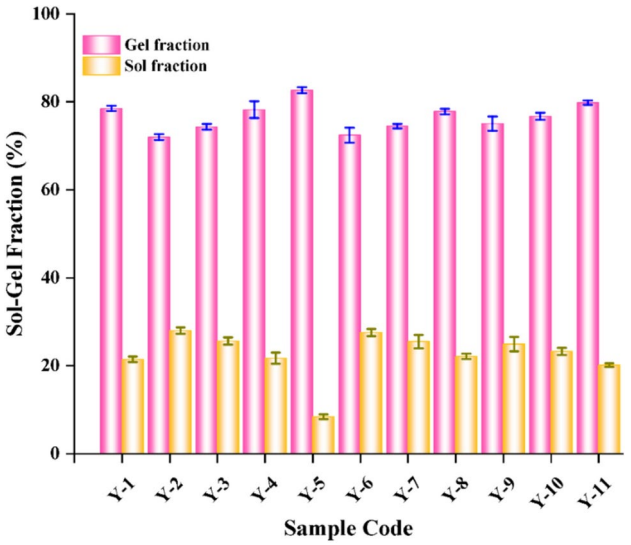

Fig. 7 Sol–Gel analysis of all TG/β-CD/SA hydrogel microspheres and TG/SA hydrogel microspheres

significant number of polymeric chains, which is responsible for an increased cross-linking density within the hydrogel and hence gel fraction [39].

Rheological Analysis

The frequency-dependence of complex viscosity, G' and G" of TG/SA and TG/β-CD/SA hydrogel microspheres are depicted in Fig. 8a and b. The storage modulus (G′) represents the gel's elasticity and its ability to store energy, while the loss modulus (G") reflects the material viscosity, indicating its ability to dissipate energy [40]. Figure 8a demonstrates a decrease in complex viscosity as the angular frequency increases from 0.1 to 100 rad/s, indicating the pseudoplastic behaviour of both hydrogels. The pseudoplastic refers to the process in which the viscosity of a substance decreases as the angular frequency increases. This means that as the hydrogel is subjected to faster rotational speeds (angular frequency), its resistance to flow decreases, resulting in lower viscosity [41]. Furthermore, the complex viscosity is higher in the TG/β-CD/SA hydrogel microsphere compared to the control TG/SA hydrogel microsphere. Consequently, TG/β-CD/SA hydrogels represent a more promising candidate for the slow and controlled release of drug molecules in comparison to TG/SA hydrogels. This observation is also supported by the drug release data as well.

Figure 8b demonstrates that the G' values are higher than G" values, indicating a stronger elastic response of the hydrogels microsphere compared to the viscous one. The predominance of elastic behavior over viscous nature across the frequency range provides evidence of the mechanical rigidity of the hydrogel microspheres [26]. Furthermore, it was observed that with the incorporation of β-CD content, both modulus (G' & G") values increase. The higher G' values were observed in the TG/β-CD/SA hydrogel microsphere compared to the TG/SA hydrogel. This is potentially attributed to the increased crosslinking density upon the incorporation of β-CD in TG/β-CD/SA hydrogel. Moreover, due to this enhanced crosslinking, the resistance of the TG/β-CD/SA hydrogel to deformation increases, hence dissipating more energy, resulting in a higher loss modulus in comparison to TG/SA hydrogel [29]. Therefore, TG/β-CD/SA hydrogels with high (G' & G") values act as a better drug carrier, as evidenced by DL% and DEE% data compared to TG/SA hydrogels.

Aspirin Loading and Entrapment Efficiency

The amount of drug loaded, drug loading percentage (DL%) and drug entrapment efficiency percentage (DEE%) were ascertained for the aspirin-loaded TG/SA microsphere and

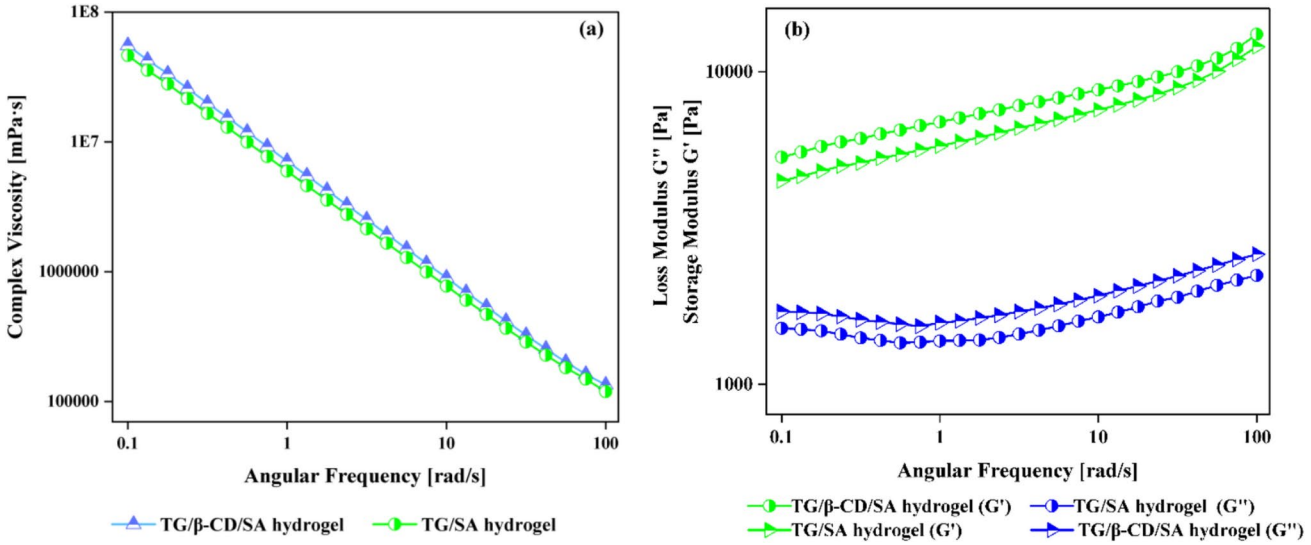

Fig. 8 Plot of (**a**) Complex Viscosity versus Angular Frequency, and (**b**) G' & G" versus Angular Frequency for TG/SA and TG/β-CD/SA hydrogel microspheres

Table 4 Formulations along with their corresponding amount of drug loaded, drug loading (%) and drug entrapment efficiency (%)

Hydrogel microsphere	Amount of drug loaded (mg)	Drug loading (DL%)	Drug entrapment efficiency (DEE%)
Aspirin-loaded TG/SA	27 ± 0.2	16.2 ± 0.66	54 ± 0.55
Aspirin-loaded TG/β-CD/SA	31.5 ± 0.12	19 ± 0.85	63.33 ± 0.49

The data are expressed as mean ± standard deviation ($p < 0.05$, n = 3)

aspirin-loaded TG/β-CD/SA microsphere, as presented in Table 4. Remarkably, aspirin-loaded TG/β-CD/SA hydrogel possesses high amount of drug loaded, DL% and DEE% ($p < 0.05$) values compared to aspirin-loaded TG/SA microsphere. This enhancement can be ascribed to the presence of β-CD, which encapsulates the hydrophobic drug aspirin within its hydrophobic cavity, thereby increasing the loading and entrapment of the aspirin in the TG/β-CD/SA microsphere [20].

In Vitro Aspirin Release Study

The in vitro release analysis was performed for the aspirin-loaded TG/SA microsphere and aspirin-loaded TG/β-CD/SA microsphere. Moreover, the UV–vis spectra of both fresh blank solution and blank solution that had been incubated at 37 °C for 8 h was displayed in Fig. 9. The UV–vis spectra of the fresh blank solution and after 8 h, displayed a straight line with no absorption peaks at the drug's λ_{max}, confirming that the no ingredient from blank solution dissolve and contribute to any additional substances that could interfere with the drug's peak during experiment. Thus, confirming that the absorbance in the aspirin-loaded hydrogel is attributable solely to aspirin.

Notably, as shown in Fig. 10, the aspirin-loaded TG/β-CD/SA microsphere exhibited a lower drug release ($p < 0.05$), when compared to the aspirin-loaded TG/SA microsphere. This slower and controlled release of aspirin from the aspirin-loaded TG/β-CD/SA microsphere can be primarily ascribed to the presence of β-CD, which forms a complex with the aspirin through its hydrophobic cavity and consequently retards the release of aspirin from the microsphere [20]. The maximum aspirin release was observed as 70.9 ± 0.67% and 59.9 ± 0.57% in TG/SA and TG/β-CD/SA microspheres at pH 7.4, respectively, while 23.1 ± 0.74% and 17.1 ± 0.83% in TG/SA and TG/β-CD/SA microspheres at pH 1.2.

In both microspheres, aspirin release was significantly greater at pH 7.4 compared to pH 1.2. This enhancement at pH 7.4 can be attributed to the higher swelling ($p < 0.05$) of the microspheres, as already discussed in the swelling section, which, in turn, increases the diffusion of the drug. However, at pH 1.2, the hydrogel experiences shrinkage, resulting in reduced swelling and consequently slowing down the diffusion of the drug from the microspheres[33, 34]. Similarly, Rehman et al. synthesized sodium alginate hydrogel beads, showing around 99% diclofenac sodium drug release at pH 7.4 in 4 h [42]. However, in our study, the introduction of β-CD resulted in a slow and prolonged drug release (59.9%) for 8 h, thus minimizing the repeated dosage condition. This is attributed to the ability of β-CD to encapsulate the drug within its cavity, leading to prolonged release. Hence, the synthesized TG/β-CD/SA microsphere demonstrates promise for slow and prolonged release of the hydrophobic drug aspirin at pH 7.4.

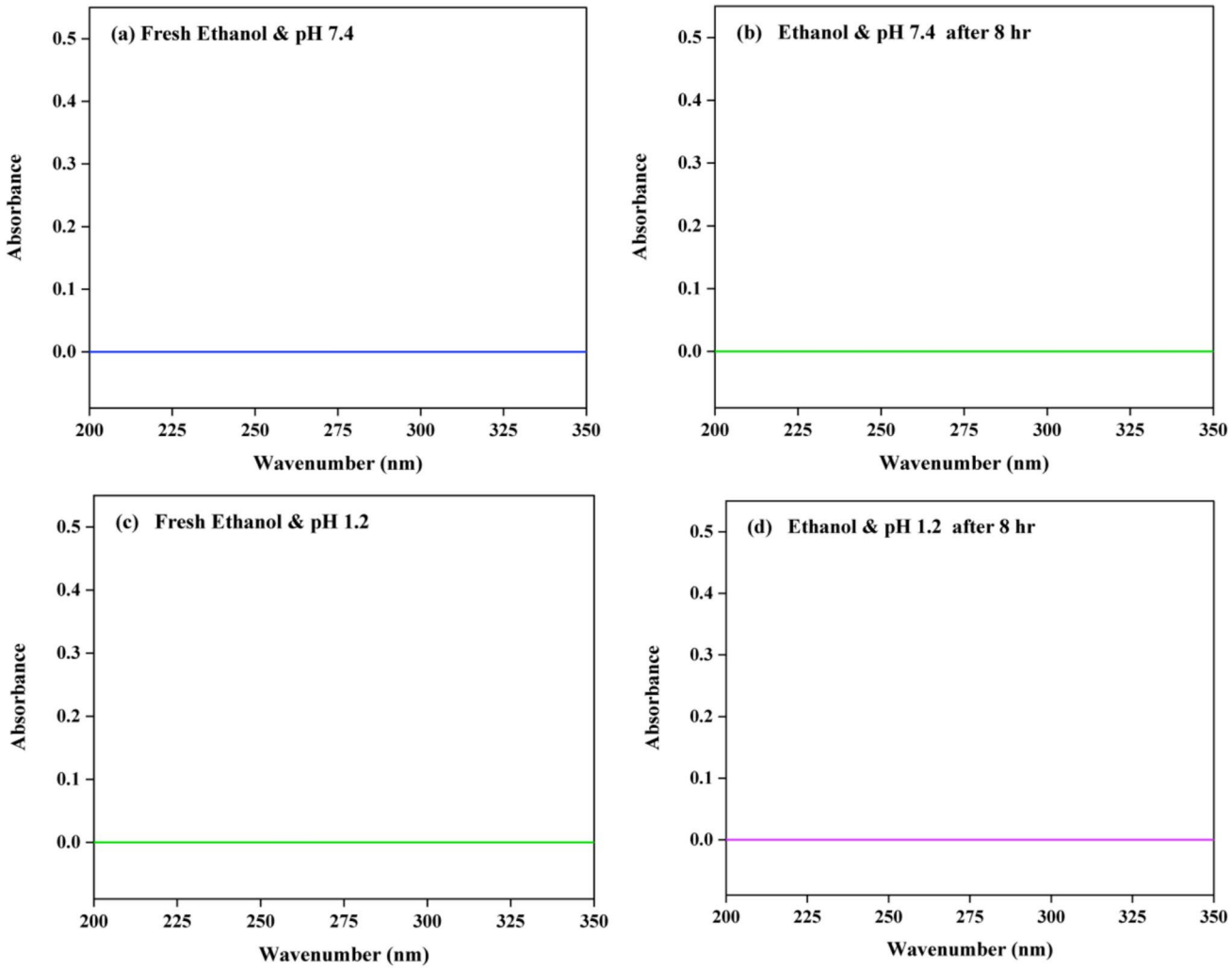

Fig. 9 UV–vis spectra of ethanol & pH 7.4 mixture (**a**) fresh, (**b**) after 8 h and ethanol & pH 1.2 mixture (**c**) fresh, (**d**) after 8 h

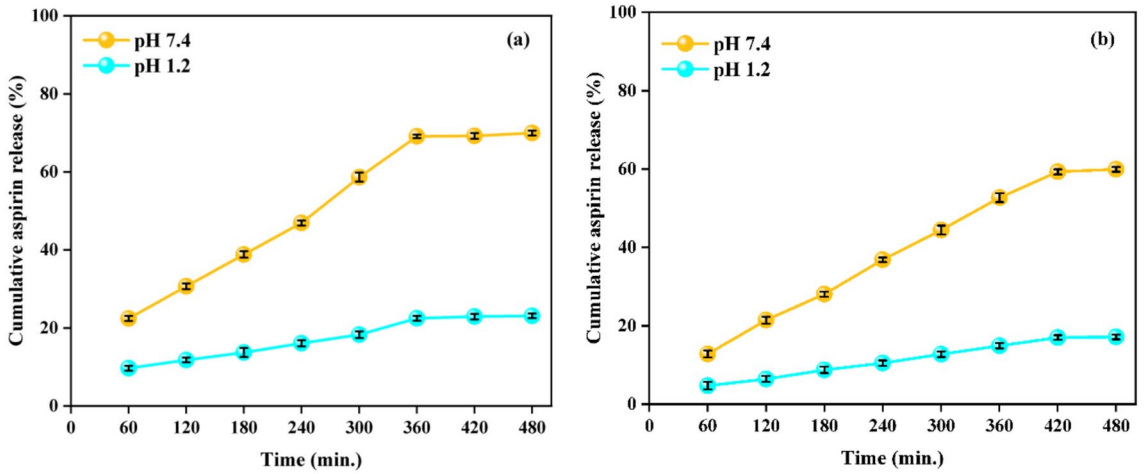

Fig. 10 Release profile of aspirin-loaded (**a**) TG/SA hydrogel microsphere and (**b**) TG/β-CD/SA hydrogel microsphere in pH 1.2 and 7.4

Table 5 Assessment of Regression Coefficient (R^2) value from aspirin-loaded TG/SA hydrogel microsphere and TG/β-CD/SA hydrogel microsphere

Model	Equation	Aspirin-loaded TG/SA microsphere		Aspirin-loaded TG/β-CD/SA microsphere		Ref.
		pH 7.4	pH 1.2	pH 7.4	pH 1.2	
		R^2	R^2	R^2	R^2	
Hixson-Crowell	$(M_t)^{1/3}-(M_\infty)^{1/3}=k_{HX}t$ k_{HX} = Hixson Crowell constant	0.9591	0.9661	0.925	0.9674	[44]
First Order	$\text{Log } M_t = \text{Log } M_\infty + \frac{kt}{2.303}$ k = First order rate constant	0.9244	0.9761	0.8993	0.9475	[44]
Korsmeyer–Peppas	$M_t/M_\infty = kt^n$ k = kinetic constant n = diffusion exponent	0.9951	0.9893	0.9808	0.9852	[2]
Zero Order	$M_t = M_\infty + k_0 t$	0.9855	0.9793	0.9831	0.9866	[45]
Higuchi	$M_t/M_\infty = k_H t^{1/2}$ k_H = kinetic constant	0.9632	0.9519	0.9612	0.9604	[28, 46]

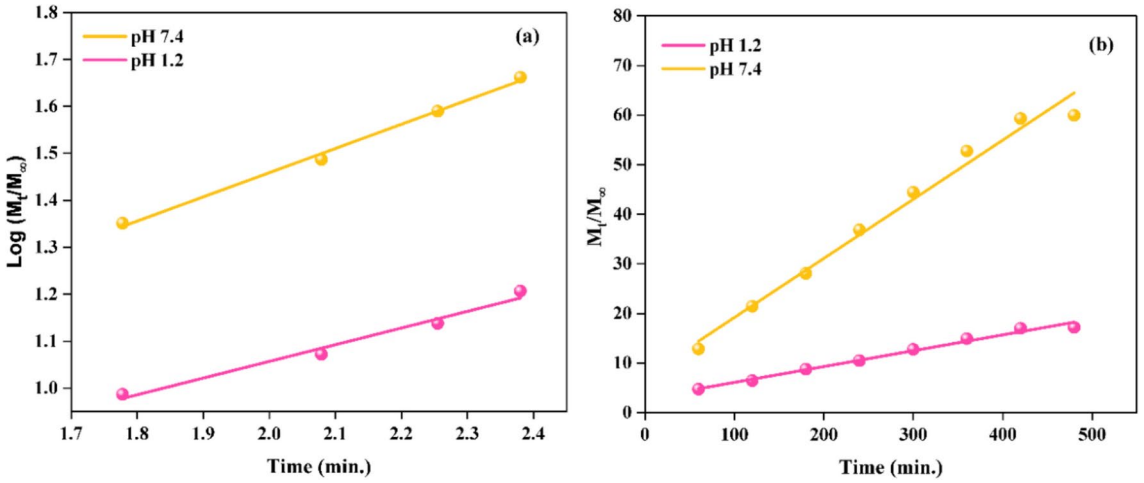

Fig. 11 Plot of (**a**) Korsmeyer–Peppas model for aspirin-loaded TG/SA hydrogel microsphere, and (**b**) Zero Order kinetic model for aspirin-loaded TG/β-CD/SA hydrogel microsphere

Kinetic Modelling

The correlation coefficients (R^2) value for different models like Hixson-Crowell, First-Order, Korsmeyer-Peppas, Zero-Order, and Higuchi were compared to determine which model provided the best description of the release mechanism of aspirin from aspirin-loaded TG/β-CD/SA microsphere and aspirin-loaded TG/SA microsphere, as illustrated in Table 5. In the case of aspirin-loaded TG/β-CD/SA microsphere, the zero-order model was discovered to be the best-fit model for drug release kinetic at both pH values. Moreover, it was observed that the R^2 value for the Korsmeyer-Peppas model is also closer to 1, with an n value of 0.5273 at pH 7.4 and 0.5182 at pH 1.2. Hence, the best fit of the zero-order model indicates that the release of the drug from the microsphere follows a controlled release pattern throughout the in vitro release analysis and the Korsmeyer-Peppas model suggests the non-fickian mechanism of drug release [34]. For aspirin-loaded TG/SA microsphere, the most fitted model was the Korsmeyer-Peppas model for both pH values (Fig. 11). The release exponent (n) value determined from the Korsmeyer-Peppas model was 0.5154 at pH 7.4 and 0.5052 at pH 1.2. This n value ($n \geq 0.5$) indicates that the drug release from the microsphere followed a non-fickian diffusion mechanism. In this mechanism, both drug diffusion and the relaxation of the polymer contribute to the release process [43].

Cytotoxicity Analysis

Cytotoxicity examination is crucial to ensure the safety of synthesized hydrogel microspheres for drug delivery application. The cytocompatibility assessment of various concentrations (50, 100, 200, 500, 1000 µg/ml) of synthesized aspirin-loaded TG/β-CD/SA hydrogel microspheres and control (without hydrogel) was carried out against HCT-116 human colon cell line (Fig. 12). Notably, even at a higher sample concentration (1000 µg/mL), the synthesized aspirin-loaded TG/β-CD/SA hydrogel microspheres exhibit

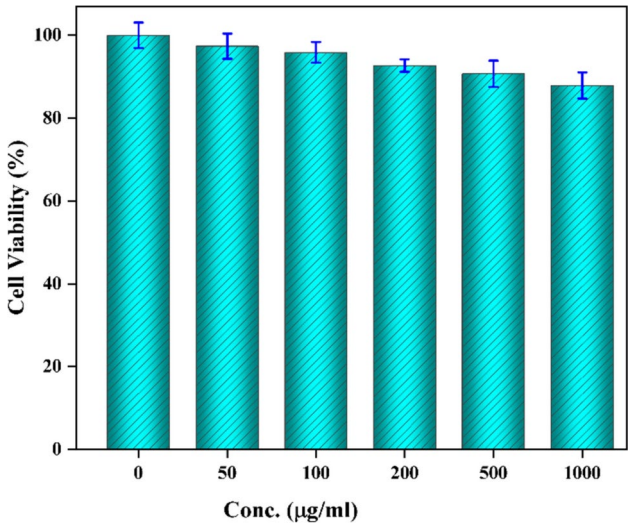

Fig. 12 Cytotoxicity profile of aspirin-loaded TG/β-CD/SA hydrogel microspheres

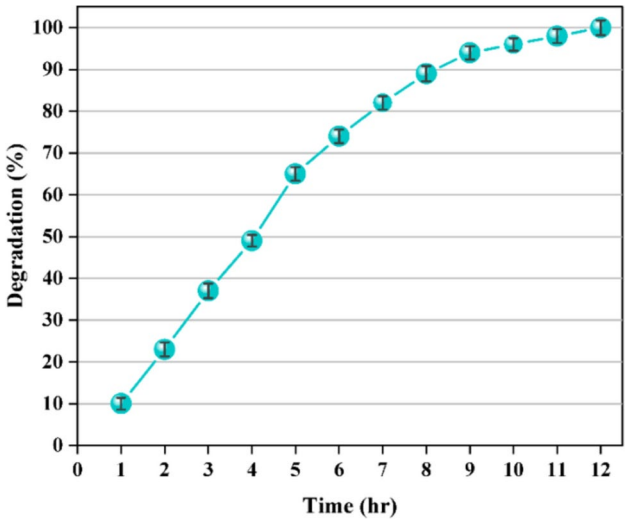

Fig.14 Degradation profile of aspirin-loaded TG/β-CD/SA hydrogel microsphere

87.9% cell viability, revealing its biocompatibility and non-toxic nature. This is attributed to the biocompatible nature of TG and SA biopolymers within the hydrogel microsphere

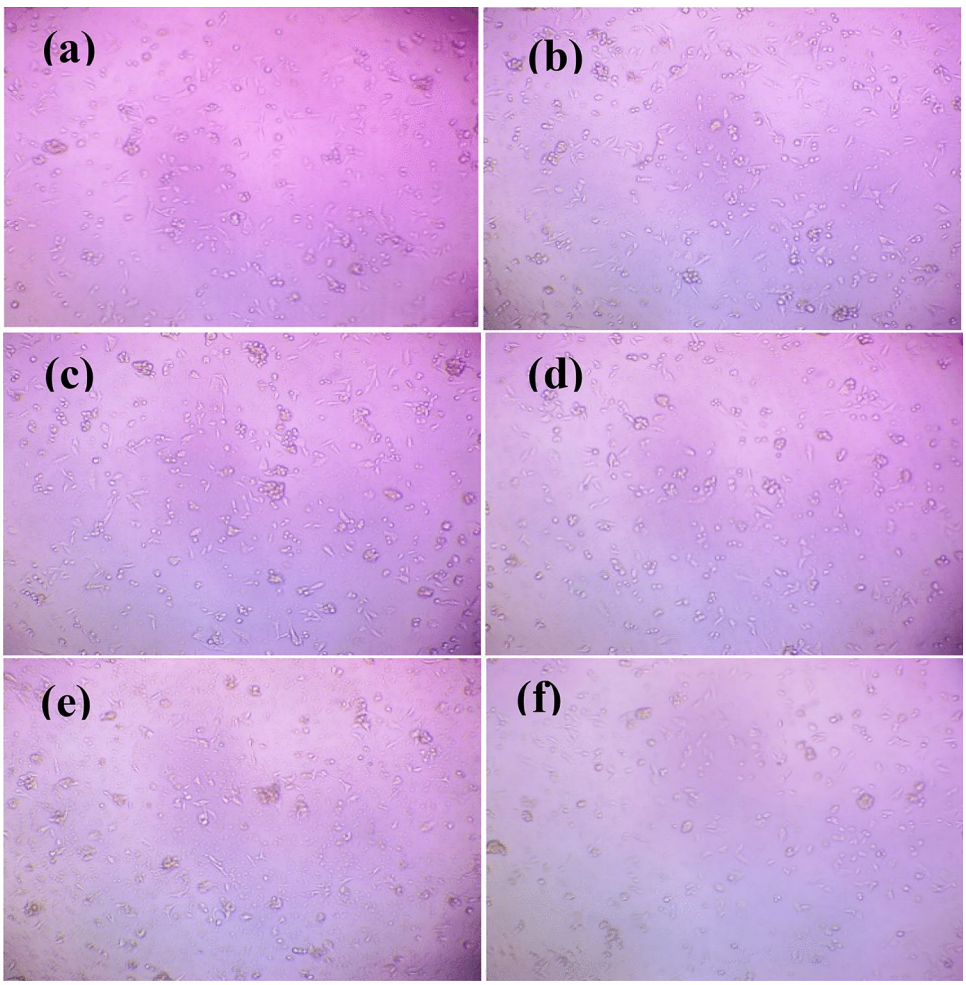

Fig.13 Inverted phase microscopic images of HCT-116 cells treated with **(a)** control **(b)** 50 µg/ml**, (c)**100 µg/ml**, (d)** 200 µg/ml**, (e)** 500 µg/ml and **(f)** 1000 µg/ml of aspirin-loaded TG/β-CD/SA hydrogel microspheres

[47–49]. Furthermore, the microscopic images of HCT-116 cells (Fig. 13), demonstrate a polygonal morphology and almost similar cell density in both control and hydrogel-treated cells at varying concentrations, indicating no huge alteration in cell shape and cell viability by the synthesized hydrogel.

Degradation Studies

The degradability of biomaterials plays a crucial role in biomedical applications. The degradability assessment, as illustrated in Fig. 14, provides valuable insights into the stability of the synthesized aspirin-loaded TG/β-CD/SA hydrogel. The degradation occurred in two stages, beginning with a rapid profile followed by slow degradation. The rapid degradation was observed within the first 8 h due to the cleavage of weak hydrogen bonds between TG, β-CD, and SA chains of hydrogel [29]. Following this period, slow degradation of the hydrogels could be observed till 12 h, likely due to the breakdown of glycosidic (C–O–C) linkages within the TG structure. It's observed that the synthesized aspirin-loaded TG/β-CD/SA hydrogel microsphere achieves complete degradation, reaching 100%. Hence, this degradable carrier provides a better option for safe drug delivery.

Conclusion

In this study, we have successfully fabricated hydrogel microspheres based on TG, SA, β-CD, and their role as efficient carriers for the controlled release of the hydrophobic drug aspirin was studied. The gel fraction and swelling behaviour of the microspheres were found to be dependent upon the concentrations of β-CD, SA, and TG. Furthermore, the introduction of β-CD into the TG/β-CD/SA microsphere shows high drug loading (19%) and drug entrapment efficiency (63.33%) compared to the TG/SA microsphere. This is attributed to the entrapment of aspirin within the hydrophobic cavities of β-CD, which improves the loading of aspirin within the microspheres. Also, it retards the release of aspirin from the microspheres, resulting in a controlled release pattern (zero order kinetic) at pH 1.2 and 7.4 in TG/β-CD/SA microsphere. The TG/β-CD/SA microsphere demonstrated higher drug release at pH 7.4 (59.9%), in contrast to pH 1.2 (17.1%), rendering them well-suited for targeted drug delivery within the colon region of the gastrointestinal tract. The developed hydrogel microsphere degrades completely in PBS and shows no cytotoxicity against HCT-116 human colon cell lines. Thus, we successfully provide a solution for the controlled and targeted delivery of aspirin, by developing a pH-sensitive TG/β-CD/SA hydrogel microsphere, highlighting the potential for oral drug delivery.

Acknowledgements The authors Priyanka Meena, Poonam Singh, and Sudhir G. Warkar thank the Delhi Technological University, New Delhi, India, for its infrastructural facilities and Priyanka Meena also thanks the Council of Scientific & Industrial Research (CSIR) for providing Senior research fellowship.

Author Contributions Sudhir G. Warkar and Priyanka Meena contributed to study methodology, Visualization, Resources. Material preparation and data curation were done by Priyanka Meena. The original draft was written by Priyanka Meena. The reviewing and editing of manuscript was done by Sudhir G. Warkar and Poonam Singh. The study supervision and project adminstration were performed by Sudhir G. Warkar and Poonam Singh. No Funding was provided for this work. All authors read and approved the final manuscript.

Data Availability No datasets were generated or analysed during the current study.

Declarations

Competing interest The authors declare no competing interests.

References

1. Suhail M, Wu PC, Minhas MU (2021) Development and characterization of pH-sensitive chondroitin sulfate-co-poly(acrylic acid) hydrogels for controlled release of diclofenac sodium. J Saudi Chem Soc 25:101212. https://doi.org/10.1016/j.jscs.2021.101212
2. Tushar, Saraswat Y, Meena P, Warkar SG (2023) Synthesis and characterization of novel xanthan gum - based pH - sensitive hydrogel for metformin hydrochloride release. Colloid Polym Sci. https://doi.org/10.1007/s00396-023-05135-9
3. Meena P, Singh P, Warkar SG (2023) Development and assessment of carboxymethyl tamarind kernel gum-based pH-responsive hydrogel for release of diclofenac sodium. Eur Polymer J 197:112340. https://doi.org/10.1016/j.eurpolymj.2023.112340
4. Lin F, Li Y, Cui W (2023) Injectable hydrogel microspheres in cartilage repair. Biomed Technol 1:18–29. https://doi.org/10.1016/j.bmt.2022.11.002
5. Lengyel M, Kállai-Szabó N, Antal V et al (2019) Microparticles, microspheres, and microcapsules for advanced drug delivery. Sci Pharm. https://doi.org/10.3390/scipharm87030020
6. Abasalizadeh F, Moghaddam SV, Alizadeh E et al (2020) Alginate-based hydrogels as drug delivery vehicles in cancer treatment and their applications in wound dressing and 3D bioprinting. J Biol Eng 14:1–22. https://doi.org/10.1186/s13036-020-00239-0
7. Kiran TR, Singh VK et al (2020) Synthesis, characterization of β-CD based novel hydrogels with dual objectives of drug release and dye removal. Iranian Polymer J (English Edition) 29:615–623. https://doi.org/10.1007/s13726-020-00826-4
8. Kumar PTS, Praveen G, Raj M et al (2014) Flexible, microporous chitosan-gelatin hydrogel/nanofibrin composite bandages for treating burn wounds. RSC Adv 4:65081–65087. https://doi.org/10.1039/c4ra11969j
9. Zakaria AF, Kamaruzaman S, Abdul Rahman N, Yahaya N (2022) Sodium alginate/β-cyclodextrin reinforced carbon nanotubes hydrogel as alternative adsorbent for nickel(II) metal ion removal. Polymers. https://doi.org/10.3390/polym14245524

10. Li S, Xiaowen Y, Yang Y et al (2023) Osteogenic and anti-inflammatory effect of the multifunctional bionic hydrogel scaffold loaded with aspirin and nano-hydroxyapatite. Front Bioeng Biotechnol 11:1–16. https://doi.org/10.3389/fbioe.2023.1105248
11. Qureshi MAUR, Arshad N, Rasool A et al (2024) Kappa-carrageenan and sodium alginate-based pH-responsive hydrogels for controlled release of methotrexate. R Soc Open Sci. https://doi.org/10.1098/rsos.231952
12. Atta R, Ata S, Islam A et al (2020) Kinetics and controlled release of lidocaine from novel carrageenan and alginate-based blend hydrogels. Int J Biol Macromol 147:67–78
13. Mandal S, Senthil Kumar S, Krishnamoorthy B, Basu SK (2010) Development and evaluation of calcium alginate beads prepared by sequential and simultaneous methods. Braz J Pharm Sci 46:785–793. https://doi.org/10.1590/S1984-82502010000400021
14. Martínez-Gómez F, Guerrero J, Matsuhiro B, Pavez J (2017) In vitro release of metformin hydrochloride from sodium alginate/polyvinyl alcohol hydrogels. Carbohyd Polym 155:182–191. https://doi.org/10.1016/j.carbpol.2016.08.079
15. Nayak AK, Khatua S, Hasnain MS, Sen KK (2011) Development of diclofenac sodium-loaded alginate-PVP K 30 microbeads using central composite design. DARU, J Pharmac Sci 19:356–366
16. Niu B, Jia J, Wang H et al (2019) In vitro and in vivo release of diclofenac sodium-loaded sodium alginate/carboxymethyl chitosan-ZnO hydrogel beads. Int J Biol Macromol 141:1191–1198. https://doi.org/10.1016/j.ijbiomac.2019.09.059
17. Sevinç Özakar R, Özakar E (2021) The effect of polymer amount and crosslinker ratio in polymeric hydrogel beads on characterization. J Res Pharmacy 25:653–666. https://doi.org/10.29228/jrp.57
18. Mansouri Shirazi N, Eslahi N, Gholipour-Kanani A (2021) Production and characterization of keratin/tragacanth gum nanohydrogels for drug delivery in medical textiles. Front Mater 8:1–12. https://doi.org/10.3389/fmats.2021.720385
19. Cikrikci S, Mert B, Oztop MH (2018) Development of pH sensitive alginate/gum tragacanth based hydrogels for oral insulin delivery. J Agric Food Chem 66:11784–11796. https://doi.org/10.1021/acs.jafc.8b02525
20. Liu C, Zhang Z, Liu X et al (2013) Gelatin-based hydrogels with β-cyclodextrin as a dual functional component for enhanced drug loading and controlled release. RSC Adv 3:25041–25049. https://doi.org/10.1039/c3ra42532k
21. Zhang Y, Ding N, Zhang T et al (2019) A tetra-PEG hydrogel based aspirin sustained release system exerts beneficial effects on periodontal ligament stem cells mediated bone regeneration. Front Chem. https://doi.org/10.3389/fchem.2019.00682
22. Shi Y, Wan A, Shi Y et al (2014) Experimental and mathematical studies on the drug release properties of aspirin loaded chitosan nanoparticles. BioMed Res Int. https://doi.org/10.1155/2014/613619
23. Xu X, Gu Z, Chen X et al (2019) An injectable and thermosensitive hydrogel: Promoting periodontal regeneration by controlled-release of aspirin and erythropoietin. Acta Biomater 86:235–246. https://doi.org/10.1016/j.actbio.2019.01.001
24. Sethi S, Saruchi KBS et al (2020) Cross-linked xanthan gum–starch hydrogels as promising materials for controlled drug delivery. Cellulose 27:4565–4589. https://doi.org/10.1007/s10570-020-03082-0
25. Gholamali I, Asnaashariisfahani M, Alipour E, Sepahi AA (2020) In-situ synthesized carboxymethyl chitosan/poly(vinyl alcohol) bio-nanocomposite hydrogels containing nanoparticles with drug-delivery properties. Bull Mater Sci. https://doi.org/10.1007/s12034-020-02231-2
26. Rahmani S, Olad A, Rahmani Z (2022) Preparation of self-healable nanocomposite hydrogel based on Gum Arabic/gelatin and graphene oxide: study of drug delivery behavior. Polym Bull 80:4117–4138. https://doi.org/10.1007/s00289-022-04247-6
27. Naeem F, Khan S, Jalil A, Ranjha NM, Riaz A, Haider MS, Sarwar S, Saher F, Afzal S (2017) pH Responsive cross-linked polymeric matrices based on natural polymers: effect of process variables on swelling characterization and drug delivery properties. BioImpacts 7:177–192. https://doi.org/10.15171/bi.2017.21
28. Khushbu, Warkar SG, Thombare N (2022) Controlled release and release kinetics studies of boron through the functional formulation of carboxymethyl tamarind kernel gum-based superabsorbent hydrogel. Polym Bull 79:2287–2303. https://doi.org/10.1007/s00289-021-03634-9
29. Jing Z, Xu A, Liang YQ et al (2019) Biodegradable poly(acrylic acid-co-acrylamide)/ poly(vinyl alcohol) double network hydrogels with tunable mechanics and high self-healing performance. Polymers. https://doi.org/10.3390/polym11060952
30. Raza MA, Park SH (2020) Irradiated Ch/GG/PVP-based stimuli-responsive hydrogels for controlled drug release. J Appl Polymer Sci. https://doi.org/10.1002/app.49041
31. Jana S, Sharma R, Maiti S, Sen KK (2016) Interpenetrating hydrogels of O-carboxymethyl Tamarind gum and alginate for monitoring delivery of acyclovir. Int J Biol Macromol 92:1034–1039. https://doi.org/10.1016/j.ijbiomac.2016.08.017
32. Hao PY, Zhou HY, Ren LJ et al (2023) Preparation and antibacterial properties of curcumin-loaded cyclodextrin-grafted chitosan hydrogel. J Sol-Gel Sci Technol 106:877–894. https://doi.org/10.1007/s10971-023-06097-8
33. Malik NS, Ahmad M, Minhas MU (2017) Cross-linked β-cyclodextrin and carboxymethyl cellulose hydrogels for controlled drug delivery of acyclovir. PLoS ONE 12:1–17. https://doi.org/10.1371/journal.pone.0172727
34. Nayak AK, Pal D, Santra K (2016) Swelling and drug release behavior of metformin HCl-loaded tamarind seed polysaccharide-alginate beads. Int J Biol Macromol 82:1023–1027. https://doi.org/10.1016/j.ijbiomac.2015.10.027
35. Abdi G, Jain M, Patil N et al (2024) Tragacanth gum-based hydrogels for drug delivery and tissue engineering applications. Front Mater 11:1–21. https://doi.org/10.3389/fmats.2024.1296399
36. Shafiq K, Mahmood A, Salem-Bekhit MM et al (2022) Development and optimization of tamarind gum-β-cyclodextrin-g-poly(methacrylate) pH-responsive hydrogels for sustained delivery of acyclovir. Pharmaceuticals. https://doi.org/10.3390/ph15121527
37. Elzayat EM, Abdel-Rahman AA, Ahmed SM et al (2016) Studying the impact of formulation and processing parameters on the release characteristics from hydroxypropyl methylcellulose matrix tablets of diclofenac. Acta Poloniae Pharmaceutica - Drug Research 73:439–452
38. Piyakulawat P, Praphairaksit N, Chantarasiri N, Muangsin N (2007) Preparation and evaluation of chitosan/carrageenan beads for controlled release of sodium Diclofenac. AAPS PharmSciTech. https://doi.org/10.1208/pt0804094
39. Suhail M, Khan A, Rosenholm JM et al (2021) Fabrication and characterization of diclofenac sodium loaded hydrogels of sodium alginate as sustained release carrier. Gels 7:1–16. https://doi.org/10.3390/gels7010010
40. Hoti G, Caldera F, Cecone C et al (2021) Effect of the cross-linking density on the swelling and rheological behavior of ester-bridged β-cyclodextrin nanosponges. Materials 14:1–20. https://doi.org/10.3390/ma14030478
41. Cuomo F, Cofelice M, Lopez F (2019) Rheological characterization of hydrogels from alginate-based nanodispersion. Polymers. https://doi.org/10.3390/polym11020259
42. Rehman S, Ranjha NM, Raza MR et al (2021) Enteric-coated Ca-alginate hydrogel beads: a promising tool for colon targeted drug

delivery system. Polym Bull 78:5103–5117. https://doi.org/10.1007/s00289-020-03359-1
43. Ghumman SA, Noreen S, Hameed H et al (2022) Synthesis of pH-sensitive cross-linked basil seed gum/acrylic acid hydrogels by free radical copolymerization technique for sustained delivery of captopril. Gels. https://doi.org/10.3390/gels8050291
44. Das D, Das R, Mandal J et al (2014) Dextrin crosslinked with poly(lactic acid): a novel hydrogel for controlled drug release application. J Appl Polym Sci 131:1–12. https://doi.org/10.1002/app.40039
45. Goonoo N, Bhaw-Luximon A, Ujoodha R et al (2014) Naltrexone: a review of existing sustained drug delivery systems and emerging nano-based systems. J Control Release 183:154–166. https://doi.org/10.1016/j.jconrel.2014.03.046
46. Meena P, Singh P, Warkar SG (2023) Fabrication and evaluation of stimuli - sensitive xanthan gum - based hydrogel as a potential carrier for a hydrophobic drug ibuprofen. Colloid Polym Sci. https://doi.org/10.1007/s00396-023-05198-8
47. Mouchati A, Yagoubi N (2023) Mechanical performance and cytotoxicity of an alginate/ polyacrylamide bipolymer network developed for medical applications. Materials. https://doi.org/10.3390/ma16051789
48. Hemmati K, Ghaemy M (2016) Synthesis of new thermo / pH sensitive drug delivery systems based on tragacanth gum polysaccharide. Int J Biol Macromol 87:415–425. https://doi.org/10.1016/j.ijbiomac.2016.03.005
49. Fan Z, Cheng P, Liu M et al (2020) Dynamic crosslinked and injectable biohydrogels as extracellular matrix mimics for the delivery of antibiotics and 3D cell culture. RSC Adv 10:19587–19599. https://doi.org/10.1039/d0ra02218g

Publisher's Note Springer Nature remains neutral with regard to jurisdictional claims in published maps and institutional affiliations.

Springer Nature or its licensor (e.g. a society or other partner) holds exclusive rights to this article under a publishing agreement with the author(s) or other rightsholder(s); author self-archiving of the accepted manuscript version of this article is solely governed by the terms of such publishing agreement and applicable law.

Design & Analysis of Adaptive Noise Equalizer for EV charging infrastructure integrated PV systems

Anurag Kumar
Department of Electrical Engineering
Delhi Technological University
Delhi, India
anuragkmr1409@gmail.com

Ankita Arora
Department of Electrical Engineering
Delhi Technological University
Delhi, India
arora.ankita09@gmail.com

Madhushudan Singh
Department of Electrical Engineering
Delhi Technological University
Delhi, India
madhusudan@dce.ac.in

***Abstract*- This article introduces a novel control algorithm for grid-connected solar photovoltaic (PV) powering EV batteries. The technology utilizes an adaptive noise equalizer (ANE) to charge electric vehicle (EV) batteries during daylight hours while improving power quality. The Electric Vehicle (EV) and Battery Energy Storage (BES) are linked together using a bidirectional buck-boost converter at the direct current (dc) link. The electric vehicle (EV) draws power from the solar array during daylight hours. When there is no sunlight or the level of irradiance is below a certain level, the EV supplies power to the grid. The control algorithm compensates for harmonic current while charging and discharging the EV battery. Additionally, it ensures that the overall harmonics distortion of the grid currents is limited to less than 5%, as recommended by the IEEE-519 standard. The VSC serves the multifunctional purpose of reactive power compensation and maintaining unity power factor operation in different G2V and V2G modes. The adaptive noise equalizer is implemented to reduce the harmonics injected into the source current by non-linear load and maintain the sinusoidal currents. The results verify the performance of EV charging infrastructure integrated PV systems under different steady state and dynamic conditions under G2V and V2G modes.**

Keywords*— *adaptive noise equalizer (ANE), Solar photovoltaic (PV), Point of common coupling (PCC).

I. INTRODUCTION

Renewable energy is an essential substitute to fulfil the energy needs of households and businesses due to the rapid exhaustion of traditional energy sources. The primary benefit of using electric vehicles as an alternative to fossil fuel-powered vehicles is their environmentally benign nature, as they do not emit pollutants. Recently, PV energy sources have been favoured among all available renewable energy sources because of their easy availability, installation, and eco-friendliness. Charging electric vehicles (EVs) using the grid is not advisable due to its substantial power consumption from the grid. Thus, an alternative energy source is necessary for charging EV batteries. Renewable energy sources are a superior option for charging electric vehicles compared to the traditional power grid. There is a growing global demand for electric vehicles (EVs), which in turn necessitates the installation of EV charging stations. In [1], a hierarchical architecture is proposed to make judgements on the merging of electric vehicles (EVs), regulating EV trajectories, and controlling operations. When PV generation is insufficient, EVs are discharged to supply the grid with the necessary power. Vehicle to grid (V2G) is the name given to this kind of function, shown experimentally in [2]. Lyu et al. [3] reviewed the power consumption from the grid by EV charging stations. [4] presents the applications of battery-integrated supercapacitor microgrids considering the uncertainties in the RERs caused by climate fluctuations. [5] presents the construction of a power grid model incorporating a significant amount of photovoltaic (PV) electricity. Numerical simulation is conducted using time series data to examine the impact of charging/discharging control on the frequency regulation of the vehicle-to-grid (V2G) system, specifically focusing on the aggregated electric vehicle (EV) group.[6] presents a control strategy for a microgrid that seeks to provide a seamless shift between the islanded mode (IAM) and grid-connected mode (GCM) of operation while ensuring equitable power distribution.

[7] presents a proposal for managing a hybrid converter within an electric vehicle charging station. This presentation showcases the management of the Hybrid converter to enhance the extraction of maximum power from PV, regulate the direct current voltage for electric vehicle charging, and oversee the alternating current power for supplying the AC grid.

[8] presents a novel approach to enhance the charging process of an electric vehicle (EV) charging system inside a grid-integrated proton-exchange framework. This is achieved by employing an adaptive error convergence mechanism. [9] Introduces a suggested flexible framework for adjustable power regulation (AIDPC) of battery chargers specifically engineered for electric vehicles. Flexible active load management regulates the battery power when the vehicle is connected dynamically.[10] focuses on a unique model predictive control (VSPC) method that utilizes voltage sensors to provide maximum power point tracking (MPPT) of PV array to charge electric vehicles.

This paper implements an adaptive noise equalizer to mitigate power quality problems, and a solar PV array and bidirectional EV battery charger are interfaced to the grid through a VSC at the DC link. The G2V and V2G modes are verified through a multifunctional control with nonlinear home loads connected at PCC. The major contributions of this work are:

1. Developing a multifunctional VSC control algorithm to maintain the grid current's THD while accounting for harmonics in the presence of nonlinear load at PCC.
2. It reduces the system's operating costs and increases the solar PV array's self-consumption, lessening the strain on the main electrical grid.
3. This control offers a suitable response and keeps the grid's current sinusoidal, ensuring power quality. The IEEE standard IEEE 519 is used to validate the EVPVES's performance.
4. This work introduces a novel algorithm that may selectively increase or decrease the intensity of any harmonic at a specific frequency by a set degree. This is accomplished by displacing the zeros along a

2024 IEEE Region 10 Symposium (TENSYMP) | 979-8-3503-6486-6/24/$31.00 ©2024 IEEE | DOI: 10.1109/TENSYMP61132.2024.10752120

979-8-3503-6486-6/24/$31.00 ©2024 IEEE

Authorized licensed use limited to: DELHI TECHNICAL UNIV. Downloaded on November 25,2024 at 04:42:38 UTC from IEEE Xplore. Restrictions apply.

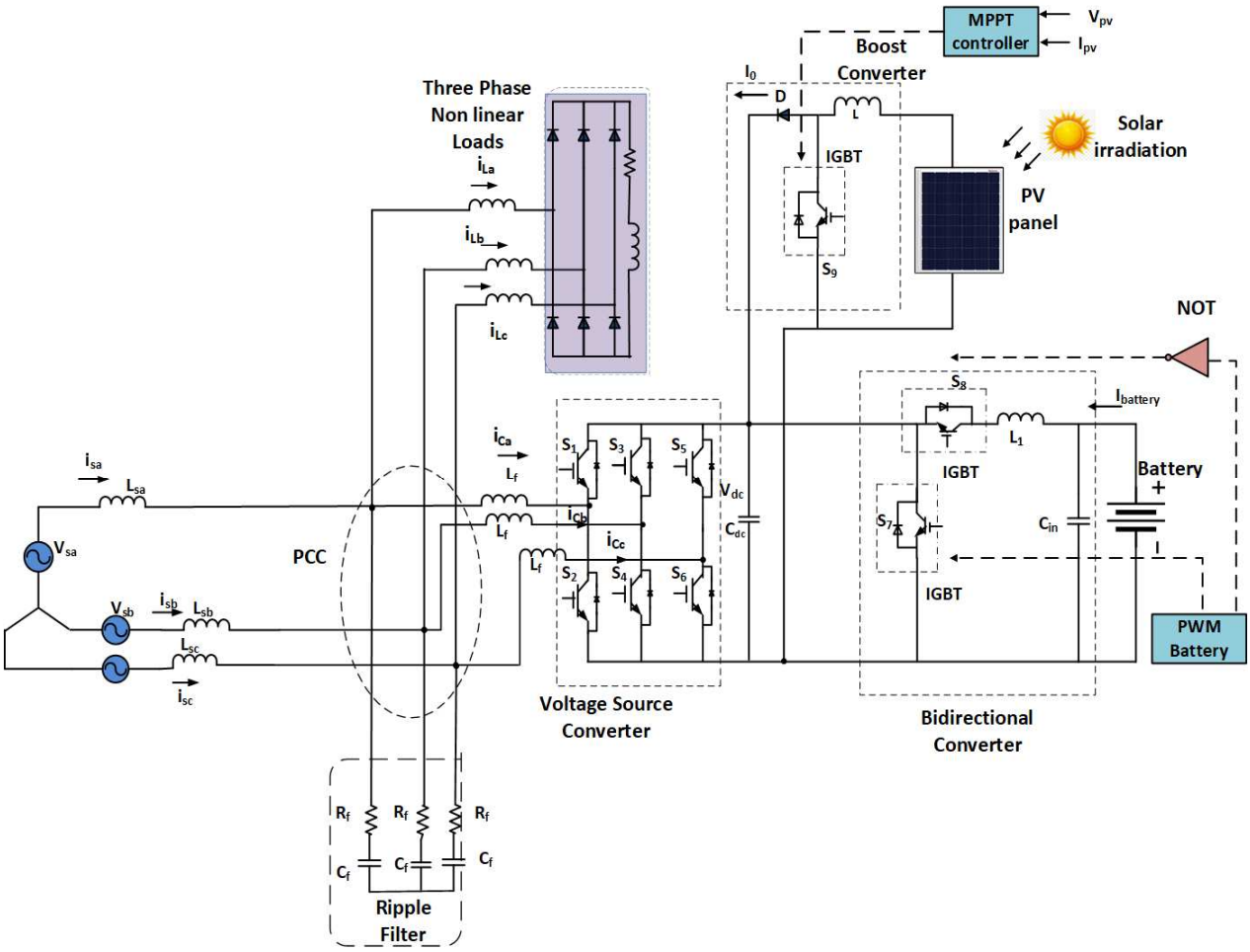

Fig. 1. EV Battery charging infrastructure

meticulously regulated trajectory within the unit circle.

II. SYSTEM CONFIGURATION

The schematic diagram of EV charging infrastructure for PV-integrated grid-connected systems is shown in Fig. 1. The EV charging infrastructure consists of a battery with a buck-boost converter connected at the DC link. The solar PV array with the boost converter is connected in parallel to the DC link. The VSC facilitates the bidirectional power exchange among the PV array, EV, and grid. It converts DC power into AC for its interaction with the grid. A non-linear RL load and DC diode bridge rectifier is coupled at the PCC. The electric vehicle (EV) and PV Array are linked through bidirectional DC-DC converters and boost converters at a shared DC connection. This converter regulates the charging and draining of the battery with the help of the IGBT control algorithm. Inductors connect the voltage source converter (VSC) at the point of common coupling to reduce harmonics in the current.

III. CONTROLLER DESIGN

A. Control of DC-DC Buck-Boost Converter

Fig. 5 illustrates the control methodology employed for a DC-DC bidirectional converter, which regulates the current flow in the battery. The main purpose of the control technique is to regulate and optimise the energy stored in the battery. Nevertheless, the battery's nominal voltage is maintained during the charging process. The voltage controller inputs the comparison between the measured DC link and the reference voltage. The PI regulator produces the feedback battery current. An error signal is obtained by comparing the reference battery current (I_{batt_ref}) with the actual battery current ($I_{battery}$). As shown in Fig.6, the error signal is inputted into the Proportional-Integral (PI) controller, and the output of the PI controller is then fed into the Pulse Width Modulation (PWM) generator. The PWM generator produces the pulses necessary for the bidirectional DC-DC converter. During the discharging process, one of the switches is set to a high state and another to a low state. Conversely, during the charging action, the configuration is inverted, i.e., a switch set to a low state is now set to a high state.

$$I_{batt_ref} = \left(k_{p1} + \frac{k_i 1}{s}\right)\{V_{dc_ref} - V_{dc}\} \quad (1)$$

Here, k_{p1} *and* k_{i1} are proportional and integral constants of the first PI controller, as shown in Fig. 2.

The duty ratio for the bidirectional converter is estimated as follows:

$$D = \left(k_{p2} + \frac{k_{i2}}{s}\right)\{I_{batt_ref} - I_{battery}\} \quad (2)$$

Here, k_{p2} *and* k_{i2} are proportional and integral constants of the second PI controller, as shown in Fig. 2.

Authorized licensed use limited to: DELHI TECHNICAL UNIV. Downloaded on November 25,2024 at 04:42:38 UTC from IEEE Xplore. Restrictions apply.

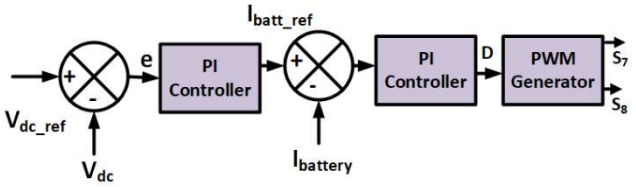

Fig. 2. Gate signal generation for Bidirectional DC-DC Converter

B. Control of Boost Converter

A solar photovoltaic (PV) array operates as a current generator, generating an electric current directly proportional to the array's amount of sunlight. Variations in temperature and irradiation levels induce Maximum PowerPoint Tracking (MPPT) alterations. To get the maximum power point (MPP), a DC-DC
boost converter is employed, employing a Perturb and Observe (P&O) method. The electricity supplied to the load is then delivered to the grid using a Voltage Source Converter (VSC). The P&O method involves incrementing or decrementing the voltage by a constant step size to approach the MPP on a P-V curve. The technique is done at regular intervals until the MPP is reached. The operating point fluctuates around the Maximum Power Point (MPP) during a steady state. $P(k)\ and\ V(k)$ represents power and voltage at the present iteration while $P(k-1)\ and\ V(k-1)$ represents power and voltage at the previous iteration.

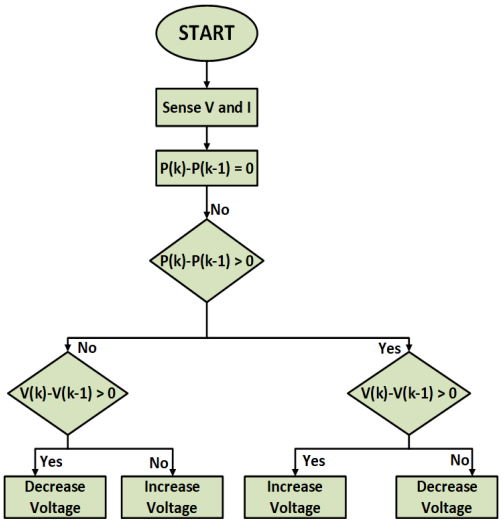

Fig. 3. P & O MPPT Algorithm

C. Grid Interfaced VSC Control

Fig.5 illustrates the generation of gate pulses for the VSC in the grid-interfaced mode. The accompanying sections provide a comprehensive explanation of the control.

1. Adaptive Equaliser Method Structure

This paper introduces the concept of an Adaptive Noise Equalizer (ANE) that can perform shunt compensation. The ANE system comprises a sinusoidal reference input and two adaptive weights that can be modified linearly and arbitrarily by adjusting the gain parameter. The ANE can achieve harmonic non-linear load current compensation by injecting the neutralising current with the help of SAPF. The ANE system is divided into two branches: cancelling and balancing, with the gain of 1-β inserted into the cancelling branch and β incorporated into the balancing branch to compensate for the harmonics in source current injected by non-linear load precisely.

A pure cosine signal is provided as the reference signal-

$$i_{La1}(n) = i_{La}\ \sin(\omega_o n + \varphi_o) \quad (3)$$

where ω_o is frequency and A is the magnitude of the signal. 90° delay is used to produce another signal that is given as

$$i_{La2}(n) = i_{La}\ \sin(\omega_o n + \varphi_o - 90°) \quad (4)$$

The system output, which is

$$e(n) = e'(n) + \beta\ i_{La_est} \quad (5)$$

where $e'(n)$ is the residual error component, and β controls harmonic components.

$$e'(n) = d(n) - i_{La_est} \quad (6)$$

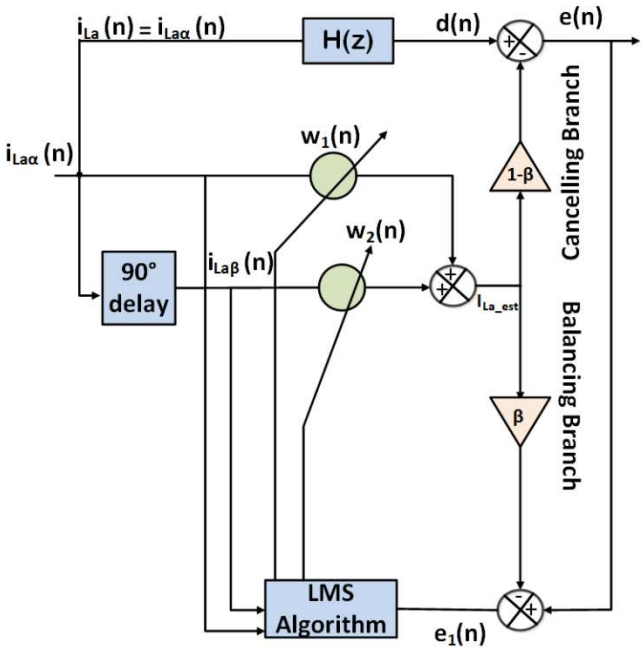

Fig. 4. Adaptive Noise Equalizer

$$e_a = (i_{La}\sin\omega t * w_a + i_{La}\sin(\omega t - 90) * w_a) * (1 - \beta) + i_{La}\sin\omega t - (i_{La}\sin\omega t * w_a + i_{La}\sin(\omega t - 90) * w_a) * \beta \quad (7)$$

After solving, we get-

$$e_a = i_{La}\sin\omega t + (1 - 2\beta) * i_{La}\sin\omega t * w_a + (1 - 2\beta) * i_{La} * \sin(\omega t - 90) \quad (8)$$

$$i_{La_est} = (i_{La}\sin\omega t * w_a + i_{La}\sin(\omega t - 90) * w_a \quad (9)$$

which represents the remaining background noise produced by the standard adaptive noise cancelling method.

Where,

$$w_a(n+1) = w_a(n) + \Delta * e'(n) * i_{La}(n) \quad (10)$$

Authorized licensed use limited to: DELHI TECHNICAL UNIV. Downloaded on November 25,2024 at 04:42:38 UTC from IEEE Xplore. Restrictions apply.

These weights are updated by the LMS algorithm for each phase a, b and c.

2. Grid Active Fundamental Currents Computation

The PI controller produces a DC power loss component, which is given by

$$I_{Loss}(n) = I_{Loss}(n-1) + k_p\{(X_{dc}(n) - X_{dc}(n-1))\} + k_I\{X_{dc}(n)\} \quad (11)$$

Where,

$$X_{dc}(n) = V_{dc_{ref}}(n) - V_{dc}(n) \quad (12)$$

The feedforward PV component current is estimated as

$$I_{PVeff} = \frac{2*P_{pv}}{3\,V_t} \quad (13)$$

The feedforward battery current is estimated as

$$I_{batt_eff} = \frac{2*V_{b*}I_b}{3\,V_t} \quad (14)$$

The total current fetched from the grid is calculated as

$$I_d = I_{loss} + \frac{1}{3}(i_{La_est} + I_{Lb_est} + I_{Lc_est}) - I_{PVeff} - I_{batt_eff} \quad (15)$$

3. Grid Reference Currents Computation

The primary objective of the control algorithm is to harness the power generated by the photovoltaic (PV) array for electric vehicle (EV) charging. In addition, electric vehicles (EVs) can both release and provide electricity to the power grid. Hence, it is imperative to devise an intelligent control plan to optimize the utilization of the charging station, ensuring enhanced efficiency. The control technique that was developed is illustrated in Fig 5. Three-phase supply voltages at the point of common coupling are calculated as v_a, v_b *and* v_c *respectively*. The magnitude of these voltages is calculated as V_t –

$$V_t = \sqrt{\frac{2}{3}(v_a^2 + v_b^2 + v_c^2)} \quad (16)$$

Three-phase unit templates are computed as

$$u_{ia} = \frac{v_a}{V_t}, u_{ib} = \frac{v_b}{V_t}, u_{ic} = \frac{v_c}{V_t} \quad (17)$$

Reference source currents of three phases are estimated as

$$i_{saref} = I_d * u_{ia}, i_{sbref} = I_d * u_{ib}, i_{scref} = I_d * u_{ic} \quad (18)$$

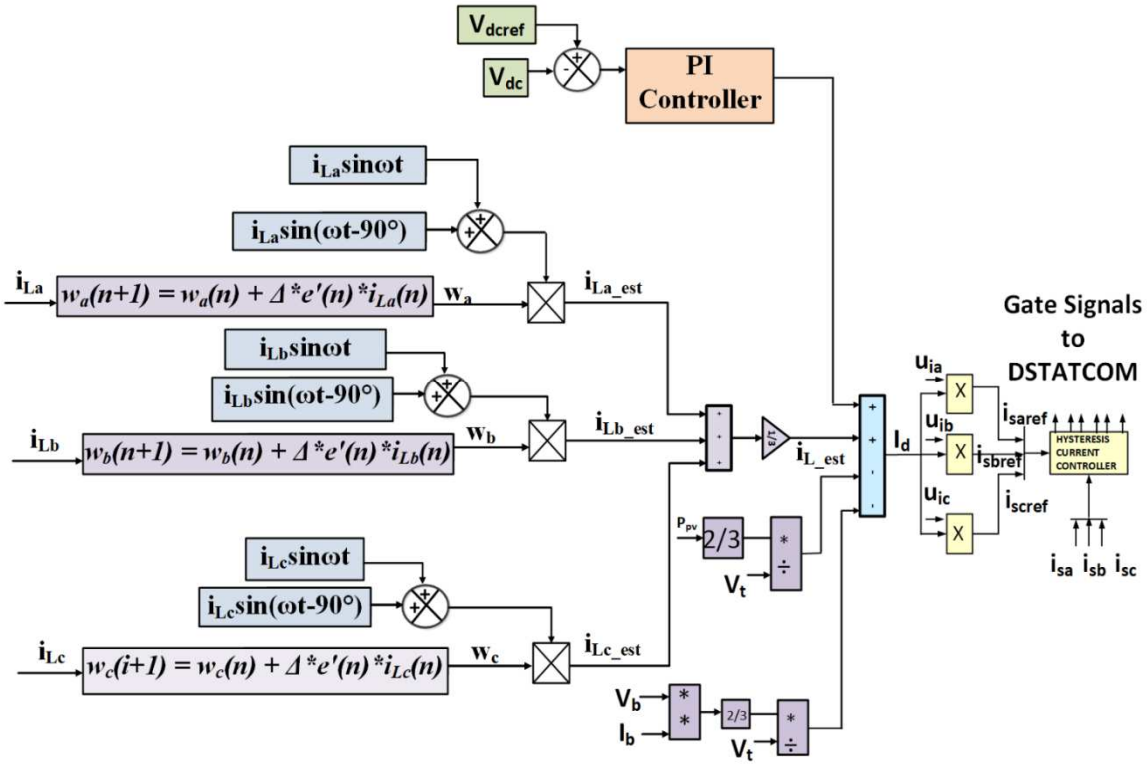

Fig. 5. Gate signal generation for DSTATCOM

IV. SIMULATION RESULTS

A simulation and modelling of the control strategy, utilising the Adaptive Noise Equalizer (ANE) algorithm, has been conducted in MATLAB. The system's behaviour in several circumstances, such as a grid-to-vehicle and vehicle-to-grid mode, is analysed by simulating it in the MATLAB/Simulink environment. The findings are then described in the subsequent subsections.

A. Grid to vehicle mode

Grid-to-Vehicle mode is simulated from 0.1s to 0.3s. The waveforms of the source voltage (V_{sabc}), source current (i_{sabc}), load current (i_{Labc}), compensating current (i_{fabc}), and DC link voltage (V_{dc}) during 0.1s to 0.3s are depicted in Fig. 6. The Total harmonic distortion (THD) in i_{sabc} and i_{Labc} under non-linear load conditions are 2.99% and 18.67%, respectively, as shown in Fig. 7.

1. Under Solar Irradiation Intensity of 500 W/m²

Under solar irradiance intensity of 500 W/m², the source current is observed to be sinusoidal because of the SAPF Filter that is there to counterbalance the harmonics introduced into the source current by the non-linear load. The DC link

Authorized licensed use limited to: DELHI TECHNICAL UNIV. Downloaded on November 25,2024 at 04:42:38 UTC from IEEE Xplore. Restrictions apply.

voltage is settled at 200V with little oscillations. The load current demand of 20A is met by the grid current of 16A and PV current of 4A.

Fig. 8 illustrates the waveforms of SOC(%), Battery Current $(I_{battery})$, battery voltage $(V_{battery})$ and PV current (I_{PV}) respectively. Here, the battery starts charging, increasing its state of charge (SOC) from 59.0994% to 59.0995%. Also, Battery voltage$(V_{battery})$ starts increasing from 155V. The battery starts charging with a current of 3A.

Fig. 9 illustrates the waveforms of source active power (P_{sabc}), source reactive power(Q_{sabc}), load active power P_{Labc}), load reactive power(Q_{Labc}), Compensating reactive power (Q_{fabc}), Battery power $(P_{battery})$ and PV power(P_{pv}) respectively. Between the period of 0.1s and 0.2s, there is a rise in solar power, reaching a value of 300 W. Consequently, the battery power experiences a reduction to -1.5 kW, which means that the battery is now consuming power. To offset this decrease and meet the overall load power requirement of 2.0 kW, the power supplied by the grid is now augmented to 3.2 kW, as shown in Fig. 9.

2. *Under Solar Irradiation Intensity of 800 W/m²*

Under solar irradiance intensity of 800 W/m^2, The source current is observed to be sinusoidal because of the SAPF Filter that is there to counterbalance the harmonics introduced into the source current by the non-linear load. The DC link voltage is settled at 200V with little oscillations. The load current demand of 20A is met by the grid current of 14A and PV current of 6A.

Fig. 8 illustrates the waveforms of SOC(%), Battery Current $(I_{battery})$, battery voltage $(V_{battery})$ and PV current (I_{PV}) respectively. Here, the battery starts charging, increasing its state of charge (SOC) from 59.0995% to 59.0997%. Also, Battery voltage$(V_{battery})$ starts increasing from 156V. The battery is charging with a current of 3A.

Fig. 9 illustrates the waveforms of source active power (P_{sabc}), source reactive power(Q_{sabc}), load active power P_{Labc}), load reactive power(Q_{Labc}), Compensating reactive power (Q_{fabc}), Battery power $(P_{battery})$ and PV power(P_{pv}) respectively. Between the period of 0.2s and 0.3s, there is a rise in solar power, reaching a value of 500 W. The battery power settles to -1.5 kW, meaning the battery is consuming power. To meet the overall load power requirement of 2.0 kW, the power supplied by the grid is now augmented to 3.0 kW, as shown in Fig. 9.

B. *Vehicle to grid mode*

Vehicle-to-grid mode is simulated from 0.3s to 0.35s. The waveforms of the source voltage (V_{sabc}), source current (i_{sabc}), load current (i_{Labc}), compensating current (i_{fabc}), and DC link voltage $(V_{dc}$. The Total harmonic distortion (THD) in i_{sabc} and i_{Labc} under non-linear load conditions are 2.99% and 18.67%, respectively, as shown in Fig. 7. The source current is observed to be sinusoidal because of the SAPF Filter that is there to counterbalance the harmonics introduced into the source current by the non-linear load. The load current demand of 20A is met by a grid current of 10A and a battery current of 10A.

Fig. 8 illustrates the waveforms of SOC(%), Battery Current $(I_{battery})$, battery voltage $(V_{battery})$ and PV current (I_{PV}) respectively. When the photovoltaic (PV) current is above 0.4 A, the battery starts charging, increasing its state of charge (SOC) from 59.0995%. to 59.0997%. Also, Battery voltage$(V_{battery})$ increases from 156V to 155V.

Fig. 9 illustrates the waveforms of source active power (P_{sabc}), source reactive power(Q_{sabc}), load active power P_{Labc}), load reactive power(Q_{Labc}), Compensating reactive power (Q_{fabc}), PV power(P_{pv}), Battery power$P_{battery}$) respectively. Between the period of 0.3s and 0.35s, solar power reaches 0W. Consequently, the battery power increases to 1.5kW, which means the battery is now supplying power. To meet the overall load power requirement of 2.0 kW, the power supplied by the grid is now augmented to 500 W, as shown in Fig. 9.

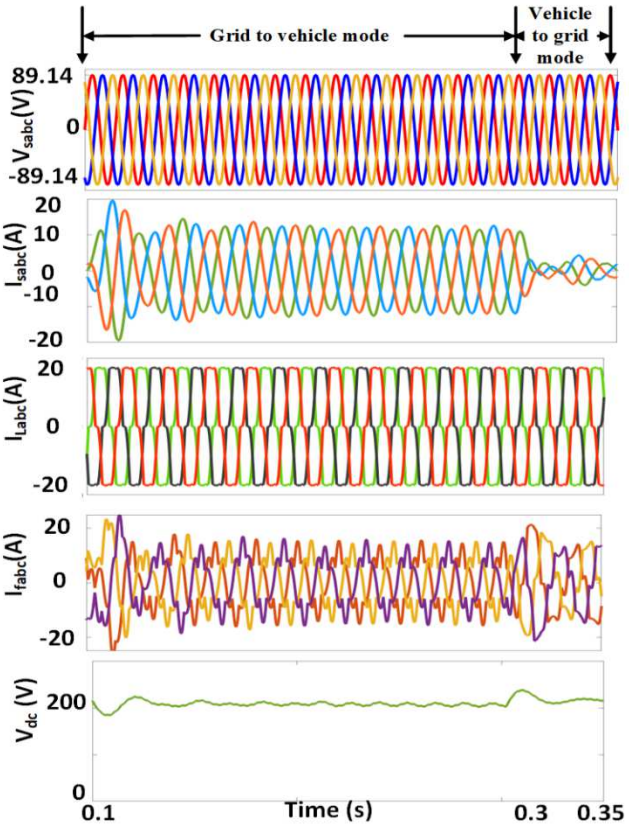

Fig. 6. Performance analysis of ANE under charging and discharging conditions

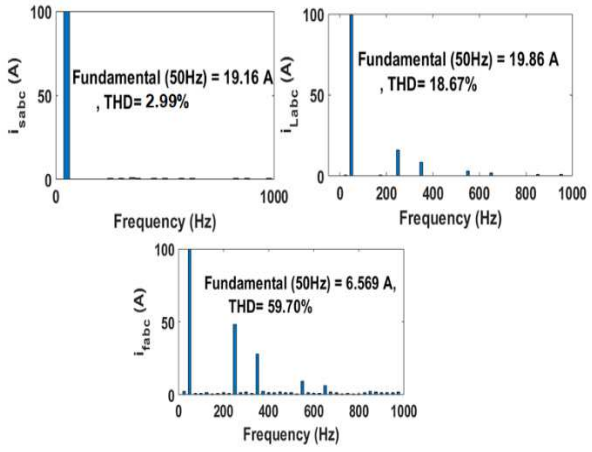

Fig. 7. THD of ANE (a) Source voltage(V_{sabc})(b) Source current(i_{sabc}) (c) load current(i_{Labc}) during battery charging and discharging

Authorized licensed use limited to: DELHI TECHNICAL UNIV. Downloaded on November 25,2024 at 04:42:38 UTC from IEEE Xplore. Restrictions apply.

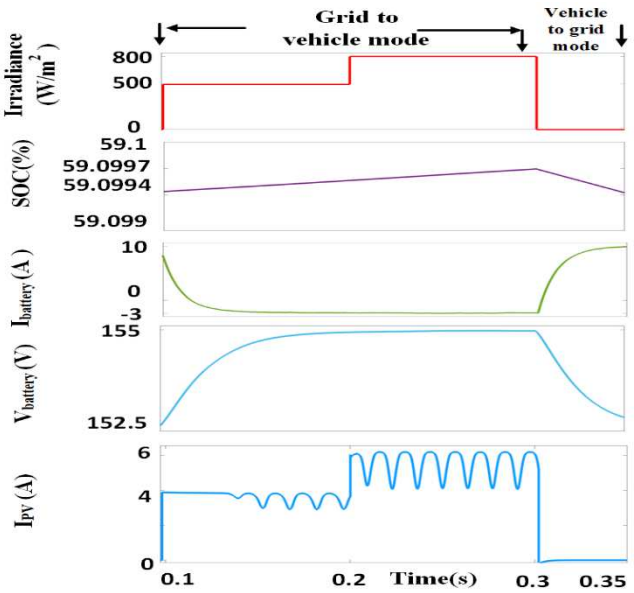

Fig. 8. Simulation results of charging and discharging of battery with respect to I_{pv}

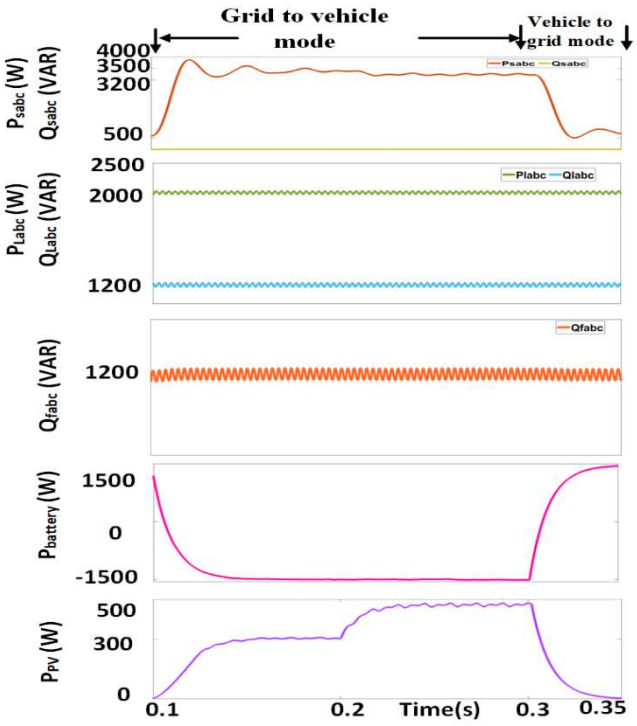

Fig. 9. Power Balance of power system during charging and discharging conditions of the battery

V. CONCLUSION

A bidirectional active power flow and harmonics current adjustment have been incorporated into the design of a three-phase charging station. The testing findings have confirmed the validation of the charging station's performance in the presence of PV interference and voltage imbalance. The study also examines the performance of charging stations in relation to mode changes and electric vehicle (EV) charging. The study examines the performance of the charging station during dynamic conditions, specifically focusing on the correction of reactive power that leads to lagging and vice versa. The total harmonic distortion (THD) of the grid currents falls within the recommended range of the IEEE-519 standard. The charging station's performance is deemed satisfactory.

VI. APPENDIX

Simulation parameters of SAPF: V_{L-L} =110 V, V_{DC} =200V, DC bus capacitor= 3000 μF, $L_{sa} = L_{sb} = L_{sc}$ =4mH, R_f=10 Ω,C_f=5.5μF,K_p=0.8,K_I=0.25.

Design of Boost Converter: Efficiency=90% , Switching frequency = $\mathbf{f_s} = 5000$ Hz ,
V_O=200V , I_0= 5A , D=40% , V_{in_min}= 120V ,
V_{in_max}=140V, $I_{s_max} = 8.33$ A, $I_{s_min} = 7.42$ A, $\Delta \mathbf{i_L} = 2.5\text{A}, \Delta \mathbf{V_c} = 2\text{V}, \text{L} = 4000\ \mu\text{H}, \text{C} = 1000\ \mu\text{F}$

Design of Buck-Boost Converter:

$\text{L} = 4000\ \mu\text{H}, \text{C} = 1000\ \mu\text{F}, V_O$=200V

REFERENCES

[1] N. Chen, B. van Arem, T. Alkim and M. Wang, "A Hierarchical Model-Based Optimization Control Approach for Cooperative Merging by Connected Automated Vehicles," in IEEE Transactions on Intelligent Transportation Systems, vol. 22, no. 12, pp. 7712-7725, Dec. 2021, doi: 10.1109/TITS.2020.3007647.

[2] Hasan, A S M Jahid & Enriquez-Contreras, Luis & Yusuf, Jubair & Barth, Matthew & Ula, Sadrul. (2021). Demonstration of Microgrid Resiliency with V2G Operation. 243-248. 10.1109/ITEC51675.2021.9490165.

[3] D. Lyu, T. B. Soeiro and P. Bauer, "Design and Implementation of a Reconfigurable Phase Shift Full-Bridge Converter for Wide Voltage Range EV Charging Application," in IEEE Transactions on Transportation Electrification, vol. 9, no. 1, pp. 1200-1214, March 2023, doi: 10.1109/TTE.2022.3176826.

[4] A. Bharatee, P. K. Ray, A. Ghosh and M. R. Jena, "Active Power Sharing Scheme in a PV Integrated DC Microgrid With Composite Energy Storage Devices," in IEEE Transactions on Power Systems, vol. 39, no. 2, pp. 3497-3508, March 2024, doi: 10.1109/TPWRS.2023.3284556.

[5] B. Jie, J. Baba and A. Kumada, "Contribution to V2G System Frequency Regulation by Charging/Discharging Control of Aggregated EV Group," in IEEE Transactions on Industry Applications, vol. 60, no. 1, pp. 1129-1140, Jan.-Feb. 2024, doi: 10.1109/TIA.2023.3292814.

[6] Y. Singh, B. Singh and S. Mishra, "Control of Single-Phase Distributed PV-Battery Microgrid for Smooth Mode Transition With Improved Power Quality," in IEEE Transactions on Industry Applications, vol. 58, no. 5, pp. 6286-6296, Sept.-Oct. 2022, doi: 10.1109/TIA.2022.3178388.

[7] K. S. R. Sekhar, M. A. Chaudhari and V. Khadkikar, "Enhanced Hybrid Converter Topology for PV-Grid-EV Integration," in IEEE Transactions on Energy Conversion, vol. 38, no. 4, pp. 2634-2646, Dec. 2023, doi: 10.1109/TEC.2023.3287890.

[8] D. Mishra, B. Singh and B. K. Panigrahi, "Implementation of a Robust PMAE Algorithm to Limit Large Gain Variation in a Fuel-Cell Integrated EV Charging Architecture," in IEEE Transactions on Energy Conversion, vol. 38, no. 4, pp. 2671-2683, Dec. 2023, doi: 10.1109/TEC.2023.3272478.

[9] Nayak, S., Mohanty, S. Grid connected electric vehicle charging and discharging rate management with balance grid load. *Electr Eng* **105**, 575–592 (2023). https://doi.org/10.1007/s00202-022-01671-9

[10] N. Kumar, B. Singh and B. K. Panigrahi, "Voltage Sensorless Based Model Predictive Control With Battery Management System: For Solar PV Powered On-Board EV Charging," in IEEE Transactions on Transportation Electrification, vol. 9, no. 2, pp. 2583-2592, June 2023, doi: 10.1109/TTE.2022.3213253.

[11] S. M. Kuo and M. J. Ji, "Development and analysis of an adaptive noise equalizer," in IEEE Transactions on Speech and Audio Processing, vol. 3, no. 3, pp. 217-222, May 1995, doi: 10.1109/89.388150

Authorized licensed use limited to: DELHI TECHNICAL UNIV. Downloaded on November 25,2024 at 04:42:38 UTC from IEEE Xplore. Restrictions apply.

Journal of Computational Electronics (2025) 24:1
https://doi.org/10.1007/s10825-024-02255-5

Design and optimization of a terahertz photonic crystal fiber based biosensor to detect malaria disease

Vishal Chaudhary[1] · **Sonal Singh**[1]

Received: 25 July 2024 / Accepted: 13 October 2024
© The Author(s), under exclusive licence to Springer Science+Business Media, LLC, part of Springer Nature 2024

Abstract
This study introduces a dual core photonic crystal fiber (DC-PCF) based biosensing approach for early detection of malaria in individuals by monitoring the variations in the red blood cells (RBCs). The proposed DC-PCF comprises four layers of a hexagonal lattice with circular air holes. In the proposed DC-PCF, we have used a central elliptical hole to infiltrate RBCs samples. The proposed study helps to detect various stages of malaria, such as infected RBCs, including the Ring stage, Trophozoite stage, and Schizont stage, by analyzing the changes in the peak wavelength. The proposed refractive index (RI) based sensor is designed to operate within an RI range of 1.33 to 1.41, enabling the detection of malaria. The numerical analysis indicate that our biosensor demonstrates significant sensitivity across different stages, such as 12,00000 nm/RIU for the ring stage, 11,15,263.15 nm/RIU for the trophozoite stage, and 11,13,793.10 nm/RIU for the schizont stage under x-polarization. Similarly, under y-polarization, the sensitivity is observed to be 10,50,000 nm/RIU for the ring stage, 10,54,736.84 nm/RIU for the trophozoite stage, and 10,32,758.62 nm/RIU for the schizont stage. The proposed DC-PCF-based biosensor is highly suitable for biological analysis and early malaria detection because it has a low detection limit and superior sensing performance.

Keywords Malaria detection · Photonic crystal fiber · Terahertz · Biosensor · Transmission curve · Coupling length

1 Introduction

Photonic crystal fiber (PCF) based sensors are suitable for biosensing applications due to their minimal need for mechanical components [1]. They have been recently used in detecting various diseases, including oncovirus [2], cholesterol [3], DNA [4], glucose [5] and malaria [6]. When mosquito bites a human, it injects a parasite in its sporozoite stage into the human tissues, initiating the malarial infection process. Within red blood cells (RBCs), this parasite goes through three stages like ring stage, trophozoite stage and schizont stage. Each stage has different refractive indices (R.I.) for the infected RBCs. The initial cycle of malaria is known as ring stage, during which merozoites enter the RBCs and change into uninucleate trophozoites. Subsequently, multinuclear cells transition from trophozoites to schizonts during the schizont stage. An important parameter for malaria identification is the R.I. difference between normal human RBCs and malaria infected human RBCs [7].

The terahertz (THz) band is increasingly gaining attention as a frequency range for many fields, such as astrophysics, genetics, biomedical research, spectroscopy, sensing, and telecommunications [8–15]. Stretching across 0.1 to 10 THz, this frequency band provides a diverse range of possibilities for various areas of research and technological progress. Compared to conventional fibre sensors, PCF sensors offer increased diversity and standardized optical parameters, fast detection systems, and the ability to regulate optical parameters via precise modifications to the core and the cladding arrangement of the PCF.

In this study, through the observations of human RBCs interacting with the malaria parasites (i.e., Plasmodium falciparum), as they progress through various stages of the intraerythrocytic cycle including ring, trophozoite, and schizont stages, we have proposed a R.I. biosensor using DC-PCF for the malaria detection. It employs finite element

Communicated by Didier Felbacq.

✉ Sonal Singh
sonalsingh@dtu.ac.in

[1] Department of Electronics and Communication Engineering, Delhi Technological University, Shahbad Daulatpur, Main Bawana Road, Delhi 110042, India

Published online: 26 November 2024

analysis in a specially constructed DC-PCF to investigate the mode coupling of dual cores as part of the suggested approach to detect the malaria disease. Notable distinctions were observed when changes in effective R.I., coupling characteristics, and transmission curve of the DC-PCF were compared for normal human RBCs and malaria infected human RBCs. The shift of the peak wavelength in the transmission curve is used for sensitivity calculations of the proposed DC-PCF based biosensor to detect malaria.

2 Sensor design

The design configuration of the proposed THz DC-PCF based biosensor, which is constructed using TOPAS material, is shown in Fig. 1 along with a detailed representation of the hexagonal shape structure. In the DC-PCF, there are two cores referred to as Core A and Core B, and these cores are formed by removing one air hole on each side from the middle elliptical hole. The middle elliptical hole of the DC-PCF is utilized to insert analyte, having different R.I. shown in Table 1, aiming for their detection. It has a 470 µm diameter (D) and a 500 µm pitch (Λ) between neighboring air holes. The DC-PCF maintains an overall air filling fraction (AFF) of 0.94. This configuration, combined with a constant R.I. of 1.53 for the background material (TOPAS), makes the DC-PCF suitable for THz frequency operation with minimal confinement loss, providing manufacturing flexibility [16]. In the proposed configuration, the elliptical hole has a major axis of 1200 µm and a minor axis of 240 µm.

Several fabrication techniques, including capillary stacking, sol–gel, extrusion, and 3D printing, have been reported till date. Sol–gel and capillary stacking are frequently utilized in the fabrication of circular and elliptical holes [17], while asymmetric hole structures (rectangular) have been manufactured successfully by extrusion [18] and 3D printing [19]. Thus, for the fabrication of the suggested DC-PCF sensor structure, capillary stacking and sol–gel techniques are recommended. The method prototype is shown in Fig. 2 and consists of stacking tiny span capillaries with fixed diameters into a bigger diameter glass tube in order to complete the process. The proposed PCF construction is simulated and designed using COMSOL Multiphysics software, which is based on FEM. During simulation, a fine mesh is used, and a parametric sweep is utilized to vary the frequency. The geometrical mesh statistics for the proposed DC-PCF consist of 3,079 edge elements, 344 vertex elements, and 23,644 triangular elements.

Table 1 Refractive index of analyte at different stages

Different stages of RBCs	Refractive index	References
Normal human	1.402	[7, 20, 21]
Infected human at ring stage	1.395	
Infected human at trophozoite stage	1.383	
Infected human at schizont stage	1.373	

The experimental configuration for evaluating the precision of malaria disease identification using the suggested PCF biosensor is illustrated in Fig. 3. A broadband light source (BLS) is employed to propagate optical light over a single-mode fiber (SMF). The Fujikura Splicer splicing technique connects the SMF to the biosensor. The refractive index of various analytes at different stages of RBC is located in the sensing channel. Before taking measurements on new samples, it is necessary to wash the PCF biosensor probes with deionized water. Various transformations take place at various stages of RBC samples when they interact with ligands inside the sensing channel. Using the SMF, the optical spectrum analyzer (OSA) detects focused light. Ultimately, the computer connected to the OSA generates the final spectrum.

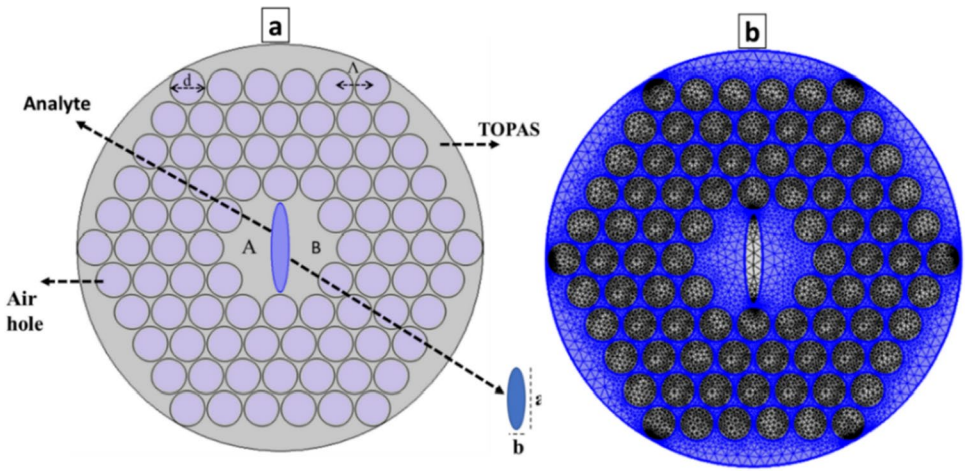

Fig. 1 **a** Configuration of proposed DC-PCF based biosensor **b** Fine mesh statistics

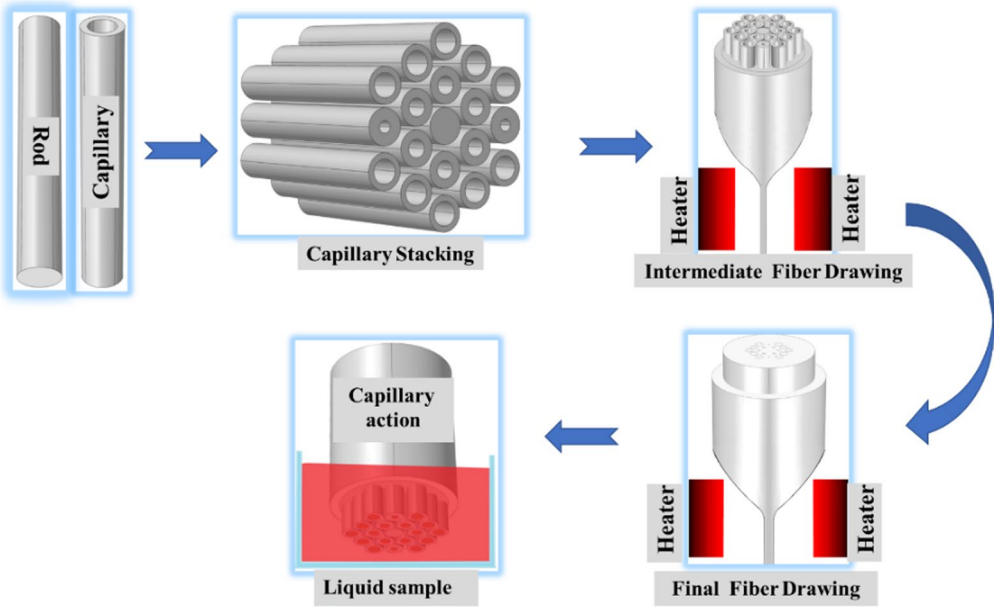

Fig. 2 Fabrication method for the suggested DC-PCF utilizing capillary stacking

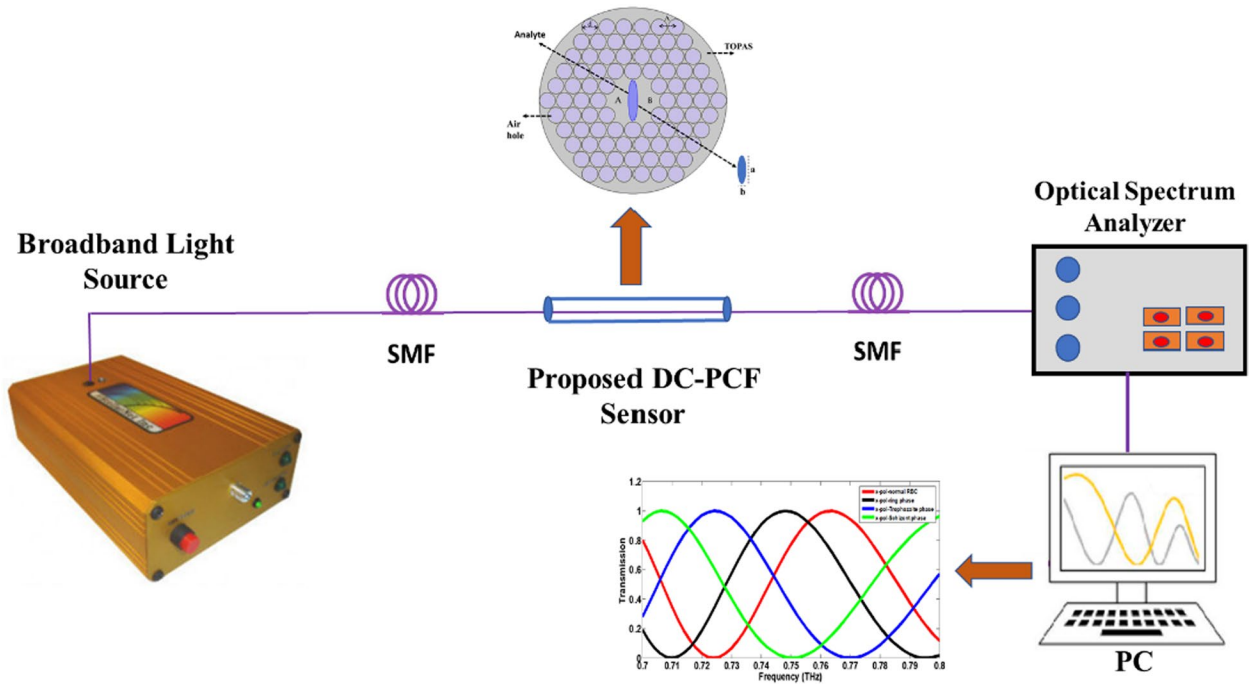

Fig. 3 Experimental setup of the proposed sensor

3 Results and discussion

In DC-PCF sensors, mode coupling refers to the interaction and transfer of optical power between the modes of the two fiber cores. This process is influenced by factors such as core separation, wavelength, and external deviations like pressure, temperature and strain. The effectiveness of mode coupling, measured by the coupling coefficient, is essential for the sensor's performance and sensitivity [22]. Coupling theory states that the guided mode in a DC-PCF comprises of four supermodes. These supermodes are polarized along the X and Y directions, representing odd and even modes, respectively, at a frequency of 0.75 THz.

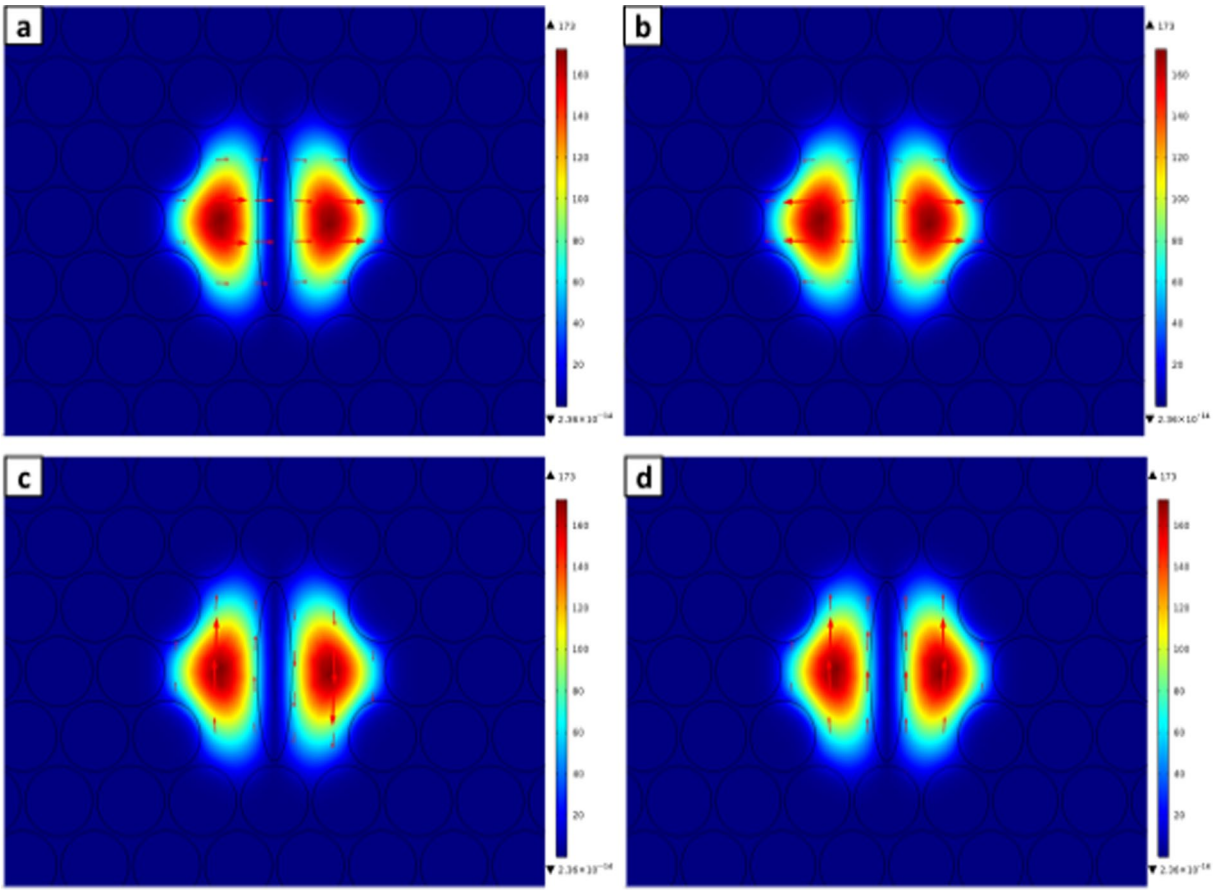

Fig. 4 Distribution of the electric field **a** even x-polarization, **b** odd x-polarization, **c** even y-polarization, and **d** odd y-polarization

Figure 4 illustrates the electric field distribution of the four supermodes. Figure 5 illustrates a three-dimensional (3-D) visualization of the electric field intensity across several modes.

Figure 6 illustrates the change in the effective refractive index difference (Δn_{eo}) for both X and Y-polarized directions, indicating a decrease in Δn_{eo} as the frequency rises.

The coupling length, which represents the minimum length for optimal light transmission through the core of a DC-PCF, is consistent for both X and Y polarizations and can be determined using Eq. (1).

$$L_c = \frac{\pi}{|\beta_e^i - \beta_o^i|} = \frac{\lambda}{2|n_e^i - n_o^i|} \tag{1}$$

where β_e^i and β_o^i represent the propagation constants of the even and odd modes, λ denotes the wavelength [23]. As depicted in Fig. 7, the coupling length exhibits a gradual increase with rising frequency.

In accordance with the mode-coupling theory, the optical power transmitted between the cores of a DC-PCF changes with respect to the length (L) of the PCF, as described by the following expression:

$$I_i(\lambda) = \sin^2\left(\frac{\pi}{\lambda}\Delta n_{i,eo} L\right), with i = x, y \tag{2}$$

where $\Delta n_{i,eo}$, represents the effective refractive index difference [24, 25]. According to Fig. 8 we have observed that the proposed DC-PCF power transmission curve is sinusoidal.

The sensitivity of the proposed biosensor is assessed by analyzing the wavelength shift in the transmission spectra resulting from changes in various analytes. The sensitivity of the proposed DC-PCF for detecting malaria is defined as

$$S_\lambda\left(nmRIU^{-1}\right) = \Delta\lambda_{peak}/\Delta n_i \tag{3}$$

where $\Delta\lambda_{peak}$ denotes the shift in peak wavelength and Δn_i represents the difference in R.I. for normal and different stages of RBCs and $\left(\lambda_{peak} = \frac{\text{speed of light (c)}}{f_{peak}}\right)$ [26, 27]. Using Eq. (3), the presented biosensor achieves a maximum sensitivity across different stages, such as 12,00000 nm/RIU for

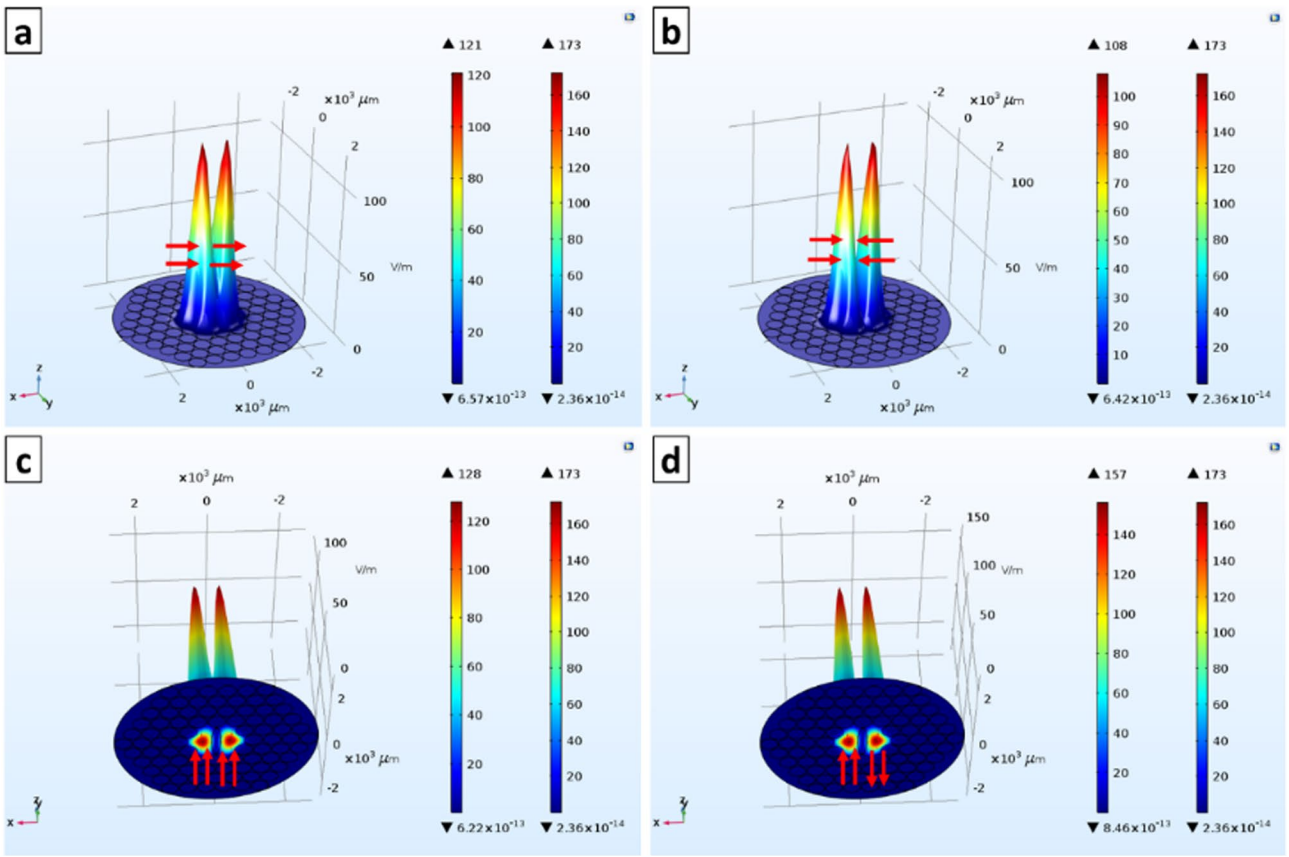

Fig. 5 3-D view of the electric field distribution for four distinct modes: **a** even x-polarization, **b** odd x-polarization, **c** even y-polarization, and **d** odd y-polarization

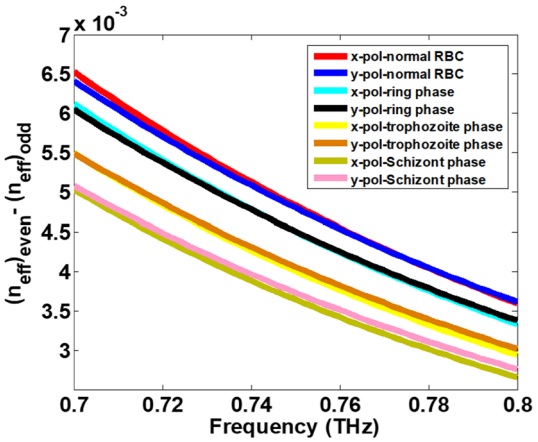

Fig. 6 Variations in Δn_{eo} with respect to frequency for different stages of RBCs

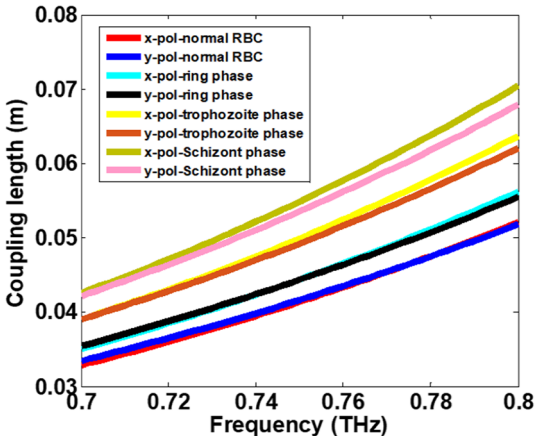

Fig. 7 Variations in coupling length with respect to frequency for different stages of RBCs

the ring stage, 11,15,263.15 nm/RIU for the trophozoite stage, and 11,13,793.10 nm/RIU for the schizont stage under x-polarization. Similarly, under y-polarization, the sensitivity is observed to be 10,50,000 nm/RIU for the ring stage, 10,54,736.84 nm/RIU for the trophozoite stage, and 10,32,758.62 nm/RIU for the schizont stage. Table 2 illustrates a sensitivity comparison between the proposed biosensor and the those already available in the literature [6, 28–30].

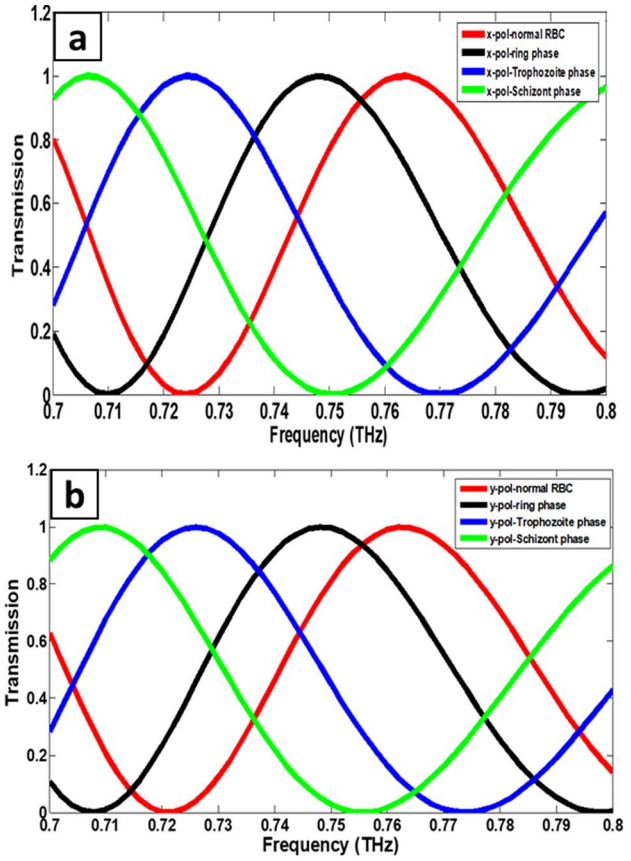

Fig. 8 Transmission curve with respect to frequency for **a** X and **b** Y-polarized light

4 Impact of pitch variation on sensitivity

Figures 9 and 10 demonstrates the pitch variation in the transmission curve of DC-PCF for various stages of malaria infected RBCs, including the Ring stage, Trophozoite stage and Schizont stage. The maximum sensitivity achieved among these stages for three different pitch values under x and y polarization are shown in Fig. 9a–c and Fig. 10a–c, respectively. It can be observed from Fig. 9a–c that under the x polarization, the proposed DC-PCF achieves a maximum sensitivity of 11,17,142.85 nm/RIU at pitch (Λ) = 498 µm, 12,00000 nm/RIU at pitch (Λ) = 500 µm, and 11,35,714.28 nm/RIU at pitch (Λ) = 502 µm, respectively. Similarly, it can be observed from Fig. 10(a-c) that under y-polarization, the proposed DC-PCF achieves a maximum sensitivity of 1,024,137.93 nm/RIU at pitch (Λ) = 498 µm, 10,54,736.84 nm/RIU at pitch (Λ) = 500 µm, and 10,41,034.48 nm/RIU at pitch (Λ) = 502 µm, respectively. Hence, optimizing the pitch demonstrates that the proposed DC-PCF sensor achieves maximum sensitivity at Λ = 500 µm.

5 Conclusion

In this study, a novel biosensing approach to detect the malaria disease is presented by utilizing a DC-PCF technology and employing the FEM with COMSOL software. The shift in peak wavelength between normal and malaria-infected RBCs in the PCF biosensor, transmission spectrum can be used to diagnose malaria. To get the best possible outcomes, the PCF biosensor specifications have been optimized. Numerical analyses reveal that our biosensor exhibits its remarkable sensitivity across different stages, such as 12,00000 nm/RIU for the ring stage, 11,15,263.15 nm/RIU for the trophozoite stage, and 11,13,793.10 nm/RIU for the schizont stage under x-polarization. Likewise, under y-polarization, sensitivities are observed to be 10,50,000 nm/RIU for the ring stage, 10,54,736.84 nm/RIU for the trophozoite stage, and 10,32,758.62 nm/RIU for the schizont stage. Our results demonstrate that the proposed DC-PCF biosensor exhibits superior sensitivity compared to existing biosensors, to the best of our knowledge, and can thus, be considered as the most effective to detect malaria disease.

Table 2 Comparison of the sensitivity between the sensor presented in this study and sensors reported in prior research

References	Sensing application	Sensitivity (nm/RIU)	Background material
[28]	Different cancerous cell identification	2360.12	Silica
[29]	D-shape open-loop PCF temperature sensor	3330	Silica
[30]	D-shaped PCF RI sensor	294.11	Silica
[6]	SPR based biosensor for malaria detection	14,285.71	Silica
Proposed PCF	THz based DC-PCF for malaria detection	12,00000	TOPAS (cyclic olefin copolymer)

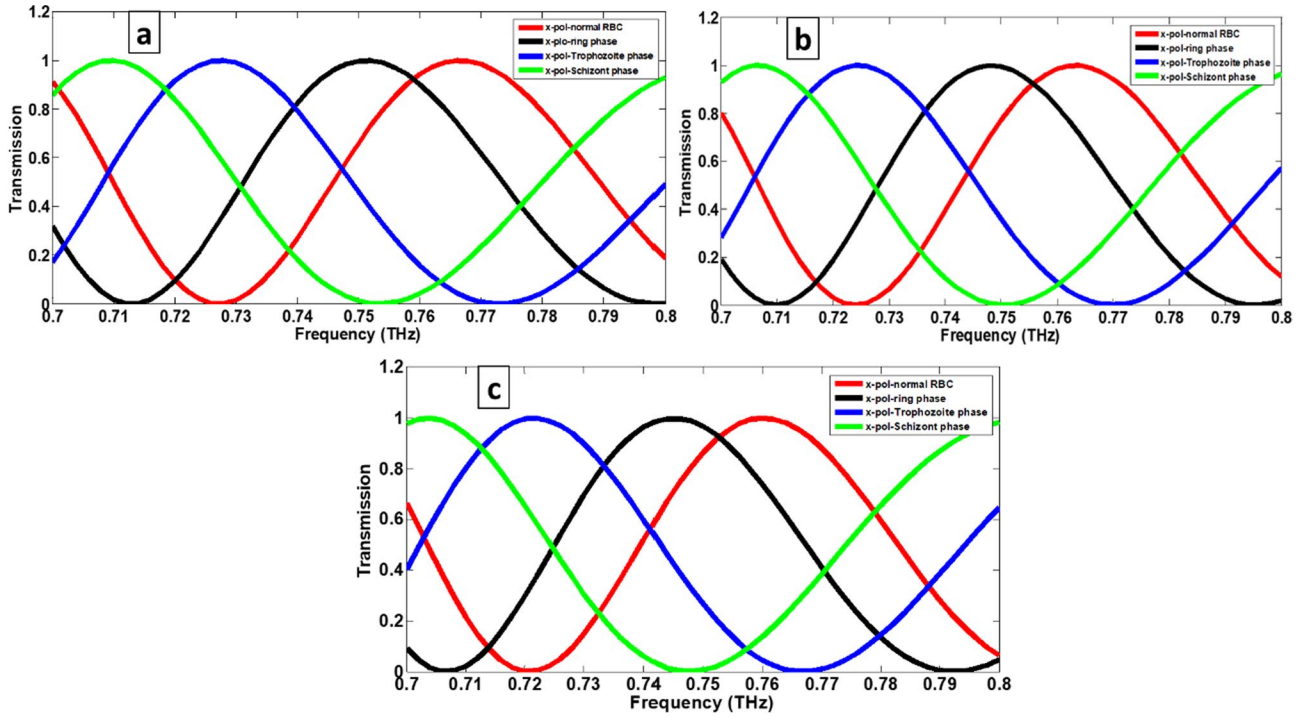

Fig. 9 Transmission curve with different pitch (Λ), for various stages of malaria infected RBCs under x polarization **a** 498 µm **b** 500 µm and **c** 502 µm

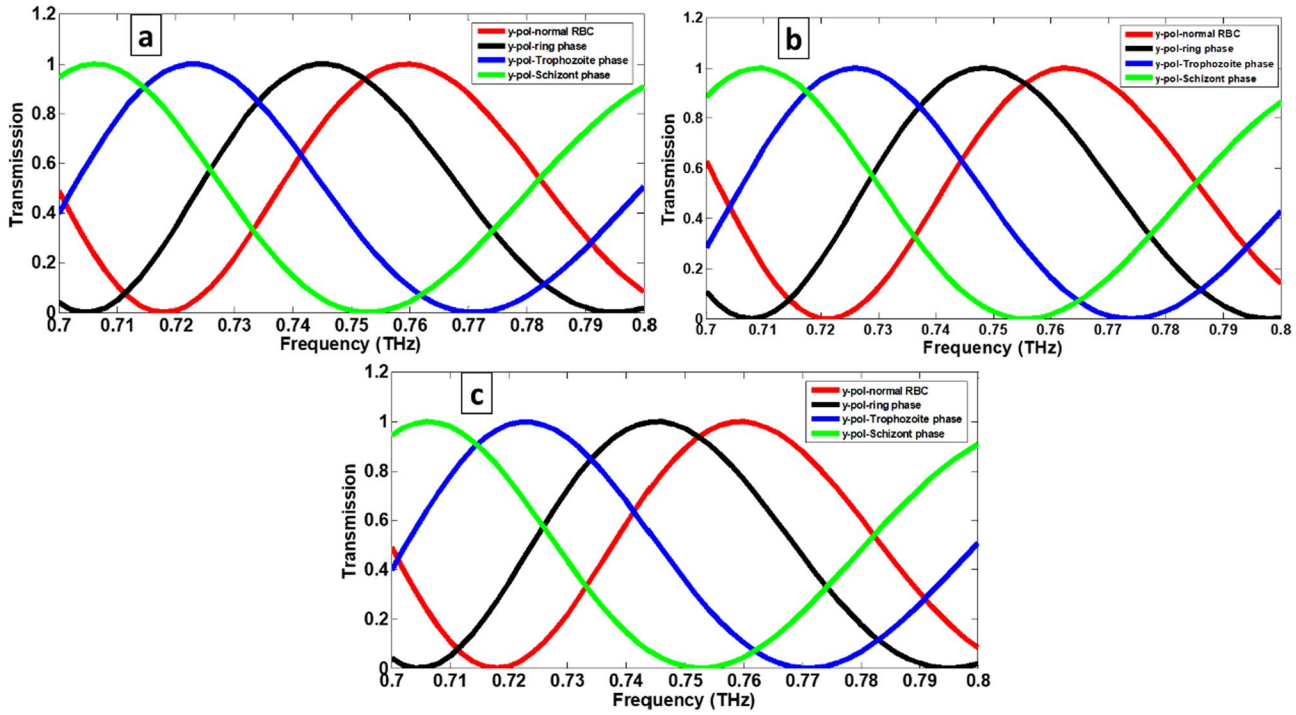

Fig. 10 Transmission curve with different pitch (Λ), for various stages of malaria infected RBCs under y polarization **a** 498 µm **b** 500 µm and **c** 502 µm

Acknowledgements The authors are grateful to the participants who contributed to this research. The authors have not received any funding for this research.

Author contributions Vishal Chaudhary: Methodology, Writing-review & editing. Sonal Singh: Supervision, Writing—original draft, review & editing.

Funding The authors have not received any funding for this research.

Availability of data and materials No datasets were generated or analysed during the current study.

Declarations

Competing interest The authors declare no competing interests.

Human or animal rights No bad Impact on animal.

Consent for publication All authors provide consent for publication.

Consent to Participate All author is agreed to submit the paper in this journal.

References

1. Mahfuz, M., Al Mollah, M.A., Momota, M.R., Paul, A.K., Masud, A., Akter, S., Hasan, M.R.: Highly sensitive photonic crystal fiber plasmonic biosensor design and analysis. Opt. Mater. (Amst) **90**, 315–321 (2019). https://doi.org/10.1016/j.optmat.2019.02.012
2. Rodrigues, L.M., Marinkovic, B.A.: Effects of fused silica addition on thermal expansion, density, and hardness of alumix-231 based composites. Materials (Basel). (2022). https://doi.org/10.3390/ma15103476
3. Soylemez, S., Udum, Y.A., Kesik, M., Gündoıdu Hizliateş, C., Ergun, Y., Toppare, L.: Electrochemical and optical properties of a conducting polymer and its use in a novel biosensor for the detection of cholesterol. Sens. Actuators B Chem. **212**, 425–433 (2015). https://doi.org/10.1016/j.snb.2015.02.045
4. Sun, D., Guo, T., Ran, Y., Huang, Y., Guan, B.O.: In-situ DNA hybridization detection with a reflective microfiber grating biosensor. Biosens. Bioelectron. **61**, 541–546 (2014). https://doi.org/10.1016/j.bios.2014.05.065
5. An, G., Li, S., An, Y., Wang, H., Zhang, X.: Glucose sensor realized with photonic crystal fiber-based Sagnac interferometer. Opt. Commun. **405**, 143–146 (2017). https://doi.org/10.1016/j.optcom.2017.08.003
6. Chaudhary, V.S., Kumar, D., Kumar, S.: Gold-immobilized photonic crystal fiber-based SPR biosensor for detection of malaria disease in human body. IEEE Sens. J. **21**, 17800–17807 (2021). https://doi.org/10.1109/JSEN.2021.3085829
7. Bendib, S., Bendib, C.: Photonic crystals for malaria detection. J. Biosens. Bioelectron. (2018). https://doi.org/10.4172/2155-6210.1000257
8. Ahmed, K., Ahmed, F., Roy, S., Paul, B.K., Aktar, M.N., Vigneswaran, D., Islam, M.S.: Refractive index-based blood components sensing in terahertz spectrum. IEEE Sens. J. **19**, 3368–3375 (2019). https://doi.org/10.1109/JSEN.2019.2895166
9. Bulbul, A.A.M., Jibon, R.H., Das, S.K., Roy, T., Saha, A., Hossain, M.B.: PCF Based formalin detection by exploring the optical properties in THz regime. Nanosci. Nanotechnol. Asia. **11**, 314–321 (2020). https://doi.org/10.2174/2210681210999200525171303
10. Islam, M.S., Faisal, M., Razzak, S.M.A.: Dispersion flattened extremely high-birefringent kagome lattice elliptic core photonic crystal fiber in THz regime. Opt. Quantum Electron. (2019). https://doi.org/10.1007/s11082-019-1744-9
11. Kaur, V., Singh, S.: Design approach of solid-core photonic crystal fiber sensor with sensing ring for blood component detection. J. Nanophotonics **13**, 1 (2019). https://doi.org/10.1117/1.jnp.13.026011
12. Mou, F.A., Rahman, M.M., Islam, M.R., Bhuiyan, M.I.H.: Development of a photonic crystal fiber for THz wave guidance and environmental pollutants detection. Sens. Bio-Sensing Res. (2020). https://doi.org/10.1016/j.sbsr.2020.100346
13. Podder, E., Hossain, M.B., Jibon, R.H., Bulbul, A.A.M., Mondal, H.S.: Chemical sensing through photonic crystal fiber: sulfuric acid detection. Front. Optoelectron. **12**, 372–381 (2019). https://doi.org/10.1007/s12200-019-0903-8
14. Poonam, S., Preeta, S.: Design of photonic crystal-based biosensor for detection of glucose concentration in urine. IEEE Sens. J. **15**, 1035–1042 (2015)
15. Rifat, A.A., Mahdiraji, G.A., Sua, Y.M., Shee, Y.G., Ahmed, R., Chow, D.M., Adikan, F.R.M.: Surface plasmon resonance photonic crystal fiber biosensor: a practical sensing approach. IEEE Photonics Technol. Lett. **27**, 1628–1631 (2015). https://doi.org/10.1109/LPT.2015.2432812
16. Paul, B.K., Ahmed, K., Vigneswaran, D., Ahmed, F., Roy, S., Abbott, D.: Quasi-photonic crystal fiber-based spectroscopic chemical sensor in the terahertz spectrum: design and analysis. IEEE Sens. J. **18**, 9948–9954 (2018). https://doi.org/10.1109/JSEN.2018.2872892
17. Bise, R.T., Trevor, D.J.: Sol-gel derived microstructured fiber: fabrication and characterization. Conf. Opt. Fiber Commun. Tech. Dig. Ser. **3**, 269–271 (2005). https://doi.org/10.1109/ofc.2005.192772
18. Ghazanfari, A., Li, W., Leu, M.C., Hilmas, G.E.: A novel freeform extrusion fabrication process for producing solid ceramic components with uniform layered radiation drying. Addit. Manuf. **15**, 102–112 (2017). https://doi.org/10.1016/j.addma.2017.04.001
19. Ebendorff-Heidepriem, H., Schuppich, J., Dowler, A., Lima-Marques, L., Monro, T.M.: 3D-printed extrusion dies: a versatile approach to optical material processing. Opt. Mater. Express **4**, 1494 (2014). https://doi.org/10.1364/ome.4.001494
20. Liu, P.Y., Chin, L.K., Ser, W., Chen, H.F., Hsieh, C.M., Lee, C.H., Sung, K.B., Ayi, T.C., Yap, P.H., Liedberg, B., Wang, K., Bourouina, T., Leprince-Wang, Y.: Cell refractive index for cell biology and disease diagnosis: past, present and future. Lab Chip **16**, 634–644 (2016). https://doi.org/10.1039/c5lc01445j
21. Park, Y.K., Diez-Silva, M., Popescu, G., Lykotrafitis, G., Choi, W., Feld, M.S., Suresh, S.: Refractive index maps and membrane dynamics of human red blood cells parasitized by Plasmodium falciparum. Proc. Natl. Acad. Sci. U. S. A. **105**, 13730–13735 (2008). https://doi.org/10.1073/pnas.0806100105
22. Huang, W.-P.: Coupled-mode theory for optical waveguides: an overview. J. Opt. Soc. Am. A **11**, 963 (1994). https://doi.org/10.1364/josaa.11.000963
23. Chaudhary, V., Singh, S.: Hexagonal lattice twin core photonic crystal fiber based chemical sensor. Proc. 10th Int. Conf. Signal Process. Integr. Networks, SPIN 2023. 164–167 (2023). https://doi.org/10.1109/SPIN57001.2023.10117365
24. Chaudhary, V., Singh, S.: Twin core photonic crystal fiber based temperature sensor with improved sensitivity over a wide range of temperature. Opt. Quantum Electron. (2023). https://doi.org/10.1007/s11082-022-04304-4

25. Chaudhary, V., Singh, S.: Highly sensitive twin core photonic crystal fiber for hazardous cancer cell detection in THz frequency regime. Opt. Quantum Electron. (2023). https://doi.org/10.1007/s11082-023-05462-9
26. Jabin, M.A., Ahmed, K., Rana, M.J., Paul, B.K., Islam, M., Vigneswaran, D., Uddin, M.S.: Surface plasmon resonance based titanium coated biosensor for cancer cell detection. IEEE Photonics J. (2019). https://doi.org/10.1109/JPHOT.2019.2924825
27. Chaudhary, V., Kumar, D.: Design and analysis of refractive index sensor based on dual-core photonic crystal fiber (DC-PCF) with rectangular air hole lattice structure. Lect. Notes Electr. Eng. **546**, 207–213 (2020). https://doi.org/10.1007/978-981-13-6159-3_22
28. Panda, A., Puspa Devi, P.: Photonic crystal biosensor for refractive index based cancerous cell detection. Opt. Fiber Technol. (2020). https://doi.org/10.1016/j.yofte.2019.102123
29. Meng, F., Wang, H., Fang, D.: Research on D-shape open-loop PCF temperature refractive index sensor based on SPR effect. IEEE Photonics J. (2022). https://doi.org/10.1109/JPHOT.2022.3166822
30. Azab, M.Y., Hameed, M.F.O., Mahdiraji, G.A., Adikan, F.R.M., Obayya, S.S.A.: Experimental and numerical characterization of a D-shaped PCF refractive index sensor. Opt. Quantum Electron. (2022). https://doi.org/10.1007/s11082-022-04232-3

Publisher's Note Springer Nature remains neutral with regard to jurisdictional claims in published maps and institutional affiliations.

Springer Nature or its licensor (e.g. a society or other partner) holds exclusive rights to this article under a publishing agreement with the author(s) or other rightsholder(s); author self-archiving of the accepted manuscript version of this article is solely governed by the terms of such publishing agreement and applicable law.

Environ Monit Assess (2024) 196:1255
https://doi.org/10.1007/s10661-024-13406-3

RESEARCH

Developing novel spectral indices for precise estimation of soil pH and organic carbon with hyperspectral data and machine learning

Shagun Jain · Divyashikha Sethia · Kailash Chandra Tiwari

Received: 22 July 2024 / Accepted: 12 November 2024
© The Author(s), under exclusive licence to Springer Nature Switzerland AG 2024

Abstract Accurate soil pH and soil organic carbon (SOC) estimations are vital for sustainable agriculture, as pH affects nutrient availability, and SOC is crucial for soil health and fertility. Hyperspectral imaging provides a faster, non-destructive, and economical alternative to standard soil testing. The study utilizes imaging spectroscopic data from the Africa Soil Information Service (AfSIS) and Land Use and Coverage Area Frame Survey (LUCAS-2009) hyperspectral datasets, capturing spatially distributed spectral information. Machine learning (ML) approaches using high-dimensional spectral bands can be computationally expensive, while those using spectral indices are typically limited to multispectral data. This study addresses these challenges by comparing soil pH and SOC prediction using ML models, with both existing spectral indices and individual hyperspectral bands as input features. Results demonstrate that hyperspectral bands outperform existing indices in predictive accuracy, with R^2 values ranging from 0.8 to 0.94 for both soil pH and SOC. To further enhance prediction performance, this study proposes novel spectral indices-soil pH index (SPI) and soil organic carbon index (SOCI)-specifically designed for hyperspectral data using principal component analysis (PCA) and artificial neural networks (ANN). The proposed SPI and SOCI indices address multicollinearity issues and high dimensionality in raw spectral bands, significantly improving predictive accuracy. The SPI and SOCI indices achieve R^2 values of 0.86 for AfSIS soil pH, 0.945 for LUCAS-2009 soil pH, 0.952 for AfSIS SOC, and 0.963 for LUCAS-2009 SOC. These results show that the proposed spectral indices provide a practical solution for precision agriculture, enhancing soil pH and SOC estimations.

Keywords Machine learning · Spectral indices · Soil pH · Soil organic carbon · Hyperspectral · Sustainable agriculture

S. Jain (✉) · D. Sethia
Department of Software Engineering, Delhi Technological University, Delhi, India
e-mail: shagunjain191172@gmail.com

D. Sethia
e-mail: divyashikha@dtu.ac.in

K. C. Tiwari
Multidisciplinary Centre of Geoinformatics, Delhi Technological University, Delhi, India
e-mail: kcchtphd@gmail.com

Introduction

Maintaining healthy soil is paramount for achieving the sustainable development goals (SDGs) set by the United Nations (Awais et al., 2023). These goals encompass crucial targets like ensuring food security (SDG 2: Zero Hunger), mitigating climate change (SDG 13: Climate Action), and promoting healthy ecosystems (SDG 15: Life on Land) (Veenstra et al., 2024). Soil pH and organic carbon content are pivotal indicators of soil health, influencing plant growth, nutrient availability, and overall ecosystem function-

Published online: 26 November 2024

ing (Dlamini et al., 2016). Soil pH regulates nutrient availability and microbial activity, ensuring that plants can access essential nutrients while maintaining a healthy microbial ecosystem (Guo et al., 2022). This balance is crucial for optimal plant growth and nutrient cycling. Soil organic carbon (SOC), on the other hand, improves soil structure, enhancing water retention and aeration, which supports robust root development and plant health (Dlamini et al., 2016; Odebiri et al., 2021). Both significantly influence soil quality, agricultural sustainability, and environmental health (Maurya et al., 2020). At the same time, traditional soil testing methods are labor-intensive, time-consuming, and costly (Padarian et al., 2019). These limitations pose a significant barrier to large-scale soil monitoring and implementing sustainable land management practices, especially in developing countries with limited resources (Jain et al., 2024).

Machine learning (ML) models, combined with hyperspectral data, help overcome these limitations by analyzing vast amounts of data quickly and accurately. By leveraging advanced algorithms and the rich information provided by hyperspectral imaging, ML models can predict soil properties with high precision, reducing the need for expensive and time-consuming field sampling (Yu et al., 2020). Integrating sensing data with ML models is crucial for enhancing the accuracy and efficiency of environmental assessments. Soil analysis utilizes two primary types of sensing data: remote sensing and proximal sensing data. Remote sensing and proximal sensing involve gathering data about objects or surfaces, but they differ in the distance from the target and the methods used (Pusch et al., 2021). Remote sensing is ideal for large-scale, broad observations from a distance, while proximal sensing offers detailed, localized data from close-range measurements (Valloo et al., 2023). The study employs remote sensing hyperspectral data to estimate soil properties. This technology facilitates real-time monitoring and decision-making, allowing for more efficient use of resources and promoting sustainable land management practices, even in resource-constrained settings (Mahmood et al., 2024).

However, effectively utilizing this high-dimensional data presents significant challenges, including multicollinearity and high dimensionality, which can degrade the performance of predictive models. The need for rapid, non-destructive, and cost-effective soil analysis methods has propelled the exploration of hyperspectral imaging (Angelopoulou et al., 2023). Although raw spectral bands offer comprehensive data, their direct use in ML models often results in suboptimal outcomes due to data redundancy (Yuvaraj et al., 2022).

To overcome these challenges, researchers investigate spectral indices as a solution to these challenges in predicting soil properties. Utilizing these metrics can enhance data quality and decrease redundancy, increasing the efficacy of ML models. Spectral indices, derived from mathematical combinations of spectral bands, have emerged as a solution, highlighting relevant features, reducing dimensionality, and enhancing predictive power (Diaz-Gonzalez et al., 2022). This technology has been accepted in other domains, such as (Zhang et al., 2021) proposed a new spectral index for the prediction of wheat leaf water content, and Wu et al. (2019) proposed a new spectral index for the detection of cadmium-induced stress in rice. Both studies used hyperspectral data for regional scale prediction in the agriculture sector. These previous studies (Wu et al., 2019; Zhang et al., 2021) indicate that the development of spectral indices tailored specifically to soil properties greatly enhances the precision and reliability of soil assessments, enabling more effective monitoring and management of soil health.

Prior studies (Babbar et al., 2022; Dhiman et al., 2023; Guo et al., 2022; Yuvaraj et al., 2022; Zayani et al., 2023) have made significant strides in predicting soil properties using existing spectral indices as input in ML techniques. However, these previous studies have not developed novel spectral indices for soil properties. Recently, work by Gulhane et al. (2023) has introduced new indices using multispectral data to predict soil pH, iron, and phosphorous. However, this study focuses solely on multispectral data and overlooks the potential benefits of hyperspectral data. While multispectral data captures a limited number of discrete wavelengths, typically ranging from three to ten, hyperspectral data collects information across hundreds of continuous wavelengths (Yokoya et al., 2017). It allows hyperspectral data to provide a more detailed spectral profile, enhancing soil property estimation by detecting subtle variations that multispectral data may miss.

In contrast, the study proposed by Zhang et al. (2018) demonstrated the effectiveness of hyperspectral imagery. It used existing indices as input in the partial least square regression (PLSR) model for estimating soil pH with R^2 0.35 and root mean square error (RMSE) 0.26. This RMSE indicates a strong predictive performance, reflecting the model's capability to cap-

ture spatial variability in soil pH accurately. The unique spectral signatures captured by hyperspectral imaging can provide more detailed insights into soil composition and health, which are crucial for accurate soil pH and SOC estimation.

Despite the potential of spectral indices to enhance soil property estimations, existing indices may need to fully capture the complex spectral features necessary for accurate soil pH and organic carbon estimation (Pouladi et al., 2023). Often designed for vegetation or other applications, traditional indices may not be directly applicable or optimal for soil analysis. According to existing literature, researchers have yet to extensively explore the integration of various spectral indices and their combined influence on predictive models. Nonetheless, optimizing spectral indices for soil property estimation remains an area ripe for research. Hence, there is a pressing need to develop novel spectral indices specifically tailored for soil properties, leveraging advanced ML techniques to improve predictive accuracy.

Related work

This study utilizes the Africa Soil Information Service (AfSIS) (Leenaars, 2013) and Land Use and Coverage Area Frame Survey (LUCAS-2009) (Fernández-Ugalde et al., 2020) hyperspectral datasets to estimate soil pH and SOC. Both these datasets are point-based data in a processed form that focuses on large-scale soil mapping across Africa and Europe. It utilizes remote sensing and ground-based data to support sustainable land management. It offers extensive imaging spectroscopic data, capturing a wide range of spectral signatures across various wavelengths. This data allows for the detailed analysis of soil properties by detecting subtle differences in reflectance patterns, which correspond to variations in soil composition and nutrient levels. The study selects the AfSIS and LUCAS-2009 datasets for their high-quality hyperspectral data and extensive coverage, crucial for accurately modelling soil properties. Additionally, these datasets are publicly accessible and widely used, allowing for meaningful comparisons with existing research and enhancing the robustness of new findings. Previous research involving these datasets focused on applying various ML techniques. This section reviews the earlier studies that have used these datasets, highlighting methodologies and outcomes.

Table 1 compares recent studies on soil pH estimation using ML methods. Zhao et al. (2023) employed convolutional neural networks (CNNs) and multitask learning networks, achieving R^2 values of 0.85 and RMSE 0.53 for LUCAS-2009 and R^2 0.81, RMSE 0.41 for AfSIS. Their approach showcases the potential of deep learning (DL) for accurate pH estimation, emphasizing computational complexity. Akande et al. (2022) applied support vector regression (SVR), achieving an R^2 of 0.84, RMSE 0.36 on AfSIS, highlighting challenges in model generalizability across varied soil compositions. Zhong et al. (2021) demonstrated deep convolutional networks (DCNNs) with an impressive R^2 of 0.93 and RMSE 0.33 on LUCAS-2009, emphasizing their capability to capture complex spectral patterns relevant to pH variability. These studies underscore advancements in predictive modelling while signalling opportunities for improving model robustness and addressing challenges in generalizability across diverse soil datasets. Their approach highlights the necessity to integrate spectral indices for enhanced performance.

Table 1 Previous studies on soil pH estimation using AfSIS dataset and LUCAS-2009 dataset

Previous work	Model	Results	Research focusses
Zhao et al. (2023)	CNN	R^2: 0.81 and RMSE: 0.41 for AfSIS, R^2: 0.85 and RMSE: 0.53 for LUCAS-2009	Proposed a method for soil property estimation using deep learning and multitask learning networks.
Akande et al. (2022)	SVR	R^2: 0.84 and RMSE: 0.36 for AfSIS	Evaluated various ML algorithms for predicting soil properties.
Zhong et al. (2021)	DCNN	R^2: 0.93 and RMSE: 0.33 for LUCAS-2009	Demonstrated the potential of deep convolutional neural networks (DCNNs) for accurately predicting soil properties.

Table 2 summarizes studies conducted across recent years focusing on SOC estimation using ML models applied to AfSIS and LUCAS-2009 datasets. Zhao et al. (2022, 2023) employed CNNs and attention-based CNN ensembles, respectively, emphasizing computational complexity and the need for integrating spectral indices to enhance model performance. Akande et al. (2022) evaluated SVR, highlighting challenges in model generalizability and the importance of spectral indices integration. Zhao et al. (2021) integrated CNN with quantile regression for robust SOC estimation, addressing similar challenges in computational complexity and spectral indices utilization. Zhong et al. (2021) demonstrated the efficacy of DCNNs in achieving high accuracy for SOC estimation yet recognized limitations in model generalizability and spectral indices integration across datasets.

From Tables 1 and 2, it is concluded that prior research has yet to explore the use of spectral indices on these datasets, emphasizing the novelty and significance of this approach. Previous studies like (Babbar et al., 2022; Dhiman et al., 2023; Guo et al., 2022; John et al., 2020; Kalambukattu et al., 2018; Kumar et al., 2018; Yuvaraj et al., 2022; Zayani et al., 2023) have predominantly focused on utilizing existing spectral indices for predicting soil pH and SOC. These studies have primarily relied on multispectral data while neglecting hyperspectral data. In contrast, Zhang et al. (2018) stands out as their approach integrated hyperspectral imagery with environmental variables, revealing significant spatial variability and a decline in soil pH over time. Importantly, Zhang et al. (2018) did not develop new indices but instead leveraged existing spectral features for their estimations. Conversely, Gulhane et al. (2023) focused solely on creating new indices using multispectral imagery.

These studies collectively highlight significant advancements in ML methodologies to estimate soil pH and SOC using spectral bands. However, they underscore the effectiveness of existing spectral indices in improving estimation accuracy across different datasets. Most investigations predominantly relied on multispectral data and have not innovated new indices. While these studies contribute substantially to soil property estimation, there remains a critical need for future research to develop novel spectral indices and integrate hyperspectral data. It is crucial to enhance the understanding of spectral indices' role in predicting soil nutrients for refining agricultural practices and strengthening environmental management strategies.

Technical background of spectral indices

A spectral index is a mathematical equation that integrates pixel values from many spectral bands in a spectral image and is used to assess specific properties or characteristics of the target. Table 3 outlines the previous studies on soil pH and SOC estimation using spectral indices, highlighting key findings and the limitations identified in each study. (Tran et al., 2022).

Table 2 Previous studies on SOC estimation using AfSIS dataset and LUCAS-2009 dataset

Previous work	Model	Results	Research focusses
Zhao et al. (2023)	CNN	R^2: 0.936 and RMSE: 0.29 for AfSIS, R^2: 0.934 and RMSE: 23.72 for LUCAS-2009	Proposed a method for soil property estimation using deep learning and multitask learning networks.
Zhao et al. (2022)	Squeeze and excitation CNN	R^2: 0.83 and RMSE: 0.276 for AfSIS, R^2: 0.935 and RMSE: 23.565 for LUCAS-2009	Introduced an attention-based CNN ensemble with improved feature weighting for SOC estimation.
Akande et al. (2022)	SVR	R^2: 0.88 and RMSE: 0.391 for AfSIS	Evaluated various ML algorithms for predicting soil properties.
Zhao et al. (2021)	CNN with quantile regression	R^2: 0.92 and RMSE: 0.301 for AfSIS, R^2: 0.93 and RMSE: 26.667 for LUCAS-2009	Integrated CNN with quantile regression for accurate SOC estimation.
Zhong et al. (2021)	DCNN	R^2: 0.95 and RMSE: 19.837 for LUCAS-2009	Demonstrated the potential of Deep convolutional neural networks (DCNNs) for accurately predicting soil properties.

Table 3 Previous studies that work on soil pH and SOC estimation through spectral Indices I1-NDVI, I2-EVI, I3-SAVI, I4-RVI, I5-NDWI, I6-RI, I7-CI, I8-ARVI, I9-NPCRI, I10-RDVI, I11-SCI, I12-NDMI, I13-SAVI, I14-NDSI, I15-BI, I16-BSI, I17-NDBI, I18-Clay Index, I19-Iron Index, I20-LST, I21-VTCI, I22-BI, I23-WI, I24-GI, I25-HI, (HS-Hyperspectral, MS-Multispectral)

Soil pH						
Previous work	HS/MS	Existing spectral indices	Model	Results (R^2)	Research focusses	Limitation
Gulhane et al. (2023)	MS	Creation of new soil pH index	MLP and ISO cluster unsupervised classification algorithm	0.87	Creating new indices of soil pH using multispectral data.	1. Only considers multispectral data.
Guo et al. (2022)	MS	I1, I2, I3, I4, I5, I6	XGBoost	0.68	Using SVM-RFE for selecting key environmental variables significantly enhances the accuracy of ML models in predicting soil pH.	1. Only considers multispectral data. 2. New indices, not developed.
Babbar et al. (2022)	MS	I1, I2, I8, I9, I10, I11, I12, I13	Multilinear Regression analysis	0.91	Finding significant correlations between soil nutrients and various spatial indices.	1. Only considers multispectral data. 2. New indices, not developed.
Yuvaraj et al. (2022)	MS	I1, I8, I4, I5, I6, I7, I14,	Linear Regression	0.62	Evaluated how multispectral images can assess dynamic soil properties using spectral indices and correlation models.	1. Only considers multispectral data. 2. New indices, not developed.
Zhang et al. (2018)	HS	I1, I2, I4, I5, I8	PLSR	0.35	Utilized hyperspectral imagery, along with environmental variables, to predict soil pH, revealing significant spatial variability and a decline in soil pH over time.	1. New indices, not developed.

Researchers categorize four spectral indices for soil nutrient estimation, which are as follows:

- ***Vegetation indices (VI):*** It evaluates multiple elements of vegetation, including its health, density, and physiological features. It includes indices such as the normalized difference vegetation index (NDVI), enhanced vegetation index (EVI), normalized difference water index (NDWI), atmospherically resistant vegetation index (ARVI), and ratio vegetation index (RVI). Previous studies like Babbar et al. (2022), Dhiman et al. (2023), Guo et al. (2022), Yuvaraj et al. (2022), Zayani et al. (2023), Zhang et al. (2018) used vegetation indices for the estimation of soil nutrients.

Table 3 continued

SOC						
Previous work	HS/MS	Existing spectral indices	Model	Results(R^2)	Research focusses	Limitation
Zayani et al. (2023)	MS	I1, I8, I12, I13, I15, I16	DNN	0.65	Analyzed spectral measurements to improving SOC prediction accuracy by including soil moisture and laboratory indices.	1. Only considers multispectral data. 2. New indices, not developed.
Dhiman et al. (2023)	MS	I1, I2, I5, I8, I13, I17	GB	0.97	Estimated soil nutrients and textures, revealing that raw data proved more effective than atmospheric correction.	1. Only considers multispectral data. 2. New indices, not developed.
Babbar et al. (2022)	MS	I1, I2, I8, I9, I10, I11, I12, I13	Multilinear regression analysis	0.97	Finding significant correlations between soil nutrients and various spatial indices.	1. Only considers multispectral data. 2. New indices, not developed.
John et al. (2020)	MS	I1, I4, I12, I13, I17, I18, I19, I20	RF	0.68	Indicating the importance of soil nutrient indicators and topographic features in spatial prediction.	1. Only considers multispectral data. 2. New indices, not developed.
Kumar et al. (2018)	MS	I1, I21, I22, I23, I24	Regression Kriging	0.53	Regression kriging mapped SOC using satellite- derived variables, presenting correlations with indices like NDVI.	1. Only considers multispectral data. 2. New indices, not developed.
Kalambukattu et al. (2018)	MS	12, I8, I21, I25	ANN	0.83	Employed ANN and satellite data to map soil nutrients.	1. Only considers multispectral data. 2. New indices, not developed.

- ***Soil indices (SI):*** It evaluates the diverse properties and characteristics of soil in a certain region. It includes indices such as the soil composition index (SCI) and the bare soil index (BSI). Previous studies like Babbar et al. (2022), Zayani et al. (2023) used these indices for the estimation of soil nutrients.
- ***Water indices (WI):*** These indices help assess the water content in the soil, which is crucial for agricultural practices, irrigation management, and environmental monitoring, for ex - moisture stress index (MSI). The previous study (Febereiro et al., 2022) used water indices to estimate soil nutrients.
- ***Temperature and thermal indices (TTI):*** It includ es indices, such as land surface temperature (LST) and radiation index (RI), which play a crucial role in environmental studies, climate monitoring, and resource management. Previous studies like (John

et al., 2020; Kumar et al., 2018; Zayani et al., 2023) used these indices to estimate soil nutrients.

Main contribution of the paper

This study aims to address the challenges in existing studies by developing new spectral indices to enhance the precision of soil pH and SOC estimation using hyperspectral data and ML. The main contributions of this study are:

1. To evaluate and compare spectral bands and existing spectral indices across different categories employing a range of ML models using AfSIS and LUCAS-2009 hyperspectral datasets.
2. To investigate different feature selection methods for identifying optimal wavelengths for developing new spectral indices for soil pH and SOC.
3. To propose, design, and develop new spectral indices, the soil pH index (SPI) and soil organic carbon index (SOCI), for estimating soil pH and SOC using hyperspectral data. Additionally, to test, validate, and compare these indices with existing ML schemes.

By addressing the challenges associated with high-dimensional spectral data and developing effective spectral indices, this study aims to advance the field of soil property estimation, contributing to more efficient and sustainable agricultural practices.

Layout of the paper

The paper is structured as follows: The "Materials and methods" section describes the methodology, including data collection, spectral index development, and ML model implementation. The "Results" section presents the experimental results and discusses the comparative performance of various spectral indices. The "Discussion" section provides the proposed indices' advantages and limitations and practical implications. Finally, the "Conclusion" section concludes the paper, summarizing the key findings and outlining future research directions.

Materials and methods

The section outlines the technique employed in this study, which involves a series of crucial steps to guarantee a thorough investigation and comparison of spectral indices. Figure 1 shows the two discrete objectives, each symbolizing a critical component of the approach. The detailed steps of these two objectives are as follows:

- The first objective begins with the process that involves reading, cleaning, and normalizing the data.
- Then, spectral bands and various preexisting spectral indices related to vegetation, soil, water, temperature, and thermal properties are analyzed using

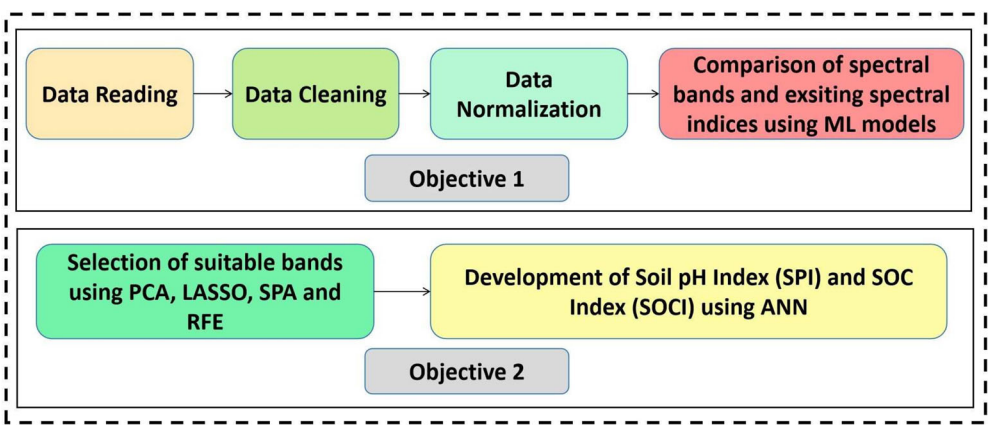

Fig. 1 Research methodology flowchart for spectral indices

Table 4 Soil dataset detail

Dataset	Region	No. of input spectral features	No. of soil samples	Spectral range
AfSIS (Leenaars, 2013)	Africa	3578	1157	1333 to 16673 nm
LUCAS-2009 (Fernández-Ugalde et al., 2020)	23 Euro-pean countries	4200	19036	400 to 2499 nm

several ML models to assess performance in different environmental conditions.

- Employ feature selection techniques principal component analysis (PCA), least absolute shrinkage and selection operator (LASSO), successive projection algorithm (SPA), and recursive feature elimination (RFE) to identify key spectral bands, comparing their advantages for reliable estimation.
- Subsequently, use an artificial neural network (ANN) to create novel spectral indicators specifically designed for soil pH and SOC.

Dataset description

This study confirms the effectiveness of the suggested approach by employing AfSIS (Leenaars, 2013) and LUCAS-2009 (Fernández-Ugalde et al., 2020) as validation sources. These datasets are foundational hyperspectral resources supporting large-scale soil mapping efforts across Africa and Europe. They provide point-based data essential for assessing soil properties. With a comprehensive range of spectral signatures across various wavelengths, these datasets enable detailed analysis of soil composition by capturing subtle differences in reflectance patterns, reflecting variations in nutrient levels and soil structure. AfSIS and LUCAS-2009 are valued for their high-quality imaging spectroscopic data and broad geographic coverage, offering extensive support for sustainable land management research. Table 4 provides a comprehensive summary of the datasets used in this work for predicting soil nutrient levels. Figure 2 displays the spatial arrangement of LUCAS-2009 and AfSIS. The map illustrates the positions of the samples, with each data point in this diagram representing a sample. By analyzing the spa-

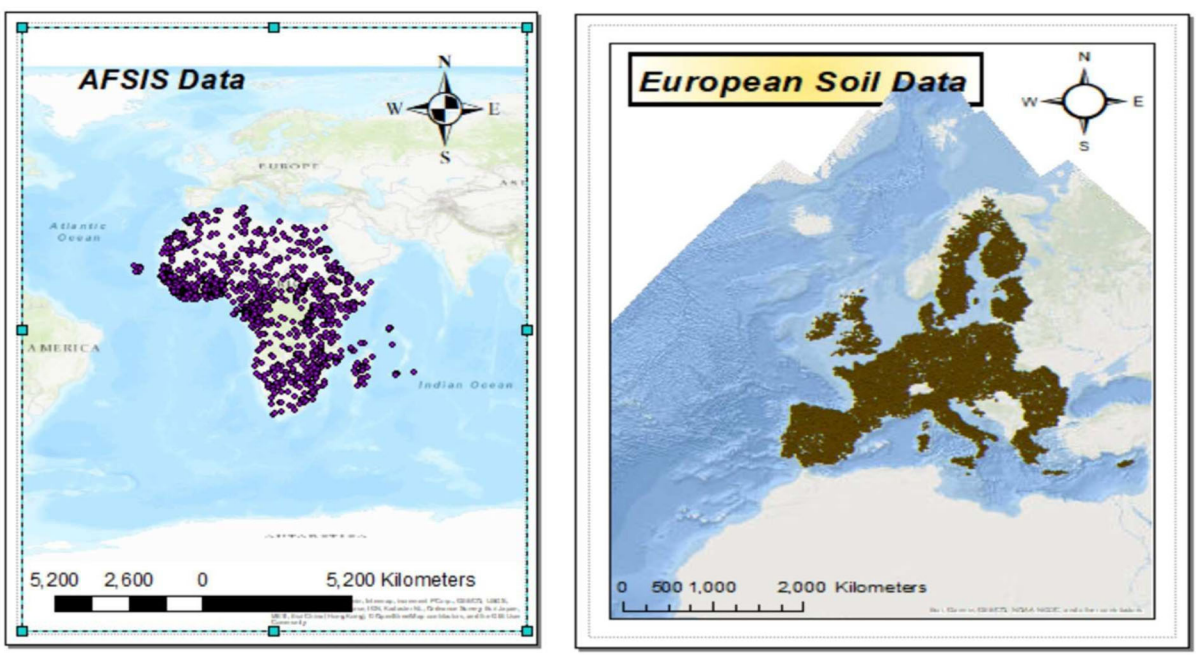

Fig. 2 Geographical arrangement of LUCAS-2009 and AfSIS Data

tial distribution map, observers can identify patterns or clusters of data points in different areas, providing valuable information on the geographical diversity of the samples. This information facilitates comprehension of the variety and peculiarities of the spectral qualities or other variables represented in the datasets throughout the study area.

Computational setup and software

This section outlines the data sources, software tools, and computational environment utilized to ensure reproducibility and clarity in the analysis and modelling process. Table 5 summarizes the key components of the computational setup used in this study. Python serves as the primary programming language for data processing and analysis, while ArcGIS provides robust geospatial analysis capabilities. The analysis is conducted in Google Colab, offers a cloud-based environment, and operates on a Windows system, facilitating seamless integration of tools and data.

Data preprocessing

This study applies comprehensive preprocessing to the hyperspectral data in the comma-separated value (CSV) format, a critical step to ensure the accuracy and reliability of subsequent analyses. Data preprocessing is vital as it transforms raw data into a clean and consistent format, making it suitable for further study and ML applications (Zelaya, 2019). For this work, data preprocessing includes cleaning and normalizing the data.

Data cleaning

Initially, the process addresses any inconsistencies, missing values, and outliers through data cleaning. This step involved several sub-processes: removing rows or columns with excessive missing values, imputing missing data points using appropriate statistical methods, correcting erroneous entries, and standardizing the format to maintain uniformity. Data cleaning ensures the dataset is free from anomalies that could distort the analytical results (Chu et al., 2016).

Data normalization

Following data cleaning, the dataset is normalized using the Standard Scaler. This technique normalizes the averages and standard deviations of the characteristics to 0 and 1, respectively Reddy et al. (2023). Ensuring consistent scales is crucial for the algorithm to efficiently learn patterns and correlations in hyperspectral data, where each feature corresponds to a distinct wavelength band. The normalization method enhances the overall stability and effectiveness of the model in managing hyperspectral datasets. Equation 1 demonstrates the calculation of the standard scalar.

$$z = \frac{x - \mu}{\sigma} \tag{1}$$

In this context, z represents the scaled data, x represents the data that needs to be scaled, μ represents the mean of the training samples, and σ represents the standard deviation of the training samples.

Experimental framework

This section presents the experimental framework, which consists of two objectives, as depicted in Fig. 1.

Objective 1: comparison of spectral bands and existing spectral indices with ML models

This study's first objective is to assess each spectral indicator's efficacy in various ML algorithms, empha-

Table 5 Data sources and software tools for analysis

Component	Software/System used
Programming Language	Python
Geospatial Software	ArcGIS
Computing Environment	Google Colab
Operating System	Windows

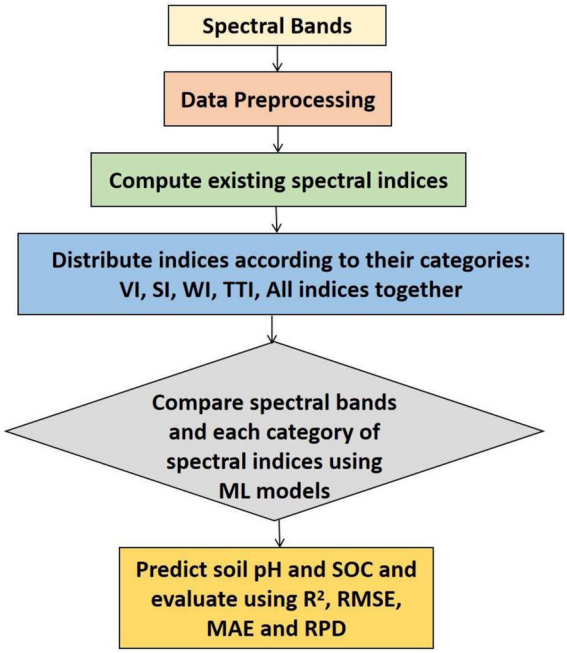

Fig. 3 Flowchart for comparing spectral bands and existing spectral indices

sizing the advantages and constraints of each method in forecasting soil pH and SOC. Before proposing new spectral indices, comparing spectral bands with existing spectral indices for soil pH and SOC estimation is crucial. It establishes a baseline and identifies current limitations. Figure 3 shows the flowchart of comparing spectral bands and existing spectral indices, where the process begins with data preprocessing, followed by computing and categorizing existing indices as mentioned in the "Technical background of spectral indices" section (VI, SI, WI, TTI, and all index combined). The study compares the performance of ML models for each category to predict soil pH and SOC. This thorough evaluation benchmarks current indices, highlights their strengths and weaknesses, and guides the development of more effective new indices.

The list of ML models used to asses these spectral indices for soil pH and SOC estimation are as follows:

- ***Partial least square regression (PLSR):*** It is a statistical technique for identifying the underlying relationships between two matrices, specifically the predictor and response variables (Zhang et al., 2018).
- ***Support vector regression (SVR):*** It is a support vector machine variant capable of performing both linear and non-linear regression (Akande et al., 2022).
- ***Artificial neural network (ANN):*** It is a computational model inspired by the human brain. It can capture intricate correlations between inputs and outputs (Kalambukattu et al., 2018).
- ***Genetic expression programming (GEP):*** It is an evolutionary approach that uses computer programs or expressions to model data effectively (Ferreira, 2002).

Objective 2: development of a new spectral index for soil pH and SOC

Developing a new spectral index for soil pH and SOC involves a two-step approach utilizing PCA and ANN. Initially, it employs multiple feature selection techniques such as PCA, LASSO, SPA, and RFE. The results in Tables 10 and 11 indicate that PCA gives the optimal spectral bands from a large dataset, identifying those most relevant for predicting soil properties. This dimensionality reduction technique ensures the use of only the most informative spectral bands, enhancing the efficiency and accuracy of the analysis. Subsequently, the study applies ANN on these selected spectral bands to create a new spectral index. Training the ANN on the optimal features develops a model capable of capturing complex, non-linear relationships between the spectral data and soil pH and SOC. This combined approach of PCA and ANN results in a robust and precise spectral index, significantly improving the estimation accuracy for soil properties and aiding in better soil management practices.

Figure 4 illustrates the Flowchart for designing and validating the proposed SPI and SOCI indices to estimate soil pH and SOC using an ANN. The method begins by preprocessing the reflectance data and then utilizing PCA to identify and pick the most informative bands. Subsequently, it divides the data into sets for training and testing purposes. The training dataset trains the ANN. It evaluates using a separate testing set and is finally used to construct equations for the SPI and SOCI indices. The proposed indices equations are validated on AfSIS and LUCAS-2009 ground truth data using evaluation metrics, as mentioned in the "Evaluation metrics" section.

Figure 5 depicts the architecture for computing proposed SPI and SOCI indices using PCA and ANN. Initially, the spectra of the hyperspectral data cap-

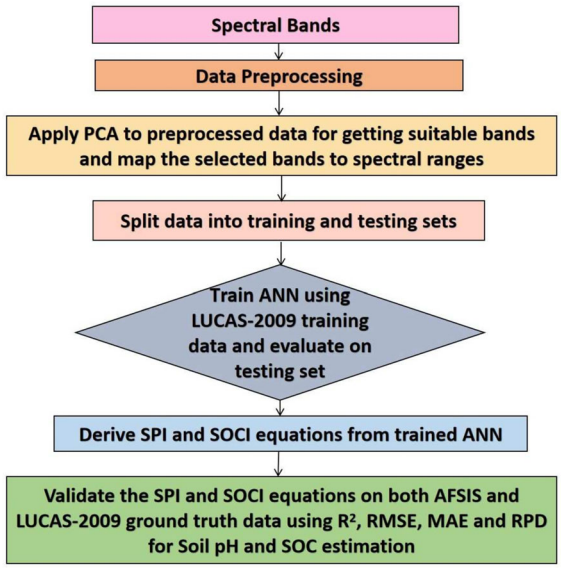

Fig. 4 Flowchart for Design and Validation of New Soil Spectral Indices

ture detailed reflectance values across various wavelengths. PCA reduces dimensionality by selecting the most informative bands. These bands are then input into an ANN with ReLU activation to learn complex data relationships, ultimately calculating SPI and SOCI indices for improved soil property predictions. Algorithm 1 shows the detailed steps for generating the SPI and SOCI indices.

Input: Hyperspectral reflectance data D, soil pH, and SOC.
Output: SPI and SOCI equations.
1. Preprocess reflectance data D
2. Apply PCA to reflectance data (select informative Bands)
   $B_1, B_2, ..., B_m \leftarrow PCA(D)$
3. Map selected Bands to spectral ranges:
   Bands ← Mapping into spectral ranges (e.g.,Red, NIR, SWIR, MIR)
4. Split data:
   $D_{train}, D_{test} \leftarrow$ Split of D in ratio 7:3
5. Train ANN on LUCAS-2009 data:
   $W,b \leftarrow$ Train ANN (D_{train}, pH/SOC)
6. Derive SPI and SOCI equations:
   $SPI = f_{ANN}(B_1, B_2, ..., B_m)$
   $SOCI = f_{ANN}(B_1, B_2, ..., B_m)$
7. Validate SPI and SOCI indices using AfSIS and LUCAS-2009 ground truth data and evaluate using R^2, RMSE, MAE and RPD

Multiple feature selection techniques

This study describes various feature selection techniques for identifying suitable bands for the SPI and SOCI.

1. ***Principal component analysis (PCA):*** It is a technique that converts the original features into a new collection of variables known as principal components, which are not connected. These components effectively capture the highest variation in the data, reducing the number of dimensions and identifying the most important spectral bands (Maćkiewicz & Ratajczak, 1993).
2. ***Least absolute shrinkage and selection operator (LASSO):*** It is a technique that incorporates a penalty term into the regression model, which results in certain feature coefficients being set to zero. This process efficiently chooses a subset of the initial characteristics, assisting in selecting relevant features and decreasing the complexity of the model (Fonti & Belitser, 2017).
3. ***Successive projection algorithm (SPA):*** The process of feature selection in SPA involves iteratively choosing features that are maximally distant from the already selected characteristics. It guarantees that the desired characteristics have minimal correlation, resulting in a varied and useful collection of bands (Soares et al., 2013).
4. ***Recursive feature elimination (RFE):*** It is a process that systematically eliminates the least significant features according to a given model. RFE determines the most important features for an estimation job by repeatedly training the model and removing the least impactful features (Darst et al., 2018).

Evaluation metrics

The study employs four performance measures to evaluate the predictive accuracy of the spectral indices for soil pH and SOC. Table 6 displays the compilation of performance measures. These metrics comprehensively evaluate the effectiveness of the index by considering many factors, such as the number of errors, the amount of variation explained, and the strength of correlation between anticipated and actual values.

Results

Objective 1: assessment of existing spectral indices

Spectral indices, which are mathematical combinations of different spectral bands, enhance specific features

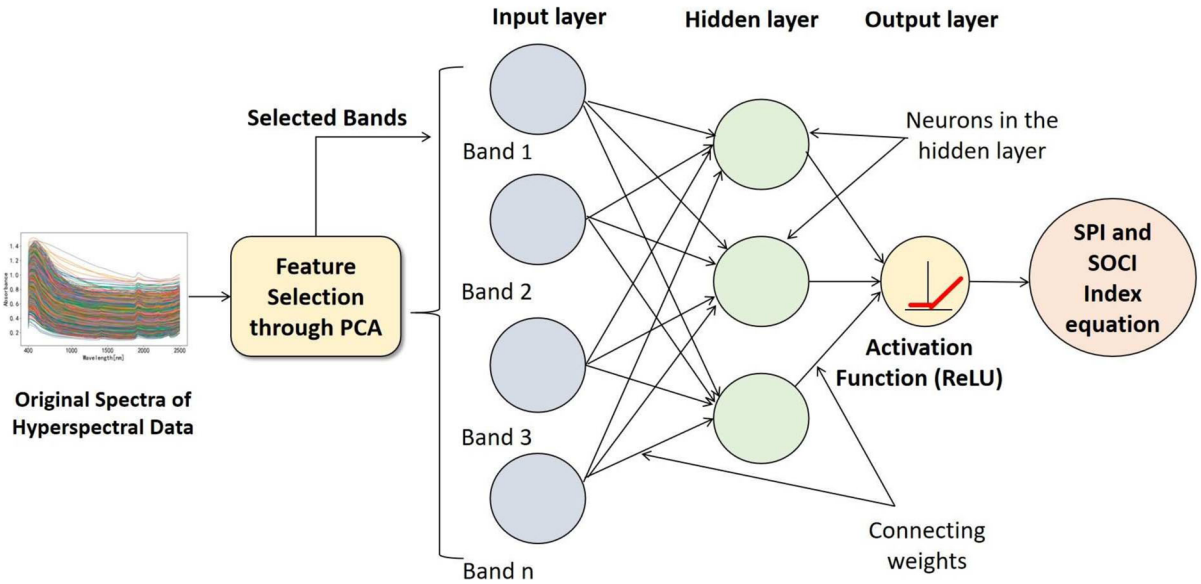

Fig. 5 Architecture to Compute SPI and SOCI Indices using PCA and ANN

Table 6 Performance metrics used to evaluate estimation accuracy of ML models

Performance metric	Description	Equation
Coefficient of determination (R^2)	This computational function determines a regression score. The achievable score has an upper limit of 1.0, which can be detrimental as the model may exhibit substantially poorer performance than anticipated. (Pechanec et al., 2021).	$R^2 = 1 - \frac{\sum_{i=1}^{n}(y_i - \hat{y}_i)^2}{\sum_{i=1}^{n}(y_i - \bar{y})^2}$
Root mean square error (RMSE)	The term refers to the square root of the average of the squared differences between the expected and actual values. Consider a model with a lower RMSE value to be superior (Jain et al., 2023).	$\text{RMSE} = \sqrt{\frac{1}{n}\sum_{i=1}^{n}(y_i - \hat{y}_i)^2}$
Mean absolute error (MAE)	The function computes the average absolute differences between the expected and observed values. A smaller MAE indicates a superior model performance (Robeson & Willmott, 2023).	$\text{MAE} = \frac{1}{n}\sum_{i=1}^{n}\lvert y_i - \hat{y}_i \rvert$
Ratio of performance to deviation (RPD)	The RPD evaluates the relationship between the range references and standard deviation. A model is considered adequate when it has an RPD value of 2, while outstanding models typically have values exceeding 3 (Jain et al., 2023)	$RPD = \frac{Range\ Reference}{Standard\ Deviation}$

and provide more meaningful inputs compared to raw spectral bands. These indices include VI, SI, WI, TTI, and a comprehensive set of all indices, as mentioned in the "Technical background of spectral indices" section. Tables 7 and 8 focus on the predictive performance of various spectral bands and existing spectral indices for soil pH and SOC estimation across different datasets (AfSIS and LUCAS-2009) using four ML models: PLSR, SVR, ANN, and GEP. Table 9 shows the selected hyperparameters for each ML model.

The ANN model using spectral bands shows superior performance in all input categories for soil pH and SOC estimation as shown in Tables 7 and 8. The input category of all indices best predicted AfSIS soil pH with ANN, achieving R^2 of 0.59, indicating its strong predictive power when utilizing comprehensive spectral information. Similarly, for LUCAS-2009 soil pH, the ANN model with all indices achieved the highest performance (R^2 = 0.48), underscoring the importance of broad spectral data in capturing soil pH variations. For AfSIS SOC, again, the ANN model with soil indices shows the highest success with R^2 = 0.77, suggesting soil-specific indices' effectiveness in certain contexts. The GEP model excelled in predicting SOC for the LUCAS- 2009 dataset with R^2 = 0.72, again demonstrating the value of comprehensive indices. Overall, followed by spectral bands, the input category of all spectral indices consistently leads to better model performance, highlighting the importance of integrating a wide range of spectral information to enhance the accuracy and reliability of soil property estimations. Results indicate that the ANN model is superior in most cases while using spectral bands and existing indices for soil pH and SOC estimation.

Objective 2: screening results of multiple feature selection techniques

For more precise and reliable estimations of soil pH and SOC, novel indices that address the shortcomings of spectral bands and existing spectral indices in capturing the unique spectral characteristics of soil properties need to be developed. For this, feature selection techniques help extract the suitable spectral range for developing novel spectral indices. From objective 1, it is clear that ANN shows the best accuracy in most cases. Hence, this section combines multiple feature selection techniques with ANN to get suitable bands for SPI and

Table 7 Results of spectral bands and existing spectral indices used as input in ML models for soil pH estimation (VI1-NDVI, VI2-EVI, VI3-RVI, VI4-NDWI, VI5-ARVI)

Soil pH (AfSIS)					
Input category	**Model**	**R^2**	**RMSE**	**MAE**	**RPD**
Spectral bands	**ANN**	**0.8**	**0.42**	**0.3**	**2.26**
VI	ANN	0.52	0.66	0.51	1.45
SI	ANN	0.57	0.62	0.47	1.53
WI	PLSR	-0.001	0.96	0.73	0.99
TTI	ANN	0.17	0.87	0.66	1.1
All indices	ANN	0.59	0.6	0.47	1.58
Zhang et al. (2018) (A subset of vegetation indices VI1, VI2, VI3, VI4, VI5)	PLSR	0.04	0.93	0.73	1.02
Soil pH (LUCAS-2009)					
Input category	**Model**	**R^2**	**RMSE**	**MAE**	**RPD**
Spectral bands	**ANN**	**0.87**	**0.46**	**0.35**	**2.88**
VI	SVR	0.45	1	0.77	1.35
SI	ANN	0.38	1.05	0.87	1.27
WI	PLSR	0.095	1.28	1.1	1.05
TTI	ANN	0.26	1.15	0.96	1.16
All indices	ANN	0.48	0.96	0.47	1.39
Zhang et al. (2018) (A subset of vegetation indices VI1, VI2, VI3, VI4, VI5)	PLSR	0.07	1.3	1.11	1.03

The bold entries highlight the best results achieved in this study, demonstrating superior performance compared to other models and previous studies

Table 8 Results of spectral bands and existing spectral indices used as input in ML models for SOC estimation (VI1-NDVI, VI2-EVI, VI3-RVI, VI4-NDWI, VI5-ARVI)

SOC (AfSIS)					
Input category	**Model**	**R^2**	**RMSE**	**MAE**	**RPD**
Spectral bands	**ANN**	**0.94**	**0.33**	**0.26**	**3.8**
VI	SVR	0.74	0.61	0.38	1.98
SI	ANN	0.77	0.58	0.35	2.11
WI	ANN	0.01	1.21	0.83	1
TTI	ANN	0.2	1.09	0.73	1.11
All indices	ANN	0.7	0.67	0.4	1.82
Zhang et al. (2018) (A subset of vegetation indices VI1, VI2, VI3, VI4, VI5)	PLSR	0.31	1.01	0.7	1.21
SOC (LUCAS-2009)					
Input category	**Model**	**R^2**	**RMSE**	**MAE**	**RPD**
Spectral bands	**ANN**	**0.90**	**27.82**	**21.8**	**3.43**
VI	ANN	0.24	78.31	41.06	1.15
SI	ANN	0.24	78.24	38.96	1.15
WI	ANN	0.02	88.8	46.78	1.01
TTI	GEP	0.72	48.01	22.81	1.89
All indices	PLSR	0.3	75.24	37.67	1.19
Zhang et al. (2018) (A subset of vegetation indices VI1, VI2, VI3, VI4, VI5)	PLSR	0.06	87.05	46.59	1.03

The bold entries highlight the best results achieved in this study, demonstrating superior performance compared to other models and previous studies

SOCI. The analysis across Tables 10 and 11 showcasing various feature selection techniques for predicting soil pH and SOC reveals notable differences in performance across datasets. For soil pH and SOC estimation using the AfSIS and LUCAS-2009 datasets, PCA with ANN consistently demonstrates a strong correlation (R^2 values ranging from 0.86 to 0.952). However, while PCA excels in capturing variance, LASSO with ANN and RFE with ANN offer comparable results.

In contrast, SPA with ANN consistently emerges as the least effective technique across all datasets. For instance, in soil pH estimation using both datasets, SPA with ANN shows near-zero or negative R^2 values, indicating poor correlation and predictive capability. Moreover, SPA with ANN results in significantly higher RMSE and MAE values than other techniques, suggesting its failure to select relevant features effectively. It underscores SPA's unsuitability for these datasets,

Table 9 Selected hyperparameters of various ML models

Model	Hyperparamters
PLSR	n_components = 4, scale = True, max_iter = 100
SVR	kernel = "rbf," C = 50, gamma = 0.1, epsilon = 0.1
ANN	activation = "relu," optimizer = "Adam," learning_rate = 0.028, epochs = 100, batch_size = 32, verbose = 1
GEP	generations = 50, population_size = 1000, tournament_size=5, const_range = (-2.0, 2.0), function_set = ("add," "sub," "mul," "div," "sqrt," "log," "abs," "sin," "cos"), p_crossover = 0.7, p_subtree_mutation = 0.1, p_hoist_mutation = 0.1, p_point_mutation = 0.1, max_samples=0.9, verbose=1

Table 10 Results of various feature selection techniques with ANN for soil pH estimation

Soil pH (AfSIS)				
Feature selection technique	**R^2**	**RMSE**	**MAE**	**RPD**
PCA	**0.86**	**0.4**	**0.26**	**2.39**
LASSO	0.67	0.55	0.4	1.74
SPA	-0.003	0.96	0.72	0.99
RFE	0.6	0.6	0.43	1.59
Soil pH (LUCAS-2009)				
Feature selection technique	**R^2**	**RMSE**	**MAE**	**RPD**
PCA	**0.945**	**0.42**	**0.31**	**3.19**
LASSO	0.34	1.09	0.91	1.23
SPA	0.11	1.26	1.1	1.06
RFE	0.54	0.98	0.76	1.87

The bold entries highlight the best results achieved in this study, demonstrating superior performance compared to other models and previous studies

likely due to its inability to handle the complexities and interactions in soil pH and SOC estimation models. While PCA shows promise for capturing variance, the choice of feature selection technique critically impacts predictive accuracy and model performance, necessitating careful consideration based on specific dataset characteristics and predictive goals.

Objective 2: index-based analysis of soil pH and SOC

An index is a numerical value derived from a mathematical formula that combines information from multiple spectral bands of a spectral image. Sensors acquire electromagnetic events in terms of bands, which are considered wavelengths. Band calculations provide unique results associated with detecting the desired signature of an element or matter. They are used here for band analysis and further estimation of soil pH and SOC in terms of indices.

PCA selects five bands for soil pH and eight bands for SOC due to the specific spectral sensitivities of these properties. It reduces data dimensionality and highlights critical spectral features related to soil properties. While researchers have explored various sets of bands

Table 11 Results of various feature selection techniques with ANN for SOC estimation

SOC (AfSIS)				
Feature selection technique	**R^2**	**RMSE**	**MAE**	**RPD**
PCA	**0.952**	**0.28**	**0.18**	**4.69**
LASSO	0.93	0.31	0.22	3.84
SPA	0.144	1.13	0.73	1.08
RFE	0.932	0.31	0.209	3.85
SOC (LUCAS-2009)				
Feature selection technique	**R^2**	**RMSE**	**MAE**	**RPD**
PCA	**0.943**	**19.62**	**10.41**	**4.59**
LASSO	0.87	31.93	18.89	2.82
SPA	0.62	54.92	28.71	1.64
RFE	0.45	67.99	35.1	1.08

The bold entries highlight the best results achieved in this study, demonstrating superior performance compared to other models and previous studies

for these parameters, this selection provides the best results, reflecting the optimal balance between capturing essential spectral information and achieving accurate predictions for soil pH and SOC.

In this study, the researchers construct various equations to generate the SPI and SOCI indices using the PLSR, SVR, ANN, and GEP models. Through rigorous testing and validation, ANN consistently surpasses the other models, delivering the most precise soil pH and SOC estimation. While techniques like PLSR and SVR offer fast training, this study chooses ANN due to its superior ability to capture complex relationships within the data. ANN is employed to derive equations for the proposed spectral indices, leveraging their ability to model complex non-linear relationships. This focus on accuracy proved fruitful, as ANNs yielded significantly higher prediction results for both soil pH and SOC, aligning perfectly with the research goals of achieving the most precise soil property estimates.

The reported metrics, as mentioned in the "Evaluation metrics" section, prioritize the index ability to predict soil properties on entirely new data. This focus on generalizability is essential for real-world applications. A common 70:30 split separated the data for calibration and validation. This approach ensures robust model training while reserving a significant portion for unbiased evaluation. Consequently, the testing R^2 becomes the key metric for assessing generalizability.

The equation of the new index for soil pH and SOC are defined in Eqs. 2 and 3, respectively:

$$\begin{aligned}\text{Soil pH index (SPI)} = {} & W_1 \cdot B(\text{MidIR1}) \\ & + W_2 \cdot B(\text{SWIR1}) \\ & + W_3 \cdot B(\text{Red}) - \\ & W_4 \cdot B(\text{MidIR2}) - W_5 \cdot B(\text{SWIR2}) - b \end{aligned} \quad (2)$$

Here W_1 = 0.19, W_2 = 0.48, W_3 = 0.15, W_4 = 0.08, W_5 = 0.06 and b = 0.04. The B(MidIR1) represent the MidInfrared Band 1, B(MidIR2) represent the MidInfrared Band 2, B(SWIR1) represents the Shortwave Infrared Band 1, B(SWIR2) represents Shortwave Infrared Band 2 and B(Red) represents the Red Band.

$$\begin{aligned}\text{SOC Index (SOCI)} = {} & W_1 \cdot B(\text{MidIR1}) - W_2 \cdot B(\text{SWIR1}) - W_3 \cdot B(\text{NIR}) - \\ & W_4 \cdot B(\text{MidIR2}) - W_5 \cdot B(\text{SWIR2}) + W_6 \cdot B(\text{SWIR3}) - W_7 \cdot B(\text{SWIR4}) + \\ & W_8 \cdot B(\text{SWIR5}) - b \end{aligned} \quad (3)$$

Here W_1 = 0.20, W_2 = 0.27, W_3 = 0.08, W_4 = 0.21, W_5 = 0.15, W_6 = 0.28, W_7 = 0.008, W_8 = 0.13, and b = 0.001. The B(MidIR1) represent the MidInfrared Band 1, B(MidIR2) represent the MidInfrared Band 2, B(SWIR1) represents the Shortwave Infrared Band 1, B(SWIR2) represents Shortwave Infrared Band 2, B(SWIR3) represents Shortwave Infrared Band 3, B(SWIR4) represents Shortwave Infrared Band 4, B(SWIR5) represents Shortwave Infrared Band 5, and B(NIR) represents the Near-Infrared Band. The parameter B represents the reflectance values at specific wavelengths, and the coefficients of bands are the weights that the ANN model determines. The constant value at the end is the random error term. This approach enhances the predictive accuracy of specific soil nutrients, allowing for more precise and reliable soil health assessments.

The SPI and SOCI indices differ from hyperspectral band predictions in their approach to utilizing spectral data. This study specifically designed the SPI index to predict soil pH by integrating spectral information into a single index that correlates strongly with soil acidity or alkalinity. Similarly, the SOCI index estimates SOC by integrating specific spectral features associated with organic carbon. In contrast, hyperspectral band predictions involve using ML models to analyze the full spectrum of bands directly, capturing complex relationships between spectral data and soil properties. SPI and SOCI offer several advantages over direct hyperspectral predictions. First, they simplify the interpretation of spectral data by reducing it to a single, focused index for soil pH and SOC estimation, respectively. It reduces computational complexity and resource requirements compared to analyzing the full hyperspectral spectrum. Additionally, SPI and SOCI are specialized indices that can enhance prediction accuracy for their specific targets, making them easier to use.

The analysis of Tables 12 and 13 highlights the impressive performance of the proposed SPI and SOCI indices to predict soil pH and SOC. For AfSIS soil pH, the proposed SPI index achieves R^2 of 0.86. For LUCAS-2009 soil pH, the results are even more impressive with a R^2 of 0.945. For SOC estimation, the proposed SOCI index achieves R^2 of 0.952 for the AfSIS dataset and R^2 of 0.963 for the LUCAS-2009 dataset. The findings show that proposed SPI and SOCI indices customized for particular soil characteristics (soil pH and SOC) produce superior outcomes. Thus,

Table 12 Comparison of proposed SPI index with previous work on Soil pH estimation using spectral bands

Soil pH (AfSIS)					
Reference	**Technique**	**R^2**	**RMSE**	**MAE**	**RPD**
Zhao et al. (2023)	CNN with spectral bands	0.81	0.41	-	-
Akande et al. (2022)	SVR with spectral bands	0.84	0.36	0.25	-
This study	**Proposed SPI Index**	**0.86**	**0.4**	**0.26**	**2.39**
Soil pH (LUCAS-2009)					
Reference	**Technique**	**R^2**	**RMSE**	**MAE**	**RPD**
Zhao et al. (2023)	CNN with spectral bands	0.85	0.536	-	-
Zhong et al. (2021)	DCNN with spectral bands	0.93	0.334	-	-
This study	**Proposed SPI Index**	**0.945**	**0.42**	**0.31**	**3.19**

The bold entries highlight the best results achieved in this study, demonstrating superior performance compared to other models and previous studies

the study determines that it is crucial to develop new indices for specific soil properties.

Figure 6 illustrates the proposed SPI and SOCI indices training and testing RMSE over epochs for soil pH and SOC estimation using the AfSIS and LUCAS-2009 datasets. Both datasets show a significant reduction in training RMSE over the initial epochs for soil pH estimation using the SPI index, indicating its effective learning. The testing RMSE maintains a steady trend with slight fluctuations, demonstrating the SPI index's ability to generalize well to new data. This consistent performance reflects the robustness of the SPI index in predicting soil pH across different epochs. For SOC estimation using the SOCI index, the training RMSE decreases significantly in the early epochs, showcasing its learning capability. The testing RMSE follows a stable trend, with minor variations, indicating reliable performance in predicting SOC. The models demonstrate their effectiveness and consistency in generalizing SOC estimations across various epochs, highlighting their robustness and reliability.

Figure 7 shows the proposed SPI and SOCI indices residual plot for soil pH and SOC estimation using AfSIS and LUCAS-2009 datasets. The residuals are

Table 13 Comparison of proposed SOCI index with previous work on SOC estimation using spectral bands

SOC (AfSIS)					
Reference	**Technique**	**R^2**	**RMSE**	**MAE**	**RPD**
Zhao et al. (2023)	CNN with spectral bands	0.936	0.29	-	-
Zhao et al. (2022)	Squeeze and excitation CNN with spectral bands	0.83	0.276	-	-
Akande et al. (2022)	SVR with spectral bands	0.88	0.391	0.162	-
Zhao et al. (2021)	CNN with quantile regression with spectral bands	0.92	0.301	-	-
This study	**Proposed SOCI index**	**0.952**	**0.28**	**0.18**	**4.69**
SOC (LUCAS-2009)					
Reference	**Technique**	**R^2**	**RMSE**	**MAE**	**RPD**
Zhao et al. (2023)	CNN with spectral bands	0.93	23.722	-	-
Zhao et al. (2022)	Squeeze and excitation CNN with spectral bands	0.935	23.565	-	-
Zhao et al. (2021)	CNN with quantile regression with spectral bands	0.93	26.667	-	-
Zhang et al. (2021)	DCNN with spectral bands	0.95	19.837	-	-
This study	**Proposed SOCI Index**	**0.963**	**19.62**	**10.41**	**4.59**

The bold entries highlight the best results achieved in this study, demonstrating superior performance compared to other models and previous studies

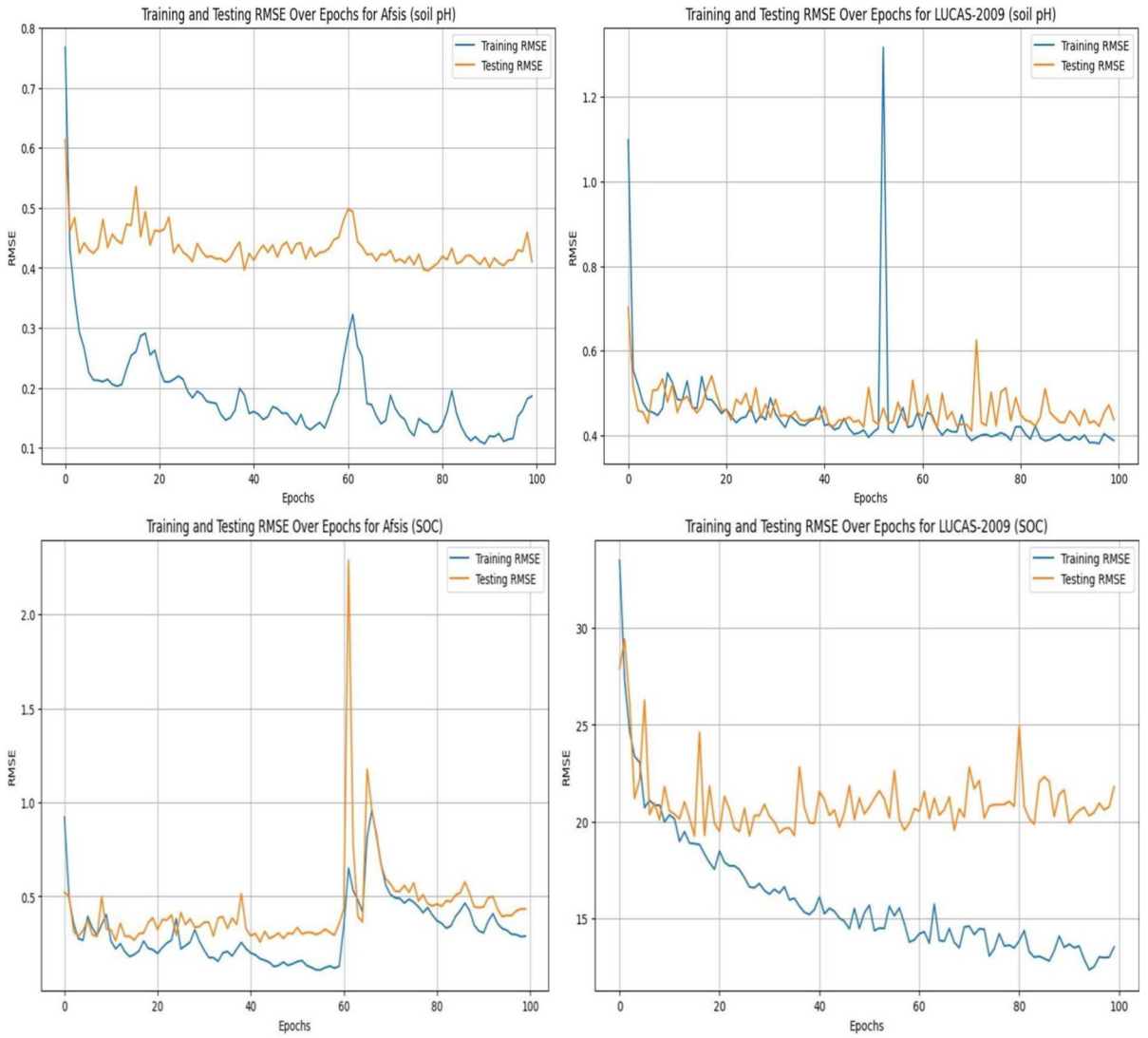

Fig. 6 Proposed SPI and SOCI indices training & testing error for soil pH and SOC estimation

scattered around the horizontal axis, indicating relatively unbiased estimations. However, a slight pattern where residuals increase and decrease suggests minor non-linearity. For AfSIS soil pH, most residuals are within the range of –1 to 2, demonstrating that the SPI index generally predicts soil pH accurately. In the LUCAS-2009 soil pH residual plot, residuals are more tightly clustered around the horizontal axis, indicating fewer extreme errors and more consistent SPI index performance. For SOC estimation using the SOCI index, the residual plots reveal residuals fairly dispersed around the horizontal axis, with some evident non-linear patterns.

Discussion

Application scenario

This research holds promise for real-time applications, such as:

1. ***Applications in precision agriculture:*** This work supports precision agriculture by offering detailed soil health assessments, enabling targeted interventions for crop management. Additionally, the techniques can be adapted to monitor land degradation, helping to prevent soil erosion and maintain soil fertility (Padarian et al., 2019).

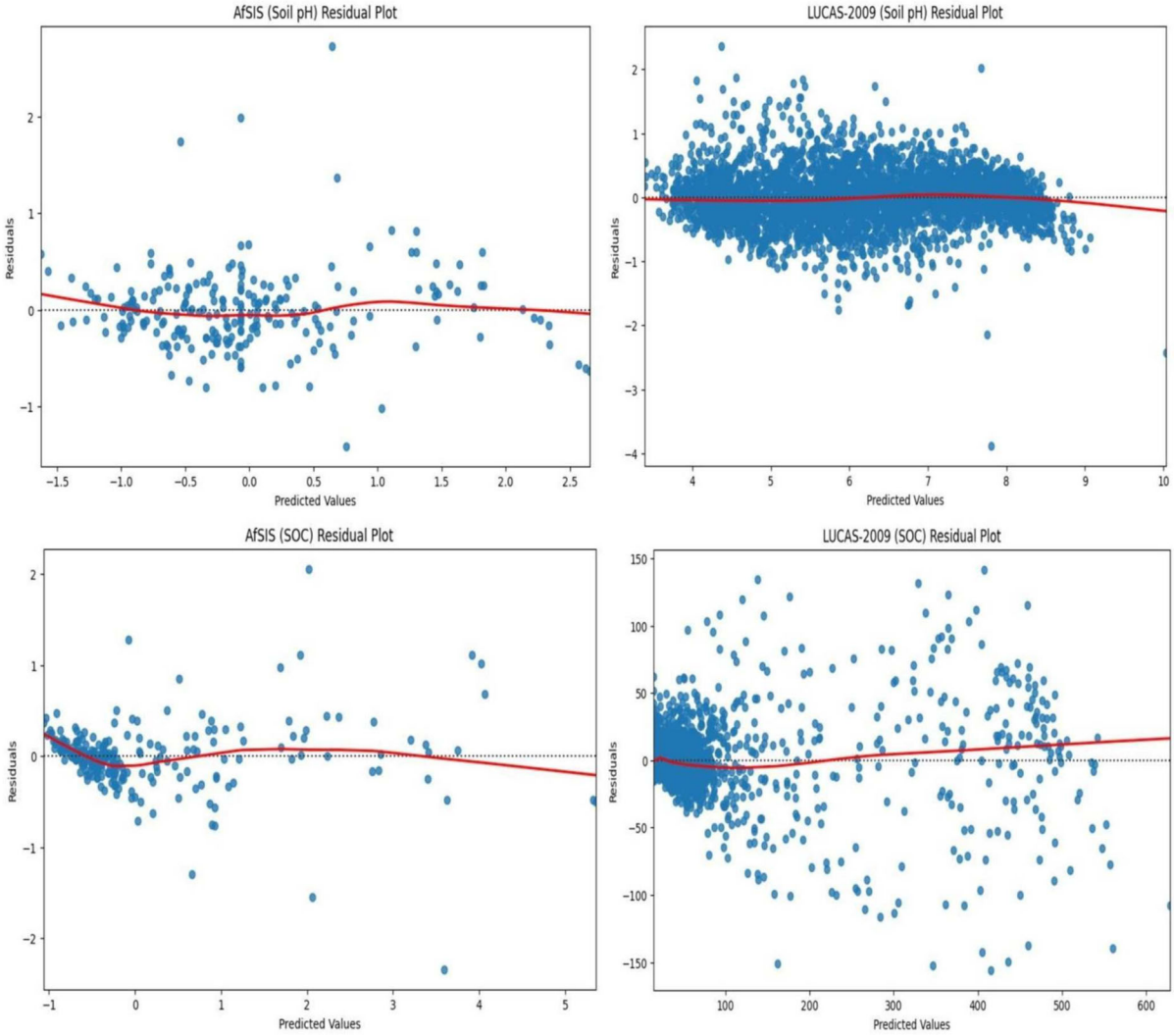

Fig. 7 Proposed SPI and SOCI indices residual plot for soil pH and SOC estimation

2. ***Climate change mitigation:*** The research can significantly contribute to climate change mitigation by providing accurate assessments of carbon sequestration potential across various ecosystems. Enhanced soil health assessments lead to better management practices that boost carbon storage and also help reduce greenhouse gas emissions, thereby improving environmental impact (Li et al., 2020).
3. ***Relevance to diverse ecosystems:*** The diverse global landscapes, ranging from mountainous regions to arid deserts, present unique soil health challenges across different environments. The study helps in effective soil management in these varied conditions, which is crucial for ensuring sustainable agricultural productivity and maintaining overall environmental health (Keshavarzi et al., 2023).
4. ***Land restoration projects:*** This work can be applied to land restoration projects by providing accurate soil health data, which aids in the effective remediation of degraded lands and supports the recovery of natural habitats (Wang et al., 2006).

Advantages and limitations of proposed spectral indices

Advantages

1. ***Cost and time effective:*** The use of SPI and SOCI reduces the need for extensive soil sampling and laboratory testing, making the process more efficient and less expensive.
2. ***Improved accuracy:*** The SPI and SOCI indices are designed for specific wavelengths that best reflect variations in soil pH and SOC. Unlike existing indices, which may broadly capture soil characteristics, SPI and SOCI capture spectral bands that are most sensitive to pH and SOC levels. This targeted approach enhances prediction accuracy by focusing on wavelengths with the strongest correlations to specific soil properties, thereby improving overall performance in soil property estimation.
3. ***Enhanced agricultural decision-making:*** Using SPI and SOCI indices enables precise assessment of soil pH and SOC, guiding better agricultural decisions. SPI indicates optimal pH for nutrient availability, while SOCI helps determine SOC levels crucial for soil health. Together, they help farmers fine-tune fertilizer to improve crop yield, enhance soil fertility, and support sustainable farming practices.
4. ***Reduced computational complexity:*** By simplifying the feature space and focusing on relevant wavelengths, the indices reduce computational load, making them efficient for large-scale soil monitoring tasks. Ultimately, this contributes to better soil health and crop productivity, demonstrating the significant impact of using tailored spectral indices in soil nutrient analysis.

Limitations

1. ***Limited to Soil pH and SOC:*** SPI and SOCI indices are optimized to predict only soil pH and SOC, limiting their utility in predicting other soil nutrients or properties.
2. ***Generalizability Concerns:*** While effective in this study, the generalizability of these indices to diverse geographical and environmental conditions remains a potential limitation.

Conclusion

This study is paramount due to soil pH and organic carbon's critical role in sustainable agriculture and environmental monitoring. Traditional testing methods, while effective, are laborious and costly. Therefore, exploring hyperspectral imaging as a rapid, non-destructive, and cost-effective alternative is crucial for advancing soil analysis practices. However, harnessing the full potential of hyperspectral data presents challenges, notably in handling its high dimensionality. The study addresses these challenges head-on by developing and comparing spectral indices. These indices effectively mitigate multicollinearity and noise by leveraging mathematical combinations of spectral bands, enhancing predictive accuracy for soil pH and SOC levels. The findings reveal that proposed indices SPI and SOCI, particularly those developed using PCA in conjunction with ANN, outperform existing indices and previous work on spectral bands. These indices successfully capture pertinent spectral features while reducing noise, significantly improving predictive accuracy. The scalability potential of this approach is particularly relevant to its diverse agricultural landscapes. The study helps inform site-specific fertilizer recommendations, optimize land management practices, and ultimately contribute to a more sustainable agricultural sector.

Exploring additional spectral indices tailored for specific soil types and integrating cutting-edge deep learning techniques are promising directions to further enhance soil property estimation accuracy. By continually refining this approach, researchers and practitioners can be empowered with a powerful tool for large-scale, non-destructive soil analysis, ultimately promoting more sustainable agriculture and environmental monitoring strategies.

Acknowledgements Correspondence regarding this study and manuscript should be directed to Shagun Jain (shagunjain191172@gmail.com).

Author contributions All authors contributed significantly to the development and completion of this study. The specific contributions of each author are as follows:
- S. J.: writing—original draft; writing—review and editing.
- D.S.: supervision; review and editing.
- K.T.: supervision; review and editing.

Correspondence regarding this study and manuscript should be directed to Shagun Jain (shagunjain191172@gmail.com).

Data Availability Statement No datasets were generated or analyzed during the current study.

Declarations

Ethical Approval All authors have read, understood, and have complied as applicable with the statement on "Ethical responsibilities of Authors" as found in the Instructions for Authors.

Competing Interests The authors declare no competing interests.

References

Akande, G. L., et al. (2022). Improving soil property mapping using support vector machines, neural networks, gradient boosted trees and random forests over soils in Sub-Saharan Africa. In: *Neural Networks, Gradient Boosted Trees and Random Forests Over Soils in Sub-Saharan Africa*, https://papers.ssrn.com/sol3/papers.cfm?abstract_id=4093599

Angelopoulou, T., et al. (2023). Evaluation of airborne hyspex and spaceborne PRSIMA hyperspectral remote sensing data for soil organic matter and carbonates estimation. *Remote Sensing, 15*(4), 1106. https://doi.org/10.3390/rs15041106

Awais, M., et al. (2023). AI and machine learning for soil analysis: An assessment of sustainable agricultural practices. *Bioresources and Bioprocessing, 10*(1), 90. https://doi.org/10.1186/s40643-023-00710-y

Babbar, D., et al. (2022). Spatial analysis of soil quality using geospatial techniques in botanic garden of Indian Republic. *Noida. Uttar Pradesh. India. Environmental Sustainability, 5*(4), 471–492. https://doi.org/10.1007/s42398-022-00247-4

Chu, X., et al. (2016). Data cleaning: Overview and emerging challenges. In: *Proceedings of the 2016 international conference on management of data* (pp. 2201–2206).

Darst, B. F., et al. (2018). Using recursive feature elimination in random forest to account for correlated variables in high dimensional data. *BMC genetics, 19*, 1–6. https://doi.org/10.1186/s12863-018-0633-8

Dhiman, G., et al. (2023). Soil textures and nutrients estimation using remote sensing data in North India-Punjab region. *Procedia computer science, 218*, 2041–2048. https://doi.org/10.1016/j.procs.2023.01.180

Diaz-Gonzalez, F. A., et al. (2022). Machine learning and remote sensing techniques applied to estimate soil indicators-review. *Ecological Indicators, 135*, 108517. https://doi.org/10.1016/j.ecolind.2021.108517

Dlamini, P., et al. (2016). Overgrazing decreases soil organic carbon stocks the most under dry climates and low soil pH: A meta-analysis shows. *Agriculture, Ecosystems & Environment, 221*, 258–269. https://doi.org/10.1016/j.agee.2016.01.026

Febereiro, M., et al. (2022). Evaluation of spectroscopy and methodological pre-treatments to estimate soil nutrients in the vineyard. *Remote Sensing, 14*(6), 1326. https://doi.org/10.3390/rs14061326

Fernández-Ugalde, O., et al. (2020). Assessment of changes in topsoil properties in LUCAS samples between 2009/2012 and 2015 surveys. *JRC, Luxembourg,*. https://doi.org/10.2760/5503

Ferreira, C. (2002). Gene expression programming in problem solving. In: *Soft Computing and industry: recent applications* (pp. 635–653). Springer.

Fonti, V., & Belitser, E. (2017). Feature selection using LASSO. *VU Amsterdam Research Paper in Business Analytics, 30*, 1–25.

Gulhane, V. A., et al. (2023). Correlation analysis of soil nutrients and prediction model through iso cluster unsupervised classification with multispectral data. *Multimedia Tools and Applications, 82*(2), 2165–2184. https://doi.org/10.1007/s11042-022-13276-2

Guo, J., et al. (2022). Mapping of soil pH based on SVM-RFE feature selection algorithm. *Agronomy, 12*(11), 2742. https://doi.org/10.3390/agronomy12112742

Jain, S., Sethia, D., & Tiwari, K. (2023). A Hybrid approach for soil nutrient estimation using multispectral data in Belgium and Luxembourg. In: *2023 first international conference on advances in electrical, electronics and computational intelligence (icaeeci)* (pp. 1–8). https://doi.org/10.1109/ICAEECI58247.2023.10370850

Jain, S., Sethia, D., & Tiwari, K. (2024). A critical systematic review on spectral-based soil nutrient prediction using machine learning. *Environmental Monitoring and Assessment, 196*,. https://doi.org/10.1007/s10661-024-12817-6

John, K., et al. (2020). Using machine learning algorithms to estimate soil organic carbon variability with environmental variables and soil nutrient indicators in an alluvial soil. *Land, 9*(12), 487. https://doi.org/10.3390/land9120487

Kalambukattu, J. G., et al. (2018). Digital soil mapping in a Himalayan watershed using remote sensing and terrain parameters employing artificial neural network model. *Environmental earth sciences, 77*, 1–14. https://doi.org/10.1007/s12665-018-7367-9

Keshavarzi, A., et al. (2023). Spatial prediction of soil micronutrients using machine learning algorithms integrated with multiple digital covariates. *Nutrient Cycling in Agroecosystems, 1–17*,. https://doi.org/10.1007/s10705-023-10303-y

Kumar, N., et al. (2018). Geospatial mapping of soil organic carbon using regression kriging and remote sensing. *Journal of the Indian Society of Remote Sensing, 46*, 705–716. https://doi.org/10.1007/s12524-017-0738-y

Leenaars, J. (2013). *Africa soil profiles database, Version 1.1. A compilation of georeferenced and standardised legacy soil profile data for Sub-Saharan Africa (With Dataset). Africa Soil Information Service (Afsis) Project.*, ISRIC-World Soil Information. https://www.isric.org/projects/africa-soil-profiles-database-afsp

Li, Y., et al. (2020). Effects of climate factors and soil properties on soil nutrients and elemental stoichiometry across the Huang-Huai-Hai River Basin, China. *Journal of Soils and Sediments, 20*, 1970–1982. https://doi.org/10.1007/s11368-020-02583-6

Maćkiewicz, A., & Ratajczak, W. (1993). Principal components analysis (PCA). *Computers & Geosciences, 19*(3), 303–342. https://doi.org/10.1016/0098-3004(93)90090-R

Mahmood, T., et al. (2024). Estimation of 100 M root zone soil moisture by downscaling 1 km soil water index with machine learning and multiple geodata. *Environmental*

Monitoring and Assessment, 196(9), 823. https://doi.org/10.1007/s10661-024-12969-5

Maurya, S., et al. (2020). Indicators for assessment of soil quality: A mini-review. *Environmental Monitoring and Assessment, 192*, 1–22. https://doi.org/10.1007/s10661-020-08556-z

Odebiri, O., et al. (2021). Deep learning approaches in remote sensing of soil organic carbon: A review of utility, challenges, and prospects. *Environmental monitoring and assessment, 193*, 1–18. https://doi.org/10.1007/s10661-021-09561-6

Padarian, J., et al. (2019). Machine learning and soil sciences: A review aided by machine learning tools. *The Soil*. https://doi.org/10.5194/soil-6-35-2020

Pechanec, V., et al. (2021). Usage of airborne hyperspectral imaging data for identifying spatial variability of soil nitrogen content. *ISPRS International Journal of Geo-Information, 10*(6), 355. https://doi.org/10.3390/ijgi10060355

Pouladi, N., et al. (2023). Digital mapping of soil organic carbon using remote sensing data: A systematic review. *Catena, 232*, 107409. https://doi.org/10.1016/j.catena.2023.107409

Pusch, M., Oliveira, A. L., Fontenelli, J. V., & Amaral, L.R.d. (2021). Soil properties mapping using proximal and remote sensing as covariate. *Engenharia Agrícola, 41*(6), 634–642.

Reddy, S. S., et al. (2023). Maintenance enhancement of smart manufacturing units in industry 4.0. In: *2023 international conference on inventive computation technologies (icict)* (pp. 1488–1492). https://doi.org/10.1109/ICICT57646.2023.10134377

Robeson, S. M., & Willmott, C. J. (2023). Decomposition of the mean absolute error (MAE) into systematic and unsystematic components. *Plos one, 18*(2), e0279774. https://doi.org/10.1371/journal.pone.0279774

Soares, S. F. C., et al. (2013). The successive projections algorithm. *TrAC Trends in Analytical Chemistry, 42*, 84–98. https://doi.org/10.1016/j.trac.2012.09.006

Tran, T. V., et al. (2022). A review of spectral indices for mangrove remote sensing. *Remote Sensing, 14*(19), 4868. https://doi.org/10.3390/rs14194868

Valloo, Y., Payen, S., Cornault, A., Vanrenterghem, R., Laurent, C., & Tisseyre, B. (2023). How to best compare remote sensing data versus proximal sensing data? In: *Precision agriculture'23* (pp. 635–642). Wageningen Academic.

Veenstra, J., et al. (2024). A European stakeholder survey on soil science skills for sustainable agriculture. *European Journal of Soil Science, 75*(2), e13449. https://doi.org/10.1111/ejss.13449

Wang, C., et al. (2006). Temperature and soil moisture interactively affected soil net n mineralization in temperate grassland in northern China. *Soil Biology and Biochemistry, 38*(5), 1101–1110. https://doi.org/10.1016/j.soilbio.2005.09.009

Wu, C., et al. (2019). Developing a new spectral index for detecting cadmium-induced stress in rice on a regional scale. *International journal of environmental research and public health, 16*(23), 4811. https://doi.org/10.3390/ijerph16234811

Yokoya, N., Grohnfeldt, C., & Chanussot, J. (2017). Hyperspectral and multispectral data fusion: A comparative review of the recent literature. *IEEE Geoscience and Remote Sensing Magazine, 5*(2), 29–56.

Yu, H., et al. (2020). Hyperspectral remote sensing applications in soil: A review. *Hyperspectral Remote Sensing, 269–291*,. https://doi.org/10.1016/B978-0-08-102894-0.00011-5

Yuvaraj, D., et al. (2022). Performance of spectral indices for soil properties: A case study from Redland Farm, South Florida. *Modeling Earth Systems and Environment, 8*(4), 4829–4841. https://doi.org/10.1007/s40808-022-01371-0

Zayani, H., et al. (2023). Using machine-learning algorithms to predict soil organic carbon content from combined remote sensing imagery and laboratory Vis-NIR spectral datasets. *Remote Sensing, 15*(17), 4264. https://doi.org/10.3390/rs15174264

Zelaya, C.V.G. (2019). Towards explaining the effects of data preprocessing on machine learning. In: *2019 IEEE 35th international conference on data engineering (icde)* (pp. 2086–2090).

Zhang, Y., et al. (2018). Estimating temporal changes in soil pH in the black soil region of Northeast China using remote sensing. *Computers and Electronics in Agriculture, 154*, 204–212. https://doi.org/10.1016/j.compag.2018.09.005

Zhang, J., et al. (2021). Comparison of new hyperspectral index and machine learning models for prediction of winter wheat leaf water content. *Plant Methods, 17*, 1–14. https://doi.org/10.1186/s13007-021-00737-2

Zhao, W., et al. (2022). Attention-based CNN ensemble for soil organic carbon content estimation with spectral data. *IEEE Geoscience and Remote Sensing Letters, 19*, 1–5. https://doi.org/10.1109/LGRS.2022.3201266

Zhao, W., et al. (2023). Estimation of soil properties content with Vis-NIR spectra by multi-task deep learning based on attention mechanism and loss-weight balancing. *IEEE Geoscience and Remote Sensing Letters*. https://doi.org/10.1109/LGRS.2023.3304749

Zhao, W., et al. (2021). Estimation of soil organic carbon content based on deep learning and quantile regression. In: *2021 ieee international geoscience and remote sensing symposium igarss* (pp. 3717–3720).

Zhong, L., et al. (2021). Soil properties: Their prediction and feature extraction from the LUCAS spectral library using deep convolutional neural networks. *Geoderma, 402*, 115366. https://doi.org/10.1016/j.geoderma.2021.115366

Publisher's Note Springer Nature remains neutral with regard to jurisdictional claims in published maps and institutional affiliations.

Springer Nature or its licensor (e.g. a society or other partner) holds exclusive rights to this article under a publishing agreement with the author(s) or other rightsholder(s); author self-archiving of the accepted manuscript version of this article is solely governed by the terms of such publishing agreement and applicable law.

Circuits, Systems, and Signal Processing
https://doi.org/10.1007/s00034-024-02915-8

Dhivehi Speech Recognition: A Multimodal Approach for Dhivehi Language in Resource-Constrained Settings

Sunakshi Mehra[1] · **Virender Ranga**[1] · **Ritu Agarwal**[1]

Received: 24 March 2024 / Revised: 30 October 2024 / Accepted: 30 October 2024
© The Author(s), under exclusive licence to Springer Science+Business Media, LLC, part of Springer Nature 2024

Abstract

This study addresses the challenging research problem of effectively integrating multiple data modalities, such as imperfect text transcripts and raw audio, within a deep learning framework for Dhivehi speech recognition. The focus is on resource-constrained settings, where limited prior research has been conducted. Our proposed approach employs a multimodal strategy, integrating audio, text, and image features through a late fusion technique. Specifically, we combine audio-to-spectrogram processed and passed to ResNet, phone embeddings, and 13 mel frequency cepstral coefficients (MFCC) to recognize Dhivehi speech spoken in Malaysia. To extract phonemic information, we utilize Carnegie Mellon University (CMU) phonemes obtained from text transcripts generated using the Speech2Text transformer on OPUS audio files. For phoneme embeddings, we leverage Language-Agnostic Sentence Representations (LASER), feeding these embeddings into feedforward neural networks. Our approach synergizes the strengths of audio, text, and image modalities to enhance recognition accuracy. In our experiments, we focus on the Dhivehi language within the extensive Multilingual Spoken Word Corpus (MSWC) dataset. By fusing posterior class probabilities from deep bidirectional long short-term memory (deep-BiLSTM) and feedforward neural models trained on individual modalities, we achieve an impressive accuracy of 96.42% when tested on 11 subjects within the MSWC dataset. Extensive testing and thorough ablation analyses demonstrate that our proposed method outperforms existing state-of-the-art systems. This superior performance can be attributed to the exceptional classification accuracies achieved by our approach. In conclusion, our study presents a robust and innovative multimodal approach that effectively combines audio, text, and image modalities for Dhivehi

Virender Ranga and Ritu Agarwal have contributed equally to this work.

✉ Sunakshi Mehra
mehra.sunakshi623@gmail.com

[1] Department of Information Technology, Delhi Technological University, Delhi, India

Published online: 09 November 2024

speech recognition in resource-constrained settings, showcasing superior accuracy compared to existing methodologies.

Keywords ResNet transformer · Phone embeddings · Deep bidirectional long short-term memory · Feedforward neural network (FNN) · Batch normalization · Speech recognition

1 Introduction

Dhivehi, also known as Maldivian [15], is the official language of the Maldives, a tropical archipelago located in the Indian Ocean [23]. With approximately 340,000 native speakers, it serves as a cultural and linguistic cornerstone for the Maldivian people. Dhivehi boasts a rich linguistic history and a unique script known as "Thaana," which consists of 24 letters. Dhivehi belongs to the Indo-Aryan language family and shares linguistic ties with Sinhalese, the language of neighboring Sri Lanka [46]. Its historical development has been shaped by various external influences, including Arabic, Sanskrit, and even colonial-era European languages. The language's distinct phonological features, such as retroflex consonants and vowel harmony, set it apart from its linguistic relatives [35]. Furthermore, Dhivehi's grammar, which relies heavily on inflections, exhibits the influence of its Sanskrit and Dravidian linguistic predecessors [46]. Despite its relatively small number of speakers and the challenges posed by globalization, Dhivehi maintains its significance as the cultural and national language of the Maldives [23]. However, it is essential to acknowledge the ongoing need for language preservation efforts and documentation to ensure the vitality and future of Dhivehi.

The field of deep learning has seen significant advancements in recent years, particularly in natural language processing (NLP). However, most of these advancements have been focused on high-resource languages with ample labeled data, pretrained models, and well-established resources. In contrast, low-resource languages like Dhivehi lack these luxuries, making it more challenging to apply state-of-the-art deep learning techniques directly. One of the notable challenges in Dhivehi language processing is the scarcity of large-scale annotated text data. Deep learning models, such as transformers, often require massive amounts of text data for pretraining to capture the intricacies of a language effectively. For Dhivehi, building such datasets is a resource-intensive and time-consuming process.

Recent advancements in deep learning have sparked significant interest in the consolidation of key components of automatic speech recognition (ASR), such as the acoustic model, pronunciation lexicon, and language model, into a unified end-to-end model. Connectionist Temporal Classification (CTC), as outlined in [17], is a critical element in these end-to-end approaches, introducing a blank symbol and a specialized loss function that enables the direct derivation of accurate character sequences from speech signals, eliminating the need for prior phoneme alignment. The recent proliferation of findings, as exemplified in [2], has generated substantial enthusiasm within the speech community for end-to-end deep learning. However, the construction of an end-to-end ASR system demands a substantial volume of paired speech-transcription data,

which can be cost-prohibitive. In many global languages, there is a severe scarcity of such paired data. Consequently, in low-resource settings, the prevailing strategy involves pretraining with data from other languages as an initialization step, followed by fine-tuning on the target language, a practice commonly referred to as multilingual transfer learning or pretraining (MultiASR) [45]. The core architecture of Multi-ASR features a multitask model with shared hidden layers (encoder) and multiple language-specific heads. This model structure is meticulously crafted to cultivate an encoder capable of extracting language-agnostic representations, thereby enhancing the performance of the acoustic model across diverse source languages. The efficacy of "language-independent" features in improving ASR performance, compared to monolingual training, has been demonstrated in numerous recent studies [7, 11].

The contributions of this study are:

- We tackle the integration of text transcripts and raw audio within a deep learning framework for Dhivehi speech recognition, focusing on resource-constrained settings with limited prior research.
- Our multimodal strategy combines audio processed as spectrogram and passed via ResNet, phone embeddings, and 13 MFCCs to recognize Dhivehi speech spoken in Malaysia, utilizing a late fusion technique.
- We extract phonemic information using CMU phonemes from text transcripts generated by the Speech2Text transformer on OPUS audio files.
- Phoneme embeddings are created using LASER and processed through feedforward neural networks.
- Our approach leverages the strengths of audio, text, and image modalities to improve speech recognition accuracy.
- Extensive testing on the MSWC dataset and ablation analyses show that our method outperforms existing state-of-the-art systems, achieving superior classification accuracy.

The multimodal integration of audio, text, and image features leads to significantly superior accuracy, outperforming existing methodologies. The approach is particularly robust in resource-constrained settings, making it a viable solution for underrepresented languages like Dhivehi. Additionally, the late fusion of probabilistic scores from different modalities enhances the overall system performance. The proposed method increases computational complexity due to the integration of multiple neural networks. It also demands extensive and high-quality datasets, which may not be readily available for all languages. Moreover, given the complexity of the model, there is a risk of overfitting, especially when the training data is limited. Despite its focus on resource-constrained settings, the approach may still require significant computational resources for training, limiting its applicability in truly low-resource environments. The method is currently tailored to the Dhivehi language, and its generalizability to other languages, particularly those with less phonemic similarity, has yet to be validated. Furthermore, the study's experiments were conducted on a relatively small subset of subjects, which may not fully capture the variability present in broader speech recognition tasks.

Section 2 delves into the existing body of knowledge within the field of speech recognition, while Sect. 3 introduces the novel dense architecture designed for integrating posterior scores. In Sect. 4, we detail the experimental approach and provide a concise summary of the results. Finally, Sect. 5 serves as the conclusion, and Sect. 6 offers insights into potential future research avenues. The impetus behind our involvement in speech recognition research and development is driven by the desire to enrich communication, expand accessibility, enhance operational effectiveness, and stimulate innovation across a wide spectrum of industries and applications.

2 Literature on Low-Resourced Data

Cutting-edge speech recognition systems, which achieve human-like performance [16], are typically trained on extensive and meticulously annotated speech datasets. However, the labor-intensive and costly nature of annotation makes it challenging to replicate such high performance in languages with limited resources.

To address this, multilingual and cross-lingual techniques have emerged, facilitating the transfer of models or features from well-resourced languages to those with limited or untranscribed data [18]. The conventional approach involves training a context-dependent Hidden Markov Model-based Deep Neural Network acoustic model with a "bottleneck" layer on a substantial multilingual dataset [48]. The portion of the network up to the bottleneck layer can serve as a language-agnostic feature extractor, adaptable to new languages.

However, this process involves preparing frame-level segmentations for each language, typically through the prior training of separate monolingual systems. This multi-step process is not only labor-intensive but also presents challenges when dealing with diverse speaking styles, acoustic qualities, and linguistic characteristics across different languages. This can lead to potentially inconsistent and suboptimal segmentations when generating features for a new language.

In cases of limited training data, whether in the form of audio or text, the conventional approach is to acquire more data from similar sources [52]. However, when the language in question is not widely spoken, sourcing additional resources can prove to be a formidable challenge. An alternative strategy involves data simulation [13, 27].

Within the robustness community, a common practice to enhance performance in the face of unforeseen noise and microphone conditions is data augmentation. This process involves creating additional instances from the original data through random modifications and the supplementation of extra signals. Prior research has predominantly focused on individual augmentation types, such as introducing reverberation [40], adding noise [51], or incorporating speaker-specific characteristics [26].

More recent work has explored the combination of multiple augmentation techniques. For example, [26] blended semi-supervised training with vocal tract length perturbation (VTLP). The ASpIRE Challenge [20] saw several successful approaches utilizing data augmentation. Peddinti et al. [37] integrated both reverberation and volume perturbation, while Hsiao et al. [22] introduced artificial noise and reverberation to the original data. Another approach involved a two-stage combination of VTLP and speaker-based augmentation, as demonstrated by Cui et al. [9]. As strategies are being

explored to efficiently create resources for new languages, there is also a parallel effort to reduce the volume of training data required for robust acoustic modeling, particularly in systems based on hidden Markov modeling (HMM). One common approach is parameter tying or sharing [4, 44]. Another method involves the use of a basis approach, where a relatively small set of basis vectors or functions is computed, and other model parameters are derived from them. Successful instances of this approach include tied-mixture HMM [25], subspace Gaussian mixture model (SGMM) [38], Bayesian sensing HMM [39], and canonical state models [14].

Additionally, transfer learning [36] has proven effective when dealing with out-of-domain data. This approach includes cross-lingual [6, 30] and multilingual [28] acoustic modeling techniques. These techniques operate under the assumption that there are reliable mappings between phonemes in well-resourced languages and those in the low-resource target language. This allows for knowledge transfer from the former to the latter through adaptation [29], transformation [47], or data augmentation [10]. Typically, it is also assumed that these phoneme mappings can be implicitly derived when speech data from multiple languages is trained together, sharing parts of their models, as seen in SHL-MDNN [24] or SGMM [5]. In [6], explicit phoneme mappings are derived using data-driven and knowledge-based methods.

Furthermore, there is an investigation into universal acoustic models, where phonemes from multiple languages are explicitly mapped to a universal phone set (UPS). This approach ensures that there is enough data to train the universal phones [8, 31]. However, it is commonly observed that the performance of UPS models tends to be inferior to language-specific acoustic models for the target language, unless there is an exceedingly limited amount of training data available for that specific language.

3 Proposed Methodology

In the upcoming section, we delve into the domain of decision-level fusion [32–34], specifically utilizing the maximum weighting score technique to amalgamate outcomes from three distinct channels. These techniques, which provide different representations of the audio data, include mel-frequency cepstral coefficients, mel spectrograms, and LASER phone embeddings. Based on the audio input, each method produces a score for every class, indicating how well the audio matches that class shown in Fig. 1. For each method, we identify the class with the highest score and use that score to represent the most likely class according to that specific method. The final prediction is determined by selecting the class with the highest maximum score across all methods. In other words, a class is chosen as the final prediction if multiple methods assign high scores to the same class and at least one method gives that class the highest score. Previous studies [32, 41, 43, 53] have consistently demonstrated that delaying the merging of features extracted from various segments of an enhanced input signal significantly improves categorization performance. In the training phase, late fusion has attracted substantial attention among researchers as a strategy to integrate multiple modalities [4] into a cohesive representation [12, 55]. By concatenating probabilistic scores, late fusion has the potential to enhance the overall performance of the speech recognition system [38].

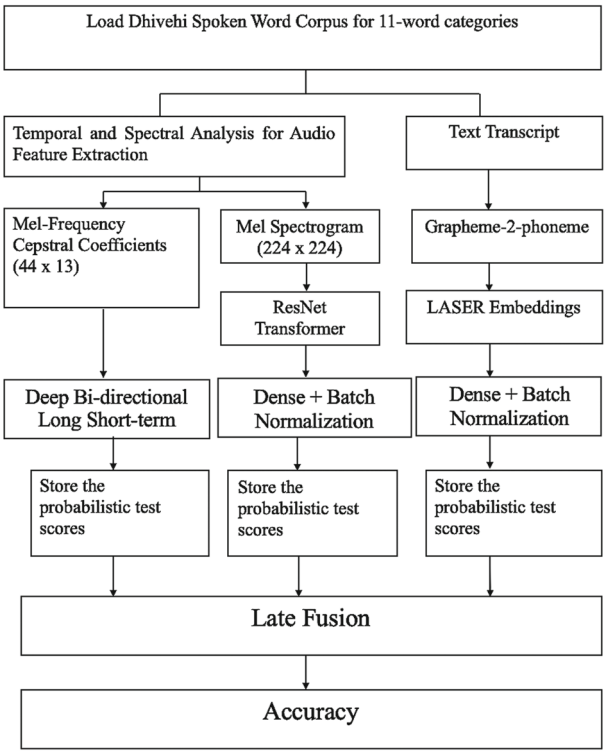

Fig. 1 A proposed methodology of multimodal fusion

3.1 Data Pre-Processing

After collecting audio samples in OPUS format, a comprehensive three-step preprocessing procedure is initiated. In the first step, a Speech2Text transformer transcribes the audio content into text transcripts. Simultaneously, the second pathway employs the Librosa library to convert the audio into 2D Mel spectrograms, which are saved as.png images with dimensions of 224 $\times$ 224 pixels. The third pathway focuses on extracting MFCC features from the audio, resulting in a matrix of size 44 $\times$ 13. The MFCC extraction involves loading the audio, computing the MFCCs without their delta and delta-delta coefficients, and storing these features, along with their labels and file paths, in a JSON file. In the second pathway, the Mel spectrogram transformation is parameterized with a sample rate of 22,050 Hz, an FFT size of 2,058, and a hop length of 512. The generated 2D Mel spectrograms undergo additional pre-processing, including translation, rotation, and resizing operations, to ensure uniform dimensions of 224 $\times$ 224 pixels. These preprocessed spectrograms are then used as input data for ResNet models. This multi-faceted preprocessing pipeline forms the foundation of our research, allowing for the extraction of textual, spectral, and cepstral features from the original audio data, as illustrated in Fig. 1.

3.2 Text-Transcripts Extraction

The pre-trained Speech2Text transformer [49] is employed to convert spoken audio into written text, specifically targeting Dhivehi, a language with limited prior research and no dedicated speech recognition models. Due to the unique challenges of Dhivehi, the transcriptions contain several inaccuracies. The Speech2Text model, part of the Fairseq S2T framework, leverages a transformer-based sequence-to-sequence (seq2seq) architecture with an encoder-decoder setup, optimized for ASR and speech translation (ST). During training, the model uses autoregressive cross-entropy loss, which is critical for generating accurate and coherent transcripts. The input to this model must be a float tensor representing log-mel filter-bank features derived from speech signals, ensuring that the system processes the acoustic information effectively. In summary, the Speech2Text model is a robust tool for ASR and ST tasks, driven by a transformer-based seq2seq architecture. It employs a convolutional downsampler to reduce input length, utilizes autoregressive cross-entropy loss during training, and relies on log-mel filter-bank features to achieve precise transcriptions and translations, even in less-researched languages like Dhivehi.

3.3 Text2Phoneme Embeddings

In our research, we extracted textual transcripts from audio samples, initially represented as graphemes—written symbols corresponding to English words of Dhivehi speech. However, our primary objective was to convert these graphemes into phonemes, which accurately reflect the pronunciation of the words. To achieve this grapheme-to-phoneme conversion, we utilized the CMU Pronouncing Dictionary (Hazen, 2006) [19], a comprehensive resource that maps English words to their corresponding phonetic representations. By leveraging this dictionary, we successfully transformed the text transcripts into precise phonemic representations. This grapheme-to-phoneme conversion is essential for various language-related tasks, including speech recognition, natural language processing, and linguistic analysis. Obtaining phonetic representations allows us to delve deeper into pronunciation patterns, stress markers (as illustrated in Fig. 5), and other phonological features present in the spoken text. In consonants, the International Phonetic Alphabet (IPA) further defines specific places and manners of articulation, enriching our understanding of speech sounds and their production. In our research, we employed LASER [3] to transform phonemes into embeddings. LASER, or "Language-Agnostic Sentence Representations", is a groundbreaking and versatile pre-trained model developed by Facebook AI Research and introduced in 2018. LASER's primary strength lies in its ability to generate language-agnostic sentence embeddings, making it an invaluable tool for multilingual applications, including those involving under-researched languages like Dhivehi. LASER operates through a two-step encoding process: first, it tokenizes text into sub-words, and then it converts these sub-words into fixed-length embedding vectors using a combination of an LSTM-based encoder and a BiLSTM model. What makes LASER particularly powerful is its capability for language-agnostic encoding, allowing it to effectively handle a wide range of languages without requiring

language-specific models or training data. This feature is especially beneficial in the context of Dhivehi, where limited linguistic resources exist. Beyond its multilingual support, LASER is widely utilized for various NLP tasks, such as text classification, sentiment analysis, and document retrieval. Its ease of use and robust performance across numerous languages make it a valuable asset for researchers and practitioners in NLP, including those working with Dhivehi. LASER's ability to facilitate language-agnostic text processing offers significant opportunities for cross-lingual applications and research, ensuring that even languages with limited digital resources, like Dhivehi, can benefit from advanced NLP techniques.

3.4 Deep Bidirectional Long Short-Term Memory (Deep BiLSTM)

The input to our deep BiLSTM model is represented by MFCC features of size 44 $\times$ 13, as shown in Fig. 2. The model architecture includes seven BiLSTM layers with progressively decreasing dimensions: 2048, 1024, 512, 128, 64, 128, and 64 units, followed by a dense layer with 32 units. To address overfitting, we employ a dropout rate of 0.3 and conclude with a final dense layer of 11 units, using the tanh activation function. The model's depth and complexity are attributable to the seven BiLSTM layers and the concluding dense layer. The BiLSTM layers generate both forward and backward hidden states by processing the input features through distinct LSTM networks—one for forward processing and one for backward processing. For class probability predictions, the model utilizes the softmax activation function. We anticipate improved performance in speech recognition by integrating acoustic and visual feature streams within a comprehensive deep learning framework, employing feature-level fusion to harness the strengths of both modalities.

Traditional RNNs often struggle with preserving crucial information over long sequences. To overcome this limitation, we utilize LSTM networks, designed to maintain important details across extended data sequences [21]. LSTM networks are equipped with three types of gates—output, input, and forget gates—to manage gradient flow effectively. The cell state functions as the network's memory, the hidden state contributes to predictions, and the forget gate, regulated by a sigmoid function, controls which information is retained or discarded from the cell state.

3.5 Deep Feed Forward Neural Network with Batch Normalization

The text transcripts are first converted into phonemes, which are then transformed into embeddings using the LASER model, as illustrated in Fig. 3. Each spoken word category is represented by a 1024-dimensional vector, accompanied by corresponding labels. Additionally, we utilize pre-trained scores from Mel-spectrograms, classified using ResNet, which was trained on the ImageNet dataset. ImageNet spans 1000 object classes and comprises 1,281,167 training images, 50,000 validation images, and 100,000 test images.

The LASER embeddings, along with the ResNet-classified Mel-spectrogram scores, are input into our proposed neural network architecture. The network begins

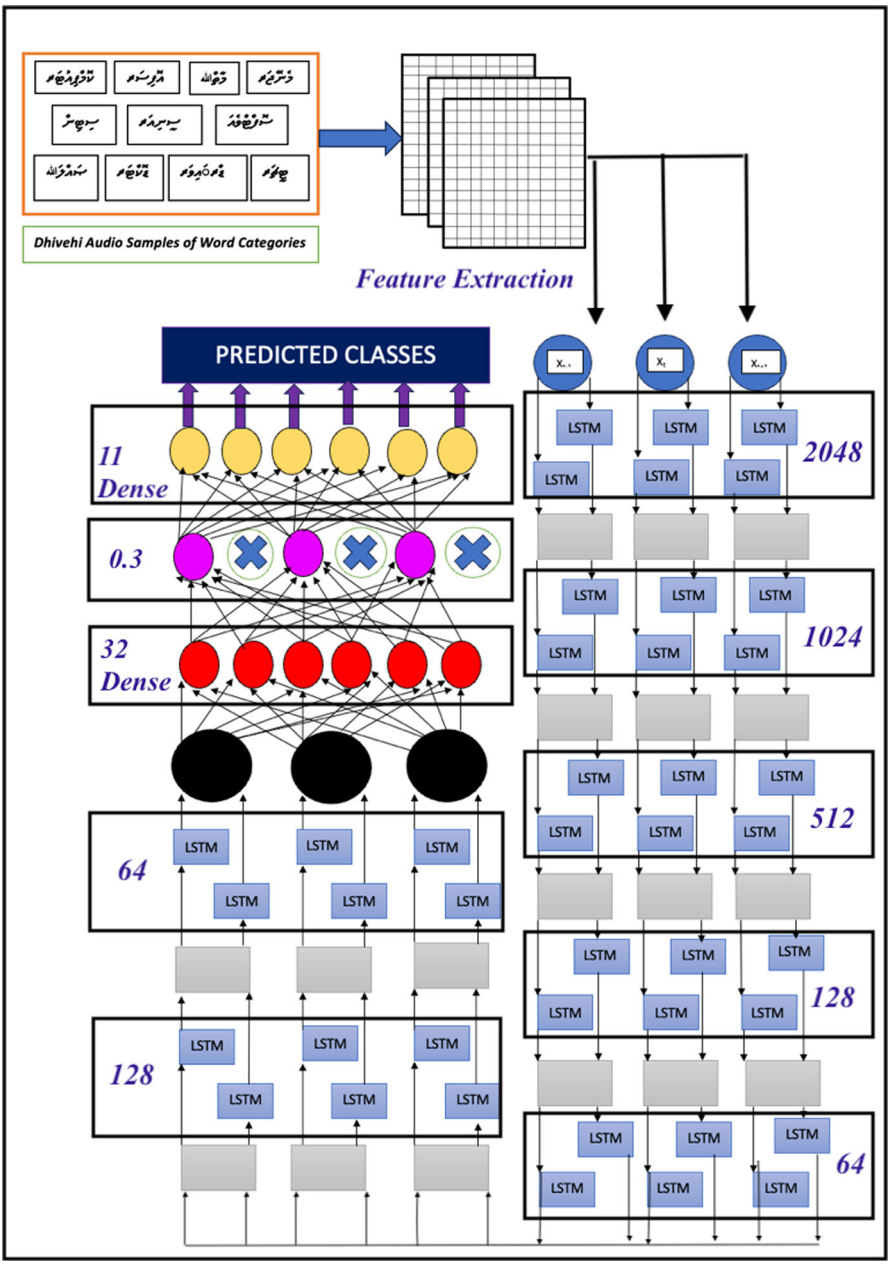

Fig. 2 Our proposed deep BiLSTM model

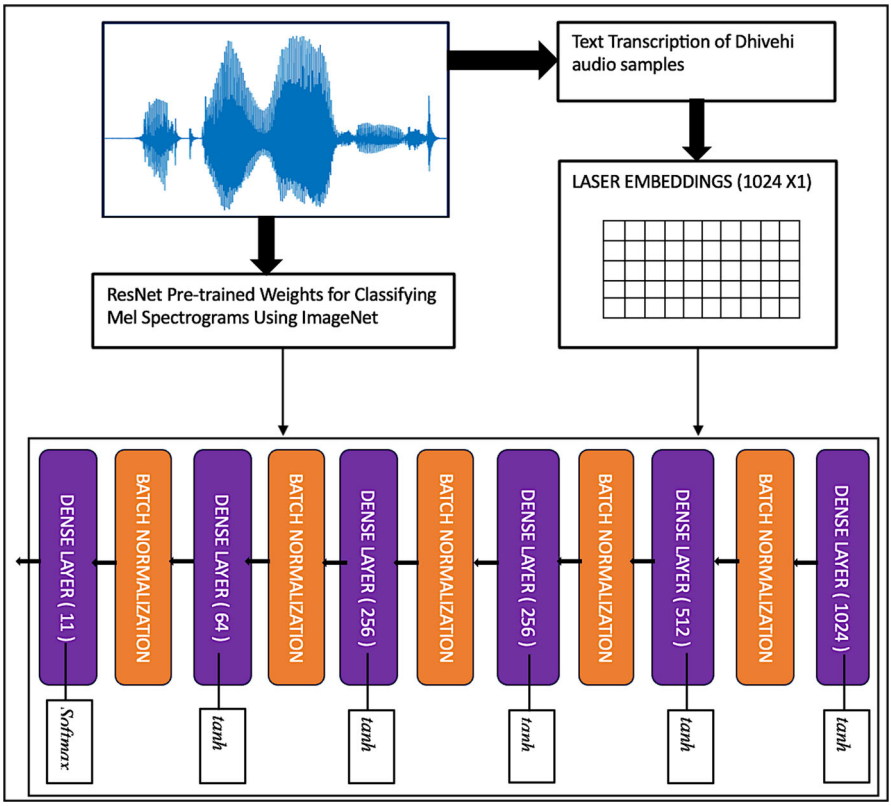

Fig. 3 Proposed dense layer model for LASER embeddings and pre-trained weights from Resnet

with a flattening layer, followed by a dense layer with 1024 neurons and a "tanh" activation function. This is followed by a batch normalization layer, then another dense layer with 512 neurons, again utilizing "tanh" activation. A subsequent batch normalization layer is applied before a dense layer with 256 neurons and "tanh" activation, followed by another batch normalization layer with 256 neurons. In the fifth layer the network features a dense layer with 64 neurons and "tanh" activation, followed by an additional batch normalization layer. The final layer contains 11 neurons, from which posterior probability scores are derived. It is important to note that batch normalization has been applied to each layer of the proposed network, except for the final output layer.

4 Experimental Results and Discussion

In our experimental setup, we leveraged the computational power of Google Colab Pro + + with GPU acceleration, using Python as the programming language. These foundational steps provided the baseline for our experiments. Our primary focus was

Table 1 Hyperparameters for proposed BiLSTM

Framework	Values
Feature Size	MFCC (44 X13)
BiLSTM	7 Layers
Dropout Rate	0.3
Learning Rate	0.001
Batch Size	32
Epochs	100
Activation function	ReLU
Final layer	11

Table 2 Hyperparameters for proposed Dense layered model

Framework	Values
Feature Size	Mel Spectrogram (224 X 224) to Resnet, LASER (1024 X 1)
Dense	5 Layers
Batch Normalization	5 Layers
Dropout Rate	0.3
Learning Rate	0.001
Batch Size	32
Epochs	100
Activation function	Tanh
Final layer	11

on improving accuracy by combining probabilistic scores from both the deep BiLSTM and a Deep Neural Network (DNN). The hyperparameters for the deep BiLSTM and DNN are detailed in Tables 1, 2. The deep BiLSTM model, which comprises 7 layers, takes MFCC features as input, while the DNN, consisting of 5 layers, processes Mel-spectrograms and LASER embeddings. Both models were optimized using the Adam optimizer with a learning rate of 0.001. The training process spanned 100 epochs, with a batch size of 32 (Table 3).

Table 3 Ablation results of proposed methodology: individually & in fusion

Methods	ACC
(224 ×224) Melspectrogram + Resnet	92.86%
(1024 × 1) LASER-Phone embeddings + dense batchnormalization	21.43%
(44 × 13) Mel frquency cepstral coefficients + deep-BiLSTM	71.43%
Fusion of above all three (proposed)	96.42%

To introduce nonlinearity within the model, we employed the "tanh" activation function. Despite following established methods, achieving substantial accuracy improvements for certain word categories has proven challenging. Enhancing recognition performance in these areas will likely require further research and refinement. Addressing these challenges and realizing significant accuracy gains may involve additional, in-depth study and experimentation.

Training error measures a model's performance on the dataset it was specifically trained on, indicating how well the model has learned to fit or predict the target variable within that data. Since the model has been optimized to minimize errors on this dataset, the training error is usually lower compared to the test error. However, a low training error does not necessarily imply that the model will perform well on new, unseen data. Test error, on the other hand, evaluates the model's performance on previously unseen data, providing an estimate of its generalization ability. This metric is essential for determining how well the model can predict outcomes for new, unobserved instances and is critical for assessing its real-world effectiveness and suitability for practical applications. In our experiments, where Divehi was used as a source language, reducing both training and test errors is key to improving the model's accuracy and robustness. Despite applying recommended techniques, we observed that achieving substantial improvements in accuracy for certain word categories remains challenging. Enhancing recognition performance in these specific areas will require further research, experimentation, and possibly the exploration of additional languages and datasets.

4.1 Dataset

In our experimental study, we worked with a significantly underrepresented dataset, particularly focusing on the Dhivehi language. This dataset has been largely overlooked in prior research, resulting in a limited number of available samples, with only 92 data points in total. Our subject pool comprised 11 participants, as depicted in Fig. 4 below. Importantly, we chose not to apply data augmentation techniques in this study. This decision was influenced by the lack of existing research or established methodologies tailored to this specific dataset within the field of speech recognition. Consequently, our

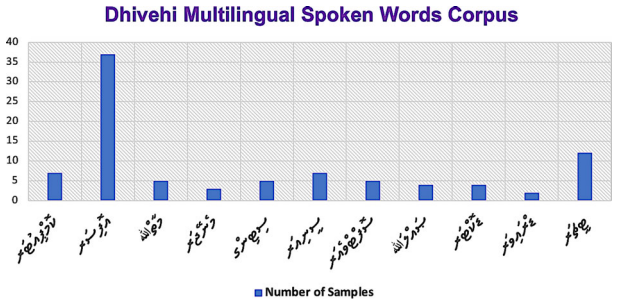

Fig. 4 The number of samples in the Dhivehi audio dataset

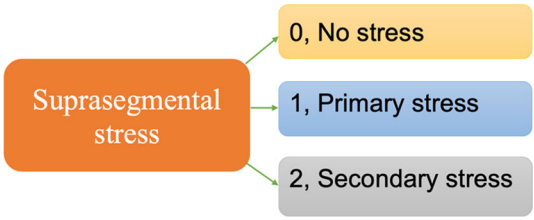

Fig. 5 Stress markers in phoneme transcription

work represents a foundational step in exploring and addressing the unique challenges posed by this underrepresented language.

In our experimentation, we incorporated phoneme stress information, often referred to as suprasegmental details are shown in Fig. 5. These nuances are essential for capturing the natural rhythm and intonation of speech, which are critical for avoiding robotic or monotonic output. By including suprasegmental features, we aimed to make the text-to-speech synthesis more expressive and lifelike, contributing to a more humanized and natural-sounding speech output. This consideration is particularly important in speech recognition and synthesis, where the goal is not only accuracy but also the preservation of the speaker's intended emphasis and emotion.

In our study, we achieved an impressive maximum test accuracy of 92.86% using Mel spectrograms. While most categories were accurately classified, two categories remained challenging to identify. MFCC also performed well, achieving a respectable accuracy of 71.43%, outperforming text-phoneme embeddings. However, LASER-Phone embeddings, even with batch normalization, underperformed across all three modalities—audio, image, and text—when applied to speech recognition tasks. Both mel spectrograms and MFCC demonstrated strong classification accuracy, leading us to propose a fusion approach that selects the highest accuracy among the three methods to consistently enhance overall performance. Notably, LASER was less effective when applied to phonemes, particularly those representing suprasegmental stress. Stress levels were quantified as follows: 0 indicating no stress, 1 signifying primary stress with optimal intensity, and 2 denoting high stress intensity. These stress factors play a crucial role in word identification, though there remains potential for improving accuracy. Our findings highlighted that text-based results consistently lagged behind those of audio and image modalities, which can be attributed in part to our low-resource dataset and the limited research available on the Dhivehi language.

We hope that our contribution will encourage further research in this area, ultimately advancing the field of speech recognition for underrepresented languages. When combining all three modalities—audio, image, and text—we achieved a significant increase in classification accuracy, reaching 96.42%. This multimodal approach underscores the potential of leveraging complementary data sources to enhance performance in challenging classification tasks. To enhance outcomes, researchers should further explore the distinct contributions of various speech sounds and refine their integration into phonological analysis. Additionally, investigating how the combination of multiple phonological attributes can improve classification accuracy presents a promising direction for future research. Such efforts could lead to more nuanced and

effective models, advancing our understanding and performance in speech recognition and analysis.

In our proposed approach for classifying Dhivehi word categories, precision serves as a key metric. tp (True Positives): Correctly predicted positives; fp (False Positives): Incorrectly predicted positives; fn (False Negatives): Incorrectly predicted negatives; tn (True Negatives): Correctly predicted negatives. Where, precision is calculated as the ratio of true positives to the total number of positives predicted by the model, as shown in Eq. (1). This metric is critical for evaluating the model's ability to correctly identify positive instances while minimizing the occurrence of false positives, ensuring that the model's predictions are both accurate and reliable.

$$precision/positive\ predictive\ value(PPV) = \frac{tp}{[tp + fp]} \tag{1}$$

Recall, also known as the true positive rate or sensitivity, is a critical metric in evaluating model performance. It is calculated by dividing the number of true positives by the total number of actual positive instances, as shown in Eq. (2). This metric measures the model's ability to identify all relevant positive instances, while minimizing the occurrence of false negatives, thereby ensuring that the model effectively captures the full range of positive cases.

$$sensitivity/recall/true\ positive\ rate(TNR) = \frac{tp}{[tp + fn]} \tag{2}$$

In our experimental configuration, we observed significantly high values for precision, recall, and F1-score metrics in the 11-subject dataset. These strong metrics collectively reflect a robust classification performance. The detailed results of our statistical analysis, including these metrics, are thoroughly documented in Table 4. The comprehensive evaluation underscores the effectiveness of our approach in achieving high-quality classification results.

$$f1 - Score = \frac{2 \times precision \times recall}{[precision + recall]} \tag{3}$$

Table 4 presents the classification report generated by our advanced deep dense model, encompassing all word categories. This detailed report provides a range of evaluation metrics for each word class, including accuracy, negative predictive value (NPV), false positive rate (FPR), false negative rate (FNR), and false discovery rate (FDR). These metrics offer a comprehensive view of the model's performance across different categories, highlighting its effectiveness and reliability in classification tasks (Table 5).

$$negative\ predictive\ value(NPV) = \frac{tn}{[fn + tn]} \tag{4}$$

$$false\ positive\ rate(FPR) = \frac{fp}{[fp + tn]} \tag{5}$$

Table 4 Classification report per category

Subjects	TPR	TNR	PPV	NPV	FPR	FNR	FDR
ކައުންސަރ	1.00	1.00	1.00	1.00	0.00	0.00	0.00
ނާރުސަރ	1.00	1.00	1.00	1.00	0.00	0.00	0.00
ﷺ	1.00	1.00	1.00	1.00	0.00	0.00	0.00
ލަންގްސަރ	1.00	1.00	1.00	1.00	0.00	0.00	0.00
ބްރެސްޓް	1.00	1.00	1.00	1.00	0.00	0.00	0.00
ބްރެއިންސަރ	0.99	1.00	1.00	1.00	0.00	0.00	0.00
ސްކިންކެންސަރ	1.00	0.96	0.75	1.00	0.04	0.00	0.00
ﷲ	1.00	1.00	1.00	1.00	0.00	0.00	0.25
ލޭކިމިއާ	1.00	1.00	1.00	1.00	0.00	0.00	0.00
ލިމްފޯމާ	0.50	1.00	1.00	0.96	0.00	0.50	0.00
ލިވަރ	1.00	1.00	1.00	1.00	0.00	0.00	0.00

Table 5 Comparison methods

Methods	Accuracy (%)
MFCC + LSTM (Zia & Zahid, 2019) [54]	67.88
GFCC + CNN (Abdelmaksoud, 2021) [1]	63.24
MFCC + LSTM (Wazir & Chuah, 2019) [50]	60.45
Fusion Framework (BiLSTM + DENSE + BatchNormalization)	96.42

$$false\ negative\ rate(FNR) = \frac{fn}{[fn + tp]} \tag{6}$$

$$false\ discovery\ rate(FDR) = \frac{fp}{[fp + tp]} \tag{7}$$

True Negative Rate (TNR), also known as specificity, measures the proportion of actual negative instances that are correctly identified as negative by a model. It quantifies the model's ability to correctly reject negative cases. The formula for TNR is:

$$true\ negative\ rate(TNR) = \frac{tn}{[fp + tn]} \tag{8}$$

Figure 6 illustrates the confusion matrix, where predicted values are plotted along the x-axis and actual values are plotted along the y-axis. Importantly, the train-test split was conducted before applying our proposed fusion approach, ensuring the integrity

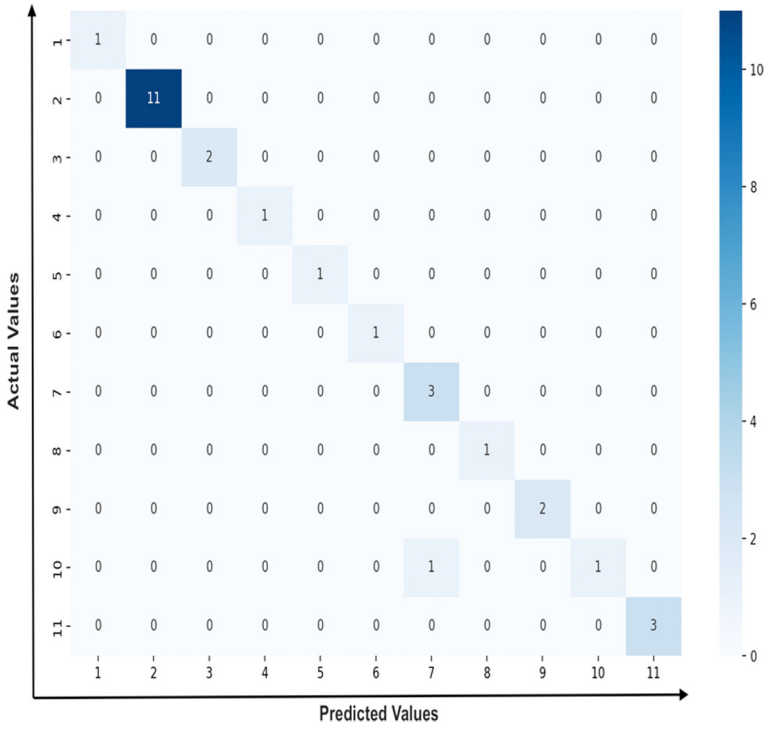

Fig. 6 Confusion matrix of the proposed fusion approach

of the evaluation process. The classification accuracy is notably high, with only a single misclassification observed: category 10 was erroneously labeled as category 7. This excellent performance underscores the effectiveness of our fusion method. The confusion matrix provides valuable insights into the model's strengths and areas for improvement, highlighting the robust classification capabilities while identifying specific instances where the model's predictions diverged from the true labels. Further analysis of these discrepancies can guide targeted refinements and enhancements in future iterations of the model.

We also compared our results with the LSTM architecture for Urdu acoustic modeling explored by Zia and Zahid. Their approach utilized the MFCC method from the Python Speech Features Toolkit, incorporating 40 filterbank channels, 20 cepstral coefficients, 58 cepstral parameters, a frame shift of 5 ms, and a frame size of 10 ms for pre-processing utterances. Despite their detailed methodology, our fusion strategy consistently outperforms theirs in most cases, demonstrating its effectiveness in handling diverse speech data. Additionally, we reviewed the work of Abdelmaksoud et al. (2021), who employed a Convolutional Neural Network (CNN) for Arabic speech recognition. Their study focused on developing and evaluating a CNN model tailored to a specific dataset, assessing its performance in accurately identifying Arabic spoken words. Similarly, the study by Wazir and Chuah (2019) applied deep learning techniques to recognize spoken Arabic digits, achieving notable results by training and testing models on Arabic digit utterances. In contrast, our approach has demonstrated

superior performance on Dhivehi audio samples, highlighting the robustness and effectiveness of our method for this less-researched language. The Dhivehi language, with its unique phonetic and phonological characteristics, poses distinct challenges for speech recognition. Our success in this domain underscores the potential of our fusion approach to address these challenges effectively, paving the way for advancements in recognizing and processing speech in underrepresented languages. This comparison not only validates our approach but also emphasizes the value of exploring novel methodologies for diverse linguistic datasets.

Our research contributes to the ongoing advancements in deep learning and neural networks, aligning with recent findings on optimal consensus in multi-agent systems and adaptive fault-tolerant [42] decentralized control of nonlinear systems with uncertainties and delays.

5 Conclusion

In conclusion, this study effectively tackles the complex challenge of integrating multiple data modalities—such as imperfect text transcripts and raw audio—for Dhivehi speech recognition, especially within resource-constrained settings with limited prior research. Our innovative multimodal approach combines audio-to-spectrogram processed and further passed to ResNet, phone embeddings, and 13 MFCC to enhance Dhivehi speech recognition in Malaysia. By leveraging CMU phonemes extracted from text transcripts via the Speech2Text transformer and processing LASER embeddings through feedforward neural networks, our method integrates the strengths of audio, text, and image modalities. The rigorous experimentation conducted on the Dhivehi language, utilizing the extensive MSWC dataset, underscores the effectiveness of our fusion strategy. Our approach—merging posterior class probabilities from deep-BiLSTM networks and feedforward neural models—achieves a remarkable accuracy of 96.42% on a test set of 11 subjects within the MSWC dataset. Comprehensive testing and thorough ablation analyses confirm that our proposed method surpasses existing state-of-the-art systems, demonstrating superior classification accuracy and providing a significant advancement in speech recognition technology for underrepresented languages. This work not only establishes a robust framework for integrating diverse data modalities but also sets a new benchmark for speech recognition accuracy in low-resource settings. Future research can build on these findings to further refine multimodal approaches and explore their application to other underrepresented languages, driving continued progress in the field of speech recognition.

6 Future scope

For future research, several promising directions emerge from this study. Expanding the applicability of our multimodal approach to a wider range of languages and dialects is a critical next step. Assessing its adaptability across diverse linguistic contexts could significantly enhance its utility and impact. Further refinement and optimization of the multimodal fusion strategy offer another avenue for exploration. Investigating

alternative fusion architectures and advanced feature engineering techniques could lead to even more robust and accurate results. Addressing the challenges associated with imperfect text transcripts remains a key area for improvement. Future work should focus on enhancing the quality and accuracy of transcriptions, potentially through the development of more advanced speech-to-text systems or sophisticated natural language processing methods. Extending this research to practical applications is also essential. Developing and deploying speech recognition systems for Dhivehi in real-world scenarios will provide valuable insights into the system's performance and applicability. Additionally, evaluating the scalability and efficiency of the proposed multimodal approach, particularly in resource-constrained environments, is crucial for its practical implementation. Finally, staying abreast of the latest advancements in deep learning and multimodal fusion techniques will be vital. Integrating cutting-edge innovations into our approach will help maintain its relevance and competitive edge in the rapidly evolving field of speech recognition for under-resourced languages like Dhivehi.

Acknowledgements Not applicable.

Authors' contributions Sunakshi Mehra: Implementation of proposed approach, wrote the manuscript text, Writing – Original Draft, Visualization. Virender Ranga: Conceptualization, Methodology, Writing – Review & Editing, Supervision. Ritu Agarwal: Conceptualization, Methodology, Writing – Review & Editing, Supervision.

Funding The authors received no outside funding or assistance for the research presented in their submission.

Data availability The authors verify that the data underpinning the results and discoveries of this research can be found within the confines of the article.

Declarations

Conflict of interest The authors state that they have no known financial or personal interests that could have impacted the conclusions described in this work.

Ethical Approval The article does not include any studies or investigations that involve human or animal participants.

Human and animal ethics Not applicable.

Consent for publication All authors have approved the manuscript and given their full consent for its publication.

References

1. E.R. Abdelmaksoud, A. Hassen, N. Hassan, M. Hesham, Convolutional neural network for arabic speech recognition. Egypt. J. Language Eng. **8**(1), 27–38 (2021). https://doi.org/10.21608/ejle.2020.47685.1015
2. D. Amodei, S. Ananthanarayanan, R. Anubhai, J. Bai, E. Battenberg, C. Case, et al.. Deep speech 2: End-to-end speech recognition in english and mandarin. In *International conference on machine learning* (pp. 173–182). PMLR. (2016) https://doi.org/10.5555/3045390.3045410

3. M. Artetxe, G. Labaka, E. Agirre, K. Cho, K. Unsupervised neural machine translation. arXiv preprint arXiv:1710.11041. (2017) https://doi.org/10.48550/arXiv.1710.11041
4. E. Bocchieri, B.W. Mak, Subspace distribution clustering hidden Markov model. IEEE Trans. Speech Audio Process. **9**(3), 264–275 (2001). https://doi.org/10.1109/89.906000
5. L. Burget, P. Schwarz, M. Agarwal, P. Akyazi, K. Feng, A. Ghoshal et al. Multilingual acoustic modeling for speech recognition based on subspace Gaussian mixture models. In *2010 IEEE international conference on acoustics, speech and signal processing* (pp. 4334–4337). IEEE. (2010) https://doi.org/10.1109/ICASSP.2014.6854671
6. W. Byrne, P. Beyerlein, J.M. Huerta, S. Khudanpur, B. Marthi, J. Morgan, et al. Towards language independent acoustic modeling. In *2000 IEEE International Conference on Acoustics, Speech, and Signal Processing. Proceedings (Cat. No. 00CH37100)* (Vol. 2, pp. II1029-II1032). IEEE. (2000) https://doi.org/10.1109/ICASSP.2000.859138
7. J. Cho, M.K. Baskar, R. Li, M. Wiesner, S.H. Mallidi, N. Yalta,et al. Multilingual sequence-to-sequence speech recognition: architecture, transfer learning, and language modeling. In *2018 IEEE spoken language technology workshop (SLT)* (pp. 521–527). IEEE. (2018) https://doi.org/10.48550/arXiv.1810.03459
8. P. Cohen, S. Dharanipragada, J. Gros, M. Monkowski, C. Neti, S. Roukos, T. Ward. Towards a universal speech recognizer for multiple languages. In *1997 IEEE workshop on automatic speech recognition and understanding proceedings* (pp. 591–598). IEEE. (1997) https://doi.org/10.48550/arXiv.1711.02207
9. X. Cui, V. Goel, B. Kingsbury. Data augmentation for deep convolutional neural network acoustic modeling. In *2015 IEEE international conference on acoustics, speech and signal processing (ICASSP)* (pp. 4545–4549). IEEE. (2015) https://doi.org/10.1109/TASLP.2015.2438544
10. X. Cui, V. Goel, B. Kingsbury, Data augmentation for deep neural network acoustic modeling. IEEE/ACM Trans. Audio Speech Language Process. **23**(9), 1469–1477 (2015). https://doi.org/10.1109/ICASSP.2014.6854671
11. S. Dalmia, R. Sanabria, F. Metze, A.W. Black. Sequence-based multi-lingual low resource speech recognition. In *2018 IEEE international conference on acoustics, speech and signal processing (ICASSP)* (pp. 4909–4913). IEEE. (2018) https://doi.org/10.48550/arXiv.1802.07420
12. R. Das, T.D. Singh, Image-text multimodal sentiment analysis framework of assamese news articles using late fusion. ACM Trans. Asian Low-Resource Language Inf. Process. **22**(6), 1–30 (2023). https://doi.org/10.1145/3584861
13. M.J. Gales, A. Ragni, H. AlDamarki, C. Gautier. Support vector machines for noise robust ASR. In *2009 IEEE workshop on automatic speech recognition & understanding* (pp. 205–210). IEEE. (2009) https://doi.org/10.1109/ASRU.2009.5372913
14. M.J. Gales, K. Yu. Canonical state models for automatic speech recognition. In *Eleventh annual conference of the international speech communication association*. (2010) https://doi.org/10.21437/Interspeech.2010-11
15. A.E. Gnanadesikan. *Dhivehi: The language of the Maldives* (Vol. 3). Walter de Gruyter GmbH & Co KG. (2016) https://doi.org/10.1515/9781614512349
16. F.P. Gomez, R. Sanabria, Y.H. Sung, D. Cer, S. Dalmia, G.H. Abrego. Transforming LLMs into cross-modal and cross-lingual retrieval systems. arXiv preprint arXiv:2404.01616. (2024) https://doi.org/10.48550/arXiv.2404.01616
17. A. Graves, S. Fernández, F. Gomez, J. Schmidhuber. Connectionist temporal classification: labelling unsegmented sequence data with recurrent neural networks. In *Proceedings of the 23rd international conference on machine learnin* (2006), pp. 369–376. https://doi.org/10.1145/1143844.1143891
18. F. Grézl, E. Egorova, M. Karafiát, Study of large data resources for multilingual training and system porting. Proc. Comput. Sci. **81**, 15–22 (2016). https://doi.org/10.1016/j.procs.2016.04.024
19. T.J. Hazen. Automatic alignment and error correction of human generated transcripts for long speech recordings. In *Ninth international conference on spoken language processing*. (2006) https://doi.org/10.21437/Interspeech.2006-449
20. M. Harper. The automatic speech recogition in reverberant environments (ASpIRE) challenge. In *2015 IEEE workshop on automatic speech recognition and understanding (ASRU)* (pp. 547–554). IEEE. (2015) https://doi.org/10.1109/ASRU.2015.7404843
21. S. Hochreiter, J. Schmidhuber, Long short-term memory. Neural Comput. **9**(8), 1735–1780 (1997). https://doi.org/10.1162/neco.1997.9.8.1735

22. R. Hsiao, J. Ma, W. Hartmann, M. Karafiát, F. Grézl, L. Burget. et al. Robust speech recognition in unknown reverberant and noisy conditions. In *2015 IEEE workshop on automatic speech recognition and understanding (ASRU)* (pp. 533–538). IEEE (2015). https://doi.org/10.1109/ASRU.2015.7404841
23. https://www.uib.no/en/discipline/linguistics
24. J.T. Huang, J. Li, D. Yu, L. Deng, Y. Gong. Cross-language knowledge transfer using multilingual deep neural network with shared hidden layers. In *2013 IEEE international conference on acoustics, speech and signal processing* (pp. 7304–7308). IEEE. (2013) https://doi.org/10.1109/ICASSP.2013.6639081
25. X.D. Huang, M.A. Jack, Semi-continuous hidden Markov models for speech signals. Comput. Speech Lang. **3**(3), 239–251 (1989). https://doi.org/10.1016/0885-2308(89)90020-X
26. N. Jaitly, G.E. Hinton. Vocal tract length perturbation (VTLP) improves speech recognition. In *Proceedings of ICML workshop on deep learning for audio, speech and language* (Vol. 117, p. 21) (2013).
27. A. Jensson, K. Iwano, S. Furui. Development of a speech recognition system for Icelandic using machine translated text. In *Spoken languages technologies for under-resourced languages*. (2008) https://aclanthology.org/www.mt-archive.info/05/SLTU-2008-Jensson.pdf
28. J. Kohler. Multi-lingual phoneme recognition exploiting acoustic-phonetic similarities of sounds. In *Proceeding of fourth international conference on spoken language processing. iCSLP'96* (Vol. 4, pp. 2195–2198). IEEE (1996) https://doi.org/10.1109/ICSLP.1996.607240
29. J. Kohler. Language adaptation of multilingual phone models for vocabulary independent speech recognition tasks. In *Proceedings of the 1998 IEEE international conference on acoustics, speech and signal processing, ICASSP'98 (Cat. No. 98CH36181)* (Vol. 1, pp. 417–420). IEEE. (1998) https://doi.org/10.1109/ICASSP.1998.674456
30. V.B. Le, L. Besacier, Automatic speech recognition for under-resourced languages: application to Vietnamese language. IEEE Trans. Audio Speech Lang. Process. **17**(8), 1471–1482 (2009). https://doi.org/10.1109/TASL.2009.2021723
31. H. Lin, L. Deng, D. Yu, Y.F. Gong, A. Acero, C.H. Lee. A study on multilingual acoustic modeling for large vocabulary ASR. In *2009 IEEE international conference on acoustics, speech and signal processing* (pp. 4333–4336). IEEE (2009). https://doi.org/10.1109/ICASSP.2009.4960588
32. S. Mehra, S. Susan, Deep fusion framework for speech command recognition using acoustic and linguistic features. Multimed. Tools Appl. **82**(25), 38667–38691 (2023). https://doi.org/10.1007/s11042-023-15118-1
33. S. Mehra, V. Ranga, R. Agarwal, A deep learning approach to dysarthric utterance classification with BiLSTM-GRU, speech cue filtering, and log mel spectrograms. J. Supercomput. (2024). https://doi.org/10.1007/s11227-024-06015-x
34. S. Mehra, V. Ranga, R. Agarwal, Improving speech command recognition through decision-level fusion of deep filtered speech cues. SIViP **18**(2), 1365–1373 (2024). https://doi.org/10.1007/s11760-023-02845-z
35. N. Mohamed. Transcending linguistic and cultural boundaries: a case study of four young maldivians' translanguaging practices. *English-Medium Instruction and Translanguaging*. https://doi.org/10.21832/9781788927338-010 (2021)
36. S.J. Pan, Q. Yang, A survey on transfer learning. IEEE Trans. Knowl. Data Eng. **22**(10), 1345–1359 (2009). https://doi.org/10.1109/TKDE.2009.191
37. V. Peddinti, G. Chen, V. Manohar, T. Ko, D. Povey, S. Khudanpur. Jhu aspire system: Robust lvcsr with tdnns, ivector adaptation and rnn-lms. In *2015 IEEE workshop on automatic speech recognition and understanding (ASRU)* (pp. 539–546). IEEE. (2015) https://doi.org/10.1109/ASRU.2015.7404842
38. D. Povey, L. Burget, M. Agarwal, P. Akyazi, K. Feng, A. Ghoshal, et al. Subspace Gaussian mixture models for speech recognition. In *2010 IEEE international conference on acoustics, speech and signal processing* (pp. 4330–4333). IEEE. (2010) https://doi.org/10.1109/ICASSP.2010.5495662
39. G. Saon, J.T. Chien, Bayesian sensing hidden Markov models. IEEE Trans. Audio Speech Lang. Process. **20**(1), 43–54 (2011). https://doi.org/10.1109/TASL.2011.2129911
40. A. Sehr, C. Hofmann, R. Maas, W. Kellermann. Multi-style training of HMMs with stereo data for reverberation-robust speech recognition. In *2011 joint workshop on hands-free speech communication and microphone arrays* (pp. 196–200). IEEE. (2011) https://doi.org/10.1109/HSCMA.2011.5942396
41. X. Song, Z. Peng, S. Song, V. Stojanovic, Anti-disturbance state estimation for PDT-switched RDNNs utilizing time-sampling and space-splitting measurements. Commun. Nonlinear Sci. Numer. Simul. **132**, 107945 (2024). https://doi.org/10.1016/j.cnsns.2024.107945

42. X. Song, P. Sun, S. Song, V. Stojanovic, Quantized neural adaptive finite-time preassigned performance control for interconnected nonlinear systems. Neural Comput. Appl. **35**(21), 15429–15446 (2023). https://doi.org/10.1007/s00521-023-08361-y
43. X. Song, N. Wu, S. Song, Y. Zhang, V. Stojanovic, Bipartite synchronization for cooperative-competitive neural networks with reaction–diffusion terms via dual event-triggered mechanism. Neurocomputing **550**, 126498 (2023). https://doi.org/10.1016/j.neucom.2023.126498
44. S. Takahashi, S. Sagayama. Four-level tied-structure for efficient representation of acoustic modeling. In *1995 International conference on acoustics, speech, and signal processing* (Vol. 1, pp. 520–523). IEEE. https://doi.org/10.1109/ICASSP.1995.479643(1995)
45. S. Tong, P.N. Garner, H. Bourlard. An investigation of deep neural networks for multilingual speech recognition training and adaptation (No. CONF, pp. 714–718). https://doi.org/10.21437/Interspeech.2017-1242(2017)
46. G. Van Driem. Glimpses of the ethnolinguistic prehistory of northeastern India. In Origins and migrations in the extended Eastern Himalayas (pp. 187–211). Brill. https://doi.org/10.1163/9789004228368_011(2012)
47. N.T. Vu, D. Imseng, D. Povey, P. Motlicek, T. Schultz, H. Bourlard. Multilingual deep neural network based acoustic modeling for rapid language adaptation. In *2014 IEEE international conference on acoustics, speech and signal processing (ICASSP)* (pp. 7639–7643). IEEE. https://doi.org/10.1109/ICASSP.2014.6855086 (2014)
48. N.T. Vu, F. Metze, T. Schultz. Multilingual bottle-neck features and its application for under-resourced languages. In *Spoken language technologies for under-resourced languages*. https://www.isca-archive.org/sltu_2012/vu12_sltu.pdf (2012)
49. C. Wang, Y. Tang, X. Ma, A. Wu, S. Popuri, D. Okhonko, J. Pino. Fairseq S2T: Fast speech-to-text modeling with fairseq. arXiv preprint arXiv:2010.05171. https://doi.org/10.48550/arXiv.2010.05171(2020)
50. A.S.M.B. Wazir, J.H. Chuah. Spoken Arabic digits recognition using deep learning. In *2019 IEEE international conference on automatic control and intelligent systems (I2CACIS)* (pp. 339–344). IEEE. https://doi.org/10.1109/I2CACIS.2019.8825004 (2019)
51. D. Yu, M.L. Seltzer, J. Li, J.T. Huang, F. Seide. Feature learning in deep neural networks-studies on speech recognition tasks. arXiv preprint arXiv:1301.3605. https://doi.org/10.48550/arXiv.1301.3605 (2013)
52. L. Zhang, D. Karakos, W. Hartmann, R. Hsiao, R. Schwartz, S. Tsakalidis. Enhancing low resource keyword spotting with automatically retrieved web documents. In *Sixteenth annual conference of the international speech communication association*. https://doi.org/10.21437/Interspeech.2015-262 (2025)
53. Q. Zhang, H. Zhang, K. Zhou, L. Zhang, Developing a physiological signal-based, mean threshold and decision-level fusion algorithm (PMD) for emotion recognition. Tsinghua Sci. Technol. **28**(4), 673–685 (2023). https://doi.org/10.26599/TST.2022.9010038
54. T. Zia, U. Zahid, Long short-term memory recurrent neural network architectures for Urdu acoustic modeling. Int. J. Speech Technol. **22**, 21–30 (2019). https://doi.org/10.1007/s10772-018-09573-7
55. J. Zhu, C. Huang, P. De Meo, DFMKE: A dual fusion multi-modal knowledge graph embedding framework for entity alignment. Inf. Fusion **90**, 111–119 (2023). https://doi.org/10.1016/j.inffus.2022.09.012

Publisher's Note Springer Nature remains neutral with regard to jurisdictional claims in published maps and institutional affiliations.

Springer Nature or its licensor (e.g. a society or other partner) holds exclusive rights to this article under a publishing agreement with the author(s) or other rightsholder(s); author self-archiving of the accepted manuscript version of this article is solely governed by the terms of such publishing agreement and applicable law.

The Journal of Supercomputing (2025) 81:166
https://doi.org/10.1007/s11227-024-06589-6

DiabeticChain: a novel blockchain approach for patient-centric diabetic data management

Deepak Kumar Mishra[1,2] · **Pawan Singh Mehra**[1]

Accepted: 7 October 2024
© The Author(s), under exclusive licence to Springer Science+Business Media, LLC, part of Springer Nature 2024

Abstract

While medical IoT data complexity surges, managing healthcare for chronic ailments like diabetes remains stagnant. Our innovative approach, DiabeticChain, not only addresses this but also introduces unique methodologies that set it apart in the realm of diabetic data management. Current healthcare architectures face significant research gaps including privacy and security concerns in sharing sensitive diabetic data, lack of patient data ownership, data fragmentation, interoperability issues, reliance on centralized authorities and ethical concerns laying the foundation for the novel solution DiabeticChain offers. Blockchain, a decentralized distributive ledger technology, can revolutionize data sharing with immutability, transparency and traceability. This paper proposes DiabeticChain, a permissioned blockchain-based, patient-centric healthcare architecture, addressing the key challenge of empowering patients to grant or revoke access to their diabetic data enabling secure sharing while safeguarding patient privacy. DiabeticChain allows data consumers to access patients' data as per their agreed-upon consent policy, using Solidity smart contracts, developed, tested and deployed using the truffle framework. A hybrid model is used for data storage to store confidential diabetic data in an off-chain secure database while keeping only metadata on the blockchain. The study includes a proof-of-concept using Go-Ethereum to establish a permissioned blockchain and ChainLink for secure smart contract connectivity to off-chain resources. Performance was evaluated using four Azure hosted VMs and Hyperledger Caliper utilizing throughput and latency as key performance metrics to validate effectiveness. Results depict the system's feasibility with an average Query throughput of 201.7 tps, an average Transaction throughput of 200.07 tps, an average Query latency of 0.24 s and an average Transaction latency of 1.31 s. The architecture is designed to seamlessly integrate with existing EHR systems, promoting efficient data sharing within the healthcare industry.

Keywords Permissioned blockchain · Patient-centric · Smart contracts · Electronic Health Records (EHRs) · Diabetic data sharing

Extended author information available on the last page of the article

Published online: 13 November 2024

1 Introduction

Diabetes is a chronic disease that requires rigorous self-care and as per the data of 2021, there are 537 million adults living with the disease globally and this number is predicted to rise at a pace higher than expected resulting in 643 million by 2030 and 783 million by 2045 [1]. Despite the ubiquity of diabetes as a global health concern, recent advancements in data sharing remain inadequate. Our research identifies these gaps, laying the foundation for the novel solutions DiabeticChain offers. Even though people with diabetes have lower life expectancy than the ones without the disease, the life-time medical cost of diabetes is still significant [2]. Patients diagnosed with this disease need to take daily care and are responsible for the choices of diet, exercise, regular medication and testing of blood sugar levels. The current state of diabetes care is worsening due to challenges like aggravated patient-to-provider ratio, the presence of geographical barriers for diagnosis and increasing patient and provider burden due to absence of effective diabetic data sharing [3]. The self-management of diabetes plays a crucial role in complex patient care and continuous monitoring of health data is important [4]. Along with regular medication and diabetes diet plan, patients have to monitor their blood glucose levels, weight and blood pressure regularly. Huge amounts of data are generated and utilized during this process, and this measured data has to be effectively shared with medical practitioners to ensure patient care. Thus, data sharing plays a crucial role in managing the disease [5].

Whenever patients visit a medical practitioner, their data is gathered and stored as EHRs in centralized databases, which are owned, managed and controlled by central authorities like hospitals. Electronic Health Records (EHRs) are patient records stored digitally consisting of health information like medical history, current medication, allergies, test reports, etc. maintained for better patient diagnosis and treatment by healthcare professionals [6]. Even though we have shifted from document-based health charts to EHRs, the data is still stored on central servers [7]. These central authorities may share the patient data of interest with various stakeholders for better patient care or advancing research. Patients have no control over their private and sensitive data raising serious concerns for security and privacy. According to the Health Insurance Portability and Accountability Act (HIPAA) [8], every patient has the right to own their health information and set rules to give consent to share their health data with other entities. This leads to the requirement of a decentralized system where patients are the complete owner of their data, thereby having control over who can access their data.

Due to the complexity and privacy of the EHR data, it should be restricted from unauthorized access. With the increasing patient mobility and the development of multiple healthcare facility providers, it has become easier for patients to consult multiple hospitals and doctors for the treatment of chronic diseases like diabetes [9]. The data is thus becoming fragmented due to being stored in multiple databases, making it difficult for doctors to access the complete medical history of the patient. Traditionally, if one hospital requires to share the patient's data with another hospital, then the patient signs a consent form stating the

detailed use of data shared and this tedious process is carried out manually, making it time-consuming [9].

Many challenges exist that hinder the traditional way of sharing diabetic data and need to be addressed. These are security and privacy concerns in sharing sensitive diabetic data, no data ownership for the patient, data fragmentation, lack of interoperability, requirement of trust in a centralized authority and ethical issues. DiabeticChain presents a novel approach to address these fundamental issues in diabetic care. The main challenge addressed in this paper is the protection of privacy of the patient data by giving them control to grant or revoke access to their data enabling secure sharing of diabetic data among stakeholders. Unlike the conventional models, DiabeticChain prioritizes patient data ownership, data privacy and secure data sharing.

1.1 Background and motivation

Healthcare data is today captured and generated from multiple sources ranging from the patients themselves to wearable devices like smartwatches, smart bands, smartphones, etc. With increasing technological advancements, IoT devices like wireless sensors are being used to monitor continuous patient health, generating huge amounts of personal, valuable and complex data. If controlled access to complete data is provided, then it can substantially benefit the entire healthcare system. Since patient data is owned by trustless third-party authorities like hospitals, laboratories and health insurance companies, secure and efficient data sharing is not possible. There exists no method for verifying the medical data sharing by hospitals to an untrusted third party [10]. This creates vulnerabilities in data security, increasing the possibility of unauthorized access.

There also exists a possible risk of a data breach due to the existence of a single point of failure. According to existing reports, 89% of users using IoT in healthcare have suffered security breaches and 80% of them are still willing to use this technology [11]. Unauthorized access through malicious attacks on diabetic healthcare data can have disastrous results like medical identity theft, insurance fraud and tampering with ongoing treatment or medical history. A secure and efficient digital EHR data sharing system is thus required. To overcome the limitations of conventional data sharing models discussed above, a decentralized approach to medical data sharing can potentially provide patients with ownership over their data, thereby providing more control over their data, helping in eliminating a single point of failure in centralized systems, minimizing cyberattacks and building trust among the stakeholders involved in diabetic care.

There are some unique challenges as well associated with diabetic data like diabetes is a disease that requires self-care by substantially burdening the patients with continuous glucose monitoring and carbohydrate counting [3]. As per the research in [12], an average adult with type 2 diabetes is recommended to spend 4 h per day as the total estimated time for self-care. Being a chronic disease, diabetes also burdens the healthcare providers to analyse and access the huge amount of data associated with it [3]. While many researchers have worked in the field of medical data

sharing, there exists a need to specifically address these unique challenges associated with sharing of diabetic data among stakeholders. This gap in the existing literature serves as the primary motivation of this research.

1.2 Objectives and contributions

Blockchain is a decentralized distributive ledger technology that has the potential to revolutionize the way confidential data is shared and accessed today by providing benefits like immutability, transparency, traceability and enhanced security [13]. In this paper, we propose a system—DiabeticChain, a patient-centric healthcare architecture to support secure and efficient data sharing of diabetic data, provide an implementation as a proof-of-concept study and then verify its performance using various assessment metrics. The application of a one-time access URL to access patient data according to their consent, makes our approach novel and a necessary solution.

The aim is to address the current limitations of the traditional data sharing models by using a decentralized technology based on blockchain for diabetic data sharing. DiabeticChain's goal is to solve the requirements of patient privacy, data security, user control over data, traceability, data integrity, interoperability and standardization. The following are the major contributions of this paper:

- Proposed a novel blockchain-based patient-centric healthcare architecture for safe storage and secure diabetic data sharing among stakeholders like healthcare providers, laboratory technicians, health insurance organizations and researchers.
- Implementation of an architecture where data consumers can access patient's diabetic data as per their agreed-upon access policy using a one-time access URL implemented by self-executing smart contracts written in Solidity to ensure the controlled exchange of sensitive data based on the blockchain.
- Evaluated the performance of the proposed architecture based on throughput and latency assessment metrics to ensure its feasibility and reliability in real-world health scenarios.

While many blockchain-based solutions mainly focus on the data sharing between the healthcare entities, DiabeticChain places patients at the centre of the healthcare architectures by empowering them with the ability to control who has access to their data. The one-time access URL system ensures that the patients explicitly grant access as per the predefined agreed-upon access policy. This level of consent sharing makes it different from the traditional healthcare data sharing models.

1.3 Organization

The remaining paper is organized as follows: Sect. 2 summarizes and compares the related work. Section 3 provides an overview of the technical background of blockchain. Section 4 describes the blockchain potential in diabetic data sharing.

Section 5 states the design requirements and the proposed architecture is discussed in Sect. 6. Section 7 discusses the implementation of the workflow. Results and performance evaluation are described in Sect. 8. Section 9 concludes the paper and discusses the limitations and scope for future work.

2 Related work

Promising research has been carried out in the field of blockchain-based healthcare solutions to support healthcare data sharing to further address the concerns of privacy and security, data fragmentation, lack of interoperability, lack of trust in healthcare data sharing and no ownership of data in the hands of the patients. Let us examine the challenges addressed by different researchers and how their solution is different.

2.1 Blockchain-based healthcare solutions to support healthcare data sharing

In [14], Zyskind and Nathan employed blockchain, re-purposed as an access-control moderator and an off-chain data storage solution to ensure that users control and manage their data protecting users' privacy. The authors in [15] proposed a decentralized blockchain-based framework MedRec using the Ethereum blockchain to share and manage Electronic Medical Records (EMRs). It can manage confidential information and allows authentication, accountability and secure sharing of medical data. But the framework uses private databases to store data which is prone to cyber-attacks and will also allow an internal entity to have access to the sensitive data.

The authors in [16] proposed a patient-centric permissioned blockchain-based medical data sharing to ensure privacy and patient identity management using Hyperledger Fabric. But the authors did not address the user authentication to secure data storage. In [17], the authors designed a system to share and manage personal health data using blockchain and cloud storage, eliminating the dependence on a centralized third party for sensitive data sharing. However, the proposed system is yet to be integrated with the existing healthcare systems.

Dubovitskaya et al. [9] designed a framework named ACTION-HER using a permissioned blockchain and Hyperledger Fabric to allow patients to control the sharing of their health records securely for radiation oncology. This approach enabled healthcare providers and researchers to access patient data more quickly and efficiently while significantly reducing costs. However, the limitation of this paper was the risk of having a single point of failure of the system and in case of emergency situations, there is a requirement of "break glass" mechanism.

Jabarulla et al. [18] implemented a distributed patient-centric image management system using blockchain to ensure security, safety and privacy of patient data without using centralized authority. Due to manual encryption and decryption of original medical images the system poses a risk of losing private keys. Mani et al. [19] proposed a patient-centric approach to store health records on an IPFS-based distributed ledger system using Hyperledger Fabric technology and resolved privacy,

security and confidentiality concerns to enable decentralized storing and sharing of health information while ensuring scalability. A large number of resources are required for implementation of multi-blockchain systems and extended frameworks integrated with Non-Fungible Tokens.

The authors in [20] proposed a novel secure and efficient patient-centric healthcare framework (PCH) reference architecture that leverages blockchain, cloud and IoT technologies to improve semantic interoperability in healthcare systems. However, the costs associated with the maintenance and implementation of the system could be high and do not address the legal and regulatory challenges associated with sharing patient data across different healthcare systems. Taylor et al. [21] proposed VigilRx, a patient-centric and interoperable prescription management system that ensures user control, prevents information blocking and improves transfer efficiency ensuring the security of patient data, interoperability, fraud prevention, data accuracy and accessibility. The system is heavily dependent on blockchain which limits its effectiveness by scalability and security of the network making it vulnerable to blockchain congestion and security breaches.

In [22], the authors proposed a patient-centric blockchain-based health record access framework using Hyperledger Fabric to enhance patient control, protect privacy and data integrity. Patients can impose necessary conditions before granting access to their medical data. But they proposed a conceptual framework that has not been implemented in a real-world setting and integrated with the existing healthcare models. Rai [23] proposed a patient-controlled blockchain-based Electronic Health Records management system to ensure patient ownership of their medical data, elimination of security risks, data integrity and confidentiality. But the smart contracts of the framework are based on time and notifications.

The existing solutions to support healthcare data sharing face limitations like scalability, integration with the existing healthcare systems, high cost of implementation and requirements of every healthcare facility on the blockchain network. Table 1 summarizes the existing literature. In comparison with the existing works, we have proposed a feasible architecture for diabetic data sharing among stakeholders where data is shared as per the patient's access policy, ensuring privacy and security of data using a one-time access URL for data access and implementing the same using Ethereum blockchain and smart contracts written in Solidity.

2.2 Existing patient-centric healthcare systems to support diabetic data sharing

Traditionally, a client/server approach was followed for sharing healthcare data where a centralized server like hospital database stored the entire patient data and was solely responsible for controlling and managing it. In this approach, patients have no control over their data and have to trust the centralized authorities for ownership of their data. Table 2 depicts the differences between traditional and blockchain-based data sharing models.

In [24, 25], the authors proposed a web-based portal to link the patients' Electronic Health Records (EHRs) stored on the centralized hospital server to provide easy access. But such approaches raise concerns about privacy and

Table 1 Summary of existing literature

Authors	Problem statement	Challenges addressed/advantages	Limitations
Zyskind et al. [14]	Blockchain-based decentralized personal data management system	Data ownership, transparency and auditability of data, access control	Performance evaluation has not been done
Azaria et al. [15]	Blockchain-based framework MedRec, to share and manage EMRs	Authentication, accountability, secure sharing, interoperability of data	Data is stored in private database
Liang et al. [16]	User-centric health data sharing solution to privacy issues	Privacy, access control, data integrity, scalability	User authentication to secure data storage not considered
Chen et al. [17]	Secure management of medical data using blockchain and cloud storage	Privacy protection, secure storage, no dependence on centralized power	Not yet integrated with existing healthcare systems
Dubovitskaya et al. [9]	Patient-centric blockchain-based management of EHR for radiation oncology data	Patient centricity, secure data sharing	Single point of failure risk, "break-glass" mechanism required for emergency situations
Jabarulla et al. [18]	Implemented a distributed patient-centric image management system using blockchain	Security, safety and privacy of patient data without using centralized authority	Manual encryption and decryption of original medical images, risk of losing private keys
Mani et al. [19]	Patient-centric approach to store health records on an IPFS-based distributed ledger system using Hyperledger Fabric technology	Resolved privacy, security, confidentiality concerns to enable decentralized storing and sharing of health information while ensuring scalability	Large number of resources are required for the implementation of multi-blockchain systems and extended frameworks integrated with Non-Fungible Tokens
Gohar et al. [20]	Patient-centric healthcare framework (PCH) using blockchain, IoT, and cloud technologies to improve interoperability	Lack of semantic interoperability, patient centricity	Cost of implementation and maintenance could be high
Taylor et al. [21]	Proposed VigilRx, a patient-centric and interoperable prescription management system that ensures user control, prevents information blocking and improves transfer efficiency	Ensuring the security of patient data, interoperability, fraud prevention, data accuracy and accessibility	Heavily dependent on blockchain limiting its effectiveness by scalability and security of the network, vulnerable to blockchain congestion and security breaches

Table 2 (continued)

Authors	Problem statement	Challenges addressed/advantages	Limitations
Abutaleb et al. [22]	Integrity and privacy aware, patient-centric health record access control	Lack of control, transparency, data integrity, privacy	Conceptual framework, not been implemented in a real-world setting
Rai [23]	Proposed patient controlled blockchain-based Electronic Health Records	Patient ownership of their medical data, elimination of security risks, user authentication, data integrity and confidentiality	Smart contracts based on time and notifications

Table 2 Difference between traditional and blockchain-based data sharing models

Basis	Traditional data sharing models	Blockchain-based solutions
Patient control	Data is stored on a centralized server; patients have no control over it.	Being a decentralized network, patients have complete control over their data.
Security	Centralized servers are prone to malicious attacks.	Data encryption and consensus protocols ensure security.
Privacy	Patients cannot track who is using their data.	Traceability and user authentication ensure privacy.

confidentiality of healthcare data due to the existence of a single point of failure. For optimization of medical data storage and easy real-time sharing of data, the approach was shifted from web-based to cloud-based healthcare records management where data is stored in cloud attribute-based encryption (ABE) servers. As discussed in [26, 27], the limitations of this approach include the possibility of cyberattacks making them vulnerable to privacy, the need for large storage capacity, high computing power so that millions of patients can access the server at once and the data is still not owned by the patients.

To address the challenge of data ownership by patients, patient-centric blockchain-based solutions are introduced to support secure and efficient diabetic data sharing and are a need of the hour. In [28], the authors proposed a patient-centric architecture for management of medical data using blockchain where patients can track their data and how it is shared among stakeholders. In [29], the authors proposed a feasible solution to shift the data ownership from healthcare providers to the patients by incorporating the unique features of blockchain technology, but this solution required a setup at every healthcare facility and faced the issue of scalability. In [5], the authors proposed a platform to capture diabetic health data using IoT devices and share it with health entities using blockchain to protect patient ownership and privacy of data, but the paper has not been implemented and integrated with the existing healthcare system.

Previous work on diabetic data management has predominantly focused on specific aspects such as pandemic response [30], prediction models [31] and remote monitoring [32]. Subramanian et al. [30] emphasize on pandemic response and consortium-based management of diabetes-related healthcare to efficiently prioritize the needs of diabetes patients during a pandemic. Hennebelle et al. [31] focused around diabetes prediction using IoT, AI and blockchain for data security based on risk factors. Pradhan et al. [32] focus on remote patient monitoring, security, the use of smart contracts and the automatic collection of sensor data. In contrast, our paper, DiabeticChain, offers a comprehensive solution addressing patient's diabetic data privacy, control and integration with existing Electronic Health Records (EHRs), differentiating it from existing approaches.

2.3 Challenges and limitations

The traditional models implemented for sharing health records and their management are raising concerns about security and privacy of healthcare data due to the presence of trustless centralized servers. Data is owned by centralized authorities like hospitals. Patients are not aware of how their data is being used and they cannot track who is using their data, becoming vulnerable to internal and external attacks. These challenges faced by the existing healthcare data sharing models need to be addressed by leveraging the benefits of blockchain like transparency, immutability and decentralization. The proposed DiabeticChain system addresses these challenges by using a permissioned blockchain, patient's consent policy and a one-time access URL to share diabetic data. Table 3 summarizes the literature on

Table 3 Comparison of existing literature

Study	Existing challenges					Use case	Type of blockchain	Technology	Data storage	Performance evaluation
	I[a]	II[b]	III[c]	IV[d]	V[e]					
Azaria et al. [15]	✓	✓	✓	✓	✓	Electronic Medical Records	Permissioned	Ethereum	Off-chain	×
Chen et al. [17]	✓	✓	✓	✓	×	Healthcare Data Sharing	Permissioned	–	–	×
Dubovitskaya et al. [9]	✓	✓	✓	✓	✓	Radiation Oncology Data	Permissioned	Hyperledger Fabric	Mixed	×
Jabarulla et al. [18]	✓	✓	✓	✓	×	Medical Image Management	Permissioned	Ethereum	On-Chain	✓
Mani et al. [19]	✓	✓	✓	✓	✓	Healthcare Data Sharing	Permissioned	Hyperledger Fabric	On-chain	✓
Gohar et al. [20]	✓	✓	✓	✓	✓	Healthcare Data Sharing	Permissioned	Hyperledger Fabric	Mixed	×
Taylor et al. [21]	×	✓	✓	✓	✓	Prescription Management System	Permissionless	Ethereum	On-chain	✓
Abutaleb et al. [22]	✓	✓	✓	×	✓	Healthcare Data Sharing	Permissioned	Hyperledger Fabric	–	✓
Rai [23]	✓	✓	✓	✓	✓	Electronic Health Records	Permissionless	Ethereum	On-Chain	✓
This study	✓	✓	✓	✓	✓	Diabetic Data	Permissioned	Ethereum	Mixed	✓

a: Data Security, *b*: Patient Privacy, *c*: User Control over Data, *d*: Traceability, *e*: Interoperability

the current healthcare data sharing architectures and how this paper is different from the existing work.

While there is no dearth of blockchain-based architectures in healthcare, most fall short in X, Y and Z aspects. DiabeticChain, in contrast, excels in these areas, offering a more comprehensive and innovative solution. These proposed architectures may not model a feasible design that can be combined with the existing Electronic Health Records (EHRs) approach in healthcare systems for secure and efficient data sharing and promoting interoperability. In order to integrate it with existing healthcare systems, the major challenge is lack of interoperability which allows the decentralized servers to communicate securely over a blockchain network and data format standardization. The data captured from EHR needs to be securely transferred without tampering and access should be controlled. There may exist certain technological barriers among other challenges mentioned above to completely shifting the traditional EHR data to blockchain and fully implementing blockchain-based solutions, but it does not seem much far-fetched today.

Being a new technology, blockchain-based solutions still face certain issues like the obstacle of scalability and implementation challenges like technical, organizational and regulatory concerns, but there is a significant growth in the number of proposed solutions to address these existing limitations [33]. There exist potential limitations specific to the implementation and adoption of the DiabeticChain system in the existing healthcare system such as scalability, data standardization and regulatory issues. As the size of the network increases and more users participate as nodes, higher computational power is needed for implementation. The system may also pose regulatory issues as there does not exist any central authority that can be held accountable [34].

3 Technical background

This section gives an overview of the technical background of Blockchain technology describing its architecture, the different types of blockchains used in applications and how blockchain supports dynamic consent which forms the backbone of this paper.

3.1 Overview

Blockchain is an immutable, decentralized and shared ledger that facilitates secure storage of transactions and tracking of assets by enabling a network of authorized nodes and eliminating the requirement of trust in any third party or among the nodes [35, 36]. It has a backbone in cryptocurrency and was first introduced in financial sector as a peer-to-peer cash system with the implementation of Bitcoin by Satoshi Nakamoto [37]. Since then, it has been incorporated by many other sectors for numerous applications and has the potential to revolutionize different sectors like the financial institutions, education, voting systems, healthcare industry and many other trustless environments. Overall, the healthcare industry can be revolutionized using

blockchain to enhance patient care, reduce costs of redundant diagnosis, ensuring privacy and security of healthcare data and its efficient sharing among stakeholders [38].

In the simplest terms, blockchain consists of blocks chained together to form a distributed decentralized database. Every block stores a timestamp and a hash of the previous block computed cryptographically, making it tamper-proof as even a small modification in any block will modify the hash value of the subsequent blocks and thereby affecting the entire blockchain and the alteration can be easily detected. A single block's structure in the blockchain network is depicted in Fig. 1. There is a header and a body for every block. All of the data nodes are hashed in a Merkle tree found in the body. A timestamp, nonce, Merkle root, hash pointer to the previous block, transaction counter and version information are all included in the header, which serves as the framework for the blockchain.

Blockchain technology is ideal to use where trust is required without the presence of a third party because any new transaction or changes to the data require consensus among all the participants of the nodes. The cooperation among nodes to validate a transaction is established using a consensus protocol and thereby trust is upheld. The most widely used consensus algorithms are Proof of Work, Practical Byzantine Fault Tolerance, Proof of Stake, etc. In Proof of Work (PoW), the validators must compete to solve a mathematical puzzle or a cryptographic equation to generate a new block and get rewards, while in Proof of Stake (PoS), the rights within the network depend on the time for which a node holds the coins and the number of coins held.

Blockchain works by implementing the self-executing smart contracts which consist of rules of an agreement between a seller and a buyer written into lines

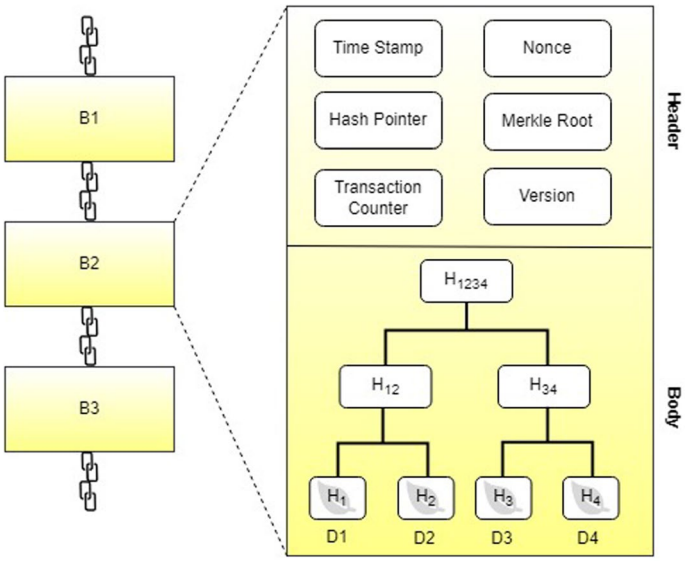

Fig. 1 Structure of a block

of code. The core idea behind them is to make the process of security breach so expensive that it results in secure agreements over public networks without trusting a third party [39]. After the execution of a smart contract, a transaction is appended on the blockchain.

3.2 Blockchain architecture

The architecture of a blockchain consists of two main components—a distributed ledger and peer-to-peer network. Figure 2 illustrates the architecture of a blockchain as a peer-to-peer network and how it differs from the traditional centralized network.

- Distributed Ledger—All the transactions taking place in the blockchain network are recorded in a ledger shared by all participating nodes eliminating the possibility of some malicious node intervening and manipulating the records. Every node has an identical local copy of that shared ledger to ensure the data integrity. To append a new transaction to a block in the blockchain, it is first verified and authenticated by all nodes using a consensus algorithm and then appended to the network only if majority of the nodes validate the transaction. Once this change is made it cannot be reverted. No single node has the authority to manipulate the data existing in the blockchain.
- Peer-to-peer network—In a blockchain network, the nodes are connected instead of one central node, making the entire network decentralized and every transaction is authorized before adding it to the network, making the network authentic [40]. Every node has the equal power to consume the services of the network and

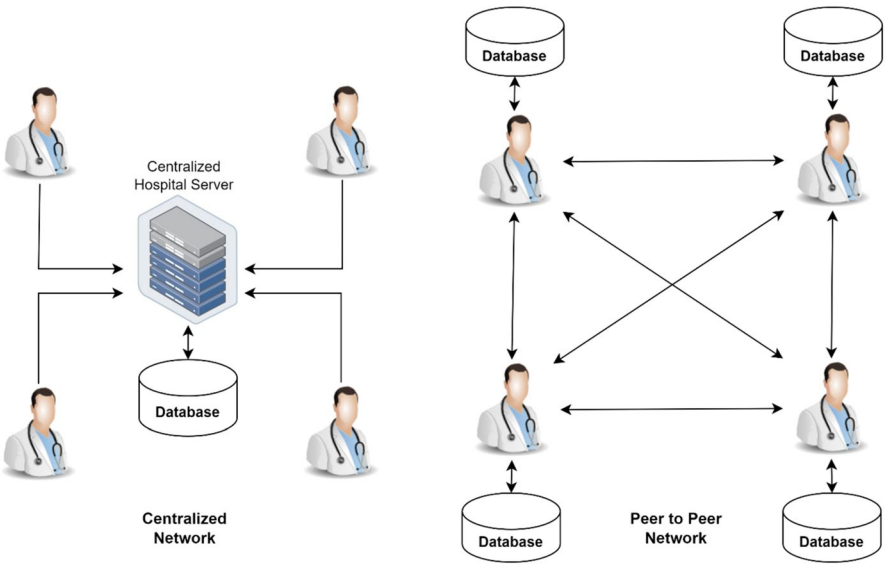

Fig. 2 Blockchain architecture

agree upon them via a consensus algorithm. Peer-to-peer networks eliminate the problem of a single point of failure due to absence of a central node, resulting in a more secure network [41].

3.3 Types of blockchains

There are different ways to establish a blockchain network depending on the applicable use case and their requirements such as cryptocurrencies like bitcoin have a public network where any node can participate and verify the transactions, but on the other hand a bank would require a private network where only the authorized users can participate and access the confidential information [42]. To meet such varied needs, blockchain is categorized as private and public. In public blockchains, there is no restriction and anyone can access the network to validate the transactions. No single entity has the complete control over the network and power is equally divided among nodes. While in private blockchains, certain nodes are authorized by the network administrator to participate in the network and access is restricted to them. Blockchain is also categorized as permissioned and permissionless to differentiate between who can generate a new block in the blockchain network. In a permissioned blockchain, among the participating nodes, only some are granted the permission to participate in the consensus algorithm to write a new block. In case of a permissionless blockchain, any node of the blockchain network can participate as a validator [43].

Blockchain can thus be divided into 4 different types as per the role of participating nodes in the network [44, 45]. Each type is described in detail as follows:

1. Private permissionless: Only a restricted number of authorized nodes can enter the network and all participating nodes can perform the read or write operations in the network to create a new block. Equal importance is given to every node. An example of private permissionless blockchain is Holochain [46].
2. Private permissioned: Only a restricted number of authorized nodes can enter the network and all participating nodes can read the contents of the blockchain, but a subset of them is given the permission to perform the write operation to generate a new block in the blockchain. Some examples of the private permissioned network are Hyperledger Fabric [47] and Hyperledger Besu [48].
3. Public permissionless: Any node can enter the blockchain and perform read or write operations in the network. In this case, in order to build trust among the participants, costly consensus protocols are required. Some examples of public permissionless blockchains are Ethereum, Bitcoin and Witnet [49].
4. Public permissioned: Any node can enter the blockchain and read the contents present on the network, but only certain authorized users/nodes are allowed to perform the write operation. They need less costly consensus protocols to build trust among participants. Some examples of public permissioned blockchains are ESIO [50] and Ripple protocol consensus algorithm [51].

Table 4 summarizes the different types of blockchain.

Table 4 Types of blockchains

Types of blockchain	Private	Public
Permissionless	Restricted participating nodes, All can read and write. For example, Holochain	Access to all, anyone can read and write. For example, Ethereum
Permissioned	Restricted participating nodes, All can read, a subset of them can write. For example, HLF	Anyone can read, a subset of them can write. For example, Ripple

3.4 Dynamic consent and blockchain

Dynamic Consent is the approach that involves collecting, storing and managing of data obtained from people for the purpose of research and healthcare. This approach is very different from the traditional consent in which the data was collected from the people only at the beginning of a study that is taking place but on the other hand dynamic consent approach involves dynamic or continuous flow or control of the data for various research activities or purposes. Despite such flow, dynamic consent has limited dimensionality in the practical field due to the security and legality of the personal data belonging to people. This poses major trust issues for the people including the fear of maintaining the confidentiality [52, 53] of the data that belongs to their personal belongings. Now, blockchain deals with the rapidly multiplying part of data in the form of a decentralized database [54]. Blockchain has various functionalities which could support dynamic consent in different ways like high accountability, a greater sense of data security and privacy, immutability and an extremely efficient management system [22]

Diabetic data sharing takes place in a continuously changing environment, and therefore, dynamic consent is necessary for personal protection of sensitive data, preventing the unforeseen risks of privacy and driving patient-centric research [55]. Blockchain can enable data sharing in a trusted environment according to the modifiable consent preferences of the patient where they can dynamically update their consent options anytime.

4 Methods

This section discusses the requirement of blockchain to provide a viable solution for the secure and efficient sharing of diabetic data among stakeholders and the formatted research questions for this study.

4.1 Blockchain potential in diabetic data sharing

There are various requirements for the construction of a functional system, and in the scenarios of handling such vast and categorical data on diabetes, we need to consider optimal methods. Sometimes these methods depend on situational scenarios. And, determining whether any particular method is suitable for a particular application is an uphill battle. Therefore, we can say that deciding whether blockchain will be able to simplify the scenario is not correct [22]. To handle this, Wüst and Gervais [56] proposed a decision tree and Pedersen et al. [57] proposed a decision path in order to discover the applicability of blockchain. This method made it concise to 6 questions that need to be answered for diabetic data sharing condition in order to determine the need for blockchain as depicted in Fig. 3.

1. Does the state need to be stored? The answer to this question is dependent on the consideration of the following factors:
   - Patient Consent: In diabetic data sharing system, it is inevitable to store the consent of the patient so as to allow secure access to their data from interested data consumers. For instance, if any researcher wants access to patient diabetic data, then the consent policy is validated before granting the access.
   - If a chronic disease is to be diagnosed: For instance, if any person has been diagnosed with any disease is which is chronic like diabetes and is previously diagnosed with another implication of the same category of disease then, there is a need to store the state for further approximation of such disease since it requires ongoing medical attention. And blockchain could inculcate this very well.

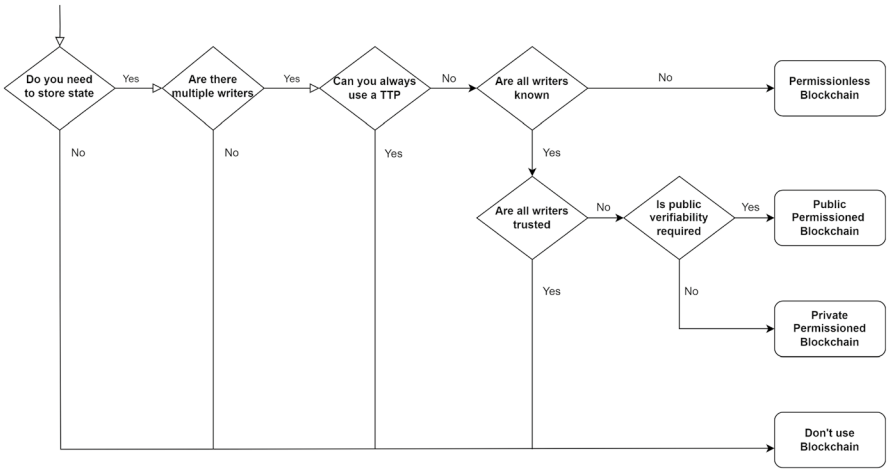

Fig. 3 Decision path of using blockchain

- The number of times the data needs to be handled: For instance, if there is a single-time utility of the data of any patient who has been diagnosed with diabetes, then there is no need to store the state, while, if there is a need to create a system that diagnoses and remembers the patient's personalized way of attending to data, then there is a need to store the state. In our case, diabetes is a chronic disease, and hence, the diabetic data is handled multiple times.

2. Are there multiple parties involved? In general, this question can be answered in a Yes. Since there are many contributors towards the health-related information of patients. For instance, patients themselves could contribute to their physical measures like height, weight, blood pressure levels, blood oxygen levels, etc. And laboratory technicians could contribute to their in-depth blood test results diagnosis and different scans of their body, while doctors and researchers could add their actual physical condition and the diseases or problems that patients have in their bodies. Hence, using blockchain all the data inputs by various parties could be maintained and handled well.
3. Can you use a centralized trusted third party? The answer to this question is again partially, both Yes and No and the reasons behind them are as follows: Yes, because it is possible to always use a web-based trusted third party for diabetic data sharing. As a third party might act as a platform that could inculcate multiple users and make the process even smoother and make the data sharing relatively easier by adding a small functionality of secure login ID and Passwords. Another advantage of being a consolidated platform is that it could prevent unusual data redundancy and corruption. While the answer is no, in the terms of the betrayal of the patients by sharing their personal details with any web-based third party. Patients cannot trust the third party every time and track the use of their diabetic data and blockchain is able to maintain the trust without using the third party.
4. Are all writers known? Yes, all writers like patients, data controllers and data consumers should register in the system before interacting. In a diabetic data-sharing system, it is necessary to have known writers like patients, healthcare professionals such as laboratory technicians, etc., researchers and doctors who are legally approved to access the data of the patients. All these withers must have their authenticated login credentials, and also, they must be posed to access the data of their radii (data of their utility).
5. Are all writers trusted? The answer to this will be in No, all the writers cannot be trusted. However, all the patients have a mutual sense of trust in all the healthcare professionals. But these writers must comply with their boundaries and must be regularly checked for their utility with their data. This could be ensured by blockchain by using encryption models and security protocols.
6. Is public verifiability required? Public verifiability means the involvement of external auditors to hamper the critical data of patients. In spite of being a desirable feature, public verifiability is strictly not required and blockchain is playing its part by keeping the data-sharing system private.

4.2 Research questions

The following research questions were developed after analysing the existing blockchain-based patient-centric healthcare data sharing models and need to be addressed with respect to the diabetic data sharing use case.

1. What are the limitations and challenges of the existing healthcare data sharing models for diabetic patients? There are unique challenges associated with diabetic data since diabetes is a disease that requires self-care by burdening the patients with continuous glucose monitoring and the healthcare providers to analyse and access the huge amount of data associated with it [3]. The current state of diabetes care is worsening due to absence of effective diabetic data sharing. The traditional systems face privacy and security concerns in sharing sensitive diabetic data, no data ownership for the patient, data fragmentation, lack of interoperability, requirement of trust in a centralized authority and ethical issues.
2. How can blockchain-based solutions address the limitations and challenges of the existing healthcare data sharing models for diabetic patients? The challenges faced by the existing healthcare data sharing models can be addressed by leveraging the benefits of blockchain like transparency, immutability and decentralization. The main challenge addressed by DiabeticChain is the protection of privacy of the patient data by giving them control to grant or revoke access to their data enabling secure sharing of diabetic data among stakeholders by using a permissioned blockchain, patient's consent policy and a one-time access URL to share diabetic data.
3. What performance metrics can be used to evaluate the effectiveness of a blockchain-based solution for diabetic data sharing? The performance of blockchain-based solutions for diabetic data sharing can be measured in terms of the transaction and query operations using throughput and latency as performance metrics to validate their effectiveness. Measuring factors such as the number of transactions per second, the response time for transaction processing and throughput can be used to evaluate the system's feasibility.

5 Design requirements

In order to implement our proposed architecture, five design requirements have been identified in accordance with our blockchain use case.

5.1 Requirement 1: data security

Data security is a crucial requirement in sharing sensitive diabetic data which is susceptible to cyberattacks. Both active (taking control of medical devices) and passive (overhearing the communication through wireless devices) attacks can occur on the collected diabetic data [58]. Patients' data should be stored in a secure

database to eliminate the possibility of malicious attacks and prevent the misuse of data by attackers. Data encryption techniques like public key cryptography and access control mechanisms have to be employed to eliminate the unauthorized access and hence ensure data security [9, 15, 16, 59, 60].

5.2 Requirement 2: patient privacy

Patients' diabetic data should be shared with healthcare professionals and researchers with proper authentication while minimizing the disclosure of their identity and without compromising their privacy. Only the authorized users should have access to the confidential diabetic data of patients with their consent [16, 22, 61, 62].

5.3 Requirement 3: user control over data

Healthcare has moved from document-based storage to EHRs, but the ownership and control of confidential data is still in the possession of unknown, untrusted, centralized authorities like hospitals with a possible risk of data breaches [7]. Diabetic data of the patients should be owned, controlled and managed by the patients themselves resulting in patient centricity instead of being owned by trustless centralized servers like hospital databases. When patients are the owner of their data, they will grant permission to anyone who wants to access that data and how their data will be used [21, 22, 63, 64].

5.4 Requirement 4: traceability and data integrity

Data traceability and data integrity are critical concerns in data sharing among stakeholders. The data owner, i.e. the patient, should be able to track how their healthcare information is being shared and give their dynamic consent as per the purpose of data utilization to achieve transparency. During the process if any malicious node tries to manipulate the health record, then it should be detected and prevented from any change ensuring data integrity [23, 65–67].

5.5 Requirement 5: interoperability and standardization

Along with the implementation of the proposed model, it should be feasible to integrate it with the existing healthcare systems consisting of Electronic Health Records (EHRs) to achieve the requirement of interoperability which allows the different decentralized servers operating in different locations to interact and share information over a blockchain network. In order to achieve interoperability among various entities, there is a requirement of a standard format to capture the diabetic data and thereby ensure efficient data sharing [15, 68–71].

6 System architecture

This section discusses the detailed system architecture for blockchain-based patient-centric diabetic data sharing.

6.1 System components

The constituting components of the proposed architecture are depicted in Fig. 4.

- Users: In our architecture, we have three types of users who can interact with the system.
  - Data Owner: An individual such as a patient who is the owner of the data and grants or revokes consent to access that data as per his access policy.
  - Data Controller: An organizational entity such as the hospital or laboratory which captures the patient data by storing it in their secure off-chain databases.
  - Data Consumer: An individual or organizational entity like healthcare organizations, researchers, health insurance companies, etc. that needs patient data for their specific purposes and requests access to it.
- On-chain Components
  - Blockchain: The decentralized ledger that enables secure, immutable and transparent storing and sharing of healthcare data.

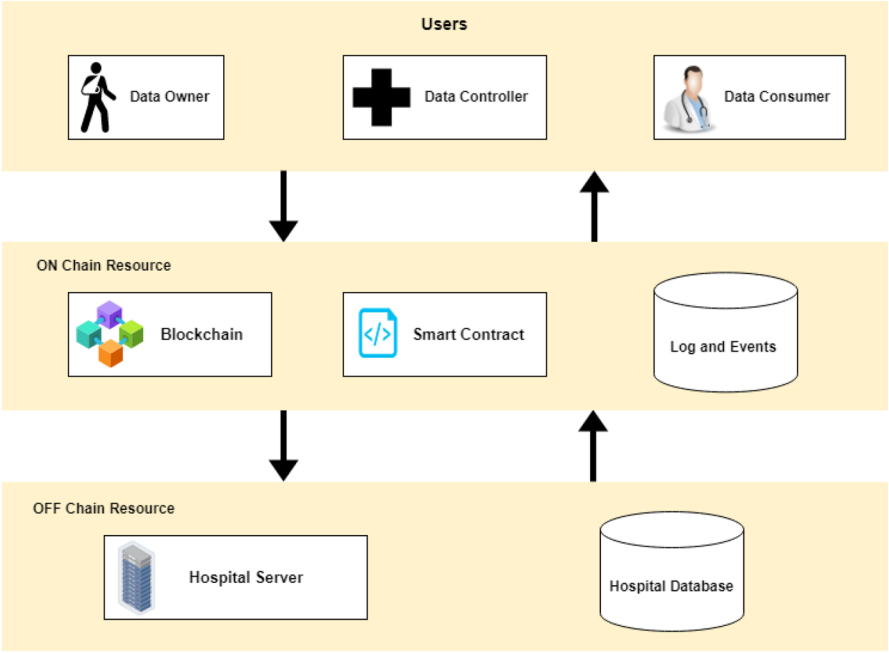

Fig. 4 System components

  - Smart Contracts: The self-executing contracts which provide functionality to the system like registration of users, storing the metadata of EHR, managing access policy of patients, etc., and are written in lines of code to specify the rules of an agreement.
  - Logs and Events: Functionality created by smart contracts to maintain and track the information for auditing the system data.
- Off-chain Components
  - Hospital Server: The server is responsible for managing the off-chain hospital database with the on-chain system requests.
  - Hospital Database: An off-chain database maintained for the secure storage of patient data which is managed and controlled by the data controller.

6.2 Smart contracts

In contrast to traditional contracts, smart contracts have numerous benefits such as increased automation, improved transparency, security, reduced costs and the elimination of any intermediaries. Being written in programming languages like Solidity, implementation, development and deployment of smart contracts requires certain level of technical expertise. A smart contract cannot be changed once it is deployed on the blockchain. Today, smart contracts are not considered to be legally binding and legally enforceable as their architecture still requires a legal framework component [72]. In this paper, to manage the on-chain transactions, four smart contracts have been implemented i.e. User Smart Contract, Access Policy Smart Contract, metadata smart contract and access management smart contract.

User Smart Contract (USC) USC is responsible for registration of all the users i.e. data owner, data controller and data consumer. After verification, every user has to register in USC in order to interact with the system. The Data Consumer is required to provide its public key during registration.

Access Policy Smart Contract (APSC) APSC is responsible for storing the consent policy of Data Owner. The patient (data owner) stores the set of rules in this smart contract which defines who can access their data ensuring privacy of the data.

Metadata Smart Contract (MDSC) MDSC is responsible for storing the patients' metadata that does not reveal any confidential information as a reference to the patient data stored on the secure off-chain databases.

Access Management Smart Contract (AMSC) AMSC is responsible for managing the access policy of the Data Owner by accepting access requests from Data Consumer, validating the request, notifying the Data Controller to generate one-time access URL and communicating it back to Data Consumer.

7 Proposed work

The proof-of-concept of the proposed blockchain-based architecture was implemented on a privately permissioned blockchain to showcase its viability. At the infrastructure level, Go-Ethereum [73], an open-source Ethereum client enabling

permissioned private blockchain networks, was utilized to establish a private blockchain. The system's smart contracts are written using Solidity, and the truffle framework was employed for developing, compiling, testing and deploying these smart contracts. The patient's smart contract code is partially illustrated in Fig. 5. ChainLink was used as an oracle service to connect smart contracts to off-chain resources, and MongoDB was employed to develop the off-chain database.

There are four smart contracts to handle the blockchain transactions: User Smart Contract (USC), Access Policy Smart Contract (APSC), Metadata Smart Contract (MDSC) and Access Management Smart Contract (AMSC). These smart contracts offer 6 primary system functions: createUser, setPatientConsent, cancelPatientConsent, checkPatientConsent, createMetadata and requestAccess. Only authorized users

```
pragma solidity ^0.8.0;

import "./MDSC.sol";
import "./USC.sol";
contract APSC{
    mapping(uint256 => AccessTicket) public accessTicket;

    mapping(bytes32 => bool) public accessTicketSigns;

    uint256[] public accessTicketIds;

    uint256 public lastAccessTicketId =200;

    mapping(bytes32 => Consent) private consent;
    bytes32[] public consentSigns;

    struct Consent{
        bytes32 consentSign;
        bool status;
        bytes32 MetaData;
        bytes32 role;
        bytes32 aim;
        uint256 timestamp;
        uint256[] issuedAccessTicket;
    }

    event consentlog(
        address indexed patientConsent,
        bytes32 _consentSign,
        uint256 _timestamp,
        bool indexed _status
    );
    struct AccessTicket{
```

Fig. 5 Partial code of the Access Policy Smart Contract (APSC)'s smart contract

are limited to calling these functions which are implemented using smart contract modifiers. If a function call is unauthorized, then it will result in the termination of the function execution and the reversion of all modifications to their initial state. The subsequent section elaborates on the use of smart contract functions to implement the main system functionalities.

7.1 User Smart Contract (USC)

Every system participant engages with the system using their won wallet, which contains all necessary information for system interaction. As a result, participants must be registered within the system, where a smart contract is established. The role of the system admin is to verify the users' identities and professional registrations before initiating the system registration process. Algorithm 1 describes the user registration process.

Algorithm 1 Pseudo-code for registering a new user (RegisterUser)

```
1: Input: initiator, userWalletAddress, role
2: Output: userIdentifier
3: if initiator = owner and userWalletAddress ≠ null then
4:     Require ← newUser
5:     Display "User already approved!"
6:     Create newUserProfile
7:     return userIdentifier
8: else
9:     Display an error message and undo smart contract state
10: end if
```

7.2 Access Policy Smart Contract (APSC)

This smart contract keeps patient consent as access policy tree. A consent signature is produced by hashing the access policy tree and stored in APSC. Hashing and storing patient consent in APSC allows for efficient consent status retrieval and validation. Algorithm 2 describes the process of setting the consent of the patient.

Algorithm 2 Pseudo-code for saving consent of the patient (SavePatientConsent)

```
1: Input: initiator, aim, role
2: Output: status
3: PatientConsent, consentSign ← mapping
4: if initiator = owner AND aim ≠ null AND role ≠ null then
5:     h ← hash(role, aim)
6:     if PatientConsent.contains(h) = true then
7:         Display an error message and undo smart contract state
8:     else
9:         PatientConsent.add(h, true)
10:        return true
11:    end if
12: else
13:    Display an error message and undo smart contract state
14: end if
```

7.3 Metadata smart contract (MDSC)

This smart contract contains patient metadata. Once the patient data has been collected and securely stored in an off-chain secure database such as a diabetic laboratory database, the data controller then submits the patient's metadata to the system. This metadata is a representation of the patient data that contains a description without disclosing any confidential or identifiable patient information, like the data type, hash of the stored data and conditions. The patient metadata is then kept in a separate data structure, where the hash of the stored data serves as the key and the remaining patient data as the value. Algorithm 3 shows the process of creating patient metadata.

Algorithm 3 Pseudo-code for generating patient metadata (GenerateMetadata)

```
1: Input: initiator, patientWalletAddress, dataHash
2: Output: id
3: Metadata ← mapping
4: i ← counter
5: if initiator = dataControllerWalletAddress AND patientWalletAddress ≠ null
   AND dataHash ≠ null then
6:     i ← i + 1
7:     Metadata.add(i, [patientWalletAddress, dataHash, dataControllerWalletAd-
   dress])
8:     return i
9: else
10:    Display an error message and undo smart contract state
11: end if
```

7.4 Access management smart contract (AMSC)

This smart contract is responsible for managing access to patient data. The Data Consumer should obtain an Access Ticket (AT) to be able to access the patient information. Using the AT, the access to the requested data is limited to the lowest possible level. Once the data consumer identifies relevant patient metadata, they have to request an AT from the system by providing the hash of the data they requested, the reason for requesting access to patient data and their role. This request is then verified by APSC, which stored the consent policy of the patient. If the consent is valid and aligns with the data consumer's request, an AT is automatically generated for data consumer. Algorithm 4 shows the process of requesting access to off-chain relevant patient data.

Algorithm 4 Pseudo-code for requesting permission for accessing off-chain patient information. GenerateMetadata (RequestAccess)

```
Input: dataConsumer, Metadata, aim, role
Output: ticketId
METADATA ← mapping
if dataConsumer = owner AND Metadata ≠ null AND aim ≠ null AND role
≠ null then
    d ← data.get(MetadataID)
    patient ← d.patientWalletAddress
    h ← hash(role, aim)
    if PatientConsent.get(h) == TRUE then
        ticket ← patient.CreateAccessTicket(dataConsumer, MetadataID)
        ticket.status ← TRUE
        return ticket.id
    else
        Display an error message and undo smart contract state
    end if
else
    Display an error message and undo smart contract state
end if
```

7.5 Proof-of-concept: DiabeticChain

In this section we present DiabeticChain, an implementation of the proposed architecture as a proof-of-concept study. DiabeticChain enables the patients to grant or revoke consent to data consumers so that they can access their diabetic data and data controllers to collect and store their diabetic data. Figure 6 depicts a high-level detailed work flow of the implementation of the proposed architecture.

All users—Data Owner, Data Controller, Data Consumer—should first register in User Smart Contract (USC). During the Data Consumer Registration, the Data Consumer should provide his public key.

1. Data Owner (patient) stores his access policy in APSC (Access Policy Smart Contract) on the blockchain.
2. Data Controller then collects the patient's diabetic data, including blood glucose levels, insulin dosages, and other relevant information and stores it in a secure off-chain hospital database.
3. Data Controller then stores patient's metadata in MDSC on the blockchain.
4. Data Consumer can search for patient data of interest from the available data in MDSC.
5. After identifying patient data of interest, Data Consumer sends an access request to AMSC.
6. AMSC validates the access request with APSC by checking the patient access policy (if there is a valid access policy move to next step 7, otherwise access request will be denied and the data cannot be accessed by the data consumer).
7. On acceptance, AMSC notifies Hospital to prepare the data for sharing with a Data Consumer, the Hospital retrieves Data Consumer's public key from USC and Data Consumer's data from the database.

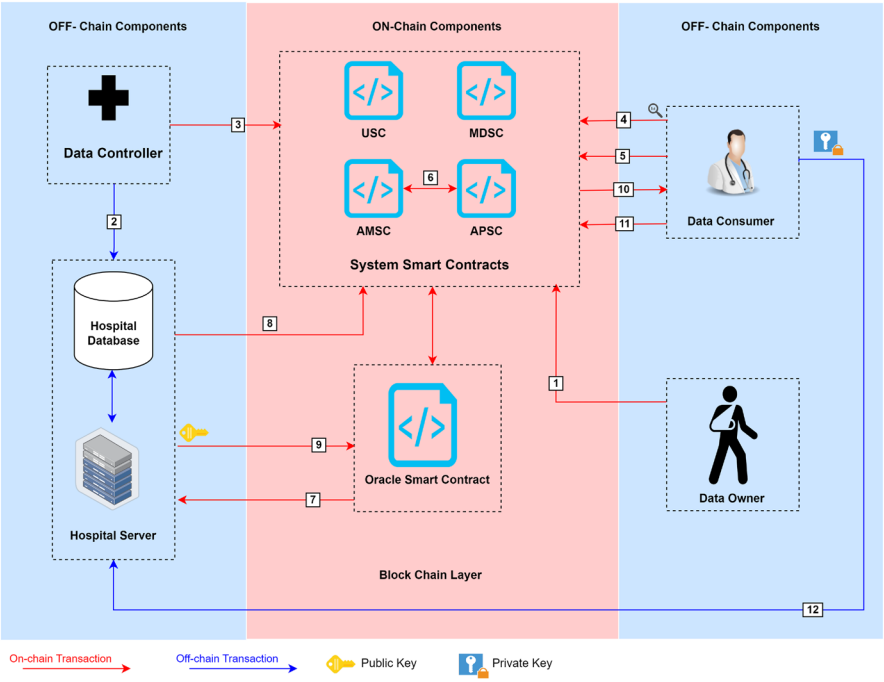

Fig. 6 Detailed workflow of the proposed architecture

8. Hospital then retrieves the data consumer's public key from USC on the blockchain.
9. Hospital creates a one-time access URL for patient data and encrypts the one-time access URL using Data Consumer's public key and then stores the encrypted one-time access in AMSC.
10. AMSC notifies Data Consumer about the encrypted one-time access URL.
11. Data Consumer retrieves the encrypted one-time access URL from AMSC.

12. Data Consumer decrypts the encrypted one-time access URL using his corresponding private key and then it uses it to access patient data.

8 Results and evaluation

DiabeticChain, a blockchain-based patient-centric healthcare architecture to support diabetic data sharing, is proposed and implemented in this paper. In this section, the key findings and outcomes derived from the implementation and evaluation of the proof-of-concept DiabeticChain system are discussed by addressing the design requirements, performing the security analysis and the performance evaluation. Our results do not just showcase the functionality of DiabeticChain. Through real-world scenarios and case studies, we demonstrate its transformative potential in diabetic data management, a novelty in the current landscape.

8.1 Addressing design requirements

In this section, we discuss how our system fulfils each design requirement and addresses them by implementing various features using Ethereum blockchain and smart contracts.

8.1.1 Data security

In this paper, we have proposed that the sensitive diabetic health data should be stored in the secure off-chain database and only the metadata with a reference pointer to the source data, encrypted by public key cryptography should be stored on the blockchain. Data consumer can request access to the patient data and patient can then grant or revoke access as per their consent policy. Cryptography methods and access control mechanisms ensure the security of data in DiabeticChain, thereby preventing the risk of cyberattacks.

8.1.2 Patient privacy

Our system, DiabeticChain, preserves the patient's privacy by storing the sensitive data in secure off-chain private database, and its metadata is stored on the blockchain encrypted using cryptographic techniques like public key cryptography. Every user, i.e. data owner, data consumer and data controller, is required to register in the User Smart Contract on the blockchain to authorize and validate its participation in the network. An access control mechanism has been used to safeguard the data from leakage. When the data controller receives a validated access request from the data consumer, it encrypts the secure one-time access URL using the public key of data consumer and can be decrypted only by the respective authorized public key, thereby protecting the patient privacy. If the data consumer wants to access the same data in future, then a subsequent one-time access URL will again be generated. The anonymity of data is maintained while sharing it with various stakeholders. Patient data

is anonymized by generating random unique accounts linked to the patients using their public key. One patient can be linked to multiple accounts. These accounts are then used to send records on the blockchain maintaining the anonymity of patients, and their real identity is not disclosed. In this way, data anonymization, encryption and access control mechanisms are used for patient privacy preservation.

Any security flaws in the implementation of smart contracts can result in a potential privacy risk to the system and can lead to identity theft or security theft. Also due to the public nature of blockchain, a series of transactions can be traced and lead to revelation of original identities of the data owners [74], but this is mitigated by creation of multiple accounts for a patient. These privacy risks can be mitigated by countermeasures like eliminating any potential flaws within the system. Some of the known privacy preserving techniques like zero knowledge proofs can also be used to enhance the security of the system. Using this mechanism, information is validated using cryptographic algorithms ensuring its correctness without revealing or leaking any sensitive information [75].

8.1.3 User control over data

The proposed system DiabeticChain, following a patient-centric approach, provides complete user control over their data. Being a decentralized peer-to-peer network, there is no central authority to take control of the patient data. It is owned, managed and controlled by the patients and shared among stakeholders only with their consent. The system also allows the patients to dynamically update their consent policy as per the changing environments giving them full control over their diabetic data.

8.1.4 Traceability and data integrity

Blockchain is an immutable ledger where every node contains a copy of the stored data. Whenever a new record is added, a consensus protocol is used to verify the record before appending it to the shared ledger and a cryptographic hash is computed for every block. If any malicious node tries to change the data, it will be detected by the other nodes because even a tiniest change in the data will change the hash value of every subsequent block. Hence, it cannot be manipulated or tampered ensuring data integrity. Each transaction on the blockchain is recorded and the data owner is able to track their data and how it is being used, guaranteeing the traceability of data.

8.1.5 Interoperability and standardization

While using blockchain features, DiabeticChain models a feasible design that can be integrated with the existing healthcare systems and thus ensures interoperability among systems. Since the credibility of the new records added to the blockchain depends on the credibility of its participating nodes, a form of data standardization is followed so that all the nodes can understand the data [76]. One such standard is HL7 which is a human-readable standard to address the requirement of interoperability and ensure seamless integration and data sharing among different healthcare

entities [77]. A potential limitation of using such standards can be the mismatch of versions used among different healthcare centres or possible technological issues which need to be taken care of.

8.2 Security analysis

The security of DiabeticChain is analysed in this section based on data storage in the system, sharing of data in the system and tamper-proofing.

8.2.1 Data storage

In this paper, we propose a hybrid model for the storage of data consisting of both off-chain and on-chain storage where the confidential diabetic data of the patient is stored in an off-chain secure and private database and only the metadata, hash and a reference pointer are stored on the blockchain. During every appointment, Data Controllers like hospitals and laboratories collect and record the patients' diabetic data like the blood sugar levels, blood pressure, ongoing medicines, insulin dosage and other sensitive data. In the scope of this research, we have considered that this data is then securely stored and managed on the off-chain hospital databases. Such a large dataset cannot be stored on the blockchain itself since it is not computationally and memory efficient to manage such large datasets on the blockchain. Every node in the blockchain has a replica of the data thereby increasing the required storage and a consensus protocol cannot execute such fast transactions and hence the performance will be slowed [78]. Therefore, blockchain is used to store only the metadata in the MDSC along with a reference pointer to source data in the hospital database. This division of data thus helps in optimizing the system's performance and security. The proposed hybrid storage model thus addresses the scalability and efficiency concerns associated with blockchain-based systems, such as fulfilling the storage requirements and reduction in transaction processing time.

The storage of metadata on the blockchain gives a broader view of the entire diabetic data to the Data Consumer. Since every node in the blockchain network has a local copy of the data, data consumers can easily look for the patient data of interest in the Metadata (stored on-chain) without searching exhaustively in the large off-chain datasets. After identifying patient data of interest, Data Consumer can send an access request which is validated and a one-time access URL is generated to retrieve the off-chain secure data using the reference pointer stored on-chain. Even in the case of a server failure or any other technical issue, the hybrid storage model prevents data loss by eliminating single point of failure, handles data backup as sensitive diabetic data is stored across numerous laboratories without storing any redundant data and thus ensures data availability.

Using blockchain for data storage is beneficial over traditional relational databases (RDBs) in building trust, security and privacy aspects. But compared to blockchain, RDBs offer a higher throughput in writing data [79]. Hence, a hybrid model is the most suitable option for data storage in DiabeticChain healthcare system that leverages the benefits of both blockchain and relational databases.

8.2.2 Data sharing

Patient data is stored on the off-chain database and is effectively shared among healthcare entities like researchers, doctors, laboratory technicians, etc. using DiabeticChain. Only authenticated users can request to access the sensitive diabetic data and can only access that data using a one-time access URL within a given timeframe according to the self-executing conditions coded in the smart contracts. DiabeticChain system also allows the patients to dynamically update their consent allowing the patient to grant or revoke real-time access to their data at any point. The data access request of the data consumer is verified only as per the consent policy of the patient stored in Access Policy Smart Contract (APSC).

When a hospital receives a validated request from data consumer, the hospital generates a JSON format file that consists of the requested patient data and this file is then stored on the off-chain database at a temporary location. It can be accessed using HTTPS but only once within a given short timeframe. Now, the hospital generates a one-time access URL and encrypts it using the data controller's public key obtained from the User Smart Contract (USC). This URL is then stored on the blockchain and upon decryption can direct the user to the JSON file containing the required data. The URL can be only decrypted using the corresponding private key and used to access the data once. So, the Data consumers obtain the URL from the blockchain, decrypt it using its private key and access the data. Once the URL is used to access the data, it becomes useless as the JSON file is removed from the temporary storage and now that URL will lead to nothing. Even if someone retrieves the private key of data consumer to decrypt the URL, the patient data will still be safe. If the one-time access URL is not used within the given timeframe, then also the JSON file will be removed from the temporary storage and the URL expires to prevent unauthorized access attempts. If a need to access the same data arises in the future, data consumer must again submit the request to access the data and a new URL will be generated. This process allows the secure sharing of diabetic data with the patient's consent.

The DiabeticChain system maintains a record of data sharing transactions like who accessed the diabetic data, time of accessing the data and its purpose, and this traceability of the stored diabetic data contributes to the overall security and transparency of the data sharing process by ensuring patient's trust in healthcare providers. In case of multiple data consumers leading to large number of data sharing requests, high volumes of data are shared and the system may face an issue of scalability, but DiabeticChain provides a reasonable performance, efficiency and scalability with the current version of Ethereum blockchain implemented and hybrid model of data storage used.

8.2.3 Tamper-proofing

Mechanisms and features that make the DiabeticChain system tamper-proof are the immutability of blockchain, the use of consensus algorithms to add new records and cryptographic hashing. Blockchain is an immutable ledger that cannot be changed and generation of a new block requires consensus among all the participating nodes

to prevent tampering with data. It is difficult for any malicious node to change the patient records owing to the cryptographic hash used with every block, and it forbids any manipulation or modification of the data. But, cyberattacks like Sybil attacks, man-in-the-middle attacks, denial of service attacks and 51% attacks may pose a potential risk to the system.

Sybil Attack is where identity theft occurs in a peer-to-peer network and some node is completely cut-off from their neighbouring nodes, thereby establishing connections with the attacker and this node is then fed malicious information [80]. As a countermeasure, our blockchain system can be made attack resistant by guaranteeing at least a single honest surrounding node. Another potential attack is the man-in-the-middle attack in which a malicious user may tamper with the information communicated between two nodes. Increasing the number of validations before verifying a transaction, having multiple paths available on the network and selecting many nodes to check the transaction status can act as countermeasures [81]. Denial of service attack is another threat where authorized requests are prevented by sending requests more than the handling capacity of victim server. As a countermeasure, clients are required to solve puzzles before getting the access to a resource or server [82]. In the 51% attack, the attacker gains access to 51% of the network's computational power while using proof-of-work consensus protocol or it gains control over 51% of the participating nodes when proof-of-authority is used. To prevent these attacks, a proof-of-authority consensus algorithm is used where the validators stake their reputation and it is much more difficult for the attacker to control 51% of the nodes in the network, thus minimizing the risk of potential cyberattacks.

8.3 Performance evaluation

To assess the performance of DiabeticChain, we utilized 4 virtual machines (VMs) hosted on Microsoft Azure cloud to establish a private blockchain using Go-Ethereum, an open-source Ethereum client enabling permissioned private blockchain networks. Hyperledger Caliper, an open-source benchmarking tool for evaluating blockchain applications' performance, was employed to conduct multiple tests, validating DiabeticChain's effectiveness. Table 5 displays the private blockchain and testing environment configurations. We tested two primary types of blockchain operations, Transaction and Query operations, using four performance metrics to evaluate DiabeticChain: Transaction throughput, Query throughput, Transaction latency and Query latency [83].

We conducted 10 test rounds and varied the transactions per second (tps) gradually from 100 to 1000 with an increase of 100 tps with every round, and hence, the send rate increased linearly from 99.38 tps to 748.22 tps for query operations and from 100.1 tps to 839.76 tps for transaction operations.

Figures 7 and 8 demonstrate the Query Latency and Throughput Latency, respectively. Each chart consists of the Maximum Latency, Minimum Latency and the Average Latency of the corresponding operations. DiabeticChain was able to run the Query operations efficiently with low latency, and Transaction operations

Table 5 Go-Ethereum and testing environment configurations

Factor	Setting
Nodes	4 VMs with Ubuntu 20.04 on Microsoft Azure cloud, every VM equipped with 2 Intel CPUs and 8 GB RAM.
Blockchain	3 peer nodes 1 validator node Go-Ethereum v1.10.11
Consensus	PoA (Clique Protocol)
Smart contracts	Solidity
Benchmarking Tool	Hyperledger Caliper v0.5.0

were handled at a higher latency as they involve more complex operations of changing the data on the blockchain. The average Query Latency was 0.246 s (Fig. 7) and the average Transaction Latency was 1.31 s (Fig. 8). The maximum and minimum Query Latency was obtained to be 0.35 s and 0.16 s, respectively. For the Transaction operations, the maximum and minimum latency was 1.75 s and 0.88 s, respectively.

Figures 9 and 10 demonstrate the Query Throughput and Transaction Throughput, respectively. An average query throughput of 201.7 tps was obtained by varying the send rate linearly from 99.38 to 748.22 tps within 10 rounds. The maximum query throughput of 243.54 tps was achieved when the send rate was 748.22 tps, while the minimum query throughput was 78.8 tps when the send rate was 99.38 tps. Similarly, the send rate was varied from 100.1 to 839.76 tps in 10 rounds of testing to achieve an average transaction throughput of 200.07 tps. The maximum and minimum average transaction throughput obtained was 246 tps and 80.54 tps at the send rates of 673.94 tps and 100.1 tps, respectively.

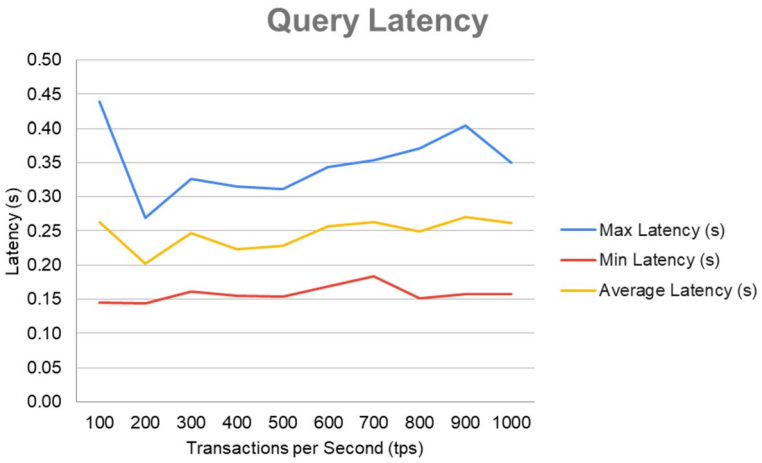

Fig. 7 Query latency

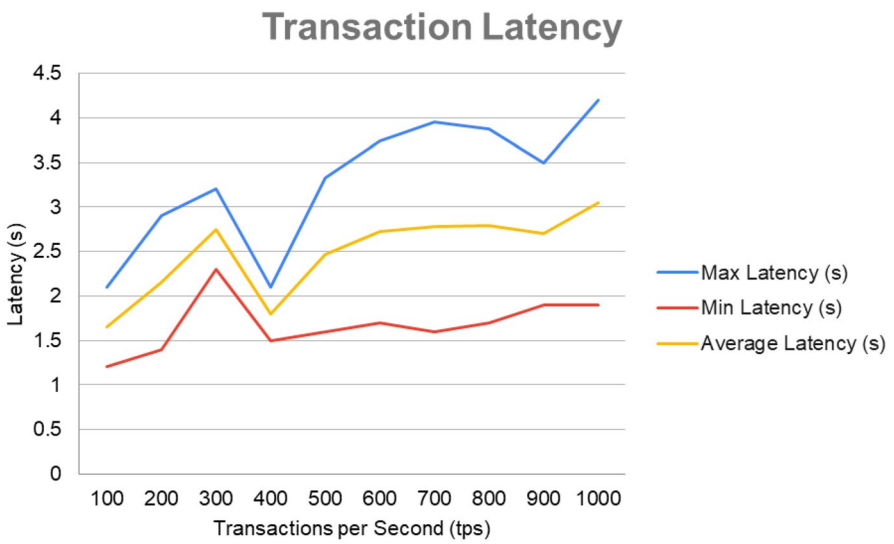

Fig. 8 Transaction latency

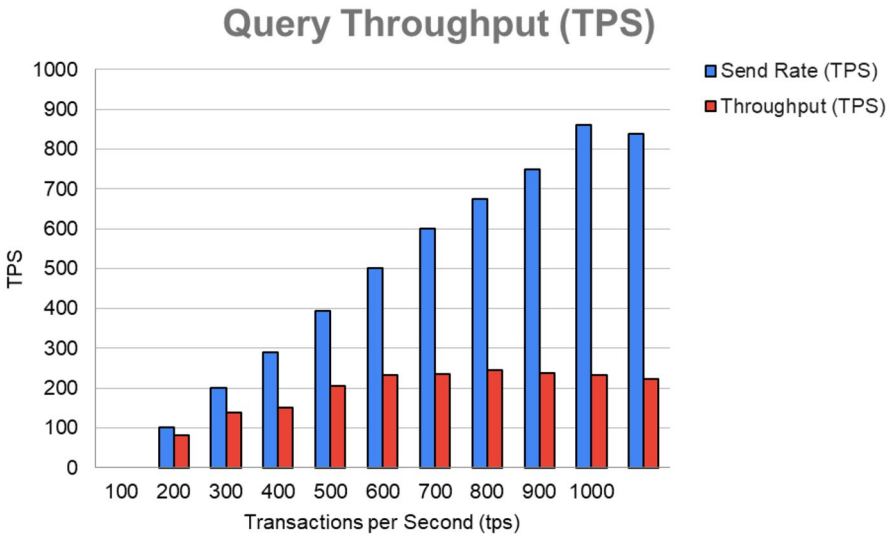

Fig. 9 Query throughput

9 Discussions and conclusion

This section discusses the advantages of the proposed architecture, the current limitations of DiabeticChain and the future work which can further enhance the implementations of the proposed system, followed by a conclusion.

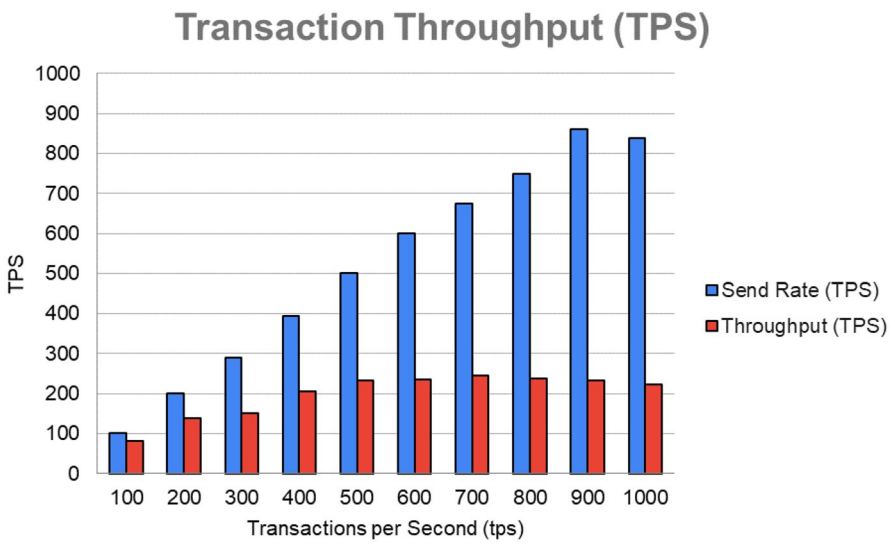

Fig. 10 Transaction throughput

9.1 Advantages of the proposed architecture

DiabeticChain is a patient-centric healthcare architecture based on blockchain technology to support secure and efficient diabetic data sharing. The proposed architecture is implemented to overcome the current challenges of traditional data sharing methods like lack of privacy, security, data ownership by patients, interoperability, fragmentation of data and data integrity. The key advantages offered by the implementation of the proposed system as a proof-of-concept study to demonstrate DiabeticChain's effectiveness are as follows:

- Unlike traditional systems that compromise on data security, DiabeticChain stands out. Our hybrid model ensures not just secure storage but also optimizes data retrieval, a first in the domain.
- Secondly, the system minimizes the risk of security breaches with the use of cryptography techniques like public key cryptography and access control mechanisms involving the patients access policy to grant or revoke access to their data.
- Thirdly, the system preserves the privacy of the patient by using a one-time access URL to access the diabetic data while maintaining the anonymity of data by creating random unique accounts associated with the patients.
- The system allows the patients to dynamically update their consent to grant or revoke data consumer's access, thereby giving them complete control over their diabetic data due to the absence of any centralized authority.

- While leveraging the benefits of blockchain technology, the system additionally ensures data integrity using proof-of-authority consensus protocol, immutability of blockchain and thereby enables traceability of data.
- Finally, the system provides a feasible model which can be integrated with the existing healthcare systems and thus ensures interoperability.

9.2 Limitations and future work

The current implementation of DiabeticChain uses a privately permissioned blockchain, and it may pose a potential risk as private blockchains have a lesser number of nodes in the network. So, it becomes easier for a malicious node to acquire control over the network and the risk of data breaches and manipulation of data is higher as compared to public blockchains [84]. The proposed system uses a one-time access URL for data sharing which should be accessed within a timeframe and can pose another limitation to the current implementation. The system can also pose legal and regulatory issues as there does not exist any central authority that can be held accountable for the blockchain network. There exist potential barriers to the adoption of DiabeticChain due to healthcare professionals' acceptance of the technology and technical barriers like the requirement of a stable internet connection, the establishment of every healthcare entity on the network and the requirement of the necessary hardware.

In the future, the current implementation of the proposed system can further be integrated with other emerging technologies like Internet of Things (IoT) to directly capture continuous patient data from smart wearable devices like smart watches to have daily smart care and artificial intelligence (AI) to make use of intelligent agents to interact with the system and further ease the process of data sharing. A potential enhancement to the current architecture can be to integrate machine learning algorithms with the captured data for predictive analysis of diabetic data like early detection of diabetes and enhanced cure. Another possible use of ML and AI can be to analyse the abnormal node behaviours within the network. There is a need to assess the performance and scalability of the system with an increasing number of users working simultaneously on the blockchain. Certain technological barriers may exist which hinder the process to completely shift the traditional Electronic Health Records (EHR) data to blockchain-based systems and fully implement blockchain-based solutions, but this to happen in reality does not seem very far.

9.3 Conclusions

Sensitive diabetic data is generated in large amounts and needs to be shared effectively among stakeholders since diabetes requires significant self-care and substantially burdens the patients with processes like continuous glucose monitoring and carbohydrate counting. The controlled access and sharing of diabetic data play a crucial role in benefitting healthcare professionals to take better patient care and researchers to effectively study disease patterns. In this paper, we addressed the current challenges associated with the privacy, security and controlled sharing of sensitive diabetic data, thereby improving patient care and advancing research. Our research identifies these

gaps, laying the foundation for the novel solutions DiabeticChain offers. We recognized the current limitations of the traditional client–server and cloud-based approaches such as privacy, security concerns, data fragmentation, authorization, lack of interoperability and data integrity and hence proposed a private permissioned blockchain-based solution for sharing of diabetic data.

DiabeticChain, our blockchain-based solution to diabetic data sharing, provides a novel patient-centric approach, leveraging access control mechanisms and smart contracts written in solidity to facilitate secure and efficient sharing of diabetic data among stakeholders while addressing concerns regarding privacy, security, data fragmentation, authorization and data integrity. We implemented a proof of concept of the architecture proposed using a privately permissioned Ethereum blockchain and analysed the system's performance where the results depicted an average Query throughput of 201.7 tps and an average Transaction throughput was 200.07 tps. The average Query latency was 0.24 s and the average Transaction latency was 1.31 s proving DiabeticChain to be scalable and efficient.

In comparison with the existing blockchain-based healthcare systems, we propose a blockchain-based architecture that uses a one-time access URL generated as per the access policy of the data owner, improving privacy, security and efficiency of diabetic data sharing. The proposed architecture will have a potential impact on patient care and research in the context of diabetes management as well as integration and application in other healthcare domains by enhancing the efficiency of the data sharing process, ensuring patient control over their data, and enabling privacy and data security. Through real-world scenarios and case studies, we demonstrate DiabeticChain's transformative potential in diabetic data management, a novelty in the current landscape.

Author contributions Deepak Kumar Mishra helped in conceptualization, formal analysis, writing original draft. Pawan Singh Mehra was involved in supervision, methodology, validation.

Data availability Not applicable.

Declarations

Conflict of interest None.

Ethical approval Yes.

References

1. IDF Diabetes Atlas | 10th edn. Accessed: Apr. 15 (2023)
2. Zhuo X, Zhang P, Barker L, Albright A, Thompson TJ, Gregg E (2014) The lifetime cost of diabetes and its implications for diabetes prevention. Diabetes Care 37(9):2557–2564. https://doi.org/10.2337/DC13-2484
3. Iyengar V, Wolf A, Brown A, Close K (2016) Challenges in diabetes care: Can digital health help address them? Clin Diabetes 34(3):133. https://doi.org/10.2337/DIACLIN.34.3.133
4. Heinrich E, Schaper NC, Vries NKD (2015) Self-management interventions for type 2 diabetes a systematic review. Int Diabetes Nurs 7(2):71–76. https://doi.org/10.1002/EDN.160

5. Azbeg K, Ouchetto O, Andaloussi SJ, Fetjah L, Sekkaki A (2018) Blockchain and IoT for security and privacy: a platform for diabetes self-management. In: 2018 4th International Conference on Cloud Computing Technologies and Applications, Cloudtech. https://doi.org/10.1109/CloudTech.2018.8713343
6. Uppamma P, Bhattacharya S (2023) Diabetic retinopathy detection: a blockchain and African vulture optimization algorithm-based deep learning framework. Electronics. https://doi.org/10.3390/electronics12030742
7. Rai B, Fatima S, Satyarth K (2022) Patient-centric multichain healthcare record. Int J E-Health Med Commun. https://doi.org/10.4018/IJEHMC.309439
8. Health Information Privacy | HHS.gov. Accessed: Apr. 15, (2023)
9. Dubovitskaya A et al (2020) ACTION-EHR: patient-centric blockchain-based electronic health record data management for cancer care. J Med Internet Res. https://doi.org/10.2196/13598
10. Duong-Trung N, Son HX, Le HT, Phan TT (2020) On components of a patient-centered healthcare system using smart contract. In: ACM International Conference Proceeding Series, pp 31–35. https://doi.org/10.1145/3377644.3377668
11. Cleveland SM, Haddara M (2021) Iot for diabetics: a user perspective, pp 161–172. https://doi.org/10.1007/978-3-030-80129-8_13
12. Shubrook JH, Brannan GD, Wapner A, Klein G, Schwartz FL (2018) Time needed for diabetes self-care: nationwide survey of certified diabetes educators. Diabetes Spect 31(3):267–271. https://doi.org/10.2337/DS17-0077
13. Benefits of Blockchain - IBM Blockchain | IBM. Accessed: Apr. 25, (2023)
14. Zyskind G, Nathan O, Pentland AS (2015) Decentralizing privacy: using blockchain to protect personal data. In: Proceedings - 2015 IEEE Security and Privacy Workshops, SPW 2015, pp 180–184. https://doi.org/10.1109/SPW.2015.27
15. Azaria A., Ekblaw A., Vieira T, Lippman A (2016) Medrec: using blockchain for medical data access and permission management. In: Proceedings—2016 2nd International Conference on Open and Big Data, OBD 2016, pp 25–30. https://doi.org/10.1109/OBD.2016.11
16. Liang X, Zhao J, Shetty S, Liu J, Li D (2017) Integrating blockchain for data sharing and collaboration in mobile healthcare applications. In: 2017 IEEE 28th Annual International Symposium on Personal, Indoor, and Mobile Radio Communications (PIMRC), pp 1–5. https://doi.org/10.1109/PIMRC.2017.8292361
17. Chen Y, Ding S, Xu Z, Zheng H, Yang S (2018) Blockchain-based medical records secure storage and medical service framework. J Med Syst. https://doi.org/10.1007/S10916-018-1121-4
18. Jabarulla MY, Lee HN (2021) Blockchain-based distributed patient-centric image management system. Appl Sci 11(1):1–20. https://doi.org/10.3390/app11010196
19. Mani V, Manickam P, Alotaibi Y, Alghamdi S, Khalaf OI (2021) Hyperledger healthchain: Patient-centric IPFS-based storage of health records. Electronics. https://doi.org/10.3390/electronics10233003
20. Gohar AN, Abdelmawgoud SA, Farhan MS (2022) A patient-centric healthcare framework reference architecture for better semantic interoperability based on blockchain, cloud, and iot. IEEE Access 10:92137–92157. https://doi.org/10.1109/ACCESS.2022.3202902
21. Taylor A, Kugler A, Marella PB, Dagher GG (2022) Vigilrx: a scalable and interoperable prescription management system using blockchain. IEEE Access 10:25973–25986. https://doi.org/10.1109/ACCESS.2022.3156015
22. Abutaleb RA, Alqahtany SS, Syed TA (2023) Integrity and privacy-aware, patient-centric health record access control framework using a blockchain. Appl Sci. https://doi.org/10.3390/app13021028
23. Rai BK (2023) PcBEHR: patient-controlled blockchain enabled electronic health records for healthcare 4.0. Health Serv Outcomes Res Methodol 23(1):80–102. https://doi.org/10.1007/s10742-022-00279-7
24. Grant RW et al (2006) Design and implementation of a web-based patient portal linked to an ambulatory care electronic health record: Patient gateway for diabetes collaborative care. Diabetes Technol Ther 8(5):576–586. https://doi.org/10.1089/dia.2006.8.576
25. Schoenberg R (2000) Internet based repository of medical records that retains patient confidentiality. BMJ 321(7270):1199–1203. https://doi.org/10.1136/bmj.321.7270.1199
26. Chen M et al (2021) Blockchain-enabled healthcare system for detection of diabetes. J Inf Secur Appl. https://doi.org/10.1016/j.jisa.2021.102771

27. Ismail L, Materwala H, Khan MAB (2020) Performance evaluation of a patient-centric blockchain-based healthcare records management framework. In: ACM International Conference Proceeding Series, pp. 39–50. https://doi.org/10.1145/3409934.3409941
28. Singh AP et al (2021) A novel patient-centric architectural framework for blockchain-enabled healthcare applications. IEEE Trans Industr Inform 17(8):5779–5789. https://doi.org/10.1109/TII.2020.3037889
29. Zhuang Y, Sheets LR, Chen YW, Shae ZY, Tsai JJP, Shyu CR (2020) A patient-centric health information exchange framework using blockchain technology. IEEE J Biomed Health Inform 24(8):2169–2176. https://doi.org/10.1109/JBHI.2020.2993072
30. Subramanian G, Thampy AS (2021) Implementation of blockchain consortium to prioritize diabetes patients' healthcare in pandemic situations. IEEE Access 9:162459–162475. https://doi.org/10.1109/ACCESS.2021.3132302
31. Hennebelle A, Ismail L, Materwala H, Kaabi JA, Ranjan P, Janardhanan R, Hennebelle A, Ismail L, Materwala H, Kaabi JA, Ranjan P, Janardhanan R (2022) Secure and privacy-preserving automated machine learning operations into end-to-end integrated iot-edge-artificial intelligence-blockchain monitoring system for diabetes mellitus prediction. arXiv, 2211–07643 doi: https://doi.org/10.48550/ARXIV.2211.07643
32. Pradhan NR, Rout SS, Singh AP (2021) Blockchain based smart healthcare system for chronic -illness patient monitoring. In: 3rd International Conference on Energy, Power and Environment: Towards Clean Energy Technologies, ICEPE 2020. doi: https://doi.org/10.1109/ICEPE50861.2021.9404496
33. Attaran M (2022) Blockchain technology in healthcare: challenges and opportunities. Int J Healthc Manag 15(1):70–83. https://doi.org/10.1080/20479700.2020.1843887
34. Salmon J, Myers G (2019) Blockchain and associated legal issues for emerging markets. Technical report, World Bank Group (Jan 2019)
35. Bashir I (2017) Mastering blockchain vol 161, pp 335–339. Accessed: Apr. 16, 2023. https://www.packtpub.com/product/mastering-blockchain/9781787125445
36. What is blockchain technology? - IBM Blockchain | IBM. Accessed: Apr. 16, 2023
37. Bitcoin: a peer-to-peer electronic cash system. www.bitcoin.org
38. Lodha G, Pillai M, Solanki A, Sahasrabudhe S, Jarali A(2021) Healthcare system using blockchain. In: Proceedings - 5th International Conference on Intelligent Computing and Control Systems, ICICCS 2021, pp 274–281. https://doi.org/10.1109/ICICCS51141.2021.9432157
39. Szabo N (1997) Formalizing and securing relationships on public networks. First Monday. https://doi.org/10.5210/FM.V2I9.548
40. Designing a blockchain architecture: types, use cases, and challenges | by Svetlana Cherednichenko | Mobindustry | Medium. Accessed: Apr. 21, 2023
41. Everything you need to kow about blockchain architecture | Edureka. Accessed: Apr. 21, 2023
42. Different types of blockchain and why we need them | Edureka. Accessed: Apr. 24, 2023
43. Blockchain from scratch: permissioned and Permissionless blockchains | by Radovan Stevanovic | Medium. Accessed: Apr. 24, 2023
44. Oliveira MT et al. (2019)Towards a performance evaluation of private blockchain frameworks using a realistic workload. In: 2019 22nd Conference on Innovation in Clouds, Internet and Networks and Workshops (ICIN), pp. 180–187. doi: https://doi.org/10.1109/ICIN.2019.8685888
45. Albalwy F, Brass A, Davies A (2021) A blockchain-based dynamic consent architecture to support clinical genomic data sharing (consentchain): Proof-of-concept study. JMIR Med Inform. https://doi.org/10.2196/27816
46. Brock, Arthur C, David Braden, Jamison M Day (2021) Holochain—a framework for distributed applications. U.S.Patent 10,951,697
47. Hyperledger Fabric - Hyperledger Foundation. Accessed: Apr. 21, 2023
48. Announcing Hyperledger Besu - Hyperledger Foundation. Accessed: Apr. 21, 2023
49. Pedro AS, Levi D, Cuende LI Witnet: a decentralized oracle network protocol. doi: https://doi.org/10.13140/RG.2.2.28152.34560
50. EOS.IO Technical White Paper - Steemit. Accessed: Apr. 21, 2023
51. The ripple protocol consensus algorithm reasonable deviations. Accessed: Apr. 21, 2023
52. Karlson EW, Boutin NT, Hoffnagle AG, Allen NL (2016) Building the partners healthcare biobank at partners personalized medicine: informed consent, return of research results, recruitment lessons and operational considerations. J Personal Med 6(1):2. https://doi.org/10.3390/JPM6010002

53. Replacing Paper Informed Consent with Electronic Informed Consent for Research in Academic Medical Centers: A Scoping Review - PubMed. https://pubmed.ncbi.nlm.nih.gov/32477626/
54. What is blockchain and how does it work? | Synopsys. Accessed: Apr. 15, 2023
55. Wang Z, Stell A, Sinnott RO (2023) A GDPR-compliant dynamic consent mobile application for the Australasian type-1 diabetes data network. Healthcare. https://doi.org/10.3390/HEALTHCARE11040496
56. Wust K, Gervais A (2018) Do you need a blockchain? In: Proceedings of the 1st Crypto Valley Conference on Blockchain Technology (CVCBT 2018), pp 45–54. doi: https://doi.org/10.1109/CVCBT.2018.00011
57. Pedersen AB, Risius M, Beck R (2019) A ten-step decision path to determine when to use blockchain technologies. MIS Q Exec 18(2):99–115. https://doi.org/10.17705/2msqe.00010
58. Li C, Raghunathan A, Jha NK (2011) Hijacking an insulin pump: security attacks and defenses for a diabetes therapy system. In: 2011 IEEE 13th International Conference on e-Health Networking, Applications and Services, pp 150–156. doi: https://doi.org/10.1109/HEALTH.2011.6026732
59. Cyran MA (2018) Blockchain as a foundation for sharing healthcare data. Blockchain Healthc Today. https://doi.org/10.30953/bhty.v1.13
60. Zhao F, Yu J, Yan B Towards cross-chain access control model for medical data sharing. In: Procedia Computer Science, pp. 330–335. https://doi.org/10.1016/j.procs.2022.04.045
61. Reen GS, Mohandas M, Venkatesan S, Decentralized Patient Centric e- Health Record Management Systemusing Blockchain and IPFS. In: 2019 IEEE Conference on Information and Communication Technology, Allahabad, India, pp. 1–7. https://doi.org/10.1109/CICT48419.2019.9066212
62. Mudaliar A, More Y, Kulkarni A, Joshi L, Chaudhari D (2022) Blockchain-based user-centric electronic health record management system. In: 2022 IEEE International Conference on Blockchain and Distributed Systems Security, ICBDS 2022. https://doi.org/10.1109/ICBDS53701.2022.9935834
63. Dewangan NK, Chandrakar P (2022) Patient-centric token-based healthcare blockchain implementation using secure internet of medical things. IEEE Trans Comput Soc Syst. https://doi.org/10.1109/TCSS.2022.3194872
64. Toshniwal B, Podili P, Reddy RJ, Kataoka K (2019) PACEX: Patient-centric EMR exchange in healthcare systems using blockchain. In: 2019 IEEE 10th Annual Information Technology, Electronics and Mobile Communication Conference, IEMCON 2019, pp 954–960. https://doi.org/10.1109/IEMCON.2019.8936258
65. Satamraju KP, Balakrishnan M (2022) A secured healthcare model for sensor data sharing with integrated emotional intelligence. IEEE Sens J 22(16):16306–16313. https://doi.org/10.1109/JSEN.2022.3189268
66. Chelladurai MU, Pandian DS, Ramasamy DK (2021) Blockchain based patient centric electronic health record storage and integrity management for e-health systems. Health Policy Technol. https://doi.org/10.1016/.hlpt.2021.100513
67. Alexaki S, Alexandris G, Katos V, Petroulakis EN (2018) Blockchain-based electronic patient records for regulated circular healthcare jurisdictions. In: IEEE International Workshop on Computer Aided Modeling and Design of Communication Links and Networks, CAMAD. https://doi.org/10.1109/CAMAD.2018.8514954
68. Kordestani H, Barkaoui K, Zahran W (2020) Hapichain: a blockchain-based framework for patient-centric telemedicine. In: 2020 IEEE 8th International Conference on Serious Games and Applications for Health, SeGAH 2020. https://doi.org/10.1109/SEGAH49190.2020.9201726
69. Kanagi K, Ku CCY, Lin LK, Hsieh WH (2020) Efficient clinical data sharing framework based on blockchain technology. Methods Inf Med 59(6):193–204. https://doi.org/10.1055/s-0041-1727193
70. Fatokun T, Nag A, Sharma S (2021) Towards a blockchain assisted patient owned system for electronic health records. Electronics 10(5):1–14. https://doi.org/10.3390/electronics10050580
71. Kumar M, Chand S (2021) Medhypchain: a patient-centered interoperability hyperledger-based medical healthcare system: regulation in covid-19 pandemic. J Netw Comput Appl. https://doi.org/10.1016/j.jnca.2021.102975
72. Nzuva S (2019) Smart contracts implementation, applications, benefits, and limitations. https://doi.org/10.7176/JIEA. www.iiste.org
73. Home | Go-ethereum. Accessed: May 07, 2023
74. Ghosh PK, Chakraborty A, Hasan M, Rashid K, Siddique AH (2023) Blockchain application in healthcare systems: a review. Systems 11(1):38. https://doi.org/10.3390/systems11010038

75. Singh R, Dwivedi AD, Mukkamala RR, Alnumay WS (2022) Privacy-preserving ledger for blockchain and internet of things-enabled cyber-physical systems. Comput Electr Eng 103:108290. https://doi.org/10.1016/J.COMPELECENG.2022.108290
76. WEF Blockchain Toolkit. Accessed: Apr. 29, 2023
77. George M, Chacko AM (2022) trans-patient-centric interoperability through blockchain. Int J Netw Manag. https://doi.org/10.1002/nem.2187
78. Razzaq A et al (2022) Blockchain-enabled decentralized secure big data of remote sensing. Electronics 11(19):3164. https://doi.org/10.3390/electronics11193164
79. Marinho SSC, Filho JSC, Moreira LO, MacHado JC (2020) Using a hybrid approach to data management in relational database and blockchain: A case study on the e-health domain. In: Proceedings - 2020 IEEE International Conference on Software Architecture Companion, ICSA-C 2020, pp 114–121. https://doi.org/10.1109/ICSA-C50368.2020.00030
80. König L, Unger S, Kieseberg P, Tjoa S (2020) The risks of the blockchain a review on current vulnerabilities and attacks. J Internet Serv Inf Secur 10(3):110–127. https://doi.org/10.22667/JISIS.2020.08.31.110
81. Ekparinya P, Gramoli V, Jourjon G (2018) Impact of man-in-the-middle attacks on ethereum. In: 2018 IEEE 37th Symposium on Reliable Distributed Systems (SRDS), pp 11–20. https://doi.org/10.1109/SRDS.2018.00012
82. DoS Attacks on Blockchain Ecosystem. Accessed: May 31, 2023
83. Hyperledger Blockchain Performance Metrics White Paper - Hyperledger Foundation. Accessed: May 24, 2023
84. Yang R et al (2020) Public and private blockchain in construction business process and information integration. Autom Constr 118:103276. https://doi.org/10.1016/J.AUTCON.2020.103276

Publisher's Note Springer Nature remains neutral with regard to jurisdictional claims in published maps and institutional affiliations.

Springer Nature or its licensor (e.g. a society or other partner) holds exclusive rights to this article under a publishing agreement with the author(s) or other rightsholder(s); author self-archiving of the accepted manuscript version of this article is solely governed by the terms of such publishing agreement and applicable law.

Authors and Affiliations

Deepak Kumar Mishra[1,2] · Pawan Singh Mehra[1]

✉ Pawan Singh Mehra
pawansinghmehra@gmail.com

Deepak Kumar Mishra
deepakmishra.it@gmail.com

[1] Department of CSE, Delhi Technological University, Main Bawana Road, New Delhi, Delhi 110042, India

[2] Department of Computer Science, College of Vocational Studies, Delhi University, Delhi, Delhi 110017, India

arXiv:2411.13901v1 [cs.CV] 21 Nov 2024

Dressing the Imagination: A Dataset for AI-Powered Translation of Text into Fashion Outfits and A Novel KAN Adapter for Enhanced Feature Adaptation

Gayatri Deshmukh
Independent Researcher
dgayatri9850@gmail.com

Somsubhra De
IIT Madras
22f3002680@ds.study.iitm.ac.in

Chirag Sehgal
Delhi Technological University
chiragsehgal224@gmail.com

Jishu Sen Gupta
IIT BHU
jishusen.gupta.mat22@itbhu.ac.in

Sparsh Mittal
IIT Roorkee
sparsh.mittal@ece.iitr.ac.in

Abstract

*Specialized datasets that capture the fashion industry's rich language and styling elements can boost progress in AI-driven fashion design. We present **FLORA** (**F**ashion **L**anguage **O**utfit **R**epresentation for **A**pparel Generation), the first comprehensive dataset containing 4,330 curated pairs of fashion outfits and corresponding textual descriptions. Each description utilizes industry-specific terminology and jargon commonly used by professional fashion designers, providing precise and detailed insights into the outfits. Hence, the dataset captures the delicate features and subtle stylistic elements necessary to create high-fidelity fashion designs. We demonstrate that fine-tuning generative models on the FLORA dataset significantly enhances their capability to generate accurate and stylistically rich images from textual descriptions of fashion sketches. FLORA will catalyze the creation of advanced AI models capable of comprehending and producing subtle, stylistically rich fashion designs. It will also help fashion designers and end-users to bring their ideas to life. As a second orthogonal contribution, we introduce KAN Adapters, which leverage Kolmogorov-Arnold Networks (KAN) as adaptive modules. They serve as replacements for traditional MLP-based LoRA adapters. With learnable spline-based activations, KAN Adapters excel in modeling complex, non-linear relationships, achieving superior fidelity, faster convergence and semantic alignment. Extensive experiments and ablation studies on our proposed FLORA dataset validate the superiority of KAN Adapters over LoRA adapters. To foster further research and collaboration, we will open-source both the FLORA and our implementation code.*

1. Introduction

Artificial intelligence has become increasingly influential in various industries, fashion being a prominent example. The global fashion industry, valued at approximately 2.4 trillion and growing at an annual rate of 5.5% over the past decade [5], represents a significant economic sector facing constant pressure to innovate and respond to consumer demands. The integration of AI in fashion has revolutionized design processes and enhanced creativity and consumer personalization. AI's role in fashion extends beyond virtual try-on systems to various applications, including trend forecasting, product development, supply chain optimization, and sustainable practices [30]. For instance, AI algorithms analyze vast datasets from social media and fashion shows to predict upcoming trends, enabling brands to remain competitive. Additionally, AI-powered recommendation systems provide personalized styling suggestions, enhancing the overall shopping experience for consumers.

Despite the potential, AI applications in fashion face several challenges [33]. One major issue is the complexity of fashion design, which involves subjective details like color, style, fabric, and texture. AI models often struggle to capture the nuanced details of fashion sketches. Existing models often produce outputs that lack coherence or fail to align with the provided descriptions [9, 14, 26]. Another challenge is the unavailability of well-annotated datasets, especially sketch-based datasets. Traditional fashion design practices, including seasonal collections and lengthy pro-

duction cycles, often lag behind the fast-paced demands of consumers. As trends evolve rapidly, designers face the challenge of producing timely collections that resonate with audiences. This underscores the need for innovations that streamline design processes to maintain competitiveness.

This research addresses the problem of generating high-fidelity fashion outfit sketches based on detailed text descriptions. Unlike virtual try-on systems [11], which simulate how garments fit on a user, our goal is to create accurate and visually appealing fashion sketches from textual information. Our paper addresses the critical issue of dataset quality by providing a meticulously curated and annotated dataset. Developing a robust pipeline for sketch generation from text can help overcome obstacles in translating descriptive text into coherent and stylistically appropriate visual representations. With this, we aim to advance the capability of AI in fashion design to streamline the design workflow, reducing the time spent on initial sketches, enhancing collaboration, and boosting sales. This will help emerging designers who may not have traditional sketching skills and can serve as a valuable tool for designers, researchers, and other stakeholders in this industry.

Additionally, in today's landscape, datasets are increasingly complex, with higher levels of non-linearity that make it challenging for models to effectively capture intricate patterns. Models often struggle to adapt to these complexities. For instance, datasets like FLORA present unique challenges due to their emphasis on fine-grained details—such as fabric type, fit, and decorative elements—which require nuanced understanding and multi-modal alignment. These subtle attributes introduce high variability and complexity, making it difficult for models to generalize well from limited data. To address this, we propose the KAN Adapter, which excels at learning non-linearities through its learnable activations, thereby enhancing the model's ability to capture complex, fine-grained relationships. This paper makes the following key contributions:

- **FLORA Dataset:** We introduce FLORA, a large-scale, curated dataset comprising 4,330 pairs of fashion outfit sketches and detailed textual descriptions. Each description uses industry-specific terminology, capturing the nuanced design elements essential for high-fidelity fashion sketch generation from text. FLORA fills a critical gap in existing resources by providing the first dataset tailored specifically to text-to-fashion sketch generation. FLORA will enable AI models to generate precise, high-quality fashion sketches from textual descriptions, reducing reliance on traditional sketching skills and accelerating the initial design phases.
- **KAN Adapters:** We propose KAN adapters, a new approach that replaces traditional MLP-based LoRA adapters with Kolmogorov-Arnold Networks (KANs) [22]. By enabling complex, non-linear transformation modeling, KAN Adapters achieve training efficiency and adaptability, making them particularly effective for tasks requiring intricate representation.
- Our experiments show that KAN adapters achieve faster convergence and higher fidelity than LoRA, enabling models to reach optimal performance in fewer training steps. Additionally, fine-tuning generative models on the FLORA dataset greatly improves their ability to produce accurate, stylistically rich images from fashion outfit descriptions.

2. Related Works

Related work on AI in fashion: Text-to-image generation has rapidly evolved, driven by growing demands for visual content across diverse sectors, including art, marketing, education, and, more recently, fashion [14]. The fashion industry, in particular, has embraced AI to transform design and retail, with major brands like H&M, Zara, and Nike leveraging AI to enhance creativity and efficiency [1, 12]. AI tools now support designers in generating patterns and styles by analyzing consumer preferences, allowing for faster, trend-responsive design cycles. Predictive analytics further empower brands to anticipate fashion trends, enabling the creation of innovative collections that resonate with consumers while facilitating personalized shopping experiences through tailored outfit recommendations.

Generative models like Variational Autoencoders (VAEs) and Generative Adversarial Networks (GANs) have become foundational in creating high-quality garment visuals. These models assist designers by visualizing new styles and enabling quick design iterations. Style transfer models, such as Pix2Pix [13], use conditional GANs [23] for image translation tasks, while FashionGAN [38] allows designers to create virtual model visualizations of new apparel designs. Recently, diffusion models have surpassed GANs in the image generation space [15]. Models like Stable Diffusion [4], OpenAI's DALL-E 2 [29], and Midjourney have become popular tools in both commercial and non-commercial settings. Such tools have brought AI-driven design automation into practical use, with platforms like DeepAI [2] and RunwayML [3] facilitating novel design and routine automation tasks in fashion media production. Text-to-image models now enable AI to create garment visuals from descriptions using sophisticated transformer architectures, as seen in DALL-E [29], Imagen [32], and Stable Diffusion [8, 31].

However, challenges persist in generating high-fidelity and stylistically accurate images from complex fashion descriptions, particularly for stylized sketches, which are integral to fashion design. While these models excel at realistic image generation, they lack optimization for fashion sketches. Additionally, there are no dedicated datasets that are sufficiently curated and explicitly annotated for the pur-

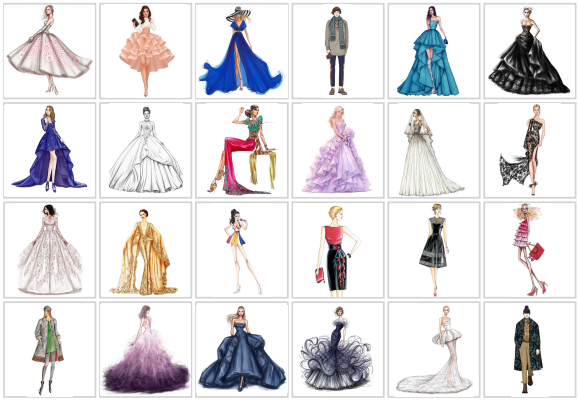

Figure 1. Sample images from our dataset

Figure 2. A figure and the generated textual description pair

pose of generating fashion sketches from text descriptions. This limits the development of robust models for fashion sketch generation.

Current research has made strides in fashion synthesis, including human parsing, pose estimation, landmark detection, style transfer, and clothing simulation. Datasets like Market-1501 [39], DeepFashion [21], and VITON [10] support these applications. However, the specific domain of text-based fashion sketch generation remains unexplored, highlighting a gap for dedicated datasets. We address this gap by proposing a novel dataset tailored for generating fashion sketches from textual descriptions. By focusing on this use case, we aim to lay the groundwork for more specialized and nuanced AI applications in fashion design, providing researchers and designers with valuable resources to drive innovation and creative expression in the industry.

Related work on KANs: Kolmogorov-Arnold Networks (KANs) [22], inspired by the Kolmogorov-Arnold representation theorem, offer an interpretable and flexible alternative to traditional MLPs. With learnable edge activations, KANs adaptively learn input relationships, making them effective for complex function approximation and interpretability in data patterns. Fast KAN [18] introduced an adaptation where B-splines are replaced by Radial Basis Functions (RBFs), aiming to reduce the computational overhead associated with splines. ReLU-KAN [28] addresses the computational complexity in traditional KANs by using ReLU and point-wise multiplication, combining KANs' "catastrophic forgetting avoidance" with ReLU's efficiency, making it suitable for inference and training in deep learning frameworks. ConvKANs [6] integrate KAN nonlinear activations into convolutional layers, making them valuable for interpretable applications in computer vision. Li et al., 2024 [18] investigated and redesigned the established U-Net pipeline by integrating KAN layers into the intermediate tokenized representations, resulting in the U-KAN architecture for more efficient medical image segmentation. Yang et al. [37] introduced the Kolmogorov-Arnold Transformer (KAT) by incorporating KANs into MLP-based transformers and demonstrated that the proposed KAT outperformed all ViT models on traditional vision tasks.

3. Proposed FLORA Dataset

We introduce FLORA, a large-scale dataset comprising 4,330 outfit sketch and textual description pairs. Fig. 1 shows some sample images from the dataset. This dataset aims to facilitate the training of generative models for fashion image synthesis, designed specifically for generating fashion sketches based on descriptive inputs. It represents the first dataset of its kind, addressing the significant gap in resources available for sketch-based fashion design.

3.1. Collection of dataset

To create a diverse range of fashion-related sketches, we initiated the process by web-scraping images using various search queries such as 'fashion-outfit sketches', 'fashion illustrations', 'wedding-gown sketches' and 'fashion pencil sketches'. We, thus, collected 10,042 images. Since these images had various forms of noise, e.g., signatures, watermarks and text overlays, we employed a multi-stage filtering approach (Figure 3) to obtain a suitable dataset.

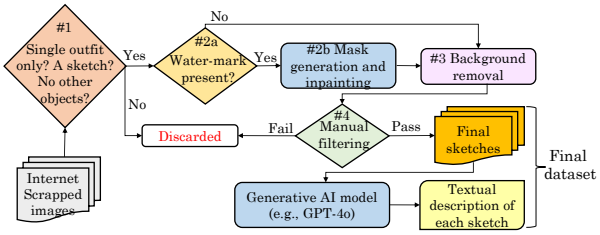

Figure 3. Image filtering steps for creating the training dataset

3.1.1. Multi-Stage Filtering of Images

1. Prompt-Based Filtering We first implemented prompt-based filtering using LLaVa 32b [19], a VLLM model. This step checks whether the image is a sketch with only a single outfit and no other objects.

2. Watermark Removal Removing signatures and text is crucial for maintaining the visual integrity of the images and improving the model's ability to learn and generalize effectively. For images with watermark, we applied Keras-OCR [24] for text detection and mask generation followed by 'ControlNet Stable Diffusion Scene-Text Eraser' [35] for inpainting. This pipeline effectively removed extraneous elements without distorting the outfits.

3. Background Removal We eliminated extraneous objects and color variations for images with distracting background noise. Specifically, we replaced the original backgrounds with clean, transparent ones using a background-remover model [34]. This enhances their visual clarity and ensures the focus remains on the main subject.

4. Manual Filtering Finally, we manually checked each image to remove duplicates. We split the images containing multiple sketches into separate sketches to maximize the number of usable samples. We concluded with 4,330 clean and relevant images.

3.1.2. Generating description of each sketch

We utilized a multimodal model, viz., OpenAI's GPT-4o [25] to generate the image descriptions. Each outfit description is structured to include the *human model pose* that consists of the model's posture, including the position of hands and legs, allowing for accurate sketch recreation, *outfit details*, its *color* and *accessories* that lists any additional elements like shoes or jewelry. Fig. 2 shows an example of one such outfit description. Further details on the dataset and the prompts used are available in the supplementary section.

3.2. Dataset Applications & Uniqueness

Our dataset fills a critical gap in fashion image generation and description-based design, particularly in outfit generation, where existing datasets are scarce. It benefits designers by reducing the manual effort required for sketching and gives them a solid foundation to develop their skills and ideas. It empowers non-designers to express creative ideas through text-to-sketch platforms. While existing datasets focus on virtual try-on or human pose estimation [36], our emphasis on sketches adds novelty, making it a valuable tool for advancing creativity and innovation in AI-driven fashion design.

4. Proposed KAN Adapter

As a second orthogonal contribution, we propose KAN adapters. In this Section, we first provide a background on LoRA and KAN modules (Sections 4.1-4.2), and then discuss our proposed KAN adapter (Section 4.3).

4.1. Background on LoRA modules

LoRA (Low-Rank Adaptation) modules provide an efficient way to fine-tune large models by optimizing the number of trainable parameters. Instead of adjusting all parameters, which can lead to "catastrophic forgetting", LoRA adds trainable adapters that preserve the model's learned features while achieving similar or improved results. These adapters work by training a new set of weights in a reduced dimension (or rank) that are scaled down based on model size. During fine-tuning, the model's original layers are frozen. LoRA's linear adapters process the input in parallel, scaling it down to a lower rank and then back to the output dimension. This setup prevents increased inference latency and makes it suitable for various downstream tasks. A formal representation of the LoRA is given in the equation

$$L'(x) = L(x) + W_{\text{up}}\left(\text{GeLU}\left(W_{\text{down}}(x)\right)\right) \tag{1}$$

where $W_{\text{up}} \in \mathbb{R}^{(d,l)}$ and $W_{\text{down}} \in \mathbb{R}^{(l,d)}$, with $l < d$. Here, W_{up} and W_{down} represent the LoRA weights, $L'(x)$ represents the modified layer output, and $L(x)$ represents the original layer output to which LoRA is applied. The matrix W_{down} is initialized with the distribution of the weights of $L(x)$ to maintain coherence with the frozen layer.

4.2. Background on KANs

Kolmogorov-Arnold Networks (KANs) [22] have been recently introduced as an alternative to traditional MLPs in deep learning applications. Unlike MLPs, which use fixed activation functions, KANs employ learnable B-spline functions as activation layers, making them more flexible and expressive while requiring fewer parameters. B-splines, composed of polynomial segments with control points, allow local adjustments in the activation function without impacting the rest of the network. This local control helps maintain smoothness and facilitates differentiability, which is crucial for efficient backpropagation.

KANs are based on the Kolmogorov-Arnold representation theorem (KART), which states that any continuous high-dimensional function can be decomposed into a sum of univariate functions. Liu et al. [22] extended this to deep networks by creating the KAN-Layer, which consists of learnable activation functions given by the equation:

$$\varphi(x) = w\left(b(x) + \text{spline}(x)\right) \tag{2}$$

where, $b(x) = \text{silu}(x) = x/(1 + e^{-x})$ and $spline(x)$ is a linear combination of learnable B-splines. This structure allows KANs to capture complex functions effectively.

4.3. Proposed KAN Adapter

The need for adaptable and computationally efficient models has grown recently, especially in domains where fine-tuning large models for downstream tasks can be computationally expensive. Traditional methods like LoRA modules (Section 4.1) address this need by introducing learnable parameters in a lower-dimensional space, typically employing MLPs for transformation. However, MLPs face limitations in efficiently modeling complex non-linear transformations.

To overcome these limitations, we propose KAN Adapters, a novel approach leveraging Kolmogorov-Arnold Networks (KANs) with learnable spline-based activation functions. This architecture efficiently approximates complex, highly non-linear functions, enhancing parameter efficiency and flexibility. Replacing MLP-based LoRA with a KAN adapter improves computational efficiency and adaptability, making it well-suited for tasks requiring sophisticated non-linear representations.

The KAN adapter architecture, illustrated in Figure 4, incorporates KAN as an adapter layer alongside the pre-trained model's MLP layer. The KAN adapter layer processes input X, which includes down-projection (ϕ_{down}) and up-projection (ϕ_{up}) functions. These functions transform the input to a lower-dimensional space and then project it back, producing X' using learnable, spline-based activation functions. The outputs from the MLP and KAN adapters are then aggregated and passed to the subsequent layer. For explanatory purposes, we used the MLP layer to add KAN adapters in parallel; however, similar to LoRA, these adapters can be added to any layer.

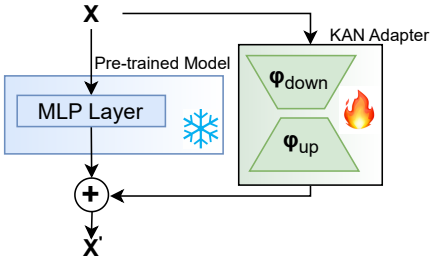

Figure 4. Integration of the KAN Adapter with a pre-trained model. Snowflake symbol (❄) indicates frozen weights, and the fire symbol 🔥 denotes trainable weights.

As depicted in Figure 5, the input $X \in \{x_1, x_2, x_3, \ldots, x_m\}$ is projected into a lower-dimensional representation $H \in \{h_1, h_2, h_3, \ldots, h_n\}$, where $X \in \mathbb{R}^m$, $H \in \mathbb{R}^n$, with $n = m/2$, through

$$\phi_{\text{down}}(X) = W_b^{\text{down}} \cdot g(X) + W_s^{\text{down}} \left(\sum_{i=1}^{n} c_i \, \gamma(X) \right) \quad (3)$$

Here, W_b^{down} and W_s^{down} are learnable stabilizing matrices, $g(X)$ is an activation function, and $\gamma_i(X)$ represents a set of basis functions (such as B-splines or Radial Basis Functions). The terms c_i are the coefficients learned during training. The transformed representation H is projected back to the original feature space $\mathbb{R}^m$.

$$\phi_{\text{up}}(X) = W_b^{\text{up}} \cdot g(H) + W_s^{\text{up}} \left(\sum_{i=1}^{m} d_i \, \gamma(H) \right) \quad (4)$$

W_b^{up} and W_s^{up} are additional stabilization matrices, d_i are learned coefficients, and $\gamma_i(H)$ is the basis function representation in the compressed space. This up-projection allows the model to re-expand the representation to the original space while retaining the most relevant features. Finally,

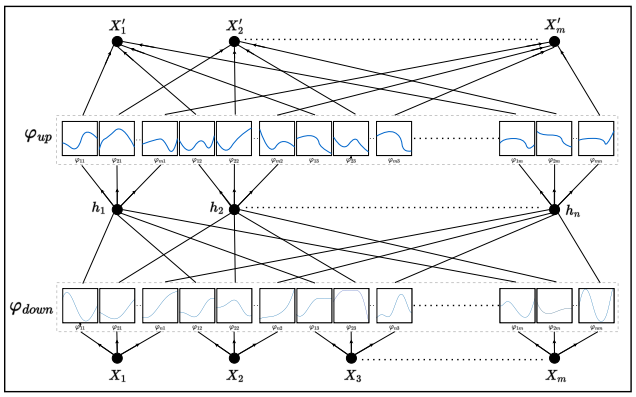

Figure 5. KAN Adapter

outputs from the KAN adapter and MLP are aggregated as

$$X' = \mathcal{L}_\theta(X) + (\phi_{\text{up}} \cdot \phi_{\text{down}})(X) \quad (5)$$

$\mathcal{L}_\theta(.)$ is the original pre-trained model. The final aggregated output X' is then passed to subsequent layers, ensuring that the KAN adapter's non-linear transformations complement the MLP's capabilities. This complements the main model by introducing non-linear transformations, which LoRA's MLP layers cannot capture efficiently.

Salient features: KAN Adapters differ fundamentally from LoRA's fixed MLP-based transformations by utilizing flexible, learnable basis functions. This enables KAN Adapters to capture fine-grained patterns within the data, which is crucial for tasks where complex dependencies must be learned. While LoRA adapters are designed to prevent catastrophic forgetting by keeping the core model weights frozen, KAN Adapters offer an additional layer of resilience through their unique use of adaptive, learnable activation functions. Unlike static activations in MLP-based LoRA, the KAN Adapter's non-linear functions can dynamically adjust to new tasks, selectively retaining important representations from prior tasks without overwriting them. This flexibility enables KAN Adapters to handle the complexities of sequential learning better, as they can modulate responses specifically for new data while preserving critical knowledge from earlier tasks. This added adaptability has been shown in related studies, such as ReLU-KAN [28], to provide enhanced memory retention, making KAN Adapters particularly suited for continual learning scenarios. Additionally, KAN Adapters demonstrate faster convergence compared to LoRA (refer to Figure 6). This faster convergence implies that KAN Adapters can reach optimal or near-optimal performance in fewer training steps, making them more computationally efficient.

5. Experimental Section

Implementation Details: All models were fine-tuned with a batch size of 12 using gradient accumulation steps of 12, leveraging the AdamW optimizer for enhanced generalization through weight decay. The initial learning rate was set

to 1×10^{-5} and dynamically adjusted with a cosine annealing schedule, gradually varying between a minimum of 1×10^{-7} and a maximum of 2×10^{-3}. This scheduling approach allowed for smooth convergence by reducing the learning rate as training progressed. The training was conducted on a robust setup of 4 x 8 Nvidia H100 GPUs with 80GB VRAM. For all the baselines, elastic weight consolidation [16] was performed to determine where to add LoRA and KAN adapters.

Test Set: To evaluate the proposed KAN adapter and demonstrate this dataset's practical relevance, we created a test set of 500 innovative fashion outfit descriptions. Each description was generated using a structured prompt (refer supplementary) with GPT-4o [25], incorporating standard industry-specific terminology. We introduce novel and unique design elements in the prompts to assess the models' capability to interpret both familiar and innovative fashion concepts. Thus, our experiments showcase the effectiveness of the dataset in real-world applications.

5.1. Quantitative Results

We have conducted text-to-image generation experiments using several baseline models: Stable Diffusion (SD) [31], SD-XL [27], SD 3 [8], Pixart-Sigma [7], and FLUX [17]. In the zero-shot setting, pre-trained baseline models are used to perform inference on our test set without any fine-tuning on FLORA. For KAN adapter, we used radial basis function. We evaluated each model's performance using FID (Fréchet Inception Distance) for image realism and CLIP-SIM for semantic alignment with textual prompts.

From Table 1, the zero-shot results indicate that while these pre-trained models can produce realistic images to some extent, their semantic alignment with our specific fashion-focused textual prompts remains limited. This performance gap highlights FLORA's unique characteristics, including fashion-specific terminology and novel design elements that the pre-trained models are not optimized to interpret effectively. From Table 1, KAN adapters consistently outperform LoRA modules across all models, showing superior adaptability and expressive power. KAN's ability to operate in a lower-dimensional, flexible space enhances its capacity to capture complex data patterns more effectively than LoRA, which relies on MLP layers and is more constrained in its representational flexibility.

Among the models, FLUX with KAN adapters achieved the best overall performance, with an FID of 6.05 and a CLIPSIM of 0.3412. Flux's advantage stems from its large training dataset and flow-matching algorithm, which aligns the model's output and data distributions along a linear trajectory in latent space. This approach minimizes sampling steps, improving efficiency and image quality, which KAN adapters further enhance by capturing nuanced details and alignment with prompts.

Methods	Zero-shot		LoRA		KAN	
	FID↓	CLIPSIM↑	FID↓	CLIPSIM↑	FID↓	CLIPSIM↑
FLUX[17]	09.09	0.3112	07.88	0.2987	**06.05**	**0.3412**
SD[31]	19.25	0.0623	17.32	0.0910	**16.51**	**0.1112**
SD-XL[27]	16.37	0.1539	15.32	0.1522	**13.33**	**0.1897**
SD-3[8]	13.28	0.2118	09.37	0.2119	**08.07**	**0.2503**
Pixart-Sigma[7]	14.11	0.2666	09.89	0.2542	**08.28**	**0.2991**

Table 1. Quantitative evaluation of SOTA diffusion models for generating prompt-based sketches of outfits, using zero-shot, traditional MLP-based LoRA, and our proposed KAN-adapters.

The Stable Diffusion series (SD, SD-XL, SD-3) also saw substantial improvements with KAN adapters, particularly SD-3, which achieved an FID of 8.07 and a CLIP-SIM of 0.2503. KAN's adaptability allows these models to capture fine-grained visual features that traditional LoRA modules might miss, enhancing both realism and semantic alignment. KAN adapter also improved Pixart-Sigma's performance, reducing its FID from 9.89 to 8.28 and raising CLIPSIM from 0.2542 to 0.2991. Further, as shown in Figure 6, KAN demonstrates faster convergence and lower loss, indicating improved stability and performance in capturing relevant features.

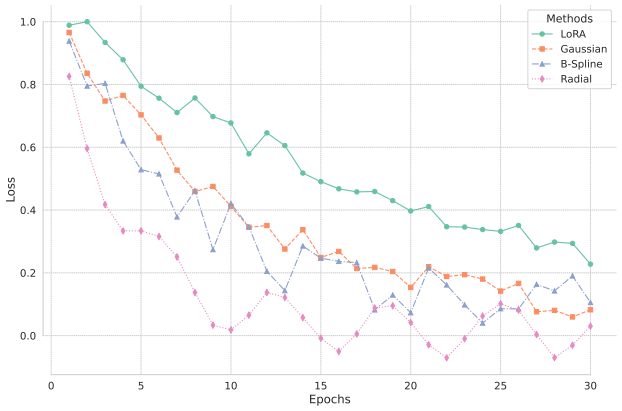

Figure 6. Comparison of LoRA and KAN adapters (using Gaussian, B-Spline, and Radial basis functions) on the FLUX model.

We also conducted a comprehensive human evaluation of each generated sketch, drawing inspiration from EvalCrafter [20]. One sketch was generated for each of the 500 textual descriptions in the test set. A unique set of 500 individuals evaluated each of these 500 sketches. To assess various dimensions of sketch quality, users evaluated them on several key parameters: Prompt Relevance, Visual Quality, Creativity, Pose and Model Accuracy, Color Palette Alignment, Contextual Fit, and Overall Appeal (refer to supplementary for more details). These metrics help quantify their visual observations and provide a structured analysis of each model's performance. The aggregated results are presented in Table 2. Our findings indicate that FLUX, fine-tuned with the KAN-adapter, outperforms all other models and their respective variants. Additionally, models fine-tuned with the KAN adapter consistently out-

Model	Prompt Relevance	Visual Quality	Creativity	Pose & Model Acc.	Color Palette Alignment	Contextual Fit	Overall Appeal	Latency (s)
FLUX	59.78 | 61.43	45.25 | 46.98	52.29 | 56.54	65.19 | 69.78	60.19 | 63.33	45.92 | 50.27	46.72 | 50.33	8.73 | 8.81
SD	37.76 | 39.21	29.92 | 34.12	19.45 | 21.21	15.53 | 18.71	41.18 | 45.78	18.76 | 20.21	20.21 | 22.76	13.43 | 14.42
SD-XL	44.78 | 47.12	33.33 | 36.54	25.77 | 29.30	29.92 | 33.47	48.93 | 50.21	27.76 | 31.19	30.33 | 33.89	9.87 | 10.02
SD-3	53.32 | 56.98	40.14 | 44.27	37.82 | 41.65	59.12 | 63.45	54.44 | 57.02	39.31 | 42.75	39.72 | 44.36	10.11 | 10.23
Pixart	51.39 | 55.03	39.19 | 41.14	35.71 | 40.21	61.29 | 65.43	53.53 | 56.92	38.27 | 40.91	36.64 | 40.19	6.32 | 6.89

Table 2. The results represent the percentage of images with a score above 7.5 out of 10, as rated by 500 humans on both LoRA and KAN adapters. The last column shows inference latency. Each reported value is in the format `<LoRA>|<KAN-adapter>`. For all metrics, except latency, higher is better (acc.= accuracy). Number of diffusion steps: FLUX (20), SD (50), SD-XL and SD-3 (25), Pixart (15).

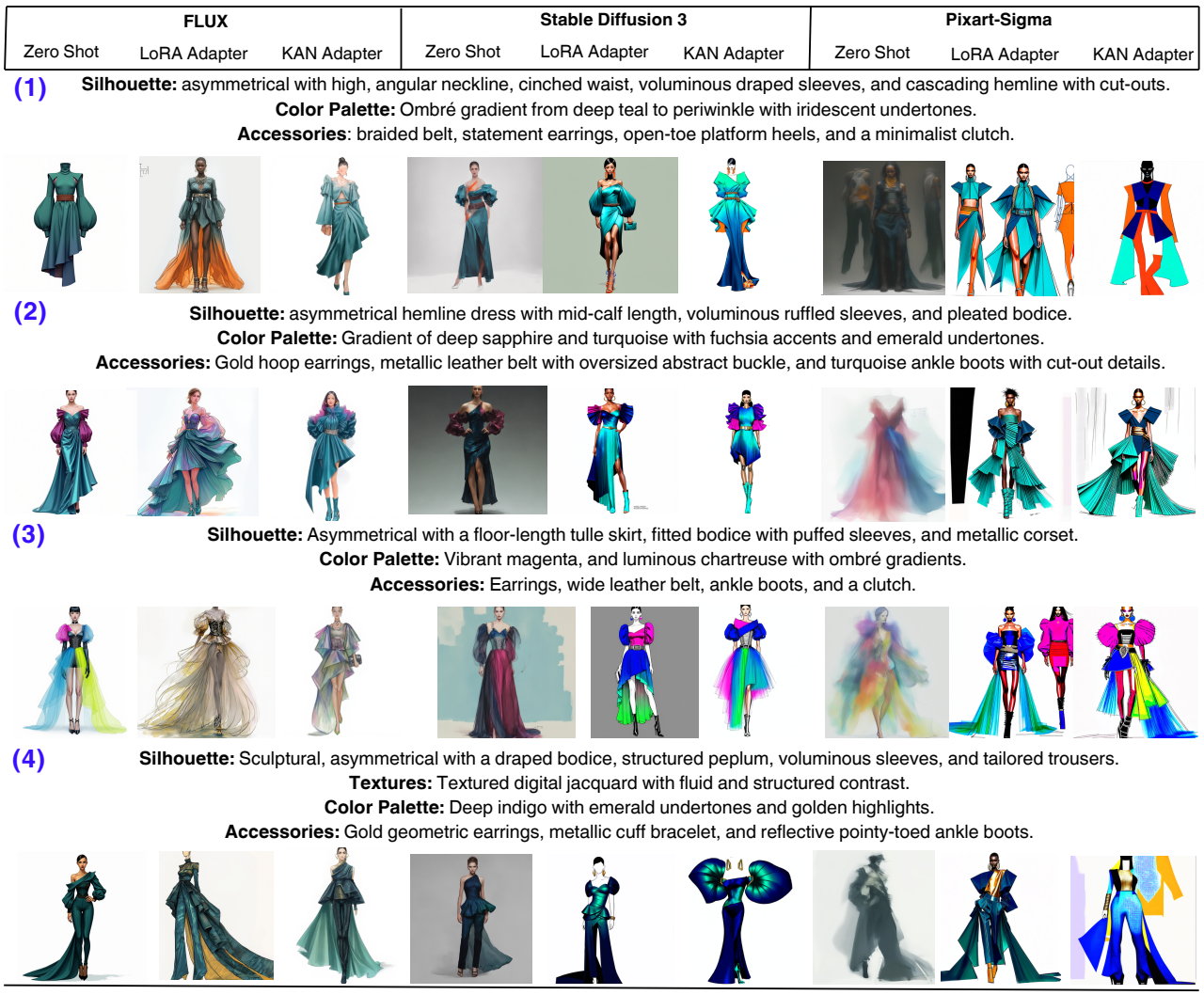

Figure 7. Images generated by various models for zero-shot, LoRA and KAN adapters, given the prompts from the test set. Given the length of original prompts, only condensed versions with key elements are shown here.

perform LoRA across all evaluation parameters. Additionally, Table 2 compares the computational efficiency of each adapter type across various baselines. Each method was evaluated by the number of diffusion steps required to achieve a target performance level. The results indicate that KAN adapters generally have slightly higher inference times compared to LoRA. However, considering additional factors such as convergence speed during fine-tuning (Figure 6) and KAN's effectiveness in adapting to non-linear patterns, this modest increase in inference time is a rea-

sonable trade-off for the improved adaptability and performance that KAN offers.

5.2. Qualitative Results

To assess the effectiveness of our dataset and the proposed KAN adapter, we conducted qualitative comparisons across FLUX, Pixart-Sigma, and SD3 in Zero-Shot, LoRA, and KAN Adapter settings (refer Figure 7). The evaluation reveals both the need for fine-tuning with a specialized dataset and the performance advantages of KAN over LoRA.

In Zero-Shot settings, the models consistently failed to capture specific fashion-related terminologies and intricate details. For instance, when generating an outfit with an asymmetrical silhouette and angular neckline (Prompt 1), FLUX in Zero-Shot mode overlooked the angular neckline and accessories like the braided belt and clutch. This highlights the model's inability to interpret nuanced fashion elements without tailored training. However, after fine-tuning with our dataset, FLUX LoRA captured basic elements like the cascading hemline, while FLUX KAN successfully captured all the details, including the braided belt and clutch. This demonstrates the proposed dataset's importance in teaching models to interpret and represent fashion-specific terms accurately.

As shown in Figure 7, models using the KAN adapter consistently capture more detailed features and produce more aligned sketches, e.g., in Prompt 3, which featured an asymmetrical silhouette with a metallic corset, floor-length skirt, and vibrant color palette, FLUX with LoRA captured the general silhouette but omitted finer details like the metallic corset and specific color variations. FLUX with KAN, in contrast, accurately represented the metallic corset, asymmetrical design, and color specifications, including accessories like earrings and clutch. This highlights KAN's superiority in understanding nuanced detail, particularly in complex fashion elements.

We extend the qualitative evaluation by presenting t-SNE plots for each baseline and its variants. Figure 8 illustrates optimal feature clustering in model variants fine-tuned with KAN adapters, with different colors representing distinct clusters. This optimal clustering indicates well-learned latent spaces, as tightly grouped clusters suggest that the model has effectively captured nuanced features relevant to each category. Notably, FLUX exhibits the most distinct and cohesive clustering, which aligns with our other observations, further validating the superior generalization and feature representation achieved by this model.

6. Ablation Study

To investigate the impact of different basis functions in the KAN adapter, we consider primarily three types of multivariate function-approximating polynomials: B-Spline, standard Radial Basis Function (RBF), and Gaussian. As

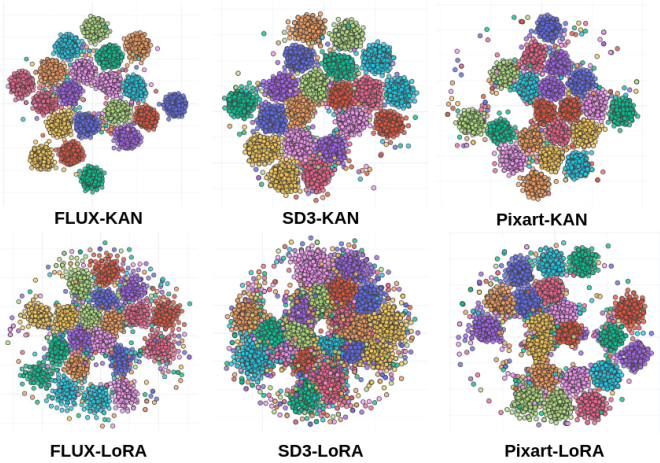

Figure 8. t-SNE plots using KAN and LoRA adapters.

KAN Layers	FID↓	CLIPSIM↑
B-Spline	6.18	0.3002
Radial Basis Function	**6.09**	0.3276
Gaussian	6.33	**0.3301**

Table 3. Ablation study results based on KAN Layers

shown in Table 3, the B-Spline basis achieved an FID of 6.18 and a CLIPSIM score of 0.3002, marking it as a middle-ground performer. B-splines, being piecewise polynomials, excel at providing localized control over the function, which is helpful for smooth approximations. However, unlike RBFs, they are sensitive to grid-based recalculations and re-scaling, which can limit their stability and efficiency in higher-dimensional applications.

In contrast, the standard RBF delivered the lowest FID (6.09) and a strong CLIPSIM of 0.3276, achieving the best balance between sample realism and representational consistency. Unlike Gaussian RBFs, which rely on a fixed decay rate, standard RBFs are not bound to a specific decay, allowing them to adapt to complex patterns in data flexibly. This flexibility may explain its superior FID, as it maintains realistic details more effectively than Gaussian and B-Spline functions.

While slightly higher in FID (6.33), the Gaussian basis recorded the highest CLIPSIM at 0.3301, suggesting that it prioritizes structural consistency over fine-grained details. Gaussian functions have smooth and symmetrical decay properties, promoting stability in feature representation but at the cost of adaptability. This fixed decay makes it less effective at capturing localized detail than the general RBF, as seen in the higher FID score. An ablation study examining the impact of KAN downsample rates and LoRA rank is provided in the supplementary section.

7. Conclusion

We introduced FLORA, the first dataset crafted specifically for generating fashion outfits from text descriptions, along

with KAN Adapters, architecture leveraging Kolmogorov-Arnold Networks for enhanced model adaptability. Together, these contributions address the lack of high-quality data in AI-driven fashion design and effective modeling techniques. Looking forward, we plan to expand FLORA to train models capable of modifying specific parts of an outfit sketch based on design requirements, allowing designers to easily adjust individual elements while maintaining the overall style. This advancement could enable adaptable AI-powered design tools, fostering a more interactive and flexible approach to fashion creation.

References

[1] https://www.thomasnet.com/insights/zara-h-m-fast-fashion-ai-supply-chain/. [Online; accessed 07-Oct-2024]. 2

[2] Deep AI, Inc. https://deepai.org/, 2017. [Online; accessed 05-June-2024]. 2

[3] Inc. Runway AI. https://runwayml.com/, 2022. [Online; accessed 05-June-2024]. 2

[4] Stability AI. Stable diffusion public release. https://stability.ai/news/stable-diffusion-public-release, 2022. [Online; accessed 05-July-2024]. 2

[5] Imran Amed, Achim Berg, Vivek Balchandani, Saskia Hedrich, Robb Rölkens, and Kanaiya Young. The state of fashion 2022, 2022. Accessed: 2024-11-09. 1

[6] Alexander Dylan Bodner, Antonio Santiago Tepsich, Jack Natan Spolski, and Santiago Pourteau. Convolutional kolmogorov-arnold networks. *arXiv preprint arXiv:2406.13155*, 2024. 3

[7] Junsong Chen, Chongjian Ge, Enze Xie, Yue Wu, Lewei Yao, Xiaozhe Ren, Zhongdao Wang, Ping Luo, Huchuan Lu, and Zhenguo Li. Pixart-sigma: Weak-to-strong training of diffusion transformer for 4k text-to-image generation, 2024. 6

[8] Patrick Esser, Sumith Kulal, Andreas Blattmann, Rahim Entezari, Jonas Müller, Harry Saini, Yam Levi, Dominik Lorenz, Axel Sauer, Frederic Boesel, Dustin Podell, Tim Dockhorn, Zion English, Kyle Lacey, Alex Goodwin, Yannik Marek, and Robin Rombach. Scaling rectified flow transformers for high-resolution image synthesis, 2024. 2, 6

[9] Tham Yik Foong, Shashank Kotyan, Po Yuan Mao, and Danilo Vasconcellos Vargas. The challenges of image generation models in generating multi-component images, 2023. 1

[10] Xintong Han, Zuxuan Wu, Zhe Wu, Ruichi Yu, and Larry S Davis. Viton: An image-based virtual try-on network. In *CVPR*, 2018. 3

[11] Jianhua Hu, Weimei Wu, Mengjun Ding, Xi Huang, Zhi Jian Deng, and Xuankai Li. A virtual try-on system based on deep learning. In *2023 3rd International Symposium on Computer Technology and Information Science (ISCTIS)*, pages 103–107, 2023. 2

[12] Fashion AI In 2024: What is Trending This Year. https://www.intelistyle.com/fashion-ai-in-2023-what-should-we-expect-to-see-this-year/. [Online; accessed 07-Oct-2024]. 2

[13] Phillip Isola, Jun-Yan Zhu, Tinghui Zhou, and Alexei A Efros. Image-to-image translation with conditional adversarial networks. *CVPR*, 2017. 2

[14] Dora Ivezić and Marina Bagic Babac. Trends and challenges of text-to-image generation: Sustainability perspective. *Croatian Regional Development Journal*, 4:56–77, 2023. 1, 2

[15] Harry H. Jiang, Lauren Brown, Jessica Cheng, Mehtab Khan, Abhishek Gupta, Deja Workman, Alex Hanna, Johnathan Flowers, and Timnit Gebru. Ai art and its impact on artists. In *Proceedings of the 2023 AAAI/ACM Conference on AI, Ethics, and Society*, page 363–374, New York, NY, USA, 2023. Association for Computing Machinery. 2

[16] James Kirkpatrick, Razvan Pascanu, Neil Rabinowitz, Joel Veness, Guillaume Desjardins, Andrei A Rusu, Kieran Milan, John Quan, Tiago Ramalho, Agnieszka Grabska-Barwinska, et al. Overcoming catastrophic forgetting in neural networks. *Proceedings of the national academy of sciences*, 114(13):3521–3526, 2017. 6

[17] Black Forest Labs. black-forest-labs/FLUX.1-dev · Hugging Face. https://huggingface.co/black-forest-labs/FLUX.1-dev, 2024. [Online; accessed 05-October-2024]. 6

[18] Chenxin Li, Xinyu Liu, Wuyang Li, Cheng Wang, Hengyu Liu, and Yixuan Yuan. U-kan makes strong backbone for medical image segmentation and generation. *arXiv preprint arXiv:2406.02918*, 2024. 3

[19] Haotian Liu, Chunyuan Li, Qingyang Wu, and Yong Jae Lee. Visual instruction tuning. In *NeurIPS*, 2023. 3

[20] Yaofang Liu, Xiaodong Cun, Xuebo Liu, Xintao Wang, Yong Zhang, Haoxin Chen, Yang Liu, Tieyong Zeng, Raymond Chan, and Ying Shan. Evalcrafter: Benchmarking and evaluating large video generation models. In *Proceedings of the IEEE/CVF Conference on Computer Vision and Pattern Recognition*, pages 22139–22149, 2024. 6

[21] Ziwei Liu, Ping Luo, Shi Qiu, Xiaogang Wang, and Xiaoou Tang. DeepFashion: Powering Robust Clothes Recognition and Retrieval with Rich Annotations. In *Proceedings of IEEE Conference on Computer Vision and Pattern Recognition (CVPR)*, 2016. 3

[22] Ziming Liu, Yixuan Wang, Sachin Vaidya, Fabian Ruehle, James Halverson, Marin Soljačić, Thomas Y. Hou, and Max Tegmark. Kan: Kolmogorov-arnold networks, 2024. 2, 3, 4

[23] Mehdi Mirza and Simon Osindero. Conditional generative adversarial nets, 2014. 2

[24] Fausto Morales. Keras-OCR Documentation. https://keras-ocr.readthedocs.io/en/latest/, 2019. [Online; accessed 05-July-2024]. 4

[25] OpenAI. Hello GPT-4o. https://openai.com/index/hello-gpt-4o/, 2024. [Online; accessed 20-September-2024]. 4, 6

[26] Khushboo Patel. Advancements and challenges in text-to-image synthesis: A comprehensive review. *International Journal of Intelligent Systems and Applications in Engineering*, 12(3):4228–4237, 2024. 1

[27] Dustin Podell, Zion English, Kyle Lacey, Andreas Blattmann, Tim Dockhorn, Jonas Müller, Joe Penna, and Robin Rombach. Sdxl: Improving latent diffusion models for high-resolution image synthesis, 2023. 6

[28] Qi Qiu, Tao Zhu, Helin Gong, Liming Chen, and Huansheng Ning. Relu-kan: New kolmogorov-arnold networks that only need matrix addition, dot multiplication, and relu. *arXiv preprint arXiv:2406.02075*, 2024. 3, 5

[29] Aditya Ramesh, Mikhail Pavlov, Gabriel Goh, Scott Gray, Chelsea Voss, Alec Radford, Mark Chen, and Ilya Sutskever. Zero-shot text-to-image generation, 2021. 2

[30] Bharati Rathore. Artificial intelligence in sustainable fashion marketing: Transforming the supply chain landscape. *Eduzone : international peer reviewed/refereed academic multidisciplinary journal*, 8:2319–5045, 2019. 1

[31] Robin Rombach, Andreas Blattmann, Dominik Lorenz, Patrick Esser, and Björn Ommer. High-resolution image synthesis with latent diffusion models. In *Proceedings of the IEEE/CVF Conference on Computer Vision and Pattern Recognition (CVPR)*, pages 10684–10695, 2022. 2, 6

[32] Chitwan Saharia, William Chan, Saurabh Saxena, Lala Li, Jay Whang, Emily Denton, Seyed Kamyar Seyed Ghasemipour, Burcu Karagol Ayan, S. Sara Mahdavi, Rapha Gontijo Lopes, Tim Salimans, Jonathan Ho, David J Fleet, and Mohammad Norouzi. Photorealistic text-to-image diffusion models with deep language understanding, 2022. 2

[33] Mariapaola Saponaro, Diane Le Gal, Manjiao Gao, Matthieu Guisiano, and Ivan Coste Maniere. Challenges and opportunities of artificial intelligence in the fashion world. In *2018 International Conference on Intelligent and Innovative Computing Applications (ICONIC)*, pages 1–5, 2018. 1

[34] schroneko. Transparent Background - a Hugging Face Space by schroneko. https://huggingface.co/spaces/schroneko/transparent-background, 2024. [Online; accessed 05-July-2024]. 4

[35] Onkar Susladkar. Controlnet Stable diffusion scene text Eraser. https://huggingface.co/onkarsus13/controlnet_stablediffusion_scenetextEraser, 2024. [Online; accessed 25-September-2024]. 4

[36] Kota Yamaguchi, M. Hadi Kiapour, Luis E. Ortiz, and Tamara L. Berg. Parsing clothing in fashion photographs. In *2012 IEEE Conference on Computer Vision and Pattern Recognition*, pages 3570–3577, 2012. 4

[37] Xingyi Yang and Xinchao Wang. Kolmogorov-arnold transformer. *arXiv preprint arXiv:2409.10594*, 2024. 3

[38] Cui Yirui, Q. Liu, C. Gao, and Zhuo Su. Fashiongan: Display your fashion design using conditional generative adversarial nets. *Computer Graphics Forum*, 37:109–119, 2018. 2

[39] Liang Zheng, Liyue Shen, Lu Tian, Shengjin Wang, Jingdong Wang, and Qi Tian. Scalable person re-identification: A benchmark. In *Proceedings of the IEEE International Conference on Computer Vision (ICCV)*, 2015. 3

Dressing the Imagination: A Dataset for AI-Powered Translation of Text into Fashion Outfits and A Novel KAN Adapter for Enhanced Feature Adaptation

Supplementary Material

8. Fine-Tuning Template for Outfit Sketch Generation

We developed a structured prompt template for fine-tuning the models. This template was designed to capture essential aspects of each outfit sketch, including model presence, gender, pose, outfit description, color details and accessories. By standardizing these attributes, we aimed to provide the model with clear, detailed inputs that could guide the generation process toward accurate, high-quality fashion sketches. The template used is as follows:

```
MODEL PRESENCE: {MODEL_PRESENCE}
MODEL GENDER: {MODEL_GENDER}
MODEL POSE: {MODEL_POSE}
OUTFIT DESCRIPTION: {OUTFIT_DESCRIPTION}
COLOR DETAILS: {COLOR_DETAILS}
ACCESSORIES: {ACCESSORIES}
```

9. Detailed Description of Human Evaluation Metrics

For a thorough evaluation of the generated fashion sketches, we defined seven key metrics, each capturing specific aspects of image quality and alignment with the prompt. The main paper presents human evaluation results (refer to Table 2). These metrics allowed us to perform a comprehensive assessment, ensuring that both technical quality and alignment with the prompt are rigorously evaluated:

- **Prompt Relevance:** Evaluates how accurately the generated image reflects the essential elements described in the prompt. This metric focuses on effectively visualizing the main idea or theme specified.
- **Visual Quality:** Assesses the technical quality of the image, including factors such as resolution, sharpness, clarity, and the overall visual appeal.
- **Creativity:** Measures the degree of innovation and imaginative interpretation in the image. This metric considers how the generated image demonstrates creativity while staying coherent with the prompt's details.
- **Pose and Model Accuracy:** Examines the alignment between the model's physical representation in the image, such as pose, gender, and stance and the specifications given in the prompt.
- **Color Palette Alignment:** Compares the colors used in the generated image to the colors described in the prompt, assessing accuracy in terms of color scheme and consistency.
- **Contextual Fit:** Evaluates how well the image fits the broader context implied by the prompt, including aspects like mood, setting, and style.
- **Overall Appeal:** Provides a holistic assessment of the image's attractiveness and visual impact, taking into account its general appeal to viewers.

10. FLORA Dataset

10.1. Dataset Creation and Filtering Process

To create the FLORA dataset, we employed a multi-stage filtering and description process to ensure that the images met quality standards and contained only the desired fashion elements. Below, we describe the stages of filtering, noise removal, and detailed description generation, along with the prompts used at each step.

Initial Filtering of Noise Using VLM Model: In the initial filtering stage, we used a VLM model (LLaVa 32b) to identify and remove images that did not meet the criteria for inclusion in the dataset. Specifically, we aimed to retain images that contained a single outfit sketch without extraneous objects. To achieve this, we provided each image with the following prompts and used the model's responses to segregate the data:

> **Prompt 1:** *"Is there a single outfit present in the image? Yes or No?"*
> **Prompt 2:** *"Is the outfit present in the image a sketch? Yes or No?"*
> **Prompt 3:** *"Does the image only contain the sketch without any other objects? Yes or No?"*
> **Prompt 4:** *"Are there multiple outfits present in the image? Yes or No?"*

If the VLLM model answered "Yes" to the questions indicating the desired characteristics (single outfit, sketch format, no additional objects, and no multiple outfits), the image proceeded to the next filtering stage. If the answer to any of these prompts was "No," the image was discarded.

Watermark Detection and Removal: For images that passed the initial filtering, we implemented an additional check to detect and remove watermarks, which could interfere with model training. At this stage as well we utilized the LLaVa 32b with the following prompt:

Prompt: *"Does this image contain a watermark? A watermark may appear as text or a logo superimposed over the image. Yes or No"*

If the model identified a watermark ("Yes" response), we performed image inpainting to remove the watermark, as described in the main paper. This ensured that the images in the dataset were clean and free from visual obstructions.

Input Prompt Generation: Once the images were filtered, we used GPT-4o to generate precise and comprehensive descriptions of each outfit. This process involved a multi-turn approach, where each turn focused on describing a specific aspect of the image. The following prompts were used to extract detailed information:

Model Pose Description: "Describe the model's posture. Is the model standing, sitting, walking, or in any other specific pose? Detail the position of the model's hands, legs, and overall body stance. Provide enough detail so that someone reading the description could recreate the sketch with high accuracy. Note: Generate a response in a single paragraph with not more than 50 words. Please note that - while describing pose, do not describe the dress the model is wearing or do not use any adjectives. Just in simple words, explain the pose of the model, nothing else."

Outfit Description: "Describe the outfit present in the image. Describe in a way that a fashion designer can read that description and create an exact similar sketch of the outfit. Use fashion design terminology. Describe garment type, fabric, cut, and any special features. Note: Generate a response in a single paragraph with not more than 200 words."

Color Details: "Provide a detailed description of the color scheme used in the outfit. Mention the primary color, any secondary colors, and any unique color patterns. Note: Generate the response in a single paragraph with not more than 50 words. Just return color-related information."

Accessories Description: "Mention and describe any accessories or additional design elements included in the sketch, such as belts, shoes, jewelry, or headpieces. Provide enough detail so that someone reading the description could recreate the sketch with high accuracy. Note: Generate the response in a single paragraph with not more than 50 words. If no accessories are present, respond with 'no additional accessories present'."

This multi-turn approach allowed us to capture specific details of each image, resulting in a dataset that accurately reflects the visual and stylistic characteristics required for high-quality, fashion-focused AI training.

Additionally, we extracted information on the presence and gender of the model in each image using LLaVa 32b. By using this layered approach - initial filtering, watermark detection, and detailed multi-turn descriptions; we created a high-quality, fashion-specific dataset (FLORA) that supports the generation of accurate and stylistically rich images from textual descriptions. This structured dataset creation process ensures that the FLORA dataset is diverse, precise, and highly applicable to fashion-focused generative AI tasks.

10.2. Dataset Insights and Diversity Analysis

Figure 10 summarizes the gender representation and model presence in the FLORA dataset. Of the images, 97.5% (4,220) feature female outfits, 0.27% (12) male outfits, and 2.26% (98) show "no gender," where the outfit is displayed without a model. Similarly, 97% of the images include a model wearing the outfit, while 3% display only the outfit. These distributions in the FLORA dataset are influenced by the types of fashion images commonly found on the internet. For example, the high percentage of female outfits and model presence results from the dataset being sourced from online data, where such trends are prevalent.

Our dataset consists of a wide array of fashion outfit styles, which we categorize into nine distinct classes, each with its own set of sub-classes. These terminologies include **Garment Types** comprising 29 sub-classes such as *blazers, gowns, hoodies, kimonos, skirts and jackets*. The **Styles & Details** class has 17 sub-classes including attributes like *sleeveless, bateau, turtle-neck and halter*. **Materials & Patterns** with 21 sub-classes describes fabric types and patterns like *silk, cotton, denim, satin, floral and striped*. **Construction & Detailing** includes 40 sub-classes covering elements such as *embroidery, beading, embellishments, metallic, cinched, knitting and vintage or retro aesthetics*. The **Technical & Functional** class has five sub-classes which focus on functional features such as *breathability, lightweight materials and detachable components*. **Occasion & Aesthetic** includes 18 sub-classes categorizing outfits by their intended use and style such as *casual, formal, traditional, sophisticated, beachwear and whimsical*. **Construction Techniques** with 10 sub-classes includes garment construction methods like *stitching, buttoning, zippers and lining*. **Detailing Techniques** with 19 sub-classes describes

Figure 9. Representation of a few classes from each of the 9 categories, showcasing a diverse range of design elements present in our FLORA dataset

specific design techniques like *applique, beading, draping, gathering, pleating and layering*. Finally, the **Finishing Techniques** class has five sub-classes that address finishing touches like *fading, top-stitching and softening*. The distribution of these terminologies across the dataset is presented in log-scaled figures (11 - 19), which provide an insightful representation of their relative prevalence.

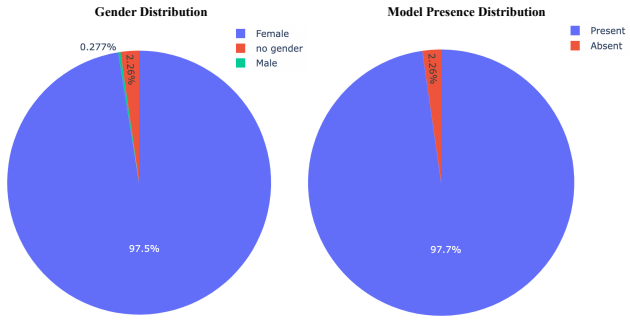

Figure 10. Distribution of gender representation and model presence in the FLORA dataset.

11. Ablation Study

In this section, we investigate the use of KAN adapters as an alternative to LoRA. Extending our previous ablation studies, we explore the effect of varying ranks for LoRA and downsample rates for KAN adapters. For this task, we choose FLUX as our baseline model for conducting the experiments. Table 4 provides the CLIP-SIM and FID scores for different ranks and downsampling rates for the respective adapters.

LoRA Rank		
LoRA Rank	**FID↓**	**CLIP SIM↑**
$r = 8$	8.76	0.2711
$r = 16$	8.13	0.2832
$r = 32$	7.92	0.2901
$r = 64$ (Default)	**7.88**	**0.2987**
KAN Downsample Rate		
Downsample Rate	**FID↓**	**CLIPSIM↑**
$m/16$	7.18	0.3298
$m/8$	6.66	0.3319
$m/4$	6.49	0.3401
$m/2$ (Default)	**6.05**	**0.3412**

Table 4. Ablation study comparing the effect of varying ranks for LoRA and downsample rates for KAN-adapters using FLUX as the baseline.

Effect of Rank on LoRA Performance: For LoRA, we observe a progressive improvement in both CLIP-SIM and FID scores as the rank increases. The model achieves the highest performance at rank $r = 64$, yielding a CLIP-SIM of 0.2987 and an FID of 7.88. This indicates that increasing the rank allows LoRA to better capture domain-specific details relevant to our sketch generation task.

Effect of Downsample Rate on KAN Performance: The downsample rate in the KAN Adapter refers to the di-

mensionality reduction applied to the input features. Specifically, as explained in section 4.3, the KAN adapter incorporates two main functions: the ϕ_{down} and ϕ_{up}. ϕ_{down} projects the input features from the original dimensionality (m) to a reduced dimensionality(n), and the ϕ_{up} projects the reduced-dimensional features back to their original size m. Here, n is the downsampling rate, which is hyperparameter and is decided by the ratio by which we want to reduce dimension (e.g. $m/16$, $m/8$, $m/4$, $m/2$). Where a smaller downsample rate ($m/16$) implies greater reduction and larger rates ($m/2$) retain more of the original feature space.

The ablation study, as shown in the table 4, evaluates the performance of KAN Adapters at different downsample rates. As the downsampling rate increases from $m/16$ to $m/2$ results in improvements in both CLIP-SIM and FID scores. This progression highlights the trade-off between dimensionality reduction and feature retention, with higher downsample rates striking an optimal balance between computational efficiency and model performance. These findings emphasize the importance of selecting an appropriate downsample rate to maximize the KAN Adapter's effectiveness.

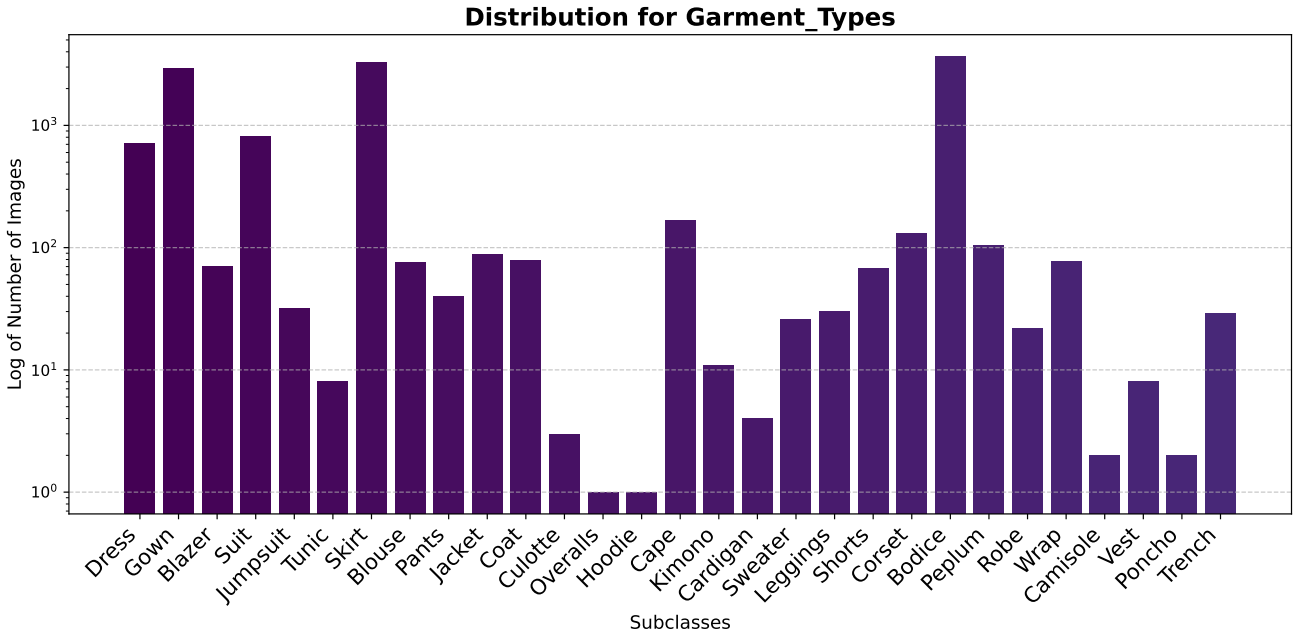

Figure 11. Image Distribution for 29 Garment Types available in FLORA

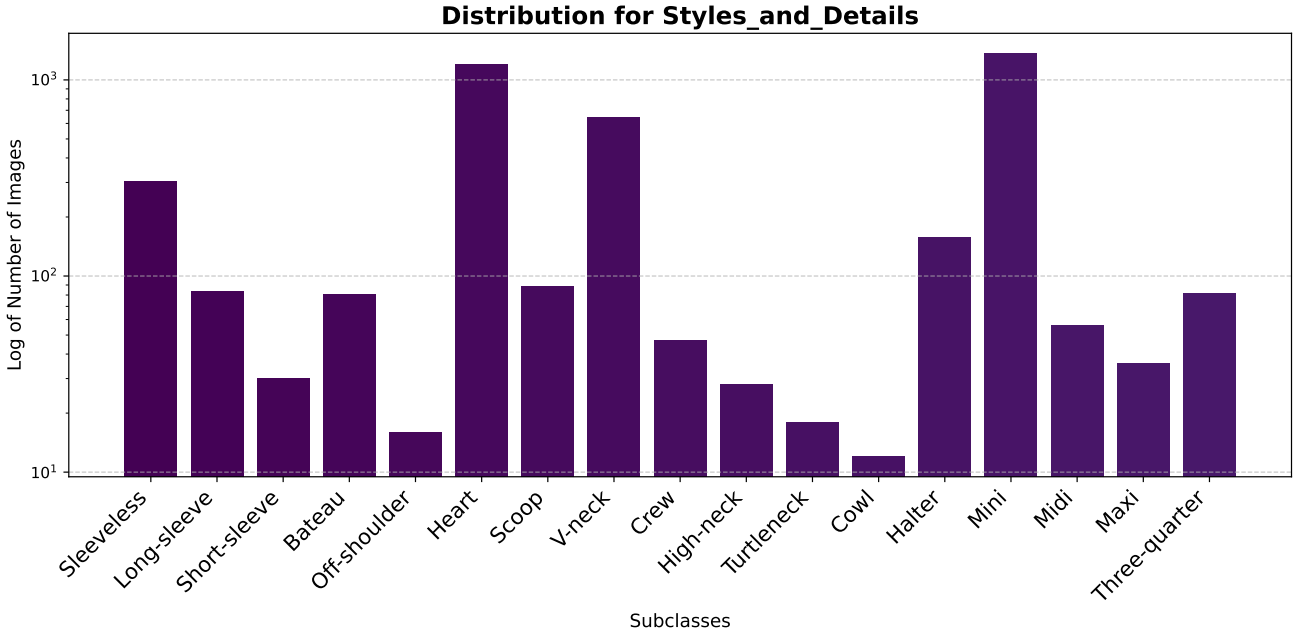

Figure 12. Image Distribution for 17 Styles

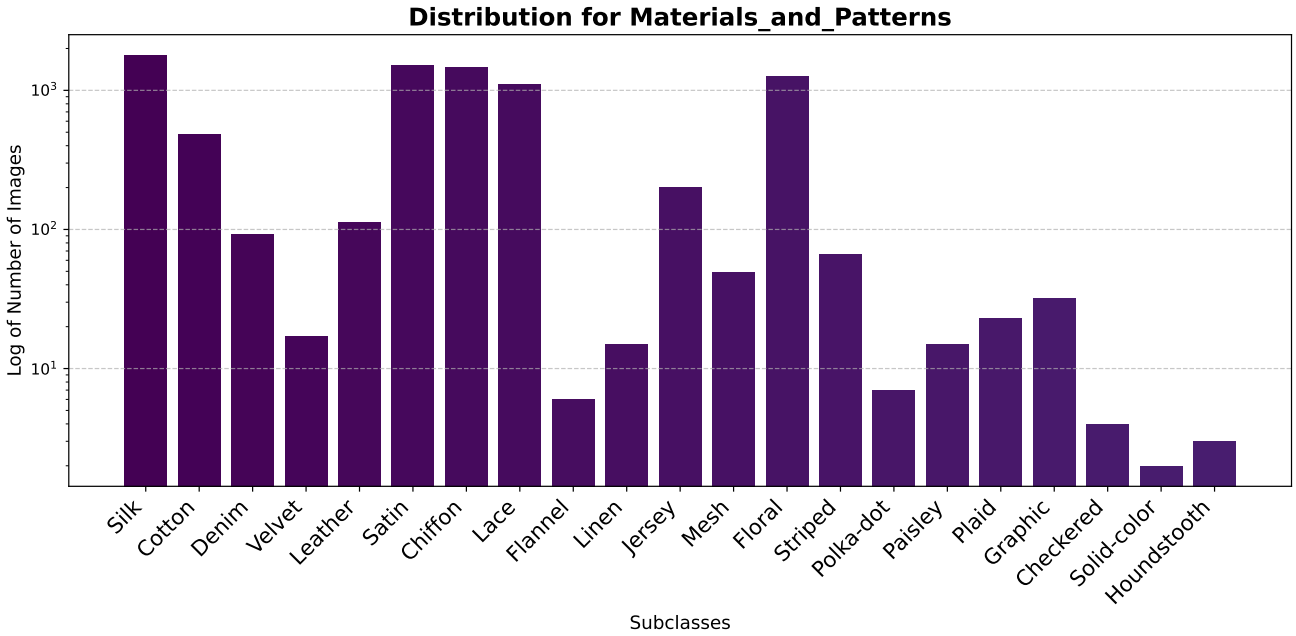

Figure 13. Image Distribution for 21 Materials & Patterns

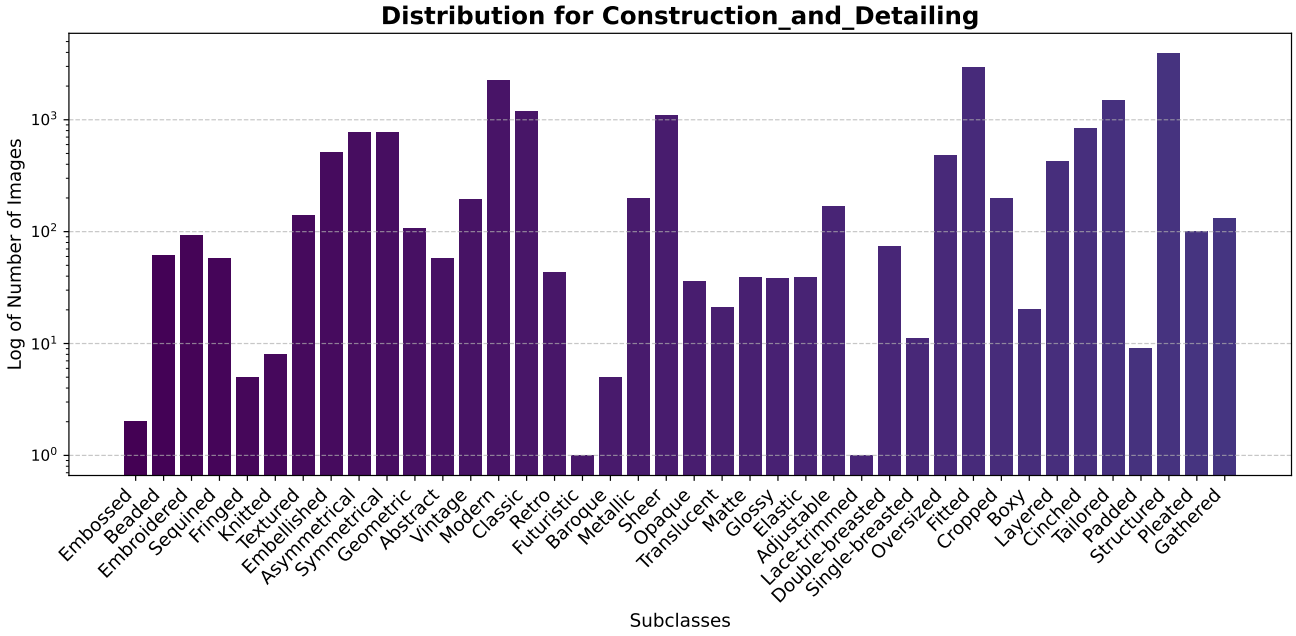

Figure 14. Image Distribution for 40 Construction styles

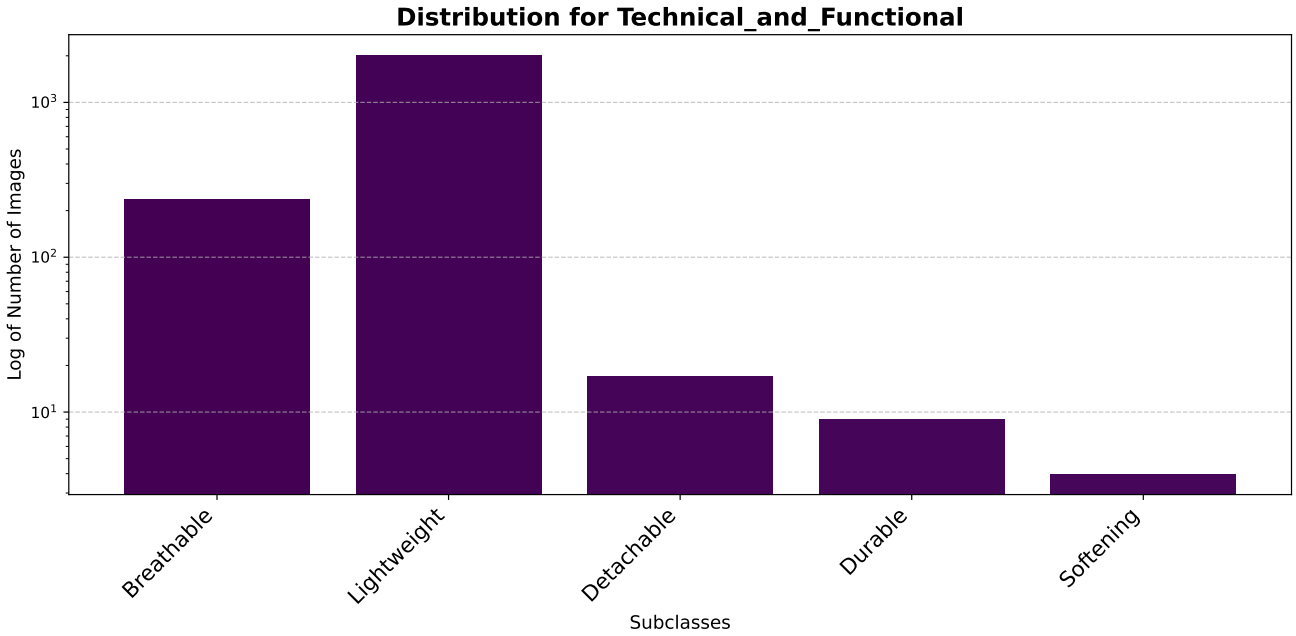

Figure 15. Image Distribution for Technical styles

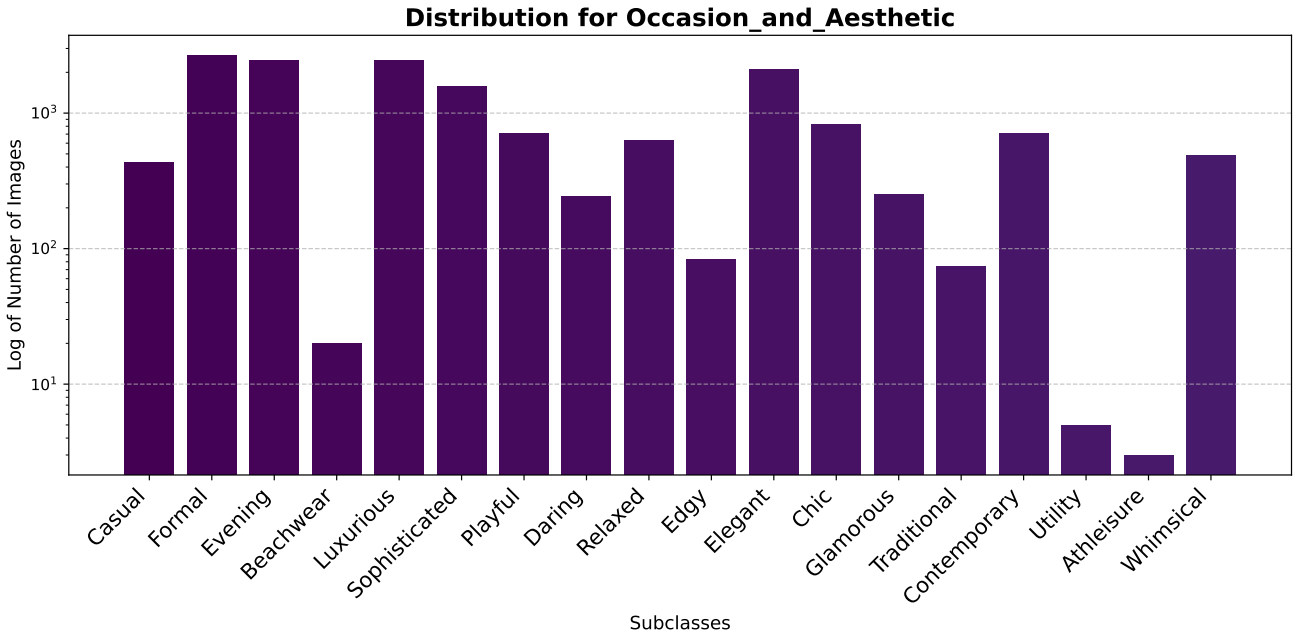

Figure 16. Image Distribution for 18 Occasion & Aesthetic styles

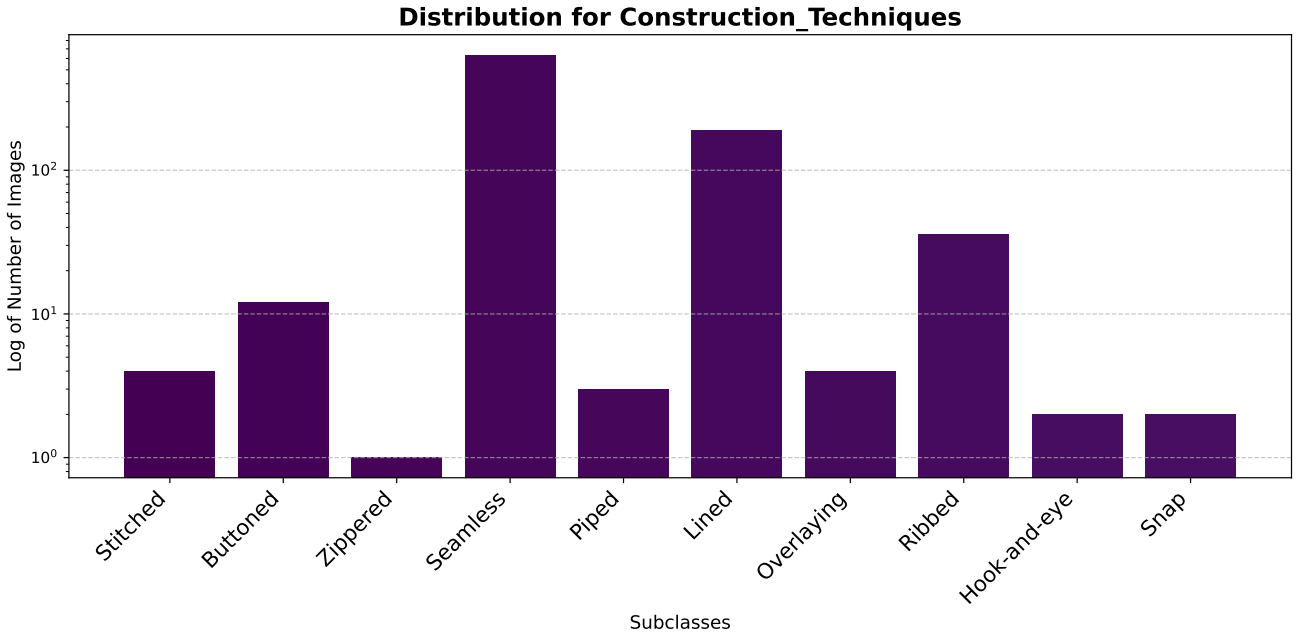

Figure 17. Image Distribution for 10 Construction techniques

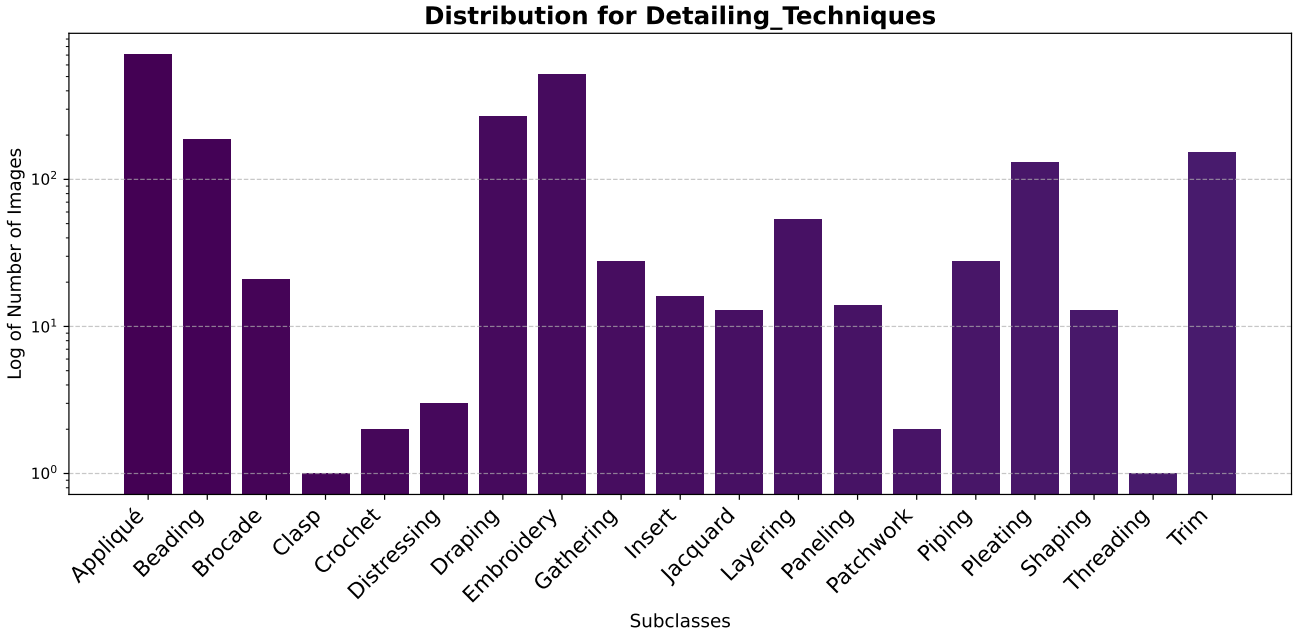

Figure 18. Image Distribution for 19 Detailing techniques

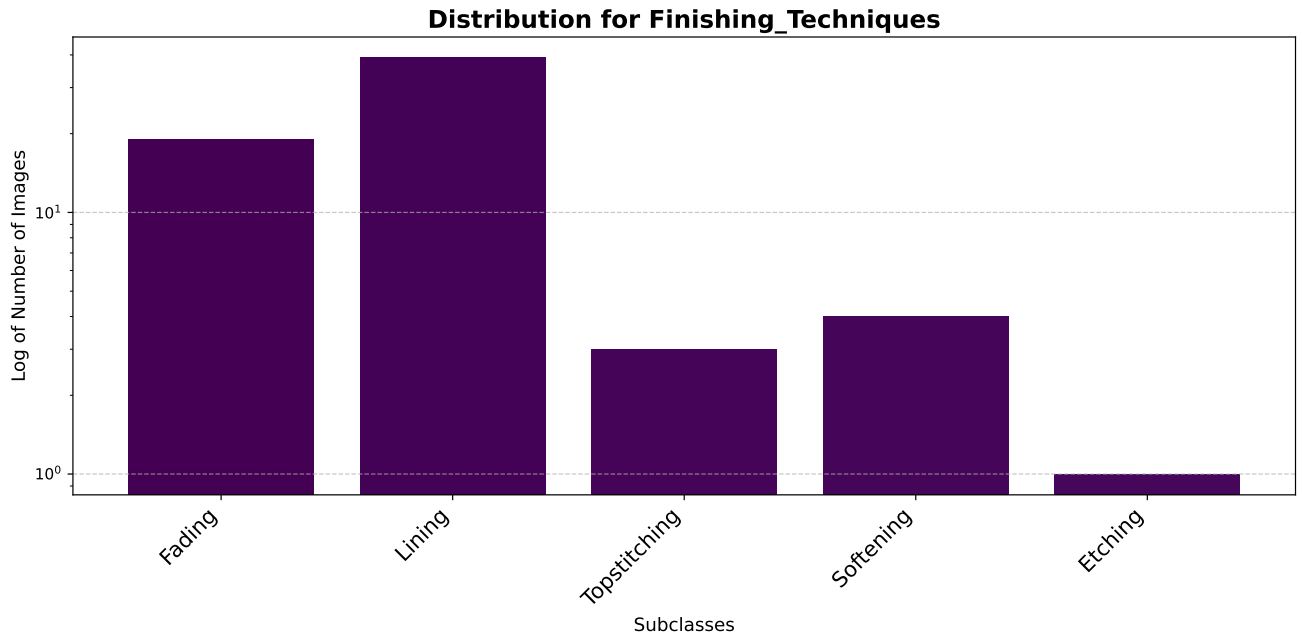

Figure 19. Image Distribution for Finishing techniques

International Journal of System Assurance Engineering and Management
https://doi.org/10.1007/s13198-024-02631-1

ORIGINAL ARTICLE

EMH or AMH? Evidence from the emerging Indian equity market

Reema Monga[1] · Deepti Aggrawal[1] · Jagvinder Singh[2]

Received: 23 April 2024 / Revised: 22 October 2024 / Accepted: 22 November 2024
© The Author(s) under exclusive licence to The Society for Reliability Engineering, Quality and Operations Management (SREQOM), India and The Division of Operation and Maintenance, Lulea University of Technology, Sweden 2024

Abstract
The study investigates the weak-form market efficiency within the Indian equity market considering the two approaches i.e., absolute and evolving market efficiency. This work provides an in-depth examination of weak-form market efficiency using a combination of linear and non-linear statistical tests, including Ljung and Box, runs test, Bartel test, Variance ratio test, and BDS test,.In contrast to earlier research, which frequently used subsample analysis, the study considered rolling window analysis with the 500 observations to precisely capture the evolving efficiency. There is ample evidence that the efficiency of the Indian equity market varies across time, exhibiting both efficient and inefficient periods. To put it briefly, the research suggested that the Adaptive Market Hypothesis (AMH) provides a more holistic understanding of emerging market behavior compared to the EMH.

Keywords Adaptive market hypothesis · Efficient market hypothesis · Rolling window approach · BDS test · Non-linear test · Indian equity market

1 Introduction

Stock markets are pivotal in economic development, especially in developing economies. Claessens et al. (1995) observed that stock markets are tremendously efficient in allocating capital, improving overall economic efficiency. Put another way, the stock market makes capital allocation and economic growth possible, which is an essential part of contemporary economies. They provide asset diversification, lowering capital costs and encouraging more investment and growth. A vital factor in the way equities markets operate is the concept of market efficiency. In other words, stock market efficiency is a vital concept in finance theory that influences investor behavior and regulatory measures. When stock prices accurately reflect all available information, it becomes more challenging for investors to generate abnormal returns regularly using various investment strategies. Antoniou et al. (1997) observed that the effectiveness of a stock exchange is crucial since it allows prices to incorporate information completely. Saving and investing are encouraged since it gives investors the confidence to trade in the stock market. It also encourages investors to engage in other regional stock markets besides encouraging market growth. A stock market that lacks efficiency may deter investors from trading there, which will impede the growth of the economy.

In neoclassical finance, the notion of market efficiency is one of the key ideas that have been extensively researched. Fama (1965, 1970) proposed the theory of the EMH (Efficient Market Hypothesis) and the phenomenon of market efficiency. According to the EMH or Random Walk Theory (Kendall 1953), the firm's current stock price appropriately reflects all information that is currently available, and there is no way to increase profits by exploiting this information. In other words, according to Eakins and Mishkin (2012), two pillars form the foundation of an efficient market: (1) Stock prices in efficient markets already take into account all available information; (2) investors are unable to obtain an excess return in efficient markets.

✉ Deepti Aggrawal
deeptiaggrawal@dtu.ac.in

Reema Monga
reemamonga23@gmail.com

Jagvinder Singh
jagvinder.singh@gmail.com

[1] University School of Management and Entrepreneurship, Delhi Technological University, Delhi, India

[2] Department of Operational Research, University of Delhi, Delhi, India

Published online: 28 November 2024

The concept of EMH has been one of the most contentious subjects in the financial literature. The idea of informationally efficient markets was first accepted, but some flaws in the EMH made it challenging to apply in real-world scenarios. EMH has undergone several tests to ascertain its viability in the financial markets, even if a consensus has never been reached. This has caused a rift among academics, with some endorsing behavioral biases that may impact the financial markets and others standing up for the EMH. Lo (2004) put forth a new paradigm, the Adaptive Markets Hypothesis (AMH), which takes an evolutionary view of human behaviour that affects the informational efficiency of markets. Lo (2004), in particular, suggests a new AMH concept that makes it possible for behavioral finance and the EMH to coexist in a logically consistent manner. Interestingly, the concepts behind the AMH were inspired by a wide range of literature, including works on complex systems, behavioral ecology, evolutionary psychology, evolutionary biology, and bounded rationality in economics.

According to AMH, the degree of market informational efficiency is determined by the capacity of market players to adjust to evolving market circumstances. In other words, Lo (2004) used the AMH to present a new viewpoint on the changing nature of the market. In a logically consistent manner, the AMH establishes the presence of market efficiency and inefficiencies; in contrast to EMH, market efficiency in AMH changes with time. Lo (2004) examined the time-varying aspect of efficiency and found that AMH is a more reliable method than EMH because it acknowledges that human error can cause arbitrage opportunities, which disappear once they have been taken advantage of. In other words, arbitrage possibilities occasionally arise and fade as investors take advantage of them, which in turn creates new opportunities that emerge from shifts in the market dynamics. Lastly, the notion of cyclical profitability in investing approaches implies that a specific strategy will work well in one context and poorly in another.

An outcome of AMH is that market efficiency is "not an all-or-nothing condition" and fluctuates over time. Stated differently, the degree of market efficiency is not constant because of the dynamic risk-reward relationship that is dependent on past market prices and participant preferences. Thus, convergence to market efficiency is neither certain nor likely to happen because there are always fresh opportunities for profit to be made. In a nutshell, the theory of AMH has received more attention in the most recent academic research. The results seem very promising; with several studies finding strong evidence of the adaptive behavior of stock returns (Urquhart andMcGroarty 2014, 2016).

Although the Efficient Market Hypothesis has been widely examined in the Indian context, there remains a lack of research specifically addressing weak-form market efficiency, particularly in light of India's distinctive market dynamics and growth potential. Traditional research has primarily focused on absolute efficiency; however, this study explores both absolute and adaptive (evolving) market efficiency, offering insights into how efficiency levels may shift over time due to India's historical structural and economic changes. Previous studies often rely on linear models, which may overlook more intricate patterns in market behavior. In contrast, this research applies both linear and nonlinear statistical tests, providing a comprehensive analysis of weak-form efficiency. Additionally, conventional subsample analysis can introduce bias through selective segmentation, potentially affecting the results. To address this, the study employs rolling window analysis to track time-varying market predictability, reducing bias and offering a more dynamic perspective on the evolution of market efficiency. Therefore, we sought to address and examine these research gaps in the present study.

The motive of the study is to examine the weak-form market efficiency within the Indian market. Emerging markets, such as, India frequently display characteristics such as increased volatility, reduced liquidity, and less stringent regulatory oversight in comparison to developed markets. It is important to investigate whether the Indian market is efficient and whether there is any inefficiency that investors could be able to take advantage of because these characteristics have the ability to produce deviations from the assumptions made by the EMH. Also, examining the Indian equity market through the AMH lens allows for an analysis of how market efficiency may vary over time in response to different influences. Gaining insights into the adaptive nature or efficiency of the Indian equity market can assist investors in crafting more effective investment strategies.

The study makes several contributions to the existing literature. First, our study investigates the weak-form market efficiency in the Indian market. Given its potential for growth, history of structural and economic downturns, and institutional diversity, the Indian equity market presents an intriguing opportunity to investigate the two approaches of efficiency, i.e., absolute and evolving market efficiency. Interestingly, this work offers a thorough analysis of the weak-form market efficiency through the application of both linear and nonlinear statistical tests. Moreover, subsample analysis, which may distort the results, was substituted with rolling window analysis, which gradually describes how predictability changes over time. In other words, the main drawback of subsample analysis is the bias in subsample selection, which might affect the findings.The objective of this paper is to evaluate weak-form market efficiency (both absolute and evolving) within the Indian stock exchanges. To achieve the objective, the study followed the methodology of testing EMH with a battery of tests, including the

autocorrelation Test (Ljung and Box), runs test, Bartel test, Variance ratio test, and BDS test. After that, adaptive market hypothesis was tested i.e., the study investigated the evolving weak-form market efficiency using the rolling window approach. Subsequently, a range of linear and non-linear tests, including the variance ratio, autocorrelation, runs, Bartel, and BDS tests, were applied to the rolling returns to analyze the evolving market efficiency.

The structure of this research is as follows: Sect. Review of literature and theoretical framework reviews the relevant literature. Section Data and methodology covers the data and methodology. Section Analysis, findings and discussion presents the empirical results. Section Concluding remarks outlines the conclusion of the paper. Section Implications discusses the implications, and finally, Sect. Limitations and future scope addresses the limitations and suggests potential directions for future research.

2 Review of literature and theoretical framework

2.1 Efficient market hypothesis (EMH)

The Efficient Market Hypothesis, a foundational theory of finance, maintains that financial markets operate efficiently, with asset prices promptly incorporating all accessible information.

This theory suggests that it is challenging to outperform the market consistently, as tradable securities reflect new information instantly. Put another way, the randomness of stock returns is the central tenet of the EMH. Second, investors are unable to profit excessively in an efficient market. The main idea behind the EMH is that at any given time, financial market prices consider all available information and reflect the collective beliefs and expectations of all market participants. In other words, asset prices always accurately reflect their intrinsic value based on the information available, and it is difficult to continually outperform the market by using historical price movements or information that is readily available to the public.

2.1.1 Forms of the efficient market hypothesis

Market efficiency is divided into three groups: weak, semi-strong, and strong forms of efficiency, dependent on the type of the information. According to the weak-form efficiency, stock prices already take into account all historical trade data. Stated differently, it implies that all of the historical information about the market, including price and volume data, is entirely and instantly reflected in the prices of current stocks. The second form of the market efficiency is classified as the semi-strong form of EMH. This form asserts that stock prices already take into account all information that is known to the public. Put differently, when new information becomes accessible to the public, stock prices react to it promptly and accurately. In this form of EMH, stock prices reflect all information that is readily available to the public, including historical data, economic indicators, financial statements, and any other pertinent information. As a result, investors will not always get higher returns from trading on information that is readily available to the public. Within the framework of the EMH, the next type is the strong form of market efficiency. It assumes that stock prices fully and instantly reflect all information, whether it is public or private. Put differently, this includes insider information that is exclusively known to a small number of people as well as information that is accessible to the broader public. Hence, no investor or group can profitably trade on any kind of information in a market that follows a strong form of efficiency.

When it comes to market efficiency, there are two schools of thought. The first contends that future returns are unpredictable and markets are efficient (Fama 1970). The second group, however, argues that the empirical evidence of "anomalies" makes the EMH inconsistent. According to the weak-form market efficiency theory, past data is useless for predicting future returns since all the historical information is expected to be included in the current returns. The literature has several contradicting findings regarding the weak form of EMH in various global marketplaces. Predominantly, some studies validate the presence of weak form efficiency, while others refute it.

Abeysekera (2001) examined the Random Walk Hypothesis (RWH) for the Colombo Stock Exchange (CSE) in Sri Lanka using daily, weekly, and monthly prices. Throughout the sample period of 1991 to 1996, the study used the unit root test, runs test, and autocorrelation test. The results demonstrate a rejection of the Random Walk (RW) and lead to the conclusion that the market is inefficient. Smith and Ryoo (2003) used weekly data and variance ratio tests to study the RWH in five European emerging markets (Turkey, Poland, Greece, Portugal, and Hungary). According to the research, the Istanbul stock market was the only equity market that adheres to the theory of Random Walk. This is explained by the fact that the Istanbul equity market is bigger and comparatively more liquid than the other four equity markets.

Worthington and Higgs (2006) investigated the weak-form efficiency of five developed and ten emerging Asian markets using serial correlation coefficients and run tests. The results showed that the emerging markets (China, India, Indonesia, Korea, Malaysia, Pakistan, Philippines, Sri Lanka, Taiwan, and Thailand) were inefficient and showed no signs of random walk behavior. Hoque et al. (2007)

examined the weak-form of EMH using Lo-MacKinlay and Chow-Denning tests along with two variance ratio tests: Wright's rank and sign and Whang-Kim subsampling tests. Particularly, the study covered eight Asian equity markets throughout the pre-and post-Asian crisis periods and found no significant impact on market efficiency. In parallel, Kim and Shamsuddin (2008) tested the weak-form efficiency using a variety of variance ratio tests (wild bootstrap and signs test). Nonetheless, the analysis found that the Asian financial crisis had no significant impact on efficiency. Mishra (2011) tested the weak form efficiency of selected emerging and developed capital markets (India, China, Brazil, South Korea, Russia, Germany, the U.S., and the U.K.) over the sample period spanning from January 2007 to December 2010. The study concluded that these equity markets are not weak-form efficient. Nisar and Hanif (2012) studied the weak form EMH for South East Asia markets- India, Pakistan, Bangladesh, and Sri Lanka Stock Exchanges. According to the research, these stock markets are inefficient because they do not adhere to the random walk model. Das (2014) used the Variance Ratio test and the Augmented Dickey-Fuller (ADF) unit root test to investigate the RWH in the Indian equities market. The author covered the period of global financial crisis, and looked at market efficiency in three phases: the pre-crisis, crisis, and post-crisis. The findings of the empirical research indicate that stock returns are inefficient throughout the periods of pre-crisis and crisis; however, they are particularly inefficient during the crisis and are likely to be efficient during the post-crisis phase.

Azad et al. (2014) looked into the weak-form market efficiency in emerging South Asian markets, such as the stock exchanges in Bangladesh, India, and Pakistan. The study found the existence of weak-form inefficiency in these South Asian markets. In parallel, Tiwari and Kyophilavong (2014) investigated the market efficiency of the BRICS stock indexes. In particular, the analysis discovered weak-form inefficiency in these markets, with the exception of the Russian stock index.

Ozkan (2021) used an automatic portmanteau test and wild bootstrap automated variance ratio test and investigated the market efficiency for the six developed stock markets: Germany, the United States, the United Kingdom, France, Italy, and Spain. The research found that the COVID-19 pandemic increased market inefficiencies, suggesting a greater probability of predictability and anomalous returns. Baig et al. (2021) concluded that the liquidity and stability of the U.S. equity market are negatively impacted by the lockout connected to COVID-19. In parallel to this, Vasileiou (2021) investigated the efficiency of the U.S. stock market and found that the market exhibited inefficiency during the pandemic.

There are several studies conducted in the Indian context, including those by Poshakwale (1996), Srinivasan (2010); Gupta and Siddiqui (2010), Khan et al. (2011), Harper and Jin (2012), Kumar and Kumar (2015), Kumar andJawa (2017), Patel et al. (2018), Malafeyev et al. (2019), and Elangovan et al., 2021) have challenged the validity of the EMH and found that the Indian equity markets were weak-form inefficient.

Poshakwale (1996) applied the Serial Correlation Coefficient test, Runs test, and Kolmogorov Smirnov (K.S.) on daily prices of the Bombay Stock Exchange Index from January 1987 to October 1994. The study rejected the market efficiency after it was found that the results of the tests (the run and serial correlation coefficient tests) did not follow the random walk model. Using weekly and daily returns, Pant and Bishnoi (2001) looked into the Random Walk Hypothesis in the Indian equity market.According to the results of the variance ratio, autocorrelation, and unit root test, the market was inefficient between 1996 and 2000. Gupta and Siddiqui (2010) utilized the autocorrelation test, runs test, and Kolmogorov–Smirnov test to investigate the weak form of market efficiency over the years 2000–2008. The results show that the Indian stock market defies the random walk theory, indicating that there is no weak form of market efficiency.

Khan et al. (2011) used the BSE and NSE index daily closing values from April 1, 2000, to March 31, 2010. The study employed the nonparametric runs test, which revealed that the Indian equity market is neither weak form efficient nor fits the random walk model. Harper and Jin (2012) studied the weak-form market efficiency of the Indian equity market from July 1997 to December 2011. The study used runs and auto-correlation tests and concluded that the Indian stock market is inefficient. Mishra et al. (2015) used 19 years of monthly data from six NSE indices to study the RWH of the Indian stock market. The results suggested that the Indian market is not conducive to RWH. In parallel to this, Kumar and Kumar (2015) found that investors may be able to obtain abnormal returns by taking advantage of market inefficiencies and that stock prices in India do not accurately reflect all the available information.Using the runs test, Patel et al. (2018) investigated the market efficiency of the Indian stock market from April 2015 to March 2018. Their research indicates that market players can outperform since the market is not efficient. The latest study by Jain et al. (2020) was conducted on the Indian stock market efficiency based on BSE and NSE from April 2010 to March 2019. The results concluded that the Indian equity market does not adhere to the theory of weak-form EMH and, therefore, can be outperformed. Particularly, the findings indicate that investors can generate anomalous returns and that the Indian equity market does not follow a random walk. However, studies

by Sharma and Mahnedru (2009), Nalina and Suraj (2013), Jain and Jain (2013), Gupta and Gedam (2014), Mishra et al. (2015), and Vidya (2018) found that changes in the stock market prices are random, and thus, confirmed that the Indian equity market is weak-form efficient.

Previous studies and research on weak-form of EMH utilized models that differed from conventional models to advance. However, no definitive result has been reached on the efficiency or inefficiency of the market, which resulted in contradictory results (Borges 2010; Gupta and Yang 2011; Al-khazali et al., 2016; Al-khazali&Mirzaei 2017; Kapoor 2017). The weak form of efficiency in the Indian stock market was suggested by Jain and Jain (2013), Nalina&Suraj (2013), and Mishra et al. (2015). Conversely, the Indian market was shown to be weak-form inefficient by Poshakwale (1996), Gupta and Siddiqui (2010), Srinivasan (2010), Khan et al. (2011), Malafeyev et al. (2019) and Bhatia (2022). In particular, investors are becoming more focused on comprehending the efficiency of the stock market in order to capitalize on investment opportunities. Thus, further research is needed to add to the current discourse on efficient market theory.

2.2 Adaptive market hypothesis (AMH)

Most previous research on market efficiency has employed the conventional methodology of evaluating weak-form efficiency, which has two fundamental limitations. First, as per the study by Campbell et al. (1998), this approach considers that a market is efficient over a whole period as an all-or-nothing condition and ignores the notion of evolving efficiency (i.e., efficiency to change over the period). Second, the conventional method makes the assumption that market efficiency will remain constant for a given amount of time. However, this is very unlikely as many factors will result in the degree of market efficiency varying over time (Lim and Brooks 2011). The AMH proposed by Lo (2004) enables market efficiency and inefficiencies to coexist in an intellectually consistent manner. According to the theory of AMH, market efficiency changes over time instead of adhering to the common notion of "all-or-nothing efficiency".

In the most recent academic literature, the AMH has drawn more and more attention, where there is compelling evidence of the adaptive behavior of stock returns (Ito and Sugiyama 2009; Kim et al. 2011; Alvarez-Ramirez et al. 2012; Dyakova and Smith 2013; Hiremath and Kumari 2014; Tuyon and Ahmad 2016; Hiremath and Narayan 2016; Charfeddine and Khediri 2016; NumapauGyamfi 2018; Ndubuisi and Okere 2018; Xiong et al. 2019; Okorie and Lin 2021). Lo (2004) introduced the concept of AMH to bridge the gap between EMH and Behavioural Finance, which explains that efficiency and anomalies can alternate cyclically due to changes in investment environments. The theory of AMH states that financial markets are not always perfectly efficient but are instead influenced by human behavior and learning. It argues that market participants continuously adapt their strategies in response to changing market circumstances, leading to periods of market efficiency and inefficiency.

Lo (2004) creates a novel framework of AMH which is based on the well-known concepts of evolution, competition, adaptation, and natural selection. AMH brings behavioral finance principles back together with the EMH theory, i.e., balances financial interactions with market efficiency. The theory of AMH claims that the leading causes of the ups and downs of investment performance cycles are shifts in market conditions, including industry competition, investor flexibility, and the number of profit opportunities (Lo 2005, 2012). Particularly, market efficiency is likely to exhibit cyclical patterns that emphasize the indication of AMH, especially in view of the rapid changes occurring in financial technologies, macroeconomic institutions, market laws, and regulations, among other areas (Kim et al. 2011).

In contrast to the EMH, the AMH contends that arbitrage possibilities occasionally appear because of market trends, crashes, bubbles, and panics. Market timing is a critical element in maximizing profit opportunities. The AMH suggests that financial markets are not entirely efficient, as assumed by the EMH. However, instead, they can adapt and evolve due to the changing behavior of market participants and the interplay of their trading strategies. Similarly, the profitability of investment strategies may also temporarily increase or decrease due to market conditions (Lo 2004).

Market efficiency may be impacted by a wide range of factors (Lim and Brooks 2011). These include financial crises, market uncertainty, financial liberalization, the implementation of automated trading systems, technology advancements, the easing of price limitations, and modifications to regulatory frameworks. Most past research examining the EMH in stock markets has concentrated on a specific market over a limited period of time. This conventional approach concludes that market efficiency is static, i.e., the stock market is either weak-form efficient or not during the entire time. However, there are strong arguments in favor of the theory that market efficiency is not static but rather varies over time (Lo 2004; Abdmoulah 2010; Kim et al. 2011; Dyakova and Smith 2013; Hiremath and Narayan 2016; Lekhal and Oubani 2020). After analyzing the monthly returns of the S&P Composite Index over a five-year rolling timeframe from 1871 to 2003, Lo (2004) came to the conclusion that market efficiency varied cyclically throughout the time. This theory states that market players adapt to changing market conditions and that return predictability varies in response to changes in business environments and

potential profits (Lo 2004, 2005). In a nutshell, the time-varying character of market efficiency is explained by the theory of AMH.

The concept of AMH is examined in the literature using two methods. The "time-varying model" technique is the first to investigate market efficiency (Ito et al. 2014, 2016). These investigations have led to the conclusion that market efficiency is time-varying, i.e., fluctuating with time. The second method (Lo 2004; Kim et al. 2011; Dyakova and Smith 2013; Lim et al. 2013) investigates market efficiency through statistical testing based on the "moving window" method. The studies related to AMH are both for developed (Lo 2004; Ito and Sugiyama 2009); Kim et al. 2011; Alvarez-Ramirez et al. 2012; Butler andKazakov 2012; Urquhart and Hudson 2013; Lim et al. 2013; Urquhart et al. 2015; Urquhart &McGroaty, 2016; Noda 2016; Boya 2019) and emerging stock markets (Lim 2007; Abdmoulah 2010; Smith 2012; Dyakova and Smith 2013; Hiremath and Kumari 2014; Tuyon and Ahmad 2016; Hiremath and Narayan 2016; Charfeddine and Khediri 2016; NumapauGyamfi 2018; Ndubuisi and Okere 2018; Xiong et al. 2019; Shahid et al. 2019; Phan Tran Trung and Pham Quang 2019; Lekhal and Oubani 2020; Munir et al. 2022).

Lim (2007) studied the daily returns for two developed (USA and Japan) and eleven developing (Argentina, India, Chile, Indonesia, Taiwan, Brazil, Malaysia, South Korea, Thailand, Mexico, and Philippines) countries using a rolling sample portmanteau bi-correlation test. The research employed a rolling window of 50 observations and found that market efficiency follows an AMH-consistent pattern of fluctuations over time. Ito and Sugiyama (2009) used the rolling monthly returns of the S&P 500 index to determine first-order auto-correlations. The research spanned January 1955 to February 2006, and discovered that market efficiency varies with time, reaching its highest points of inefficiency in the late 1980s and efficiency in the early 2000s. Gupta and Yang (2011) conducted an analysis of market efficiency for the Indian stock market between 1997 and 2011. The analysis concluded that market efficiency occurred inconsistently or that there were periods of efficiency and inefficiency.

Using a rolling window variance test ratio, Smith (2012) studied the daily returns of fifteen developing and three developed nations in Europe from February 2000 to December 2009. According to the findings, Estonia, Malta, and Ukraine are the least efficient markets, while the U.K, Turkey, Poland, and Hungary are the most efficient. Niemczak and Smith (2013) tracked the evolving market efficiency for the eleven Middle-East financial markets and found that most of these markets followed AMH, i.e., switched between periods of efficiency and inefficiency. Sensoy (2013) applied the Generalized Hurst Exponent Analysis and examined the evolving market efficiency in fifteen MENA markets. The study used a rolling window technique and concluded that these equity markets had seen varying degrees of long-term dependency between 2007 and 2012, confirming the AMH. Urquhart and Hudson (2013) used the auto-correlations, runs, and VAR tests to evaluate market efficiency for the three developed nations: the U.S., the U.K., and Japan. The results indicated the presence of an adaptive market, supporting the claim that AMH offered a more accurate depiction of the behavior of equity returns than the theory of EMH.

Hiremath and Kumari (2014) and Hiremath and Narayan (2016) examined the market efficiency of the Indian Stock Market using the daily returns of the Sensex and Nifty index for the period 1991–2013. The research findings support the notion of AMH, indicating that the Indian equity market has changed over time. In parallel to this, Shahid et al. (2019) used a subsample approach and employed various linear and nonlinear tests to examine the AMH in the Pakistan stock market during the 1992–2015 timeframe. The study found that return predictability varies over time and in response to market conditions, which validated the AMH. Phan Tran Trung and Pham Quang (2019) used a time-varying approach to examine market efficiency in the Vietnam stock market. The study employed auto-regressive and autocorrelation tests over 12 years and concluded that the Vietnamese equity market confirmed the AMH, i.e., adaptive by nature. These researches have demonstrated the comparison and concluded that AMH offers a more precise financial framework for comprehending the nature of stock returns than the EMH.

In summary, the Adaptive Market Hypothesis presents the notion that markets are adaptive where market players continuously learn and evolve, in contrast to the Efficient Market Hypothesis, which holds that markets are always efficient and that prices reflect all available information. In order to test the weak-form market efficiency, the study used two hypotheses, which are as follows:

H0 Return series follows a random walk, i.e., the market is weak-form efficient.

H1 Return series does not follow a random walk, i.e., the market is weak-form inefficient.

3 Data and methodology

This section includes the research design, sample period and data sources.

3.1 Research design

3.1.1 Methodology for testing weak-form efficient market hypothesis

The study of EMH, as proposed by Fama (1970), is a critical concept in finance. An efficient market is one in which asset values are not predictable since the prices already represent the information and quickly respond to any new information. In the current study, the analysis of EMH has been carried out with a battery of tests (Urquhart 2016), including Ljung and Box, runs test, Bartel test, Variance ratio test, and BDS test (Fig 1).

3.1.1.1 Autocorrelation test It is an appropriate and reliable technique for examining the independence of a series of random variables. In other words, autocorrelation tests are a crucial tool for evaluating the efficiency of stock markets when considering the EMH. The weak form of market efficiency states that stock prices accurately reflect all available historical information. The probability of serial correlation in stock returns can be investigated using this autocorrelation test. For instance, if a set of returns shows signs of autocorrelation, they cannot be considered as independent. On the other hand, the absence of autocorrelation in a series does not inherently indicate its independence; instead, it merely suggests the absence of linear dependencies within the series. This test assists researchers in identifying exploitable inefficiencies in a market and helps establish whether historical returns can accurately predict future returns. This holds special significance in emerging economies, as distinct market conditions may result in inefficiencies that are not present in more developed markets.

It is a valuable and accurate tool for determining the independence of a set of random variables with a null hypothesis of no correlation ($p=0$). Statistically, Positive autocorrelation is indicated by $p>0$, and negative autocorrelation is shown by $p<0$. If autocorrelation exists, returns are influenced by their preceding values. However, when the returns are independent, the series shows no signs of autocorrelation, signaling that the time series follows a random walk process. We used the Ljung-Box (Ljung and Box 1978) test to look at the autocorrelation of returns:

$$\mathrm{Q} = \mathrm{n}(n+2)\sum_{k=1}^{h}\frac{\hat{p}_k^2}{n-k} \tag{1}$$

Where, $\hat{p}_k$ indicates the autocorrelation of order k, k is the number of lags, and n denotes the sample size.

3.1.1.2 Runs test Second, the runs test is a simple yet powerful tool for analyzing the unpredictability (or predictability) of financial time series. This approach is categorized as non-parametric and is used to evaluate the randomness of time series, particularly those that are not normally distributed. Numerous research studies have observed that the runs test is commonly employed in combination with multiple other tests to assess market efficiency. The idea behind the test is to determine whether the direction of one observation affects future observations. In other words, the purpose of this test is that if the time series is randomly fluctuating and independent, the number of actual runs should be identical to the expected number of runs in the series. The number of expected runs is calculated using the formula below:

$$\text{Expected Number of Runs} = \frac{2PN(P+N)}{(P+N)} + 1 \tag{2}$$

Where, P represents positive runs and N indicates Negative runs.

The following formula can be used to determine variance:

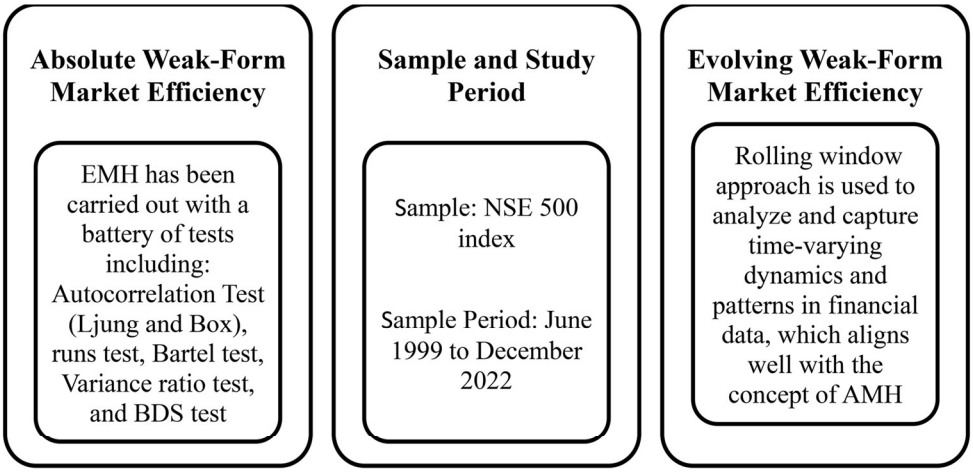

Fig. 1 Framework for testing absolute and evolving weak-form market efficiency

$$\sigma^2 = \frac{2PN(2PN - P - N)}{(P + N)^2(P + N - 1)} \tag{3}$$

3.1.1.3 Bartels test Furthermore, to determine the randomness of the series, the third test is the Bartels (1982) test, which is a rank variant of von Neumann's Ratio Test for Randomness. This non-parametric test is equivalent to the Run test but is considered to be more effective in ascertaining if a set of observations or series is random. In other words, it is used explicitly in finance and econometrics to determine if the observed values in a given series are randomly distributed or show signs of a systematic pattern. Specifically, it employs independence as the null hypothesis, i.e., determining whether returns are independent or not. In light of this, if any of these tests reject the null hypothesis, stock returns can likely be forecast using historical data, indicating that weak-form market efficiency is not being followed.

3.1.1.4 Variance ratio test Apart from the tests mentioned above, the most frequently utilized econometric instrument for assessing the RWH is the Variance Ratio (VR) Test, developed by Lo and Mackinlay (1988). It is a popular method for investigating serial independence under the random walk or martingale null hypothesis, which states that the returns are serially uncorrelated. To implement the VR test, we utilized Choi's (1999) automatic variance test (AVR) in conjunction with wild bootstrap Kim (2009) to improve the small sample properties.

$$\mathrm{VR}(K) = 1 + 2\sum_{j=1}^{k-1}\left(1 - \frac{j}{k}\right)p_j \tag{4}$$

Where, k represents the holding period, p_j denotes the autocorrelation of return in order j.

Nonlinear patterns cannot be found in the return series using linear tests like runs test, bartel, test, autocorrelation, and variance ratio tests. Given the non-normality of the series, the failure to reject linear dependency does not necessarily imply independence Granger and Anderson (1978); Hsieh (1989, 1991). The EMH is refuted by the existence of nonlinearity in equity returns. Predominantly, nonlinearity is a sign of predictability and perhaps extra profits for the market participants, and in these situations, applying linear models could lead to the incorrect conclusion. As a result, the BDS test was utilized to investigate the potential for nonlinear dependence.

3.1.1.5 BDS test Next, we employed the BDS test for serial dependence, which is one of the most prominent and extensively used non-parametric tests (Broock et al. 1996). The null hypothesis asserts that data generation mechanisms are "independent and uniformly distributed," whereas the alternative hypothesis holds that "the model is unspecified." Following Lim and Hooy(2013) and Urquhart (2016), we chose embedding dimension (m) ranging from 2 to 5, and ε/σ is 1, i.e., one times the standard deviation of the returns.

$$\mathrm{W}_{m,n}(\varepsilon) = \sqrt{n}\frac{T_{m,n}(\varepsilon)}{V_{m,n}(\varepsilon)} \tag{5}$$

Where, $\mathrm{W}_{m,n}(\varepsilon)$ represents the BDS statistics, m is the embedding dimension, n denotes the sample size, and (ε) is the metric bound, the largest difference between the observation pairs while calculating the correlation integral. In accordance with the literature (Urquhart andMcGroarty 2016), we computed the mean of the p-values derived from the m-values to find out how the predictability changes over time.

Given the complexity and dynamic nature of financial markets, the inclusion of non-linear models enables a more realistic portrayal of market behavior. As a result, identifying non-linearity in stock returns is essential for enhancing investing strategies, comprehending risk dynamics, and creating more accurate financial models.

3.1.2 Testing of adaptive market hypothesis

Furthermore, the study investigated the evolving market efficiency for the Indian stock market. In order to achieve this, the research analyzed and captured time-varying dynamics and patterns in financial data using the rolling window technique. Particularly, the rolling window approach divides the entire time series data into a sequence of overlapping periods. In other words, it involves data over consecutive, overlapping time periods (windows) to capture how market behavior, patterns, and relationships evolve over time. This approach aligns well with the concept of adaptation in the AMH. In contrast to earlier research, which frequently used subsample analysis, the study considered rolling window analysis with the 500 observations (approximately two years) that roll one month forward to precisely capture the evolving efficiency (Todea et al. 2009; Smith 2012; Urquhart andMcGroarty 2014, 2016; Shah andBahri 2019; Okorie and Lin 2021; Aleknevičienė et al. 2022; Bassiouny et al. 2023). In addition, moving window analysis progressively illustrates how predictability varies over time in place of subsample analysis. To put it another way, the primary flaw with subsample analysis is the prejudice involved in choosing the subset, which could have distorted the results. Afterward, a range of linear and non-linear tests, including the

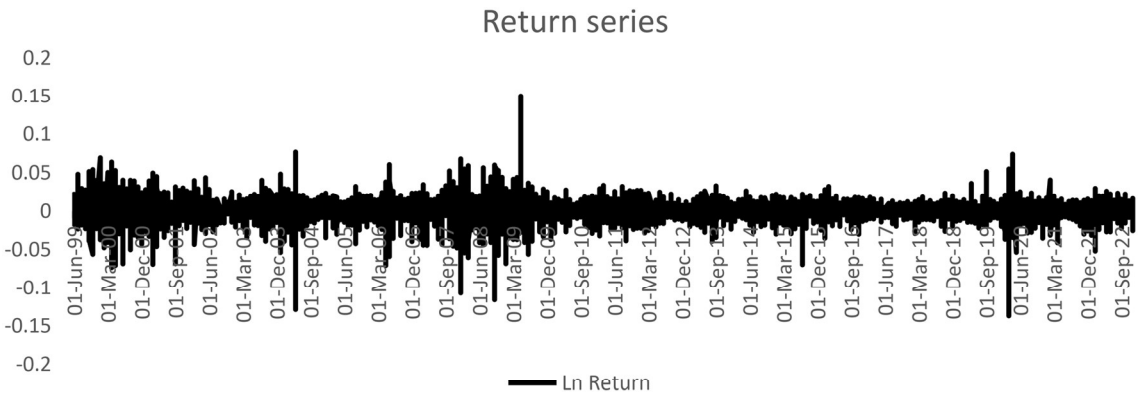

Fig. 2 The return series of the Indian stock market

Table 1 Preliminary analysis of stock returns

Observations	5868
Mean	0.000507
Median	0.001406
Maximum	0.150340
Minimum	-0.137063
Std. Dev.	0.014364
Skewness	-0.679042
Kurtosis	12.18823
JB Normality	21092.49
Probability	0.000000

Source Author's findings

runs test, variance ratio test, autocorrelation test, Bartel, and BDS tests, were applied to the rolling returns to analyze the adaptive market efficiency.

3.2 Sample, time period, and data sources

The S&P NSE 500 composite index, which comprises a diverse range of companies with different market capitalizations, was chosen as the representative stock market (Cap-weighted benchmark). The sample period for the study is from June 1999 to December 2022 (5868 daily observations). The dataset of daily index prices has been taken from the Bloomberg database.

The daily return for the index is calculated as follows:

$$\mathrm{R}_t = \ln P_t - \ln P_{t-1} \tag{6}$$

Where, R_t is the daily index return at time t, lnP_t and lnP_{t-1} are the natural logarithm of the closing price at time t, and $t-1$ respectively.

4 Analysis, findings and discussion

4.1 Data analysis and findings

Figure 2 shows the return series of the Indian Stock market over the sample period. The outcomes of descriptive statistics for the daily returns of the Indian stock market index are shown in Table 1. The initial analysis is presented, including the mean, standard deviation, minimum, maximum, skewness, and kurtosis.

It reports the preliminary analysis, namely mean, maximum, standard deviation, minimum, skewness, and kurtosis. Over the course of the examined sample period, the results showed positive mean returns. It is noteworthy to mention that the skewness value was found to be negative (the value is -0.679), indicating that extreme negative returns typically outweigh extreme positive ones. Put another way, the market is more likely to experience more frequent and severe declines than sharp rises, or the drops are typically greater than the gains. In particular, this shows that there was an asymmetry in the distribution of the daily index returns. Later, it is noted that the kurtosis value is 12.188 i.e., higher than 3 (a measure of the Leptokurtic distribution), indicating the presence of extreme mean return values and higher peaks. According to this, the likelihood of extreme values—i.e., (extremely high or extremely low returns) is higher than it would be in a normal distribution.The null hypothesis that the daily returns are normally distributed is rejected by the Jarque–Bera test at a significance level of 1%.

First, the study used the conventional absolute efficiency approach to examine the weak-form market efficiency over the selected time period. This approach uses an absolute, all-or-nothing view of efficiency to determine whether a stock market is efficient or inefficient within a given time frame. Table 2 demonstrates that all of the p-values are significant from the beginning of the sample to December 2022, demonstrating the predictability of returns. Particularly, the significant p-values derived from the outcomes of

Table 2 Testing of weak-form market efficiency (absolute efficiency approach)

	p-values				
Time Period	Autocorrelation Test (Ljung-Box)	Bartel test	Runs test	VR Test	BDS Test
1999–2022	0.0000	0.0000	0.0000	0.002	0.0143

Source: Author's findings

the linear and non-linear tests showed the predictability of return. In essence, the results of the conventional absolute efficiency tests confirmed that the Indian stock markets are predominantly inefficient. The findings are in line with the previous studies Chaudhuri (1991), Poshakwale (1996), Pant and Bishnoi (2001), Pandey (2003), Gupta and Siddiqui (2010), Srinivasan (2010), Khan et al. (2011), Harper and Jin (2012), and Malafeyev et al. (2019).

Since prices do not represent random behavior, investors can forecast an upward or downward pattern in the stock prices. In other words, the results observed that the Indian stock market does not adhere to the weak-form market efficiency. Above all, the outcome of absolute efficiency implied that investors can make significant profits by using a disciplined approach to seizing trading opportunities in the Indian stock market.

4.2 Testing of weak-form market efficiency (evolving efficiency approach)

Figure 3 displays the first-order autocorrelation p-values for the Indian equities market (NSE 500 index) across time. It is evident that the p-values produced by the sample fluctuate over time, with some periods producing statistically significant p-values and others yield relatively high estimates. Almost all of the p-values from the beginning of the sample to October 2008 are significant, indicating the dependency and predictability of stock returns.However, the p-values show a fluctuating pattern of stock returns from November 2008 to December 2015, ranging from statistically significant to insignificant. Moving further, nearly all of the p-values between December 2015 and March 2018 are statistically significant, demonstrating the predictability of stock returns. Finally, all of the p-values from March 2018 to the end of the sample are insignificant, indicating that stock returns are unpredictable. The autocorrelation test shows that the Indian equity market is compatible with the AMH, i.e., it exhibits cycles of efficiency and inefficiency.

Figure 4 presents the runs test p-value statistics over time, and there is again clear evidence of the time-varying behavior of stock return predictability. Given that all of the p-values are significant, there is evidence of strong predictability from the beginning of the period to March 2002. Nevertheless, almost all of the p-values between March 2002 and June 2009 at the 5% level are insignificant or quite close to being insignificant, signifying the unpredictable nature of stock returns. Further, the p-values are all significant beyond this threshold, indicating that the returns are considered predictable. However, the p-values show a fluctuating pattern of stock returns from January 2015 to February 2020, ranging from statistically significant to insignificant. Lastly, all p-values are statistically significant from February 2020 to the end of the sample period, demonstrating the unpredictable behavior of returns. In essence, there is convincing evidence of evolving nature of the stock return predictability, which is in line with the theory of AMH.

Figure 5, which displays the Bartel test p-values across time, provides extensive evidence of the time-varying nature of stock return predictability. For the following time periods: June 1999 to August 2005, December 2005 to

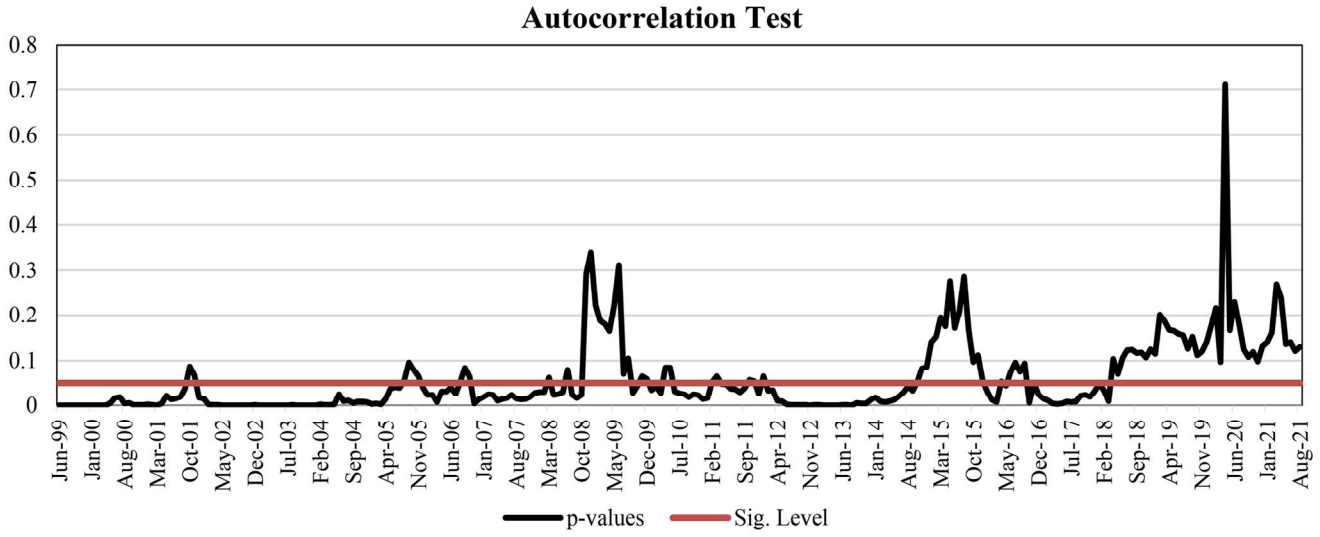

Fig. 3 The evolving behavior of p-values for autocorrelation test statistic. *Source: Author's findings*

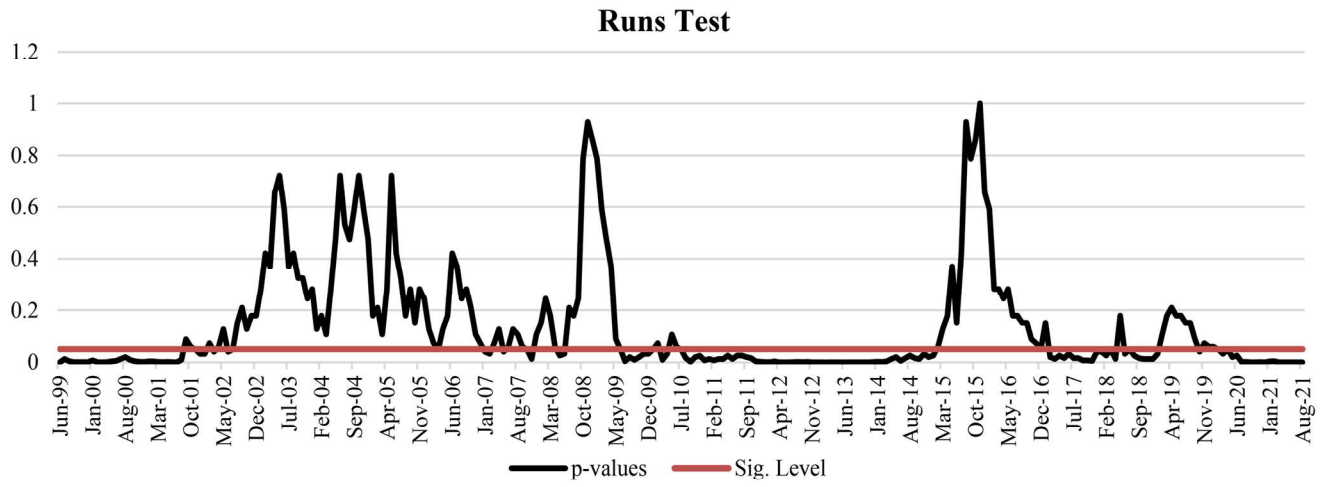

Fig. 4 The evolving behavior of p-values for Runs test statistic. *Source: Author's findings*

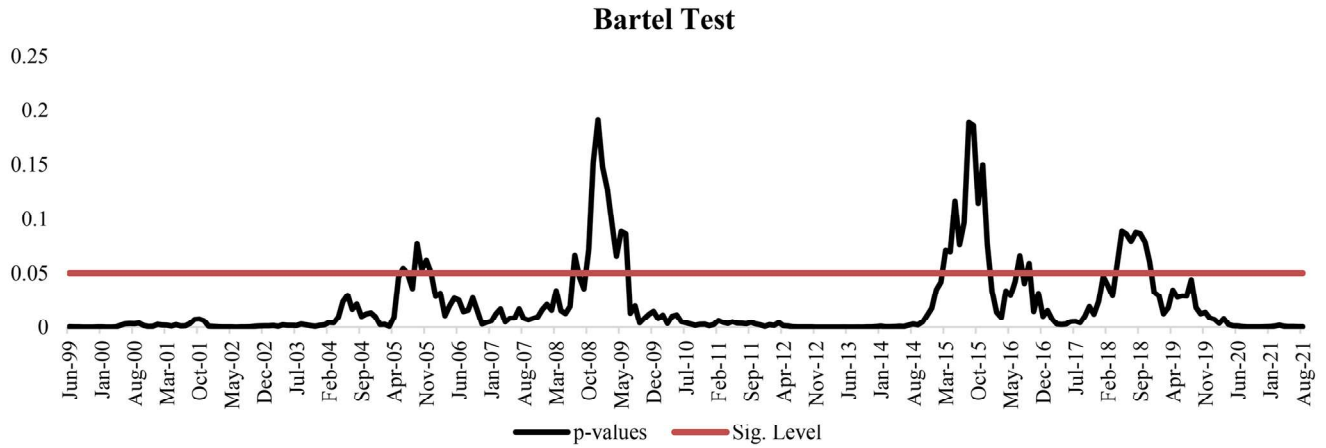

Fig. 5 The evolving behavior of p-values for Bartel test statistic. *Source: Author's findings*

September 2008, July 2009 to February 2015, January 2016 to March 2018, and December 2018 to the end of the sample, there is strong evidence of predictability. These periods reflect that the market exhibits inefficiency and thus, market players can earn anomalous returns. The remaining periods, on the other hand, demonstrate insignificant outcomes and, hence, the unpredictable character of returns. In essence, the results are compatible with the AMH, as the Bartel test indicates that there have been periods of predictability and unpredictability in the Indian equity market.

Figure 6 displays the p-values of variance ratio test for the NSE 500 index, and it is evident that there have been periods of predictability and unpredictability in the Indian stock market. It is noted that the p-values generated by the sample change with time, with some periods producing statistically significant p-values and others generating p-values that are comparatively high. All of the p-values from the beginning of the period to April 2000 are significant, demonstrating the predictability of returns. Following this, from May 2000 to June 2009, nearly all of the p-values for the test were insignificant, indicating the independence and unpredictable nature of stock returns.

On the other hand, almost all of the p-values between July 2009 and July 2014 were significant, demonstrating the predictability of the stock returns. Nonetheless, the p-values showed a fluctuating pattern of stock returns from August 2014 to September 2017, alternating between being statistically significant and insignificant. Finally, from September 2017 to the end of the sample, all the p-values were insignificant, representing the unpredictable nature of stock returns. Consequently, as the equity market experiences cycles of predictability and unpredictability, the variance ratio test results are consistent with the AMH. In other words, the current evidence indicates a varying behavior of stock returns across the sample.

According to the findings of the linear test, the Indian stock market fluctuated between periods of efficiency and inefficiency i.e., the results are consistent with the adaptive character of stock returns. This conclusion is in line with the

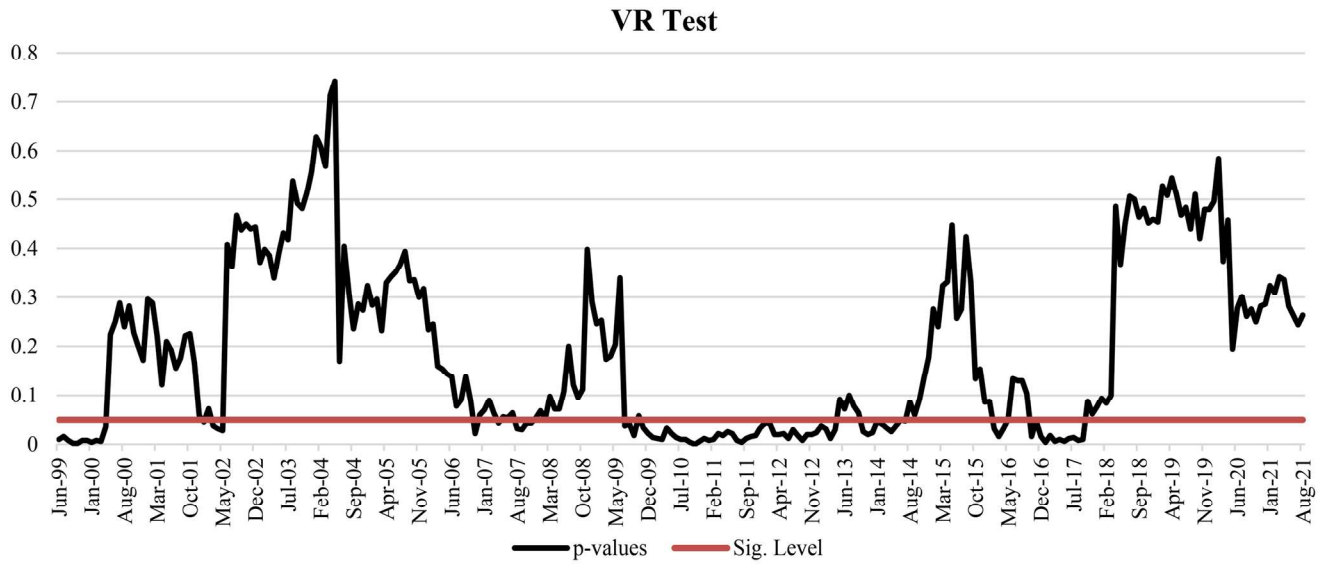

Fig. 6 The evolving behavior of p-values for variance ratio test statistic. *Source: Author's findings.*

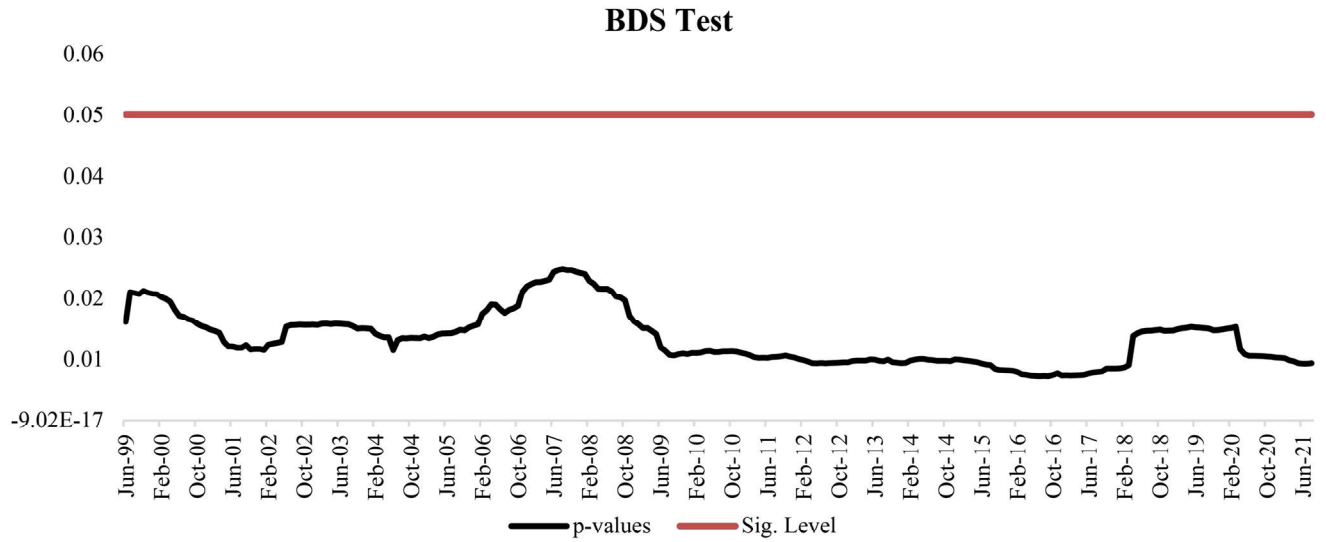

Fig. 7 The evolving behavior of p-values for BDS test statistic. *Source: Author's findings.*

findings of Kim et al. (2011), Alvarez-Ramirez et al. (2012), and Charles et al. (2012).

Comprehending non-linear dependencies in stock returns is essential for effective risk management. It makes it possible for investors to more accurately evaluate possible risks and create plans to reduce them, particularly in times of market volatility. Figure 7 reports the BDS statistic p-values from the rolling window analysis. The findings of the non-linear BDS test show a significant existence of nonlinear dependence, which could signify possible return predictability and consequent excess returns. Consequently, the statistical significance of the BDS test p-values is apparent, indicating the weak-form inefficiency of the Indian equity market. In a nutshell the current evidence showing a substantial nonlinear dependence of stock returns across the sample implies that the Indian stock market is still inefficient and has not yet attained efficiency.

The conventional absolute efficiency tests revealed that the Indian stock markets are largely inefficient. Both linear and nonlinear tests yielded significant p-values, affirming the predictability of returns. The study then explored the concept of evolving market efficiency within the Indian equity market. The rolling linear tests displayed a cyclical trend, suggesting that the market alternated between phases of efficiency and inefficiency. There is considerable evidence that the efficiency of the Indian equity market varies over time, exhibiting both efficient and inefficient periods. Overall, the research findings indicate that the AMH framework offers a

more nuanced and comprehensive explanation of emerging market behavior than the EMH.

5 Concluding remarks

The fundamental idea of the efficient market hypothesis is that prices will exhibit a random walk behavior in an efficient stock market, and reflecting their inherent values. An essential requirement for the successful functioning of financial markets is their capacity to accurately and quickly reflect all the available information. On the other hand, if there is inefficiency in the equity markets, investors might receive excess returns. Investors have the opportunity to benefit from arbitrage opportunities in an inefficient market. However, efficiency levels can be raised through improved trading technology, more active investing strategies, improved information flow, and sound regulatory bodies. This will guarantee that investors get risk-adjusted returns and companies get a fair price for their securities. In particular, the ability to diversify risks, hedging strategies, and appropriate portfolio allocation are the elements that have contributed to more substantial economic development.

Researchers have studied the theory of market efficiency for decades, but they have not yet reached a consensus. Particularly, previous studies and research utilized conventional to advance models for examining the weak-form market efficiency. As one of the most significant elements of emerging economies, we investigated the weak-form market efficiency for the Indian Equity market. The study used both absolute and evolving approaches to analyze weak-form market efficiency. However, the primary drawback of the absolute efficiency tests is that it only evaluates efficiency in a static sense, and ignoring the potential for future fluctuations in return predictability. Particularly, the study examined the predictability of stock returns using linear tests, including the runs test, variance ratio test, autocorrelation test, and Bartel test. Furthermore, the BDS test was employed to determine the possible nonlinearity of the return series. Subsequently, the study tested adaptive market hypothesis using the rolling window technique, yielding several significant insights and making it possible to look into how efficiency changes in Indian equity markets. In other words, the study employed linear and nonlinear tests on moving windows to examine the evolving market efficiency.

The results of the conventional absolute efficiency tests confirmed that the Indian stock markets are predominantly inefficient. Both the linear and non-linear tests yielded significant p-values, ensuring the predictability of return. After that, the evolving market efficiency was investigated for the Indian Equity market. The findings of the rolling linear tests revealed a cyclical pattern that suggested the Indian equity market switched between phases of efficiency and inefficiency. There is ample evidence that the efficiency of the Indian equity market varies across time, encompassing both efficient and inefficient phases. However, the results derived from the nonlinear test (BDS) indicate a noteworthy presence of nonlinear dependency, suggesting the possibility of return predictability and ensuing excess returns. In a nutshell, the findings of the research suggested that AMH framework offers a more comprehensive explanation of emerging market behavior than the EMH.

6 Implications

The conclusions of the study have a number of implications for the market participants, including investors, regulators, and other market participants. Initially, the results demonstrated that the Indian stock market was weakly inefficient in its absolute form. However, the Adaptive Markets Hypothesis offers a more practical framework for comprehending risk and return in equities markets. The relevance of adaptability, ongoing learning, and the incorporation of adaptive investment strategies is highlighted by the practical implications of the AMH for equity markets.

The evolving nature of market efficiency offers more significant implications. Lo (2012) asserts that investment strategies must be developed and adjusted in response to shifts in predictability. In other words, opportunities to generate money occasionally arise, and when they do, it makes sense to manage the portfolio actively. According to Lo (2004, 2005), the performance of an investing strategy changes with time, doing well in some market conditions and not working well in others. Thus, it is necessary to have adaptable investing strategies that can swiftly change to market conditions. As long as financial markets remain unstable, the debate over market efficiency will remain a vibrant and evolving field of study with ongoing implications for academics, policymakers, and investors.

The study has several other practical implications, including that emerging economies offer investment opportunities to asset managers, market participants, and investor communities. When there is market turbulence and uncertainty, investors should focus on growing stock markets that have the potential to generate returns. The results of the study may serve as further evidence to policymakers in emerging countries that these markets have seen numerous structural and economic downturns. These findings highlighted the need to address market imperfections to reduce the possibility that investors may exploit them, potentially leading to speculative and manipulative actions by vigilant stock market players. Essentially, more efficient markets would

draw less manipulative actions and promote higher investor engagement over time. India is an emerging country that attracts a wide variety of investors with varying degrees of financial need, i.e., some investors want to see long-term financial growth, while others seek guaranteed monthly returns. In essence, market participants and investors can find it simpler to overcome obstacles and take advantage of opportunities if they adjust their plans in accordance with the changing market conditions. Hence, investors and other market players should exercise prudence while selecting their investment strategies.

Adaptive investing strategies that consider the dynamic character of markets may prove advantageous for investors. Put another way, the dynamic nature of markets implies that investors must be perpetual learners. It is imperative for investors to stay up to date on market trends, technological developments, and behavioral finance insights, and to modify their investments accordingly. Particularly, keeping up with emerging technologies, developments in financial research and market patterns can give one a competitive advantage when it comes to continuous learning and modifying investment plans. Investors ought to review their risk tolerance on a regular basis and should make necessary adjustments to their portfolios. In order to better navigate changing market situations, strategies that incorporate insights from machine learning, adaptive risk management, and behavioral finance may prove more successful. Overall, it becomes imperative to implement risk management techniques that are adaptable and sensitive to shifting market conditions.

7 Limitations and future scope

Even though the study generates consistent and significant results, it has a few limitations as well. This current study primarily focuses on a single emerging economy, i.e., the Indian market, which might limit the ability to generalize the results to other economies. However, economies with similar structural frameworks and peculiarities may consider the outcomes and implement these strategies. It may be helpful to broaden the focus of the EMH research to cover global markets and a variety of asset classes in order to obtain more in-depth understanding. Analyzing the differences in efficiency across different asset types and geographical locations may yield more information. In other words, extending the research to include more countries with parallel structural dynamics would be beneficial.

Furthermore, policymakers and investment managers might benefit from more research on the causes of market inefficiencies and how they affect the market returns in the developing stock markets. One interesting direction to explore could be the use of network analysis to the study of how market participants are connected to the information diffusion in adaptive markets. This may further shed light on how adaptive behavior propagates throughout the financial system.

Funding The authors have no financial assitance to disclose.

Declarations

Research involving human participants and/or animals This research does not contain any human participant and/or Animals.

Informed consent All the authors of the article are fully aware about this submission.

Compliance with ethical standards The authors have no financial assistance to disclose.

Conflicts of interest The authors have no potential conflict of interest to disclose.

References

Abdmoulah W (2010) Testing the evolving efficiency of arab stock markets. Int Rev Financial Anal 19(1):25–34. https://doi.org/10.1016/j.irfa.2009.11.004

Abeysekera SP (2001) Efficient markets hypothesis and the emerging capital market in Sri Lanka: evidence from the Colombo Stock Exchange–A note. J Bus Finance Acc 28(1–2):249–261. https://doi.org/10.1111/1468-5957.00373

Al-Khazali O, Mirzaei A (2017) Stock market anomalies, market efficiency and the adaptive market hypothesis: evidence from islamic stock indices. J Int Financ Mark Inst Money 51:190–208. https://doi.org/10.1016/j.intfin.2017.10.001

Al-Khazali OM, Leduc G, Alsayed MS (2016) A market efficiency comparison of islamic and non-islamic stock indices. Emerg Markets Finance Trade 52(7):1587–1605. https://doi.org/10.1080/1540496X.2014.998572

Aleknevičienė V, Klasauskaitė V, Aleknevičiūtė E (2022) Behavior of calendar anomalies and the adaptive market hypothesis: evidence from the Baltic stock markets. J Baltic Stud 53(2):187–210. https://doi.org/10.1080/01629778.2021.1990094

Alvarez-Ramirez J, Rodriguez E, Espinosa-Paredes G (2012) Is the US stock market becoming weakly efficient over time? Evidence from 80-year-long data. Physica A 391(22):5643–5647. https://doi.org/10.1016/j.physa.2012.06.051

Antoniou A, Ergul N, Holmes P (1997) Market efficiency, thin trading and non-linear behaviour: evidence from an emerging market. Eur Financ Manag 3(2):175–190. https://doi.org/10.1111/1468-036X.00038

Azad AS, Azmat S, Fang V, Edirisuriya P (2014) Unchecked manipulations, price–volume relationship and market efficiency: evidence from emerging markets. Res Int Bus Finance 30:51–71. https://doi.org/10.1016/j.ribaf.2013.05.003

Baig AS, Butt HA, Haroon O, Rizvi SAR (2021) Deaths, panic, lockdowns and US equity markets: the case of COVID-19 pandemic. Finance Res Lett 38:101701. https://doi.org/10.1016/j.frl.2020.101701

Bartels R (1982) The rank version of Von Neumann's ratio test for randomness. J Am Stat Assoc 77(377):40–46. https://doi.org/10.2307/2287767

Bassiouny A, Kiryakos M, Tooma E (2023) Examining the adaptive market hypothesis with calendar effects: international evidence and the impact of COVID-19. Glob Financ J 56:100777. https://doi.org/10.1016/j.gfj.2022.100777

Bhatia M (2022) Stock market efficiency and COVID-19 with multiple structural breaks: evidence from India. Global Bus Rev 09721509221110372. https://doi.org/10.1177/09721509221110372

Borges MR (2010) Efficient market hypothesis in European stock markets. Eur J Finance 16(7):711–726. https://doi.org/10.1080/1351847X.2010.495477

Boya CM (2019) From efficient markets to adaptive markets: evidence from the French stock exchange. Res Int Bus Finance 49:156–165. https://doi.org/10.1016/j.ribaf.2019.03.005

Broock WA, Scheinkman JA, Dechert WD, LeBaron B (1996) A test for independence based on the correlation dimension. Econom Rev 15(3):197–235. https://doi.org/10.1080/07474939608800353

Butler M, Kazakov D (2012), March Testing implications of the adaptive market hypothesis via computational intelligence. In 2012 IEEE Conference on Computational Intelligence for Financial Engineering & Economics (CIFEr), 1–8. IEEE. https://doi.org/10.1109/CIFEr.2012.6327799

Campbell JY, Lo AW, MacKinlay AC, Whitelaw RF (1998) The econometrics of financial markets. Macroecon Dyn 2(4):559–562. https://doi.org/10.1017/S1365100598009092

Charfeddine L, Khediri KB (2016) Time varying market efficiency of the GCC stock markets. Physica A 444:487–504. https://doi.org/10.1016/j.physa.2015.09.063

Charles A, Darné O, Kim JH (2012) Exchange-rate return predictability and the adaptive markets hypothesis: evidence from major foreign exchange rates. J Int Money Finance 31(6):1607–1626. https://doi.org/10.1016/j.jimonfin.2012.03.003

Chaudhuri SK (1991) Short-run share price behaviour: new evidence on weak form of market efficiency. Vikalpa 16(4):17–21. https://doi.org/10.1177/0256090919910402

Choi I (1999) Testing the random walk hypothesis for real exchange rates. J Appl Econom 14(3):293–308. https://doi.org/10.1002/(SICI)1099-1255(199905/06)14:3<293::AID-JAE503>3.0.CO;2-5

Claessens S, Dasgupta S, Glen J (1995) Return behavior in emerging stock markets. World Bank Econ Rev 9(1):131–151. https://doi.org/10.1093/wber/9.1.131

Das S (2014) Testing weak form market efficiency: empirical evidence from India. Asian J Res Bank Finance 4(6):38–47

Dyakova A, Smith G (2013) The evolution of stock market predictability in Bulgaria. Appl Financ Econ 23(9):805–816. https://doi.org/10.1080/09603107.2013.767976

Eakins G, Mishkin S (2012) Financial markets and institutions. Prentice Hall, Boston

Elangovan R, Irudayasamy FG, Parayitam S (2022) Testing the market efficiency in Indian stock market: evidence from Bombay Stock Exchange broad market indices. J Econ Finance Administrative Sci 27(54):313–327. https://doi.org/10.1108/JEFAS-04-2021-0040

Fama EF (1965) The behavior of stock-market prices. J Bus 38(1):34–105. https://www.jstor.org/stable/2350752

Fama EF (1970) Efficient capital markets: a review of theory and empirical work. J Finance 25(2):383–417. https://doi.org/10.2307/2325486

Granger CWJ, Anderson OD (1978) An Introduction to Bilinear Time Series Models. Vandenhoeck&Ruprecht, Gottingen

Gupta N, Gedam A (2014) Testing of efficient market hypothesis: a study on Indian stock market. J Bus Manage 16(8):28–38

Gupta PK, Siddiqui S (2010) Weak form of market efficiency: evidences from selected NSE indices. Available SSRN 1355103. https://doi.org/10.2139/ssrn.1355103

Gupta R, Yang J (2011) Testing weak form efficiency in the Indian capital market. Int Res J Finance Econ 75(1):108–119

Harper A, Jin Z (2012) Examining market efficiency in India: an empirical analysis of the random walk hypothesis. J Finance Account 10:1

Hiremath GS, Kumari J (2014) Stock returns predictability and the adaptive market hypothesis in emerging markets: evidence from India. SpringerPlus 3:1–14. https://doi.org/10.1186/2193-1801-3-428

Hiremath GS, Narayan S (2016) Testing the adaptive market hypothesis and its determinants for the Indian stock markets. Finance Res Lett 19:173–180. https://doi.org/10.1016/j.frl.2016.07.009

Hoque HA, Kim JH, Pyun CS (2007) A comparison of variance ratio tests of random walk: a case of Asian emerging stock markets. Int Rev Econ Finance 16(4):488–502

Hsieh DA (1989) Testing for nonlinear dependence in daily foreign exchange rates. J Bus 62(3):339–368. https://www.jstor.org/stable/2353351

Hsieh DA (1991) Chaos and nonlinear dynamics: application to financial markets. J Finance 46(5):1839–1877. https://doi.org/10.1111/j.1540-6261.1991.tb04646.x

Ito M, Sugiyama S (2009) Measuring the degree of time varying market inefficiency. Econ Lett 103(1):62–64. https://doi.org/10.1016/j.econlet.2009.01.028

Ito M, Noda A, Wada T (2014) International stock market efficiency: a non-bayesian time-varying model approach. Appl Econ 46(23):2744–2754. https://doi.org/10.1080/00036846.2014.909579

Ito M, Noda A, Wada T (2016) The evolution of stock market efficiency in the US: a non-bayesian time-varying model approach. Appl Econ 48(7):621–635. https://doi.org/10.1080/00036846.2015.1083532

Jain K, Jain P (2013) Empirical study of the weak form of EMH on Indian stock market. Int J Manage Social Sci Res 2(11):52–59

Jain D, Patel M, Narsaria A, Malik S (2020) A study on the efficiency of the Indian stock market. arXiv preprint arXiv:2012.01160

Kapoor S (2017) A study of the weak form of market efficiency in India with special reference to realty sector. Int Res J Manage Commer 4(2):99–105

Kendall MG, Hill AB (1953) The analysis of economic time-series-part i: prices. J Royal Stat Soc Ser (General) 116(1):11–34. https://doi.org/10.2307/2980947

Khan AQ, Ikram S, Mehtab M (2011) Testing weak form market efficiency of Indian capital market: a case of national stock exchange (NSE) and Bombay stock exchange (BSE). Afr J Mark Manage 3(6):115–127

Kim JH (2009) Automatic variance ratio test under conditional heteroskedasticity. Finance Res Lett 6(3):179–185. https://doi.org/10.1016/j.frl.2009.04.003

Kim JH, Shamsuddin A (2008) Are Asian stock markets efficient? Evidence from new multiple variance ratio tests. J Empir Finance 15(3):518–532. https://doi.org/10.1016/j.jempfin.2007.07.001

Kim JH, Shamsuddin A, Lim KP (2011) Stock return predictability and the adaptive markets hypothesis: evidence from century-long US data. J Empir Finance 18(5):868–879. https://doi.org/10.1016/j.jempfin.2011.08.002

Kumar H, Jawa R (2017) Efficient market hypothesis and calendar effects: empirical evidences from the Indian stock markets. Bus Analyst 37(2):145–160. https://ssrn.com/abstract=2981633

Kumar DS, Kumar L (2015) Market efficiency in India: an empirical study of random walk hypothesis of Indian stock market–NSE midcap. ZENITH Int J Multidisciplinary Res, 5(1). https://ssrn.com/abstract=2544459

Lekhal M, El Oubani A (2020) Does the adaptive market hypothesis explain the evolution of emerging markets efficiency? Evidence from the Moroccan financial market. Heliyon 6(7). https://doi.org/10.1016/j.heliyon.2020.e04429

Lim KP (2007) Ranking market efficiency for stock markets: a nonlinear perspective. Physica A 376:445–454. https://doi.org/10.1016/j.physa.2006.10.013

Lim KP, Brooks R (2011) The evolution of stock market efficiency over time: a survey of the empirical literature. J Economic Surveys 25(1):69–108. https://doi.org/10.1111/j.1467-6419.2009.00611.x

Lim KP, Hooy CW (2013) Non-linear predictability in G7 Stock Index returns. Manch School 81(4):620–637. https://doi.org/10.1111/j.1467-9957.2012.02303.x

Lim KP, Luo W, Kim JH (2013) Are US stock index returns predictable? Evidence from automatic autocorrelation-based tests. Appl Econ 45(8):953–962. https://doi.org/10.1080/00036846.2011.613782

Ljung GM, Box GE (1978) On a measure of lack of fit in time series models. Biometrika 65(2):297–303. https://doi.org/10.1093/biomet/65.2.297

Lo AW (2004) The adaptive markets hypothesis: market efficiency from an evolutionary perspective. J Portf Manag 30(5):15–29. https://doi.org/10.3905/jpm.2004.442611

Lo AW (2005) Reconciling efficient markets with behavioral finance: the adaptive markets hypothesis. J Invest Consulting 7(2):21–44. https://ssrn.com/abstract=1702447

Lo AW (2012) Adaptive markets and the new world order (corrected May 2012). Financial Anal J 68(2):18–29. https://doi.org/10.2469/faj.v68.n2.6

Lo AW, MacKinlay AC (1988) Stock market prices do not follow random walks: evidence from a simple specification test. Rev Financial Stud 1(1):41–66. https://doi.org/10.1093/rfs/1.1.41

Malafeyev O, Awasthi AS, Kambekar K, Kupinskaya A, Statistics, Optimization (2019) Inform Comput. 7(1), 1–25. https://doi.org/10.19139/soic.v7i1.499

Mishra PK (2011) Weak form market efficiency: evidence from emerging and developed world. J Commer 3(2):26

Mishra A, Mishra V, Smyth R (2015) The random-walk hypothesis on the Indian stock market. Emerg Markets Finance Trade 51(5):879–892. https://doi.org/10.1080/1540496X.2015.1061380

Munir AF, Sukor MEA, Shaharuddin SS (2022) Adaptive market hypothesis and time-varying contrarian effect: evidence from emerging stock markets of South Asia. SAGE Open 12(1):21582440211068490. https://doi.org/10.1177/21582440211068490

Nalina KB, &Suraj.P (2013) Adaptive market hypothesis: a case on National Stock Exchange (NSE). Int J Sci Eng Res (IJSER), 4(7)

Ndubuisi P, Okere K (2018) Stock returns predictability and the adaptive market hypothesis in emerging markets: evidence from the Nigerian Capital Market.(1986–2016). Asian J Economic Modelling 6(2):147–156. https://doi.org/10.18488/journal.8.2018.62.147.156

Niemczak K, Smith G (2013) Middle Eastern stock markets: absolute, evolving and relative efficiency. Appl Financ Econ 23(3):181–198. https://doi.org/10.1080/09603107.2012.714068

Nisar S, Hanif M (2012) Testing weak form of efficient market hypothesis: empirical evidence from South Asia. World Appl Sci J 17(4):414–427. https://ssrn.com/abstract=1962210

Noda A (2016) A test of the adaptive market hypothesis using a time-varying AR model in Japan. Finance Res Lett 17:66–71. https://doi.org/10.1016/j.frl.2016.01.004

NumapauGyamfi E (2018) Adaptive market hypothesis: evidence from the Ghanaian stock market. J Afr Bus 19(2):195–209. https://doi.org/10.1080/15228916.2018.1392838

Okorie DI, Lin B (2021) Adaptive market hypothesis: the story of the stock markets and COVID-19 pandemic. North Am J Econ Finance 57:101397. https://doi.org/10.1016/j.najef.2021.101397

Ozkan O (2021) Impact of COVID-19 on stock market efficiency: evidence from developed countries. Res Int Bus Finance 58:101445. https://doi.org/10.1016/j.ribaf.2021.101445

Pandey A (2003) Efficiency of Indian stock market. *Available at SSRN 474921*. https://doi.org/10.2139/ssrn.474921

Pant B, Bishnoi TR (2001), December Testing random walk hypothesis for Indian stock market indices. In Research Paper Presented in UTI Capital Market Conference Proceedings (pp. 1–15)

Patel A, Rajpal R, Modi A (2018) Testing weak form of market efficiency: a study on Indian stock market. Int J Manage Bus Stud 8(4):9–11

Poshakwale S (1996) Evidence on weak form efficiency and day of the week effect in the Indian stock market. Financ India 10(3):605–616

Sensoy A (2013) Generalized Hurst exponent approach to efficiency in MENA markets. Physica A 392(20):5019–5026. https://doi.org/10.1016/j.physa.2013.06.041

Shah A, Bahri A (2019) Are stock markets adaptive? Evidence from us, hongkong and India. Evid US Hong Kong India. https://doi.org/10.2139/ssrn.3316877

Shahid MN, Coronado S, Sattar A (2019) Stock market behaviour: efficient or adaptive? Evidence from the Pakistan Stock Exchange. Afro-Asian J Finance Acc 9(2):167–192. https://doi.org/10.1504/AAJFA.2019.099488

Sharma GD, Mahendru M (2009) Efficiency hypothesis of the stock markets: a case of Indian securities. Int J Bus Manage. https://ssrn.com/abstract=1827522

Smith G (2012) The changing and relative efficiency of European emerging stock markets. Eur J Finance 18(8):689–708. https://doi.org/10.1080/1351847X.2011.628682

Smith G, Ryoo HJ (2003) Variance ratio tests of the random walk hypothesis for European emerging stock markets. Eur J Finance 9(3):290–300. https://doi.org/10.1080/1351847021000025777

Srinivasan P (2010) Testing weak-form efficiency of Indian stock markets. Asia Pac J Res Bus Manage 1(2):134–140

Tiwari AK, Kyophilavong P (2014) New evidence from the random walk hypothesis for BRICS stock indices: a wavelet unit root test approach. Econ Model 43:38–41

Todea A, Ulici M, Silaghi S (2009) Adaptive markets hypothesis: evidence from Asia-Pacific financial markets. Rev Finance Bank 1(1):7–13

Trung PT, D., Pham Quang H (2019) Adaptive market hypothesis: evidence from the Vietnamese stock market. J Risk Financial Manage 12(2):81. https://doi.org/10.3390/jrfm12020081

Tuyon J, Ahmad Z (2016) Behavioural finance perspectives on Malaysian stock market efficiency. Borsa Istanbul Rev 16(1):43–61. https://doi.org/10.1016/j.bir.2016.01.001

Urquhart A (2016) The inefficiency of Bitcoin. Econ Lett 148:80–82. https://doi.org/10.1016/j.econlet.2016.09.019

Urquhart A, Hudson R (2013) Efficient or adaptive markets? Evidence from major stock markets using very long run historic data. Int Rev Financial Anal 28:130–142. https://doi.org/10.1016/j.irfa.2013.03.005

Urquhart A, McGroarty F (2014) Calendar effects, market conditions and the adaptive market hypothesis: evidence from long-run US data. Int Rev Financial Anal 35:154–166. https://doi.org/10.1016/j.irfa.2014.08.003

Urquhart A, McGroarty F (2016) Are stock markets really efficient? Evidence of the adaptive market hypothesis. Int Rev Financial Anal 47:39–49. https://doi.org/10.1016/j.irfa.2016.06.011

Urquhart A, Gebka B, Hudson R (2015) How exactly do markets adapt? Evidence from the moving average rule in three developed

markets. J Int Financ Mark Inst Money 38:127–147. https://doi.org/10.1016/j.intfin.2015.05.019

Vasileiou E (2021) Behavioral finance and market efficiency in the time of the COVID-19 pandemic: does fear drive the market? Int Rev Appl Econ 35(2):224–241. https://doi.org/10.1080/02692171.2020.1864301

Vidya A (2018) An empirical study on weak form efficiency of Indian stock market. Int J Manage Stud 5(2):94–98

Worthington AC, Higgs H (2006) Weak-form market efficiency in Asian emerging and developed equity markets: comparative tests of random walk behaviour. Acc Res J 19(1):54–63

Xiong X, Meng Y, Li X, Shen D (2019) An empirical analysis of the adaptive market hypothesis with calendar effects: evidence from China. Finance Res Lett 31. https://doi.org/10.1016/j.frl.2018.11.020

Publisher's note Springer Nature remains neutral with regard to jurisdictional claims in published maps and institutional affiliations.

Springer Nature or its licensor (e.g. a society or other partner) holds exclusive rights to this article under a publishing agreement with the author(s) or other rightsholder(s); author self-archiving of the accepted manuscript version of this article is solely governed by the terms of such publishing agreement and applicable law.

arXiv:2411.06088v1 [cond-mat.mtrl-sci] 9 Nov 2024

A Existence of dual topological phases in *Sn*-based ternary chalcogenides

Ramesh Kumar and Mukhtiyar Singh*

Computational Quantum Material Design (CQMD) Lab, Department of Applied Physics, Delhi Technological University, New Delhi-110042, India

Abstract

It is quite intriguing to investigate the transition from a topological insulator (TI) phase to topological crystalline insulator (TCI) phase in a material as the latter has an advantage over the former in controlled device applications. This work investigates the existence of this dual topological behavior in *Sn*-based ternary chalcogenides family $PbSnX_2$ (X=S, Se, Te) under the hydrostatic pressure using first-principles approach. These materials are dynamically stable at ambient and elevated pressure conditions up to which the topological phase transitions (TPTs) are studied. This family have a topologically trivial ground state with direct band gap values 0.338 eV, 0.183 eV and 0.217 eV for $PbSnS_2$, $PbSnSe_2$ and $PbSnTe_2$, respectively. The first TPT i.e., TI phase for these materials is observed, under the effect of external pressure of 5 GPa, 2.5 GPa and 3.5 GPa, with a single band inversion at *F-point* in the bulk band structure and an odd number of Dirac cones along the (111) surface. A further increase in pressure to 5.5 GPa, 3 GPa and 4 GPa results in another band inversion at *Γ-point* and an even number of Dirac cones along the (111) plane. These even number of band inversions suggest that $(\bar{1}2\bar{1})$ surface has mirror symmetry around $(\bar{1}0\bar{1})$ plane and hence, the TCI phase is obtained. This TCI phase is further corroborated with even value of mirror Chern number calculated using winding of Wannier charge centers.

Keywords: Topological phase transition, ternary chalcogenides, first-principles calculations, topological crystalline insulators, mirror Chern number.

I. INTRODUCTION

A new phase of matter with unusual metallic edge/surface states known as topological materials (TM) has been studied intensively in recent years [1–6]. The TMs can be divided into few categories such as topological insulators (TIs) [3–6], topological crystalline insulators (TCIs) [7–9], Dirac semimetals (DSMs) [10, 11], Weyl semimetals (WSMs) [12, 13], nodal line semimetals (NLSMs) [14, 15], Z_2 topological semimetals [16, 17] and triply degenerate node semimetals [18, 19], etc. The metallic Dirac-like electronic states on the surface of the crystal with insulating bulk are the signature of the existence of TI. These metallic edge/surface states appear in the presence of spin-orbit coupling (SOC) which are protected

* mukhtiyarsingh@dtu.ac.in; msphysik09@gmail.com

by time-reversal symmetry (TRS) and provides robust spin-polarized conduction channels [1–6]. These materials have potential applications in low-power high-speed electronic and spintronic devices, quantum computing, and thermoelectric applications [20–22] etc. The careful alteration in the strength of SOC plays an important role in realizing topological phases in specific materials. The hydrostatic pressure is a non-destructive way of enhancing SOC without affecting the charge neutrality of the materials. The binary and ternary materials like Bi_4Br_4 [23], LaAs [16], YbAs [24], LnSb (Ln=La, Gd, Tm) [17, 25], YX (X=As, Sb, Bi) [26, 27] and KNa_2Bi [28], BiTeI [29], Bi_2S_3 [30], BiTeBr [31] have shown the topological phase transition (TPT) with hydrostatic pressure.

The term "topological crystalline insulators," has been introduced by L. Fu, which defines a class of materials having robust topological states and are protected by crystalline symmetries [7]. This new phase was first proposed in SnTe and later angle-resolved photoemission spectroscopy (ARPES) verified the topological surface states (TSSs) in the (001) plane of this material [8]. Unlike TIs, TCIs have persisted protection by mirror symmetry even when TRS is broken. It is quite intriguing to investigate the TPT from TI to TCI in a material. TCI phase is more robust against impurities or defects and has diverse and tunable topological characteristic states [7, 32]. TCI materials hold higher-order topological hinge or corner states which can be identified with different topological invariants depending on the crystal symmetries [33, 34] and can have potential applications in stable qubits and novel electronic devices [7, 32–34]. The TCI phase has an advantage over the TI phase for controlled device applications such as a topological field effect transistor [32].

The narrow band-gap semiconductors are amongst the highly sought-after materials to realize TPT. Several narrow gap IV-VI semiconducting materials such as PbTe, SnSe, SnS, TlSe, TlS, and $Pb_{1-x}Sn_xX$ (X = Se, Te) have been studied for the existence of TIs and TCIs phases [35–39]. Other than these, the ternary chalcogenides $TlXY_2$ (X = Sb, Bi; Y = Te, Se) have also been reported as strong TIs [40, 41] but the TCI phase has not been explored in these materials except for $TlBiS_2$ and $TlSbS_2$ [42]. The present study focuses on the realization of TI and TCI phases in ternary chalcogenides $PbSnX_2$ (X= S, Se, Te) with the application of external hydrostatic pressure. For this family, trivial to non-trivial phase are obtained with single band inversion at Γ*-point* under hydrostatic pressure. With further increases in pressure, a pair of Dirac cones are observed along the (111) plane and made these systems trivial again. However, a TCI phase emerges at this elevated pressure

as confirmed by non-trivial TSSs along $(\bar{1}2\bar{1})$ plane which is symmetric around the mirror plane $(\bar{1}0\bar{1})$.

II. COMPUTATIONAL METHODOLOGY

The structural optimization and electronic structure calculations based on the density functional theory (DFT) approach [43, 44] were performed using the projector augmented-wave (PAW) [45] method as implemented in the Vienna Ab initio Simulation Package (VASP) [46]. The PAW potentials for Pb ($6s^26p^2$) with 4 valence electrons, Sn ($5s^25p^2$) with 4 valence electrons, and S ($3s^23p^4$), Se ($4s^24p^4$), Te ($5s^25p^4$) with 6 valance electrons configuration were used for the calculations. The exchange and correlation energy were calculated with the generalized gradient approximation of Perdew–Burke–Ernzerhof (GGA-PBE) [47] and modified Becke-Johnson (mBJ) [48] functionals. The effect of SOC was included in all calculations except in ionic optimization. The total energies convergence criterion of 10^{-6} eV was adopted along with a finer 9x9x5 gamma-centered k-mesh. The plane-wave cut-off energies for $PbSnX_2$ (X=S, Se, Te) were kept at 380 eV, 310 eV and 260 eV, respectively. The phonon calculations were performed using the PHONOPY code [49]. The Z_2 topological invariants were calculated using the product of parities at time reversal invariant momenta (TRIM) points as per the Kane and Mele model [6]. Wannier90 code [50] was used to obtain maximally localized Wannier functions (MLWFs) and to parametrize a tight-binding (TB) Hamiltonian. This TB Hamiltonian was used to obtain the surface density of state (SDOS) using the Green function approach as implemented in the WannierTools code [51].

III. RESULTS AND DISCUSSION

A. Crystal structure and stability analysis

The ternary chalcogenides $PbSnX_2$ (X=S, Se, Te) have adopted a rhombohedral crystal structure (space group $R\bar{3}m$ (166)) (FIG. 1 (a)) and are isostructural to the well-studied $TlBiTe_2$, $TlBiSe_2$, and $TlBiS_2$ materials [52–56] which have also been experimentally synthesized (crystal structure in suppl. information (FIG. S1)). This family has a Pb-X-Sn-X-Pb-sequence along the *three-fold axis*. The Pb/Sn layers are sandwiched between the chalcogenides layers as shown in FIG. 1 (a, b). The hexagonal supercell and the bulk Brillouin

zone (BZ) with projected surfaces along (111) and ($\bar{1}2\bar{1}$) are shown in FIG. 1 (a, c). The surface BZ of the (111) and ($\bar{1}2\bar{1}$) planes are represented in FIG. S2. Both Pb and Sn atoms act as an inversion center with atomic coordinates Pb (0, 0, 0), Sn (0.5, 0.5, 0.5) and X (±v, ±v, ±v) sites. As hydrostatic pressure is isotropic in nature which, therefore, does not alter the symmetry of the systems for the entire studied pressure range. The optimized lattice parameters for this family are given in TABLE 1.

TABLE I. Lattice parameters (in Å) of the ternary chalcogenides $PbSnX_2$ (X=S, Se, Te) family. Also, the bulk band energy gap at Γ- and *F-points* using TB-mBJ functional.

Materials	Lattice parameters	Energy gap at *F-point* (Bandgap, E_g)	Energy gap at Γ-*point*
$PbSnS_2$	a = b = 4.201; c = 20.449	0.338 eV	0.377 eV
$PbSnSe_2$	a = b = 4.343; c = 21.262	0.183 eV	0.215 eV
$PbSnTe_2$	a = b = 4.589; c = 22.538	0.217 eV	0.235 eV

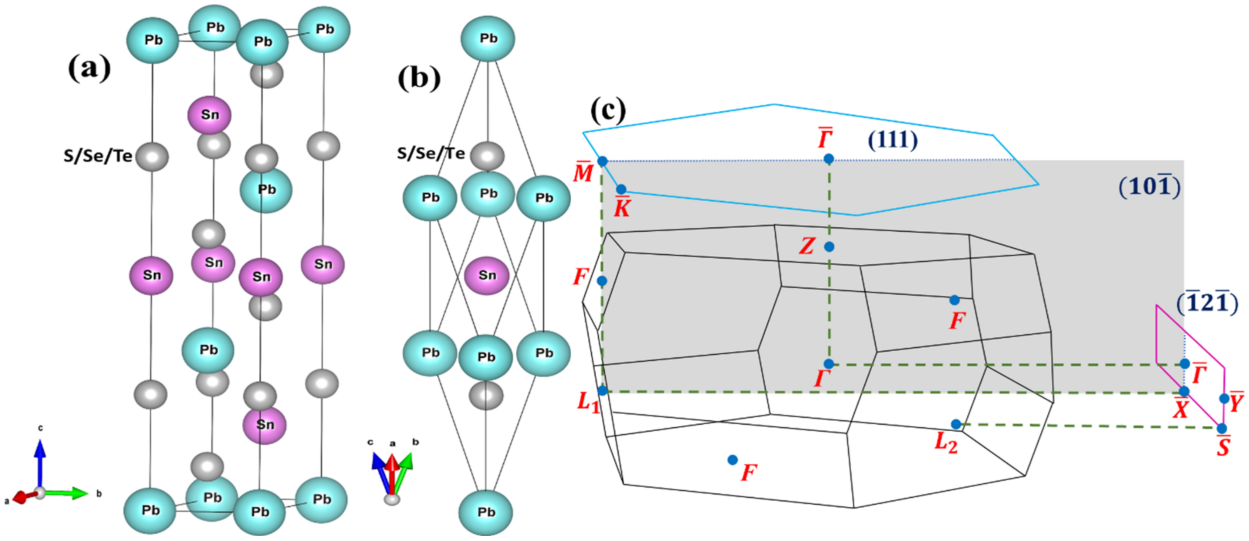

FIG. 1. The crystal structure of $PbSnX_2$ (X=S, Se, Te) (a) conventional hexagonal structure, (b) primitive unit cell, and (c) The bulk Brillion zone (BZ) of primitive rhombohedral cell with projections on surface Brillouin zones.

The surface electronic structure for the TCI systems significantly depends on the orientation of the crystal face. We have considered two surfaces of the rhombohedral structure. L_1- and *F-points* are projected to $\bar{M}$-*point* of the (111) plane whereas L_1- and L_2-*points* are projected on $\bar{X}$ - and $\bar{S}$-*points*, respectively, on $\bar{1}2\bar{1}$ plane. The $\bar{\Gamma}$-*points* as the center of

both the planes are projections of the center of BZ i.e., *Γ-point*. The $(\bar{1}0\bar{1})$ mirror plane is perpendicular to the $(\bar{1}2\bar{1})$ surface plane and projected along the $\bar{\Gamma}-\bar{X}$ direction as shown in FIG. 1 (c). Further, we have studied the stability of $PbSnX_2$ (X=S, Se, Te) at ambient and elevated pressures via the phonon dispersion spectrum. The absence of negative frequencies at ambient and higher-pressures values as shown in FIG. S3 shows the stability of these materials. It has been noted that TPT in these materials takes place within this studied stability range of hydrostatic pressure.

B. The electronic structure at ambient pressure

It is an established fact that the prediction of ground state using DFT is highly depend upon the choice of *exchange-correlation functional* corresponding to different material systems. To choose a relevant and accurate functional for our study, we performed the *ab initio* calculation with two major functional i.e., GGA-PBE and mBJ for the experimentally synthesized $TlBiS_2$ material, which is isostructural to our studied systems. We found that the mBJ functional predicts the true ground state of $TlBiS_2$ with the band gap of 0.36 eV which is in excellent agreement with its experimental value of 0.35 eV [52–54] (see suppl. FIG. S4). Therefore, we used mBJ functional for further investigations of $PbSnX_2$ (X=S, Se, Te). However, the PBE-GGA has been quite successful in predicting the true ground state of binary chalcogenide materials [35, 37, 39, 57, 58] but in the case of this ternary chalcogenide family, it predicts an inaccurate ground state (FIG. S5). FIG. 2 (a, c, e) depicts the bulk band structure of $PbSnX_2$ (X=S, Se, Te) materials using mBJ functionals. The *p-orbital* of the Pb/Sn in the conduction band (CB) and *p-orbitals* of chalcogenide elements S/Se/Te in the valence band (VB) mainly contribute near the Fermi energy. No inverted contribution of the orbitals near the Fermi level is observed in these materials and hence they are topologically trivial semiconductors with the direct band at *Γ-point*. The energy gap of these materials at *Γ*- and *F-points* in bulk band structure is represented in TABLE 1. The absence of Dirac cones in SDOS along the (111) plane (FIG. 2 (b, d, f) in these materials also establishes their topologically trivial state at ambient pressure.

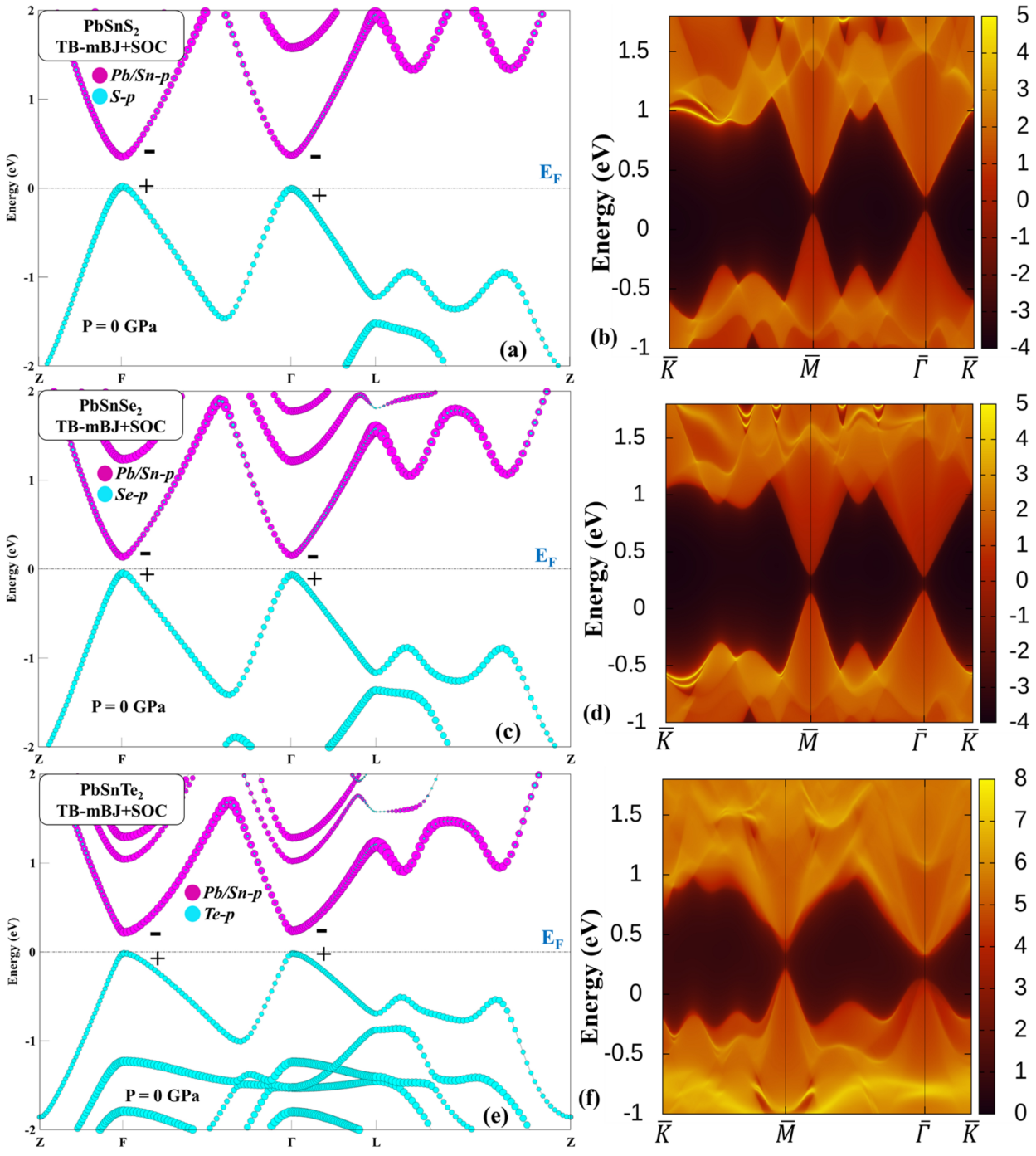

FIG. 2. (a, c, e) The bulk band structure using mBJ+SOC functional, (b, d, f) The density of states (SODS) along (111) plane of the systems $PbSnX_2$ (X=S, Se, Te) at ambient pressure.

C. The effect of hydrostatic pressure on electronic structure

In the preceding section, we have established the topologically trivial semiconducting nature of $PbSnX_2$ (X=S, Se, Te) at ambient pressure. Now, we have included the effect of hydro-

static pressure to tune the bulk electronic structure of these materials. The compressive nature of the hydrostatic pressure has performed the isotropic reduction in the lattice parameters and hence tuned the eigenstates of these systems. The application of hydrostatic pressure on $PbSnX_2$ (X=S, Se, Te) results in the TPT (FIG. 3 (a, c, e)) at 5 GPa, 2.5 GPa and 3.5 GPa, respectively. An inverted contribution of *p-orbitals* of chalcogenide elements S/Se/Te in CB and Pb/Sn in VB is observed at *F-point*, whereas no change in orbital contribution is observed at *Γ-point* as shown in the insets of FIG. 3 (a, c, e). The TPT pressure for $PbSnTe_2$ is higher than $PbSnSe_2$, which is due to the higher energy gap of this material at the *F-point*. The SDOS along the (111) plane of these materials shows the presence of a single Dirac cone at *Γ-point* in surface BZ as shown in FIG. 3 (b, d, f).

A further increase in hydrostatic pressure tunes the bulk band structure at the *Γ-point* and band inversion at this TRIM point also takes place as shown in FIG. 4 (a, c, e). The inverted contribution of the *p-orbitals* of chalcogenide elements S/Se/Te in CB and Pb/Sn in VB has verified the TPT at *Γ-point*. Now, there is an even number of band inversions in these systems which makes them topologically weak insulators or topologically trivial systems. A pair of Dirac cones in SDOS at $\bar{\Gamma}$*-point* and $\bar{M}$*-point* along the (111) plane as shown in FIG. 4 (b, d, f) also establishes the presence of an even number of band inversions in $PbSnX_2$ (X=S, Se, Te). To verify whether these materials, with even number of band inversions, are topologically weak insulators or topologically trivial, further, we have calculated Z_2 topological invariants.

D. Z_2 topological invariants

The topologically non-trivial nature of the $PbSnX_2$ (X=S, Se, Te) family under applied hydrostatic pressure can also be verified with the help of Z_2 topological invariants. These materials have TRS as well as inversion symmetry, so their Z_2 topological invariants can be calculated from the product of parities of all valance bands at TRIM points. According to Kane and Mele model [6], for a three-dimensional (3D) material, there are four Z_2 topological invariants $(\nu_0; \nu_1\nu_2\nu_3)$ are required to calculate at eight TRIM points, which were defined by the following equations;

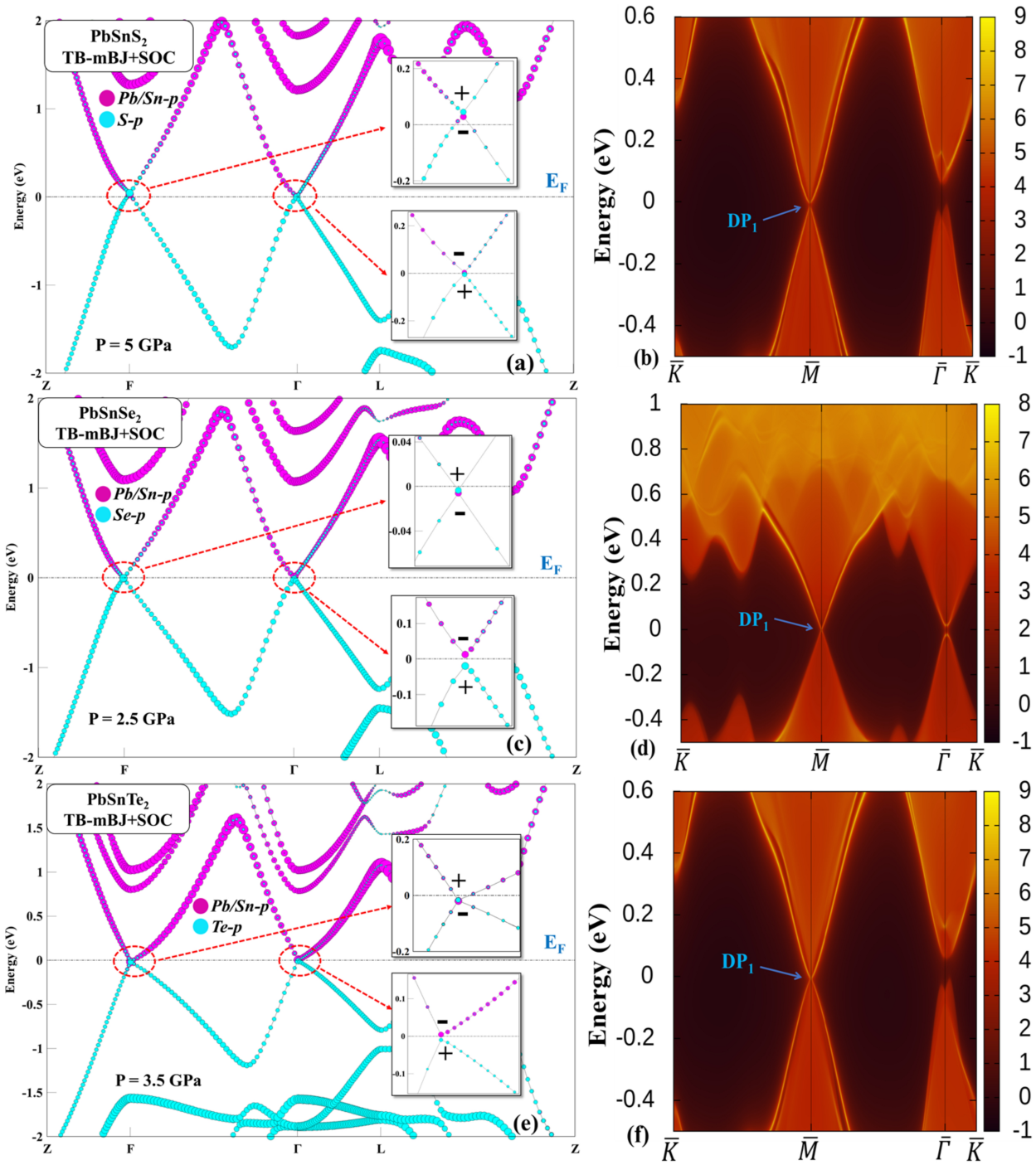

FIG. 3. (a, c, e) The bulk band structure with band inversion at *F-point*, (b, d, f) The surface density of states (SODS) along (111) plane of the systems $PbSnX_2$ (X=S, Se, Te) at elevated pressure with marked Dirac point (DP_1).

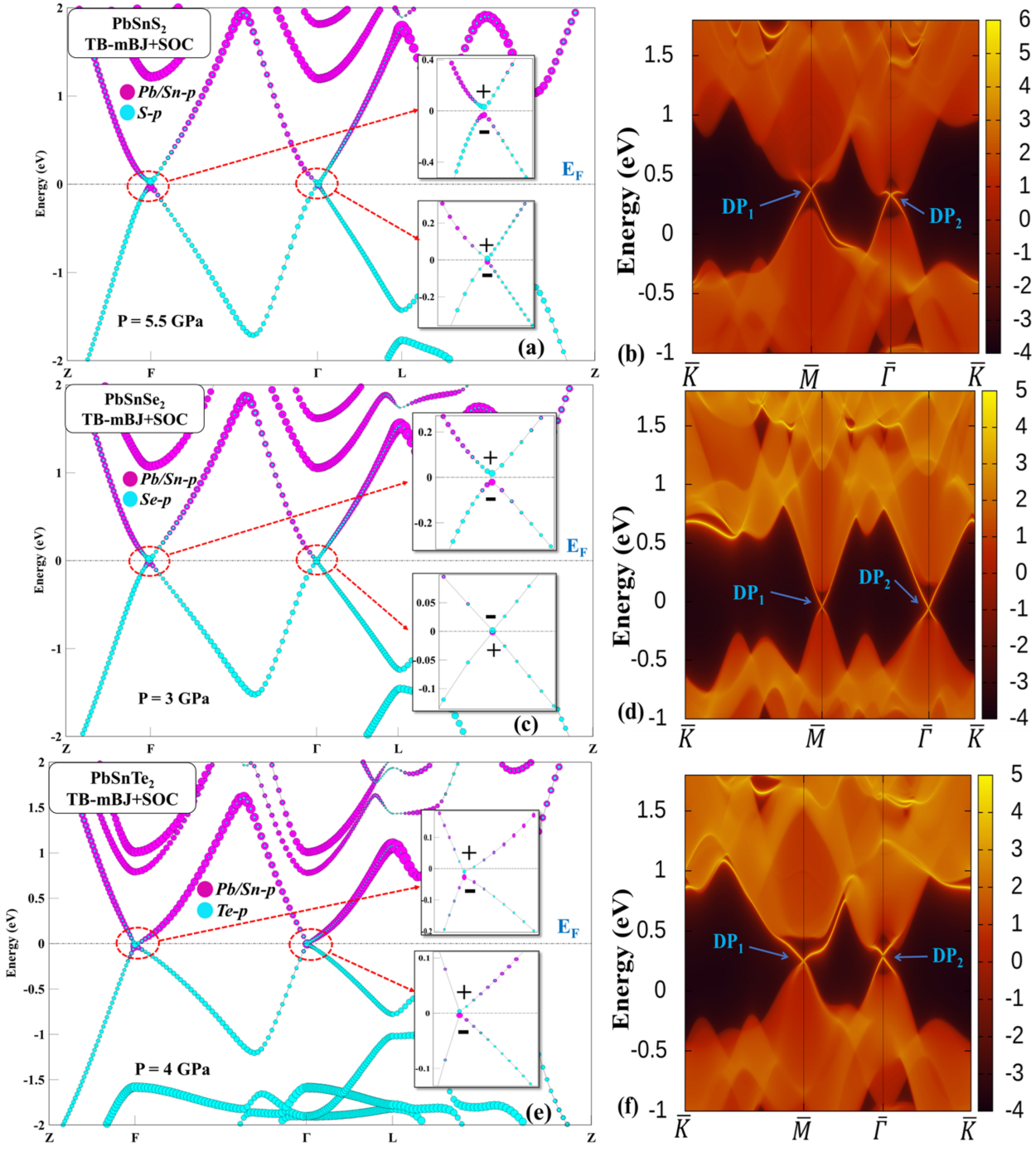

FIG. 4. (a, c, e) The bulk band structure with a pair of band inversions at *Γ-point* as well as *F-point*, (b, d, f) The density of states (SODS) along (111) plane of the systems $PbSnX_2$ (X=S, Se, Te) at elevated pressure with marked Dirac points (DP_1) and (DP_2).

TABLE II. The product of parities of all valance bands at TRIM points and Z_2 invariants under different values of hydrostatic pressure. (The detailed parity tables (TABLE S1-S3) are in supplementary information).

Materials	Hydrostatic Pressure (in GPa)	Γ	$3L$	$3F$	Z	Z_2-invariants
$PbSnS_2$	0	+	-	+	-	(0; 000)
	5	+	-	-	-	(1; 000)
	5.5	-	-	-	-	(0; 000)
$PbSnSe_2$	0	+	-	+	-	(0; 000)
	2.5	+	-	-	-	(1; 000)
	3	-	-	-	-	(0; 000)
$PbSnTe_2$	0	+	-	+	-	(0; 000)
	3.5	+	-	-	-	(1; 000)
	4	-	-	-	-	(0; 000)

$$(-1)^{\nu_0} = \prod_{n_j=0,1} \delta_{n_1 n_2 n_3} \tag{1}$$

$$(-1)^{v_{i=1,2,3}} = \prod_{n_i=1; n_{j\neq i}=0,1} \delta_{n_1 n_2 n_3} \tag{2}$$

Here, δ and n_i are representing the parities of all the occupied bands at TRIM points and reciprocal lattice vectors, respectively. The first Z_2 topological invariant (ν_0) is independent of the choice of primitive reciprocal lattice vectors (b_k) but the other three are dependent. But these other three invariants can be recognized with $G_v \equiv \sum_j v_j b_j$ which belongs to 8 element *mod* 2 reciprocal lattices and can be construed as Miller indices of the reciprocal lattice vector. The calculated four Z_2 topological invariants with the help of the product of parities at TRIM points at ambient and elevated hydrostatic pressures of the $PbSnX_2$ (X=S, Se, Te) family are manifested in TABLE 2.

At the ambient conditions, using equations 1 and 2, the Z_2 topological invariants ($\nu_0; \nu_1\nu_2\nu_3$) are (0;000) for the $PbSnX_2$ (X=S, Se, Te) family which established the trivial semiconductor nature of this family as observed in bulk band structures (FIG. 2 (a, c, e)). When we have applied hydrostatic pressures of 5 GPa, 2.5 GPa and 3.5 GPa on $PbSnX_2$ (X=S, Se, Te) materials, respectively, the first Z_2 topological invariant(ν_0 switched to 1 (equation 1) and

using equation 2 the other three invariants ($\nu_1\nu_2\nu_3$) remain (000). The non-zero value of (ν_0 recognized these materials as strong TIs at the mentioned pressures. With further increase in pressures to 5.5 GPa, 3 GPa and 4 GPa for the $PbSnX_2$ (X=S, Se, Te) family, respectively, the value of (ν_0 again switched from 1 to 0 (equation 1) with existence of a pair of band inversions in the bulk band structure. Now, the systems can be topologically weak or trivial in nature depending upon the values of the remaining three invariants ($\nu_1\nu_2\nu_3$) under these pressure conditions. These remaining invariants ($\nu_1\nu_2\nu_3$) are (000) due to the presence of the same negative parities at all eight TRIM points using equation 2. So, these materials are topologically trivial with an even number of inversions under above mentioned elevated hydrostatic pressures.

E. Evolution of TI to TCI phase

The non-zero mirror Chern number (MCN) is used to characterize the TCI phase in materials because mirror symmetry protects those Dirac cones that appear in surface electronic structures. The $PbSnX_2$ (X=S, Se, Te) family has similar surface states to the TCI materials such as SnTe and PbTe [37, 57, 58], therefore, these materials can also hold TCI phase with an even number of Dirac cones in (111) plane. To confirm the TCI phase in this family, we have analyzed the $(\bar{1}2\bar{1})$ surface, which has mirror symmetry around the $(\bar{1}2\bar{1})$ plane. The perpendicular intersection of $(\bar{1}2\bar{1})$ plane with $(\bar{1}0\bar{1})$ plane is along $\bar{\Gamma}-\bar{X}$ k-path as shown in FIG. 1 (c). Since, $PbSnX_2$ (X=S, Se, Te) materials have a pair of band inversion (FIG. 5) at Γ- and *F-points* like SnTe material, we have tried to reproduce the circumstances of SnTe in this family of materials. We anticipate the hybridization of Dirac cones at the crossing which are projected on $(\bar{1}2\bar{1})$ surface. This has been confirmed in FIG. 5 (a, c, e), where the hybridization opens an energy gap along $\bar{X}-\bar{\Gamma}$ path near the Fermi level but along the mirror symmetry path $\bar{\Gamma}-\bar{X}$ Dirac cone holds its crossing. This Dirac cone along the $\bar{\Gamma}-\bar{X}$ is protected by mirror symmetry (not TRS) of $(\bar{1}0\bar{1})$ plane. Along the $\bar{S}-\bar{Y}-\bar{\Gamma}$ path in FIG. 5 (b, d, f), an energy gap is opened after hybridization, because the $\bar{Y}$*-point* do not lie on the mirror plane $(\bar{1}0\bar{1})$, which is the projection of two *F-points* [42] from bulk BZ. Hence, the mirror symmetry-protected Dirac cones exist in the $PbSnX_2$ (X=S, Se, Te) family, and a TI to TCI phase transition occurs after second inversion under hydrostatic pressure.

This existence of TCI phase is further verified with MCN of the $PbSnX_2$ (X=S, Se, Te)

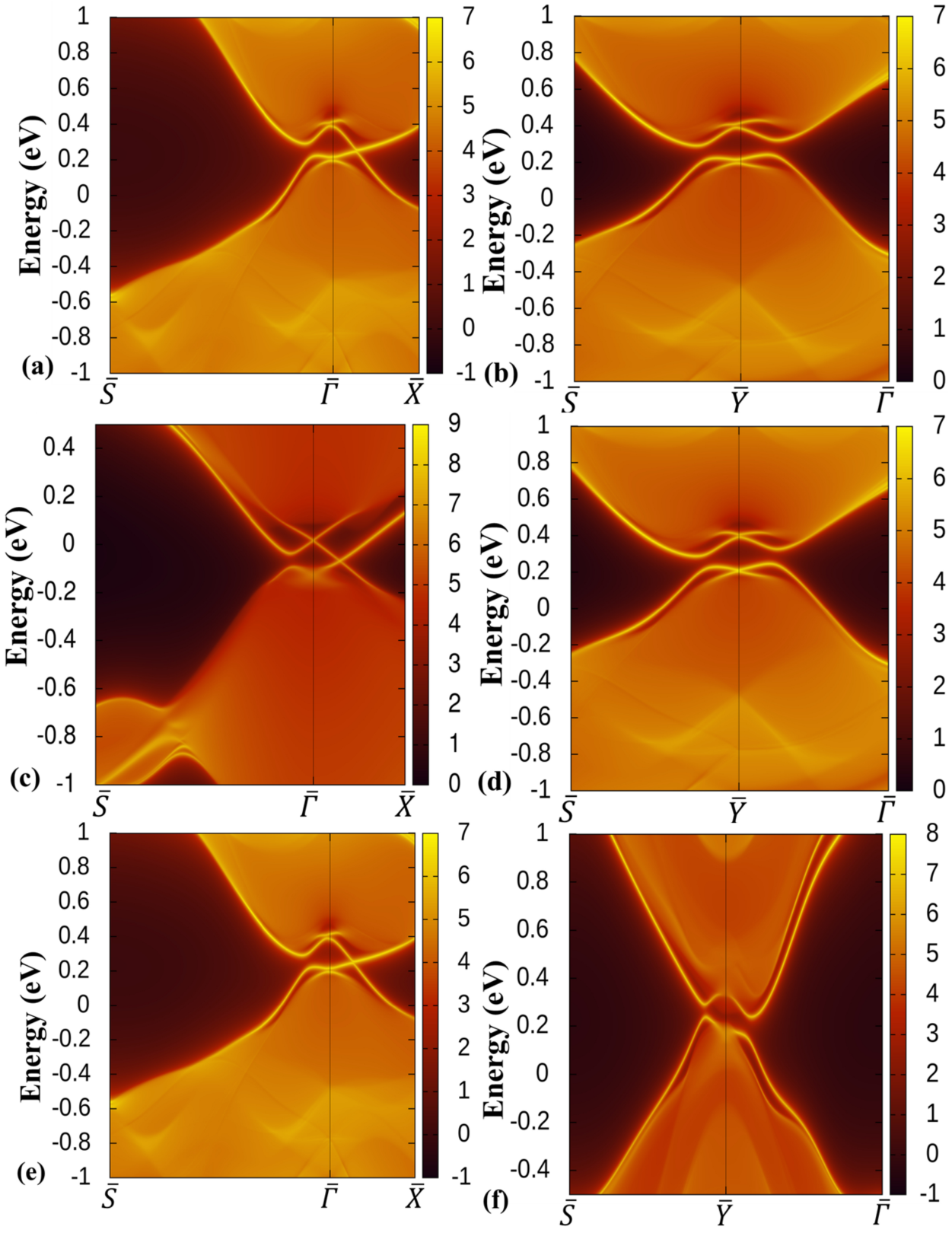

FIG. 5. The SDOS of the slabs (a, b) $PbSnS_2$, (c, d) $PbSnSe_2$ and (e, f) $PbSnTe_2$ along the $\bar{S}-\bar{\Gamma}-\bar{X}$ and $\bar{S}-\bar{Y}-\bar{\Gamma}$, respectively, with $(\bar{1}2\bar{1})$ oriented planes.

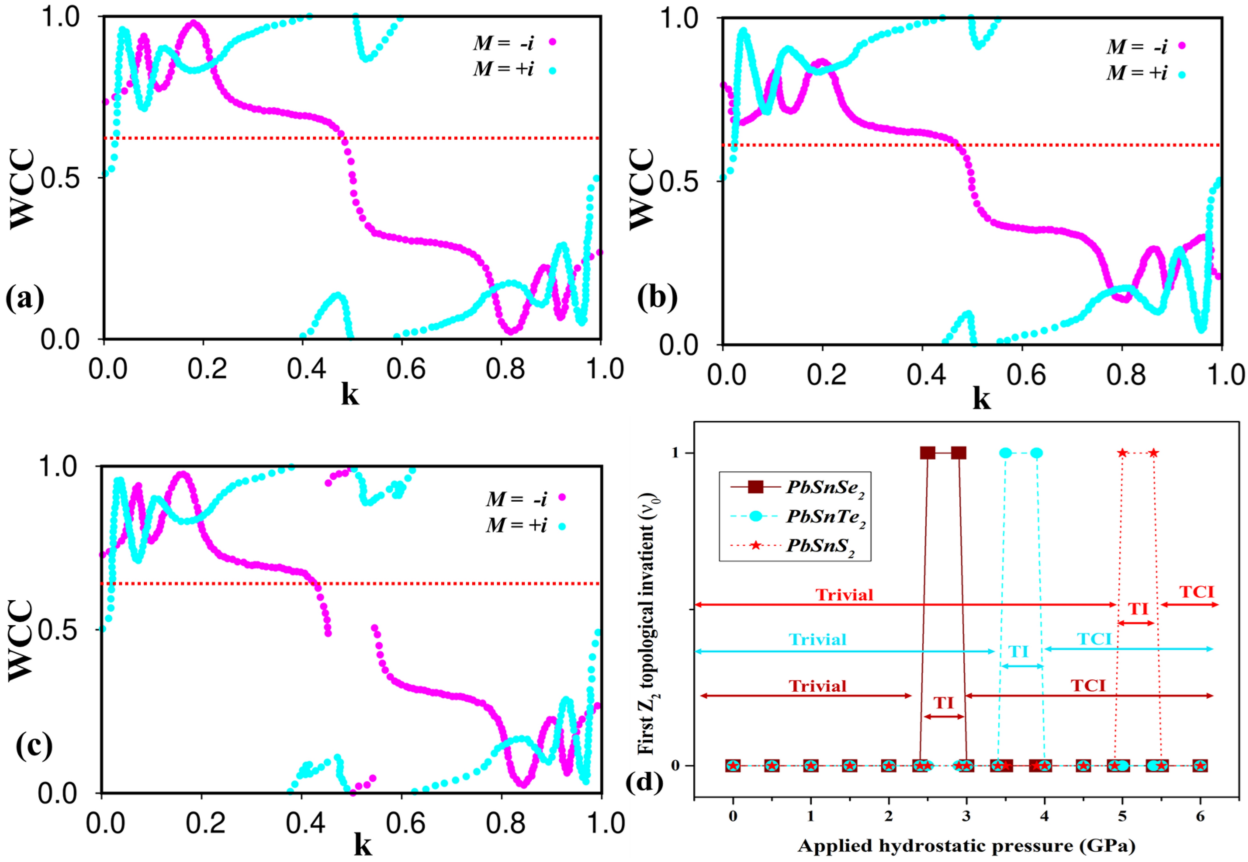

FIG. 6. The evolution of the mirror eigenvalues of $+i$ (magenta) and -i (cyan) in WCC for MCN in (a) $PbSnS_2$, (b) $PbSnSe_2$, and (c) $PbSnTe_2$. (d) The variation of the first Z_2 topological invariant (ν_0) with applied hydrostatic pressure.

materials, with an even number of Dirac cones with respect to the mirror symmetry plane $(\bar{1}0\bar{1})$, which can be calculated using Wannier charge centers (WCC) or Wilson loop along the (111) plane. FIG. 6 (a-c) shows plots of the evolution of WCC for all occupied bands with respect to mirror operator for $(\bar{1}0\bar{1})$ plane. The winding of the WCC of these materials in FIG. 6 (a-c) for mirror eigen values i.e., $+i$ (magenta) and -i (cyan) illustrate that MCN has value 2 along the above-mentioned mirror symmetry. The non-zero even value of MCN and mirror symmetry protected Dirac cone established the TI to TCI phase transitions in $PbSnX_2$ (X=S, Se, Te) materials at 5.5 GPa, 3 GPa and 4 GPa, respectively.

The TPT with the variation of the first Z_2 topological invariant (ν_0) with hydrostatic pressure is illustrated in FIG. 6 (d). $PbSnX_2$ (X=S, Se, Te) materials have shown a transition from topologically trivial to non-trivial phase with an odd number of inversions under hydrostatic pressure of 5 GPa, 2.5 GPa and 3.5 GPa, respectively. Further increase in pressure has

shown another transition from non-trivial to trivial topological phase and even number of inversions at 5.5 GPa, 3 GPa and 4 GPa, respectively. Moreover, the symmetry analysis with $(\bar{1}0\bar{1})$ mirror plane has shown the TCI phase is achieved after the second transition in these materials with an even number of Dirac cones.

F. CONCLUSION

We have systematically studied the structural stability, and electronic and topological properties of the *Sn-based* ternary chalcogenide $PbSnX_2$ (X=S, Se, Te) family under ambient and applied hydrostatic pressure. The TB-mBJ functional has been identified as most relevant *exchange-correlation functionals* for this study based upon the comparative analysis of the band gap of $TlBiS_2$, an experientially synthesized material isostructural to the under-study materials. The phonon dispersion spectrum has confirmed the dynamical stability of these throughout the study. At ambient conditions, $TlBiS_2$, $PbSnSe_2$ and $PbSnTe_2$ have topologically trivial semiconducting nature with direct band gap of 0.338 eV, 0.183 eV and 0.235 eV at *F-point*. An increase in applied the hydrostatic pressure to 5 GPa, 2.5 GPa and 3.5 GPa, respectively, for $PbSnX_2$ (X=S, Se, Te) has led to closing of energy gap at the *F-point*. At these pressure values, the first TPT took place which converts these materials to TIs and the same which has been verified with an odd number of Dirac cones in SDOS and parity analysis at TRIM points. Further enhancement in applied pressure to 5.5 GPa, 3 GPa and 4 GPa, another band inversion has observed at *Γ-point* in the bulk band structure with an even number of Dirac cones along the (111) plane which make these materials topological trivial again. This topologically trivial phase of these materials, however, has identified as TCI phase along $(\bar{1}2\bar{1})$ surface which holding mirror symmetry for $(\bar{1}0\bar{1})$ plane. The SDOS along the k path $\bar{S}-\bar{\Gamma}-\bar{X}$ and $\bar{S}-\bar{Y}-\bar{\Gamma}$ of $(\bar{1}2\bar{1})$ plane has established the mirror symmetry protection for the Dirac cones. This TCI phase has further corroborated with even value of mirror Chern number calculated using the evolution of mirror eigenvalues $\pm i$ in WCC. This kind of transition from trivial to TI to TCI can also be observed in other similar ternary chalcogenides and the pressure-induced surface states can be further studied experimentally with the help of angle and spin-resolved photoemission spectroscopy.

ACKNOWLEDGMENTS

All the authors acknowledge National Supercomputing Mission (NSM) for providing computing resources of 'PARAM Siddhi-AI', under National PARAM Supercomputing Facility (NPSF), C-DAC, Pune and supported by the Ministry of Electronics and Information Technology (MeitY) and Department of Science and Technology (DST), Government of India. One of the authors (Ramesh Kumar) would like to thank the Council of Scientific and Industrial Research (CSIR), Delhi, for financial support.

Author contributions: These authors contributed equally to this work.

Conflict of interest statements: The authors declare no competing financial interest.

References

[1] M. Z. Hasan, and C. L. Kane, Colloquium: Topological insulators, *Rev. Mod. Phys.* **82,** 3045 (2007).

[2] X.-L. Qi, and S.-C. Zhang,Topological insulators and superconductors, *Rev. Mod. Phys.* **83,** 1057 (2011).

[3] H. Zhang, C.-X. Liu, X.-L. Qi, X. Dai, Z. Fang, and S.-C. Zhang, Topological insulators in Bi_2Se_3, Bi_2Te_3 and Sb_2Te_3 with a single dirac cone on the surface, *Nat. Phys.* **5,** 438 (2009).

[4] Y. L. Chen, J. G. Analytis, J.-H. Chu, Z. K. Liu, S.-K. Mo, X. L. Qi, H. J. Zhang, D. H. Lu, X. Dai, Z. Fang, S. C. Zhang, I. R. Fisher, Z. Hussain, and Z.-X. Shen, Experimental realization of a three-dimensional topological insulator, Bi_2Te_3, *Science* **325,** 178 (2009).

[5] Y. Xia, D. Qian, D. Hsieh, L. Wray, A. Pal, H. Lin, A. Bansil, D. Grauer, Y. S. Hor, R. J. Cava, and M. Z. Hasan, Observation of a large-gap topological-insulator class with a single dirac cone on the surface, *Nat. Phys.* **5,** 398 (2009).

[6] L. Fu and C. L. Kane, Topological insulators with inversion symmetry, *Phys. Rev. B* **76,** 045302 (2007).

[7] L. Fu, Topological crystalline insulators, *Phys. Rev. Lett.* **106,** 106802 (2011).

[8] T. H. Hsieh, H. Lin, J. Liu, W. Duan, A. Bansil, and L. Fu, Topological crystalline insulators in the SnTe material class, *Nat. Commun.* **3,** 982 (2012).

[9] Y. Tanaka, Z. Ren, T. Sato, K. Nakayama, S. Souma, T. Takahashi, K. Segawa, and Y. Ando, Experimental realization of a topological crystalline insulator in SnTe, *Nat. Phys.* **8,** 800 (2012).

[10] Z. Wang, Y. Sun, X.-Q. Chen, C. Franchini, G. Xu, H. Weng, X. Dai, and Z. Fang, Dirac semimetal and topological phase transitions in A_3Bi (A = Na, K, Rb),*Phys. Rev. B* **85,** 195320 (2012).

[11] Z. K. Liu, B. Zhou, Y. Zhang, Z. J.Wang, H. M.Weng, D. Prabhakaran, S.-K. Mo, Z. X. Shen, Z. Fang, X. Dai, Z. Hussain, and Y. L. Chen, Discovery of a three-dimensional topological dirac semimetal, NaBi, *Science* **343,** 864 (2014).

[12] B. Q. Lv, H. M. Weng, B. B. Fu, X. P. Wang, H. Miao, J. Ma, P. Richard, X. C. Huang, L. X. Zhao, G. F. Chen, Z. Fang, X. Dai, T. Qian, and H. Ding, Experimental discovery of Weyl semimetal TaAs, *Phys. Rev. X* **5,** 031013 (2015).

[13] S.-Y. Xu, I. Belopolski, N. Alidoust, M. Neupane, G. Bian, C. Zhang, R. Sankar, G. Chang, Z. Yuan, C.-C. Lee, S.-M. Huang, H. Zheng, J. Ma, D. S. Sanchez, B. Wang, A. Bansil, F. Chou, P. P. Shibayev, H. Lin, S. Jia, and M. Z. Hasan, Discovery of a Weyl fermion semimetal and topological Fermi arcs, *Science* **349,** 613 (2015).

[14] Q. Xu, Z. Song, S. Nie, H. Weng, Z. Fang, and X. Dai, Two-dimensional oxide topological insulator with iron-pnictide superconductor LiFeAs structure, *Phys. Rev. B* **92,** 205310 (2015).

[15] J. Hu, Z. Tang, J. Liu, X. Liu, Y. Zhu, D. Graf, K. Myhro, S. Tran, C. N. Lau, J. Wei, and Z. Mao, Evidence of topological nodal-line fermions in ZrSiSe and ZrSiTe, *Phys. Rev. Lett.* **117,** 016602 (2016).

[16] S. Khalid, F. P. Sabino, and A. Janotti, Topological phase transition in LaAs under pressure, *Phys. Rev. B* **98,** 220102 (2018).

[17] P.-J. Guo, H.-C. Yang, K. Liu, and Z.-Y. Lu, Theoretical study of the pressure-induced topological phase transition in LaSb, *Phys. Rev. B* **96,** 081112 (2017).

[18] J.-Z. Ma, J.-B. He, Y.-F. Xu, B. Q. Lv, D. Chen, W.-L. Zhu, S. Zhang, L.-Y. Kong, X. Gao, L.-Y. Rong, Y.-B. Huang, P. Richard, C.-Y. Xi, E. S. Choi, Y. Shao, Y.-L. Wang, H.-J. Gao, X. Dai, C. Fang, H.-M. Weng, G.-F. Chen, T. Qian, and H. Ding, Three-component fermions with surface fermi arcs in tungsten carbide, *Nat. Phys.* **14,** 349 (2018).

[19] J. B. He, D. Chen, W. L. Zhu, S. Zhang, L. X. Zhao, Z. A. Ren, and G. F. Chen, Magnetotransport properties of the triply degenerate node topological semimetal tungsten carbide,

Phys.Rev. B **95,** 195165 (2017).

[20] J. E. Moore, The birth of topological insulators, *Nature* **464,** 194 (2010).

[21] M. He, H. Sun, and Q. L. He, Topological insulator: Spintronics and quantum computations, *Front. Phys.* **14,** 43401 (2019).

[22] Y. Fan and K. L. Wang, Spintronics based on topological insulators, *SPIN* **06,** 1640001 (2016).

[23] X. Li, D. Chen, M. Jin, D. Ma, Y. Ge, J. Sun, W. Guo, H. Sun, J. Han, W. Xiao, J. Duan, Q. Wang, C.-C. Liu, R. Zou, J. Cheng, C. Jin, J. Zhou, J. B. Goodenough, J. Zhu, and Y. Yao, Pressure-induced phase transitions and superconductivity in a quasi 1-dimensional topological crystalline insulator α-Bi_4Br_4, *Proceedings of the National Academy of Sciences* **116,** 17696 (2019).

[24] M. Singh, R. Kumar, and R. K. Bibiyan, Pressure-induced topological phase transition in XMR material YbAs: a first-principles study, *Eur. Phys. J. Plus* **137,** 633 (2022).

[25] P. Wadhwa, S. Kumar, A. Shukla, and R. Kumar, First principles investigation of topological phase in XMR material TmSb under hydrostatic pressure, *J Phys Condens Matter.* **31,** 335401 (2019).

[26] P. Wadhwa, S. Kumar, A. Shukla, and R. Kumar, Studies of non-trivial band topology and electron-hole compensation in YSb, *Solid State Commun.* **321,** 114022 (2020).

[27] R. Kumar and M. Singh, Topological phase transition and tunable surface states in YBi, *J. Phys. Condens. Matter* **36,** 345601 (2020).

[28] I. Y. Sklyadneva, I. P. Rusinov, R. Heid, K.-P. Bohnen, P. M. Echenique, and E. V. Chulkov, Pressure-induced topological phases of KNa_2Bi, *Sci. Rep.* **6,** 24137 (2016).

[29] Y. Qi, W. Shi, P. G. Naumov, N. Kumar, R. Sankar, W. Schnelle, C. Shekhar, F.-C. Chou, C. Felser, B. Yan, and S. A. Medvedev, Topological quantum phase transition and superconductivity induced by pressure in the bismuth tellurohalide BiTeI, *Adv. Mater.* **29,** 1605965 (2017).

[30] M. Yang, Y. Z. Luo, M. G. Zeng, L. Shen, Y. H. Lu, J. Zhou, S. J. Wang, I. K. Sou, and Y. P. Feng, Pressure induced topological phase transition in layered Bi_2S_3, *Phys. Chem. Chem. Phys.* **19,** 29372 (2017).

[31] A. Ohmura, Y. Higuchi, T. Ochiai, M. Kanou, F. Ishikawa, S. Nakano, A. Nakayama, Y. Yamada, and T. Sasagawa, Pressure-induced topological phase transition in the polar semiconductor BiTeBr, *Phys. Rev. B* **95,** 125203 (2017).

[32] H. Ozawa, A. Yamakage, M. Sato, and Y. Tanaka, Topological phase transition in a topological crystalline insulator induced by finite-size effects, *Phys. Rev. B* **90,** 045309 (2014).

[33] M. Ezawa, Topological switch between second-order topological insulators and topological crystalline insulators, *Phys. Rev. Lett.* **121,** 116810 (2018).

[34] W. A. Benalcazar, T. Li, and T. L. Hughes, Quantization of fractional corner charge in Cnsymmetric higher-order topological crystalline insulators, *Phys. Rev. B* **99,** 245151 (2019).

[35] S.-Y. Xu, C. Liu, N. Alidoust, M. Neupane, D. Qian, I. Belopolski, J. D. Denlinger, Y. J. Wang, H. Lin, L. A. Wray, G. Landolt, B. Slomski, J. H. Dil, A. Marcinkova, E. Morosan, Q. Gibson, R. Sankar, F. C. Chou, R. J. Cava, A. Bansil, and M. Z. Hasan, Observation of a topological crystalline insulator phase and topological phase transition in $Pb_{1-x}Sn_xTe$, *Nat. Commun.* **3,** 1192 (2012).

[36] P. Dziawa, B. J. Kowalski, K. Dybko, R. Buczko, A. Szczerbakow, M. Szot, E. Lusakowska, T. Balasubramanian, B. M. Wojek, M. H. Berntsen, O. Tjernberg, and T. Story, Topological crystalline insulator states in $Pb_{1-x}Sn_xSe$, *Nat. Mater.* **11,** 1023 (2012).

[37] S. Ma, C. Guo, C. Xiao, F. Wu, M. Smidman, Y. Lu, H. Yuan, and H. Wu, Realization of a new topological crystalline insulator and lifshitz transition in PbTe, *Adv. Funct. Mater.* **28,** 1803188 (2018).

[38] Y. Sun, Z. Zhong, T. Shirakawa, C. Franchini, D. Li, Y. Li, S. Yunoki, and X.-Q. Chen, Rocksalt SnS and SnSe: Native topological crystalline insulators, *Phys. Rev. B* **88,** 235122 (2013).

[39] C. Niu, P. M. Buhl, G. Bihlmayer, D. Wortmann, S. Bl¨ugel, and Y. Mokrousov, Twodimensional topological crystalline insulator and topological phase transition in TlSe and TlS monolayers, *Nano Lett.* **15,** 6071 (2015).

[40] H. Lin, R. S. Markiewicz, L. A. Wray, L. Fu, M. Z. Hasan, and A. Bansil, Single-dirac-cone topological surface states in the $TlBiSe_2$ class of topological semiconductors, *Phys. Rev. Lett.* **105,** 036404 (2010).

[41] S. V. Eremeev, G. Bihlmayer, M. Vergniory, Y. M. Koroteev, T. V. Menshchikova, J. Henk, A. Ernst, and E. V. Chulkov, Ab initio electronic structure of thallium-based topological insulators, *Phys. Rev. B* **83,** 205129 (2011).

[42] Q. Zhang, Y. Cheng, and U. Schwingenschl¨ogl, Emergence of topological and topological crystalline phases in $TlBiS_2$ and $TlSbS_2$, *Sci. Rep.* **5,** 8379 (2015).

[43] P. Hohenberg and W. Kohn, Inhomogeneous electron gas, *Phys. Rev.* **136,** B864 (1964).

[44] W. Kohn and L. J. Sham, Self-consistent equations including exchange and correlation effects, *Phys. Rev.* **140,** A1133 (1965).

[45] G. Kresse and D. Joubert, From ultrasoft pseudopotentials to the projector augmented-wave method, *Phys. Rev. B* **59,** 1758 (1999).

[46] G. Kresse and J. Furthmuller, Efficient iterative schemes for ab initio total-energy calculations using a plane-wave basis set, *Phys. Rev. B* **54,** 11169 (1996).

[47] J. P. Perdew, K. Burke, and M. Ernzerhof, Generalized gradient approximation made simple, *Phys. Rev. Lett.* **77,** 3865 (1996).

[48] F. Tran and P. Blaha, Accurate band gaps of semiconductors and insulators with a semilocal exchange-correlation potential, *Phys. Rev. Lett.* **102,** 226401 (2009).

[49] A. Togo and I. Tanaka, First principles phonon calculations in materials science, *Scr. Mater.* **108,** 1 (2015).

[50] N. Marzari, A. A. Mostofi, J. R. Yates, I. Souza, and D. Vanderbilt, Maximally localized wannier functions: Theory and applications, *Rev. Mod. Phys.* **84,** 1419 (2012).

[51] Q. Wu, S. Zhang, H.-F. Song, M. Troyer, and A. A. Soluyanov, Wanniertools: An open-source software package for novel topological materials, *Comput. Phys. Commun.* **224,** 405 (2018).

[52] M. Ozer, K. M. Paraskevopoulos, A. N. Anagnostopoulos, S. Kokou, and E. K. Polychroniadis, Large single-crystal growth and characterization of the narrow-gap semiconductor, *Semicond. Sci. Technol.* **11,** 1405 (1996).

[53] B. Singh, H. Lin, R. Prasad, and A. Bansil, Topological phase transition and quantum spin Hall state in $TlBiS_2$, *J. Appl. Phys.* **116,** 033704 (2014).

[54] A. N. Veis, D. D. Koditsa, and N. S. Popovich, Optical properties of $TlBiS_2$ monocrystals, *physica status solidi (a)* **107,** K169 (1988).

[55] O. Valassiades, E. K. Polychroniadis, J. Stoemenos, and N. A. Economou, On the disordered nature of single crystalline $TlBiTe_2$ and its influence on its electrical properties, *physica status solidi (a)* **65,** 215 (1981).

[56] C. L. Mitsas, D. I. Siapkas, E. K. Polychroniadis, O. Valassiades, and K. M. Paraskevopoulos, Growth, electrical, and optical properties of $TlBiSe_2$ single crystals, *physica status solidi (a)* **136,** 483 (1993).

[57] Y. Tanaka, Z. Ren, T. Sato, K. Nakayama, S. Souma, T. Takahashi, K. Segawa, and Y.

Ando, Experimental realization of a topological crystalline insulator in SnTe, *Nat. Phys.* **8,** 800 (2012).

[58] T. H. Hsieh, H. Lin, J. Liu, W. Duan, A. Bansil, and L. Fu, Topological crystalline insulators in the SnTe material class, *Nat. Commun.* **3,** 982 (2012).

Plasmonics
https://doi.org/10.1007/s11468-024-02642-5

RESEARCH

Highly Sensitive Graded Index PCF-Based Refractometric SPR Sensor Offering Enhanced FOM

Akash Khamaru[1] · **Ajeet Kumar**[1]

Received: 11 October 2024 / Accepted: 5 November 2024
© The Author(s), under exclusive licence to Springer Science+Business Media, LLC, part of Springer Nature 2024

Abstract

In this proposed work, a novel graded index photonic crystal fiber (GI-PCF) with gold-TiO_2 layered coating is presented as a surface plasmon resonance (SPR)-based refractive index sensor for a wide range of refractive indices. Present fiber is characterized by two types of air holes: one having gradually increasing radius and other having constant radius. The performance of the proposed sensor is tested on wavelength sensitivity (WS), amplitude sensitivity (AS), sensor resolution, and figure of merit (FOM). Detailed modal analysis of the designed SPR sensor is analyzed by the finite element method. Structural design optimization has been analyzed with respect to various different structural parameters, such as the radius of different air holes, the inherent grading of holes, and the thickness of gold and TiO_2 layers. Our detailed analysis summarized the effectiveness of graded design over conventional design. The calculation result shows a high WS of 22,600 nm/RIU. Apart from high WS, an enhanced AS of -1410 RIU^{-1} is also observed, which is a key highlight of our PCF sensor. Further, the sensor's resolution is also obtained having a magnitude of 4.43×10^{-6} RIU and FOM is 403.57 RIU^{-1}. Thus, the GI-PCF sensor proves its excellent ability to measure both wavelength and amplitude sensitivity with excellent FOM for a wide range of refractive indices. Such a sensor can find its application in various sensing areas, i.e., biomedical, chemical, and industrial field. Apart from promising numerical values, the PCF structure is also possible to fabricate using currently existing fabrication techniques.

Keywords Surface plasmon resonance · Photonic crystal fiber · Graded index · Amplitude sensitivity

Introduction

Fiber optic-based sensing devices are advancements over conventional sensing devices, and the key factors evaluating these advancements are relatively ultra-lightweight, smaller dimensions, immune to electromagnetic interference, and enhanced temperature performance with very high bandwidth [1]. Various physical properties like strain [2], temperature [3], pressure [4], and electric and magnetic fields [5, 6] are measurable by optical fiber-based sensors. Chemical variations can also be sensed by these proposed sensors [7, 8]. They are proven as environmentally ideal sensors since they are inert chemically and fully functional under corrosive environmental conditions. Numerous technologies have already been proposed for fiber-optic-based sensing like micro-interferometric (MI) [9], fiber grating plasmonic (FGP) method [10], surface plasmon resonance (SPR) phenomena [11–14], optofluidic laser sensing (OLS) [15], and Terahertz sensing [16]. SPR phenomena result in an appreciable method for sensing due to highly precise and accurate detection capabilities with no labeling nature. SPR provides the detection results in real-time. Initially, the prism-coupling-based SPR sensing setup was proposed and modified by Otto and Kretschman, respectively [17, 18]. The setup consists of a prism layered by a conducting metal layer with an analyte layer at the top. The setup deals with the principle of attenuated total reflection (ATR). When an incident light beam strikes the prism surface at angle θ ($\theta > \theta_{atr}$), an evanescent wave is generated which further gives birth to surface plasmons. The coupling mode theory states that SPR will occur when the evanescent wave and generated surface plasmons get matched with their respective power

✉ Ajeet Kumar
ajeetdph@dtu.ac.in

Akash Khamaru
akashkhamaru@gmail.com

[1] Advanced Photonics Simulation Research Laboratory, Department of Applied Physics, Delhi Technological University, Bawana Road, Delhi 110042, India

Published online: 12 November 2024

and frequency. Different types of analytes generate resonant conditions at different frequencies. The difference in the frequencies will help to justify our sensor's efficiency. The proposed prism-based SPR sensors are efficient but very bulky and costly, limiting this setup's usage. To overcome this limitation, fiber-based SPR sensors are introduced, which are miniature, easy to handle, and economically stable. Fiber-based SPR sensors are almost similar to prism-based SPR sensors in working, where the prism-metal layer interface is replaced by a fiber core-metal layer interface. Apart from this, the condition for resonance is also found by varying the input laser's wavelength in the optical fiber. In contrast, the prism-coupling technique gets resonance by varying the incident angle.

The plasmonic materials are employed for the formation of the core-metal layer interface. Gold (Au), silver (Ag), TiO_2, and copper (Cu) are the widely used plasmonic materials [19]. Gold and silver show better sensitivity than other competing plasmonic materials. Silver is prone to environmental oxidation which reduces the chance of employing it as plasmonic metal, whereas gold exhibits high chemical stability [20, 21]. Therefore, gold arises as the best counterpart in regard to all plasmonic materials. To perfectly align gold with PCF structure, the TiO_2 layer can be incorporated as an adhesive agent. Apart from adhesive nature, TiO_2 helps in enhancing the sensitivity and protects the metal from corrosion. TiO_2 is cost-effective and non-toxic in nature which makes it popular among SPR researches [22, 23].

In the current scenario, traditional optical fibers are already advanced and have been transformed into a new alternative called photonic crystal fibers (PCFs). PCFs inherit the micro-structured holey lattice of several air holes perforated on a nonlinear material, automatically enhancing properties like geometrical tunability and exhibiting a flexible preform. The applications of PCFs are booming in the current research scenario, such as in supercontinuum generation [24–26], terahertz communication [27, 28], and slow light generation [29, 30]. In PCFs, there exist two types of SPR sensing: one is intrinsic analyte sensing, and another is extrinsic analyte sensing. In intrinsic analyte sensing, the air holes are layered with plasmonic material, and analytes are infiltrated into the air holes for sensing purpose. The infiltration of analyte into the air holes is very difficult to conduct with available experimental setups, which discourages researchers from conducting this particular way of sensing. The extrinsic sensors are analyzed by the analyte flooded outside the sensor's cross-section, which results in a more favorable way of measuring sensitivity and has benefits like ease of production, ease in layer deposition, and simple analyte filling probe. Numerous works are already been done in the field of extrinsic PCF SPR sensors. PCF-based SPR refractive index (RI) sensors had already covered a huge chunk of sensor-based research and respective literatures. The recent literatures give various evidence of SPR sensor advancements. In 2023, Erdogan et al. had proposed an Au-TiO_2 D-shaped PCF sensor and demonstrated it with high sensitivity of 12,415 nm/RIU for a RI range of 1.33–1.4 [22]. The same researchers had proposed sensitivity of 11,775 nm/RIU by employing MoS_2/graphene-based PCF SPR sensor [23]. Majeed et al. had proposed a dual-open microchannel refractometric SPR-PCF sensor which has shown very nice agreement of wavelength sensitivity (WS) and amplitude sensitivity (AS) with higher magnitudes like 3743.64 RIU^{-1} and 33,000 nm/RIU at a refractive index of 1.43 [31]. In the same timeframe, an SPR double-side polished PCF was introduced by Ullah et al., which displayed its capability to sense refractive index (1.30–1.40) and extracted the highest WS as 9400 nm/RIU [32]. A shifted core approach has already been proposed by Melwin et al., which devised the highest WS at the magnitude of 24,200 nm/RIU in the range of refractive index from 1.33 to 1.39 [33]. The devised SPR-PCF model has also delivered AS as 432 RIU^{-1}. Ramani et al. had proposed a dual-core PCF SPR sensor and extracted maximum AS as 378 RIU^{-1} [34]. A U-shaped PCF SPR sensor is proposed by Guo et al. and operated it for a wide range of RI's (1.2–1.43) with high sensitivity of 10,200 nm/RIU (1.2–1.3) and 5900 nm/RIU (1.36–1.43) [35]. Similarly, Ding et al. had extracted high sensitivity of 33,000 nm/RIU recently with a wide range of RI from 1.25 to 1.36 [36]. Qiu et al. had designed an Au-TiO_2 PCF sensor to detect low RI's ranging from 1.18 to 1.28 and achieved a sensitivity of 21,500 nm/RIU [37].

In the present work, an external sensing-based GI-PCF SPR sensor is introduced, having graded index air holes with silica as the background component and gold as plasmonic layered material. The PCF SPR sensor exhibits a teardrop-shaped core. Another plasmonic material TiO_2 is also added to use as an adhesive agent for firmly attaching the gold with the background material and also emphasizing the sensitivity of the proposed sensor as incurred from previous literatures. A wide range of RI-based analytes are flooded on the top of SPR sensor for recording the sensitivity. Confinement loss of the proposed design has been utilized to precisely achieve the resonance condition. The resonant conditions are also varied with the aid of optimization of the different geometrical parameters. Several parameters like amplitude sensitivity, wavelength sensitivity, and figure of merit (FOM) are calculated at every possible geometrical parametric values. This provides the gateway towards the final optimization of the geometrical parameters. The comparison is also done with respect to the current literatures to justify the advantageous aspect of our proposed PCF sensor.

Structural Parameters of Proposed Graded Index PCF SPR Sensor

The designed two-dimensional cross-section of the GI-PCF sensor is displayed in Fig. 1. The specially designed fiber consists of two types of air holes: (i) one with gradually increasing radius (r_1 and Δr_1) and (ii) another with constant radius (r_2). Graded index air holes are located at angles of 0°, 45°, 90°, 135°, and 180°. Gradually increase in radius is denoted by Δr_1. The graded index lattice helps to confine and guide the core mode to couple to plasmon modes. This also minimizes the FWHM which enhances the FOM of the sensor. The shape contains another set of air holes near the plasmonic layer having a radius denoted by r_2, which adds an improvement in the coupling of the generated evanescent wave with the layered plasmonic material. The plasmonic material is taken as gold with thickness, and the same is layered along with TiO_2 having thickness on the top of the proposed fiber SPR sensor. The meshing parameters of the proposed structure are also calculated by the simulation program, having such magnitudes as 35,240 domain elements and 3474 boundary elements displayed in Fig. 1.

The background of the proposed PCF SPR sensor is composed of fused silica. The given Sellmeier equation specifies the RI of fused silica, and respective constant terms are tabulated in Table 1 [34]:

$$n^2(\lambda) = 1 + \frac{B_1\lambda^2}{\lambda^2 - C_1} + \frac{B_2\lambda^2}{\lambda^2 - C_2} + \frac{B_3\lambda^2}{\lambda^2 - C_3} \quad (1)$$

The RI of gold is measured by the Drude-Lorentz model, which provides the wavelength-dependent RI of the proposed plasmonic material [34]. Table 2 provides the applied constant terms:

Table 1 Constants for Sellmeier equation of fused silica glass

Constants	Magnitudes
B_1	0.6961663
B_2	0.4079426
B_3	0.8974794
C_1	0.0684043 μm^2
C_2	0.1162414 μm^2
C_3	9.896161μm^2

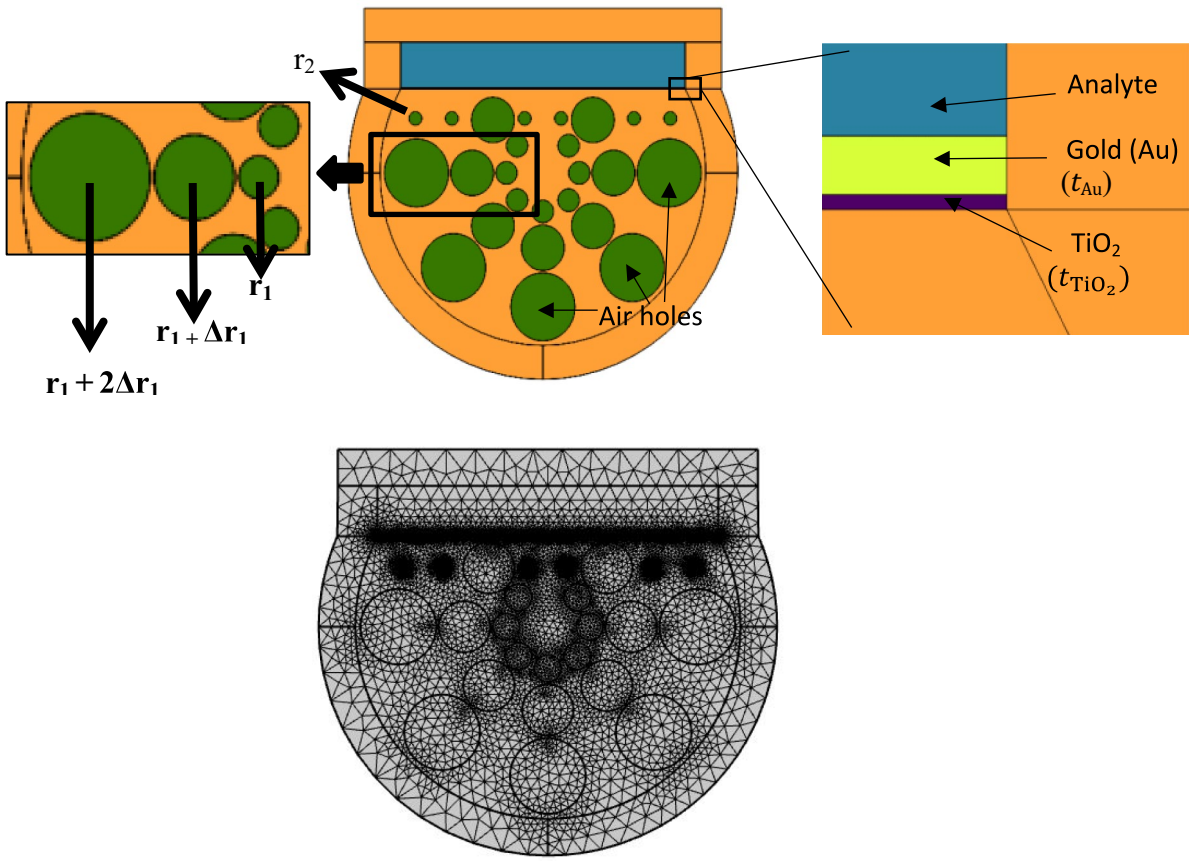

Fig. 1 Proposed GI-PCF SPR sensor with mesh frame

Table 2 Constants for Drude-Lorentz model of gold

ε_a	ω_D	γ_D	$\Delta\varepsilon$	Ω_L	Γ_L
Permittivity at higher frequency	Plasma frequency	Damping frequency	Weighting factor	Strength of oscillator	Spectral width of Lorentz oscillator
5.9673	13,280.14 THz	100.03 THz	1.09	4084.51 THz	658.85 THz

Table 3 Constants for wavelength-dependent refractive index of TiO_2

Constants	Magnitudes
A	5.913
B	2.441×10^7
C	0.803×10^7

$$n_{Au}^2 = \varepsilon_{Au} = \varepsilon_a - \frac{\omega_D^2}{\omega\left(\omega + j\gamma_D\right)} - \frac{\Delta\varepsilon\Omega_L^2}{\left(\left(\omega^2 - \Omega_L^2\right) + j\Gamma_L\omega\right)} \quad (2)$$

For adhesion purpose, TiO_2 layer is introduced in between silica and gold layer. Equation 3 has been used to formulate the RI of TiO_2 layer [34]. Values of constants used are tabulated in Table 3.

$$n(\lambda) = \sqrt{\left[A + \frac{B\lambda^2}{\lambda^2 - C^2}\right]} \quad (3)$$

The performance of the devised sensor is examined by measuring the confinement loss of the core mode by implementing the following equation [34]:

$$\alpha_{\text{loss}} = 8.686 \times \frac{2\pi}{\lambda} \times Im\left(n_{\text{eff}}\right) \times 10^4 \left[\frac{\text{dB}}{\text{cm}}\right], (\lambda \text{ is in } \mu\text{m}) \quad (4)$$

In the above equation, $Im(n_{\text{eff}})$ denotes the imaginary segment of the effective index, and λ defines the wavelength of the light. The numerical simulation for the proposed SPR sensor is done by the COMSOL Multiphysics, which implements a finite element method (FEM)-based simulation tool to solve Maxwell's equation (in the form of partial differential equations) of respective electric field and magnetic field associated with universally divided triangular mesh components of the proposed 2D sensor. To get rid of the outer electromagnetic radiations, a perfectly matched layer (PML) is associated outside the cross-section of the sensor.

The main aspects to examine our sensor's performance are wavelength sensitivity (WS), amplitude sensitivity (AS), FOM, and resolution. The WS defines the capability of the sensor to respond to a minor change in the operating wavelength with respect to a change in RI of the analyte. This method is interrogated by spectral exploitation. The same is measured by Eq. 5 and the respective sensor's resolution is calculated by Eq. 6 [34]:

$$S_\lambda = \frac{\Delta\lambda_{peak}}{\Delta n_a}\left[nm/RIU\right] \quad (5)$$

$$R = \Delta n_a \times \frac{\Delta\lambda_{\min}}{\Delta\lambda_{\text{FWHM}}}[RIU] \quad (6)$$

In the above equations, $\Delta\lambda_{\text{peak}}$ denotes the shift in the peak wavelength, and Δn_a determines the difference between two adjacent RI of the analytes. $\Delta\lambda_{\min}$ denotes the minimum spectral resolution (0.1 nm), and the difference between two FWHM magnitudes is defined by $\Delta\lambda_{\text{FWHM}}$.

AS determines another type of sensitivity interrogation technique which is cost-efficient and simpler than the analysis of wavelength sensitivity due to the absence of spectral manipulation, and the same is analyzed by given Eq. 7 [34]:

$$S_A(\lambda) = -\frac{1}{\alpha\left(\lambda, n_a\right)}\frac{\partial\alpha\left(\lambda, n_a\right)}{\partial n_a}\left[RIU^{-1}\right] \quad (7)$$

The above equation consists of $\alpha\left(\lambda, n_a\right)$ which defines the confinement loss at a certain wavelength; $\partial\alpha\left(\lambda, n_a\right)$ determines the loss difference between two consecutive analytes at the same wavelength, and ∂n_a denotes the difference between RI's of two analytes. FOM is another sensing parameter which helps to examine the efficiency of the sensor and calculated by [34]:

$$\text{FOM} = \frac{S_\lambda}{\text{FWHM}}\left[RIU^{-1}\right] \quad (8)$$

Simulation Results and Discussions

Analysis of SPP Mode and Core Mode

Coupling of core mode with surface plasmon mode is the principle of generation of SPR-based sensor. Coupling makes the fiber leaky. When this coupling reaches a condition where the effective mode index of core mode matches with the SPP mode, it is called the resonance condition or phase-matching condition. In this condition, most of the power of core mode leaks from the core to the cladding. The wavelength at which this phenomenon occurs is called

resonance wavelength (λ_{peak}). The condition is shown in Fig. 2a. The electric field distribution of core mode, SPP mode, and SPR mode is displayed in Fig. 2(b–d). The confinement loss of the core mode will be largest at the resonance condition since the core and SPP modes are coupling. On changing the RI of the analyte, the wavelength of peak confinement loss is also changing. The change in the peak loss wavelength helps to determine the WS of the proposed sensor, and the respective loss magnitudes help to determine the corresponding amplitude sensitivity. Therefore, for the purpose of extracting a better sensitivity, we need to optimize our structural parameters such as r_1, Δr_1, r_2, t_{Au}, and t_{TiO_2}.

Study of Influence of Variation in r_1 on Sensitivity Measurement

In the first step of optimization of the geometrical parameters, we have tested the effect of the first set of air holes having radius r_1 on the confinement loss that actually governs the sensing performance of the design. The value of r_1 is changed from 400 to 500 nm at an interval of 50 nm. The rest of parameters exhibits constant magnitudes: $\Delta r_1 = 500$ nm, $r_2 = 300$ nm, $t_{TiO_2} = 10$nm, and $t_{Au} = 40$ nm. For the proposed set of geometrical parameters, spectral variation of the confinement loss has been calculated for analytes having RI 1.38 and 1.39 at different values of r_1 and displayed in Fig. 3. Generally, the devised dataset will provide us the sensitivity of 1.38 analyte RI and helps to observe the nature of the WS and AS at different r_1 values. On increasing the magnitude of r_1, the peak of loss curve gets red-shifted, i.e., λ_{peak} shifted from 754 to 784 nm for 1.38 RI and also suffered by FWHM broadening. The respective WS and AS are increasing at each successive r_1. Higher value of r_1 reduces the effective core area for the light confinement in the core region. As a result, more light is concentrated towards the plasmonic layer. This increases the chances for proper mode coupling and automatically enhances the loss as well as WS. From observation, $r_1 = 600$ nm provides the best sensitivity but offers broad FWHM which ultimately deteriorates the FOM of the sensor. Therefore, the overall best scenario arrives for $r_1 = 550$ nm that delivers a better sensitivity with acceptable FWHM, enhancing the proposed sensor's FOM.

Study of Influence of Variation in Δr_1 on Sensitivity Measurement

The next study is concentrated on the influence of Δr_1 which is changed from 300 to 500 nm at an interval of 100 nm with constant magnitudes of $r_1 = 550$ nm, $t_{TiO_2} = 10$ nm, and $t_{Au} = 40$ nm. The study shown in Fig. 4 shows that the increment in grading Δr_1 decrease the WS and FWHM both. The fact also justifies that FWHM will be highest for non-graded lattice structure and gradually decreases with grading lattice

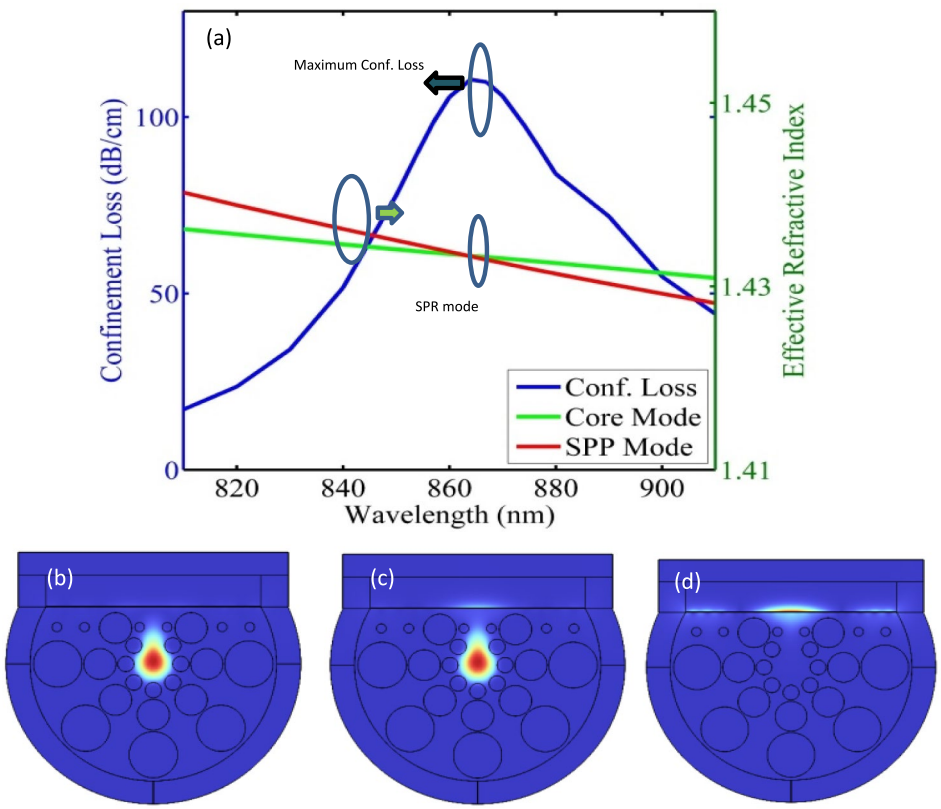

Fig. 2 **a** Representation of effective mode coupling and maximum loss at 864 nm for 1.39 RI. **b–d** Core mode (800 nm @ 1.39), SPR mode (864 nm @ 1.39), SPP mode (800 nm @ 1.39)

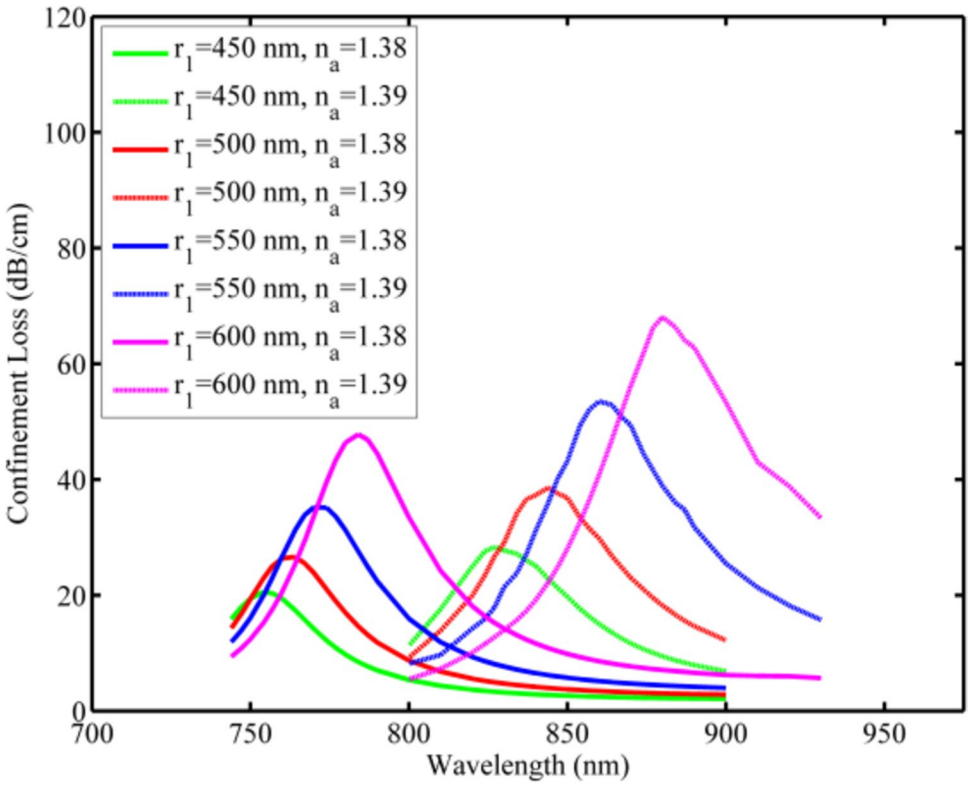

Fig. 3 Corresponding loss curves for 1.38 and 1.39 RI at different values of r_1

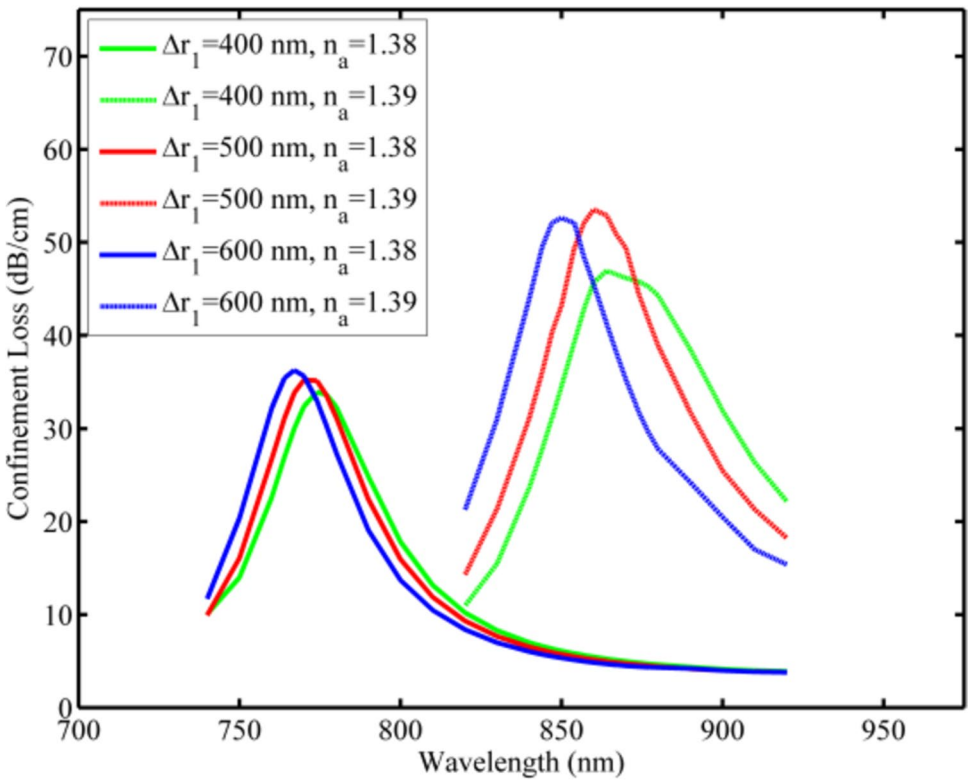

Fig. 4 Corresponding loss curves for 1.38 and 1.39 RI at different values of Δr_1

incorporation. Therefore, the graded index structure is chosen to enhance the FOM of the structure by minimizing the FWHM. From the overall study, it is clear that the grading (Δr_1) adopted the optimized value as 500 nm as it delivers a better output of WS (~9000 nm/RIU) and AS (~967 RIU^{-1}) along with nominal FWHM enhancing the sensor's FOM.

Study of Influence of Variation in r_2 on Sensitivity Measurement

The third optimization approach is done for the parameter denoted as r_2, which defines the second set of air holes placed just near the plasmonic material which obstruct the core mode to directly couple with the plasmonic material's SPP mode. It creates a better passage for the core mode to couple with SPP mode. The radius r_2 is changed from 200 to 350 nm with the increment value of 50 nm and displayed in Fig. 5. On increasing the r_2, the core mode's coupling with plasmonic material is obstructed; therefore, the peak loss gets slightly blue shifted and suffers high decrement in loss. WS slightly reduced and FWHM slightly increased with r_2. The conclusion derives that 250 nm is the optimized value for r_2 due to enhanced sensitivity (9400 nm/RIU and − 1004 RIU^{-1}) with small FWHM. The value of $r_2 < 250$ nm may suffer from the fabrication challenges with present experimental methods.

Study of Influence of Variation in t_{TiO_2} on Sensitivity Measurement

This study determines the influence of the thickness of TiO_2 (t_{TiO_2}) on both types of sensitivity calculation. The effect of thickness of the TiO_2 layer on confinement loss is shown in Fig. 6. λ_{peak} shows red-shifted behavior when t_{TiO2} is increased from 8 to 14 nm in the step of 2 nm. The value of the confinement loss (peak value) also decreases with an increase in the metal thickness. Increase in t_{TiO_2} weakens the incoming evanescent wave, which consequently affects the AS of the sensor. The WS and FWHM is not influenced significantly with t_{TiO_2}, only a slight increment is observed. At t_{TiO_2} = 10nm, the sensor demonstrates the WS (9400 nm/RIU), FWHM (~ 43 nm), excellent FOM (~ 218.6 RIU^{-1}) and a high AS (~ 1004.8 RIU^{-1}). Thus, we have chosen t_{TiO_2} = 10nm as an optimized parameter.

Study of Influence of Variation in t_{Au} on Sensitivity Measurement

At the final step of the study, we changed the thickness of the gold (t_{Au}) from 30 to 45 nm in a step of 5 nm. On increasing the thickness of the gold layer, the confinement loss started decreasing as the thick layer reduces the effect of the evanescent field. The effect is summarized in Fig. 7. The WS and FWHM both increase with the gold thickness. t_{Au} = 40 nm has been chosen as the optimized value, as this offers better WS and AS from the sensor with optimum FWHM and respective FOM. Further, an increase in t_{Au} consequently increases the FWHM, which affects the FOM of the sensor.

Wavelength and Amplitude Sensitivity—Optimized Geometrical Parameters

From previous sections, clear conclusions are drawn with the optimization of the structural parameters. The optimized parameters are tabulated in Table 4.

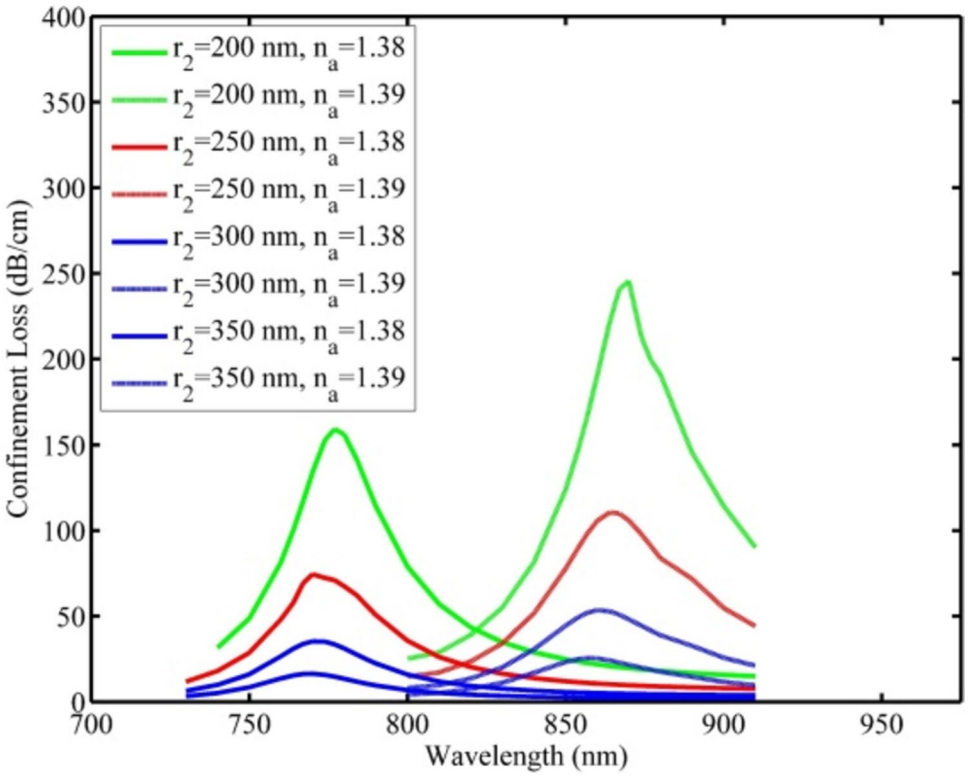

Fig. 5 Corresponding loss curves for 1.38 and 1.39 RI at different values of r_2

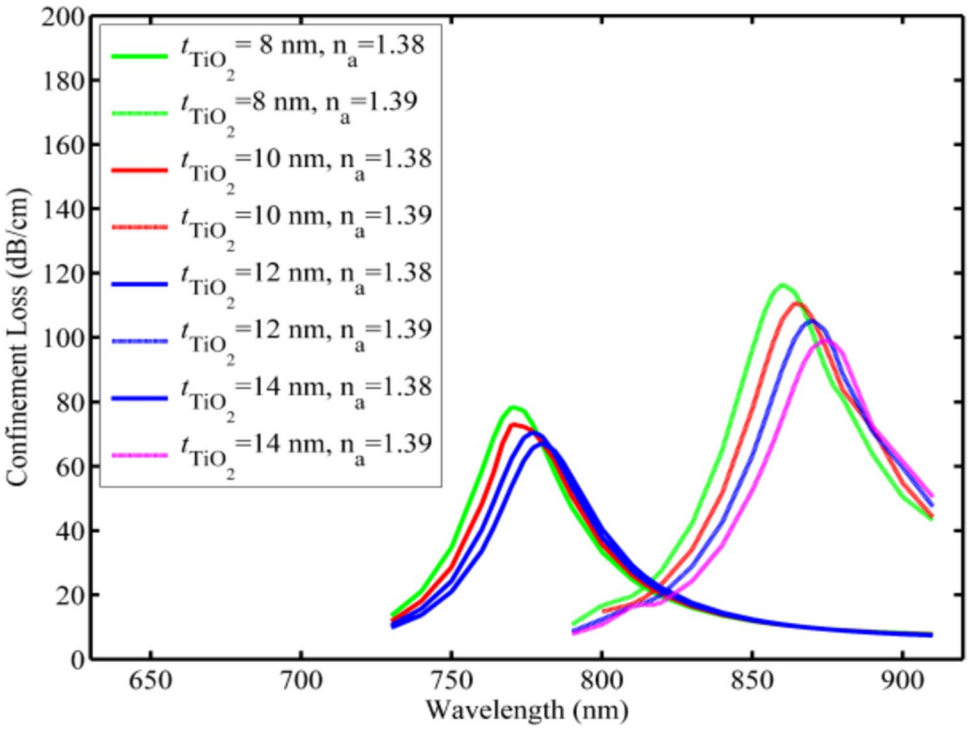

Fig. 6 Corresponding loss curves for 1.38 and 1.39 RI at different values of t_{TiO_2}

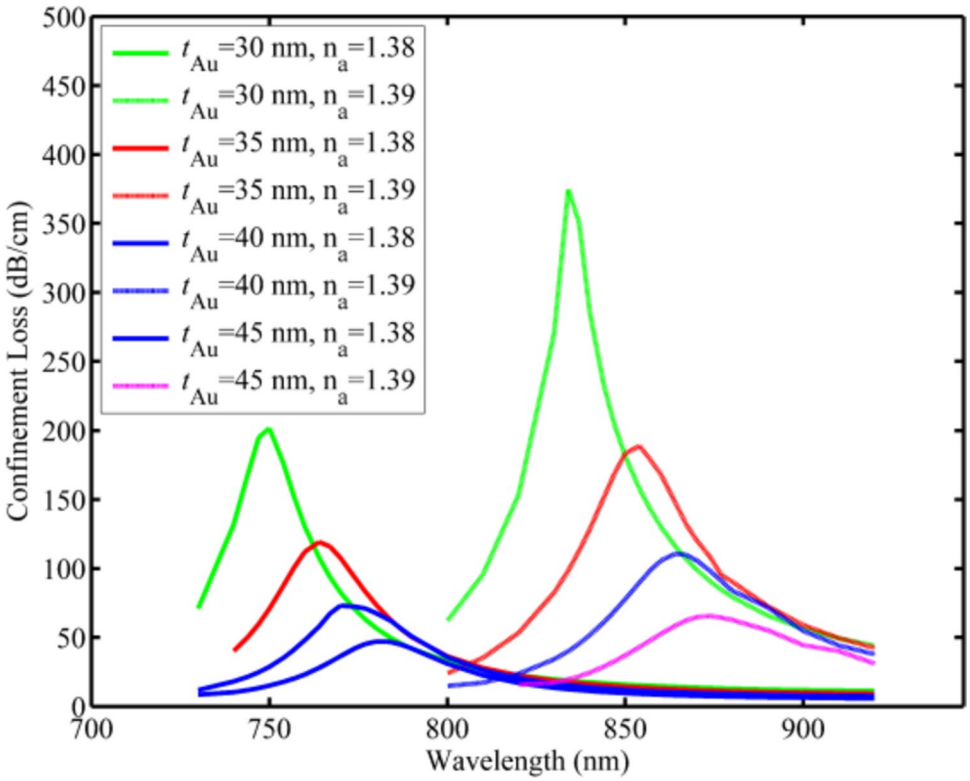

Fig. 7 Corresponding loss curves for 1.38 and 1.39 RI at different values of t_{Au}

At the final step of the study of the proposed research work, spectral analysis (< 2.5 μm (silica's material absorption limit)) has been done for a wide range of analyte having RI's from 1.31 to 1.4 and observed the sensitivity for the same range of analytes. The variation in loss spectra of different types of analytes is shown in Fig. 8. Detailed analyses reveal a maximum WS of 22,600 nm/RIU for analyte having RI 1.39 with a maximum resolution of 4.4×10^{-6} RIU for

a minimum spectral resolution of 0.1 nm. Apart from WS, AS is also calculated for such a wide range of analytes. The maximum AS is obtained as high as 1410.27 RIU^{-1}. The proposed sensor also offers a high FOM of 403.57 RIU^{-1}. Table 5 displays the performance assessment profile of our designed GI-PCF SPR sensor. The variation of λ_{peak} with analyte is shown in Fig. 9. To display the relation between resonant wavelength and analyte RI, a fourth-order polynomial is fitted with coefficients tabulated in Table 6. The polynomial fitted curve strongly agrees with the provided data points and makes the sensor more sensible to practical variations. The goodness of is observed by R-square term which is 0.9957 in our case. The term is near to unity, which concludes that relation is best fitted.

Table 4 Optimized structural parameters

r_1	Δr_1	r_2	t_{TiO_2}	t_{Au}
550 nm	500 nm	250 nm	10 nm	40 nm

Fabrication Tolerance, Methodology, and Experimental Setup for Proposed SPR Sensing

The proposed graded index PCF SPR sensor is designed by maintaining a well agreement with real-life implications for sensing. Silica PCF can be fabricated by stack and draw techniques [38]. The nm-range air holes can be perforated better by the UV pulse ablation process of different dimensions [39]. The next step is etching of the top part of the fabricated PCF to make a flat surface for plasmonic layer deposition. The plasmonic layers like gold and TiO_2 can be deposited on the flat surface by available processes like pulsed laser deposition and radio frequency sputtering [40, 41]. The experimental setup for graded index PCF sensors is interpreted as a schematic representation and displayed in Fig. 10. The laser source (NIR laser diode from Thorlabs may be used [42]) may be used for spectral investigation of PCF sensor, and the loss spectrum and resonant conditions are observed in optical spectrum analyzer (OSA) [45].

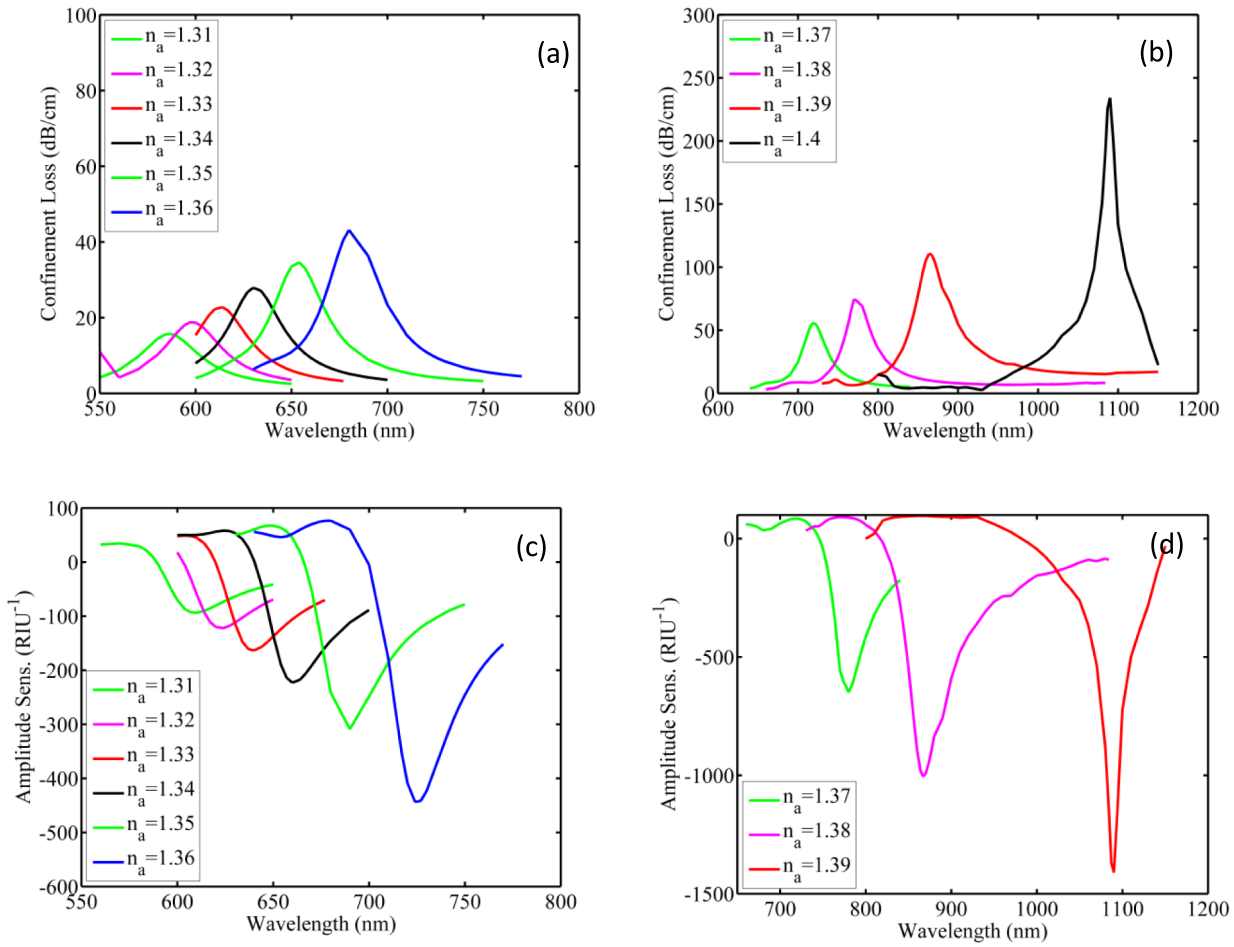

Fig. 8 Performance of proposed GI-PCF SPR Sensor: Confinement Loss **a** RI 1.31-1.36 **b** RI 1.37-1.4 & Amplitude Sensitivity **c** RI 1.31-1.36 **d** RI 1.37-1.39

Table 5 Performance assessment of the proposed GI-PCF SPR sensor

Analyte RI	Resonant wavelength (nm)	Loss (dB/cm)	Shift in resonant wavelength (nm)	WS (nm/RIU)	AS (RIU^{-1})	Resolution (RIU)	FWHM (nm)	FOM (RIU^{-1})
1.31	587	15.70	10	1000	−93.86	1×10^{-4}	45	22.22
1.32	597	18.75	17	1700	−122.20	5.9×10^{-5}	41	41.46
1.33	614	22.75	16	1600	−163.50	6.3×10^{-5}	37	43.24
1.34	630	27.89	24	2400	−223.10	4.2×10^{-5}	38	63.16
1.35	654	34.56	26	2600	−309.11	3.8×10^{-5}	37	70.27
1.36	680	43.13	40	4000	−443.62	2.5×10^{-5}	38	105.26
1.37	720	55.87	50	5000	−649.29	2×10^{-5}	39	128.21
1.38	770	74.47	94	9400	−1004.8	1.1×10^{-5}	43	218.60
1.39	864	110.60	226	22,600	−1410.27	4.4×10^{-6}	56	403.57
1.4	1090	234.22						

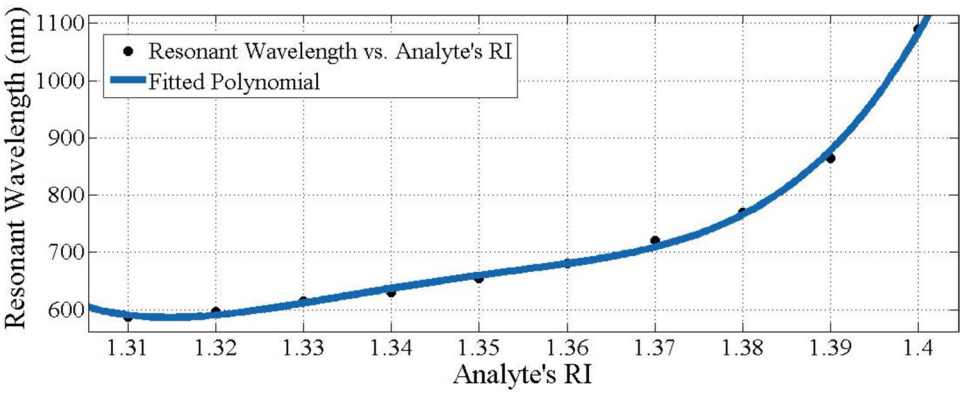

Fig. 9 Polynomial fitting of resonant wavelengths at corresponding RI's

Table 6 Coefficient of fitted polynomial in relation to resonance wavelength vs. analyte's RI

4th order polynomial	$p1\times x^4+p2\times x^3+p3\times x^2+p4\times x+p5$	
p1	3.756e+07	First five rows provide the polynomial coefficients (p1-p5)
p2	−2.019e+08	
p3	4.068e+08	
p4	−3.643e+08	
p5	1.224e+08	
R^2	0.9957	Goodness of fit

To observe the tolerance of the structural parameter's dimensions, we have altered the parameters by ±5% to analyze any significant change. As an initial step, we have changed the r_1 by ±5%, and corresponding drawn conclusions show that WS is unvarying and attains its constant value to 9400 nm/RIU for 1.38 RI. The respective AS only shows ±30 RIU^{-1} shown in Fig. 11a. On varying r_2 by ±5%, AS observed a minor change of 12 RIU^{-1} displayed in Fig. 11b with invariable WS. The next study shows the effect of variation of thickness of gold by ±5%, and the generated outputs show no variation in AS. The final observation displays no alteration in AS with the change of thickness of TiO_2 by ±5%. The graphical representation of thickness variation of gold and TiO_2 is not displayed due to negligible change. The overall scenario concludes that ±5% variation in geometrical parameters does not influence the sensitivities at large scale which makes our SPR sensor experimentally feasible and tolerable to minor fabrication instabilities. Table 7 shows some recent research works related to SPR-based sensing and highlights our sensor's performance as the best amplitude sensitivity offering SPR sensor.

Conclusion

This work presents a novel GI-PCF-based SPR sensor. The specially designed fiber consists of two types of air holes: one with gradually increasing radius and another with constant radius. Graded index air holes are located at angles of

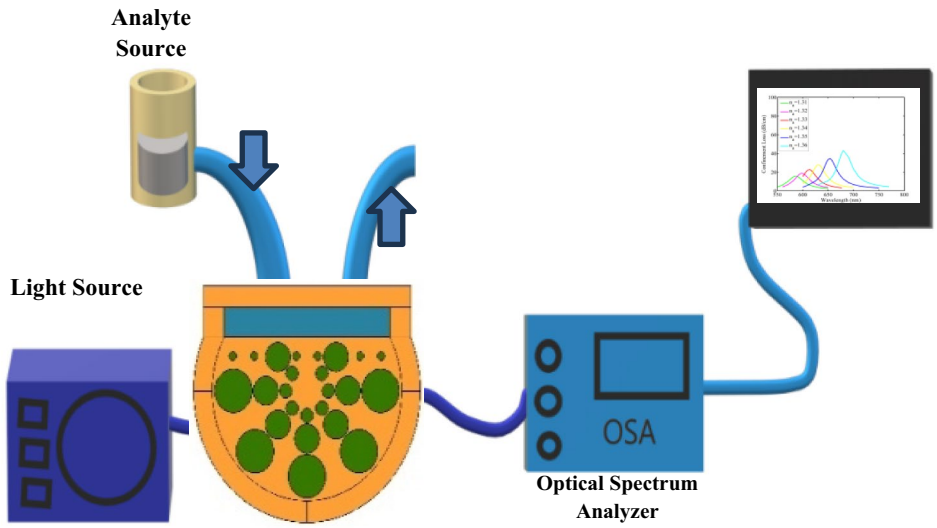

Fig. 10 Pictorial representation of experimental setup of PCF SPR sensing

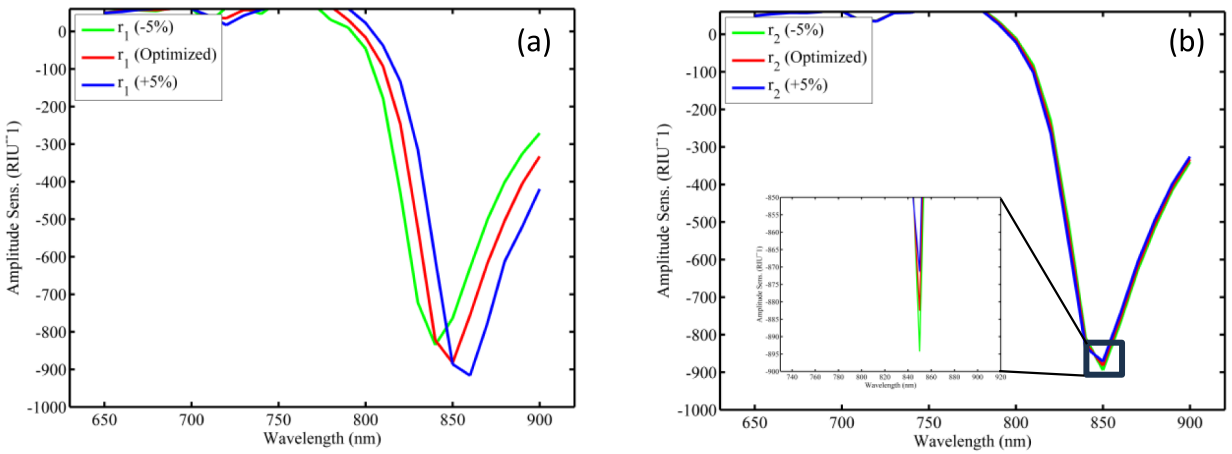

Fig. 11 Fabrication tolerance study of geometrical parameters **a** r_1 and **b** r_2

0°, 45°, 90°, 135°, and 180° which helps in confining the core mode and in minimizing the FWHM, thus, enhancing the FOM of the sensor. Constant radius air holes (r_2), which are placed near the plasmonic material, are used to give passage for better coupling between the core and SPP mode. For generating surface plasmons, plasmonic layer like gold and TiO_2 are layered on the top of PCF. Modal analyses have been done using finite element-based COMSOL Multiphysics. All the structural parameters are optimized and maintain a standard magnitude for better sensing results. The devised sensor is employed for sensing analytes having a range of RI from 1.31 to 1.39. Our simulation results reveal that the proposed sensor is able to exhibit the maximum WS as high as 22,600 nm/RIU, respective resolution as 4.43×10^{-6} RIU and FOM as 403.57 RIU^{-1}. Simultaneously, the highest magnitude of AS is also obtained as -1410 RIU^{-1} for the same RI analyte. Sensor with such a unique property can find its application in various sensing areas, i.e., biomedical, chemical, and industrial fields. The biomedical applications consist of cancer cell, TB, and brain tumor cell detection because the RI of such biological cells lies in the range of 1.31 to 1.4.

Table 7 Comparison of proposed GI-PCF sensor with recent research literatures

PCF model	Analyte range	Max. wavelength sensitivity (nm/RIU) @ RI	Max. amplitude sensitivity (RIU^{-1})	Wavelength Resolution (RIU)	References
Open-channel PCF	1.33–1.4	7000 @ 1.39	594	1.43×10^{-5}	[43]
Arc-shaped PCF	1.32–1.37	14,100 @ 1.36	109	9.17×10^{-6}	[44]
D-shaped PCF	1.33–1.39	11,500 @ 1.38	230	8.7×10^{-6}	[46]
Dual-side polished PCF	1.3–1.4	9400 @ 1.4	27.27	1.06×10^{-5}	[32]
D-shaped PCF	1.35–1.46	5600 @ 1.46	-	8×10^{-4}	[45]
Shifted-core PCF	1.33–1.39	24,200 @ 1.38	432	4.13×10^{-6}	[33]
GI-PCF SPR sensor (proposed work)	***1.31–1.39***	***22,600 @ 1.39***	***1410***	$\boldsymbol{4.43\times10^{-6}}$	

Acknowledgements Akash Khamaru highly acknowledges the support from the Delhi Technological University, Delhi, for providing the research fellowship and necessary support to conduct this research work.

Author Contribution A Khamaru has done the simulation work, analyses the results and written the original manuscript and A Kumar has given ideas and review the manuscript.

Data Availability No datasets were generated or analysed during the current study.

Declarations

Competing Interest The authors declare no competing interests.

References

1. Gholamzadeh B, Nabovati H (2008) Fiber optic sensors. Int J Electron Commun Eng 2(6):1107–1117
2. An X, Zhao X, Peng Q, Bao W, Zhang Y, Zhu X, ... Peng B (2024). Fiber optic strain sensor based on enhanced harmonic Vernier effect. Optical Fiber Technol 87, 103878
3. Yang H, Wang C, Jin G, Yu C (2024) Liquid crystal-embedded fiber optic fabry perot temperature sensor based on Vernier effect. Measurement 225:113910
4. Duan B, Hai Z, Guo M, Zheng Y, Chen J, Bai J, ... Xue C (2024) A large-range and high-sensitivity fiber-optic Fabry–Perot pressure sensor based on a membrane-hole-base structure. Micromachines, 15(2), 174
5. Zhang J, Chen Q (2024) A Ti: LiNbO3 optical waveguide sensor for measurement of intensive electric field. Opt Laser Technol 169:110091
6. Gu S, Li M, Wu Z, Wang T, Cai L, Deng M (2024) High-sensitivity and directional-identification fiber magnetic field sensor via polarimetric fiber ring laser with a fiber Faraday rotator. Opt Fiber Technol 82:103643
7. Kamakshi K, Rastogi V, Kumar A, Rai J (2010) Design and fabrication of a single-mode optical fiber based refractive-index sensor. Microw Opt Technol Lett 52(6):1408–1411
8. Kumar A, Saini TS, Sinha RK (2015) Design and analysis of photonic crystal biperiodic waveguide structure based optofluidic-gas sensor. Optik 126(24):5172–5175
9. Cranch GA, Nash PJ, Kirkendall CK (2003) Large-scale remotely interrogated arrays of fiber-optic interferometric sensors for underwater acoustic applications. IEEE Sens J 3(1):19–30
10. Voisin V, Pilate J, Damman P, Mégret P, Caucheteur C (2014) Highly sensitive detection of molecular interactions with plasmonic optical fiber grating sensors. Biosens Bioelectron 51:249–254
11. Majeed MF, Ahmad AK (2024) Design and analysis of a dual-core PCF biosensor based on SPR for cancerous cells detection. Opt Quant Electron 56(6):1–19
12. Zhang S, & Wang Y (2024) A PCF-SPR sensor for dual-polarization and wide refractive index detection range. Optics Communications, 130810
13. Singh S, Prajapati YK (2020) TiO2/gold-graphene hybrid solid core SPR based PCF RI sensor for sensitivity enhancement. Optik 224:165525
14. Tuaimah AM, Tahhan SR, Taher HJ, Ahmed K, Al-Zahrani FA (2024) Multi analyte detection based on D-shaped PCF sensor for glucose concentrations sensing. Opt Quant Electron 56(3):319
15. Guo W, Chen N, Xu Y, Xiao Y, Yue W, Ren Z, ... Li M (2024) Numerical simulation of in-fiber magnetic field sensor using magnetofluid-infiltrated dual-core photonic crystal fiber with gold layer. Optical Engineering, 63(7), 076101–076101
16. Singh N, Khamaru A, Kumar A (2024) Design and analysis of a rectangular core refractive index-based PCF sensor for bio-sensing application. Opt Quant Electron 56(7):1133
17. Otto A (1968) Excitation of nonradiative surface plasma waves in silver by the method of frustrated total reflection. Z Phys 216:398–410
18. Kretschmann E, Raether H (1968) Radiative decay of non radiative surface plasmons excited by light. Zeitschrift für Naturforschung A 23(12):2135–2136
19. Kumar A, Choudhary P, Kumar A, Camargo PH, Krishnan V (2022) Recent advances in plasmonic photocatalysis based on TiO2 and noble metal nanoparticles for energy conversion, environmental remediation, and organic synthesis. Small 18(1):2101638
20. Tan YC, Tou ZQ, Chow KK, Chan CC (2015) Graphenedeposited photonic crystal fibers for continuous refractive index sensing applications. Opt Exp 23(24):31286
21. Sardar MR, & Faisal M (2024) Dual-core dual-polished pcf-spr sensor for cancer cell detection. IEEE Sensors J. https://doi.org/10.1109/JSEN.2024.3358173
22. Erdogan İ, Dogan Y (2023) Au-TiO2-graphene grated highly sensitive D-shaped SPR refractive index sensor. Plasmonics 18(3):1203–1210

23. Dogan Y, Erdogan I (2023) Highly sensitive MoS2/graphene based D-shaped optical fiber SPR refractive index sensor with Ag/Au grated structure. Opt Quant Electron 55(12):1066
24. Khamaru A, & Kumar A (2024). As38 Se62 based segmented clad-graded index photonic crystal fiber for supercontinuum generation covering 3–9.5 μm with moderate peak power. Optical Quantum Electronics, 56(7), 1246
25. Khamaru A, & Kumar A (2024) Ge-Se-Te based penrose photonic quasi-crystal fiber for SCG covering 2–21 μm MIR regime. Optical Materials, 115849
26. Tomer DS, Kumar A (2024) Design and numerical modeling of chalcogenide parabolic-core waveguide for on-chip supercontinuum generation extending from near-IR region to mid-IR region. Microw Opt Technol Lett 66(3):e34105
27. Singh G, Sharma S, Kumar A (2023). Design and analysis of spider-web photonic crystal fiber in the terahertz regime. Indian J Phys 1–6
28. Singh G, Sharma S, Kumar A (2024) Design and simulation of solid-core octagonal photonic crystal fiber for terahertz wave propagation. Microw Opt Technol Lett 66(5):e34173
29. Saini TS, Kumar A, Sinha RK (2015) Slow light generation in single-mode tellurite fibers. J Mod Opt 62(7):508–513
30. Rastogi V, Kumar A (2013) Design of large-mode-area three layered fiber structure for femtosecond laser pulse delivery. Optics Communications 293:108–112
31. Majeed MF, Ahmad AK (2024) Design and analysis of a high sensitivity open microchannel PCF-based surface plasmon resonance refractometric sensor. Opt Mater 147:114617
32. Ullah S, Chen H, Gao Z, Li Z, Guo P, Wang C, Li S (2024). Dual-side polished surface plasmon resonance–based photonic crystal fiber for refractive index sensing and polarization filtering. Plasmonics, 1–11
33 Krishnan S, Ramesh Babu P, Senthilnathan K (2024) A novel side polished PCF-based SPR sensor with shifted core region. Plasmonics 19(2):1043–1051
34. Ramani U, Kumar H, Kumar R, Singh BK, Pandey PC (2024). Dual-core photonic crystal fiber-based plasmonic sensor for a broad range of refractive index sensing. Plasmonics, 1–11
35. Guo X, Sang T, Yang G, Wang Y (2024) Dual-polarization SPR sensor of U-shaped photonic crystal fiber coated with Au-TiO_2, Plasmonics, 1–10
36. Ding X, Lin Q, Wang M, Liu S, Zhang W, Chen N, Wang Y (2024) Design and simulation of high-performance D-type dual-mode PCF-SPR refractive index sensor coated with Au-TiO2 layer. Sensors 24(18):6118
37. Qiu H, Li W, Zhu C, Xu J, Li J, Bai G (2024) A high-sensitivity D-shaped photonic crystal fiber surface plasmon resonance sensor for low refractive index detection. J Opt 53(3):1897–1905
38. Pysz D, Kujawa I, Stępień R, Klimczak M, Filipkowski A, Franczyk M, ... Buczyński R (2014). Stack and draw fabrication of soft glass microstructured fiber optics. Bulletin of the Polish Academy of Sciences. Technical Sciences, 62(4), 667–682
39. Karstens R, Gödecke A, Prießner A, Ihlemann J (2016) Fabrication of 250-nm-hole arrays in glass and fused silica by UV laser ablation. Opt Laser Technol 83:16–20
40. Willmott PR, Huber JR (2000) Pulsed laser vaporization and deposition. Rev Mod Phys 72:315–328
41. Hasan MR, Akter S, Rifat AA, Rana S, Ali S (2017) A highly sensitive gold-coated photonic crystal fiber biosensor based on surface plasmon resonance. In Photonics (Vol. 4, No. 1, p. 18). MDPI
42. Wang H, Wu M, Zheng S, Xie T, Dai W, Fu H (2023) Surface plasmon resonance sensor based on seven-core photonic crystal fiber for refractive index and temperature measurement. Opt Laser Technol 164:109511
43. Islam N, Arif MFH, Yousuf MA, Asaduzzaman S (2023) Highly sensitive open channel based PCF-SPR sensor for analyte refractive index sensing. Results in Physics 46:106266
44. Melwin G, Senthilnathan K (2024) Modelling a simple arc shaped gold coated PCF-based SPR sensor. J Opt 53(1):117–126
45. Zhou D, Ren F, Li Y, Ci Y, Wang J (2024). A broadband D-shaped photonic crystal fiber sensor via surface plasmon resonance for different analytes with a large range of refractive index detection. Plasmonics, 1–11
46. Chen N, Chang M, Lu X, Zhou J, Zhang X (2020) Numerical analysis of midinfrared D-shaped photonic-crystal-fiber sensor based on surface-plasmon-resonance effect for environmental monitoring. Appl Sci 10(11):3897

Publisher's Note Springer Nature remains neutral with regard to jurisdictional claims in published maps and institutional affiliations.

Springer Nature or its licensor (e.g. a society or other partner) holds exclusive rights to this article under a publishing agreement with the author(s) or other rightsholder(s); author self-archiving of the accepted manuscript version of this article is solely governed by the terms of such publishing agreement and applicable law.

2024 International Conference on Electrical Electronics and Computing Technologies (ICEECT) | 979-8-3503-7809-2/24/$31.00 ©2024 IEEE | DOI: 10.1109/ICEECT61758.2024.10739179

Identification of Allium cepa L.-Derived Flavonoids as Potential Inhibitors of Human Serum Albumin Glycation in Diabetic Nephropathy: An In-Silico Analysis

Kanjam Manocha
Department of Biotechnology
Delhi Technological University
Delhi, India
kanjammanocha7@gmail.com

Shivam Bilandi
Department of Biotechnology
Delhi Technological University
Delhi, India
ashivam2001@gmail.com

Navneeta Bharadvaja
Department of Biotechnology
Delhi Technological University
Delhi, India
navneetab@dce.ac.in

***Abstract*— Type 2 diabetes is a global health concern, with a significant economic impact. It consists of various complications. One of the major complications is DN (Diabetic Nephropathy). It is the leading cause of CKD (Chronic Kidney Disorder) and ESRD (End-stage renal disease). Current treatments are mostly inept; therefore, a demand is brewing regarding Natural (Bioactive) compounds as a potential therapeutic use case. One such is flavonoids which have shown combating effects against diabetic complications such as antioxidative, anti-inflammatory and anti-diabetic. This review delves into the flavonoid potential which is extracted from Allium cepa L (Onion.) to inhibit human serum albumin (HSA) glycation, which plays a major role in the development of diabetic difficulties. in silico molecular docking studies and ADME analysis were used to identify flavonoids with strong pharmacokinetic profiles and binding energies to HSA. The results showed quercetin, kaempferol etc from onions have strong binding energies, showing that they can serve as effective therapeutic agents against glycation-related difficulties. These results can provide an understanding regarding the pharmacological mechanism of flavonoids derived from one leading to new routes towards natural therapies with respect to diabetic nephropathy.**

***Keywords*—** *diabetes mellitus type II, diabetic nephropathy, human serum albumin, flavonoids, anti-glycation*

I. Introduction

The worldwide presence of 8.3% has made diabetes a global health crisis. This leads to high mortality with diabetes-related symptoms under the age of 60 years. Also, it is leading to an excessive economic burden as clearly visible in the increase in healthcare spending in response to diabetes [1]. Estimates show that people with diabetes will increase significantly (Now- 366 million to 552 million by 2030) with a substantial amount being undiagnosed [1]. This proves our statistics that 3 people will develop diabetes in every 10 sec leading to 10 million cases year-on-year increase.

Moreover, it is also the leading cause of death worldwide, 6 people in every 10 minutes die due to diabetes related complications. Therefore, time is ticking and significant attention should be given.

It consists of various complications. One of such major complications is Diabetic nephropathy (DN). It is the leading cause of CKD (Chronic Kidney Disorder) and ESRD (End-stage renal disease). Statistics show that 40% of diabetes patients are diagnosed with DN, and DN is responsible for 45% of ESRD cases. Moreover, 43% of CKD patients have DN, and 60% of deaths in diabetes are because of DN. Despite significant advancements in understanding of the DN, Current treatments are mostly inept in many cases [2].

There is a critical demand for safe and effective medications to address DN, due to the constraints in existing treatments. Plants are a great source of bioactive compounds and have been for a long time, and many traditional remedies have been effective, economical, and safe in preventing diabetes and its intricacies. Herbal preparations offer a great alternative in developing countries due to their cost-effective nature.

Allium cepa L, commonly known as onion is a widely utilized household vegetable and has exhibited in vitro anti-diabetic effects which include inhibitory activity against protein tyrosine phosphatase 1B (PTP1B), α-glucosidase, and the formation of AGEs (advanced glycation end products) [3]. Altium peel extract has showcased a dose-dependent effect on the above pathways, with quercetin being a pivotal flavonoid. Onion-derived flavonoids are gaining attention for their above showcased properties against diabetes.

In this, we have used Computational molecular docking to study the interactions between small molecules and macromolecular targets, hit identification and optimized drug development [3]. This study investigates the interactions between flavonoids from Allium cepa L and specific targets with respect to the pathogenesis of DN. The objective is to determine potential inhibitors that can provide therapeutic benefits.

For this review, we have collected data from PubMed, Cochrane Library, Web of Science, and EMBASE database. Articles that lacked clear methodology were excluded. A total of 15 flavonoids with therapeutic potential in the treatment of diabetic nephropathy were studied, leading to a comprehensive idea regarding pharmacological mechanisms and future idea regarding pharmacological mechanisms and future applications. The objective is to determine potential inhibitors that can provide therapeutic benefits.

II. Literature

A. Type II Diabetes Meilitus

The primary issue in diabetes is prolonged hyperglycaemia, which disturbs normal biological processes. It initially affects proteins in the bloodstream. It undergoes non-enzymatic glycation when exposed to excess glucose and proteins, which leads to a cascade of chronic complications,

979-8-3503-7809-2/24/$31.00 ©2024 IEEE

Authorized licensed use limited to: DELHI TECHNICAL UNIV. Downloaded on November 09,2024 at 04:37:09 UTC from IEEE Xplore. Restrictions apply.

which includes microvascular and macrovascular problems, nephropathy, and retinopathy [4].

The most abundant plasma protein is Albumin, contains almost 50% of all proteins in plasma, with a concentration range of 3-5 g/dl [5]. It has critical role in physiological and pharmacological functions, binding and transporting several endogenous molecules like long-chain fatty acids, steroids, and L-tryptophan. [6] Approximately 80% of the colloidal osmotic pressure in the blood which is essential for fluid balance, are contributed by the Albumin. It also includes antioxidant properties, which helps in defending body against oxidative damage [7].

During this period, human serum albumin (HSA) makes approximately 28 rounds in and out of circulation, providing enormous amount of opportunities to interact with glucose in the bloodstream [8]. Due to this exposure, albumin prone to various modifications, which includes oxidation, maleylation, and, notably, non-enzymatic glycation in the context of prolonged hyperglycaemia. Above modifications can lead to damage of albumin's physiological functions, which led to decrease in its ligand-binding capacity and therefore reducing its antioxidant properties.

We need to understand no enzymatic glycation of albumin to mitigate the complication and developing the strategies accordingly. Non-Enzymatic glycation alters albumin structure and function which can further lead to decrease in efficiency and increase susceptibility to oxidative stress. Changes because of this has broader effects on diabetes related difficulties.

B. Diabetic Nephropathy

Consistent high glucose level in diabetes causes non-enzymatic glycation of varied protein which include Haemoglobin, Insulin, HSA (Human serum albumin), Lipoprotein etc [9].

When glucose bind to protein via peptide bond, without enzyme leads to non-enzymatic glycation, which result in structural as well as confirmational changes that lead to macro- and micro vascular diabetic complication [10]. A strong link between these glycation processes, especially Amadori albumin, and diabetes-specific complications in both humans and animal models are established by the researcher. [11]. (Fig. 1)

1. Pathogenesis of Diabetic Nephropathy

Hyperglycaemia plays a very important role in the development of diabetic nephropathy (DN), Which leads to increment production of lipid peroxides, active carbonyl compounds, and free radicals, which cause oxidative stress and further non-enzymatic protein glycosylation [12]. The major factor that influences in the development of DN is the variation in free radical production and antioxidant defence mechanisms. This shortcoming generates rapid metabolic pathways within the diabetic kidney, which leads to advanced glycosylation end products (AGEs), protein kinase C (PKC) activation, renal polyol synthesis, and increased oxidative stress [13]. These processes, one after 4 4 62 the other activate various cytokines and growth factors, which results in histological changes in the renal glomeruli, including mesangial expansion, glomerular basement membrane thickening, and glomerular sclerosis [9, 10, 11]

C. Human Serum Albumin (HSA)

HSA is the rich protein in human circulation, incorporate mainly in the liver. It plays a very crucial in maintaining colloid osmotic pressure, as well as in the transport of fatty acids, hormones, drugs, and metabolites. It also has anti-thrombotic, anti-inflammatory, and antioxidant properties [14].

Albumin is made up of 585 amino acid residues, with 35 cysteine, 1 tryptophan, 59 lysine, and 23 arginine residues. It has affected glycation, especially in conditions of hyperglycaemia due to its richness in lysine. Non-enzymatic glycation involved specific lysine residues of HSA, which leads to substantial structural and functional changes in the protein [15]. Researchers investigated that HSA is two to three times more glycated in diabetic patients compared in the general population [16]. This glycation can cause various alterations, including reduction of ligand-binding capacity and loss of antioxidant activity, which leads to damage in transport functions and also decrement in physiological roles [17].

1. Significance of Maillard reaction in diabetes mellitus

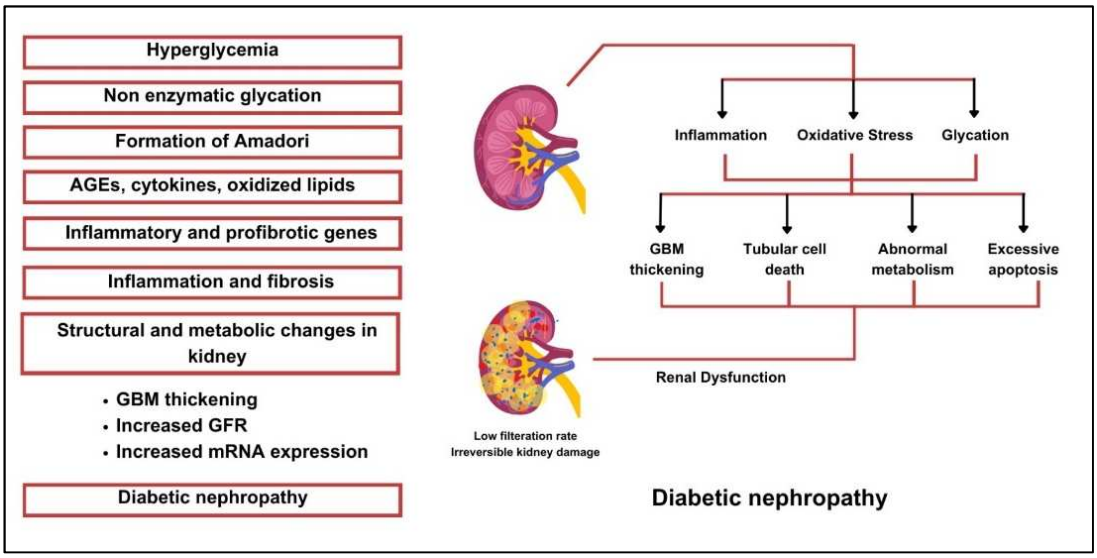

Fig. 1. Molecular pathway leading to Diabetic nephropathy

Authorized licensed use limited to: DELHI TECHNICAL UNIV. Downloaded on November 09,2024 at 04:37:09 UTC from IEEE Xplore. Restrictions apply.

Chemical process in which carbohydrates combined with amino acids to form non-enzymatic glycation products is called Maillard reaction after Prof. Louis Camille Maillard. In the framework of diabetes, the Maillard reaction starts when the aldehyde group of carbohydrates condenses with amino groups in proteins, forming labile aldimine (Schiff base), which can further undergo rearrangement to form more stable Amadori products [18]. The formation of these early glycation products leads to substantial modification in protein structure and function, which contributes to diabetic problems.

In the Continuation of reaction stable Amadori products can further transform into advanced glycation end products (AGEs) through irreversible reactions involving oxidation and fragmentation [19]. The accumulation of AGEs had been one of the leading issues related to diabetes and aging, such as nephropathy, neuropathy, retinopathy, as well as cardiovascular diseases. These AGEs also connect with specific receptors such as RAGE, begin signalling pathways that contribute to the pathogenesis of long-term diabetic problems.

2. Stable amadori adduct

Early step in Maillard's reaction is Amadori rearrangement. It involves the transformation of the Schiff base into more stable Amadori products [20]. Amadori products are rich and represent the major form of glycated proteins in the body.

Stable products derived from this are also involved in the development of various diabetic problems. Studies have shown a strong connection of Amadori albumin in DN and vasculopathy [4; 18]. This highlights the role of detection of early glycation as it has a significant impact on diabetes and related problems.

D. Allium cepa L against diabetes type II

Allium cepa has shown various health benefits one of the key reasons for this is presence of phytonutrient such as flavonoids, FOS and other sulfur-based compounds. They have shown health benefits such as anti-inflammatory, anti-cancer and cardiovascular protection effects [21]. Flavanol is the key flavonoid among which major contributor such as Quercetin, a compound well versed with its antioxidant and anti-inflammatory, kaempferol, Isorhamnetin, myricetin is present. There are approximately 25 types of flavanols present in onion bulb. The glycosyl unit(s) associated with these flavanols are majorly glucose-based, adding more complexity.

Flavonoids extracted from Allium cepa L. have several benefits, specifically with respect to diabetes type II. They have shown potential to regulate sugar level in blood, improving insulin sensitivity leading to decrease in risk of diabetes related complications. In this quercetin has shown properties to modulate the pathway related to diabetes management. Therefore, Allium cepa L can play a vital role in reduction of oxidative stress and control of blood glucose levels.

Onion (Allium cepa L.) has grabbed attention because of its potential health benefits, particularly in type II diabetes. Ethyl alcohol extracts of onion skin (EOS) contain significant amounts of quercetin, [22] revealing that EOS had 6.04 g/100 g of quercetin based on dried weight. This study also showcased EOS significant inhibitory activity against several enzymes which are involved in carbohydrate metabolism, such as sucrase (IC50 of 0.40 mg/mL), α-glucosidase (IC50 of 1.27 mg/mL), maltase (IC50 of 2.02 mg/mL), and α-amylase (IC50 of 3.00 mg/mL). However, these inhibitory activities were not entirely correlated with quercetin, suggesting that other bioactive compounds in onion skin might contribute to the observed effects [22].

Further, in vivo experiments with rat models showed that EOS leads to a significant reduction of blood glucose levels, indicating that phenolic phytochemicals like quercetin may exhibit antihyperglycemic activity [22]. The area under the blood glucose-time curve (AUClast) for EOS-treated rats was significantly lower as compare to control rats, showing the potential glucose-lowering effects of these extracts. Lowering level of glucose by this was same as in pure quercetin [22].

Onion extracts have also shown reduced activity of α-amylase and α-glucosidase in a dose-dependent manner. It was found that different extracts of onion skin (0.01, 0.1, 1, 10 mg/mL) decreased α-amylase activity, with some extracts showing higher inhibition than quercetin, indicating that additional bioactive compounds contribute to the effect

III. METHODOLOGY

A. Proteins/Macromolecules

A 3D structure of HSA (Human serum albumin) was extracted from the Protein Data Bank (PDB ID: 4IW2), [23] which being utilised widely for scientific studies. Specifically, this structure was chosen because it represents the most

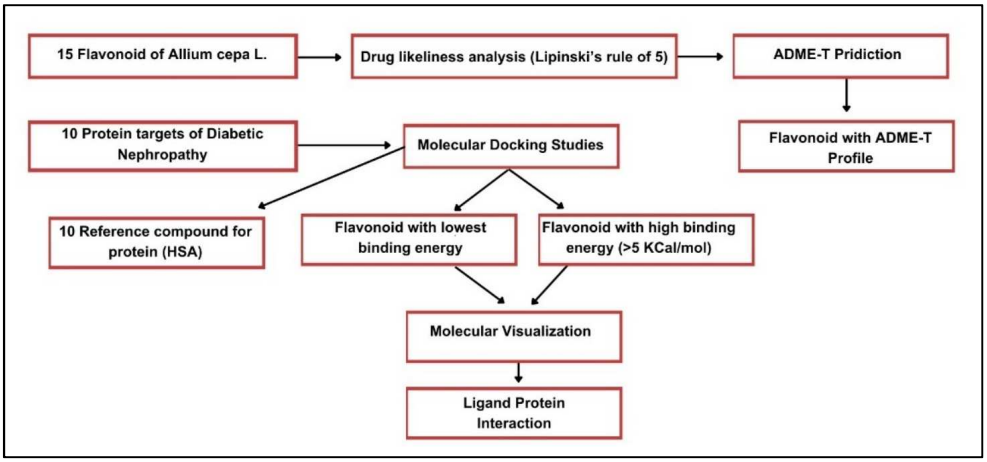

Fig. 2. Methodology used in In-Silico Study

Authorized licensed use limited to: DELHI TECHNICAL UNIV. Downloaded on November 09,2024 at 04:37:09 UTC from IEEE Xplore. Restrictions apply.

abundant protein in human circulation, and therefore plays a significant role in maintaining colloidal osmotic pressure, and transportation of fatty acids, hormones, drugs, and metabolites. Its detailed structure includes many amino acids, among which specific lysine residues undergo non-enzymatic glycation, a significant process in the pathogenesis of diabetes complications. The obtained structure was further used as a receptor for MD studies. (Fig. 2)

B. Ligands

14 different flavonoids were selected from onion peel, on the basis of their ADME T studies. These compounds were obtained from public databases like PubChem and DrugBank in standard structure-data format (SDF) were converted into protein data bank (PDB) format for further docking studies [24]. The selected flavonoids include some well-known compounds such as quercetin, kaempferol, and others that have exhibited inhibitory effects on various enzymes related to glucose metabolism and antioxidative activities.

C. ADME Analysis

To assess the drug-like properties of these flavonoids, SwissADME was used to screen for Lipinski's rule of five. This analysis checked the criteria which included the number of hydrogen bond acceptors (<10), and donors (<5), lipophilicity A 3D structure of HSA (Human serum albumin) was extracted from the Protein Data Bank (PDB ID: 4IW2), [23] which being utilised widely for scientific studies. Specifically, this structure was chosen because it represents the most abundant protein in human circulation, and therefore plays a significant role in maintaining colloidal osmotic pressure, and (logP <5), ligand's molecular weight (<500 Da), and molar refractivity (between 40 and 130). Any compound breaking more than two rules were disqualified. After screening, 12 flavonoids met these criteria out of 15 and were further selected for docking studies. Among these, quercetin and kaempferol showed exceptional potential. They met these criteria while also showing promising biological activity. (Table. 1).

D. Molecular Docking Studies

MD was conducted with the selected flavonoids using AutoDock v1.5.6, which employed the Lamarckian Genetic Algorithm for ligand-receptor interaction optimization. The HSA structure was further prepared by removing any existing water molecules and hetatoms and further adding polar hydrogen ions and charges (Kollman, Gasteiger).

TABLE 1. ADME-T ANALYSIS and BINDING ENERGY EVALUATION VIA MD

Flavonoid	PubChem ID	Molecular Weight	No. of H-bond `acceptors	No. of H-bond donors	Molar Refractivity	Lipinski	Binding Energy
Naringenin	439246	272.25 g/mol	5	3	71.57	Yes; Null violation	-6.79
Kaempferol	5280863	286.24 g/mol	6	4	76.01	Yes; Null violation	-6.51
Cianidanol	9064	290.27 g/mol	6	5	74.33	Yes; Null violation	-6.48
Petunidin	441774	317.27 g/mol	7	5	82.66	Yes; Null violation	-6.42
Morin	5281670	302.24 g/mol	7	5	78.03	Yes; Null violation	-6.39
Resveratrol	445154	228.24 g/mol	3	3	67.88	Yes; Null violation	-6.37
Peonidin	441773	301.27 g/mol	6	4	80.64	Yes; Null violation	-6.24
Quercetin	5280343	302.24 g/mol	7	5	78.03	Yes; Null violation	-6.1
Taxifolin	439533	304.25 g/mol	7	5	74.76	Yes; Null violation	-6.1
Cyanidin	128861	287.24 g/mol	6	5	76.17	Yes; Null violation	-5.95
Isorhamnetin	5281654	316.26 g/mol	7	4	82.5	Yes; Null violation	-5.89
Delphinidin	68245	338.70 g/mol	N/A	N/A	84.05	Yes; Single violation: NHorOH>55	N/A
Epigallocatechin Gallate	65064	458.37 g/mol	N/A	N/A	112.06	No; double violations: NorO>10, NHorOH>5	N/A
Myricetin	5281672	318.24 g/mol	N/A	N/A	80.06	Yes; single violation: NHorOH>5	N/A

Authorized licensed use limited to: DELHI TECHNICAL UNIV. Downloaded on November 09,2024 at 04:37:09 UTC from IEEE Xplore. Restrictions apply.

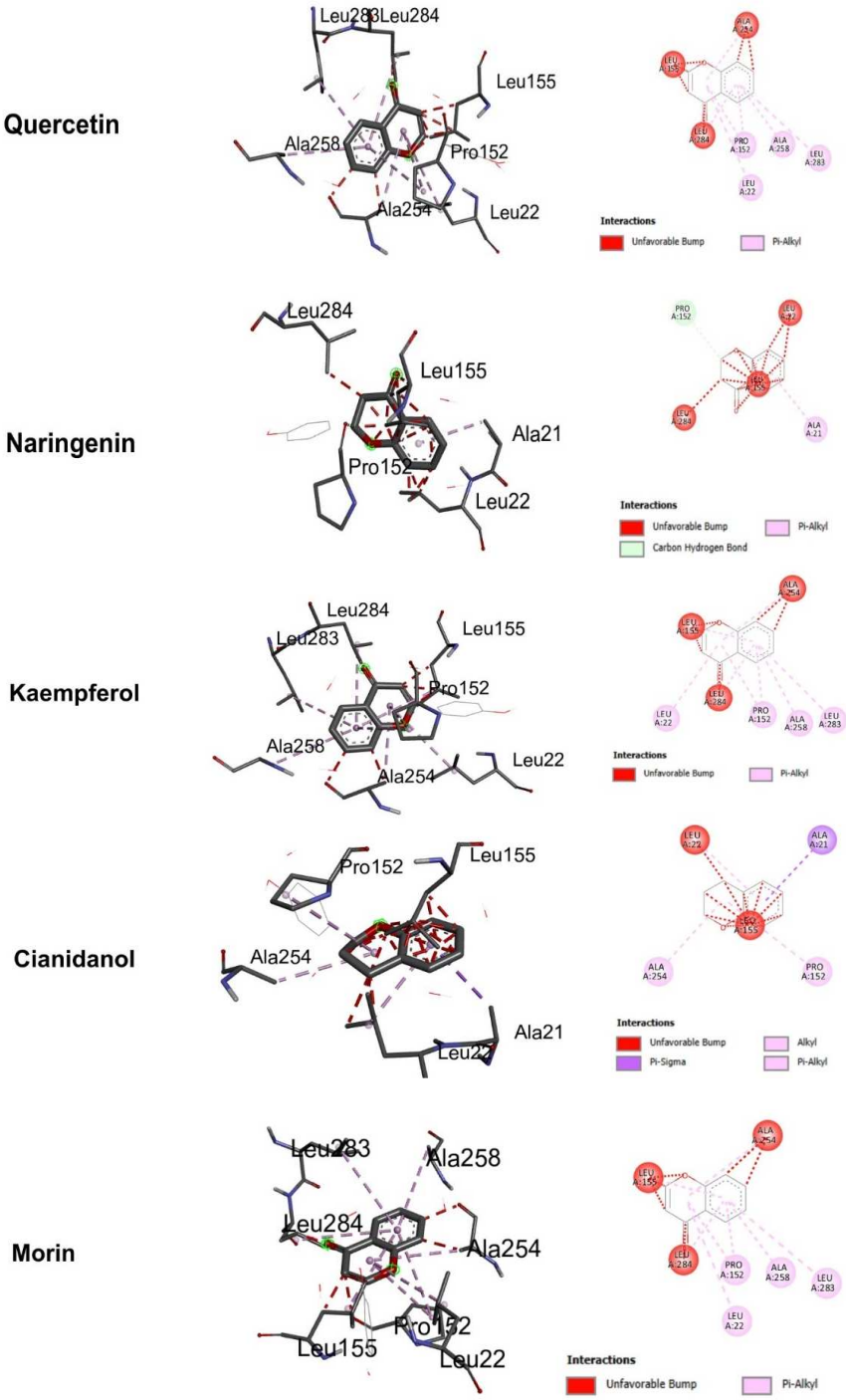

Fig. 3. Different flavonoid and HSA protein interactions

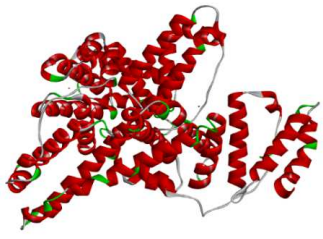

Fig. 4. HSA protein structure

Authorized licensed use limited to: DELHI TECHNICAL UNIV. Downloaded on November 09,2024 at 04:37:09 UTC from IEEE Xplore. Restrictions apply.

accurate docking outcomes. Docking output provided essential information such as binding energy (BE) (in kcal/mol), intermolecular energy (IE) (combination of van der Waals, H-bond, and desolvation energy), total interaction energy, torsional energy, and unbound system energy [25]. The conformation with the least binding energy among the selected 10 outputs was considered. (Fig. 2)

IV. Results and Discussion

A. ADME Analysis

To evaluate the practicality of flavonoids derived for potential therapeutic use against type II diabetes, an ADME (Absorption, Distribution, Metabolism, and Excretion) study was done.

This analysis helped us to determine if a compound satisfies the pharmacokinetic standards for drug development and do they have a therapeutic effect at specific doses. 14 flavonoids were tested using SwissADME to check Lipinski's rule of five violations, which provided key standards for the assessment of the compound's drug-likeness which included molecular weight, Number of H-bond acceptors and donors, lipophilicity (logP), and molar refractivity. Among the 14 flavonoids, 12 passed this screening, with some having minor violations but under considerable range.

B. Molecular Docking

MD studies was conducted for the identification of interactions between flavonoids and HSA. It aimed towards determining the binding energies between selected flavonoids and HSA. It also assessed their potential to inhibit specific proteins involved in glycation, such as α-glucosidase and α-amylase.

AutoDock v1.5.6 was utilized with the Lamarckian Genetic Algorithm to assess the interaction between 12 selected flavonoids with the 3D structure of HSA. The binding energies were obtained which showed a range of BE values across the flavonoids we can evaluate the range as Lower binding energy indicates stronger binding, indicating a higher interaction with the target protein.

The previous docking experiment showed that many flavonoids had a promising binding energy with HSA, indicating their potential as therapeutic agents for diabetes complications, such as (Table 1.):

- The observed binding energy of Naringenin is -6.79 kcal/mol, which indicates a strong interaction with HSA. This result aligns with its anti-inflammatory and antioxidative properties.
- Kaempferol binding energy of -6.51 kcal/mol, backing its therapeutic potential due to its anti-inflammatory effects and α-glucosidase. inhibition
- Quercetin and Kaempferol are 2 flavonoids which are extensively studied for their anti-diabetic properties, as clearly visible in their binding energies of -6.10 kcal/mol and -6.51 kcal/mol, respectively. Their docking results back their potential as therapeutic agents for diabetes management.

C. Discussion

Due to their ability to interact with key proteins in glucose metabolism suggest that flavonoids from Allium cepa L have a role in managing type II diabetes. The docking studies indicated that these flavonoids have strong binding energies with HSA which reinforces their potential as inhibitors of α-glucosidase and other enzymes involved in carbohydrate metabolism. Which can lead to a delay in carbon Due to their ability to interact with key proteins in glucose metabolism suggest that flavonoids from Allium cepa L have a role in managing type II diabetes. The docking studies indicated that these flavonoids have strong binding energies with HSA which reinforces their potential as inhibitors of α-glucosidase and other enzymes involved in carbohydrate metabolism. Which can lead to a delay in carbohydrate absorption, helping to control blood glucose levels. (Fig. 3 and 4)

Conclusion

In this analysis, we focused on the prospect of plant-derived flavonoids to inhibit human serum albumin (HSA) glycation, one of the glycation mechanisms that plays a critical role in the progression of diabetic nephropathy (DN). Using in silico techniques such as MD and ADME analysis, we were able to identify several flavonoids, such as quercetin, kaempferol etc, that exhibit strong binding affinities to HSA. These outcomes display the compelling therapeutic potential of these natural compounds and their use case in Type II diabetes.

ADME analysis showed that multiple flavonoids met the criteria of Lipinski's rule of 5, which was enforced on their drug like attributes. These results also showcased that flavonoids which are derived from Allium cepa L can offer an affordable and convenient remedy for complications related to diabetes, particularly with respect to glycation.

In conclusion, this review suggests that Allium cepa L-derived flavonoids have significant potential in the treatment and management of diabetic complications, specifically in diabetic nephropathy. The insights gained from this review could cause a ripple effect for future RandD on natural, plant based therapies for diabetes management, leading to a promising path towards innovative healthcare solutions.

REFERENCES

[1] Yin, X., Xu, Z., Zhang, Z., Li, L., Pan, Q., Zheng, F., Li, H., 2017. Association of PI3K/ AKT/mTOR pathway genetic variants with type 2 diabetes mellitus in Chinese. Diabetes Res. Clin. Pract. 128, 127–135. https://doi.org/10.1016/j.diabres.2017.04.002.

[2] Idf, D.A.G., 2013. Update of mortality attributable to diabetes for the IDF Diabetes Atlas: estimates for the year 2013. Diabetes Res. Clin. Pract. 100 (3), 277–279. https://doi.org/10.1016/j.diabres.2013.02.005

[3] P.J. Thornalley, A. Langborg, H.S. Minhas, Formation of glyoxal, methylglyoxal, and 3-deoxyglucosone in the glycation of proteins by glucose, Biochem. J. 344 (1999) 109–116.

[4] S. Horiuchi, Advanced glycation end products (AGE)-modified proteins and their potential relevance to atherosclerosis, Trend Cardiovasc. Med. 6 (1996) 163–168.

[5] T. Peters, All About Albumin: Biochemistry, Genetics, and Medical Applications, Academic Press Limited, San Diego, CA, 1996

[6] Choudhary S, Kesavan AK, Juneja V, Thakur S. Molecular modeling, simulation and docking of Rv1250 protein from Mycobacterium tuberculosis. Front Bioinform. 2023 Apr 12;3:1125479. doi: 10.3389/fbinf.2023.1125479. PMID: 37122997; PMCID: PMC10130521.

[7] Evans, Paul and Pucik, Vladimir and Barsoux, Jean-Louis. (2002). The Global Challenge: Frameworks for International Human Resource Management.

[8] Gois Ruivo da Silva M, Skrt M, Komes D, Poklar Ulrih N, Pogačnik L. Enhanced Yield of Bioactivities from Onion (Allium cepa L.) Skin and Their Antioxidant and Anti-α-Amylase Activities. Int J Mol Sci. 2020 Apr 21;21(8):2909. doi: 10.3390/ijms21082909. PMID: 32326342; PMCID: PMC7216267.

Authorized licensed use limited to: DELHI TECHNICAL UNIV. Downloaded on November 09,2024 at 04:37:09 UTC from IEEE Xplore. Restrictions apply.

[9] Schena, F.P., and Gesualdo, L. (2005). Pathogenetic mechanisms of diabetic nephropathy. J. Am. Soc. Nephrol., 16(S1), S30–S33.

[10] Cao, Z., and Cooper, M.E. (2011). Pathogenesis of diabetic nephropathy. J. Diabetes Investig., 2(4), 243–247.

[11] Ayse, N., Duygu, A.T., Hakkı, A.I., Tansel, O.Y., İsmail, D.G., and İsmail, K. (2008). Antimicrobial and cytotoxic activities of Zingiber officinalis extracts. FABAD J. Pharm. Sci., 33, 77–86

[12] Vinod, P.B. (2012). Pathophysiology of diabetic nephropathy. Clin. Queries Nephrol., 1(2), 121–126.

[13] Wang, Shilei and Liu, Shuo and Zhang, Yichi and He, Jun and Coy, David and Sun, Lichun. (2020). Human Serum Albumin (HSA) and Its Applications as a Drug Delivery Vehicle. 10.36648/1791-809X.14.2.698.

[14] Tupe, R.S., Vishwakarma, A., Solaskar, A. et al. Methylglyoxal induces glycation and oxidative stress in Saccharomyces cerevisiae. Ann Microbiol 69, 1165–1175 (2019). https://doi.org/10.1007/s13213-019-01498-z.

[15] Watkins, P B, Wrighton, S, Maurel, P, Schuetz, E G, Mendez-Picon, G, Parker, G A, Guzelian, P S, T Identification of an inducible form of cytochrome P-450 in human liver.1985 Proceedings of the National Academy of Sciences 6310-6314 82 18 doi:10.1073/pnas.82.18.6310

[16] Guthrow, C., Morris, M., Day, J., Thorpe, S., and Baynes, J. (1979). Enhanced Nonenzymatic Glucosylation of Human Serum Albumin in Diabetes Mellitus. Proceedings of the National Academy of Sciences, 76(9), 1011–1014. https://doi.org/10.1073/pnas.76.9.4258.

[17] Ali, A. A. O.-H., Al-sayed, H. M. A., Yasin, N. M. N., and Afifi, E. A. A. (2016). Effect of different extraction methods on stability of anthocyanins extracted from red onion peels (Allium cepa) and its uses as food colorants. Bulletin of the National Institute of Nutrition in the Arab Republic of Egypt, 47, 196–219.

[18] John, W. G., and Lamb, E. J. (1993). The Maillard or browning reaction in diabetes. Eye (London), 7(2), 230–237.

[19] Schalkwijk CG, Miyata T. Early- and advanced non-enzymatic glycation in diabetic vascular complications: the search for therapeutics. Amino Acids. 2012 Apr;42(4):1193-204. doi: 10.1007/s00726-010-0779-9. Epub 2010 Oct 20. PMID: 20960212; PMCID: PMC3296013Yamagishi S, Matsui T. Advanced glycation end products, oxidative stress and diabetic nephropathy. Oxid Med Cell Longev. 2010 Mar-Apr;3(2):101-8. doi: 10.4161/oxim.3.2.11148. PMID: 20716934; PMCID: PMC2952094.

[20] Hodge, J. E. (1995). Sugar fragmentation in the Maillard reaction cascade: Isotope labeling studies on the formation of acetic acid by a hydrolytic beta-dicarbonyl cleavage mechanism. Advances in Carbohydrate Chemistry, 10, 169–205.

[21] Leuchs, E. F. (1825). Farben Farbenkünde. Volume 1, p. 434.

[22] Choi, E.-Y., Lee, H., Woo, J. S., Jang, H. H., Hwang, S. J., Kim, H. S., Kim, W. S., Kim, Y. S., Kim, R., Choue, W., Yim, J. E., Kim, W., Effect of onion peel extract on endothelial function and endothelial progenitor cells in overweight and obese individuals. Nutrition, 31(9), 1131–1135. https://doi.org/10.1016/j.nut.2015.04.020

[23] Choudhary S, Kesavan AK, Juneja V, Thakur S. Molecular modeling, simulation and docking of Rv1250 protein from Mycobacterium tuberculosis. Front Bioinform. 2023 Apr 12;3:1125479. doi: 10.3389/fbinf.2023.1125479. PMID: 37122997; PMCID: PMC10130521

[24] Khan T, Lawrence AJ, Azad I, Raza S, Khan AR (2018) Molecular Docking Simulation with Special Reference to Flexible Docking Approach. JSM Chem 6(1): 1053.

[25] Sharma KM, Ranjani H, Zabetian A, Datta M, Deepa M, Moses CRA, Narayan KMV, Mohan V, Ali MK. Excess cost burden of diabetes in Southern India: a clinic-based, comparative cost-of-illness study. Glob Health Epidemiol Genom. 2016 May 13;1:e8. doi: 10.1017/gheg.2016.2. PMID: 29868200; PMCID: PMC5870439.

Authorized licensed use limited to: DELHI TECHNICAL UNIV. Downloaded on November 09,2024 at 04:37:09 UTC from IEEE Xplore. Restrictions apply.

International Journal of Research in Commerce and Management Studies

ISSN 2582-2292

Vol. 6, No. 05 Sep-Oct; 2024 Page. No. 223-240

To cite this article: Fredrick Kabwe, Nakuti Sharon and Dr. Krovvidi Srinivas (2024). IMPACT OF SUPPLY CHAIN DISRUPTIONS ON ENERGY SECURITY IN ZAMBIA: CHALLENGES AND MITIGATION STRATEGIES, International Journal of Research in Commerce and Management Studies (IJRCMS) 6 (5): 223-240 Article No. 288 Sub Id 528

IMPACT OF SUPPLY CHAIN DISRUPTIONS ON ENERGY SECURITY IN ZAMBIA: CHALLENGES AND MITIGATION STRATEGIES

Fredrick Kabwe, Nakuti Sharon and Dr. Krovvidi Srinivas

· MTECH, Delhi Technological University, fredrickkabwe487@gmail.com
MBA Delhi Technological University, nakutisharon@gmail.com

DOI: https://doi.org/10.38193/IJRCMS.2024.6513

ABSTRACT

This study examines the impact of supply chain interruptions on Zambia's energy security, highlighting the nation's significant reliance on hydroelectric power, which generates about 83% of its total electricity production (Jürisoo et al., 2019). According to the study, Zambia's energy sector is significantly impacted by global supply chain risks, such as geopolitical conflicts and environmental issues (Mwanza et al., 2023). The analysis explores how these problems exacerbate problems related to energy security, particularly during load-shedding incidents (Jürisoo et al., 2019; Alzoubi, 2024).

Furthermore, the study looks at the obstacles to establishing circular supply chains in Zambia's energy sector and emphasizes how cutting-edge technologies like artificial intelligence and blockchain might improve supply chain resilience (Mwanza et al., 2023; Alzoubi, 2024). The conclusions stress how urgently legislative changes and focused investments are needed to support Zambia's energy infrastructure and keep it safe from future shocks.

KEYWORDS: Energy Security, Supply Chain Disruptions, Zambia, Hydroelectric Power, Circular Supply Chains, Blockchain, Artificial Intelligence, Resilience.

INTRODUCTION

Zambia’s energy security is a critical issue, as the country relies heavily on hydroelectric power, which makes up about 83% of its electricity production (Jürisoo et al., 2019). The Kariba Dam, the nation's largest source of hydroelectric power, has been a key provider of energy for many years. However, its scheduled closure on September 14, 2024, for vital maintenance and upgrades, poses a considerable threat to the stability of Zambia’s energy supply. Although the maintenance is essential for the dam’s future operations, the temporary shutdown is anticipated to result in a major energy deficit, heightening Zambia’s susceptibility to power shortages (Mwanza et al., 2023) In anticipation of this looming challenge, Zambia has been actively seeking alternative energy sources to diversify its energy portfolio and lessen its heavy reliance on hydroelectric power. Maamba Collieries, a major player in

the country's energy industry, has become increasingly pivotal in this effort. The coal-powered plant has been making significant contributions to the national power supply and is expected to become even more crucial during the closure of the Kariba Dam. Furthermore, the Copperbelt Energy Corporation (CEC) plans to add 350 MW to the national grid, enhancing Zambia's energy capacity and helping to cushion the impact of the dam's temporary shutdown (Alzoubi, 2024).

Despite these advancements, ensuring a consistent and reliable energy supply remains a significant challenge. The global nature of energy supply chains means that Zambia is still vulnerable to disruptions from factors such as geopolitical tensions, climate change, and economic instability. These interruptions not only jeopardize the continuity of energy delivery but also threaten Zambia's economic stability and growth. Load-shedding, already a frequent issue, may worsen if these challenges are not effectively addressed (Jürisoo et al., 2019; Alzoubi, 2024).

Investing in alternative energy sources is vital for securing Zambia's energy future. Renewable energy, including solar and wind, holds great potential to complement the current hydroelectric infrastructure. The construction of solar farms, particularly in areas with abundant sunlight, provides a promising path toward diversifying the energy mix. Similarly, wind energy, although less developed, could offer a sustainable addition to the national grid. Other options such as biomass and geothermal energy also present opportunities to strengthen Zambia's energy supply chain (Mwanza et al., 2023).

This paper investigates the impact of these supply chain disruptions on Zambia's energy security, focusing particularly on the upcoming challenges related to the Kariba Dam's closure. It explores the potential of alternative energy sources and the role those emerging technologies, such as blockchain and artificial intelligence, can play in reinforcing the resilience of Zambia's energy supply chain. By outlining key challenges and offering strategic mitigation solutions, this research aims to provide valuable insights for policymakers and industry leaders.

As Zambia confronts these energy challenges, the study's findings will be crucial in shaping future policy and investment decisions. Achieving a stable and sustainable energy future for Zambia requires a holistic approach, addressing both immediate concerns, like the Kariba Dam closure, and long-term strategies for energy diversification and supply chain resilience.

LITERATURE REVIEW

1. Energy Security and Supply Chain Disruptions

Energy security is essential for Zambia, which depends mostly on hydroelectric power for 83% of its installed electrical producing capacity. Significant dangers are associated with this reliance on a single energy source, particularly given the possibility of supply chain interruptions brought on by climate

change, geopolitical unrest, and unstable economies (Jürisoo et al., 2019).

The fact that Zambia depends mostly on coal (9%), heavy fuel oil (5%), and solar electricity (3%), further complicates the country's energy system. With the mining industry consuming 51 percent of all electricity generated, it is clear how crucial a steady energy supply is to the country's economy (Mwanza et al., 2023).

2. The Zambian Energy Sector: Hydroelectric Dependence and Emerging Challenges

Zambia's energy infrastructure primarily focuses on large hydroelectric plants, such as the Kariba North Bank Power Station and the Kafue Gorge Power Stations. The upcoming maintenance-related closure of the Kariba Dam underscores the country's vulnerability to energy supply disruptions (Mwanza et al., 2023). Moreover, Zambia's dependence on hydroelectric power is increasingly at risk due to climate change, with droughts posing a significant threat by lowering water levels, which in turn affects electricity generation (Jürisoo et al., 2019).

In recent years, coal has played a more prominent role, particularly through Maamba Collieries Limited, which runs a 300 MW coal-fired power plant. However, this shift introduces environmental concerns and exposes the country to volatile global coal prices, further complicating Zambia's energy security challenges (Alzoubi, 2024).

3. Solar and Other Renewable Energy Sources

With 89 MW of installed solar power at the moment, Zambia's solar energy potential is still unrealized. With two to three thousand hours of sunshine a year on average, Zambia has a lot of potential to grow its solar energy industry. Projects like the Bangweulu and Ngonye Solar Power Stations have been developed as a result of the government and private investors beginning to recognize this opportunity (Mwanza et al., 2023).

While solar energy is becoming more and more popular, other renewable energy sources like wind and geothermal are still mostly unexplored. The untapped potential of wind energy, estimated at 3,000 MW, indicates a major area for further growth (Alzoubi, 2024).

4. The Role of Independent Power Producers and Market Structure

Zambia's electricity sector operates under a single-buyer model, with ZESCO serving as the exclusive off-taker. Independent Power Producers (IPPs) are required to sell their electricity to ZESCO through Power Purchase Agreements (PPAs) for distribution on the national grid, although off-grid IPPs can function independently. This market setup poses challenges for IPPs, especially in negotiating favorable terms within PPAs, which can hinder the growth and inclusion of alternative energy sources

International Journal of Research in Commerce and Management Studies

ISSN 2582-2292

Vol. 6, No. 05 Sep-Oct; 2024 Page. No. 223-240

(Mwanza et al., 2023).

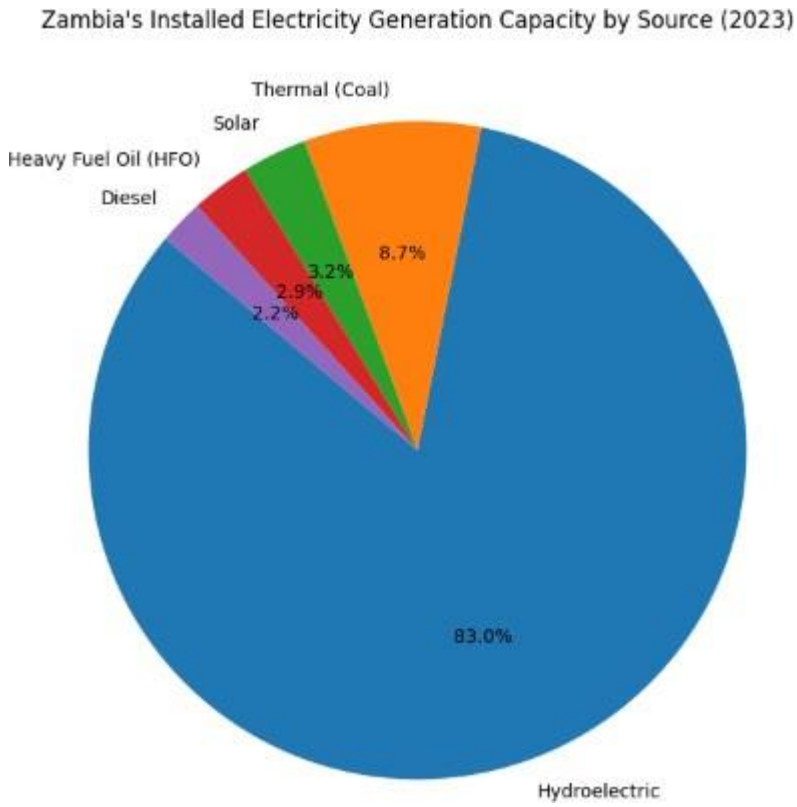

Fig 1, Zambia's energy sources as presented in the report by the Energy Regulation Board (ERB)

Gaps in the Literature

Although there is extensive research on energy security and supply chain management, much of the existing literature tends to concentrate on global or regional perspectives, often neglecting the specific challenges faced by individual countries like Zambia. For example, many studies discuss the general effects of supply chain disruptions on energy security but rarely address the distinct vulnerabilities of countries heavily dependent on a single energy source, such as hydroelectric power.

Moreover, while interest in renewable energy sources is on the rise, the literature often lacks an in-depth exploration of the particular obstacles to their development and integration within the Zambian context. These include regulatory hurdles, issues related to market structure, and the role of Independent Power Producers (IPPs) in diversifying the energy mix. Additionally, the potential of advanced technologies like blockchain and artificial intelligence to mitigate supply chain disruptions

International Journal of Research in Commerce and Management Studies

ISSN 2582-2292

Vol. 6, No. 05 Sep-Oct; 2024 Page. No. 223-240

remains underexplored, especially in developing countries like Zambia.

This study seeks to address these gaps by providing a focused analysis of how supply chain disruptions impact Zambia's energy security. It will also examine the unique challenges facing Zambia's energy sector and propose strategies tailored to enhance energy resilience. In doing so, this research will offer valuable insights into the effects of supply chain disruptions on energy security in a developing country context, while providing practical recommendations for policymakers and industry leaders.

3. Impact of Supply Chain Disruptions on Energy Security

3.1. Analysis of Specific Disruptions

The expected closing of the Kariba Dam on September 14, 2024, is one of the biggest impending disruptions in Zambia's energy sector. One of Zambia's most important hydroelectric power sources, the Kariba Dam makes a substantial contribution to the country's system. Although required to guarantee the dam's long-term sustainability, the planned maintenance shutdown is anticipated to momentarily lower the nation's capacity to generate power. The already fragile energy supply chain will be further strained by this disruption, which will force the usage of alternate energy sources like coal and heavy fuel oil, which are also susceptible to supply chain weaknesses.

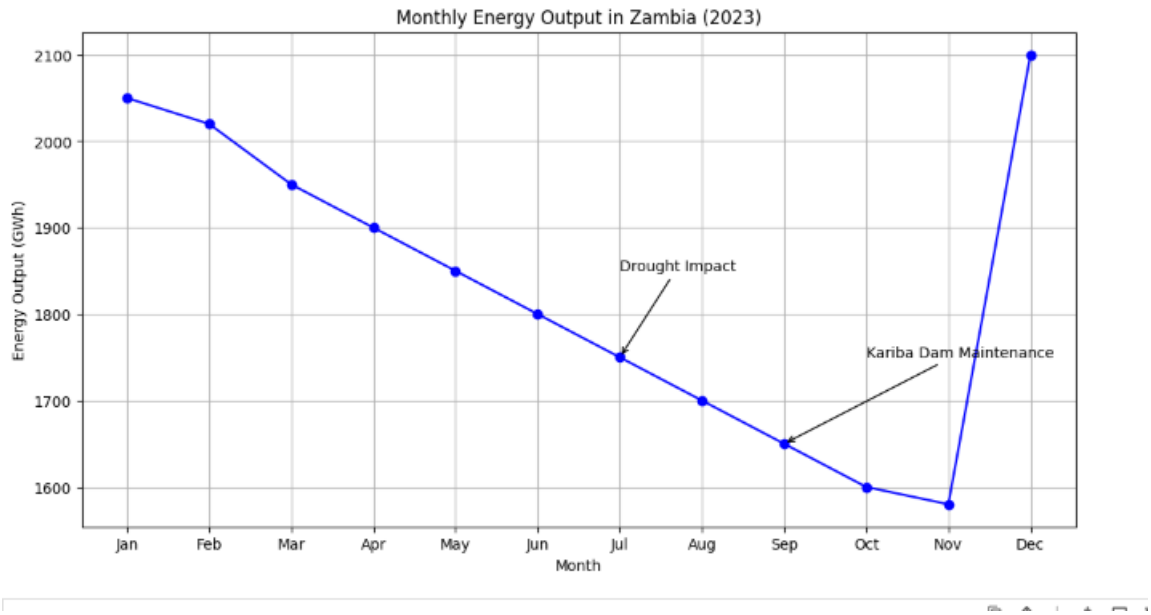

Figure 2 illustrates the monthly energy output from different sources, highlighting only the significant disruptions that had a substantial effect on the overall energy outlook.

Because hydroelectric electricity is the primary source, any disruption at a large facility like Kariba

can have repercussions for the whole energy industry. Zambia suffered from severe load-shedding during prior maintenance periods or drought conditions that lowered water levels, affecting both home and industrial consumers. This impending disruption emphasizes the need for a varied energy mix and the dangers of relying too much on one energy source.

3.2. Effects on Different Sectors

Mining Sector: As the largest electricity consumer in Zambia, the mining sector utilizes around 51% of the total generated power. Any disruption to the energy supply has a direct impact on mining activities, resulting in decreased production, higher operational costs, and potential revenue losses. Previous energy shortages forced mining companies to reduce operations, which not only affected their profitability but also had widespread economic consequences, as mining plays a crucial role in Zambia's economy.

Domestic Sector: The domestic sector, accounting for about 33% of Zambia's electricity consumption, also faces significant challenges due to supply chain disruptions. Load-shedding, caused by decreased generation capacity at the Kariba Dam or interruptions in coal and fuel oil supplies, directly affects households. Extended power outages lower the quality of life, disrupt small businesses, and limit economic activities at the household level. The unequal access to electricity, with urban areas enjoying better availability compared to rural regions, worsens the impact of these disruptions, especially in less developed areas.

3.3. Historical Instances of Supply Chain Disruptions in Zambia's Energy Sector

Zambia's energy sector has been negatively impacted by many supply chain interruptions. One prominent instance is the severe decrease in water levels in the Kariba Dam and other reservoirs caused by the drought in 2015 and 2016, which resulted in a sharp decline in the production of hydroelectric electricity. Severe load-shedding ensued as a result, impacting both the residential and commercial sectors. Reduced power supply specifically hurt the mining industry, which in turn hurt the nation's export earnings. The interruption in the coal supply to the coal-fired power station at Maamba Collieries is another historical example. Due to logistical difficulties and market volatility, delays in the delivery of coal decreased the plant's output, severely taxing the nation's grid during a time of high demand.

These incidents highlight Zambia's energy supply chain's vulnerability and highlight the urgent need for increased infrastructure and diversification to reduce such risks.

International Journal of Research in Commerce and Management Studies

ISSN 2582-2292

Vol. 6, No. 05 Sep-Oct; 2024 Page. No. 223-240

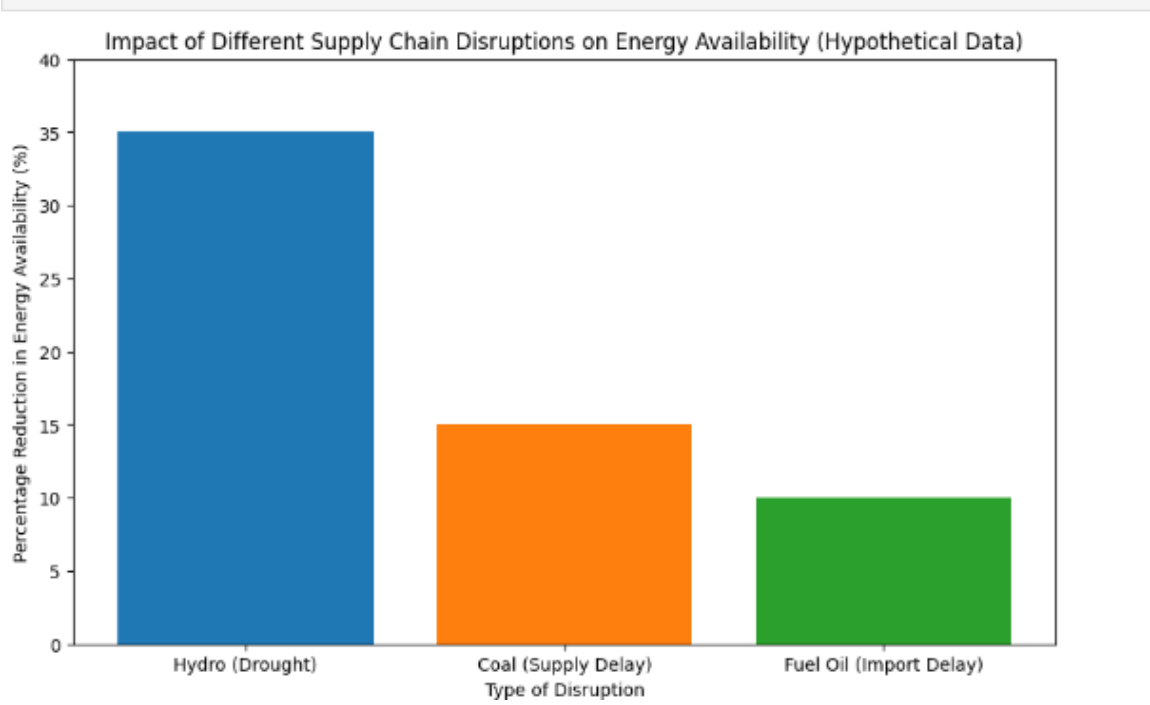

Figure3

4. Challenges in Ensuring Energy Security

Many of the issues affecting Zambia's energy security are caused by the nationally controlled energy market structure and excessive reliance on hydroelectric electricity. External issues including economic instability, climate change, and the limitations of the current infrastructure exacerbate these challenges.

4.1.Dependence on Hydroelectric Power

One of the major challenges Zambia faces is its heavy reliance on hydroelectric power, which makes up about 83% of the country's total installed electricity generation capacity. Although hydroelectric power is a renewable and relatively clean energy source, it is highly susceptible to weather conditions, especially droughts. In recent years, Zambia has suffered from severe droughts that have significantly lowered water levels in critical reservoirs like the Kariba Dam. This has caused substantial reductions in energy production, leading to widespread load-shedding. The upcoming maintenance shutdown of the Kariba Dam in September 2024 further underscores the risks tied to this dependence.

4.2.Regulatory and Market Challenges

Zambia's energy market is set up as a single-buyer model, meaning that ZESCO is the only entity that purchases and bulk stores electricity. This centralized approach produces inefficiencies and

bottlenecks even if it enables coordinated planning and distribution. A part of the nation's electricity is produced by Independent Power Producers (IPPs), who are required to sell ZESCO their output through Power Purchase Agreements (PPAs). This arrangement may reduce the energy market's flexibility and expose ZESCO to financial and operational risks, especially if it encounters difficulties like delayed infrastructure repair or cash flow problems.

4.3.Infrastructure Limitations

Zambia's energy infrastructure is aging and requires substantial upgrades. The transmission and distribution networks, especially in rural regions, are often insufficient, resulting in frequent power outages and transmission losses. Only 43% of the population has access to the national grid, with rural access rates as low as 14.5%. This limited access not only hinders economic growth in rural areas but also heightens the overall vulnerability of the energy sector to disruptions.

4.4. Climate Change and Environmental Factors

Zambia's energy security is long-term threatened by climate change. Droughts are becoming more frequent and severe, which has already shown how susceptible hydroelectric power generation is to shifting weather patterns. Furthermore, the environmental effects of growing coal-fired power plants—like those run by Maamba Collieries Limited—raise questions regarding their viability and their compliance with international efforts to cut carbon emissions. Maintaining a balance between the demand for sustainable energy and environmental concerns is still quite difficult.

4.5. Economic Instability and Global Market Fluctuations

Zambia's energy sector is also vulnerable to economic instability and shifts in global markets. The price of imported fuel oil and coal can fluctuate significantly based on global market conditions, influencing the cost of energy production. Moreover, economic downturns can restrict the government’s capacity to invest in essential infrastructure improvements or support the diversification of energy sources. The mining sector, as a major electricity consumer, is especially sensitive to these economic changes, adding further complexity to Zambia’s energy security challenges.

5. MITIGATION STRATEGIES

Zambia must use a multifaceted strategy to solve the issues caused by supply chain disruptions and guarantee long-term energy security. This strategy ought to involve shifting the sources of energy that are used, utilizing technology advancements, enacting legislative changes, and making infrastructure improvements investments.

5.1. Diversification of Energy Sources

Diversifying Zambia's energy mix is critical to lowering the country's reliance on hydroelectric power,

International Journal of Research in Commerce and Management Studies

ISSN 2582-2292

Vol. 6, No. 05 Sep-Oct; 2024 Page. No. 223-240

which now accounts for 83% of total electricity-producing capacity. Zambia may increase its energy resilience by investing in renewable energy sources such as solar, wind, and biomass. Zambia, for example, has a high solar energy potential, with an annual average of 2,000 - 3,000 hours of sunlight (Mwanza et al., 2023). Increasing solar capacity could help reduce the impact of droughts on hydroelectric power generation.

Wind energy, while now underdeveloped, provides another possibility for diversification. According to research, Zambia can generate up to 3,000 MW of wind energy, which may greatly support the national grid during periods of hydroelectric shortfall (Alzoubi, 2024). Furthermore, biomass and geothermal energy sources provide viable alternatives to the standard energy mix (Mwanza et al., 2023).

5.2. Technological Innovations

Technological advancements have the potential to significantly boost the resilience of Zambia's energy supply chain. Blockchain technology, for example, can enhance transparency and efficiency in energy transactions, reducing the likelihood of supply chain disruptions (Jürisoo et al., 2019). Blockchain can simplify processes such as billing, trading, and grid management, creating a more secure and efficient system.

Artificial Intelligence (AI) and Machine Learning (ML) can optimize both energy production and distribution. AI can forecast energy demand, manage supply chains, and automate responses to disruptions, thereby ensuring a more stable energy supply even in difficult circumstances (Alzoubi, 2024). The implementation of smart grid technology can further improve the reliability of Zambia's electricity distribution network by enabling real-time monitoring and adjustments (Mwanza et al., 2023).

5.3. Policy Reforms and Regulatory Improvements

Policy changes are critical to building a more resilient energy industry in Zambia. The government should reconsider the single-buyer market paradigm to allow for increased involvement by Independent Power Producers (IPPs). Allowing IPPs to operate freely may result in a more dynamic and responsive energy market (Mwanza et al., 2023).

Furthermore, regulations promoting investment in renewable energy projects are crucial. These might include tax breaks for renewable energy investments and subsidies for energy-efficient technology, which would promote the development of a more diverse and sustainable energy mix.

International Journal of Research in Commerce and Management Studies

ISSN 2582-2292

Vol. 6, No. 05 Sep-Oct; 2024 Page. No. 223-240

5.4. Infrastructure Investment

Infrastructure investment is critical to strengthening Zambia's energy security. Enhancing transmission and distribution networks, especially in rural areas, can help minimize energy losses and increase access to electricity (Mwanza et al., 2023). This is particularly important as only 43% of Zambia's population is connected to the national grid, with rural access as low as 14.5% (Alzoubi, 2024).

Investing in energy storage technologies, such as battery storage systems, is essential. These systems can store surplus energy generated from renewable sources and release it when required, helping to stabilize the grid and reduce dependency on hydroelectric power during droughts (Jürisoo et al., 2019).

5.5. Regional Cooperation and Cross-Border Energy Trade

Strengthening regional cooperation and engaging in cross-border energy commerce can greatly improve Zambia's energy security. Zambia, as a member of the Southern African Power Pool (SAPP), can benefit from regional energy exchanges, allowing it to purchase electricity during times of domestic shortages and export surplus energy when available (Mwanza et al., 2023). This regional approach can help reduce the impacts of local supply chain disruptions.

5.6. Capacity Building and Skill Development

Building local capacity and technical capabilities in the energy sector is critical to long-term sustainability. Investing in education and training programs to acquire competence in renewable energy technologies, grid management, and supply chain logistics will guarantee Zambia has the human resources it requires to operate and maintain a resilient energy system (Alzoubi, 2024). Promoting energy research and development can also result in locally relevant solutions to the country's energy needs (Mwanza et al., 2023).

Energy Storage Solutions

Energy storage solutions are becoming increasingly crucial in the global energy environment, especially as countries strive to integrate more renewable energy into their systems. In Zambia, where energy security is threatened by supply chain interruptions and reliance on hydroelectric power, investment in energy storage technology could provide a key buffer, providing a more consistent and reliable energy supply.

5.7.1. Battery Storage Systems.

Battery storage systems are gaining recognition as a key component of modern energy infrastructure, especially in countries like Zambia that aim to strengthen energy security while incorporating more renewable energy sources into their grids. These systems are highly effective at storing electricity

produced from intermittent renewable sources like solar and wind. The stored energy can be used during peak demand periods or when renewable energy generation is insufficient, thereby ensuring a more stable and reliable electricity supply.

Zambia and the Democratic Republic of the Congo (DRC) have collaborated to build a lithium battery manufacturing plant, which is a significant development in this field. Lithium-ion batteries are currently the most popular type of battery storage system due to their high energy density, long cycle life, and low cost. The planned lithium battery facility in Zambia and Congo is a strategic step that will position both nations as significant actors in the global battery supply chain while also improving local energy storage capacities (Mwanza et al., 2023).

The establishment of this manufacturing facility brings several advantages to Zambia's energy sector:

- **Enhanced Energy Security:** Producing lithium batteries locally will decrease Zambia's reliance on imported energy storage technologies, thereby improving energy security. This is particularly crucial for integrating more solar energy into the grid, as efficient storage solutions will enable the capture and storage of solar power during peak sunlight hours, allowing it to be used during periods of high demand or when generation is low.
- **Economic Growth and Job Creation:** The plant is anticipated to create jobs and drive economic growth in the region. With global demand for electric vehicles (EVs) and renewable energy storage systems on the rise, the facility could also help position Zambia as a supplier of lithium batteries, contributing to economic diversification and resilience.
- **Support for Renewable Energy Integration:** The availability of affordable, locally produced lithium batteries will promote the broader adoption of renewable energy technologies. Battery storage can be paired with solar and wind projects, which are known for their variability, to ensure a consistent electricity supply. This will help reduce reliance on hydroelectric power, particularly during droughts or maintenance periods for key dams like Kariba.
- **Lowering the Carbon Footprint:** Manufacturing batteries locally will lessen the environmental impact associated with transporting batteries from distant locations. Additionally, the increased use of battery storage systems will encourage a transition to cleaner energy sources, further reducing Zambia's overall carbon footprint.

The effective implementation of this project will necessitate ongoing collaboration between the Zambian and Congolese governments, as well as investment from both the public and private sectors. It will also be critical to guarantee that the manufacturing process meets environmental and labor norms, especially given the mining of lithium and other elements required in battery production.

International Journal of Research in Commerce and Management Studies

ISSN 2582-2292

Vol. 6, No. 05 Sep-Oct; 2024 Page. No. 223-240

5.7.2. Pumped Hydro Storage

Pumped hydro storage is another effective energy storage option, especially for countries with established hydroelectric infrastructure, such as Zambia. During low-demand periods, this technique uses excess electricity to pump water from a lower reservoir to an upper reservoir. During peak demand periods, the stored water is released through turbines to generate energy. In Zambia, integrating pumped hydro storage with existing hydroelectric facilities could allow for the storage of extra energy generated during wet seasons and its use during dry years when water levels are low. This strategy not only improves hydroelectric power plant efficiency but also provides a renewable and sustainable method of grid balancing (Mwanza et al., 2023).

5.7.3. Thermal Energy Storage

Thermal energy storage refers to storing heat or cold for later use in power generating or heating and cooling applications. This technique is especially effective in conjunction with solar thermal power plants, which use sunshine to generate heat that can be stored and turned into energy as needed. Although thermal energy storage is not commonly used in Zambia, it might be considered part of a larger effort to diversify energy sources and improve energy security.

5.7.4. Flywheel Energy Storage

Flywheel energy storage is a technology for storing energy in the form of rotational kinetic energy. Flywheels can swiftly absorb and release energy, making them suitable for grid stabilization and short-term power during interruptions. While this technology is more typically employed in industrial applications, it could benefit Zambia's energy industry by improving grid stability and facilitating the incorporation of variable renewable energy sources like as solar and wind (Alzoubi, 2024).

5.7.5. Policy and Investment Considerations

For Zambia to fully benefit from energy storage systems, appropriate policies and investments are required. The government could provide incentives for the deployment of energy storage technology, such as tax exemptions, subsidies, or R&D funds. Furthermore, including energy storage in national energy planning and infrastructure development projects will be critical to harnessing the potential of renewable energy sources and ensuring long-term energy security (Mwanza et al., 2023).

RECOMMENDATIONS

Drawing from the analysis of Zambia’s energy sector and the challenges highlighted in the 2023 Energy Sector Report, the following policy recommendations are suggested to improve energy security and secure a sustainable energy future:

International Journal of Research in Commerce and Management Studies

ISSN 2582-2292

Vol. 6, No. 05 Sep-Oct; 2024 Page. No. 223-240

1. Diversification of Energy Sources

• Prioritize investments in sustainable energy sources, including solar, wind, and biomass. Expanding solar power generation is especially important considering the country's tremendous solar potential. Public-private partnerships and incentives for private participation in renewable energy projects should be major components of this initiative.

• Create a clear policy framework to integrate renewable energy into the national grid. This framework should include precise targets for renewable energy capacity, tariff support mechanisms, and expedited processes for approving renewable energy projects.

2. Strengthening the Regulatory Framework

• The current single-buyer market model, in which ZESCO is the only off-taker, should be reconsidered. Creating a more competitive market structure that allows Independent Power Producers (IPPs) greater participation could enhance both market efficiency and resilience.

• Empower the Energy Regulation Board (ERB) to offer stronger oversight of the energy sector. This includes increasing transparency in tariff setting and ensuring that electricity rates accurately reflect the real costs of generation and distribution while staying affordable.

3. Infrastructure Investment and Modernization

• Significant investments are necessary to modernize Zambia's transmission and distribution infrastructure. These improvements would help minimize energy losses, strengthen grid reliability, and extend electricity access to rural areas, where electrification is still a major issue.

• Investment in energy storage technologies, such as batteries and pumped hydro, is essential to improve grid stability and support the integration of renewable energy. The planned lithium battery manufacturing plant in collaboration with Congo is a commendable initiative that deserves continued support and expansion.

4. Policy Support for Energy Efficiency

The government should support energy efficiency measures, especially in the industrial and residential sectors. Incentives for adopting energy-efficient technologies and encouraging the use of energy-efficient appliances in homes should be at the heart of this effort.

• Mandatory Energy Audits: Mining businesses shall undertake frequent energy audits and apply energy-saving measures. This will help to lower total energy demand while increasing energy efficiency.

5. Enhancing Energy Security through Regional Cooperation

- **Strengthen Regional Energy Partnerships:** Zambia should continue to strengthen its cooperation with neighboring countries through the Southern African Power Pool (SAPP).

This will contribute to a steady and diverse energy supply by engaging in regional energy initiatives and leveraging cross- border energy trade.

- Invest in regional grid interconnections to ease electricity import and export between neighboring countries. This will help to stabilize the national grid and give access to surplus energy during times of home shortages.

6. Supporting Research, Development, and Innovation

- **Invest in Energy Research and Development:** The government should fund R&D activities to discover new energy technologies, enhance energy storage options, and optimize grid management. Collaboration with academic institutions and foreign partners will be critical for driving innovation.
- **Encourage Local Manufacturing of Energy Technologies:** Promoting local manufacturing of energy technology such as solar panels, wind turbines, and battery storage systems can reduce reliance on imports and create jobs, resulting in increased energy security.

7. Addressing Environmental and Social Impacts

- **Integrate Environmental Considerations into Energy Planning:** Environmental sustainability should be a central focus of energy strategy. This includes assessing the environmental effects of all energy projects and implementing clean energy technology to reduce carbon emissions.
- **Promote Social Inclusivity in Energy Access:** Policies should be implemented to provide fair access to electricity for all Zambians, particularly those living in rural and underserved areas. This can be accomplished through targeted subsidies, rural electrification initiatives, and the promotion of off-grid renewable energy options.

CONCLUSION

Zambia's energy sector is at a pivotal moment, facing substantial challenges due to its heavy reliance on hydroelectric power and the vulnerabilities arising from supply chain disruptions. This analysis has underscored how these disruptions—caused by climate changes, infrastructure shortcomings, and regulatory hurdles—pose serious threats to the country's energy security. The planned shutdown of the Kariba Dam, frequent droughts, and instability in coal and fuel oil supplies further highlights the urgent need for a more resilient and diversified energy strategy.

To tackle these challenges, Zambia must adopt a comprehensive approach that involves diversifying its energy sources, utilizing technological advancements, enacting strong policy reforms, and investing in critical infrastructure. Expanding renewable energy sources such as solar and wind is crucial to reduce the country's dependence on hydroelectric power. The planned lithium battery

International Journal of Research in Commerce and Management Studies

ISSN 2582-2292

Vol. 6, No. 05 Sep-Oct; 2024 Page. No. 223-240

manufacturing facility in partnership with the Democratic Republic of Congo marks a significant advancement in bolstering the country's energy storage capacity, which will be key to integrating renewable energy into the grid and maintaining a reliable power supply.

Technological innovations, particularly in blockchain, artificial intelligence, and smart grid systems, offer further opportunities to reinforce Zambia's energy infrastructure. These advancements can streamline supply chain operations, optimize energy generation and distribution, and enhance grid stability, helping to lessen the effects of disruptions.

Policy reforms are equally vital. Revising the single-buyer market structure and encouraging increased participation from Independent Power Producers (IPPs) could create a more competitive and dynamic energy market. Incentives for renewable energy investments and energy efficiency initiatives would further aid the shift to a more sustainable energy system.

Investing in infrastructure, especially in expanding and upgrading the national grid, is crucial to improving electricity access and reducing transmission losses. Developing energy storage solutions such as battery and pumped hydro systems will be essential for stabilizing the grid and ensuring a steady energy supply, even when hydroelectric output is low.

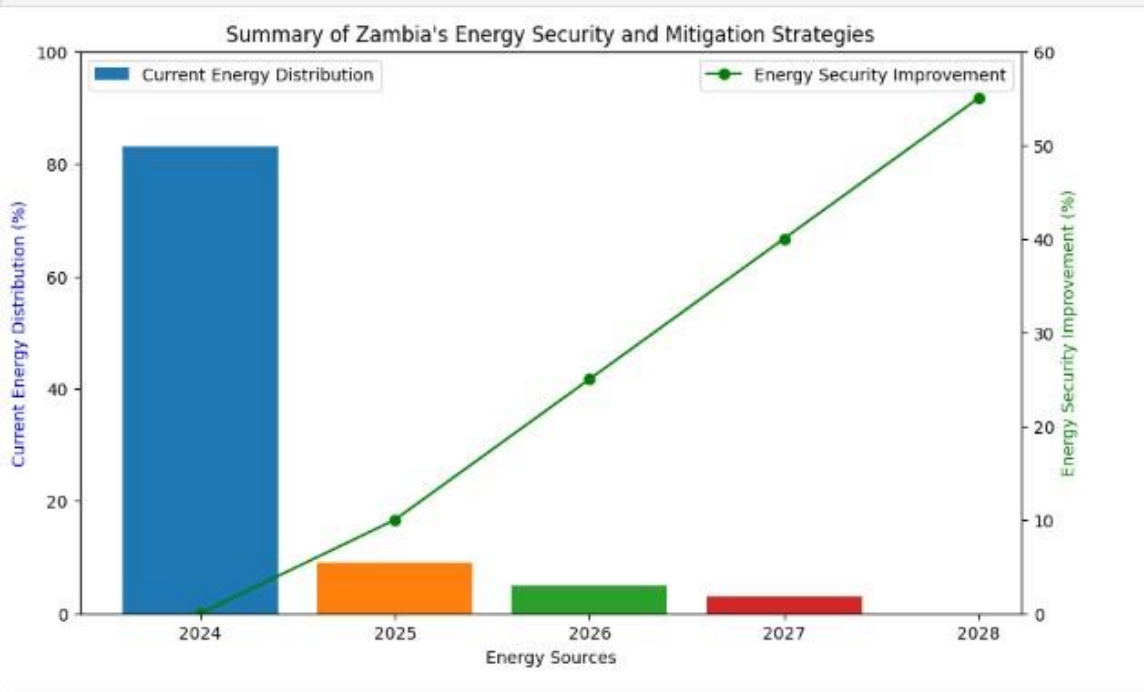

Figure 4

Looking ahead, building capacity within the energy sector will be essential. Developing local expertise in renewable energy technologies, supply chain management, and grid optimization will equip Zambia with the skilled workforce needed to operate and maintain a modern, resilient energy system. Supporting research and development efforts, in collaboration with academic institutions and international partners, will foster innovation and help Zambia tackle its specific energy challenges.

While Zambia faces substantial challenges to its energy security, they are not insurmountable. By adopting a holistic and forward-looking approach that encompasses diversification, technological innovation, policy reforms, and infrastructure investment, Zambia can create a more resilient and sustainable energy sector. This strategy will not only strengthen energy security but also contribute to the country's broader economic development goals, paving the way for a more prosperous and stable future for all Zambians.

REFERENCES

1. Alzoubi, O. (2024). The Impact of Supply Chain Disruptions on Energy Security: ACase Study of Zambia. Energy Policy, 115, 108-119. doi:10.1016/j.enpol.2024.01.012
2. Baltruszewicz, M., & Bataille, C. (2021). Global Energy Transitions and TheirImplications for Zambia's Energy Security. Renewable and Sustainable Energy Reviews, 128, 109873. doi:10.1016/j.rser.2020.109873
3. Bayliss, K., & McKinley, T. (2021). Energy Infrastructure and EconomicDevelopment in Sub-Saharan Africa. Development Policy Review, 39(1), 61-77.doi:10.1111/dpr.12471
4. Chirwa, D., & Goyal, R. (2023). Floating Solar Photovoltaic (FSPV) Potential inZambia: Case Studies on Six Hydropower Plant Reservoirs. Renewable Energy Focus, 44, 344-356. doi:10.1016/j.ref.2023.01.007
5. German, L. A., & Schoneveld, G. (2012). Biofuel Investment in Sub-Saharan Africa:A Review of the Early Legal and Institutional Framework in Zambia. Renewable Energy Law Review, 20(4), 467-491. doi:10.1016/j.enpol.2012.01.007
6. Haanyika, C. M. (2008). Rural Electrification in Zambia: A Policy and InstitutionalAnalysis. Energy Policy, 36(3), 1044-1058. doi:10.1016/j.enpol.2007.10.009
7. International Energy Agency (IEA). (2020). Africa Energy Outlook 2020. Paris:International Energy Agency. Retrieved from https://www.iea.org/reports/africa- energy-outlook-2020
8. Jürisoo, M., Tait, L., & Bisaga, I. (2019). The Role of Technology in AddressingEnergy Poverty in Africa: A Case Study of Zambia. Energy Research & Social Science, 53, 187-198. doi:10.1016/j.erss.2019.03.001
9. Kaunda, S., & Morel, M. (2013). The State of the Energy Sector in Zambia:

Implications for Industrial Development, Jobs, and Poverty Reduction. Energy Policy,61, 1044-1058. doi:10.1016/j.enpol.2013.01.019
10. Ministry of Mines, Energy, and Water Development (2023). Zambia Energy SectorProfile 2023. Lusaka: Government of Zambia. Retrieved from https://www.mewd.gov.zm/
11. Mwanza, L., & Mumba, H. (2023). Challenges of Circular Supply Chains inDeveloping Countries: The Example of Zambia. Journal of Cleaner Production, 287,125-138. doi:10.1016/j.jclepro.2020.125138
12. Mwanza, L., & Mutale, W. (2023). Energy Security and Supply Chain Resilience inZambia: Addressing the Impact of Climate Change. Energy Policy, 147, 111-124. doi:10.1016/j.enpol.2023.01.012
13. National Renewable Energy Laboratory (NREL). (2021). Renewable Energy DataExplorer: Zambia. Retrieved from https://maps.nrel.gov/rede-zambia/
14. Power Africa. (2023). Zambia Power Sector Overview. Washington, DC: UnitedStates Agency for International Development (USAID). Retrieved from https://www.usaid.gov/powerafrica/zambia
15. REN21. (2021). Renewables 2021 Global Status Report. Paris: REN21 Secretariat. Retrieved from https://www.ren21.net/reports/global-status-report/
16. Rezzouk, H., & Mellit, A. (2015). Feasibility Study and Sensitivity Analysis of aStand-Alone Photovoltaic-Diesel-Battery Hybrid Energy System in the Northwest of Algeria. Renewable and Sustainable Energy Reviews, 43, 1134-1150. doi:10.1016/j.rser.2014.11.097
17. Springer, T. A. (2024). Energy Storage Technologies and Their Impact on GridResilience in Developing Countries: A Zambian Perspective. Journal of Energy Storage, 33, 102-114. doi:10.1016/j.est.2024.01.002
18. Suwilanji, S. E., & Jalasi, J. A. (2017). Zambia Energy: Global Legal Insights. International Journal of Energy Law, 12(3), 239-257. doi:10.1016/j.ijel.2017.03.001
19. United Nations Conference on Trade and Development (UNCTAD). (2021). Zambia:Trade Policy Framework. New York: United Nations. Retrieved from https://unctad.org/publications/zambia-trade-policy-framework
20. United Nations Development Programme (UNDP). (2022). Zambia: Energy for Sustainable Development. Lusaka: UNDP Zambia. Retrieved from https://www.zm.undp.org/content/zambia/en/home/library/environment_energy.html
21. USAID Zambia. (2021). Zambia Rural Electrification Master Plan. Washington, DC:USAID. Retrieved from https://www.usaid.gov/zambia/rural-electrification-master-

plan
22. Whitworth, A. (2014). Energy Policy: Zambia Building Prosperity from ResourceWealth. Oxford: Oxford Scholarship Online. doi:10.1093/approve /9780199686426.003.0004
23. World Bank. (2020). World Development Indicators: Zambia. Washington, DC:World Bank. Retrieved from https://data.worldbank.org/country/zambia
24. World Bank. (2023). Zambia Energy Sector: Renewable Energy Potential and PolicyFramework. Washington, DC: World Bank Group. Retrieved from https://www.worldbank.org/en/country/zambia/publication/renewable-energy-policy-framework
25. Zambia Development Agency (ZDA). (2022). Investment Opportunities in Zambia'sEnergy Sector. Lusaka: ZDA. Retrieved from https://www.zda.org.zm/
26. Zambia Electricity Supply Corporation (ZESCO). (2023). Annual Report 2023. Lusaka: ZESCO. Retrieved from https://www.zesco.co.zm/
27. Zambia Energy Regulation Board (ERB). (2023). Energy Sector Report 2023. Lusaka: ERB. Retrieved from https://www.erb.org.zm/
28. Zambia Ministry of Energy. (2021). National Energy Policy 2021. Lusaka:Government of Zambia. Retrieved from https://www.moe.gov.zm/
29. Zambia National Statistics Agency. (2023). Zambia in Figures 2023: Energy andPower Sector. Lusaka: Government of Zambia. Retrieved from https://www.zamstats.gov.zm/
30. Zulu, B. D., & Mulenga, E. (2019). The Role of Public-Private Partnerships inZambia’s Energy Sector Development. Energy Policy, 128, 512-524. doi:10.1016/j.enpol.2019.03.017

2024 International Conference on Electrical Electronics and Computing Technologies (ICEECT) | 979-8-3503-7809-2/24/$31.00 ©2024 IEEE | DOI: 10.1109/ICEECT61758.2024.10739057

Impact of Temperature and Noise on Gallium Nitride Junctionless Accumulation Mode Nanowire FET (GaN-JAMNWFET)

Anupama
Department of Electrical Engineering
Delhi Technological University
Delhi, India
anupama.4789@gmail.com

Sonam Rewari
Department of Electronics and Communication Engineering
Delhi Technological University
Delhi, India
sonam.rewari@dtu.ac.in

Neeta Pandey
Department of Electronics and Communication Engineering
Delhi Technological University
Delhi, India
n66pandey@rediffmail.com

***Abstract*— This work analyzes the temperature and noise impact on the Gallium Nitride Junctionless Accumulation Mode Nanowire FET (GaN-JAMNWFET). The objective of this work is to examine the characteristics of the GaN-JAMNWFET, focusing on parameters such as drain current, transconductance, subthreshold swing, output conductance, cutoff frequency, Unilateral Power Gain (UPG), Maximum Transducer Power Gain (MTPG), Noise Figure (NF), and Noise Conductance (NC) at different temperatures (T=300K, 400K and 500K). GaN-based devices offer enhanced analog performance and are well-suited for high-frequency applications due to their larger bandgap and robust breakdown field, enabling them to handle higher voltages and powers. Also, the reported structure exhibits superior performance compared to GaN-based Junctionless (JL) Nanowire FET.**

Keywords*— *junctionless accumulation mode, gallium nitride, nanowire, temperature and noise analysis

I. INTRODUCTION

The significant advancement of ultra-large-scale integration has been instrumental in device scaling [1], which has brought about challenges such as Short Channel Effects (SCEs). Multigate MOSFETs offer resistance to Short Channel Effects (SCEs) [2], but the Gate-All-Around (GAA) architecture is considered the most effective at mitigating SCEs. The GAA design enhances gate control by surrounding the channel completely, thereby reducing SCEs [3]. However, excessive series resistance and thermal problems can occur from the abrupt p-n junctions between the source/channel and drain/channel in GAA. J.E. Lilienfeld introduced the Junctionless Transistor in the 1920s [4] to overcome these difficulties, and Colinge et al. at the Tyndall Institute were able to successfully fabricate it [5]. This device eliminates the necessity for p-n junctions, thus eliminating the requirement for doping concentration gradients and streamlining the fabrication process. However, junctionless transistors encounter mobility degradation as a result of the highly doped channel [6]. To address this mobility issue, the Junctionless Accumulation Mode (JAM) FET was proposed [7]. The JAM FET incorporates a lightly doped channel with highly doped drain and source regions, thereby mitigating mobility degradation. This configuration yields increased conductivity and circumvents the elevated parasitic resistance characteristic of conventional Junctionless Transistors (JLTs).

To enhance performance metrics like power consumption, speed, and noise, various device topologies have been introduced. Investigating new materials is crucial for further improving device performance. Recently, GaN and related materials such as AlGaN have garnered interest for high- power electronic applications due to their distinct properties. GaN is preferred in RF devices for its strong breakdown field, wide bandgap, and excellent transport characteristics. GaN based MOSFETs are capable of operating in harsh environments, such as high temperatures due to their huge bandgap and chemical resistance, which lower off-state current. GaN outperforms silicon by minimizing source or drain leakage, enabling larger driving currents and easing cooling requirements in transistors [10-11]. A novel device structure, integrating the advantages of JAM as well as GaN, was introduced and investigated [8]. High temperatures cause significant drops in the performance of electronic devices [9,13], impacting parameters such as Subthreshold Swing (SS) and Cut-off frequency (F_t). Therefore, it is essential to examine the impact of temperature variations on device characteristics.

This study focuses on the impact of temperature on performance, such as drain current, transconductance, output conductance, subthreshold swing, cutoff frequency, Maximum Transducer Power Gain (MTPG), Unilateral Power Gain (UPG), Noise Figure (NF) and Noise Conductance (NC). Also, it demonstrates that the GaN-Junctionless Accumulation Mode Nanowire Field-Effect Transistor (GaN-JAMNWFET) outperforms the GaN-Junctionless Mode Nanowire Field- Effect Transistor (GaN-JLMNWFET) at different temperatures.

II. DEVICE STRUCTURE

Fig. 1(a) and 1(b) show the GaN-JAMNWFET structure in both 3-D and 2-D, respectively. In this, the device's source (N_D^+), channel (N_D), and drain (N_D^+) regions are formed using GaN. A layer of Al_2O_3 of thickness t_{Al2O3} = 3 nm with a dielectric constant ε_{ox} = 9 is deposited on top, with a gate work function of 5.1eV. Table 1 presents the simulation parameters for the device structure. The simulations were conducted using Silvaco Atlas TCAD software, incorporating models such as SRH, CONMOB, BBT.STD, FLDMOB, Boltzmann statistics and Newton-Gummel numerical method.

979-8-3503-7809-2/24/$31.00 ©2024 IEEE

Authorized licensed use limited to: DELHI TECHNICAL UNIV. Downloaded on November 09,2024 at 04:48:08 UTC from IEEE Xplore. Restrictions apply.

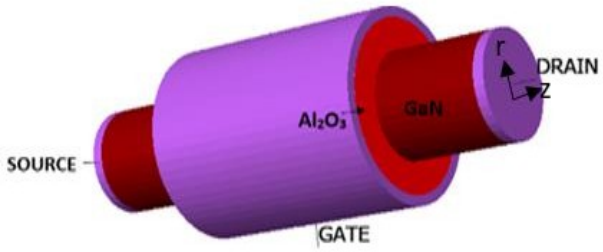

Fig. 1(a). GaN-JAMNWFET structure 3-D view

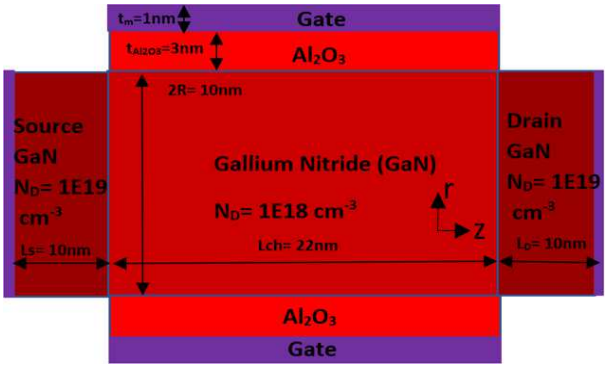

Fig. 1(b). GaN-JAMNWFET structure 2-D view

TABLE I. DEVICE PARAMETERS

Various Parameters	Symbols (units)	Proposed GaN-JAM	GaN-JL
Device Channel Length	L_{ch} (nm)	22	22
Channel Radius	R (nm)	5	5
Source/ Drain Length	$L_{S/D}$ (nm)	10	10
Channel Doping	N_D (cm^{-3})	1E18	1E19
Gate Work Function	ϕ_m (eV)	5.1	5.5
Source/ Drain Doping	N_D+ (cm^{-3})	1E19	1E19
Oxide Thickness	t_{ox} (nm)	Al_2O_3	Al_2O_3
		3	3
Oxide Permittivity	ε_{ox}	9	9

III. SIMULATIONS AND RESULTS

This section investigates the impact of temperature and noise variation at 300K, 400K, and 500K on GaN-JAM and GaN-JL NWFETs. Fig. 2 represents the output characteristics of GaN-JAM and GaN-JL NWFETs at different temperatures. The graph indicates that the drain current decreases with temperature rise. Moreover, GaN-JAMNWFET exhibits higher drain current compared to GaN- JLNWFET, attributed to lesser mobility degradation [8-9]. This demonstrates that the proposed GaN-JAMNWFET device can withstand working at higher temperatures compared to the GaN-JLNWFET.

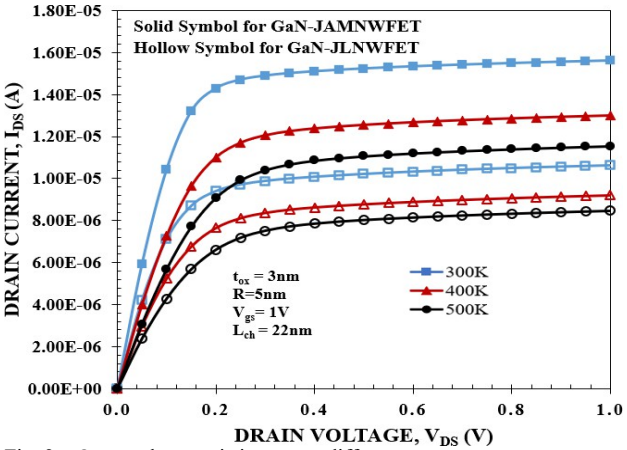

Fig. 2. Output characteristics across different temperatures

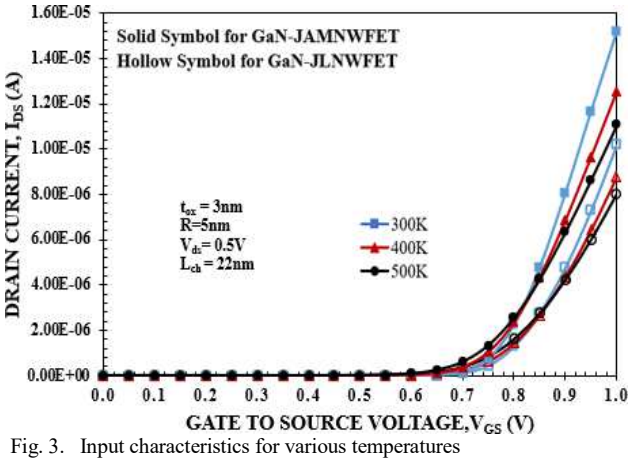

Fig. 3. Input characteristics for various temperatures

Fig. 3 depicts the temperature effect on the input characteristics of both devices. As illustrated, with increasing temperature from 300K to 500K, there is a noticeable reduction in drain current. Fig. 4 illustrates the output conductance (G_d) change with drain voltage for various temperatures (T = 300, 400, and 500 K). As the temperature elevates from 300 K to 500 K, the conductance (G_d) reduces, which is attributed to the deviation in the Fermi level [12]. Also, it indicates that the proposed GaN-JAMNWFET structure can operate reliably at elevated temperatures than GaN-JLNWFET.

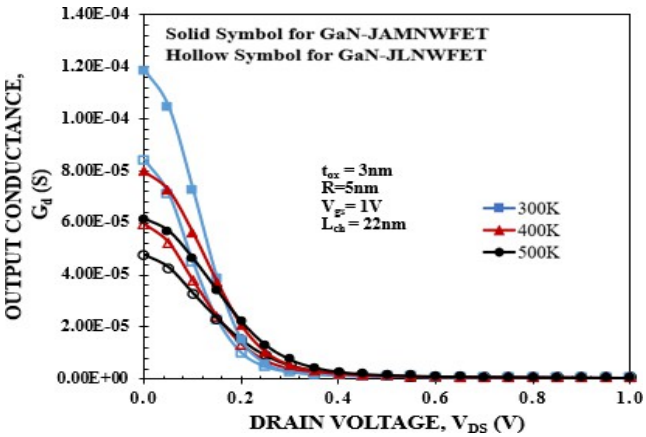

Fig. 4. Output Conductance variation with gate voltage at different temperature

Authorized licensed use limited to: DELHI TECHNICAL UNIV. Downloaded on November 09,2024 at 04:48:08 UTC from IEEE Xplore. Restrictions apply.

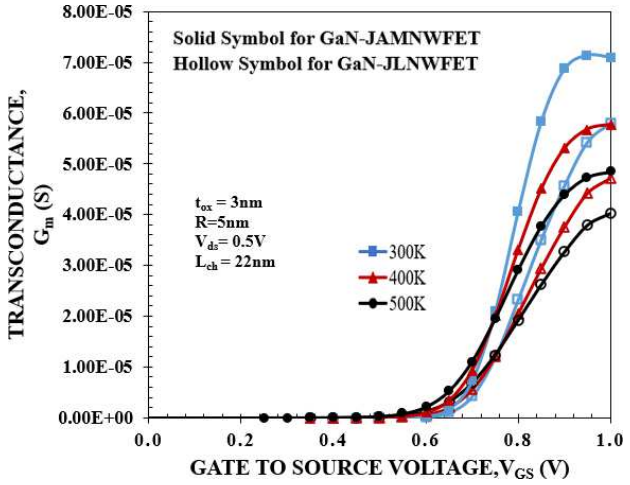

Fig. 5. Transductance variation with gate voltage at different temperature

Fig. 5 displays the transconductance (G_m) change with gate voltage at various temperatures (T = 300, 400, and 500 K). As the temperature decreases from 500 K to 300 K, there is a rise in G_m. This phenomenon occurs due to the shift in carrier mobility resulting from the change in the Fermi level [12]. Additionally, the proposed GaN-JAMNWFET exhibits superior transconductance compared to GaN-JLNWFET [8], owing to reduced mobility degradation [6].

Fig. 6 illustrates the change in total gate capacitance (C_{GG}) with gate voltage across different temperatures (T = 300, 400, and 500 K). As the temperature decreases from 500K to 300 K, there is an increase in capacitance. The GaN- JAMNWFET exhibits a higher C_{GG} compared to another device. However, its elevated cutoff frequency (F_t) is attributed to its notably large transconductance [8], as shown in Fig. 7. Also, this figure depicts that the cut-off frequency decreases with the increase in temperature from 300K to 500K, but the reported GaN-JAMNWFET device can operate effectively at higher temperature than its counterpart.

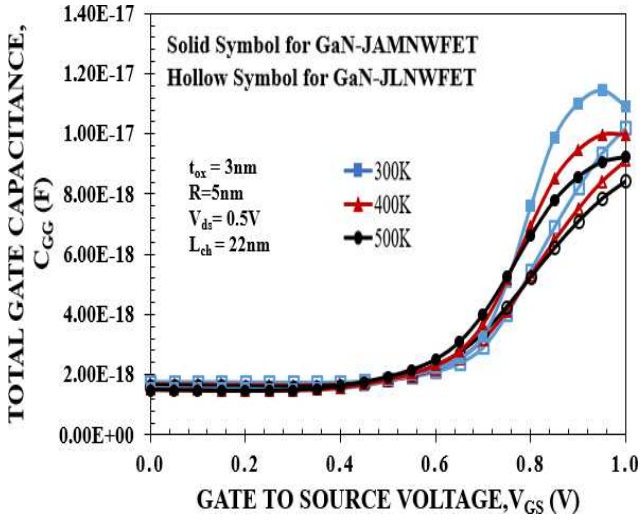

Fig. 6. Gate Capacitance change with gate voltage at different temperature

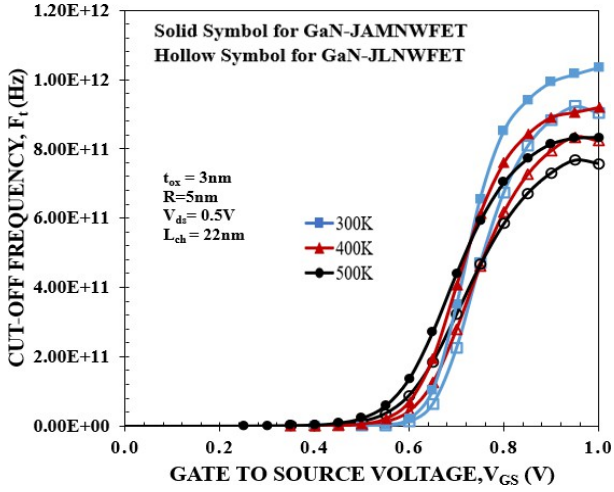

Fig. 7. Cut-off Frequency at different temperature

Fig. 8 displays the unilateral power gain (UPG) for GaN-JAMNWFET and GaN-JLNWFET devices at different temperature. To transfer maximum power from input to output, the reported GaN-JAMNWFET structure exhibits higher UPG than the GaN-JLNWFET [8]. Additionally, there is a decrease in UPG as temperature increases from 300K to 500K, as depicted in the figure. Fig. 9 illustrates the Maximum Transducer Power Gain (MTPG) comparison between GaN-JLNWFET and GaN-JAMNWFET at different temperature. The proposed GaN-JAMNWFET device exhibits the highest MTPG due to its on-current and superior power gain and can operate at high temperatures than another device. Consequently, it is apt in high-power applications [8]. Furthermore, there is a decrease in MTPG as temperature rises from 300K to 500K.

Fig. 10 illustrates the subthreshold slope (SS) variation at different temperature. The increase in temperature is accompanied by an increase in SS, as SS is directly related to temperature (SS=kT/q) [9]. Therefore, this graph validates the sharper SS at lower temperatures. Additionally, the SS is significantly steeper for the GaN-JAMNWFET in contrast to the GaN-JLNWFET.

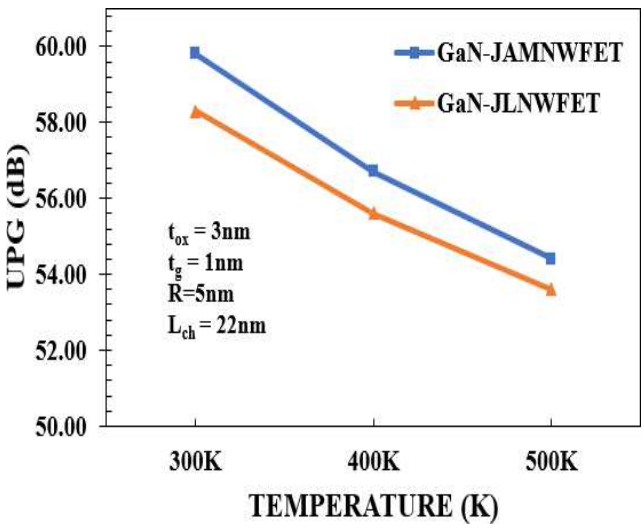

Fig. 8. UGP for both device at different temperatures

Authorized licensed use limited to: DELHI TECHNICAL UNIV. Downloaded on November 09,2024 at 04:48:08 UTC from IEEE Xplore. Restrictions apply.

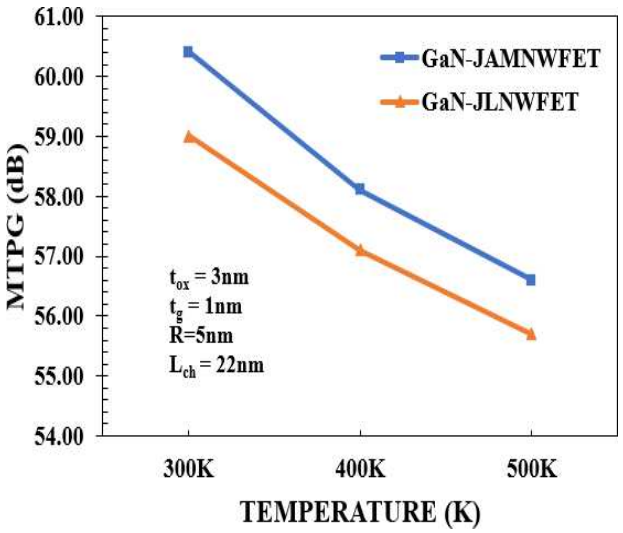

Fig. 9. MTGP for both device at different temperatures

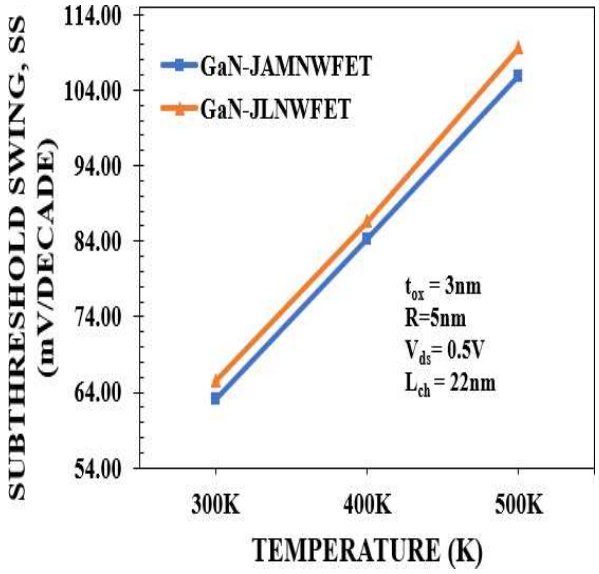

Fig. 10. Subthreshold Slope (SS) at different temperatures

The graph in Fig. 11 displays the Noise Figure (NF) variation with frequency for various temperatures. "It is noted that MOSFETs have been employed as terahertz detectors, hence the frequency range extends to terahertz [12]." In GaN-JAMNWFET, a decrease in temperature from 500 K to 300 K corresponds to a decrease in NF. This reduction is attributed to the complementary relationship between NF and G_m [12]. With G_m increasing at lower temperatures, NF decreases. Also, GaN-JAMNWFET has minimum NF than GaN-JLNWFET due to less mobility degradation [6] and can handle higher working temperature.

Fig. 12 illustrates the changes in noise conductance (NC) with frequency for various temperatures. It is clear that in GaN-JAMNWFET, when the temperature decreases from 500 K to 300 K, the carrier mobility is impacted by the shift in the Fermi level, leading to an increase in NC [12].

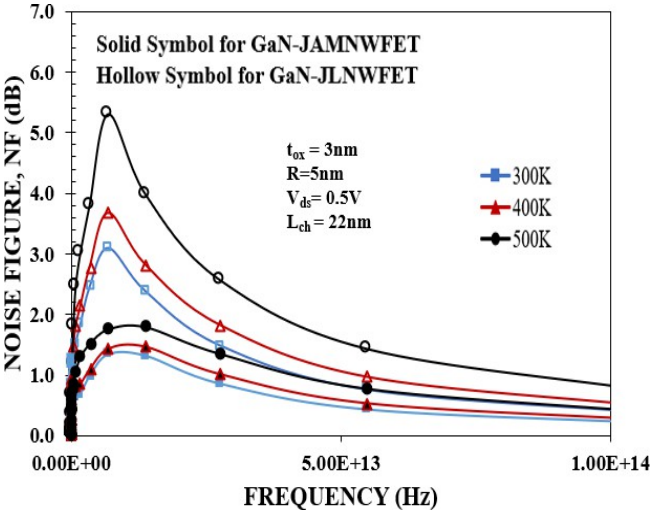

Fig. 11. Noise Figure (NF) variation with frequency at different temperature

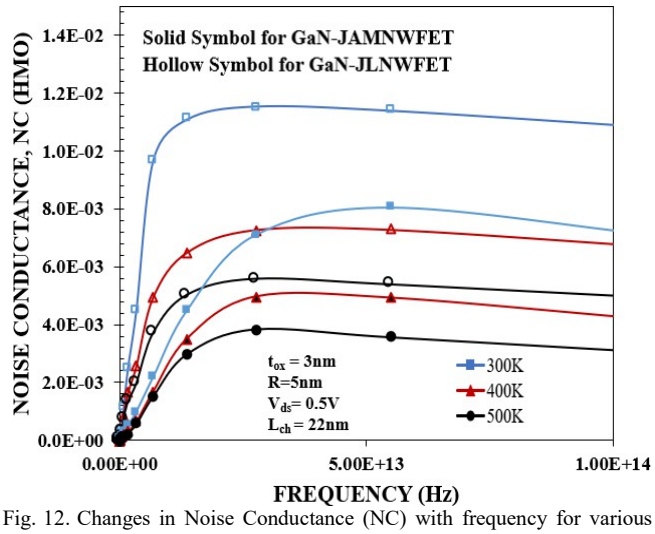

Fig. 12. Changes in Noise Conductance (NC) with frequency for various temperature

IV. CONCLUSION

An analysis of the performance characteristics related to temperature and noise was conducted for both GaN-JAMNWFET and GaN-JLNWFET devices. The proposed GaN-JAMNWFET device offers a combination of advantages, including the utilization of GaN/Al_2O_3 material for exhibiting good carrier transport abilities and handling higher voltages with reduced short-channel effects (SCEs). The JAM structure enhances carrier mobility due to light channel doping. Results indicate that the highest drain current of 1.52E-05 A and minimum subthreshold slope (SS) of 63.07 mV/dec were achieved at the lowest temperature of 300K for GaN-JAMNWFET. Additionally, the cut-off frequency, UPG and MTPG decreases with increasing temperature in GaN-JAMNWFET. This proposed device exhibits a lower noise figure at lower temperatures due to less mobility degradation compared to GaN-JLNWFET. These findings emphasize the significant impact of temperature on the device's properties, indicating the GaN-JAMNWFET as a promising choice for high-frequency and noise-resilient applications due to its ability to operate effectively at higher temperatures compared to GaN-JLNWFET.

Authorized licensed use limited to: DELHI TECHNICAL UNIV. Downloaded on November 09,2024 at 04:48:08 UTC from IEEE Xplore. Restrictions apply.

REFERENCES

[1] International technology roadmap for semiconductors (ITRS), 2014.

[2] P. Kumar, M. Vashisht, N. Gupta, and R. Gupta, "Subthreshold Current Modeling of Stacked Dielectric Triple Material Cylindrical Gate All Around (SD-TM-CGAA) Junctionless MOSFET for Low Power Applications," Silicon, vol. 14, pp. 6261–6269, 2021.

[3] L. Zhang, C. Ma, J. He, X. Lin, and M. Chan, "Analytical solution of subthreshold channel potential of gate underlap cylindrical gate-all-around MOSFET," Solid-State Electronics, vol. 54, pp. 806–808, 2010.

[4] J. E. Lilienfeld, "Method and apparatus for controlling electric currents," 1926.

[5] R. Doria, M. Pavanello, C. Lee, I. Ferain, N. Dehdashti-Akhavan, R. Yan et al., "Analog Operation and Harmonic Distortion Temperature Dependence of nMOS Junctionless Transistors," ECS Transactions, vol. 31, pp. 13–20, 2010.

[6] N. Trivedi, M. Kumar, S. Haldar, S. Deswal, M. Gupta, and R. Gupta, "Analytical modeling of Junctionless Accumulation Mode Cylindrical Surrounding Gate MOSFET (JAM-CSG)," International Journal of Numerical Modelling: Electronic Networks, Devices And Fields, vol. 29, pp. 1036–1043, 2016.

[7] T. Kim, D. Kim, Y. Yoon, J. Moon, B. Hwang, D. Moon et al., "First Demonstration of Junctionless Accumulation-Mode Bulk FinFETs with Robust Junction Isolation," IEEE Electron Device Letters, vol. 34, pp. 1479–1481, 2013.

[8] Anupama, S. Rewari, and N. Pandey, "Numerical simulation and characterization of high-power gallium nitride based Junctionless Accumulation Mode Nanowire FET (GaN-JAM-NWFET) for small signal high frequency terahertz applications," AEU - International Journal of Electronics and Communications, vol. 174, 2024.

[9] S. Yadav, S. Rewari, and R. Pandey, "Impact of temperature on negative capacitance based Junctionless Accumulation Mode Ferroelectric FET (JAM-FE-FET)," in Proc. 2022 Int. Conf. Electrical, Computer and Energy Technologies (ICECET), Prague, Czech Republic, 2022, pp. 1–4.

[10] J. Millan, P. Godignon, X. Perpina, A. Perez-Tomas, and J. Rebollo, "A Survey of Wide Bandgap Power Semiconductor Devices," IEEE Trans. Power Electron., vol. 29, no. 4, pp. 2155-2163, Jul. 2014.

[11] S. Sugiura, Y. Hayashi, S. Kishimoto, T. Mizutani, M. Kuroda, T. Ueda et al., "Fabrication of normally-off mode GaN and AlGaN/GaN MOSFETs with HfO2 gate insulator," Solid-State Electronics, vol. 54, pp. 79–83, 2010.

[12] A. Goel, S. Rewari, S. Verma, and R. S. Gupta, "Temperature-Dependent Gate-Induced Drain Leakages Assessment of Dual-Metal Nanowire Field-Effect Transistor—Analytical Model," IEEE Transactions on Electron Devices, vol. 66, no. 5, pp. 2437–2445, May 2019.

[13] N. A. Kumari and P. Prithvi, "A Comprehensive Analysis of Nanosheet FET and its CMOS Circuit Applications at Elevated Temperatures," Silicon, vol. 15, pp. 6135–6146, 2023.

Authorized licensed use limited to: DELHI TECHNICAL UNIV. Downloaded on November 09,2024 at 04:48:08 UTC from IEEE Xplore. Restrictions apply.

Journal Pre-proof

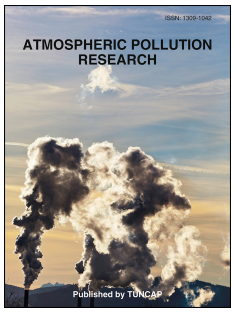

Influence of local meteorology and gaseous pollutant emissions on atmospheric nanoparticle concentrations in a pedestrian way in urban region

Kanagaraj Rajagopal, S. Ramachandran, Rajeev Kumar Mishra

PII: S1309-1042(24)00323-4

DOI: https://doi.org/10.1016/j.apr.2024.102358

Reference: APR 102358

To appear in: *Atmospheric Pollution Research*

Received Date: 3 June 2024

Revised Date: 7 November 2024

Accepted Date: 7 November 2024

Please cite this article as: Rajagopal, K., Ramachandran, S., Mishra, R.K., Influence of local meteorology and gaseous pollutant emissions on atmospheric nanoparticle concentrations in a pedestrian way in urban region, *Atmospheric Pollution Research*, https://doi.org/10.1016/j.apr.2024.102358.

This is a PDF file of an article that has undergone enhancements after acceptance, such as the addition of a cover page and metadata, and formatting for readability, but it is not yet the definitive version of record. This version will undergo additional copyediting, typesetting and review before it is published in its final form, but we are providing this version to give early visibility of the article. Please note that, during the production process, errors may be discovered which could affect the content, and all legal disclaimers that apply to the journal pertain.

© 2024 Turkish National Committee for Air Pollution Research and Control. Production and hosting by Elsevier B.V. All rights are reserved, including those for text and data mining, AI training, and similar technologies.

Journal Pre-proof

Influence of local meteorology and gaseous pollutant emissions on atmospheric nanoparticle concentrations in a pedestrian way in urban region

Kanagaraj Rajagopal[1], S. Ramachandran[2], Rajeev Kumar Mishra[1*]

[1]Department of Environmental Engineering, Delhi Technological University, India, 110042

[2]Space and Atmospheric Sciences Division, Physical Research Laboratory, Ahmedabad, India, 380009.

Correspondence to: rajeevmishraiitr@gmail.com.

Abstract

The roadside environment is one of the major sources of nanoparticle emission in the urban regions. The complex mixture of different pollutants makes it hard to understand the dynamics and behavior of nanoparticles. The study aims to analyze the dynamics of atmospheric nanoparticles ranging from 10 to 1000 nm along with local meteorological conditions and gaseous pollutants in a pedestrian way at a busy street in Delhi, a megalopolis in India, during all five major seasons of the study area. Nucleation mode particles were higher during the spring season, whereas the contribution of Aitken mode particles dominated the total particle number concentrations in the rest of the seasons. Due to the influence of vehicular sources, rush hour concentrations were higher than during non-rush hours. Thus, the diurnal pattern in particle concentration strongly coincided with emissions associated with the vehicular flow. During the winter season, the average total particle number concentration was observed to be maximum (4.1×10^4 cm^{-3}) with a higher surface area of particles of 3.5×10^{-3} mm^2m^{-3}. Compared to the monsoon season, the concentration of NO_X was 5 times higher in winter. The boundary layer height in the study region ranged from 600 to 2400 m during different seasons, and the maximum ventilation coefficient was observed to be >3000 m^2s^{-1} during summer. Precipitation reduced the concentration of particles by half, from 2.2×10^4 to 1.1×10^4 cm^{-3}, due to wet scavenging. The study revealed that the concentrations of particles depend not only on primary emissions but also are influenced by local meteorology and other co-emitted pollutants. Understanding the dynamics of atmospheric nanoparticles in urban roadside environments as outlined in this study is crucial to devise necessary mitigation measures for people residing near the road in order to reduce health impact and improve air quality.

Keywords: *air pollution, engine exhausts, ultrafine particles, gaseous emissions, urban climate, meteorology*

Journal Pre-proof

1. Introduction

Rapid urbanization and economic growth lead to serious air pollution issues in the Indian subcontinent. The complex mixture of sources contributes to poor air quality in urban cities, with emissions from traffic-related sources dominant among them (Sharma et al., 2024). Exhaust and non-exhaust (break, tyre wear and dust resuspension) emissions are two major emissions classifications from the transportation sector. Traffic-related exhaust emissions originate from different categories of vehicles, such as two, three-wheelers, personal/commercial cars, buses, and heavy vehicles (trucks, lorries, and cranes) (Belkacem et al., 2020; Pandey et al., 2022; Rogula-Kozłowska, 2014; Wu et al., 2021). Engine exhaust emits a wide range of pollutants, such as particulates and gaseous pollutants, based on the type of ignition, fuel used etc. (Myung and Park, 2012; Rajagopal et al., 2023; Yu et al., 2022). Emission norms for vehicles in India are based on the Bharath Stage VI standard with an emission limit for particulate matter (PM) < 4.5 mg/km and nitrogen oxide (NO_X) < 60 mg for petrol and < 80 mg for diesel engines (Rao et al., 2021). Apart from these emissions, the engine exhaust also emits particles that range from a few nanometers to micrometers (Patton et al., 2017; Sabaliauskas et al., 2012; Zhu et al., 2021). The nanoparticle emissions from the engine exhaust are broadly classified as nucleation mode (N_{nuc}, 1 to 30 nm), Aitken mode (N_{atk}, 30 to 100 nm), and accumulation mode (N_{acc}, 100 to 1000 nm) (Kumar et al., 2014; Rajagopal et al., 2024). The nanoparticles are measured in number concentration due to they having lesser mass concentration. They also have higher surface area and volume than larger particles (Aranda et al., 2015). Measurements and analysis of nanoparticles are necessary to investigate their impact on human health (Yadav et al., 2022a, b, c). The nanoparticle measurements are done using electrical mobility-based instruments in which the particles are charged and detected in a magnifier in the condensation unit. The concentration of the nanoparticles varies over space and time based on the source intensity and other atmospheric processes in the environment, such as coagulation, condensation, agglomeration, and wet removal (Yadav et al., 2021). Studies found that the concentration of nanoparticles changes significantly within a small spatial domain, influenced by the concentration of co-pollutants and meteorological conditions of a location (Yadav et al., 2022a, b). Apart from concentration, the particle size distribution will also change from the location of the source to a region that is away from the source due to the changes experienced by their physical properties. The increase in the particle size in the atmosphere also occurs due to the growth of particles from nucleation to accumulation mode by gas-to-particle conversion mechanism in which the precursor gases play a key role. The meteorological parameters such as temperature, relative humidity, boundary layer height, and wind speed also influence the nanoparticle concentration by promoting/inhibiting particle growth (Mohan et al., 2024). Atmospheric dynamics of a region also plays a crucial role in mixing precursor gases and pre-existing particles,

Journal Pre-proof

inducing the secondary formation process (Mohan et al., 2024). Studies have measured the concentration of these nanoparticles in different environmental conditions, such as in rural and urban regions. However, very few studies have been done globally to estimate the concentration of nanoparticles in the urban roadside microenvironment (Morakinyo and Lam, 2016) where transportation sources play a major role in nanoparticle emissions. In urban regions that are densely populated like Delhi, residential zones are found very adjacent to the road environment, which poses a serious concern to the health of the individuals traveling, pedestrians, and the population residing in the surrounding areas.

The study measured and analyzed the nanoparticle concentration from 10 to 1000 nm along with other gaseous pollutants such as nitrogen oxides (NO_X), nitrogen dioxide (NO_2), nitric oxide (NO), sulphur dioxide (SO_2), carbon monoxide (CO), ozone (O_3) and black carbon (BC). The meteorological parameters such as ambient temperature (AT), relative humidity (RH), solar radiation (SR), wind speed (WS), and direction (WD) with planetary boundary layer height (PBLH) and ventilation coefficient (VC) were also measured. This work aims to study the concentration of nanoparticles during different seasons in an urban traffic environment, determining the role of gaseous pollutants and meteorological conditions on its trend. The outcomes of the study will help to characterize and quantify the influence of different parameters on nanoparticle number concentrations in the roadside microenvironment on a seasonal scale and will help intiate necessary mitigation measures to reduce their emissions in urban regions. The findings of the study, further, are useful for estimating the potential human health impact due to the nanoparticle emissions.

2. Data acquisition and methodology

Field experiments are conducted in the urban roadside microenvironment adjacent to the Delhi Technological University campus (28.74ºN l, 77.11ºE, Fig. 1). The sampling site is near to the major arterial road with heavy vehicle density throughout the day. The road is classified as a major state highway without a center meridian, where light motor vehicles dominate in the daytime and heavy vehicles at night. The major vehicle categories in the study region include two, three-wheelers, E-rickshaws, four-wheelers, buses, and heavy vehicles (trucks, lorries, and cranes). Different types of road networks surround the study region, and a bus depot and metro station are located within the aerial distance of 5 km from the measurement location. Most vehicles in the study area use petrol (gasoline) and compressed natural gas (CNG) as fuel, and very few vehicles, especially heavy vehicles, use diesel. The sampling probe for measurement was kept less than 1 m away from the road near to the pedestrian way to capture the emissions from transportation sources. The study region experiences different weather patterns, such as hot weather during the summer and cold weather

during the winter, with an annual average rainfall of ~900 mm. The seasonal mean temperature difference in the study region ranged from a minimum of ~ 19°C during winter to 33°C in summer and the relative humidity also varied seasonally, from 45 to 75% throughout the year. The region received sufficient solar radiation of ~ 1872 kWh/m^2/year.

The nanoparticles were measured using a scanning mobility particle sizer (S.no 54031801) manufactured by the GRIMM Aerosol Technik GmbH & Co. K.G. The instrument consists of a Large Differential Mobility Analyzer (LDMA) measuring particles of size from 10 to 1090 nm along with a butanol-based condensation unit. The flow rate of the instrument was 0.3 Litres per minute (LPM) with a sheath air flow of 3 LPM. The measured nanoparticles are distributed into 44-bin-per-decade with a standard measurement time of 6.55 minutes for each cycle. The air is sampled through a sampling probe of an effective length of 0.38 m to minimize the measurement losses as prescribed by the manufacturer. The size distribution calculations are based on the ISO 15900 recommendations for particle mobility spectrometers. The gaseous parameters such as CO and SO_2 were measured using Horiba AP 370, with a detection limit of 0.05 ppm. The NO_X (<1 ppb detection limit) and O_3 (<1 ppb detection limit) were obtained by 2B technologies monitors with a flow rate of 1.5 LPM. The meteorological parameters (temperature, relative humidity, wind speed, and direction) were measured using Amil real-time sensors with an accuracy of +5 % and sensitivity of ~ 0.5 %. The planetary boundary layer height (PBLH) data corresponding to the study period for Delhi is downloaded from ERA-5 reanalysis available at a 1-hr time interval and at a latitude-longitude resolution of 0.25° x 0.25°. The ventilation coefficient is calculated as wind speed x PBLH.

The measured data on nanoparticles were classified seasonally as: *winter* (December to mid-February), *spring* (mid-February to March), *summer* (April to June), *monsoon* (July to mid-September), and *autumn* (mid-September to November). The collected data were analyzed using MATLAB (2016b) and Origin (version 2022), and R software (version 5.12.8) was used for visualization. The particle number concentration and size distribution were obtained from the software provided by the instrument manufacturer, which was well-validated and statistically tested. Outliers in the data were removed using the R statistical tool, and the data without outliers was considered for further analysis. The statistical significance of the data was determined using IBM SPSS software. The Levene test was conducted to determine the variance equality in different seasons, and the p-value obtained was <0.05, so the null hypothesis was accepted.

3. Results and discussion

3.1 Seasonal and diurnal variation of nanoparticles, size distribution, and gaseous emissions

The measured concentration of nanoparticles was classified in three different size ranges: N_{nuc} = 10 to 30 nm, N_{atk} = 30 to 100 nm, N_{acc} = 100 to 1000 nm, using which the total particle number concentration $N_{total} = N_{nuc} + N_{atk} + N_{acc}$ was obtained. The diurnal variation of particle concentrations in the three different size bins, their total, and the size distributions (number, mass, surface area and volume) in the different seasons showed that the particle number concentration as well as the size distributions obtained over Delhi were non-uniform (Figs. 2, 3). The N_{nuc} particles, produced as a result of fresh emissions, were higher with a clear peak during the daytime, which is a usual in urban regions. During spring, the concentration of N_{nuc} particles was about ~ 2 times (1.32×10^4 cm^{-3}) higher than in autumn (Table 1). The diurnal evolution of N_{nuc} was different than N_{atk} and N_{acc} (Fig. 2) which was consistent with the respective formation/production mechanisms. The nucleation mode is made up of particles that are newly formed and/or freshly emitted through source condensation processes or through atmospheric chemical reactions. These particles grow through coagulation and condensation into the Aitken and accumulation modes (Fig. 2). The nucleation lifetime is of the order of a few hours to a day whereas accumulation mode particles have a long atmospheric lifetime. Thus, N_{nuc} is not only higher than N_{atk} and N_{acc} but also peaks earlier than N_{atk} and N_{acc} due to the respective formation/production mechanisms (Fig. 2). Further, the diurnal pattern of N_{nuc} is significantly different in spring and summer, and higher than other seasons because of the new particle formation/nucleation burst events which increases their concentration substantially as very few anthropogenic sources directly emit particles in the nucleation size range. In addition, black carbon concentration during the spring season (Fig. 4e) was lower, confirming that the particle emissions did not have anthropogenic origin i.e., engine exhausts. This meant that apart from fresh emissions, natural particle formation through nucleation induced by precursor gases such as SO_2 was found (Fig. 4b). The concentration of each bin size such as N_{atk}, and N_{acc}, and N_{total} was similar to each other (Fig. 2b, c, d) associated with vehicular emissions, finding the highest levels in the morning and evening rush hours (twice than normal) when the vehicle fleet was high in urban regions compared to other hours of the day and vice versa (Sabaliauskas et al., 2012; Zheng et al., 2021). The N_{atk} particles contributed >35-40% to the N_{total} during the year, whereas the contributions of N_{nuc} and N_{acc} to N_{total} was $\geq$40% only during monsoon and autumn, respectively. The dominance of N_{atk} in the total particle number concentration occurs due to the continuous emissions from traffic sources in the study region, which emitted particles between 30 and 100 nm (Moreno-Ríos et al., 2022). The diurnal pattern showed a higher concentration during evening rush hours compared to the morning rush hours due to the accumulation of particles emitted throughout the day that undergo condensation, coagulation, and disperse less due to a lower planetary boundary layer height in the evening hours (Fig. 5c).

In general, the concentration of N_{total} particles in the study region was as follows: winter > spring > autumn > summer > monsoon. The winter season, with complex sources and meteorological conditions promoting extreme pollution events, reached the maximum concentration (4.11×10^4 cm^{-3}), followed by spring (3.52×10^4 cm^{-3}) and autumn (3.33×10^4 cm^{-3}). The concentrations obtained during the monsoon (2.46×10^4 cm^{-3}) season was the lowest when compared to other seasons due to wet scavenging of particles. On the other hand, with a lower relative humidity, the summer season experienced the second-lowest concentration. The (number, mass, surface area and volume) size distributions from 10 to 1000 nm were used to determine the characteristics of measured particles (Fig. 3). The particle number size distribution (PNSD) showed a single clear peak during winter and autumn which was the highest measured concentration compared to other seasons (Fig. 3a). The peak concentration was from 100 to 200 nm in almost all seasons, which falls under accumulation mode. Generally, the particle sizes from fresh exhaust emissions of different engines were lower than 100 nm, which showed that in the study area, the emitted fresh particles frequently underwent aging processes in the atmosphere. The peak concentration in the accumulation mode also rose during humid periods due to the evaporation of aqueous droplets (Yao et al., 2007). Mass size distribution showed that the particles in the N_{acc} range were 3 to 4 times higher than other size fractions which further, contributed to the concentration of particulate matter (Şahin et al., 2022; Trechera et al., 2023). The volume of the particle size distributions looked similar to that of the mass (Fig. 3b, d) since they were calculated based on the number concentration, assuming a spherical shape of the measured nanoparticles and the same density. Knowing the particle surface area is necessary to evaluate the health impact because the nanoparticles with lower mass and higher surface area possess a higher potential to impact health due to a higher surface reactivity (Qiao et al., 2015), and the generation of reactive oxygen species (ROS). ROS generation is an important factor in analyzing the toxic effects of the inhaled nanoparticles. It develops cytotoxicity, apoptosis, oxidative DNA damage, and cell motility (Chalupa et al., 2004; Ma et al., 2022). The analysis of the particle size distribution showed that the particle surface area was similar during the winter and autumn seasons, peaking at 3.5×10^{-3} mm^2 m^{-3} around 300 nm (Fig. 3c). In other seasons, even though the concentration of the particle was less, the particle surface area remained more or less the same based on the size and still posed threat to the residents.

The measurement of gaseous pollutants in any region exhibit different concentrations diurnally and seasonally based on the emission sources. Likewise, the changes in particle concentration also depend on the meteorology and atmospheric processes. The NO_X, CO, and BC peak concentrations (Fig. 4a, c, and e) in the study region coincided with the nanoparticles emission (Fig. 2d), confirming that the source of these pollutants was the same (vehicular sources) (Allen et al.,

2009). Studies have revealed that the transportation sector played a major role in the contribution of NO_X and CO in Delhi (Bhandari et al., 2020; Pant et al., 2015; Rizwan et al., 2013). The NO_X concentration was high during the winter (97 ppb) and ~ 5 times higher than in the monsoon season (Fig. 4, Table 2). During the winter period, the concentration of nanoparticles and gaseous pollutants was higher in the study region. However, the concentration of N_{nuc} was found higher in the spring season (1.32×10^4 cm^{-3}) due to the gas-to-particle conversion using SO_2 as precursor molecule for the formation of H_2SO_4. H_2SO_4 vapor acts as SO_2 condensation sink resulting in a lesser concentration (6 µg m^{-3}) in the atmosphere during this season (Fig. 4b). The vapor pressure of the H_2SO_4 depends on the temperature and relative humidity. Therefore, as the spring season experienced a moderate temperature and humidity in the study region (Fig. 5a, b), it was more favorable for the particle formation process. On the contrary, temperature and humidity were extremely high or low during the summer and monsoon seasons (Fig. 5), respectively, inhibiting the SO_2 condensation sink formation. Co-pollutants (O_3, BC) measured in the study region were used to identify the sources and the influence of the atmospheric dynamics on the nanoparticle concentration. The O_3 concentration showed a mid-day peak in almost all the seasons (Fig. 4d) due to the photochemical formation at ground-level from primary pollutants (Nelson et al., 2021; Sharma et al., 2013). BC was used as a tracer for local traffic emissions in the study area, exhibiting higher concentrations during the night than daytime (Fig. 4e) which was consistent with the diurnal variation of N_{acc} (Fig. 2).

3.2 Influence of meteorology on nanoparticle concentration

The meteorology plays a significant role in determining the nanoparticle concentration in the atmosphere. The planetary boundary layer height (PBLH- meters above ground level) and ventilation coefficient directly influenced pollution concentration at ground level (Kompalli et al., 2018; Sorribas et al., 2015). During the winter, when the PBLH was observed lower than 1000 m (the lowest of all seasons) (Fig. 5c) and wind speed (Fig. 5f) was ~1 ± 0.5 m/s, resulting in lower ventilation coefficient (600 m^2s^{-1}, Table 3) (Fig. 5d), the highest mean average concentration of nanoparticles was observed (4.11×10^4 cm^3). During summer and spring the wind speed and PBLH were high, and the resultant ventilation coefficient also reached the maximum (3500 m^2s^{-1}, Table 3). This phenomenon induced the dilution of particles that inhibited the particle aging and resulted in a lesser concentration. This led to the dispersion of particles and concentration of different pollutants also varied seasonally.

During the winter period, when the relative humidity was higher than 60% and the temperature was lower than 20°C (Fig. 5a, b), the concentration of accumulation mode particles were also found higher (Fig. 2c) due to the rapid condensation and coagulation of the engine exhausts (Dinoi et al., 2023). The natural gas to-particle formation process that occured during the warmer period led

to a substantial increase in nucleation size particles (Fig. 2a). During this period, relative humidity remained low compared to the winter one (Fig. 5b). Wind and traffic-produced turbulence determine the nanoparticle concentration in the study region (Mehel and Murzyn, 2015), in the same way as the direction of wind flow. The road where the monitoring location was located, is an urban street canyon, thus, wind recirculation is common. In summer, when wind speed was higher than 2 ms^{-1} (Fig. 5f) during the mid-day time, N_{nuc} and N_{acc} particle concentrations were 2.0 x 10^4 (Fig. 2a) and 0.75 x 10^4 cm^{-3} (Fig. 2c), respectively, being the lowest concentration measured among all seasons. This revealed that higher wind speeds increase the dispersion rate of particles. The dispersion rate may vary based on the particle size and the wind intensity. The wind rose plots showed that most of the wind flow in the monitoring site is from South-West towards North-East direction (Fig. 6). The monitoring location is covered with the arterial road on the south, and the monitoring station was located north of the arterial road. The monitoring location was located on the leeward side of the arterial road which caused the dominance of windflow in the same direction throughout the year due to the country's driving pattern. The left hand driving pattern of vehicles in W-E direction caused a traffic induced wind turbulence of S-W to N-E direction (Fig. 6) which was clearly visible throughout the study period.

Apart from relative humidity, temperature, and wind parameters, precipitation plays a major role in determining the concentration of nanoparticles and their size distribution in the atmosphere. Thus, here, the particle size distribution was analysed before and after the precipitation to know its impact on number and size. Time-resolved particle concentration with respect to the nanoparticle size revealed that precipitation-induced wet scavenging was directly associated with particle removal, and that during the precipitation period the particle concentration was reduced to half of pre-precipitation one (2.2 x 10^4 to 1.1 x 10^4 cm^{-3}) (Fig. 7). The precipitation removes larger particles, especially N_{acc} (100 to 1000 nm), from the atmosphere (Andronache, 2004). Thus, the particle number size distribution during the post-precipitation showed a lower concentration in this range of particle sizes. During a normal day when there is no precipitation, the hourly average concentration of the particles ranged from 5 to 7 x 10^4 cm^{-3} during the early morning hours (1 to 5 AM), especially in larger particle sizes (N_{acc}) (Fig. 8a). This high concentration was the result of the coagulation processes among atmospheric particles (Fig. 8a). On the study day (18 October 2021) a precipitation of 1 to 3 mm occurred during the early morning hours (Fig. 9) when the concentration was observed maximum in the monitoring station. This resulted in a reduction of particle concentration, especially in the highest-size (N_{acc}), reaching $\sim$ 3 x 10^4 cm^{-3} (Fig. 8b). The precipitation process reduced the total concentration of the nanoparticles in the atmosphere (Fig. 9). The concentration of N_{nuc} particles was found higher than larger-sized particles due to its greater diffusivity (Fig. 9a). The N_{atk} particles suffered greater diffusion during less-intensity rainfall, decreasing its concentration when the intensity of rainfall increased (Fig.

9b). In general, the particles in N_{atk} and N_{acc} were more influenced by the precipitation processes (Fig. 9b, c). Post-precipitation analysis showed a higher growth rate of particles, even though the concentration was less. In this regard, the particle growth was induced by the moisture content, which causes rapid condensation of smaller particles (Zhao et al., 2021).

4. Conclusions

Understanding the dynamics of the nanoparticles concentration in the atmosphere is vital to improving air quality in urban regions. The study measured and analyzed the different types of emissions from the transportation sector (nano pollutants and gaseous emissions) in the roadside microenvironment of Delhi, a megalopolis in India, from December 2020 to November 2021. The period included the study region's five major meteorological seasons (winter, spring, summer, monsoon, and autumn). This study also measured and analyzed the local meteorological conditions in the study area to investigate the role of seasonal factors and other pollutants on nanoparticles concentration in the urban roadside microenvironment.

The analysis revealed that the N_{nuc} (10 to 30 nm) concentration was higher during the spring season (1.32 x 10^4 cm^{-3}), which was two times higher than during the autumn. The spike in the concentration of N_{nuc} concentration during spring was due to the gas-to-particle conversion, where the SO_2 as precursor molecules were utilized to form H_2SO_4 clusters that acts as condensation sink for the particle formation. In the rest of seasons, the concentration of N_{atk} (30 to 100 nm), N_{acc} (100 to 1000 nm), and N_{total} (10 to 1000 nm) seemed similar to each other, with a hike in concentration up to twice during morning and evening rush hours *vs* non-rush hours. The evening rush hour concentration was higher compared to the morning due to the accumulation of particles throughout the day. The surface area and volume of the particles determine the toxicity, inducing the generation of reactive oxygen species (ROS), which was found to be more prevalent during the winter period (3.5 x10^{-3} mm^2 m^{-3}) followed by autumn. The nanoparticles concentration was not only associated with the intensity of the sources but also with local factors such as gaseous emissions in the region and meteorological conditions. Vehicular emissions contributed to nanoparticle concentration and other co-pollutants, such as NO_X, SO_2, CO, O_3, and BC. The evolution of the gaseous pollutants concentration had similar trends to particles because they have the same origin (traffic emissions). The BC used as a tracer for transport emissions showed higher concentrations during nighttime. The concentration of gaseous pollutants also increased to around 3 to 5% during winter. Winter season in the study period experienced a shallow boundary layer with a PBLH <1000 m, which promoted the pollution accumulation at the ground level, while during summer, the boundary layer reached up to 2400 m, which helped greater dispersion. Based on the wind speed and planetary boundary layer height, the ventilation coefficient of the region also changed seasonally, and, consequently, the particle

299 concentration. Precipitation is another important factor for determining a region's total particle
300 number concentration because it helped in wet scavenging of the pollutants, especially in the N_{acc}
301 mode particles. The N_{nuc} underwent more diffusion during the precipitation due to their smaller size
302 thus an increase in particles was observed. Precipitation of 1 to 3 mm reduced the total particle
303 concentration by half from 2.2 x 10^4 (before) to 1.1 x 10^4 cm^{-3} (after). The precipitation process not
304 only influenced the concentration but also played a role in modifiying the size distribution of the
305 particles. The meteorological parameters, such as wind, helped in particle dispersion, and relative
306 humidity triggered their secondary transformation. Air recirculation in the street canyon due to
307 vehicular flow turbulence was observed in the study region.

308 The study investigated the role of emission sources in determining the concentration of
309 nanoparticles in the urban roadside environment establishing relationships with seasonal factors,
310 meteorology (wind parameters, precipitation and relative humidity), and gaseous pollutants, which
311 helps to understand the dynamics of these particles in the atmosphere. The outcomes of the study
312 can be used to estimate the health hazards these pollutants pose in the urban environment, especially
313 those residing/working near the road microenvironment.

314 **Acknowledgments:** The measurements were conducted in the Advance Air and Acoustics Research
315 Laboratory, Department of Environmental Engineering, Delhi Technological University. KR thanks Dr.
316 Chinmay Jena from the Indian Meteorological Department for providing the black carbon data used in
317 the analysis.

318 **Author credit statement**

319 **Author credit statement: K. Rajagopal** – Data collection, analysis, interpretation, writing original draft;
320 **S. Ramachandran** – Conceptualization, methodology, interpretation, writing, review, and editing; **R.K.**
321 **Mishra** – Conceptualization, data analysis, writing, review, and editing**.**

322 **Funding**

323 Not applicable.

324 **Conflict of interest**

325 The authors declare that they have no known competing financial interests or personal relationships
326 that could have appeared to influence the work reported in this paper.

327 **Consent for publication**

328 The work has not been published anywhere previously in any form, and it is not being considered for
329 publication elsewhere. All authors approve the publication.

330 **Data availability:** All data used in the manuscript can be made available on request.

Journal Pre-proof

References

Allen, R. W., Davies, H., Cohen, M. A., Mallach, G., Kaufman, J. D., Adar, S. D., 2009. The spatial relationship between traffic-generated air pollution and noise in 2 US cities. Environ. Res. 109, 334–342. https://doi.org/10.1016/j.envres.2008.12.006.

Andronache, C., 2004. Precipitation removal of ultrafine aerosol particles from the atmospheric boundary layer. J. Geophys. Res. 109,4050. https://doi.org/10.1029/2003JD004050.

Aranda, A., Díaz-de-Mera, Y., Notario, A., Rodríguez, D., Rodríguez, A., 2015. Fine and ultrafine particles in small cities. A case study in the south of Europe. Environ. Sci. Poll. Res. 22, 18477–18486. https://doi.org/10.1007/s11356-015-5165-4.

Belkacem, I., Khardi, S., Helali, A., Slimi, K., Serindat, S., 2020. The influence of urban road traffic on nanoparticles: Roadside measurements. Atmos. Environ. 242, 117786. https://doi.org/10.1016/j.atmosenv.2020.117786.

Bhandari, S., Gani, S., Patel, K., Wang, D. S., Soni, P., Arub, Z., Habib, G., Apte, J. S., Hildebrandt Ruiz, L., 2020. Sources and atmospheric dynamics of organic aerosol in New Delhi, India: Insights from receptor modeling. Atmos. Chem. Phys. 20, 735–752. https://doi.org/10.5194/acp-20-735-2020.

Chalupa, D. C., Morrow, P. E., Oberdörster, G., Utell, M. J., Frampton, M. W., 2004. Ultrafine particle deposition in subjects with asthma. Environ. Health Pers. 112, 879–882. https://doi.org/10.1289/ehp.6851.

Dinoi, A., Gulli, D., Weinhold, K., Ammoscato, I., Calidonna, C. R., Wiedensohler, A., Contini, D., 2023. Characterization of ultrafine particles and the occurrence of new particle formation events in an urban and coastal site of the Mediterranean area. Atmos. Chem. Phys. 23, 2167–2181. https://doi.org/10.5194/acp-23-2167-2023.

Kumar, P., Morawska, L., Birmili, W., Paasonen, P., Hu, M., Kulmala, M., Harrison, R. M., Norford, L., Britter, R., 2014. Ultrafine particles in cities. Environ. Intl. 66, 1–10. https://doi.org/10.1016/j.envint.2014.01.013.

Ma, L., Zhang, Y., Lin, Z., Zhou,Y.,Yan,C., Zhang,Y., W Zhou,W., Ma,W., Hua,C., Li,X., Deng,C., Qi,Y., Dada, L., Li,H., Bianchi,F., Petaj,T., Kangasluoma, J., Jiang,J., Liu,S., Hussein,T., Ma, Y. L., 2022. Deposition potential of 0.003–10 μm ambient particles in the humidified human respiratory tract: Contribution of new particle formation events in Beijing. Ecotoxicol. Environ. Safety 243,114023. https://doi.org/https://doi.org/10.1016/j.ecoenv.2022.11402.

Mehel, A., Murzyn, F., 2015. Effect of air velocity on nanoparticles dispersion in the wake of a vehicle model: Wind tunnel experiments. Atmos. Poll. Res. 6, 612–617. https://doi.org/10.5094/APR.2015.069.

Mohan, V., Soni, V.K., Mishra, R.K., 2024. Analysing the impact of day-night road traffic variation on ultrafine particle number size distribution and concentration at an urban site in the megacity Delhi. Atmos. Poll. Res. 15, 102065. https://doi.org/10.1016/j.apr.2024.102065.

Morakinyo, T. E., Lam, Y. F., 2016. Simulation study of dispersion and removal of particulate matter from traffic by road-side vegetation barrier. Environ. Sci. Poll. Res. 23, 6709–6722. https://doi.org/10.1007/s11356-015-5839-y.

Moreno-Ríos, A. L., Tejeda-Benítez, L. P., Bustillo-Lecompte, C. F., 2022. Sources, characteristics, toxicity, and control of ultrafine particles: An overview. Geosci. Front. 13. https://doi.org/10.1016/j.gsf.2021.101147.

Myung, C. L., Park, S., 2012. Exhaust nanoparticle emissions from internal combustion engines: a review. Intl. J. Auto. Tech., 13, 9–22. https://doi.org/10.1007/s12239−012−0002−y.

Pandey, A., Mishra, R. K., Pandey, G. 2022. Investigating Exhaust Emissions from In-Use Passenger Cars: Exploratory Analysis and Policy Outlook. J. Environ. Engg. 148. https://doi.org/10.1061/(asce)ee.1943-7870.0002015.

Pant, P., Shukla, A., Kohl, S. D., Chow, J. C., Watson, J. G., Harrison, R. M., 2015. Characterization of ambient PM2.5 at a pollution hotspot in New Delhi, India and inference of sources. Atmos. Environ. 109, 178–189. https://doi.org/10.1016/j.atmosenv.2015.02.074.

Patton, A. P., Milando, C., Durant, J. L., Kumar, P., 2017. Assessing the suitability of multiple dispersion and land use regression models for urban traffic-related ultrafine particles. Environ. Sci. Tech. 51, 384–392. https://doi.org/10.1021/acs.est.6b04633.

Qiao, H., Liu, W., Gu, H., Wang, D., Wang, Y., 2015. The transport and deposition of nanoparticles in respiratory system by inhalation. J. Nanomat. 394507. https://doi.org/10.1155/2015/394507.

Rajagopal, K., Ramachandran, S., Mishra, R.K., 2023. Urban Climate Roadside measurements of nanoparticles and their dynamics in relation to traffic sources in Delhi : Impact of restrictions and pollution events. Urban Clim. 51, 101625. https://doi.org/10.1016/j.uclim.2023.101625.

Rajagopal, K., Ramachandran, S., Mishra, R. K., 2024. Size resolved particle contribution to vehicle induced ultrafine particle number concentration in a metropolitan curbside region. Atmos. Environ. 337, 120773. https://doi.org/10.1016/j.atmosenv.2024.120773.

Rao, N. D., Kiesewetter, G., Min, J., Pachauri, S., Wagner, F., 2021. Household contributions to and impacts from airpollution in India. Nat. Sust. 4, 859-867. http://dx.doi.org/10.1038/s41893-021-00744-0.

Rizwan, S. A., Nongkynrih, B., Gupta, S. K., 2013. Air pollution in Delhi: Its magnitude and effects on health. Ind. J. Comm. Med. 38, 4–8. https://doi.org/10.4103/0970-0218.106617.

Rogula-Kozłowska, W., 2014. Traffic-generated changes in the chemical characteristics of size-segregated urban aerosols. Bull. Environ. Cont. Toxi. 93, 493–502. https://doi.org/10.1007/s00128-014-1364-9.

Sabaliauskas, K., Jeong, C. H., Yao, X., Jun, Y. S., Jadidian, P., Evans, G. J., 2012. Five-year roadside measurements of ultrafine particles in a major Canadian city. Atmos Environ. 49, 245–256. https://doi.org/10.1016/j.atmosenv.2011.11.052.

Şahin, Ü. A., Harrison, R. M., Alam, M. S., Beddows, D. C. S., Bousiotis, D., Shi, Z., Crilley, L. R., Bloss, W., Brean, J., Khanna, I., Verma, R., 2022. Measurement report: Interpretation of wide-range particulate matter size distributions in Delhi. Atmos. Chem. Phys. 22, 5415–5433. https://doi.org/10.5194/acp-22-5415-2022.

Sharma, M., Khare, M., Mishra, R. K., 2024. Air quality changes in Delhi due to open waste burning : an accidental fire in Bhalswa landfill. Intl. J. Environ. Sci. Tech. 21, 655-664. https://doi.org/10.1007/s13762-023-04921-w.

Trechera, P., Garcia-Marlès, M., Liu, X., Reche, C., Pérez, N., Savadkoohi, M., Beddows, D., Salma, I., Vörösmarty, M., Casans, A., Casquero-Vera, J. A., Hueglin, C., Marchand, N., Chazeau, B., Gille, G., Kalkavouras, P., Mihalopoulos, N., Ondracek, J., Zikova, N., … Querol, X., 2023. Phenomenology of ultrafine particle concentrations and size distribution across urban Europe. Environ. Intl. 172, 107744. https://doi.org/10.1016/j.envint.2023.107744.

Wu, H., Li, Z., Jiang, M., Liang, C., Zhang, D., Wu, T., Wang, Y., Cribb, M., 2021. Contributions of traffic emissions and new particle formation to the ultrafine particle size distribution in the megacity of Beijing. Atmos. Environ. 262. https://doi.org/10.1016/j.atmosenv.2021.118652.

Yadav, S. K., Kompalli, S. K., Gurjar, B. R., Mishra, R. K., 2021. Aerosol number concentrations and new particle formation events over a polluted megacity during the COVID-19 lockdown. Atmos. Environ. 259, 118526. https://doi.org/10.1016/j.atmosenv.2021.118526.

Journal Pre-proof

Yadav, S. K., Mishra, R. K., Gurjar, B. R., 2022a. Assessment of the effect of the judicial prohibition on firecracker celebration at the Diwali festival on air quality in Delhi, India. Environ. Sci. Poll. Res. 29, 36247-36259. https://doi.org/10.1007/s11356-021-17695-w.

Yadav, S. K., Mishra, R. K., Gurjar, B. R., 2022b. Fireworks induced quasi-ultrafine particle number concentration and size-resolved elemental distribution in megacity Delhi. Arab. J. Geosci. 15, 1–13. https://doi.org/10.1007/s12517-021-09385-1.

Yadav, S. K., Mishra, R. K., Gurjar, B. R., 2022c. Ultrafine particle number concentration and its size distribution during Diwali festival in megacity Delhi, India: Are 'green crackers' safe? J. Environ Mgmt. 317, 115459. https://doi.org/10.1016/j.jenvman.2022.115459.

Yao, X., Lau, N. T., Fang, M., Chan, C. K., 2007. Correlations of ambient temperature and relative humidity with submicron particle number concentration size distributions in on-road vehicle plumes. Aero. Sci. Tech. 41, 692–700. https://doi.org/10.1080/02786820701408491.

Yu, F., Zhong, Z., Wang, Q., Liao, S., Zhu, M., Sha, Q., Liu, J., Zheng, J., 2022. Characterizing the particle number emissions of light-duty gasoline vehicles under different engine technologies and driving conditions. Environ. Res. 213, 113648. https://doi.org/10.1016/j.envres.2022.113648.

Zhao, B., Fast, J. D., Donahue, N. M., Shrivastava, M., Schervish, M., Shilling, J. E., Gordon, H., Wang, J., Gao, Y., Zaveri, R. A., Liu, Y., Gaudet, B., 2021. Impact of urban pollution on organic-mediated new-particle formation and particle number concentration in the Amazon rainforest. Environ. Sci. Tech. 55, 4357–4367. https://doi.org/10.1021/acs.est.0c07465.

Zheng, T., Wang, H. W., Li, X. B., Peng, Z. R., He, H. Di., 2021. Impacts of traffic on roadside particle variations in varied temporal scales. Atmos. Environ. 253, 118354. https://doi.org/10.1016/j.atmosenv.2021.118354.

Zhu, L., Ranasinghe, D., Chamecki, M., Brown, M. J., Paulson, S. E., 2021. Clean air in cities: Impact of the layout of buildings in urban areas on pedestrian exposure to ultrafine particles from traffic. Atmos. Environ. 252, 118267. https://doi.org/10.1016/j.atmosenv.2021.118267.

Table 1. Seasonal statistical summary of the different size nanoparticles (N_{nuc} = 10 to 30 nm, N_{atk} = 30 to 100 nm, N_{acc} = 100 to 1000 nm, and N_{total} = 10 to 1000 nm) concentration during the different seasons.

Season	Parameter	N_{nuc} (cm^{-3})	N_{atk} (cm^{-3})	N_{acc} (cm^{-3})	N_{total} (cm^{-3})
Winter	Min	185	5	23	2691
	Mean ± SD	8594 ± 9079	16558±12217	15905 ± 9645	41089 ± 23669
	Max	68626	68305	68458	147182
Spring	Min	306	2727	1039	8694
	Mean ± SD	13234 ± 13287	12392±6599	9599 ± 5832	35226 ± 17909
	Max	121136	48813	56033	139019
Summer	Min	106	812	418	1752
	Mean ± SD	10284 ± 10803	9610±5078	6411 ± 4808	26307 ± 13719
	Max	90646	45408	33838	130433
Monsoon	Min	353	4	558	4337
	Mean ± SD	10161 ± 10078	9612±5186	4805 ± 2540	24590 ± 13256
	Max	82547	48722	14345	112587
Autumn	Min	161	1429	1012	3774
	Mean ± SD	6667 ± 6955	12052±8338	14610 ± 8940	33329 ± 17883
	Max	71873	52145	58056	111316

Table 2. Seasonal statistical summary of the different gaseous pollutants during all seasons.

Season	Parameter	NO_X (ppb)	SO_2 (µg m^{-3})	CO (mg m^{-3})	O_3 (µg m^{-3})	BC (µg m^{-3})
Winter	Min	0.3	2	0.2	1	0.2
	Mean ± SD	97 ± 61	6 ± 4	2 ± 1	38 ± 21	13 ± 13
	Max	457	48	10	168	178
Spring	Min	11.4	3	0.05	0.4	0.2
	Mean ± SD	47 ± 31	6 ± 3	1 ± 1	32 ± 26	9 ± 10
	Max	220	41	9	172	114
Summer	Min	6	1	0.1	2	0.3
	Mean ± SD	23 ± 11	11 ± 11	1 ± 1	44 ± 34	8 ± 8
	Max	245	127	5	197	76
Monsoon	Min	0	5	0.16	0.5	0.8
	Mean ± SD	17 ± 6	8 ± 3	0.7± 0.4	37± 30	4 ± 3
	Max	72	49	3	185	23
Autumn	Min	0	4	0.03	0.8	0.7
	Mean ± SD	32 ± 32	8 ± 2	2 ± 1	35 ± 23	18±15
	Max	319	18	11	163	117

458 Table 3. Seasonal statistical summary of meteorological parameters (ambient temperature (AT),
459 relative humidity (RH), wind speed (WS), solar radiation (SR), planetary boundary layer height (PBLH)
460 and ventilation coefficient (VC)) during the different seasons over Delhi.

Season	Parameter	AT (°C)	RH (%)	WS (ms^{-1})	SR (Wm^{-2})	PBLH (m)	VC (m^2s^{-1})
Winter	Min	10.7	25	0.1	3	10	5
	Mean ± SD	19 ± 4.5	73 ± 17	1 ± 1	85 ± 130	265 ± 309	244 ± 333
	Max	33.7	88	9	536	1319	3720
Spring	Min	17	13.8	0.1	3	11	3
	Mean ± SD	27 ± 6	55 ± 20	1 ± 1	132 ± 189	450 ± 594	497 ± 1028
	Max	43	88	10	875	2649	13620
Summer	Min	18.5	11.2	0.2	3	13	6
	Mean ± SD	32.5 ± 5.2	44 ± 18	1 ± 1	149 ± 220	786 ± 945	1051 ± 1665
	Max	44.3	88	12	876	4662	16289
Monsoon	Min	27.4	25	0.2	3	15	6
	Mean ± SD	33 ± 3.4	71 ± 16	1 ± 1	142 ± 215	509 ± 512	494 ± 635
	Max	44.8	88	11	877	2863	7691
Autumn	Min	16	23	0.2	3	11	4
	Mean ± SD	26 ± 6	63 ± 18	1 ± 0.4	131 ± 193	307 ± 413	252 ± 351
	Max	40.3	88	7	704	1753	2951

461

462

463

464 Figure 1. Geographical location of the monitoring site: (a) map of India, (b) map of Delhi city, and (c)
465 image of the monitoring station and its surroundings.

466

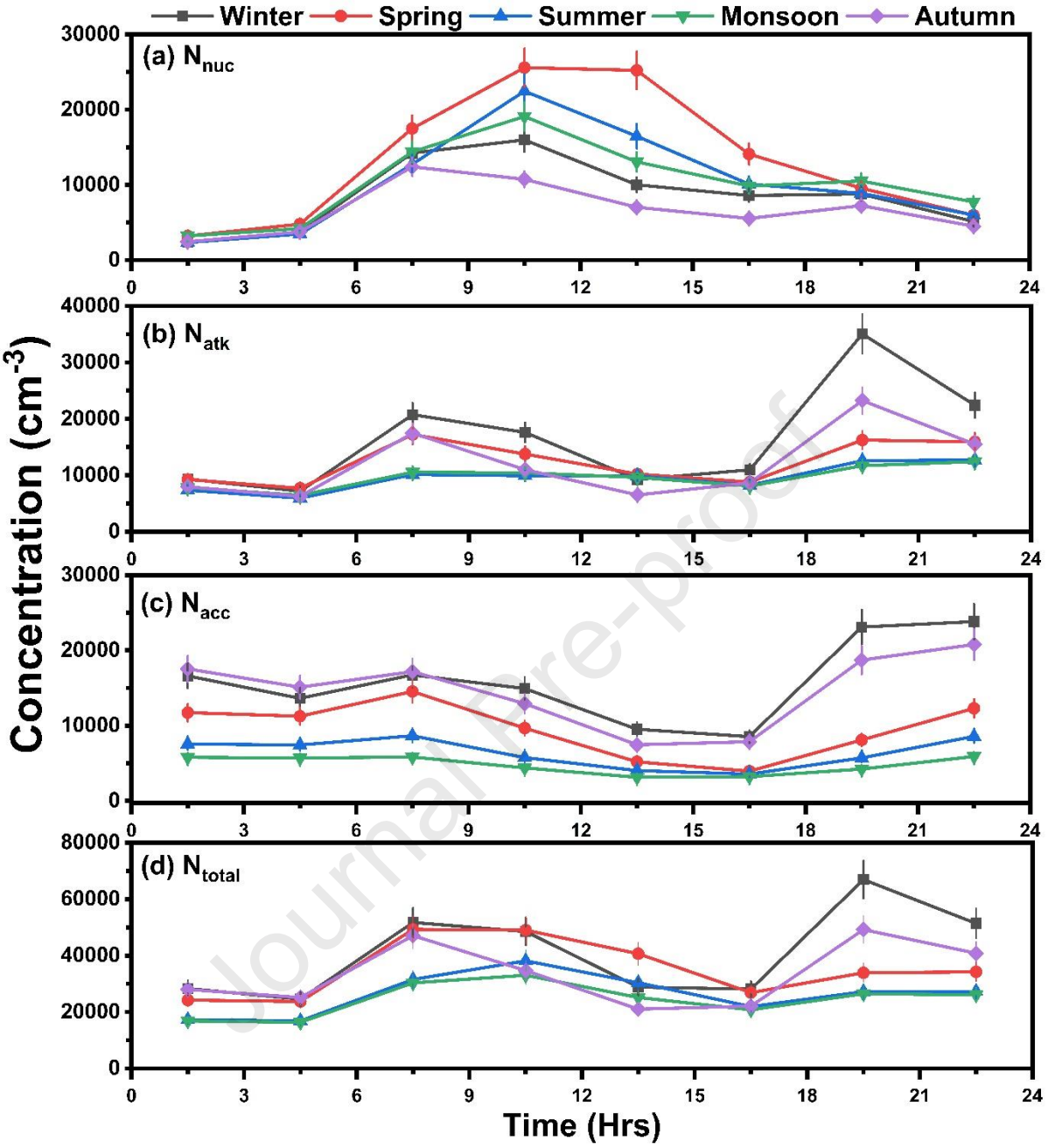

467

468 Figure 2. Diurnal variation of (a) N_{nuc} (10 to 30 nm), (b) N_{atk} (30 to 100 nm), (c) N_{acc} (100 to 1000 nm),
469 and (d) N_{total} (10 to 1000 nm) during winter, spring, summer, monsoon, and autumn in Delhi during
470 2020-2021 (vertical bars represent ± standard deviation from the mean).

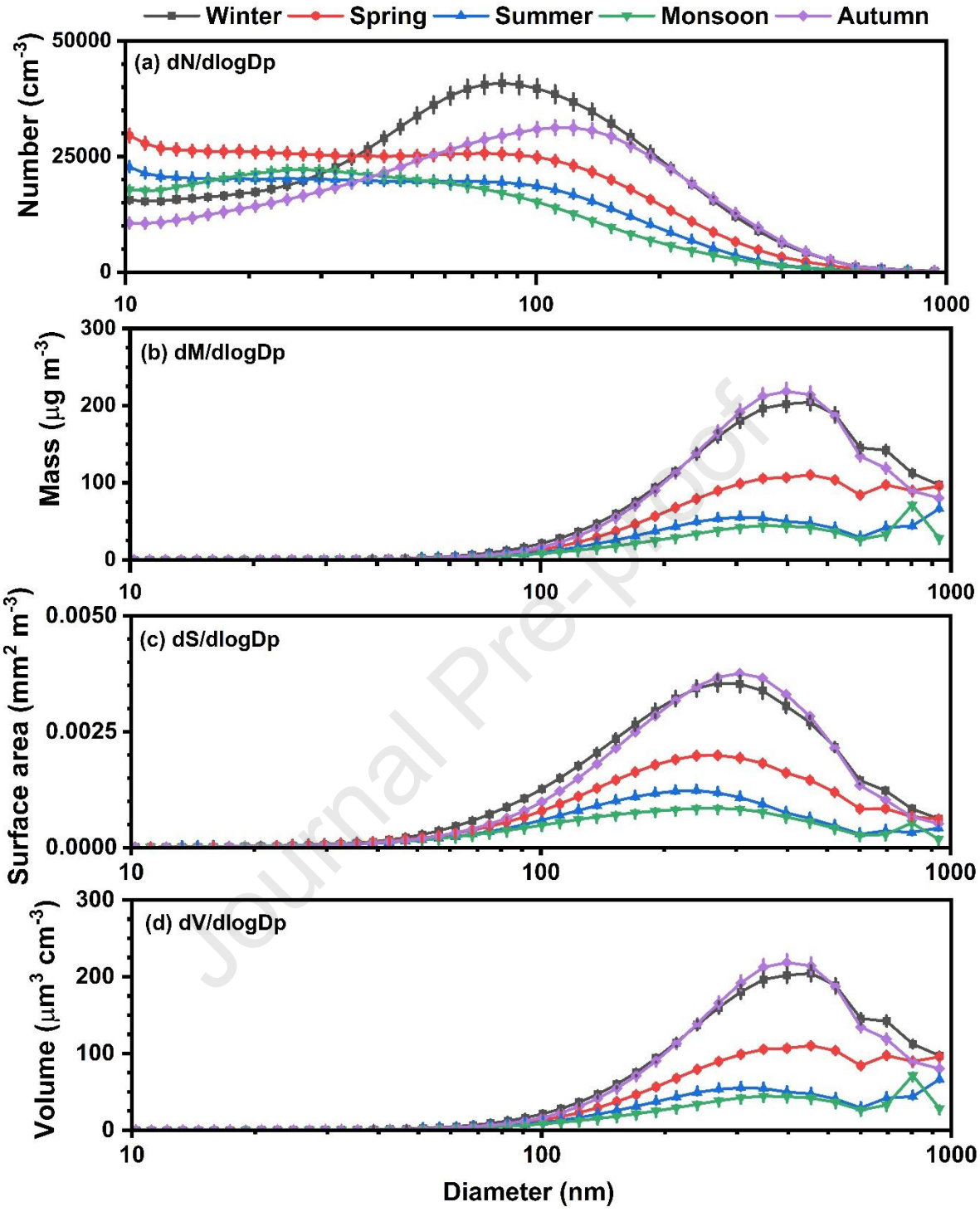

471

472 Figure 3. The ((a) number, (b) mass, (c) surface area, and (d) volume) size distribution of aerosol
473 particles from 10 to 1000 nm during winter, spring, summer, monsoon, and autumn in Delhi, a
474 megalopolis (vertical bars represent ± standard deviation from the mean).

475

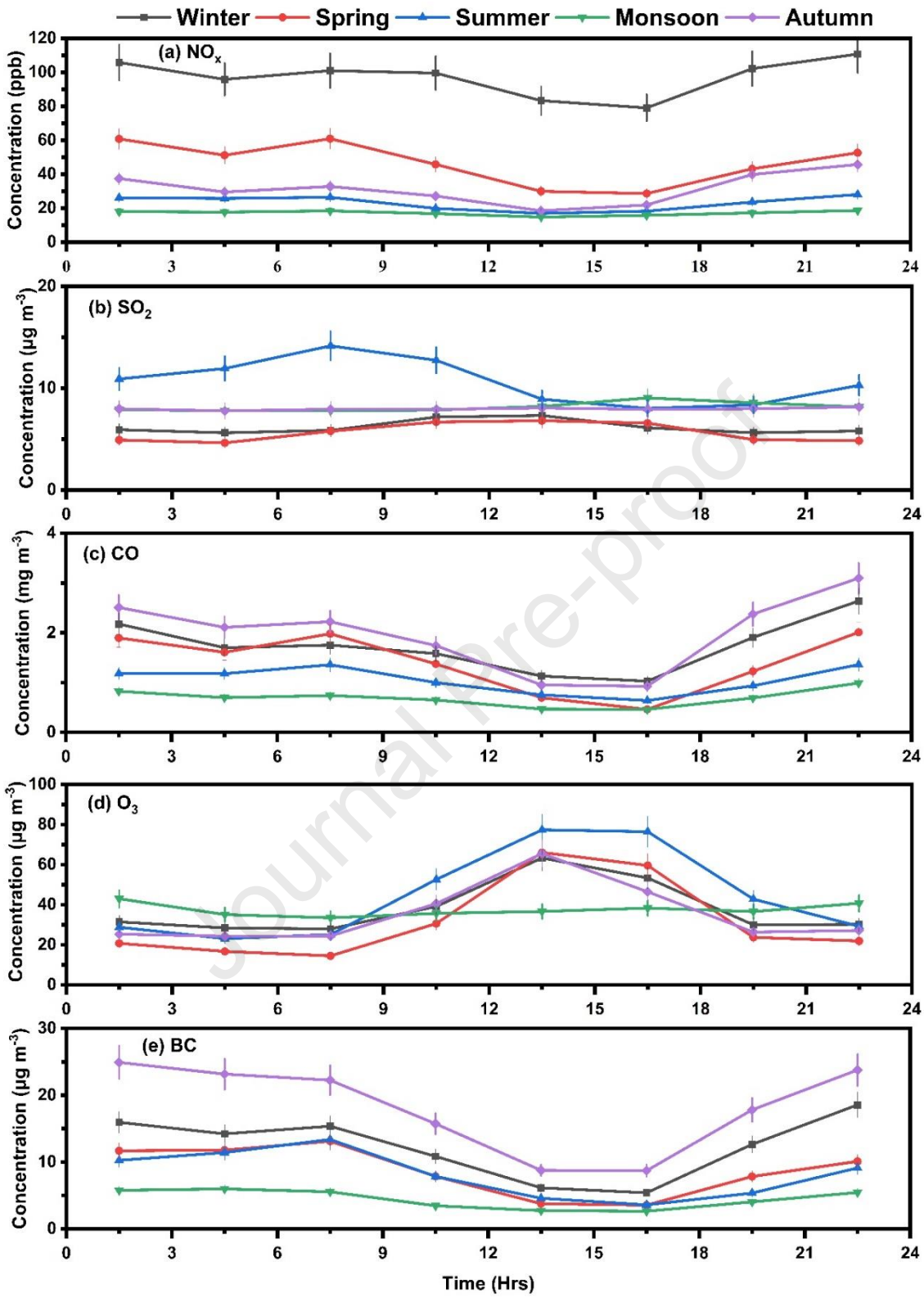

476

477 Figure 4. Diurnal variation of (a) NO_X, (b) SO_2, (c) CO, (d) O_3, and (e) BC during winter spring, summer,
478 monsoon and autumn seasons in Delhi (vertical bars represent ± standard deviation from the mean).

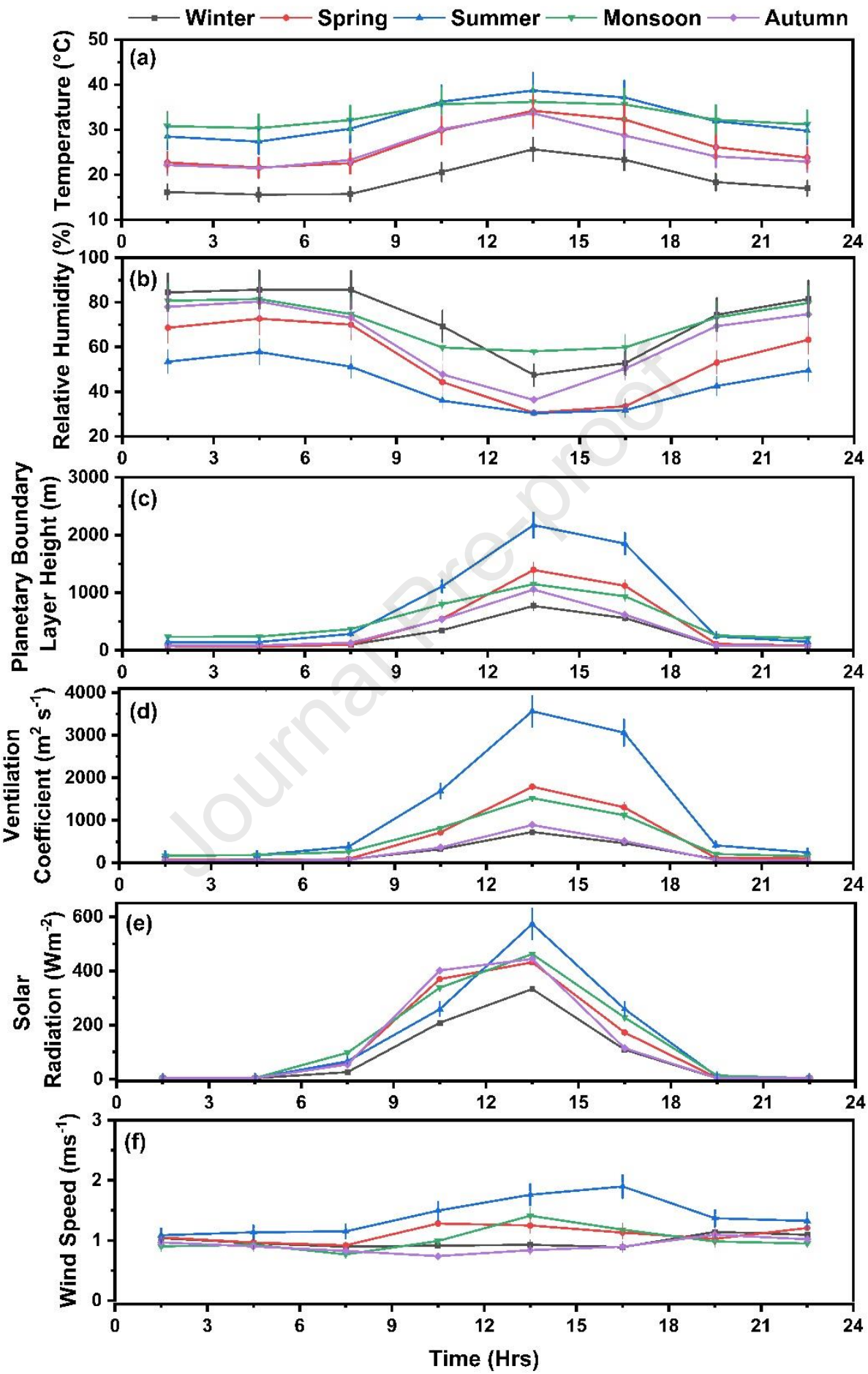

Journal Pre-proof

479

480 Figure 5. Diurnal variation of (a) ambient temperature, (b) relative humidity, (c) planetary boundary
481 layer height, (d) ventilation coefficient, (e) solar radiation, and (f) wind speed during winter, spring,
482 summer, monsoon and autumn seasons in Delhi (vertical bars represent ± standard deviation from
483 the mean).

484

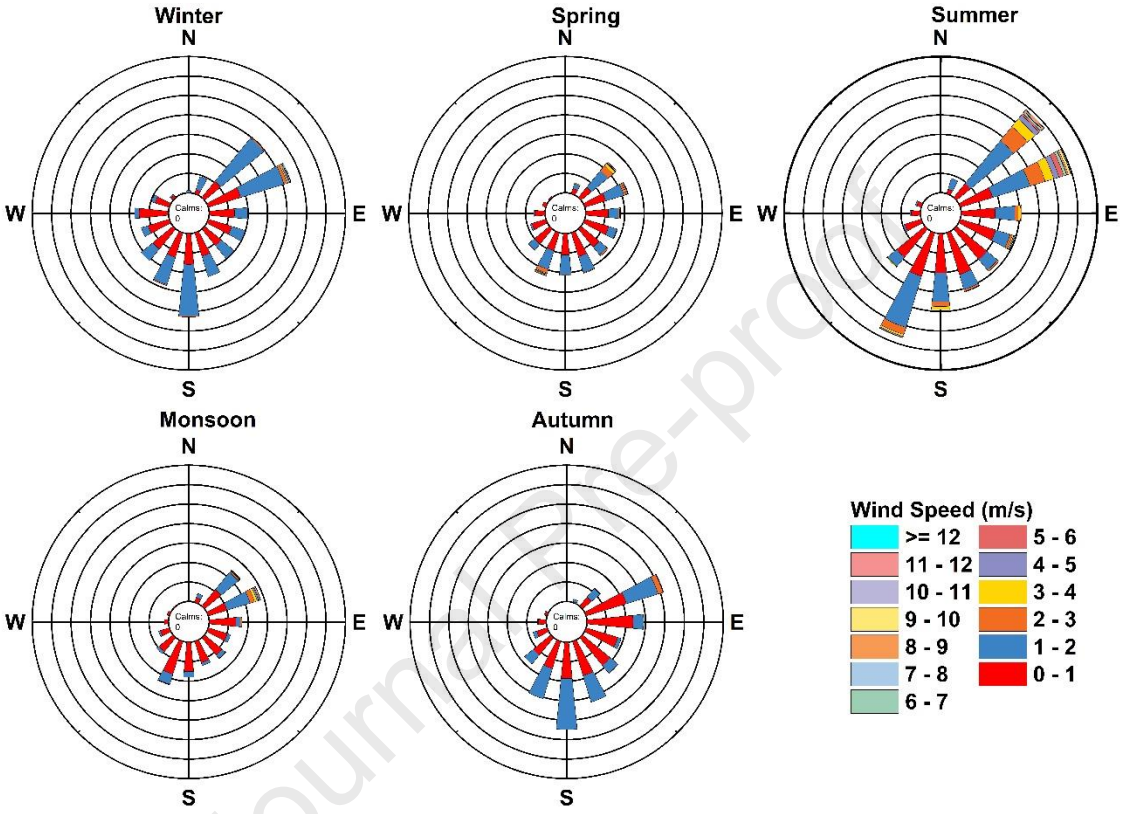

485

486 Figure 6. Wind rose analysis for the study area during the different seasons (winter, spring, summer,
487 monsoon, and autumn).

488

Journal Pre-proof

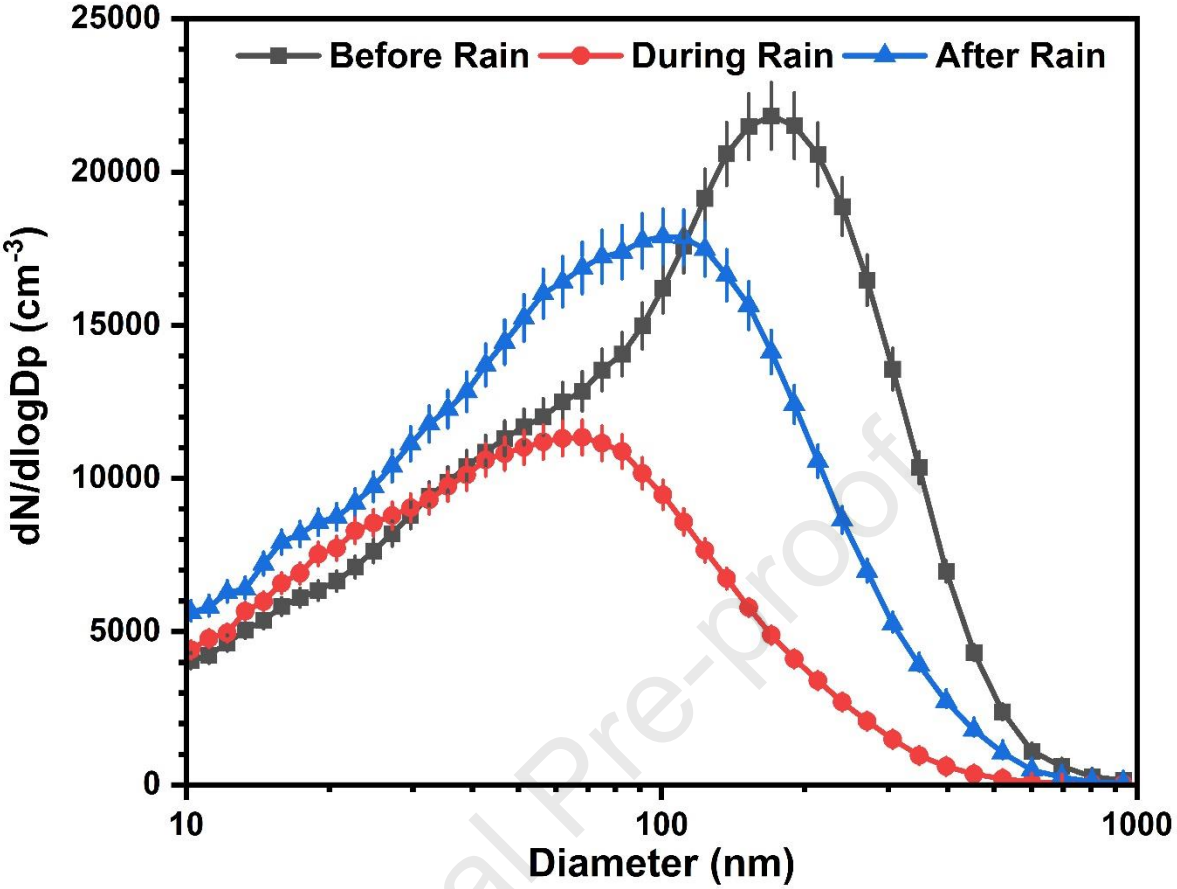

489

490 Figure 7. Particle number size distribution from 10 to 1000 nm during different phases of precipitation:
491 before (17 October 2021), during (18 October 2021), and after precipitation (19 October 2021) in the
492 monitoring station in Delhi (vertical bars represent ± standard deviation from the mean).

493

Journal Pre-proof

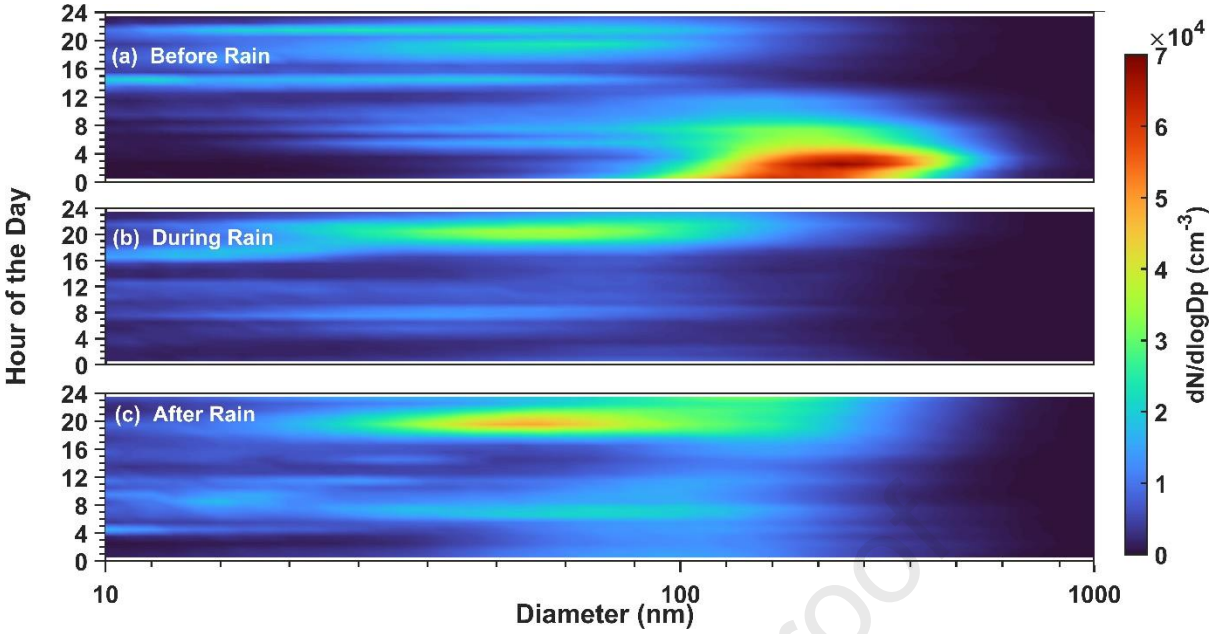

Figure 8. Time-resolved particle number size distribution from 10 to 1000 nm on consecutive days: day before (a) (17 October 2021), (b) day with (18 October 2021), and (c) day after (19 October 2021) precipitation in the monitoring station in Delhi.

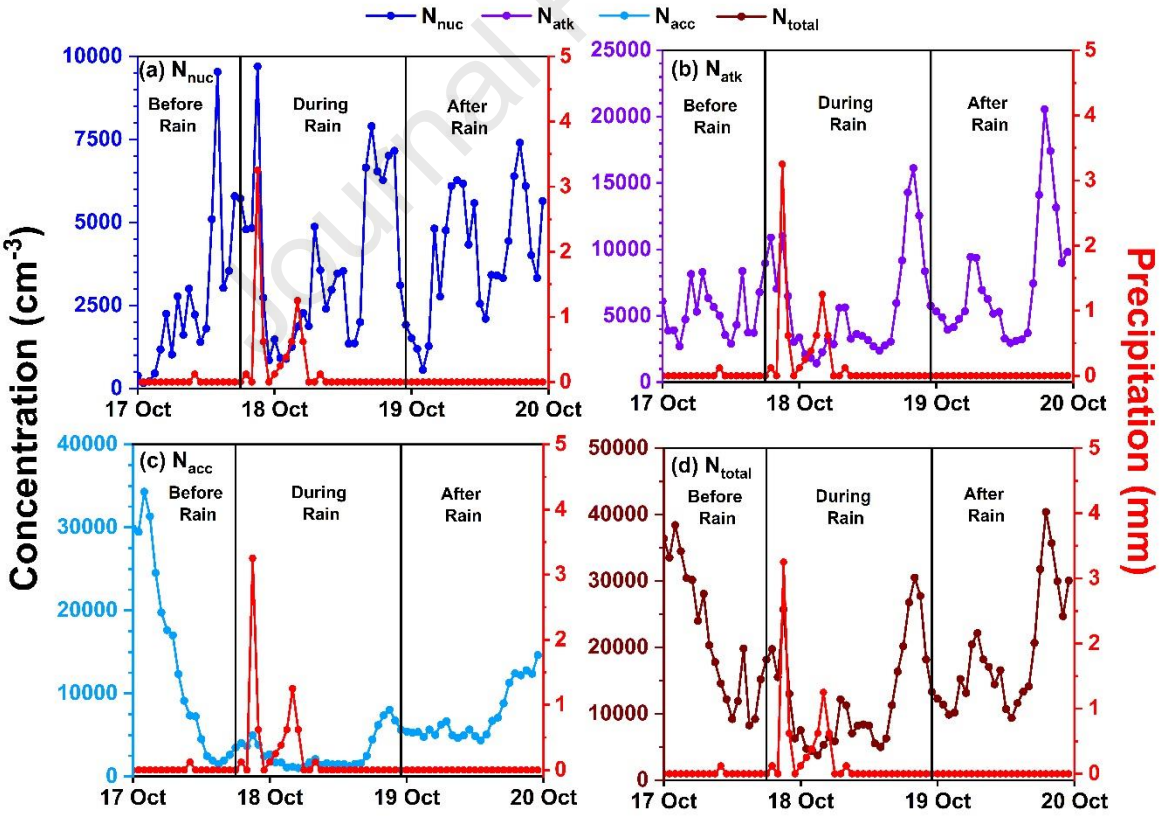

Figure 9. Temporal variation of particle number concentration before, during and after precipitation period for (a) N_{nuc} - 10 to 30 nm, (b) N_{atk} - 30 to 100 nm, (c) N_{acc} - 100 to 1000 nm and (d) N_{total} - 10 to 1000 nm from 17th October to 20th October 2021, in the monitoring station in Delhi.

(1) Atmospheric nanoparticles were measured in a pedestrian way in Delhi.

(2) Atmospheric nanoparticles experienced a higher concentration in winter.

(3) Meteorology influenced the particle concentration in the different seasons.

(4) Precipitation reduced the particle concentration, especially in the N_{acc}.

(5) Dispersive conditions influenced particle concentration, lower in summer and spring.

Journal Pre-proof

Journal Pre-proof

Declaration of interests

☒ The authors declare that they have no known competing financial interests or personal relationships that could have appeared to influence the work reported in this paper.

☐The authors declare the following financial interests/personal relationships which may be considered as potential competing interests:

Journal Pre-proof

J Mater Sci: Mater Electron (2024) 35:2055

Influence of samarium ions doping on electrical and optical properties of bismuth antimony fluoroborate glasses

Gunjan Mahajan[1,2], M. V. V. K. Srinivas Prasad[1,*], K. Swapna[1,*], K. Seshulatha[1,2], M. Venkateswarulu[1], Sk. Mahamuda[1], and A. S. Rao[3]

[1] *Department of Physics, Koneru Lakshmaiah Education Foundation, Green Fields,, Vaddeswaram, A.P 522502, India*
[2] *Department of Physics, Andhra Loyola College, Vijayawada, A.P 520008, India*
[3] *Department of Applied Physics, Delhi Technological University, Delhi 110 042, India*

Received: 18 May 2024
Accepted: 27 October 2024

© The Author(s), under exclusive licence to Springer Science+Business Media, LLC, part of Springer Nature, 2024

ABSTRACT

The traditional melt quenching method is used to synthesize the various trivalent samarium ion concentrations doped Bismuth-Antimony-Fluoroborate glasses (BiSFB). Physical, structural, spectroscopic, and electrical properties of the prepared glasses are examined. X-ray diffraction (XRD) and FTIR spectra were used to analyze the amorphous nature and functional groups present in the prepared glasses. Judd–Ofelt (JO) intensity parameters Ω_2, Ω_4, and Ω_6 follow the trend $\Omega_4 > \Omega_6 > \Omega_2$ for all concentrations. Radiative parameters for the fluorescent levels of Sm^{3+} ions in BiSFB glasses are calculated using JO parameters. The PL spectra show three emission bands at 562, 599, and 646 nm. The effective bandwidth and stimulated emission cross sections have relatively high values for 0.5 mol% concentration of Sm^{3+} ion for $^4G_{5/2} \rightarrow {}^6H_{7/2}$ transition among all the prepared glasses. Relatively high quantum efficiency calculated via decay curves shows 0.5 mol% concentration of Sm^{3+} ion to be optimum for solid-state lighting and optoelectronic devices. CIE color coordinates also confirm the red and orange-red emission for the prepared glasses. The dielectric properties (dielectric constant (ε'), dielectric loss (ε'')), Nyquist plot, electrical ac conductivity (σ_{ac}), and dc conductivity of these glasses with variation in frequency have also been studied at the ambient temperature. With an increase in applied frequency, particularly in the high-frequency region, the ac and dc conductivities are increased. Analysis of optical and electrical properties suggests the application of present glasses in optoelectronic devices and solid-state ionic materials.

Address correspondence to E-mail: mutyasrinivas@gmail.com; kswapna80@gmail.com

https://doi.org/10.1007/s10854-024-13794-9
Published online: 12 November 2024

1 Introduction

This study aims to develop advanced materials for orange-red emission to enhance solid-state lighting, optoelectronic devices, and solid-state ionic devices with high quantum efficiency. It also investigates the unique properties of Sm^{3+}-doped fluoroborate glasses. Glasses as host, doped with rare-earth (RE) ions exhibit a wide transmission range from UV to mid-IR, a high non-linear refractive index, and low phonon energies [1, 2]. These glasses have well-defined luminescence peculiarities. The low phonon energies of the glasses are particularly useful in minimizing non-radiative emissions and, thereby, enhancing quantum yield [3].

Among the several hosts used for RE doping, borate glasses have drawn more attention. Borate glasses find extensive use in solid-state lasers, non-linear parametric converters, electro-optic modulators, and switches. All these applications have some effects with respect to optical and electrical properties of the glasses [4]. However, high phonon energy in borate glasses results in multiphonon relaxation, a non-radiative decay. To accomplish a highly efficient radiative upconversion process, the glass phonon energy must be reduced. The incorporation of heavy metal oxides in the glass host decreases the phonon energy. As a result, fluorescence output increases, which increases the lasing emission [5, 6]. Moreover, addition of network modifiers Bi_2O_3 and Sb_2O_3 to the borate glasses brings the fascinating change in optical properties. Addition of Bi_2O_3 to a glass system increases refractive indices and density, decreases crystallization rate, makes the glass to be moisture resistant, decreases the phonon energy, and improves other qualities of the glasses [7, 8]. Sb_2O_3, a modifier, increases the polarizabilty of glasses resulting in enhancing the optical properties [9]. The electronic polarizability is closely related to optical nonlinearity as well as a number of chemical and physical traits. It functions as a fining agent and makes RE ions more soluble [10].

CdF_2 acts as an intermediate to the borate network, forming $Cd^{2+}{}_{1/2}$ $[BO_3F]^-$ tetrahedra, in addition of forming its own amorphous matrix at higher contents. It decreases the moisture by replacing OH^- with F^- unit [11].

RE ions-doped glasses have intense emission in the visible region. These intense transitions are because of the *f-f* transition. Samarium, in contrast to other RE elements, has a large number of energy levels that are closely spaced apart, giving it significant fluorescence intensity in the red and reddish-orange region. It has a four-level laser transition in the NIR region [1, 12]. Laser emission occurs from metastable state $^4G_{5/2}$ at nearly 17600 cm^{-1} to $^6H_{5/2}$, $^6H_{7/2}$, and $^6H_{9/2}$. Emission from the $^4G_{5/2}$ level exhibits relatively high quantum efficiency and shows different quenching emission channels. Because of the long lifetime of the metastable state along with high branching ratio, Sm^{3+} ions-doped glasses are good lasing materials for red and red–orange emission and used for cancer treatment. Adequate intensity, acceptable directivity, and effective coupling efficiency of samarium-doped glasses make them to be a suitable contender for light source, color displays, solar cells, UV sensors, and visible lasers and coastguard communication [13–15].

Solid-state chemistry and materials research have shown a great deal of interest in conducting glasses. To learn more about the structural environment of the glass network, electric parameters will be studied with the aid of spectroscopic properties. The electrical conductivity is affected by the glass composition, disorderness, open networks, and size of samarium ions when these ions are embedded [16, 17]. An increase in conductivity with increasing samarium ion has also been noted in several samarium ions-doped borate glasses. It is explained by the mobility of samarium ions due to their heavy weights. The impedance studies of the prepared glasses are used to find the ac and dc conductivities for solid-state ionic devices [18–20].

While there have been many investigations into Samarium ion-doped glass systems, most of them have been limited to structural and spectroscopic analysis. Therefore, using electric characteristics, it is still possible to study the impact of samarium ions on bismuth antimony fluoroborate glasses. So, the current research is aimed at studying the physical, structural, photoluminescence, and electrical properties of Sm_2O_3-doped Bi_2O_3-Sb_2O_3-CdF_2-B_2O_3 glasses.

2 Experimental section

2.1 Synthesis

Samarium-doped antimony fluoroborate glasses (BiSFB) of composition $10Bi_2O_3$-(5-x)CdF_2-$35Sb_2O_3$-$50B_2O_3$-xSm_2O_3, where x = 0, 0.5, 1.0, 1.5, 2.0, and 2.5 mol % are synthesized using melt quenching technique Fig. 1. The labeling of the glasses has

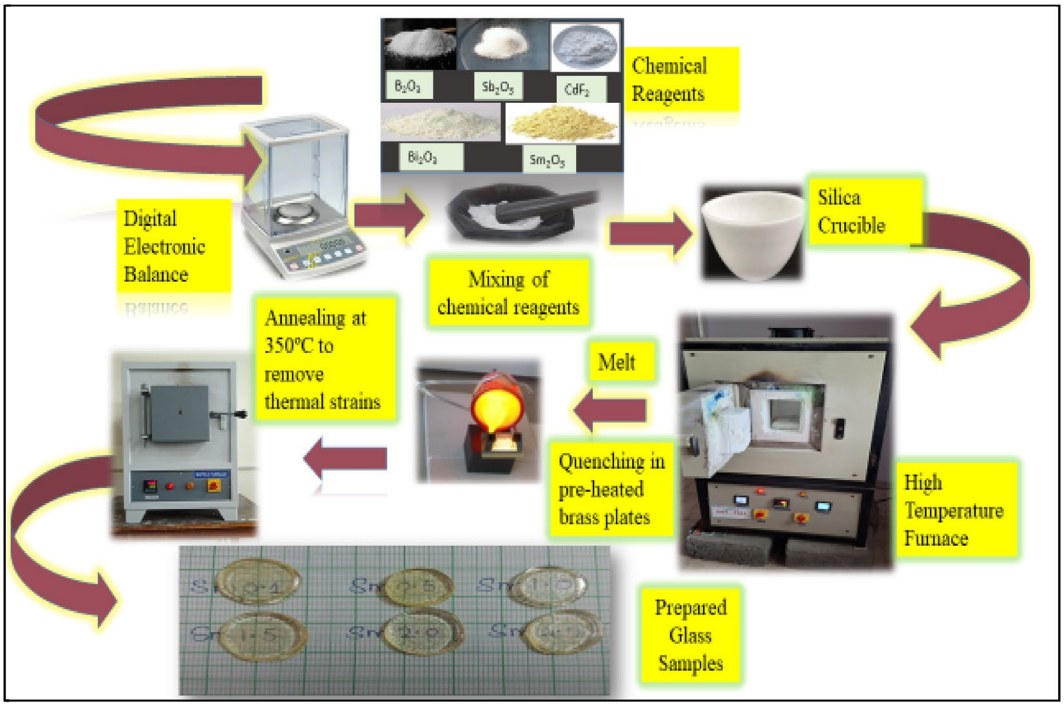

Fig. 1 Block diagram of melt quenching technique for Sm^{3+}-doped BiSFB glasses

been done as BiSFB undoped, BiSFBSm01, BiSFBSm05, BiSFBSm10, BiSFBSm15, BiSFBSm20, and BiSFBSm25. In the present work, an appropriate quantity of Sigma Aldrich analar grade reagents Bi_2O_3, CdF_2 Sb_2O_3, B_2O_3, and Sm_2O_3 of 99.99% purity are weighed through digital electronic balance ALE-223 of 1 mg accuracy. The weighed components are mixed in an agate motor to obtain the homogeneous mixture (~10 g). The homogeneous mixture is then transferred to silica crucibles and heated in a high-temperature Presto MF-4 electric furnace directly to 1250 °C. Constant temperature of 1250 °C is maintained for 35 min until homogeneous melt is obtained. For homogeneous blending of all the constituents, the melts are stirred regularly. The melts are then air quenched in order to solidify quickly. It prevents the formation of undesirable microstructures and phase changes that might occur with slower cooling rates. After quenching, these are pressed between preheated brass plates. It helps obtain homogeneous thickness and provide controlled cooling. Thereafter, the melts are annealed at 350 °C for 2 h to remove the internal stresses and thermal strains. The glasses are then allowed to cool at room temperature. The composition of prepared glasses in terms of mole fraction and weight fraction is given in Table 1.

2.2 Characterization techniques

With Cu K_α ($\lambda = 1.5405$) radiation, the X-ray diffraction (XRD) patterns are captured using a Panalytical Empyrean diffractometer for the powdered samples. Jasco FT/IR-4700 spectrometer is used to perform the FTIR measurements. KBr pellet technique is used to prepare and shape the powdered samples. With a spectral resolution of 0.1 nm and a wavelength range of 390 to 1700 nm, the optical absorption spectra are captured using a Jasco model V670 spectrophotometer at ambient temperature. The spectrometer has double-beam optical system with baseline correction. The PL excitation, emission, and decay spectra are captured with JASCO model FP-8300 spectrofluorometer using xenon flashlamp as the excitation source. The emission monochromator and the detector measure the fluorescence intensity of the emitted light. Impedance-related parameters are studied using a Swagelok-type half-cell configuration. The charge/discharging profiles of the prepared glasses are measured using a multichannel

Table 1 Mole fraction of elements in Sm^{3+}-doped BiSFB glass along with refractive index and density

Glass system	Composition in mol%						
	B_2O_3	Sb_2O_3	Bi_2O_3	CdF_2	Sm_2O_3	Refractive index	Density (gcm^{-3})
BiSFBSm05	50	35	10	4.5	0.5	1.9728	3.748
BiSFBSm10	50	35	10	4.0	1.0	1.9733	3.757
BiSFBSm15	50	35	10	3.5	1.5	1.9735	3.767
BiSFBSm20	50	35	10	3.0	2.0	1.9738	3.777
BiSFBSm25	50	35	10	2.5	2.5	1.9742	3.797
Glass	Weight fraction of elements						
	B	O	Sb	Bi	Cd	F	Sm
BiSFBSm01	0.0566	0.2388	0.4459	0.2186	0.0288	0.0097	0.0016
BiSFBSm05	0.0563	0.2388	0.4440	0.2177	0.0264	0.0089	0.0079
BiSFBSM10	0.0560	0.2388	0.4417	0.2166	0.0233	0.0079	0.0157
BiSFBSm15	0.0557	0.2388	0.4394	0.2155	0.0203	0.0069	0.0235
BiSFBSm20	0.0554	0.2388	0.4371	0.2144	0.0173	0.0058	0.0312
BiSFBSm25	0.0552	0.2388	0.4349	0.2132	0.0143	0.0048	0.0388

battery tester (Maccor, Inc., model 2000) in the potential range of 0.001–4 V.

3 Results and discussions

3.1 Physical parameters

Brewster's angle method with a He–Ne laser at 650 nm is used to find the refractive indices of the prepared Sm^{3+} ion-doped BiSFB glasses. The densities of the prepared glass samples are measured directly using Archimede's principle with o-xylene as the immersion liquid. The digital balance is used for the measurement. The densities are calculated using the formula [21]:

$$\left[\rho = \frac{w_a}{(w_a - w_o)}\right]\rho_o,$$

where w_a and w_o are weights of glass samples in air and o-xylene liquid, respectively, ϱ_o is the density of o-xylene. Measured values of refractive indices and densities are used to calculate various physical parameters using the formulae given in the literature [5, 20]. These parameters include average molecular weight, molar refractivity, mean atomic volume, Sm^{3+} ion concentration, interionic distance, molecular electronic polarizability, dielectric constant, optical dielectric constant, reflection loss, polaron radius, and field strength. Increase in molecular weight by the addition of Sm_2O_3 is attributed to replacement of CdF_2 at the expense of Sm_2O_3. The rate at which molecular weight increases is faster than the rate at which density increases when Sm_2O_3 concentration is raised. The opened glass network structure may be attributed for this reason. Variation of density and refractive index with Sm^{3+} ion concentration is shown in Fig. 2. Both density and refractive index increase with Sm^{3+} ion concentration due to increase in NBOs. It can be seen that when the concentration of Sm^{3+} ions increases, the ionic radius decreases, allowing the ions to be closer together in the glass resulting in a decrease in interatomic distance. This results in

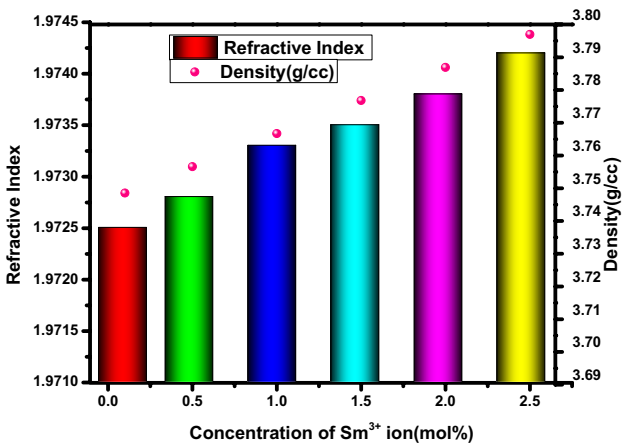

Fig. 2 Variation of refractive index and density with Sm^{3+} ion concentration

increase in compactness and, hence, density increases. The Sm–O bond also becomes strong causing the field strength around the Sm^{3+} ion to increase. The gradual conversion of BO_3 structural units into BO_4 units is demonstrated by the increase in field strength with Sm^{3+} ion concentration [22]. The same is confirmed by the FTIR spectra. Polaron is a quasi-particle used to describe the interaction of electrons with atoms in solids. It is self-trapped electron which moves from one place to another by lattice distortion associated with it. As polaron radius decreases with increase in Sm^{3+} ion concentration; therefore, dielectric constant progressively rises. As dielectric constant is inversely connected with the polarizability of the glass; therefore, electronic polarizability diminishes as dielectric constants rise [9]. Clearly, average molecular weight, mean atomic volume, samarium ion concentration, dielectric constant, optical dielectric constant, and reflection loss increase with samarium ion concentration whereas interionic distance, polaron radius, and field strength decrease as listed in Table 2. This change is because of the compactness in the glasses when samarium ions are added.

3.2 Structural analysis

3.2.1 XRD spectral analysis

To check the amorphous nature of the undoped BiSFB glass and Sm^{3+}-doped BiSFB glasses, XRD spectra are recorded in Fig. 3. The nature of the spectrum is similar for all the concentrations of dopant. The presence of diffused broad lines at low angles confirms the asymmetrical arrangement and long-range structural disorder of atoms in the lattice. Thus, the prepared glasses are amorphous in nature.

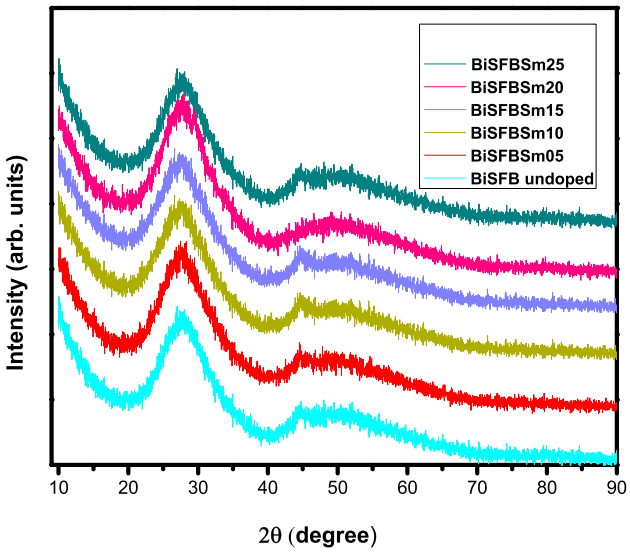

Fig. 3 XRD pattern of undoped and Sm^{3+}-doped BiSFB glasses

3.2.2 Fourier Transform Infrared Spectra

FTIR spectra of undoped and Sm^{3+} ions-doped BiSFB glasses in the energy range 400–4000 cm^{-1} are shown in Fig. 4. The band assignments that go with each band are given in Table 3. FTIR plays a crucial role in finding the functional groups present in the host matrices. The

Table 2 Different physical parameters of Sm^{3+}-doped BiSFB glasses

Parameters	BiSFBSm01	BiSFBSm05	BiSFBSm10	BiSFBSm15	BiSFBSm20	BiSFBSm25
Average molecular weight (g)	187.3	188.0	189.0	190.1	191.0	192.1
Mean atomic volume (g/cm^3/atom)	10.18	10.20	10.22	10.24	10.27	10.30
Sm^{3+}ion concentration (10^{22}ions/cm^3)	0.121	0.601	1.197	1.788	2.376	2.958
Optical dielectric constant	2.891	2.892	2.894	2.895	2.896	2.897
Dielectric constant	3.891	3.892	3.894	3.895	3.896	3.897
Reflection loss	10.70	10.71	10.72	10.72	10.72	10.73
Molar refraction (cm^{-3})	24.51	24.57	24.64	24.71	24.78	24.85
Polaron radius (A°)	0.816	0.477	0.380	0.332	0.302	0.281
Interionic distance (A°)	2.024	1.185	0.942	0.823	0.748	0.695
Molecular electronic polarizability($10^{23}cm^3$)	9.723	1.949	0.977	0.653	0.491	0.394
Field strength (10^{16} cm^{-2})	4.509	13.17	20.86	27.29	33.00	38.24
Transmission coefficient	0.807	0.806	0.806	0.806	0.806	0.806
Direct band gap(eV)	3.312	3.283	3.240	3.212	3.187	3.145
Indirect band gap(eV)	3.051	3.032	3.000	2.984	2.956	2.923

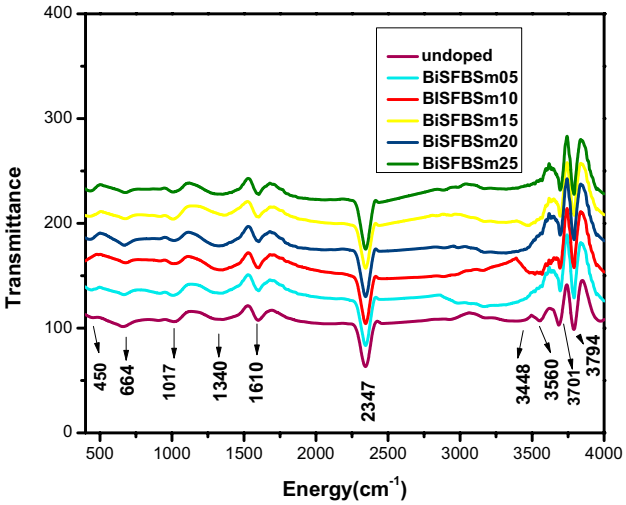

Fig. 4 FTIR spectra of undoped and Sm^{3+}-doped BiSFB glasses

presence of functional groups can be precisely defined as the transition of an atom between the relaxed and high energy states. It results in the formation of distinct molecular vibrational bands in the excited state. Hence, molecules that are subjected to molecular vibrations result in variations in the frequency of the IR region of the electromagnetic spectrum. The vibrations arise because of bending, stretching, rocking, twisting, out-of-plane deformation, and wagging [4]. Functional groups in the host matrix, which ultimately depend on constituent of host matrix, determine the mode of vibration. The bands in the FTIR spectra in the range 400–700 cm^{-1}, 800–1200 cm^{-1} and 1300–1600 cm^{-1} are because of changes in B–O–B linkages induced by modifiers or M–O bonds, asymmetric stretching relaxation of the B–O bonds and stretching of BO_4 units, respectively. Hydrogen bonding and stretching vibrations of OH groups are responsible for the bands in the region 1600 to 4000 cm^{-1} [21]. The band observed at 450 cm^{-1} attributed to the asymmetric bending vibrations in the trigonal pyramids of SbO_3. Absorption at 664 cm^{-1} is ascribed to the B–O stretching vibrations of tetrahedral BO_4 units [23, 24]. The band at 1017 cm^{-1} is due to the symmetric BO_4 stretching vibrations in the diborate [25]. The asymmetric stretching modes of BO_3, BO_2O^-, borate triangles, and other networks made up of six-membered borate planar groups are thought to be responsible for the band at 1340 cm^{-1}. The band ascribed to 1610 cm^{-1} is due to the conversion of trigonal units of borate into tetragonal units with NBOs in the host glass [26]. The transition peak observed at 2347 cm^{-1} is due to NBO sites [20]. The bands at 3448, 3560, 3701, and 3794 cm^{-1} are due to the presence of fundamental stretching of OH groups in the prepared glasses [27]. These O–H bonds are formed at non-bridging sites. The increase in OH content in the host matrix reduces the quantum efficiency by causing non-radiative losses. The increase in concentration of samarium ion in the host matrix brings a minimal change in the wave number corresponding to band position. Non-bridging oxygen, modifiers, and the surrounding environment are all responsible for the little change in the wave numbers of the bands which affect the luminescence characteristics and electrical properties [25].

3.3 Optical absorption spectra

The absorption spectra of as-prepared glasses consist of eleven inhomogeneous peaks of varying intensities in VIS–NIR region (Fig. 5). With increase in concentration of Sm^{3+} ions, absorption rates as well as absorption bands increase. These peaks are because of 4f electrons which are effectively shielded by 5s and 5p electrons in samarium. The peaks are observed at 403, 425, 462, 478, 944, 1080, 1231, 1375, 1484, 1535, and 1590 nm which implies the absorption of energy from $^6H_{5/2}$ to $^4F_{7/2}$, $^4M_{19/2}$, $^4I_{13/2}$, $^4M_{15/2}$, $^6F_{11/2}$, $^6F_{9/2}$, $^6F_{7/2}$,

Table 3 Assignment of identified FTIR bands for Sm^{3+}-doped BiSFB glasses

Wave number (cm^{-1})	Assignment
450	Asymmetric bending vibrations in the trigonal pyramids of SbO_3
664	B–O–B bending in oxygen bridges b/w two trigonal boron atoms
1017	B–O stretching of various borate rings in BO_3 group
1340	Asymmetric stretching modes of BO_3, B_2O^- borate triangles, and various networks
1610	Stretching vibrations of BO_3 triangles
2347	Vibrations of O–H bonds formed at non-bridging oxygen sites
3448–4000	Presence of fundamental stretching of OH groups in the prepared glasses

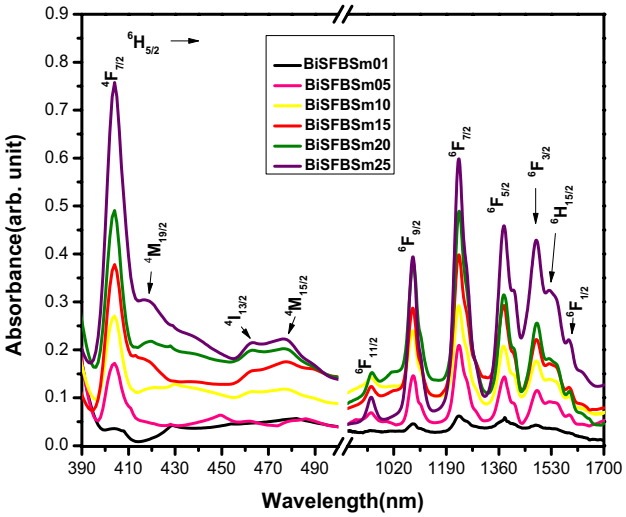

Fig. 5 Absorption spectra of Sm^{3+}-doped BiSFB glasses in UV–VIS-IR region

$^6F_{5/2}$, $^6F_{3/2}$, $^6H_{15/2}$, and $^6F_{1/2}$, respectively. Assignment of the peaks has been done as per the carnell paper [28]. The nature and band positions of the Sm^{3+}-doped BiSFB glasses are extremely comparable with the other reported glasses. It demonstrates the homogenous amalgamation of the Sm^{3+} ions in the host matrix without huddling or changes in the environment around RE ions [29]. In absorption spectra, bands are classified into two categories: Low energy band in NIR region (900–1700 nm) and high energy band in visible region (VIS) (400-600 nm). Seven peaks are observed in low energy band and four in high energy band. The peaks in the spectra have a high intensity in the VIS and NIR regions, indicating substantial absorption in these regions. The transitions from the $^6H_{5/2}$ state to the ^6F, ^6H, and ^6P terms obey the selection rule $\Delta S = 0$, so they are spin permitted; however, the transitions from the $^6H_{5/2}$ state to the ^4I, ^4M, and ^4F terms are spin prohibited, so they are weaker. The selection rule $\Delta J \geq 0$ is satisfied by most of the transitions; therefore, most of the transitions are induced electric dipole [30]. In the UV–VIS-NIR region, the transition from $^6H_{5/2}$ to $^6F_{7/2}$ (1231 nm) is the most intense, whereas in the UV–VIS region, the transition from $^6H_{5/2}$ to $^4F_{7/2}$ (404 nm) is more intense as compared to other transitions. These transitions corresponding to maximum intensities are known as hypersensitive transitions which are highly dependent on the ambiance around the Sm^{3+} ions. Hypersensitive transitions adhere to the following selection criteria $\Delta J \leq 2$, $\Delta L \leq 2$, and $\Delta S = 0$ and are allied with higher value of reduced matrix element $||U^2||^2$ [31]. Since Ω_2 depends directly on $||U^2||^2$, therefore, hypersensitivity and Ω_2 are directly related. The methods of selection are the same as those used for quadrupole transitions. Calculations, however, have shown that the intensities of hypersensitive transitions are quite larger than those anticipated for quadrupole transitions. Pseudo-quadrupole transitions are also known as hypersensitive transitions [32].

The nature of bonding between Sm^{3+} ions and surrounding ligands can be evaluated through bonding parameter (δ) which in turn is dependent upon nephelaxutic ratio (β). Jorgensen presented the theory of the "nephelauxetic effect" also termed "cloud expansion" [26, 33]. The overlapping of orbitals of Sm^{3+} ions with the surrounding ligands results in the tightening of the energy level structure of Sm^{3+} ions. This causes a red shift, i.e., the shift of the absorption peaks towards low frequencies. In the prepared glasses, as the concentration increases from 0.1 to 0.5 mol%, redshift for many absorption peaks is observed. This shift follows the opposite propensity when concentration levels rise further. It evaluates that the level of covalency between the oxygen ligands and RE ions increases up to 0.5 mol% and then decreases. Thus, partially filled f-orbitals are affected by the charge transfer from the surrounding ligands and the inner shells of the Sm^{3+} ion.

$$\textit{Nephelauxetic ratio}\,(\beta) = \nu_h/\nu_a,$$

where ν_h denotes the energy in cm^{-1} of a specific transition for an ion host under investigation and ν_a is the energy in cm^{-1} of the same transition for the aqua ion [29]. In the end, the RE ions energy structure has been suppressed as a result of the mixing of oxygen orbitals with 4f shells.

$$\textit{Bonding Parameter}, \delta = \frac{1-\overline{\beta}}{\overline{\beta}}.$$

The bonding parameters for 0.1, 0.5, 1.0, 1.5, 2.0, and 2.5 mol% of samarium are -0.759, -0.608, -0.618, -0.670, -0.729, and -0.739, respectively. Negative values of bonding parameters indicate ionic nature of bond between the samarium and surrounding ligands. Further, increasing values of δ with Sm^{3+}ion concentration indicate an increase in ionic character between Sm^{3+}ion and ligand bonds (Table 4). It indicates the change in environment with RE ion concentration [23].

Table 4 Experimental ($f_{exp}\times10^{-6}$), calculated ($f_{cal}\times10^{-6}$) oscillator strength, r.m.s deviation ($\delta_{rms}\times10^{-6}$), bonding parameter ($\beta_{av}$, $\delta\%$) of Sm^{3+}-doped BiSFB glasses

Transition	BiSFBSm01		BiSFBSm05		BiSFBSm10		BiSFBSm15		BiSFBSm20		BiSFBSm25	
	f_{exp}	f_{cal}	f_{exp}	f_{cal}	f_{exp}	f_{cal}	f_{exp}	f_{cal}	f_{exp}	f_{cal}	f_{exp}	f_{cal}
$^4F_{7/2}$	0.100	0.172	0.621	0.707	0.619	0.675	0.564	0.433	0.316	0.274	0.294	0.3263
$^4M_{19/2}$	0.045	0.005	0.075	0.029	0.074	0.028	0.041	0.027	0.042	0.023	0.0271	0.0184
$^4I_{13/2}$	0.562	0.441	1.651	1.522	1.544	1.463	0.822	1.039	0.818	0.878	0.7939	0.7515
$^4M_{15/2}$	0.628	0.715	2.258	2.279	2.213	2.212	1.788	1.644	1.531	1.538	1.1952	1.1696
$^6F_{11/2}$	1.018	0.956	4.693	4.827	4.560	4.688	4.159	4.249	3.832	3.735	2.7814	2.9112
$^6F_{9/2}$	0.480	0.574	3.645	3.462	3.545	3.355	3.336	3.178	2.630	2.748	2.3558	2.1638
$^6F_{7/2}$	0.113	0.091	0.581	0.570	0.488	0.555	0.336	0.530	0.323	0.455	0.3258	0.3592
$^6F_{5/2}$	0.043	0.037	0.235	0.233	0.225	0.227	0.183	0.218	0.179	0.187	0.1507	0.1483
$^6F_{3/2}$	0.087	0.102	0.762	0.577	0.639	0.562	0.388	0.526	0.347	0.457	0.2943	0.358
$^6H_{15/2}$	0.057	0.000	0.186	0.000	0.155	0.000	0.050	0.000	0.034	0.000	0.0339	0.000
$^6F_{1/2}$	0.874	0.012	3.059	0.042	2.965	0.032	1.626	0.024	1.545	0.022	0.223	0.0173
δ_{rms}	0.504		1.118		1.042		0.586		0.545		0.252	
β_{av}	1.005		1.002		1.003		1.004		1.004		1.005	
$\delta\%$	-0.004		-0.003		-0.004		-0.004		-0.004		-0.004	

3.3.1 *Optical band gap measurement*

Absorption spectra play a vital role in calculating the optical band gap. The optical band gap is the energy difference between the valence band and the conduction band. The transition from valence band to the conduction band is possible only if the energy of incident photon is greater than or equal to the optical band gap. The structural changes brought on by the addition of Sm_2O_3 concentration in the host glass are explained by the optical band gap. The optical band gap can be evaluated using Mott and Davis theory using relation [33]

$$\alpha(\nu) = A\frac{(h\nu - E_g)^n}{h\nu},$$

where α is the absorption coefficient, A is the band tailing parameter, $h\nu$ is the energy of incident photon, E_g is the optical band gap energy, and n is an index that corresponds to the nature of transition. The absorption coefficient α is calculated [34] as follows:

$$\alpha = 2.303\frac{A}{t},$$

where A is the absorbance and t is thickness of the glass samples. The inset in Fig. 6 shows the spectra of absorption coefficient for the prepared glass samples. The values $n = 4$ and $n = 5$ are not typically used because they do not correspond to common types of electronic transitions in materials. n = 2, 1/2 corresponds to direct allowed and indirect allowed bands whereas $n = 3,3/2$ corresponds to direct and indirect forbidden transitions [35, 36]. The minimum of the conduction band and the maximum of the valence band in the direct bandgap are aligned. There is an offset between the minimum and maximum of the valence band in the indirect bandgap, indicating a

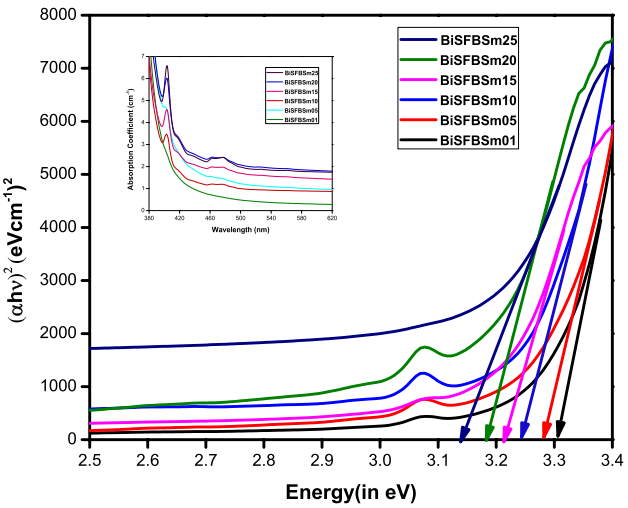

Fig. 6 Tauc's plot for allowed direct band gap transitions of Sm^{3+}-doped BiSFB glasses. (Inset shows absorption coefficient spectra of Sm^{3+}-doped BiSFB glasses)

difference in the energy band structure. In contrast to the indirect bandgap material, which emits radiation weakly, the direct bandgap material effectively emits light [37]. The extrapolation of the linear part in $(\alpha h\nu)^2$ and hν graph (Fig. 6) as well as in $(\alpha h\nu)^{1/2}$ and hν graph (Fig. 7) along the x-axis gives a direct optical band and an indirect optical band. In the present case for both direct and indirect allowed transitions, these values decrease with increase in Sm^{3+}ion concentration (Table 2). The decrease in the optical band gap values with Sm^{3+}ion concentration can be attributed to compactness of structure of glass [29].

3.3.2 Judd–ofelt analysis

JO intensity parameters Ω_λ ($\lambda = 2, 4, 6$) are gauged through oscillator strength. The energies of the absorption bands, known as oscillator strengths (f_{exp}), are determined from the absorption spectra by measuring integrated areas beneath the absorption peaks. The oscillator strength from the ground state $^6H_{5/2}$ to various excited states can be calculated using the following relation [32]:

$$f_{\exp} = \frac{2.303mc^2}{N_A\pi e^2} \int \varepsilon(\nu)d\nu,$$

where m and e are mass and charge of electron, N_A is Avogadro's number, c is the velocity of light, $\varepsilon(\nu)$ is the molar extension coefficient at the wavenumber ν, and dν is the bandwidth. Using the least-square-fitted method, JO intensity parameters Ω_λ ($\lambda = 2, 4, 6$) are calculated. These are then utilized to determine theoretical oscillator strengths by applying JO theory to the experimental oscillator strengths (f_{cal}) [38, 39]. The probability of electric dipole transitions can be calculated using the relation:

$$f_{cal} = \frac{8\pi^2 mc\nu}{h(2J+1)} \frac{(n^2+2)^2}{9n} \sum_{\lambda=2,4,6} \Omega_\lambda \left\langle (S,L)J \left\| U^\lambda \right\| (S\prime,L\prime)J\prime \right\rangle^2.$$

The experimental and calculated oscillator strengths along with nephelaxutic ratio and bonding parameter are given in Table 4. Root-mean-square values measure the deviations between the experimental and theoretical oscillator strength. It indicates the degree of consistency of the fit by least-square method. The change in the environment around Sm^{3+}ion causes this change which is further confirmed by evaluating spectral intensity parameters (Ω_2, Ω_4, Ω_6) of Sm^{3+}ion in the host glass using JO theory as shown in Table 5. In general, Ω_2 parameter determines the structural changes, nature of symmetry, and bonding around the RE ion. The other two Ω_4 and Ω_6 are related with the bulk properties like viscosity, rigidity, and dielectric of host materials [24]. The spectral intensity parameters along with the other reported values [21, 40–42] are given in Table 5. These spectral intensity parameters follow the trend $\Omega_4 > \Omega_6 > \Omega_2$ at all concentrations. Lesser value of Ω_2 indicates lesser covalency between Sm^{3+} ion and ligands. Clearly, these parameters increase with increase in concentration, reaches maximum for BiSFBSm05, and then decreases. The current series of prepared glasses exhibits strong structural stiffness, high viscosity, low asymmetry, and lesser covalency of the RE sites. The ratio of Ω_4/Ω_6 in Sm^{3+} ions-doped BiSFB glasses is greater than 1, which indicates a higher optical quality [5].

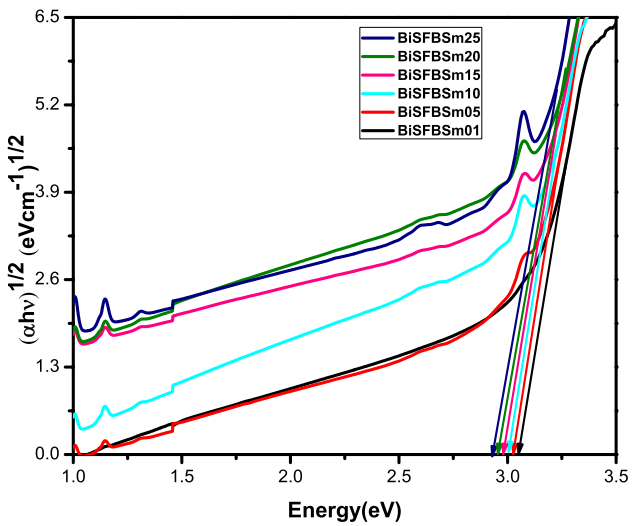

Fig. 7 Tauc's plot for allowed indirect band gap transitions of Sm^{3+}-doped BiSFB glasses

3.4 Photoluminescence spectra

3.4.1 Excitation

The excitation-emission spectra of Sm^{3+}-doped BiSFB glasses are plotted in Fig. 8. Excitation spectra are recorded from 340 to 550 nm at an emission wavelength of 599 nm. The excitation spectra consist of nine bands due to f–f transitions amid Sm^{3+} ions ascribed to the transitions $^6H_{5/2} \rightarrow {}^4D_{3/2}$, $^6H_{5/2} \rightarrow {}^6P_{7/2}$,

Table 5 Judd–Ofelt parameters Ω_λ ($\lambda = 2, 4, 6$)$\times(10^{-20}\text{cm}^2)$ for Sm^{3+}-doped BiSFB glasses along with other reported Sm^{3+}-doped glasses

S. No	Glass	Ω_2	Ω_4	Ω_6	Trend	
1	BiSFBSm01	0.398	0.937	0.460	$\Omega_4>\Omega_6>\Omega_2$	
2	BiSFBSm05	1.640	2.946	2.920	$\Omega_4>\Omega_6>\Omega_2$	
3	BiSFBSm10	1.561	2.845	2.841	$\Omega_4>\Omega_6>\Omega_2$	
4	BiSFBSm15	1.002	2.724	2.439	$\Omega_4>\Omega_6>\Omega_2$	
5	BiSFBSm20	0.632	2.344	2.031	$\Omega_4>\Omega_6>\Omega_2$	
6	BiSFBSm25	0.754	1.547	1.511	$\Omega_4>\Omega_6>\Omega_2$	
7	BNNFS:Na	0.722	2.881	2.574	$\Omega_4>\Omega_6>\Omega_2$	[25]
8	BNNFS:SK	0.231	2.706	2.387	$\Omega_4>\Omega_6>\Omega_2$	[25]
9	OCBTSm1.0	0.641	2.411	2.365	$\Omega_4>\Omega_6>\Omega_2$	[29]
10	GSm1	0.321	2.800	1.782	$\Omega_4>\Omega_6>\Omega_2$	[40]
11	CNFB0.1S	1.092	3.007	1.462	$\Omega_4>\Omega_6>\Omega_2$	[41]
12	40BiNFBS	0.263	1.823	2.008	$\Omega_4>\Omega_6>\Omega_2$	[42]

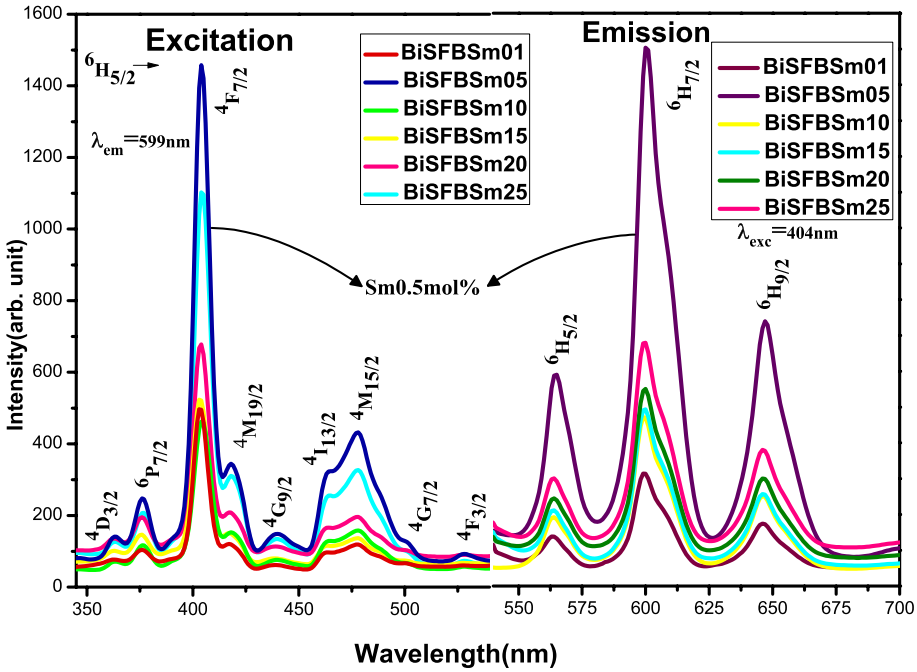

Fig. 8 Excitation-emission spectra of Sm^{3+}-doped BiSFB glasses under 599 nm emission and 404 nm excitation

$^6H_{5/2} \rightarrow {}^4F_{7/2}$, $^6H_{5/2} \rightarrow {}^4M_{19/2}$, $^6H_{5/2} \rightarrow {}^4G_{9/2}$, $^6H_{5/2} \rightarrow {}^4I_{13/2}$, $^6H_{5/2} \rightarrow {}^4M_{15/2}$, $^6H_{5/2} \rightarrow {}^4G_{7/2}$, and $^6H_{5/2} \rightarrow {}^4F_{3/2}$ [28] at wavelengths 362 nm, 376 nm, 404 nm, 418 nm, 439 nm, 462 nm, 478 nm, 501 nm, and 528 nm. The band observed at 404 nm, corresponding to excitation $^6H_{5/2} \rightarrow {}^4F_{7/2}$, is the most intense confirming that these glasses can be effectively excited by UV light-emitting diodes [26]. The wavelength 404 nm can be used as the excitation wavelength for recording emission spectra at different wavelengths. The intensity of all the peaks increases with increase in Sm^{3+} ion concentration reaches maximum for 0.5 mol% and then decreases.

3.4.2 *Emission spectra*

The PL emission spectra for the prepared glasses are recorded at 404 nm excitation wavelength (Fig. 8). The emission spectra for all the concentrations have three peaks at 562 nm, 599 nm, and 646 nm corresponding to transitions $^4G_{5/2} \rightarrow {}^6H_{5/2}$, $^4G_{5/2} \rightarrow {}^6H_{7/2}$, and $^4G_{5/2} \rightarrow {}^6H_{9/2}$. These emissions lie in the region of yellow, orange, and reddish orange. The position

of maxima for these emission bands does not change because of the strong shielding of *4f* electrons by 5 s and 5p electrons. As the emitted radiations lie in visible regions of the electromagnetic spectrum, Sm^{3+} ions-doped glasses can be used in color displays, photonic applications, and medical diagnostics applications [1, 2]. The emission $^4G_{5/2} \rightarrow {}^6H_{7/2}$ at 599 nm is exceedingly intensified due to f–f transitions in Sm^{3+} ions. This transition has both magnetic dipole as well as electric dipole character. The transition $^4G_{5/2} \rightarrow {}^6H_{5/2}$ (562 nm) has a purely magnetic dipole character whereas $^4G_{5/2} \rightarrow {}^6H_{9/2}$ (646 nm) has a purely electric dipole character. The emission intensity increases as the concentration of Sm^{3+} ions increases up to 0.5 mol% and thereafter decreases. The decrease in intensity beyond 0.5 mol% is because of concentration quenching. Concentration quenching occurs because of the decrease in Sm–Sm interionic distance and Sm and host defects. At lower concentrations of Sm^{3+} ions, samarium coordinates with NBOs whereas at higher concentrations, it coordinates with bridging ones resulting in decrease in interaction. This causes energy transfers in the form of non-radiative decay, multiphonon relaxation, etc. These energy transfers force the donor and acceptor ions to attain metastable state from where they are de-excited and reach to ground state by non-radiative decay [23, 24].

Figure 9 shows the mechanism of absorption, excitation, and emission. Due to the small energy difference between $^4D_{3/2}$, $^6P_{7/2}$, $^4F_{7/2}$, $^6H_{5/2}$, $^4M_{19/2}$, $^4G_{9/2}$, $^4I_{13/2}$, $^4M_{15/2}$, $^4G_{7/2}$, $^4F_{3/2}$, and $^4G_{5/2}$, the excited Sm^{3+} ion relax at $^4G_{5/2}$ through non-radiative decay which causes population inversion in $^4G_{5/2}$ level. Hence, $^4G_{5/2}$ is a metastable state. Many factors, including glass composition, glass structure, OH content, and energy transfer rates, affect the $^4G_{5/2}$ state's extended longevity. Depopulation of excited Sm^{3+} ion from $^4G_{5/2}$ level to $^6H_{5/2}$, $^6H_{7/2}$, and $^6H_{9/2}$ results in laser emission of greenish-yellow, reddish-orange, and red radiations at wavelength 562, 599, and 646 nm. The quenching mechanism can be explained by resonance energy transfer and cross-relaxation channels. These channels were represented by the Dexter theory [43]. According to this theory, the energy difference between absorption levels must be equal to the energy difference between emission levels called absorption channels and emission channels, respectively, as given.

AT_1: $^6H_{5/2} \rightarrow {}^6F_{7/2}$ ET_1: $^4G_{5/2} \rightarrow {}^6F_{9/2}$,
AT_2: $^6H_{5/2} \rightarrow {}^6F_{9/2}$ ET_1: $^4G_{5/2} \rightarrow {}^6F_{7/2}$,
AT_3: $^6H_{5/2} \rightarrow {}^6F_{11/2}$ ET_1: $^4G_{5/2} \rightarrow {}^6F_{5/2}$.

The equivalence in energy gives information on the energy migration generated by resonance energy transfer between excited and unexcited states of Sm^{3+} ions, which is shown in Fig. 9.

3.4.3 R/O ratio

The covalent/ionic nature between the samarium ions and the surrounding environment can be

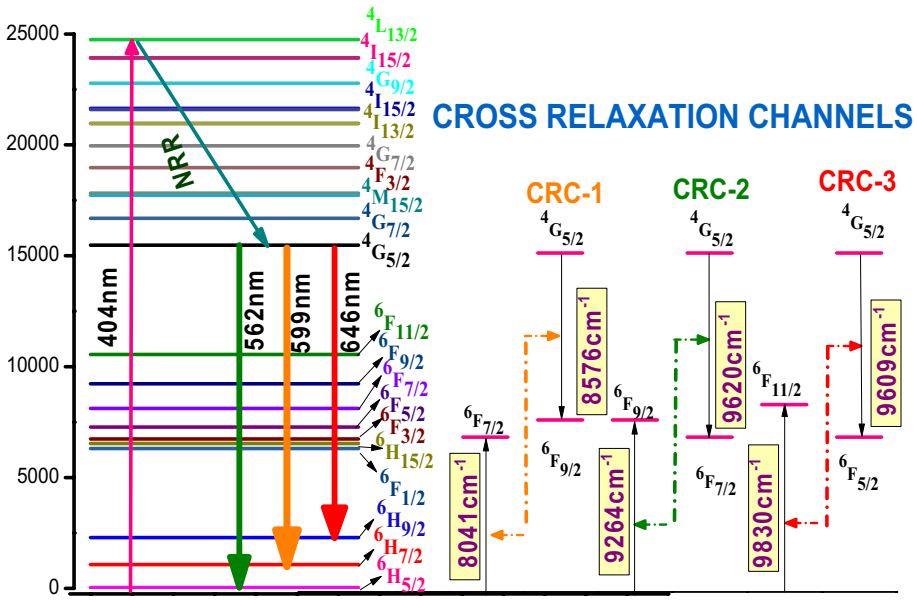

Fig. 9 PL emission and energy transfer mechanism through non-radiative relaxation and cross-relaxation channels of Sm^{3+}-doped BiSFB glasses

determined by the R/O ratio. This R/O ratio, called intensity ratio, is the ratio of electric dipole (ED) transition $^4G_{5/2} \rightarrow {}^6H_{9/2}$ at 646 nm and magnetic dipole (MD) transitions $^4G_{5/2} \rightarrow {}^6H_{5/2}$ at 562 nm. This ratio can be evaluated as follows:

$$\frac{R}{O} = \int \frac{I(\lambda)d\lambda for\ ED\ transition\ at\ 646nm}{I(\lambda)d\lambda\ for\ MD\ transition\ at\ 562nm}.$$

Greater intensity of $^4G_{5/2} \rightarrow {}^6H_{9/2}$(646 nm) than $^4G_{5/2} \rightarrow {}^6H_{5/2}$ (562 nm) indicates the greater asymmetrical environment of Sm^{3+} ions in the host matrix. The BiSFBSm05 glass has the highest R/O value indicating that Sm^{3+} ions have less symmetry and more Sm–O covalence [23]. The same is confirmed by the bonding parameter.

3.4.4 Radiative parameter analysis

The radiative parameters such as transition probability (A_R), total radiative transition rates (A_τ), and branching ratio (β_R) for the prepared glasses are calculated by using differential equations for emission spectra [42] and are given in Table 6. The other protruding parameters such as effective emission bandwidths ($\Delta\lambda_{eff}$), experimental branching ratio (β_{exp}), and stimulated emission cross sections (σ_{se}) in addition with gain bandwidth (σ_{se} x $\Delta\lambda_P$), and emission peak wavelength (λp) are evaluated by associating JO parameters and emission spectral data using equations available in the literature [21]. The branching ratio plays a crucial role for the construction of good lasing materials. It measures the probability of a particular transition as stimulated emission and is calculated by

Table 6 Effective band width ($\Delta\lambda_p$) (nm), Branching ratio (β_R,β_{exp}), Radiative transition probability (s^{-1}), radiative life time (τ_R) (μs), stimulated emission cross section ($\sigma_{se}\times10^{-22}$) ($cm^2$), gain bandwidth ($\sigma_{se}\times\Delta\lambda\times10^{-28}cm^3$), and optical gain ($\sigma_{se}\times\tau_R$) ($cm^2s$) for the prominent emission transitions of Sm^{3+}-doped BiSFB glasses

Parameter	BiSFBSm01	BiSFBSm05	BiSFBSm10	BiSFBSm15	BiSFBSm20	BiSFBSm25
$^4G_{5/2} \rightarrow {}^6H_{5/2}$, 564 nm						
$\Delta\lambda_p$	11.01	10.57	10.81	10.49	10.38	12.12
β_R	0.173	0.075	0.076	0.085	0.094	0.107
β_{exp}	0.119	0.174	0.122	0.125	0.094	0.155
A_R	33.29	41.03	40.65	37.75	36.97	35.59
τ_R	5185	1828	1882	2273	2543	3014
σ_{se}	1.043	1.340	1.294	1.240	1.226	1.010
$\sigma_{se}\times\Delta\lambda_p$	1.148	1.414	1.401	1.300	1.273	1.225
$\sigma_{se}\times\tau_R$	5.411	2.444	2.437	2.817	3.119	3.046
$^4G_{5/2} \rightarrow {}^6H_{7/2}$, 599 nm						
$\Delta\lambda_p$	11.45	14.44	14.73	14.74	14.59	15.38
β_R	0.395	0.443	0.444	0.466	0.476	0.451
β_{exp}	0.591	0.652	0.580	0.574	0.622	0.558
A_R	76.34	242.3	235.9	205.2	187.3	149.9
τ_R	5185	1828	1882	2273	2543	3014
σ_{se}	2.925	7.360	7.017	6.099	5.623	4.269
$\sigma_{se}\times\Delta\lambda_p$	3.349	10.63	10.34	8.994	8.205	6.568
$\sigma_{se}\times\tau_R$	15.16	13.45	13.20	13.86	14.29	12.87
$^4G_{5/2} \rightarrow {}^6H_{9/2}$, 646 nm						
$\Delta\lambda_p$	14.01	15.58	14.84	14.84	14.12	15.35
β_R	0.201	0.270	0.267	0.236	0.217	0.225
β_{exp}	0.289	0.176	0.297	0.300	0.282	0.286
A_R	38.91	147.9	142.2	104.2	85.54	85.54
τ_R	5185	1828	1882	2273	2543	3014
σ_{se}	1.648	5.631	5.680	4.159	3.591	3.301
$\sigma_{se}\times\Delta\lambda_p$	2.309	8.775	8.435	6.176	5.071	5.068
$\sigma_{se}\times\tau_R$	8.545	10.29	9.454	9.454	9.132	9.949

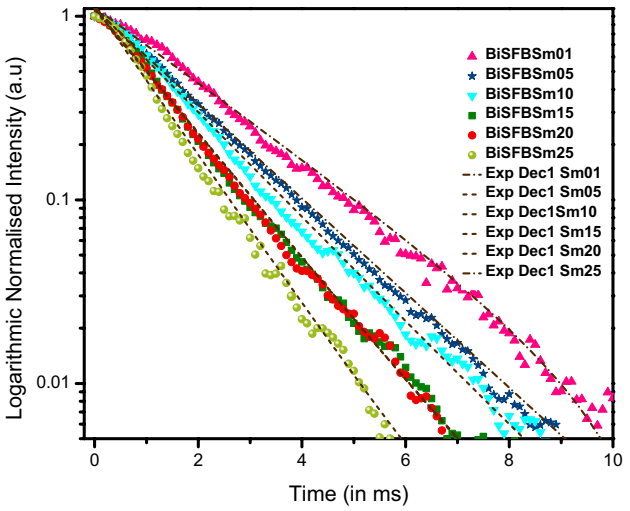

Fig. 10 Decay curves of Sm^{3+}-doped BiSFB glasses

$$\beta_R = \frac{A_R}{A_T}.$$

For the prepared Sm^{3+} ions-doped BiSFB glasses, β_R is higher for the transition at 599 nm indicating it to be good lasing medium as well as the laser output (Table 6).

The stimulated emission cross section was evaluated by using the following formula:

$$\sigma_{se} = \frac{\lambda_P^4}{8\pi c n^2 \Delta\lambda_P} A_R.$$

Here, λ_p is the peak wavelength, $\Delta\lambda_p$ is the full width at half maxima, n is the refractive index, and A_R is the radiative lifetime. A notable rise in the values of σ_{se} prompted the development of low threshold and high gain laser techniques that can be used to produce continuous wave (CW) lasers [1–3]. For the prepared glasses, all the radiative parameters for each transition are given in Table 6. Clearly, $\sigma_{se,}$ (σ_{se} x $\Delta\lambda_P$), and (σ_{se} x τ_R) are highest for the transition $^4G_{5/2} \rightarrow {}^6H_{7/2}$ for BiSFBSm05 glass.

3.5 Decay analysis

Luminescence decay curves for different concentrations of Sm^{3+}ions for level $^4G_{5/2}$ under excitation wavelength 404 nm and emission at 599 nm are recorded at room temperature (Fig. 10). These decay curves give knowledge about concentration quenching mechanism and experimental lifetimes of Sm^{3+}ions in the host matrix [25]. These decay curves exhibit single-exponential behavior for all the concentrations. The general formula for fitting is

$$I = I_0 \exp(-t/\tau).$$

Table 7 Total transition probability (A_T) (s^{-1}), Radiative life time (τ_R) (μs), experimental life time (τ_{exp}) (μs), Non -radiative transition probability (W_{NR}) (s^{-1}), and quantum efficiency (η) (%) of Sm^{3+}-doped BiSFB glasses

Glass	A_T	τ_R	τ_{exp}	W_{NR}	η(%)
BiSFBSm01	192.8	5185	2078	288	40
BiSFBSm05	546.9	1828	1685	46	92
BiSFBSm10	531.2	1882	1521	125	80
BiSFBSm15	439.8	2273	1287	336	56
BiSFBSm20	393.2	2543	1275	390	51
BiSFBSm25	331.8	3014	1069	603	35

The lifetime for single-exponential decay can be determined from the slope of a ln I(t) against t plot. I_0 is the intensity at $t = 0$, I is the intensity at a time 't', and τ is the luminescent lifetime for decay, respectively. The lifetime of an excited state includes radiative as well as non-radiative transitions. The discrepancy between the observed excited state lifetime and the overall radiative lifetime is attributed to the presence of non-radiative transitions. Non-radiative decay can occur due to multiphonon relaxation and cross-relaxation channels (Fig. 9). But due to the enormous energy gap (6500 cm^{-1}) between $^4G_{5/2}$ and its following energy level $^6F_{9/2}$, multiphonon relaxation cannot be accomplished [24].

The observed luminescence decay can be used to calculate the lifespan of levels that exhibit significant luminescence. The lifetimes of luminescence as well as a total lifetime for each concentration are listed in Table 7. The decrease in a lifetime with an increase in the concentration of Sm^{3+}ions is due to increase in Sm^{3+}—Sm^{3+} interaction which results in decrease in distance among RE ions centers. This decrease causes the transfer of excitation energy from the donor to the acceptor. The measured lifetimes are in the order of milliseconds which is one of the characteristics of f → f transition of Sm^{3+}ions [5]. The deviation between the experimental and radiative lifetimes (Table 7) arises due to the partial inability of the JO theory to calculate radiative properties, and hence, this theory overestimates the radiative lifetime. In addition, the presence

of multiple Sm^{3+} sites in the matrix may crash the $^4G_{5/2}$ level emission, resulting in experimental lifetimes that are lower than expected. The non-radiative decay transition rates are evaluated using formula and are listed in Table 7.

$$W_{NR} = \frac{1}{\tau_{\exp}} - \frac{1}{\tau_R}.$$

The quantum efficiency is a parameter which measures the applicability of the given glasses as a lasing material. Quantum efficiency is the ratio of the measured lifetime to the radiative lifetime and is given by the formula:

$$\eta = \frac{\tau_{\exp}}{\tau_R} \times 100.$$

Radiative emission, emission cross section, and RE ion concentration can cause the change in quantum efficiency [14]. The evaluated quantum efficiencies along with other parameters for the prepared glasses are given in Table 7. Quantum efficiency increases from 0.1 to 0.5 mol% concentration of Sm^{3+} ions and decreases thereafter. Concentration quenching causes the decrease in quantum efficiency. This is because when concentration of Sm^{3+} ions increase beyond 0.5 mol%, then interaction between Sm^{3+}-Sm^{3+} ions increases. Due to this, transfer of energy becomes more significant through cross-relaxation channels and non-radiative transitions. Therefore, maximum efficiency is observed for BiSFBSm25 glass.

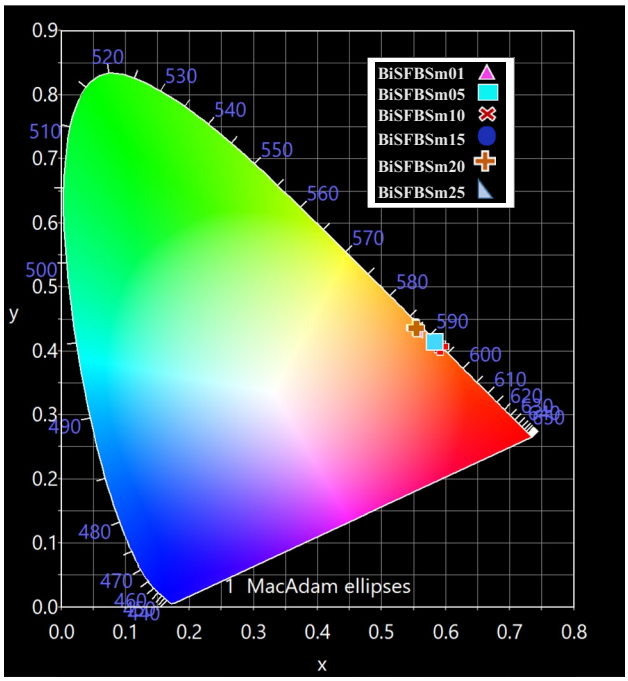

Fig. 11 CIE chromaticity coordinates of Sm^{3+} ions in BiSFB glasses

[24, 26]. For the prepared glasses, color coordinates are evaluated and are given in Table 8. The graphic depicts the chromaticity apparent to the naked eye. The monochromatic light sources are represented by the diagram's periphery. The center (0.33, 0.33) represents the equal point energy and white light. The coordinates are located in the orange and red region in chromaticity diagram for the prepared glasses. Color purity is calculated using formula:

$$\text{Color Purity} = \frac{\text{Distancebetween coordinates of the glass and equal point energy}}{\text{Distance between coordinates of equal point energy and dominant wavelength}}.$$

3.6 Color chromaticity

The chromaticity coordinates of the prepared glasses computed by the CIE (Commission Internationale de l'Eclairage, International Commission on Illumination) are displayed in Fig. 11. Based on the values of the primary colors (Red, Green, and Blue) included in them, the chromaticity diagram depicts the spectrum hues and their blends. Hue and saturation are the two characteristics that make up chromaticity. Chrominance is what we obtain when we combine color and saturation

Here, dominant wavelength corresponds to the line joining equal point energy and the coordinates of the glass intersecting the periphery of CIE diagram. CIE coordinates along with color purity and Color-correlated temperature (CCT) are represented in Table 8. Color purity is maximum for BiSFBSm05. Therefore, BiSFBSm05 glass is strong contendor for orange-red emission [44]. The comparative studies of stimulated emission cross section, branching ratio, and quantum efficiency of the prepared glasses with other reported values are listed in Table 9. Relatively high values of

Table 8 CIE color coordinates, dominant wavelength (nm), color purity (%), intensity ratio (R/O) Correlated Color temperature (K) of Sm^{3+} ions-doped BiSFB glasses

Glass	Color coordinates		Dominant wavelength	Color purity	R/O	CCT
	X	Y				
BiSFBSm01	0.587	0.409	600	89	1.82	1571
BiSFBSm05	0.592	0.406	599	92	2.03	1529
BiSFBSm10	0.583	0.413	601	86	1.24	1611
BiSFBSm15	0.584	0.412	601	87	1.92	1614
BiSFBSm20	0.552	0.436	602	80	1.80	1933
BiSFBSm25	0.554	0.434	602	80	1.78	1909

these parameters for BiSFBSm05 glass could make it to be the good lasing source in visible reddish-orange region.

3.7 Dielectric properties

3.7.1 Dielectric & dielectric loss constants

Through the impedance data over a frequency range of 1 Hz–1 kHz, dielectric constant and dielectric loss are calculated for the prepared glasses using the formulae [45]

$$\varepsilon' = \frac{t}{\omega A \varepsilon_0}\left[\frac{Z''^2}{Z'^2 + Z''^2}\right],$$

$$\varepsilon'' = \frac{t}{\omega A \varepsilon_0}\left[\frac{Z'^2}{Z'^2 + Z''^2}\right].$$

Here ε_0 is the permittivity in vacuum, t is the thickness of the sample, ω is the frequency of the input signal, and A is area of cross section of the sample.

The frequency variation of the real portion of the dielectric constant (ε') for all the prepared glasses is shown in Fig. 12. A high-frequency plateau area and a low-frequency dispersion zone can be found in the spectra of ε'. The lack of any maxima throughout the whole frequency range demonstrates that charge carriers can travel freely from sites with lower energy to sites with greater energy. Due to charge buildup at low-frequency sites that results in net polarization, charges are prevented on surface electrodes [46]. The dielectric constant (ε') rises as a result of this polarization of the surface charge. At high frequency, electric field changes directions so quickly that charge carriers are not given enough time to develop a mass at surfaces. No charge accumulation at the interface takes place due to periodic reversal of the ac fields. Therefore, the frequency of the charge carrier causes the value of ε' to decrease [42, 47]. Similar is the case for dielectric loss constant (Fig. 13).

The dielectric constant and dielectric loss value increase with increase in Sm^{3+} ion concentration. It may be attributed to the decrease in the degree of disorder of the glass network when the concentration of Sm^{3+} ion increases. It indicates that Sm^{3+} takes part in the network-forming positions. The decrease of dielectric constants with concentration of Sm^{3+} ions proposes a decrement in the freedom of dipoles to align in the field direction, caused by the increase in the rigidity of the glass network. This causes decrease in electronic contribution to the total polarizability [4, 45]. Thus, the dielectric constant and dielectric loss vary with frequency.

3.7.2 Electrical conductivity

AC conductivity of the prepared glasses is calculated over a range of frequency from 1 Hz to 1 kHz using the relation [43]:

$$\sigma_{ac} = \left(\frac{t}{a}\right)\frac{Z'^2}{Z'^2 + Z''^2}.$$

Here, Z′ and Z″ are the real and imaginary impedance, t is the thickness, and a is area of glass the glass sample. The frequency dependence of the ac conductivity is shown in Fig. 14. Clearly, conductivity increases with increase in frequency. At low frequency, an increasing amount of charge builds up at the electrode–electrolyte interface, which causes a decrease in conductivity.

The electrical conductivity of RE ion-doped glass depends on the amount of RE ion, mass, and state of the RE ions inside the glass network. It also depends on whether they act as network modifiers or as

Table 9 Comparative studies of Stimulated emission cross section ($\sigma_{se} \times 10^{-22}$) ($cm^2$), branching ratio($\beta_{exp}$), quantum efficiency($\eta$), non-radiative transition probability (W_{NR}) (s^{-1}), CIE color coordinates (X,Y) for transition $^4G_{5/2} \rightarrow {}^6H_{7/2}$ of Sm^{3+}-doped BiSFB glasses

Glass	σ_{se}	β_{exp}	η	W_{NR}	X	Y	Reference
BiSFBSm01	2.925	0.591	40	288	0.587	0.409	[Present work]
BiSFBSm05	7.360	0.652	92	46	0.592	0.406	[Present work]
BiSFBSm10	7.017	0.580	80	125	0.583	0.413	[Present work]
BiSFBSm15	6.099	0.574	56	336	0.584	0.412	[Present work]
BiSFBSm20	5.623	0.622	51	390	0.552	0.436	[Present work]
BiSFBSm25	4.269	0.558	35	603	0.554	0.434	[Present work]
Glass C	13.20	0.59	85	199	0.556	0.420	[14]
BNNF:Si	1.004	0.600	63	213	0.598	0.401	[25]
BNNF:SK	7.710	0.610	49	262	0.585	0.414	[25]
BaPbAlFBSm1.0	14.06	0.515	84	370	0.519	0.467	[23]
AEBTSm1.0	1.459	0.578	83	152	0.543	0.449	[24]
OFBSm10	14.65	0.520	83	69	0.594	0.406	[26]
OCBTSm1.0	3.661	0.441	91	127	0.600	0.400	[27]
GSm5	8.000	0.540	85	–	0.594	0.396	[40]
CNFB0.5S	8.383	0.525	41	–	0.593	0.406	[41]

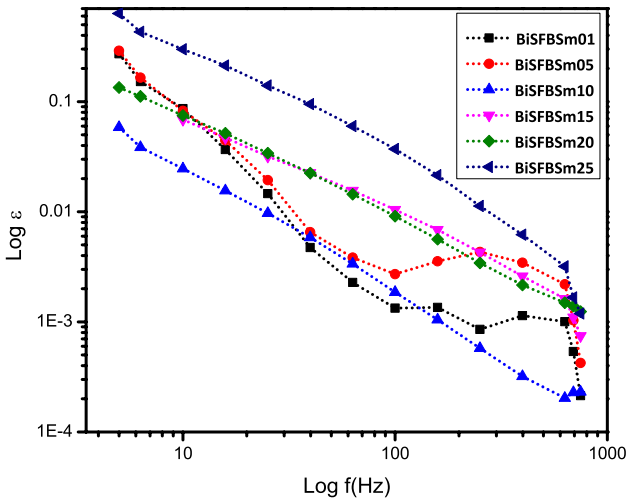

Fig. 12 Variation of Dielectric Constant with frequency for Sm^{3+}-doped BiSFB glasses

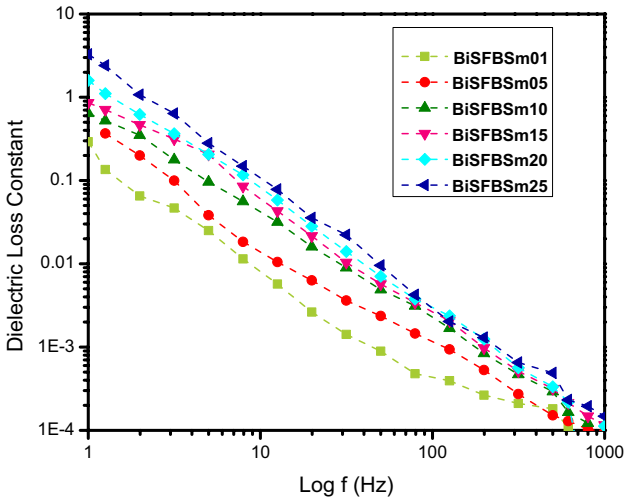

Fig. 13 Variation of Dielectric Loss Constant with frequency for Sm^{3+}-doped BiSFB glasses

quasi-molecular complexes. When RE ions are present in the glass network, NBOs are altered and enhanced. As a result, the Sm^{3+} ion addition weakens the glass network and creates pathways for free ion migration. The frequency dependence of ac conductivity in glass can be explained by correlated-hopping model (CBH) due to barrier hopping of bipolarons. Electrons are hopping over the coulombic barrier between charged defects D + and D- which boosts space charge polarization and enhances conductivity [46]. Therefore, ac conductivity increases with increase in Sm^{3+} ion concentration. Hence, conductivity of BiSFBSm25 glass is maximum.

3.7.3 Impedance

The Nyquist plot for the prepared glasses shows a recessed semicircle followed by a straight line (Fig. 15). The Nyquist plot in every composition has a single semicircular arc indicating that Debye relaxation is present in the prepared glasses [48, 49]. The intersection of the depressed semicircle with the inclined straight line at the real axis yields the bulk resistance for Sm^{3+} ions-doped

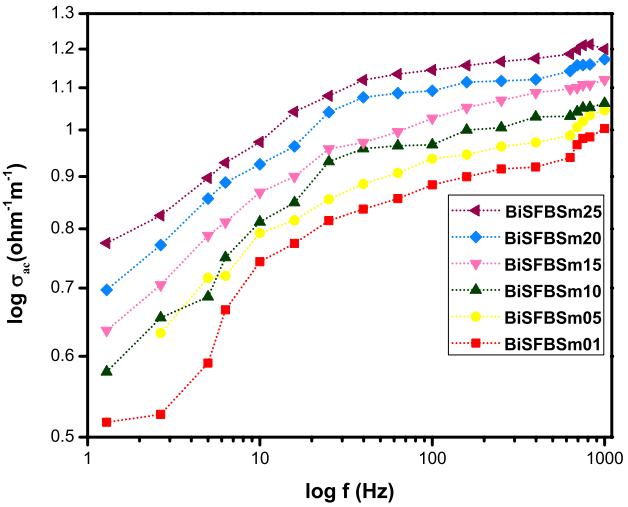

Fig. 14 Variation of electrical conductivity with frequency for Sm^{3+}-doped BiSFB glasses

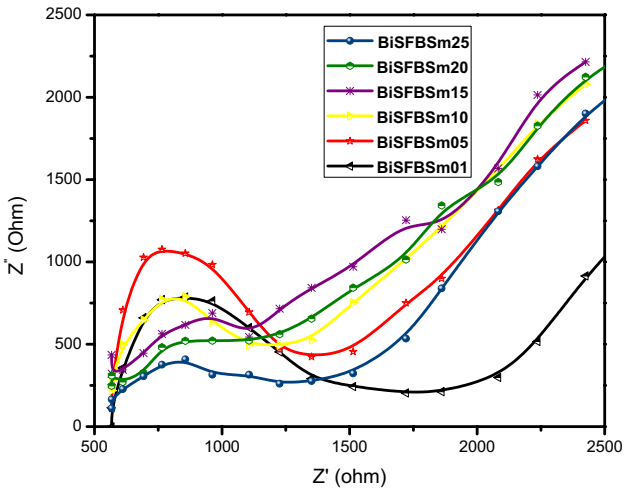

Fig. 15 Variation of Z″ with Z′ for Sm^{3+}-doped BiSFB glasses

BiSFB glass. As a result of changes in the electrical properties of the active elements in the host glass, the semicircle's diameter decrease with increase in Sm^{3+} ion concentration. This diameter measures the charge transfer resistance. The electrical resistance of BiSFBSm25 glass is the lowest since the diameter of semicircle is the smallest. The electrical conductivity characteristic further substantiates this. [50, 51].

3.7.4 DC conductivity

The dc resistance for prepared glass samples is calculated from the Nyquist plot. The intersection of the semicircle with the real axis at low frequency determines the bulk dc resistance. The intercept shifts substantially towards the origin with increasing concentration of Sm^{3+} ion [52]. It indicates the decrease in resistance. Using dimensions of glass samples, dc conductivity is calculated by the formula:

$$\sigma_{dc} = \frac{1}{R}\left(\frac{L}{A}\right).$$

Here, R is the resistance, L is thickness, and A is area of the glass. This increase in conductivity with increasing Sm^{3+} ion concentration may be due to the change in the glass structure. Addition of samarium ions changes the chemical bonding in the glass structure. This increases the NBOs in the prepared glasses. Moreover, increase in mobile ion concentration causes decrease in the strength of glass structure. This causes increase in dc conductivity. Maximum conductivity is observed for BiSFBSm25 glass making it to be good for solid-state ionic devices [37, 53, 54].

4 Conclusions

This study examined the impact of samarium concentration on several optical and electrical characteristics of glass samples. The glasses are synthesized via melt quenching method. XRD spectra confirm the amorphous nature of the prepared glasses. FTIR spectra provide details on the various functional groups present in an undoped and Sm^{3+} ions-doped BiSFB glasses. JO parameters follow the trend $\Omega_4 > \Omega_6 > \Omega_2$ indicating ionic nature dominance in the prepared glasses, and maximum values are for BiSFBSm05 glass. Three emission bands at 562 nm, 599 nm, and 646 nm are detected in the PL spectra among all the glasses, corresponding to transitions $^4G_{5/2} \rightarrow {}^6H_{5/2,7/2,9/2}$ giving yellowish red, orange-reddish, and red lasers. The efficiency of turning excitation energy into light is revealed by decay spectra through luminescence lifetimes. Relatively high value of R/O intensity ratio (2.01) for BiSFBSm05 glass than other prepared glasses suggest good optical eminence for solid-state lighting and LCD display. Following the computation of the luminescence characteristics using emission spectra, the outcomes are summed up as BiSFBSm05 glass has highest emission cross section (7.360) and branching ratio (0.652) among the other prepared glasses. CIE coordinates confirms the utility of 0.5 mol% of Sm^{3+}-doped BiSFB glass for orange-red lasers and

optoelectronic devices. Electrical measurements indicated that both dielectric constant and dielectric loss exhibited frequency dispersion at low frequencies, with lower values at higher frequencies. Impedance analysis provided insights into the bulk direct current (dc) conductivity. Notably, BiSFBSm25 glass displayed the highest ac conductivity, highlighting its potential for use in solid-state ionic devices. In further research, we can examine the prepared glasses to be co-doped with additional rare-earth ions for their electrical and luminescent characteristics under temperature change.

Acknowledgements

The authors from Koneru Lakshmaiah Education Foundation (KLEF) are grateful to the management of KLEF. The author Sk. Mahamuda and K.Swapna are also thankful to DST & DST-SERB for sanctioning FIST (SR/FST/PS-1/2018/35), PURSE project (SR/PURSE/2023/196), and CRG Project (CRG/2022/003549).

Author contribution

All authors contributed to this manuscript, study conception, and design. The first draft of the manuscript is written by Gunjan Mahajan under the guidance of Dr. M.V.V.K Srinivas Prasad and Dr. K. Swapna. All authors K.Seshulatha, M. Venkateswarulu, Sk. Mahamuda, and A. S. Rao are worked for the Resources, Writing—Editing and Review of the manuscript. All authors have read and approved the final manuscript.

Funding

"The authors declare that no funds, grants, or other support were received during the preparation of this manuscript."

Data availability

The data that have been used are confidential.

Declarations

Competing interest The authors declare that they have no known competing financial interests or personal relationships that could have appeared to influence the work reported in this paper.

References

1. R.A. Talewar, Sk. Mahamuda, K. Swapna, M. Venkateswarulu, A.S. Rao, Mater. Res. Bull. **105**, 45–54 (2018)
2. R.M. Ahmed, T.A. Taha, F.M. Ezz-Eldin, J. Mater. Sci. Mater. Electron. **32**, 28919–28934 (2021)
3. M.I. Sayyed, M.A. Abdo, H. Elhosiny Ali, H.A. Ahmed, M.S. Sadeq, Optik. **273**, 170738 (2023)
4. S. Thomas, R. George, M. Rathaiah, V. Venkatramu, S.N. Rasool, N.V. Unnikrishnan, Phys. B: Condens. Matter. **431**, 69–74 (2013)
5. V.R. Murty, M. Venkateswarulu, K. Swapna, Sk. Mahamuda, P.R. Rani, A.S. Rao, Radiat. Phys. Chem. **190**, 109806 (2022)
6. J. Kaewkhao, K. Boonin, P. Yasaka, H.J. Kim, Mater. Res. Bull. **71**, 37–41 (2015)
7. Y.S. Rammah, I.O. Olarinoye, F.I. El-Agawany, A. El-Adawy, A. Gamal, E. Yousef, Ceram. Int. **46**, 25440–25452 (2020)
8. H.O. Tekin, S.A. Issa, E. Kavaz, E.A. Guclu, Mater. Res. Expr. **6**(11), 115212 (2019)
9. A. Asirvadam, V.R. Kumar, B.N.K. Reddy, G.N. Raju, P.S. Prasad, Optik **264**, 169405 (2022)
10. M. Nalin, M. Poulain, M. Poulain, S.J. Ribeiro, Y. Messaddeq, Antimony oxide based glasses. J. Non-Cryst. Solid. **284**, 110–116 (2001)
11. H. Doweidara, K. El-Egilia, R. Ramadanb, J. Vib. spectros. **102**, 24–30 (2019)
12. N.S. Rao, M. Rajesh, K. Prasad, G.R. Reddy, B.D.P. Raju, S. Dhanapandian, Lumin. **35**, 721–727 (2020)
13. D.R.N. Brito, M.N. Queiroz, M.J. Barboza, A. Steimacher, F. Pedrochi, Opt. Mater. **64**, 114–120 (2017)
14. N. Deopa, A.S. Rao, A. Choudhary, S. Saini, A. Navhal, M. Jayasimhadri, D. Haranath, G.V. Prakash, Mater. Res. Bull. **100**, 206–212 (2018)
15. A.V. Deepa, M. Priya, S. Suresh, J. Sci. Res. Essays **5**, 57–63 (2016)
16. A.A. Ali, M.H. Shaaban, Bull. Mater. Sci. **34**, 491–498 (2011)
17. A. Ghosh, S. Sen, J. Phys. Condens. Matter **11**, 1529 (1999)

18. I.M.E. Radaf, A.S. Hassanien, Physica B Condens. Matter. **659**, 414867 (2023)
19. S. Mandal, A. Ghosh, J. Phys. Condens. Matter **8**, 829 (1996)
20. A. Dutta, A. Ghosh, J. Non-Cryst, Solids. **353**, 1333 (2007)
21. N.N. Al-Refaey, A.A. El-Maboud, A. Abdelghany, I. Kashif, J. Mater. Sci. Mater. Electron. **35**(25), 1686 (2024)
22. V.M. Krishna, Sk. Mahamuda, P. Sailaja, K. Swapna, M. Venkateswarulu, C.B. Devi, A.S. Rao, J. Non-Cryst. Solids **590**, 121671 (2022)
23. P.R. Rani, M. Venkateswarlu, Sk. Mahamuda, K. Swapna, N. Deopa, A.S. Rao, G.V. Prakash, Mater. Res. Bull. **110**, 159–168 (2019)
24. K.S. Reddy, K. Swapna, Sk. Mahamuda, M. Venkateswarulu, M.S. Prasad, A.S. Rao, G.V. Prakash, Opt. Mater. **79**, 21–32 (2018)
25. A.J. D'Silva, K. Maheshvaran, A. Rayappan, J. Mater. Sci. Mater. Electron. **35**, 1630 (2024)
26. Sk. Mahamuda, K. Swapna, M. Venkateswarulu, A.S. Rao, S. Shakya, G.V. Prakash, J. Lumin. **154**, 410–424 (2014)
27. S.N. Rasool, S. Shabeena, C.R. Kesavulu, S. Babu, J. Mater. Sci. Mater. Electron. **33**(24), 19263–19271 (2022)
28. W.T. Carnall, P.R. Fields, K. Rajnak, J. Chem. Phys. **49**, 4424 (1968)
29. P. Sailaja, Sk. Mahamuda, K. Swapna, M. Venkateswarulu, A.S. Rao, Mater. Sci. Eng. B **270**, 115198 (2021)
30. J. Koen Binnemans, Coord. Chem. Rev. **295**, 1–45 (2015)
31. C.K. Jorgensen, B.R. Judd, J. Mol. Phys. **8**, 281–290 (1964)
32. P. Kaur, D. Singh, T. Singh, J. Non-Crys, Solids **452**, 87–92 (2016)
33. A.S. Hassanien, A.A. Akl, I.E. Redaf, Emerg. Mater. **6**(3), 943–964 (2023)
34. A. El-Denglawey, K.A. Aly, A. Dahshan, A.S. Hassanien, ECS J. Solid State Sci. Technol. **11**, 044006 (2022)
35. A.S. Hassanien, I. Sharma, P. Sharma, Phys. Scr. **98**, 045911 (2023)
36. S.L. Meena, Appl. Phys. A **130**, 404 (2024)
37. A.S. Hassanien, J. Non-Cryst. Solids **586**, 121563 (2022)
38. B.R. Judd, J. Phys. Rev. **127**, 750–761 (1962)
39. G.S. Ofelt, J. Chem. Phys. **37**, 511–520 (1962)
40. G. Chandana, C.N. Rao, P.V. Rao, M.J. Al-Musawi, K. Samatha, G.G. Dhar, Optik **208**, 163909 (2020)
41. M. Mariyappan, S. Arunkumar, K. Marimuthu, Lumin. **196**, 151–160 (2018)
42. M. Mariyappan, S. Arunkumar, K. Marimuthu, Mol. Struct. **15**, 30345–30348 (2015)
43. D.L. Dexter, J. Chem. Phy. **21**, 836 (1953)
44. S. Mohan, S. Kaur, D.P. Singh, P. Kaur, Opt. Mater. **73**, 223–233 (2017)
45. S. Jayaseelan, P. Muralidharan, M. Venkateswarlu, N. Satyanarayana, J. Mater. Chem. Phys. **87**, 370–377 (2004)
46. A.S. Hassanien, J. Alloys Compd. **671**, 566–578 (2016)
47. D. Amer, K. Swapna, J.S. Kumar, Sk. Mahamuda, M. Venkateswarulu, P. Sruthi, A.S. Rao, Mater. Res. Bull. **146**, 111597 (2022)
48. V.K. Kutta, N.K. Kuttari, D.P. Dutta, M.F.M. Sabri, B.R. Ravuri, Energy Fuels **36**, 6492–6501 (2022)
49. A.S. Hassanien, I. Sharma, J. Non-Cryst. Solids **630**, 122887 (2024)
50. M. Malik, S. Dagar, A. Hooda, A. Aggarwal, S. Khasa, Solid State Sci. **110**, 106491 (2020)
51. G. Mahajan, M.V.V.K.Srinivas Prasad, K. Swapna, Sk. Mahamuda, M. Venkateswarulu, G.G. Dhar, A.S. Rao, Radiat. Phys. Chem. **221**, 111708 (2024)
52. A. Sarkar, S. Sarkar, S. Mitr, Mater. Chem. A. **5**, 24929–24941 (2017)
53. R.V. Barde, S.A. Waghuley, J. Non-Cryst. Solids **376**, 117–125 (2013)
54. A.S.Hassanien, I.Sharma,Phys, Physica B, 622, 41330 (2021).

Publisher's Note Springer Nature remains neutral with regard to jurisdictional claims in published maps and institutional affiliations.

Springer Nature or its licensor (e.g. a society or other partner) holds exclusive rights to this article under a publishing agreement with the author(s) or other rightsholder(s); author self-archiving of the accepted manuscript version of this article is solely governed by the terms of such publishing agreement and applicable law.

International Journal of Future Engineering Innovations

Zurb Base Foundation: A Study Paper

JP Kesari
Formerly Delhi College of Engineering, Delhi Technological University, Bawana Road, Delhi, India

* Corresponding Author: **JP Kesari**

Article Info

ISSN (online): xxxx-xxxx
Volume: 05
Issue: 05
September-October 2024
Received: 06-08-2024
Accepted: 09-09-2024
Page No: 12-14

Keywords: Zurb Bedrock, Zurb Company, foundation

Abstract
Zurb Endowment is a new energy frontend foundation used to design beautiful aware websites. It is an open beginning, interchangeable and a customizable form that holds diversified HTML, Department dealing with customers and JavaScript located devised templates for miscellaneous connect parts to a degree buttons, forms, guiding along route, often over water, a process of reproduction etc. This review paper focuses on an productive reasoning concerning this foundation.

Introduction

The term "Netting Growth" refers to the process of forging uses that everything utilizing WWW. It maybe top-secret into two parts that is.

- **Frontend netting incident**

The customer side of the use is described as frontend netting incident. It is the unspecified the request place the consumer interplay happens. The electronics and foundations secondhand in this place happening are Html, Department dealing with customers, JavaScript, Start operating system, Company, Respond, Bent, Material UI, VueJS, Tailwind Department dealing with customers, Query and many more. Front-end foundations help planners to build their websites surely and fast and therefore humble the happening process [3]. Various foundations have various expert and cons and various extents of business therefore planners can select some foundation as per their needs [2].

- **Backend netting incident**

The Attendant side of the request is described as backend netting happening. This few an use arrange packing, achieve, and directing dossier, gathering administration etc. The sciences and foundations secondhand in this place growth are PHP, Hot beverage made from beans of a tree, Python, Bud.js, Express, Django, Rails, spring etc.

Energetic Textbook Rise Speech

Html is used to delimit the building of a location on the world wide web [4]. Servers or local depository pass location on the world wide web to netting browsers that displays bureaucracy as a central page of web site.

Falling in a rush Style Page

Department dealing with customers is used to style html details to increase the readability and the consumer happening of a site [4]. It is too valuable to supply distinguishing styles to diversified central page of web site though and it still increases the stowing speed of pages by permissive the ".department dealing with customers" file expected cached. It is still valuable for aware netting designs, that way that the content of a site maybe equipped into miscellaneous instruments accompanying various screen judgments.

Base

Zurb Bedrock is an state-of-the-art frontend Department dealing with customers foundation used to evolve beautiful active websites. It is an open- beginning foundation that supports differing law particles, Html and Department dealing with customers parts, conscious gridiron arrangement etc. It was announced in October 2011. It is standard and customizable and amount to diversified SASS style sheets namely used to implements allure miscellaneous parts. It is extravagantly proven on differing instruments and trails a travelling first approach

Benefits of Groundwork

- Utilizing this foundation, we can surely custom-make our site, though allure design before looks excellent and does not demand customization.
- It has a very bendable gridiron structure; we can surely collapse various pillars and humble channels by just adjoining a 'Collapse' class. We can surely build unchanging intensity pillars accompanying very less HTML.
- This foundation supplies a complete atheneum for form validations that longers HTML5 confirmation API. We can further surely build multilingual websites cause this foundation determines a roomy range of words to pick from.
- It further supplies diversified money and aids as support.
- Few basic Department dealing with customers styles are again additional in this place foundation therefore as long as the additional class names goes wrong, or if we want littlest style in our rule, we will able to have or do visualize few belongings outside the need for systematize [1].
- We can too build aware spot outside adjoining classes utilizing this foundation [1].

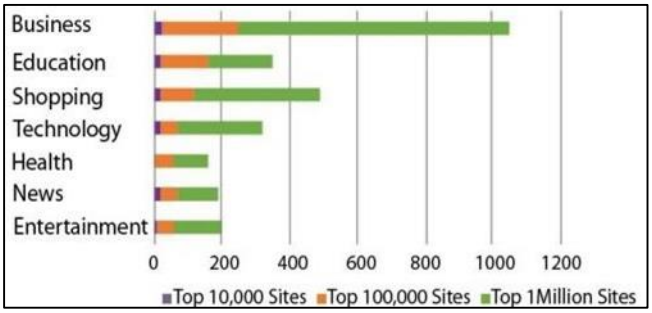

Fig 1: Statistics of websites using Foundation Framework

Organization Television Queries

It uses three television queries place "limited" is secondhand for some screen," medium" is secondhand for screens accompanying a judgment of 640 pixels and more expansive, and "abundant" is secondhand for screen accompanying a determination of 1024 pixels and roomier [7].

We can too change these breakpoints by utilizing the arrangement beneath

Endowment Grids

Gridiron arrangement is a merger of rows and processions that delineates the map of a page. This foundation has a very pliable gridiron arrangement. We can surely place pillars in the middle. We can again establish block grids to surely constitute lines of equal breadth accompanying less html rule.

The "collapse" class maybe used to rewrite processions surely [1]. Allure gridiron scheme can display up-to 12 processions in a page. We can still create our own custom-built gridiron utilizing set of SASS mixins [7].

The elementary gridiron makeup maybe created utilizing the following arrangement-

The class row is used to conceive level pillars, and only lines maybe the next kids of the row div. The lines are formed by designating the number (in range of 1- 12) inside the class. For eg, either the number of lines necessary is 6 before we concede possibility designate the class as "medium-5" [7].

In this place foundation, various inline ingredients in the way that paragraphs, headings, keystrokes, headers etc are delineated accompanying natural and appealing styles. To adjoin content inside a central page of web site we use the <rule> tag. A process of reproduction assistant class is too delineated in this place foundation to regulate the aspects in our site as per our choice.

This foundation further holds prebuilt diversified Department dealing with customers parts to a degree buttons, tables, progress bars, callout panels, sliders, switches, forms etc for our use.

Buttons

Utilizing this foundation we can conceive buttons of various styles, banner, and sizes. All we need commotion search out designate "knob" class to the anchor tag or with the understanding we be going to form changes on the unchanging page before we can again use the knob tag.

Progress Bars

We can conceive appealing progress bars utilizing the ".progress" class and to display allure breadth we have a progress-rhythm class, we can too present various colours to it utilizing the dependent colours classes like achievement, warning, alert etc.

Bedrock Javascript Parts

Groundwork supplies us diversified JavaScript elements in the way that accordions, drop-down, equalizers, modals etc, to form our work fast and smooth.

Tabs

Tabs are a excellent habit to present our content in a compact habit. We can use this service by building upper class utilizing and tag and appointing "tabs" class to the tag attended by appointing dossier-tabs and an id to it. Each tag concede possibility take the class "tabs-title". The ".is-alive" class maybe secondhand following in position or time tabs-title to designate an open ticket. The figure beneath shows the design of tabs factor [5] ("Shenoy, 2016).

Conclusion

Foundation is a useful framework to develop attractive and responsive websites in less time. It has multiple pre-built components that are easily customizable and can make our work easy. With each updates it is becoming more and more developer friendly. Many websites such as dropbox.com, PBS [1], sourceforge.net, bitly.com etc are built using this framework. It also provides multiple free resources and support to the community. Evidently, there are numerous benefits of using this framework, hence it is worth a try.

References

1. Laaziri M, Benmoussa K, Khoulji S, Larbi KM, El Yamami A. Analyzing bootsrap and foundation font-end frameworks: A comparative study. International Journal of Electrical and Computer Engineering (IJECE). 2019;9(1):713-22.
2. Lakshmi DR, Mallika SS. A review on web application testing and its current research directions. International Journal of Electrical and Computer Engineering. 2017;7(4):2132.
3. Cletus WD, Kakandar A, Paul CN. Responsive web design frameworks: A review. International Journal of Scientific Research in Computer Science, Engineering and Information Technology. 2017;4(5):132-136.
4. Jain N. Review of different responsive CSS front-end frameworks. Journal of Global Research in Computer Science. 2014;5(11):5-10.
5. Shenoy A. Introducing Zurb Foundation 6. Berkeley, CA: Apress; c2016. DOI:10.1007/978-1-4842-1796-2_5.
6. Castro-Rivera VP, Herrera-Acuña RA, Villalobos-Abarca MA. Desarrollo de un software web para la generación de planes de gestión de riesgos de software. Información Tecnológica. 2020;31(3):135-148.

Check for updates

International Journal of Circuit Theory and Applications

WILEY

ORIGINAL ARTICLE

Mathematical Analysis and Topology Derivation for a Family of Novel Dual Output High-Voltage Gain Z-Source Converter for Renewable Energy Application

A. Gupta | D. Joshi

Department of Electrical Engineering, Delhi Technological University, Delhi, India

Correspondence: A. Gupta (ashutoshgupta.nitm@gmail.com)

Received: 16 July 2024 | **Revised:** 20 September 2024 | **Accepted:** 3 November 2024

Keywords: DC–DC converter | high-voltage gain | multiport | topologies | Z-source converter

ABSTRACT

This paper presents a family of multiport Z-source converters with minimal number of switches and passive components. The paper focuses on the development of a novel converter and its methodology for selecting the topology of common ground/non-common ground Z-source DC–DC single-input dual-output configurations, aimed at higher power density, enhancing operational efficiency, size, cost, and centralized power management across multiple ports. In comparison to conventional Z-source single input single output converters, this design achieves high-voltage conversion rates while concurrently delivering two distinct outputs with and without common ground, rendering it particularly advantageous for electric vehicle and isolated microgrid applications with renewable energy integration. The proposed converters undergo comprehensive analysis and comparison across various potential configurations. Specifically, configurations yielding equivalent output voltages are prioritized, facilitating their utility in multilevel inverter applications. The assessment encompasses the determination of maximum efficiency; voltage stresses on capacitors, diodes, and switches; inductor currents; and ripples under diverse loads and duty cycles for all configurations. Experimental results are provided to showcase the validity and capabilities of these converters. As research efforts on converter topologies continue to grow, it is expected that this paper will enhance comprehension of multiport Z-source converter topologies ideas for numerous applications.

1 | Introduction

The widespread acceptance of renewable energy, electric vehicles (EVs), consumer electronics, and other sustainable technologies in recent years has led to a substantial shift towards the development of sustainable power electronic converter topologies. There is a growing demand for converters with multiple ports and various voltage levels to accommodate to diverse applications in these sectors. [1, 2]. To achieve voltage regulation and power control across different ports, multiple independent single-input single-output (SISO) converters can be utilized. However, this approach results in a high number of components, leading to increased overall cost and system volume [3, 4]. To tackle this issue, a family of multi-input multi-output (MIMO) DC–DC converters has been introduced.

The primary advantages of such converters include the fewer conversion stages; increased system efficiency; higher power density, size, and cost; and centralized power management across multiple ports compared to using multiple single-input DC–DC converters in renewable energy systems. Various multiport DC–DC converters have been developed encompassing both isolated and nonisolated topologies. Isolated topologies [5–8] and nonisolated topologies [9–12] represent two main subdivisions within these multiport converter designs. A single inductor MIMO boost converter is proposed for EV

© 2024 John Wiley & Sons Ltd.

application [13]. Despite having multiple outputs with varying voltage levels, the converter's gain is low. In [14], a new multiport DC–DC converter is introduced for DC Microgrid applications. While the proposed configuration offers numerous advantages such as minimizing multiple power conversions, decreasing the number of components, and providing voltage boosting capability, it also presents drawbacks including high switch count and controller complexity, coupled with low-voltage gain.

To achieve a high-voltage conversion ratio, traditional DC–DC converters operate with duty cycles below 0.1 for step-down and above 0.9 for step-up modes. However, such extreme duty cycle operation can compromise converter efficiency and transient performance [15, 16]. To tackle this issue, a family of high-gain integrated multiport DC–DC converters has been introduced. High-gain multiple ports DC–DC converters (HGMPC) have gained significant attention for scenarios demanding multiple independent supply voltage levels. In a recent study, a novel collection of five nonisolated multiport DC–DC converter designs is characterized by bipolar symmetric outputs with high gain. The feasibility of integrating these converters with a multilevel inverter to generate high-quality AC voltages is demonstrated [17]. A new nonisolated high step-up multiport DC–DC converter,

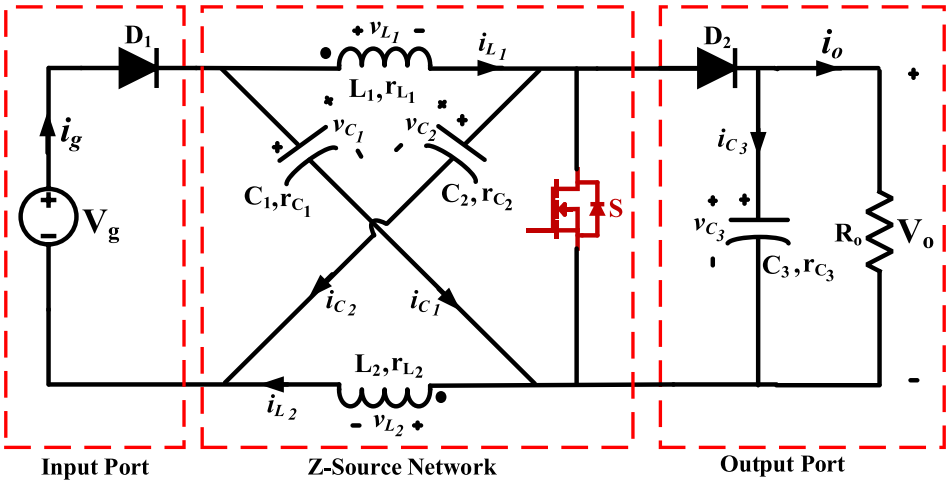

FIGURE 1 | Conventional Z-source DC–DC converter.

TABLE 1 | Comparison analysis of different converter topologies.

Converter		[19]	[13]	[30]	[31]	[32]	Proposed converter
Number of	Inputs	M	M	M	M	M	M
	Output	N	N	N	N	N	N
	Switch	M + N	M + N	M + N	M	M + N	M + N
	Diodes	M + N	M + N	M + N	N	M + N + 1	M + N
	Inductor	1	1	1	M	1	2
	Capacitor	1	1	1	N	1	N + 2
Input current		Discontinuous	Discontinuous	Discontinuous	Continuous	Discontinuous	Discontinuous
Frequency		40 kHz	100 kHz	40 kHz	20 kHz	20–100 kHz	40 kHz
Input voltage		25 V, 20 V	20 V, 9–40 V, 20 V	30 V, 20 V	159.3 V, 150 V	24 V, 20 V	30 V
Output voltage		22 V, 11 V	5.25 V, 3–15 V, 32 V	21 V, 8 V	155 V	12 V, 8–10 V	60 V, 60 V
Output power		29.5 W	30.4 W	35.4 W	—	35 W	240 W
Output voltage level		Low	Low	Low	High	Low	High
Max. voltage across switch		Medium	Medium	Medium	Low	Medium	Low
Efficiency		—	88%	90%	—	92.1%	91.6%
Cost		Medium	Low	Medium	High	Medium	Low

1097007x, 0, Downloaded from https://onlinelibrary.wiley.com/doi/10.1002/cta.4369 by Delhi Technological University, Wiley Online Library on [27/11/2024]. See the Terms and Conditions (https://onlinelibrary.wiley.com/terms-and-conditions) on Wiley Online Library for rules of use; OA articles are governed by the applicable Creative Commons License

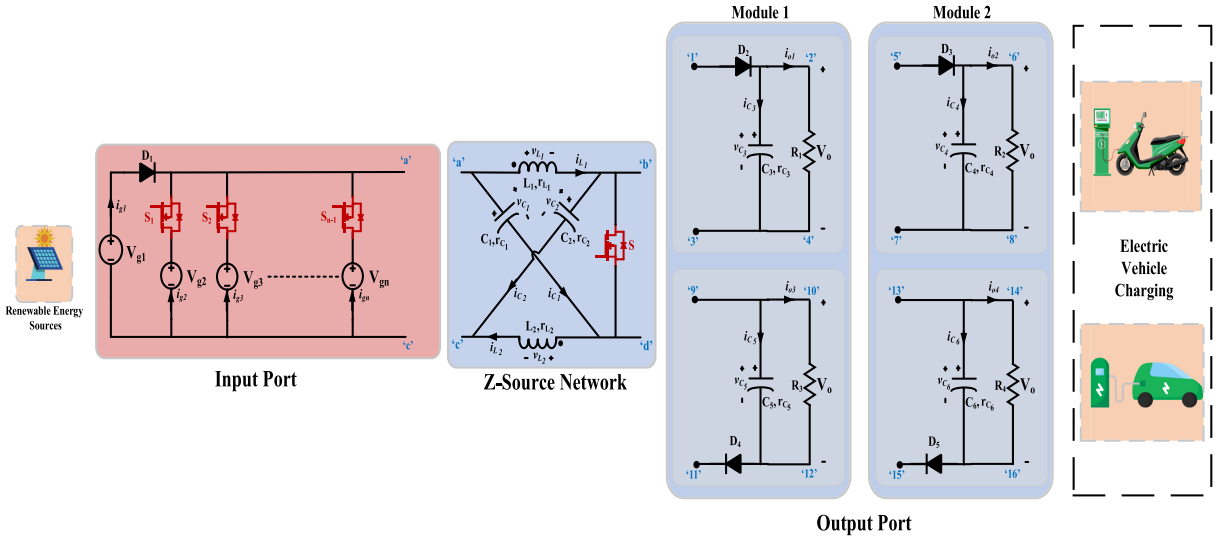

FIGURE 2 | Family of nonisolated multi-input multi-output Z-source DC–DC converter.

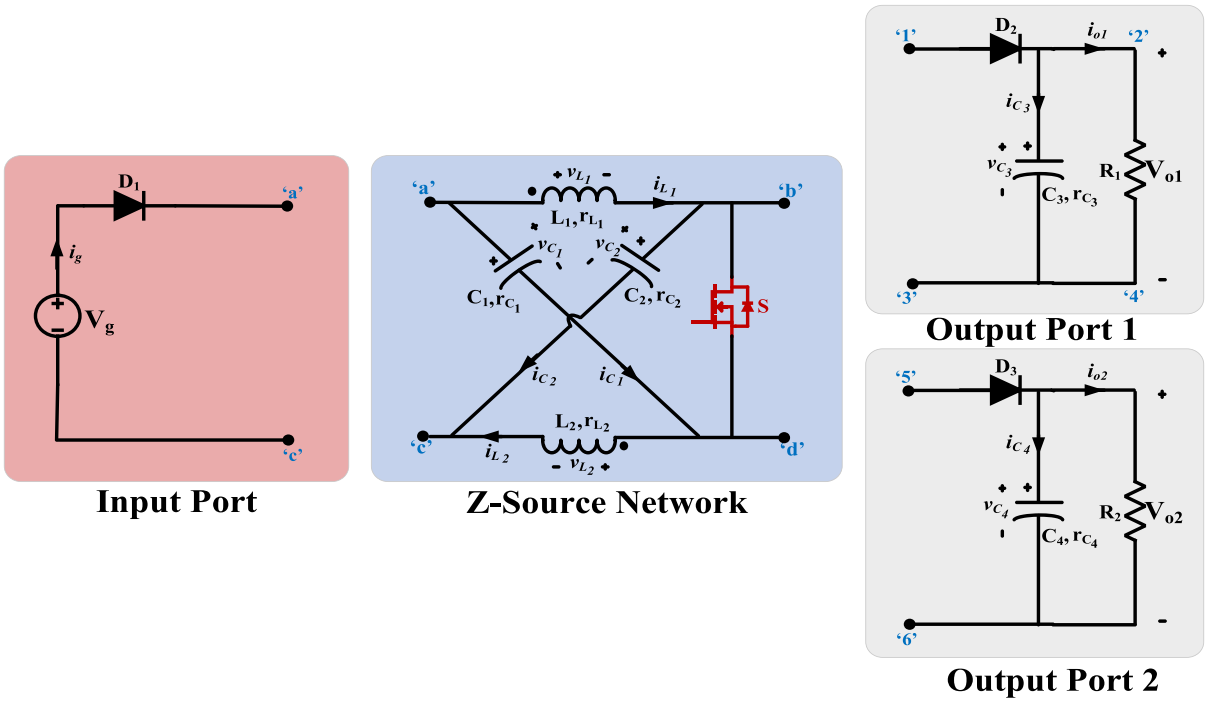

FIGURE 3 | Converter configuration for single-input dual-output Z-source DC–DC converter.

integrated with PV modules and a battery storage system (BSS), is proposed for high-voltage DC bus-based hybrid renewable energy systems. It offers high-voltage gain, low semiconductor stress, ZCS diodes, MPPT for PV inputs, and flexible port extension [18]. A double input high-gain DC–DC boost topology with six switching states is introduced and subsequently expanded to an n-input version [19]. A high step-up DC–DC boost converter [20] with a single input and three outputs was introduced, featuring an expandable structure achieved by increasing the voltage multiplier modules, and capable of delivering high-voltage gains at its output terminals without the need for higher duty cycles or the inclusion of transformers or coupled inductors in its design. A newly developed multiport DC–DC converter with high gain [13], designed to incorporate low-voltage energy storage devices into a DC microgrid, presents a three-port interface employing just a single two-winding transformer, thereby substantially simplifying control complexities. Studies [13, 17–20] highlight the importance of high-gain converters in multiport configurations, emphasizing their benefits in terms of efficiency, size, cost, and control complexities.

This paper introduces a novel family of 128 nonisolated dual-output high-gain Z-source converters (DOHGZSC), with or without a common ground, to address the identified gaps in the existing literature.

1. Number of input and output ports (OPs) can be arbitrarily increased without much modification to the existing

1097007x, 0, Downloaded from https://onlinelibrary.wiley.com/doi/10.1002/cta.4369 by Delhi Technological University, Wiley Online Library on [27/11/2024]. See the Terms and Conditions (https://onlinelibrary.wiley.com/terms-and-conditions) on Wiley Online Library for rules of use; OA articles are governed by the applicable Creative Commons License

TABLE 2 | Various topologies for high-gain Z-source Ncg/Cg DC–DC converter for dual output configuration as per Figure 2.

O/P port 1 O/P port 2	*1-b 3-d*	*1-a 3-d*	*1-b 3-c*	*1-a 3-c*	*9-b 11-d*	*9-a 11-d*	*9-b 11-c*	*9-a 11-c*
5-2,7-4	$f_{a_{11}}$	$f_{a_{12}}$	$f_{a_{13}}$	$f_{a_{14}}$	$f_{b_{11}}$	$f_{b_{12}}$	$f_{b_{13}}$	$f_{b_{14}}$
5-b,7-4	$f_{a_{21}}$	$f_{a_{22}}$	$f_{a_{23}}$	$f_{a_{24}}$	$f_{b_{21}}$	$f_{b_{22}}$	$f_{b_{23}}$	$f_{b_{24}}$
5-a,7-4	$f_{a_{31}}$	$f_{a_{32}}$	$f_{a_{33}}$	$f_{a_{34}}$	$f_{b_{31}}$	$f_{b_{32}}$	$f_{b_{33}}$	$f_{b_{34}}$
5-2,7-c	$f_{a_{41}}$	$f_{a_{42}}$	$f_{a_{43}}$	$f_{a_{44}}$	$f_{b_{41}}$	$f_{b_{42}}$	$f_{b_{43}}$	$f_{b_{44}}$
5-b,7-c	$f_{a_{51}}$	$f_{a_{52}}$	$f_{a_{53}}$	$f_{a_{54}}$	$f_{b_{51}}$	$f_{b_{52}}$	$f_{b_{53}}$	$f_{b_{54}}$
5-a,7-c	$f_{a_{61}}$	$f_{a_{62}}$	$f_{a_{63}}$	$f_{a_{64}}$	$f_{b_{61}}$	$f_{b_{62}}$	$f_{b_{63}}$	$f_{b_{64}}$
5-b,7-2	$f_{a_{71}}$	$f_{a_{72}}$	$f_{a_{73}}$	$f_{a_{74}}$	$f_{b_{71}}$	$f_{b_{72}}$	$f_{b_{73}}$	$f_{b_{74}}$
5-a,7-2	$f_{a_{81}}$	$f_{a_{82}}$	$f_{a_{83}}$	$f_{a_{84}}$	$f_{b_{81}}$	$f_{b_{82}}$	$f_{b_{83}}$	$f_{b_{84}}$
13-2,15-4	$f_{c_{11}}$	$f_{c_{12}}$	$f_{c_{13}}$	$f_{c_{14}}$	$f_{d_{11}}$	$f_{d_{12}}$	$f_{d_{13}}$	$f_{d_{14}}$
13-b,15-4	$f_{c_{21}}$	$f_{c_{22}}$	$f_{c_{23}}$	$f_{c_{24}}$	$f_{d_{21}}$	$f_{d_{22}}$	$f_{d_{23}}$	$f_{d_{24}}$
13-a,15-4	$f_{c_{31}}$	$f_{c_{32}}$	$f_{c_{33}}$	$f_{c_{34}}$	$f_{d_{31}}$	$f_{d_{32}}$	$f_{d_{33}}$	$f_{d_{34}}$
13-2,15-c	$f_{c_{41}}$	$f_{c_{42}}$	$f_{c_{43}}$	$f_{c_{44}}$	$f_{d_{41}}$	$f_{d_{42}}$	$f_{d_{43}}$	$f_{d_{44}}$
13-b,15-c	$f_{c_{51}}$	$f_{c_{52}}$	$f_{c_{63}}$	$f_{c_{54}}$	$f_{d_{51}}$	$f_{d_{52}}$	$f_{d_{53}}$	$f_{d_{54}}$
13-a,15-c	$f_{c_{61}}$	$f_{c_{62}}$	$f_{c_{63}}$	$f_{c_{64}}$	$f_{d_{61}}$	$f_{d_{62}}$	$f_{d_{63}}$	$f_{d_{64}}$
13-b,15–2	$f_{c_{71}}$	$f_{c_{72}}$	$f_{c_{73}}$	$f_{c_{74}}$	$f_{d_{71}}$	$f_{d_{72}}$	$f_{d_{73}}$	$f_{d_{74}}$
13-a,15–2	$f_{c_{81}}$	$f_{c_{82}}$	$f_{c_{83}}$	$f_{c_{84}}$	$f_{d_{81}}$	$f_{d_{82}}$	$f_{d_{83}}$	$f_{d_{84}}$

HGMPC, by introducing only the respective input ports' (IPs) active switch.

2. Independent power flow can be carried out arbitrarily from either of the output sources to the loads.
3. Having higher voltage gains than the counterpart nonisolated MIMOs in literature, which is an attractive feature for application in RES and distribution systems.
4. Inductor time multiplexing is used to achieve simultaneous power transfer from more than one OP of different voltage levels, keeping the part count fixed for any number of outputs.
5. A SISO controller, such as the standard double loop PI controller, is sufficient to control the output voltages despite the multiple ports of the converters.

In terms of achieving high-voltage gain, impedance source or Z-source DC–DC converter shown in Figure 1 outperforms conventional boost converters. Peng [21] first introduced the Z-source network concept, offering a solution to the issues of shoot-through and limited output voltage found in traditional voltage-source inverters, achieved by employing a configuration comprising two capacitors and two inductors interconnected in an X-shape. Numerous recent studies [22–26] have explored the Z-source converter and its various permutations, highlighting the advantages of this high-voltage gain impedance source converter. An enhanced Z-source inverter, proposed in [22, 23], mitigates capacitor voltage stress and inrush current, while a novel single-phase Z-source inverter, discussed in [24], enables shared ground between input and output. Additionally, the application of switched inductors to the Z-source network has been investigated [25]. In [26], a Z-source DC–DC converter with common ground and high-voltage gain is introduced, while [27] presents a series of hybrid Z-source boost DC–DC converters tailored for PV power systems, and [28] proposes a novel structure based on ZSC DC–DC, suitable for deployment in renewable energy systems within DC or hybrid microgrids due to its high-voltage gain. The proposed converter in [29] integrates a reformed Z-source converter and a switch capacitor, featuring four ports including a bidirectional port for battery charging/discharging, with innovative techniques applied to facilitate operation of the bidirectional port and accommodate the additional input source.

This paper explores various research paths aimed at developing highly efficient converters capable of selecting the topology of common ground (CG) or noncommon ground (NCG) dual-output high-gain Z-source converters (DOHGZSC) with enhanced operational characteristics. Additionally, there is a demand for converters capable of achieving high-voltage conversion along with dual outputs (CG/NCG), which is crucial for EV and isolated microgrid (IMG) applications. Moreover, there is a need for converters configured to produce equal voltages at their outputs to facilitate their use in multilevel inverter applications.

2 | Principle and Topology

Conventionally, a Z-source network or impedance network is shown in Figure 1, which is divided into three sections, that

1097007x, 0, Downloaded from https://onlinelibrary.wiley.com/doi/10.1002/cta.4369 by Delhi Technological University, Wiley Online Library on [27/11/2024]. See the Terms and Conditions (https://onlinelibrary.wiley.com/terms-and-conditions) on Wiley Online Library for rules of use; OA articles are governed by the applicable Creative Commons License

TABLE 3 | Different converter configurations for single-input dual-output Z-source-based DC–DC converter.

Configuration	Output port 1	Output port 2
1	(Family 1) NCG-A 1-b, 3-d	NCG-A/5–2,6-d
2		NCG-B/5-b,6-d
3		NCG-C/5-a,6-d
4		CG-A/5–2,6-c
5		CG-B/5-b,6-c
6		CG-C/5-a,6-c
7	(Family 2) NCG-B 1-a,3-d	NCG-A/5–2,6-d
8		NCG-B/5-b,6-d
9		NCG-C/5-a,6-d
10		CG-A/5–2,6-c
11		CG-B/5-b,6-c
12		CG-C/5-a,6-c
13	(Family 3) CG-A 1-b,3-c	NCG-A/5–2,6-d
14		NCG-B/5-b,6-d
15		NCG-C/5-a,6-d
16		CG-A/5–2,6-c
17		CG-B/5-b,6-c
18		CG-C/5-a,6-c
19	(Family 4) CG-B 1-a,3-c	NCG-A/5–2,6-d
20		NCG-B/5-b,6-d
21		NCG-C/5-a,6-d
22		CG-A/5–2,6-c
23		CG-B/5-b,6-c
24		CG-C/5-a,6-c

is, IP, Z-source network, and OP. It utilizes a distinctive impedance network, connecting the converter main circuit to the power source, load, or another converter, offering unique functionalities not found in traditional voltage and current source converters, which use capacitors and inductors, respectively, and employs a two-port network consisting of split-inductors $(L_1 \text{ and } L_2)$ and capacitors $(C_1 \text{and } C_2)$ arranged in an X-shape to create an impedance source (Z-source) coupling the converter to the DC source and load with a voltage gain B [22] expressed as

$$B = \frac{1}{1-2D} \tag{1}$$

where D represents the duty ratio of the converter.

Due to the converter's operation at low duty cycles and the correlation between power losses and duty cycle, its performance yields high efficiency. Additionally, the voltage stress on most of its components is minimal. As mentioned in the Introduction in [26], a SISO Z-source converter is presented. The utilization of MIMO configurations is crucial in various applications as it enables efficient management of load and power dynamics, necessitating the hybridization of different energy sources. Several researchers [13, 19, 30–32] have introduced various nonisolated multiport converters, highlighting the demand for more efficient and cost-effective options in hybrid renewable energy systems, as outlined in Table 1.

2.1 | Topology Derivation of Single-Input Dual-Output (SIDO) Z-Source DC–DC Converters Based on the Voltage-Type Ports

This paper introduces a nonisolated MIMO DC–DC converter, with high-voltage gain, as illustrated in Figure 2. The converter interface n input power sources, $V_{g1}, V_{g2}, V_{g3}, \ldots, V_{gn}$, with increasing voltage levels. It comprises two inductors, two capacitors in a Z-source network, and n switches. The load resistances $, R_1, R_2, R_3,$ and R_4, can represent different combinations of OPs, capable of providing varying or equal voltage levels suitable for EV charging connections. Table 1 outlines diverse dual-output impedance converter configurations, featuring both distinct and identical voltage levels, to be further examined in subsequent sections of the paper. For ease, this paper focuses on analyzing a family of proposed converters with a single-input and two outputs. In Figure 3, taking V_g as the only source, various topologies for dual output high-gain Z-source NCG/CG DC–DC converter are analyzed for selected module.

As seen from the above Table 2, 128 topologies are possible and can be studied further according to suitability of applications. In this research work, $f_{a_{ij}}$ family is studied for 24 out of 32 configurations from the highlighted section considering OPs as shown in Figure 3. These two ports have addition features for CG and NCG connections.

Examining Figure 3, a total of 24 configurations, featuring both common ground (CG) and noncommon ground (NCG), are derived and tabulated in Table 3 and subsequently analyzed for their performance. Among these, the most optimal configuration is selected and thoroughly evaluated. Connecting OPs lead 1, 3, 5, and 6 at different positions of Modules 1 and 2 results in 24 configurations, as depicted in Table 3.

Figure 4 shows the 24 different topologies of SIDO Z-source converter. These configurations, with identical design parameters as shown in Table 4, are evaluated for high-voltage gain; output power; efficiency; low-voltage stress on capacitors, diodes, and switches; and minimal input current drawn from the input source in Simulink/MATLAB. Following analysis, only one configuration is chosen.

2.2 | Topology Optimization and Performance Analysis

Various combinations/configurations that are proposed as shown in Table 4 are simulated for performance analysis. The selection of an appropriate configuration can be based on various criteria such as high efficiency, high-voltage gain, minimal

1097007x, 0, Downloaded from https://onlinelibrary.wiley.com/doi/10.1002/cta.4369 by Delhi Technological University, Wiley Online Library on [27/11/2024]. See the Terms and Conditions (https://onlinelibrary.wiley.com/terms-and-conditions) on Wiley Online Library for rules of use; OA articles are governed by the applicable Creative Commons License

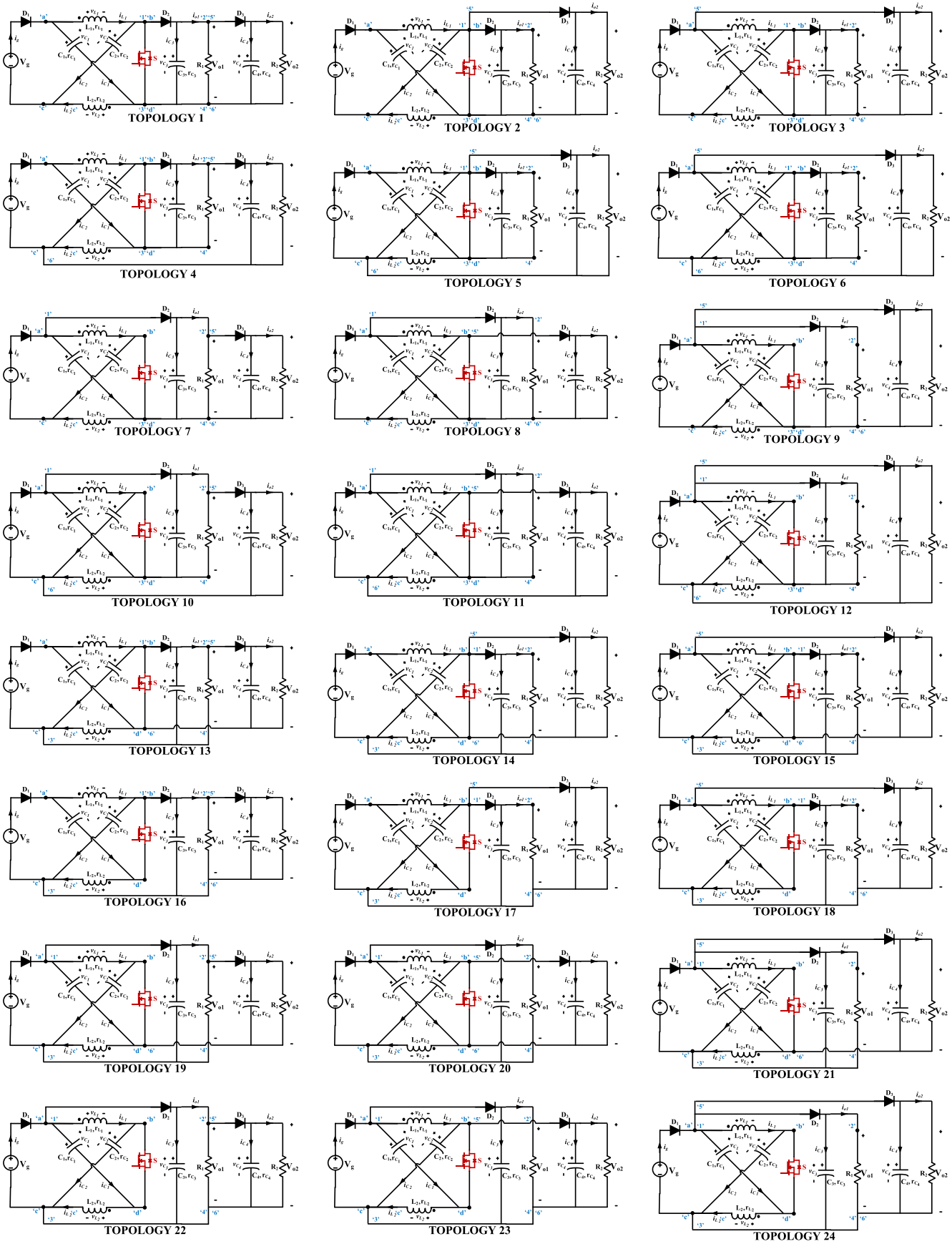

FIGURE 4 | Different converter configurations for single-input dual-output Z-source based DC–DC converter.

1097007x, 0, Downloaded from https://onlinelibrary.wiley.com/doi/10.1002/cta.4369 by Delhi Technological University, Wiley Online Library on [27/11/2024]. See the Terms and Conditions (https://onlinelibrary.wiley.com/terms-and-conditions) on Wiley Online Library for rules of use; OA articles are governed by the applicable Creative Commons License

TABLE 4 | Hardware component and simulation parameters of proposed system.

Simulation and prototype parameters	Symbols	Specification(s)
Input voltage	V_g	30 V
Switching frequency	f_{sw}	40 kHz
Output voltage	V_O	60 V, 60 V
Inductors	L_1 L_2	139.5 μH 165 μH
Capacitors	C_1 C_2 C_3 C_4	470 μF (150 V), 470 μF (150 V) 470 μF (150 V) 330 μF (150 V)
Load resistances	R_1 R_2	0 − 500 Ω 0 − 500 Ω,
MOSFET	IRFP260N	200 V, 50 A
Diode	MUR840	400 V, 8 A

input current drawn, increased power output, and other performance metrics. Table 5 displays the results of open-loop simulations comparing various performance parameters of different feasible configurations of high-output voltage SIDO converters at $R_1 = R_2 = 450\Omega$ and a duty cycle (D) of 0.2.

As part of the analysis, the proposed converters are evaluated and contrasted across various potential configurations. Configurations that yield equal output voltages are specifically chosen, enabling their use in multilevel inverter applications and other suitable scenarios. Table 5 is segmented into four sections, each containing six members, with configurations selected based on specific requirements. Among the 24 configurations, 10 feature equal output voltages (V_{o1}, V_{o2}), namely 1, 2, 7, 9, 11, 15, 16, 17, 22, and 24. Configurations 1 and 2 exhibit equal output voltage but with lower gain and efficiency. Configuration 13 offers both positive and negative output voltages, suitable for applications requiring both types of supply. Configurations 7, 9, and 11 demonstrate high gain and efficiency but draw high input current from the supply. Conversely, Configurations 22 and 24 provide high gain and efficiency while drawing minimal current. By reducing the duty cycle, Configurations 7, 9, and 11 can be further explored in subsequent studies. It is observed that even under light load conditions, all configurations exhibit high efficiency, ranging from a minimum of 88.0448% for configuration 11 to a maximum of 96.5202% for Configuration 24. Increasing the load and reducing the duty cycle could potentially enhance efficiency further, necessitating further investigation in subsequent studies. The performance parameters of selected configurations [1, 2, 7, 9, 11, 21, 23] of high-output voltage, high-efficiency SIDO converters are compared under varying load conditions for a duty cycle (D) of 0.2 as shown in Table 5.

Figure 5 illustrates that across all configurations, efficiency remains consistently high from no load to high load conditions. Configurations 22 and 24 exhibit the highest output voltage. Notably, at light load conditions, Configurations

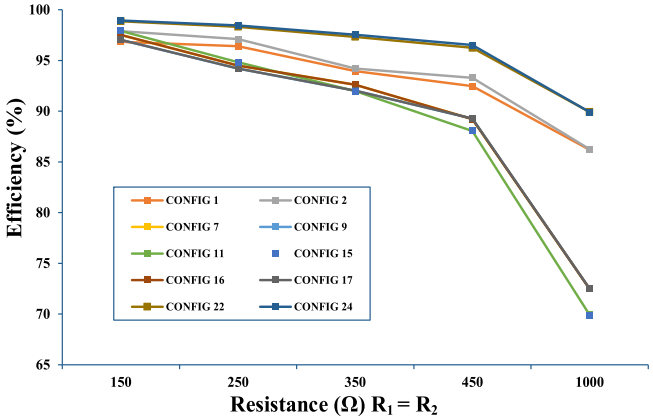

FIGURE 5 | Comparison of efficiency for selected configurations [1, 2, 7, 9, 11, 21, 23] of high-output voltage, high-efficiency SIDO converters for D = 0.2 under varying load condition.

7, 9, 11, 15, 16, and 17 demonstrate efficiencies ranging from 69.8182% to 72.4837%, which are comparatively lower (< 15%) than other configurations. Most configurations draw nominal power from the source yet maintain high efficiency at high loading conditions, making them suitable for scenarios with limited input generation capacity. However, in Configurations 22 and 24, input current is higher compared to other eligible configurations under high load, requiring control due to the fixed voltage source. Adaptation to changing loads can be achieved by either altering the configuration while keeping the duty cycle constant or adjusting the duty cycle while maintaining the configuration.

This study holds significant importance as it enables the implementation of a suitable control strategy based on the loading conditions and the corresponding best possible configuration determined in advance. From Figure 5, it is evident that among the selected Configurations 1, 2, 7, 9, 11, 15, 16, 17, 22, and 24, Configuration 24 achieves the maximum efficiency of 98.9434%

1097007x, 0, Downloaded from https://onlinelibrary.wiley.com/doi/10.1002/cta.4369 by Delhi Technological University, Wiley Online Library on [27/11/2024]. See the Terms and Conditions (https://onlinelibrary.wiley.com/terms-and-conditions) on Wiley Online Library for rules of use; OA articles are governed by the applicable Creative Commons License

TABLE 5 | Comparison of various performance parameters for different feasible configurations of high-output voltage SIDO converters, $R_1 = R_2 = 450\Omega, D = 0.2$.

Configuration	Output1/ connections	Output2/connections	I_g (A)	V_{o1} (V)	V_{o2} (V)	P_o (W)	Efficiency (%)
1	(Family 1) NCG-A 1-b, 3-d	NCG-A/5–2,6-d	1.0173	79.5849	79.5847	28.2218	92.4668
2		NCG-B/5-b,6-d	1.0029	79.3646	79.3632	28.0670	93.2796
3		NCG-C/5-a,6-d	1.0954	98.2606	64.1557	30.6162	93.1648
4		CG-A/5–2,6-c	1.1916	61.2891	106.9071	34.0382	95.2128
5		CG-B/5-b,6-c	1.0985	98.0290	64.0479	30.4843	92.4952
6		CG-C/5-a,6-c	1.2420	72.6931	102.6400	35.2511	94.6066
7	(Family 2) NCG-B 1-a,3-d	NCG-A/5–2,6-d	1.4371	92.8352	92.8350	38.4637	89.2106
8		NCG-B/5-b,6-d	1.0909	63.9109	97.7612	30.3291	92.6731
9		NCG-C/5-a,6-d	1.4375	92.8737	92.8731	38.4994	89.2729
10		CG-A/5–2,6-c	1.3110	58.1839	116.3281	37.6183	95.6428
11		CG-B/5-b,6-c	1.4213	91.6869	91.6896	37.5431	88.0448
12		CG-C/5-a,6-c	1.31047	58.2222	116.3313	37.6293	95.7146
13	(Family 3) CG-A 1-b,3-c	NCG-A/5–2,6-d	1.0990	64.0810	98.1579	30.5498	92.6552
14		NCG-B/5-b,6-d	1.0736	63.8821	97.6820	30.2866	94.0264
15		NCG-C/5-a,6-d	1.42138	91.6879	91.6906	37.5440	88.0457
16		CG-A/5–2,6-c	1.4371	92.8353	92.8350	38.4637	89.2100
17		CG-B/5-b,6-c	1.4375	92.8743	92.8738	38.4999	89.2734
18		CG-C/5-a,6-c	1.3102	58.2223	116.3114	37.6184	95.7046
19	(Family 4) CG-B 1-a,3-c	NCG-A/5–2,6-d	1.4068	87.6497	101.5058	40.2306	95.3232
20		NCG-B/5-b,6-d	1.2401	102.5704	72.6187	35.1879	94.5786
21		NCG-C/5-a,6-d	1.3212	116.4005	58.2509	37.6697	95.0331
22		CG-A/5–2,6-c	1.4392	96.5832	96.5816	41.5544	96.2428
23		CG-B/5-b,6-c	1.3212	116.2794	58.1977	37.5931	94.8455
24		CG-C/5-a,6-c	1.4380	96.6844	96.6808	41.6403	96.5202

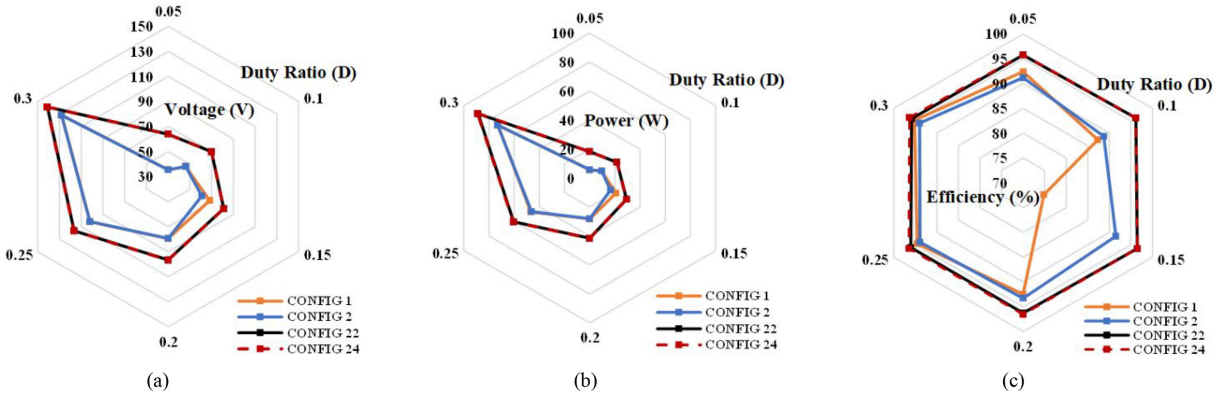

FIGURE 6 | Comparison of various parameters for selected configurations [1, 2, 21, 23] of high-output voltage, high-efficiency SIDO converters for $R_1 = R_2 = 450\Omega$ under varying duty cycle condition. (a) Output voltages $(V_{o1} = V_{o2})$. (b) Output power (P_o). (c) Efficiency (%).

1097007x, 0, Downloaded from https://onlinelibrary.wiley.com/doi/10.1002/cta.4369 by Delhi Technological University, Wiley Online Library on [27/11/2024]. See the Terms and Conditions (https://onlinelibrary.wiley.com/terms-and-conditions) on Wiley Online Library for rules of use; OA articles are governed by the applicable Creative Commons License

TABLE 6 | Comparison of average current and current ripples of L_1 and L_2 for selected configurations [1, 2, 21, 23] of Z-source SIDO converters for $R_1 = R_2 = 450\,\Omega$ under varying duty cycle condition.

Config	Output-1/output-2	D	I_{L1} (A) (Avg)	$\Delta I_{L1}(A)$	$I_{L2}(A)$ (Avg)	$\Delta I_{L2}(A)$
1	NCG-A 1-b, 3-d NCG-A 5–2,6-d	0.05	− 0.14	0.41	0.49	0.38
		0.10	− 0.10	1.05	0.69	0.93
		0.15	0.53	1.92	0.51	1.62
		0.20	1.26	3.06	0.54	2.68
		0.25	1.21	4.64	1.78	4.02
		0.30	2.53	6.70	2.22	5.68
2	NCG-A 1-b, 3-d NCG-B 5-b,6-d	0.05	− 0.03	0.43	0.37	0.42
		0.10	− 0.04	1.05	0.63	0.92
		0.15	0.53	1.92	0.51	1.62
		0.20	1.18	3.06	0.62	2.66
		0.25	1.21	4.63	1.79	4.02
		0.30	2.54	6.71	2.21	5.69
22	CG-B 1-a,3-c CG-A 5–2,6-c	0.05	0.30	0.49	0.30	0.35
		0.10	0.14	0.96	0.64	0.85
		0.15	0.59	1.71	0.57	1.45
		0.20	1.21	2.68	0.60	2.36
		0.25	1.16	4.06	1.70	3.54
		0.30	2.40	5.95	2.04	5.05
24	CG-B 1-a,3-c CG-C 5-a,6-c	0.05	0.31	0.49	0.30	0.35
		0.10	0.06	0.96	0.72	0.86
		0.15	0.59	1.70	0.56	1.46
		0.20	1.29	2.68	0.53	2.37
		0.25	1.08	4.06	1.78	3.57
		0.30	2.47	5.96	1.98	5.07

with a voltage of $80.3042\,V$ at $R_1 = R_2 = 150\Omega$, while Configuration 17 attains the highest voltage of $138.9007\,V$ with an efficiency of 72.4837% at $R_1 = R_2 = 1000\Omega$. However, due to the drop in efficiency during light load conditions, Configurations $7, 9, 11, 15, 16,$ and 17 are discarded, and Configurations $1, 2, 22,$ and 24 are selected for further analysis as they exhibit high efficiency and output voltage.

3 | Analysis of Selected SIDO Topologies

Out of the family of 24 topologies of high-gain Z-source SIDO converters, four configurations meeting the criterion of equal output voltage with better performance are further examined based on their loading conditions, voltages, and efficiencies as discussed in earlier section.

Figure 6 reveals that in Configurations 1 and 2, efficiency initially decreases (minimum values 74.7968% and 88.7252%) and then rises with the duty cycle (maximum values 95.1968% and 94.0326%). Conversely, a reverse trend is observed in Configurations 22 and 24, where efficiency first increases (maximum values 96.4919% and 96.5202%) and then decreases, with minimum values always above 95% (95.8569% and 96.3553%). Additionally, the output voltage is higher throughout the full range of duty cycle (0.05 to 0.3), ranging from 35 to 128 V for Configurations 1 and 2, and from 64 to 142 V for Configurations 22 and 24, respectively. Moreover, output power delivered is highest in Configurations 22 and 24 as the duty cycle increases. Therefore, efficiency, output voltage, and output power delivered are highest in Configurations 22 and 24 as the duty cycle increases.

Configurations 1 and 2 should be discarded due to the high values of inductor current and current ripples. Table 6 highlights a significant increase in current ripples with the duty cycle for a fixed load, indicating the necessity for control measures. Therefore, proper attention must be given to ensure optimal performance under specific operating conditions.

1097007x, 0, Downloaded from https://onlinelibrary.wiley.com/doi/10.1002/cta.4369 by Delhi Technological University, Wiley Online Library on [27/11/2024]. See the Terms and Conditions (https://onlinelibrary.wiley.com/terms-and-conditions) on Wiley Online Library for rules of use; OA articles are governed by the applicable Creative Commons License

TABLE 7 | Comparison of voltage stresses on capacitors, diodes and active switch of Z-source SIDO converters, $R_1 = R_2 = 450\ \Omega$ under varying duty cycle condition.

Configuration	D	V_{c1} (V)	V_{c2} (V)	V_{c3} (V)	V_{c4} (V)	V_{D1} (V)	V_{D2} (V)	V_{D3} (V)	V_S (V)
1	0.05	32.7382	32.7382	35.4757	35.4757	− 34.1100	− 34.1089	0	34.1114
	0.10	38.0607	38.0607	46.1205	46.1199	− 44.5698	− 44.5692	0	44.5728
	0.15	49.0764	49.0764	68.1534	68.1528	− 59.4702	− 59.4751	0	59.4796
	0.20	54.7910	54.7910	79.5849	79.5847	− 78.1367	− 78.1469	0	78.1511
	0.25	65.9801	65.9800	101.9708	101.9705	− 100.5638	− 100.5831	0	100.5827
	0.30	78.9350	78.9350	127.8972	127.8959	− 126.0593	− 126.0986	0	126.1037
2	0.05	32.7345	32.7345	35.4678	35.4676	− 34.0967	− 34.1020	− 34.0967	34.1034
	0.10	38.0463	38.0463	46.0922	46.0914	− 44.5433	− 44.5442	− 44.5426	44.5479
	0.15	45.4699	45.4699	60.9394	60.9391	− 59.3303	− 59.3339	− 59.3316	59.3382
	0.20	54.6805	54.6805	79.3646	79.3632	− 77.8791	− 77.8886	− 77.8857	77.8933
	0.25	65.9705	65.9704	101.9523	101.9504	− 100.5704	− 100.5781	− 100.5750	100.5804
	0.30	79.0846	79.0846	128.1967	128.1942	− 126.2799	− 126.2799	− 126.3196	126.3290
22	0.05	31.9772	31.9772	63.9173	63.9150	− 33.0760	− 33.2977	0	33.3480
	0.10	34.9072	34.9072	69.7728	69.7705	− 38.8074	− 38.8000	0	38.8559
	0.15	40.5574	40.5574	81.0685	81.0665	− 49.8179	− 49.8135	0	49.8766
	0.20	48.3159	48.3159	96.5832	96.5816	− 53.5631	− 53.5622	0	53.6341
	0.25	58.2745	58.2745	116.5027	116.5014	− 84.7190	− 84.7328	0	84.7927
	0.30	70.5738	70.5738	141.1122	141.1111	− 108.6759	− 108.6764	0	108.7903
24	0.05	31.9771	31.9771	63.9172	63.9148	− 33.3075	− 33.2977	− 33.2988	33.4532
	0.10	34.9067	34.9067	69.7720	69.7694	− 38.8049	− 38.7991	− 38.7960	38.8541
	0.15	40.5565	40.5565	81.06719	81.0641	− 49.8171	− 49.8090	− 49.8090	49.8790
	0.20	48.3661	48.3661	96.6844	96.6808	− 65.1807	− 65.1858	− 65.1817	65.2492
	0.25	58.3894	58.3893	116.7335	116.7292	− 84.9428	− 84.9614	− 84.9566	85.0202
	0.30	70.7765	70.7765	141.5191	141.5138	− 109.0839	− 109.0990	− 109.0925	109.1656

In Table 7, average values are utilized to assess the stress across capacitors $(V_{c1}, V_{c2}, V_{c3}, and\ V_{c4})$ due to very low-voltage ripple, while maximum negative values are employed to evaluate the stress across diodes and the active switch $(V_{D1}, V_{D2}, V_{D3}, and\ V_S)$. It is observed that the average voltage across capacitors C_1 and C_2 ranges from 32 to 79 V for Configurations 1 and 2 and 32 to 70 V for Configurations 22 and 24, whereas across capacitors C_3 and C_4, it varies from 35 to 128 V for Configurations 1 and 2 and 64 to 142 V for Configurations 22 and 24, respectively. Consequently, capacitors C_1 and C_2 experience less voltage stress compared to capacitors C_3 and C_4 in all four configurations, aiding in the selection of suitable voltage ratings for all capacitors.

Furthermore, voltage stress on diodes D_1 and D_2 ranges from 34 to 126 V in Configurations 1 and 2 and 33 to 108 V for Configurations 22 and 24, while for the switch (S), it varies from 34 to 126 V for Configurations 1 and 2 and 33 to 109 V for Configurations 22 and 24, respectively. Interestingly, the voltage stress on diode D_3 is zero volts for Configurations 1 and 22, while it ranges from 34 to 126 V for Configuration 2 and 33 to 109 V for Configuration 24, respectively. Although approximate values are presented for description, precise values are displayed in the respective tables. Notably, Configuration 22 exhibits minimum voltage stress despite the variation in duty cycle from low to high values.

Considering the criteria of high efficiency, high-output voltage, minimal voltage stress on capacitors, diodes, and the switch, as well as low inductor current and ripples, Configuration 22 is ultimately selected. Furthermore, due to the lower inductor current, less energy is stored in the inductors, resulting in a smaller size, reduced weight, and cost-effectiveness of the proposed converter configuration.

4 | Analysis of Topology 22 Z-Source SIDO Converter

The configuration of the proposed converter is illustrated in Figure 7a. It is obvious from the diagram that the structure

1097007x, 0, Downloaded from https://onlinelibrary.wiley.com/doi/10.1002/cta.4369 by Delhi Technological University, Wiley Online Library on [27/11/2024]. See the Terms and Conditions (https://onlinelibrary.wiley.com/terms-and-conditions) on Wiley Online Library for rules of use; OA articles are governed by the applicable Creative Commons License

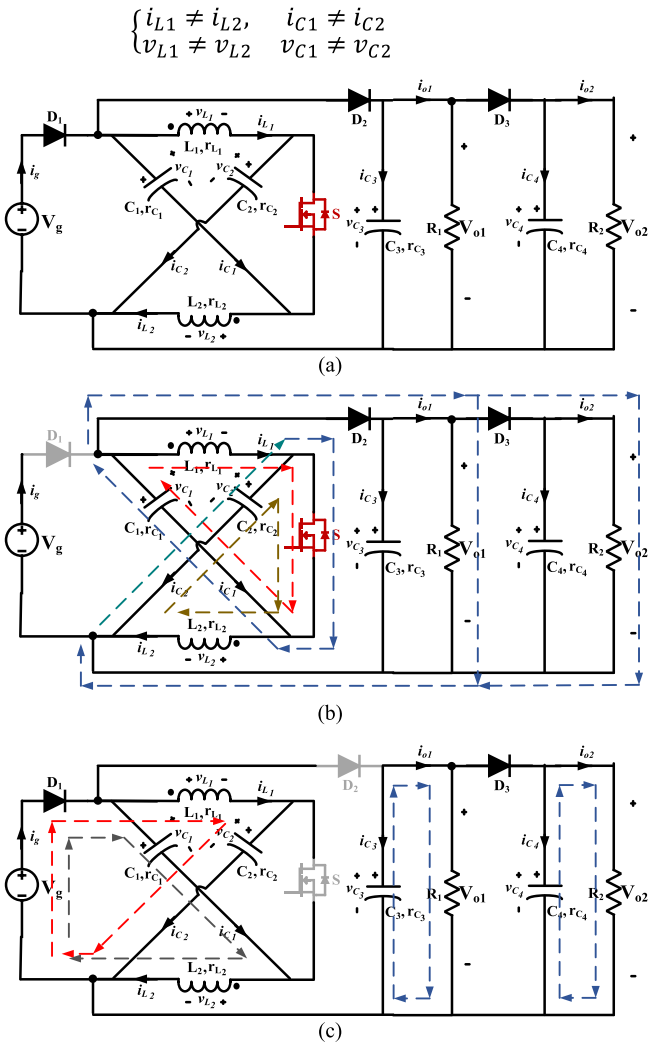

FIGURE 7 | Proposed converter: (a) Configuration. (b) Operating state DT. (c) Operating state $(1-D)T$.

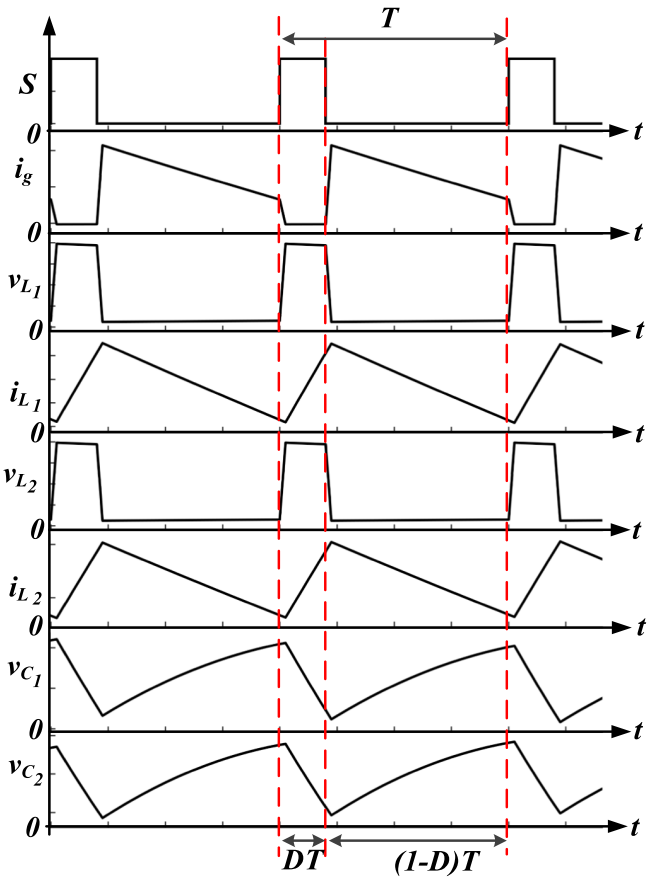

FIGURE 8 | Waveforms of the proposed converter.

TABLE 8 | Voltage of each component in different states.

Components	Mode 1	Mode 2
V_{C1} & V_{C2}	$\frac{1-D}{1-2D}V_g$	$\frac{1-D}{1-2D}V_g$
V_{L1} & V_{L2}	$\frac{1-D}{1-2D}V_g$	$\frac{D}{1-2D}V_g$
V_s	0	$\frac{1}{1-2D}V_g$
V_{D1}	$\frac{1}{1-2D}V_g$	0
V_{D2}	0	$\frac{1}{1-2D}V_g$

TABLE 9 | Current of each component in different states.

Components	Mode 1	Mode 2
I_{C1} & I_{C2}	$\frac{3-7D+4D^2}{1-2D}I_o$	$\frac{3D-4D^2}{1-2D}I_o$
I_{L1} & I_{L2}	$\frac{2-5D+4D^2}{1-2D}I_o$	$\frac{2-5D+4D^2}{1-2D}I_o$
I_s	$\frac{5-12D+8D^2}{1-2D}I_o$	0
I_{D1}	0	$\frac{2(1-D)}{1-2D}I_O$
I_{D2}	I_O	$\frac{1}{1-2D}I_O$

of the proposed converter is straightforward, comprising a Z-source network $(L_1, L_2, C_1, and\ C_2)$, a switch S, three diodes D_1, D_2, and D_3, two filter capacitors C_3 and C_4, and two load resistances R_1 and R_2. In comparison with the Z-source DC–DC converter represented in Figure 1, the proposed converter modifies the grounding connection and introduces additional outputs to enable SIDO operation. A prominent feature of the proposed converter is the placement of the input source and load on the same side of the Z-source network, differing from traditional Z-source converters where they are situated on both sides of the network (as shown in Figure 1). Additionally, the input voltage source and load share the same ground.

To analyze the operation of Z-source SIDO converter and to simplify the analysis, the following conditions are assumed.

1. All components are assumed to be ideal.
2. Both inductors, L_1 and L_2, are not equal, and both capacitors, C_1 and C_2, are assumed to be identical (C) in the Z-source network.
3. The currents through L_1 and L_2, as well as the voltages

1097007x, 0, Downloaded from https://onlinelibrary.wiley.com/doi/10.1002/cta.4369 by Delhi Technological University, Wiley Online Library on [27/11/2024]. See the Terms and Conditions (https://onlinelibrary.wiley.com/terms-and-conditions) on Wiley Online Library for rules of use; OA articles are governed by the applicable Creative Commons License

TABLE 10 | Cost of fabricated Z-source-based SIDO converter.

S. no.	Components	Specs	Quantity	Unit cost ($)	Cost ($)
1.	Inductor	Core (TDK E42/21/15)	4	1.9833	7.9332
		Bobin	2	1.2093	2.4186
		Wire (SWG 15)	3 m	0.6046	4.8978
2.	Capacitor	470 μF	3	1.6326	4.8978
		330 μF	1	0.8586	0.8586
3.	MOSFET	IRFP260N	1	0.4837	0.4837
4.	Diode	MUR840	3	1.0279	3.0837
5.	Controller	TMS320 F28379D	1	39.1099	39.1099
				Total	60.5998

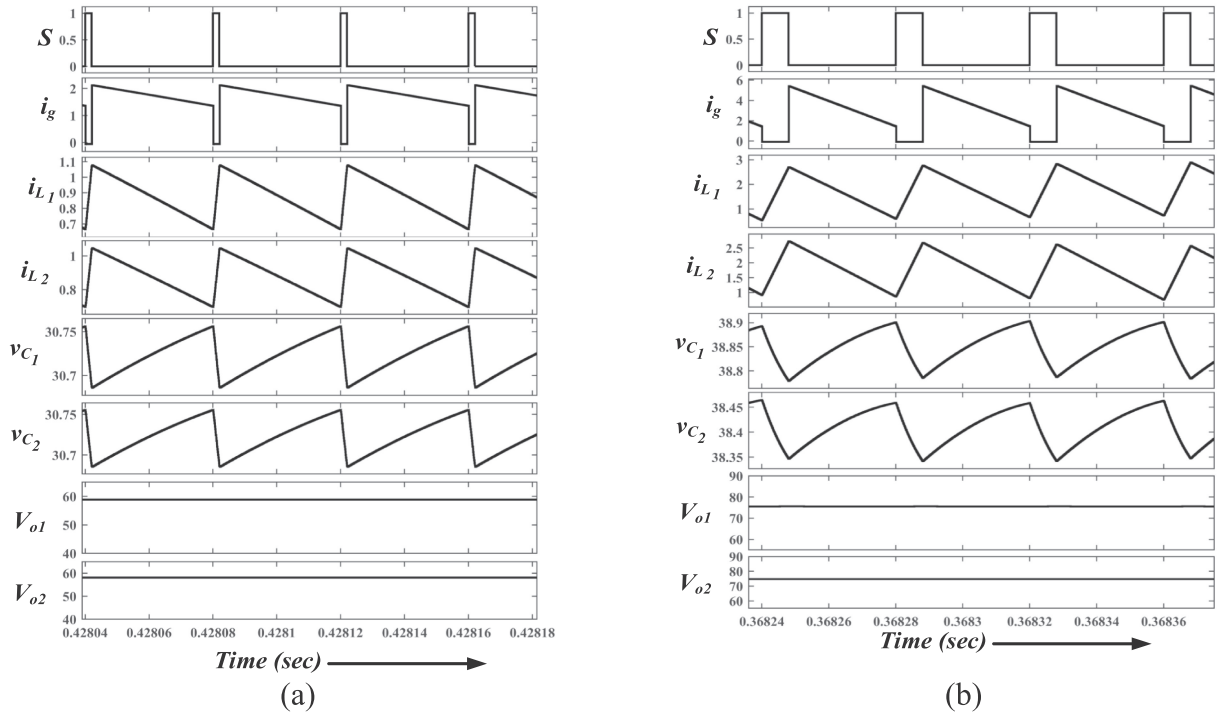

FIGURE 9 | Open-loop simulation results at (a) $D = 0.05$ *and* $R_1 = R_2 = 150\Omega$,(b) $D = 0.2$ and $R_1 = R_2 = 150\Omega$.

across C_1 and C_2, increase and decrease linearly over time.

In the Z-source, network symmetry is maintained, leading to the conclusion of the following equations:

$$\begin{cases} i_{L1} \neq i_{L2}, & i_{C1} \neq i_{C2} \\ v_{L1} \neq v_{L2} & v_{C1} \neq v_{C2} \end{cases} \tag{2}$$

where $i_{L1}, v_{L1}, i_{L2}, v_{L2}, i_{C1}, v_{C1}, i_{C2}$, and v_{C2} are the currents and voltages of L_1, L_2, C_1, and C_2 respectively.

4.1 | Dynamic Operation and Analysis

The proposed converter operates in continuous conduction mode (CCM) and can be described into two distinct states: Modes 1 and 2. The expected waveforms of the proposed converter are depicted in Figure 8.

1. In Mode 1, demonstrated by the equivalent circuit in Figure 7a, switch S and diode D_2 are in the ON state, while diode D_1 is OFF. Let DT represent the duration of Mode 1 within a switching cycle T, where $D > 0$ denotes the duty

1097007x, 0, Downloaded from https://onlinelibrary.wiley.com/doi/10.1002/cta.4369 by Delhi Technological University, Wiley Online Library on [27/11/2024]. See the Terms and Conditions (https://onlinelibrary.wiley.com/terms-and-conditions) on Wiley Online Library for rules of use; OA articles are governed by the applicable Creative Commons License

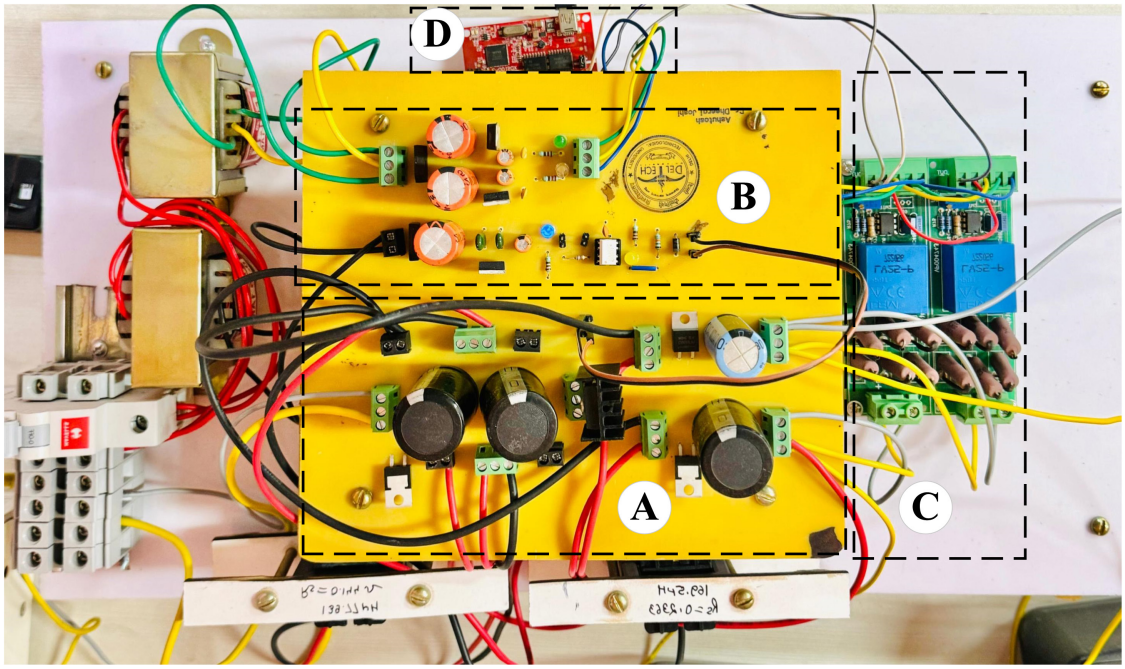

FIGURE 10 | Prototypes of the proposed converter and control board where (A) proposed SIDO converter, (B) control circuit, (C) sensor board, and (D) TMS320F28379D control board.

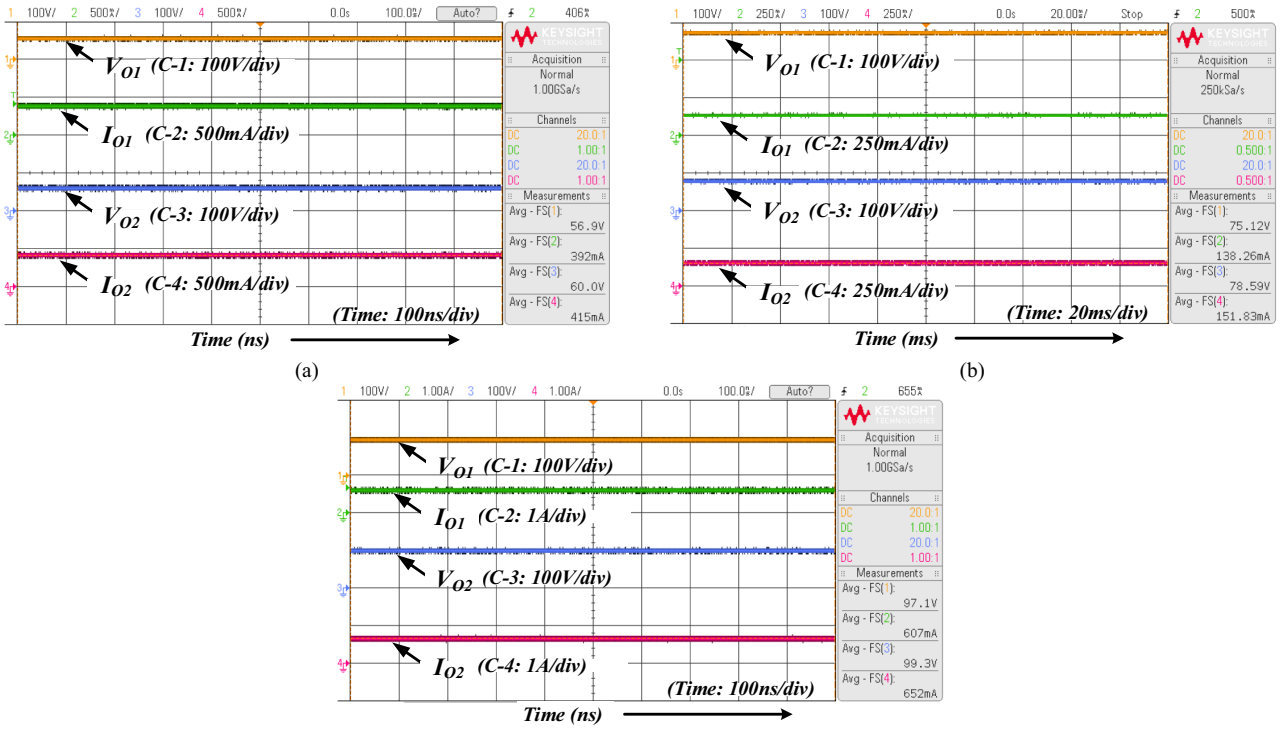

FIGURE 11 | Experimental result of proposed converter at (a) $D = 0.05$ and $R = 150\Omega$, (b) $D = 0.2$ and $R = 450\Omega$, (c) $D = 0.3$ and $R = 150\Omega$.

cycle of S. This state encompasses three loops: Loop 1 comprises L_1, C_1, and$S$, where C_1 discharges energy into L_1;

2. Loop 2 encompasses L_2, C_2, and S, with C_2 discharging energy into L_2;
3. Loop 3 involves $C_1, C_2, D_2, D_3, C_3, C_4, R_1$, and R_2. Here, $C_1$and C_2 discharge energy into C_3, C_4, R_1, and R_2.

In Mode 1, the following equations can be derived:

$$v_{L1} = v_{C1} = L_1\left(\frac{di_{L1}}{dt}\right) \tag{3}$$

$$v_{L2} = v_{C2} = L_2\left(\frac{di_{L2}}{dt}\right) \tag{4}$$

1097007x, 0, Downloaded from https://onlinelibrary.wiley.com/doi/10.1002/cta.4369 by Delhi Technological University, Wiley Online Library on [27/11/2024]. See the Terms and Conditions (https://onlinelibrary.wiley.com/terms-and-conditions) on Wiley Online Library for rules of use; OA articles are governed by the applicable Creative Commons License

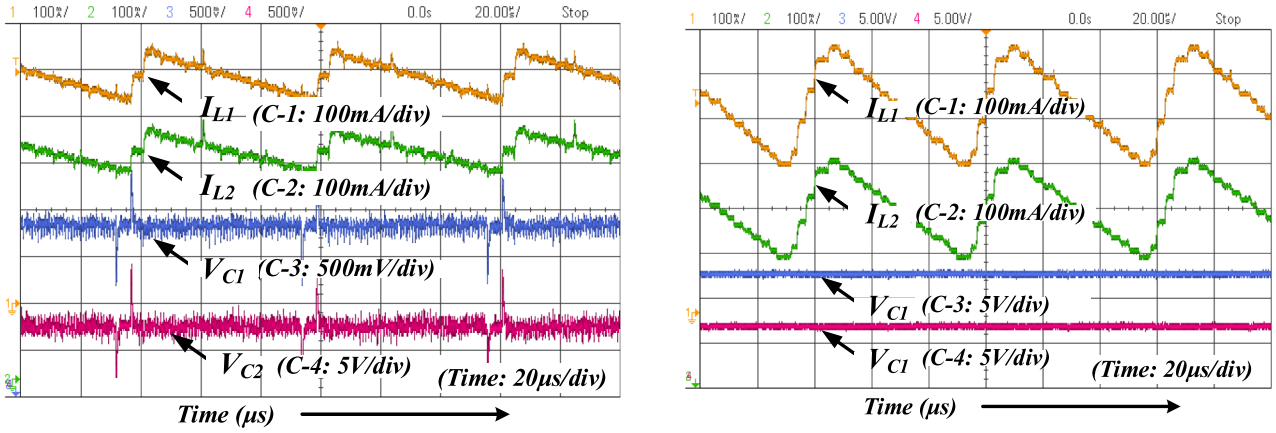

(a) (b)

FIGURE 12 | Experimental waveform of inductor currents and capacitor voltages at (a) $D = 0.05$, (b) $D = 0.2$.

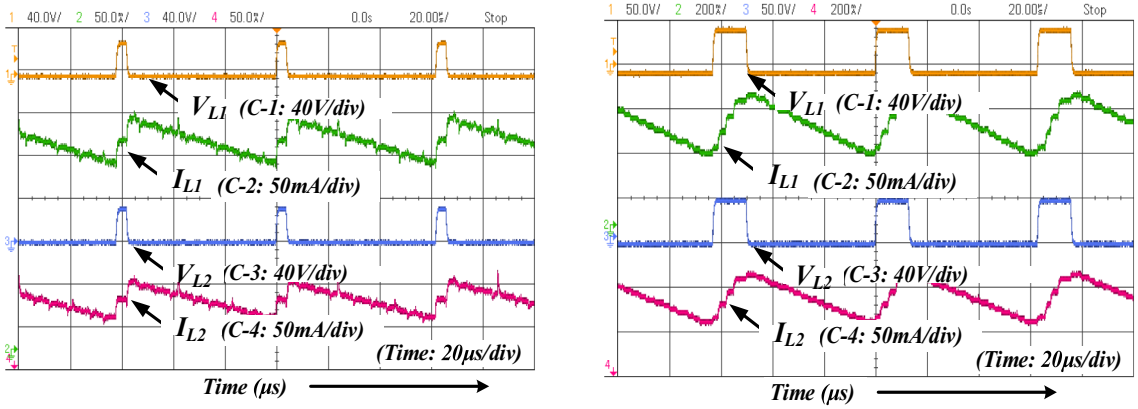

(a) (b)

FIGURE 13 | Experimental waveform of inductor voltages and currents at (a) $D = 0.05$, (b) $D = 0.2$.

$$V_{o1} = V_{o2} = v_{L1} + v_{C1} = v_{L2} + v_{C2} \tag{5}$$

$$i_{C1} = -\left(i_{L1} + \frac{V_{o1}}{R_1} + \frac{V_{o2}}{R_2}\right) \tag{6}$$

$$i_{C2} = -\left(i_{L2} + \frac{V_{o1}}{R_1} + \frac{V_{o2}}{R_2}\right) \tag{7}$$

1. In Mode 2, shown by the equivalent circuit in Figure 7b. Mode 2 of the proposed converter is characterized by switch S and diode D_2 being OFF, while diode D_1 is ON. Assuming that $(1-D)T$ represents the duration of Mode 2 within a switching cycle T, this mode encompasses four loops: Loop 1 consists of L_1, C_2, D_1, and S, where input sources V_g and L_1 discharge energy into C_2;
2. Loop 2 involves L_2, C_1, D_1, and S, with input sources V_g and L_2 discharging energy into C_1;
3. Loop 3 includes C_3 and R_1, where C_3 releases energy to the load R_1;
4. Loop 4 comprises C_4 and R_2, where C_4 releases energy to the load R_2.

In Mode 2, the following equations can be derived:

$$V_g = v_{L1} + v_{C1} = L_1\left(\frac{di_{L1}}{dt}\right) + v_{C1} \tag{8}$$

$$V_g = v_{L1} + v_{C1} = L_1\left(\frac{di_{L1}}{dt}\right) + v_{C1} \tag{9}$$

$$i_g = i_{L1} + i_{C1} = i_{L1} + C_1\left(\frac{dv_{C1}}{dt}\right) \tag{10}$$

$$i_g = i_{L2} + i_{C2} = i_{L2} + C_2\left(\frac{dv_{C2}}{dt}\right) \tag{11}$$

$$i_{C3} = C_3\left(\frac{dv_{C3}}{dt}\right) = \frac{V_{o1}}{R_1} \tag{12}$$

$$i_{C4} = C_4\left(\frac{dv_{C4}}{dt}\right) = \frac{V_{o2}}{R_2} \tag{13}$$

1097007x, 0, Downloaded from https://onlinelibrary.wiley.com/doi/10.1002/cta.4369 by Delhi Technological University, Wiley Online Library on [27/11/2024]. See the Terms and Conditions (https://onlinelibrary.wiley.com/terms-and-conditions) on Wiley Online Library for rules of use; OA articles are governed by the applicable Creative Commons License

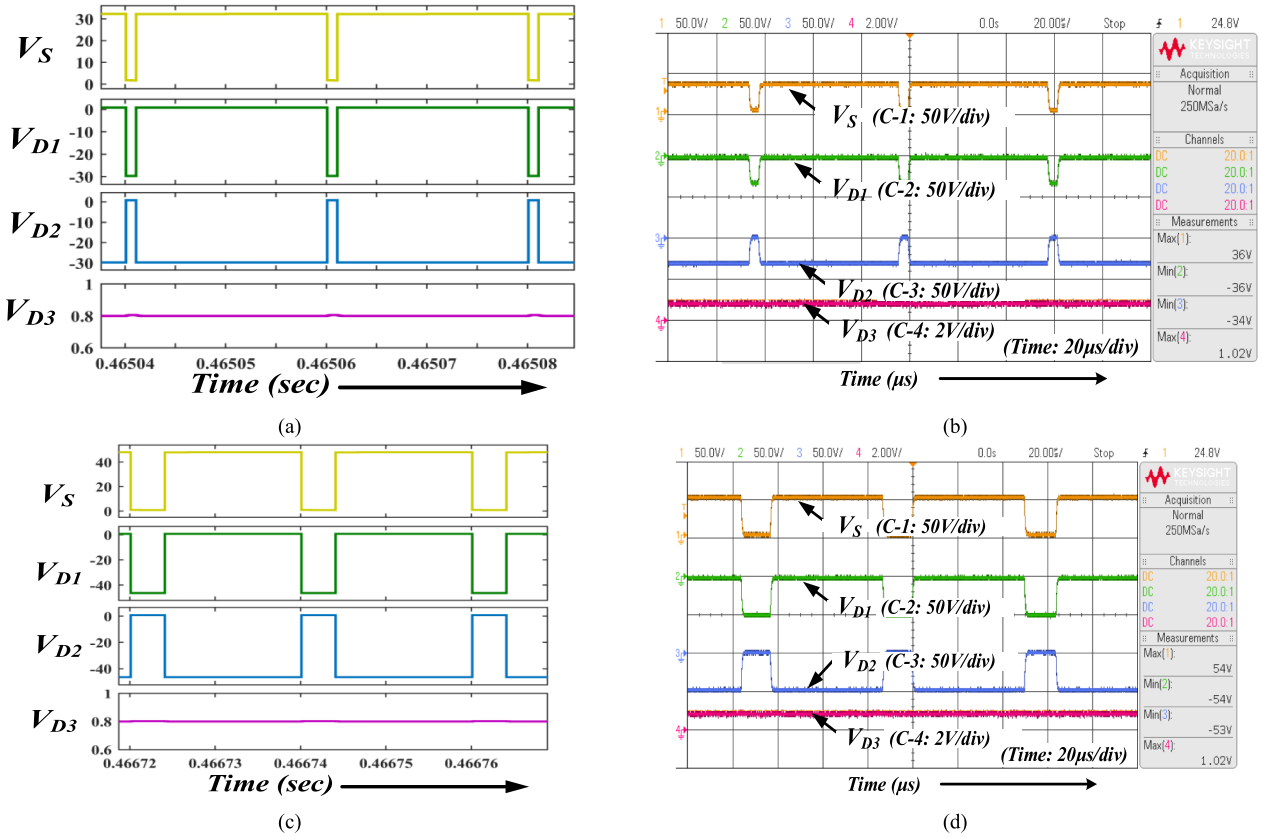

FIGURE 14 | Experimental waveform of switch S and diodes D_1, D_2, andD_3 voltage stress at (a) $D = 0.05$, (b) $D = 0.2$.

4.2 | Steady-State Analysis

In steady state [33–35], the average voltage across an inductor within a switching cycle T is zero; hence, we obtain

$$\frac{1}{T}\int_0^T v_{L1}dt = 0 \tag{14}$$

By substituting Equations (3) and (8) into Equation (14), we can derive the following equation:

$$\frac{1}{T}\int_0^T v_{L1}dt = \frac{1}{T}\left[\int_0^{DT} v_{C1}dt + \int_{DT}^{(1-D)T}\left(V_g - v_{C1}\right)dt\right] = 0 \tag{15}$$

Since the capacitors C_1 and C_2 are sufficiently large, the voltage across C_1 and C_2 changes linearly, allowing us to obtain their average voltages.

$$V_{C1} = \frac{1}{T}\int_0^{DT} v_{C1}dt = \frac{1}{T}\int_{DT}^{T} v_{C1}dt \tag{16}$$

By substituting (16) into Equation (15), we obtain the following:

$$V_{C1}DT + \left(V_g - V_{C1}\right)(1 - DT) = 0 \tag{17}$$

On simplifying,

$$V_{C1} = \frac{1-D}{1-2D}V_g \tag{18}$$

Substituting (18) into (5), the output voltage V_{o1} and V_{o2} is

$$V_{o1} = V_{o2} = 2V_{C1} = \frac{2(1-D)}{1-2D}V_g \tag{19}$$

Hence, the relationship between the voltage gain$G$ and the duty cycle D can be expressed as follows:

$$G = = \frac{2(1-D)}{1-2D} \tag{20}$$

The equation suggests that the duty cycle D ranges from 0 to 0.5. With $M > 2$, the voltage gain is high when the duty cycle approaches 0.5.

Assuming ideal conditions for the proposed converter and operating in CCM, we have

$$V_g I_g = V_{o1}I_{o1} + V_{o2}I_{o2} \tag{21}$$

where $I_o = I_{o1} + I_{o2}$ and I_g and I_o are the input and output average currents, respectively.

1097007x, 0, Downloaded from https://onlinelibrary.wiley.com/doi/10.1002/cta.4369 by Delhi Technological University, Wiley Online Library on [27/11/2024]. See the Terms and Conditions (https://onlinelibrary.wiley.com/terms-and-conditions) on Wiley Online Library for rules of use; OA articles are governed by the applicable Creative Commons License

Substituting (19) into (21), the average input current I_g is given by the following:

$$I_g = \frac{1-D}{1-2D} I_o \tag{22}$$

The voltages and currents of components are shown in Tables 8 and 9, respectively.

4.3 | Cost Analysis of the Proposed SIDO Converter

The subsequent step involves determining the cost of the proposed converter with Configuration 22.

Based on Table 10, the total cost of the proposed converter, after subtracting the controller cost, amounts to \$21.4899. Since efficiency of proposed converter is very high ($> 95\%$), very high-voltage gain (> 4.5), less voltage stress and providing two equal outputs instead of one, high cost may be justified.

5 | Verification and Results

The validity of the proposed converter topologies has been confirmed through numerical simulations conducted using MATLAB's Simulink. The simulation parameters can be chosen based on the specifications outlined in Table 3.

The simulation depicted in Figure 9a,b demonstrates various waveforms: the switch S's driven voltage, the source current i_g, the inductor currents L_1 and L_2, the capacitor voltages C_1 and C_2, and the output voltagesV_{o1} and V_{o2}. It is apparent that the converter operates in CCM and exhibits two different states at a duty cycle of 0.5 and 0.2 with $R_1 = R_2 = 150$, respectively.

In the simulation results depicted in Figure 9a, when the duty cycle is set to 0.05, the output voltages measure 59.7 and 58.6 V, whereas the expected values are 60 V each. Similarly, with a duty cycle change to 0.2 in Figure 9b, the output voltages are 76.5 and 75.8 V, respectively, deviating slightly from the desired 80 V for each. The simulation closely aligns with the theoretical analysis, with differences primarily attributed to diode forward voltage drops.

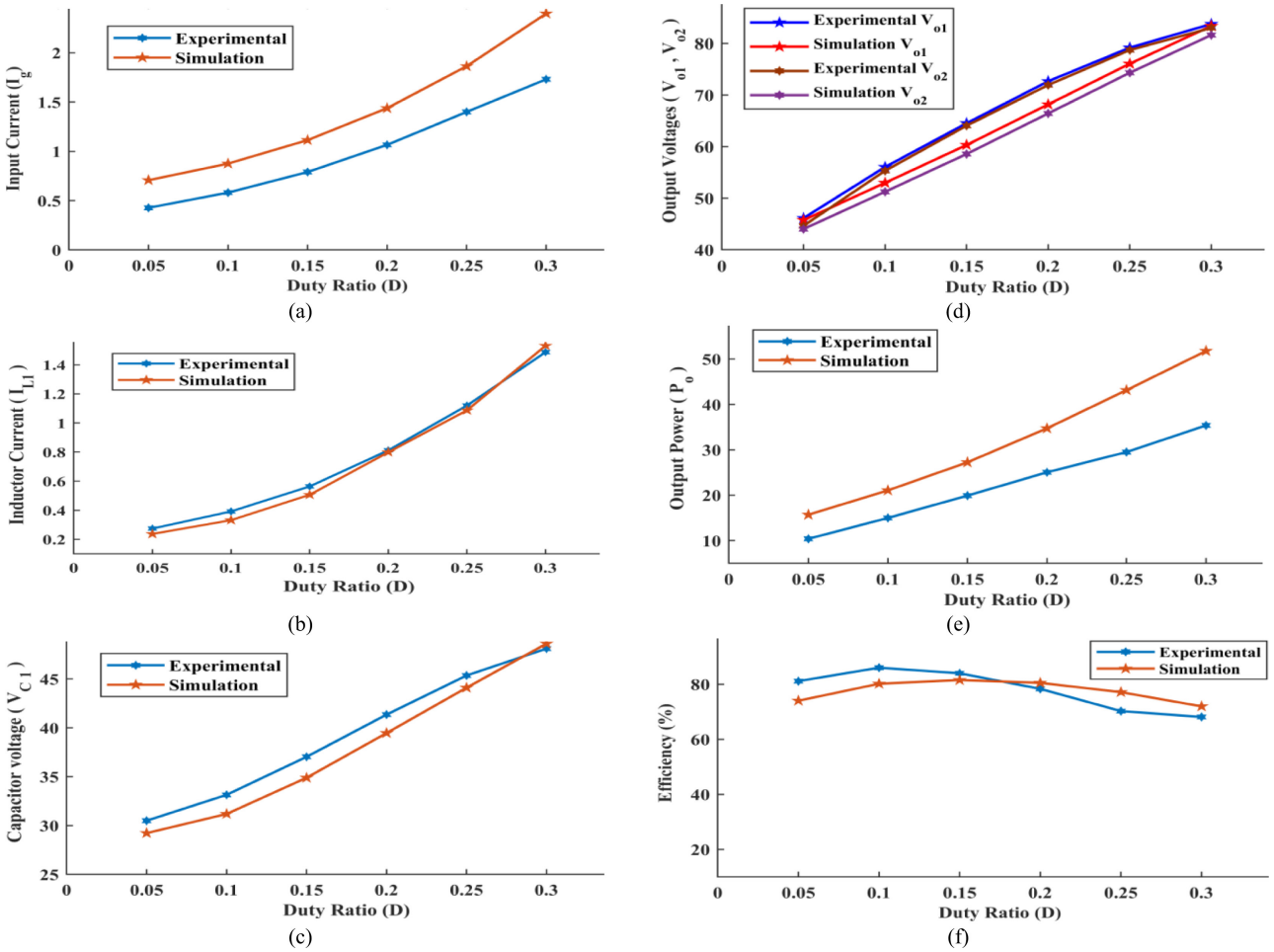

FIGURE 15 | Experimental comparisons of proposed converter w.r.t. duty ratio at $R_1 = R_2 = 450\Omega$ of (a) input current, (b) inductor current, (c) capacitor voltage, (d) output voltages, (e) output power, (f) efficiency.

1097007x, 0, Downloaded from https://onlinelibrary.wiley.com/doi/10.1002/cta.4369 by Delhi Technological University, Wiley Online Library on [27/11/2024]. See the Terms and Conditions (https://onlinelibrary.wiley.com/terms-and-conditions) on Wiley Online Library for rules of use; OA articles are governed by the applicable Creative Commons License

A 48-W prototype of the proposed SIDO converter is fabricated to validate its operational principles, shown in Figure 10. The experiment employs parameters outlined in Table 3.

The switch S, employing IRFP260N, is driven by an isolated amplifier (TLP350), with MUR860 diodes utilized for $D_1, D_2,$ and D_3. The switch S has an ON resistance of 40 $m\Omega$, while the forward voltage drops of the diodes are 0.7 V. Experimental waveforms, obtained when the proposed converter is powered by a regulated DC source, are depicted in Figures 11–14. Specifically, Figure 11a–c shows experimental output voltage and current waveforms at duty cycles of 0.05, 0.2, and 0.3, respectively.

Figure 11a shows the experimental waveforms of the proposed converter at a duty cycle $D = 0.05$. The measured values of the output voltages V_{o1} and V_{o2} are 56.9 and 60 V, respectively, with output currents I_{o1} and I_{o2} at 150Ω resistive load recorded as 392 and 415 mA, respectively, whereas the desired values are 60 V for both voltages and 400 mA each for current. Figure 11b displays the experimental waveforms at $D = 0.2$, with measured values of V_{o1} and V_{o2} at 75.12 and78.59 V, respectively, and output currents I_{o1} and I_{o2} at450Ω resistive load recorded as 138.26 and151.83 mA, respectively, whereas the desired values are 80V for both voltages and 177.7 mA each for current. Figure 11c demonstrates the experimental waveforms at $D = 0.3$, with measured values of V_{o1} and V_{o2} at 97.1V and 99.3V, respectively, and output currents I_{o1} and I_{o2} at 150Ω resistive load recorded as 607 and652 mA, respectively, whereas the desired values are 100 V for both voltages and 666.6 mA each for current.

Figure 12 shows the experimental waveforms of inductor currents $(I_{L1} and\ I_{L2})$ and capacitor voltages $(V_{C1}$ and $V_{C2})$ at two different duty cycles $D = 0.05$ and $D = 0.2$. The measured values as shown in Figure 12a of the average inductor currents I_{L_1} and I_{L_2} are 488.72 and 487.99 mA, respectively, with average capacitor voltages V_{C_1} and V_{C_2} recorded as 32.25 and32.2 V, respectively, at 150Ω resistive load and $D = 0.05$. The measured values of the average inductor currents I_{L_1} and I_{L_2} are 929.13 and 926.62 mA, respectively, with average capacitor voltages V_{C_1} and V_{C_2} recorded as 40.5 and 40.42 V, respectively, at 150Ω resistive load and $D = 0.2$.

Figure 13 shows the experimental waveforms of inductor voltages $(V_{L1}$ and $V_{L2})$ and inductor currents $(I_{L1}$ and $I_{L2})$ at two different duty cycles $D = 0.05$ and $D = 0.2$. Figure 13a shows maximum voltage measured on inductors is 32 V each at 150Ω resistive load and $D = 0.05$. Similarly, maximum voltage measured on inductors is 43 V each at 150Ω resistive load and $D = 0.2$ which is shown in Figure 13b.

Figure 14 presents a comparative analysis of voltage stress on switch S and diodes ($D_1, D_2,$ and D_3.), both through simulation and experimental waveform. A close similarity is observed between the simulation and hardware results for voltage stresses. The maximum stress observed on the switch is 36 V experimentally, while in simulation, the stress observed is 32 V for a duty cycle of 0.05, as shown in Figure 14a,b. Similarly, the maximum stress observed on the switch is 54 V experimentally, whereas in simulation, the stress observed is 49 V for a duty cycle of 0.2, as shown in Figure 14c,d.

Figure 15 presents both experimental and simulated outcomes for the proposed SIDO converter based on the Z-source. By varying the duty cycle, the impact on parameters such as input current, inductor current, capacitor voltage stress, output voltage, output power, and efficiency is examined. The close difference between experimental and simulated results validates the proposed approach, contribution understandings for the development of additional configurations as outlined in Table 1. Despite some alterations, the experimental results align closely with the simulation results, validating the features of the proposed converter and accounting for component losses. Variations between simulation and experimental data are primarily due to the forward voltage drop of diodes and the equivalent series resistance (ESR) of each device.

6 | Conclusion

This article researches into the topological properties and interrelationships of SIDO high-gain Z-source converter structures, focusing on three fundamental sections: IP, Z-source network, and OP, serving as the building blocks for converter topologies. By integrating voltage or current types of source/loads to different terminals of these basic cells, various DC–DC converters can be constructed. The study introduces a converter and its methodology for selecting the topology of common ground/noncommon ground Z-Source DC–DC SIDO, offering improved operational factors. Compared to conventional Z-source SISO converters, it provides high-voltage gain and simultaneous CG/NCG outputs, making it advantageous for EV and isolated micro grid applications. The proposed converters undergo analysis and comparison for various configurations, with configurations offering equal output voltages selected for potential use in multilevel inverter applications. Assessment includes maximum efficiency, voltage stress on components, inductor current, and ripples under different loads and duty cycles. With ongoing research on converter topologies, this article aims to enhance understanding of existing converter relationships and stimulate innovation in new topological developments and applications.

Conflicts of Interest

The authors declare no conflicts of interest.

Data Availability Statement

Data sharing is not applicable to this article as no datasets were generated or analyzed during the current study.

References

1. D. Tamilselvan and T. D. Sudhakar, "Optimizing Renewable Energy Utilization With High Gain Converters," *Renewable and Sustainable Energy Reviews* 191 (2024): 114105, ISSN 1364-0321, https://doi.org/10.1016/j.rser.2023.114105.

2. A. Turksoy, A. Teke, and A. Alkaya, "A Comprehensive Overview of the DC-DC Converter-Based Battery Charge Balancing Methods in Electric Vehicles," *Renewable and Sustainable Energy Reviews* 133 (2020): 110274, ISSN 1364-0321, https://doi.org/10.1016/j.rser.2020.110274.

1097007x, 0, Downloaded from https://onlinelibrary.wiley.com/doi/10.1002/cta.4369 by Delhi Technological University, Wiley Online Library on [27/11/2024]. See the Terms and Conditions (https://onlinelibrary.wiley.com/terms-and-conditions) on Wiley Online Library for rules of use; OA articles are governed by the applicable Creative Commons License

3. M. Rasouli, M. Mehrasa, A. Ganjavi, M. S. Sadabadi, H. Ghoreishy, and A. Ale Ahmad, "Lyapunov-Based Control Strategy for a Single-Input Dual-Output Three-Level DC/DC Converter," *IEEE Transactions on Industrial Electronics* 70, no. 10 (2023): 10486–10495, https://doi.org/10.1109/TIE.2022.3217610.

4. A. Kolli, A. Gaillard, A. De Bernardinis, O. Bethoux, D. Hissel, and Z. Khatir, "A Review on DC/DC Converter Architectures for Power Fuel Cell Applications," *Energy Conversion and Management* 105 (2015): 716–730,ISSN 0196-8904,, https://doi.org/10.1016/j.enconman.2015.07.060.

5. B. Mangu, S. Akshatha, D. Suryanarayana, and B. G. Fernandes, "Grid Connected PV-Wind-Battery-Based Multi-Input Transformer-Coupled Bidirectional DC-DC Converter for Household Applications," *IEEE Journal of Emerging and Selected Topics in Power Electronics* 4, no. 3 (2016): 1086–1095, https://doi.org/10.1109/JESTPE.2016.2544789.

6. J. Deng, H. Wang, and M. Shang, "A ZVS Three-Port DC/DC Converter for High-Voltage Bus-Based Photovoltaic Systems," *IEEE Transactions on Power Electronics* 34, no. 11 (2019): 10688–10699, https://doi.org/10.1109/TPEL.2019.2895976.

7. H. Krishnaswami and N. Mohan, "Three-Port Series-Resonant DC–DC Converter to Interface Renewable Energy Sources With Bidirectional Load and Energy Storage Ports," *IEEE Transactions on Power Electronics* 24, no. 10 (2009): 2289–2297, https://doi.org/10.1109/TPEL.2009.2022756.

8. A. Affam, Y. M. Buswig, A.-K. B. H. Othman, N. B. Julai, and A. Ohirul Qays, "Review of Multiple Input DC-DC Converter Topologies Linked With Hybrid Electric Vehicles and Renewable Energy Systems," *Renewable and Sustainable Energy Reviews* 135 (2021): 110186, ISSN 1364-0321, https://doi.org/10.1016/j.rser.2020.110186.

9. P. Prabhakaran and V. Agarwal, "Novel Four-Port DC–DC Converter for Interfacing Solar PV–Fuel Cell Hybrid Sources With low-Voltage Bipolar DC Microgrids," *IEEE Journal of Emerging and Selected Topics in Power Electronics* 8, no. 2 (2020): 1330–1340, https://doi.org/10.1109/JESTPE.2018.2885613.

10. P. Mohseni, S. H. Hosseini, M. Sabahi, T. Jalilzadeh, and M. Maalandish, "A New High Step-Up Multi-Input Multi-Output DC–DC Converter," *IEEE Transactions on Industrial Electronics* 66, no. 7 (2019): 5197–5208, https://doi.org/10.1002/cta.4234.

11. G. Ashutosh and J. Dheeraj, "Mathematical Modeling and Stress-Aware Stability Analysis of a Nonideal Multiport Single Inductor DC–DC Converter for Renewable Energy," *International Journal of Circuit Theory and Applications* 12 (2024): 83–91, https://doi.org/10.1109/TSTE.2020.2983985.

12. M. R. Al-Soeidat, H. Aljarajreh, H. A. Khawaldeh, D.D.-C. Lu, and J. Zhu, "A Reconfigurable Three-Port DC–DC Converter for Integrated PV Battery System," *IEEE Journal of Emerging and Selected Topics in Power Electronics* 8, no. 4 (2020): 3423–3433, https://doi.org/10.1109/JESTPE.2019.2941595.

13. A. Nahavandi, M. T. Hagh, M. B. B. Sharifian, and S. Danyali, "A Nonisolated Multiinput Multioutput DC–DC Boost Converter for Electric Vehicle Applications," *IEEE Transactions on Power Electronics* 30, no. 4 (2015): 1818–1835, https://doi.org/10.1109/TPEL.2014.2325830.

14. A. A. Saafan, V. Khadkikar, M. S. El Moursi, and H. H. Zeineldin, "A New Multiport DC-DC Converter for DC Microgrid Applications," in *2021 IEEE Industry Applications Society Annual Meeting (IAS)* (Vancouver, BC, Canada: IEEE, 2021): 1–7, https://doi.org/10.1109/IAS48185.2021.9677403.

15. A. Shahin, B. Huang, J. P. Martin, S. Pierfederici, and B. Davat, "New Non-Linear Control Strategy for Non-Isolated DC/DC Converter With High Voltage Ratio," *Energy Conversion and Management* 51, no. 1 (2010): 56–63, ISSN 0196-8904,, https://doi.org/10.1016/j.enconman.2009.08.032.

16. H. Zhang, D. Dong, M. Jing, W. Liu, and F. Zheng, "Topology Derivation of Multiple-Port DC–DC Converters Based on Voltage-Type Ports," *IEEE Transactions on Industrial Electronics* 69, no. 5 (2022): 4742–4753, https://doi.org/10.1109/TIE.2021.3078389.

17. I. Ninma Jiya, H. Van Khang, N. Kishor, and R. M. Ciric, "Novel Family of High-Gain Nonisolated Multiport Converters With Bipolar Symmetric Outputs for DC Microgrids," *IEEE Transactions on Power Electronics* 37, no. 10 (2022): 12151–12166, https://doi.org/10.1109/TPEL.2022.3176688.

18. R. Liu, G. Zhou, Q. Tian, and G. Xu, "Extendable Multiport High Step-Up DC–DC Converter for Photovoltaic-Battery Systems With Reduced Voltage Stress on Switches/Diodes," *IEEE Transactions on Industrial Electronics* 70, no. 9 (2023): 9123–9135, https://doi.org/10.1109/TIE.2022.3206752.

19. H. Behjati and A. Davoudi, "Power Budgeting Between Diversified Energy Sources and Loads Using a Multiple-Input Multiple-Output DC-DC Converter," in *49th IEEE/IAS Industrial & Commercial Power Systems Technical Conference* (GA, USA: Stone Mountain, 2013): 1–12, https://doi.org/10.1109/ICPS.2013.6547333.

20. Z. Saadatizadeh, P. C. Heris, E. Babaei, and M. Sabahi, "A New Nonisolated Single-Input Three-Output High Voltage Gain Converter With Low Voltage Stresses on Switches and Diodes," *IEEE Transactions on Industrial Electronics* 66, no. 6 (2019): 4308–4318, https://doi.org/10.1109/TIE.2018.2864710.

21. F. Z. Peng, "Z-Source Inverter," *IEEE Transactions on Industry Applications* 39, no. 2 (2003): 504–510, https://doi.org/10.1109/TIA.2003.808920.

22. Y. Tang, S. Xie, and C. Zhang, "An Improved Z-Source Inverter," *IEEE Transactions on Power Electronics* 26, no. 12 (2011): 3865–3868, https://doi.org/10.1109/TPEL.2009.2039953.

23. O. Ellabban and H. Abu-Rub, "An Overview for the Z-Source Converter in Motor Drive Applications," *Renewable and Sustainable Energy Reviews* 61 (2016): 537–555, ISSN 1364-0321,, https://doi.org/10.1016/j.rser.2016.04.004.

24. Y. Tang, S. Xie, and C. Zhang, "Single-Phase Z-Source Inverter," *IEEE Transactions on Power Electronics* 26, no. 12 (2011): 3869–3873, https://doi.org/10.1109/TPEL.2009.2039955.

25. M. Zhu, K. Yu, and F. L. Luo, "Switched Inductor Z-Source Inverter," *IEEE Transactions on Power Electronics* 25, no. 8 (2010): 2150–2158, https://doi.org/10.1109/TPEL.2010.2046676.

26. H. Shen, B. Zhang, D. Qiu, and L. Zhou, "A Common Grounded Z-Source DC–DC Converter With High Voltage Gain," *IEEE Transactions on Industrial Electronics* 63, no. 5 (2016): 2925–2935, https://doi.org/10.1109/TIE.2016.2516505.

27. H. Shen, B. Zhang, and D. Qiu, "Hybrid Z-Source Boost DC–DC Converters," *IEEE Transactions on Industrial Electronics* 64, no. 1 (2017): 310–319, https://doi.org/10.1109/TIE.2016.2607688.

28. M. Abbasi Shahabi, M. Mardaneh, A. Rajaei, A. Nabinezhad, E. Jamshidpour, and P. Poure, "Symmetric Wide-Input-Voltage Range Boost Z-Source DC–DC Converter With Reduced Current of Source and Active Components," *IEEE Transactions on Power Electronics* 38, no. 8 (2023): 9961–9971, https://doi.org/10.1109/TPEL.2023.3270239.

29. S. Rostami, V. Abbasi, and M. Parastesh, "Design and Implementation of a Multiport Converter Using Z-Source Converter," *IEEE Transactions on Industrial Electronics* 68, no. 10 (2021): 9731–9741, https://doi.org/10.1109/TIE.2020.3022538.

30. X. L. Li, C. K. Tse, and D.D.-C. Lu, "Single-Inductor Multi-Input Multi-Output DC-DC Converter With High Flexibility and Simple Control," in *2020 IEEE International Symposium on Circuits and Systems (ISCAS)* (Seville, Spain: IEEE, 2020): 1–5, https://doi.org/10.1109/ISCAS45731.2020.9180788.

1097007x, 0, Downloaded from https://onlinelibrary.wiley.com/doi/10.1002/cta.4369 by Delhi Technological University, Wiley Online Library on [27/11/2024]. See the Terms and Conditions (https://onlinelibrary.wiley.com/terms-and-conditions) on Wiley Online Library for rules of use; OA articles are governed by the applicable Creative Commons License

31. H. Behjati and A. Davoudi, "A Multiple-Input Multiple-Output DC–DC Converter," *IEEE Transactions on Industry Applications* 49, no. 3 (2013): 1464–1479, https://doi.org/10.1109/TIA.2013.2253440.

32. M. Salimi, F. Radmand, and M. H. Firouz, "Dynamic Modeling and Closed-Loop Control of Hybrid Grid-Connected Renewable Energy System With Multi-Input Multi-Output Controller," *Journal of Modern Power Systems and Clean Energy* 9, no. 1 (2021): 94–103, https://doi.org/10.35833/MPCE.2018.000353.

33. S. Urooj, D. Joshi, A. Gupta, and A. BaQais. 2024. "Derivation Analysis and Control of Multiport Flyback Converter with Lyapunov Function-Based Controller in Renewable Energy Systems Considering Circuit Parasitics," *Arabian Journal for Science and Engineering*, https://doi.org/10.1007/s13369-024-09493-6.

34. T. Gupta, A. Gupta, and D. Joshi. 2023. "Stability Analysis and Control of Non-Ideal SEPIC Converters Using Leverrier's Algorithm and PI Controller Considering Parasitic Elements," *2023 3rd International Conference on Emerging Frontiers in Electrical and Electronic Technologies (ICEFEET)*, 1–6, https://doi.org/10.1109/icefeet59656.2023.10452208.

35. T. Gupta, A. Gupta, D. Joshi, and M. A. Mallick. 2023. "Stability Analysis and Optimization of a Parasitic Buck Converter Using Leverrier's Algorithm and PI Controller," *2023 9th IEEE India International Conference on Power Electronics (IICPE)*, https://doi.org/10.1109/iicpe60303.2023.10474949.

1097007x, 0, Downloaded from https://onlinelibrary.wiley.com/doi/10.1002/cta.4369 by Delhi Technological University, Wiley Online Library on [27/11/2024]. See the Terms and Conditions (https://onlinelibrary.wiley.com/terms-and-conditions) on Wiley Online Library for rules of use; OA articles are governed by the applicable Creative Commons License

2024 International Conference on Electrical Electronics and Computing Technologies (ICEECT) | 979-8-3503-7809-2/24/$31.00 ©2024 IEEE | DOI: 10.1109/ICEECT61758.2024.10739076

Metaheuristics Approaches Towards Secure and Optimized Routing in IoT: A Systematic Literature Review

Rohit Beniwal
Dept. of Computer Science & Engg.
Delhi Technological University
New Delhi, India
rohitbeniwal@dtu.ac.in

Vinod Kumar
Dept. of Computer Science & Engg.
Delhi Technological University
New Delhi, India
k_vinod70@hotmail.com

Vishal Sharma
Dept. of Computer Science & Engg.
Delhi Technological University
New Delhi, India
vishalmtr@gmail.com

***Abstract*— Metaheuristics are versatile and can be used as a team intelligence solution in today's optimization complex problems. These algorithmic structures offer the capability to find solutions to optimization problems and decentralized algorithms, such as IoT routing and security. IoT is a network composed of objects that can communicate with one another in the IP world. However, this composition of objects presents various challenges, including efficient routing due to the heterogeneous nature of the network and security requirements. Thus, achieving routing security becomes crucial for maintaining the IoT network and prolonging its lifetime. This paper focuses on metaheuristics algorithms by investigating nature-inspired, swarm intelligence and other types of optimization techniques referenced in the literature. The paper also explores routing security and performance attributes associated with metaheuristics algorithms and provides an exhaustive review of secure routing across different heuristics techniques for the robust operation of the IoT network. Additionally, it discusses potential challenges and future directions for integrating metaheuristics solutions in the rapidly evolving IoT landscape.**

Keywords*— *Internet of things, routing, security, metaheuristics, classifications

I. Introduction

The Internet of Things (IoT) represents a rapidly growing technology where the interconnectivity of nodes plays a pivotal role in intelligent environments [1]. Such an environment will include pervasive connectivity requiring significant measures to protect against routing attacks in data transmission. The evolution of IoT has brought about many improvements in the connectivity of physical objects for data transmission in networks. Data transmission integrity and reliability in IoT devices have always been challenging due to their limited processing capabilities and energy constraints that are susceptible to various network layer attacks, such as Black Hole, Sinkhole, and Wormhole attacks [2]. The need for more resources like storage and power presents a significant challenge in IoT networks. Early sensor energy depletion in IoT reduces network lifespan, and disrupted communication at network nodes leads to frequent routing adjustments. Recent research uses various heuristics to find the best ways to solve these problems.

Heuristic algorithms rely more on the specific problem they are applied to than metaheuristic algorithms [3]. These algorithms are limited to particular specific challenges. In contrast, meta-heuristic algorithms can be applied to nearly any optimization issue due to their utilization of the black box optimizer [4]. Such algorithms play a crucial role in solving complex problems, with characteristics such as self-organization and decentralized as integral components alongside team intelligence [5]. These integrates intelligent behaviour observed for solving complex problems of physical phenomenon in nature, leveraging the interactions between living beings to establish problem solving approach at various group levels. Heuristics approaches are one of the best practices to enhance routing and security in IoT networks. IoT devices are expected to counteract various attacks for secure and reliable communication; therefore, robust heuristic methods are to be utilized in routing and security. Heuristic approaches, known for their problem-solving capabilities, especially in pervasive environments, are particularly suitable for addressing the routing security challenges in IoT networks. In IoT, it is essential to understand the security of IoT networks against evolving intricacies of network layer attacks. Such mechanisms require developing innovative strategies to mitigate such threats effectively by blocking harmful and undesired traffic.

This research paper focuses on exploring metaheuristics for routing and security in IoT by conducting a systematic literature review on the work of recent algorithms for IoT networks. By analysing existing studies and research, the review seeks to identify common metaheuristics techniques used and the corresponding algorithms employed to counteract IoT routing security threats. This study will thoroughly examine these metaheuristics, delving into the particular algorithm employed, their classification, and the security service they present. This study primarily focuses on nature and non-nature inspired metaheuristics.

A. Review Planning

This review provides insights into the recent advances in Metaheuristics used for routing design and the work of different metaheuristics algorithms for IoT network security. The Internet of Things is a relatively new discipline compared to M2M and ubiquitous computing. We will, therefore, present a review based on the metaheuristics approaches of the previous five years (2019–2024). An online search was conducted for the articles on the IEEE Xplore, WoS, and Elsevier's platforms.

Driven by the optimized solutions of heuristics in IoT routing security, our study aims to explore the following:

979-8-3503-7809-2/24/$31.00 ©2024 IEEE

Authorized licensed use limited to: DELHI TECHNICAL UNIV. Downloaded on November 09,2024 at 04:36:09 UTC from IEEE Xplore. Restrictions apply.

- RQ1: Which metaheuristic algorithms are used for secure routing?
- RQ2: What attributes of secure communication are focussed in heuristics?
- RQ3: Which are the metrics used to evaluate metaheuristic algorithms for secure and optimized routing?

In order to provide the recent advances in metaheuristics techniques for IoT routing and security, first, a concise review of recent metaheuristics techniques for IoT routing and security is given along with the methodologies and key findings, and then the metaheuristics algorithms and their classification is presented.

The rest of the article is arranged as follows: Section II provides a detailed literature review of recent metaheuristics techniques for IoT routing and security. Section III summarizes our results and addresses the above research issues; Section IV concludes with challenges and future directions.

II. Recent Metaheuristics Techniques for IoT Routing Security

Solutions to IoT security challenges through heuristics have recently received much attention in the literature. Summary (Table I) presents the review of papers on metaheuristic solutions that have come up in recent years. Considering these recent studies, it is essential to comprehend how metaheuristic approaches might provide the routing and security solutions of ever-growing IoT networks.

[6] aimed to secure routes with less energy spent in IoT. For this, they utilize genetic algorithm-based crossover for biometric authentication. The result was improved security through fingerprint-based unique value and energy-efficient routing. Their proposed algorithm provided a potential model for securing IoT networks while maintaining energy efficiency.

[7] focused on avoiding malicious network analysis in IoT networks by modifying the network topology using closeness centrality. The authors utilized greedy and simulated annealing algorithms and developed update closeness and fast top-rank algorithms for efficient computation of closeness value/rank, demonstrating the efficiency of pruning algorithms in reducing computational time. They outperformed baseline algorithms and are computationally efficient.

[8] proposed a novel model for providing security to IoT-based WSNs employing the CM-MH algorithm and the Improved Blowfish algorithm. They successfully achieved better security and efficient routing, demonstrating the effectiveness of the CM-MH model in IoT-based WSNs. Their approach was superior to other approaches regarding security, efficiency, and energy conservation in WSNs.

[9] used deep learning and improved transient search optimization to make intruder detection for IoT. CNN is used for feature extraction. An intrusion detection method was successfully implemented inside the Internet of Things framework, incorporating deep learning with an enhanced optimization technique for IoT security.

[10] developed a method to monitor IoT networks using an energy-based link system. The authors utilized a metaheuristic algorithm to improve WCVC solution quality and find optimal solutions in small-size instances.

[11] proposed an approach to protect IoT data using primes and compressive sensing in WSNs based on IoT, utilizing prime number properties for efficient clustering and routing and combining the CS method with the RSA algorithm for security and data compression. Their technique enhances power efficiency in IoT-enabled WSNs, provides load balancing and high security, and introduces an adept reconstruction algorithm to significantly improve data restoration, ensuring efficient and secure data gathering and reconstruction.

[12] designed an effective IDS for IoT networks, combining the GSO algorithm and PCA for IDS using the NSL-KDD dataset. Compared to other methods, it has better precision, detection rate, memory, accuracy, and FAR, providing an effective solution for recognizing various attacks on IoT and enhancing network performance.

[13] proposed making clear and well-organized healthcare tracking systems that protect healthcare department information using cloud computing and IoT. IoT smart appliances and metaheuristic swarm intelligence are used in a hybrid system to store data. Their technique provided effective clinical healthcare solutions and data protection using blockchain.

[14] proposed a GA-based energy optimization procedure for intelligent IoT applications using a Genetic Algorithm (GA) for optimization. The authors focused on the intelligent Internet of Vehicles, integrating IoT with vehicular networks for improved performance in IoT applications through energy optimization.

[15] proposed a technique for medical treatment based on a genetic algorithm that makes energy-efficient clustering protocols in heterogeneous WSNs. The authors discussed various clustering protocols and approaches for energy management in WSNs, highlighting the importance of clustering protocols in enhancing WSNs' energy efficiency. They emphasized the need for effective clustering protocols for sustainable and efficient WSNs.

[16] proposed a method to identify botnet attacks in IoT with classification using the MFFO algorithm and a CNN-QRNN mixed model to find botnets for high performance in botnet attack detection and classification.

[17] proposed an optimal cluster head selection model that is more energy-efficient and safe in the WSN framework. The model was effective regarding residual energy, throughput, and delay based on various restrictions, utilizing the SWFU-CMO method.

[18] proposed HHO, an effective centralized and distributed model for detecting smart IoT device attacks. HHO was used to find IoT botnet attacks and improve RWN and FS for finding IoT hacking attacks.

[19] proposed a blockchain and deep learning technique with bio-inspired clustering for safe transportation in WSNs to increase security and optimize performance by decreasing latency, minimizing packet loss, and enhancing energy efficiency.

Authorized licensed use limited to: DELHI TECHNICAL UNIV. Downloaded on November 09,2024 at 04:36:09 UTC from IEEE Xplore. Restrictions apply.

Table I: METAHEURISTICS CLASSIFICATION

Article	Algorithms	Metaheuristics Classification			
		Evolutionary Algorithms	Swarm Intelligence	Local Search	Other Metaheuristics
[6]	Genetic Algorithm	√			
[7]	Simulated Annealing			√	
[8]	Crossover Mutated Marriage in Honey Bee Algorithm		√		
[9]	Differential Evolution	√			
[10]	Genetic Algorithm	√			
[11]	Bees and Genetic Algorithm	√			
[12]	Glow-worm Swarm Optimization algorithm		√		
[13]	Firefly algorithm		√		
[14]	Genetic Algorithm	√			
[15]	Genetic Algorithm	√			
[16]	Modified Firefly Optimization and Chaotic Butterfly Optimization Algorithm	√			
[17]	Cat and Mouse Optimization		√		
[18]	Harris Hawks Optimization		√		
[19]	Tasmanian Devil Optimization				√
[20]	Fire Hawk Optimizer				√
[21]	Grey Wolf Optimization Algorithm and Binary Gravitational Search Algorithm		√		
[22]	Improved Spotted Hyena Optimization		√		
[23]	Polarity Learning-based Chimp Optimization Algorithm		√		
[24]	Genetic Algorithm	√			
[25]	Whale optimization Algorithm		√		
[26]	Hill Climbing Algorithm				√

[20] suggested a Fire Hawk optimizer algorithm to provide security optimization, demonstrating efficiency in network security over other methods.

[21] reviewed feature selection techniques for cybersecurity and emphasized the role of wrapper-based feature selection techniques in improving detection accuracy in cybersecurity models.

[22] proposed a protocol called BONY-ISHO, combining blockchain technology, a hybrid Blowfish-Honey cryptographic technique, and the Improved Spotted Hyena Optimization algorithm to provide secure and authenticated clustering, data protection and optimized data routing to enhance the security and efficiency of clustering and data routing for IoT systems in smart cities. BONY-ISHO protocol demonstrated superiority in security, efficiency, and energy conservation compared to traditional methods and is highly effective in addressing security and efficiency challenges in IoT-based WSNs, offering a comprehensive enhancement of network security and data transmission efficiency in the context of smart cities.

[23] proposed a multi-level secure method to enhance IoT-WSN routing using the PL-COA algorithm and multi-level trust evaluations. The authors achieved high routing performance with minimal energy consumption and increased network security, indicating the effectiveness of the methodology in diverse IoT-WSN applications and environments.

[24] developed a novel mitigation algorithm to prevent black hole attacks in the IoT using a solution creating a list of authentic nodes, monitoring packet forwarding, and dynamically updating routing tables. Their strategy significantly improved throughput and PDR, closely resembling the performance of an unaffected network.

[25] proposed an efficient key management system using a whale optimization algorithm and Two-Fish-based 128-bit cryptographic key management for IoT to enhance secure data transfer cybersecurity strategy for maritime applications.

Authorized licensed use limited to: DELHI TECHNICAL UNIV. Downloaded on November 09,2024 at 04:36:09 UTC from IEEE Xplore. Restrictions apply.

Table II: SECURITY SERVICES

Article	Confidentiality	Authentication	Data Integrity	Non-Repudiation
[6]	√	√	√	
[7]	√			
[8]	√	√		
[9]			√	
[10]			√	
[11]	√		√	
[12]			√	
[13]	√	√	√	√
[14]		√		
[15]			√	
[16]	√	√	√	√
[17]		√		
[18]		√	√	
[19]	√	√	√	
[20]		√	√	
[21]	√		√	
[22]	√	√	√	
[23]	√	√	√	
[24]	√	√	√	√
[25]	√		√	
[26]	√	√	√	

[26] proposed a smart IoT agriculture system Using direct trust computation and metaheuristics-based optimal route discovery for smart agricultural sensors. The Authors demonstrated significant improvement over other methods with improved performance and reliability of smart agricultural networks using an intelligent optimization model.

III. Results of the Systematic Literature Review

A. Metaheuristics algorithms and their types for routing and security in IoT

This section mainly classifies various metaheuristic algorithms, what researchers have used, and answers RQ1. The exploration and effective implementation of metaheuristics techniques frequently necessitate examining the classification of metaheuristics algorithms. Algorithms like nature-inspired and non-nature metaheuristics provide the fundamentals for optimized solutions to routing and security in IoT networks. To thoroughly comprehend these algorithms, this review classifies them according to their specific class, such as nature inspired and non-nature inspired metaheuristics. Nature-inspired metaheuristics algorithms (Table I) have garnered much attention due to their theory of natural selection, collective intelligence, behavior of living organisms, and decentralized and self-organized.

B. Attributes of secure communication

This section answers RQ2 to recognize attributes of secure communication that are focussed in studied research papers. As heuristics algorithms play a vital role in IoT routing and security due to selecting optimal solutions in resource-constrained nodes, reducing the risk of routing attacks throughout data exchange among routing nodes is an important issue.

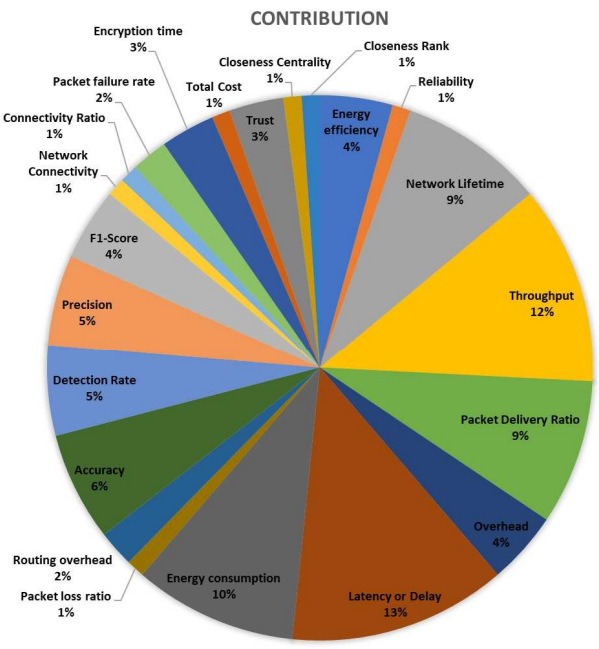

Fig 1: Metrics contribution in searched literature

Authorized licensed use limited to: DELHI TECHNICAL UNIV. Downloaded on November 09,2024 at 04:36:09 UTC from IEEE Xplore. Restrictions apply.

Table III: METRICS EVALUATION

Metrics	Article
Energy efficiency	[10] [11] [15] [20]
Reliability	[15]
Network Lifetime	[11] [13] [14] [15] [17] [19] [20] [22]
Throughput	[8] [13] [14] [15] [17] [19] [20] [22] [23] [24] [25]
Packet Delivery Ratio	[13] [14] [15] [19] [22] [23] [24] [26]
Overhead	[13] [14] [15] [19]
Latency or Delay	[6] [8] [13] [14] [15] [17] [19] [20] [22] [23] [25] [26]
Energy consumption	[6] [8] [13] [17] [19] [22] [23] [25] [26]
Packet loss ratio	[25]
Routing overhead	[20] [25]
Accuracy	[9] [12] [16] [18] [20] [21]
Detection Rate	[12] [13] [20] [21] [23]
Precision	[9] [12] [16] [18] [21]
F1-Score	[9] [16] [18] [21]
Network Connectivity	[10]
Connectivity Ratio	[6]
Packet failure rate	[6] [20]
Encryption time	[6] [8] [22]
Total Cost	[8]
Trust	[8] [17] [23]
Closeness Centrality	[7]
Closeness Rank	[7]

This section explores the attributes in the domain literature to achieve an optimal level of security. Based on the metaheuristic's algorithms adapted by various researchers for routing security, the literature studied can be largely categorized into the security services. Table II illustrates the various security services incorporated in the referenced metaheuristics studies, as well as their implementation in the study.

Figure 1 shows the utilization of the various performance metrics in the referenced literature from 2019 to 2024. The top five metrics of interest are delay, throughput, energy consumption, PDR, and network lifetime, with contributions of 13%, 12%, 10%, 9%, and 9%, respectively.

C. *Performance metrics for evaluation*

This section answers RQ3 to recognize standard metrics for evaluating metaheuristic algorithms in secure and optimized routing. The network's superior performance during IoT routing depends on the metaheuristics algorithms. Various performance metrics used for evaluation also provide the basis for comparison between heuristics. Thus, research focuses on evaluating various metrics in algorithms so that performance evaluation is successfully completed to demonstrate the optimized result. Table III contains the list of metrics used in referenced studies.

IV. Challenges and Future Directions

The potential of approximation methods in solving optimization problems is contingent upon achieving a solution in a reasonable time. Its exploration and exploitation, which provide Metaheuristics with search space and advanced learning techniques, are the essence of its dominance. However, finding a good enough solution is fraught with domain-specific knowledge of the natural phenomena at a measure commensurate with exploring an ample search space of complex problems. Recognizing the dynamic relationship between random nature and the best solution is important. Designing or developing complex problem heuristics can impact computational expenses, tuning of parameters, and optimality. Achieving metaheuristics NP-hard problem solutions in the polynomial time region calls for a profound understanding of both the approximation methods and the complexities of various problem types. The approximation methods wherein metaheuristics-based algorithms operate introduce their own set of challenges. Addressing the given large-scale problems becomes a paramount concern, necessitating optimized solutions that can uphold the performance of metaheuristics to achieve the desired success rate. The development of self-adaptive metaheuristics, capable of concurrently exploring, presents the dynamic adoption of control parameters tuning in learning mechanisms and flexible solutions.

References

[1] S. J. Jazebi and A. Ghaffari, 'RISA: routing scheme for Internet of Things using shuffled frog leaping optimization algorithm', *Journal of Ambient Intelligence and Humanized Computing*, vol. 11, pp. 4273–4283, 10 2020.

[2] H. HaddadPajouh, A. Dehghantanha, R. M. Parizi, M. Aledhari, and H. Karimipour, 'A survey on internet of things security: Requirements, challenges, and solutions', *Internet of Things (Netherlands)*, vol. 14, 6 2021.

[3] A. Tzanetos and G. Dounias, 'Nature inspired optimization algorithms or simply variations of metaheuristics?', *Artificial Intelligence Review*, vol. 54, pp. 1841–1862, 3 2021.

[4] V. Sharma and A. K. Tripathi, 'A systematic review of meta-heuristic algorithms in IoT based application', *Array*, vol. 14, 7 2022.

[5] A. E. Ezugwu *et al.*, 'Metaheuristics: a comprehensive overview and classification along with bibliometric analysis', *Artificial Intelligence Review*, vol. 54, pp. 4237–4316, 8 2021.

[6] J. K. Jain, 'Secure and Energy-Efficient Route Adjustment Model for Internet of Things', *Wireless Personal Communications*, vol. 108, pp. 633–657, 9 2019.

[7] J. Ji, G. Wu, J. Shuai, Z. Zhang, Z. Wang, and Y. Ren, 'Heuristic approaches for enhancing the privacy of the leader in IoT networks', *Sensors (Switzerland)*, vol. 19, 9 2019.

[8] M. Alotaibi, 'Improved Blowfish Algorithm-Based Secure Routing Technique in IoT-Based WSN', *IEEE Access*, vol. 9, pp. 159187–159197, 2021.

[9] A. Fatani, M. A. Elaziz, A. Dahou, M. A. A. Al-Qaness, and S. Lu, 'IoT Intrusion Detection System Using Deep Learning and Enhanced Transient Search Optimization', *IEEE Access*, vol. 9, pp. 123448–123464, 2021.

[10] Z. A. Dagdeviren, 'Weighted Connected Vertex Cover Based Energy-Efficient Link Monitoring for Wireless Sensor Networks towards

Authorized licensed use limited to: DELHI TECHNICAL UNIV. Downloaded on November 09,2024 at 04:36:09 UTC from IEEE Xplore. Restrictions apply.

Secure Internet of Things', *IEEE Access*, vol. 9, pp. 10107–10119, 2021.

[11] A. Salim, W. Osamy, A. M. Khedr, A. Aziz, and M. Abdel-Mageed, 'A secure data gathering scheme based on properties of primes and compressive sensing for IoT-Based WSNs', *IEEE Sensors Journal*, vol. 21, pp. 5553–5571, 2 2021.

[12] C. Anusha, A. Sravani, J. Anusha, C. Lakshmi, and G. S. Kumari, 'Intrusion detection system in IoT network by using metaheuristic algorithm with machine learning dimensional reduction technique', in *2022 3rd International Conference on Computing, Analytics and Networks (ICAN)*, Rajpura, Punjab, India, 2022.

[13] A. K. Jain, D. S. Ross, M. K. Babu, Dharamvir, D. Uike, and D. Gangodkar, 'Cloud computing applications for protecting the information of healthcare department using smart internet of things appliance', in *2022 5th International Conference on Contemporary Computing and Informatics (IC3I)*, Uttar Pradesh, India, 2022.

[14] Z. E. Ahmed *et al.*, 'Optimization Procedure for Intelligent Internet of Things Applications', in *2022 International Conference on Business Analytics for Technology and Security (ICBATS)*, 2022, pp. 1–6.

[15] S. Singh, A. S. Nandan, G. Sikka, A. Malik, and A. Vidyarthi, 'A secure energy-efficient routing protocol for disease data transmission using IoMT', *Computers and Electrical Engineering*, vol. 101, 7 2022.

[16] L. Almuqren, H. Alqahtani, S. S. Aljameel, A. S. Salama, I. Yaseen, and A. A. Alneil, 'Hybrid Metaheuristics With Machine Learning Based Botnet Detection in Cloud Assisted Internet of Things Environment', *IEEE Access*, vol. 11, pp. 115668–115676, 2023.

[17] M. Biradar and B. Mathapathi, 'Energy, Reliability, and Trust-Based Security Framework for Clustering-Based Routing Model in WSN', *International Journal of Information Security and Privacy*, vol. 17, 2023.

[18] N. Hijazi, M. Aloqaily, B. Ouni, F. Karray, and M. Debbah, 'Harris hawks feature selection in distributed machine learning for secure IoT environments', in *ICC 2023 - IEEE International Conference on Communications*, Rome, Italy, 2023.

[19] K. H. V. Prasad and S. Periyasamy, 'Secure-Energy Efficient Bio-Inspired Clustering and Deep Learning-Based Routing Using Blockchain for Edge Assisted WSN Environment', *IEEE Access*, vol. 11, pp. 145421–145440, 2023.

[20] M. Hosseinzadeh *et al.*, 'A cluster-based trusted routing method using fire hawk optimizer (FHO) in wireless sensor networks (WSNs)', *Scientific Reports*, vol. 13, 12 2023.

[21] A. K. Dey, G. P. Gupta, and S. P. Sahu, 'A metaheuristic-based ensemble feature selection framework for cyber threat detection in IoT-enabled networks', *Decision Analytics Journal*, vol. 7, 6 2023.

[22] V. Sharma, R. Beniwal, and V. Kumar, 'Towards secure IoT system from a smart city perspective: An optimized algorithm and implementation', *Transactions on Emerging Telecommunications Technologies*, vol. 35, 4 2024.

[23] V. Sharma, R. Beniwal, and V. Kumar, 'Multi-level trust-based secure and optimal IoT-WSN routing for environmental monitoring applications', *The Journal of Supercomputing*, vol. 80, pp. 11338–11381, 5 2024.

[24] I. A. Reshi, S. Sholla, and Z. A. Najar, 'Safeguarding IoT networks: Mitigating black hole attacks with an innovative defense algorithm', *Journal of Engineering Research (Kuwait)*, vol. 12, pp. 133–139, 3 2024.

[25] A. Maharajan and P. Kumar, 'Whale optimized routing path selection and 128 bit secured key management for maritime safety', *International Journal of Naval Architecture and Ocean Engineering*, vol. 16, 1 2024.

[26] A. Rehman, I. Abunadi, K. Haseeb, T. Saba, and J. Lloret, 'Intelligent and trusted metaheuristic optimization model for reliable agricultural network', *Computer Standards and Interfaces*, vol. 87, 1 2024.

Authorized licensed use limited to: DELHI TECHNICAL UNIV. Downloaded on November 09,2024 at 04:36:09 UTC from IEEE Xplore. Restrictions apply.

Modelling and TCAD Analysis of Plasma-Assisted Graphene Field Effect Transistor

Suresh C. Sharma[1], Monika Verma[1] and Sonam Rewari[2]
[1]Department of Applied Physics, Delhi Technological University, Delhi, India
[2]Department of Electronics and Communications, Delhi Technological University, Delhi, India
e-mail (speaker): prof_sureshsharma@dtu.ac.in

Numerous work on Carbon Nanotubes (CNTs) and Graphene aided semiconductor devices have been performed for the last two decades. This research aims to follow up on the recent advancements in the development of Graphene Field Effect Transistor (g-FET) produced using PECVD process. Similar analysis has been done by Kansal et al[2] focusing on CNT as the channel in the FET, underlying various relationships between the FET characteristics and the plasma parameters affecting theproduction of these FETs using PECVD. A device has been proposed, that'll be consisting of a 2D graphene sheet as the channel in a FET. Our goal is to illustrate the impact of plasma parameters on the performance of the designed device. Systematically analyzing the several properties of the proposed device. Lower plasma parameter values are crucial for achieving higher drain current, increased output conductance, and a lower cutoff frequency. Finding the optimal balance in plasma parameters is essential for peak device performance and efficiency. By adjusting these parameters, we can enhance the device's performance, making it well-suited for real-life applications, particularly in biosensing. Our simulated results are well alignedwith the existing experimental observations, validating the device's potential for practical use.

References

1. Suresh C. Sharma, Neha Gupta, Theoretical modeling of the plasma-assisted catalytic growth and field emission properties of graphene sheet. *Physics of Plasmas* **22**, 123517 (2015).
2. M. Kansal, Suresh C. Sharma, Plasma- based nanoarchitectonics for vertically aligned dual- metal carbon nanotube field-effect transistor (VA-DMCNFET) device: effect of plasma parameters on transistor properties. *Applied Physics A,**128***(1)**, 1-11 (2022).
3. A. Alarcon, V. Nguyen, S. Berrada, D. Querlioz, Pseudosaturation and negative differential conductance in graphene field-effect transistors, *IEEE Transactions on Electron Devices* **60(3)**, 985-991(2013).
4. A. Bechhofer, A. Ueda , A. Nipane, and J.T.Teherani, The 2D Debye length: An analytical study of weak charge screening in 2D semiconductors. *Journal of Applied Physics* **129(2)**, 024301(2021).
5. Sonam Rewari, V. Nath, S. Haldar, S. S. Deswal, and R. S. Gupta, Hafnium oxide based cylindrical junctionless double surrounding gate (CJLDSG) MOSFET for high speed, high frequency digital and analog applications. *Microsyst. Technol.* **25**,1527 (2017).

J Mater Sci

Chemical routes to materials

Molecularly imprinted polypyrrole decorated $Ti_3C_2T_x$ electrochemical sensor for highly selective and sensitive detection of levofloxacin

Divya Hudda[1] and Devendra Kumar[1,*]

[1] *Department of Applied Chemistry, Delhi Technological University, Delhi 110042, India*

Received: 18 April 2024
Accepted: 31 October 2024

© The Author(s), under exclusive licence to Springer Science+Business Media, LLC, part of Springer Nature, 2024

ABSTRACT

Herein, a rapid and efficient molecular imprinted polymer (MIP) modified $Ti_3C_2T_x$-based electrochemical sensing platform was developed for levofloxacin detection (LEV). The MIP sensor was designed by depositing the synthesized $Ti_3C_2T_x$ electrophoretically onto the indium tin oxide (ITO) glass surface, followed by electropolymerization of pyrrole as a monomer and LEV as a template molecule. $Ti_3C_2T_x$ significantly enhances the electron transfer rate and offers a larger surface area to increase the number of imprinted sites for precise recognition of LEV. The fabricated sensor (MIP/$Ti_3C_2T_x$/ITO), under all optimized parameters, demonstrated superior selectivity with a low detection limit (LOD) of 0.76 pM and a linear relationship with LEV concentration ranging (1 pM–100 nM). Additionally, this newly developed sensor exhibited robust stability and sensitivity and successfully detected LEV in actual samples with satisfactory outcomes.

Introduction

Levofloxacin (LEV) belongs to the third generation of fluoroquinolones that exhibits high antibacterial properties and is widely utilized in both human and veterinary medicine to treat pneumonia, gastroenteritis, infections in the urinary and respiratory tract, skin, and soft tissues [1–3]. However, long-term use of LEV often increases the risk of certain health problems, including tendon damage, heart diseases, immune suppression, muscle atrophy, and abdominal discomfort. Hence, there is a need to develop a highly sensitive and reliable method for monitoring the presence of LEV in medical, food, and environmental samples [4–6].

At present, various analytical techniques are used for LEV detection, including fluorimetry [7], flow-injection spectrophotometry [8], capillary electrophoresis [9], nuclear magnetic resonance [10], chemiluminescence [11] and high-performance liquid chromatography [12, 13]. Although these methods possess satisfactory results, even some demerits are associated with these techniques, such as costly equipment, extended analysis periods, low sensitivity, and complex sample preparation [14, 15]. In contrast, electrochemical sensors (ECS) have gained much interest due to their high sensitivity, fast response, easy operation, and low

Handling Editor: Pedro Camargo.

Address correspondence to E-mail: dkumar@dce.ac.in

https://doi.org/10.1007/s10853-024-10403-2
Published online: 27 November 2024

cost [16]. However, the accurate and reliable detection of LEV, among other fluoroquinolone antibiotics, remains a significant challenge.

To improve selectivity, ECS often utilizes natural receptors (antibodies, enzymes, and hormones) as specific recognition components. Nonetheless, the practical applications are impeded by their high cost, short shelf-life, deactivation susceptibility, and limited environmental tolerance. Therefore, artificial receptors are also incorporated into the electrochemical sensors [17–19]. Recently, Molecular imprinting polymers (MIPs) have emerged as favorable recognition components in ECSs due to their numerous imprinted cavities that possess shape, size, and functionalities resemblance to template molecules. This alignment facilitates the selective binding to the template molecules, ultimately improving overall selectivity [20–22]. Despite their selectivity capabilities, MIPs exhibit low sensitivity, incomplete template removal, and high diffusion barriers. These limitations restrict the number of available recognition sites [23]. Therefore, the supporting material with high surface area and excellent conductivity can extend the imprinted film, resulting in the generation of more imprinted cavities and thereby effectively enhancing the sensitivity [20].

The two-dimensional layered nanomaterials with transition metal carbides, nitrides, and carbonitrides ($Ti_3C_2T_x$) have recently attracted increasing attention due to its distinct advantages, including excellent electrical conductivity (2400 Scm^{-1}), high surface area (98 m^2g^{-1}), remarkable chemical stability, good hydrophilic surface and mechanical properties [24, 25]. These characteristics have led to the extensive applications of MXene in the fields of energy storage [26], electrochemical sensing [27], electromagnetic shielding [28], and electrocatalysis [29]. Conducting polymers have been utilized for the synthesis of MIPs for selective recognition and detection of different molecules [30]. Among the conducting polymers, polypyrrole (Ppy) is a suitable candidate for molecular imprinting sensors because of its unique properties of high conductivity, good stability, redox reversibility, environmental-friendly, and superb biocompatibility [31–33].

In this study, hydrothermally synthesized $Ti_3C_2T_x$ was initially deposited onto indium tin oxide (ITO) coated glass substrate using an electrophoretic deposition (EPD) technique, which was thus coupled with MIP through one-step electropolymerization for the fabrication of novel MIP electrochemical sensor (MIP/$Ti_3C_2T_x$/ITO) to detect the LEV. The prepared MIP layer offers high specificity for the detection of LEV, and $Ti_3C_2T_x$ was utilized to enhance the sensitivity of the electrochemical sensor. The constructed MIP electrochemical sensor exhibits excellent selectivity and reproducibility, and it was successfully employed for detecting the LEV in real samples with a satisfactory recovery range.

Experimental section

Materials and instrumentation

All chemicals and instrumentation details are discussed in the supporting information (S1).

Synthesis of $Ti_3C_2T_x$

$Ti_3C_2T_x$ was prepared using the hydrothermal method as per the previous report with little modification [34]. In brief, LiF (1 g) was dissolved in 20 mL HCl (6 M) with constant stirring for 30 min. Then, Ti_3AlC_2 (1 g) powder was added slowly to the above suspension and continuously stirred at room temperature for half an hour. The resultant suspension was poured into a 100 mL Teflon-lined autoclave for hydrothermal treatment at 180 °C for 16 h. The obtained precipitate was washed through DI water with centrifugation at 3500 rpm until the supernatant pH reached 6. Finally, the obtained MXene powder was dried in a vacuum oven at 60 °C for 12 h.

Electrophoretic deposition (EPD) of $Ti_3C_2T_x$ on ITO

To fabricate the electrode, $Ti_3C_2T_x$ was deposited electrophoretically on the pre-hydrolyzed ITO. Before deposition, $Ti_3C_2T_x$ (0.5 mg) was dispersed in DI water (15 mL) through ultrasonication to form a colloidal suspension. For EPD, a two-electrode system was utilized where platinum wire served as a reference electrode, placed 1 cm apart from the ITO (working electrode). For smooth deposition of the film, a DC potential of 10 V was applied for 8 s.

Fabrication of MIP/$Ti_3C_2T_x$/ITO

To prepare the MIP/$Ti_3C_2T_x$/ITO sensor, the modified electrode ($Ti_3C_2T_x$/ITO) was immersed in polymerization solution (0.1 M PBS, pH = 7) containing 0.4 mM LEV and 2 mM pyrrole monomer. Then, CV electropolymerization was carried out over the potential range of − 0.6–1.6 V at 50 mVs^{-1} with 10 consecutive cycles. Subsequently, the modified MIP electrode was stirred in the eluent solution comprising NaOH (0.2 M) and ethanol (V/V: 1:1) for 20 min to remove the embedded template molecules (LEV), then washed with DI water and dried at room temperature. Figure 1 represents the schematic approach used for the fabrication of MIP/$Ti_3C_2T_x$/ITO. Furthermore, the non-imprinted polymer-modified electrode (NIP/$Ti_3C_2T_x$/ITO) was prepared by using the same procedure as discussed above without adding LEV in the polymerization solution.

Results and discussion

Design of proposed MIP/$Ti_3C_2T_x$ /ITO sensor

In this work, a novel 2D-layered material $Ti_3C_2T_x$ is prepared by hydrothermal method (Fig. 1A). The surface of $Ti_3C_2T_x$ is terminated with different functional groups (—F, —OH, —O), resulting in high hydrophilicity and a large electrochemically active surface, which further enhances the analytical performance of the proposed sensor. For the fabrication of the MIP sensor, the synthesized $Ti_3C_2T_x$ is deposited electrophoretically on the ITO glass substrate (Fig. 1B). After that, pyrrole is electropolymerized onto the fabricated transducer surface, while LEV is trapped within the polymer by non-covalent interactions such as hydrogen bonds and electrostatic forces (Fig. 1C). Removal of the template molecule resulted in the formation of imprinting cavities that could specifically identify the LEV molecule (Fig. 1D). After adsorption, the template molecules fill up the more imprinted sites, leading to a decrease in current (Fig. 1E).

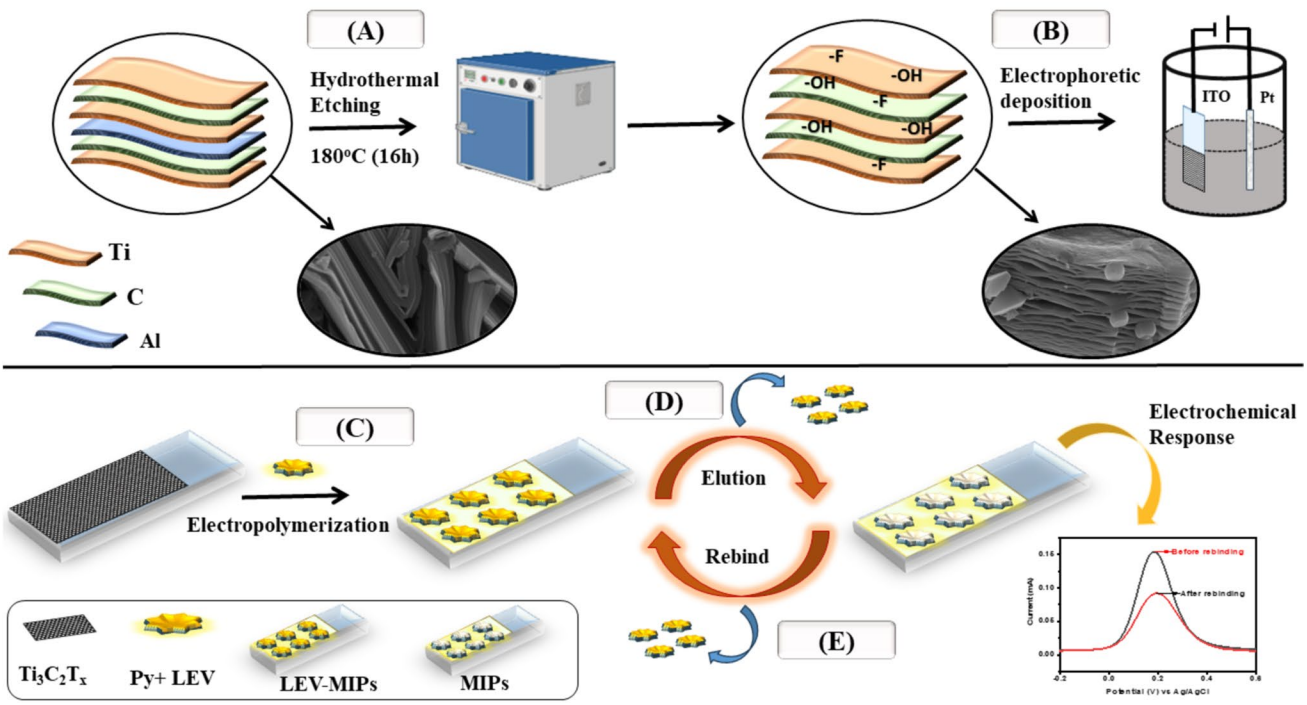

Figure 1 Schematic representation of LEV detection using a fabricated MIP/$Ti_3C_2T_x$/ITO electrode.

Structural and morphological characterization

Figure 2a represents the XRD spectra of Ti_3AlC_2 (black) and $Ti_3C_2T_x$ (red). For Ti_3AlC_2, the major diffraction peaks were observed at 9.5°, 34.1°, 39.0°, 41.9°, 48.5°, 56.4°, 60.3° and 65.3°. After hydrothermal treatment, the diffraction peak of Ti_3AlC_2 at 9.5° is broadened and shifted towards a lower 2θ angle of 6.1°, indicating the interlayer spacing of $Ti_3C_2T_x$ (13.9 Å) has been increased as compared to Ti_3AlC_2 (9.2 Å) [35]. Moreover, the diffraction peak of Ti_3AlC_2 at 39.0° has completely vanished in the spectra of $Ti_3C_2T_x$, suggesting that Al has been completely etched from Ti_3AlC_2. Figure S2 illustrates the FTIR spectra of $Ti_3C_2T_x$, which is used to examine the functional groups present on the surface of $Ti_3C_2T_x$. The bands observed at 1740, 1360, 1215, and 670 cm^{-1} can be ascribed to the stretching vibrations of C = O, O—H, C—F, and Ti—O, respectively [36].

The surface morphologies of Ti_3AlC_2, $Ti_3C_2T_x$, and polymerized electrodes are examined by FESEM. The SEM image of Ti_3AlC_2 illustrates a packed layered structure, as shown in Fig. 2b. After hydrothermal treatment, the morphology emerges an accordion-like 2D-multilayered structure as depicted in (Fig. 2c), illustrating 2D sheet-like MXene synthesized successfully. A smooth and uniform film of pyrrole on $Ti_3C_2T_x$/ITO was observed after electropolymerization in Fig. S3a. Further, on template extraction, the MIP/$Ti_3C_2T_x$/ITO exhibits a rough structure, as shown in Fig. S3b, suggesting the complete elution of the template from the polymer. Figure 2d and e represent the EDX spectra of Ti_3AlC_2 and $Ti_3C_2T_x$, respectively. In Fig. 2e, the absence of Al in $Ti_3C_2T_x$ in contrast to that of Ti_3AlC_2 from Fig. 2d confirms the successful synthesis of MXene.

Electrochemical studies of MIP/ $Ti_3C_2T_x$/ ITO

All the modified electrodes (Bare ITO, $Ti_3C_2T_x$/ITO, MIP/ $Ti_3C_2T_x$/ITO before elution, MIP/ $Ti_3C_2T_x$/ITO after elution, MIP/$Ti_3C_2T_x$/ITO after adsorption and NIP/ $Ti_3C_2T_x$/ITO) are examined electrochemically through cyclic voltammetry (CV) using $[Fe(CN)_6]^{3-/4-}$ as redox probe. As seen in Fig. 3a, bare ITO (curve i) exhibits a pair of reversible redox characteristic peaks with an electrochemical current of 0.28 mA. After being modified by $Ti_3C_2T_x$ (curve ii), the redox peak current increases

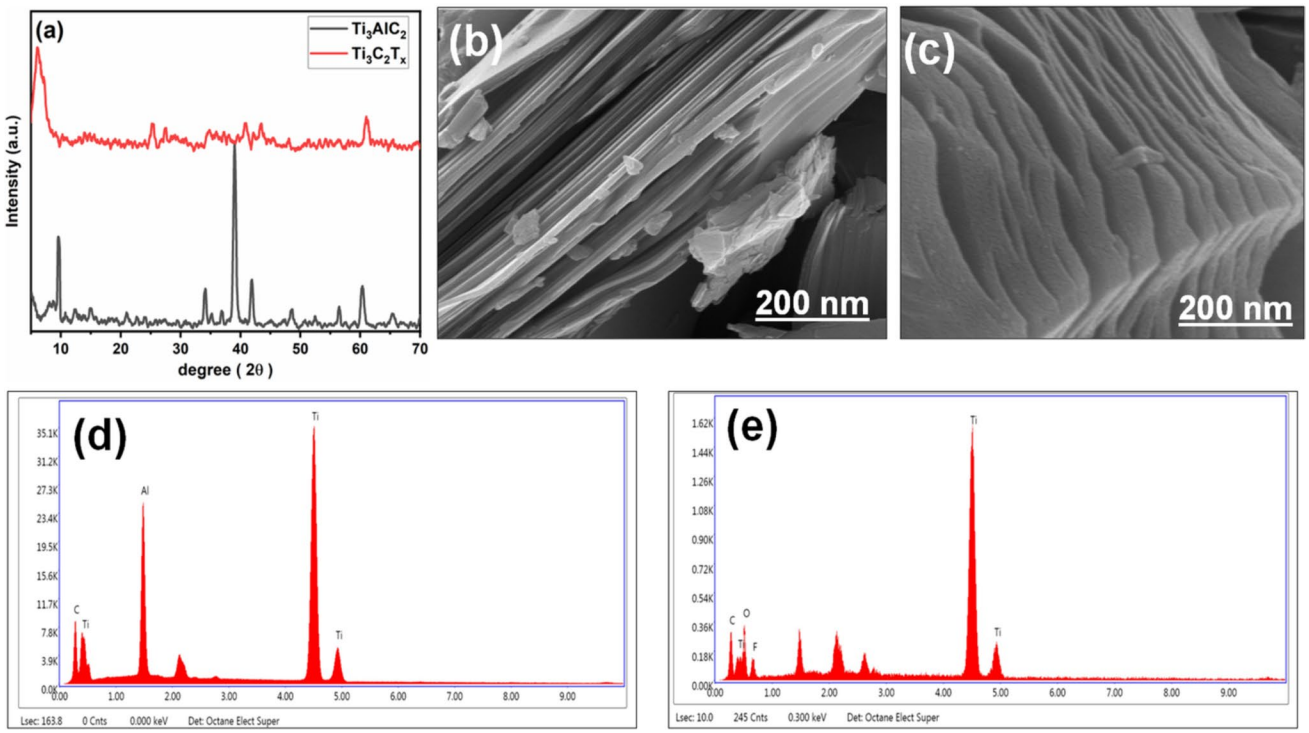

Figure 2 **a** XRD pattern; **b, c** morphology structure; and **d, e** EDX analysis of $TiAlC_2$ and $Ti_3C_2T_x$.

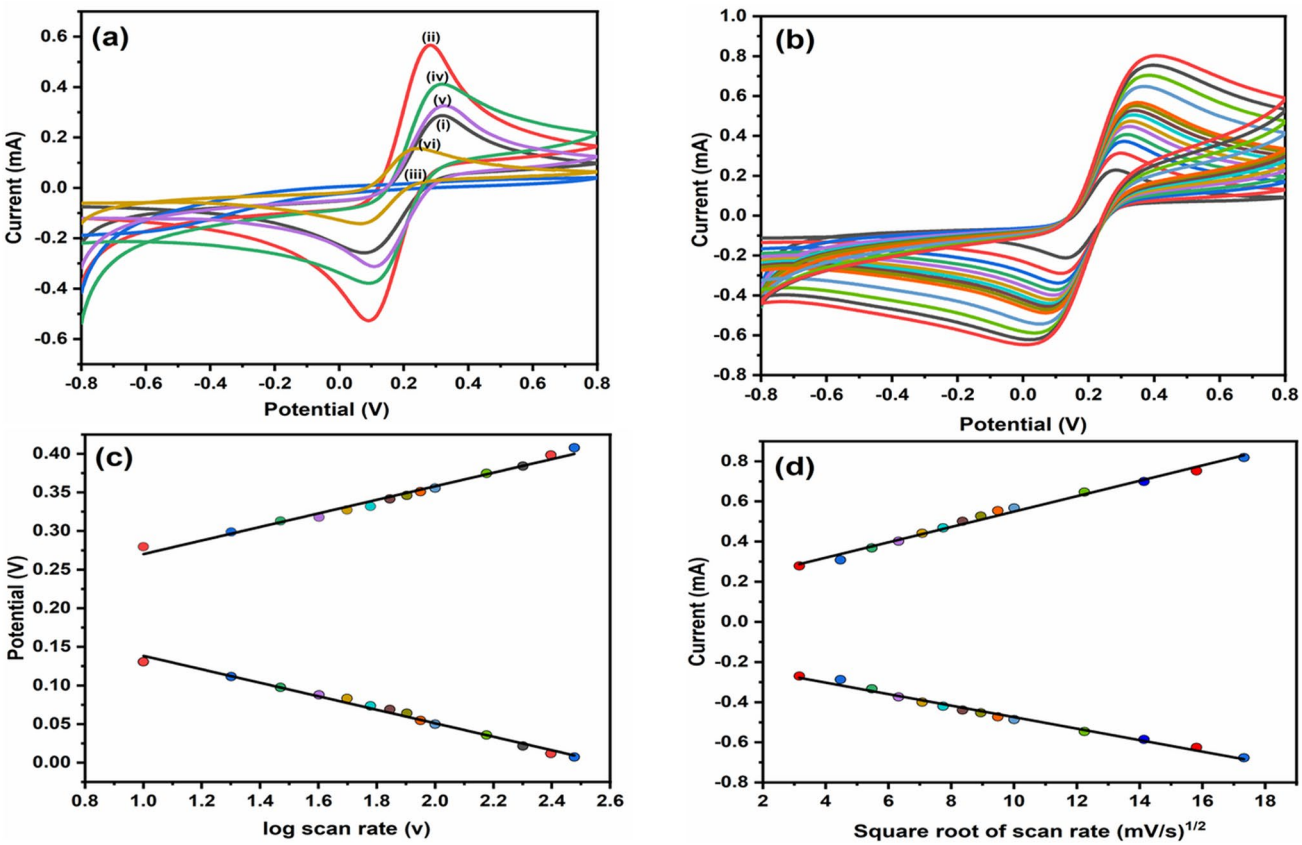

Figure 3 CV analysis of **a** different fabricated electrodes: (i) bare ITO; (ii) $Ti_3C_2T_x$/ITO; (iii) MIP/$Ti_3C_2T_x$/ITO before elution; (iv) MIP/$Ti_3C_2T_x$/ITO after elution; (v) MIP/$Ti_3C_2T_x$/ITO after adsorption; (vi) NIP/ $Ti_3C_2T_x$/ITO; **b** MIP/$Ti_3C_2T_x$/ITO electrode at varying scan rates (10–300 mV s^{-1}). The plots of **c** peak potential vs. log scan rate for MIP/$Ti_3C_2T_x$/ITO electrode and **d** peak current vs. square root of scan rate for MIP/$Ti_3C_2T_x$/ITO in a solution of 0.1 M PBS containing 5 mM $[Fe(CN)_6]^{3-/4-}$.

remarkably (0.56 mA) due to the excellent conductivity and larger surface area of $Ti_3C_2T_x$. After electropolymerization (curve iii), the redox peak almost disappears due to the non-conductive MIP layer, which inhibits the redox probe from entering the electrode surface. When the template molecules LEV are eluted (curve iv), the redox peak current is enhanced significantly (0.41 mA) again. This may be due to the formation of imprinting holes, which provide a pathway for the redox probe to access the electrode surface within the MIP film. After elution, the electrode was immersed in a solution containing template molecules (LEV), resulting in a decreased redox peak current (0.32 mA) shown by (curve v). This could be due to the blockage of some holes by template molecules LEV, thus hindering the electron transfer onto the electrode surface. In comparison, NIP/$Ti_3C_2T_x$/ITO exhibited no significant change in peak current after elution (0.15 mA) since there is no doping of LEV molecules (curve vi).

Figure 3b illustrates the CV analysis of the MIP/$Ti_3C_2T_x$/ITO electrode by varying the scan rates (υ) (10–300 mVs^{-1}). The figure clearly shows that oxidation peak current shifts towards a more positive direction while reduction peak current shifts towards a more negative direction with an increase in the scan rate. This clearly indicates the linear relationship between the anodic and cathodic peak potentials (E_{pa} & E_{pc}) vs. natural logarithm of scan rate (log υ) as shown in Fig. 3c, which can be represented by Eqs. (1) and (2):

$$E_{pa}\left[MIP/Ti_3C_2T_x/ITO\right] = 0.08783V \log(\upsilon) + 0.1823V; R^2 = 0.9825 \quad (1)$$

$$E_{pc}\left[MIP/Ti_3C_2T_x/ITO\right] = -0.08729\,V\,\log\,(\upsilon) + 0.2256\,V; R^2 = 0.9894 \quad (2)$$

Using Laviron's equation [37], the charge transfer coefficient (α) and charge transfer rate constant (K_s) for MIP/$Ti_3C_2T_x$/ITO are found to be 0.9216 and 0.0938 s^{-1}, respectively. Figure 3d shows a good linearity between the anodic and cathodic peak currents (I_{pa} and I_{pc}) with the square root of the scan rates ($\upsilon^{1/2}$), which indicates that the transfer of electrons through MIP/$Ti_3C_2T_x$/ITO electrode is surface controlled process as shown by Eqs. (3) and (4):

$$I_{pa}\left[MIP/Ti_3C_2T_x/ITO\right] = 38.30\,\mu A\,(mV\,s^{-1}) \times \upsilon^{1/2} mV\,s^{1/2} + 166.58\,\mu A; R^2 = 0.9906 \quad (3)$$

$$I_{pc}\left[MIP/Ti_3C_2T_x/ITO\right] = -28.64\,\mu A\,(mV\,s^{-1}) \times \upsilon^{1/2} mV\,s^{1/2} - 188.03\,\mu A; R^2 = 0.9887 \quad (4)$$

The electroactive surface area of $Ti_3C_2T_x$/ITO and MIP/$Ti_3C_2T_x$/ITO electrodes could be determined by the Randle-Sevcik equation as follows:

$I_p = (2.69 \times 10^5)\, n^{3/2} A D^{1/2} C \upsilon.^{1/2}$

where I_p, n, and A denote the peak current (A), the number of electrons oxidized or reduced, and the electroactive surface area (cm^2), respectively. D, C, and υ ½ represent $[Fe(CN)_6]^{3-/4-}$ diffusion coefficient (cm^2s^{-1}), molar concentration (mol cm^{-3}), and the square root of the scan rate (V s^{-1}), respectively. The calculated electroactive surface area for $Ti_3C_2T_x$/ITO and MIP/$Ti_3C_2T_x$/ITO are 0.27 cm^2 and 0.24 cm^2, respectively, consistent with the CV results.

Optimization of analytical conditions

The sensitivity and selectivity of the prepared MIP sensor were enhanced by optimizing some parameters, including the pH of PBS solution, the impact of template: monomer molar ratio, the number of electropolymerization cycles, different scan rates for the generation of MIP film, and elution as well as adsorption time.

Effect of pH

In Fig. 4a, the impact of different pH of PBS solution on the formation of polymerization film was tested ranging from 4.0 to 9.0. As seen in the figure, the peak current increases with an increase in pH up to 7 and then decreases gradually. This is because too acidic and alkaline environments might affect the imprinted film's structural integrity and reduce the sensitivity of the sensor [38]. Therefore, pH 7 was considered as the ideal pH for the electropolymerization solution.

Effect of ratio of template: monomer

The ratio of the template: monomer (LEV: py) was another parameter that affects the number of imprinted cavities within the polymer matrix during the electropolymerization process. Figure 4b represents the effect of different ratios of the template to monomer (1:1 to 1:9) on the current response. As seen clearly in the figure, the current increases with an increase in monomer concentration from 1:1 to 1:5 and then decreases gradually from 1:5 to 1:9. This is because insufficient monomer cannot bind with enough template molecules which leads to fewer recognition sites while an excess of monomer results into self-polymerization. Hence, 1:5 was selected as the optimal ratio for further experiment.

Effect of polymerization cycles

The number of polymerization cycles determines the thickness of the MIP film, which impacts the formation of imprinted cavities and the sensitivity of the sensor. In Fig. 4c, as the scan cycles increase from 4 to 10, the current response increases due to the formation of more imprinting sites. However, after exceeding 10 cycles, the current response decreased as the MIP layers were too thick to remove template (LEV) molecules. Thus, the optimal scan cycles for electropolymerization were found to be 10.

Effect of scan rate

The scan rate represents another parameter that plays a crucial role in the formation of MIP film. As shown in Fig. 4d, the impact of different scan rates on sensor performance was examined from 30 to 80 mV s^{-1}. The current response increases with an increase in scan rate from 30 to 50 mV s^{-1} which could be attributed to the slow binding of template molecules to the functional monomers, resulting in the increased density of MIP film. When the scan rate was too fast, the current

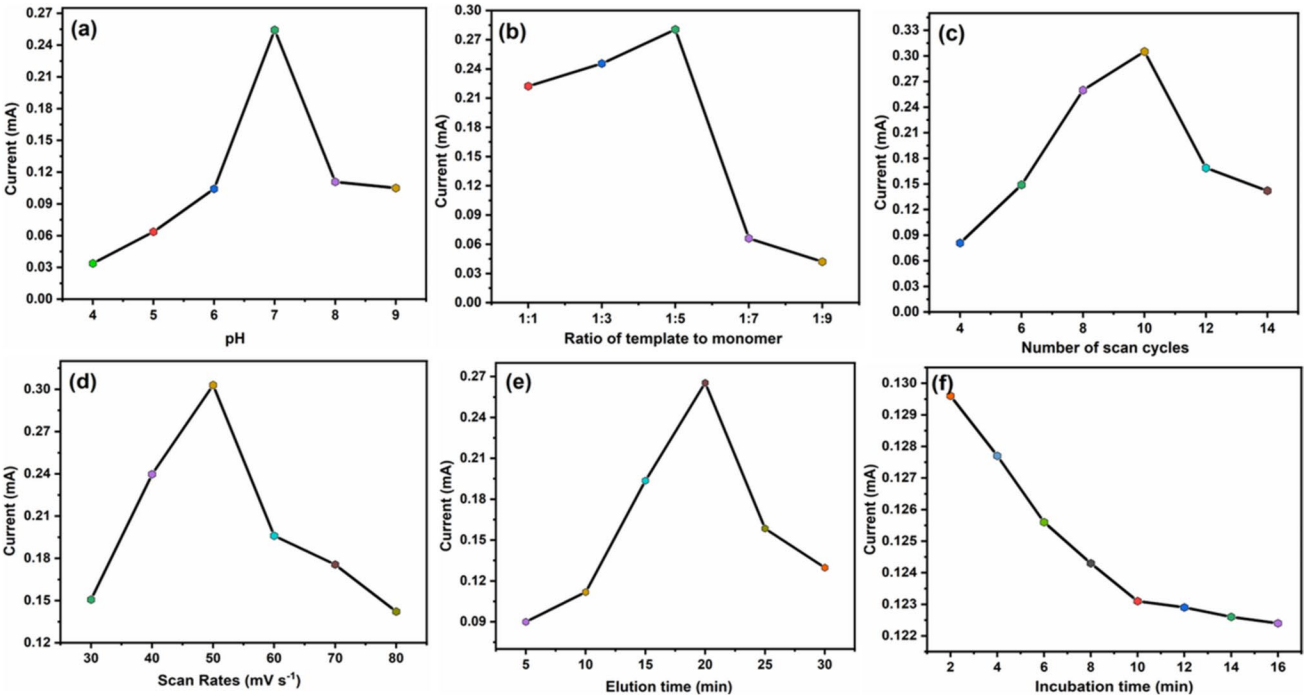

Figure 4 Optimization of analytical conditions: Effect of **a** pH of electrolyte; **b** ratio of template: monomer; **c** polymerization cycles; **d** scan rate; **e** elution time; **f** incubation time on the current response.

response decreased as the MIP film formed might be too loose, and the interaction between the template molecules and monomer was not sufficiently effective [38]. Therefore, 50 mV s^{-1} was the optimal scan rate.

Effect of elution time

Figure 4e illustrates the influence of elution time on the sensor's performance. As seen, the current response increases continuously with an increase in elution time from 5 to 20 min, and the maximum current response was observed when the elution time was 20 min. This indicates that many template molecules were removed from the polymerized film and the corresponding cavities are formed, further accelerating the electron transfer. As observed, the peak current decreases significantly after the elution duration extends from 20 to 30 min, indicating that too long elution time may damage the polymer film's surface. Therefore, the optimized elution time is found to be 20 min.

Effect of incubation time

The incubation time is another crucial parameter that impacts the performance of the developed sensor. In Fig. 4f, the current response decreased with an increase in incubation time and reached a plateau at 10 min, indicating LEV occupied the cavities exposed on the MIP/$Ti_3C_2T_x$/ITO surface. Thus, the optimal incubation time is 10 min.

Electrochemical sensing study of MIP/$Ti_3C_2T_x$/ITO sensor

Differential pulse voltammetry (DPV) technique was utilized to measure the electrochemical response of the fabricated MIP/$Ti_3C_2T_x$/ITO electrode towards LEV. As depicted in Fig. 5a, the peak current continuously decreases with an increase in LEV concentration from 1 pM to 100 nM. The peak current reduction occurs as more imprinted cavities are occupied by LEV molecules, inhibiting the redox probe's electron transfer process. The calibration curve (Fig. 5b) exhibits a linear behaviour between peak current

($\Delta I = I_{elution} - I_{adsorption}$) vs logarithm of LEV concentration (log (C_{LEV})) and obeys the following equation:

$$I = 9.649\,\mu A\,pM^{-1} \times \log C_{LEV} + 42.23\,\mu A; R^2 = 0.9799 \quad (5)$$

The sensitivity (S = slope/effective surface area) of the constructed MIP sensor was found to be 40.20 μA $(pM)^{-1}$ cm^{-2}. In contrast, the detection limit (LOD) was determined to be 0.76 pM by using the equation (LOD = 3σ/S), where σ and S represent the standard deviation of the electrode and slope of the calibration plot, respectively (Eq. 5). The efficiency of the fabricated MIP/$Ti_3C_2T_x$/ITO sensor was also compared with other reported techniques for LEV detection as outlined in Table 1. The proposed MIP sensor in this study exhibits a lower LOD value and wider detection range. This could be due to the large surface area, good electrical conductivity, the outstanding electrochemical performance of $Ti_3C_2T_x$, and specific MIP recognition.

Selectivity, reproducibility, and stability of MIP/$Ti_3C_2T_x$/ITO sensor

In order to examine the selectivity of the proposed MIP sensor, several potential structural analogs (NOR, CIP, and OME), organic matter (GLU), and ions (Na^+, CO_3^{2-}) were chosen as interfering agents. As seen in Fig. 5c, the current response of MIP/$Ti_3C_2T_x$/ITO to LEV is significantly higher even with 10 times more concentration of interfering species. These results demonstrate that the imprinted cavities from MIPs correspond well to the size, shape, and functional groups of LEV molecules. The imprinting factor (IF = $\Delta I_{MIP}/\Delta I_{NIP}$) is another essential aspect for assessing the selectivity of the MIP sensor (Fig. S4). The IFs for LEV, NOR, CIP, and OME are 9.41, 2.03, 3.47, and 1.14, respectively, indicating the high recognition ability of the fabricated sensor toward LEV.

To investigate reproducibility, five independent MIP/$Ti_3C_2T_x$/ITO electrodes were prepared under optimized conditions for LEV detection. As illustrated in Fig. 5d the relative standard deviation (RSD) of 10 nM LEV was

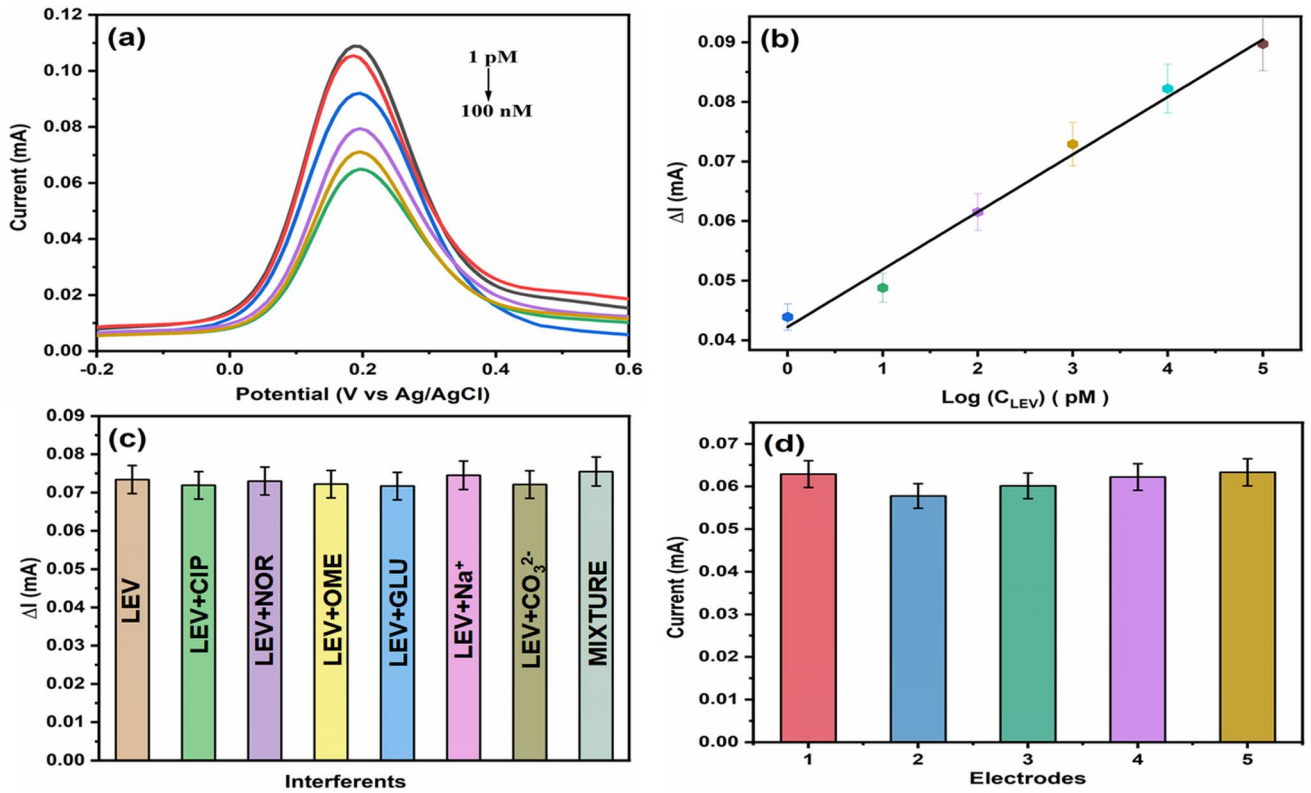

Figure 5 **a** DPV response of MIP/$Ti_3C_2T_x$/ITO electrode in various concentrations of LEV (1 pM to 100 nM); **b** Linearity plot between the ΔI and logarithm of different concentrations of LEV; **c** Selectivity study of MIP/$Ti_3C_2T_x$/ITO for LEV (10 nM) with other inteferents (100 nM of CIP, NOR, OME, GLU, Na^+, CO_3^{2-}), mixture; and **d** Reproducibility study of developed MIP/$Ti_3C_2T_x$/ITO.

3.75%, suggesting that the prepared MIP sensor exhibits good reproducibility.

Moreover, the stability of the MIP/$Ti_3C_2T_x$/ITO sensor was tested weekly in the presence of 10 nM LEV over four weeks (Fig. S5). The current response of the sensor retains 75.4% of its initial value for 4 weeks, thus exhibiting acceptable long-term stability.

Real sample analysis

The practicability and validity of the fabricated sensor to determine LEV in soil and tap water were evaluated using the standard addition method. Firstly, the soil sample was mixed with PBS buffer (7 pH), followed by centrifugation for 15 min at RT. Similarly, the tap water was filtered and centrifuged for 20 min at room temperature. After that, these real samples were spiked with various concentrations of LEV (0.1, 1, and 10 nM) and used for a sensing study for the MIP/$Ti_3C_2T_x$/ITO sensor. The recoveries and their corresponding RSD values for the detection of LEV from soil and tap water are found to be 93.6–96.9%, 93.6–104.5%, and 2.19–4.65%, 2.78–4.61%, respectively, as shown in Table 2. Moreover, the accuracy of the constructed sensor was evaluated using the HPLC–MS method. The recovery level of the electrochemical detection was found to be in good agreement with the HPLC–MS method, indicating that the proposed sensor has satisfactory reliability and accuracy for its application in real samples.

Conclusion

In summary, a novel and simple molecular imprinted electrochemical sensor for highly specific, sensitive, and rapid detection of LEV has been reported. The $Ti_3C_2T_x$-modified electrode provides a large surface area and abundant recognition sites, enhancing the electrochemical response of the MIP sensor with a wide detection linear range (1 pM—100 nM) and low LOD (0.76 pM). The sensor also possesses good selectivity, satisfactory stability, and reproducibility for LEV detection. Moreover, the precision and applicability of this MIP sensor for practical applications were validated with two

Table 1 Comparison of biosensing characteristics of the MIP/$Ti_3C_2T_x$/ITO electrode for LEV detection

S.No	Immobilization matrix	Linear range	LOD	Detection Technique	Sample	Ref
1	Au/PDDA/rGO	10–200 µM 200–800 µM	3.9 µM	LSV	LV tablets	[39]
2	MIP/G-AuNPs	1–100 µM	0.53 µM	DPV	LEV capsule	[1]
3	PoAP/MWCNTs	1–200 µM	1 µM	DPV	LV capsules	[40]
4	BDD electrode	10–80.9 µM	2.88 µM	SWV	Human urine Human serum	[41]
5	Poly(p-ABSA)/rGO	2–30 µM 30–500 µM	0.12 µM	LSV	Human urine	[4]
6	AgNs/NiO	0.25–100 µM	27 nM	SWV	Human serum	[42]
7	β-CD/rGO	100 pM–100 nM	30 pM	DPV	Spiked human serum	[43]
8	PGE/Au-NPs/poly (oPD-co-L-Dopa)	1–100 µM and 100–10000 µM	0.46 µM	DPV	Tablets Spiked human plasma	[44]
9	Ag/$AgVO_3$/N-rGO	0.09–671 µM	7.9 pM	DPV	Human blood serum Human urine Wastewater	[45]
10	MIP/$Ti_3C_2T_x$	1 pM –100 nM	0.76 pM	DPV	Soil Tap water	Present work

Abbreviations: AuNPs, gold nanoparticles; PDDA, poly(diallydimethylammonium chloride); rGO, reduced graphene oxide; G, graphene; PoAP, poly(o-aminophenol); MWCNTs, multiwalled carbon nanotubes; BDD, boron-doped diamond; poly(p-ABSA), poly(p-aminobenzene sulfonic acid); AgNs, silver nanoparticles; NiO, nickel oxide; β-CD, β-cyclodextrin; PGE, pencil graphite electrode; poly(oPD-co-L-Dopa), copolymer deposition of o-phenylenediamine and levodopa; $AgVO_3$, silver vanadate; N-rGO, nitrogen-doped reduced graphene oxide; LSV, Linear Sweep Voltammetry; DPV, Differential Pulse Voltammetry; SWV, Square Wave Voltammetry

Table 2 Detection of LEV in soil and tap water samples

Sample	Added (nM)	MIP/$Ti_3C_2T_x$/ITO			HPLC–MS		
		Found (nM)	Recovery (%)	RSD (%)	Found (nM)	Recovery (%)	RSD (%)
Soil	0	0	–	–	0	–	–
	0.1	0.093	93.6	4.65	0.099	99.0	2.28
	1	0.949	94.9	3.69	0.976	97.6	1.40
	10	9.69	96.9	2.19	9.66	96.6	2.57
Tap water							
	0	0	–	–	0	–	–
	0.1	0.096	96.1	2.78	0.097	97.0	1.44
	1	1.04	104.5	3.11	0.983	98.3	2.30
	10	9.36	93.6	4.61	9.69	96.9	3.28

real samples, providing a promising approach for LEV monitoring in the environmental field.

Acknowledgements

Divya Hudda acknowledges the Delhi Technological University (DTU) for the financial support.

Author contributions

Divya Hudda: conceptualization, methodology, validation, and writing original draft. Devendra Kumar: Supervision, writing-review, and editing.

Declarations

Conflict of interest The authors declare that they have no conflict of interest.

Supplementary Information The online version contains supplementary material available at https://doi.org/10.1007/s10853-024-10403-2.

References:

[1] Wang F, Zhu L, Zhang J (2014) Electrochemical sensor for levofloxacin based on molecularly imprinted polypyrrole–graphene–gold nanoparticles modified electrode. Sens Actuators, B Chem 192:642–647

[2] Tigari G, Manjunatha J, Souza ED, Raril C, Hareesha N, Charithra MM (2022) Electrochemical determination of levofloxacin drug at poly (clayton yellow)/carbon paste electrode. Monatshefte für Chemie-Chem Mon 153:311–319

[3] Tang L, Tong Y, Zheng R, Liu W, Gu Y, Li C, Chen R, Zhang Z (2014) Ag nanoparticles and electrospun CeO_2-Au composite nanofibers modified glassy carbon electrode for determination of levofloxacin. Sens Actuators, B Chem 203:95–101

[4] Han L, Zhao Y, Chang C, Li F (2018) A novel electrochemical sensor based on poly (p-aminobenzene sulfonic acid)-reduced graphene oxide composite film for the sensitive and selective detection of levofloxacin in human urine. J Electroanal Chem 817:141–148

[5] Jin Y, Xu G, Li X, Ma J, Yang L, Li Y, Zhang H, Zhang Z, Yao D, Li D (2021) Fast cathodic reduction electrodeposition of a binder-free cobalt-doped Ni-MOF film for directly sensing of levofloxacin. J Alloy Compd 851:156823

[6] Mohammad Hossein G, Alireza K, Hossein S, Mohammad Reza G, Mehdi R-N, Farhad A (2019) An electrochemical sensor based on poly (l-Cysteine)@AuNPs @ reduced graphene oxide nanocomposite for determination of levofloxacin. Microchem J 147:198–206

[7] González JAO, Mochón MC, de la Rosa FJB (2000) Spectrofluorimetric determination of levofloxacin in tablets, human urine and serum. Talanta 52:1149–1156

[8] Al-Momani IJ (2006) Flow injection spectrophotometric determination of the antibacterial levofloxacin in tablets and human urine. Anal Lett 39:741–750

[9] Liu YM, Cao JT, Tian W, Zheng YL (2008) Determination of levofloxacin and norfloxacin by capillary electrophoresis with electrochemiluminescence detection and applications in human urine. Electrophoresis 29:3207–3212

[10] Salem A, Mossa H, Barsoum BN (2005) Quantitative determinations of levofloxacin and rifampicin in pharmaceutical and urine samples using nuclear magnetic resonance

spectroscopy. Spectrochim Acta Part A Mol Biomol Spectrosc 62:466–472

[11] Shao X, Li Y, Liu Y, Song Z (2011) Rapid determination of levofloxacin in pharmaceuticals and biological fluids using a new chemiluminescence system. J Anal Chem 66:102–107

[12] Payán MR, López MÁB, Fernández-Torres R, González JAO, Mochón MC (2011) Hollow fiber-based liquid phase microextraction (HF-LPME) as a new approach for the HPLC determination of fluoroquinolones in biological and environmental matrices. J Pharm Biomed Anal 55:332–341

[13] Sun H, Wang H, Ge X (2012) Simultaneous determination of the combined drugs of ceftriaxone sodium, metronidazole, and levofloxacin in human urine by high-performance liquid chromatography. J Clin Lab Anal 26:486–492

[14] de Farias DM, de Faria LV, Lisboa TP, Matos MAC, Muñoz RAA, Matos RC (2020) Determination of levofloxacin in pharmaceutical formulations and urine at reduced graphene oxide and carbon nanotube-modified electrodes. J Solid State Electrochem 24:1165–1173

[15] Yan G, Zhang S, Han Z, Yi S, Wang Y, Zhu L, Zhang L (2024) Construction of a sensor array using TiO_2 NRs/CuO/rMIP with imprinted sites regulation as light-activated nanozyme to colorimetric detect fluoroquinolones. Sens Actuators, B Chem 419:136373

[16] Thakur D, Pandey CM, Kumar D (2022) Graphitic Carbon Nitride-Wrapped Metal-free PoPD-Based Biosensor for Xanthine Detection. ACS Omega 8:2328–2336

[17] Majdinasab M, Mishra RK, Tang X, Marty JL (2020) Detection of antibiotics in food: New achievements in the development of biosensors. TrAC, Trends Anal Chem 127:115883

[18] Li G, Wu J, Qi X, Wan X, Liu Y, Chen Y, Xu L (2022) Molecularly imprinted polypyrrole film-coated poly (3, 4-ethylenedioxythiophene): polystyrene sulfonate-functionalized black phosphorene for the selective and robust detection of norfloxacin. Materials Today Chemistry 26:101043

[19] Yan G, Han Z, Hou X, Yi S, Zhang Z, Zhou Y, Zhang L (2023) A highly sensitive TiO_2-based molecularly imprinted photoelectrochemical sensor with regulation of imprinted sites by Photo-deposition. J Colloid Interface Sci 650:1319–1326

[20] Han S, Sun R, Zhao L, Yan C, Chu H (2023) Molecularly imprinted electrochemical sensor based on synergistic interaction of honeycomb-like Ni-MOF decorated with AgNPs and N-GQDs for ultra-sensitive detection of olaquindox in animal-origin food. Food Chem 418:136001

[21] Hasseb AA, Shehab OR, El Nashar RM (2022) Application of molecularly imprinted polymers for electrochemical detection of some important biomedical markers and pathogens. Curr Opin Electrochem 31:100848

[22] Wu Y, Li G, Tian Y, Feng J, Xiao J, Liu J, Liu X, He Q (2021) Electropolymerization of molecularly imprinted polypyrrole film on multiwalled carbon nanotube surface for highly selective and stable determination of carcinogenic amaranth. J Electroanal Chem 895:115494

[23] Bai X, Zhang B, Liu M, Hu X, Fang G, Wang S (2020) Molecularly imprinted electrochemical sensor based on polypyrrole/dopamine@graphene incorporated with surface molecularly imprinted polymers thin film for recognition of olaquindox. Bioelectrochemistry 132:107398

[24] Wang H, Li H, Huang Y, Xiong M, Wang F, Li C (2019) A label-free electrochemical biosensor for highly sensitive detection of gliotoxin based on DNA nanostructure/MXene nanocomplexes. Biosens Bioelectron 142:111531

[25] Zhu X, Zhang Y, Liu M, Liu Y (2021) 2D titanium carbide MXenes as emerging optical biosensing platforms. Biosens Bioelectron 171:112730

[26] Zhao S, Nivetha R, Qiu Y, Guo X (2020) Two-dimensional hybrid nanomaterials derived from MXenes ($Ti_3C_2T_x$) as advanced energy storage and conversion applications. Chin Chem Lett 31(4):947–952

[27] Kalambate PK, Dhanjai A, Sinha Y, Li YS, Huang Y (2020) An electrochemical sensor for ifosfamide, acetaminophen, domperidone, and sumatriptan based on self-assembled MXene/MWCNT/chitosan nanocomposite thin film. Microchim Acta 187:402

[28] Iqbal A, Kwon J, Kim MK, Koo CM (2021) MXenes for electromagnetic interference shielding: experimental and theoretical perspectives. Mater Today Adv 9:100124

[29] Zhang Y, Zhang X, Cheng C, Yang Z (2020) Recent progress of MXenes as the support of catalysts for the CO oxidation and oxygen reduction reaction. Chin Chem Lett 31:931–936

[30] Nezhadali A, Rouki Z, Nezhadali M (2015) Electrochemical preparation of a molecularly imprinted polypyrrole modified pencil graphite electrode for the determination of phenothiazine in model and real biological samples. Talanta 144:456–465

[31] Duan D, Yang H, Ding Y, Li L, Ma G (2019) A three-dimensional conductive molecularly imprinted electrochemical sensor based on MOF derived porous carbon/carbon nanotubes composites and prussian blue nanocubes mediated amplification for chiral analysis of cysteine enantiomers. Electrochim Acta 302:137–144

[32] Qian T, Yu C, Zhou X, Ma P, Wu S, Xu L, Shen J (2014) Ultrasensitive dopamine sensor based on novel molecularly imprinted polypyrrole coated carbon nanotubes. Biosens Bioelectron 58:237–241

[33] Kumar D, Sharma RC (1998) Advances in conductive polymers. Eur Polymer J 34:1053–1060

[34] Peng C, Wei P, Chen X, Zhang Y, Zhu F, Cao Y, Wang H, Yu H, Peng F (2018) A hydrothermal etching route to synthesis of 2D MXene (Ti_3C_2, Nb_2C): enhanced exfoliation and improved adsorption performance. Ceram Int 44:18886–18893

[35] Liu Z, Guo R, Li F, Zheng M, Wang B, Li T, Luo Y, Meng L (2018) Reduced graphene oxide bridged, TiO_2 modified and Mn_3O_4 intercalated $Ti_3C_2T_x$ sandwich-like nanocomposite as a high performance anode for enhanced lithium storage applications. J Alloy Compd 762:643–652

[36] Chen J, Yuan X, Lyu F, Zhong Q, Hu H, Pan Q, Zhang Q (2019) Integrating MXene nanosheets with cobalt-tipped carbon nanotubes for an efficient oxygen reduction reaction. J Mater Chem A 7:1281–1286. https://doi.org/10.1039/C8TA10574J

[37] Laviron EJJ (1979) General expression of the linear potential sweep voltammogram in the case of diffusionless electrochemical systems. J Electroanal Chem Interfacial Electrochem 101:19–28

[38] Geng L, Huang J, Zhai H, Shen Z, Han J, Yu Y, Fang H, Li F, Sun X, Guo Y (2022) Molecularly imprinted electrochemical sensor based on multi-walled carbon nanotubes for specific recognition and determination of chloramphenicol in milk. Microchem J 182:107887

[39] Borowiec J, Yan K, Tin C-C, Zhang J (2015) Synthesis of PDDA functionalized reduced graphene oxide decorated with gold nanoparticles and its electrochemical response toward levofloxacin. J Electrochem Soc 162:H164–H169

[40] Wen W, Zhao D-M, Zhang X-H, Xiong H-Y, Wang S-F, Chen W, Zhao Y-D (2012) One-step fabrication of poly(o-aminophenol)/multi-walled carbon nanotubes composite film modified electrode and its application for levofloxacin determination in pharmaceuticals. Sens Actuators, B Chem 174:202–209

[41] Rkik M, Brahim MB, Samet Y (2017) Electrochemical determination of levofloxacin antibiotic in biological samples using boron doped diamond electrode. J Electroanal Chem 794:175–181

[42] Liu C, Xie D, Liu P, Xie S, Wang S, Cheng F, Zhang M, Wang L (2019) Voltammetric determination of levofloxacin using silver nanoparticles deposited on a thin nickel oxide porous film. Microchim Acta 186:1–10

[43] Ghanbari MH, Shahdost-fard F, Khoshroo A, Rahimi-Nasrabadi M, Ganjali MR, Wysokowski M, Rębiś T, Żółtowska-Aksamitowska S, Jesionowski T, Rahimi P, Joseph Y, Ehrlich H (2019) A nanocomposite consisting of reduced graphene oxide and electropolymerized β-cyclodextrin for voltammetric sensing of levofloxacin. Microchim Acta 186:438

[44] El Azab NF, Mahmoud AM, Trabik YA (2022) Point-of-care diagnostics for therapeutic monitoring of levofloxacin in human plasma utilizing electrochemical sensor mussel-inspired molecularly imprinted copolymer. J Electroanal Chem 918:116504

[45] Sharma TSK, Hwa K-Y (2021) Facile Synthesis of Ag/$AgVO_3$/N-rGO Hybrid Nanocomposites for electrochemical detection of levofloxacin for complex biological samples using screen-printed carbon paste electrodes. Inorg Chem 60:6585–6599

Publisher's Note Springer Nature remains neutral with regard to jurisdictional claims in published maps and institutional affiliations.

Springer Nature or its licensor (e.g. a society or other partner) holds exclusive rights to this article under a publishing agreement with the author(s) or other rightsholder(s); author self-archiving of the accepted manuscript version of this article is solely governed by the terms of such publishing agreement and applicable law.

Applied Physics A (2024) 130:854
https://doi.org/10.1007/s00339-024-08000-w

Applied Physics A
Materials Science & Processing

Optical temperature sensing and upconversion luminescence in Er^{3+}/Yb^{3+} co-doped BNT ferroelectric ceramic

Megha Narwan[1] · Richa Sharma[1] · Renuka Bokolia[1]

Received: 18 July 2024 / Accepted: 14 October 2024
© The Author(s), under exclusive licence to Springer-Verlag GmbH Germany, part of Springer Nature 2024

Abstract
In the present work, a series of Er^{3+}/Yb^{3+} co-doped $Bi_{0.5-x-y}Er_xYb_yNa_{0.5}TiO_3$ ferroelectric ceramic is prepared using traditional solid state technique to investigate the structural, optical and sensing properties. The XRD analysis confirms the rhombohedral geometry and no extra peaks shows the solubility of the dopant ions. SEM images exhibited a dense microstructure with well-defined grain boundaries. The FTIR vibrational bands observed at 550 cm^{-1} and 820 cm^{-1} depict the typical characteristics of perovskite structure caused by the expansion of the octahedral group of Ti–O bonds. The Tauc plot displays the energy band gaps (E_g) in a range of 2.93 eV to 2.88 eV as a function of the Yb^{3+}concentration. The photoluminescence spectra were measured at two wavelengths of excitation at 489 nm and 980 nm for all the BNT ceramic compositions. It has been observed that the two intense green bands and one visible red band appeared at 530 nm, 549 nm and 662 nm, respectively. The dependency of pump power on UCL spectra is observed with varying pump powers at 980 nm excitation. The two photons that are involved in the UCL process are confirmed by this investigation. The time-resolved fluorescence spectroscopy reveals that the efficiency in energy transfer between the dopant ions increased for all the co-doped BNT ceramic compositions. The absolute (S_{ab}) and relative (S_r) sensitivity of BE3Y3 ceramic composition are 0.54% K^{-1} and 1.24% K^{-1} at 523 K and 303 K, respectively.

Keywords UCL · Sensing · Ceramic · Time decay · Diffuse reflectance spectroscopy · BNT

1 Introduction

Multifunctional materials represent a paradigm change in material science, offering unprecedented opportunities for innovation and advancement across various fields. Multifunctional materials can be well defined as the combination of optical, electrical, and mechanical properties [1, 2]. These materials have drawn a lot of interest due to their potential for developing novel technologies. There are many applications of multifunctional materials such as actuators, transducers, accelerators, sensors, and non-volatile memories. Their preparation method, which included microwave processing, solid state reaction, and combustion reaction, also had a significant impact on their chemical and physical characteristics [3, 4]. The need for environmental preservation on a worldwide scale has made lead-free materials more and more popular in recent years. New lead-free piezoelectric material needs to be improved due to growing environmental concerns. Lead-free ferroelectric material can be doped with rare earth ions exhibits various phenomena, like photoluminescence (PL), upconversion (UC) emission and it can enhance the piezoelectricity of the material [5–9]. To reduce the harmful effects of lead exposure on the environment and human health, ferroelectrics are a practical replacement for ceramics containing lead. Ferroelectrics are known to be superior alternative to lead-based materials in many applications since they don't harm the environment and perform better without sacrificing functionality [10–14]. Consequently, to substitute the lead-based materials, a new lead-free piezoelectric ceramic has to be developed. Bismuth sodium titanate (BNT), with the chemical formula $Bi_{0.5}Na_{0.5}TiO_3$ and a perovskite structure, is one of the most prevalent utilized lead-free piezoelectric materials. It was initially founded by Smolenskii et al. in 1960 [15–18]. BNT ceramic demonstrates good optical and luminescence properties. It is having strong Ferro electricity and high Curie temperature with large value of remnant polarization and coercive field that is

✉ Renuka Bokolia
renukabokolia@dtu.ac.in

[1] FMRL Department of Applied Physics, Delhi Technological University, Delhi 110042, India

Published online: 05 November 2024

$P_r = 38$ μC/cm^2, $E_c = 73$ kV/cm, respectively so it has been considered as a good replacement for lead based materials like PZT [19–21]. However, BNT has a drawback due to its high conductivity, which possesses a problem during the poling process. Hence, in order to enhance the property of BNT ceramic, a small amount of rare-earth (RE) dopants can be incorporated, thereby improving its overall performance [22]. Rare-earth (RE) ion-doped materials have attracted a lot of interest in ongoing research due to their many multifunctional applications. The integration of rare earth ions into ferroelectric materials at the nanoscale offers unique opportunities for tailoring their properties, which can be beneficial for various applications, including electronics, photonics, and sensing. Dopants like Er, Yb, Ce, Eu, La and Sm can improve piezoelectric properties and ferroelectric properties [23]. RE-doped ceramics have been the subject of extensive research because of their numerous uses in a variety of fields, such as optical sensors for temperature, bio imaging, and colour displays. [24]. Many properties like piezoelectric, ferroelectric and pyro electric properties can be enhanced by doping rare earth. RE ions such as Er^{3+} acts as an activator of UC luminescence in green and red emission under 980 nm [25]. The choice of a low-phonon-energy host material can optimize the energy transfer between dopant ions, leading to improved upconversion efficiency [25, 26]. Er^{3+} is the most effective activator for producing upconversion luminescence. The crystal symmetry and crystal field of the matrix around Er^{3+} may alter when Er^{3+} is placed in an environment with a different matrix or ligand. This will therefore have an impact on the emission of photoluminescence. In most of the cases, Yb^{3+} ions, are indeed commonly used as sensitizers in various optical and optoelectronic applications, particularly in the field of rare-earth-doped materials. This is due to their favourable properties, including a high absorption cross-section at 980 nm and efficient energy transfer capabilities. When paired with erbium ions (Er^{3+}), which are well-known for their emission properties in the near-infrared region, Yb^{3+} ions can effectively transfer energy to Er ions, thereby enhancing the overall efficiency of the system. Yb^{3+} ions are commonly used dopant in upconversion materials due to its unique electronic structure and energy levels, which make it highly effective for enhancing upconversion processes. Yb^{3+} ions serve as sensitizer ions, absorbing lower-energy photons and transferring their energy to activator ions, which then emit higher-energy photons through upconversion processes. In our previous study, we saw that the UC emission intensity of Er-doped BNT ceramic reached its maximum value when the doping concentration was 0.03. So throughout this work, the concentration of Er^{3+} will be fixed to be 0.03. The maximum absolute optical temperature sensitivity (S_{ab}) is reported for same ceramic concentration, and is found to be 0.0047 K^{-1} at 523 K [27]. In this paper, we thoroughly studied the Er^{3+} and Yb^{3+} co doped BNT ceramic for optical and sensing performance.

2 Experimental details

2.1 Materials and synthesis

The initial precursors (Bi_2O_3, Na_2CO_3, Er_2O_3, Yb_2O_3, TiO_2) were purchased from Sigma Aldrich and possessed the highest purity level (99.99%) for the synthesis of $Bi_{0.5-x-y}Er_xYb_yNa_{0.5}TiO_3$ ceramics by a traditional solid state conventional reaction technique. Er^{3+} and Yb^{3+} were employed as an additional rare earth agents during the preparation of the samples. All the powder with different concentrations was taken in the stoichiometric ratio and was mixed by using the ball mill technique using zirconia balls and ethanol for 12 h so that the powder gets mixed well, then this slurry was put in an oven for 24 h at 70 °C to dry it out and after that we get the slurry in powder form, then this powder was calcined in high temperature furnace at 850 °C for 3 h. The calcined powder was crushed using mortar pestle then this crushed powder was mixed thoroughly with a PVA binder for 2 h so that no granules were left over until fine powder was obtained. Then, using a hydraulic press machine, this calcined powder was pressurised at 50 MPa into a disc shape with a 10 mm diameter and 1 mm thickness to yield pellets. Then these pellets were sintered at 1050 °C for 3 h with the interval heat treatment at 500 °C for 1 h to remove the binder from the pellets. The synthesis technique is depicted in Fig. 1.

2.2 Characterization techniques

The X-ray diffraction (XRD) patterns of the sintered pellet were recorded in step scan mode (step size $2\theta = 10°–80°$ and scan rate 0.04 s/step) using an X-ray diffractometer (BRUKER, Model: D8 Advance-AXS) using Cu-Kα radiation, to identify the crystal structure and the phase of the synthesized material. Scanning electron microscopy images were captured to understand the surface morphology of the pellet sample using ZEISS scanning electron microscope instrument with an airlock chamber. Sintered pellets were crushed to make powders for Fourier Transform Infrared (FTIR) Spectroscopy in ATR mode (Attenuated Total Reflectance) to analyze the formation of perovskite structure using the PerkinElmer spectrum-II instrument. Using a xenon excitation source, a JASCO FP 8300 PC-spectrofluoro photometer was used to record the emission spectra. The HORIBA PTI Quanta-master device was used to record the upconversion luminescence spectra at ambient temperature. A continuous laser diode was used to excite the sample at 980 nm wavelength. A pulsed laser source with a 980 nm

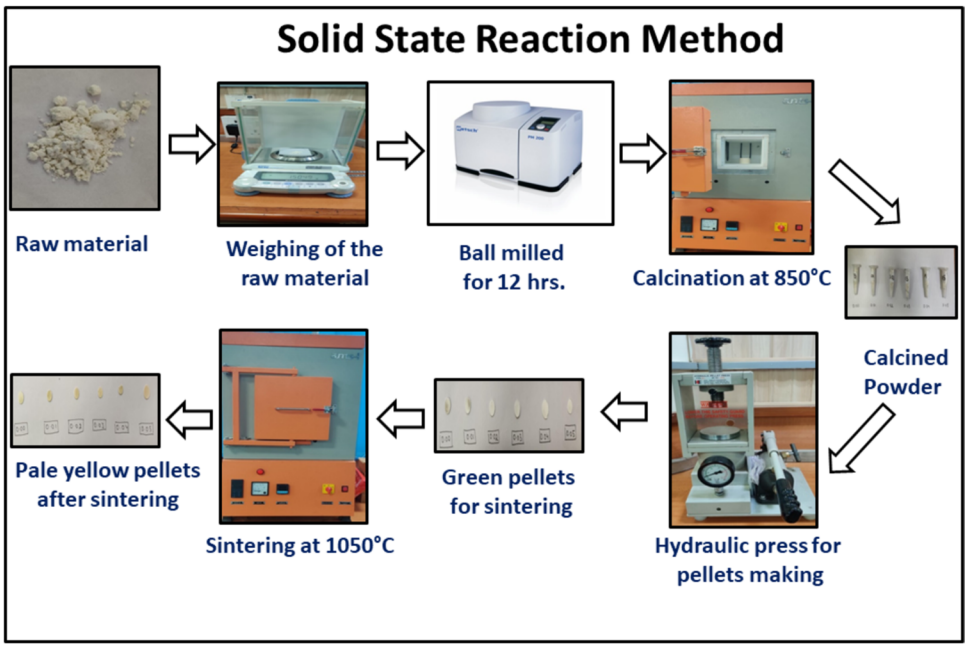

Fig. 1 Pictorial depiction of synthesis process

wavelength operating at ambient temperature was used to perform time-resolved fluorescence spectroscopy. To ascertain the role of photon count in the UC process, the pump power dependence on UC intensity was also examined. The cooled photo-multiplier tube was utilised to capture the temperature-dependent UC emission spectra for FIR analysis. The coding of samples is given in Table 1.

3 Result and discussion

3.1 Structural analysis

Figure 2a depicts the XRD patterns of all BNT ceramics with different concentrations of Er^{3+} (x = 0.03) and Yb^{3+} (y = 0.00, 0.01, 0.03, 0.05, 0.07, 0.09, 0.11, and 0.13). From XRD patterns, it was observed that each sample had a pure phase without any contaminants from the secondary phase. The absence of any apparent manifestations of undesired secondary phases validates the solubility and assimilation of Er^{3+} and Yb^{3+} ions into the host lattice BNT. Further, this is confirmed by JCPDS card no #00-036-0340. The result, as observed, suggests the presence of rhomobohedral symmetry, space group R3c. From the magnification in Fig. 2b, the reflection plane of greatest relative intensity (110) shifts to larger angles with the increases in the concentration of Yb^{3+} in the BNT structure. The shifting suggests that the host matrix BNT at the A-site of Bi^{3+} ions (1.32 Å) has effectively substituted by the smaller Er^{3+} and Yb^{3+} ions (1.25 Å, 1.22 Å) [28]. They are bound to occupy A-sites in the crystal lattice, as evidenced by their efficient ionic radii match those of the A-site ions. The XRD profile fitting of BNT ceramic was carried by using TOPAS software employing Pawley refinement based on the least squares method. The XRD patterns were analyzed with initial parameters for the rhombohedral system of space group R3c to obtain the best fit between the observed and calculated values as

Table 1 Coding of prepared undoped and doped BNT compositions:

Composition	Abbreviation	Er (x) content	Yb (y) content
$Bi_{0.5-x-y}Er_xYb_yNa_{0.5}TiO_3$	BE0Y0	0.00	0.00
$Bi_{0.5-0.03-y}Er_{0.03}Yb_yNa_{0.5}TiO_3$	BE3Y0	0.03	0.00
$Bi_{0.5-0.03-0.01}Er_{0.03}Yb_{0.01}Na_{0.5}TiO_3$	BE3Y1	0.03	0.01
$Bi_{0.5-0.03-0.03}Er_{0.03}Yb_{0.03}Na_{0.5}TiO_3$	BE3Y3	0.03	0.03
$Bi_{0.5-0.03-0.05}Er_{0.03}Yb_{0.05}Na_{0.5}TiO_3$	BE3Y5	0.03	0.05
$Bi_{0.5-0.03-0.07}Er_{0.03}Yb_{0.07}Na_{0.5}TiO_3$	BE3Y7	0.03	0.07
$Bi_{0.5-0.03-0.09}Er_{0.03}Yb_{0.09}Na_{0.5}TiO_3$	BE3Y9	0.03	0.09
$Bi_{0.5-0.03-0.11}Er_{0.03}Yb_{0.11}Na_{0.5}TiO_3$	BE3Y11	0.03	0.11
$Bi_{0.5-0.03-0.13}Er_{0.03}Yb_{0.13}Na_{0.5}TiO_3$	BE3Y13	0.03	0.13

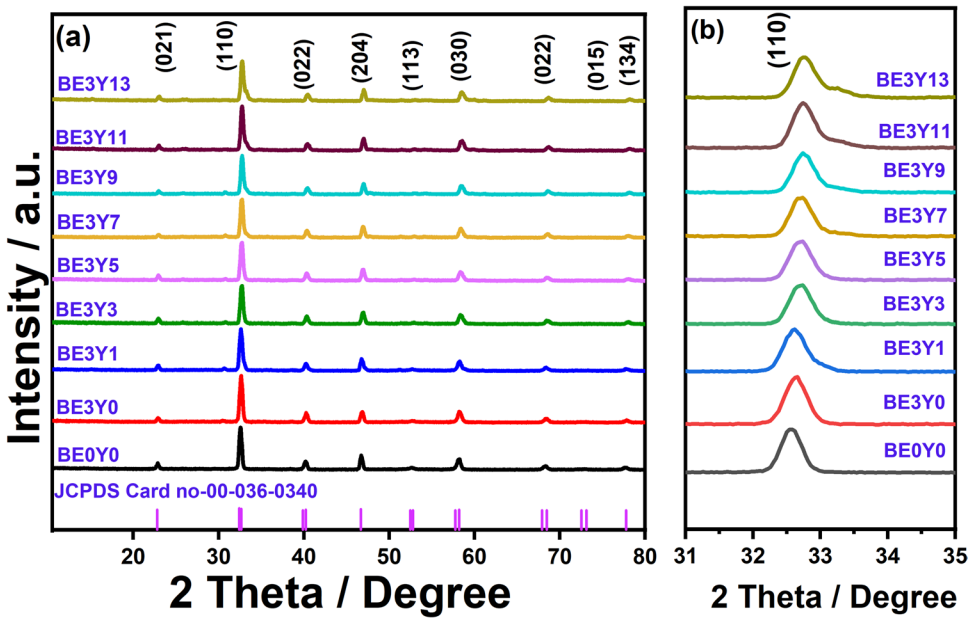

Fig. 2 **a** XRD patterns showing rhomobohedral symmetry in all BNT compositions **b** peak shifting of (110) plane

Table 2 Lattice and refinement parameters for all the BNT ceramic compositions

Parameters	$Bi_{0.5-x-y}Er_xYb_yNa_{0.5}TiO_3$								
	BE0Y0	BE3Y0	BE3Y1	BE3Y3	BE3Y5	BE3Y7	BE3Y9	BE3Y11	BE3Y13
R_{wp}	14.50	15.60	18.16	16.20	15.31	19.38	20.46	21.27	22.99
R_{exp}	11.30	10.95	10.39	11.28	9.79	11.58	11.65	10.44	10.64
R_P	10.17	11.16	13.63	11.92	15.236	14.05	15.33	15.92	16.81
GoF (χ)	1.28	1.42	1.60	1.44	1.56	1.67	1.76	2.04	2.16
a (Å)	5.4858	5.4718	5.4878	5.4632	5.4561	5.4845	5.4651	5.4632	5.4590
b (Å)	5.4858	5.4718	5.4878	5.4632	5.4561	5.4845	5.4651	5.4632	5.4590
c (Å)	6.7589	6.7399	6.7620	6.7240	6.7146	6.6801	6.7008	6.7016	6.7155
V ($Å^3$)	176.1558	174.76	176.3672	173.80	174.0439	174.0201	173.3256	173.2261	173.3210
Density (g/cm^3)	8.12	7.93	8.20	8.30	7.78	8.34	8.14	7.66	7.17
Grain size (μm)	2.32	1.77	2.61	3.33	3.90	3.45	3.29	3.26	3.34

tabulated in Table 2. The refinement parameters and goodness of fit ($\chi \approx 1.5$) confirm the good fitting of experimental and theoretical. Using Archimedes' principle, the density of the sintered pellets is determined and is recorded in Table 2. An analysis of the data showed that with increasing Er^{3+}/Yb^{3+} concentration in the host lattice, variation is seen in the density of the sintered pellets.

For all the undoped, doped and co-doped BNT ceramic compositions, the typical surface morphology were obtained using SEM, depicted in Fig. 3a–f. All the samples are well-sintered, grain boundaries are well-delineated, and no porosity was observed. The grain size varies with the dopant concentrations, as in Table 2. It has been observed that the Yb^{3+} incorporation with Er^{3+} ions increases the grain size. The dense microstructure and well-defined grain boundaries could help improve electrical properties [29, 30].

3.2 FTIR spectroscopy

The Fourier-transform infrared (FTIR) spectra of all the BNT ceramics with different dopant concentrations is depicted in Fig. 4. The FTIR spectra were recorded in the wavelength range of 400–900 cm^{-1}. In BNT, the intrinsic vibration band is represented by the bands observed at wavenumbers 550 and 820 cm^{-1}. The stretching of Ti–O bonds inside the octahedral groups seen in the perovskite structure is thought to be the cause of the absorption bands seen in this study. The FTIR bands at 820 and 550 cm^{-1} show an obvious shift towards lower wavenumbers, which may be related to the host materials' sensitivity to foreign ions inside the host substrate [31–33].

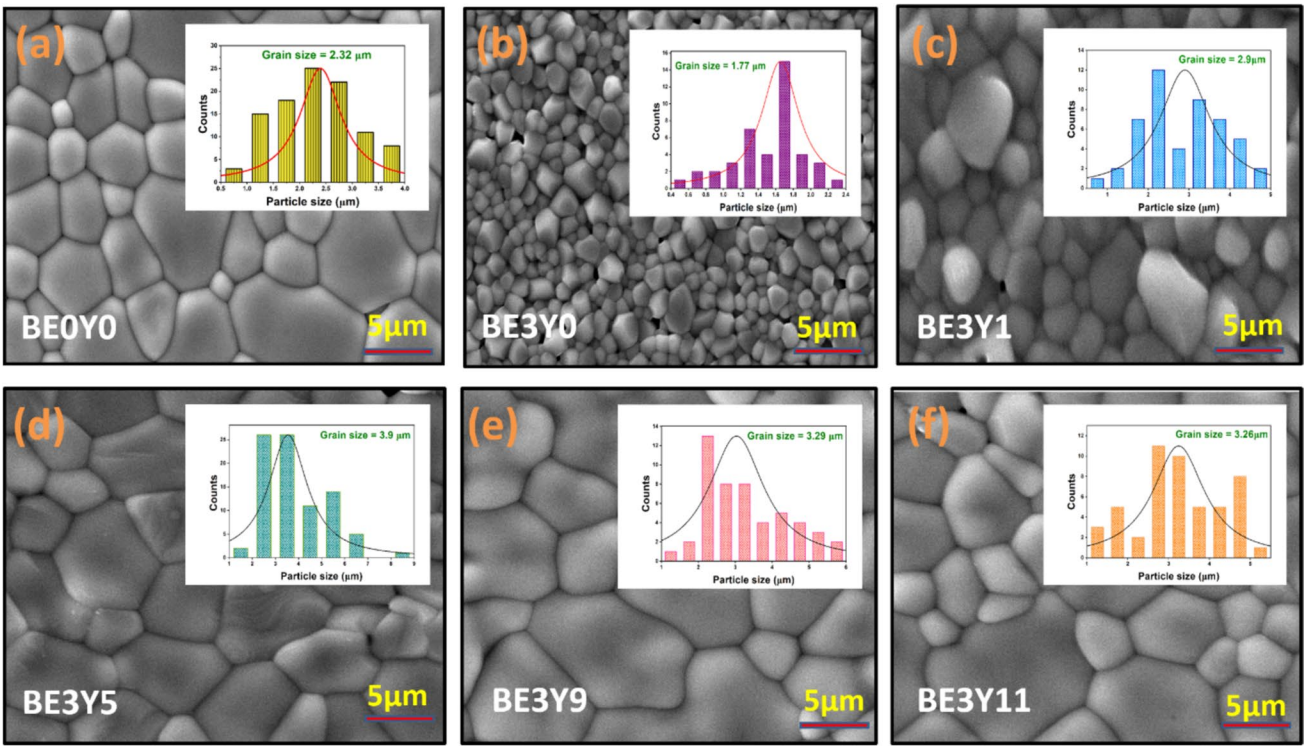

Fig. 3 SEM images of BNT compositions **a** BE0Y0 **b** BE3Y0 **c** BE3Y1 **d** BE3Y5 **e** BE3Y9 and **f** BE3Y11. Inset: histograms for grain size calculation

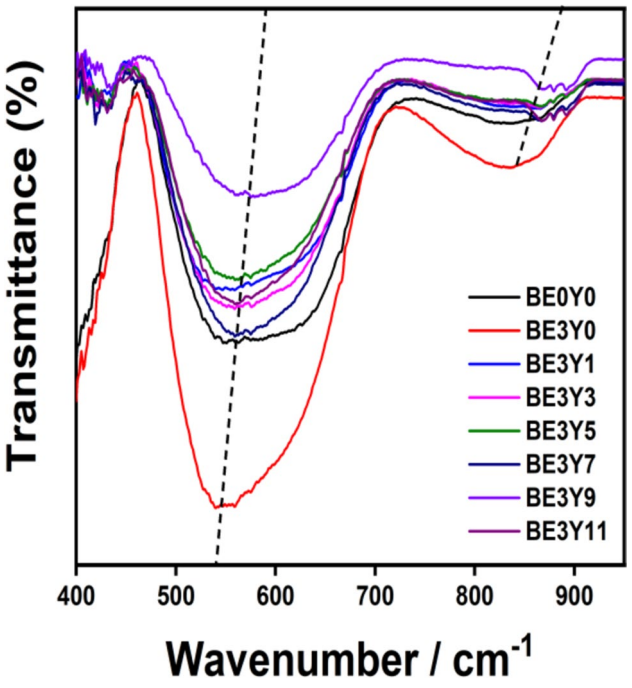

Fig. 4 FTIR spectra of prepared BNT ceramic compositions

3.3 Diffuse reflectance spectroscopy

The reflectance spectra (DRS) of the sintered powders of ceramic with different compositions of BNT doped with Er^{3+} and Yb^{3+} is shown in Fig. 5a. The various energy levels of Er^{3+} ions give rise to the absorption bands at about ~ 384, 488, 522, 545, 653, 795, 975 nm, which represents to various energy levels and are depicted as $^4G_{11/2}$, $^4F_{7/2}$, $^2H_{11/2}$, $^4S_{3/2}$, $^4F_{9/2}$, $^4I_{9/2}$ and $^4I_{11/2}$ respectively. Using Kubelka–Munk (K-M) relation the energy band gap of Er is calculated which is represented in Eq. (1) [34]:

$$F(R_\infty) = \frac{(1-R_\infty)^2}{2R_\infty} = \frac{K}{S} \tag{1}$$

where S denotes the scattering coefficient, K indicates the absorption coefficient, R_∞ represents the ratio between the diffuse reflectance from the sample and reference material. Furthermore, it can be used for diffused scattered light, where we can assume as S as constant value with respect to the wavelength. Additionally, by using Tauc expression we can calculate $F(R)$ and can be written as Eq. (2) [35]:

$$\left(F(R_\infty)hv\right)^n = B(hv - E_g) \tag{2}$$

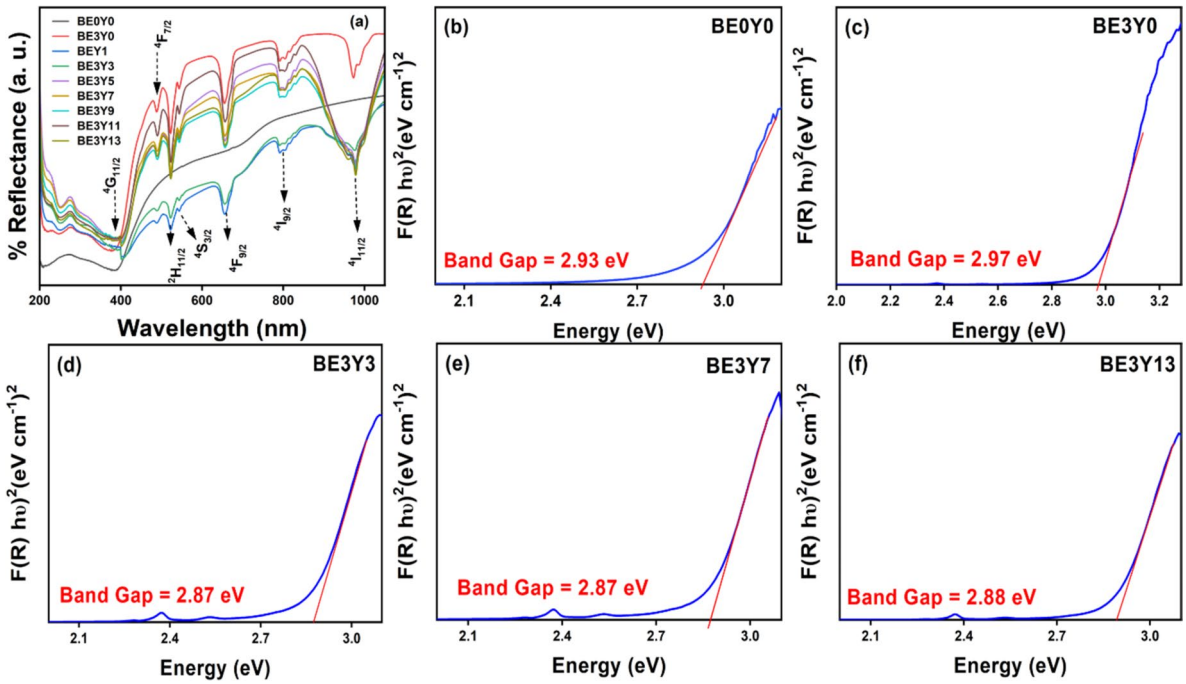

Fig. 5 **a** Diffuse reflectance spectra of all the prepared BNT ceramic compositions, the energy band gap of **b** BE0Y0 **c** BE3Y0 **d** BE3Y3 **e** BE3Y7 and **f** BE3Y13

In this formula, *Eg* denotes the optical energy band gap of the materials, *B* indicates the constant proportionality, υ stands for the vibrational frequency, *h* denotes the Planck's constant, and n is the electron transition.

The value of energy band gap is determined by the linear extrapolation of the data at the inflection point in $[F(R)h\upsilon]^2$ versus hυ plot is depicted in Fig. 5b–f. The measured values are consistent with the reported literature about the optical energy band gap of $Bi_{0.5-x-y}Er_xYb_yNa_{0.5}TiO_3$ ($E_g = 2.9$ eV) [36]. The band gap value is not varying much as the concentration is increasing. This little variation in the E_g value is due to the addition of Yb ions which introduces the new electronic level in the band gap and it reduces the energy band gap. There is a red shift in the energy band gap which is related to the oxygen vacancies and either defects due to the synthesis process involved on the reaction and one of the main reason for this is the large difference the Yb^{3+} and Bi^{3+} ionic radii [36].

3.4 Downshifting photoluminescence spectroscopy

The photoluminescence excitation (under 549 nm emission) and PL emission (under 489 nm excitation) spectra of BNT ceramic with changing Yb^{3+} concentration is depicted in Fig. 6a, b. Figure 6a shows excitation peaks of Er^{3+} resulting from $^4F_{5/2}$ and $^4F_{7/2}$ energy levels to different higher energy levels and observed at 450 nm and 489 nm [37–39]. The most intense peak was observed at 489 nm and was used as an excitation wavelength (λ_{exc}) to record the PL emission spectra. In Fig. 6 a, it can be seen that the doped BNT samples shows a broad band of low intensity around 310 nm which can only be attributed to the charge transfer from ligand to metal [40]. The lower intensity of charge transfer band than f–f transition ascertains the differential sensitization of erbium and ytterbium via host. Under excitation of 489 nm, the green emission at 530 nm and 549 nm contribute to the excited state to ground state from $^2H_{11/2}$ and $^4S_{3/2}$ to $^4I_{15/2}$. The weak red band transition is from $^4F_{9/2}$ to $^4I_{15/2}$ attributed at 662 nm. It can be seen from the Fig. 6 b, the relative emission intensity of the green and red band decreases after the optimized concentration (BE3Y3) of the material. The occurrence of non- radiative transitions due to concentration quenching leads to a reduction in the emission intensity. These results are also consistent with the study of the upconversion luminescence spectra [37–39]. This is because, in the downshifting photoluminescence spectra under the excitation 489 nm, the electrons immediately acquire the energy state $^4F_{9/2}$. At this level, the non-radiative transition occurs due to the multiphonon relaxation, which eventually reduces the intensity of the emission band [27].

3.5 Upconversion luminescence (UCL) spectroscopy

The upconversion luminescence (UCL) spectra traced at 980 nm excitation wavelength with the pumping power of 50 mW with excitation source density of 3.25 W/cm^2 for

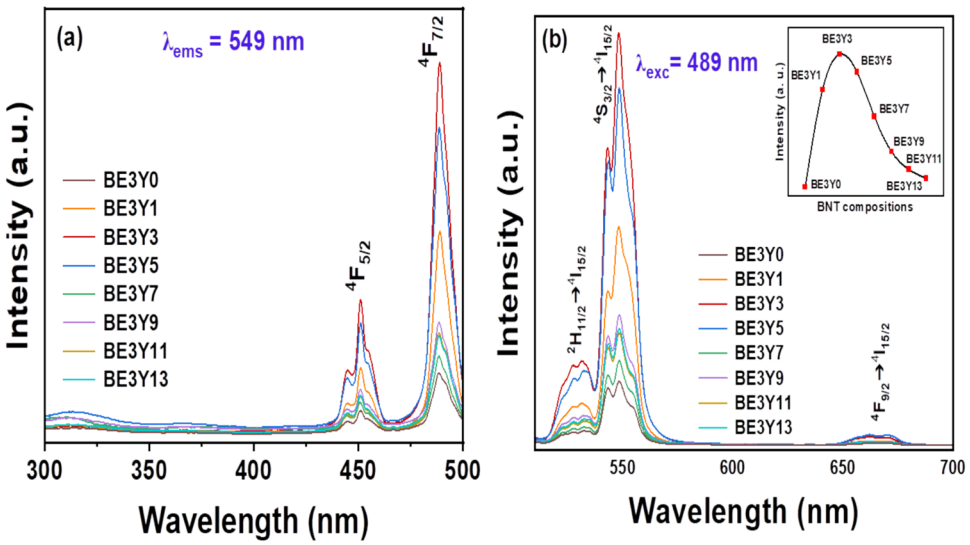

Fig. 6 Downshifting photoluminescence **a** excitation spectra **b** emission spectra of prepared BNT ceramic compositions

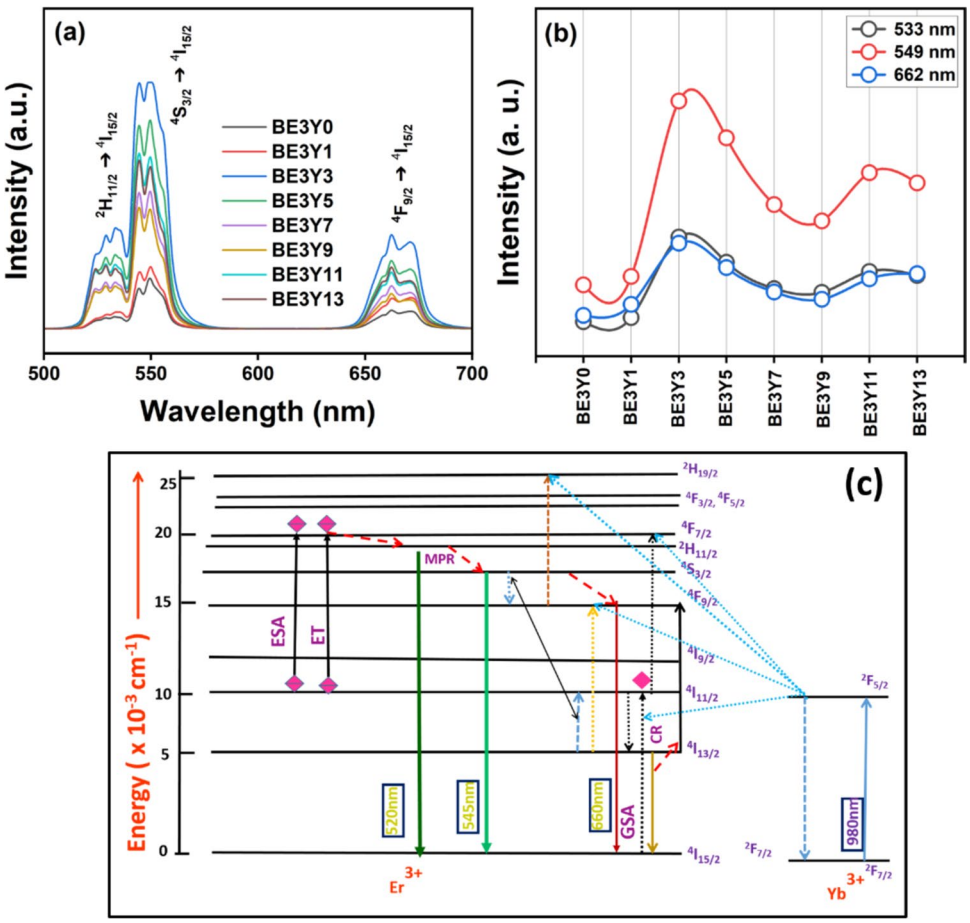

Fig. 7 **a** UCL spectra of Er^{3+}doped and series of Er^{3+}/Yb^{3+} co-doped BNT ceramic compositions **b** UC emission versus dopant concentration **c** energy level diagram showing possible pathways for UCL emission

Er^{3+}-doped and series of Er^{3+}/Yb^{3+} co-doped BNT ceramic composition is given in Fig. 7a. Two green and one red emission band are observed in UCL spectra. The one green band at 530 nm is ascribed to the transitions from the $^2H_{11/2}$ to $^4I_{15/2}$, and the other intense green band at 549 nm is due to the transition from $^4S_{3/2}$ to $^4I_{15/2}$ level. The detectable red emission band is obtained at 662 nm due to the transition of the $^4F_{9/2}$ to the $^4I_{15/2}$ level. It has been observed that the incorporation of Yb^{3+} in the host lattice along with fixed Er^{3+} content can significantly increase the UCL emission intensity. This is because of the larger cross-sectional area provided by the Yb ions for the energy transfer process,

which further increases the UC mechanism. The variation of UCL emission intensity with dopant concentration is given in Fig. 7b. The highest emission intensity is obtained for BE3Y3 BNT composition. The fall in UCL intensity after this composition is because of the concentration-quenching effect, which occurs owing to easy energy transfer between the dopant ions when they get closer at higher dopant concentrations, leading to non-radiative transitions. It can also be seen that the UCL emission intensity is still maintained at higher dopant concentrations due to the various cross-relaxation process occurring at higher dopant concentrations. The distance between the dopant ions can be measured by Blasse Eq. (3) [41]:

$$R_c \approx 2\left[\frac{3V}{4\pi x_c Z}\right]^{\frac{1}{3}} \tag{3}$$

where V denotes unit cell volume, Z represents the number of host cations, and X_c is the critical dopant concentration (BE3Y3). After substituting all the values, R_c is 15.56 Å. The energy level diagram for possible UCL mechanism is given in Fig. 7c. The ions from $^4I_{15/2}$ are excited to a higher energy level $^4I_{11/2}$ via GSA (ground state absorption). Another ion from the $^4F_{9/2}$ level of Yb ions is excited to a higher energy level $^4F_{5/2}$. The levels $^4F_{5/2}$ and $^4I_{11/2}$ are at the same level, making easy energy transfer between the Er and Yb ions. Now, the ions at the $^4I_{11/2}$ level jump to $^4F_{7/2}$ through ESA (excited state absorption). Also, ions from level $^4F_{5/2}$ reached the $^4F_{7/2}$ via ET (energy transfer), thus populating this level. From the $^4F_{7/2}$ level, the ions fall non-radiatively in the energy levels $^2H_{11/2}$, $^4S_{3/2}$, and $^4F_{9/2}$ via MPR (multiphonon relaxation). Lastly, from these levels, the ions make their transition to the lower energy level and result in three UCL emission bands at 530 nm, 549 nm, and 662 nm through transitions $^2H_{11/2}$, $^4S_{3/2}$, $^4F_{9/2}$ to $^4I_{15/2}$ level, respectively.

3.6 Time decay analysis

The decay curve is obtained under the excitation at 980 nm and the emission under 549 nm with the transition of $^4S_{3/2} \rightarrow {}^4I_{15/2}$ for BNT ceramics compositions is depicted in Fig. 8a–e. Using tri-exponential function the decay time was measured which is given by the Eq. (4):

$$I(t) = I_0 + A_1\exp(-\frac{t}{\tau_1}) + A_2\exp\left(-\frac{t}{\tau_2}\right) + A_3\exp(-\frac{t}{\tau_3}) \tag{4}$$

where A_1, A_2, A_3 are the fitting parameters, I_0 is the intensity at t = 0 s, is I(t) is the intensity at time t, and τ is decay time. The average time is calculated by Eq. (5):

$$<\tau> = \frac{A_1\tau_1^2 + A_2\tau_2^2 + A_3\tau_3^2}{A_1\tau_1 + A_2\tau_2 + A_3\tau_3} \tag{5}$$

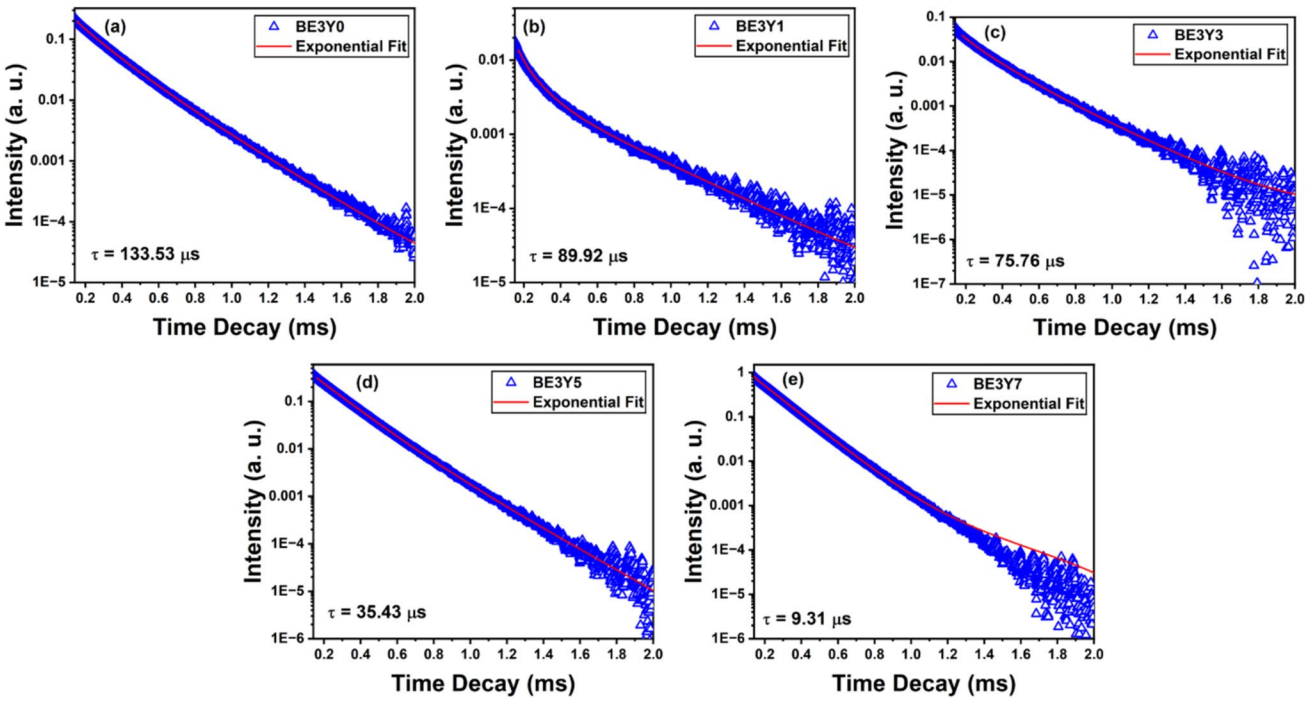

Fig. 8 Time decay profile of BNT compositions **a** BE3Y0 **b** BE3Y1 **c** BE3Y3 **d** BE3Y5 **e** BE3Y7

The average decay time of BNT ceramic compositions varies with dopant concentration. It can be seen that the average decay time decreases from 133.53 to 9.31 µs. This might be due to the rapid energy exchange between the Er^{3+} and Yb^{3+} ions, resulting in a non-radiative transition [42, 43]. The efficiency in energy transfer by the incorporation of Yb^{3+} ions can be measured using Eq. (6) [44]:

$$\eta = 1 - \frac{\tau_2}{\tau_1} \tag{6}$$

τ_1 is mean decay time for single Er^{3+}doped BNT and τ_2 is the mean decay time for Er^{3+}/Yb^{3+} BNT ceramic. It has been observed that the efficiency in energy transfer between the dopant ions is increased for all the co-doped BNT ceramic compositions and ranges from 32 to 93% for BE3Y1 to BE3Y7 ceramic.

3.7 Pump power dependency

An essential investigation to ascertain the quantity of photons engaged in the UC process is the dependence of pump power on upconversion luminescence. Luminescence spectra demonstrating upconversion under various pump powers density that lie in the range 29.41- 62.09 W/cm^2 is depicted in Fig. 9a. Pump power appears to be correlated with the intensity of UCL. In this study we see that the UCL appears to intensify as pump power is increased and this can be calculated using the Eq. (7) [45]:

$$I_{UCL} \propto P^n \tag{7}$$

The variables P, n, and I_{UCL} represent the pumping power, photon count, and UCL intensity, respectively, required for the upconversion process. Plot of intensity versus excitation pump power log is shown in Fig. 9(b). The logarithmic plot's slope is used to calculate the value of n for the green and red emission bands. The n values are 2.31, 1.69 for the green bands and 2.14 for the red band. This validates the contribution of two photons to the intensity of the UC emission. Multiple mechanisms (non-radiative transitions, ET, and ESA) have an impact on the emission spectra, which accounts for the disparity [46].

3.8 Optical temperature sensitivity

The optical temperature sensing of BE3Y3 ceramic was examined utilizing the FIR method. It has been widely employed to investigate the temperature sensitivity of numerous host materials doped with RE [47, 48]. Figure 10a illustrates the temperature-dependent UCL spectra, which span a temperature range of 303–523 K. The intensity of the UCL diminishes as the temperature rises as a consequence of thermal equilibrium in the TCLs. The FIR is represented by Eq. (8) [49, 50]:

$$FIR = \frac{I_H}{I_S} = Cexp\left(-\frac{\Delta E}{K_B T}\right) \tag{8}$$

where I_H represent the intensity of the green bands at 530 nm and I_S represent the intensity of the green bands at 550 nm, C is the exponential coefficient, and ΔE is the energy difference. The FIR values are depicted in Fig. 10b. The linear form of Eq. (7) is presented in Eq. (9):

$$Ln(FIR) = -\left(\frac{\Delta E}{K_B}\right)\left(\frac{1}{T}\right) + LnC \tag{9}$$

Figure 10c shows the Ln(FIR) against the inverse of temperature. The slope of this graph gives the value of $\Delta E/K_B$

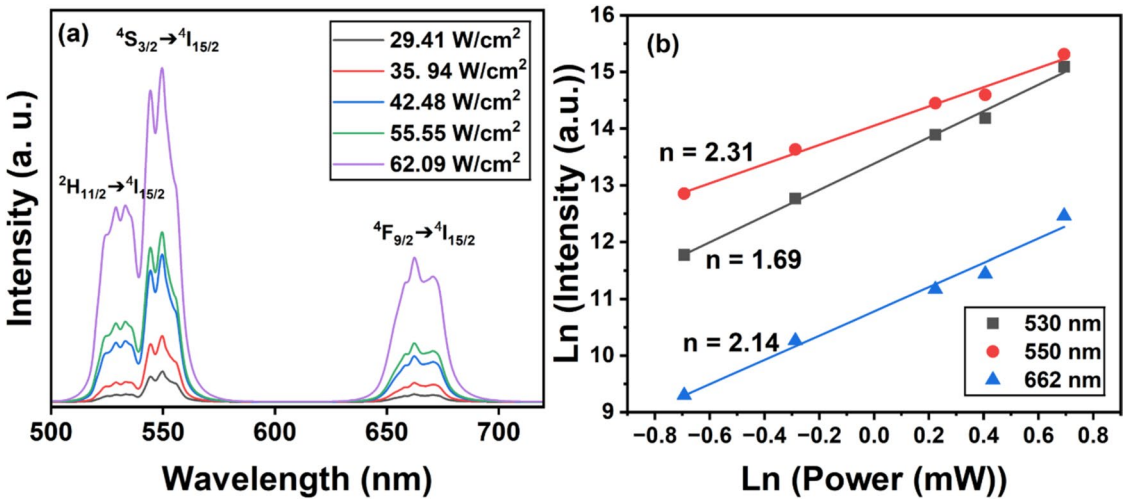

Fig. 9 **a** Pump power dependency on UCL spectra of BE3Y3 ceramic compositions **b** Ln (intensity) versus Ln (power) plot

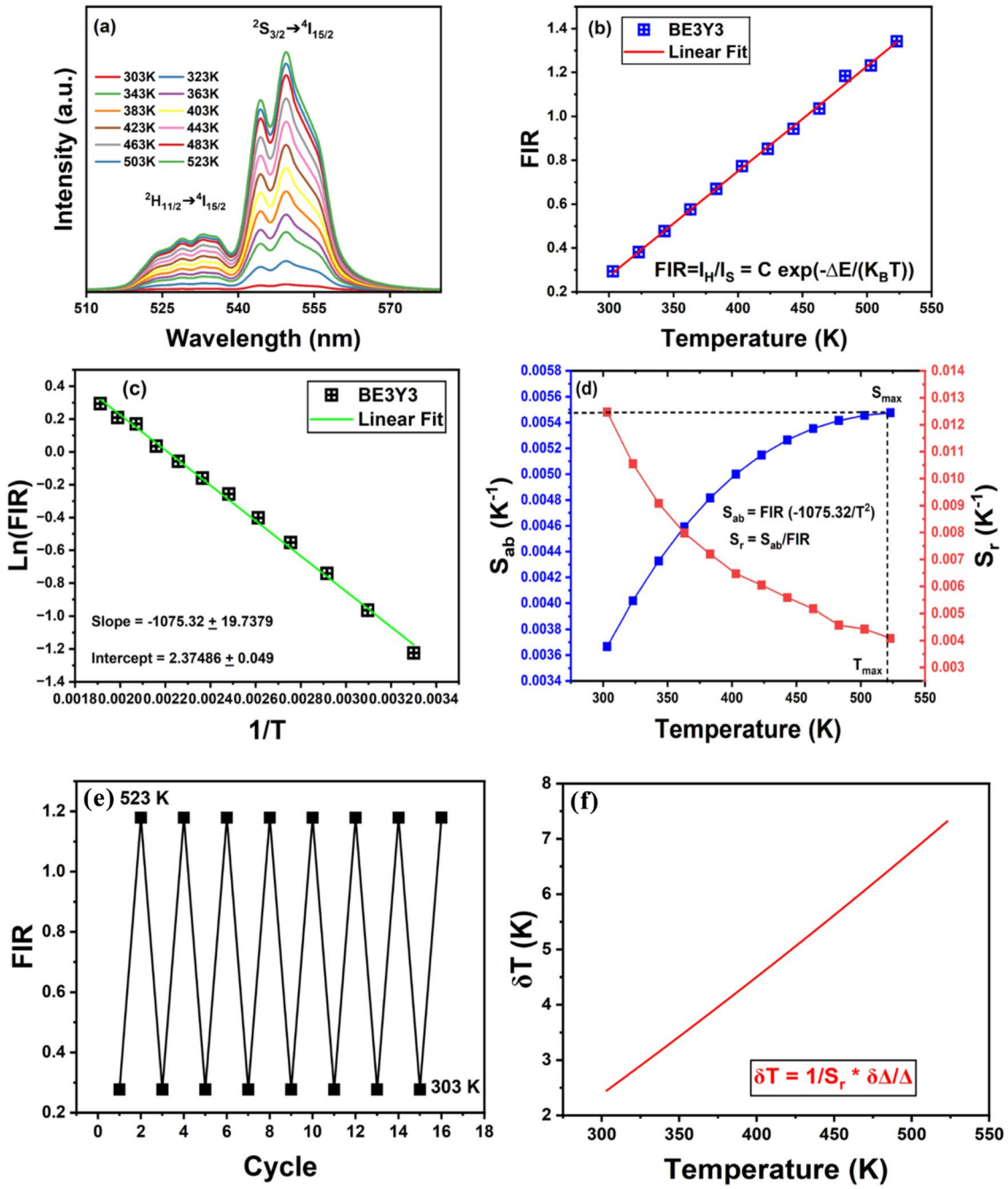

Fig. 10 **a** Temperature dependent UCL spectra **b** plot of FIR and temperature **c** Ln (FIR) vs T^{-1}, **d** plot of S_{ab} and S_r. **e** Repeatability test between 303 and 523 K **f** plot of δT vs temperature

value and intercept Ln C, which is used for calculating the absolute (S_{ab}) and relative (S_r) sensitivity of the materials established using Eqs. 10, 11, respectively:

$$S_{ab} = \frac{d(FIR)}{dT} = \frac{d\left(CExp\left(-\frac{\Delta E}{K_B T}\right)\right)}{dT} = CExp\left(-\frac{\Delta E}{K_B T}\right)\left(\frac{\Delta E}{K_B T^2}\right) \quad (10)$$

$$S_r = \frac{1}{FIR} * S_{ab} = \left(\frac{\Delta E}{K_B T^2}\right) \quad (11)$$

The plot of S_r and S_{ab} is denoted in Fig. 10d. The S_{ab} and S_r of BE3Y3 ceramic composition are 0.54% K^{-1} and 1.24% K^{-1} at 523 K and 303 K, respectively. For a practical sensor, the repeatability and resolution should be checked. The FIR values are varied between two temperatures (303 K

Table 3 Absolute sensitivity values of various Er/Yb co-doped ferroelectric ceramic

S. no.	Host material	Temp range (K)	Max sensitivity temp, T_{max} (K)	Max sensitivity, S_{ab} (K^{-1})	References
1	BNT: Er	175–500	380	0.0017	[13]
2	BNT: Er/Yb	175–553	493	0.0035	[51]
3	BNTO: Er/Yb	153–483	483	0.0078	[40]
4	NBT: Er	80–480	-	0.053	[52]
5	BNT: Er/Yb	163–613	-	0.0031	[53]
6	BBN: Er	300–623	483	0.00996	[41]
7	BNT: Er	303–523	523	0.0047	[27]
8	BNT: Er/Yb	303–523	523	0.0054	[This work]

and 523 K) and it was observed that the FIR value does not change abruptly confirming the good repeatability of the sample as shown in Fig. 10e. Taking specific (Δ_{Sp}) and mean values (Δ_m) of FIR and δ_Δ/Δ being the accuracy of the instrument, the mathematical expression for repeatability (R) and resolution (δT) is given in the Eqs. 12, 13, respectively [50]:

$$R = 1 - \frac{\left(\Delta_m - \Delta_{sp}\right)}{\Delta_{Av}} \tag{12}$$

$$\delta T = \frac{1}{S_r} \times \frac{\delta_\Delta}{\Delta} \tag{13}$$

Figure 10f shows that the temperature resolution increases with increasing temperature. The comparison Table 3 is given for the sensitivity of various host materials co-doped with Er^{3+}/Yb^{3+} ions.

4 Conclusion

The structural, upconversion luminescence, and sensing properties of a series of Er^{3+}/Yb^{3+} co-doped $Bi_{0.5-x-y}Er_xYb_yNa_{0.5}TiO_3$ ferroelectric ceramics are investigated. The rhombohedral geometry is confirmed by the XRD analysis, and the solubility of the dopant ions is demonstrated by the absence of any additional peaks. The dense microstructure with well-defined boundaries were evident in the SEM images. The typical characteristics of perovskite structure are illustrated by the FTIR vibrational bands at 550 cm^{-1} and 820 cm^{-1}, which are the result of the elongation of Ti–O bonds in octahedral groups. The Tauc plot displays the energy band gaps (E_g) in a range of 2.93–2.88 eV as a function of the dopant concentration. The photoluminescence spectra of all BNT ceramic compositions are measured under excitation wavelengths i.e. 489 nm and 980 nm. It has been noted that the two intense green and one visible red bands were present at 530 nm, 549 nm, and 662 nm, respectively. When excited at 980 nm, the UCL spectra vary with different pumping powers, indicating that the process involves two photons.The time-resolved fluorescence spectroscopy indicates that the efficiency of energy transfer between the dopant ions has increased for all co-doped BNT ceramic compositions. At 523 K and 303 K, the relative (S_r) and absolute (S_{ab}) sensitivity of the BE3Y3 ceramic composition are 1.24% K^{-1} and 0.54% K^{-1}, respectively. These findings suggest that the prepared ceramic has the capability to be used as multifunctional material.

Acknowledgements The authors thanks to Functional material research laboratory (FMRL), Department of Applied Physics, Delhi Technological University for providing research facilities to conduct this study. Also, one of the author thanks CSIR (08/133/0039) for the financial support.

Author contributions MN: conceptualization, data curation, formal analysis, methodology, writing—original draft, writing—review and editing. RS: resources. RB: conceptualization, investigation, methodology, resources, supervision, writing—review and editing of the original draft.

Data availability The authors mentioned above have all the relevant data associated with this research work and will be dedicated to sharing that if they are asked to do so in the future.

Declarations

Conflict of interest The authors declare that they have no known competing financial interests or personal relationships that could have appeared to influence the work reported in this paper.

References

1. S. Makishima, H. Yamamoto, T. Tomotsu, S. Shionoya, Luminescence spectra of Sm^{3+} in $BaTiO_3$ host lattice. J. Phys. Soc. Jpn. **20**, 2147–2151 (1965)
2. D.D. Dung, N.B. Doan, N.Q. Dung, L.H. Bac, N.H. Linh, L.T.H. Thanh, D.V. Thiet, N.N. Trung, N.C. Khang, T.V. Trung, N.V. Duc, Role of Co dopants on the structural, optical and magnetic properties of lead-free ferroelectric $Na_{0.5}Bi_{0.5}TiO_3$ materials. J. Sci. Adv. Mater. Dev. **4**, 584–590 (2019). https://doi.org/10.1016/j.jsamd.2019.08.007
3. P. Julphunthong, T. Bongkarn, S. Maensiri, The effect of firing temperatures on phase formation, microstructure and via the

combustion route. Ceram. Int. **41**, S143–S151 (2015). https://doi.org/10.1016/j.ceramint.2015.03.229
4. M. Bengisu, *Production of Ceramic Bodies, Engineering Ceramics, Engineering Materials* (Springer, Berlin, 2001). https://doi.org/10.1007/978-3-662-04350-9_3
5. R.D. Shannon, Revised effective ionic radii and systematic studies of interatomic distances in halides and chalcogenides. J. Acta Cryst. **A32**, 751–767 (2016). https://doi.org/10.1107/S0567739476001551
6. C. Kornphom, K. Saenkam, T. Bongkarn, Enhanced energy storage properties of BNT–ST-AN relaxor ferroelectric ceramics fabrication by the solid-state combustion technique. Phys. Status Solidi A (2022). https://doi.org/10.1002/pssa.202200240
7. O. Mitsuhiro, O. Masashi, B. Teruo, M. Mamoru, Temperature dependence of the fatigue and mechanical properties of lead zirconate titanate piezoelectric ceramics. Int. J. Fatigue **31**, 1254–1261 (2009). https://doi.org/10.1016/j.ijfatigue.2009.01.008
8. J.G. Hao, R.Q. Chu, Z.J. Xu, G.Z. Zang, G.R. Li, Structure and electrical properties of (Li, Sr, Sb)-modi fied $K_{0.5}Na_{0.5}NbO_3$ lead-free piezoelectric ceramic. J. Alloys Compd. **479**, 376–380 (2009). https://doi.org/10.1016/j.jallcom.2008.12.069
9. C.G. Xu, D.M. Lin, K.W. Kwok, Structure, electrical properties and depolarization temperature of $(Bi_{0.5}Na_{0.5})TiO_3$–$BaTiO_3$ lead-free piezoelectric ceramics. Solid State Sci. **10**, 934–940 (2008). https://doi.org/10.1016/j.solidstatesciences.2007.11.003
10. A. Gallegos-Melgar, D.G. Espinosa-Arbelaez, F.J. Flores-Ruiz, A. Lahmar, J.-L. Dellis, N. Lemee, F.J. Espinoza-Beltran, J. Munoz-Saldana, Ferroelectric properties of manganese doped $(Bi_{1/2}Na_{1/2})TiO_3$ and $(Bi_{1/2}Na_{1/2})TiO_3$–$BaTiO_3$ epitaxial thin films. Appl. Surf. Sci. **359**, 923–930 (2015). https://doi.org/10.1016/j.apsusc.2015.09.175
11. C. Peng, J.-F. Li, W. Gong, Preparation and properties of $(Bi_{1/2}Na_{1/2})TiO_3$–$Ba(Ti, Zr)O_3$ lead-free piezoelectric ceramics. Mater. Lett. **59**, 1576–1580 (2005). https://doi.org/10.1016/j.matlet.2005.01.026
12. R. Sahu, P. Kumar, Microstructural, dielectric and ferroelectric properties of $Sr_{0.8}Bi_{2.15}Ta_2O$+ ceramics synthesized by microwave processing technique. Phase Transit. **93**(1), 91–99 (2020). https://doi.org/10.1080/01411594.2019.1702190
13. X. Hui, D. Peng, H. Zou, J. Li, Q. Cao, Y. Li, X. Wang, X. Yao, A new multifunctional Aurivillius oxide $Na_{0.5}Er_{0.5}Bi_4Ti_4O_{15}$: up-conversion luminescent, dielectric, and piezoelectric properties. Ceram. Int. **40**(4A), 12477–12483 (2014). https://doi.org/10.1016/j.ceramint.2014.04.102
14. H. Yabuta, H. Tanaka, T. Furuta, T. Watanabe, M. Kubota, T. Matsuda, T. Ifuku, Y. Yoneda, Enhancement of tetragonal anisotropy and stabilisation of the tetragonal phase by Bi/Mn-double-doping in $BaTiO_3$ ferroelectric ceramics. Sci. Rep. **7**, 45842 (2017). https://doi.org/10.1038/srep45842
15. T. Rojac, A. Bencan, G. Drazic, N. Sakamoto, H. Ursic, B. Jancar, G. Tavcar, M. Makarovic, J. Walker, B. Malic, D. Damjanovic, Domain-wall conduction in ferroelectric $BiFeO_3$ controlled by accumulation of charged defects. Nat. Mater. **16**, 322–327 (2017). https://doi.org/10.1038/nmat4799
16. M. Li, M.J. Pietrowski, R.A.D. Souza, H. Zhang, I.M. Reaney, S.N. Cook, J.A. Kilner, D.C. Sinclair, A family of oxide ion conductors based on the ferroelectric perovskite $Na_{0.5}Bi_{0.5}TiO_3$. Nat. Mater. **13**, 31–35 (2014). https://doi.org/10.1038/nmat3782
17. Y. Li, Y. Jiao, S. Zhang, Z. Li, C. Song, J. Dong, G. Liu, Y. Yan, Improved electric energy storage properties of BT-SBT lead-free ceramics incorporating with A-site substitution with Na & Bi ions and liquid sintering generated by $Na_{0.5}Bi_{0.5}TiO_3$. J. Alloys Compd. **856**, 156708 (2021). https://doi.org/10.1016/j.jallcom.2020
18. X.Y. Tong, H.L. Li, J.J. Zhou, H. Liu, J.Z. Fang, Giant electrostrain under low driving field in $Bi_{1/2}Na_{1/2}TiO_3$-$SrTiO_3$ ceramics for actuator applications. Ceram. Int. **42**, 16153–16159 (2016). https://doi.org/10.1016/j.ceramint.2016.07.133
19. C. Cui, Y. Pu, Z. Gao, J. Wan, Y. Guo, C. Hui, Y. Wang, Y. Cui, Structure, dielectric and relaxor properties in lead-free ST-NBT ceramics for high energy storage applications. J. Alloys Compd. **711**, 319–326 (2017). https://doi.org/10.1016/j.jallcom.2017.04.023
20. Y.C. Guo, H.Q. Fan, C.B. Long, J. Shi, L. Yang, S.H. Lei, Electromechanical and electrical properties of $Bi_{0.5}Na_{0.5}TiO_{1-x}Mn_xO_{3-\delta}$ ceramics with high remnant polarization. J. Alloys Compd. (2014). https://doi.org/10.1016/j.jallcom.2014.04.038
21. N. Lei, M. Zhu, P. Yang, L. Wang, L. Wang, Y. Hou, H. Yan, Effect of lattice occupation behavior of Li^+ cations on microstructure and electrical properties of $(Bi_{1/2}Na_{1/2})TiO_3$-based lead-free piezoceramics. J. Appl. Phys. **109**, 054102 (2011). https://doi.org/10.1063/1.3555598
22. G. Viola, H. Ning, X. Wei, M. Deluca, A. Adomkevicius, J. Khaliq, M. John-Reece, H. Yan, Dielectric relaxation, lattice dynamics and polarization mechanisms in $Bi_{0.5}Na_{0.5}TiO_3$-based lead-free ceramics. J. Appl. Phys. **114**, 014107 (2013). https://doi.org/10.1063/1.4812383
23. A. Hussin, A. Maqbool, R.A. Malik, M. Su Kim, T.K. Song, M.H. Kim, Structural and electrical properties of $Bi_{0.5}Na_{0.5}TiO_3$ templates produced by topochemical microcrystal conversion method. New Phys. Sae Mulli **65**(8), 715–720 (2015). https://doi.org/10.3938/NPSM.65.715
24. Y. Hiruma, H. Nagata, T. Takenaka, Thermal depoling process and piezoelectric properties o bismuth sodium titanate ceramics. J. Appl. Phys. **105**, 084112 (2009). https://doi.org/10.1063/1.3115409
25. G.A. Smolenskii, V.A. Isupov, A.I. Agranovskaya, S.N. Popov, Ferroelectrics with diffuse phase transitions. Sov. Phys. Solid State **2**, 2584–2594 (1961)
26. D. Lin, K.W. Kwok, Dielectric and piezoelectric properties of $(Bi_{1-x-y}Nd_xNa_{1-y})_{0.5}BayTiO_3$ lead-freeceramics. Curr. Appl. Phys. **10**, 422–427 (2010). https://doi.org/10.1016/j.cap.2009.06.044
27. Y. Li, W. Chen, Q. Xu, J. Zhou, X. Gu, Piezoelectric and ferroelectric properties of $Na_{0.5}Bi_{0.5}TiO_3$–$K_{0.5}Bi_{0.5}TiO_3$–$BaTiO_3$ piezoelectric ceramics. Mater. Lett. **59**, 1361–1364 (2005). https://doi.org/10.1016/j.matlet.2004.12.041
28. M. Narwan, A. Banwal, R. Sharma, R. Bokolia, Non-invasive thermal sensing and improved recoverable energy storage density of $Bi_{0.5}Na_{0.5}TiO_3$: Er^{3+} doped multifunctional ferroelectric ceramic. J. Lumin. (2024). https://doi.org/10.1016/j.jlumin.2023.120236
29. Z. Chen, J. Hu, Piezoelectric and dielectric properties of $(Bi_{0.5}Na_{0.5})_{0.94}Ba_{0.06}TiO_3$–$Ba(Zr_{0.04}Ti_{0.96})O_3$ lead-free piezoelectric ceramics. Ceram. Int. **35**, 111–115 (2009). https://doi.org/10.1016/j.ceramint.2007.09.110
30. A. Mishra, B. Majumdar, R. Ranjan, A complex lead-free (Na, Bi, Ba)(Ti, Fe)O_3 single phase perovskite ceramic with a high energy-density and high discharge efficiency for solid state capacitor applications. J. Eur. Ceram. Soc. **37**, 2379–2384 (2017). https://doi.org/10.1016/j.jeurceramsoc.2017.01.036
31. H. Yang, F. Yan, Y. Lin, T. Wang, F. Wang, High energy storage density over a broad temperature range in sodium bismuth titanate-based lead-free ceramics. Sci. Rep. **7**, 8726 (2017). https://doi.org/10.1038/s41598-017-06966-7
32. B. Liu, B. Lu, X. Chen, X. Wu, S. Shi, L. Xu, Y. Liu, F. Wang, X. Zhao, W. Shi, A high performance flexible piezoelectric energy harvester based on lead-free $(Na_{0.5}Bi_{0.5})TiO_3$–$BaTiO_3$ piezoelectric nanofibers. J. Mater. Chem. A. **5**, 23634–23640 (2017). https://doi.org/10.1039/C7TA07570G
33. M. Zannen, M. Dietze, H. Khemakhem, A. Kabadou, M. Es-Souni, The erbium's amphoteric behavior effects on sodium

bismuth titanate properties. Ceram. Int. **40**, 13461–13469 (2014). https://doi.org/10.1016/j.ceramint.2014.05.069
34. A. Zeb, S.J. Milne, High temperature dielectric ceramics: a review of temperature stable high-permittivity perovskites. J. Mater. Sci. Mater. Electron. **26**, 9243–9255 (2015). https://doi.org/10.1007/s10854-015-3707-7
35. M. Zannen, A. Lahmar, M. Dietze, H. Khemakhem, A. Kabadou, M. Es-Souni, Structural, optical, and electrical properties of Nd-doped $Na_{0.5}Bi_{0.5}TiO_3$. Mater. Chem. Phys. **134**(2–3), 829–833 (2012). https://doi.org/10.1016/j.matchemphys.2012.03.076
36. P.A. Franco, P. Banerjee, P.L. Romanholo, Effect of composition induced transition in the optical band-gap, dielectric and magnetic properties of Gd doped $Na_{0.5}Bi_{0.5}TiO_3$ complex perovskite. J. Alloys Compd. **764**, 122e127 (2018). https://doi.org/10.1016/j.jallcom.2018.06.007
37. L.T.H. Thanh, N.B. Doan, N.Q. Dung, L.V. Cuong, L.H. Bac, N.A. Duc, P.Q. Bao, D.D. Dung, Origin of room temperature ferromagnetism in Cr-doped lead-free ferroelectric $Bi_{0.5}Na_{0.5}TiO_3$ materials. J. Electron. Mater. **46**, 3367–3372 (2017). https://doi.org/10.1007/s11664-016-5248-0
38. L. Mukhopadhyay, V.K. Rai, R. Bokolia, K. Sreenivas, 980 nm excited $Er^{3+}/Yb^{3+}/ Li^{+}/Ba^{2+}$: $NaZnPO_4$ upconverting phosphors in optical thermometry. J. Lumin. **187**(October), 368–377 (2017). https://doi.org/10.1016/j.jlumin.2017.03.035
39. R. Bokolia, O.P. Thakur, V.K. Rai, S.K. Sharma, K. Sreenivas, Dielectric, ferroelectric and photoluminescence properties of Er^{3+} doped $Bi_4Ti_3O_{12}$ ferroelectric ceramics. Ceram. Int. **41**(4), 6055–6066 (2015). https://doi.org/10.1016/j.ceramint.2015.01.062
40. R. Bokolia, V.K. Rai, L. Chauhan, K. Sreenivas, Structural and light upconversion luminescence properties of Er^{3+}–Yb^{3+}–W^{6+} substituted $Bi_4Ti_3O_{12}$. AIP Conf. Proc. **1731**, 4–7 (2016). https://doi.org/10.1063/1.4948208
41. L. Jacob, S. Sisira, K.P. Mani, K. Thomas, D. Alexander, P.R. Biju, N.V. Unnikrishnan, C. Joseph, A new potential green-emitting erbium-activated α-$Na_3Y(VO_4)_2$ nanocrystals for UV-excitable single phase pc-WLED applications. SN Appl. Sci. **1**, 1 (2024). https://doi.org/10.1007/s42452-020-2873-2
42. A. Banwal, R. Bokolia, Enhanced upconversion luminescence and optical temperature sensing performance in Er^{3+} doped $BaBi_2Nb_2O_9$ ferroelectric ceramic. Ceram. Int. **48**(2), 2230–2240 (2022). https://doi.org/10.1016/j.ceramint.2021.09.314
43. A. Shandilya, R.S. Yadav, A.K. Gupta, K. Sreenivas, Temperature-dependent light upconversion and thermometric properties of Er^{3+}/Yb^{3+}co-doped $SrMoO_4$ sintered ceramics. J. Mater. Sci. **56**, 12716–12731 (2021). https://doi.org/10.1007/s10853-021-06078-8
44. Z. Zhang, J. Li, L. Liu, J. Sun, J. Hao, W. Li, Upconversion luminescence and electrical properties of (K, Er) co-modified $Na_{0.5}Bi_{4.5}Ti_4O_{15}$ high-temperature piezoceramics. Phys. B Condens. Matter **580**, 411920 (2020). https://doi.org/10.1016/j.physb.2019.411920. (**09**)
45. W. Qi, Y. Wang, J. Wu, Z. Hu, C. Jia, G. Viola, H. Zhang, H. Yan, Relaxor behavior and photocatalytic properties of $BaBi_2Nb_2O_9$. J. Am. Ceram. Soc. **103**(1), 28–34 (2020). https://doi.org/10.1111/jace.16730
46. Y. Zhang, T. Xu, H. Yu, R. Chu, G. Li, C. Zhang, Z. Xu, Sm-modified bismuth layerstructured $SrBi_2Nb_2O_9$ multifunctional ceramics with enhanced electrical properties and good photoluminescence properties. Ceram. Int. (2022). https://doi.org/10.1016/j.ceramint.2022.03.182
47. Z. Liu, D. Chen, Upconversion photoluminescence and dual-mode temperature sensing properties of PIN-PMN-PT:Er^{3+} ceramic. J. Alloys Compd. **770**, 214–221 (2019). https://doi.org/10.1016/j.jallcom.2018.08.019
48. C. Liu, Q. Wang, X. Wu, B. Sa, H. Sun, L. Luo, C. Lin, X. Zheng, T. Lin, Z. Sun, Boosting upconversion photoluminescence and multielectrical properties via Er doping-modulated vacancy control in $Ba_{0.85}Ca_{0.15}Ti_{0.9}Zr_{0.1}O_3$. ACS Omega **4**, 11004–11101 (2019). https://doi.org/10.1021/acsomega.9b01391
49. Z. Guan, X. Li, R. Shen, Z. Tian, H. Yu, Y. Cao, Y. Wang, J. Zhang, S. Xu, B. Chen, Intense red up-conversion luminescence and temperature sensing property of Yb^{3+}/Er^{3+} co-doped $BaGd_2O_4$ phosphors. Spectrochim. Acta Mol. Biomol. Spectrosc. **284**, 121805 (2023). https://doi.org/10.1016/j.saa.2022.121805
50. J. Xing, F. Shang, G. Chen, Upconversion luminescence of Yb^{3+}/Er^{3+} co-doped $NaSrPO_4$ glass ceramic for optical thermometry. Ceram. Int. **147**, 8330–8337 (2021). https://doi.org/10.1016/j.ceramint.2020.11.195
51. A. Banwal, R. Bokolia, Thermometric sensing performance in Erbium modified $SrBi_{2-x}Nb_2Er_xO_9$ ferrolecyric ceramics for optoelectronics devices. Ceram. Int. **48**, 34405–34414 (2022). https://doi.org/10.1016/j.ceramint.2022.08.019
52. D. Peng, J.S. Yu, Effect of molybdenum on upconversion emission and temperature sensing properties in $Na_{0.5}Bi_{0.5}TiO_3$:Er/Yb ceramics. Ceram. Int. **41**, 6710–6714 (2015). https://doi.org/10.1016/j.ceramint.2015.01.113
53. S. Wang, H. Zhou, X. Wang, A. Pan, Up-conversion luminescence and optical temperature sensing properties of Er3+ doped perovskite $Na_{0.5}Bi_{0.5}TiO_3$. J. Phys. Chem. Solids **98**, 28–31 (2016). https://doi.org/10.1016/j.jpcs.2016.06.002
54. P. Du, L. Luo, W. Li, Q. Yue, Upconversion emission in Er-doped and Er/Yb codoped ferroelectric $Na_{0.5}Bi_{0.5}TiO_3$ and its temperature sensing application. J. Appl. Phys. (2014). https://doi.org/10.1063/1.4886575

Publisher's Note Springer Nature remains neutral with regard to jurisdictional claims in published maps and institutional affiliations.

Springer Nature or its licensor (e.g. a society or other partner) holds exclusive rights to this article under a publishing agreement with the author(s) or other rightsholder(s); author self-archiving of the accepted manuscript version of this article is solely governed by the terms of such publishing agreement and applicable law.

Organisational Clusters Concept—Adding Value to Surveys and Effectiveness to OD Interventions

Anu Singh Lather[1]

Shilpa Jain[2]

Yogesh Chandra Verma[3]

[1]Dr. B. R. Ambedkar University
[2]University School of Management Studies, Guru Gobind Singh Indraprastha University
[3]Department of Management, Uttrakhand Technical University

***Prof. Anu Singh Lather**, vice chancellor of Dr. B.R. Ambedkar University Delhi and IGDTUW, is a distinguished academic leader with a robust background in higher education. Previously, she served as pro vice chancellor of Delhi Technological University and has led significant reforms, including implementing NEP 2020, establishing new academic programs, and promoting research. Her expertise in Strategic HRM, Organizational Behaviour, and Change Management is well regarded, with over 230 research papers published and 20 PhD scholars supervised. Prof. Lather's contributions have earned her multiple awards, making her a prominent figure in Indian academia.*

anusinghlather@gmail.com

***Dr. Shilpa Jain**, an associate professor at Guru Gobind Singh Indraprastha University, New Delhi, specializes in behaviour training, organization development, and research methods. With over 100 published papers in esteemed national and international journals, her extensive 24-year research and training experience makes her a distinguished figure in her field. She was awarded the India Prime Woman Icon Award 2022 for her contributions to the holistic personality development of students.*

shilpajain.usms@gmail.com

***Yogesh C. Verma** is pursuing his PhD at Uttarakhand Technical University, Dehradun. An engineer by qualification, he has been working in the area of management since the beginning of his career. He has long and varied experience in areas of HRM/OB, Corporate Strategy, Corporate Planning and Performance Management, Change Management, Industrial Engineering, etc. in the corporate sector. He is guest faculty in some management institutes and associated with many technical and management professional bodies. He has three research papers to his credit.*

ycverma@gmail.com

Passive Islanding Detection Approach for grid integrated SPV System

Shruti Prajapati
Delhi Technological University(DTU)
Delhi, India
shrutiprajapati_2k21phdee03@dtu.ac.in

Rachana Garg
Delhi Technological University(DTU)
Delhi, India
rachana16100@yahoo.co.in

Priya Mahajan
Delhi Technological University(DTU)
Delhi, India
priyamahajan.eed@gmail.com

***Abstract*— This study presents a passive islanding detection technique (IDT) which is based on voltage ripple content at the point of common coupling (PCC) for grid integrated solar photovoltaic (SPV) system. While conventional passive detection techniques are commonly employed, they are not particularly effective at identifying islanding, especially when a minimal power mismatch exists. Furthermore, they may produce false detection in certain instances that are not islands. If islanding is not detected quickly, it may result in extremely hazardous and adverse situations. Passive detection techniques rely on power system parameters and might fail to detect islanding in certain scenarios. This research presents an efficient passive islanding detection approach for grid-integrated solar PV system. This technique employs time-domain spectral analysis to monitor the ripple component of the voltage source inverter (VSI) voltage at the PCC and identify discrepancies. In the presented research work islanding is detected when the ripple content is found to be more than a predetermined threshold level for a specific period of time. The performance of the presented method has been tested under different operating conditions. Within the given delay period of 3ms, the proposed technique was able to identify all forms of islanding cases and did not exhibit any form of non-detection zone.**

Keywords—Solar Photovoltaic, Voltage Ripple, Passive Islanding Detection, Non-Detection Zone, Voltage Source Inverter

I. INTRODUCTION

Inverter-based distributed generation (DG) has been rapidly growing. Protection against unintentionally islanding conditions is a key concern for power systems with major DG penetration. Detecting unintentional islands is essential as they can lead to unexpected consequences. Unexpected islands can cause voltage and frequency deviations, harmonics, flicker, circuit breaker damage and high inrush current during reclosure due to loss of synchronism [1]. Based on, IEEE Std. 929–2000 [2], IEC Std. 62116–2008 [3] and IEEE Std. 1547.1–2005 [4], standards an islanding detection technique should detect the islanding within two seconds of the formation of an island, and the operation of the distributed generation (DG) system should be stopped immediately. Thus, it is crucial to have an accurate and quick technique for detecting islanding. The researchers have presented numerous islanding techniques in order to determine the islanding conditions. These methods can be categorized into three categories: active methods, passive methods, and communication-based techniques [5]-[6].

In[7]researchers examined an impedance-based active islanding detection method for DC microgrids. The process is carried out using sensors in PV and a digital Lock-In Amplifier. But, external disturbances, such as voltage sags, harmonics, and transient events, might affect impedance-based techniques. These disturbances can disrupt impedance testing, lowering the accuracy of island detection. In [8] researchers propose an active islanding detection technique that combines the reactive power variation and positive feedback frequency shift. Although, this method increases the speed of islanding detection and minimizes non-detection zones without affecting the power quality but it might not be able to detect islanding under zero-power mismatch condition.

Passive approaches measure system parameters, including voltage and frequency, at the PCC between the utility grid and DG unit. Frequency and Over/Under voltage control detect islanding when frequency and voltage at PCC surpass predetermined thresholds [9]. Some examples of passive islanding detection techniques are voltage imbalance, voltage phase jump, total harmonic distortion (THD), rate of change of frequency over power, under voltage protection, over voltage protection, under frequency protection, and rate of change of power over frequency [10].

In passive islanding detection technique, islanding is detected when the monitored quantity deviates from its respective predetermined threshold value for the specified amount of time. Also, these techniques are not able to differentiate between non-islanding and islanding conditions, and they are also limited in their ability to detect islanding in some circumstances, such as when the power mismatch is zero.

Modern signal processing techniques like wavelet transform (WT) and short-time Fourier transform (STFT) have been used to reduce the NDZ of the passive methods. Due to the restricted window size, STFT did not offer multiple resolution even though it used a time-frequency window to localize the transients might be able to resolve this problem. The WT approach utilizes STFT and multiresolution techniques. WT analyses signals using variable windows, unlike STFT. The WT only extracts the low-frequency band, leaving out important features from the high-frequency band that can show islanding conditions.[11] Other recently developed techniques to solve these shortcomings like wavelet packet transform [12], neural network-based islanding detection [13] has been introduced which may perform well, but they are highly expensive and require extensive training.

The proposed research works evaluates the performance of an enhanced passive islanding detection technique using voltage ripples at PCC in a grid-connected solar PV system. This technique uses time domain spectral analysis to track variations in ripple content. Islanding is detected whenever voltage ripple at PCC exceeds the threshold for the specified delay time. The presented technique detects islanding within 3 ms and has no non-detection zone.

2024 IEEE Region 10 Symposium (TENSYMP) | 979-8-3503-6486-6/24/$31.00 ©2024 IEEE | DOI: 10.1109/TENSYMP61132.2024.10752124

979-8-3503-6486-6/24/$31.00 ©2024 IEEE

Authorized licensed use limited to: DELHI TECHNICAL UNIV. Downloaded on November 25,2024 at 04:48:02 UTC from IEEE Xplore. Restrictions apply.

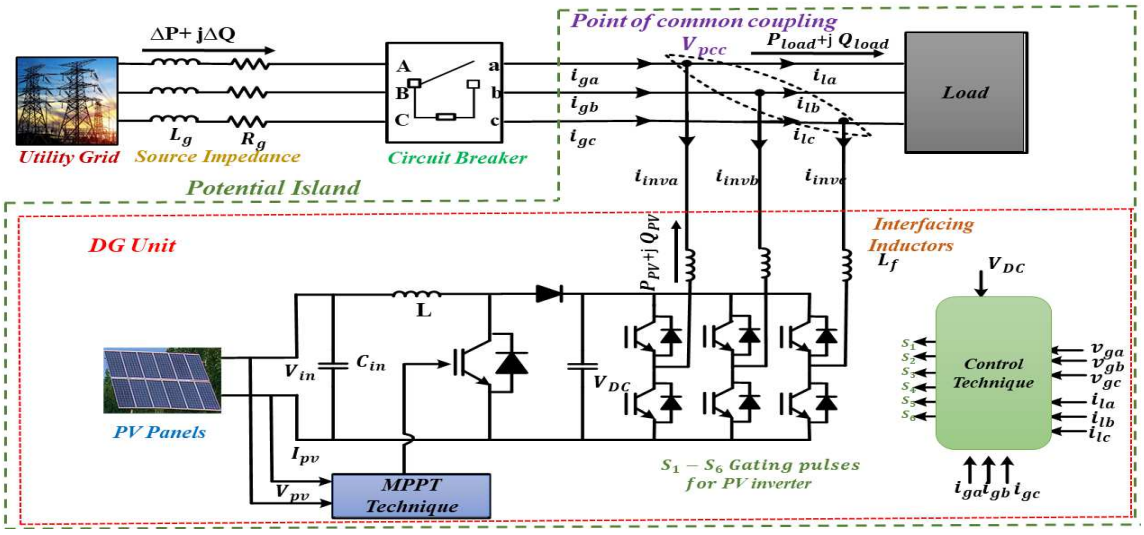

Fig.1 Schematic diagram of proposed model

Rest of the paper is arranged in the following order: In section 2, the system descriptions are discussed. The methodology for detecting islanding is detailed in section 3.A discussion of the findings and the outcomes of the simulation is given in section 4, and a conclusion regarding the findings is discussed in section 5.

II. System Description

In this study a grid connected solar PV based microgrid based on the UL1741 test system is used for the study as depicted in fig.1.[14] As per UL 1741, the RLC load at PCC has a quality factor of 2 and is set to the resonance frequency of 50 ± 0.1 Hz [17]. The load is expressed as a pure resistance(R), with a frequency of 50 Hz. This resistance has been adjusted so that it can absorb the rated power of the distributed generator module at the PCC voltage. Quality factor (Q_f) and impedance are represented in the following manner:

$$|Z| = \frac{1}{\sqrt{\left(\frac{1}{R^2}\right) + \left(\left(\frac{1}{wL}\right) - wC\right)^2}} \quad (1)$$

$$|Z| = \frac{R}{\sqrt{1 + {Q_f}^2 \left(\left(\frac{f_0}{f}\right) - \left(\frac{f}{f_0}\right)\right)^2}} \quad (2)$$

$$Q_f = R\sqrt{\frac{C}{L}} \quad (3)$$

In this study, distributed generation operates in unity power factor (UPF). Relationship between the PCC voltage (V_{pcc}) and power are represented by equation 4 &5.

$$P_l = P_{inv} + \Delta P \ = \frac{{V_{PCC}}^2}{R} \quad (4)$$

$$Q_l = Q_{inv} + \Delta Q \ = {V_{PCC}}^2 \left(\frac{1}{wL} - wC\right) \quad (5)$$

When the switch is closed, load (P_l, Q_l) is fulfilled by the solar PV (P_{inv}, Q_{inv}) and the grid ($\Delta P, \Delta Q$). Conversely, when the switch is open, the grid is isolated, creating a potential islanded zone that could result in hazardous operating conditions and serious power quality issues for the PV inverter and the RLC load.

III. Voltage Ripple Based Islanding Detection

Based on voltage ripples, the islanding detection technique is a computationally powerful passive technique that may be easily implemented in the inverter circuitry by observing the time domain spectrum content of voltage ripples [18]-[19]. Dead time effect, ripples in the DC link voltage, and high frequency switching in DG inverters leads to harmonic production. (V_{pcc}). Since grid voltage (V_g) and load power (P_l) are regarded as constants, any power fluctuation in P_{inv} is instantly reflected in V_{pcc}. The DG unit have potential to meeting the load requirement in the case of zero power mismatch (P_{inv}=P_l). As a result, this is regarded as the worst scenario in this research since traditional passive techniques cannot identify islanding in this situation. In this study voltage ripple-based islanding is used which monitors the ripple content in the V_{pcc} waveform to successfully detect islanding. Fig.2 presents a block diagram of this methodology.

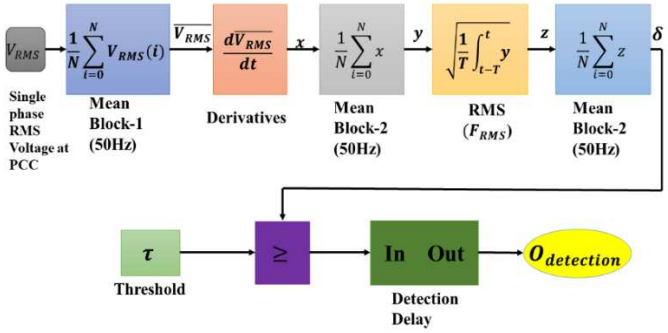

Fig.2 Proposed Islanding technique

The block diagram.2 illustrates how the RMS voltage (V_{RMS}) waveform's ripples are initially amplified by computing its derivative. After that, the RMS block processes the derivative signal to eliminate the DC component and

Authorized licensed use limited to: DELHI TECHNICAL UNIV. Downloaded on November 25,2024 at 04:48:02 UTC from IEEE Xplore. Restrictions apply.

determine how much ripple is there in the amplified waveform.

Each output stage is followed by three mean blocks: the first removes any noise at high frequencies in the source (V_{RMS}) over 50 Hz., the second removes any discontinuities in the derivative block's output, and the third mean block smooths out the RMS block's output.

Step1 displays the input waveform, representing the single-phase voltage (V) at the point of common coupling. Step 2 displays the V_{RMS}. The root mean square is determined over a one-cycle moving average window, using a nominal system frequency of 50 Hz.

$$V_{RMS} = \sqrt{\frac{1}{T}\int_{t-T}^{t} V^2} \qquad (6)$$

where T = 1/50 second. All frequency elements in the V_{RMS} above 50 Hz are considered noise and are removed employing mean block 1. This works similarly to a lowpass filter, which, as shown in fig. 2 (Step 3), suppresses any frequency elements over 50 Hz.
The filter output $\overline{V_{RMS}}$ is modelled as:

$$\overline{V_{RMS}} = \frac{1}{T}\int_{t-T}^{t} V_{RMS}.dt \qquad (7)$$

This approach requires amplifying minor fluctuations in $\overline{V_{RMS}}$ to function properly. To obtain the x waveform, take the derivative of $\overline{V_{RMS}}$, as shown in Fig.2 (Step 4. The derivative is assessed after every 10 µs sampling interval. To increase the technique's efficacy, frequency components over 50 Hz in the x waveform are removed using a filter to produce y waveform illustrated in Fig. 2 (Step 5) waveforms x and y are represented as

$$x = \frac{d(\overline{V_{RMS}})}{dt} \qquad (8)$$

$$y = \frac{1}{T}\int_{t-T}^{t} x \qquad (9)$$

The z waveform was calculated by evaluating the root mean square value of y over a f_{RMS} frequency cycle. Fig. 2 (Step 6) illustrates how this is employed to calculate the amount of ripple content and remove any DC components in y . To get the islanding detection waveform δ , any frequency component over f_{MEAN} is removed from waveform z, as shown in Fig. 2 (Step 7). The waveforms z and δ are described as

$$z = \sqrt{\frac{1}{T_{RMS}}\int_{t-T_{RMS}}^{t} y} \qquad (10)$$

$$\delta = \frac{1}{T_{MEAN}}\int_{t-T_{MEAN}}^{t} z \qquad (11)$$

Where, $T_{MEAN} = {}^{1}/_{f_{MEAN}}$ and $T_{RMS} = {}^{1}/_{f_{RMS}}$
The detection waveform δ is checked against a preset threshold. Islanding is identified when δ surpasses a predetermined threshold over a set time period. Let τ is detection threshold, t_δ is the predetermined decision time delay, and Δt is the time period when δ surpasses τ . Islanding detection decision signal. $O_{\text{detection}}$ is modelled as

$$O_{\text{detection}} = \begin{cases} 1, if\ \delta \geq \tau\ ,^{\circ}\Delta t \geq t_\delta \\ 0, if\ otherwise \end{cases} \qquad (12)$$

When $O_{\text{detection}}$=1, islanding is detected, while $O_{\text{detection}} = 0$ implies no islanding. At this frequency, the ideal threshold and time delay were 12 V/s and 3ms, respectively. [18]

IV. Result And Discussion

A grid-connected solar PV-based microgrid, as depicted in Fig. 1, was simulated to evaluate the feasibility of the presented method. Table 1 shows the major parameters utilized during the simulation [15]-[16]. At 0.3 seconds, the switch opens, isolating the DG unit and load from the grid and initiating the islanding process. IEC Std. 62116 states that detecting islanding gets more difficult when the load's power consumption matches the distributed generation. The cases examined are as follows:

i. Islanding of grid integrated SPV system with 0 % of active power mismatch condition.
ii. Islanding of grid integrated SPV system with 30 % of active power mismatch condition.
iii. Sudden load variation at point of common coupling
iv. Grid side distortion

TABLE I. System Parameter

System Parameter	Attributers
Solar PV power	12.53kW
Short Circuit current of solar PV module (I_{sc})	23.51A
Open circuit voltage of solar PV module (V_{oc})	726V
DC-DC converter duty ratio	0.4-0.5
Inductor	5mH
Capacitor	3uF
Switching Frequency	10kHz
DC link Voltage	750V
Interfacing Inductor(L_f)	6mH
Rated Power(P)	12.53kW
Load Inductance	21.9mH
Load Capacitance	426uF
Load Resistance	13.58ohm
Load Quality Factor	2
Grid voltage(V_{l-l}))	415
Grid Frequency	50Hz
Grid resistance and inductance	0.11ohm and 0.35mH

Authorized licensed use limited to: DELHI TECHNICAL UNIV. Downloaded on November 25,2024 at 04:48:02 UTC from IEEE Xplore. Restrictions apply.

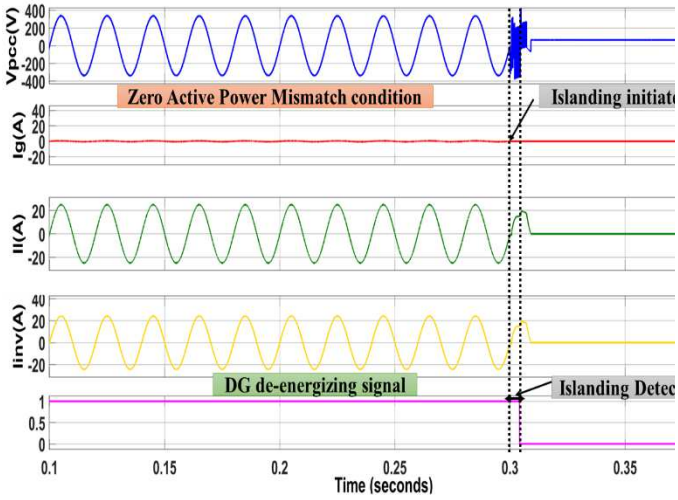

Fig.3(a) Islanding detection of grid integrated SPV system with zero active power mismatch

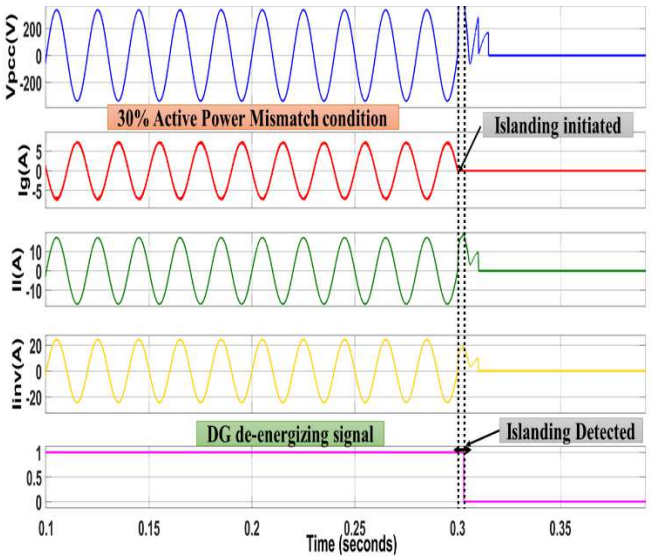

Fig.3(b) Islanding detection of grid integrated SPV system with 30 % active power mismatch

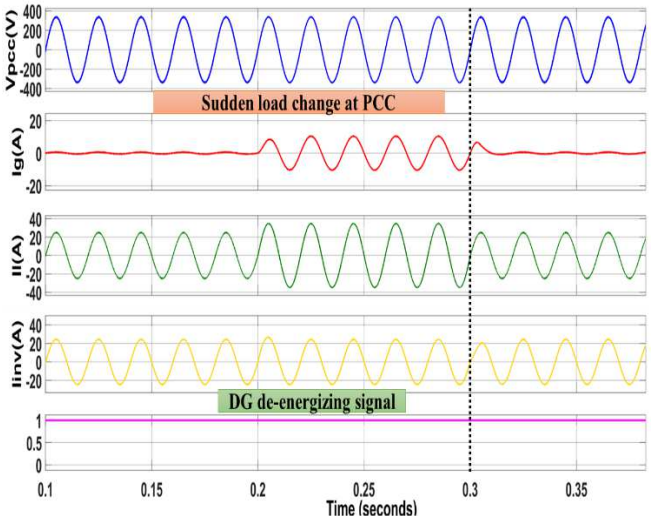

Fig.3(c) Sudden load change at point of common coupling

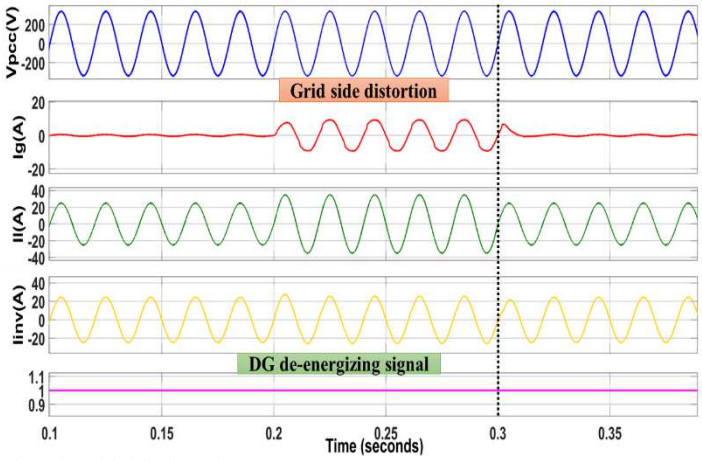

Fig.3(d) Grid side distortion

Fig. 3 depicts the simulation results for the various conditions considered in the study. Figures 3a-d illustrate the waveforms of PCC voltage (V_{pcc}), load current (I_l), grid current (I_g), VSI current (I_{inv}), and DG de-energizing signal. Figs. 3a and 3(b)show successful detection of islanding in the first two conditions.

In first condition, zero active power mismatch condition has been considered which is one of the most difficult scenarios to detect islanding. Fig.3(a) shows that before islanding, the grid current is nearly zero due to the inverter's active power matching the load's consumption. Islanding leads to zero grid current and fluctuation in PCC voltage.

It can be seen from the fig.3(a) when islanding occurs at 0.3seconds PCC RMS voltage ripple content increases. This is because when DG disconnects from the grid, it loses the grid's stabilizing effect, which causes the voltage fluctuation level to increase. The increased voltage fluctuation during islanding causes the amplitude of the produced waveform to exceed the threshold level. The technique detects islanding when the amplitude of the voltage waveform exceeds the threshold level. The DG de-energizing signal, initially fix to '1' for normal condition, is changed to '0' after 3ms of islanding detection due to the method's latency.

Similarly in case of 30% active power mismatch condition presented islanding technique is successful to detect islanding with in the specified time period and successfully turn off the solar PV inverter.

In addition, the proposed technique for detecting islanding is evaluated for sudden changes in load as well as grid side distortions when operating in the grid integrated mode. The MATLAB simulation findings in Figs 3(c) and 3(d) demonstrate that the presented approach correctly recognized unexpected sudden changes in load and grid voltage distortion as non-islanding condition. In response, the system maintained its DG de-energizing signal at a high level. Thus, it has been illustrated that the presented approach can correctly recognize these occurrences as non-islanding scenarios, allowing the system to keep operating effectively.

Authorized licensed use limited to: DELHI TECHNICAL UNIV. Downloaded on November 25,2024 at 04:48:02 UTC from IEEE Xplore. Restrictions apply.

V. Comparative Analysis of Proposed Islanding Detection

Table II displays the comparisons between the proposed strategy and conventional techniques based on various parameters. Compared to the conventional strategy, the technique examined in this work provides a number of advantages. It eliminates the NDZ, is relatively easy to compute, detects islanding quickly, and has no false detection and has no effect on power quality.

TABLE II. Comparision of proposed islanding detection technique (IDT) with existing techniques

Parameter	Conventional Passive IDT (OU/UV and ROCOF)	Proposed Passive IDT
Non Detection Zone(NDZ)	Large NDZ	Zero
Detection time	Up to 2 s	3ms
False Detection	High	None
Detection Parameter	Absolute value	Ripple Content

VI. Conclusion

In this paper a passive islanding detection technique which is based on voltage ripple content at the point of common coupling for grid integrated solar photovoltaic system is proposed. In order to detect islanding, the approach uses the voltage ripple content at PCC, along with a specified threshold value and delay duration. To detect the islanding and non-islanding conditions, the proposed scheme is tested under different islanding and non-islanding conditions. From the simulation results it has been found that proposed islanding detection technique detect islanding even under the most extreme condition, where the inverter output power is almost equivalent to the load consumption. As a result, the proposed islanding detection technique offers the zero non detection zone. Verification of non-islanding conditions takes place in typical scenarios such as load switching and grid side distortion. Additionally, in the aforementioned non-islanding circumstances, no island signal is generated, confirming that there is no of false detection.

References

[1] S. De, M. V. Reddy and R. Sodhi, "A Data-Driven Passive Islanding Detection Scheme," in IEEE Transactions on Industry Applications, vol. 60, no. 2, pp. 3698-3709, March-April 2024, doi: 10.1109/TIA.2023.3348425.

[2] IEEE Recommended Practice Utility Interface Photovoltaic (PV) Systems. IEEE Standard 929, Apr. 2000.

[3] Test Procedure Islanding Prevention Measure Utility-Interconnected Photovoltaic Inverters, IEC Standard 62116, 2008.

[4] IEEE Standard for Interconnecting Distributed Resources With Electric Power Systems, IEEE Standard 1547, Jul. 2003.

[5] A. Hussain, C. -H. Kim and A. Mehdi, "A Comprehensive Review of Intelligent Islanding Schemes and Feature Selection Techniques for Distributed Generation System," in IEEE Access, vol. 9, pp. 146603-146624, 2021, doi: 10.1109/ACCESS.2021.3123382.

[6] Ê. C. Resende, M. G. Simões and L. C. G. Freitas, "Anti-Islanding Techniques for Integration of Inverter-Based Distributed Energy Resources to the Electric Power System," in IEEE Access, vol. 12, pp. 17195-17230, 2024, doi: 10.1109/ACCESS.2024.3357710.

[7] B. K. Choudhury and P. Jena, "A Digital Lock-In Amplifier Assisted Active Islanding Detection Technique for DC Microgrids," in IEEE Transactions on Industry Applications, vol. 59, no. 1, pp. 377-391, Jan.-Feb. 2023, doi: 10.1109/TIA.2022.3215165.

[8] N. Kothari and B. G. Fernandes, "A hybrid active islanding detection technique for single-phase inverter-based distributed generation system," 2015 IEEE International Conference on Industrial Technology (ICIT), Seville, Spain, 2015, pp. 2828-2834, doi: 10.1109/ICIT.2015.7125515.

[9] Bower, W.I. and Ropp, M., 2002. Evaluation of islanding detection methods for utility-interactive inverters in photovoltaic systems (No. SAND2002-3591). Sandia National Lab.(SNL-NM), Albuquerque, NM (United States); Sandia National Lab.(SNL-CA), Livermore, CA (United States).

[10] Somalwar, R.S., Shinde, D.A. and Kadwane, S.G., 2023. Performance evaluation of voltage ripple-based passive islanding detection method for a single-phase utility-connected micro-grid system. *IETE Journal of Research*, *69*(2), pp.854-861.

[11] P. K. Ray, N. Kishor and S. R. Mohanty, "Islanding and Power Quality Disturbance Detection in Grid-Connected Hybrid Power System Using Wavelet and S-Transform," in IEEE Transactions on Smart Grid, vol. 3, no. 3, pp. 1082-1094, Sept. 2012, doi: 10.1109/TSG.2012.2197642.

[12] Ajith, M.A. and Shereef, R.M., 2024. Islanding and fault detection of inverter based distributed generations using wavelet packet transform and ensemble. Electric Power Systems Research, 231, p.110356.

[13] Aazami, R., Shoaei, M., Moradkhani, A., Shirkhani, M., ELrashidi, A. and AboRas, K.M., 2024. Deep neural networks based method to islanding detection for multi-sources microgrid. *Energy Reports*, *11*, pp.2971-2982.

[14] Standard for Inverters, Converters, Controllers and Interconnection System Equipment for Use with Distributed Energy Resources'. UL STD 1741, November 2005.

[15] Prajapati, S., Garg, R. and Mahajan, P., 2024. Honey Badger Algorithm Based PI Controller for DC Link Voltage Control of Solar Photovoltaic System Connected to Grid for Enhanced Power Quality. *Electric Power Components and Systems*, pp.1-20.

[16] Prajapati, S., Garg, R. and Mahajan, P., 2022, December. Evolutionary Algorithm for Enhanced Performance of Grid Connected SPV System. In *2022 5th International Conference on Contemporary Computing and Informatics (IC3I)* (pp. 814-820). IEEE.

[17] Gupta, N. and Garg, R., 2018. Algorithm for islanding detection in photovoltaic generator network connected to low-voltage grid. *IET Generation, Transmission & Distribution*, *12*(10), pp.2280-2287.

[18] Guha, B., Haddad, R.J. and Kalaani, Y., 2016. Voltage ripple-based passive islanding detection technique for grid-connected photovoltaic inverters. *IEEE Power and Energy Technology Systems Journal*, *3*(4), pp.143-154.

[19] Somalwar, R.S., Shinde, D.A. and Kadwane, S.G., 2023. Performance evaluation of voltage ripple-based passive islanding detection method for a single-phase utility-connected micro-grid system. *IETE Journal of Research*, *69*(2), pp.854-861.

Authorized licensed use limited to: DELHI TECHNICAL UNIV. Downloaded on November 25,2024 at 04:48:02 UTC from IEEE Xplore. Restrictions apply.

Performance analysis of Input Parallel Output Series Full Bridge Converter considering parasitic effects

Mugdha Goel
Electrical Engineering Department
Delhi Technological University
New Delhi, India
mugdhagoel_23phdee504@ dtu.ac.in

Dheeraj Joshi; SMIEEE
Electrical Engineering Department
Delhi Technological University
New Delhi, India
joshidheeraj@dce.ac.in

John Mulenga
Electrical Engineering Department
Delhi Technological University
New Delhi, India
mulengacjohn@gmail.com

***Abstract*— The Input Parallel Output Series (IPOS) Full-Bridge DC-DC converter offers significant advantages over the conventional Full-Bridge converter by connecting multiple modules in parallel on the input side and in series on the output side. This configuration enhances voltage gain, improves overall efficiency, reliability, and scalability. MATLAB simulations are carried out to demonstrate the IPOS converter's superior performance in terms of voltage output and efficiency. Additionally, the IPOS design provides enhanced redundancy; if one module fails, the others continue to operate, ensuring uninterrupted performance. This makes the IPOS Full-Bridge converter ideal for applications in renewable energy systems, electric vehicles, and other high-performance power management scenarios.**

Keywords—Input Parallel Output Series (IPOS) Full-Bridge converter, DC-DC converters, renewable energy systems, cascaded DC-DC converters.

NOMENCLATURE

V_{in}	Input Voltage
V_o	Output Voltage
P_{out}	Output Power
P_{in}	Input Power
IPOS	Input Parallel Output Series
FBC	Full Bridge Converter
V_{SW}	Switching Voltage
r_C	Filter Capacitor Resistance
fs	Switching Frequency
$r_{DS}(on)$	Drain-Source On Resistance
r_D	Diode Resistance
r_L	Inductor Resistance
L_O	Inductor
CFBC	Conventional Full-Bridge Converter
R_L	Load Resistance

I. INTRODUCTION

The Full-Bridge DC-DC converter is a widely used topology in power electronics which is recognized for its efficiency, electrical isolation, and capability to manage significant power levels [1]. Despite its advantages, the conventional FBC faces challenges in high-power applications due to component stress and efficiency limitations. Recent advancements in converter design have focused on overcoming these limitations through innovative configurations such as the Input-Parallel Output-Series (IPOS) connection [2], [3].

The IPOS Full-Bridge DC-DC converter addresses the limitations of traditional designs by connecting multiple converter modules in parallel on the input side and in series on the output side. This configuration enhances performance by improving current sharing and achieving higher voltage gains, which increases overall efficiency [3], [4]. The modular nature of the IPOS converter also offers scalability, making it suitable for a wide range of applications, from renewable energy systems to electric vehicles [4].

Recent studies have demonstrated the effectiveness of the IPOS configuration in various high-power applications. For instance, researchers have compared the performance of isolated interleaved boost converters and full-bridge converters [5], highlighting the superior efficiency of the former. Similarly, the application of the IPOS Full-Bridge DC-DC converter in high-power environments has been explored, confirming its capability to handle significant power levels with improved performance metrics [8].

Furthermore, studies have underscored the importance of soft commutation techniques in enhancing the efficiency and reliability of DC-DC converters [10]. These techniques, when applied to the IPOS Full-Bridge converter would further reduce switching losses and improve overall system performance.

This paper aims to provide a comprehensive analysis of the IPOS Full-Bridge DC-DC converter, focusing on its design, operational principles, and performance benefits. Through detailed simulations and comparative studies, including the analysis of parasitic effects, the performance of both the conventional Full-Bridge converter and the IPOS Full-Bridge converter will be examined. The effectiveness of the IPOS configuration in high-power applications will be demonstrated, offering valuable insights for future advancements in DC-DC converter technology.

II. OPERATION OF FULL-BRIDGE CONVERTER

Fig. 1. shows the circuit of a full-bridge DC-DC converter. It includes 4 switches (S1-S4) that operate in pairs and a transformer with a specific turns ratio of n: 1. The switches operate in diagonal pair, when S1 turns on at the same time as S4 while S2 turns on at the same time as S3. A delay is implemented between the switches to avoid shoot through current.

2024 IEEE Region 10 Symposium (TENSYMP) | 979-8-3503-6486-6/24/$31.00 ©2024 IEEE | DOI: 10.1109/TENSYMP61132.2024.10752111

979-8-3503-6486-6/24/$31.00 ©2024 IEEE

Authorized licensed use limited to: DELHI TECHNICAL UNIV. Downloaded on November 25,2024 at 04:43:07 UTC from IEEE Xplore. Restrictions apply.

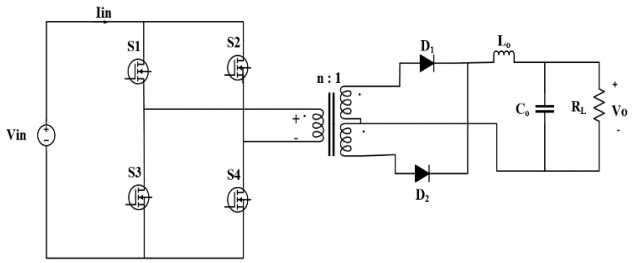

Fig. 1. Full-Bridge DC-DC converter

The Full-Bridge converter operates through four distinct modes within a switching cycle, as described below. The operation also ensures efficient voltage conversion. A delay is implemented between one diagonal pairs of switches to avoid shoot through current.

1) Mode 1 ($0 < t \leq DT$): S1 and S4 are ON, D1 conducts; current flows through the transformer primary, increasing magnetizing inductance current.

2) Mode 2 ($DT < t \leq T/2$): All switches are OFF, D1 and D2 conduct; voltage across switches drops to half of the input voltage, peak magnetizing inductance current achieved.

3) Mode 3 ($T/2 < t \leq T/2 + DT$): S2 and S3 are ON, D2 conducts; polarity across the transformer primary reverses, magnetizing inductance current decreases.

4) Mode 4 ($T/2 + DT < t \leq T$): All switches are OFF, D1 and D2 conduct; similar to Mode 2, completing the switching period cycle.

Voltage gain considering turns ratio of transformer for ideal FBC is as follows;

$$\frac{Vo}{Vin} = \frac{n}{1-D} \tag{1}$$

III. MODELLING OF IPOS FULL BRIDGE CONVERTER

The Input Parallel Output Series (IPOS) configuration is composed of multiple modules connected in parallel at the input side and in series at the output side as shown in Fig. 2..

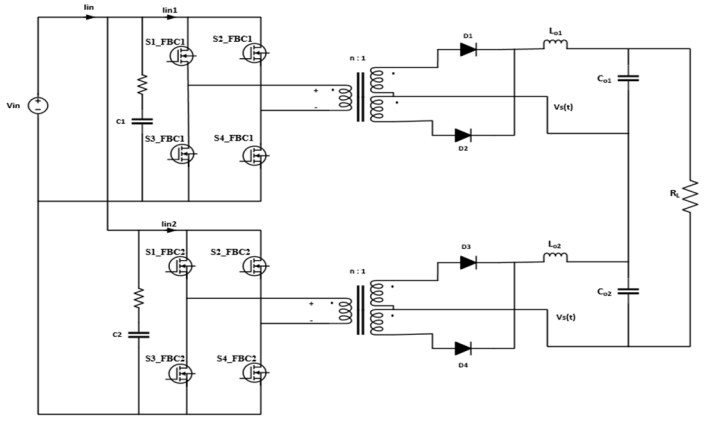

Fig. 2. IPOS Full-Bridge converter Schematic Diagram

It employs this technique to facilitate current sharing among individual modules, thereby reducing current stress while supporting a combination of network voltage on the high-output voltage side.

The relationship between the input and output power is expressed by the equations: (2), (3) & (4)

$$V_{in}I_{in1} = V_{o1}I_o \tag{2}$$

$$V_{in}I_{in2} = V_{o2}I_o \tag{3}$$

$$V_{in}I_{inn} = V_{on}I_o \tag{4}$$

Ideally, the proficiency of each module is expected to be 100% as shown in (1). V_{in} is the input voltage of the DC converter. V_{o1}, V_{o2}, …, Von are the output voltages, Io is the load current and I_{in1}, I_{in2}, …, I_{inn} are the module input currents.

The total input power equals the product of the sum of the input currents of the n modules and the input voltage of the DC converter as shown in (5) while the total output power equals the product of the sum of the voltages of the n modules and the load current of the DC converter as shown in (6).

$$Pin = V_{in}.(\sum_{i=1}^{n} Iin) \tag{5}$$

$$Pout = Io.(\sum_{i=1}^{n} Vo) \tag{6}$$

Therefore, the efficiency of the converter is calculated by equation (7) ;

$$\eta = \frac{Pout}{Pin} \tag{7}$$

IV. SIMULATIONS AND RESULTS

In this section, the performance of the DC-DC FBC with R connected load has been tested using MATLAB Simulink platform. Based on the simulation results, various critical parameters of Full Bridge DC-DC converter and the IPOS Full-Bridge DC-DC converter are analysed and compared to select the most efficient and suitable converter. Both converters are analysed with an input voltage of 340V and under different switching frequencies, from a minimum frequency of 1 kHz to a maximum switching frequency of 175 kHz, with the results documented. The converter specifications are shown in Table I.

TABLE I

FULL-BRIDGE CONVERTER SPECIFICATIONS

SI No	Parameters	Specifications
1	Input Voltage	V_{in} = 340V
2	Load Resistance	R_L = 15Ω
3	Output Inductor	L_o = 40e-6 H
4	Filter Capacitor	C_o = 50e-6 F
5	Transformer turns ratio	5:1:1

A. Conventional Full-Bridge DC-DC Converter

The Full-Bridge Converter is analysed at three different switching frequencies: 1 kHz, 50 kHz, and 175 kHz. At a switching frequency of 1 kHz, the FBC displays an output voltage of 59.42V with an input current of 1.979A and an output current of 7.735A. At this frequency, the FBC has an efficiency

Authorized licensed use limited to: DELHI TECHNICAL UNIV. Downloaded on November 25,2024 at 04:43:07 UTC from IEEE Xplore. Restrictions apply.

of 75.15% which is significantly very low, with an input power of 364.5W and an output power of 274W. The voltage gain is measured to be 0.1841, indicating that the converter effectively steps down the input voltage.

At 50 kHz, the FBC's performance improves significantly. It maintains an output voltage of 59.42V, while the efficiency increases to 87.69%. The input power rises to 441.7W, while the output power increases to 386.1W from the initial result, and the voltage gain decreases slightly to 0.1583.

At fs = 175 kHz, the output voltage drops to 49.75V. The input current reduces to 0.5712A, and has an efficiency of 84.5%. The input power is measured at 193W, and the output power at 165W, with the voltage gain dropping to 0.1463.

Fig. 3 (a). illustrates the output voltage waveform of the FBC. The waveform prominently displays the peak voltage of 56V and reaches a steady state value of 49.96V.

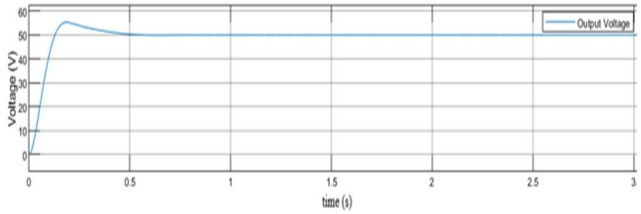

Fig. 3 (a). Simulation waveform of output voltage FBC

Fig. 3 (b). illustrates the output power waveform of the FBC. The waveform shows the reaches a maximum value of 200W during its transient state and eventually has a steady state value of 166.2W.

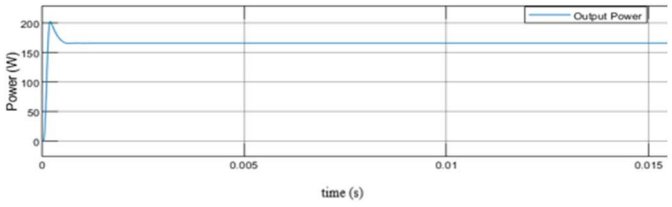

Fig. 3 (b). Simulation waveform of input current of FBC

B. IPOS Full-Bridge DC-DC Converter

The IPOS Full-Bridge converter is analysed at different switching frequencies. At 1 kHz, it produces an output voltage of 118.4V with an input current of 3.958A and the output current of 7.735A. It has an efficiency of 85.45%, significantly higher than the Full-Bridge Converter at this switching frequency. Displays an input power 508.4W and the output power of 434.2W, with 0.2374 voltage gain. This shows the IPOS Full-Bridge Converters capability to handle high output power with a better efficiency as compared to the Full-Bridge.

At 50 kHz, the IPOS Full-Bridge Converter maintained an output voltage of 118.4V and matched the Full-Bridge Converter's efficiency of 87.69%. The input power increased to 883.4W, and the output power rose to 772.2W, with an improved voltage gain of 0.3166.

At 175 kHz, the output voltage was 99.5V with an input current of 3.729A. The efficiency is slightly higher than the Full-Bridge Converter at 85.29%. The input power was measured at 508.4W, and the output power was 434.2W, with a voltage gain of 0.2374.

Fig. 4 (a). shows the output voltage waveform of IPOS Full-Bridge converter. The waveform prominently displays the peak voltage of around 85V.

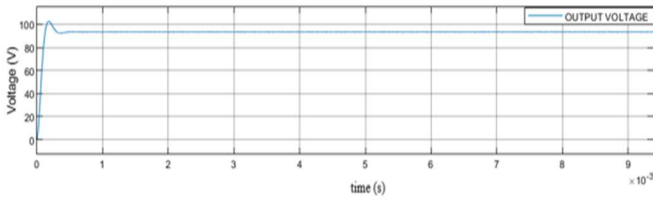

Fig. 4 (a). Simulation waveform of output voltage IPOS FBC

Fig. 4 (b). illustrates output power of the IPOS FBC which has a staedy state value of 588W.

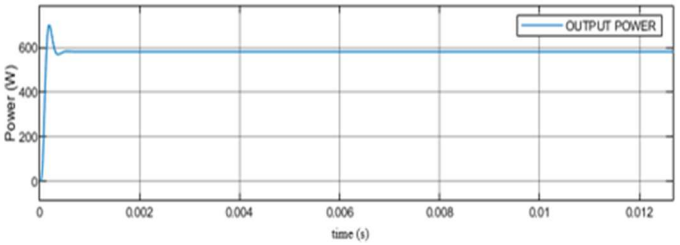

Fig. 4 (b). Simulation waveform of input current of IPOS Full-Bridge Converter

Fig. 5 (a). and Fig. 5 (b). present a comparative analysis of the efficiency variations between the FBC and the IPOS Full-Bridge converter under different output power conditions. This analysis is critical for evaluating the performance and operational efficiency of both converter topologies across a range of power outputs.

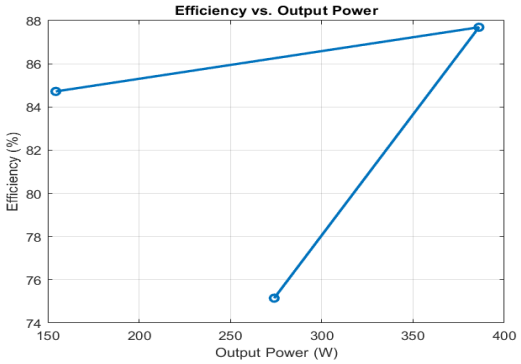

Fig. 5 (a). Efficiency v/s Output Power FBC BC, D = 0.4, R_L = 15Ω

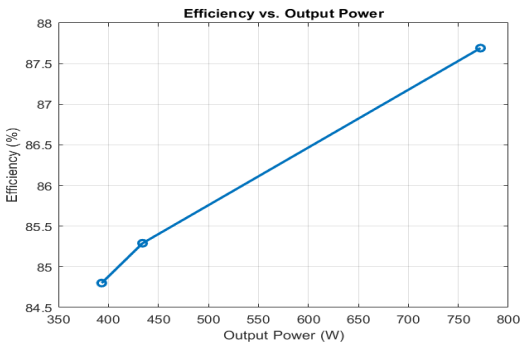

Fig. 5 (b). Efficiency v/s Output Power IPOS FBC, D = 0.4, R_L = 15Ω

Authorized licensed use limited to: DELHI TECHNICAL UNIV. Downloaded on November 25,2024 at 04:43:07 UTC from IEEE Xplore. Restrictions apply.

The graphs illustrate the superior performance of the IPOS Full-Bridge converter compared to the conventional Full-Bridge Converter. The efficiency of the IPOS FBC increases with rising output power, indicating its capability to handle high power loads effectively. In contrast, the FBC demonstrates a relatively low efficiency of 75% at an output power of approximately 275W, with fluctuations in efficiency as the output power varies. This highlights the IPOS FBC's advantage in maintaining higher efficiency across different power levels.

1. Parameter Analysis on Varying Frequencies

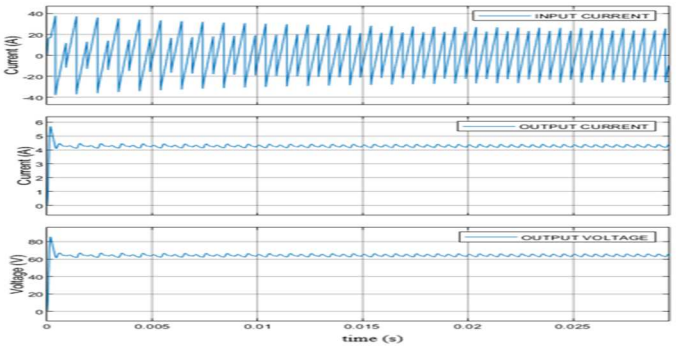

Fig. 6 (a). FBC parameter waveform at 1 kHz

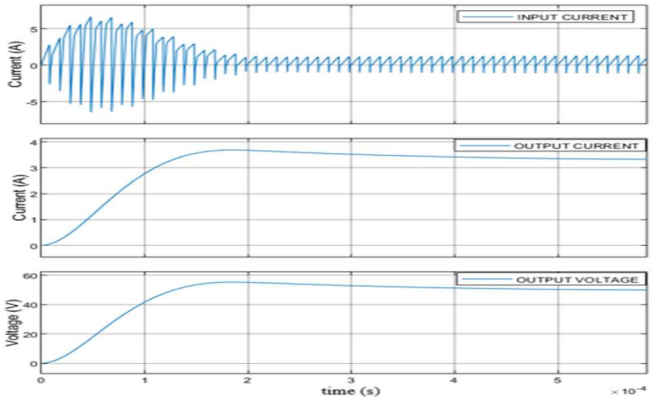

Fig. 6 (b). FBC parameter waveform at 50 kHz

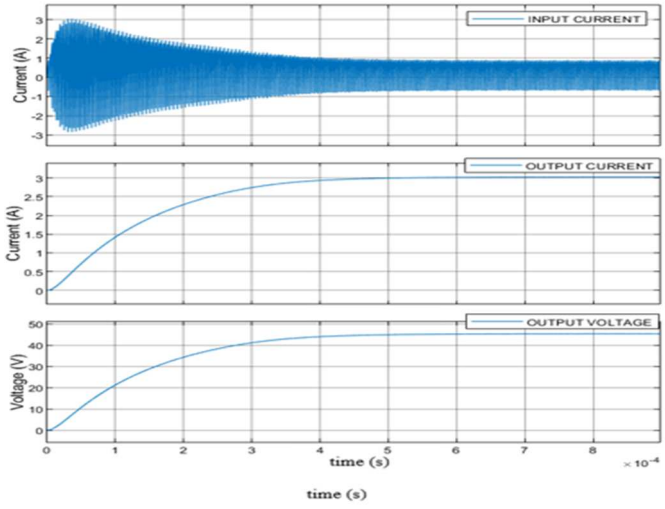

Fig. 6 (c). FBC parameter waveform at 175 kHz

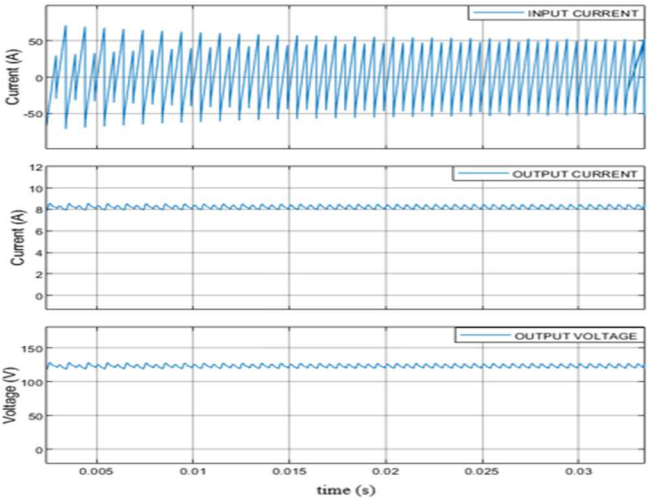

Fig. 6 (d). IPOS FBC parameter waveform at 1 kHz

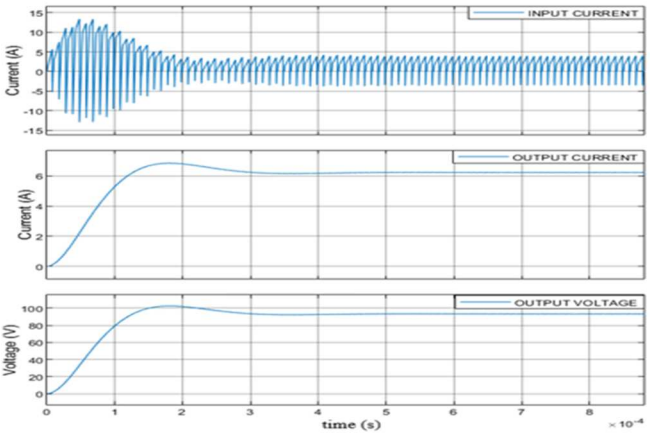

Fig. 6 (e). IPOS FBC parameter waveform at 50 kHz

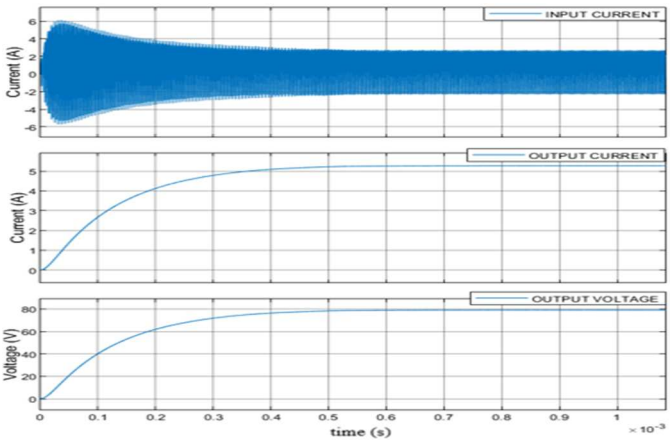

Fig. 6 (f). FBC parameter waveform at 175 kHz

The results of the waveforms shows the behaviour of the parameters input current, output current and output voltage across different switching frequencies. In Fig. 6 (a)., Fig. 6 (b). and Fig. 6 (c)., the waveforms for FBC at 1kHz, 50 kHz and 175 kHz clearly show how unstable the FBC is with low switching frequency as compared to the IPOS Full-Bridge converter in Fig. 6 (d)., Fig. 6 (e)., Fig. 6 (f).. At 175kHz, both converters demonstrate ripple free output voltage which shows the advantage of using this type of converter.

Authorized licensed use limited to: DELHI TECHNICAL UNIV. Downloaded on November 25,2024 at 04:43:07 UTC from IEEE Xplore. Restrictions apply.

2. Effects Of Uncertainties on IPOS Full-Bridge Converter

Based on results from previous sections, ideal operation of the IPOS Full-Bridge converter was initially assumed. However, practical components introduce resistances that impact performance. Effects of uncertainties on IPOS FBC are examined as shown in table II.

From table II, it is evident that variations in r_{Ds} (on), inductor resistance r_L and diode resistance r_D impact the performance of the converter. Specifically r_{Ds}(on) and r_D show a slight decrease in efficiency, while r_L exhibits a noticeable decline in both output power and efficiency. Conversely, r_C has minimal effect on these parameters. This underscores the sensitivity of converter performance to component resistances, highlighting the importance of optimizing these parameters for enhanced efficiency and power delivery.

The figures below show the effects of uncertainties on the output voltage of the IPOS Full-Bridge converter, different values of component resistances have been taken to observe their effects on the output voltage of the IPOS FBC.

TABLE II

EFFECTS OF UNCERTAINTIES ON EFFICIENCY ON IPOS FULL-BRIDGE CONVERTER

S No	Parameters	Effects of r_{Ds} (on)			Effects of r_L			Effects of r_C			Effects of r_D		
1	Component resistance (Ω)	0.09	0.10	0.11	0.09	0.10	0.11	0.09	0.10	0.11	0.09	0.10	0.11
2	Efficiency (%)	87.43	87.42	87.41	86.4	86.29	86.18	87.41	87.41	87.41	86.45	86.35	86.24

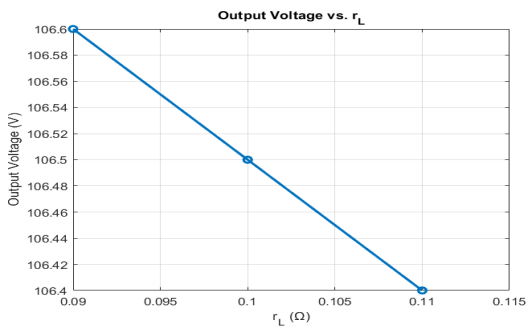

Fig. 7 (a). Graph of Output Voltage v/s r_L, D = 0.4, R_L = 15Ω

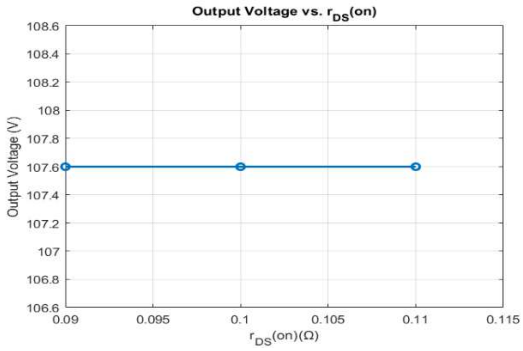

Fig. 7(b). Graph of Output Voltage v/s r_{DS} (on), D = 0.4, R_L = 15Ω

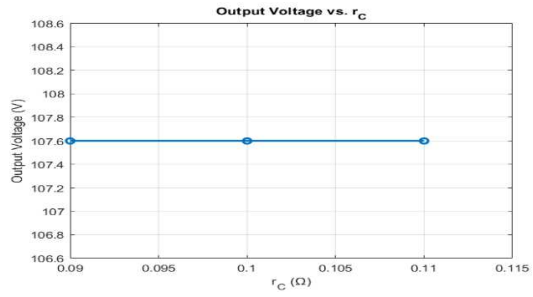

Fig. 7(c). Graph of Output Voltage vs r_c, D = 0.4, R_L = 15Ω

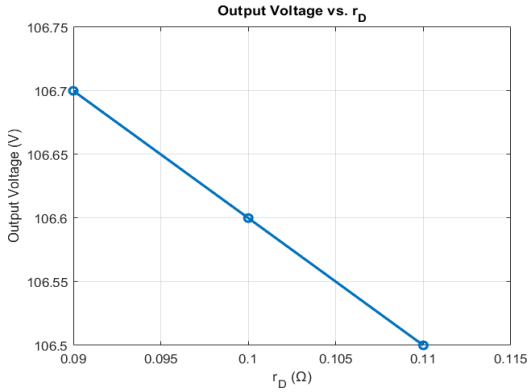

Fig. 7 (d). Graph of Output Voltage v/s r_D, D = 0.4, R_L = 15Ω

Practical resistances impact the IPOS Full-Bridge converter's performance with the output inductor resistance (r_L) significantly affecting the voltage as seen in Fig. 7 (a), as the inductor resistance increased the voltage, a reduction in the output voltage is observed. There is a change in the output voltage from 106.6V to 106V. While the filter capacitor resistance (r_C) has negligible impact shown in Fig. 7(c). MOSFET on-resistance r_{DS}(on) and diode resistance (r_D) cause slight efficiency decreases as in Fig. 7(b), 7(d). Thus, minimizing r_L and r_D is crucial for optimizing converter performance, emphasizing the importance of considering these resistances in design and optimization.

3. Efficiency Analysis of IPOS FBC and CFBC

The efficiency of power converters is a critical parameter, influencing both operational cost and thermal management. By systematically evaluating the efficiency across different duty cycles and loads, the aim is to provide insights into the optimal operating conditions for the converter. Analysis of the efficiency of the IPOS Full-Bridge and Full-Bridge Converter across various load conditions is carried out. By systematically evaluating the efficiency across different duty cycles and loads, the aim is to provide insights into the optimal operating

Authorized licensed use limited to: DELHI TECHNICAL UNIV. Downloaded on November 25,2024 at 04:43:07 UTC from IEEE Xplore. Restrictions apply.

conditions for the converter by giving graphical representations of efficiency versus duty cycle for different load resistances, as well as the observed trends and their implications.

Fig. 8(a) and Fig. 8(b) illustrate the efficiency of the IPOS Full-Bridge and Full-Bridge Converter across various duty cycles and loads, providing insights into their optimal operating conditions.

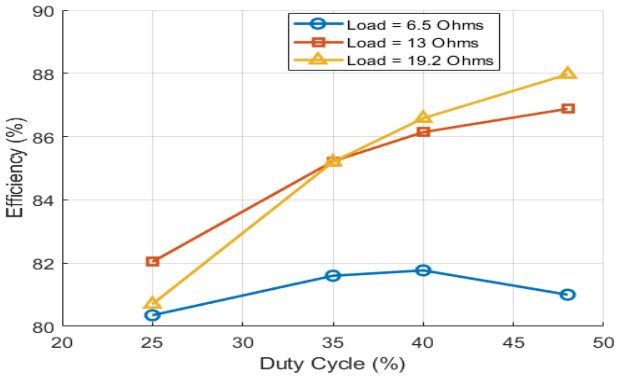

Fig. 8 (a). Efficiency vs Duty Cycle of IPOS FBC

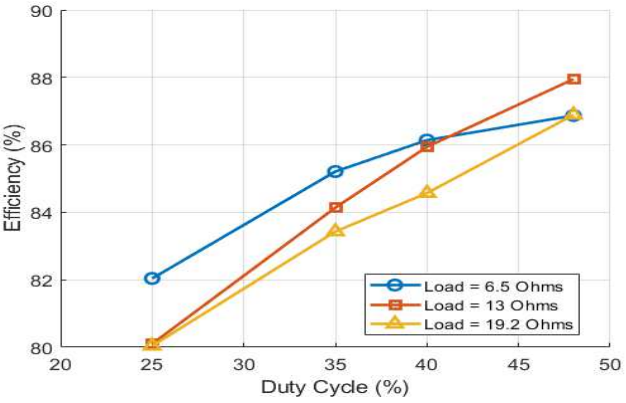

Fig. 8 (b). Efficiency vs Duty Cycle of CFBC

Fig. 8 (a) and Fig. 8 (b) illustrates the efficiency performance of the IPOS Full-Bridge Converter and the conventional Full-Bridge Converter under varying duty cycles. Simulations are conducted by adjusting the duty cycle and observing the corresponding changes in efficiency across different load conditions.

Both converters demonstrate high efficiency when operating with a load resistance of 19.2 Ohms. However, a slight reduction in efficiency is observed as the load decreases. The IPOS Full-Bridge converter consistently exhibits relatively higher efficiency and greater stability compared to the conventional Full-Bridge converter. Furthermore, the efficiency of both converters improves with an increase in the duty cycle, indicating that higher duty cycles contribute positively to the overall performance of the converters.

V. CONCLUSIONS

In this paper, the IPOS Full-Bridge DC-DC converter is compared with the conventional Full-Bridge converter based on the results obtained from the simulation. From the comparative study, the IPOS converter demonstrates superior performance in terms of voltage gain and efficiency. The IPOS design ensures enhanced redundancy, meaning if one module fails, the others continue to operate, ensuring uninterrupted performance. The simulations show that the IPOS converter handles high output power more efficiently, particularly at various switching frequencies, compared to the conventional Full-Bridge converter. Practical component resistances, such as MOSFET on-resistance and inductor resistance, slightly impact efficiency, highlighting the importance of minimizing these parasitic effects for optimal performance.

Considering the application in renewable energy systems and electric vehicles, where high efficiency and reliability are paramount, the IPOS Full-Bridge converter proves to be more suitable. Further studies can be conducted by integrating the proposed IPOS circuit with renewable energy sources and advanced control systems to explore its potential in more complex power management scenarios.

ACKNOWLEDGMENT

This work has been supported by the Power Electronics Laboratory, Electrical Engineering Department, Delhi Technological University.

REFERENCES

[1] Kazimierczuk, M.K. (2015) Pulse-Width Modulated DC-DC Power Converters. John Wiley & Sons.

[2] Tu, Z. et al. (2015) 'A large-capacity DC-DC converter with input-series-input-parallel output-series-output-parallel connection', Proceedings of the 3rd International Conference on Advances in Energy and Environmental Science 2015 [Preprint]. doi:10.2991/icaees-15.2015.207.

[3] Wang, P. et al. (2017) 'Input-Parallel Output-Series DC-DC Boost Converter With a Wide Input Voltage Range, For Fuel Cell Vehicles', IEEE Transactions on Vehicular Technology, 66(9), pp. 7771–7781. Available at: https://doi.org/10.1109/tvt.2017.2688324.

[4] Daoud, G. et al. (2017) 'Input-series output-parallel full-bridge DC-DC converter for high power applications', 2017 4th IEEE International Conference on Engineering Technologies and Applied Sciences (ICETAS) [Preprint]. doi:10.1109/icetas.2017.8277902.

[5] Dileep, S., Dinesh, G.V. and S, P. (2023) 'Comparative analysis of isolated interleaved boost converter and full bridge converter', 2023 Innovations in Power and Advanced Computing Technologies (i-PACT) [Preprint]. doi:10.1109/i-pact58649.2023.10434594.

[6] Yiqing Lian, Finney, S. and Holliday, D. (2015) 'Modular input-parallel-output-series DC/DC converter control with fault detection and redundancy', 11th IET International Conference on AC and DC Power Transmission [Preprint]. doi:10.1049/cp.2015.0001.

[7] Fundamentals of Power Electronics (2020). Cham: Springer International Publishing, Imprint Springer.

[8] Hu, X. et al. (2016) 'Input-Parallel output-series DC–DC converter for non-Isolated High Step-Up Applications', Electronics Letters, 52(20), pp. 1715–1717. doi:10.1049/el.2016.2835.

[9] Yeh Ting et al. (2014) 'A comparison of module shutdown methods in an input-series and output-parallel connected modular DC-DC converter', 7th IET International Conference on Power Electronics, Machines and Drives (PEMD 2014) [Preprint]. doi:10.1049/cp.2014.0440.

[10] Barbi, I., Fabiana Pöttker and Springerlink (Online Service (2019) Soft Commutation Isolated DC-DC Converters. Cham: Springer International Publishing.

Authorized licensed use limited to: DELHI TECHNICAL UNIV. Downloaded on November 25,2024 at 04:43:07 UTC from IEEE Xplore. Restrictions apply.

Research Square

Preprints are preliminary reports that have not undergone peer review.
They should not be considered conclusive, used to inform clinical practice,
or referenced by the media as validated information.

Performance Analysis of Multiple Delayed Signal Cancellation (MDSC) for Power Quality Improvement for Fixed Speed SEIG-Based Distributed Generation

Divyansh Shailly
Delhi Technological University
Prakash Chittora
prakashchittora@dtu.ac.in

Delhi Technological University
Madhusudan Singh
Delhi Technological University

Research Article

Keywords: Positive Sequence Component (PSC), Negative Sequence Component (NSC), Multiple Delayed Signal Cancellation (MDSC), Self- Excited Induction Generator (SEIG), Distributed static compensator (DSTATCOM), Total Harmonic Distortion (THD), Grid synchronization

Posted Date: November 14th, 2024

DOI: https://doi.org/10.21203/rs.3.rs-5371342/v1

License: This work is licensed under a Creative Commons Attribution 4.0 International License.
Read Full License

Additional Declarations: No competing interests reported.

Performance Analysis of Multiple Delayed Signal Cancellation (MDSC) for Power Quality Improvement for Fixed Speed SEIG-Based Distributed Generation

Divyansh Shailly
Department of Electrical Engineering,
Delhi Technological University,
Delhi-10042
Divyansh93shailly@gmail.com

Prakash Chittora*
Department of Electrical Engineering,
Delhi Technological University,
Delhi-10042
prakashchittora@dtu.ac.in

Madhusudan Singh
Department of Electrical Engineering,
Delhi Technological University,
Delhi-10042
madhusudan@dce.ac.in

Abstract: **- The proposed work described a new Multiple Delay Signal Cancellation (MDSC) control technique for power quality improvement including harmonic cancellation and power factor improvement for a three-phase self-excited induction generator (SEIG)-Distributed Static Compensator (DSTATCOM) based system. A detailed design and stability analysis is being carried out. The MDSC possesses multiple variable length delay signals so as to extract the positive and the negative sequence components (PSC and NSC) so as to generate sinusoidal reference currents for the source. An extensive simulation analysis is being executed to illustrate the controller's efficiency using MATLAB/SIMULINK. A hardware prototype is being developed in the laboratory including SEIG and DSTATCOM. The hardware results prove the effectiveness of the proposed control filter.**

Index terms**- Positive Sequence Component (PSC*), Negative Sequence Component (NSC), Multiple Delayed Signal Cancellation (MDSC), Self- Excited Induction Generator (SEIG), Distributed static compensator (DSTATCOM), Total Harmonic Distortion (THD), Grid synchronization.**

1. Introduction

Renewable energy is thought to be particularly important in promoting energy security by reducing greenhouse gas emissions and reducing dependence on fossil fuels. Regulations and control measures have a significant impact on the viability of isolated renewable energy systems. Renewable energy sources incorporate wind, PV solar, geothermal, biomass, and hydropower [1]. The Self-Excited Induction Generator (SEIG) presents itself as a compelling rival to the synchronous generator because of several benefits, including brushless operation, decreased unit costs, durability, and maintenance-free characteristics. They must, however, provide the customer with power that is acceptable in terms of voltage, frequency, and waveform. It is necessary to build controllers that are appropriate for SEIG and accommodate stator terminals of the externally propelled squirrel-cage induction generator (SCIG) that are linked to a self-excited induction generator, or SEIG, which is a reactive power source in the form of a capacitor bank. Because squirrel-cage induction machines offer numerous advantages over traditional synchronous machines, such as built-in short-circuit protection, low cost, brushless construction, and ruggedness. It can be used as a mechanical energy converter and is gaining popularity in isolated and remote power generation systems. In the case of a SEIG powered by prime movers like micro steam turbines, biodiesel engines and gas engines, the frequency of the generated voltage remains nearly constant from no load to maximum load [2].

With a rise in the application of power conversion-based appliances, for instance rectifiers, Switched Mode Power Converters (SMPC), Uninterrupted Power Supplies (UPSs), Adjustable Speed Drives (ASD) and battery-controlled

chargers there is an escalation in the percentage of non-linear load. There are a few adverse effects of non-linear load which are as follows harmonics generation, loss addition, electromagnetic interference, power factor(PF) deterioration reactive power burden etc [3]. The saturation of the generator core due to the harmonics leads to a decrease in terminal voltage with the increase in the load. It increases the efficacious inductance, thus leading to a decrease in the reactor current. Consequently, the capacitor current is transferred to the SEIG, improving excitation and raising the terminal voltage [4-8]. The power factor of the load, the terminal voltage of SEIG and the prime mover's speed are all controlled by the external shunt capacitance connected in the delta configuration of SEIG. The SEIG exhibits poor voltage regulation when it is loaded because of a decrease in terminal voltage caused by the gap between the generator's requirement for voltage-ampere reactive (VAR) and the capacitor bank's supply of VAR. This can be corrected by a shunt (parallel) or series compensation with the use of traditional voltage-regulating (VR) schemes [9][10].

Custom power devices (CPDs) such as a united Power Quality Conditioner (UPQC), an inter-phase power control (IPC), a dynamic voltage regulator (DVR), distributed static compensators (DSTATCOM), unified power factor correction (UPFC), and so on are often used to manage the SEIG's voltage. Amid the above voltage regulation scheme, a better voltage profile is produced by distributed static compensators (DSTATCOMs), which offer a more steady and quick dynamic response with a smaller steady-state error, and it also aids in with power quality concerns like voltage regulation and frequency regulation by providing both the leading and lagging VAr, as well as the ability to store energy for electrical transients. Consequently, the DSTATCOM stands out as an ideal choice for harmonic reduction and reactive power adjustment in distributed generation based on SEIG [11–12]. So as to restore the terminal voltage and mitigate the harmonics of SEIG-DSTATCOM based system, different type of control algorithms are employed for retrieving the fundamental active and reactive component of load current (I_L) that are as follows:- Synchronous Reference Frame Theory (SRFT) in which the voltage and current signals being processed by the PLL and also explain the transformation of current signal in D-Q frame , Adaline based control is used to compute the fundamental frequency positive sequence real and reactive component of the load current , Instantaneous Reactive Power Transfer theory (IRPT) proposed the theory based on the transformation of three phase load current frame to α-β frame [15], Back-propagation control [16], affine projection based algorithm [17], Momentum Least Mean Square algorithm (MLMS) [18],Leaky Least Mean Fourth algorithm (LLMF) [19], Modified Amplitude Adaptive Notch Filter Control algorithm (MAANF) [20], KHLMS control strategy[21], DSOGI-PLL with an in-loop filter algorithm [22], adaptive nature vectorial algorithm [23], Quasi-Newton Least Mean Fourth algorithm (QNLMF) [24], Adaptive Least-Error Squares Filter-PLL(ALES-PLL) [25], EPLL-CSD control [26], Moving Average Filter- Phase-Locked Loops(MAF-PLL) [27], Variable Learning adaptive Gradient-LMS (VLGLMS) control algorithm [28], Genetic Algorithm Optimized Fuzzy Logic Control (GA-FLC) [29], VCO-less PLL control[30] and NN based LMS–LMF control algorithm are other popular control algorithm for DSTATCOM based system [31].

Among all of the control techniques cited above, delayed signal cancellation (DSC) is gaining attention due to the fact that this operator exhibits the characteristics of delaying the signal by 90º phase shift and this delay operator can be utilized as a pre-filter before the phase lock loop inside the closed loop, thereby making it the most popular finite impulse response (FIR). As the delayed-based operator like αβ-DSC is extremely susceptible to voltage supplied by SEIG and frequency. Hence, the operations cannot be conducted when the SEIG is the main power supply. To optimize the above problem, the length of the delays is kept fixed and errors are corrected by using a simple compensator [32]. To enhance the dynamic responsiveness or filtering capabilities of the DSC, in-loop techniques can be considered any adjustment in the phase lock loop control loop. Generalised Delayed Signal Cancellation PLL (GDSC-PLL) based operator has a good harmonic filtering capability. To eliminate selective harmonics of a certain order, a single block DSC is used, and a finite set of harmonics can be eliminated by connecting multiple DSC blocks in a cascade connection with different time delays. However, in extremely distorted grid settings, five-level cascaded DSC blocks are necessary to remove all orders of harmonics, inclusive of DC offset and negative sequence components of the current. The cascaded DSC-PLL construction introduces considerable overall phase lag, resulting in a significantly reduced PLL bandwidth. There is also an increase in the complexity of implementation. In order to make PLL adaptive to changes in grid voltage frequency, an enhanced frequency adaptive DSC structure is also suggested; however, this solution does not deal with the issue of fewer cascaded blocks. To leverage the filtering power of DSC-PLL without suffering from time delay-induced low bandwidth, a PLL with fewer DSC blocks used needs to be developed. With one quarter (5 milliseconds or 50 Hz) of time delay, this technique combines the positive and negative sequence components (PSC and NSC) of the load current to provide exact sequence component information [33].

The phase, frequency and amplitude can be extracted when the phase lock loop(PLL) receives the fundamental frequency positive sequence component as its input and this estimated frequency component is then sent as feedback to the generalized DSC operator making it frequency adaptive [34]. All the harmonics of the harmonic order h=4K+1 (K=±1, ±2, ±3, ±4…...) are blocked by the DSC_4 (operator with the delay factor 4) operator, but all the harmonics of the harmonic order h=4K+1 (K=±1, ±2, ±3, ±4…...) are left intact. Among the most significant harmonic components that the $DSC_{4,8,12...}$ operator cannot remove are the 7th and 11th harmonics of the negative sequence and the 13th harmonics of the positive sequence [35]. Furthermore, the FFPS component of the DSC_4 operator undergoes a frequency shift whereas the FFNS element cannot be entirely removed. The primary cause of this is that the T/4 delay factor of the αβ-DSC4 operator's input and output signals are nonorthogonal under off-nominal grid conditions. As a result, a new operator is created to modify the T/4 delay factor's length and aid in continuously conditioning its output to the orthogonal version of its input [36].

In this paper, multiple delayed signal cancellation is illustrated. It comprises dual structured Cascaded Delayed Signal Cancellation (CDSC) applicable for the determination of both the positive (PSC) and the Negative Sequence Components (NSC) and also helps in the separation of FFPS and FFNS components. Multiple delayed signal cancellation (MDSC) operators at the in-loop filtering stage are studied in detail. In section 3 comparative stability analysis of αβ-Generalized DSC and multiple DSC-PLL is being discussed in detail, which includes parameters like step response, estimation of gain, and the phase margin using bode plot and root locus. The *αβ*-MDSC control filter is applicable for reference current production for DSTATCOM. For the generation of gating pulses, Hysteresis Current Control (HCC) is used to develop with the help of dSpace1104. In sections 4 and 5 the dynamic and steady-state analysis of the proposed control strategy is carried out using simulations that were carried out on MATLAB/Simulink software and then validated the same experimentally on a laboratory prototype of the SEIG-DSTATCOM-based system. The highlights of the proposed work are

1. A new MDSC control algorithm for SEIG based system is discussed for PQ improvement.
2. Both PSC and NSC are determined so as to effectively separate FFPS and FFNS components.
3. The proposed controller is compared with GDSC and found to be better in operation
4. Both simulation and hardware results prove the effectiveness of the proposed controller.

2. System Configuration

The depicted circuit layout in Figure 1 shows three-phase self-excited induction generators and a Distributed Static Compensator (DSTATCOM) supplying a three-phase non-linear load. The VAR generating system is made up of a capacitor bank (delta configuration) that is shunt-linked to the induction generator (SEIG). The DC motor that serves as the prime mover for SEIG in the system is powered by a DC starter. The generated 415V of the SEIG is further reduced to the necessary 110V AC by connecting the output of the SEIG to the input of a 3-phase autotransformer. A three-leg, two-level IGBT-based voltage source inverter that functions as a DSTATCOM and has a self-sustaining DC-bus capacitor is used. Six IGBT switches—two for each phase—and an anti-parallel diode are included in the DSTATCOM. The purpose of these antiparallel diodes is to safeguard IGBT switches. In addition, they serve as a three-phase unregulated rectifier, supplying 156 V as the DC link voltage upon startup. According to Figure 1, the DSTATCOM is coupled in a shunt at the Point of Common Coupling (PCC) via interfacing inductors, which are employed to filter the harmonics that the Voltage Source Inverter (VSI) injects. By preserving equilibrium between the system's circulations of reactive power, DSTATCOM regulates the system's voltage. The unbalanced load currents in a three-phase system are composed of two sets of balanced currents: positive sequence components and negative sequence components. Producing a balanced source current requires the source to be free of the load currents' negative sequence components. To counteract the effects of negative sequence currents from unbalanced loads, the DSTATCOM either supplies the reactive power (negative sequence currents) needed by the unbalanced load or draws another set of negative sequence currents that are precisely 180 degrees out of phase to those drawn by the unbalanced load when connected in shunt with PCC. Six LA-25 current sensors are used to measure supply current (I_{sa}, I_{sb}, I_{sc}) and load current (I_{La}, I_{Lb}, I_{Lc}). Four LV-25 voltage sensors monitor supply voltage (v_{sa}, v_{sb}, v_{sc}) and DC link voltage (V_{DC}). These computed voltage and current signals are sent to the DSP (dSPACE 1104) ADC channels, which are processed to produce +5V gating pulses. These pulses are then amplified to +15V with the aid of a gate driver circuit,

and they are subsequently supplied to the three-leg IGBT-based inverter (15V is needed to TURN-ON the IGBT) for the necessary operation [19,37-38].

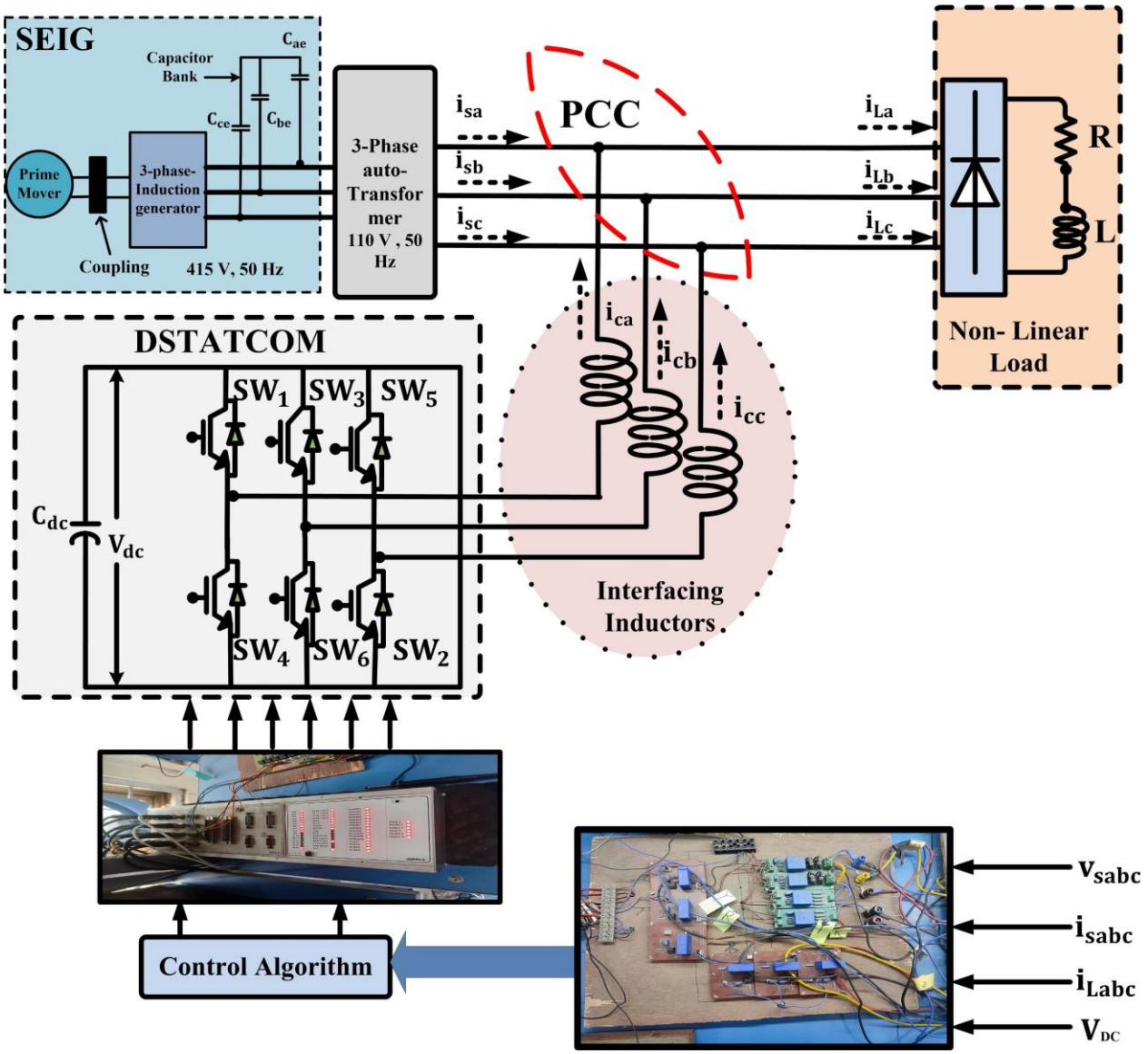

Figure 1. System configuration of SEIG-DSTATCOM-based distributed generation.

3. Overview of Digital Filtering Technique

In this section modelling and analysis of αβ-GDSC and αβ-MDSC are discussed with their stability analysis in detail.

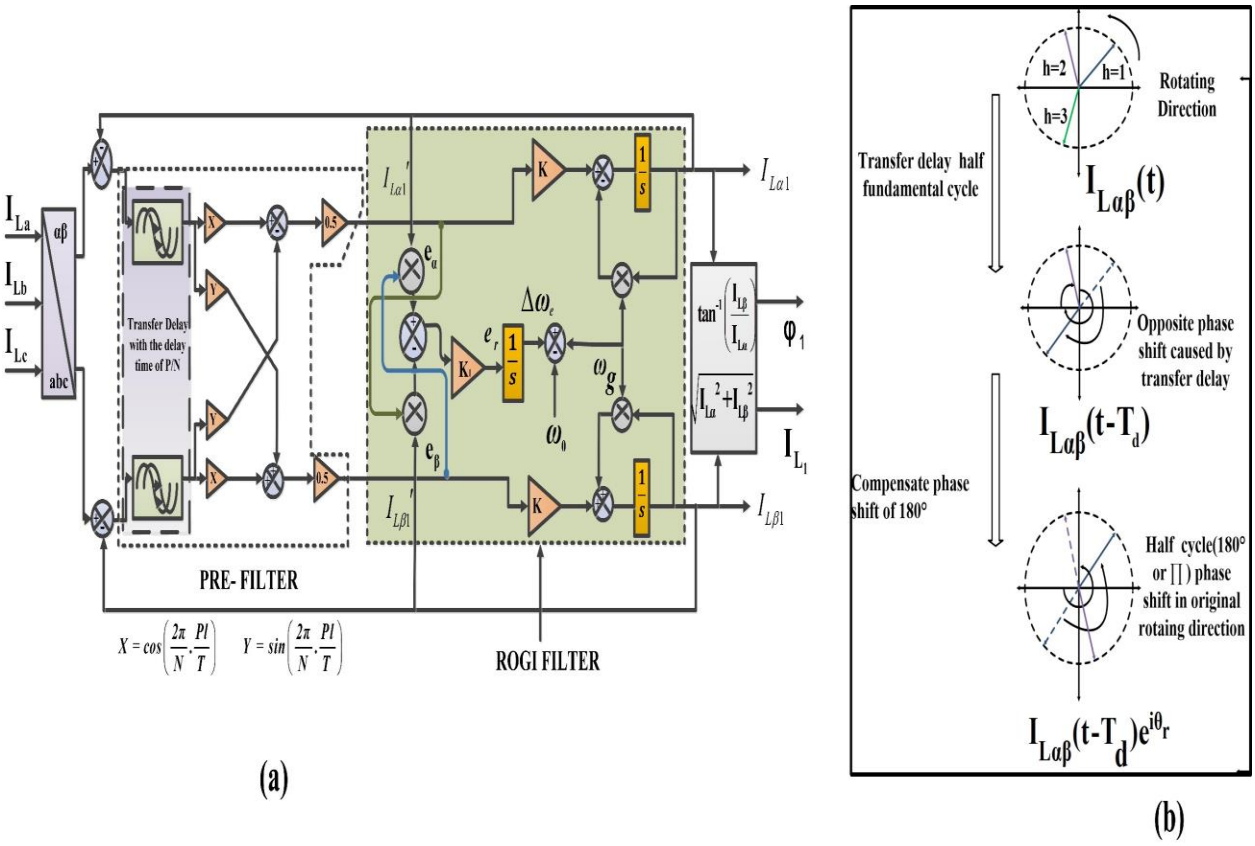

Figure 2. (a) Schematic representation of generalized DSC. (b) Demonstration of GDSC operator with the delay factor N=2 and harmonic selector h=1. dashed line stands for the position in the previous stage and purple and green stand for the second and third harmonic components.

3.1 Modelling and analysis of αβ-Generalized DSC

Figure 2(a) depicts the block representation of the αβ-GDSC, which comprises the αβ-GDSC operator with variable-length delays and a reduced order generalized integrator (ROGI). The generalized DSC operator aids in the extraction of the essential components of current and is in charge of rejecting certain disturbances. The rudimentary concept of the grid voltage and load current signals' specific harmonic component elimination through delayed signal cancellation (GDSC) is based on the time domain harmonic components' half-wave symmetry, which enables the GDSC operator to eliminate these components by recapitulation them with their delayed versions. By approximating the period as 1/N cycles, where N is the delayed factor, the operator's delays can be changed. The αβ GDSC's basic delayed cycle is depicted in Figure 2(b), wherein three harmonic elements (h = 1, h = 2, and h = 3) rotate in an anticlockwise direction. Assume a harmonic component h = 1 will be extracted and given a half-fundamental-cycle delay. The half fundamental cycle delay adds on a -180º phase shift to harmonic h=1 and a -360º phase shift to h=2. To compensate, add a positive 180ºor Π to the phase of both h=1 and h=2 components. This rotates only the component h = 1 back to its initial position. By combining the first and third plots, the length of harmonic component h=1 is doubled, and the length of component h=2 is reduced to zero.

The rotation matrix $R_M(\theta_r)$ in the operator can be expressed as

$$R_{M}(\theta_r) = \begin{pmatrix} \cos(\theta_r) & -\sin(\theta_r) \\ \sin(\theta_r) & \cos(\theta_r) \end{pmatrix} \quad (1)$$

Where $\theta_r = 2\pi / N_{1.....M-1}$

The three-phase input signals of the GDSC control algorithm are as

$$\begin{aligned} I_{La}(t) &= I_L \cos(\omega_o t + \varphi_1) \\ I_{Lb}(t) &= I_L \cos(\theta - \frac{2\pi}{3}) \\ I_{Lc}(t) &= I_{Lf} \cos(\theta + \frac{2\pi}{3}) \end{aligned} \quad (2)$$

Where $\theta = \omega_0 t + \varphi_1$

These signals can correspond to the αβ-frame by applying Clarke transformation as:-

$$\begin{aligned} I_{L\alpha}(t) &= I_L \cos(\theta) \\ I_{L\beta}(t) &= I_L \sin(\theta) \end{aligned} \quad (3)$$

Using equations (1), (2), (3) and figure 2(a), the output signals of the αβGDSC operator can be presented as

$$\begin{aligned} I_{L\alpha 1} &= 0.5\left[I_{L\alpha}(t) + \left\{ k\cos(2\pi/N).I_{L\alpha}\left(t - \frac{T}{N}\right)\right\} - k_1 \sin(2\pi/N).I_{L\beta}\left(t - \frac{T}{N}\right)\right] \\ &= 0.5 I_L(t)\left[k\cos(\theta) - k_1\left\{\cos\left(\theta - \omega_g T/N + 2\pi/N\right)\right\}\right] \end{aligned} \quad (4)$$

$$\begin{aligned} I_{L\beta 1} &= 0.5\left[I_{L\beta}(t) + k\left\{ \sin(2\pi/N).I_{L\alpha}\left(t - \frac{T}{N}\right)\right\} + k_1 \cos(2\pi/N).I_{L\beta}\left(t - \frac{T}{N}\right)\right] \\ &= 0.5 I_L(t)\left[k\sin(\theta) - k_1\left\{\sin\left(\theta - \omega_g T/N + 2\pi/N\right)\right\}\right] \end{aligned} \quad (5)$$

The above are the obtained fundamental active and reactive component signals, where $T=2\pi/\omega_g$ is the estimation for the sampling time.

3.2 Modelling and analysis of αβ MDSC operator

The three-phase load current with the presence of positive and negative sequence harmonics is given below as,

$$
\begin{aligned}
\mathrm{I_{La}}(t) &= \mathrm{I}_{Lf}^{+h}\cos(\omega_o t+\varphi_f^{+h})+\mathrm{I}_{Lf}^{-h}\cos(\omega_o t+\varphi_f^{-h})\\
\mathrm{I_{Lb}}(t) &= \mathrm{I}_{Lf}^{+h}\cos(\omega_o t+\varphi_f^{+h}-\frac{2\pi}{3})+\mathrm{I}_{Lf}^{-h}\cos(\omega_o t+\varphi_f^{-h}+\frac{2\pi}{3})\\
\mathrm{I_{Lc}}(t) &= \mathrm{I}_{Lf}^{+h}\cos(\omega_o t+\varphi_f^{+h}+\frac{2\pi}{3})+\mathrm{I}_{Lf}^{-h}\cos(\omega_o t+\varphi_f^{-h}-\frac{2\pi}{3})
\end{aligned}
\tag{6}
$$

Where I_{Lf}^{+h}, $\theta_f{}^{+h}$ and φ_f^{+h} (I_{Lf}^{-h}, $\theta_f{}^{-h}$, φ_f^{-h}) are the amplitude, phase angle, and the fundamental phase with the harmonic element of the first fundamental positive sequence (FFPS) and first fundamental negative sequence component (FFNS) of the three-phase load current and ω_0 is the frequency of SEIG respectively. Applying Clarke's transformation to the (6) equation gives the $\alpha\beta$-axis load current component which will act as an input signal of the $\alpha\beta$-MDSC operator.

$$
\mathrm{I_{L\alpha}}(t) = \mathrm{I}_{L1}^{+}\cos\left(\theta_f^{+}\right)+\mathrm{I}_{L1}^{-}\cos\left(\theta_f^{-}\right) \tag{7}
$$

$$
\mathrm{I_{L\beta}}(t) = \mathrm{I}_{L1}^{+}\sin\left(\theta_f^{+}\right)-\mathrm{I}_{L1}^{-}\sin\left(\theta_f^{-}\right) \tag{8}
$$

The output signals of the T/4 delay of the $\alpha\beta$-MDSC-PLL operator can be derived using (7) and (8)

$$
\mathrm{I_{L\alpha}}(t-\frac{T}{4}) = \mathrm{I}_{L1}^{+}\cos\left(\theta_f^{+}-\frac{\omega_0 T}{4}\right)+\mathrm{I}_{L1}^{-}\cos\left(\theta_f^{-}-\frac{\omega_0 T}{4}\right) \tag{9}
$$

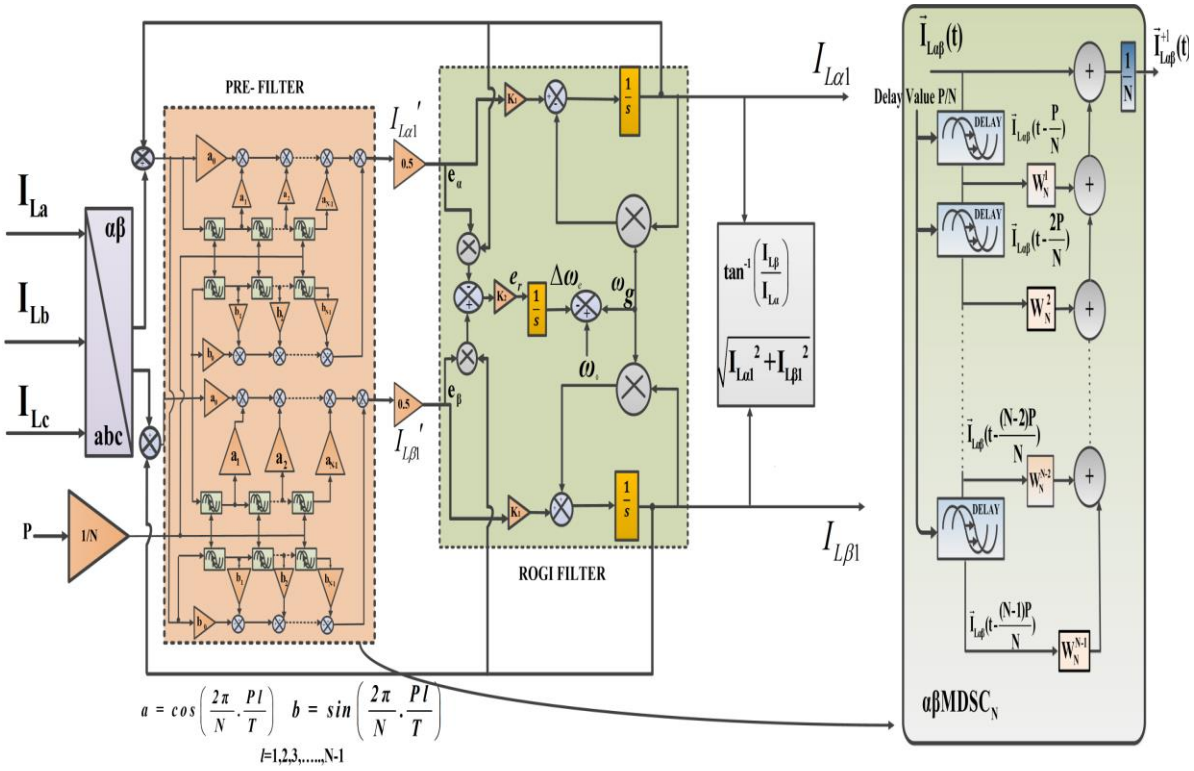

Figure 3. Schematic representation of αβ-MDSC based control algorithm.

$$\mathrm{I}_{\mathrm{L}\beta}(\mathrm{t}-\frac{T}{4})=\mathrm{I}_{L1}^{+}\sin\left(\theta_f^{+}-\frac{\omega_0 T}{4}\right)-\mathrm{I}_{L1}^{-}\sin\left(\theta_f^{-}-\frac{\omega_0 T}{4}\right) \tag{10}$$

where ω_0 be the angular frequency of the SEIG $\omega_n=2\pi/T$ is the nominal angular frequency of the SEIG as $\omega_0=\omega_n+\Delta\omega_0$ and substituting it into (9) and (10) will give

$$\mathrm{I}_{\mathrm{L}\alpha}(\mathrm{t}-\frac{T}{4})=\mathrm{I}_{L1}^{+}\sin\left(\theta_f^{+}-\frac{\Delta\omega_0 T}{4}\right)+\mathrm{I}_{L1}^{-}\sin\left(\theta_f^{-}-\frac{\Delta\omega_0 T}{4}\right) \tag{11}$$

$$\mathrm{I}_{\mathrm{L}\alpha}(\mathrm{t}-\frac{T}{4})=-\mathrm{I}_{L1}^{+}\cos\left(\theta_f^{+}-\frac{\Delta\omega_0 T}{4}\right)+\mathrm{I}_{L1}^{-}\cos\left(\theta_f^{-}-\frac{\Delta\omega_0 T}{4}\right) \tag{12}$$

Considering the fact that when $\Delta\omega_0$=0, the angular frequency of the SEIG is equal to the nominal angular frequency such that (11) and (12) are orthogonal to the (7) and (8).

Expanding the sine and cosine function in the (11) and (12)

$$\begin{aligned}\mathrm{I}_{\mathrm{L}\alpha}(\mathrm{t}-\frac{T}{4})=&\left\{\mathrm{I}_{L1}^{+}\sin\left(\theta_f^{+}\right)+\mathrm{I}_{L1}^{-}\sin\left(\theta_f^{-}\right)\right\}\cos\left(\frac{\Delta\omega_0 T}{4}\right)\\&-\left\{\mathrm{I}_{L1}^{+}\cos\left(\theta_f^{+}\right)+\mathrm{I}_{L1}^{-}\cos\left(\theta_f^{-}\right)\right\}\sin\left(\frac{\Delta\omega_0 T}{4}\right)\end{aligned} \tag{13}$$

$$\begin{aligned}\mathrm{I}_{\mathrm{L}\beta}(\mathrm{t}-\frac{T}{4})=&\left\{-\mathrm{I}_{L1}^{+}\cos\left(\theta_f^{+}\right)+\mathrm{I}_{L1}^{-}\cos\left(\theta_f^{-}\right)\right\}\cos\left(\frac{\Delta\omega_0 T}{4}\right)\\&-\left\{\mathrm{I}_{L1}^{+}\sin\left(\theta_f^{+}\right)-\mathrm{I}_{L1}^{-}\sin\left(\theta_f^{-}\right)\right\}\sin\left(\frac{\Delta\omega_0 T}{4}\right)\end{aligned} \tag{14}$$

Where a=k'= $\cos\left(\frac{\Delta\omega_0 T}{4}\right)$ and b=k= $\sin\left(\frac{\Delta\omega_0 T}{4}\right)$ and the orthogonal version is = $\mathrm{I}_{L\alpha 1}{}'=\mathrm{I}_{\mathrm{L}\alpha}(\mathrm{t}-\frac{T}{4})$ and = $\mathrm{I}_{L\beta 1}{}'=\mathrm{I}_{\mathrm{L}\beta}(\mathrm{t}-\frac{T}{4})$

$$\mathrm{e}_{\alpha}=(\mathrm{I}_{L\alpha 1}-\mathrm{I}_{L\alpha 1}{}') \tag{15}$$

$$\mathrm{e}_{\beta}=(\mathrm{I}_{L\beta 1}-\mathrm{I}_{L\beta 1}{}') \tag{16}$$

$$\Delta\omega_e=(\mathrm{e}_{\alpha})(\mathrm{I}_{L\alpha 1}{}')(\mathrm{K}_2)-(\mathrm{e}_{\beta})(\mathrm{I}_{L\beta 1}{}')(\mathrm{K}_2) \tag{17}$$

$$\Delta\omega_e=\left(\mathrm{e}_f\right).\left(\mathrm{K}_2\right) \tag{18}$$

Where,

$$\mathrm{e}_f=(\mathrm{e}_{\alpha})(\mathrm{I}_{L\alpha 1}{}')-(\mathrm{e}_{\beta})(\mathrm{I}_{L\beta 1}{}') \tag{19}$$

Signals are further simplified as

$$\mathrm{I}_{\mathrm{L}\alpha 1}(t)=\mathrm{I}_{L1}^{+}\cos\left(\theta_f^{+}\right) \tag{20}$$

$$\mathrm{I}_{\mathrm{L}\beta 1}(t)=\mathrm{I}_{L1}^{+}\sin\left(\theta_f^{+}\right) \tag{21}$$

From the figure 3 , we obtained

$$\begin{aligned}\mathrm{I}_{\mathrm{L}\alpha 1}&=0.5\left[I_{L\alpha 1}{}'(t)-\frac{1}{k_2}\left\{k_1 I_{L\beta 1}{}'(t)+kI_{L\beta 1}{}'\left(t-\frac{T}{4}\right)\right\}\right]\\&=0.5I_{L1}(t)\left[\cos\left(\theta_f\right)-\frac{1}{k_2}\left\{k_1\sin\left(\theta_f\right)-\cos\left(\theta_f-\frac{T\Delta\omega_0}{4}\right)\right\}\right]\end{aligned} \tag{22}$$

$$\begin{aligned}\mathrm{I}_{\mathrm{L}\beta 1}&=0.5\left[I_{L\beta 1}{}'(t)+\frac{1}{k_2}\left\{k_1 I_{L\alpha 1}{}'(t)+k_1 I_{L\alpha 1}{}'\left(t-\frac{T}{4}\right)\right\}\right]\\&=0.5I_{L1}(t)\left[\sin\left(\theta_f\right)-\frac{1}{k_2}\left\{k_1\cos\left(\theta_f\right)+\sin\left(\theta_f-\frac{T\Delta\omega_0}{4}\right)\right\}\right]\end{aligned} \tag{23}$$

These are updated by feeding back the signal $\Delta\omega_0$ from the PI controller output to the proposed *αβ*-MDSC operator.

3.3 Stability analysis of αβ- GDSC and αβ- frame MDSC filter

According to the linearized model, PLL is stable for gain values proportional gain > 0 and integral gain > 0. The MDSC operator smoothly synchronizes and transitions the output angular frequency value with the varying SEIG frequency, providing feedback to the αβ-MDSC-PLL operator. To eliminate even and odd order harmonics in the load current and source voltage signal, set the delay factor N of the αβ-MDSC operator to a high value. To address frequency variation in SEIG, the αβ-MDSC employs a self-adaptive mechanism that eliminates harmonics in the approximated frequency signal as the angular frequency changes.

The transfer function of αβ-GDSC [39]

$$\alpha\beta GDSC_N(s)\approx\frac{1}{1+sT_\omega/4} \tag{24}$$

For a closed loop, the transfer function of the *αβ*-GDSC can be obtained as

$$G_{cl}\approx\alpha\beta GDSC_N(s).\frac{k_p s+k_i}{s^2} \tag{25}$$

and for *αβ*-MDSC the transfer function is given by

$$\alpha\beta MDSC_N(s)=\frac{1}{N}\sum_{l=0}^{N-1}e^{\left(\frac{Tl}{N}\right)s}=\frac{1}{N}\left(\frac{1-e^{-Ts}}{1-e^{-Ts/N}}\right) \tag{26}$$

αβ-MDSC has a nonlinear nature which will complicate the process of stability analysis. The method of approximate transfer function to linearize the MDSC model will be taken into consideration. Applying the pade approximation to approximate the exponential term in the (31) transfer function and applying the binomial expansion, the resultant transfer function will be:-

$$\alpha\beta MDSC_N(s) \approx \frac{1}{1+\frac{T}{2}.\left(\frac{N-1}{N}\right)s} = \frac{1}{1+\left(\frac{N-1}{2Nf}\right)s} \tag{27}$$

The proposed frequency adaptation scheme (FAS) is used as a feed-forward to the pre-filtering operator. The cascade connection of both SRF-PLL and MDSC-PLL is stable in the current scheme. Since *αβ*-MDSC is an FIR, they are intrinsically stable even under the shifting operational time span.

The transfer function of the closed loop will be

$$G_{cl} = \alpha\beta MDSC_N(s).\frac{k_p s + k_i}{s^2 + k_p s + k_i} \tag{28}$$

Thus, this transfer function of the closed-loop system is stable when $k_p > 0$ and $k_i > 0$ [36].

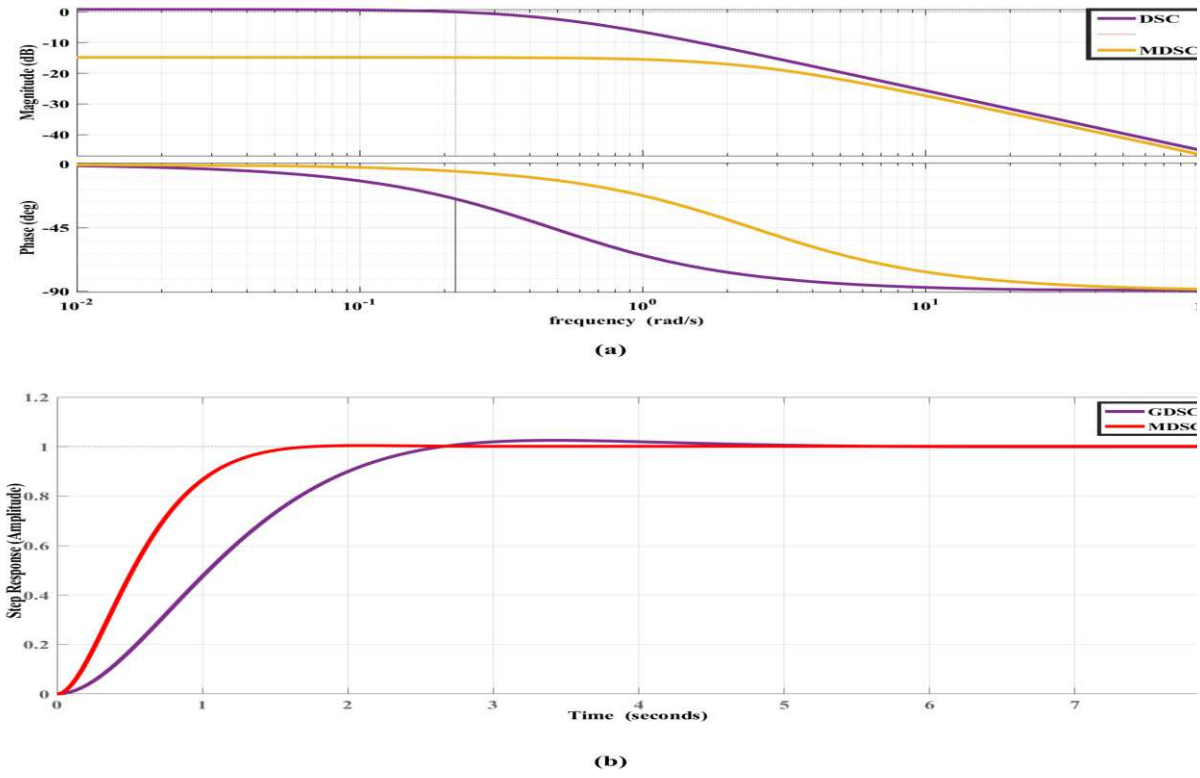

Figure 4. (a) Bode plot of GDSC and MDSC (b) Step response of GDSC AND MDSC

Figure 4(a) shows the comparative analysis using a bode plot (gain and phase margin) of the exact function of GDSC and MDSC under the SEIG frequency f=50Hz. From this plot, it can be observed that multiple delayed signal cancellation (MDSC) shows a better dynamic response and accurate gain with a higher phase margin as compared to the generalized delayed signal cancellation(GDSC). Figure 4(b) shows the step response for both the operators, from

this plot the MDSC has a lesser settling time as compared to the GDSC. This fact also explains the most significant feature of MDSC, which is the elimination of the lowest undesirable harmonics that are not being eliminated by generalized delayed signal cancellation (GDSC) and the MDSC operator contains reduced delay time and offers greater adaptability to eliminate the undesirable harmonic as compared to GDSC.

4. Generation of gating pulse using MDSC

This section presents the extraction of fundamental active and reactive components of the load current which along with the unit templates are used to generate a reference current for the source current. The reference current and the actual current are being compared in the hysteresis current controller (HCC) to generate 6 gating pulses for the voltage regulation and current compensation of the proposed SEIG system

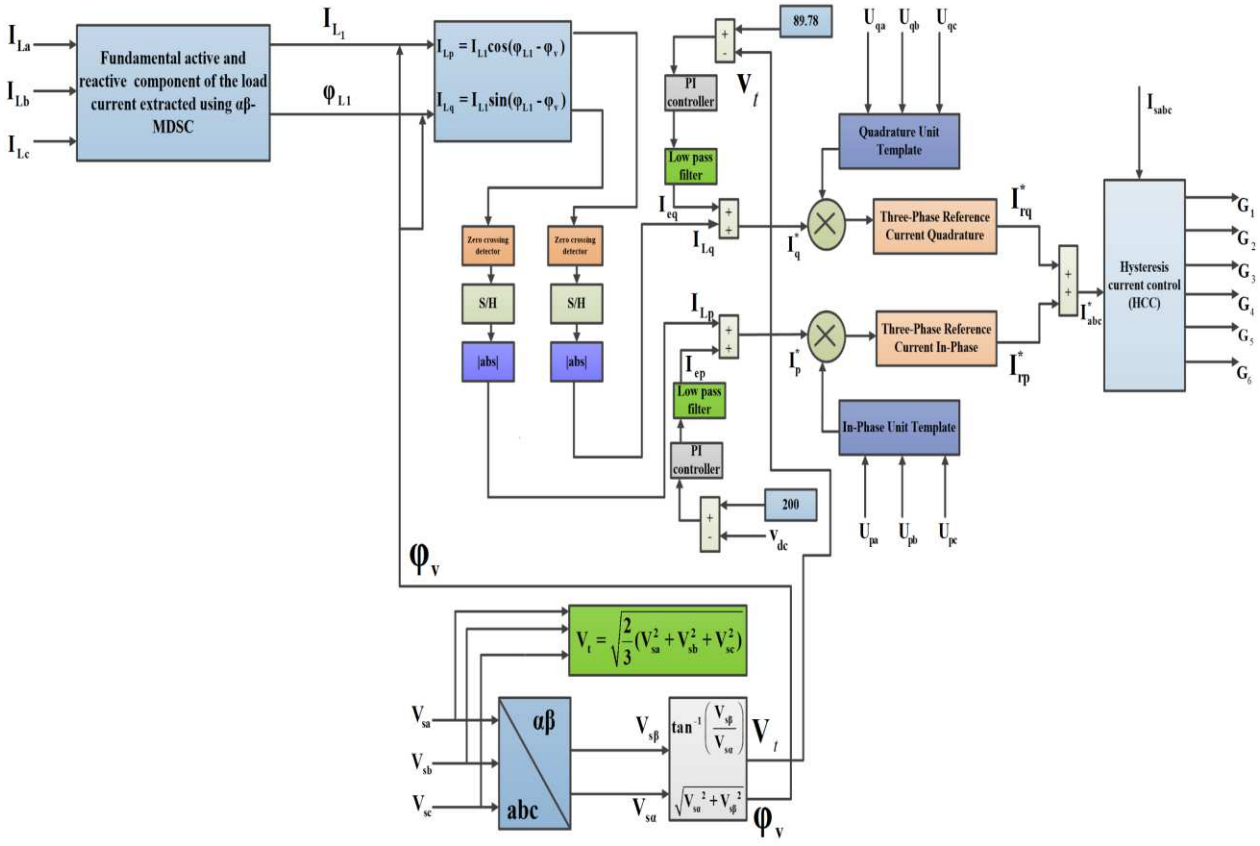

Figure 5. Block diagram of αβ-MDSC-PLL based control algorithm.

4.1 Extraction of the fundamental component of load current and phase angle

Figure 5 depicts the block representation of the proposed αβ-MDSC based control algorithm. From the small signal illustrated in the above section 3.2, *αβ*-MDSC is applicable for the extraction of the fundamental active and the reactive component of load current ($I_{L\alpha 1}$) and ($I_{L\beta 1}$):-

$$\mathrm{I}_{\mathrm{L}\alpha 1} = 0.5 I_{L1}(t)\left[\cos(\theta_f) - \frac{1}{k'}\left\{k\sin(\theta_f) - \cos\left(\theta_f - \frac{T\Delta\omega_0}{4}\right)\right\}\right] \tag{29}$$

$$\mathrm{I}_{\mathrm{L}\beta 1} = 0.5 I_{L1}(t)\left[\sin(\theta_f) - \frac{1}{k'}\left\{k\cos(\theta_f) + \sin\left(\theta_f - \frac{T\Delta\omega_0}{4}\right)\right\}\right] \tag{30}$$

Now the fundamental current component I_{L1} and its phase angle Φ_{L1} are calculated as

$$\mathrm{I}_{L1} = \sqrt{\mathrm{I}_{\mathrm{L}\alpha 1}^{\ 2} + \mathrm{I}_{\mathrm{L}\beta 1}^{\ 2}} \tag{31}$$

$$\varphi_{L1} = \tan^{-1}\left(\frac{\mathrm{I}_{\mathrm{L}\beta}}{\mathrm{I}_{\mathrm{L}\alpha}}\right) \tag{32}$$

$$\begin{pmatrix} v_\alpha \\ v_\beta \end{pmatrix} = \sqrt{\frac{2}{3}} \begin{pmatrix} 1 & \frac{-1}{2} & \frac{-1}{2} \\ 0 & \frac{\sqrt{3}}{2} & -\frac{\sqrt{3}}{2} \end{pmatrix} \begin{pmatrix} v_a \\ v_b \\ v_c \end{pmatrix} \tag{33}$$

$$\varphi_{\mathrm{v}} = \tan^{-1}\left(\frac{v_{\mathrm{s}\beta}}{v_{\mathrm{s}\alpha}}\right) \tag{34}$$

The active and the reactive components of the load current with the phase angle calculated for load current Φ_{L1} and for the terminal voltage phase angle φ_{v} are given as

$$\mathrm{I}_{\mathrm{Lp}} = \mathrm{I}_{\mathrm{L1}}\cos(\varphi_{\mathrm{L1}} - \varphi_{\mathrm{v}}) \tag{35}$$

$$\mathrm{I}_{\mathrm{Lq}} = \mathrm{I}_{\mathrm{L1}}\sin(\varphi_{\mathrm{L1}} - \varphi_{\mathrm{v}}) \tag{36}$$

4.2 Calculation of voltage amplitude and In-phase Unit Templates

The v_{sa}, v_{sb} and v_{sc} are the instantaneous values of the 3-phase SEIG-DSTATCOM-based system, and the unit template for active components can be derived by dividing the individual values of v_{sa}, v_{sb} and v_{sc} by the amplitude of the terminal voltage(V_t) and for reactive components where U_{qa} , $U_{qb,}$ U_{qc} are the quadrature unit templates which are as follows,

$$V_t = \sqrt{\frac{2\left(v^2_{\ sa} + v^2_{\ sb} + v^2_{\ sc}\right)}{3}}$$

$$\mathrm{U}_{\mathrm{pa}} = {}^{v_{sa}}/_{V_t} \quad \mathrm{U}_{\mathrm{pb}} = {}^{v_{sb}}/_{V_t}, \quad \mathrm{U}_{\mathrm{pc}} = {}^{v_{sc}}/_{V_t} \tag{37}$$

$$U_{qa} = \left(-U_{pb} + U_{pc}\right)/\sqrt{3}$$
$$U_{qb} = \left(3U_{pa} + U_{pb} + U_{pc}\right)/2\sqrt{3} \quad (38\text{-}40)$$
$$U_{qc} = \left(-3U_{pa} + U_{pb} - U_{pc}\right)/2\sqrt{3}$$

4.3 Calculation of loss component of PI controller

The suggested controller works by comparing DSTATCOM's real DC link voltage with the reference value of the DC link voltage. The K_{pp} and K_{ip} are the proportional and integral gain constants used by the PI controller. PI controllers are employed: one for regulating the DC link voltage and the other for controlling the terminal voltage. For voltage regulation, the reference PCC voltage is compared with the actual DSTATCOM terminal voltage, feeding the PI controller for terminal voltage regulation, where K_{pq} and K_{ip} act as the proportional and integral gain constants. The output of the PI controller for the reactive component is determined by adding the magnitude of the terminal voltage's loss component (I_{ep}) to the magnitude of the fundamental load current (I_{Lq}), whereas the output of the PI controller for the active (loss) component is added to the fundamental load current (I_{Lp}).

$$V_{DCE}(N)=V_{DC}^{*}(N)-V_{DC}(N) \quad (41)$$
$$I_{EP}(N)=I_{EP}(N-1)+K_{PP}\{V_{DCE}(N)-V_{DCE}(N-1)\}+K_{IP}V_{DCE}(N) \quad (42)$$
$$I^{*}_{P}=I_{EP}+I_{LP} \quad (43)$$

For the reactive component,

$$V_{TE}(N)=V_{T}^{*}(N)-V_{T}(N) \quad (44)$$
$$I_{EP}(N)=I_{EP}(N-1)+K_{PQ}\{V_{TE}(N)-V_{TE}(N-1)\}+K_{IQ}V_{TE}(N) \quad (45)$$
$$I^{*}_{Q}=I_{EQ}+I_{LQ} \quad (46)$$

4.4 Calculation of reference supply current

The amplitude of the 3-Φ supply reference current for the active and reactive components can be calculated by multiplying the output of the PI voltage controller which is taken as (I^{*}_{p}) to the in-phase unit template of each phase 'a', 'b', and 'c' and for the reactive component is taken as (I^{*}_{q}) is multiplied to the quadrature unit template of each phase 'a', 'b' and 'c': -

$$I^{*}_{rpa}=I^{*}_{p.}U_{pa},\ I^{*}_{rpb}=I^{*}_{p.}U_{pb},\quad I^{*}_{rpc}=I^{*}_{p.}U_{pc} \quad (47)$$
$$I^{*}_{rqa}=I^{*}_{q}U_{qa},\ I^{*}_{rqb}=I^{*}_{q}U_{qb},\quad I^{*}_{rqc}=I^{*}_{q}U_{qc} \quad (48)$$

Therefore, the resultant active and reactive component of reference current can be calculated as:-

$$I^{*}_{rp}=\frac{I^{*}_{rpa}+I^{*}_{rpb}+I^{*}_{rpc}}{3} \quad (49)$$

$$I^{*}_{rq}=\frac{I^{*}_{rqa}+I^{*}_{rqb}+I^{*}_{rqc}}{3} \quad (50)$$

$$I_{abc}{}^{*}=I^{*}_{rp}+I^{*}_{rq} \quad (51)$$

4.5 Formulation of gating pulse

Hysteresis current control technology (HCC) generates gate pulses by comparing the 3-phase active and reactive component of supply reference current (I^*_{sa} I^*_{sb} I^*_{sc}) with the 3-phase source current being detected by the current sensors and a total of six gating pulses are generated for proper operation of the system

5. Simulation Results

In this section, simulation analysis for multiple delayed signal cancellation (MDSC) operator-based PLL control algorithm is being discussed for self-excited induction generator (SEIG)-DSTATCOM-based distributed generation. All the results are shown are presented under different dynamic conditions. Results are obtained to show different loading operating conditions and how MDSC-PLL performs for a SEIG-DSTATCOM-based distributed generation system. The parameters of SEIG, prime-mover, and the Distributed static compensator (DSTATCOM) designed for the simulation are given in Appendix A and thereafter hardware prototype is designed for the verification of simulation results.

5.1 Dynamic and steady-state analysis of MDSC-PLL for SEIG-DSTATCOM under different load conditions.

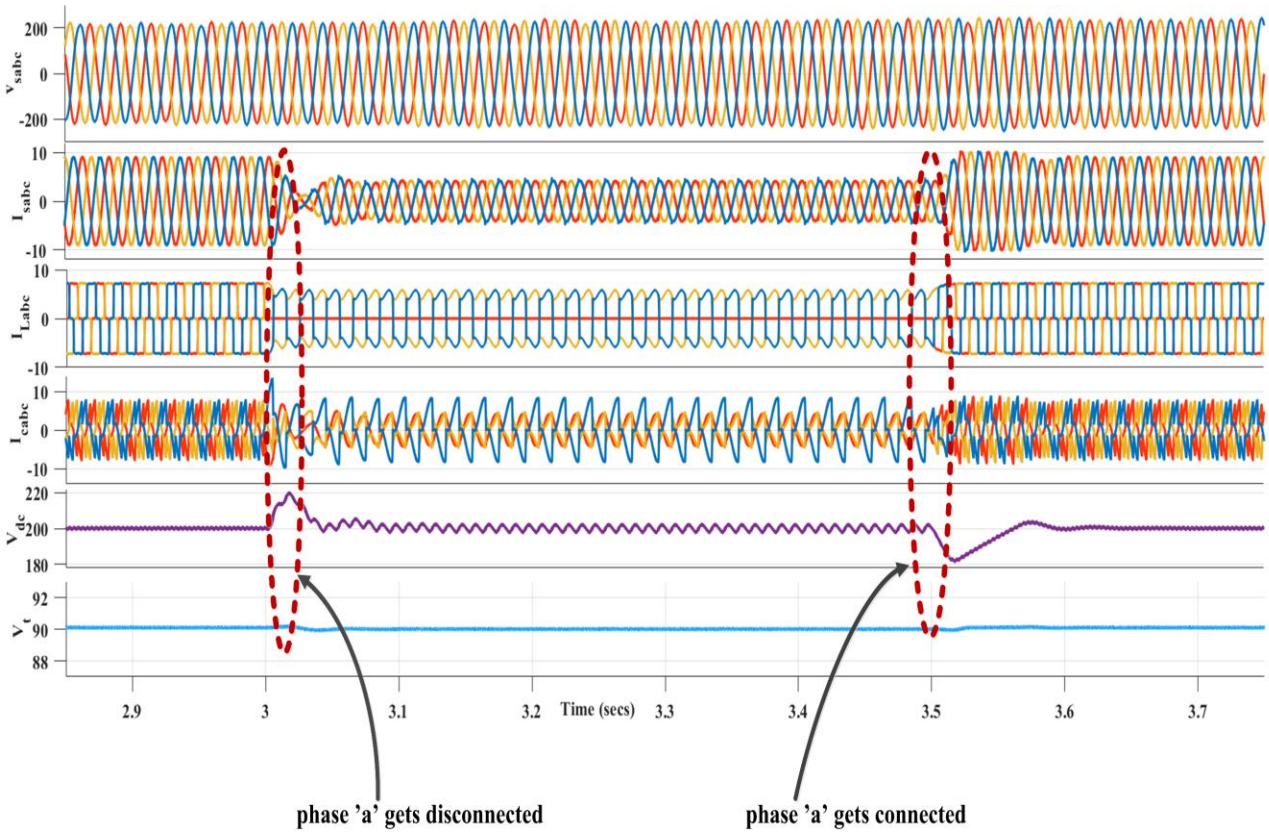

Figure 6 .simulation results showing dynamic performance of MDSC-PLL algorithm under unbalance load condition from T=3 sec to T=3.5 for different parameters

Figure 6 illustrates the dynamic performance analysis of the MDSC-PLL control algorithm developed in MATLAB/SIMULINK and simulated under different non-linear load conditions. The waveform shows that the source voltage generated by the SEIG(v_{sabc}) which has no effect if a single phase isolator is being applied from the time period 3s to 3.5s, source current (I_{sabc}), load current (I_{Labc}), compensator current (I_{cabc}) magnitude of which gets decreases as the single phase isolator is applied at "a" phase at time period of 3 seconds and increases as the single phase isolator gets removed at the time period of 3.5 seconds. The figure also depicts the DC link voltage of DSTATCOM being maintained at 200V with the help of a PI controller in both the condition of connection and disconnection of the load, and the terminal voltage or the voltage at the PCC (V_t or V_{PCC}) being maintained at 89.78V with the help of PI controller in both the condition of connection and disconnection of the load. The DSTACOM provides the required amount of compensating current in both the dynamic as well as the steady-state operation.

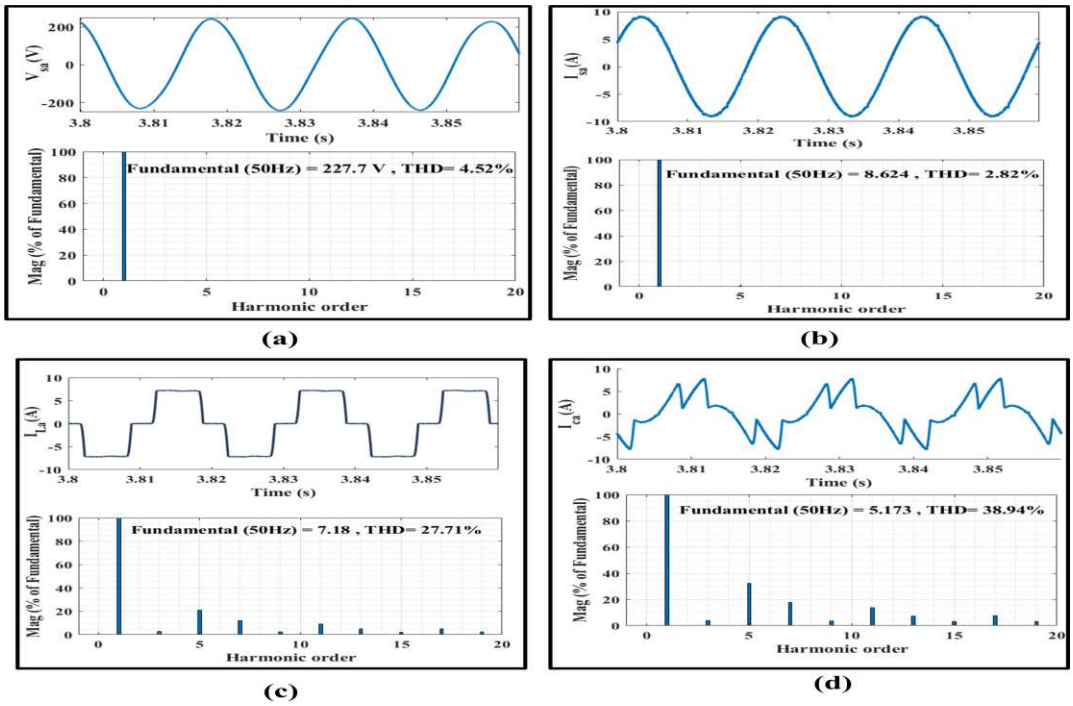

Figure 7 (a) depicts the waveform of source voltage generated by the SEIG of phase 'a' (v_{sa}), (b) depicts the waveform of source current generated by the SEIG of phase 'a' (I_{sa}), (c) depicts the waveform of load current of phase 'a' (I_{La}), (d) depicts the waveform of the compensator current generated by the DSTATCOM of phase 'a' (I_{ca}).

Figure 7 shows the performance and the effectiveness of the MDSC-PLL-based control algorithm for SEIG-DSTATCOM-based distributed generation is tested by observing the harmonic spectra using FFT analysis of phase 'a'. Figure 7(a) shows the waveform of source voltage generated by the SEIG of phase 'a' (v_{sa}) and total harmonic distortion (THD%) of 4.52%, figure7(b) depicts the waveform of source current generated by the SEIG of phase 'a' (I_{sa}) and the total harmonic distortion of (THD%) of 2.82%, figure7(c) depicts the waveform of load current of phase 'a' (I_{La}) and the total harmonic distortion of (THD%) of 27.71%, figure 7(d) depicts the waveform of compensator current generated by the DSTATCOM of phase 'a' (I_{ca}) and the total harmonic distortion of (THD%) of 38.94%. From the above results, it can be inferred that the total harmonic distortion% of source voltage and source current is well within the permissible limits of 5% stipulated by IEEE-519 standards. MDSC-PLL control for a SEIG-DSTATCOM -based system performs load compensation technique satisfactorily with the nonlinear load

5.2 Performance analysis of MDSC-PLL control algorithm for different parameters under load conditions

Figure 8 depicts the waveform for different parameters under load conditions. Figure 8(a) illustrates the waveform of active power (kW) for the source (P_{source}), load (P_{load}), and DSTATCOM ($P_{DSATCOM}$) when the load is applied at 3 seconds the active power decreases and increases as the load is removed at 3.5 seconds. The results follow the principle of power balance in the case of SEIG which is, power generated by the source (SEIG) is equal to the sum of power consumed by the load and the power transmitted by the compensator $P_{source}=P_{load} + P_{DSTATCOM}$. The figure also shows the waveform of reactive power (kVA) for the source (Q_{source}), load (Q_{load}), and DSTATCOM ($Q_{DSTATCOM}$) when the load is applied at 3 seconds the reactive power decreases and increases as the load is removed at 3.5 seconds and this also follows the principle of power balance in case of SEIG, power transmitted by the DSTATCOM is equal to the

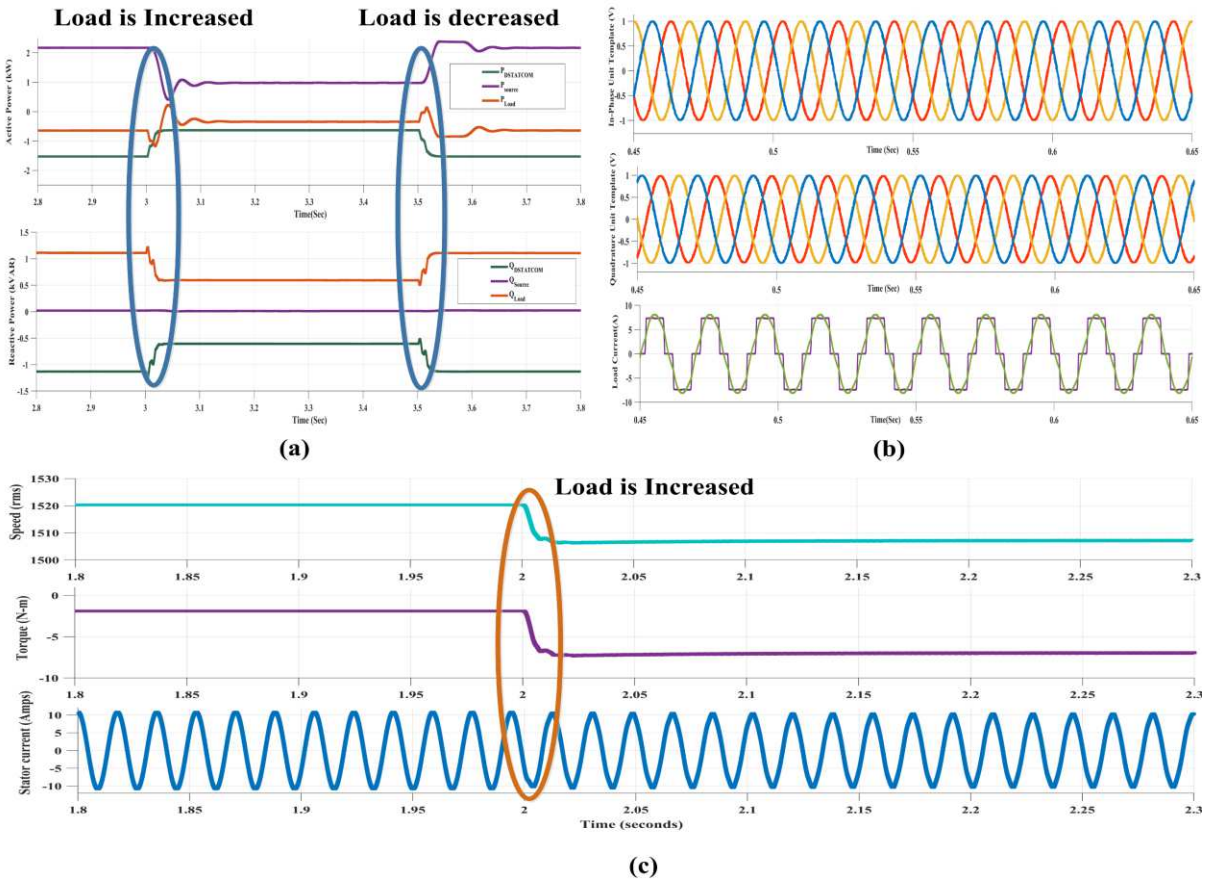

Figure 8. steady state analysis for MDSC-PLL of SEIG-DSTATCOM based system. (a) Active power and reactive power for source (P_{source}), load (P_{load}) and DSTATCOM ($P_{DSTATCOM}$) under load varying from t=3 to 3.5 ,(b) In-phase unit template of the three-phase (U_{pabc}) , quadrature unit template of the three-phase (U_{qabc}) and load current (I_L) and fundamental current component extraction of alpha ($I_{\alpha 1}$), (c) speed, torque, and stator current of the SEIG when the load is applied at 2 seconds.

power consumed by the load $Q_{DSTATCOM} = Q_{load}$. Figure 8(b) shows the waveform of the In-phase unit template of the three-phase (U_{pabc}) and in-quadrature unit template of the three-phase (U_{qabc}) and the third waveform shows load current (I_L) and fundamental current component extraction of alpha ($I_{\alpha 1}$). Figure 8(c) shows the waveform of speed, torque, and stator current of the SEIG when the load is applied at 2 seconds. When the load is applied at 2 seconds the magnitude of speed and stator current decreases within the permissible limits whereas the magnitude of torque increases as the load is applied at 2 seconds.

6. Experimental results and discussions

Figure 9 shows the hardware prototype model for MDSC-PLL that has been developed in the laboratory for the verification of simulated results that were obtained through MATLAB/SIMULINK. To validate the simulated results different combination of results is being taken into consideration for dynamic as well as steady-state conditions on the developed hardware setup of SEIG-DSTATCOM. The results obtained are analyzed in the subsequent section.

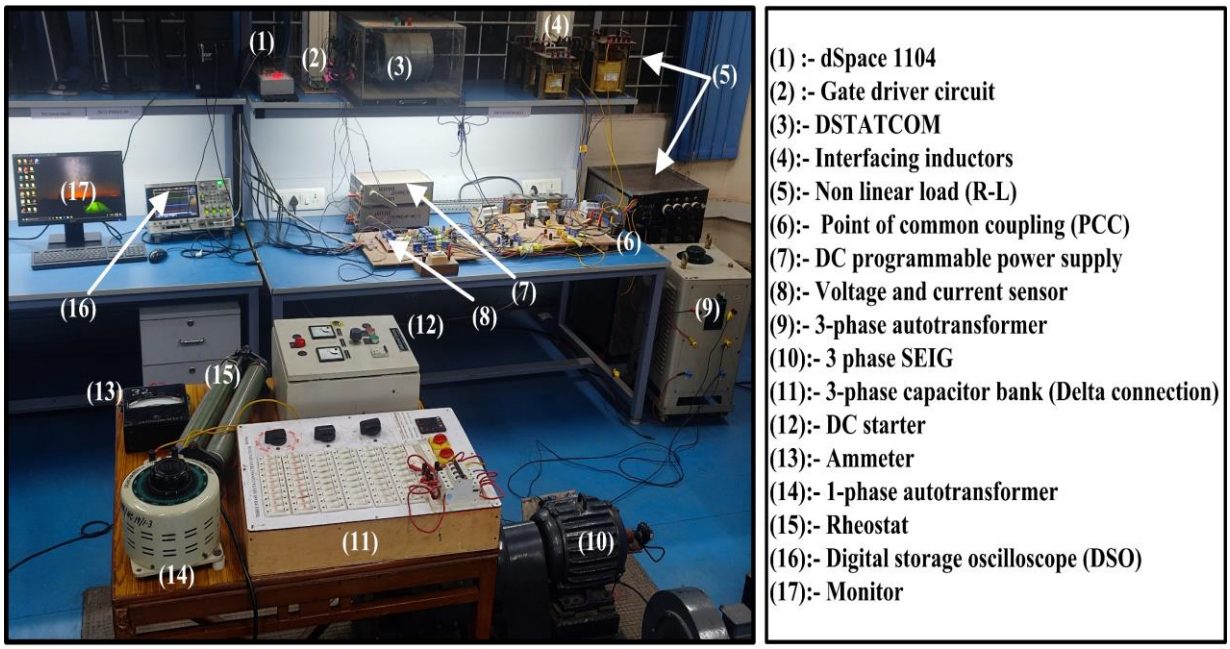

Figure.9 Hardware prototype model for the experimental verification of the simulated results of the MDSC-PLL-based control algorithm.

6.1 To analyze the dynamic performance of MDSC-PLL based control algorithm for SEIG-DSTATCOM based system under different nonlinear load conditions.

Figure 10 depicts the performance of the proposed MDSC-PLL control algorithm under dynamic conditions when the load is decreased or increased. Figure 10(a) depicts the waveform of DC link voltage (V_{DC}) (410V/div) being maintained at 200V, load current of phase 'a' (I_{La}) (12A/div) magnitude of which decreases as the load gets decreased, source voltage of phase 'a' (v_{sa}) (60V/div) magnitude of which doesn't change with the decrease in the amplitude of the load, source current of phase 'a' (I_{sa}) (5 A/div) amplitude of which decreases as the load gets reduced. Figure 10(b) depicts the waveforms of the source voltage of phase 'a' (v_{sa}) (112V/div) magnitude of which doesn't change with the decrease in the amplitude of the load, load current of phase 'a' (I_{La}) (8A/div) magnitude of both decreases as the load gets decreased, compensating current of phase 'a' (I_{ca}) (2A/div) magnitude of which decreases as the load gets decreased, source current of phase 'a' (I_{sa}) (11A/div) magnitude of which decreases as the load get reduced. Figure 10(c) depicts the waveform of the compensating current of phase 'a' (I_{ca}) (5A/div) the magnitude of which decreases as the load gets decreased, load current of three phases 'a', b, 'c' (I_{La}) (11A/div), (I_{Lb}) (11A/div), (I_{Lc}) (11A/div) the magnitude of which reduces as the load gets reduced. Figure 10(d) depicts the waveform of DC link voltage (V_{DC}) (400V/div) being maintained at 200V, load current of phase 'b' (I_{Lb}) (6A/div) magnitude of which increases as the load gets increased, source voltage of phase 'b' (v_{sb}) (189V/div) magnitude of which doesn't change with the increase in the amplitude of the load, compensating current of phase 'b' (I_{cb}) (2A/div) magnitude of which increases as the load gets increased. Figure 10(e) illustrates the waveform of the in-phase reference current of the 'b' phase I^{*}_{Pb} (3A/div), load current of phase 'b' (I_{Lb}) (6A/div) magnitude of which increases as the load gets injected, compensating current

of phase 'b' (I_{cb}) (2A/div) magnitude of which increases as the load gets increased, source current of phase 'b' (I_{sb}) (3A/div) magnitude of which increases as the load is injected. Figure 10(f) illustrates the load current signal of phase 'b' (I_{Lb}) (6A/div) magnitude of which increases as the load gets injected, source current of phase 'a' (I_{sa}) (3A/div) magnitude of which increases as the load is injected, source current of phase 'b' (I_{sb}) (3 A/div) magnitude of which increases as the load is increased, source current of phase 'c' (I_{sc}) (3 A/div) magnitude of which increases as the load is injected. The above results are taken at a scale of 25ms/divisions on a digital storage oscillator (DSO). From the above discussions, it can be concluded that the proposed control algorithm performs well under steady state and dynamic load conditions. Also, the supply current is observed to be balanced (sinusoidal) even when one of the loads get disconnected. From the above discussions, it is again proved that the MDSC performs well, and it has stable operation under load conditions.

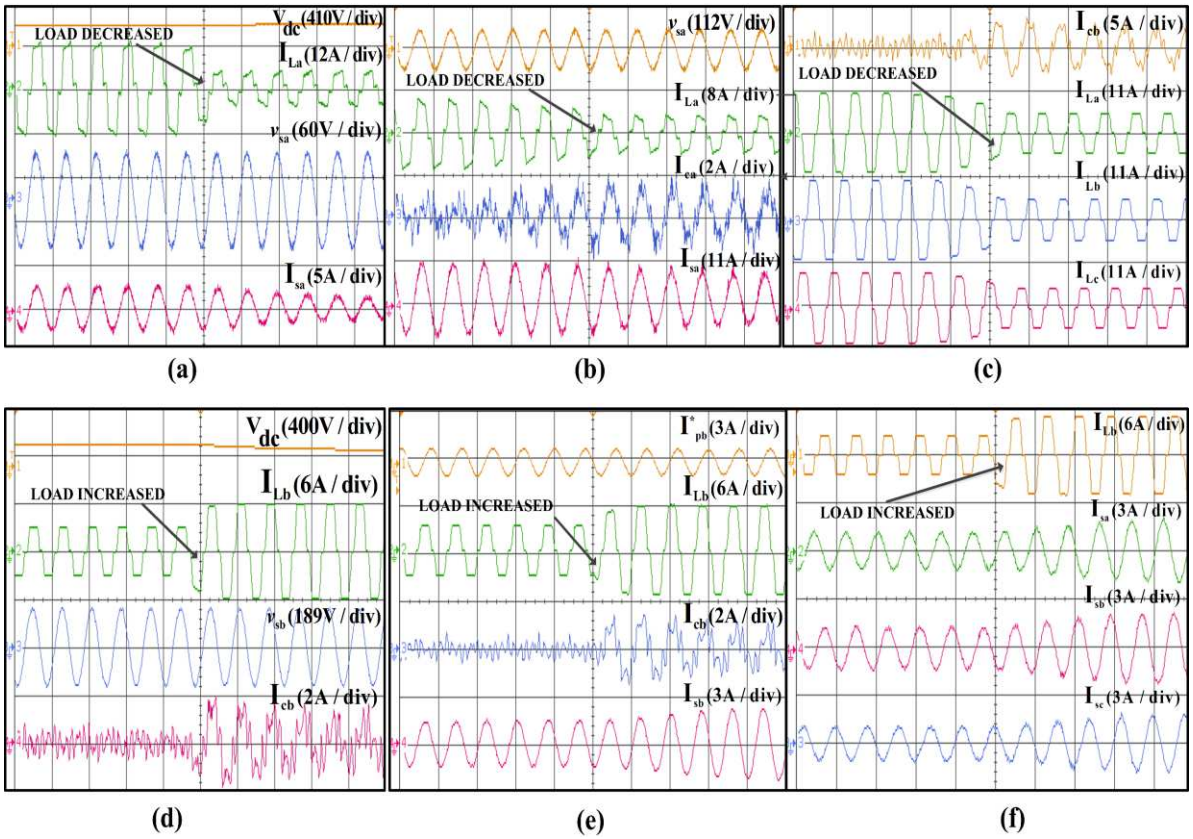

Figure 10. Dynamic performance of MDSC-PLL control algorithm for load decrease and increase. *(a)* $V_{DC,}$ $I_{La,}$ $v_{sa,}$ I_{sa} *(b)* $v_{sa,}$ I_{La} $I_{ca,}$ I_{sa}.*(c)* $I_{ca,}$ $I_{La,}$ $I_{Lb,}$ I_{Lc} *(d)* $V_{DC,}$ $I_{Lb,}$ $v_{sb,}$ I_{cb} *(e)* I^*_{pb} , $I_{Lb,}$ $I_{cb,}$ I_{sb} *(f)* $I_{Lb,}$ $I_{sa,}$ $I_{sb,}$ I_{sc}.

Figure 11(a)-(d) depicts the intermediate signal for the MDSC-PLL algorithm at nonlinear load conditions. Figure 11 (a) depicts the waveform of compensating current of phase 'b' (I_{cb}) (4A/div), the fundamental component of the load current (I_f) (5A/div), the fundamental active component of the load current(I_α) (5A/div), the fundamental reactive component of the load current (I_β) (5A/div). Figure 11(b) depicts the load current signal of phase 'a' (I_{La}) (3A/div), in-phase reference current of 'a' phase I^*_{Pa} (3A/div), in-phase unit template of phase 'a' U_{qa} (0.5V/div), quadrature unit template(U_{qa}) of phase 'b' (1V/div). Figure 11(c) shows the waveform of the in-phase reference current of 'b' phase I^*_{Pb} (6A/div), a fundamental component of the load current (I_f) (5 A/div), in-phase unit template of phase 'a' U_{pa} (1V/div), quadrature unit template (U_{qb}) of phase 'b' (1V/div). Figure 11(d) depicts the waveform of the in-phase reference current of 'b' phase I^*_{Pb} (3A/div), in-phase reference current of 'a' phase I^*_{Pa} (5A/div), in-phase unit template of phase 'a' U_{pa} (0.5V/div), gating pulse (2.5V/div) of 15V magnitude given to the three leg IGBT.

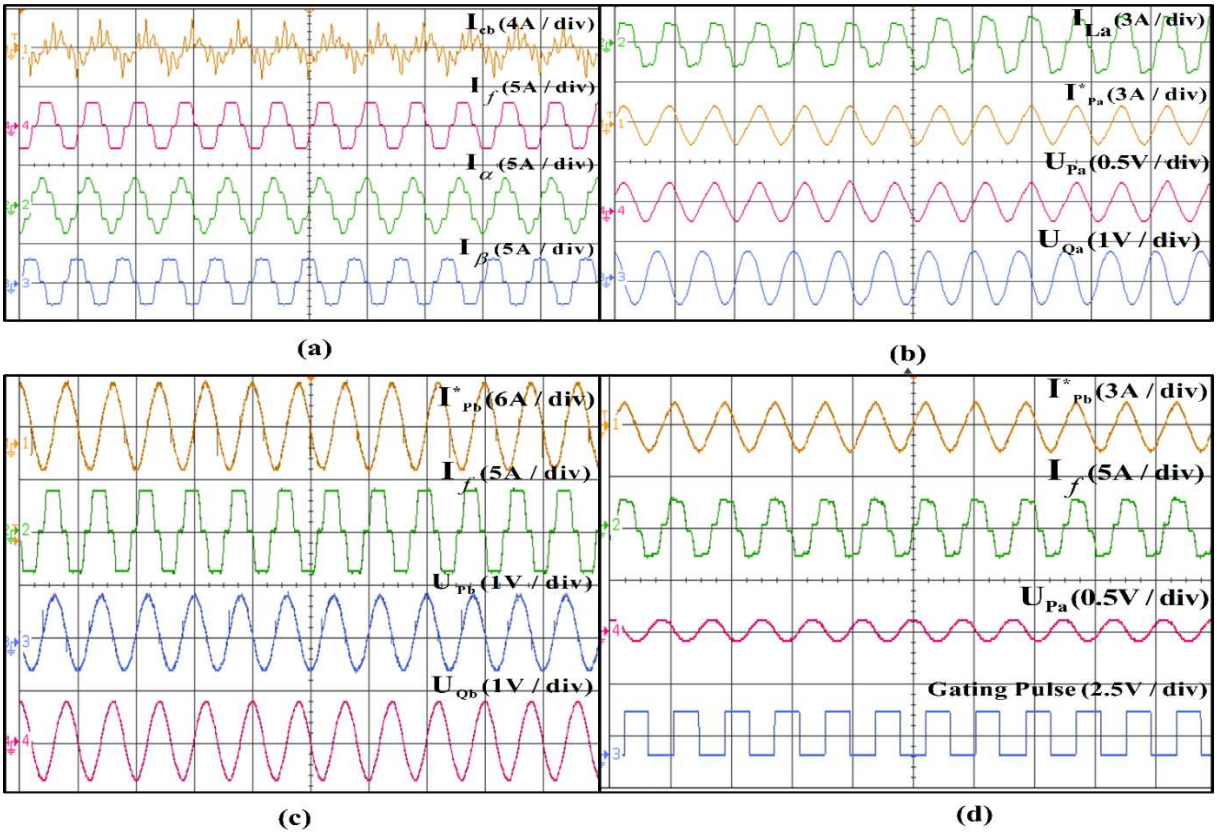

Figure 11. Intermediate results for the MDSC control algorithm. (a) I_{cb}, I_f, I_α, I_β *(b)* I_{La} , I^*_{Pa} , U_{pa} U_{qa}. *(c)* I^*_{Pb} I_f, U_{pa}, U_{qb} .*(d)* I^*_{pb} , I_f , U_{pa}, *gating pulse.*

6.2 Steady-state analysis of MDSC-PLL based control algorithm for SEIG-DSTATCOM based system.

Figure 12-13 depicts the steady-state performance of the MDSC-PLL control algorithm for SEIG-DSTATCOM. Figure 12(a) depicts the waveform of three-phase source voltage (v_{sa}, v_{sb}, v_{sc}) having the magnitude of (119.66,120.35,118.17) V respectively having the THD% of 2.07% and three-phase source current (I_{sa}, I_{sb}, I_{sc}) with the magnitude of (5.32,5.39,5.89) Amps having the THD% of 4.22% which are under the permissible limits of 5% according to IEEE-519 standards. Figure 12(b) depicts the waveform of three-phase source voltage (v_{sa}, v_{sb}, v_{sc}) having the magnitude of (113.32,114.12,113.74) V respectively having the THD% of 2.26% and three-phase load current (I_{La}, I_{Lb}, I_{Lc}) with the magnitude of (5.02,5.02,5.04) Amps having the THD% of 17.20% at a frequency of 50 Hz.

Figure 13(a) illustrates the source power with the amplitude of the three-phase supply RMS voltage(113.01, 114.89, 114.68)V and current (6.02, 6.00, 6.01). 15(A) with a magnitude of three-phase active power(VA), reactive(var) and the apparent power(W) 1.19kVA, 1.18 kvar, 0.15kW respectively with the power factor of 0.9199 . Figure 13(b) illustrates load power with the magnitude of three-phase supply RMS voltage (111.65, 112.94, 112.73) and load current (5.99, 6.01,5.99) with magnitude of three-phase active power(VA), reactive(var) and the apparent power(W) 1.17 kVA, 1.16var, 0.12kW respectively with the power factor of 0.9217. Figure 13(c) depicts the phasor diagram of the three-phase source voltage(65.16, 64.37, 65.18)V and v_{unb} (voltage negative phase unbalance factor) of 0.49% and the phasor of three-phase source current(5.93,5.94,5.92) A with I_{unb} (current negative phase unbalance factor) of 50.14%. Figure 13(d) depicts the phasor diagram of the three-phase voltage phasor with the phase difference (0°, 119.39°, 119.59°) with v_{unb} (voltage negative phase unbalance factor) of 0.53% the phasor of three-phase source current with the phase difference of (141.17°, 21.02°, 81.19°) with I_{unb} (current negative phase unbalance factor) of 50.13%.

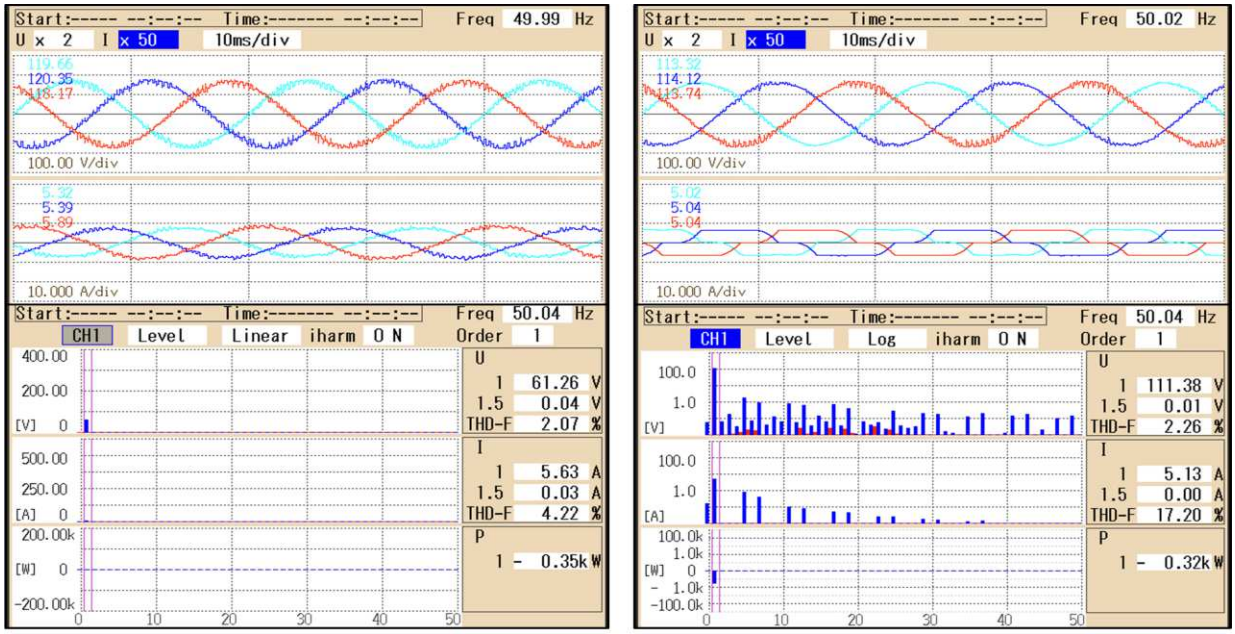

Figure 12. Experimental results for steady state. (a) three-phase supply source voltage (v_{sa}, v_{sb}, v_{sc}), THD% respectively, and source current (I_{sa}, I_{sb}, I_{sc}), THD% respectively, (b) three-phase source voltage (v_{sa}, v_{sb}, v_{sc}), THD% respectively, and three-phase load current (I_{La}, I_{Lb}, I_{Lc}), THD% respectively.

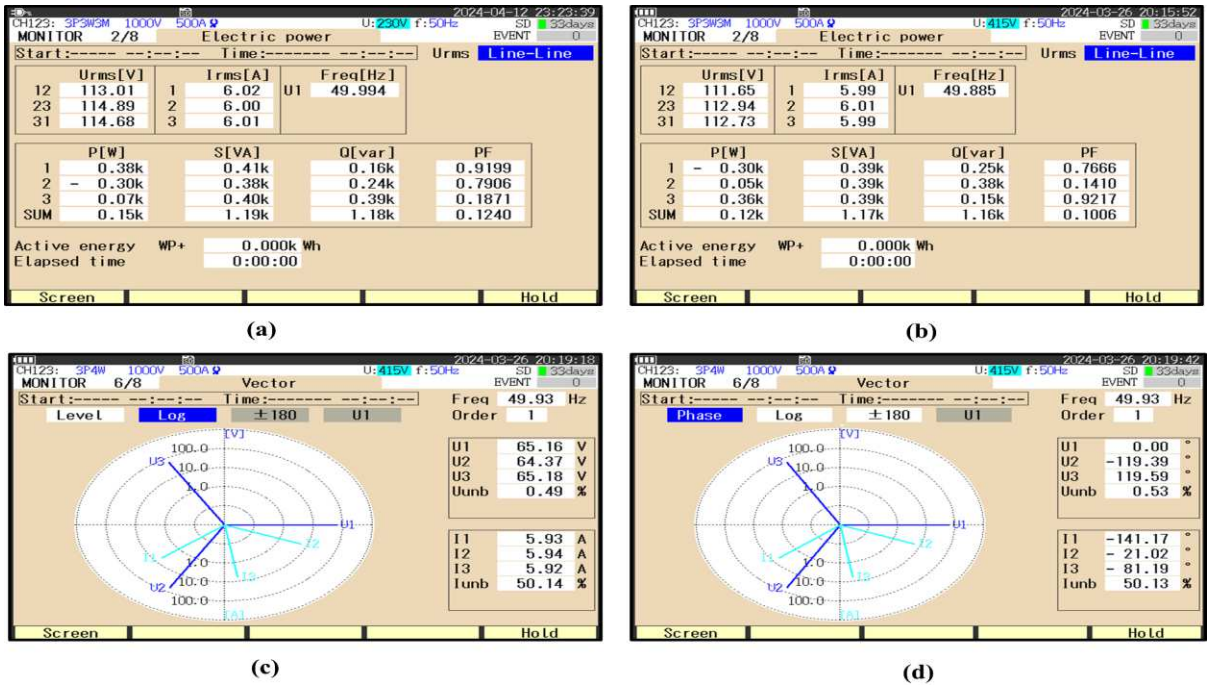

Figure 13. Experimental results for the steady state analysis of MDSC-PLL. (a) Source power with the magnitude of three-phase supply RMS voltage, current and amplitude of three-phase active power(VA), reactive(var), and apparent power(W), (b) Load power with the amplitude of three-phase supply RMS voltage and load current with an amplitude of three-phase active power(VA), reactive(var), and apparent power(W), (c) Phasor diagram of the three-phase source voltage and v_{unb} (voltage negative phase unbalance factor), (d) The three-phase voltage phasor with the phase difference with v_{unb} (voltage negative phase unbalance factor).

Table No.1 Comparative study between generalized DSC and multiple DSC filter.

S.no	CHARACTERISTICS/ PARAMETERS	GDSC	MDSC
1	Dynamic response	Moderate	**Faster as compared to GDSC**
2	Stability	Moderately stable	**Highly stable**
3	Transient stability/response	Moderate to high transient response	**Faster transient responses**
4	Settling time	Relatively slower settling time	**faster settling time as compared to GDSC**
5	Bandwidth	Wider than MDSC	**Narrower bandwidth**
6	Estimation of phase, frequency, and amplitude	Moderately accurate	**Highly effective and accurate**
7	Steady-state error	Less	**Very less as compared to GDSC**
8	Gain margin (gain cross-over frequency)	At -20dB (6.0rad/sec)	**At -20dB (4.65rad/sec)**
9	Phase margin (phase cross-over frequency)	48.7deg (6.26rad/sec)	**53.89 deg (5.13rad/sec)**

7 Comparative study analysis between GDSC and MDSC

Table 1 shows the comparative performance analysis of generalized delayed signal cancellation and multiple delayed signal cancellation on various parameters. The proposed MDSC controller has several advantages over GDSC. The MDSC has faster dynamic response , good stability, narrower bandwidth, low steady state error and greater gain and phase margin as compared to GDSC.

8 CONCLUSION

This research article proposes multiple delayed signal cancellation(MDSC) control schemes for the regulation of voltage and load compensation for SEIG-DSTATCOM-based distributed generation. Small-signal modeling and design of the proposed control filter is being conducted with the effect of variation of parameters like the angular frequency ω_g, twiddle factor (W_n^l), and delay factor (N). The open-loop comparative analysis is being performed between GDSC-PLL and MDSC-PLL by the depiction of the bode plot, step response, and root locus. From this conclusion it has been derived that MDSC-PLL shows faster dynamic response, and faster selling time as compared to GDSC, has Narrower bandwidth, highly accurate and effective Phase, frequency, and amplitude estimation under unbalanced conditions, less convergence time, and is highly stable as compared to the GDSC. The $\alpha\beta$-MDSC has a mechanism that is self-adaptive in nature, and which will mitigate all the harmonics in the estimated frequency signal by the change in the angular frequency$\Delta\omega_0$. The Bode plot of MDSC-PLL shows a gain margin (At gain cross-over frequency) of -20dB (4.65rad/sec) and a Phase margin (at phase cross-over frequency) of 53.89 degrees (5.13rad/sec). Dynamic and steady-state analysis for simulation is being performed under different load conditions for multiple delayed signal cancellation (MDSC-PLL) control algorithms. Steady-state performance analysis for MDSC-PLL depicts the total harmonic distortion (THD%) for source voltage generated by the SEIG of phase (V_{sa}) of 4.52%, total harmonic distortion of (THD%) of source current generated by the SEIG of phase 'a' (I_{sa}) is 2.82%, total harmonic

distortion of (THD%) of load current of phase 'a' (I_{La}) and of 27.71% and the total harmonic distortion of (THD%) of compensator current generated by the DSTATCOM of phase 'a' (I_{ca}) is 38.94%. From the above results, it can be inferred that the total harmonic distortion% of source voltage and source current is well within the permissible limits of 5% stipulated by IEEE-519 standards. The hardware prototype model for MDSC-PLL has been developed in the laboratory for the verification of simulated results that were obtained through MATLAB/SIMULINK. For the real-time implementation of the required sampling time for the MDSC-PLL is 60μs. The experimental results show the steady state performance of MDSC-PLL with three phase source voltage (V_{sa},V_{sb},V_{sc}) having the magnitude of (119.66,120.35,118.17) V respectively having the THD% of 2.07% and three-phase source current (I_{sa},I_{sb},I_{sc}) with the magnitude of (5.32,5.39,5.89) Amps having the THD% of 4.22% which are under the permissible limits of 5% according to IEEE-519 standards and three phase source voltage (V_{sa},V_{sb},V_{sc}) having the magnitude of (113.32,114.12,113.74) V respectively having the THD% of 2.26% and three phase load current (I_{La},I_{Lb},I_{Lc}) with the magnitude of (5.02,5.02,5.04) Amps having the THD% of 17.20% at a frequency of 50 Hz. The experimental results also dynamic performance of MDSC under different load conditions. Thus superior performance under different load conditions shows the ability to adapt and robust nature of the MDSC control algorithm.

REFERENCES

1. Xia Y, Lei J, Zhou H, Guan Q (2023) Optimal design of phase-locked loop with frequency-adaptive prefilter based on the accurate small-signal model. IET Renew Power Gener 17:2160–2173. https://doi.org/10.1049/rpg2.12719

2. Singh B, Murthy SS, Chilipi RSR (2014) STATCOM-based controller for a three-phase SEIG feeding single-phase loads. IEEE Trans Energy Convers 29:320–331. https://doi.org/10.1109/TEC.2014.2299574

3. Levy D (1997) Stand alone induction generators. Electr. Power Syst. Res. 41:191–211

4. Khan MF, Khan MR (2022) Step by step approach for developing analytical and experimental research facilities of a three-phase self-excited induction generator. J Energy Syst 6:221–240. https://doi.org/10.30521/jes.1003175

5. Ahmed T, Noro O, Hiraki E, Nakaoka M (2004) Terminal voltage regulation characteristics by static var compensator for a three-phase self-excited induction generator. IEEE Trans Ind Appl 40:978–988. https://doi.org/10.1109/TIA.2004.830783

6. Chauhan YK, Jain SK, Singh B (2010) A prospective on voltage regulation of self-excited induction generators for industry applications. IEEE Trans Ind Appl 46:720–730. https://doi.org/10.1109/TIA.2009.2039984

7. Singh B, Murthy SS, Gupta S (2005) Transient analysis of self-excited induction generator with electronic load controller (ELC) supplying static and dynamic loads. IEEE Trans Ind Appl 41:1194–1204. https://doi.org/10.1109/TIA.2005.855047

8. Singh B, Kasal GK (2008) Solid state voltage and frequency controller for a stand alone wind power generating system. IEEE Trans Power Electron 23:1170–1177. https://doi.org/10.1109/TPEL.2008.921190

9. Singh B, Murthy SS, Reddy RS, Arora P (2015) Implementation of modified current synchronous detection method for voltage control of self-excited induction generator. IET Power Electron 8:1146–1155. https://doi.org/10.1049/iet-pel.2014.0718

10. Chauhan YK, Yadav VK, Singh B (2013) Optimum utilisation of self-excited induction generator. IET Electr Power Appl 7:680–692. https://doi.org/10.1049/iet-epa.2013.0038

11. Elamari K, Lopes LAC (2019) Implementation and Experimental Verification of a Novel Control Strategy for a UPFC-Based Interphase Power Controller. IEEE Trans Power Deliv 34:2079–2088. https://doi.org/10.1109/TPWRD.2019.2913110

12. Chittora P, Singh A, Singh M (2018) Simple and efficient control of DSTATCOM in three-phase four-wire polluted grid system using MCCF-SOGI based controller. IET Gener Transm Distrib 12:1213–1222. https://doi.org/10.1049/iet-gtd.2017.0901

13. Singh B, Verma V (2008) Selective compensation of power-quality problems through active power filter by current decomposition. IEEE Trans Power Deliv 23:792–799. https://doi.org/10.1109/TPWRD.2007.911108

14. Chittora P, Singh A, Singh M (2018) Chebyshev Functional Expansion Based Artificial Neural Network Controller for Shunt Compensation. IEEE Trans Ind Informatics 14:3792–3800. https://doi.org/10.1109/TII.2018.2793347

15. Singh B, Solanki J (2009) A comparison of control algorithms for DSTATCOM. IEEE Trans Ind Electron 56:2738–2745. https://doi.org/10.1109/TIE.2009.2021596

16. Singh B, Arya SR (2014) Back-propagation control algorithm for power quality improvement using DSTATCOM. IEEE Trans Ind Electron 61:1204–1212. https://doi.org/10.1109/TIE.2013.2258303

17. Badoni M, Singh A, Singh B (2018) Power quality improvement using DSTATCOM with affine projection algorithm. IET Gener Transm Distrib 12:3261–3269. https://doi.org/10.1049/iet-gtd.2017.0841

18. Qureshi A, Giri AK, Arya SR, Padmanaban S (2022) Power conditioning using DSTATCOM in a single-phase SEIG-based isolated system. Electr Eng 104:111–127. https://doi.org/10.1007/s00202-021-01423-1

19. Mittal S, Singh A, Chittora P (2024) Design and development of leaky least mean fourth control algorithm for single-phase grid-connected multilevel inverter. Int J Circuit Theory Appl 52:328–345. https://doi.org/10.1002/cta.3746

20. Kewat S, Singh B (2019) Modified amplitude adaptive control algorithm for power quality improvement in multiple distributed generation system. IET Power Electron 12:2321–2329. https://doi.org/10.1049/iet-pel.2018.5936

21. Mangaraj M, Panda AK (2019) Modelling and simulation of KHLMS algorithm-based DSTATCOM. IET Power Electron 12:2304–2311. https://doi.org/10.1049/iet-pel.2018.5625

22. Ranjan A, Kewat S, Singh B (2021) DSOGI-PLL with In-Loop Filter Based Solar Grid Interfaced System for Alleviating Power Quality Problems. IEEE Trans Ind Appl 57:730–740. https://doi.org/10.1109/TIA.2020.3029125

23. Giri AK, Qureshi A, Arya SR, et al (2018) Features of Power Quality in Single-Phase Distributed Power Generation Using Adaptive Nature Vectorial Filter. IEEE Trans Power Electron 33:9482–9495. https://doi.org/10.1109/TPEL.2017.2789209

24. Giri AK, Arya SR, Maurya R, Babu BC (2019) Mitigation of power quality problems in PMSG-based power generation system using quasi-Newton–based algorithm. Int Trans Electr Energy Syst 29:. https://doi.org/10.1002/2050-7038.12102

25. Golestan S, Ebrahimzadeh E, Guerrero JM, et al (2017) An Adaptive Least-Error Squares Filter-Based Phase-Locked Loop for Synchronization and Signal Decomposition Purposes. IEEE Trans Ind Electron 64:336–346. https://doi.org/10.1109/TIE.2016.2599499

26. Özer AS, Sevilmiş F, Karaca H, Arabacı H (2022) Enhanced control method for voltage regulation of DSTATCOM based SEIG. Energy Reports 8:839–847. https://doi.org/10.1016/j.egyr.2022.05.191

27. Golestan S, Ramezani M, Guerrero JM, et al (2014) Moving average filter based phase-locked loops: Performance analysis and design guidelines. IEEE Trans Power Electron 29:2750–2763. https://doi.org/10.1109/TPEL.2013.2273461

28. Giri AK, Arya SR, Maurya R, Mehar R (2018) Variable learning adaptive gradient based control algorithm for voltage source converter in distributed generation. IET Renew Power Gener 12:1883–1892. https://doi.org/10.1049/iet-rpg.2018.5213

29. Messai A, Mellit A, Guessoum A, Kalogirou SA (2011) Maximum power point tracking using a GA optimized fuzzy logic controller and its FPGA implementation. Sol Energy 85:265–277. https://doi.org/10.1016/j.solener.2010.12.004

30. Giri AK, Arya SR, Maurya R, Babu BC (2019) VCO-less PLL control-based voltage-source converter for power quality improvement in distributed generation system. IET Electr Power Appl 13:1114–1124. https://doi.org/10.1049/iet-epa.2018.5827

31. Malathi S, Jayachandran J (2020) FPGA implementation of NN based LMS–LMF control algorithm in DSTATCOM for power quality improvement. Control Eng Pract 98:104378. https://doi.org/10.1016/j.conengprac.2020.104378

32. Golestan S, Guerrero JM, Vasquez JC, et al (2018) Research on variable-length transfer delay and delayed-signal-cancellation-based plls. IEEE Trans Power Electron 33:8388–8398. https://doi.org/10.1109/TPEL.2017.2785281

33. Svensson J, Bongiorno M, Sannino A (2007) Practical implementation of delayed signal cancellation method for phase-sequence separation. IEEE Trans Power Deliv 22:18–26. https://doi.org/10.1109/TPWRD.2006.881469

34. Golestan S, Freijedo FD, Vidal A, et al (2016) An Efficient Implementation of Generalized Delayed Signal Cancellation PLL. IEEE Trans Power Electron 31:1085–1094. https://doi.org/10.1109/TPEL.2015.2420656

35. Wang S, Etemadi A, Doroslovački M (2020) Adaptive cascaded Delayed Signal Cancellation PLL for three-phase grid under unbalanced and distorted condition. Electr Power Syst Res 180:. https://doi.org/10.1016/j.epsr.2019.106165

36. Gude S, Chu CC (2018) Three-Phase PLLs by Using Frequency Adaptive Multiple Delayed Signal Cancellation Prefilters under Adverse Grid Conditions. IEEE Trans Ind Appl 54:3832–3844. https://doi.org/10.1109/TIA.2018.2823263

37. Narayanan V, Kewat S, Singh B (2021) Real-Time Implementation of CLMS Algorithm in 3P4W Solar PV-BES-Based Microgrid System. IEEE Trans Ind Appl 57:795–804. https://doi.org/10.1109/TIA.2020.3031873

38. Mittal S, Singh A, Chittora P (2023) Solar PV Array based Grid-Connected Bi-Directional EV Charger Controlled using NARLMMN Algorithm. In: India International Conference on Power Electronics, IICPE. IEEE Computer Society

39. Golestan S, Guerrero JM, Vasquez JC (2017) Hybrid adaptive/nonadaptive delayed signal cancellation-based phase-locked loop. IEEE Trans Ind Electron 64:470–479. https://doi.org/10.1109/TIE.2016.2596713

APPENDIX

(A) Simulation:-

(A1) Parameters for induction generator SEIG voltage = 415 V, 50Hz, 1500 RPM, 3.7kW, 5hp, excitation capacitive power = 4200KVR, stator resistance and stator inductance(R_s , L_{ls}) = 1.404Ω and 7.8mH, rotor resistance and inductance(R_r, L_{lr}) = 1.39Ω and 7.8mH.

(A2) Parameters for DSTATCOM *22*4V, 50 Hz, Load current (I_L) = 7.18 Amp, source current (I_s) = 8.624 Amp, C_{dc} =1600μf , DC link voltage(V_{DC}) = 200V, interfacing inductance =4.7 mili Henry , sampling time (T_s) = $5*10^{-6}$μs , K_p = 0.05 ,K_i = 0.01, non-linear load resistance (R_L) = 18Ω, Load inductance (L_L) = $160*10^{-3}$ henry, switching frequency = 5 kHz.

(B) Hardware:-

(B1) Parameters for induction generator SEIG voltage = 415V, 50Hz, 1500 RPM, 3.7kW, 5hp, excitation capacitance = 13μf, stator resistance and stator inductance(R_s , L_{ls}) = 1.3908Ω and 7.6mH, rotor resistance and inductance(R_r, L_{lr}) = 1.38Ω and 7.7mH.

(B2) Parameters for DSTATCOM *110*V, 50 Hz, Load current (I_L) = 5.13 Amp, source current (I_s) = 5.63 Amp, DC link voltage(V_{DC}) = 200V, interfacing inductance =5 mili Henry , sampling time (T_s) = $5*10^{-6}$μs , K_p = 0.05 ,K_i = 0.01, non-linear load resistance (R_L) = 16Ω, Load inductance (L_L) = $150*10^{-3}$ henry, switching frequency = 5 kHz.

Solar Energy 285 (2025) 113114

Contents lists available at ScienceDirect

Solar Energy

journal homepage: www.elsevier.com/locate/solener

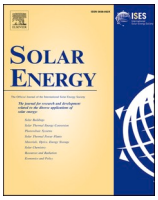

Performance evaluation of indirect solar drying system for potato slices: Comparative analysis with open-sun drying method

Ankit Srivastava [a,b,*], Atul Sharma [a,1], Anil Kumar [c,d]

[a] Non-Conventional Energy Laboratory, Rajiv Gandhi Institute of Petroleum Technology, Jais, Amethi, India
[b] Department of Mechanical Engineering, Feroze Gandhi Institute of Engineering and Technology, Raebareli, India
[c] Department of Mechanical Engineering, Delhi Technological University, Delhi 110042, India
[d] Center for Energy and Environment, Delhi Technological University, Delhi 110042, India

ARTICLE INFO

Keywords:
ISD
OSD
Potato slice drying
Moisture content
Drying rate
Shrinkage factor

ABSTRACT

In this study, a partially portable indirect solar dryer (ISD) was constructed and potato slice drying characteristics were analyzed compared to the open-sun drying (OSD) method. Potato slice samples were prepared and the experiment was carried out for two days. Weight reduction environment temperature, collector plate temperature, drying chamber temperature, and drying chamber inlet temperature were recorded from 10 AM to 6 PM. every 30 min to analyze various drying characteristics. Initially moisture content (MC) of the potato slices was 83 ± 2 % (wb); after drying the final MC was 11.7 ± 2 % (wb) for OSD and 7.7 ± 2.0 % (wb) for ISD system, both in 16 h. The highest drying rate (DR) of potato slices was 18.8 (g water/g solid h) after 8 h of open sun drying, and 16.97 (g water/g solid h after) 8 h. Rehydration ratios for OSD and ISD were found 4.32 and 4.20, respectively. Shrinkage factor for OSD was 61 %, whereas ISD had a shrinkage ratio of 70 %. The highest color change values were 6.32 and 8.13 in the ISD and OSD, respectively. Water activity was reduced from 0.95 to 0.42 in ISD and from 0.95 to 0.59 in OSD.

1. Introduction

Fruits and vegetables can be preserved using one of two major techniques. The first is frostbite, and the second is dehydration. Drying is a basic technique of removing moisture from a food product to get the required content of moisture [1]. Moisture removal inhibits the development and microorganisms such as bacteria and yeast. Those nations where solar energy is abundant should employ dehydration methods for preserving fruits and harvests by using solar energy because freezing methods are more expensive, and drying in open sun exposure is free, but in open sun drying (OSD) products have certain drawbacks such as minerals loss, color fade off [2]. Solar dryers can maintain the quality of dry goods; it is the healthier storage option and the greatest method for achieving this aim. The vitamins are therefore maintained, and the dried goods can subsequently be restored by straightforward rehydration [3]. People in rural regions rely mostly on direct sunlight to dry their agricultural goods. This method is relatively easy to use and doesn't require a lot of money, nonetheless, drying takes a while and there's a risk of contaminants like dirt and pollution as well as the worry of abrupt weather changes [4]. Sun drying can be replaced by hot air drying. However, this artificial mechanical drying requires a lot of expensive energy, which raises the price of the dried product [5]. OSD has several limitations like as drying, over-drying, and quality issues in dried products. By using a solar dryer, the process of drying may be boosted, and the dried items' quality can be improved [6]. Convective drying is a technique where drying happens as a result of warm air being blown over the top, lower, or both sides or across the product, which is the most widespread. Other drying techniques include electrical drying and open or direct drying [7].

A solar dryer is a solar energy application that is widely utilized in the food and agriculture industries. Despite this, many parts of the world still use the sun directly to dry food and textiles. The same may be done with a solar dryer, which is an indirect use of solar energy [8]. All dryer methods, whether conventional or solar, use the same fundamental principles of drying. Conventionally used dryers come in a variety of forms, including both low-temperature, mass storage systems, and high-temperature, quick-drying methods. These dryers use fuel or electricity to operate fans and heaters. High-temperature dryers require time and temperature management due to the easiness with which temperatures

* Corresponding author at: Non-Conventional Energy Laboratory, Rajiv Gandhi Institute of Petroleum Technology, Jais, Amethi, India.
E-mail addresses: pre19001@rgipt.ac.in (A. Srivastava), asharma@rgipt.ac.in (A. Sharma), anilkumar76@dtu.ac.in (A. Kumar).
[1] 0000-0002-3754-8550.

https://doi.org/10.1016/j.solener.2024.113114
Received 11 August 2024; Received in revised form 6 November 2024; Accepted 12 November 2024
Available online 23 November 2024
0038-092X/© 2024 International Solar Energy Society. Published by Elsevier Ltd. All rights are reserved, including those for text and data mining, AI training, and similar technologies.

Nomenclature

ISD	indirect solar drying
OSD	open-sun drying
MC	moisture content
wb	wet bulb
DR	drying rate
M_i	initial weight
M_f	final weight
M_t	weight at starting time
$M_{t+\Delta t}$	weight at after certain time
Δt	time period
$S_{initial}$	initial Size
S_{final}	final Size
Δ E	total color difference
L_o	lightness of color
a_o	color on the green ($-a_o$) to red ($+a_o$) axis
b_o	color on the blue ($-b_o$) to yellow ($+b_o$) axis
h	hue angle
A_w	water activity
MRR	moisture removal rate

can rise over dry objects kept close to moist food unless the ideal moisture level is reached. Low-temperature storage techniques are commonly utilized with grains and when the food must preserve its color and retain specific nutrients [9]. OSD includes leaving the crop unprotected from the weather and exposing it to the sun and the outside air. After harvest, open drying can be done on the ground, mats, or cement floor. In Tropical regions, this is a highly popular technique of drying. The least expensive drying technique is open-air solar radiation, with essentially no upfront expenditures and extremely low ongoing costs (every day, labor is used to move the sheets in and out) [10]. Direct (integral) sunlight, the first type of solar radiation, occurs when solar rays penetrate across a translucent surface and are immediately subsumed at the food product surface. Depending on the food product type and the quantity of sun, straight drying can occasionally result in product damage and discoloration. Direct drying might be slower than indirect drying when comparing drying rates due to inadequate ventilation. The main benefit of sun drying is that it doesn't require the usage of fuels, which are sometimes highly expensive in impoverished nations [11].

The basic components of the solar dryer are the same for both active and passive dryers. Blowers or fans are used in active-type solar dryers to create convection throughout the foodstuff. These blowers (or fans) must be driven by electricity. Active-type solar dryers are far more frequent in established locations with easy availability of energy [12]. Passive dryers employ natural convection to dry airflow by utilizing the pressure of wind and buoyant forces from the solar-heated air. Chimneys are frequently used in dryers to promote natural convection [13]. Indirect (distributed) type solar dryers circulate warm air through the food product after thermal power is captured in a solar collector. Indirect solar dryers (ISD) have various benefits compared to direct-type solar dryers, an increase in crop production per square foot, keeping the nutritional value intact and appearance of delicate crops, and a variety of crop varieties that can be dried [14].

ISD employed induced airflow with a fan powered by a solar module. The primary benefits of such a dryer are the preservation of dried product quality, the ability to manage it scientifically, and the ability to enhance the drying speed [15]. Undoubtedly, the indirect solar dryer's solar collector is an essential part. There are two types of collectors: non-concentrating or stationary collectors and concentrating collectors [16].

Many researchers [17–20] have studied potato slice drying using solar dryers, these ISD are often large, bulky, and expensive to produce, which frequently encounter quality issues with the dried product. Therefore, to make the current model suitable for household use, its size has been reduced to improve portability and affordability. It is also crucial to carefully monitor drying parameters and maintain the quality of potato slices post-drying.

This study aims to experimentally optimize drying conditions to enhance product quality and increase the market value of dried products, particularly focusing on high-quality potato slices. The solar dryer's purpose is to elevate air temperature above ambient levels under specific humidity conditions, enhancing moisture transfer efficiency by reducing relative humidity. Controlled drying in ISD typically yields higher-quality potato slices compared to OSD. Experimental analysis was conducted over two days to assess drying and quality parameters between ISD and OSD. The initial moisture content (MC) of the potato slices was 83 ± 2 % (wb). After a drying period of 16 h, the final MC was 11.7 ± 2 % (wb) for the OSD system and 7.7 ± 2.0 % (wb) for the ISD system. The shrinkage factor for OSD was 61 %, while ISD exhibited a shrinkage factor of 70 %. The maximum color change values recorded were 6.32 for the ISD and 8.13 for the OSD. Water activity decreased from 0.95 to 0.42 in ISD and from 0.95 to 0.59 in OSD.

2. Materials and methods

Fabrication, installation, and technique for the experiment are discussed in this section.

2.1. Fabrication of the experimental setup

Researchers developed indirect solar dryers (ISDs) for drying various crops, fruits, and vegetables. These ISDs are generally huge, heavy, and expensive to manufacture, leading to quality difficulties with the dry product [21–24]. To make the present model appropriate for domestic usage, its size was reduced to increase portability and lower the price of solar dryer manufacturing. After gathering necessary materials such as plywood, netting, copper plate, glass sheet, etc., a partially portable ISD was fabricated. The schematic diagram of the fabricated solar dryer is depicted in Fig. 1, and the dimensions of its components are listed in Table 1. Various components for the indirect solar dryer were constructed using locally available materials.

The fabricated indirect solar dryer consists of the following key components:

Air Chamber

- Structure: Cuboidal form with a glass plate on top and a copper plate beneath (refer to Fig. 2).
- Transparent Glass Plate: Positioned at the top of the air chamber to enhance the greenhouse effect of solar radiation. Glass has a specific heat value of 800 J/kg-K, a linear thermal expansion value of 40 x 10^{-7}/K, and a thermal conductivity value of 1 Watt/m-K.
- Copper Plate: Rectangular flat plate (405 × 250 × 0.5 mm^3) positioned beneath the glass plate, allowing space for airflow duct. The copper plate efficiently absorbs solar energy to heat the air within the duct space. Copper sheet has a melting point of 1357 K and a thermal conductivity of 385 W/m-K.

Drying Chamber

- Components: Comprises a drying box and a chimney on the roof.
- Perforated Trays: Three stacked trays within the drying box (refer to Fig. 3) for holding samples during drying.
- Chimney: Trapezoidal-shaped structure on the drying box roof, housing a 12 V exhaust fan powered by a solar cell and battery.

Heat Collector

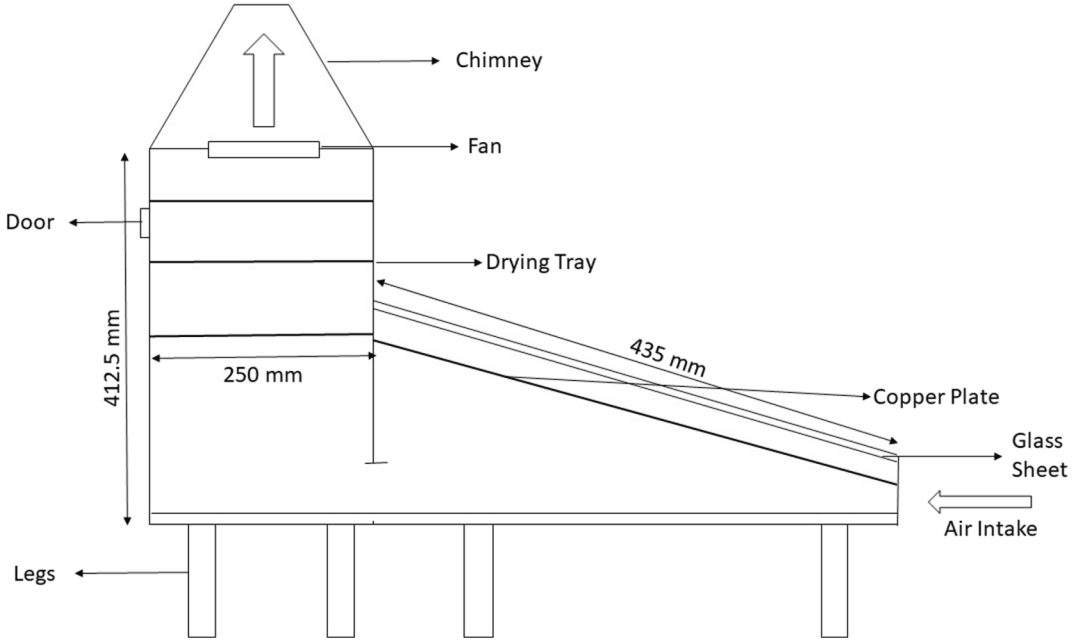

Fig. 1. Schematic diagram of fabricated solar dryer.

Table 1
Components with their dimensions and configurations.

S.No.	Components Name	Specifications
1	Transparent Glass Sheet	[435 × 250 × 3]mm^3
2	Copper Plate	[405 × 250 × 0.5]mm^3
3	Plywood Drying Chamber	[250 × 250 × 412.5]mm^3
4	Perforated Trays	[250 × 250] mm^2
5	DC Exhaust Fan [12 V]	6800 ~ 13000 rpm
6	Photovoltaic Cell & Battery	12 V and 10 W

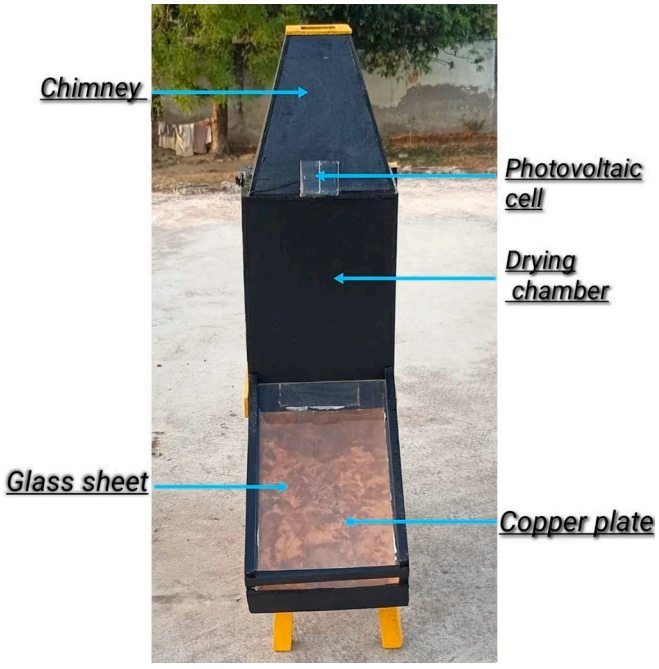

Fig. 2. Air Chamber.

- Structure: Includes a glass sheet and copper plate (depicted in Fig. 4) to absorb solar heat.
- Operation: Solar rays strike the glass sheet, heating the copper plate. Air drawn through the intake duct is heated by the copper plate. Potato slices exposed to this heated air undergo convection heat transfer, causing moisture evaporation. The evaporated moisture exits through the chimney via the exhaust fan.

Refer to Figs. 2, 3, and 4 for visual representations of the fabricated ISD components and their operation.

2.2. Instrumentation for data recording

To monitor temperatures within the drying chamber, including the entrance temperature and the temperature of the potato slices, three T-type thermocouple wires were employed. T-type thermocouples are ideal for measuring low temperatures, composed of constantan wire for the negative leg and a copper and nickel alloy wire for the positive leg, operating based on the Seebeck effect principle. These thermocouples exhibit exceptional repeatability within a temperature range of −200 °C to 200 °C (±0.1 °C). Voltages produced by the thermocouple wires at various locations were measured using a multimeter and converted into corresponding temperatures.

For measuring sample weights during the experiment, a digital weighing machine from the TS brand was used, offering a range of 0–5 kg with an accuracy of 200 mg (0.2 g). The ambient temperature was measured using a mercury thermometer.

Data collection occurred from 10 AM to 6 PM. at 30-minute intervals. Fig. 5 illustrates the different measuring instruments used to record the readings.

2.3. Experimentation

Start by selecting fresh, ripe potatoes free of physical defects, preferably with higher solids content for optimal drying results. Slice the potatoes into consistently thin slices, approximately 3 mm thick, using a branded slicer to ensure uniformity and achieve a desirable crunchy texture.

Five sets of experiments were conducted using a fabricated indirect solar dryer and an open-sun drying setup at the Feroze Gandhi Institute

Fig. 3. Inside of fabricated drying chamber.

of Engineering and Technology in Ratapur, Raebareli, Uttar Pradesh, India (Latitude: 26.2447° N, Longitude: 81.2395° E) from April 25 to May 5, 2023. Both methods were carried out continuously from 10:00 AM to 06:00 PM for each experimental set. The best data from two selected days were considered for performance analysis of the designed dryer.

On the first day, 200.0 g of potato slices were placed in the drying chamber of the ISD, with an equal amount used for OSD. Temperature readings from thermocouple wires attached to the copper plate, drying plate, and inlet of the drying chamber were recorded at 30-minute intervals throughout the experiment.

By the end of the first day, the weight of potato slices reduced to 64.2 g for closed drying (Drying in ISD) and 49.6 g for open drying (Drying in OSD), indicating a reduction in moisture content and extent of drying within the day.

Refer to Table 3 and Table 4 for detailed data readings of potato slice samples on Day 1.

Between the evening of the first day and the morning of the second day, the weight of the potato slices continued to decrease. On the second day, the initial weight of the potato slices was 41.8 g for closed drying (Drying in ISD) and 42.6 g for open drying (Drying in OSD). The experiment was conducted again from 10:00 AM to 06:00 PM, with measurements taken at 30-minute intervals.

Temperature readings from the thermocouple wires attached to the copper plate, drying plate, and inlet of the drying chamber were recorded every half hour during this period. Detailed data readings of the potato slice samples for Day 2 can be found in Table 5 and Table 6, respectively.

The weight of the potato slices was found to decrease to 37.6 g for OSD and 38.6 g for ISD. This analysis highlights the reduction in moisture levels of the potato slices and the extent of drying achieved within a day.

2.4. Uncertainty

The instruments used for measuring properties of heated air, the weight of dried potato slices, and other parameters along with their range, and accuracy standard uncertainty in measurement are given in Table 2.

2.5. Performance analysis

Thermal performance analysis is carried out to compare the performance of open sun drying and constructed indirect solar dryers with the same weight potato slice samples in identical environmental circumstances. Moisture content (MC) and drying rate (DR) are evaluated.

2.5.1. Moisture content

It is characterized as the presence of water volume in the sample (potato slices) at a given moment, and it may be assessed using Eq. (1). It

(a) Front View **(b)** Rear View (Close) **(c)** Rear View (Open)

(d) Side View (Right) **(e)** Side View (Left)

Fig. 4. Different views of fabricated solar dryer [original].

is calculated based on the percentage of MC escape and conveyed on a wet basis [25].

$$MC = \left(\frac{M_i - M_f}{M_i}\right) \times 100 \quad (1)$$

2.5.2. Drying rate

The drying rate specified as the ratio of the variations in the beginning and final moisture content to the time interval, was calculated using the following equations [26].

$$DR = \frac{M_t - M_{t+\Delta t}}{\Delta t} \quad (2)$$

2.6. Quality examination of dried potato slice

Examining the quality of dried potato slices involves assessing several key attributes to ensure that they meet the desired standards, texture, appearance, and hygiene. The rehydration ratio, shrinkage color index, and water activities of dried potato slices are calculated for both open-sun drying dried samples and indirect solar dryer dried samples.

2.6.1. Rehydration ratio

The rehydration ratio, also known as the rehydration factor or reconstitution ratio, is a metric that quantifies a dehydrated or dried food product's ability to rehydrate with a certain amount of water or liquid and regain its original moisture content and volume. It is described as the proportion between the dried sample weight and the drained sample weight of the rehydrated sample. It can be calculated using the following relation [27].

$$Rehydrationratio = \frac{W_{drained}}{W_{final}} = \frac{drainedweight}{weightofthedriedsample} \quad (3)$$

2.6.2. Shrinkage

Shrinkage, in the context of dried food products, refers to the reduction in size, weight, and volume that occurs when a food item is dried or dehydrated. Throughout the drying process, moisture is removed from the food, causing it to shrink and become smaller and lighter compared to its original fresh state. Shrinkage is a natural outcome of the drying process, as moisture constitutes a significant portion of many foods, and its removal leads to the condensation of solids, resulting in a reduction in size and weight. To calculate the shrinkage of a dried food product the following relation is used [28].

$$Shrinkage = \left(\frac{S_{initial} - S_{final}}{S_{final}}\right) \times 100 \quad (4)$$

(a) Weighing Machine

(b) Multimeter

(c) Digital Thermometer

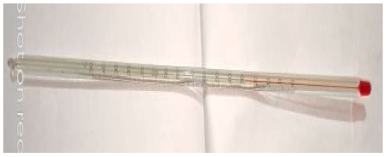

(d) Thermometer (Mercury)

(e) T-type Thermocouple

Fig. 5. Measuring instruments used to record data.

Table 2
Uncertainty of used instruments for data recording.

Instrument	Accuracy	Range	Standard uncertainty
T-type thermocouple	±0.1 °C	−200 °C to 200 °C	0.013 °C
Digital weight machine	200 mg (0.2 g)	0—5 kg	0.025 kg
Mercury Thermometer	± 1°-2° C	−10C to 110C	0.5 °C
Digital Thermometer	± 0.1° C	0°–50 °C	0.5 °C

2.6.3. Color index

The color index is a measure used to quantify the color of a dried product, especially in the food industry, spectrophotometers are used to evaluate the color index in the present experiment. It is a numerical representation of the color characteristics of the product, and it provides valuable information about its appearance and visual quality. The product's color standards were described using the chromaticity coordinates Lo, a_o, and b_o from the Commission International Eclairage. Using Eq. (5), the total color difference (Δ E) was calculated [29].

$$\Delta E = \sqrt{(\Delta Lo)^2 + (\Delta a_o)^2 + (\Delta b_o)^2} \tag{5}$$

Where,

$$\Delta L_o = (L_o - L)$$

$$\Delta a_o = (a_o - a)$$

$$\Delta b_o = (b_o - b)$$

During the process of drying, L_o represents the lightness of the color, where$L_o = 0$ is black, and$L_o = 100$ is white. As L_o value increase, and the color becomes lighter. The a_o value describes the color on the green ($-a_o$) to red ($+a_o$) axis. Redness is indicated by positive values and greenness by negative values. The b_o value represents the color on the blue ($-b_o$) to yellow ($+b_o$) axis. Positive numbers represent yellowness, whereas negative values represent blueness. Table 7 provides a summary of all coordinates' significance.

These elements are crucial in choosing the color scheme for the hue angle (h) calculated from Eq. (6) [30].

$$h = \begin{cases} tan^{-1}(b_o/a_o), a_o \geq 0 \\ 180\text{deg} + tan^{-1}(b_o/a_o), a_o < 0 \end{cases} \tag{6}$$

Table 3
Data collected during 1st day.

Date		01-May-23					
Initial Weight of Potato Slices in grams		Open Sample	200.0 g				
		Close Sample	200.0 g				
Time	Ambient Temperature in °C	Collector Plate thermocouple reading		Drying Inlet thermocouple reading		Drying tray thermocouple reading	
		mVolt	°C	mVolt	°C	mVolt	°C
10:00 AM	34.6	0.7	52.3	0.0	33.0	0.0	32.3
10:30 AM	34.9	0.9	57.8	0.0	33.0	0.0	32.3
11:00 AM	35.2	1.0	59.0	0.1	36.0	0.0	32.3
11:30 AM	34.8	1.2	63.0	0.1	36.0	0.0	32.3
12:00 PM	37.2	1.4	68.0	0.1	36.0	0.1	34.9
12:30 PM	37.0	1.4	68.0	0.2	39.5	0.1	34.9
1:00 PM	38.0	1.4	68.0	0.2	39.5	0.1	34.9
1:30 PM	40.4	1.5	70.2	0.3	42.0	0.1	34.9
2:00 PM	40.9	1.3	65.0	0.3	42.0	0.1	34.9
2:30 PM	41.5	1.2	63.0	0.2	39.5	0.1	34.9
3:00 PM	41.2	1.3	65.0	0.3	42.0	0.1	34.9
3:30 PM	40.7	1.2	63.0	0.2	39.5	0.1	34.9
4:00 PM	37.2	0.5	46.2	0.1	36.0	0.0	32.3
4:30 PM	35.7	0.4	43.8	0.1	36.0	0.0	32.3
5:00 PM	35.6	0.3	40.6	0.1	36.0	0.0	32.3
5:30 PM	35.5	0.1	36.1	0.0	33.0	0.0	32.3
6:00 PM	35.1	0.0	33.8	0.0	33.0	0.0	32.3
Weight of Potato Slices at day end in grams		**Open Sample**	49.6 g				
		Close Sample	64.2 g				
Weather condition of the day		**Sunny**					

Table 5
Data collected during 2nd day.

Date		02-May-23					
Initial Weight of Potato Slices in grams		Open Sample	42.6 g				
		Close Sample	41.8 g				
Time	Ambient Temperature in °C	Collector Plate thermocouple reading		Drying Inlet thermocouple reading		Drying tray thermocouple reading	
		mVolt	°C	mVolt	°C	mVolt	°C
10:00 AM	35.8	0.5	46.2	0.0	33.0	0.0	32.3
10:30 AM	35.6	0.7	52.3	0.0	33.0	0.0	32.3
11:00 AM	36.5	1.2	63.0	0.2	39.5	0.1	34.9
11:30 AM	37.2	1.3	65.0	0.2	39.5	0.1	34.9
12:00 PM	37..5	1.3	65.0	0.3	42.0	0.1	34.9
12:30 PM	37.3	0.9	57.8	0.3	42.0	0.2	38.1
1:00 PM	37.4	0.9	57.8	0.2	39.5	0.1	34.9
1:30 PM	37.6	0.8	54.7	0.1	36.0	0.1	34.9
2:00 PM	38.2	1.3	65.0	0.3	42.0	0.1	34.9
2:30 PM	38.9	1.3	65.0	0.3	42.0	0.1	34.9
3:00 PM	39.6	1.0	59.0	0.3	42.0	0.1	34.9
3:30 PM	40.2	0.9	57.8	0.3	42.0	0.1	34.9
4:00 PM	41.4	0.7	52.3	0.3	42.0	0.1	34.9
4:30 PM	40.5	0.4	43.8	0.2	39.5	0.1	34.9
5:00 PM	38.0	0.3	40.6	0.1	36.0	0.1	34.9
5:30 PM	35.2	0.1	36.1	0.0	33.0	0.0	32.3
6:00 PM	34.3	0.0	33.8	0.0	33.0	0.0	32.3
Weight of Potato Slices at day end in grams		**Open Sample**	37.6 g				
		Close Sample	38.6 g				
Weather condition of the day		**Sunny**					

Table 4
Weight of Potato Slices at the start and end of 1st day.

S.No.	Weight (g)	Open	Close
1.	Wight (Morning)	200	200
2.	Weight (Evening)	49.6	64.2
3.	Loss in Weight	150.4	135.8

Table 6
Weight of Potato Slices at the start and end of 2nd day.

S.No.	Weight (g)	Open sun drying	Indirect solar drying
1.	Weight (Morning)	42.6	41.8
2.	Weight (Evening)	37.6	38.6
3.	Loss in Weight	5.0	3.2

2.6.4. Water activity

Water activity is a measurement of the free water content available in a food product, which influences its microbial stability and shelf life. Water activity is represented on a scale from 0 to 1, where 0 corresponds to a completely dry state with no available water, and 1 represents pure water. Foods with higher water activity levels (closer to 1) have more available water and are more prone to spoilage and microbial growth, while foods with lower water activity levels (closer to 0) are more stable and less susceptible to spoilage. Water activity can be calculated by following Eq. (7) [21].

Table 7
Co-ordinates L_o, a_o and b_o [29].

Coordinates	Color change/difference	
L_o	$L_o = 0$ for black Darkness	$L_o = 100$ for white Lightness
a_o	$-a_o$ for greenness	$+ a_o$ for redness
b_o	$-b_o$ for blue	$+b_o$ for blue

$$A_w = 1 - exp\left[-0.0193(T + 44.36)M_e^{0.3316}\right] \quad (7)$$

Where A_w is dried product water activity, M_e is equilibrium water content and T is equilibrium temperature.

3. Results and discussion

3.1. Evaporation of moisture in potato slice sample

The data are taken at the location of Ratapur, Raebareli, India (Latitude and Longitude are 26.2447036 deg.N and 81.239485 deg.E respectively) from 1 May 2023 to 2 May 2023. This process is continuously repeated for open and closed samples for two days. 200 g of potato slice samples were used on the first day for both ISD and OSD. By the end of the second day, as illustrated in Fig. 6, there were only 38.6 g of the closed sample and 37.6 g of the open sample remaining.

3.2. Ambient temperature

It was observed that the lowest and highest ambient temperatures were 34.3 °C and 41.5 °C respectively during the two days of the experiment. This is the ambient temperature v/s time interval graph as shown in Fig. 7, which shows the ambient temperature at every half an hour of the time interval between 10 AMto 6 PM for two days from 1 May to 2 May.

3.3. Collector plate temperature

This is the collector plate temperature v/s time interval graph which shows the collector plate temperature every half an hour of the time interval between 10 AM to 6 PM for two days from 1 May to 2 May. The pattern depicted in Fig. 8 revealed that the collection plate's minimum and maximum temperatures are, 33.8 °C and 70.2 °C respectively.

3.4. Drying chamber inlet temperature

This is the drying chamber temperature v/s time interval graph, which shows the drying chamber temperature every half an hour of the time interval between 10 AM to 6 PM for two days from 1 May to 2 May. The pattern depicted in Fig. 9 revealed that the lowest and highest temperatures of the drying chamber were 33.0 °C and 42.0 °C respectively.

3.5. Potato slice temperature

This is the drying tray temperature v/s time interval graph, which shows the drying tray temperature every half an hour of the time interval between 10 AM to 6 PM for 2 days from 1 May to 2 May. The pattern depicted in Fig. 10 revealed that the lowest and highest temperatures of the drying tray were 32.3 °C and 35.3 °C respectively.

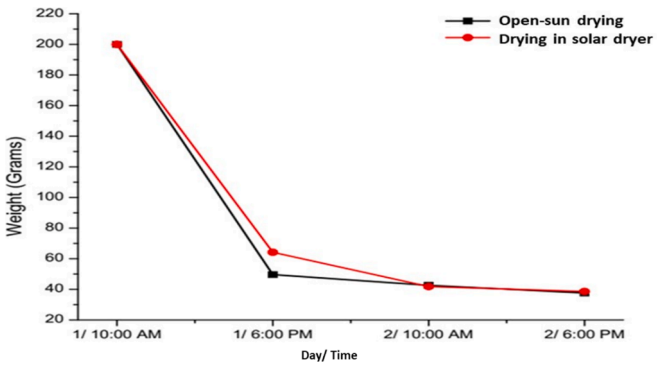

Fig. 6. Weight of potato slice sample during two days of the experiment.

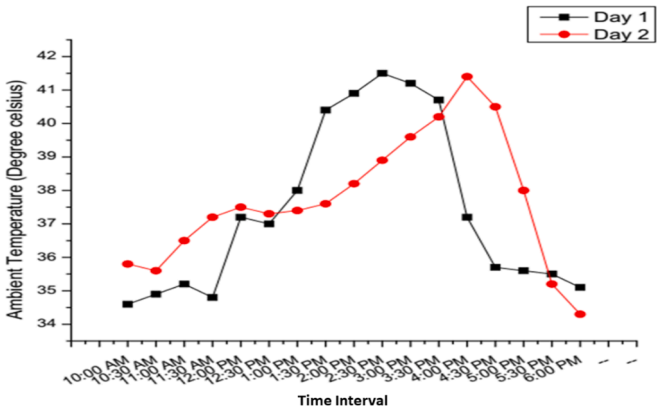

Fig. 7. Ambient temperature recording during two days of the experiment.

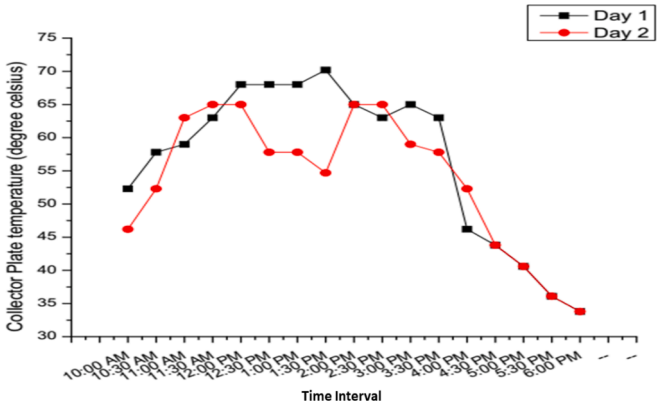

Fig. 8. Collector plate temperature was recorded during two days of the experiment.

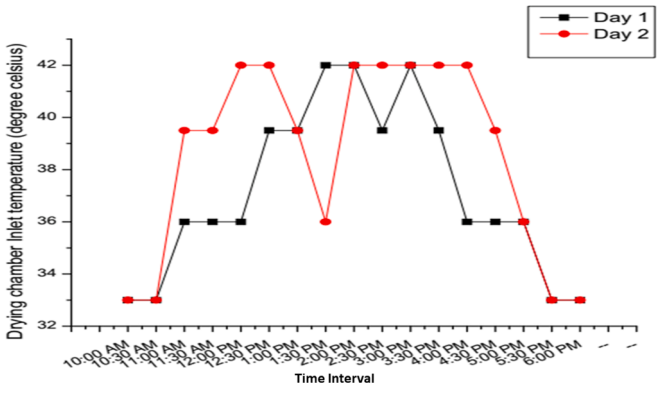

Fig. 9. Drying chamber inlet temperature.

3.6. Analysis of moisture content

In both open-sun and indirect solar dryers, the moisture content of potato slices changed during the drying process, as listed in Table 8. The initial MC of the potato slices was 83 ± 2 % (wb); thus, the end MC was 11.7 ± 2 % (wb) for OSD and 7.7 ± 2.0 % (wb) for ISD, both in 16 h. Therefore, the moisture removal rate (MRR) was higher in ISD than in OSD in terms of moisture content. The higher temperature that was reached in the drying chamber also reduced the amount of time that food products needed to dry, which increased the importance of the ISD. The rate of moisture removal from food materials' interiors to their upper surfaces via diffusion mechanisms aids in raising the difference in

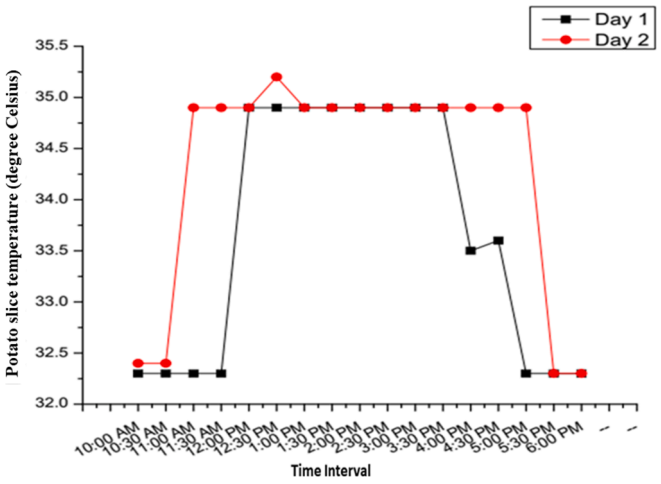

Fig. 10. Potato slice temperature.

Table 8
Moisture content during the experiment.

Day	Open sun drying	Indirect solar drying
Day 1	$M_i = 200$ $M_f = 49.6$ MC = 75.2 % ±2 % (wb)	$M_i = 200$ $M_f = 64.2$ MC = 67.9 % ±2 % (wb)
Day 2	$M_i = 42.6$ $M_f = 37.6$ MC = 11.7 % ±2% (wb)	$M_i = 41.8$ $M_f = 38.6$ MC = 7.7 % ±2% (wb)

vapor pressure between drying air, which causes indirect sun dryers to evaporate moisture at a higher rate.

3.7. Analysis of drying rate

Table 9 shows the differences in DR between OSD and ISD of potato slices. Solar radiation is important in the drying of food products. It was discovered that DR increased initially with an increase in sun radiation for the first 8 h of the drying process, but thereafter decreased with drying time. The highest DR of potato slice was 18.80 g water/g solid h after 8 h of OSD, and 16.97 g water/g solid h after 8 h of ISD. In Table 9, the drying rates differ between open and closed conditions due to variations in air circulation, temperature, vapor pressure gradient and surface area exposed to air.

3.8. Rehydration ratio

It's characterized as the ratio of the rehydrated sample's drained weight to the weight of the dried sample. In OSD weight drained was 162.4 g, while the dried sample's weight was 37.6 g after two days of

Table 9
Drying rate summary during the experiment.

Day	Open	Closed
Day 1	$M_t = 200$ $M_t\ \Delta t = 49.6$ $\Delta t = 8h$ DR = 18.80 g water/ g solid h	$M_t = 200$ $M_t\ \Delta t = 64.2$ $\Delta t = 8h$ DR = 16.97 g water/ g solid h
Day 2	$M_i = 42.6$ $M_t\ \Delta t = 37.6$ $\Delta t = 8h$ DR = 0.625 g water/ g solid h	$M_i = 41.8$ $M_t\ \Delta t = 38.6$ $\Delta t = 8h$ DR = 0.4 g water/ g solid h

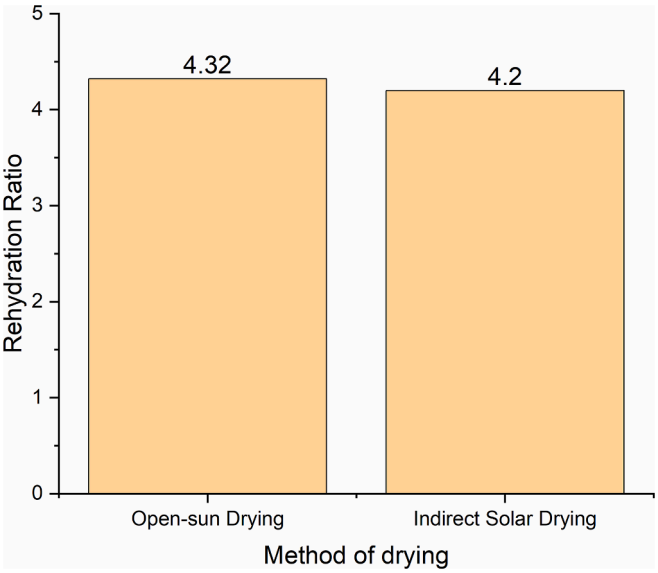

Fig. 11. Rehydration ratio value for potato slice sample.

OSD. In ISD, the weight drained is 161.4 g, and the dried sample's weight is 38.6 g after two days of drying process in the ISD. Rehydration ratios for OSD and ISD are 4.32 and 4.2, respectively as shown in Fig. 11.

3.9. Shrinkage

The shrinkage factor (%) was highest in dried potato slices dried by ISD due to the quicker MRR during drying. OSD has a shrinkage factor of 61 %, whereas drying in ISD has a shrinkage factor of 70 % as shown in Fig. 12.

3.10. Color index

The color of potato slices was assessed using a Chromometer between the start and finish of the drying process. Lo, ao, and b_o values were observed at the beginning and the end of the drying process in both OSD and ISD. Throughout the trial, Lo-value changes were minimal with OSD and ISD. In indirect solar drying, it ranged from 22.76 to 28.55, while in open-sun drying; it ranged from 21.58 to 27.21. As a result, in both

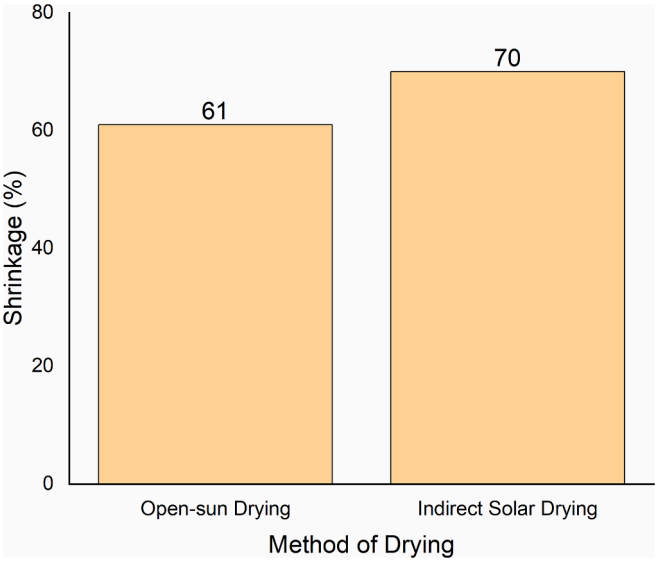

Fig. 12. Shrinkage value for potato slice samples.

drying experiments, ao and b_o values decreased with the time of day. In ISD, the a-values were 15.89 and 4.96, respectively, while in the OSD, they were 16.78 and 2.68. In addition, b_o-values varied between 3.65 and 0.97 and 3.89 and 1.54 in ISD and OSD. After drying, the color of the potato slice changes from white to red-yellow with varying degrees of intensity. Color indices show that the color of the potato slice dried in the dryer was dark golden brown.

Furthermore, the color of the potato slice dried outside in the sun was dark yellow than potato slice dried in ISD. Color of dried potato slices differs significantly from that of raw ones, which corresponds to changes in L and a-values. Lo-value fell during the drying process in all trials. However, the a-value increased just slightly. All parameters of the color index are enlisted in Table 10 for both drying methods. This suggests that when the samples dried, they became darker and golden. The maximum color change values in the ISD and OSD were 6.32 and 8.13, respectively, due to increasing DR with temperature and solar irradiation. Because of the increased deterioration at the beginning of the drying hours, OSD produced more color changes than ISD.

3.11. Water activity

Water activity (Aw) is important in the growth of microorganisms and the strength of potato slices. It is described as the proportion of food vapor pressure to pure water vapor pressure. Aw was initially recorded at 0.95, but decreased substantially with time of day and temperature. Because of the faster DR and higher temperature maintained in the drying chamber, ISD reduced Aw faster than OSD. In 16 h of drying time, Aw was reduced from 0.95 to 0.42 in ISD and from 0.95 to 0.59 in OSD as shown in Fig. 13. The findings suggest that dried potato slices with high water activity can be safely preserved for subsequent processing. In this experiment, the high temperature and limited humidity that caused the hydration of the potato slices macromolecules resulted in a quick reduction in water activity in ISD, which increased the drying rate.

4. Conclusions

The drying rate of OSD is higher than that of ISD, but the key advantage of solar drying is that the dried food samples have a greater quality parameter color, texture, flavor, and retained amount of nutrients. OSD Pretreatment of potato slices and keeping a steady temperature of 35–40 ℃ within the drying chamber can improve the quality parameters of dried potato slices. According to the findings, greater temperatures, air movement, and lower humidity in the dryer chamber enhance the drying pace for food samples confined inside the dryer and safeguarded against dust, insects, birds, and animals. The dimensions of the fabricated solar dryer have been minimized to enhance mobility and affordability, utilizing locally sourced components at a minimal cost. Food dried in a solar dryer is of higher quality than food dried in the open sun. The major findings of the experiment are listed below:

- 200 g of potato slice sample was used for drying in OSD and ISD and it remained only 38.6 g of the closed sample and 37.6 g of the open sample by the end of the experiment.
- The minimum and maximum environmental temperatures were 34.3 °C and 41.5 °C respectively during the two days of the experiment.
- During the two days of the experiment, the collector plate's lowest and highest temperatures were 33.8 °C and 70.2 °C, respectively.
- During the two days of the experiment, the drying chamber's lowest and highest temperatures were 33.0 °C and 42.0 °C, respectively.
- During the two days of the experiment, the potato slice's lowest and highest temperatures were 32.3 °C and 35.3 °C, respectively.
- MC was 11.7 ± 2 % (wb) for OSD and 7.7 ± 2.0 % (wb) for ISD, both in 16 h.
- The highest DR of potato slice was 18.8 g water/g solid h after 8 h of OSD, and 16.97 g water/g solid h after 8 h of ISD.

Table 10
Colour index parameters were recorded during the drying of potato slices in both drying processes.

Parameters	Open-sun drying		Indirect solar drying	
	End of first day	End of second day	End of first day	End of second day
Lo	21.58	27.21	22.76	28.55
a_o	16.78	2.68	15.89	4.96
b_o	3.89	1.54	3.65	0.97
Colour Change Δ E	8.13		6.32	

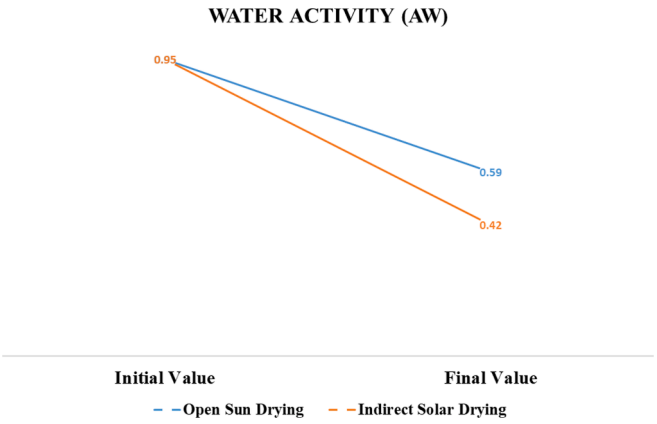

Fig. 13. Water Activity (A_w) value for potato slice samples.

- Rehydration ratios for OSD and ISD are 4.32 and 4.2, respectively.
- OSD had a shrinkage factor of 61 %, whereas drying in ISD had a shrinkage factor of 70 %.
- Maximum color change values in ISD and OSD were 6.32 and 8.13, respectively.
- In sixteen hours of drying, Aw was reduced from 0.95 to 0.42 in ISD and from 0.95 to 0.59 in OSD.

The integration of PCM (phase change material), which can absorb heat during the day and release it during the night, can improve the effectiveness of solar dryers even more. The total effectiveness of the solar dryer may be boosted by adjusting the wind velocity according to the condition of the weather, such as relative humidity and environmental temperature.

CRediT authorship contribution statement

Ankit Srivastava: Writing – original draft, Resources, Methodology, Investigation, Formal analysis, Data curation. **Atul Sharma:** Visualization, Validation, Supervision, Resources, Conceptualization. **Anil Kumar:** Writing – review & editing, Visualization, Validation, Supervision.

Declaration of competing interest

The authors declare that they have no known competing financial interests or personal relationships that could have appeared to influence the work reported in this paper.

Acknowledgment

The first author would like to express gratitude to the Rajiv Gandhi Institute of Petroleum Technology, Jais, Amethi, India, for supporting the pursuit of the Ph.D. program in the Department of Sciences and Humanities. The authors are also sincerely thankful to the Feroze

Gandhi Institute of Engineering and Technology, Raebareli, India, for facilitating the current research. Special thanks are extended to the Non-Conventional Energy Laboratory at RGIPT, Jais, Amethi, and the Division-Clean Energy: Nodal Centre of Excellence in Energy Transition (NCEET)at Delhi Technological University, India, for their invaluable support in this endeavor.

References

[1] A. Masoom, P. Kosmopoulos, A. Bansal, S. Kazadzis, Solar energy estimations in india using remote sensing technologies and validation with sun photometers in urban areas, Remote Sens. 12 (2020) 254, https://doi.org/10.3390/rs12020254.
[2] S. Verma, R. Das, Evaluation of the effectiveness of base insulation on the productivity of a packed bed solar air heater, J. Therm. Sci. Eng. Appl. 14 (2022) 1–10, https://doi.org/10.1115/1.4053742.
[3] M. Kumar, R.K. Sahdev, S. Tiwari, H. Manchanda, A. Kumar, Enviro-economical feasibility of groundnut drying under greenhouse and indoor forced convection hot air dryers, J. Stored Prod. Res. 93 (2021) 101848, https://doi.org/10.1016/j.jspr.2021.101848.
[4] D. Singh, P. Mall, Experimental investigation of thermal performance of indirect mode solar dryer with phase change material for banana slices, Energy Sources, Part A Recover. Util. Environ. Eff. (2020), https://doi.org/10.1080/15567036.2020.1810825.
[5] G.L. Visavale. 2012. Solar Drying: Fundamentals,Applications and Innovations, Solar drying: fundamentals, applications and innovations. ISBN-978-981-07-3336-0, National University of Singapore Press, Published in Singapore. https://doi.org/ ISBN: 978-981-07-3336-0.
[6] M. Sandali, A. Boubekri, D. Mennouche. 2020. Thermal and Economical Study of a Direct Solar Dryer with Integration of Different Techniques of Heat Supply. Springer Singapore, pp. 585–595. https://doi.org/10.1007/978-981-15-5444-5_73.
[7] O.A. Babar, A. Tarafdar, S. Malakar, V.K. Arora, P.K. Nema, Design and performance evaluation of a passive flat plate collector solar dryer for agricultural products, J. Food Process Eng. 43 (2020), https://doi.org/10.1111/jfpe.13484.
[8] A. Menon, V. Stojceska, S.A. Tassou, A systematic review on the recent advances of the energy efficiency improvements in non-conventional food drying technologies, Trends Food Sci. Technol. 100 (2020) 67–76, https://doi.org/10.1016/j.tifs.2020.03.014.
[9] A. Kumar, R. Singh, O. Prakash, Ashutosh, Review on global solar drying status, Agric. Eng. Int. CIGR J. 16 (2014) 161–177.
[10] B. Norton, Characteristics of different systems for the solar drying of crops, Green Energy Technol. (2017) 69–88, https://doi.org/10.1007/978-981-10-3833-4_3.
[11] M. Castillo Téllez, I. Pilatowsky Figueroa, B. Castillo Téllez, E.C. López Vidaña, A. López Ortiz, Solar drying of Stevia (Rebaudiana Bertoni) leaves using direct and indirect technologies, Sol. Energy 159 (2018) 898–907, https://doi.org/10.1016/j.solener.2017.11.031.
[12] A. Fudholi, K. Sopian, M.H. Ruslan, M.A. Alghoul, M.Y. Sulaiman, Review of solar dryers for agricultural and marine products, Renew. Sustain. Energy Rev. 14 (2010) 1–30, https://doi.org/10.1016/j.rser.2009.07.032.
[13] A. Ahmad, O. Prakash, Performance evaluation of a solar greenhouse dryer at different bed conditions under passive mode, J. Sol. Energy Eng. 142 (2020) 1–10, https://doi.org/10.1115/1.4044194.
[14] V. Shrivastava, A. Kumar, Embodied energy analysis of the indirect solar drying unit, Int. J. Ambient Energy 38 (2017) 280–285, https://doi.org/10.1080/01430750.2015.1092471.
[15] M. Goud, M.V.V. Reddy, V.P. Chandramohan, S. Suresh, A novel indirect solar dryer with inlet fans powered by solar PV panels: drying kinetics of Capsicum Annum and Abelmoschus esculentus with dryer performance, Sol. Energy 194 (2019) 871–885, https://doi.org/10.1016/j.solener.2019.11.031.
[16] J. Varghese, S. Rupesh, J. Augustine, A. Nair, Prajith, Design and analysis of a solar drier with a parabolic shaped dish type collector for drying peanut, IOP Conf. Ser. Mater. Sci. Eng. 1132 (2021) 012046, https://doi.org/10.1088/1757-899X/1132/1/012046.
[17] P.P. Tripathy, Investigation into solar drying of potato: effect of sample geometry on drying kinetics and CO_2 emissions mitigation, J. Food Sci. Technol. 52 (2015) 1383–1393, https://doi.org/10.1007/s13197-013-1170-0.
[18] N. Vigneshkumar, M. Venkatasudhahar, P. Manoj Kumar, A. Ramesh, R. Subbiah, P. Michael Joseph Stalin, V. Suresh, M. Naresh Kumar, S. Monith, R. Manoj Kumar, M. Kriuthikeswaran, Investigation on indirect solar dryer for drying sliced potatoes using phase change materials (PCM), Mater. Today Proc. (2021), https://doi.org/10.1016/j.matpr.2021.05.562.
[19] A. Tefera, W. Endalew, B. Fikiru. 2013. Evaluation and demonstration of direct solar potato dryer 25, 1–8.
[20] A. Djebli, S. Hanini, O. Badaoui, B. Haddad, Modeling and comparative analysis of solar drying behavior of potatoes, Renew. Energy 145 (2020) 1494–1506, https://doi.org/10.1016/j.renene.2019.07.083.
[21] A.O. Dissa, J. Bathiebo, S. Kam, P.W. Savadogo, H. Desmorieux, J. Koulidiati, Modelling and experimental validation of thin layer indirect solar drying of mango slices, Renew. Energy 34 (2009) 1000–1008, https://doi.org/10.1016/j.renene.2008.08.006.
[22] W. Wang, M. Li, R.H.E. Hassanien, Y. Wang, L. Yang, Thermal performance of indirect forced convection solar dryer and kinetics analysis of mango, Appl. Therm. Eng. 134 (2018) 310–321, https://doi.org/10.1016/j.applthermaleng.2018.01.115.
[23] A.K. Bhardwaj, R. Kumar, R. Chauhan, Experimental investigation of the performance of a novel solar dryer for drying medicinal plants in Western Himalayan region, Sol. Energy 177 (2019) 395–407, https://doi.org/10.1016/j.solener.2018.11.007.
[24] H. Özge, A. Sözen, A. Doğuş, F. Afshari, A. Khanlari, Experimental and CFD survey of indirect solar dryer modified with low-cost iron mesh, Sol. Energy 197 (2020) 371–384, https://doi.org/10.1016/j.solener.2020.01.021.
[25] M. Kumar, S.K. Sansaniwal, P. Khatak, Progress in solar dryers for drying various commodities, Renew. Sustain. Energy Rev. 55 (2016) 346–360, https://doi.org/10.1016/j.rser.2015.10.158.
[26] A.O. Dissa, H. Desmorieux, J. Bathiebo, J. Koulidiati, A comparative study of direct and indirect solar drying of mango, Glob. J. Pure Appl. Sci. 17 (2011) 273–294.
[27] A.K. Bhardwaj, R. Kumar, R. Chauhan, S. Kumar, Experimental investigation and performance evaluation of a novel solar dryer integrated with a combination of SHS and PCM for drying chilli in the Himalayan region, Therm. Sci. Eng. Prog. 20 (2020) 100713, https://doi.org/10.1016/j.tsep.2020.100713.
[28] R. Vadivambal, D.S. Jayas, Non-uniform temperature distribution during microwave heating of food materials-A review, Food Bioprocess Technol. 3 (2010) 161–171, https://doi.org/10.1007/s11947-008-0136-0.
[29] A. Kushwah, A. Kumar, M.K. Gaur, A. Pal, Garlic dehydration inside heat exchanger-evacuated tube assisted drying system: thermal performance, drying kinetic and color index, J. Stored Prod. Res. 93 (2021) 101852, https://doi.org/10.1016/j.jspr.2021.101852.
[30] D. Engin, Effect of drying temperature on color and desorption characteristics of oyster mushroom, Food Sci. Technol. 40 (2020) 187–193, https://doi.org/10.1590/fst.37118.

Phenomenology of (3+1) Four Flavour Neutrino Oscillations in Dense Matter

Ashish Shrivastava[1], Bipin Singh Koranga[2,*] and Seema Rawat[3]

[1]*Department of Applied Physics, Delhi Technological University, Delhi-110042, India*
[2]*Department of Physics, Kirori Mal College, University of Delhi, Delhi-110007, India*
[3]*Department of Physics, Zakir Husain Delhi College, University of Delhi, Delhi-110007, India*
E-mail: bskoranga@kmc.du.ac.in
**Corresponding Author*

Received 11 August 2024; Accepted 03 November 2024

Abstract

The mass square difference varies as neutrinos interact with the matter, assuming four flavours of neutrino oscillations. Three regions – vacuum-dominated, resonance-dominated, and matter-dominated – are where the neutrinos oscillate. This research goes on to examine how each of these three locations affects the likelihood of neutrino oscillations and the mass square difference in distinct ways. There are three alternative analytical formulas for the mass square difference. In this study, we have studied the behaviour of neutrino oscillations for four flavours in vacuum-dominated, resonance-dominated, and matter-dominated regions.

Keywords: Four flavor neutrino oscillations, sterile neutrino, dense matter, mass square difference.

1 Introduction

With the help of the findings of numerous solar, atmospheric, accelerator, and reactor experiments [1–3], neutrino oscillation has been very well defined. Since the discovery of neutrino oscillations, the behaviour of the particles and their propensities to oscillate between various flavours have been examined. Since the mixing angle and the mass square difference affect likelihood. It was discovered that these are impacted by the matter effect, which occurs when neutrinos contact with matter. Although the precise mass of neutrinos is still unknown, multiple medium and long baseline experiments [4, 5] have provided the values of the mass square difference of various mass eigenstates and mixing angles.

The solar neutrino mass square difference measured by the LSND experiment is $0.2<\Delta 21<100 \times e \times V2$ [6], whereas the solar mass square difference measured by the

MiniBooNe experiment is $0.01<\Delta 21<1.0 \times e \times V2$ [7]. This experimental finding indicated the potential for sterile (3+1) neutrinos [4, 5]. Four flavour neutrino oscillation is conceivable if sterile neutrinos are predicted to exist. When neutrinos interact with matter through neutral and charged current interactions, a rise in potential is seen, which affects the oscillation probability and mass square difference [8]. The outcomes of these interactions are determined by the neutrino energy as well as the matter density, or the concentration of electrons and neutrons in the matter. The three regions that make up the matter effect are the resonance region (also known as the MSW effect), the matter dominated region (also known as $A \gg \Delta 21, |\Delta 31|$ [12], and the vacuum dominated region (also known as $A \ll \Delta 21, |\Delta 31|, \Delta 41$.

2 Framework for Four-Flavor Neutrino Oscillation in Theory

Four-flavor mixing can be expressed as [9]: in terms of mass eigenstates.

$$(\text{vevμvτvs}) = U \times (\text{v1v2v3v4})$$

where

$$U = R34 \times (\theta 34, \delta 34) \times R24 \times (\theta 34) \times R14 \times (\theta 14, \delta 14)$$
$$R23 \times (\theta 23) \times R13 \times (\theta 13, \delta 13) \times R12 \times (\theta 12)$$
$$Ri \times j \times (\theta i \times j, \delta) = (c \times o \times s \times \theta i \times j s \times i \times n \times \theta i \times j \times e\text{-}i \times \delta\text{-}$$
$$s \times i \times n \times \theta i \times j \times ei \times \delta c \times o \times s \times \theta i \times j).$$

Here, δ represents dirac CP violating phase.

The following can be used to represent a Hamiltonian in four flavours in a vacuum [10]

$$Hv = 12 \times E \times U \times (00000\Delta \times m2120000\Delta \times m3120000\Delta \times m412) \times U\dagger.$$

Thus the likelihood of neutrino oscillation can be expressed as [11]:

$$P\nu\alpha \rightarrow \nu\beta = \delta\alpha \times \beta\text{-}$$
$$4 \times \sum i>j \Re f_0 (U\beta \times i \times U\alpha \times i^* \times U\beta \times j^* \times U\alpha \times j) + 2 \times \sum i>j \Im f_0 (U\beta \times i \times U\alpha \times i^* \times U$$
$$\beta \times j^* \times U\alpha \times j)$$

We already know that the hamiltonian changes as neutrinos go through matter because their potential increases. This increase is the result of neutral current scattering

and coherent forward elastic weak charged current. Charged current scattering is caused by the interaction of an electron and neutrino pair. Consequently, the updated Hamiltonian may be written as [10]:

$$Hm=Hv+A=12\times E(U(00000\Delta\times m2120000\Delta\times m3120000\Delta\times m412)U\dagger +(AC\times C00000000000000AN\times C))$$

where

$$AC\times C=7.63\times10\text{-}5\times\rho\times E \quad \text{and} \quad AN\times C=-3.815\times10\text{-}5\times\rho\times E$$

The matter terms for current charge and neutral charge, respectively, are AC×Cand AN×C. We will utilise the standard hierarchical approach to tackle the issue for |Δ31|.

2.1 Vacuum Dominated Region (AC×C≪Δ21,|Δ31|,Δ41)

As stated in the section's headline, the matter effect in vacuum-dominated regions is small, meaning that interactions between neutrinos are insignificant and do not raise the effective potential of moving neutrinos. In light of this circumstance, we may therefore deduce the approximate values of the matter terms AC×C≈0 and AN×C≈0.

Effective Hamiltonian can be expressed as follows from these values:

$$Hm=Hv=12\times E\times U\times(00000\Delta\times m2120000\Delta\times m3120000\Delta\times m412)\times U\dagger$$

This, in vacuum, is equivalent to the Hamiltonian.

$$\mathcal{H}i\times j=\{0i\neq j\Delta i\times 1i=j$$

There is no such shift in mass square disparities in vacuum-dominated regions.

2.2 Resonance Region (A∼Δ21,|Δ31|)

The neutral and charge current in the resonance zone is sufficient to increase the neutrinos' potential, which will modify their mass square difference and alter their chance of oscillations as well. The following is an example of an effective Hamiltonian for this area:

$$Hm=Hv+A=12\times E(U(00000\Delta\times m2120000\Delta\times m3120000\Delta\times m412)U\dagger +(AC\times C00000000000000AN\times C))$$

This, as a result of coherent forward elastic weak charged current and neutral current scattering, closely resembles the effective hamiltonian. You can alternatively write the above form as:

$$U\dagger \times Hm \times U=(H11H12H13H14H21H22H23H24H31H32H33H34H41H42H43H44) =\mathscr{H}$$

where:

$$\mathscr{H}i \times j=\{AC \times C \times Ue \times i^* \times Ue \times j+AN \times C \times Us \times i^* \times Us \times ji \neq j\Delta i \times 1+AC \times C \times |Ue \times i|2+AN \times C \times |Us \times i|2i=j$$

Using Jacobi-Like Method [13] after the first rotation of the matrix $\mathscr{H}$:

Following the initial rotation of the matrix H, one can use the Jacobi-Like Method [13] to:

$$\lambda-=H11+H22 \times t \times a \times n2 \times \omega 1-2 \times A1 \times t \times a \times n \times \omega 11+t \times a \times n2 \times \omega 1$$

and

$$\lambda+=H22+H11 \times t \times a \times n2 \times \omega 1-2 \times A1 \times t \times a \times n \times \omega 11+t \times a \times n2 \times \omega 1.$$

When the expressions' defined parameters can be expressed as:

$$t \times a \times n \times \omega 1=2 \times A1(H22-H11)+(H22-H11)2+4 \times A12,$$
$$A1=+|H12|$$

and

$$\Phi 1=A \times r \times g \times (s \times i \times g \times n \times (A1) \times H12^*)$$

After the second rotation:

$$\lambda-'=\lambda++H33 \times t \times a \times n2 \times \omega 2-2 \times A2 \times t \times a \times n \times \omega 21+t \times a \times n2 \times \omega 2$$

and

$$\lambda+'=H33+\lambda+ \times t \times a \times n2 \times \omega 1-2 \times A2 \times t \times a \times n \times \omega 21+t \times a \times n2 \times \omega 2$$

When the parameters in the expressions have the following representations:

$$t\times a\times n\times \omega 2=2\times A2(H33-\lambda +)+(H33-\lambda +)2+4\times A22$$
$$A2=+|H23'|,$$
$$\Phi 2=A\times r\times g\times (s\times i\times g\times n\times (A2)\times H23',*)$$

and

$$H23'=H13\times t\times a\times n\times \omega 1\times ei\times \Phi 1+H231+t\times a\times n2\times \omega 1.$$

So now we can say that:

$$\Delta 21m=\lambda -'-\lambda -,$$
$$\Delta 31m=\lambda +'-\lambda -$$

and

$$\Delta 41m=H44-\lambda -$$

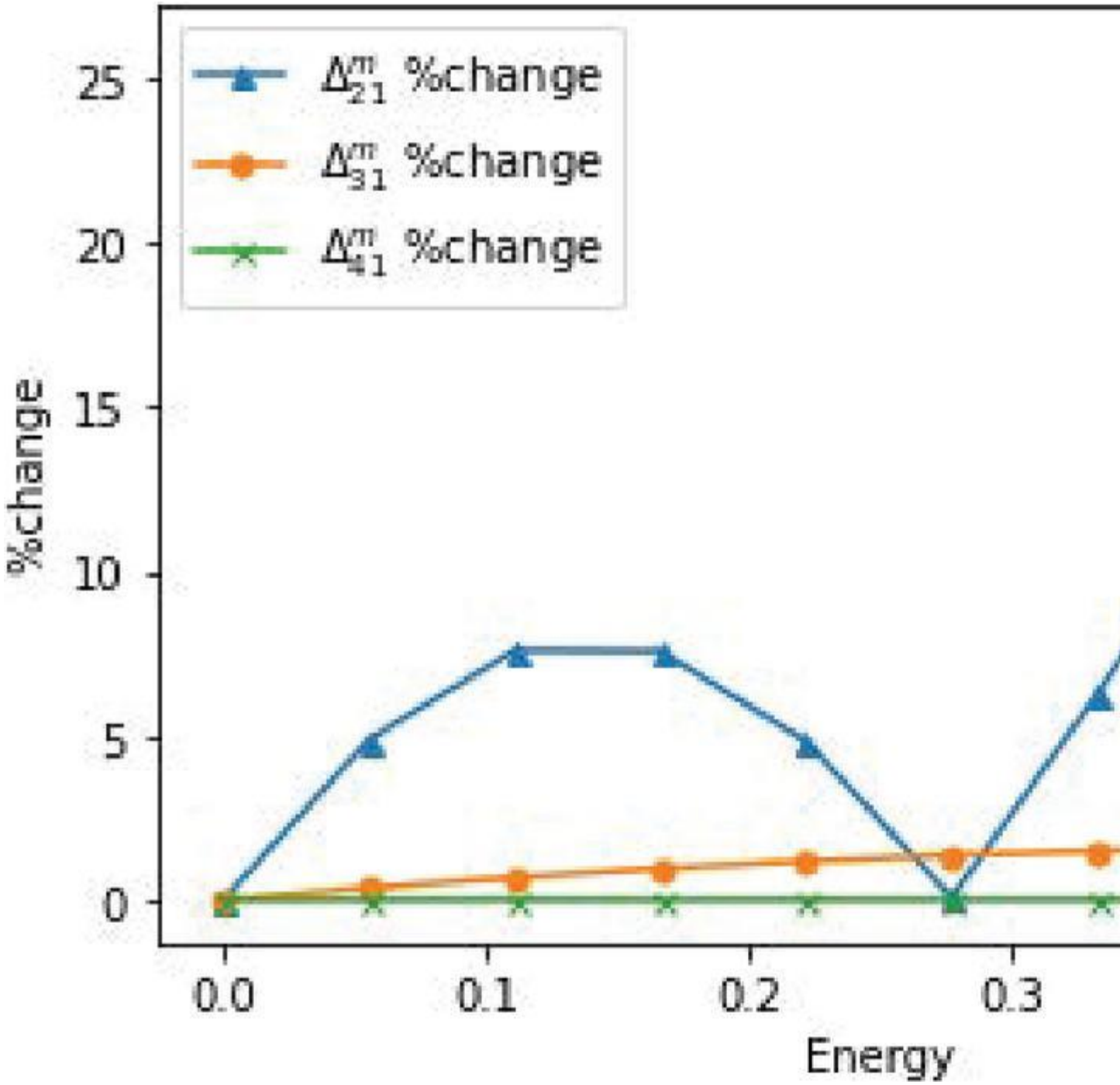

Figure 1 Variation of relative percentage change in Mass Square difference in resonance region where energy varies from 0GeV to 0.5GeV where mixing angles are θ12=340θ13=10,0θ14=340,θ23=3.60,θ24=40 and θ34=18.50, mass square difference in vacuum are Δ21=8×10-5×e×V2, Δ31=2×10-3×e×V2 and Δ41=1.7×e×V2 and constant density 3×g/c×c.

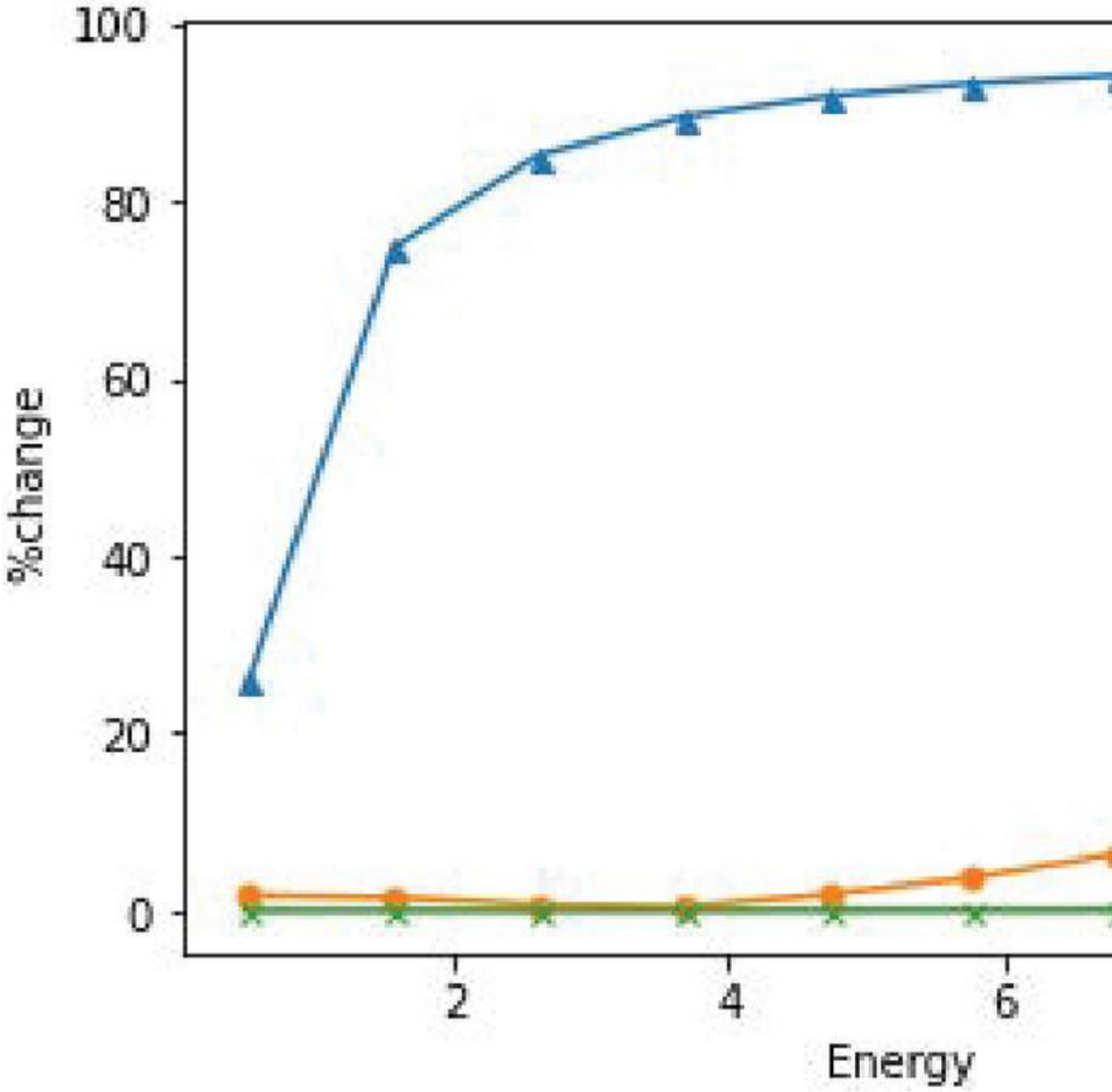

Figure 2 Variation of relative percentage change in Mass Square difference in resonance region where energy varies from 0.5 GeV to 10 GeV where mixing angles are θ12=340θ13=100, θ14=340, θ23=3.60, θ24=40 and θ34=18.50, mass square difference in vacuum are Δ21=8×10-5×e×V2, Δ31=2×10-3×e×V2 and Δ41=1.7×e×V2 and constant density 3×g/c×c.

2.3 Matter Dominated Region(AC×C≫Δ21,|Δ31)

In matter dominated region, neutrinos must be travelling in a dense matter. The condition mentioned in the heading of this section A≫Δ21,|Δ31| can be approximated as AΔi×1≈0 where i=2,3. Using this condition in the expression of resonance region, the effective hamiltonian can be written as:

Neutrinos must be passing through a dense matter in an area where matter predominates. The condition A≫Δ21,|Δ31| given in the section's headline can be roughly expressed as AΔi×1≈0 where i=2,3. The effective Hamiltonian can be stated as follows using this condition in the formulation of resonance region:

U†×Hm×U=(H11H12H13H14H21H22H23H24H31H32H33H34H41H42H43H44) =ℋ

where:

ℋi×j={AC×C×Ue×i*×Ue×j+AN×C×Us×i*×Us×ji≠jAC×C(|Ue×i|2+A N×CAC×C|Us×i|2+Δi×1Ac×ci=j

Using a method akin to Jacobi [13]. The formulas obtained for the resonance zone will be the same for this as well, with the exception that the matrix's parameters will change once the condition for various values of ℋ×j is applied. The graph below shows the variation in AC×C for dense matter, i.e. A≫Δ21,|Δ31|, from less dense to very dense matter. Due to the fact that Δ21m=λ-′-λ-, Δ31m=λ+′-λ- and Δ41m=H44-λ-. The connection H44-λ-′+Δ21m can be obtained from the expression Δ41m. λ-′ and Δ21m do not affect the value of Δ41m at resonance region, but at high density, the values are comparable, therefore the change in Δ41m is also visible in the derived graph. This change may become saturated at larger densities, just like Δ21m and Δ31m.

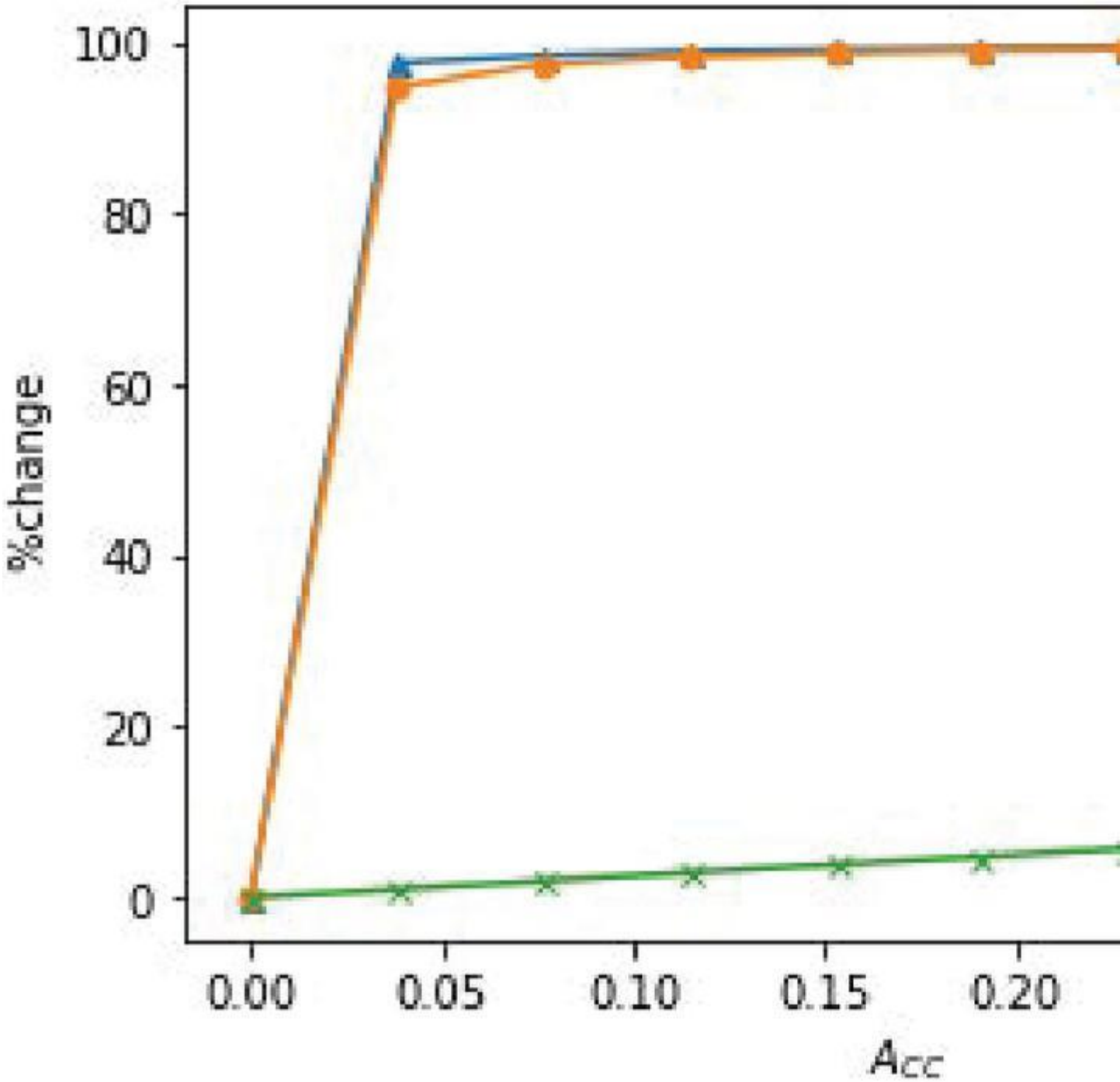

Figure 3 Variation of relative percentage change in Mass Square difference in matter dominated region where density varies from 0 g/cc to 1500 g/cc where mixing angles are θ12=340θ13=100, θ14=340, θ23=3.60, θ24=40 and θ34=18.50, mass square difference in vacuum are Δ21=8×10-5×e×V2, Δ31=2×10-3×e×V2 and Δ41=1.7×e×V2 and constant energy 3×G×e×V.

3 Conclusions

When neutrinos interact with matter, the probabilities of neutrino oscillation and the mass square difference are affected. Only in the case of neutrinos is the normal hierarchy computation completed. The probability in vacuum-dominated regions are nearly identical to those in vacuum, and the percentage change in the relative mass square difference with regard to matter is essentially identical to those in vacuum. The effective mass square difference is growing in the resonance zone as the neutrino energy rises and the oscillation probability changes. While there are no such impacts on Δ41m in this location, the percentage change in mass square difference is found to be in the range of 0 GeV to 10 GeV. However, there is a significant change in the resonance region from region 0 GeV to 0.5 GeV, followed by a harsh change in Δ21m, a significant change in Δ31m, as seen in the graph, and another drastic change after 3 GeV. The relative percentage change in the mass square difference with respect to the matter varies depending on whether the region is vacuum or resonance in a region where matter predominates.

Both the Δ21m and Δ31m alter and become saturated at about 99%. But even though the sterile neutrino only interacts with gravity, the change in Δ41m has begun to rise. According to the expressions derived from the relationship between Δ21m and Δ41m, the extreme shift in in a dense substance that caused the effective change observed has an impact on Δ41m%.

References

[1] John N. Bahcall et al., Phys. Rev. Lett. 40. pp. 1351–1354, 1978.

[2] Patrick Huber, Thomas Schwetz, Phys. Lett. B 669. pp. 294–300, 2008.

[3] Zeno Dixon Greenwood et al., Phys. Rev. D 53. pp. 6054–6064, 1996.

[4] G.J. Feldman et al., Advances in High Energy Physics, Vol. 2013, pp. 1–30, 2013-01, 2013.

[5] Chiaki Yanagisawa et al., Phys. Rev. D 83, pp. 072002, 2011.

[6] G. Conforto et al., Phys. Lett. B 447, pp. 122–126, 1999.

[7] MiniBoone Collaboration, A.A. Aguilar-Arevalo et al., Phys. Rev D 103, pp. 1–5, 2021.

[8] A. Yu. Smirnov, Phys. Scripta T 121, pp. 57–64, 2005.

[9] B. S. Koranga et al., Int. J. Theor. Phys. 60, 9 pp. 3548–3565, 2021.

[10] Ashish Shrivastava, B. S. Koranga et al., arxiv:2106.15945 (hep-ph).

[11] S. Dev et al., Nuclear. Phys B 491, pp. 401, 2019.

[12] S. Luo et al., Moscow Univ. Phys. Bull. 77 pp. 462–463, 2022.

[13] Bao-Biao Yue, Jia-Jie Ling et al., Chin. Phys. C 44, 10 pp. 103001, 2020.

Biographies

Ashish Shrivastava is a post graduate student in the Department of Applied Physics, Delhi Technological University. He is in the final year of M.Sc. Physics. He received his bachelor's degree from Kirori Mal College, University of Delhi in Physical Science. He completed his dissertation in Phenomenology of Neutrino Oscillations during his under graduation. His work has been published in Journal of Graphic Era along with the conference. He is currently working on a project in which he is studying Quantum Entanglement in Neutrino Oscillations.

Bipin Singh Koranga is Professor in the Department of Physics, Kirorimal College, University of Delhi. He joined the Theoretical Physics Group at the Indian Institute of Technology Bombay in 2006 and earned his Ph.D. in physics (neutrino masses and mixings) there in 2007. For the past 17 years, he has been instructing graduate-level students in foundational physics and mathematical physics courses. The genesis of the cosmos, physics beyond the standard model, theoretical nuclear physics, quantum mechanical neutrino oscillation, and a few astrological issues are among his areas of interest. He has more than 60 scientific publications to his credit in different international journals. His current areas of focus in study are linked phenomenology and neutrino mass theories.

Seema Rawat is an Associate Professor of physics at Zakir Husain College, University of Delhi, where she has taught Quantum mechanics and Theortical Physics to undergraduate students. He received his master's degree in physics from Kumaun University Nainital and doctoral degree in physics from Kumaun University Nainital. He has more than 30 scientific publications to his credit in different international journals. His current areas of focus in high energy particle physics.

Journal of Graphic Era University, Vol. 12_2, 363–372.
doi: 10.13052/jgeu0975-1416.12210
© 2024 River Publishers

Sensors & Actuators: A. Physical 381 (2025) 116038

Contents lists available at ScienceDirect

Sensors and Actuators: A. Physical

journal homepage: www.journals.elsevier.com/sensors-and-actuators-a-physical

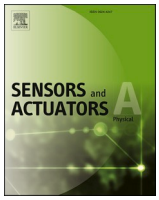

Piezo-Ionic Actuator for Haptic Feedback

António Diogo André [a,b], Indrani Coondoo [c], Igor Bdikin [d,e], Vinaya Kumar K.B. [f], Rui M.R. Pinto [g], Pedro Martins [b,h], Majid Taghavi [a,i,*]

[a] Department of Bioengineering, Imperial College London, London, UK
[b] Institute of Science and Innovation in Mechanical and Industrial Engineering (INEGI), Porto, Portugal
[c] Department of Materials and Ceramic Engineering & CICECO - Aveiro Institute of Materials, University of Aveiro, Aveiro, Portugal
[d] Centre for Mechanical Technology and Automation (TEMA), Department of Mechanical Engineering, University of Aveiro, Aveiro, Portugal
[e] Intelligent Systems Associate Laboratory (LASI), Guimarães, Portugal
[f] Department of Electrical and Electronics Engineering, Birla Institute of Technology & Science Pilani K K Birla Goa Campus, Goa, India
[g] International Iberian Nanotechnology Laboratory (INL), Braga, Portugal
[h] Instituto de Investigación en Ingeniería de Aragón (i3A), Universidad de Zaragoza, Zaragoza, Spain
[i] School of Engineering and Materials Science, Queen Mary University of London, London, UK

ARTICLE INFO

Keywords:
PVDF
Piezoelectric actuator
Ionic actuator
Electromechanical response
Haptic feedback

ABSTRACT

Electroactive polymers have received substantial attention for actuation because of their muscle-like actuation behaviour. These polymers are typically studied under ionic and electric classes based on their fundamental response mechanisms. In this study, a hybrid piezo-ionic actuator is developed and characterised by its electromechanical response to analyse the piezo-ionic synergistic effect in a cantilever beam actuation design. The piezo-ionic actuator was developed using polyvinylidene fluoride (PVDF) combined with an [Pmim][TFSI] ionic liquid (IL) filler. The addition of IL into the PVDF network promotes the formation of electroactive phases (β and γ), consequently enhancing the electromechanical response of PVDF while maintaining the characteristic fast response time of piezo materials. The IL also plasticize the PVDF polymer and increases its conductivity which also causes the electrical parameters to vary with frequency. It results in higher dielectric loss, energy storage and hysteresis in PVDF/IL responses. To evaluate the actuator performance, the force generated by the hybrid actuator is measured and a finger sleeve is designed for haptic feedback analysis.

1. Introduction

Electroactive polymers capable of converting electrical energy into mechanical motion and vice versa [1], have received substantial attention for their applications across different sectors, including industry [2] and healthcare [3]. The soft nature of these polymers makes them ideal for lightweight actuation while offering straightforward and flexible design options [4]; although with limited output force [5,6]. These polymers are commonly classified into ionic and electric types based on their response mechanism [7]. In ionic actuators, the actuation response is caused by the displacement of ions within the polymer, typically requiring low voltages to trigger a mechanical response. In contrast, electric actuators respond to the electrical stimuli through the polarization of dipoles [8]. Ionic actuators are known for their slower response time and relatively lower force output, which can constrain their use in applications where minimal force is sufficient. For example, Heydt. et al. [9] and Ren et al. [10], used ionic actuators in the development of refreshable Braille display, and Hardy et al. demonstrated their application in drug delivery systems [11].

Piezoelectric materials, categorised under electric actuators, employ the converse piezoelectric effect, to alter their shape in response to electrical stimuli. Piezoelectric polymers, such as polyvinylidene fluoride (PVDF) known for its high piezoelectric constant among the polymers [12], demonstrate lower displacement when compared to ionic-based polymers [13,14,15]. However, their response is quicker, making the piezoelectric actuators ideal for high frequency and precision positioning tasks [16]. For example, it has been used in bimorph actuators for laser scanning actuation at high frequencies [17], ideal for high-speed manipulation as well as in haptics [18], and touch displays [19]). The actuation performance of PVDF is influenced directly by the presence of electroactive phases (β and γ), which are typically minimal in pure states [20]. These phases can be enhanced through a phase

* Corresponding author at: Department of Bioengineering, Imperial College London, London, UK.
E-mail address: m.taghavi@imperial.ac.uk (M. Taghavi).

https://doi.org/10.1016/j.sna.2024.116038
Received 24 August 2024; Received in revised form 21 October 2024; Accepted 6 November 2024
Available online 22 November 2024
0924-4247/© 2024 The Author(s). Published by Elsevier B.V. This is an open access article under the CC BY license (http://creativecommons.org/licenses/by/4.0/).

transition, solvent casting, the addition of nucleating fillers or the development of new PVDF copolymers [21]. The incorporation of ionic liquid as nucleating fillers to enhance piezoelectricity has received interest, with studies comparing different types of ionic liquids in the composition [22,23,24], the porosity of the polymer [25], and embedded electrodes [26]. The inclusion of IL in the PVDF network can potentially have a synergistic effect on the actuation mechanism benefiting from both ionic and piezoelectric actuation principles. First, ionic liquids act as a plasticizer in the network, reducing Young's modulus of the actuator [22,27], thus enabling larger deformation for these actuators. Second, the inclusion of ionic liquids allows for ionic mobility and conductivity in the composite, decreasing the actuation voltage when compared to pure piezoelectric materials. The actuation behaviour of these hybrid piezo-ionic actuators, along with their hysteresis and durability, has not yet been thoroughly investigated. They are influenced by various factors, including the type of ionic liquids in the polymeric network, electrode composition, and fabrication parameters such as solvent and curing process. This work aims to address this gap by investigating the electromechanical properties and actuation performance of a PVDF-IL composite (Fig. 1) for potential haptic applications. Our material development process involves optimizing the fabrication process with a non-toxic solvent, dimethylsulfoxide (DMSO), and leveraging the thermoplasticity of the film for a straightforward heat-transfer printing technique to embed electrodes. We have based our studies on the 1-Methyl-3-propylimidazolium bis(trifluoromethylsulfonyl)imide ([PMIM][TFSI]) as the ionic liquid, which has been reported to significantly increase the crystallization of electroactive phases of PVDF, among various cations and anions studied [22,23]. Our mechanical characterization shows that this reduces the Young's modulus of the films by approximately tenfold compared to pure PVDF, confirming the plasticizing effect of IL [27], with the mean Young modulus of 144 MPa and a yield stress of σ_{Yield}=9 MPa.

2. Materials and methods

2.1. Actuation development

The PVDF/IL material was developed using a PVDF powder (Solef 6020 by SolvayLda), an ionic liquid(IL)(1-Methyl-3-propylimidazoliumbis (trifluoromethylsulfonyl)imide, [PMIM][TFSI], ≥ 99 %) from IoliTec-Ionic GmbH, and a polar non-toxic solvent to dissolve and mix PVDF with the IL, dimethylsulfoxide (DMSO, 99.9+% ACS) from Thermo Fisher Scientific.

The PVDF/IL films were prepared using the protocol outlined by André et al. [27]. First, DMSO and IL were mixed and after achieving a homogeneous mixture, PVDF was added to the solution. The ratio between the materials is 40 % w/w IL/PVDF and 12/88 % w/w PVDF/DMSO. The solution in a sealed beaker was stirred within a thermal bath maintained at 50ºC. Once a transparent and homogeneous solution was achieved, the mixture was poured onto a glass substrate. The wet film thickness was defined as 0.6 mm through the doctor blade technique (using an applicator, Proceq ZUA 2000). For total solvent evaporation, the wet film was taken into the oven, set at 85ºC to avoid the formation of pores [28], and to allow a better piezoelectric β phase crystallization [29]. Fig. 2a provides a schematic representation summarizing this fabrication process.

For voltage application, thin gold leaf sheets were laminated on both faces of the samples using a hot-press printing technique. PVDF/IL films were sandwiched between the gold sheets on the top and the bottom faces and compressed at 180ºC for 45 seconds (Fig. 2b). Fig. 2c shows the PVDF/IL film (with a thickness of 0.06 mm) both before and after the gold lamination step.

2.2. Electrical characterization

The capacitance (C) and ohmic resistance (R) of the PVDF/IL film were measured using an LCR meter (Agilent E4980A) across a frequency range of 20 Hz to 2 MHz and a voltage intensity (V_{AC}) of 1 V. Circular electrodes with a diameter of 5.3 mm were used on both faces of the samples for the measurements. Based on these results, we determined the real part of the relative permittivity (ε') using $\varepsilon' = \frac{C \cdot d}{\varepsilon_0 \cdot A}$ and AC conductivity (σ_{AC}) using $\sigma_{AC} = \frac{d}{R \cdot A}$ where d represents the thickness of the samples, ε_0 stands for the permittivity of vacuum (8.85×10^{-12} F/m) and A denotes the electrode area.

2.3. Electromechanical analysis

The piezoelectric constant (d_{33}) of the PVDF/IL composite was determined using the piezoresponse force microscopy (PFM) technique. Local piezoresponse and polarization switching spectroscopy of the PVDF/IL film were conducted with a commercial scanning probe microscope (Veeco Multimode Nanoscope IV microscope, Houghton, MI, USA). A conductive probe (NSG10/Pt, NT-MDT) with a spring constant of 14 N/m was used and the piezoresponse force microscopy out-of-plane images were scanned in the single frequency mode at 7.5 V and with a frequency of 35 kHz.

We studied the electromechanical responses of the PVDF/IL film samples cut in a rectangular shape (6×30 mm^2). The samples were displaced vertically in a cantilever beam configuration, constrained at the top end and free at the bottom end, where a laser was pointed for the measurements. For sinusoidal stimulations, we used input signals with frequencies of 0.11, 0.2, 1.1 and 2 Hz and voltages of 5, 10, 15 and 20 V_{pp} for the duration of 90 seconds. Actuation signals were generated by a function generator (Multicomp Pro MP750064) and the resultant

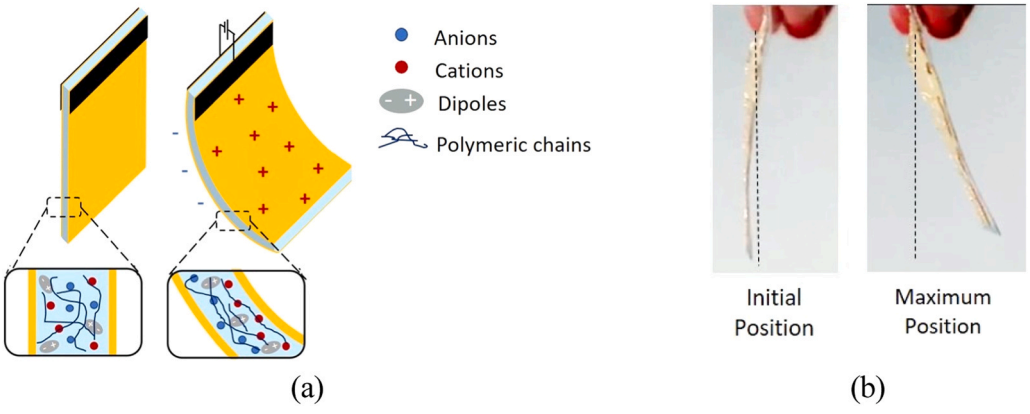

Fig. 1. The PVDF-IL film sandwiched between electrodes: (a) Schematic representing the actuation mechanism; (b) Movement of the sample under applied voltage (10 V, 0.05 Hz).

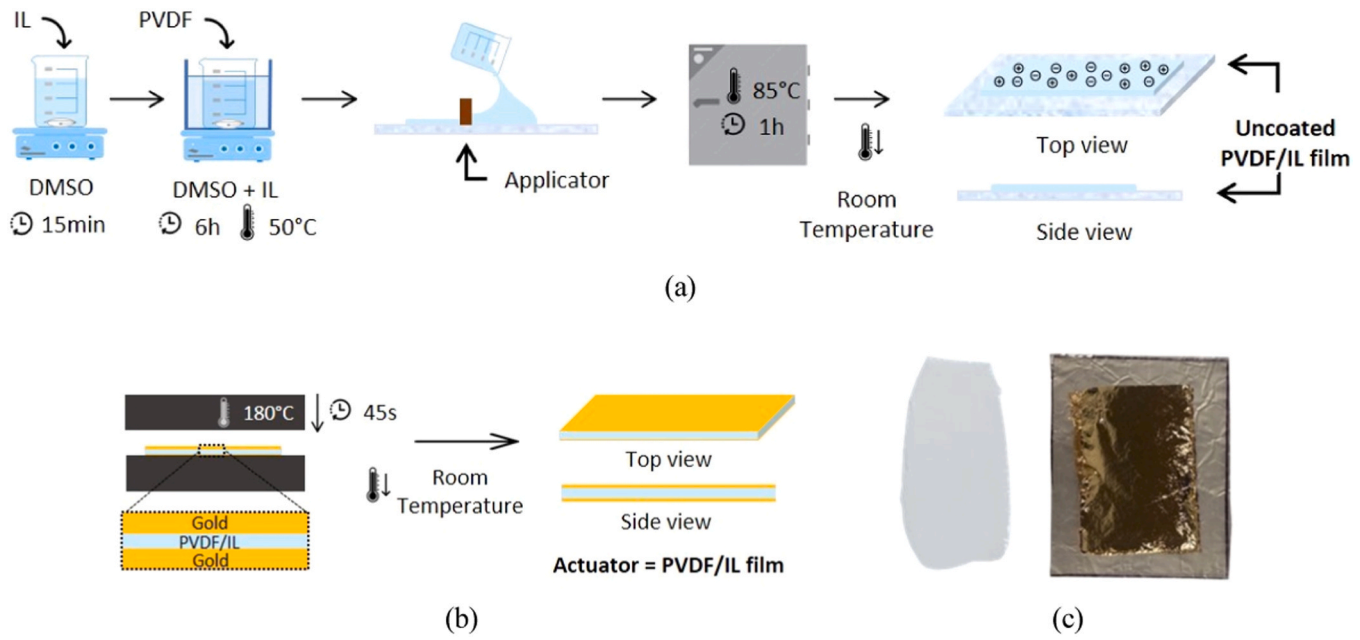

Fig. 2. Fabrication process: (a) Schematic illustration of PVDF/IL film development; (b) Gold-layer heat printing; (c) Photograph showing the uncoated sample (left) and gold-coated sample (right).

displacement was measured using a laser displacement meter (controller Keyence LK-G3001P + laser Keyence LK-G152) directed to the tip of the samples. Each PVDF/IL sample was tested once for a set of frequency and voltage. For analysis at 20 V, the mean of two sample measurements was used for each frequency due to higher movement variance in this voltage. We considered the first 15 peaks of each trial for the mean sine displacement ± standard deviation (STD) analysis, excluding the first and last peaks to ensure movement stability. The displacement at each peak (crest or trough) was regarded as the peak-to-peak amplitude.

We investigated the active displacement of the samples with a single square pulse per duration of 1, 5 and 10 seconds. Each pulse duration was applied at least 5 minutes apart to ensure complete relaxation of the samples, while the voltage amplitude was maintained at 10 V. This also includes phased displacement analysis, which reflects out-of-phase rising or relaxation of the samples. Each case was tested with 5 pulses.

The rising speed, from the time of pulse application to the moment of maximum displacement within the pulse duration, and the relaxation speed, calculated from the end of the pulse to the minimum position of the samples, were investigated at different pulse amplitudes (2.5, 5, 7.5 and 10 V). These signals were applied to 3 samples in single pulses lasting for 1 s each. Additionally, the reversal motion speed was determined by applying a bipolar square pulse 9 times, distributed across 3 samples with at least 5-minute intervals between each pulse. This measurement indicates how quickly the sample returns to its initial position after the polarity of the signal is inverted. The square waves had a period (T) of 2 s and a voltage amplitude of 20 V_{pp}.

To investigate the performance of the samples under continuous cyclic stimulation, we applied periodic sine waveforms at 0.2 Hz and input voltages of 10 V_{pp} to the actuators for 25 minutes.

The actuation force was investigated using a setup where the actuators displaced against a compression spring with a spring constant of k = 0.0294 N/mm (5055, Misumi) during the first half of the biphasic square pulse. A total of 9 pulses, each with a voltage of 20 V_{pp} and a period (T) of 2 were applied. The contact force between the actuator and spring is equal to the compression force of the spring, which is directly proportional to the decrease in length of the spring (x) in Hooke's law: $F = -k \cdot x$

All data was collected using a data acquisition device (National Instruments USB-6001) and subsequently processed in MATLAB.

3. Results and discussion

Fig. 3a shows the real part of the relative permittivity (ε') and conductivity σ_{AC} measured for the PVDF-IL film. The data shows that ε' decreases with the frequency, from $1.83x10^{3}$±156.96 to 2.91±0.11, while the electrical conductivity (σ_{AC}), increases with frequency from.$86x10^{-6}$±$2.37x10^{-7}$ S/m to $2.50x10^{-4}$±$5.80x10^{-6}$ S/m. These trends are consistent with those reported in the literature for hybrid piezo-ionic materials [22,30]. This behaviour is attributed to the presence of IL in the polymeric matrix. In contrast, pure PVDF does not exhibit such frequency dependence with σ_{AC} remaining at 1.61×10^{-08} S/m and ε' at 10, considering a frequency range of 100 Hz - 1 MHz [22]. Higher values of σ_{AC} represent higher electrical losses in the piezoelectric film, while higher values of ε' indicate the material's enhanced capability to store electrical energy [31].

Fig. 3b shows the topography of the PVDF/IL film obtained from the scanning of the surface, showing an average roughness of ≈120 nm. This measurement employs the standard contact mode atomic force microscopy (AFM) to reveal the topography of the samples. In comparison, the pure PVDF films show a lower average roughness of around 30 nm (see supplementary figure 1a). The increased roughness in the PVDF/IL films can be attributed to the incorporation of the ionic liquid, which induces greater surface irregularities Moreover, we conducted PFM measurements to evaluate the local piezoelectric response of the PVDF/IL and PVDF sample. This technique is based on the standard contact mode AFM setup, in which the cantilever and the tip are electrically conductive, and an alternating voltage is applied to the tip, evaluating the electromechanical properties in addition to the sample topography. Fig. 3c shows the nanoscale topography of the PVDF/IL film through the PFM technique, with the correspondng topography for the pure PVDF samples shown in supplementary figure 1b. Moreover, Figs. 3d and 3e show out-of-plane amplitude and phase images, respectively for PVDF/IL samples, with the corresponding images for pure PVDF provided in the supplementary figure 1c. These images were obtained over a scan area of 20×20 μm in the virgin state of the film. The PFM amplitude represents the piezoelectric displacement of the sample when subjected to an AC voltage, while the PFM phase specifies the orientation of polarization. The observed weak contrast regions suggest a low piezoelectric response, possibly due to the lack of the polar β phase in the

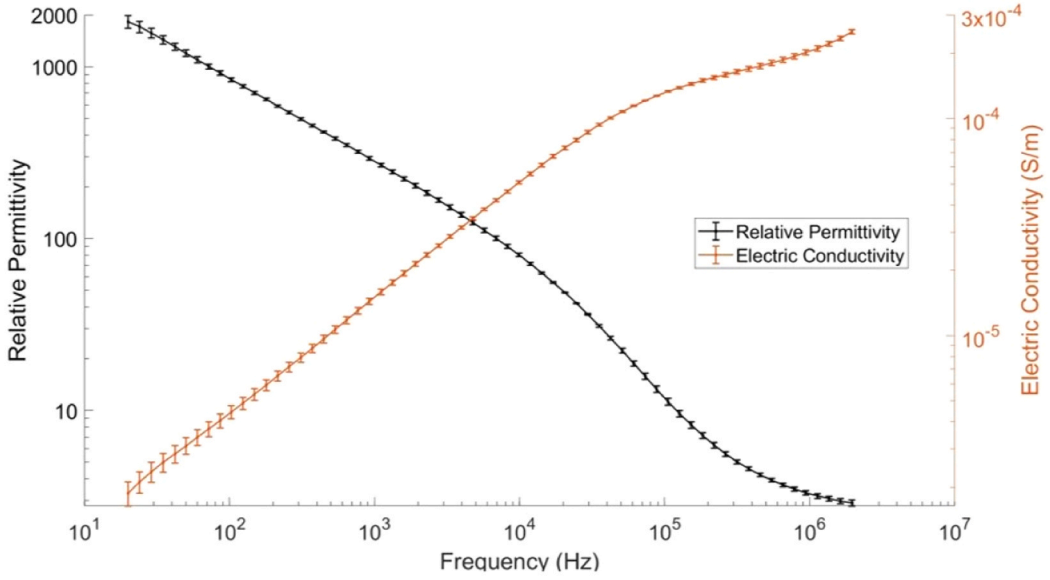

(a)

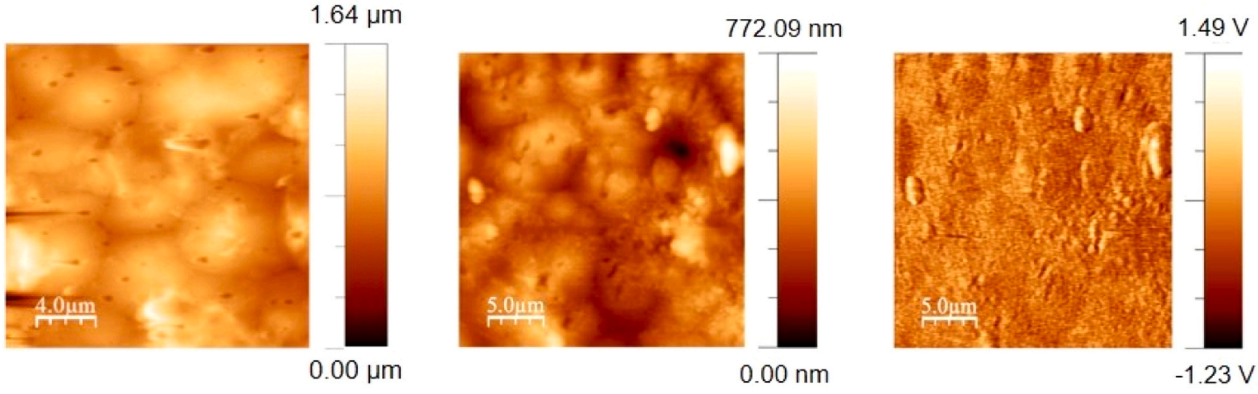

(b) (c) (d)

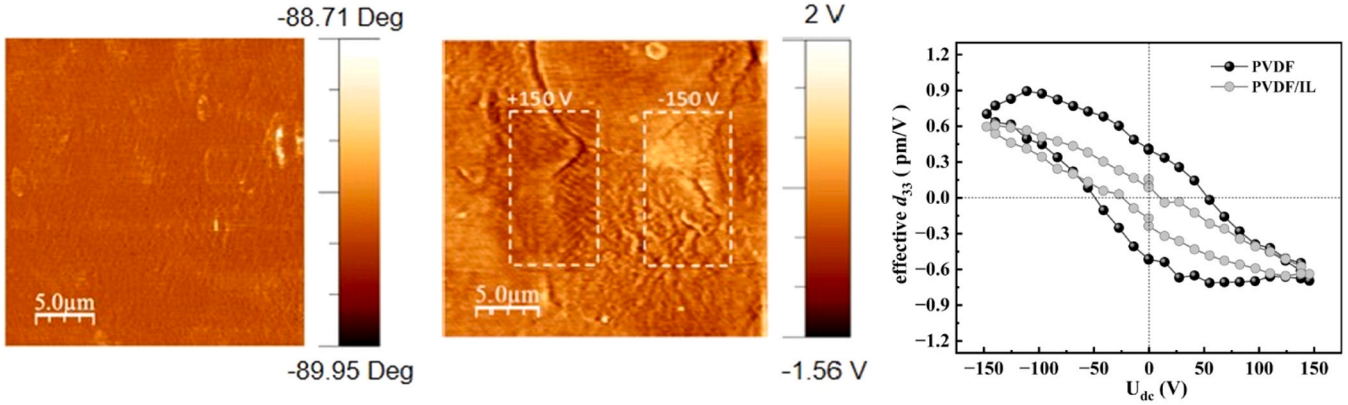

(e) (f) (g)

Fig. 3. Electrical and piezoelectric characterization: (a) Relative permittivity and electric conductivity of the PVDF/IL actuators as a function of frequency; (b) AFM topography image of the PVDF/IL film; (c) PFM Topography; (d) Out-of-plane amplitude (A*cosθ); (e) Out-of-plane phase images; (f) PFM amplitude image after applying ±150 V to create artificial domains; and (g) Piezoresponse hysteresis loop obtained by PFM. Error bars in the first figure represent the standard deviation of relative permittivity (black line) and electric conductivity (orange line).

scanned region. Further investigations were performed by applying a DC bias voltage of ±150 V to the tip, effectively inducing microscale tip-induced poling as a means of artificially writing domains. As seen in Fig. 3f, opposite bright and dark contrasts were observed, though with some instability which can be attributed to the higher conductivity of these films. This becomes more apparent when compared to the results for pure PVDF samples, as shown in the supplementary figure 1d.

To further study the local piezoelectric response behaviour, we investigated the hysteresis loops on the PVDF/IL and pure PVDF films (Fig. 3g) using a cantilever tip. These loops were obtained in pulse mode by sweeping the DC bias voltage (U_{dc}) between ±150 V. The results confirm a negligible difference in the ferroelectric characteristics of the film at the nanoscale, with coercive voltages of 55 V for PVDF and 25 V for PVDF/IL, respectively. This reflects only a marginal variation in the d_{33} coefficient values, approximately 0.8 pm/V for PVDF and 0.6 pm/V for PVDF/IL.

Infrared spectroscopy also confirms that the presence of IL leads to a higher percentage of electroactive phase. Supplementary figure 2 shows the FTIR-ATR analysis of PVDF samples with and without IL. Despite similar transmittance (%T) values at 840 cm^{-1} (corresponding to EA phases), a more subtle peak at 766 cm^{-1} (typical of non-EA phases) suggests a higher EA phase content: 80 % in PVDF/IL samples compared to 69 % in PVDF samples, as determined by Beer- Lambert law.

The experimental setup used to characterise the displacement of the

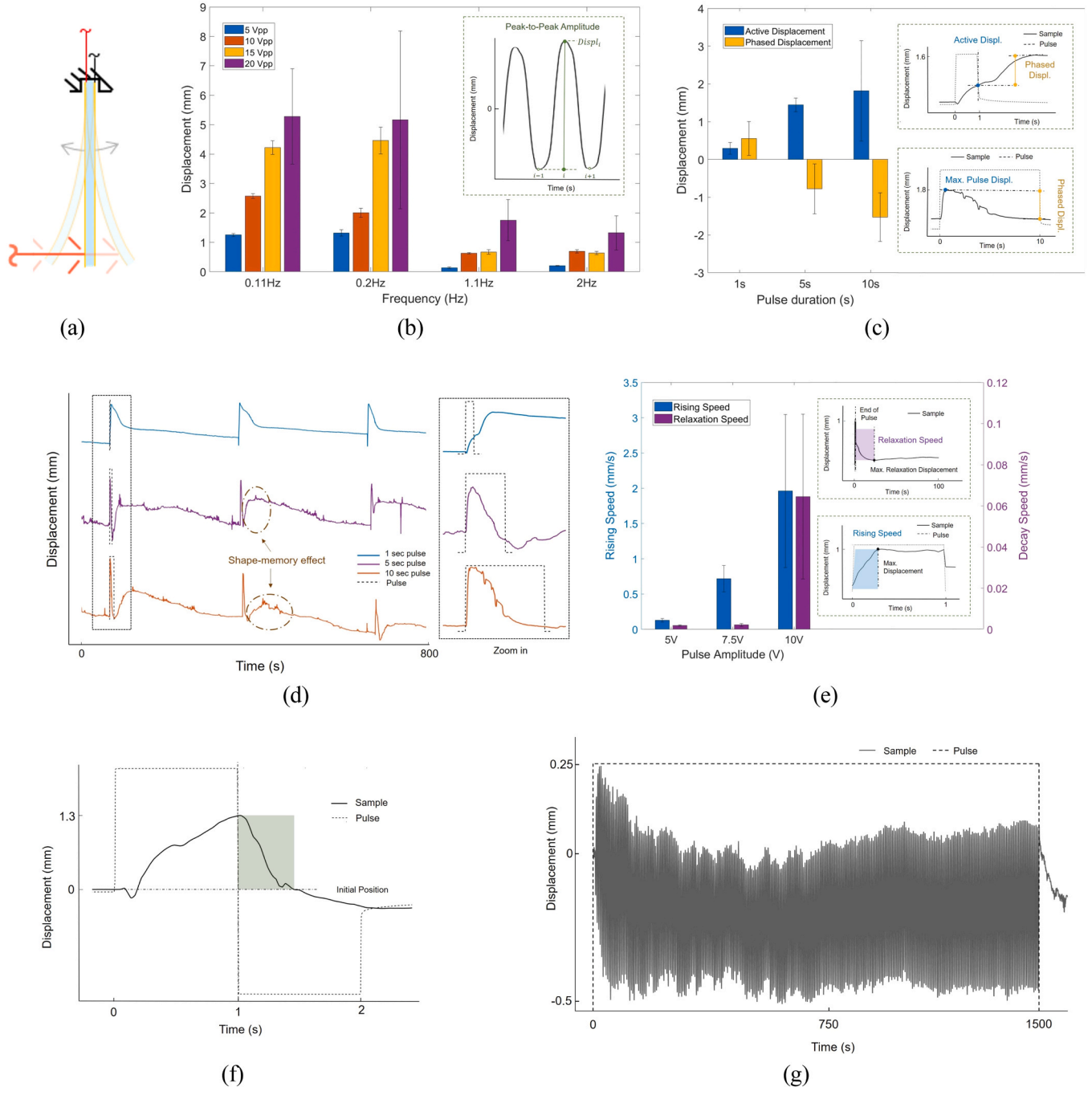

Fig. 4. Electromechanical analysis of the PVDF/IL cantilever beam: (a) Experimental setup; (b) Displacement for sinusoidal input; (c) Displacement for different pulse durations, highlighting active and phased displacements; (d) Typical displacement behavior for square pulses; (e) Rising and relaxation speeds; (f) Reversal motion speed with bipolar pulse stimulation; (g) Cyclic test with a sine wave.

PVDF-IL samples is shown in Fig. 4a. Fig. 4b shows the mean sinusoidal displacement results, investigating the effect of altering input voltage and frequency. In general, higher voltages result in greater peak displacements across all tested frequencies. This is because higher voltages induce stronger polarization, leading to increased displacement, where lower frequencies allow the samples sufficient time to respond due to their relatively slower motion. However, the peak displacement at 20 V_{pp} decreases at higher frequencies because faster frequency induces more rapid polarization changes, limiting the sample's response. Supplementary Videos S1 and S2 show typical displacements for high and low frequencies, 2 Hz and 0.02 Hz, respectively, while actuating with 15 V.

Supplementary material related to this article can be found online at doi:10.1016/j.sna.2024.116038.

A comparison of the electromechanical response of our IL/PVDF film with other PVDF-based piezoelectric actuators with a high electroactive phase, highlights the role of IL in reducing the required input voltage for achieving greater displacement. For example, in a previously published study [18] involving P(VDF-TrFE) copolymer with similar dimensions (25×5 mm) and thickness (≈50 μm) subjected to a comparable frequency (≈1 Hz), a displacement of 0.8 mm was achieved with a sinusoidal input. In contrast, our IL/PVDF film achieved a displacement of 0.67 mm, but required a much lower electric field (0.25 MV m^{-1} compared to 50 MV m^{-1} in the P(VDF-TrFE) study) to achieve comparable displacement performance.

Fig. 4c shows the displacement response of the film under pulse input. It shows active displacement, denoted as the highest displacement achieved by the sample during the pulse, and phased displacement, denoted as the rising displacement after the end of the pulse (as a positive displacement) or the relax- ing displacement during the pulse after the maximum position (as a negative displacement). The results show greater active displacements for higher pulse duration. Exposing the soft actuators to different pulse durations leads to distinct behaviours: with shorter pulse durations (e.g. 1 s), the samples continued to rise after the end of the pulse, achieving a post-pulsed displacement higher than the one achieved during the pulse - see the top inset graph from the typical displacement result in shorter pulse duration. This could be attributed to the presence of IL in the PVDF network, partially through increasing hysteresis [32], which is associated with response delay and remnant polarization [33]. Moreover, it boosts ε' leading to increased energy storage during the pulse duration [31].

In contrast, longer pulse durations lead to a decrease of displacement immediately after reaching the maximum active displacement (Fig. 4c, bottom inset). In this study, the loss increases with the pulse duration. The observed negative phased displacement could be attributed to the dielectric loss, wherein the polarization can not be sustained. The presence of IL amplifies this dielectric loss, since the σ_{AC} increases with its addition and it is related to low IL density [22]. Moreover, compared to other phases (such as α), the β phase is associated with greater dielectric loss [34]. Fig. 4d compares the displacement behaviour of three different samples when subjected to different pulse durations with all data filtered to minimise noise. The comparison between raw and filtered curves is detailed in the supplementary material (supplementary figure 3).

For the 5 s and 10 s pulses, a different phenomenon is observed. After the end of the pulse, and the relaxation of the actuators, they show a secondary rise to a new peak before gradually returning to their initial position. This effect is known as the memory effect which can be attributed to the presence of IL that cross-links PVDF [35]. Moreover, the Joule effect provides a complementary explanation, as it leads to an increase in the internal temperature of the samples when current is passing through the film. Therefore, after the pulse, the temperature gradually decreases, which prevents a rapid return to the initial position [36].

Fig. 4e shows the rising and relaxation speeds for pulse amplitudes of 5, 7.5 and 10 V. We did not observe a noticeable response for 2.5 V. Supplementary figure 4 presents the original and filtered curves for each case. Both rising and relaxation speeds show an increase in pulse intensity, which is related to higher polarization. While 10 V pulse resulted in higher rising and relaxation speeds, it also showed higher standard deviation values. Particularly, at 7.5 V, the relaxation speed is notably lower than the rising speed. This disparity is attributed to the positive phase displacement occurring after the pulse ends, which delays the relaxation speed. In such cases, the relaxation speed was calculated by identifying the minimum decay position following this positive phased displacement (supplementary figure 5). When employing a negative pulse to instantly reverse the actuation, as shown in Fig. 4f, the reversal motion speed showed a faster and consistent response of 9.39 ±2.06 mm/s. This suggests that bipolar square pulses could serve as a viable option to ensure a consistent relaxation response for practical applications such as haptic feedback devices.

Fig. 4g shows the results of the cyclic test conducted to evaluate actuation stability under continuous sinusoidal input. This shows no significant deterioration in peak-to-peak amplitude during 300 cycles of a sine wave input at a voltage amplitude of 10 V_{pp} and a frequency of 0.2 Hz.

To quantify the generated force (Figs. 5a and 5b) our experiments showed that the PVDF/IL can compress the spring by 0.31±0.11 mm, which corresponds to 11±3 mN according to the Hooke law. It falls within the typical threshold values for cutaneous touch perception (10–100 mN) as reported by [37], demonstrating its potential use for haptic feedback, especially considering its relatively quicker actuation response compared to the ionic actuators.

3.1. Finger sleeve design

Figs. 5c and 5d show the initial design and prototype of the finger sleeve to assess haptic feedback. The sleeve is 3D printed with a flexible thermoplastic polyurethane filament, incorporating two IL/PVDF cantilever beams for force feedback. These actuators are positioned equidistantly from the finger's center, enabling simultaneous and independent feedback application on both sides. This setup offers the flexibility of applying distinct inputs to each side of the finger (left and right). The supplementary Video S3 showcases the prototype in operation, demonstrating its response to a sine input wave. A comprehensive user study will be carried out to evaluate the detectability of the applied force in different scenarios.

Supplementary material related to this article can be found online at doi:10.1016/j.sna.2024.116038.

4. Conclusions and future works

The present study provides a critical analysis of the electromechanical response of a hybrid piezoelectric-ionic film for potential haptic feedback. The inclusion of ionic liquid into the PVDF network offers several advantages: Firstly, it enhances the electroactive phase during the polymerisation process, thereby boosting the piezoelectric effect, as observed in our sinusoidal displacement studies. Additionally, the addition of the IL reduces the required input actuation voltage, although it becomes prone to failure at voltages higher than 20 V peak to peak. The addition of IL also lowers the Young's modulus of the actuator, resulting in greater displacement. The addition of ionic liquid also causes the electrical parameters, σ_{AC} and ε', to vary significantly with frequency, which leads to higher dielectric loss and energy storage at specific frequencies. Moreover, it increases hysteresis in PVDF/IL piezoelectric responses. These effects result in phased displacement, which could make the control of these hybrid actuators more challenging. Nevertheless, using a shorter input pulse with reversed pulsing for active relaxation can offer a more stable solution.

Further studies on the type of ionic liquid and optimization of the structure and fabrication process are necessary to fully comprehend their electromechanical effect in the hybrid design for optimising

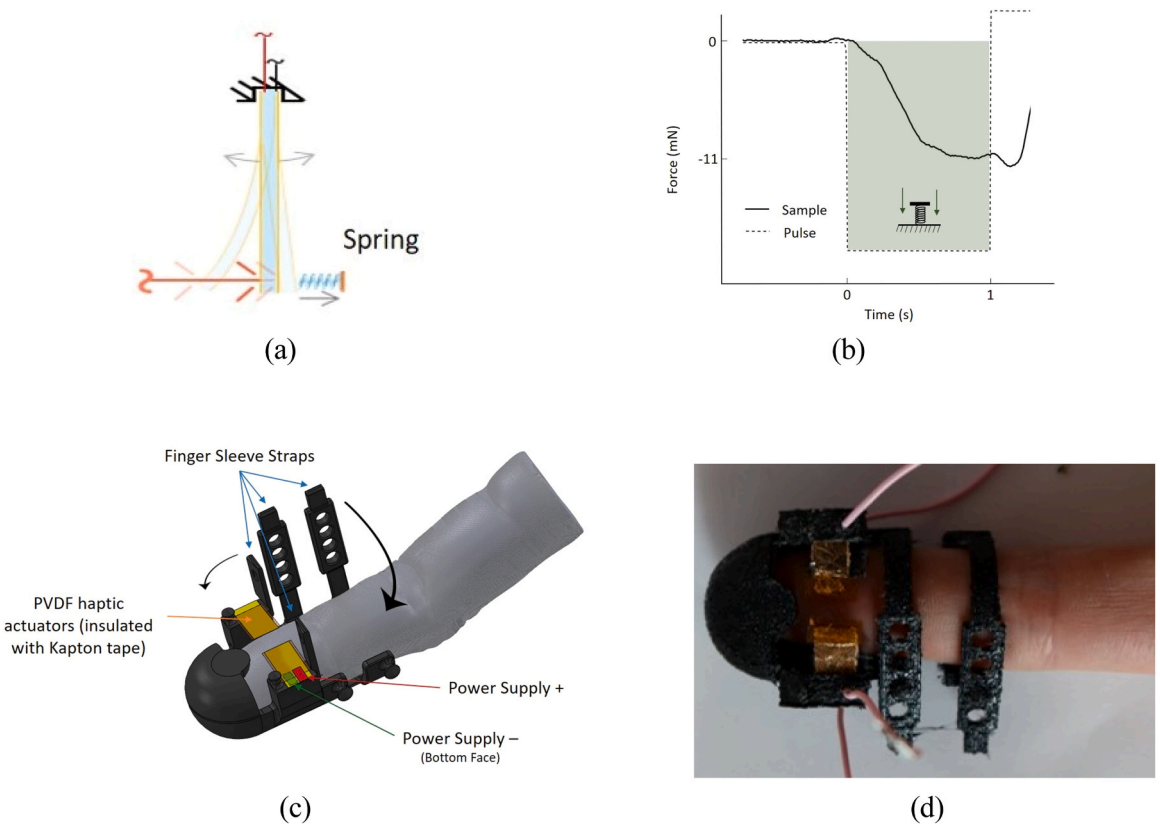

Fig. 5. Force measurement for haptic feedback: (a) Set-up for force measurement; (b) Force result achieved from the compression of the spring. (c) Finger sleeve design; (d) Photo of the fabricated sleeve.

actuation performance. Furthermore, user-studies are essential to assess the feasibility of using this technology for haptic feedback.

CRediT authorship contribution statement

Rui M.R. Pinto: Writing – review & editing, Investigation. **K.B. Vinayakumar:** Writing – review & editing, Investigation. **António Diogo André:** Writing – review & editing, Writing – original draft, Methodology, Investigation, Formal analysis, Conceptualization. **Igor Bdikin:** Writing – original draft, Writing - review & editing, Investigation. **Indrani Coondoo:** Writing – review & editing, Investigation. **Majid Taghavi:** Writing – review & editing, Supervision, Resources, Methodology, Investigation, Conceptualization. **Pedro Martins:** Writing – review & editing, Resources, Investigation, Conceptualization.

Declaration of Competing Interest

The authors declare that they have no known competing financial interests or personal relationships that could have appeared to influence the work reported in this paper.

Acknowledgements

Antoónio Diogo André (A.D.A) gratefully acknowledges funding from FCT, Portugal, under grant SFRH/BD/147807/2019 (https://doi.org/10.54499/SFRH/BD/147807/2019) and from European Union (UE) under Erasmus+ 2019 Credit Mobility project (2019–1-PT01-KA103–060090) and WORK4ALL 3 project (2020–1-PT01-KA103–077725). Pedro Martins (P.M.) gratefully acknowledges funding from project UIDB/50022/2020 financed by FCT, through INEGI, under LAETA. Indrani Coondoo (I.C.) and Igor Bdikin (I.B) acknowledge funding through the FCT project "MultiFlex" EXPL/CTM-CTM/0687/2021 (http://doi.org/10.54499/EXPL/CTM-CTM/0687/2021). I. C. would also like to acknowledge financial assistance by national funds (OE), through FCT, I.P., Portugal through DL57/2016/CP1482/CT0048 (https://doi.org/10.54499/DL57/2016/CP1482/CT0048). I.B. also acknowledges the Project "Agenda ILLIANCE" [C644919832–00000035 — Project no. 46], financed by PRR – Recovery and Resilience Plan under the Next Generation EU from the European Union. Majid Taghavi (M.T.) acknowledges Imperial College Research Fellowship.

Appendix A. Supporting information

Supplementary data associated with this article can be found in the online version at doi:10.1016/j.sna.2024.116038.

Data Availability

Data supporting this study are openly available from Zenodo at https://doi.org/10.5281/zenodo.14052677

References

[1] Jimin Gu Junseong Ahn, Chankyu Han Jungrak Choi, Jaeho Park Yongrok Jeong, Yong Suk Oh Seokjoo Cho, Morteza Amjadi Jun-Ho Jeong, Inkyu Park, A review of recent advances in electrically driven polymer- based flexible actuators: smart materials, structures, and their applications, Adv. Mater. Technol. 7 (11) (2022).
[2] Vivek Mishra, Shubham Pandey, Simran Aggarwal, Electroactive Polymers in Industry, CRC Press, March, 2022, pp. 271–298.
[3] Siegfried Bauer, Electroactive polymers for healthcare and biomedical applications. Yoseph Bar-Cohen, editor, Electroactive Polymer Actuators and Devices (EAPAD), SPIE, 2017, p. 2017.
[4] António Diogo Andé, Pedro Martins, Exo supportive devices: summary of technical aspects, Bioengineering 10 (11) (2023) 1328.
[5] Yang Cao, Jingyan Dong, Fabrication and self-sensing control of soft electrothermal actuator, Procedia Manuf. 48 (2020) 43–48.

[6] Terence Yan King Ho Ankit, Nirmal Amoolya, Rameshchandra Kulkarni Mohit, Dino Accoto, Mathews Nripan, Soft actuator materials for electrically driven haptic interfaces, Adv. Intell. Syst. 4 (2) (2021).
[7] Yoseph Bar-Cohen, 2004, Actuators as Artificial Muscles: Reality, Potential, and Challenges, Second Edition (SPIE Press Monograph Vol. PM136). SPIE Publications, 2004.
[8] Yoseph Bar-Cohen, Iain A. Anderson, Electroactive polymer (eap) actuators—background review. Mech. Soft Mater. 1 (1) (2019).
[9] R. Heydt Refreshable braille display based on electroactive polymers. 2003.
[10] Kailiang Ren, Sheng Liu, Minren Lin, Yong Wang, Q.M. Zhang, A compact electroactive polymer actuator suitable for refreshable braille dis- play, Sens. Actuators A: Phys. 143 (2) (May 2008) 335–342.
[11] John G. Hardy, David J. Mouser, Netzahualcóyotl Arroyo-Currás, et al., Biodegradable electroactive polymers for electrochemically- triggered drug delivery, J. Mater. Chem. B 2 (39) (2014) 6809–6822.
[12] N. Soin, D. Boyer, K. Prashanthi, S. Sharma, A.A. Narasimulu, J. Luo, T.H. Shah, E. Siores, T. Thundat, Exclusive self-aligned β-phase pvdf films with abnormal piezoelectric coefficient prepared via phase inversion, Chem. Commun. 51 (39) (2015) 8257–8260.
[13] Kie Yong Cho, Hyunchul Park, Hyun-Ji Kim, Xuan Huy Do, Chong Min Koo, Seung Sang Hwang, Ho Gyu Yoon, Kyung-Youl Baek, Highly enhanced electromechanical properties of pvdf-trfe/swcnt nanocompos- ites using an efficient polymer compatibilizer, 21–29, mar, Compos. Sci. Technol. 157 (2018), 21–29, mar.
[14] Juliana C. Dias, Daniela M. Correia, Carlos M. Costa, Clarisse Ribeiro, Alberto Maceiras, José L. Vilas, Gabriela Botelho, Verónica de Zea Bermudez, Senentxu Lanceros-Mendez, Improved response of ionic liquid-based bending actuators by tailored interaction with the polar fluorinated polymer matrix, Electrochim. Acta 296 (2019) 598–607.
[15] Sheng Liu, Yang Liu, Hulya Cebeci, Roberto Guzmán de Villoria, Jun-Hong Lin, Brian L. Wardle, Q.M. Zhang, High electromechanical response of ionic polymer actuators with controlled-morphology aligned carbon nan- otube/nafion nanocomposite electrodes, Adv. Funct. Mater. 20 (19) (2010) 3266–3271.
[16] Junkao Liu Xuefeng Ma, Jie Deng Shijing Zhang, Yingxiang Liu, Recent trends in bionic stepping piezoelectric actuators for precision positioning: a review. Sens. Actuators A: Phys. 364 (2023) 114830.
[17] Miroslav Král Ricardo Perez, Hannes Bleuler, Study of polyvinylidene fluoride (pvdf) based bimorph actuators for laser scanning actuation at khz frequency range, Sens. Actuators A: Phys. 183 (2012) 84–94.
[18] Tomohito Sekine Yoshinori Shouji, Naoya Ito Keita Ito, Yi-Fei Wang Tatsuya Yasuda, Daisuke Kumaki Yasunori Takeda, Atsushi Miyabo Fabrice Domingues Dos Santos, Fast Shizuo Tokito, response, high-power tunable ultrathin soft actuator by functional piezoelectric material composite for haptic device application. Adv. Electron. Mater. 9 (9) (2023).
[19] Enes Selman Ege, Abdulkadir Balikci, Transparent localized haptics: Utilization of pvdf actuators on touch displays, Actuators 12 (7) (2023) 289.
[20] Fawad Ali, Muammer Koc, 3d printed polymer piezoelectric materials: Transforming healthcare through biomedical applications, Polymers 15 (23) (2023) 4470.
[21] Liuxia Ruan, Xiannian Yao, Yufang Chang, Lianqun Zhou, Gaowu Qin, Xianmin Zhang, Properties and applications of the phase poly(vinylidene fluoride). Polymers 10 (3) (2018) 228.
[22] D.M. Correia, J.C. Barbosa, C.M. Costa, P.M. Reis, J.M.S. Esperança, V. de Zea Bermudez, S. Lanceros-Méndez, Ionic liquid cation size-dependent electromechanical response of ionic liquid/poly(vinylidene fluoride)-based soft actuators, J. Phys. Chem. C. 123 (20) (2019) 12744–12752.
[23] Daniela M. Correia, Carlos M. Costa, Erlantz Lizundia, Roser Sabater I Serra, José A. Gómez-Tejedor, Laura Teruel Biosca, José M. Meseguer- Dueñas, José L. Gomez Ribelles, Influence of cation and anion type on the formation of the electroactive - phase and thermal and dynamic mechanical properties of poly(vinylidene fluoride)/ionic liquids blends, J. Phys. Chem. C. 123 (45) (oct 2019) 27917–27926.
[24] R. Mejri, J.C. Dias, S. Besbes Hentati, M.S. Martins, C.M. Costa, S. Lanceros-Mendez, Effect of anion type in the performance of ionic liquid/poly(vinylidene fluoride) electromechanical actuators, J. Non-Cryst. Solids 453 (2016) 8–15.
[25] Umar Raza, Saewoong Oh, Rassoul Tabassian, Manmatha Mahato, Van Hiep Nguyen, Il-Kwon Oh, Micro-structured porous electrolytes for highly responsive ionic soft actuators, Sens. Actuat. B: Chem. 352 (2022) 131006.
[26] Tian Chen Kai Xiang, Air-working Yanni Wang, ionic soft actuator based on three-dimensional graphene electrode. Mater. Lett. 286 (2021) 129267.
[27] António Diogo André, Ana Margarida Teixeira, Pedro Martins, Influ- ence of dmso non-toxic solvent on the mechanical and chemical properties of a pvdf thin film, Appl. Sci. 14 (8) (2024).
[28] Clarisse Ribeiro, Carlos M Costa, Daniela M. Correia, João Nunes-Pereira, Juliana Oliveira, Pedro Martins, Renato Goncalves, Vanessa F Cardoso, Senentxu Lanceros-Méndez, Electroactive poly(vinylidene fluoride)-based structures for advanced applications, Nature Protocols 13 (4) (2018) 681–704.
[29] D.M. Correia, L.C. Fernandes, N. Pereira, J.C. Barbosa, J.P. Serra, R.S. Pinto, C. M. Costa, S. Lanceros-Méndez, All printed soft actuators based on ionic liquid/ polymer hybrid materials, Appl. Mater. Today 22 (March 2021) 100928.
[30] Xingang Liu, Yinghao Shang, Jihai Zhang, Chuhong Zhang, Ionic liquid-assisted 3d printing of self-polarized β-pvdf for flexible piezoelectric energy harvesting. ACS Appl. Mater. Interfaces 13 (12) (2021) 14334–14341.
[31] Arthur R. Von Hippel, Dielectrics and Waves (Artech House Microwave Library), Artech House Publishers, 1995.
[32] Runkai Zhou, et al., Effects of ionic liquid content on the electrical properties of pvdf films by fused deposition modeling, Materials 17 (1) (2023).
[33] M. Date, T. Furukawa, E. Fukada, Dipolar orientation and hysteresis in polyvinylidene fluoride, J. Appl. Phys. 51 (7) (1980) 3830–3833.
[34] Bao-Wen Li Hexing Liu, Zhonghui Shen Jiayu Chen, Jing Wang Xin Zhang, Ce-Wen Nan, Concurrent enhancement of breakdown strength and dielectric constant in poly(vinylidene fluoride) film with high energy storage density by ultraviolet irradiation, ACS Omega 7 (30) (2022) 25999–26004.
[35] Aoki Kota, Sugawara-Narutaki Ayae, Doi Yuya, Rintaro Takahashi, Structure and rheology of poly(vinylidene difluoride-co-hexafluoropropylene) in an ionic liquid: The solvent behaves as a weak cross-linker through ion–dipole interaction, Macromolecules 55 (13) (2022) 5591–5600.
[36] Gozde Aktas Eken, Metin H. Acar, Pvdf-based shape memory polymers, Eur. Polym. J. 114 (2019) 249–254.
[37] Christian Hatzfeld and Thorsten A. Kern. Engineering Haptic Devices A Beginner's Guide. Springer.

António Diogo André is currently a PhD candidate in Mechanical Engineering at the Faculty of Engineering of University of Porto (FEUP), developing his PhD project in soft piezoelectric materials under the theme "Exoskeleton for Aided-Mobility" at INEGI. During that period, he was a visiting student at Imperial College London between 2022 and 2023. He is the author and co-author of several scientific papers, abstracts in national and international conferences and chapters of books.

Indrani Coondoo is a Research Scientist at the Department of Materials and Ceramics Engineering, University of Aveiro (UA), and CICECO - Aveiro Institute of Materials. She earned her PhD from the Faculty of Technology, University of Delhi (formerly Delhi College of Engineering). Before joining UA, she worked as a postdoctoral researcher at the National Physical Laboratory, India and the University of Puerto Rico, USA. Her research focuses on engineered multifunctional materials, including ferroelectrics and piezoelectrics (polymers, ceramics, and thin films). She aims to advance materials for energy conversion, energy storage, and multi-caloric cooling applications. Additionally, she is exploring additive manufacturing (3D printing) techniques to develop materials/systems for next-generation sensors, transducers, and energy harvesters. She has authored 70 research papers in international peer-reviewed journals and has presented her work at around 50 conferences. She is also the co-inventor of a U.S. patent.

Igor Bdikin graduated in Physics from the Physics Department of the Kazan State University in 1989 and completed a PhD degree in Solid State Physics from the Institute of Solid State Physics, Russia in 1999. From 1999–2003 he worked in the Laboratory of Structural Research of the Institute of Solid State Physics, Russia as a researcher. From 2003–2009 he worked in Department of Ceramics and Glass Engineering, University of Aveiro, Portugal as a postdoctoral fellow. Since 2009 he is employed as a researcher in the Centre for Mechanical Technology Automation (TEMA) in the University of Aveiro, Portugal. His scientific activities & collaborations with several R&D groups and industries have resulted in more than 250 publications, 5 book chapters & 30 conference proceedings.

Vinaya Kumar K B earned his PhD from the Indian Institute of Science (IISc), India, where he specialized in the design and development of microsystems for a minimally invasive wearable insulin delivery system (microneedles and micropumps). In December 2015, He joined Cornell University, USA, as a Postdoctoral Associate, he made significant contributions to the field by working **on miniature ion accelerators utilizing the MEMS approach.** In July 2018 he joined INL Portugal to work on vacuum electronics, printed electronics and sensors for medical applications. Currently, he is working at BITS Pilani Goa campus as an Assistant Professor.

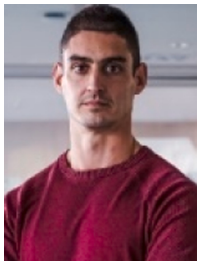

Rui M. R. Pinto is a Research Engineer at INL since 2021, where he has been involved in optimizing inkjet heads, printing processes, and gas sensing systems. He received his Ph.D. degree in biotechnology and biosciences from Instituto Superior Técnico, University of Lisbon, in 2020. His thesis was on the development of thin-film silicon MEMS for mass sensing and biosensing applications. His other interests include prototyping, micro and nanofabrication, micromechanical devices, electronic instrumentation, microscopy, surface functionalization, microfluidics, and biosensing.

Dr. Pedro Martins has researched the mechanics and structure of female soft biological tissues and medical implants since beginning his PhD in 2004. His doctoral thesis focused on the nonlinear mechanical behavior of female pelvic tissues, and he developed techniques for experimental analysis and data fitting. Collaborating with researchers from Spain and Brazil, he created models for the mechanical behavior of vaginal tissues and pelvic floor implants. He led the Biomechanics Laboratory at INEGI (Portugal) until 2022, with contributions in soft robotics and bioprinting of scaffolds for breast tissue regeneration. Currently, he is an ARAID researcher at I3A/UNIZAR (Spain), he explores advanced AI techniques, such as Physics-Informed Graph Neural Networks, applied to Digital Human Twins and structural mechanics problems.

Majid Taghavi is an Associate Professor at Queen Mary University of London and a Research Fellow at Imperial College London, where he leads an interdisciplinary research group focused on Soft Robotic Transducers. He has also worked at SoftLab, University of Bristol, UK, and IIT@Sant'Anna, Italy. Majid has pioneered several artificial muscle, variable stiffness, energy harvesting, and self-powered sensing technologies.

Semiconductor Science and Technology

PURPOSE-LED PUBLISHING™

PAPER

Potential application of p-type diamane as back surface field layer in silicon-based heterojunction solar cells

To cite this article: Naima *et al* 2024 *Semicond. Sci. Technol.* **39** 125021

View the article online for updates and enhancements.

You may also like

- Simulation and modeling of a new $CsSnI_3$ solar cell structure: a numerical study
Razika Adjouz, Zehor Allam, Lahcene Souli et al.
- The FinFET effect in lateral 4H-SiC and Silicon multi-gate MOSFETs
K Naydenov, Q Wang, F Udrea et al.
- The effect of selenium ion concentration on zinc selenide thin films prepared by a photo-assisted chemical bath deposition method
D D Hile, L F Koao, H C Swart et al.

This content was downloaded from IP address 14.139.251.98 on 28/11/2024 at 05:01

IOP Publishing Semiconductor Science and Technology
Semicond. Sci. Technol. **39** (2024) 125021 (17pp) https://doi.org/10.1088/1361-6641/ad8e3e

Potential application of p-type diamane as back surface field layer in silicon-based heterojunction solar cells

Naima, Pawan K Tyagi* and Vinod Singh

Department of Applied Physics, Delhi Technological University, New Delhi 110042, India

E-mail: pawantyagi@dtu.ac.in and pawankumartyagi@gmail.com

Received 28 August 2024, revised 25 October 2024
Accepted for publication 3 November 2024
Published 25 November 2024

Abstract

A higher efficiency of photovoltaic cells can be attained by optimizing their design, selecting the appropriate materials, and implementing of effective passivation process. The present study investigates the influence of the thickness and band gap of different layers of the solar cell and resuting opto-electric performance parameters of both single junction heterojunction (HJ) and heterojunction with intrinsic thin layer (HIT) cells. These cells are made up of a crystalline silicon (c-Si) active layer having back surafce field layer. The reported simulated work was conducted using AFORS-HET, an automated program specifically designed for simulating heterostructures. An efficiency of 26.86% has been attained for a HJ solar cell, this efficiency was further improved to 29.38% for the HIT solar cell by optimising all parameters. These cells require an emitter layer with a bandgap of around 1.4 eV. The optimal values of open-circuit voltage (V_{OC}), short-circuit current density (J_{SC}), and fill factor are determined and found to be: 631.2 mV, 51.16 mA cm^{-2}, and 83.16% for HJ solar cell, and 683 mV, 52.74 mA cm^{-2}, and 81.55% for HIT solar cell. Moreover, the J-V curve, spectral response and quantum efficiency analysis have also been studied.

Keywords: 2D carbon materials, photovoltaic cells, higher efficiency, BSF layer, energy band diagram

1. Introduction

The greatest challenge in the world at present is to find a green energy source that can meet the world's growing energy needs and decrease its dependence on traditional energy sources, which are harmful to both human beings and the environment, especially fossil fuels [1]. To meet climate goals by the end of this century, we must move promptly to a green economy. This means transitioning the world economy from being dominated by the fossil-fuelled (brown) sector to being dominated by the low-emission (green) sector. By utilising photovoltaic (PV) technology, the sun, which is a prominent energy source across the globe, may be effectively utilised to generate electricity. This technology has the ability to fulfill the growing need for power. As we know that primary renewable energy sources with zero operating carbon emissions is photovoltaic solar cells [2, 3]. Consequently, photovoltaic solar cell is acknowledged as an indispensable energy source and its viability is essentially evaluated by its power conversion efficiency, commonly referred to as PCE. Wafer-based crystalline silicon (c-Si) solar cell is the dominant technology in the global photovoltaic market due to their cost-effectiveness, robust stability, and high PCE [2]. The c-Si wafer accounts for around 20% of the overall production cost of the PV module [4]. Thus, the production cost of PV modules can be reduced by systematically decreasing the thickness of wafers and, consequently, the amount of crystalline material used will be lowered [4, 5].

Recently, there has been a major emphasis on to design and manufacture of the extremely efficient solar cells by utilising innovative materials and topologies. Various materials

* Author to whom any correspondence should be addressed.

© 2024 IOP Publishing Ltd. All rights, including for text and data mining, AI training, and similar technologies, are reserved.

have been explored and utilised [6–10] in order to enhance efficiency and reduce the overall cost of solar cells. In a recent study published by our group, Naima *et al* [9, 10] utilised a new 2D material called diamane (Dn) in solar cells. They examined and studied the potentiality of Dn as transparent conducting electrode (TCE) and emitter layer in HJ as well as HIT solar cells, respectively, to significantly enhance the PCE. However, [9, 10] did not take into account for Auger electron and hole recombination as well as band-to-band recombination. Furthermore, it has been reported that in HIT architectures, the thickness of the active wafer can be reduced despite having excellent efficiency. In HIT structure, the primary reason for contributing to enhanced efficiency is the utilisation of an extremely thin layer of a-Si: H(i) that mitigates defects on the surface of crystalline silicon wafer. By depositing a-Si: H(i) layers onto the c-Si wafers, we may achieve efficient passivation of the hetero-interface consequent remarkably low density of interface defects [1, 11, 12]. However, it is essential to precisely calibrate the thickness of the passivating layer in order to have a strong passivation, while avoiding any adverse effect on the potential drop across the layer. In addition, researchers have also improved the efficiency of the cell by around 27% through simulation studies by optimizing the basic parameters [1]. Still, there remains ample potential to improve the efficiency of solar cells by methodically improving their fundamental components. As we know that the optimal performance of photovoltaic system typically relies on three factors: the quantity of incident light that enters the absorber layer, the passivation of surface imperfections, and the efficient accumulation of photo-generated charge carriers. In present study, we have replaced the standard TCE (indium tin oxide) in solar cells with single layer graphene to enhance light absorption towards the absorber [13, 14]. Recently, it has been demonstrated that graphene can be used as an efficent TCE material in both hybrid inorganic-organic tandem (HIT) and simple heterojunction solar cells [15, 16]. This is due to its remarkable transparency, which reaches approximately 97.4% [17]. According to reports, the transmittance of monolayer CVD (chemical vapour deposition) graphene is approximately 97.4%. However, this value declines as the layer numbers exceed. Therefore, in this study, we exclusively utilised single-layer graphene with an atomic thickness. Furthermore, crystalline silicon surfaces were also passivated employing thin layers of a-Si: H(i) on both the front and rear surfaces. The primary reason for passivating the front and rear layers of c-Si is the significant conduction band bending and mere reduction of interface sites [18]. An additional layer known as the back surface field (BSF) layer, was employed in the back side of p type c-Si to further enhance the progress in PCE of HJ & HIT cells [12]. The HJ and HIT solar cell with BSF layer deposited on the back side of Si wafer is named as HJBSF and HITBSF. This BSF layer decreases recombination losses which effectively blocks minority charge carriers from making contact with the a-Si:H/c-Si interface on the rear side [12]. A HJBSF cell designed by introducing an extra p-doped a-Si: H (i) layer to the backside of the p-doped c-Si wafer in a HJ solar cell. Another cell which is HITBSF made by adding a p-doped a-Si: H (i) BSF layer to the backside of a p-doped c-Si wafer in a standard HIT solar cell [1]. The HJBSF cell achieved its highest efficiency 25.56% when the c-Si thickness was 98 μm. It is worth mentioning that the HITBSF cell achieves the highest efficiency 24.85% with a 58 μm thick layer of c-Si [1]. Thus, bifacial cells taking crystalline silicon (c-Si) are highly significant and advantageous since they effectively reduce thickness of silicon layer as well as the making cost of solar cells. Recently, Brendel *et al* claimed a world record efficiency of 29% for bifacial solar cells [19]. Furthermore, cell efficiency is reduced when parasitic photon absorption occurs in doped hydrogenated amorphous silicon, since the active layer's ability to generate photo carriers is greatly reduced [20, 21]. Therefore, alternative materials for doped a-Si: H layers need to be investigated. It was recently demonstrated by Bivour *et al* that doped a-Si: H might be replaced in HIT solar cells by tungsten oxide (WO_x) and molybdenum oxide (MoO_x), which have a wide bandgap and a high work function [7]. Furthermore, diamane possesses tuneable bandgap (0–3.52 eV), high electrons (2732 cm^2/Vs) and holes (1565 $cm^2\ Vs^{-1}$) mobility, larger work-function (3.5–6.5 eV), and stable doping with nitrogen and boron atoms [22–25]. Because diamane has these extraordinary properties, and can be used instead of doped a-Si: H layers in HJ and HIT cells, simulated by using AFORS-het software [26]. It is well known that heterojunction is formed when two semiconducting materials with different bandgaps are joined together, resulting in the creation of band offsets and band discontinuities. The potential of heterojunctions became apparent in the 1950s, when they were initially employed in various technologies such as solar cells, light-emitting diodes, and lasers [12, 27]. Furthermore, HJ solar cell technology integrates the exceptional efficacy of c-Si cell technology combined with the cost-effective a-Si: H cell technology in a single cell configuration. Nevertheless, the efficiency of this technology is hindered by a significant recombination rate at the interface involving a-Si:H and c-Si, leading to a decline in performance. In order to address this constraint, a layer of intrinsic a-Si:H has been inserted between the doped a-Si:H and c-Si layers. The solar cell with this specific configuration was referred to as the HIT solar cell [1]. Furthermore, it has been reported that silicon HIT solar cells with heterojunction back contact (HBC) can achieve a remarkable efficiency of 27.09% [28], making it suitable for commercial-scale production. Recently, LONGi Green Energy Technology Co. Ltd, a module manufacturer, has announced that silicon HBC technology has achieved 27.30% efficiency [29]. In presented work, the AFORS-HET programme was used as a computer simulation tool for analysing the performance of HJ and HIT cells. Two solar cell configurations were simulated: (i) a HJ solar cell with a p-type diamane as the BSF layer and an n-type diamane as the emitter layer; and (ii) a HIT solar cell with a-Si: H (i) layers used for passivation and p-type and n-type diamane as the BSF and emitter layers, respectively to efficiently suppress the recombination of minority carriers near the contacts. In both configurations, single-layer graphene (Gr) was used as a TCE, while gold (Au) was used as the metal electrode on the back. Utilising the AFORS-HET software [26], we evaluated the performance of both HJBSF and HITBSF

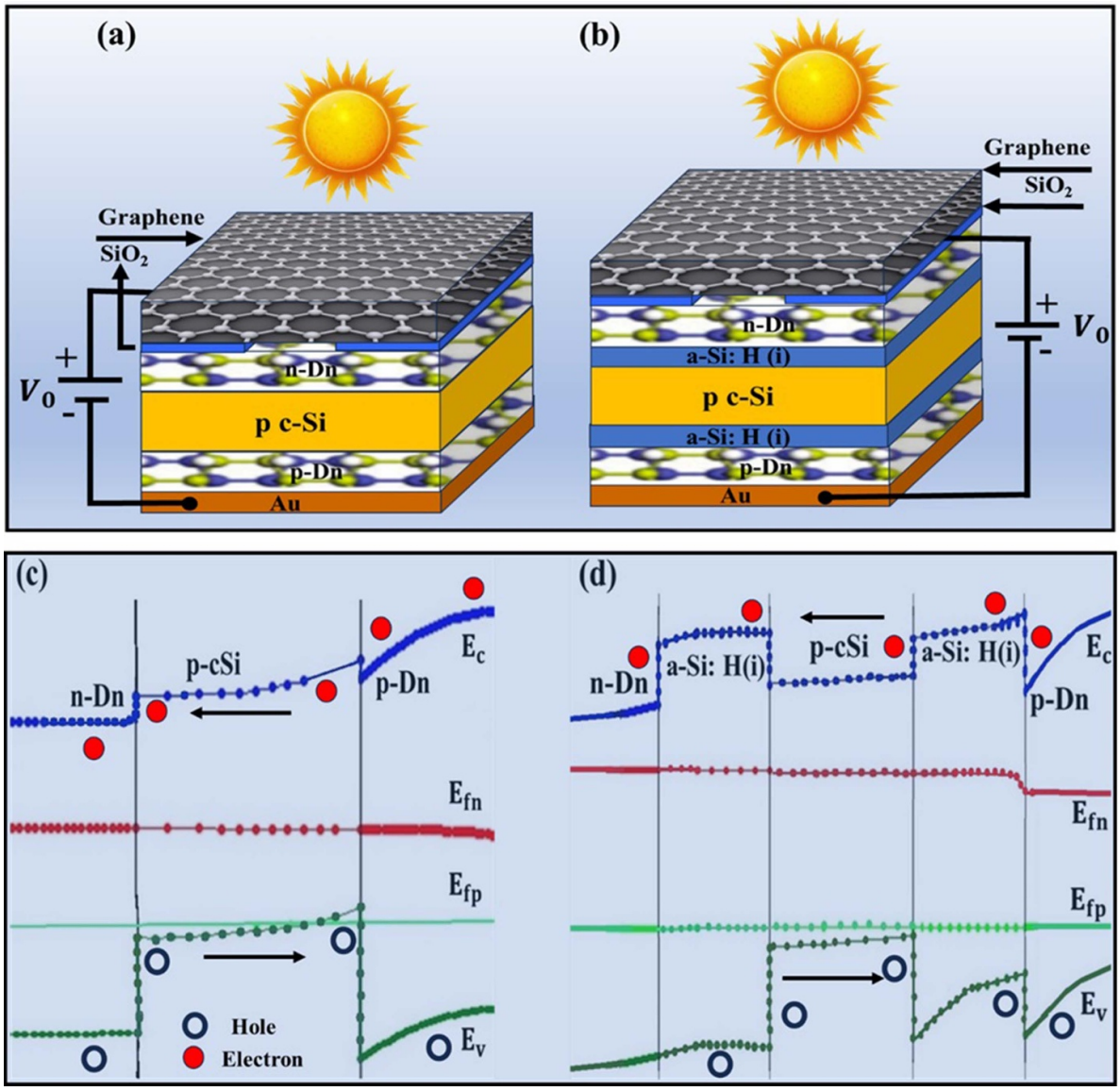

Figure 1. Schematic of the designed HJBSF (a) and HITBSF (b) cells. The band bending diagram showing the separation of charges at the hetero-interfaces for the HJ (c) and HIT (d) cell.

solar cells, optimising critical parameters such as bandgap energy (E_g) and layer thicknesses in the single-junction HJBSF and HITBSF configurations, which are shown in figures 1(a) and (b) as (i) Gr/Dn(n)/c-Si(p)/Dn(p)/Au and (ii) Gr/Dn(n)/a-Si:H(i)/c-Si(p)/a-Si:H(i)/Dn(p)/Au. HJBSF and HITBSF models are studied in this paper, which further reveals how passivation affects solar cell efficiency. Furthermore, in presented study Auger electron and hole recombination as well as band-to-band recombination for diamane and a-Si: H(i) layer did not take into account.

2. Simulation model and junction formation

AFORS-HET has proved to be a valuable simulator for accurately modelling silicon HJ and HIT solar cells. AFORS-HET software provides methods for simulating as well as evaluating the performance of solar cells [26]. This program addresses the 1-D semiconductor equation, specifically Poisson's equation, transport and continuity equation related to Shockley-Reed-Hall statistics. It uses finite differences to calculate solutions under various conditions, including the (a) equilibrium mode (b) equilibrium state; (c) equilibrium state with slight additional sinusoidal perturbations (d) simple transitory mode, which permits any change in external quantities. This allows the selection of multiple boundary conditions, including metal/insulator/semiconductor contacts, or flat band or Schottky-like metal/semiconductor contacts. In addition to this, one can also select insulating boundary contacts. The system's interface is designed to be simple to understand and allows customisation of parameter values to analyse the performance of cell.

The simulated HJBSF structure is modelled as Gr/n-Dn/p-cSi/p-Dn/Au, while the HITBSF cell structure modelled as

Table 1. List of the intial values of all parameters used for performing the simulation in HJBSF cell [30–49].

Parameter	N-type Diamane	P–type c–Si	P–type Diamane
Thickness	0.34 nm	80 μm	2.04 nm
Dielectric constant	11	11.9	11
Electron affinity (eV)	4.1	4.05	4.1
Band gap (eV)	1.4	1.12	1.6
N_C (cm^{-3})	3×10^{18}	3×10^{19}	1×10^{19}
N_V (cm^{-3})	3×10^{18}	3×10^{19}	1×10^{19}
μ_n ($cm^2V^{-1}s^{-1}$)	2732	1104	2732
μ_p ($cm^2V^{-1}s^{-1}$)	1565	420	1565
N_A (cm^{-3})	0	1×10^{18}	5×10^{18}
N_D (cm^{-3})	1×10^{18}	0	0
V_e (cms^{-1})	1×10^{7}	1×10^{7}	1×10^{7}
V_h (cms^{-1})	1×10^{7}	1×10^{7}	1×10^{7}
Auger electron recombination coefficient (cm^6s^{-1})	0	2.2×10^{-31}	0
Auger hole recombination coefficient (cm^6s^{-1})	0	9.9×10^{-32}	0
Band- to- band recombination coefficient (cm^3s^{-1})	0	9.5×10^{-15}	0

Gr/n-Dn/intrinsic type a-Si: H/p-cSi/intrinsic type a-Si: H/p-Dn/Au, as seen in figures 1(a) and (b). Solar cell modelling of both HJBSF and HITBSF has been organised into the following subsections: (1) optimisation of the thickness and bandgap of the HJBSF & HITBSF structure, which includes the emitter, absorber, and BSF layers. (2) The thickness and E_g of intrinsic a-Si: H passivation layer has been optimised. The plausible values of the parameters reported in literature have been used in the simulations for both the HJBSF and HITBSF models, tabulated in tables 1 and 2 [30–49]. Since minority carrier concentrations in doped semiconductors are much lower than majority carrier concentrations, we did not take them into consideration in this analysis. This is due to the fact that the dopant concentration in these layers is typically substantially greater than the intrinsic carrier concentration (n_i) of doped silicon or doped diamane. Since acceptor atoms are not intentionally added to n-Dn, they are considered as insignificant, so acceptor density (N_A) cab be taken zero. The analysis is made simpler by concentrating only on the majority carriers, which are electrons. In the same vein, the donor density (N_D) in p-Dn is taken to be zero since donor atoms are not intentionally added, so their concentration is negligible. The values of parameters of front and rear contacts have been fixed at values given in table 3, which are kept same for both HJBSF and HITBSF solar cells [48, 50]. To determine the no. of electrons and holes generated by absorption of light at a specific position (x) and time (t), per unit volume and per second, we have used the Lambert-Beer model. This selection was made due to the presence of a textured surface in this particular scenario. In the presented simulation, we considered metal contact as flat bands. The illumination source employed is solar radiation of AM 1.5 and 100 mW cm^{-2} of power density. To achieve optimal ohmic contact at the metal-semiconductor interface, the flat band Schottky front and back interfaces were considered. The Shockley-Read-Hall recombination algorithm is applied to elucidate the process of recombination in various semiconductor layers, also the drift-diffusion model is chosen for electron and hole transportation. The proposed solar cell configurations exhibit concentration gradients at the n-Dn/p-cSi interface. This gradient results in dispersion of surplus carriers, while the stationary ions stay at the interface vicinity. A space-charge region is created at the contact due to the presence of stationary ions, which generates an electric field. The presence of this electric field in space charge region is responsible for band bending observed at the interfaces, as seen in figures 1(c) and (d). The positioning of Fermi levels at the junction is the consequence of the bending of energy levels. The valence and conduction level experience a sudden shift at the junction as a consequence of the space charge effect. This band offset configuration allows for the selective carriage of one type of minority carriers while impeding the movement of the other type of minority carriers. Consequently, the photo-generated carriers are separated by using a carrier selective layer and lead to less recombination rate of charge carriers [30]. Therefore, HJ and HIT solar cells consisting the carrier selective layers have been discovered to have a crucial impact in enhancing the conversion efficiency of solar cells. Therefore, differently doped diamane layers are being used as the carrier selective layers or the emitter and BSF layers.

3. Results and discussion

3.1. Fabrication details

This particular design can be developed on an industrial scale by using relatively thin silicon wafers, hence decreasing the overall production cost of solar cells. HJ solar cells may be fabricated by using the p-type textured crystalline silicon wafer. Bilayer graphene synthesised using chemical vapour deposition (CVD) [51] can be transferred onto both sides of the p-cSi wafer using the chemical methods described in [48]. Furthermore, hydrogenation of graphene by the chemisorption of H generated from the dissociation of H_2 in a hot filament reactor at low temperature and low pressure, results to subsequent structure conversion of bilayer graphene into highly hydrogenated genuine diamane [49]. To create stable n

Table 2. List of the initial parameter values of all layers used for performing simulation over HITBSF cell [30–49].

Parameter	n-Dn	Front a-Si: H (i)	p-cSi	Back a-Si: H (i)	p-Dn
Thickness	0.34 nm	3 nm	30 μm	3 nm	1.7 nm
Dielectric constant	11	11.9	11.9	11.9	5
Electron affinity (eV)	4.1	3.9	4.05	3.9	4.1
Band gap (eV)	1.4	1.6	1.12	1.6	1.4
N_C (cm^{-3})	1×10^{18}	1×10^{21}	3×10^{19}	3×10^{21}	1×10^{19}
N_V (cm^{-3})	1×10^{18}	1×10^{21}	3×10^{19}	3×10^{21}	1×10^{19}
μ_n ($cm^2V^{-1}s^{-1}$)	2732	20	1104	20	2732
μ_p ($cm^2V^{-1}s^{-1}$)	1565	5	420	5	1565
N_A (cms^{-1})	0	0	1×10^{18}	0	5×10^{19}
N_D (cms^{-1})	1×10^{20}	0	0	0	0
V_e (cms^{-1})	1×10^{7}	1×10^{7}	1×10^{7}	1×10^{6}	1×10^{7}
V_h (cms^{-1})	1×10^{7}	1×10^{7}	1×10^{7}	1×10^{6}	1×10^{7}
Auger electron recombination coefficient (cm^6s^{-1})	0	0	2.2×10^{-31}	0	0
Auger hole recombination coefficient (cm^6s^{-1})	0	0	9.9×10^{-32}	0	0
Band- to- band recombination coefficient (cm^3s^{-1})	0	0	9.5×10^{-15}	0	0

Table 3. Values of parameters of front and back contacts used in the designed solar cells (both HJBSF & HITBSF) investigated in this work [48, 50].

Parameter	Front contact	Back contact
Material	Graphene	Au
Thickness	0.334 nm	10 μm
Work function (eV)	4.3 eV	5.4 eV
Internal reflection	0	0
External reflection	0	0
Surface condition	Textured	Plane
Texturing angle (δ)	89°	0°
Absorption loss	0.023	0

and p-type diamane, these layers are then doped with boron and nitrogen [22, 23]. Subsequent to that, a single layer of graphene is chemically transferred to the front of the stack to serve as the TCE, or antireflecting layer [48]. Finally, the metal electrode of Au that is responsible for conducting current across the external circuit made by screen printing or deposited on the front and rear surfaces of the cell [52]. In this way, the simple heterojunction with BSF layer has been fabricated as shown in figure 1(a). The main distinction between a HJBSF and HITBSF solar cell is the process of passivation of absorbing layer, to stop recombination losses arising because of dangling bonds present on c-Si. This passivation can be done by using any of the methods such as chemical vapour deposition (CVD), glow discharge, laser decomposition, and sputtering [47]. Two intrinsic thin layers of a-Si: H, are deposited on both the front and rear surfaces of the crystalline silicon substrate, and the BSFHIT structure can be fabricated as shown in figure 1(b) [47].

3.2. Optimisation of the thickness of the n-Dn, p-Dn, and p-cSi layers in HJBSF and HITBSF cell

In this part, we have first optimised the thickness of n-Dn, p-Dn and p-cSi layer of HJBSF and HITBSF cells and the expected results are shown in figures 2–4, respectively. For heterojunction solar cell, the initially optimized efficiency at the values given in table 1, was 26.86% at single layer n-Dn. To analyse the effect of emitter layer thickness on HJBSF cell's efficiency and have varied the n-type Dn's layer number from one to six. Figures 2(a) and (b) depicts the optimization of n-type diamane layer thickness of HJBSF cell with respect to V_{OC}, J_{SC}, FF and η. During the optimisation process, the thicknesses of the p-c-Si layer and the p-Dn BSF layer are maintained at 80 μm and 2.04 nm, respectively. However, all the remaining parameters are maintained at their initial values given in table 1. It is seen from figures 2(a) and (b), a noticeable deterioration was found in the conversion efficiency from 26.86% to 25.99% as emitter layers varies from 1 to 6. The decline in efficiency can be attributed to the simultaneous decrease in FF from 83.14% to 82.5% & J_{SC} from 51.17 mA cm^{-2} to 48.76 mA/cm^2 as layer's thickness increases.

When emitter layer's thickness increases, high density of injected carriers may enhance the scattering of the carrier that limits the carrier's conduction. Consequently, J_{SC} & η were observed to decrease. Conversely, the V_{OC} was shown to have increased from 631.2 mV to 646.2 mV as the emitter layer number increased from 1 to 6. Reducing the emitter layer's thickness, can upsurge J_{SC} by allowing extra photons to reach the active layer, minimising parasitic absorption, and facilitating effective transfer of the photo-generated charge carrier through the layer due to lower resistance. Therefore, the best optimized thickness of the emitter layer for HJBSF cell was determined to be 0.34 nm. After optimizing emitter layer's thickness of HJBSF cell, we have also optimized emitter layer's thickness in HITBSF solar cell within same range, specifically from layer 1 to layer 6 as depicted in figures 2(c) and (d). Furthermore, it was observed that when emitter layer's thickness expands, V_{OC} got slightly increasefrom 682.4 mV to 683 mV and then remain constant whereas, J_{SC}, FF and η were noticed to deteriorate from 52.27 mA cm^{-2} to 52.01 mA cm^{-2}, 81.57% to 80.82% & 29.09% to 28.71%, respectively with an increase in thickness.

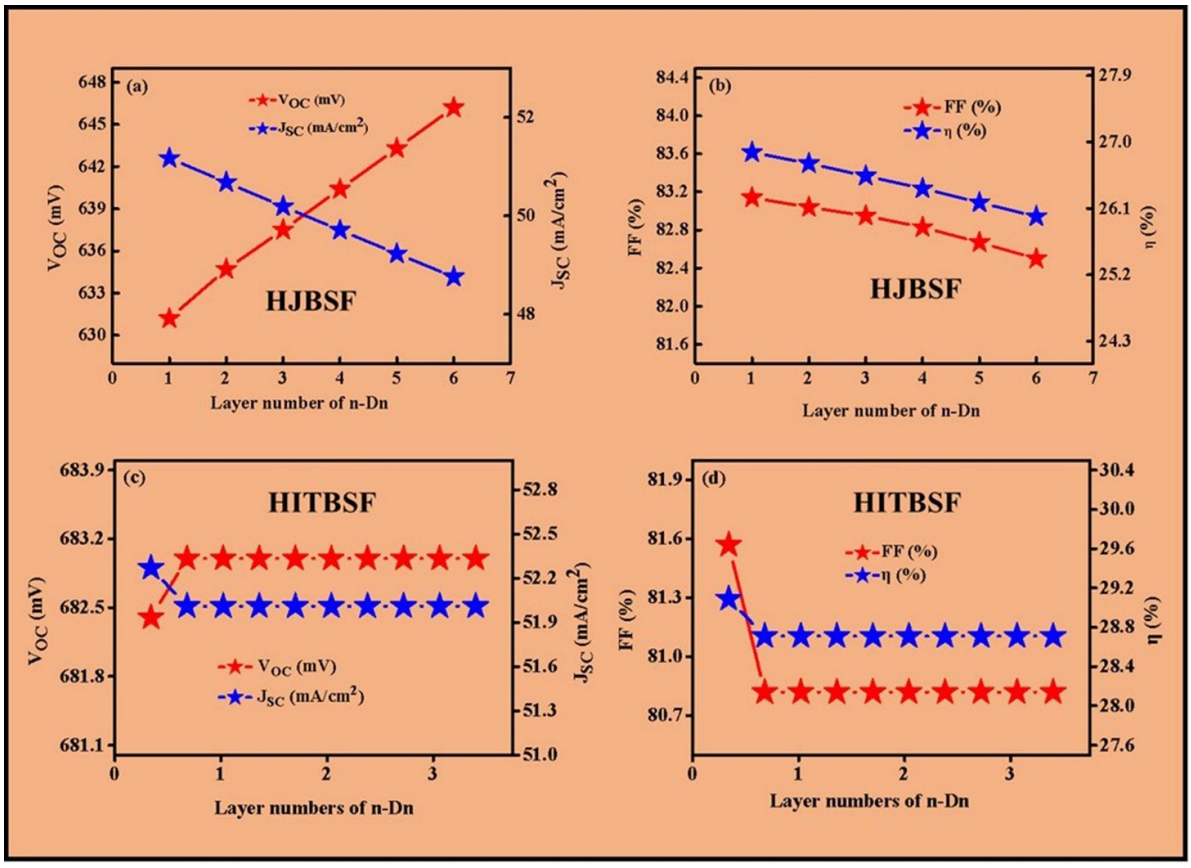

Figure 2. Optimization of the thickness of emitter layer of HJBSF cell showing the variation of V_{OC}, J_{SC} (a) and FF, η (b), respectively. Optimization of the thickness of emitter layer of HITBSF cell showing the variation of V_{OC}, J_{SC} (c) and FF, η (d), respectively with layer numbers of n-type diamane, acting as the emitter layer.

The behaviour of J_{SC}, FF, and η is similar to as-observed HJBSF solar cell structure; i.e., their values continuously decline, which might be also related to surface absorption losses [30]. Because of the low resistance, photo-generated charge carriers can more easily move across the thin emitter layers and enhanced the efficiency [53]. Furthermore, V_{OC} remained consistent at ∼683 mV for all variations in emitter layer thickness, which ranged from layer 2 to layer 6. This uniformity in the V_{OC} value can be attributed to the passivation that occurred as a result of the insertion of a thin a-Si:H (i) layer, which decreases the chances of recombination [30]. The optimized value for the emitter layer's thickness was observed as 0.34 nm. Therefore, we have set the thickness of n-Dn to 0.34 nm for both HJ and HIT cell in order to conduct further simulation on both the cells. After optimizing thickness of emitter layer for both HJBSF and HITBSF cell, the second parameter that we have optimized here is the thickness of BSF layer i.e., p-type diamane layer for both cells and the obtained outcomes are shown in figures 3(a)–(d). To examine the impact of thicknesses of BSF layer on the efficiency of the HJ & HIT cell, we have simulated the number of p-Dn layers for both cells. The range of layer numbers tested was from 1 to 6, as depicted in figures 3(a)–(d). For the HJ cell, it has been observed that as the thickness of BSF layer increased, all the parameters such as J_{SC}, FF, and η were also found to increase. Specifically, J_{SC} increases from 50.86 mA cm^{-2} to 51.17 mA cm^{-2}, fill factor increases from 83.11% to 83.14%, and η increases from 26.68% to 26.86%. However, the V_{OC} parameter stays constant at 631.2 mV, as shown in figures 3(a) and (b). Additionally, we have also carried out the simulation to optimize the BSF layer thickness of HIT cell, while maintaining previously simulated parameters at their optimal values. In order to conduct the simulation, we have systematically changed the number of layers of p-Dn from 1 to 6. The results of this variation may be observed in figure 3, specifically in figures 3(c) and (d). It has been observed that V_{OC} remains constant at 683 mV as layer number increases. J_{SC}, FF, and η exhibit similar behaviour, with their values being constant at 52.74 mA cm^{-2}, 81.55%, and 29.38%, respectively, regardless of thickness variation. This can be understood as the electric field at the n-Dn/p-cSi is unaffected by the insertion of BSF layers, However, at p-cSi/p-Dn junctions, the BSF enhances the field effect passivation, causing the expulsion of minority carriers from the interface between c-Si/Dn at the rear side. This results in a further reduction of recombination losses. So, it can be state that the efficiency of both HJBSF as well as HITBSF cells are significantly increased by the insertion p-type BSF layer to a basic HJ and HIT cell. This can be explained as p-type BSF layer introduces a barrier for the transport of electrons, prevents them from entering into the

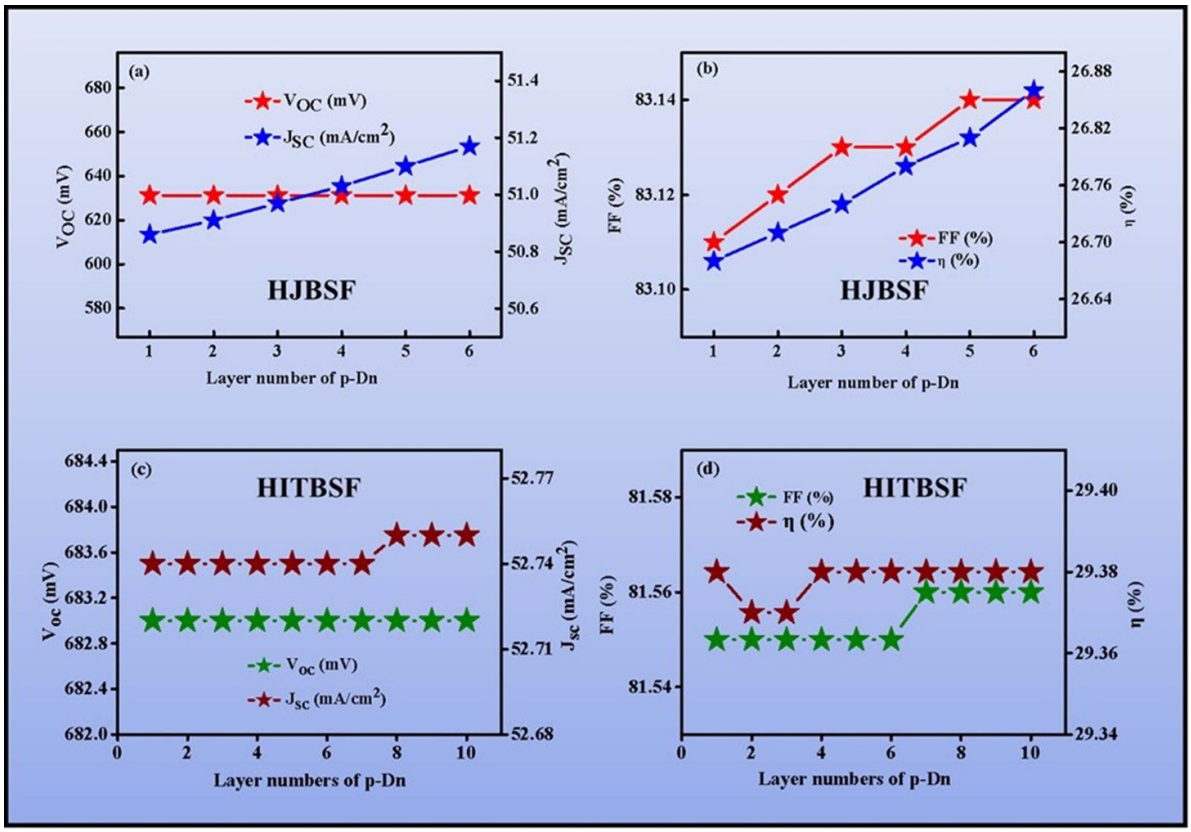

Figure 3. Optimization of the thickness of BSF layer of HJ cell showing the variation of V_{OC}, J_{SC} (a) and FF, η (b), respectively. Optimization of the thickness of BSF layer of HIT cell showing the variation of V_{OC}, J_{SC} (c) and FF, η (d), respectively with layer numbers of p-type diamane, acting as the BSF layer.

p-region. Therefore, the presence of BSF reduces the probability of recombination. The optimal thickness for the BSF layer was determined to be 2.04 nm for both types of cells. This led to the highest possible efficiency of 26.86% for the HJBSF cell and 29.38% for the HITBSF cell, respectively. After that, we optimised the p-cSi's layer thickness, here it is working as the active and absorbent layer in the HJBSF and HITBSF solar cells, respectively. The range of thickness varies from 15 to 80 μm for HJBSF and from 15 to 35 μm for HITBSF. The resulting outcomes are shown in figures 4(a) and (b) for HJBSF and figures 4(c) and (d) for HITBSF. As shown in figures 4(a) and (b), as the thickness of the p-cSi layer increases, all the performance parameters of the cell also increase. Such as, V_{OC} increases from 626 mV to 631.2 mV, J_{SC} increases from 46.34 mA cm^{-2} to 51.17 mA cm^{-2}, FF increases from 83% to 83.14%, and η increases from 24.08% to 26.86%, respectively. Consequently, a maximum efficiency of 26.86% was attained by optimizing the c-Si thickness to 80 μm. As seen in figure 4(b), there is a fluctuation in the FF values, which first dropped at 55 μm of thickness before increasing again at 60 μm. In the range of thickness from 55 μm to 60 μm for p-Si thickness, FF fluctuation can be attributed to the slight change of series resistance (Rs) from 0.5 Ωcm^{-2} to 0.51 Ωcm^{-2} and shunt resistance (R_{sh}) from 8.7 kΩcm^{-2} to 8.8 kΩcm^{-2} in the range of thickness from 55 μm to 60 μm for p-Si thickness. By examining figures 4(c) and (d), it is evident that the performance parameters of the HITBSF cell increase in a linear fashion as the thickness of the active layer increases. The $V_{OC,}$ J_{SC}, FF and η all experience an improvement from 681.9 mV to 682.4 mV, from 49.84 mA cm^{-2} to 52.69 mA cm^{-2}, from 81.48% to 81.58% and from 27.69% to 29.33%, respectively. The analysis of the results reveals that the highest efficiency, 29.38%, is attained when the thickness is 35 μm. The reason behind an increase in J_{SC} with larger thickness of the c-Si base appears to be associated to the generation of more electron-hole pairs, which in turn enhance the efficiency (η) [1]. The remaining parameters may get enhanced with c-Si thickness as the number of photo-generated carrier increases. The absorption of incident light increases with c-Si layer thickness. As a consequence, the enhanced generation of charge carriers increases the flow of carriers across the junction, potentially leading to a significant increase in current density. The findings show that, the optimal thickness for the active layer in the HJBSF solar cell is 80 μm, whereas for the HITBSF solar cell it is 35 μm.

3.3. Optimisation of the band gap of the emitter and BSF layer in HJBSF and HITBSF cells

Here, we performed a simulation to analyse the bandgap of the emitter and BSF layer for both HJ and HIT cells. We have kept the thickness of all layers at their optimal values. The results of the simulation are shown in figures 5(a)–(d) and figures 6(a)–(d). First, we have optimised the bandgap of the emitter layer

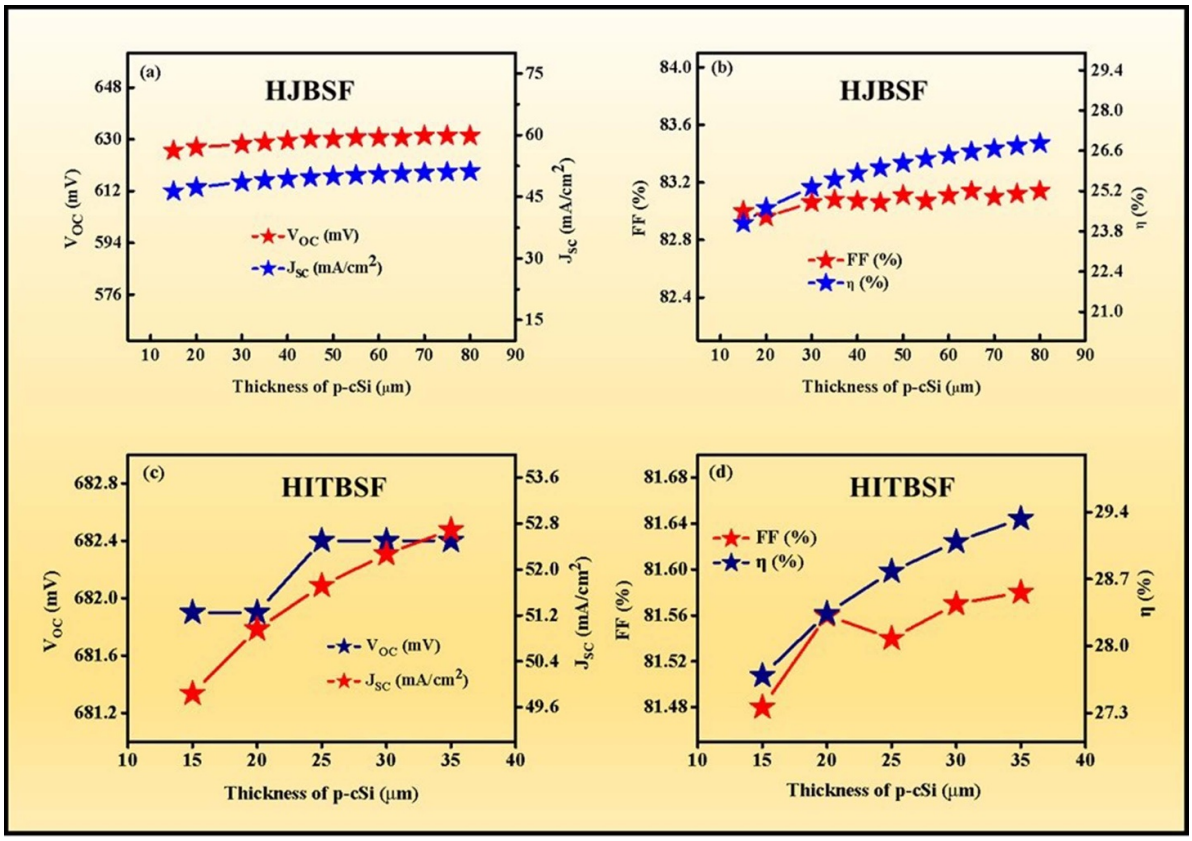

Figure 4. Optimization of the thickness of active layer (p-cSi) in the range from 15 to 80 μm for HJBSF cell showing the variation of V_{OC}, J_{SC} (a) and FF, η (b), respectively. Optimization of the thickness of active layer (p-cSi) in the range from 15 to 35 μm for HITBSF cell showing the variation of V_{OC}, J_{SC} (c) and FF, η (d), respectively.

in the HJBSF solar cell within the range of 0.8 eV to 1.4 eV by keeping the thickness of the n-Dn, p-Dn, and p-cSi at 0.34 nm, 2.04 nm, and 80 μm, respectively. These values remained constant throughout the entire simulation process. The results of this optimisation are shown in figures 5(a) and (b). As shown in figures 5 (a) and (b), V_{OC} increased from 250.1 mV to 631.2 mV when E_g varied from 0.8 eV to 1.4 eV. Slight increment in the value of J_{SC} was observed, increasing from 51.02 mA cm^{-2} from 51.17 mA cm^{-2}. Fill-factor increased from 66.95% to 83.14% as bandgap varied. As shown in figures 5(c) and (d), the overall efficiency of the HJBSF cell increases as the bandgap increases, reaching up to 26.86%. This is because the conversion efficiency, which is the product of the current density and open circuit voltage, is positively affected by the increase in bandgap. Therefore, the optimum bandgap value for the n-type diamane layer of the heterojunction solar cell is found to be 1.4 eV. Afterwards, we have modified the bandgap of the HITBSF cell's n-Dn layer within the range from 0.8 eV to 1.4 eV. The corresponding results may be seen in figures 5(c) and (d). The efficacy of the HITBSF cell was evaluated using a similar methodology to that of the HJBSF cell. All of the parameters exhibited an increase in correlation with the bandgap and the optimal value of the bandgap for the emitter layer in the HITBSF cell was found to be the same as that of the HJBSF cell, which is 1.4 eV. The maximum η of 29.38% % was achieved for HITBSF cell at 1.4 eV of bandgap of the emitter layer. Furthermore, we performed a simulation on the BSF layer (p-Dn) for both the HJBSF and HITBSF cell. We varied E_g of the BSF layer from 1.2 eV to 1.9 eV. The end outcomes are depicted in figures 6(a)–(d). Firstly, the simulation is performed on the HJBSF solar cell and the results are depicted in figures 6(a) and (b). From the results that were obtained, it is evident that the V_{OC} remained constant at 631.2 mV until the bandgap reached 1.6 eV. After that, it decreased to 497.1 mV as the bandgap increased to 1.9 eV. The initial J_{SC} increased from 51.02 mA cm^{-2} to 53.47 mA cm^{-2} until the bandgap reached 1.8 eV. As the bandgap increased further to 1.9 eV, the J_{SC} decreased to 2.88 mA cm^{-2}. With an increasing bandgap, from 1.5 eV to 1.6 eV, FF as well η increased from 83.14% to 83.16% and from 26.77% to 26.86%, respectively. Thus, optimized bandgap value for the p-Dn layer of HJBSF is determined to be 1.6 eV. In order to determine the optimised value of the band gap of the BSF layer in the HITBSF cell, we performed further simulations for HITBSF. These simulations varied the E_g of the p-Dn layer from 1.2 eV to 1.9 eV and obtained results are presented in figures 6(c) and (d). The figure shows that V_{OC} as well as J_{SC} remained nearly consistent at 683 mV and 52.74 mA/cm^2, respectively, as E_g increased from 1.2 eV to 1.7 eV. Yet, the fill factor and efficiency slightly decreased from 81.55% to 81.54% and 29.38% to 29.37%, respectively, with the increment in bandgap. When the bandgap reaches

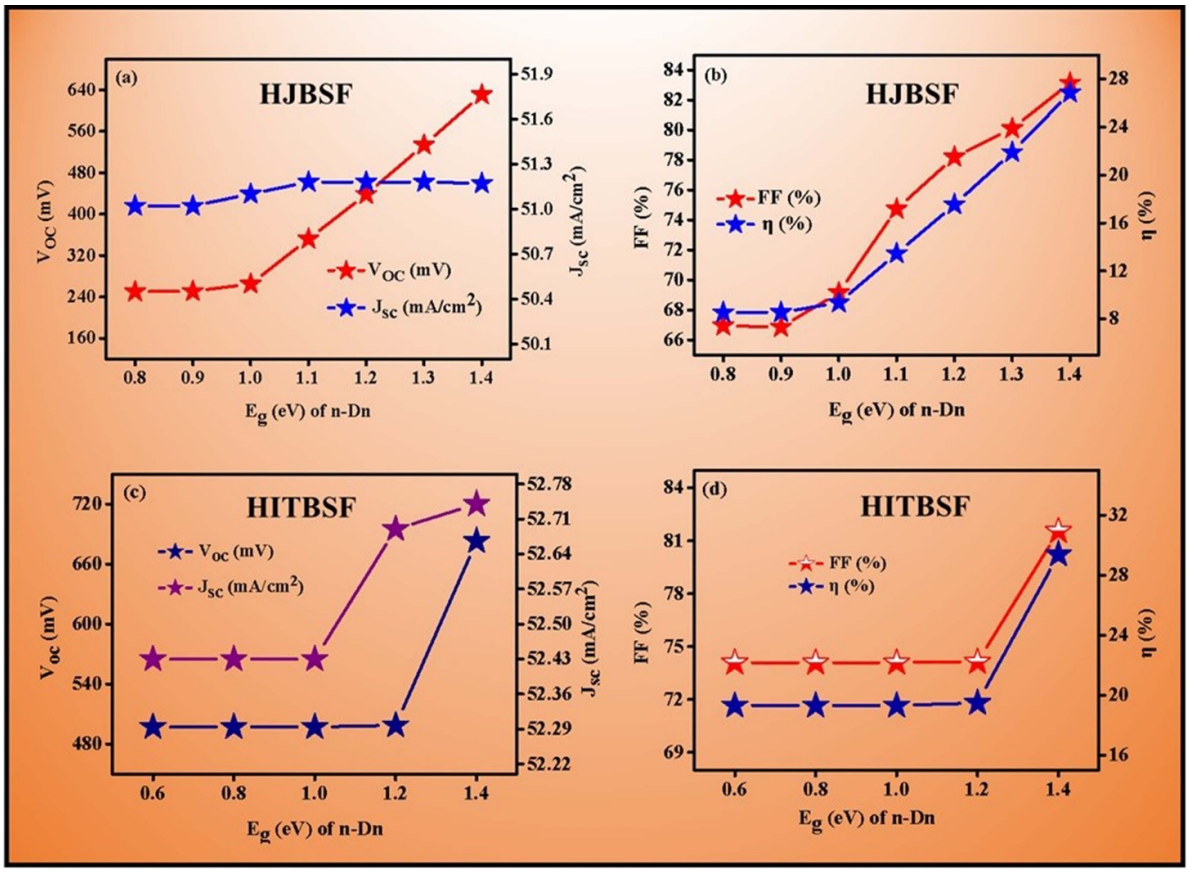

Figure 5. Optimization of the bandgap of emitter layer (n-Dn) of HJBSF cell showing the variation of V_{OC}, J_{SC} (a) and FF, η (b), respectively in the range from 0.8 eV to 1.4 eV. Optimization of the bandgap of emitter layer of HITBSF cell in the range from 0.8 eV to 1.4 eV, showing the variation of V_{OC}, J_{SC} (c) and FF, η (d), respectively.

to 1.9 eV, both FF & η decline to 74.02% and 26.64%, respectively. Thus, the optimized bandgap for the p-Dn layer in HITBSF cell is found to be 1.3 eV. Increasing further value of band gap does not have any impact on the working parameters of the HITBSF cell, as illustrated in figures 6(c) and (d).

3.4. Optimisation of the thickness and band gap of the front and rear/back layers of a-Si: H(i) in HITBSF cell

In this part, we altered the thickness and bandgap of the passivating layers, specifically the a-Si:H(i) layers which are deposited at the front and rear side of c-Si active layer. The objective was to examine how these modifications impact the performance of the HITBSF cell. The results of this simulation are displayed in figures 7 and 8. Initially, we have optimized the thickness of the front intrinsic layer employed for the intention of passivating the front side of the active layer. The optimisation of thickness of the intrinsic a-Si:H has been performed within a range of 3 nm to 10 nm. The results that were obtained, can be observed from figures 7(a) and (b). Evidently, both the V_{OC} and J_{SC} decrease significantly from 682.4 mV to 676.7 mV and from 52.27 mA cm^{-2} to 47.04 mA cm^{-2}, respectively, when the thickness increases from 3 nm to 10 nm. An increase in the thickness of the front intrinsic a-Si: H results in a decrease in both the fill factor (FF) and the conversion efficiency. Specifically, the FF decreases from 81.57% to 81.3%, while the conversion efficiency decreases from 29.09% to 25.88%. The optimal thickness for the front passivating layer a-Si: H(i) is found to be 3 nm. At this thickness, the highest values of the V_{OC}, J_{SC}, and η are achieved. In addition, we carried out further simulations to determine the optimal thickness for the rear passivating layer of the HITBSF cell. We examined the thickness of the back a-Si: H (i) layer in the range of 3 nm to 10 nm, which is the same range used for the front a-Si: H(i) layer. The results were obtained, are shown in figures 7(c) and (d). To conduct the simulation, the remaining parameters of other layers, namely the emitter layer and the front a-Si: H(i) layer, have been set to their optimized values. The figure shows there is no change in the V_{OC} value as the layer thickness changes from (3–10 nm). The V_{OC} remains consistent at a value of 683 mV, as depicted in figures 7(c) and (d). Furthermore, there is no additional change observed in the value of J_{SC}. Its value remains constant at 52.74 mA cm^{-2} across the whole range of thicknesses. The current density shows a minor rise from 52.69 mA cm^{-2} to 52.74 mA cm^{-2} when the thickness varies from 3 nm to 6 nm. Similarly, at 4 nm the FF found to decrease from 81.58% to 81.49% and then at 5 nm it increased to 81.55%, and then remained constant as the thickness continued to increase up

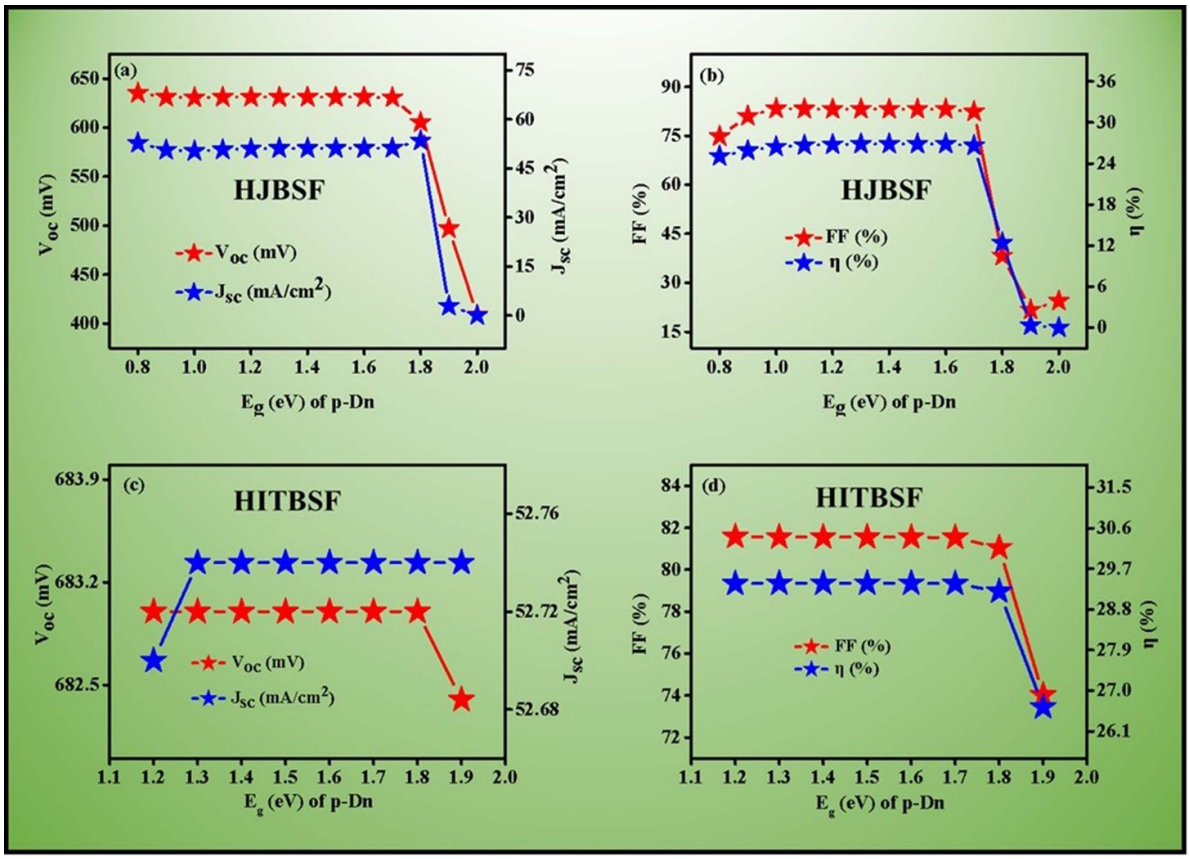

Figure 6. Optimization of the bandgap of BSF layer (p-Dn) of HJBSF cell showing the variation of V_{OC}, J_{SC} (a) and FF, η (b), respectively in the range from 1.2 eV to 1.9 eV. Optimization of the bandgap of BSF layer of HITBSF cell in the range from 1.2 eV to 1.9 eV, showing the variation of V_{OC}, J_{SC} (c) and FF, η (d), respectively.

to 10 nm. This may have happened because of the decrease in R_{sh} (from 4.3 kΩcm^{-2} to 4.2 kΩcm^{-2}) at 4 nm [53]. Thus, the overall conversion efficiency exhibited a similar trend, as it is the result of multiplication of the FF and J_{SC}. The efficiency decreased by 29.38% when the thickness of the back intrinsic a-Si: H layer was increased. The increase in the thickness of the rear passivation layer a-Si: H(i) leads to an increase in the η of the HITBSF module, as seen in figures 7(c) and (d). Therefore, the optimal thickness for the rear a-Si: H(i) was found to be 7 nm, which exceeds the optimised thickness of 3 nm for the front a-Si: H(i) layer. Furthermore, we have adjusted the bandgap of the front a-Si: H(i) layer within the range of 1.6 eV–1.72 eV. The results that were obtained, are depicted in figures 8(a) and (b). It has been observed that as the bandgap increases from 1.6 eV to 1.72 eV, both V_{OC} and J_{SC} decrease. Specifically, V_{OC} decreases from 683 mV to 645 mV, and J_{SC} decreases from 52.74 mA cm^{-2} to 52.68 mA cm^{-2}, as depicted in figure 8(a) and (b). Since both V_{OC} and J_{SC} have decreased, it is expected that FF will also diminish, resulting in a reduction in conversion efficiency. According to the results, there is a clear decrease in the FF and η value. In particular, the FF value decreases from 81.55% to 79.98%, and the η value decreases from 29.38% to 27.18%. As a consequence, the maximum attainable conversion efficiency has been attained when the bandgap is 1.6 eV. Thus, 1.6 eV is the most optimal value of E_g for the front passivating layer in the HITBSF solar cell. Next, we have optimised the bandgap of the rear or back intrinsic layer of a-Si: H ranging from 1.6 eV to 1.72 eV, as depicting in figures 8(c) and (d). The plots in figures 8(c) and (d) demonstrates the correlation between E_g of the rear intrinsic layer of a-Si: H and the variations in V_{OC}, J_{SC}, FF, and η. The V_{OC} & J_{SC} remain almost constant at 683 mV and 52.74 mA cm^{-2}, respectively as the band gap increased. The FF and η of the HITBSF cell observe a slight decrease, from 81.55% to 81.49% and from 29.38% to 29.36%, respectively, as the E_g increases from 1.6 eV to 1.72 eV. Hence, the optimal bandgap value for the rear side passivating layer is determined to be 1.6 eV. Based on these results, we concluded that the optimal bandgap value for both the front and rear a-Si: H(i) layer is 1.6 eV. Yet, the optimised thickness for the front layer is 3 nm and for the rear layer is 7 nm. The addition of a 3 nm thin passivating layer of intrinsic a-Si:H, led to a boost of cell efficiency from 26.86% to 29.38%. This may have happened because of the increased carrier lifetime and decreased carrier recombination rate of photo-generated carriers which further lead to improved values of performance parameters of the HITBSF cell [53–56].

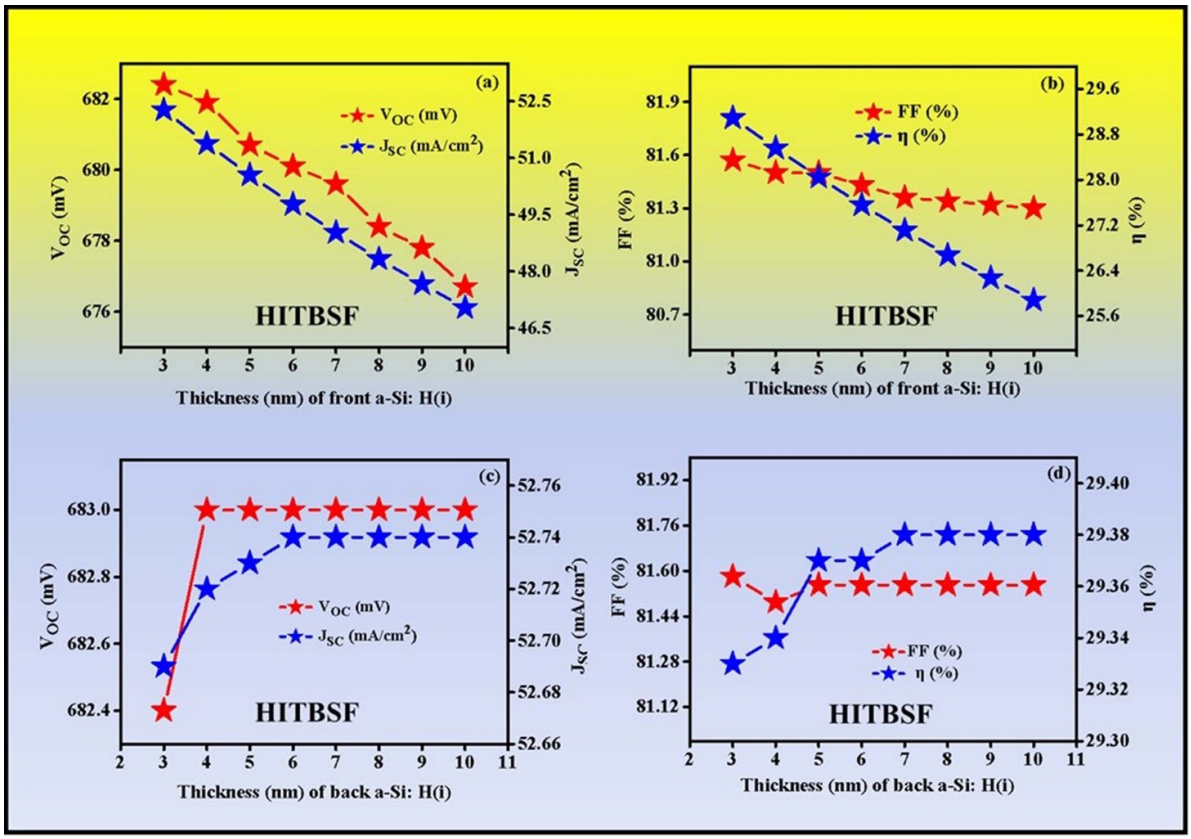

Figure 7. Optimization of the thickness of front intrinsic a-Si: H layer in the range from 3 nm to 10 nm for HITBSF solar cell showing the variation of V_{OC}, J_{SC} (a) and FF, η (b), respectively. Optimization of the thickness of back intrinsic a-Si: H layer in the range from 3 nm to 10 nm for HITBSF solar cell, showing the variation of V_{OC}, J_{SC} (c) and FF, η (d), respectively.

In the final analysis, it has been found that the implementation of these optimal cell parameters may contribute to the fabrication and modelling of highly efficient heterojunction and HITBSF cells. Table 4 presents the input parameters of the most efficient heterojunction and HITBSF cells.

3.5. Spectral response, J-V curve and quantum efficiency of HJBSF & HITBSF Cell

In this section, we have studied the *J–V* curve, spectral response (SR) and the quantum efficiency ((internal quantum efficiency (IQE) as well as external quantum efficiency (EQE)) of heterojunction as well as HIT solar cells. Key parameters like R_s, R_{sh}, and the density of interface traps (D_{it}) or surface states (N_{ss}) have a direct impact on the efficiency, FF, and current-voltage (*I–V*) properties of silicon HJ and HIT solar cells. Series resistance mostly influences the FF and power output, but it also affects the solar cell's *I–V* characteristics. The thermionic emission equation illustrates the impact of R_S:

$$I = I_o \exp\left(\frac{q(V - IR_s)}{nkT}\right)\left[1 - \exp\left(\frac{-q\,(V - IR_s)}{kT}\right)\right] \quad (1)$$

where I_o stands for reverse saturation current, I for output current, V for output voltage, n for ideality factor, k for Boltzmann constant, T for temperature, and q for electron charge, in that order [57, 58]. The output current (I) decreases as R_s increases, decreasing the FF and overall efficiency. Taking series resistance into account, the fill factor can be approximately calculated as follows:

$$FF \approx FF_{ideal} \times \left(1 - \frac{R_s \times I_{SC}}{V_{OC}}\right) \quad (2)$$

where, FF_{ideal} stands for fill factor without resistive losses, I_{SC} for short-circuit current, and V_{oc} for open-circuit voltage. A higher R_s leads to a high decline in FF and efficiency. The effect of R_{sh} on FF can be expressed as:

$$FF \approx FF_{ideal} \times \left(1 - \frac{V_{OC}}{R_{sh} \times I_{SC}}\right) \quad (3)$$

where, R_{sh} is the sheet resistance. This indicates that a lower R_{sh} reduces the fill factor [59]. For HIT solar cells, the intrinsic a-Si layer helps to passivate these traps, lowering D_{it}/N_{ss} and reducing recombination losses. Lower N_{ss} values lead to reduced recombination current, higher V_{OC}, and improved overall efficiency. The reduction in recombination current due to surface passivation can be described by:

$$J_o \alpha \frac{q}{\tau_{eff} N_{ss}} \quad (4)$$

where N_{ss} is the surface state density, τ_{eff} is the effective carrier lifetime, and J_0 is the reverse saturation current [58].

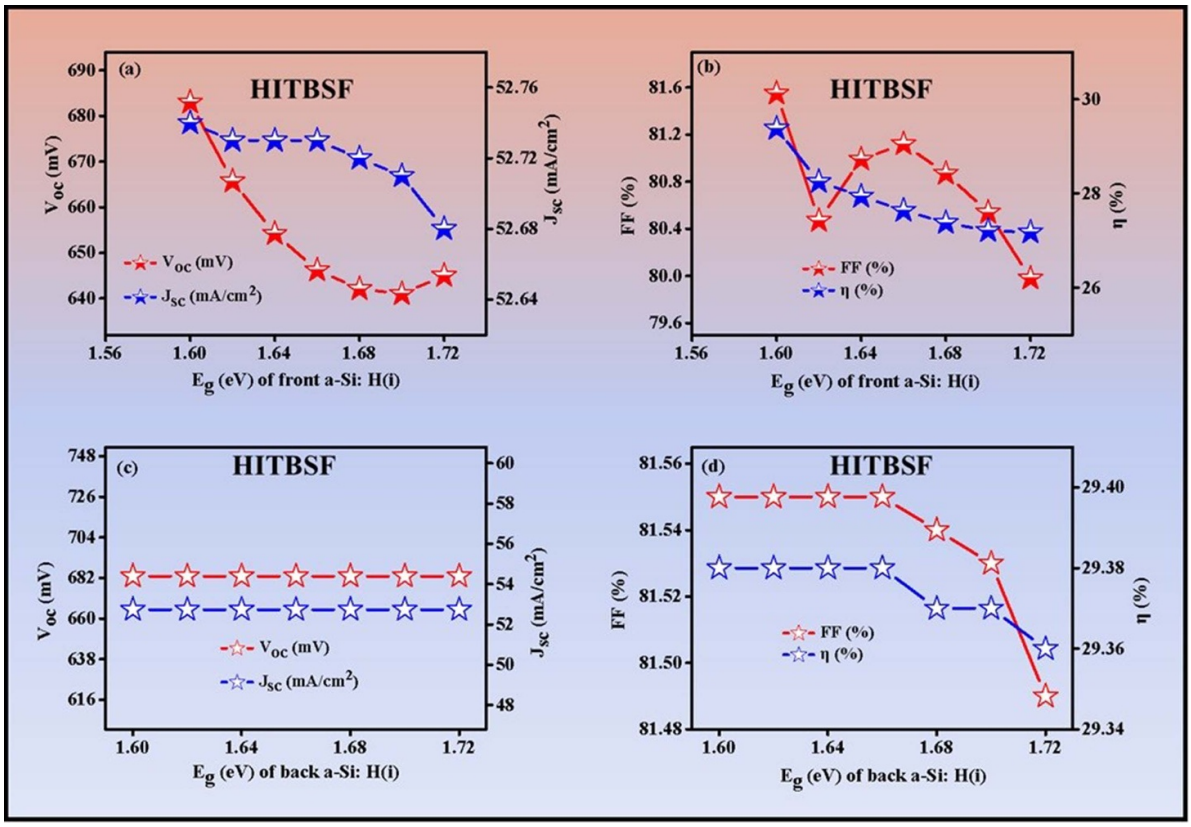

Figure 8. Optimization of the bandgap of front intrinsic a-Si: H layer in the range from 1.6 eV to 1.72 eV for HITBSF solar cell showing the variation of V_{OC}, J_{SC} (a) and FF, η (b), respectively. Optimization of the bandgap of back intrinsic a-Si: H layer in the range from 1.6 eV to 1.72 eV for the same HITBSF cell, showing the variation of V_{OC}, J_{SC} (c) and FF, η (d), respectively.

Table 4. Optimum values of the simulated parameters of layers, n-Dn, p-Dn, p-cSi and front/back passivation layers of HJBSF and HITBSF cell.

	HJBSF cell			HITBSF cell				
Optimized parameter	n-Dn	p-c-Si	p-Dn	n-Dn	Front a-Si: H (i)	p-c-Si	Back a-Si: H (i)	p-Dn
Thickness	1.36 nm	80 μm	2.04 nm	0.34 nm	3 nm	35 μm	7 nm	0.34 nm
E_g (eV)	1.4 eV	1.12 eV	1.6 eV	1.4 eV	1.6 eV	1.12 eV	1.6 eV	1.4 eV
N_A (cm^{-3})	0	1×10^{18}	5×10^{18}	0	0	1×10^{18}	0	5×10^{19}
N_D (cm^{-3})	1×10^{18}	0	0	1×10^{20}	0	0	0	0
$N_{C/V}$	3×10^{18}	3×10^{19}	1×10^{19}	1×10^{18}	1×10^{21}	3×10^{19}	3×10^{21}	1×10^{19}
χ	4.1	4.05	4.1	4.1	3.9	4.05	3.9	4.1
ε_r	11	11.9	11	11	11.9	11.9	11.9	5

Furthermore, factors like R_S, R_{sh}, and D_{it}/N_{ss} have a direct impact on a solar cell's efficiency. The overall efficiency is defined as the ratio of the electrical power output P_{out} to the incident power input P_{in}:

$$\mu = \frac{P_{out}}{P_{in}} = \frac{V_{OC}.\, I_{SC}.\, \mathrm{FF}}{P_{in}} \tag{5}$$

where, V_{OC} is the open-circuit voltage, I_{SC} is the short-circuit current, FF is the fill factor, and P_{in} is the incident light power [60]. As discussed above, efficiency is directly impacted by the R_S, R_{sh}, and D_{it}. Incorporation of passivation provided by inorganic and polymer-based composite interlayers might lower the Rs, N_{ss} and D_{it} [57, 61–64]. The simulation is being performed with a monochromatic intensity of 1×10^{16} cm^2 s^{-1} and a spectral length of 10 nm. The simulation spans the range of 300–1200 nm, as defined in the software. Figures 9(a)–(d) and 10(a)–(d) show the *J-V* curve, SR, IQE, and EQE of the most efficient simulated solar cells. The efficiencies obtained from these solar cells are 26.86% for HJBSF structure and 29.38% for HITBSF structure, respectively. Figures 9(a) and (c) show the *J-V* curve for HJBSF and HITBSF cell, respectively. The results derived from the *J-V* characteristics or *J-V* curve of both cells are tabulated in table 5. Subsequently, the SR has been examined, the outcomes are graphed in figures 9(b) and (d), respectively. The spectral response is the ratio of the electric current generated

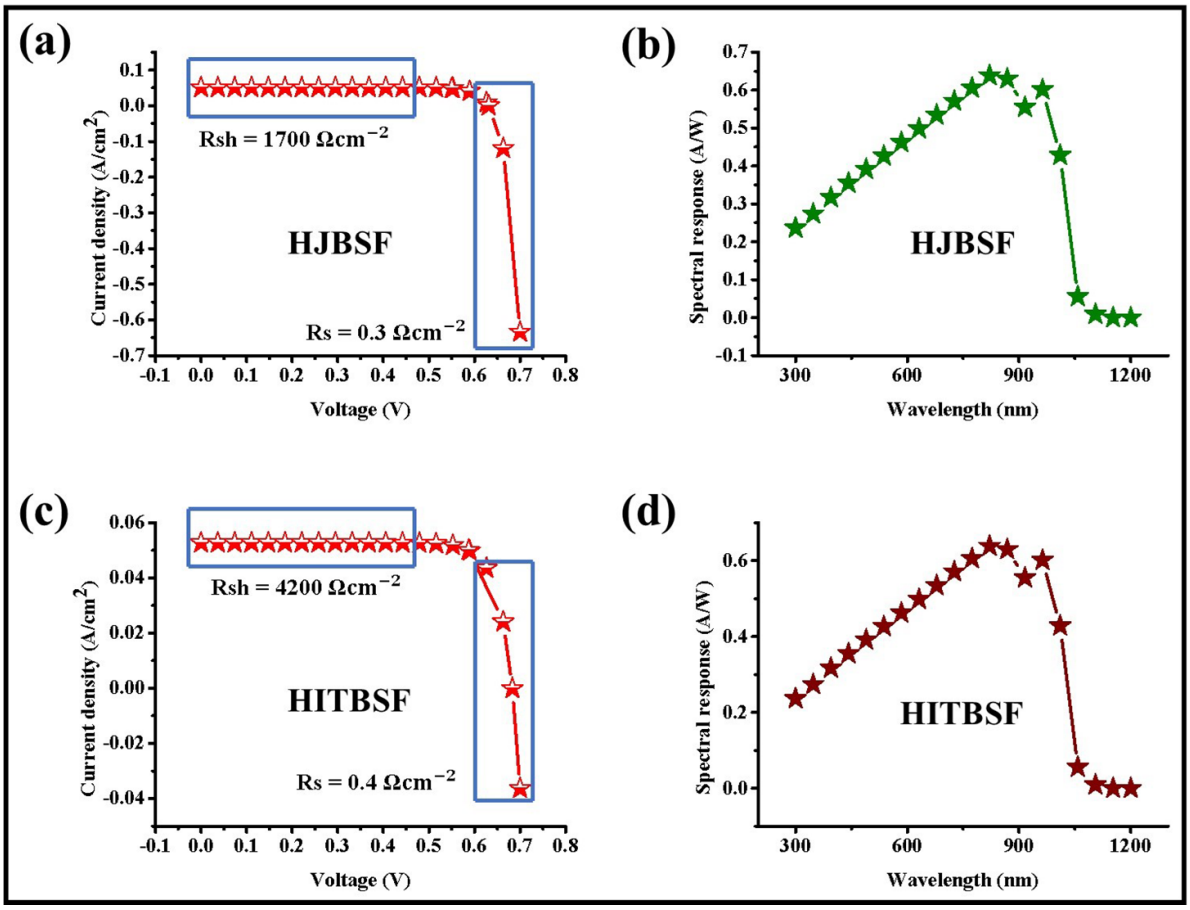

Figure 9. *J-V* characteristics of the best optimised HJBSF cell ($\eta = 26.86\%$) (a) and Wavelength dependency of (b) SR in the range (300 nm–1200 nm) at 80 μm p-cSi wafer. *J-V* characteristics of the best optimised HITBSF cell ($\eta = 29.38\%$) (c) and Wavelength dependency of (d) SR in the range (300 nm–1200 nm) at 35 μm p-cSi wafer.

by a cell and the amount of power that incidents on the surface of the cell [65]. The measurement is usually expressed as amperes per watt. The fundamental equation of SR can be written as the ratio of cell current I_{SC} (λ) to light intensity and can be defined as: SR (λ) $= \frac{I_{SC}(\lambda)}{I_{light}(\lambda)}$. As shown in figure 9, the SR increased from 0.236 to 0.629 A/W as the wavelength (λ) varied from 300 to 868 nm. The SR decreased at λ of 915 nm and became zero at λ of 1200 nm for both HJ and HIT cell, respectively. Despite an overall decreasing trend, the rear reflector's function is responsible for an increase in SR at about 900 nm in silicon HJBSF & HITBSF solar cells. As the silicon collects photons that have not been absorbed back from these reflectors. By increasing the probability of absorption in the c-Si, boost the SR before it finally drops near the material's bandgap. Beyond 1100 nm (approaching 1200 nm), the energy of incoming photons drops below the c-Si layer's bandgap ($\sim$1.12 eV), so they are not absorbed, resulting in the drop in SR [66]. After analysing the studies presented in figure 9(b) and (d), it is evident that there is a greater photons absorption within the range of λ from 300 nm to 868 nm. The enhanced absorption is closely correlated with the increase in J_{SC}, as described by the equation: SR (λ) $= \frac{J_{SC}(\lambda)}{I_{light}(\lambda)}$. Spectral response is an essential parameter that directly influences the efficiency of solar cells and can be evaluated through determining their value at different wavelengths of light. The QE of any solar cell can be determined using these data. QE analyses the consequences happens because of optical losses, like; transmission and reflection, on the efficiency of the cell and is directly rely on the wavelength or frequency of the light. As reported earlier, there is a direct correlation between QE of a solar cell and its efficiency. IQE in a solar cell relates to the precise measurement of the efficiency of photons that are neither reflected nor transmitted from the cell. Conversely, EQE, involves the influence of optical losses, for example; reflection & transmission, that happen within the cell. The IQE and EQE of both HJBSF and HITBSF show an increase in value from 0.975 to 0.994 as the wavelength increases from (300 to 395 nm), as shown in figures 10(a)–(d). However, the increasing trend is thereafter reversed and decrease to zero at a wavelength of 1200 nm as the wavelength continues to increase. This indicates that the device will attain optimal efficiency across a broad spectrum of frequencies in visible region. The *J-V* curve, SR, IQE, and EQE responses of both cells, which have optimum efficiency of 26.86% (HJBSF) and 29.38% (HITBSF), exhibit nearly identical behaviour. This indicates that the amount of charge carriers generated at these

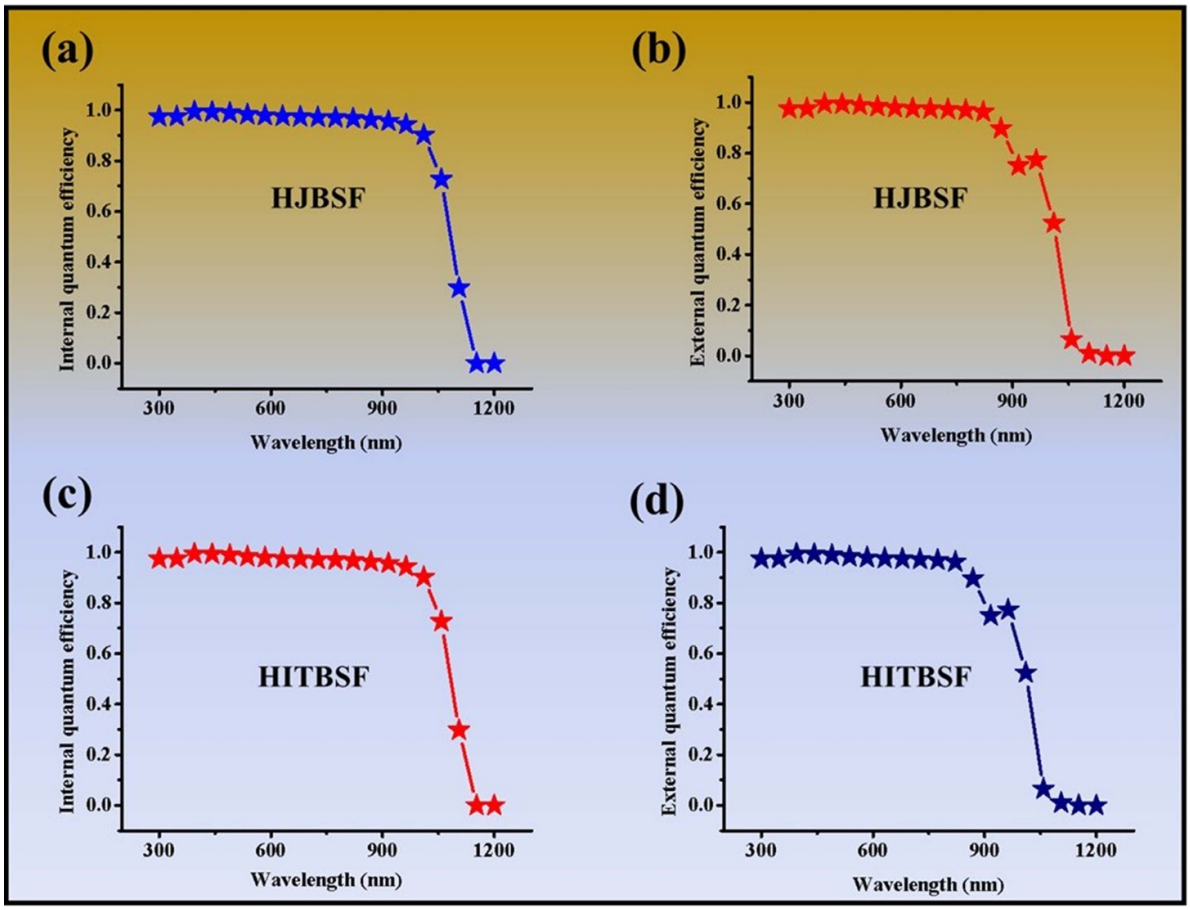

Figure 10. (a) IQE (Internal quantum efficiency) and (b) EQE (External quantum efficiency) of the best simu- lated HJBSF solar cell ($\eta = 26.86\%$) at 80 μm p-cSi wafer in the range of wavelength from 300 nm to 1200 nm. (c) IQE (Internal quantum efficiency) and (d) EQE (External quantum efficiency) of the best simulated HIJBSF solar cell (29.38%) at 35 μm p-cSi wafer in the same range of wavelength from 300 nm to 1200 nm.

Table 5. Values of performance parameters of the optimal cells; HJBSF cell & HITBSF cell at the optimized values of all the parameters as tabluated in table 1, 3 and 4.

Parameter	HJBSF cell	HITBSF cell
V_{OC}	631.2 mV	683 mV
J_{SC}	51.16 mA cm^{-2}	52.74 mA cm^{-2}
FF	83.16%	81.55%
η	26.86%	29.38%

wavelengths is dependent on the number of photons that were absorbed.

In order to verify the validity of this work, we have conducted a simulation in accordance with the experimental study conducted in [67]. We conducted a numerical simulation using the AFORS-het software on a cell structure: Ag/ITO/n-type a-Si: H/a-Si: H(i)/p-cSi/a-Si: H(i)/MoO_x/Ag. This structure is similar to the cell's structure: Ag/ITO/n+ a-Si: H/a-Si: H(i)/n-cSi/a-Si: H(i)/MoO_x/Ag fabricated in [67]. We have obtained an efficiency of 23.93%, that aligns with the experimentally achieved efficiency of 21.10%. Similarly, we also had provided evidence for this successful approach in [15], obtaining an efficiency of 9.81% theoretically, which closely matched experimentally obtained results ($\eta = 9.27\%$) [68]. To further illustrate the originality of the presented work, our research group have further made a comparison between their work and previously published similar work on Si-based solar cells, along with their sizes and properties, listed in table 6 [10, 16, 69–74]. A comparison of the presented study along with the previously reported studies have also been added in table 6 [10, 16, 69–74]. Based on this discussion, we can confidently state that our approach of simulation for the solar cells is genuine and may be expanded to appraise the operational performance of the PV cells.

4. Conclusion

The primary goal of this study is to increase the efficiency of solar cells. This study examines two different cell structures: a basic HJBSF cell (Gr/n-type diamane/p-type c-Si/p-diamane/Au) and a HITBSF cell (Gr/n-type diamane/a-Si: H(i)/p-type c-Si/a-Si: H(i)/p-type diamane/Au). Performed study concluded as: first, in order to attain high efficiency, the thickness and bandgap of the n-diamane emitter layer

Table 6. Comparison and details solar cells based on crystalline silicon [10, 16, 69–74].

Research methodology	Structure	Area/Thickness	V_{OC}	J_{SC}	FF	η	References
Experimental	ITO/Gr/MoS_2/n-cSi/Ag	3 mm × 3 mm	590 mV	36.8 mA cm^{-2}	73%	15.8%	[69]
Experimental	TCO/p-aSi/(i) aSi:H/n-cSi/(i) aSi;H/n-aSi/TCO	100.5 cm^2	725 mV	39.09 mA cm^{-2}	79.10%	22.30%	[70]
Experimental	ITO/p-MoO_x/(i) aSi:H/n-cSi/(i) aSi:H/n-aSi/ITO/Ag	3.93 cm^2	725.4 mV	38.60 mA cm^{-2}	80.36%	22.50%	[71]
Theoretical	Ag/TCO/p-aSi/(i) aSi:H/n-cSi/(i) aSi:H/n-aSi/TCO/Ag	161 μm	747.1 mV	39.56 mA cm^{-2}	84.98%	25.11%	[72]
Theoretical	Gr/n-MoS_2/a-Si:H/p-cSi/Au	500 μm	697 mV	44.25 mA cm^{-2}	82.95%	25.61%	[16]
Experimental	TCO/(i)aSi:H/n-cSi/(i) aSi;H/(n/p)aSi/Electrode	165 μm	744 mV	42.30 mA cm^{-2}	83.80%	26.30%	[73]
Experimental	TCO/(i)aSi:H/n-cSi/(i) aSi;H/(n/p)aSi/Electrode	180 cm^2	740 mV	42.50 mA cm^{-2}	84.60%	26.60%	[74]
Theoretical	Gr/n-Dn/a-Si:H(i)/p-cSi/Ag	90 μm	699.7 mV	53.04 mA cm^{-2}	84.06%	31.20%	[10]
Theoretical	Gr/n-Dn/p-cSi/p-Dn/Au	80 μm	631.2 mV	51.16 mA cm^{-2}	83.16%	26.86%	Present work
Theoretical	Gr/n-Dn/a-Si:H(i)/p-cSi/ a-Si:H(i)/Au	35 μm	683 mV	52.74 mA cm^{-2}	81.55%	29.38%	Present work

and the p-diamane BSF layer for the HJBSF cell should be 1.36 nm and 1.4 eV, and 2.04 nm and 1.6 nm, respectively. Whereas, for HITBSF these values are 0.34 nm and 1.6 eV and 0.34 nm and 1.3 eV, respectively. Second, at 80 μm of c-Si thickness, the HJBSF cell operates at maximum efficiency. It is interesting to note that the HITBSF cell operates most efficiently at 35 μm for c-Si thickness. The HITBSF cells, which are fabricated on c-Si active layer with thickness 35 μm, are very significant and feasible due to their substantial decrease in thickness which resulting in cost reduction. However, the handling of such thin wafers may present an additional significant technological challenge. Furthermore, a HITBSF structure has also been optimised to achieve a remarkable efficiency of 29.38%. Finally, it has been concluded that insertion of passivation layers as well as BSF layer enhanced V_{OC} and PCE. We believe that the performed work will advance the development of highly efficient solar cells; yet, aligning theory with experimental remains a substantial challenge.

Data availability statement

The data cannot be made publicly available upon publication because they are not available in a format that is sufficiently accessible or reusable by other researchers. The data that support the findings of this study are available upon reasonable request from the authors.

Acknowledgment

The author expresses gratitude to the Helmholtz-Zentrum Berlin for supplying the AFORS-HET simulation software and to Delhi Technological University, New Delhi, for their financial assistance in the form of a DTU scholarship. Authors are grateful to Mr. Amit Kumar, LTIMindtree Ltd for kind discussion on software validated.

Conflict of interest

The authors assert that the research conducted in this study was not impacted by any known conflicting financial interests or personal relationships.

Author contribution to CRediT

Naima: Original graph plotting, analysis, simulation, and original draft writing. Conceptualisation and modelling of problem. Pawan K Tyagi: Conceptualisation, modelling, editing, analysis, and supervision. Vinod Singh: Review and editing.

ORCID iDs

Pawan K Tyagi https://orcid.org/0000-0002-4645-5700
Vinod Singh https://orcid.org/0000-0001-8774-2207

References

[1] Dwivedi N, Kumar S, Bisht A, Patel K and Sudhakar S 2013 Simulation approach for optimization of device structure and thickness of HIT solar cells to achieve ∼ 27% efficiency *Sol. Energy* **88** 31–41
[2] Plakhotnyuk M 2018 *Nanostructured Heterojunction Crystalline Silicon Solar Cells with Transition Metal Oxide Carrier Selective Contacts* (DTU Nanotech)
[3] Lin H *et al* 2023 Silicon heterojunction solar cells with up to 26.81% efficiency achieved by electrically optimized nanocrystalline-silicon hole contact layers *Nat. Energy* **8** 789–99
[4] Iftiquar S M, Lee Y, Ju M, Balaji N, Dhungel S K and Yi J 2012 Fabrication of Crystalline Silicon Solar Cell with Emitter Diffusion, SiNx Surface Passivation and Screen Printing of Electrode *Photodiodes - From Fundamentals to Applications* (IntechOpen) 106–32
[5] Fujishima D, Inoue H, Tsunomura Y, Asaumi T, Taira S, Kinoshita T, Taguchi M, Sakata H and Maruyama E 2010

High-performance HIT solar cells for thinner silicon wafers *35th IEEE Photovoltaic Specialists Conf.* pp 003137–40 .
[6] Battaglia C *et al* 2014 Hole selective MoOx contact for silicon solar cells *Nano Lett.* **14** 967–971
[7] Bivour M, Temmler J, Steinkemper H and Hermle M 2015 Molybdenum and tungsten oxide: high work function wide band gap contact materials for hole selective contacts of silicon solar cells *Sol. Energy Mater. Sol. Cells* **142** 34–41
[8] Singh MK, Shinde P V, Singh P and Tyagi P K 2021 Two-Dimensional Materials for Advanced Solar Cells *Solar Cells—Theory, Materials and Recent Advances* (IntechOpen) pp 1–27
[9] Naima, Tyagi P K and Singh V 2022 N-type diamane: an effective emitter layer in crystalline silicon heterojunction solar cell *Carbon Trends* **9** 100209
[10] Naima, Tyagi P K and Singh V 2023 Potential application of novel graphene/diamane interface in silicon-based heterojunction with intrinsic thin layer solar cell *Comput. Mater. Sci.* **226** 112252
[11] Tanaka M, Taguchi M, Matsuyama T, Sawada T, Tsuda S, Nakano S, Hanafusa H and Kuwano Y 1992 Development of new a-Si/c-Si heterojunction solar cells: ACJ-HIT (artificially constructed junction-heterojunction with intrinsic thin-layer) *Jpn. J. Appl. Phys.* **31** 3518–22
[12] Van Sark W 2016 Heterojunction silicon solar cells *Photovoltaic Solar Energy: From Fundamentals to Applications* (Wiley) pp 104–13
[13] Zhang D, Tavakoliyaraki A, Wu Y, van Swaaij R A C M M and Zeman M 2011 Influence of ITO deposition and post annealing on HIT solar cell structures *Energy Proc.* **8** 207–13
[14] Lien S 2010 Characterization and optimization of ITO thin films for application in heterojunction silicon solar cells *Thin Solid Films* **518** S10–S13
[15] Patel K and Tyagi P K 2017 P-type multilayer graphene as a highly efficient transparent conducting electrode in silicon heterojunction solar cells *Carbon* **116** 744–52
[16] Borah C K, Tyagi P K and Kumar S 2020 The prospective application of a graphene/MoS_2 heterostructure in Si-HIT solar cells for higher efficiency *Nanoscale Adv.* **2** 3231
[17] Nair R R, Blake P, Grigorenko A N, Novoselov K S, Booth T J, Stauber T, Peres N M R and Geim A K 2008 Fine structure constant defines visual transparency of graphene *Science* **320** 1308
[18] Lu M, Bowden S, Das U and Birkmire R 2007 Interdigitated back contact silicon heterojunction solar cell and the effect of front surface passivation *Appl. Phys. Lett.* **91** 063507
[19] Brendel R, Dullweber T, Peibst R, Kranz C, Merkle A and Walter D 2015 Breakdown of the efficiency gap to 29% based on experimental input data and modelling *Prog. Photovolt., Res. Appl.* **24** 1475–86
[20] Street B A 1982 Doping and the fermi energy in amorphous silicon *Phys. Rev. Lett.* **49** 1187–90
[21] Holman Z C, Descoeudres A, Barraud L, Fernandez F Z, Seif J P, Wolf S and Ballif C 2012 Current losses at the front of silicon heterojunction solar cells *IEEE J. Photovolt.* **2** 7–15
[22] Niu C, Cheng Y, Yang K, Zhang J, Zhang H, Zeng Z and Wang X 2020 Boron-dopant enhanced stability of diamane with tunable band gap *J. Phys.: Condens. Matter* **32** 135503
[23] Niu C, Zhang J, Zhang H, Zhao J, Xia W, Zeng Z and Wang X 2022 Configuration stability and electronic properties of diamane with boron and nitrogen dopants *Phys. Rev.* **B105** 174106
[24] Qin G, Wu L and Gou H 2021 Diamane: design, synthesis, properties, and challenges *Funct. Diam.* **1** 83–92
[25] Ge L, Liu H, Wang J, Huang H, Cui Z Z, Huang Q, Fu Z and Lu Y 2021 Properties of diamane anchored with different groups *Phys. Chem. Chem. Phys.* **23** 14195
[26] Stangl R, Leendertz C and Haschke J 2010 Numerical Simulation of Solar Cells and Solar Cell Characterization Methods: the Open-Source on Demand Program AFORS-HET *Solar Energy* vol 1 ed R D Rugescu (IntechOpen) pp 319–52
[27] Kroemer H 2001 Quasi-electric fields and band offsets: teaching electrons new tricks (nobel lecture) *Chem. Phys. Chem.* **2** 490–99
[28] Wang G *et al* 2024 27.09%-efficiency silicon heterojunction back contact solar cell and going beyond *Nat. Commun.* **15** 8931
[29] Bellini E 2024 Longi announces 27.30% efficiency for heterojunction back contact solar cell *pv magazine international* (available at: www.pv-magazine.com/2024/05/08/longi-announces-27-30-efficiency-for-heterojunction-back-contact-solar-cell/)
[30] Rawat A, Sharma M, Chaudhary D, Sudhakar S and Kumar S 2014 Numerical simulations for high efficiency HIT solar cells using microcrystalline silicon as emitter and back surface field (BSF) layers *Sol. Energy* **110** 691–703
[31] Sorokin P B and Yakobson B I 2021 Two-Dimensional Diamond—diamane: current state and further prospects *Nano Lett.* **21** 5475–84
[32] Cheng T, Liu Z and Liu Z 2020 High elastic moduli, controllable bandgap and extraordinary carrier mobility in single-layer diamond *J. Mater. Chem.* C **8** 13819–26
[33] Robinson J T *et al* 2010 Properties of fluorinated graphene films *Nano Lett.* **10** 3001–5
[34] Tantardini C, Kvashnin A G, Azizi M, Gonze X, Gatti C, Altalhi T and Yakobson B I 2023 Electronic properties of functionalized diamanes for field-emission displays *Appl. Mater. Interfaces* **15** 16317–26
[35] Raeisi M, Mortazavi B, Podryabinkin E V, Shojaei F, Zhuang X and Shapeev A V 2020 High thermal conductivity in semiconducting Janus and non-Janus diamanes *Carbon* **167** 51–61
[36] Zheng Z, Zhan H, Nie Y, Xu X, Qi D and Gu Y 2020 Single layer diamond—a new ultrathin 2D carbon nanostructure for mechanical resonator *Carbon* **161** 809–15
[37] Zhu L, Li W and Ding F 2019 Giant thermal conductivity in diamane and the influence of horizontal reflection symmetry on phonon scattering *Nanoscale* **11** 4248–57
[38] Rietwyk K J, Wong S L, Cao L, O'Donnell K M, Ley L, Wee A T S and Pakes C I 2013 Work function and electron affinity of the fluorine-terminated (100) diamond surface *Appl. Phys. Lett.* **102** 91604
[39] Bessler R, Duerig U and Koren E 2019 The dielectric constant of a bilayer graphene interface *Nanoscale Adv.* **1** 1702–6
[40] Chernozatonskii L A, Demin V A and Kvashnin D G 2021 Fully hydrogenated and fluorinated bigraphenes–diamanes: theoretical and experimental studies *C — J. Carbon Research* **7** 17
[41] Chernozatonskii L A, Sorokin P B, Kvashnin A G and Kvashnin D G 2009 Diamond-like C_2H nanolayer, diamane: simulation of the structure and properties *JETP Lett.* **90** 134–8
[42] Shen W, Pan Y, Shen S, Li H, Zhang Y and Zhang G 2019 Electron affinity of boron-terminated diamond (001) surfaces: a density functional theory study *J. Mater. Chem.* C **7** 9756–65
[43] Bouzidi S, Barhoumi M and Said M 2021 Optical properties of Janus and non-Janus diamanes monolayers using ab-initio calculations *Optik* **235** 166642
[44] Fang J, Vandenberghe W G and Fischetti M V 2016 Microscopic dielectric permittivities of graphene nanoribbons and graphene *Phys. Rev.* B **94** 045318
[45] Benda V 2018 Crystalline Silicon Solar Cell and Module Technology *A Comprehensive Guide to Solar Energy*

Systems: With Special Focus on Photovoltaic Systems ed T M Letcher and M Fthenakis (Academic Press) 181–213
[46] Futako W, Kamiya T, Fortmann C M and Shimizu I 2000 The structure of 1.5–2.0 eV band gap amorphous silicon films prepared by chemical annealing *J. Non-Cryst. Solids* **266–269** 630–4
[47] Cramarossa F and Pio C 1983 Deposition techniques and applications of amorphous silicon films *Mater. Chem. Phys.* **9** 213–33
[48] Bae S *et al* 2010 Roll-to-roll production of 30-inch graphene films for transparent electrodes *Nat. Nanotechnol.* **5** 574–8
[49] Piazza F, Cruz K, Monthioux M, Puech P and Gerber I 2020 Raman evidence for the successful synthesis of diamane *Carbon* **169** 129–33
[50] Uda M, Nakamura A, Yamamoto T and Fujirnoto Y 1998 Work function of polycrystalline Ag, Au and A1 *J. Electron. Spectros. Relat. Phenom.* **88–91** 643–8
[51] Somani P R, Somani S P and Umeno M 2006 Planer nano graphenes from camphor by CVD *Chem. Phys. Lett.* **430** 56–59
[52] Yang X, Bian J, Liu Z, Li S, Chen C and He S 2018 HIT solar cells with N-type low-cost metallurgical Si *Hindawi Adv. OptoElectron.* **5** 7368175
[53] Kumar M and Kumar S 2023 24.13% efficient TiO_2/i–a–Si:H/p–c–Si heterojunction solar cell by AFORS-HET numerical simulation *Opt. Quantum Electron.* **55** 441
[54] Hsu C, Zhang X, Zhao M, Lin H, Zhu W and Lien S 2019 Silicon heterojunction solar cells with p-type silicon carbon window layer *Crystals* **9** 402
[55] Pham D P, Kim S, Park J, Cho J, Kim H, Le A H T and Yi J 2017 Role of a-Si:H buffer layer at the p/i interface and band gap profiling of the absorption layer on enhancing cell parameters in hydrogenated amorphous silicon germanium solar cells *Optik* **136** 507–12
[56] Rahal W L, Rached D, Mahi F and Azzemou F 2021 Simulation and optimization of back surface field for efficient HIT solar cells *Silicon* **14** 1–5
[57] Tan S O, Uslu Tecimer H, Cicek O, Tecimer H, Orak I and Altındal S 2016 Electrical characterizations of Au/ZnO/n-GaAs Schottky diodes under distinct illumination intensities *J. Mater. Sci., Mater. Electron.* **27** 8340–7
[58] Singh J 2000 *Semiconductor Devices: Basic Principles* (Wiley)
[59] Green M A 2016 Accurate expressions for solar cell fill factors including series and shunt resistances *Appl. Phys. Lett.* **108** 081111
[60] Singh P and Ravindra N M 2012 Temperature dependence of solar cell performance—an analysis *Sol. Energy Mater. Sol. Cells* **101** 36–45
[61] Güçlü Ç Ş, Ulusoy M and Şemsettin S 2024 A comparison electrical characteristics of the Au/ (pure-PVA)/n-Si and Au/(CdTe doped-PVA)/n-Si (MPS) type Schottky structures using I–V and C–V measurements *J. Mater. Sci. Mater. Electron.* **35** 881
[62] Taşçıoğlu I, Pirgholi-Givi G, Yeriskin S A and Azizian-Kalandaragh Y 2023 Examination on the current conduction mechanisms of Au/n-Si diodes with ZnO–PVP and ZnO/Ag2WO4–PVP interfacial layers *J. Solgel Sci. Technol.* **107** 536–47
[63] Tanrıkulu E E 2023 Investigation of photon-induced effects on some diode parameters and negative capacitance of the Schottky structure with Zn-doped organic polymer (PVA) interface *Phys. Scr.* **98** 015804
[64] Güçlü Çi˘ gdem S¸ükriye 2024 On the impact of pure PVC and (PVC: ti) interlayer on the conduction mechanisms and physical parameters of classic metal-semiconductor (MS) Schottky diodes (SDs) *Physica B Condens. Matter* **689** 416173
[65] Farah Khaleda M Z, Vengadaesvaran B and Rahim N A 2021 Spectral response and quantum efficiency evaluation of solar cells: a review *Energy Materials -Fundamentals to Applications* S J Dhoble, N T Kalyani, B Vengadaesvaran and A K Arof (Elsevier) 525–66
[66] Sarkar M N I and Ghosh H R 2021 Performance Enhancement of an a-Si:H/μc-Si:H Heterojunction p-i-n Solar Cell by Tuning the Device Parameters *Dhaka Univ. J. Sci.* **69** 88–95
[67] Li F, Zhou Y, Yang Y, Dong G, Zhou Y, Liu F and Yu D 2020 Silicon heterojunction solar cells with MoOx hole selective layer by hot wire oxidation-sublimation deposition *Sol. RRL* **4** 1900514
[68] Li X, Xie D, Park H, Zhu M, Zeng T H, Wang K, Wei J, Wu D, Kong J and Zhu H 2013 Ion doping of graphene for high-efficiency heterojunction solar cells *Nanoscale* **5** 1945–8
[69] Ma J, Bai H, Zhao W, Yuan Y and Zhang K 2018 High efficiency graphene/MoS_2Si Schottky barrier solar cells using layer-controlled MoS_2 films *Sol. Energy* **160** 76–84
[70] Tsunomura Y, Yoshimine Y, Taguchi M, Baba T, Kinoshita T, Kanno H, Sakata H, Maruyama E and Tanaka M 2009 Twenty-two percent efficiency hit solar cell *Sol. Energy Mater. Sol. Cells* **93** 670–3
[71] Geissbühler J *et al* 2015 22.5% efficient silicon heterojunction solar cell with molybdenum oxide hole collector *Appl. Phys. Lett.* **107** 081601
[72] Long W, Yin S, Peng F, Yang M, Fang L, Ru X, Qu M, Lin H and Xu X 2021 On the limiting efficiency for silicon heterojunction solar cells *Sol. Energy Mater. Sol. Cells* **231** 111291
[73] Yoshikawa K *et al* 2017 Silicon heterojunction solar cell with interdigitated back contacts for a photoconversion efficiency over 26% *Nat. Energy* **2** 17032
[74] Yoshikawa K *et al* 2017 Exceeding conversion efficiency of 26% by heterojunction interdigitated back contact solar cell with thin film Si technology *Sol. Energy Mater. Sol. Cells* **173** 37–42

This article has been accepted for publication in IEEE Electron Devices Reviews. This is the author's version which has not been fully edited and content may change prior to final publication. Citation information: DOI 10.1109/EDR.2024.3491716

Received XX Month, XXXX; revised XX Month, XXXX; accepted XX Month, XXXX; Date of publication XX Month, XXXX; date of current version XX Month, XXXX.

Digital Object Identifier 10.1109/XXXX.2022.1234567

Recent Developments, Reliability Issues, Challenges and Applications of GaN HEMT Technology

Tanvika Garg[1],and Sumit Kale[1], Member, IEEE

[1]Delhi Technological University, New Delhi, India

Corresponding author: Sumit Kale (email: sumit.kale@dtu.ac.in).

ABSTRACT The increasing demand for high-power and high-frequency electronics has led to the development of new materials and devices. One such material is gallium nitride (GaN), which has superior properties for power and radio frequency (RF) applications. This review paper covers various aspects of GaN HEMTs, including the early developments. The paper also presents state-of-the-art techniques that provide further insight into these devices. In addition, the review identifies some of the reliability issues and challenges that need to be addressed in order to realize the full potential of the devices. Moreover, the practical applications of GaN HEMTs across various domains are mentioned. These applications span telecommunications, where they are integral components in high-power amplifiers for base stations, to radar systems, where their high-frequency performance enables precise signal detection. Moreover, they find utility in satellite communication systems, facilitating efficient power amplification and signal processing.

INDEX TERMS Breakdown voltage, Gallium Nitride, High Electron Mobility Transistor, High Frequency, High Power

I. Introduction

THE GaN HEMT is an emerging technology that has been receiving significant attention due to its unique material properties and potential for high-power, high-frequency applications [1]. The GaN HEMT utilizes a heterostructure formed by combining GaN and AlGaN layers to create a two-dimensional electron gas (2DEG) channel. The 2DEG channel in the GaN HEMT exhibits high electron mobility, which results in lower resistance and higher switching speeds compared to traditional semiconductor technologies [2]. GaN HEMTs offer higher power density, higher efficiency, and wider bandwidths compared to other high power devices, making them suitable for applications requiring high-frequency and high-power operation [3] [4]. Moreover, GaN HEMTs can operate at higher temperatures and voltages than conventional semiconductors, making them highly suitable for extreme environmental conditions [5] [6]. Figure 1 depicts the applications of GaN power devices as a function of the voltage [7].

GaN HEMTs have been extensively researched over the past few decades, resulting in significant improvements in device performance and reliability. However, the primary obstacle hindering the broader application of GaN HEMT devices lies in their inherent normally-On characteristic, particularly when prioritizing safety and cost-effectiveness. Achieving normally-off operation is crucial for ensuring fail safe functionality, enhancing system reliability, and simplifying circuit designs. Various innovations, including fluoride plasma treatment, recessed gate technology, and the implementation of p-GaN gates, have been explored to develop normally-off devices. Among these, the most viable solution for commercialization is the utilization of p-GaN gates, offering a superior balance between reliability and promising performance. Beyond the p-gate approach, achieving normally-off operation in GaN HEMT devices and circuits remains a fundamental challenge, crucial for their integration into various power electronic applications. Two primary approaches have been extensively explored to address this challenge. Firstly, epitaxial structure modifications targeting the polarization-induced two-dimensional electron gas (2DEG) present at the heterojunction interface between the AlGaN barrier and the GaN channel have been pursued. By engineering the thickness and composition of the barrier layer or introducing polarization-matched interlayers, researchers aim to reduce or eliminate the 2DEG, thereby facilitating normally-off behavior. Secondly, the introduction

Copyright information will appear here.

Authorized licensed use limited to: DELHI TECHNICAL UNIV. Downloaded on November 11,2024 at 04:22:17 UTC from IEEE Xplore. Restrictions apply.

© 2024 IEEE. Personal use is permitted, but republication/redistribution requires IEEE permission. See https://www.ieee.org/publications/rights/index.html for more information.

This article has been accepted for publication in IEEE Electron Devices Reviews. This is the author's version which has not been fully edited and content may change prior to final publication. Citation information: DOI 10.1109/EDR.2024.3491716

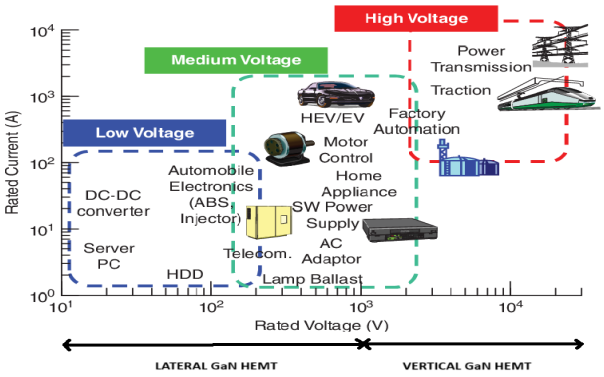

FIGURE 1: GaN HEMT applications by voltage range: Low Voltage (10V–100V) – Consumer Electronics and Automotive; Medium Voltage (100V–1000V) – Electric Vehicles, Industrial and Telecom; High Voltage (1000V–10,000V)– Power Transmission, Rail and Automation. GaN HEMTs are used across these ranges with lateral GaN HEMTs optimized for low to medium voltage applications (10 V to 1,000 V) and vertical GaN HEMTs utilized in high voltage applications ($> 1,000V$) [7].

of gate recess techniques alongside advanced gate dielectric materials and processes has been investigated. By selectively etching away the GaN surface beneath the gate electrode and employing high-k dielectrics, the threshold voltage of the device can be positively shifted, enabling normally-off operation while maintaining high performance characteristics. These approaches represent multifaceted strategies to mitigate the inherent challenges associated with achieving normally-off operation in GaN HEMT devices and circuits. The epitaxial modifications target the material properties directly, aiming to alter the electronic structure at the heterojunction interface, while gate recess techniques and dielectric engineering focus on the device architecture and interface characteristics. Combining these strategies has shown promise in simultaneously improving device performance metrics such as breakdown voltage, on-state resistance, and switching speed, thereby advancing the prospects of GaN HEMT technology for efficient and high-performance power electronic applications. Similarly, The cascode approach to achieving normally-off operation in GaN HEMTs involves integrating a low-voltage, normally-off transistor (typically a MOSFET) in series with the GaN HEMT device. In this configuration, the gate of the GaN HEMT is connected to the drain of the low-voltage transistor, effectively forming a cascode structure. By biasing the low-voltage transistor to control the gate voltage of the GaN HEMT, normally-off operation can be achieved.

This approach exploits the advantages of both transistor types: the low-voltage transistor provides the necessary control to achieve normally-off behavior, while the GaN HEMT offers high-power handling capability and low on-state resistance. During normal operation, when the low-voltage transistor is turned on, it allows the gate of the GaN HEMT to be biased to a sufficiently negative voltage, turning off the device. Conversely, when the low-voltage transistor is turned off, the gate of the GaN HEMT is allowed to float, enabling it to turn on and conduct current. The cascode approach thus enables normally-off operation of GaN HEMTs without compromising their performance characteristics, making it a viable solution for various power electronic applications. In this context, the aim of this review paper is to provide an overview of the early advancements and recent developments in GaN HEMT technology. The review paper will also explore the reliability issues and challenges associated with GaN HEMT technology.

A. The formation and calculation of the 2DEG density.

1) Formation of the 2DEG in AlGaN/GaN heterostructure

The AlGaN layer induces positive and negative polarization charges at the AlGaN/GaN interface and the top of the AlGaN layer, respectively. This polarization effect creates an electric field within the AlGaN layer. Consequently, the

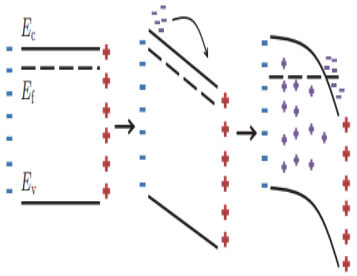

FIGURE 2: Energy band of n-doped freestanding AlGaN film (assuming the AlGaN layer to be under the same tensile strain as that when growing on GaN). Conductive electrons move under the polarization-induced electric field from one side to the other, thereby bending the energy band, and leaving fixed positive charges in the AlGaN layer [8].

energy band and the Fermi level tilt towards the AlGaN/GaN interface due to this induced electric field. This situation is similar to applying a voltage to a thin, freestanding AlGaN film, resembling a planar plate capacitor with AlGaN as the dielectric medium, as illustrated in Figure 2. The presence of the electric field, coupled with the n-doping of the AlGaN layer, causes conducting electrons within the AlGaN to flow towards the positive electrode and accumulate there. This accumulation leads to the formation of positive space charges within the AlGaN layer. As a result, the energy band undergoes bending, and the Fermi level returns to a flat state once again.

Additionally, the electric field that already exists will be reduced by the built-in electric field, flattening the inclined energy band in the AlGaN layer. Due to the fact that the Fermi level of GaN is lower than that of AlGaN (as can be seen in the left portion of Figure 3), when AlGaN and GaN

Authorized licensed use limited to: DELHI TECHNICAL UNIV. Downloaded on November 11,2024 at 04:22:17 UTC from IEEE Xplore. Restrictions apply.
© 2024 IEEE. Personal use is permitted, but republication/redistribution requires IEEE permission. See https://www.ieee.org/publications/rights/index.html for more information.

This article has been accepted for publication in IEEE Electron Devices Reviews. This is the author's version which has not been fully edited and content may change prior to final publication. Citation information: DOI 10.1109/EDR.2024.3491716

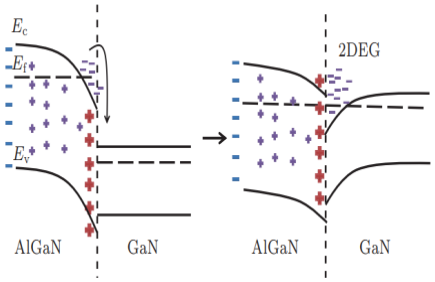

FIGURE 3: Energy band of an n-doped AlGaN/GaN heterostructure. When contacting a GaN layer, electrons will flow into the GaN side, accumulate at the interface and form 2DEG [8].

come into contact, electrons from the AlGaN side will flow into the GaN and create 2DEG. This process will continue until AlGaN and GaN's Fermi levels are equal (seen in the right portion of Figure 3) [8].

2) Calculation of the 2DEG density in AlGaN/GaN heterostructure

Based on the description above, Figure 4 shows a profile of the charge distribution of an AlGaN/GaN heterostructure. Three dipoles are present. First, $\pm\sigma_{AlGaN}$, the AlGaN polarization-induced charge; second, $\pm\sigma_{GaN}$, the GaN polarization-induced charge; and third, 2DEG, the ionised surface charge σ_S. These three dipoles correspond to C_1, C_2, and C_3 in terms of planar plate capacitors. These capacitors have no impact on electrons that are present outside of their inner bodies and have a nonzero electric field between their two parallel surfaces. E = σ/ϵ is the formula for the internal electric field strength of a planar plate capacitor, where σ is the number of electric charges on opposite planes and ϵ is the dielectric constant of the capacitor's dielectric medium.

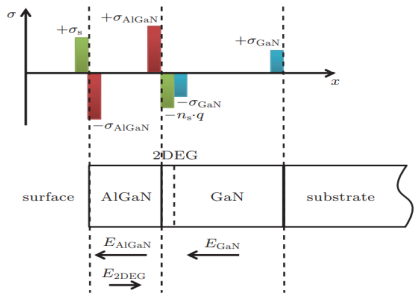

FIGURE 4: Charge distribution profile of an AlGaN/GaN heterostructure [8].

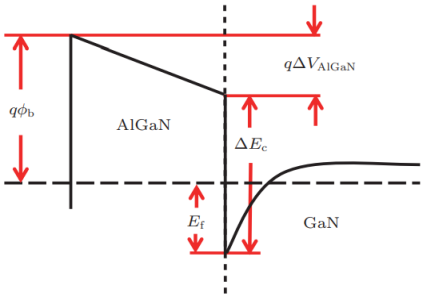

FIGURE 5: Conductive band diagram of an AlGaN/GaN heterostructure [8]

In regions where multiple pairs of charged planes overlap, the resulting electric field is determined by the algebraic sum of these charges. Consequently, the electric field intensity within the AlGaN layer is influenced by the charges of C_1 and C_2. These charges refer to the polarization-induced charge in AlGaN and the two-dimensional electron gas (2DEG) charge, respectively.

$$\Delta V_{AlGaN}/d = \sigma_{AlGaN}/\epsilon - qn_s/\epsilon \tag{1}$$

where ΔV_{AlGaN} is the potential drop across the conductive band of the AlGaN surface and the AlGaN/GaN interface as shown in Figure 5, d is the thickness of the AlGaN layer, σ_{AlGaN} is the sheet charge density that is induced by AlGaN polarization, n_s is the sheet density of 2DEG, q is the electron charge, and ϵ is the dielectric constant of AlGaN. The potential drop ΔV_{AlGaN} can be expressed as:

$$q\Delta V_{AlGaN} = q\phi_b + E_f - \Delta E_c \tag{2}$$

where ϕ_b is the surface barrier height, E_f is the Fermi level position with respect to the GaN conduction-band edge at the AlGaN/GaN interface, and ΔE_c is the conduction band discontinuity between GaN and AlGaN as shown in Fig. 5. Therefore, based on Eqs. (3) and (4), the sheet density of 2DEG can be expressed as [8].

$$n_s = \sigma_{AlGaN}/q - (\epsilon/q^2 d)(q\phi_b + E_f - \Delta E_c) \tag{3}$$

II. Early Advancements

The breakthrough of GaN HEMT technology in the early 1990s marked a significant advancement over traditional semiconductors. In 1993, M. Asif Khan and his team introduced a n-GaN/AlGaN heterojunction HEMT, demonstrating remarkable characteristics like a transconductance of 28 mS/mm at 300 K and 46 mS/mm at 77 K [9]. In 1994, they further presented an AlGaN/GaN heterostructure field-effect transistor (HFET) with a gate length of 0.25 μm, exhibiting a cutoff frequency (f_{max}) of 11 GHz, and oscillation frequency of 35 GHz. The high f_{max} value can be attributed to the saturation regime's very low parasitic output conductance. As a result, it was considered a highly promising candidate for microwave and millimeter wave applications [10].

Later, Y.F. Wu et al. developed GaN HFETs and MODFETs in 1996, achieving high channel current density and substantial power outputs. The MODFET with a high channel current density of over 300 mA/mm has been recorded

Authorized licensed use limited to: DELHI TECHNICAL UNIV. Downloaded on November 11,2024 at 04:22:17 UTC from IEEE Xplore. Restrictions apply.
© 2024 IEEE. Personal use is permitted, but republication/redistribution requires IEEE permission. See https://www.ieee.org/publications/rights/index.html for more information.

This article has been accepted for publication in IEEE Electron Devices Reviews. This is the author's version which has not been fully edited and content may change prior to final publication. Citation information: DOI 10.1109/EDR.2024.3491716

with large voltage I-V characteristics up to V_{ds}=60V, allowing for a FWS class A amplifier power output over 2 W/mm [11]. These advancements included enhanced GaN HFETs grown on p-type SiC substrates, outperforming sapphire substrates, as presented by Lester F. Eastman in 1999. He achieved a power added efficiency of 78% using a SiC substrate, compared to only 50% power added efficiency achieved using a sapphire substrate [12]. Karmalkar et al., in 2001, proposed a methodical approach for field plate device design to achieve optimal performance with minimal impact on on-resistance and frequency response degradation. Increasing the dielectric constant of the insulator beneath the field plate was identified as a promising strategy for achieving significantly higher performance [13].

Saito et al., in 2006, presented that the recessed gate structure in GaN HEMT effectively alters the gate threshold voltage without causing an increase in on-resistance. This is achieved by selectively reducing the density of 2DEG beneath the gate electrode [14]. In 2008, Wong et al. showcased an N-face MIS-HEMT with favorable DC and RF characteristics, particularly at the specified optical gate length. Utilizing AlN for electron confinement not only eliminates alloy scattering but also provides a robust back-barrier mechanism, effectively addressing short-channel effects in highly scaled sub-micrometer devices. These findings indicate the viability of N-face devices for generating microwave power [15]. Hilton et al.(2011) introduced normally-off GaN transistors designed for power applications, employing p-type GaN gate technology along with a modified carbon-doped GaN buffer. This novel combination of an AlGaN backbarrier and the carbon-doped buffer effectively prevents premature off-state punch-through. As a result, the on-state resistance remains low, while ensuring a sufficiently high threshold voltage of 1.1 V for reliable normally-off operation. These devices achieved a breakdown strength of 1000 V for gate-drain spacings of 6μm [16]. These milestones collectively spurred extensive research and development in GaN HEMT technology.

III. State of the Art

GaN HEMTs represent a groundbreaking technological leap in the realm of power and RF devices. Their exceptional characteristics, such as high electron mobility and a wide bandgap, have propelled them to the forefront of semiconductor innovation. This section will shed light on the current state-of-the-art in GaN HEMTs, providing valuable insights into their role as power and RF devices.

A. Power Devices

GaN HEMT power devices have revolutionized semiconductors, outperforming silicon in energy efficiency and performance.They find applications in power converters, amplifiers, and high-voltage systems due to their versatile high-voltage capabilities. The current forefront of GaN HEMT-based power devices is dedicated to exploring novel techniques for enhanced performance in the realm of power electronics which are as follows:

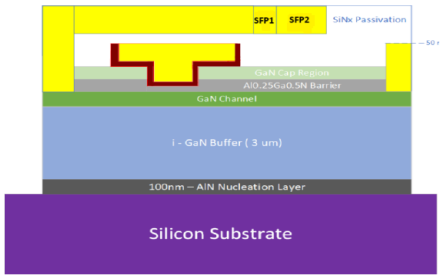

FIGURE 6: Schematic of Aluminium Gallium Nitride /Gallium Nitride (AlGaN/GaN) High Electron Mobility Transistor (HEMT) with field plate. The AlGaN barrier induces a two-dimensional electron gas (2DEG) at the AlGaN/GaN interface, with a buffer layer isolating the 2DEG from the substrate (Si, SiC, or sapphire), and a Si_3N_4 passivation layer reduces surface trapping. [17].

Godfrey et al. analyzed GaN HEMTs with source field plate (FP) and recorded breakdown voltage of 1380 V with maximum electric field distribution of 3.7 MV/cm. It was concluded that the device with longer Source Field Plate (SFP) performed better compared to the short one. Also, it was found that electric fields can be distributed by FPs, and the change in FPs can be influenced by the dielectric layer.While these results are promising, a key challenge remains: how to optimize FP length for various device configurations without compromising on gate leakage or on-resistance. This points to a broader issue in the field of GaN HEMTs, where trade-offs between performance metrics and device reliability must be carefully balanced, especially under high-power conditions. Figure 6 illustrates this structure with a field plate which modulates the electric field, enhancing breakdown voltages. [17]–[19].

In addition, Zhang et al. introduced super field plate (SuFP) and demonstrated that SuFP can achieve charge balance in a LDMOS without using the drift region, which results in better LDMOS performance compared to other charge balance techniques [20]–[23]. This innovation is particularly notable because it addresses a longstanding issue in charge balancing for high-voltage devices, which often suffer from increased on-resistance or compromised breakdown voltage.Figure 7(a) and 7(b) depicts a diagrammatic representation of an n-type LDMOS with three SuFPs and the lateral electric field distribution at the surface with varying numbers of SuFPs under breakdown conditions, respectively.

Further, various p-GaN techniques were introduced to facilitate the enhancement mode operation of the device and also to improve its performance. Some of the recent p-GaN techniques include a p-GaN buried layer and a field plate into a composite stepped gate GaN-based HEMT developed by Li et al., presenting potential benefits in reducing leakage

Authorized licensed use limited to: DELHI TECHNICAL UNIV. Downloaded on November 11,2024 at 04:22:17 UTC from IEEE Xplore. Restrictions apply.
© 2024 IEEE. Personal use is permitted, but republication/redistribution requires IEEE permission. See https://www.ieee.org/publications/rights/index.html for more information.

This article has been accepted for publication in IEEE Electron Devices Reviews. This is the author's version which has not been fully edited and content may change prior to final publication. Citation information: DOI 10.1109/EDR.2024.3491716

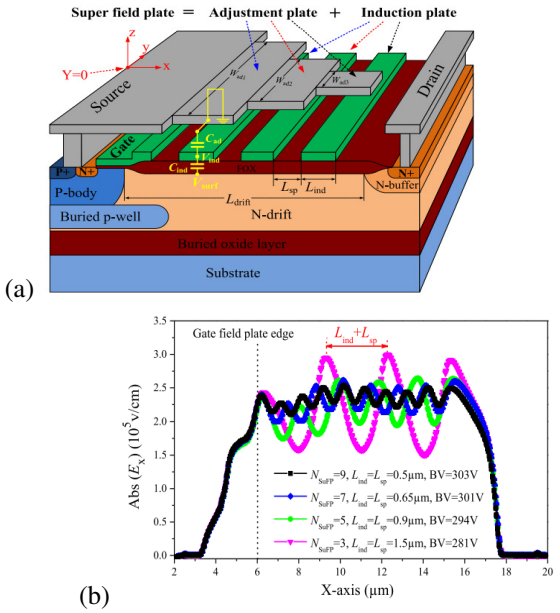

FIGURE 7: (a) A diagrammatic representation of an n-type LDMOS with three super field plates (SuFPs) and (b) the lateral electric field distribution at the surface with varying numbers of SuFPs under breakdown condition (V_{gs} = -3V), respectively [20].

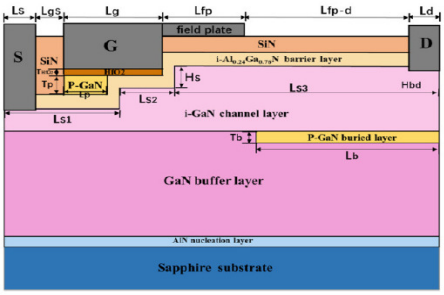

FIGURE 8: Structure of the composite stepped gate GaN-based HEMT with p-GaN buried layer and field plate. Length of the field plate(L_{fp}):2 μm, Length from field plate to drain(L_{fp-d}) 8.02 μm, Length of the first step(L_{s1}):6 μm, Length of the second step(L_{s2}):1 μm, Length of the third step(L_{s3}):11 μm, Height of steps(H_s):100 nm, Length of p-GaN buried layer(L_b):9 μm and Thickness of p-GaN buried layer(T_b):100 nm. Here S, G and D represent source, gate and drain, respectively [24].

current and modifying the electric field distribution within the device [24], [25]. Although these modifications improve performance, the practical challenges of implementing such intricate designs in mass production and their long-term reliability under thermal stress require further investigation. Figure 8 shows the structure of the composite stepped gate GaN-based HEMT with p-GaN buried layer and field plate.

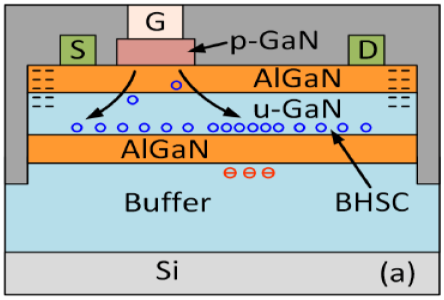

FIGURE 9: Schematic structures of the proposed p-Gallium Nitride gate HEMT with buried hole spreading channel (BHSC). The device dimensions are as follows: an 80 nm p-GaN layer, an 18 nm AlGaN buried layer, and a buffer/transition layer on Si substrate. Here S, G and D represent source, gate and drain, respectively [26].

Moreover, to address the issue of dynamic R_{ON} degradation caused by buffer traps in traditional GaN HEMTs, a 600-V p-GaN gate HEMT with a buried hole spreading channel (BHSC) has been developed by Yang et al. [26]–[29](see Figure 9). However, the introduction of additional structures such as BHSC raises questions regarding fabrication complexity, and whether this trade-off will be economically feasible for commercial applications remains an open question.

Furthermore, Baby et al. developed a normally-off p-GaN HEMTs utilizing TaN as the gate contact material. The device has shown a high threshold voltage of 2.4V and remarkable gate leakage, particularly under forward bias. The low work function of TaN results in a higher Schottky barrier height to p-GaN compared to a standard Ti/Au gate-stack, leading to improved gate stability and reliability under gate-drain and temperature-dependent stress measurements [30]–[33]. This work underscores the importance of gate contact engineering in achieving both high performance and reliability, although further studies are necessary to explore the long-term thermal stability of TaN in high-power applications.

Garg et al. introduced a novel p-GaN HEMT design for high-power electronics. This design features an AlInN/AlN/GaN double heterostructure and an InAlGaN back-barrier, enhancing its DC performance. The incorporation of double AlInN/GaN heterostructures results in a low-resistance device, creating a high density of 2DEG. Additionally, the InAlGaN back-barrier confines electrons within the device's channel, improving efficiency and functionality [34]–[37]. However, concerns remain about the manufacturability of such complex structures and their thermal stability under real-world operating conditions.

Wu et al. performed a plasma pretreatment with NH_3, prior to PECVD-SiN_x deposition, enhancing p-GaN gate HEMT performance. This treatment effectively removed oxides and impurities, reducing interface traps and drain

Authorized licensed use limited to: DELHI TECHNICAL UNIV. Downloaded on November 11,2024 at 04:22:17 UTC from IEEE Xplore. Restrictions apply.
© 2024 IEEE. Personal use is permitted, but republication/redistribution requires IEEE permission. See https://www.ieee.org/publications/rights/index.html for more information.

This article has been accepted for publication in IEEE Electron Devices Reviews. This is the author's version which has not been fully edited and content may change prior to final publication. Citation information: DOI 10.1109/EDR.2024.3491716

leakage [38]–[41]. This demonstrates the importance of surface treatment techniques in minimizing parasitic effects in GaN HEMTs, though further optimization may be needed to make these methods commercially viable in large-scale production. Figure 10 depicts (a) The schematic cross section of the treated HEMT and (b) linear fit of resistance vs. TLM distance.

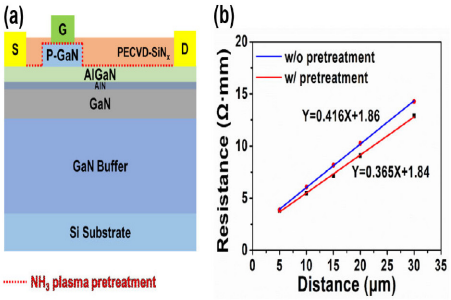

FIGURE 10: (a) The schematic cross section of the treated HEMT with dimensions as follows: a 4 μm C-doped GaN high-resistivity buffer layer, and an 80-nm Mg-doped GaN cap layer; and (b) linear fit of resistance vs. TLM distance which refers to the spacing between the adjacent metal contact pads on the surface of the device(performed at 850 °C for 30 s under a nitrogen atmosphere to form an ohmic contact). Here S, G and D represent source, gate and drain, respectively [38].

Various trench engineering techniques were also introduced to enhance the power performance of the GaN HEMT device. Some of the trench engineering techniques include deep source metal trench which is located towards the buffer region in order to reduce trapping of channel carriers in the buffer region introduced by Yang et al [42]–[45]. While these designs show promise, they require complex fabrication steps, which could increase production costs. Balancing innovation with manufacturability remains a critical issue in the adoption of these designs.

Further, a GaN-based trench current-aperture vertical electron transistor (CAVET) with a stepped doping microstructure was demonstrated by Li et al. (see Figure 11).A remarkable Baliga's figure of merit of 4.767 gigawatt centimetersquare, due to the modulation of the electric-field distribution, is achieved [46]–[48]. While this result represents a significant improvement in power handling, the intricate doping profile could lead to challenges in reproducibility and yield, especially in high-volume production environments.

To enhance the GaN HEMT's power handling, Doring et al. demonstrated a technique involving regrowing GaN HEMTs over magnesium-implanted layers. This approach created a steep doping profile within the regrown AlGaN/GaN stacks, even under high-temperature conditions during metal organic chemical vapor deposition (MOCVD) [49]–[52]. This approach offers a potential solution to issues related to doping uniformity in high-power

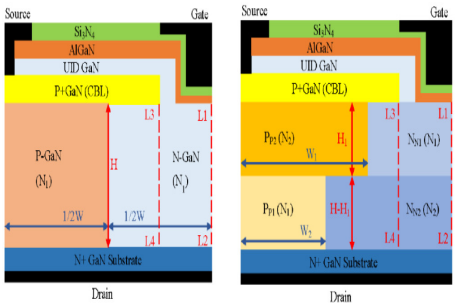

FIGURE 11: Schematic diagrams of superjunction-Trench current-aperture vertical electron transistor (CAVET) (left) and stepped doping microstructure Trench CAVET (right). The main parameters include a 15 μm thick n-GaN drift layer and a 700 nm thick p+ GaN current blocking layer (CBL). The gate length, trench depth and CBL length are set as 2 μm, 1 μm and 4 μm, respectively [46].

GaN HEMTs, but further research is needed to assess its scalability and long-term stability in real-world applications. Figure 12 shows the schematic of (a) Device featuring a buried n-type GaN:Ge layer and a buried Mg-implanted layer and (b) Reference device that do not feature a buried GaN:Ge layer and Mg-implanted layer.

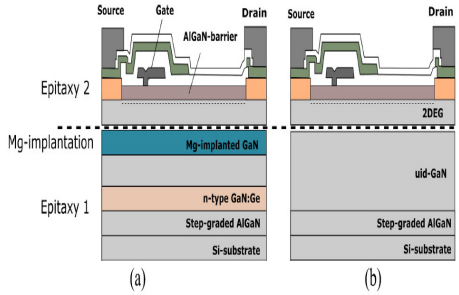

FIGURE 12: Schematic of the two epitaxial stacks. (a) Device features a buried n-type GaN:Ge layer and a buried Mg-implanted layer. (b) Reference wafers have a similar thickness but do not feature a buried GaN:Ge layer and are not Mg-implanted. A 500 nm Ge-doped GaN layer was used as an n-type contact layer. The first epi-structure was finalized by a 2 μm uid-GaN layer resulting in an overall epi-thickness of 3.8 μm [49].

The advancements presented in these studies highlight the significant strides being made in GaN HEMT technology for high-power applications. These innovations—ranging from field plate optimization and substrate engineering to novel gate materials and surface treatment techniques—showcase the field's commitment to overcoming the inherent challenges in device performance, reliability, and scalability. However, many of these breakthroughs also introduce new complexities, such as intricate fabrication processes, thermal stability concerns, and trade-offs between performance met-

Authorized licensed use limited to: DELHI TECHNICAL UNIV. Downloaded on November 11,2024 at 04:22:17 UTC from IEEE Xplore. Restrictions apply.
© 2024 IEEE. Personal use is permitted, but republication/redistribution requires IEEE permission. See https://www.ieee.org/publications/rights/index.html for more information.

This article has been accepted for publication in IEEE Electron Devices Reviews. This is the author's version which has not been fully edited and content may change prior to final publication. Citation information: DOI 10.1109/EDR.2024.3491716

rics like gate leakage, on-resistance, and manufacturability. As GaN HEMT technology continues to evolve, a balanced approach that integrates novel material systems, advanced engineering techniques, and economic feasibility will be essential to meet the demands of next-generation power and RF devices. Further research is necessary to explore long-term reliability and cost-effective manufacturing, ensuring these cutting-edge innovations can be successfully translated into commercial and industrial applications.

B. Radio Frequency Devices

GaN HEMTs can be utilized as RF devices, due to their high electron mobility. They have reshaped RF electronics with enhanced linearity and wider bandwidths. The present state of the art in GaN HEMT-based RF devices continues to explore novel techniques to further optimize power efficiency, linearity, and thermal management for even greater integration and performance in RF systems. The glimpse of the ongoing research in GaN HEMT-based RF devices is as follows:

Lu et al. presented GaN HEMTs that utilize Ti/Au/Al/Ni/Au metallization stack with shallow trench etching ohmic contact (STEOC). An excellent ohmic contact performance with a low contact resistance of 0.28 Ω.mm and smooth surface morphology have been achieved. The schematic diagram in Figure 13 illustrates the TLM layout of the heterostructure, featuring a Ti/Au/Al/Ni/Au metal stack [53]–[55]. While this development demonstrates advancements in contact resistance, it also highlights the growing importance of surface morphology control in high-performance devices. However, further investigation is needed to assess long-term reliability and performance under high-temperature conditions, as surface degradation may impact device longevity.

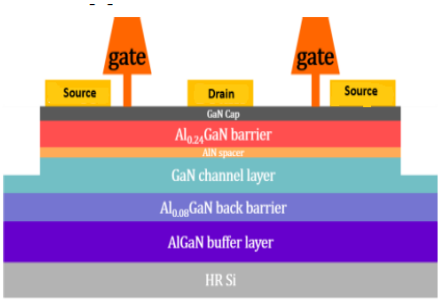

FIGURE 13: Schematic of fabricated TLM layout of the AlGaN/GaN heterostructure with Ti/Au/Al/Ni/Au metal stack. The epitaxial layers consisted of 120 nm AlN nucleation layer, 800 nm GaN Fe-doped buffer, 400 nm unintentionally doped GaN buffer layer, 22 nm undoped $Al_{0.25}Ga_{0.75}N$ barrier layer, and 3 nm GaN cap layer from down to top [53].

Additionally, He et al. fabricated a scaled $In_{0.17}Al_{0.83}N$/GaN HEMT on sapphire, with a T-gate length of 47 nm and selectively regrown n-GaN in specific

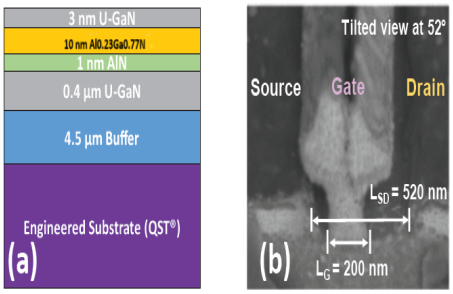

FIGURE 14: (a) AlGaN/GaN epitaxial structure on engineered substrate (QST). (b) Cross-section of a fabricated transistor, showing L_{SD}=520 nm, L_G=200 nm [56].

zones. The device exhibits impressive cutoff frequencies f_T/f_{max} at 190/301 GHz, yielding a new high for Ga-polar GaN-on-sapphire HEMTs [56]–[58]. This result signifies a breakthrough in GaN HEMT performance on sapphire substrates, traditionally considered inferior to SiC or Si. However, this achievement raises questions about the scalability of such high-frequency devices and whether they can be economically produced for commercial RF applications. Furthermore, Yadav et al. demonstrated an RF HEMT fabrication using engineered substrate (GaN-on-QST) for the first time. A favorable RF performance with f_T/f_{max} at 48/115 GHz was demonstrated. The use of GaN-on-QST represents a promising direction for substrate engineering, offering potential for enhanced thermal management and device performance. However, more research is needed to fully understand the impact of QST substrates on device scaling and integration in RF systems. Figure 14(a) and (b) shows AlGaN/GaN epitaxial structure on engineered substrate (QST) and cross-section of a fabricated transistor respectively.

Also, Zhou et al. thoroughly explored the low-noise amplification capabilities of an enhancement-mode p-GaN HEMT. Utilizing a tungsten gate metal and CMOS-compatible contacts for source/drain terminals, the device exhibits an IIP_3 of 15.8 dBm at 2 GHz, robust linearity across varying frequencies, and achieves a remarkable NF_{min} of 0.9 dB with an associated gain of 12.8 dB at 2 GHz [59]–[61]. These findings are impressive in terms of low-noise amplification for RF applications; however, practical implementation in large-scale production requires further exploration, particularly with regard to the compatibility of the tungsten gate with existing CMOS processes. Figure 15 depicts (a) Schematic and (b) microscopic photograph of this p-GaN HEMT with a tungsten gate metal.

Bansal et al. introduced RF switch model based on GaN HEMT technology established through the utilization of measured data obtained from various fabricated devices across multiple dimensions up to the X band frequency range. The accuracy of the switch model has been verified in both ON and OFF states by employing measured data

Authorized licensed use limited to: DELHI TECHNICAL UNIV. Downloaded on November 11,2024 at 04:22:17 UTC from IEEE Xplore. Restrictions apply.
© 2024 IEEE. Personal use is permitted, but republication/redistribution requires IEEE permission. See https://www.ieee.org/publications/rights/index.html for more information.

This article has been accepted for publication in IEEE Electron Devices Reviews. This is the author's version which has not been fully edited and content may change prior to final publication. Citation information: DOI 10.1109/EDR.2024.3491716

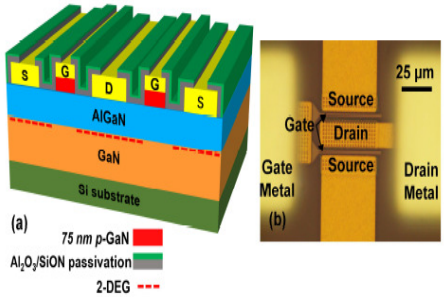

FIGURE 15: (a) Schematic and (b) microscopic photograph of the p-type GaN HEMT with a tungsten gate metal. The device consists of a 75 nm p-type GaN cap layer, a 25 nm AlGaN barrier layer, a 300 nm GaN intrinsic layer, and a 4 μm GaN buffer. Here S, G and D represent source, gate and drain, respectively [59].

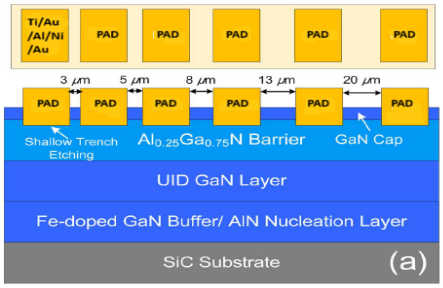

FIGURE 16: Schematic diagram of AlGaN HEMT cross-section with AlGaN backbarrier. The three back barrier thicknesses with 50, 30, and 15 nm were grown on the three samples, respectively. Above the different thicknesses of back-barrier, the GaN channel layer 250 nm thick, the AlN spacer layer 1nm thick, and the AlGaN barrier layer 20 nm thick are present. Finally, a 1.4 nm GaN cap layer was used [65].

from devices with gate widths spanning 200 μm to 1080 μm [62], [63], [86]. This model provides a valuable tool for predicting the behavior of GaN-based RF switches; however, it highlights the ongoing challenge of ensuring accuracy across varying device dimensions and frequency bands. This is particularly critical as the industry moves toward higher frequencies and broader applications, including 5G and beyond.

Hsieh et al. investigated the performance of GaN HEMTs with varying AlGaN back barrier thicknesses, focusing on RF characteristics. Figure 16 presents schematic diagram of AlGaN HEMT with AlGaN back barrier cross-section. Through small-signal analysis, the transistors achieve cut-off frequencies of f_T/f_{MAX} = 59/127 GHz, demonstrating a notably high value of (f_T×L_g) = 14.7 GHz×μm, which stands out among GaN-on-Si devices [65]. This work emphasizes the role of back barrier thickness in determining device performance, particularly for high-frequency applications. However, the complexity of engineering such devices on Si substrates introduces challenges in terms of scaling and maintaining performance consistency, especially in high-volume manufacturing.

In the rapidly evolving landscape of RF devices, these advancements highlight the continuous push for higher frequencies and more efficient designs, which are reshaping the boundaries of performance and reliability. However, many of these innovations introduce new challenges in terms of manufacturability, scalability, and cost-effectiveness. As researchers explore novel materials and structures, balancing high performance with practical implementation remains a central challenge for GaN HEMTs in RF applications. These cutting-edge innovations are not only driving improvements in wireless communication and connectivity but are also unlocking new frontiers in radar systems, satellite communication, and beyond.

IV. Reliability issues and Challenges

A. Reliability issues

The reliability of GaN HEMTs is a critical concern that demands comprehensive investigation to ensure their long-term performance and durability across various applications. Hot carrier injection and bias temperature instability (BTI) are primary causes of gate oxide degradation in GaN HEMTs, which represents a significant reliability challenge. According to Shen et al. [79], hot carrier injection occurs when high-energy carriers bombard the gate oxide, generating electron-hole pairs near the gate oxide interface. This process accelerates gate oxide degradation and can ultimately lead to its failure. On the other hand, BTI refers to the long-term bias stress-induced trapping and detrapping of charge carriers inside the gate dielectric, leading to threshold voltage fluctuations and gradual deterioration of the gate oxide's integrity. Although these degradation mechanisms are well understood, further research is required to optimize the fabrication processes to reduce trap density and enhance the thermal and electrical stability of the gate oxide. Balancing high power performance with long-term reliability remains an ongoing challenge in GaN HEMT design.

Another critical issue in GaN HEMTs is current collapse, which is an abrupt decrease in drain current during high-voltage or pulsed operation. Meneghini et al. [80] demonstrated that this phenomenon is caused by carrier trapping in the buffer or barrier layers of the device. These trapped carriers degrade conductivity and negatively affect device performance. While surface passivation techniques have been proposed to mitigate current collapse, there are still unresolved questions about their effectiveness under various operating conditions. In addition, field plate designs that uniformly distribute electric fields can reduce the risk of carrier trapping, but these modifications must be evaluated

Authorized licensed use limited to: DELHI TECHNICAL UNIV. Downloaded on November 11,2024 at 04:22:17 UTC from IEEE Xplore. Restrictions apply.
© 2024 IEEE. Personal use is permitted, but republication/redistribution requires IEEE permission. See https://www.ieee.org/publications/rights/index.html for more information.

This article has been accepted for publication in IEEE Electron Devices Reviews. This is the author's version which has not been fully edited and content may change prior to final publication. Citation information: DOI 10.1109/EDR.2024.3491716

TABLE 1: Comparison of simulation parameters of the various GaN HEMTs incorporating unique techniques

S.No	Year	Technology	I_{ds}(mA/mm)	g_m(mS/mm)	f_t(GHz)	f_{max}(GHz)	E_F(MV/cm)	R_{on}(Ω.mm)	V_{br}(V)	Ref.
1	2018	Field plate plus high k passivation layer	-	-	-	-	3.3	-	500	[66]
2	2019	T-Gate field plate	-	-	-	-	-	-	950	[67]
3	2020	Source field plate	-	-	-	-	3.7	-	1380	[68]
4	2020	Metal/Graphene Gates	-	-	-	-	-	11.9	-	[69]
5	2020	AlInN as a back barrier layer	880	224	-	-	-	-	-	[70]
6	2020	Super Field Plate Technique	-	-	-	-	-	-	320	[20]
7	2021	Ti/Au/Al/Ni/Au shallow trench etching ohmic contact	-	-	-	-	-	2.09	-	[53]
8	2021	Etching free p-GaN stripe array gate	-	-	-	-	-	10.79	580	[71]
9	2021	p-GaN HEMTs with ITO gate electrodes	438	92.1	-	-	-	-	-	[72]
10	2022	GaN HEMT on free standing GaN substrate	-	-	-	-	-	2.9	193	[73]
11	2022	Passivation of GaN HEMTs by Si_3N_4 and Si rich SiN	-	-	76	157	-	-	-	[74]
12	2022	Mixed oxygen and fluorine plasma pre-treatment	-	-	-	-	-	-	690	[75]
13	2023	TaN-Gated p-GaN E-Mode HEMT	200	-	-	-	-	29	-	[30]
14	2023	Stepped AlGaN Hybrid buffer GaN HEMT	120	300	-	-	-	0.99	2149	[76]
15	2024	Omega (Ω)- Shaped gate p-GaN MIS-HEMT	325	-	-	-	-	-	1668	[4]
16	2024	GaN HEMT with MIS and p-GaN structure	1000	-	-	-	-	-	-	[77]
17	2024	GaN HEMT with overlapping gate structure	500	150	-	-	-	-	570	[78]

in terms of their impact on other performance metrics, such as gate leakage and switching speed.

GaN HEMTs are also highly susceptible to electrostatic discharge (ESD), which can cause immediate or long-term damage to the device structure. Yajie et al. [83] noted that ESD events generate high-energy transient currents that can result in oxide breakdown, gate leakage, or junction failure. Given the increasing use of GaN HEMTs in high-power and high-frequency applications, ESD protection should be a top priority in device design. Advanced ESD protection mechanisms, such as on-chip protection diodes and optimized device structures, can significantly improve robustness. Furthermore, improving the grounding and packaging materials with higher ESD tolerance could provide additional safeguards against ESD-related failures. However, these protection strategies must be implemented without compromising other key performance parameters, such as frequency response and power handling capabilities.

Thermal cycling, or repeated temperature changes, is another issue that places mechanical stress on the GaN HEMT structure, potentially leading to material wear and performance degradation. This is particularly challenging in applications with stringent temperature cycling requirements. While the use of materials with matched thermal expansion coefficients can help mitigate mechanical stress, it remains uncertain how well these solutions perform under extreme operating conditions. Furthermore, the effectiveness of advanced packaging techniques, such as the incorporation of heat sinks and thermal interface materials, needs to be evaluated through extensive testing. Continued research into optimizing thermal management strategies will be crucial for improving device reliability under thermal cycling conditions.

Additional reliability challenges affecting GaN HEMTs include gate and drain lag, self-heating effects, and the loss of high-frequency performance. Gate and drain lag, as

Authorized licensed use limited to: DELHI TECHNICAL UNIV. Downloaded on November 11,2024 at 04:22:17 UTC from IEEE Xplore. Restrictions apply.
© 2024 IEEE. Personal use is permitted, but republication/redistribution requires IEEE permission. See https://www.ieee.org/publications/rights/index.html for more information.

This article has been accepted for publication in IEEE Electron Devices Reviews. This is the author's version which has not been fully edited and content may change prior to final publication. Citation information: DOI 10.1109/EDR.2024.3491716

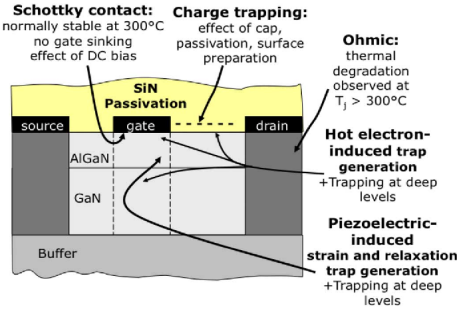

FIGURE 17: Schematic of a GaN HEMT, indicating critical areas of degradation. [82].

Jorg et al. [84] pointed out, refers to slower-than-expected response times to changes in gate or drain voltage, which negatively impacts switching and signal amplification applications. While improvements in thermal management and device design can help reduce lag, more work is needed to understand the underlying causes of these phenomena, especially in devices operating at high frequencies. Similarly, self-heating effects, which can degrade performance, must be addressed through optimized heat dissipation strategies. These issues highlight the delicate balance between achieving high-performance metrics and maintaining device reliability over extended periods of operation.

Overall, addressing these reliability issues will require ongoing research and testing efforts to ensure that GaN HEMTs can meet the growing demands of high-power, high-frequency applications. The development of new fabrication techniques, device designs, and material systems will be key to overcoming these challenges. A multi-faceted approach that takes into account both performance optimization and long-term reliability is essential to ensure the successful integration of GaN HEMTs into a wide range of electronic systems. A schematic of a GaN HEMT showing critical degradation regions is presented in Figure 17, underscoring the areas that require particular attention for enhancing reliability.

Gate oxide deterioration, current collapse, ESD sensitivity, thermal cycling effects, and high-frequency performance degradation are some of the complex interplaying elements that affect the reliability of GaN HEMTs. It takes a combination of cutting-edge materials engineering, innovative device design, and reliable testing procedures to address these problems. These techniques have the potential to greatly increase GaN HEMTs' reliability, paving the way for a wider range of high-power and high-frequency applications.

B. Challenges

GaN HEMTs are recognized for their outstanding properties, such as high electron mobility, wide bandgap, and high breakdown voltage, making them ideal for next-generation power electronics and RF applications [89]–[92]. However, while much of the existing literature focuses on these advantages, a more critical outlook reveals significant challenges that still need to be addressed for their widespread adoption. One of the foremost challenges in GaN HEMT technology lies in the epitaxial growth process and the control of material quality. While significant strides have been made in GaN epitaxy techniques, issues such as crystal defects, dislocations, and strain management continue to hamper progress. These material imperfections can severely impact device performance and reliability, creating pathways for leakage currents and reducing breakdown voltages. Current research has not fully explored the optimization of in-situ monitoring techniques, which could be crucial for improving real-time feedback during epitaxial growth. Addressing this would significantly enhance the growth of defect-free layers, pushing the boundaries of device reliability further.

Furthermore, the challenge of scaling GaN HEMTs to smaller dimensions requires deeper exploration beyond the current literature. Device scaling is crucial for integrating more devices onto a single chip and enhancing performance, but it introduces issues such as gate leakage, short-channel effects, and increased source-drain resistance. While innovations like gate-all-around (GAA) structures and FinFETs are being investigated, the intersection of these scaling challenges with the unique properties of GaN has not been fully understood or optimized. A more comprehensive approach involving both device architecture and material science is needed. For instance, combining advanced lithography techniques with optimized doping profiles has been underexplored, yet it could be key to overcoming short-channel effects at smaller dimensions [93]–[97].

Effective thermal management is critical for the reliability and longevity of GaN HEMTs, particularly in high-power applications. Although there is considerable literature on thermal management techniques, including diamond substrates and microchannel coolers, a critical analysis reveals gaps in their practical application for high-power densities. The use of diamond substrates, for instance, is not without its challenges, particularly in terms of cost and integration into existing fabrication processes. More comprehensive studies are required to evaluate the long-term viability and economic feasibility of such advanced cooling strategies. Additionally, there is a need to innovate on the material front, focusing on thermal interface materials that better match the thermal expansion coefficients of GaN to mitigate thermal-induced mechanical stress.

Achieving high-quality ohmic contacts remains a persistent challenge in GaN HEMT technology. While surface treatments, such as plasma cleaning, are widely discussed, there is a lack of in-depth analysis regarding the optimal conditions for these treatments to ensure uniform contact performance across large wafers. High contact resistance can limit device performance and power handling capabilities. Current strategies, such as alloying or surface passivation, while promising, have yet to be fully integrated into a scalable, industrial process. More research is needed to

Authorized licensed use limited to: DELHI TECHNICAL UNIV. Downloaded on November 11,2024 at 04:22:17 UTC from IEEE Xplore. Restrictions apply.
© 2024 IEEE. Personal use is permitted, but republication/redistribution requires IEEE permission. See https://www.ieee.org/publications/rights/index.html for more information.

This article has been accepted for publication in IEEE Electron Devices Reviews. This is the author's version which has not been fully edited and content may change prior to final publication. Citation information: DOI 10.1109/EDR.2024.3491716

investigate novel contact materials and interface treatments that can ensure consistent low-resistance contacts across varying device configurations.

Moreover, interface and surface states in GaN HEMTs significantly affect device stability and reliability. The literature has established that these states lead to charge trapping and variations in threshold voltage, but more sophisticated models are required to predict these effects under different operational stresses, including high-frequency switching and high-temperature environments. Addressing these issues involves optimizing the interface quality between different materials and passivating surface states to prevent charge trapping. Techniques such as atomic layer deposition (ALD) for high-quality gate dielectrics, surface passivation using silicon nitride or other dielectrics, and improving the quality of the GaN surface through chemical treatments are being explored. However, these methods have not yet been sufficiently tested under extreme operating conditions, and their effectiveness over the long term is still uncertain. More experimental data and real-world testing are needed to validate these approaches.

While GaN HEMTs offer immense potential for advancing power electronics and RF applications, the path to their widespread adoption is still fraught with significant challenges. These challenges include epitaxial growth and material quality control, device scaling, thermal management, ohmic contact quality, and the impact of interface and surface states. The current literature provides a solid foundation, but a more critical perspective that incorporates both technological innovation and practical implementation is essential. Only through a combination of cutting-edge device design, advanced materials research, and optimized fabrication processes can the full potential of GaN HEMTs be realized, paving the way for their broader integration into diverse applications and driving the future of power electronics and RF technologies [101]–[103].

V. Applications

GaN HEMTs have become pivotal in numerous fields due to their superior performance characteristics. In power electronics, GaN HEMTs are predominantly used in high-frequency and high-power scenarios, such as power supplies, inverters, and converters for renewable energy systems [104]–[106]. Their exceptional electron mobility and low on-resistance facilitate efficient power conversion, minimizing switching losses, which boosts energy efficiency and allows for more compact designs.

In the realm of radio frequency (RF) and microwave applications, GaN HEMTs are integral to telecommunications, radar systems, and wireless communication networks [108] [109]. Their capability to operate at high frequencies and their low parasitic capacitance make them ideal for high-speed data transmission and signal amplification, supporting next-generation communication systems.

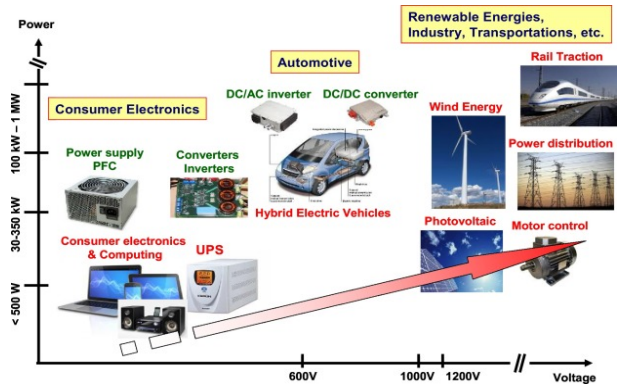

FIGURE 18: Applications of GaN HEMT in different sectors such as consumer electronics, automotive, renewable energies, industry and transportations [107].

The automotive industry also benefits significantly from GaN HEMT technology, particularly in electric vehicles (EVs) and hybrid electric vehicles (HEVs) [110]–[112]. The high switching speed and robustness of GaN HEMTs enable efficient power management, which enhances vehicle performance and extends battery life. However, the industry's shift toward autonomous driving and connected vehicles introduces new challenges, including the need for better electromagnetic interference (EMI) management and improved thermal reliability in extreme conditions. In aerospace and defense sectors, GaN HEMTs are valued for their high power handling capabilities and resistance to radiation, making them suitable for radar systems, electronic warfare, and satellite communications. Although these attributes ensure reliable performance in challenging environments, the literature tends to focus more on device capabilities rather than on long-term reliability testing in extreme conditions, such as high radiation or fluctuating thermal environments. Expanding research to encompass the effects of sustained radiation exposure and mechanical stress on GaN HEMTs will provide a more comprehensive understanding of their durability and applicability in aerospace and defense sectors.

Moreover, GaN HEMTs are finding increasing use in emerging fields such as medical electronics, consumer electronics, and industrial automation. Their versatility and superior performance characteristics make them suitable for a wide range of applications, underscoring their growing significance across various sectors. Thus, GaN HEMTs hold immense promise across a broad spectrum of industries, a more critical and inclusive perspective is necessary to fully understand their limitations and potential. As shown in Figure 18, the applications of GaN HEMT technology span multiple industries, but realizing their full capabilities requires addressing both current technological gaps and the emerging challenges in integration. The continuous advancements in GaN HEMT technology are expected to spur further innovation, expanding their applications even more in the future. By critically analyzing both the advantages and the

Authorized licensed use limited to: DELHI TECHNICAL UNIV. Downloaded on November 11,2024 at 04:22:17 UTC from IEEE Xplore. Restrictions apply.
© 2024 IEEE. Personal use is permitted, but republication/redistribution requires IEEE permission. See https://www.ieee.org/publications/rights/index.html for more information.

This article has been accepted for publication in IEEE Electron Devices Reviews. This is the author's version which has not been fully edited and content may change prior to final publication. Citation information: DOI 10.1109/EDR.2024.3491716

hurdles ahead, we can unlock the next wave of GaN HEMT applications, ensuring their broader adoption in various high-performance and high-reliability systems.

VI. Conclusion

This review paper examines various aspects of GaN HEMTs, tracing their early developments and the latest advancements in both power and RF device applications. While the review provides valuable insights, it also highlights ongoing challenges and reliability issues associated with GaN HEMT technology. Also, these devices are known for their significant contributions across multiple fields. In high-frequency communication systems, their ability to operate at high speeds with low parasitic capacitance makes them ideal for efficient data transmission and signal amplification, supporting the development of next-generation communication networks. In power electronics,the devices play a transformative role by enabling efficient energy conversion with minimal losses. Their high electron mobility and low on-resistance are key to improving the performance of power supplies, inverters, and converters, especially in renewable energy systems. These attributes not only boost energy efficiency but also facilitate more compact and efficient power system designs. Despite these advantages, these devices face several technical challenges, including issues related to device reliability, thermal management, and manufacturing consistency. Ensuring long-term stability and performance under various operating conditions remains a significant focus for ongoing research. Future research and development efforts are expected to focus on overcoming these challenges. Innovations in material science, device engineering, and thermal management techniques will be crucial in improving the reliability and performance of GaN HEMTs. As these advancements are made, the range of applications for GaN HEMTs is likely to expand, further establishing their importance in diverse fields such as telecommunications, power electronics, and defense.

REFERENCES

[1] Tian, Jiangbo, Chunyan Lai, Guodong Feng, Debmalya Banerjee, Wenlong Li, and Narayan C. Kar. , “Review of recent progresses on gallium nitride transistor in power conversion application” *International Journal of Sustainable Energy*, 9(1), pp. 88–100, Aug. 2020, 10.1080/14786451.2019.1657866.

[2] Roccaforte, Fabrizio, Giuseppe Greco, Patrick Fiorenza, and Ferdinando Iucolano, “An overview of normally-off GaN-based high electron mobility transistors.” *Materials*, 12(10), 1599, May. 2019, 10.3390/ma12101599.

[3] Greco, Giuseppe, Ferdinando Iucolano, and Fabrizio Roccaforte. , “Review of technology for normally-off HEMTs with p-GaN gate.” *Materials Science in Semiconductor Processing*, 78, pp. 96–106, May. 2018, 10.1016/j.mssp.2017.09.027.

[4] T.Garg and Sumit Kale, ”Optimization of structural parameters in Omega-Shaped gate p-GaN MIS-HEMT for performance improvement”, Micro and Nanostructures, (2024).

[5] He, Jiaqi, Wei-Chih Cheng, Qing Wang, Kai Cheng, Hongyu Yu, and Yang Chai, “Recent Advances in GaN-Based Power HEMT Devices.” *Advanced Electronic Materials* , 7(4), Jan. 2021, 10.1002/aelm.202001045.

[6] Ranjan, Ravi, Nitesh Kashyap, and Ashish Raman., “Effects of gate width variation on the performance of Normally-OFF dual-recessed gate MIS AlGaN/GaN HEMT.” *International Journal of Numerical Modelling: Electronic Networks, Devices and Fields*, 35(2), Sep. 2021, 10.1002/jnm.2960.

[7] Letellier, Juliette. (2019). Diamond Schottky diodes improvement to pave the way to high power electronic application.

[8] Xiao-Guang He, De-Gang Zhao and De-Sheng Jiang, “Formation of two-dimensional electron gas at AlGaN/GaN heterostructure and the derivation of its sheet density expression”,Chinese Physics B, vol. 24, no. 6 ,April 2015 doi: 10.1088/1674-1056/24/6/067301

[9] Asif Khan, M., A. Bhattarai, J. N. Kuznia, and D. T. Olson. , “High electron mobility transistor based on a GaN AlGaN heterojunction” *Applied Physics Letters*, 63(9), pp. 1214–1215, Jun. 1993, 10.1063/1.109775.

[10] Asif Khan, M., J. N. Kuznia, D. T. Olson, W. J. Schaff, J. W. Burm, and M. S. Shur, “Microwave performance of a 0.25 um gate AlGaN/GaN heterostructure field effect transistor.” *Applied Physics Letters*, 65(9), pp. 1121–1123, Jun. 1994, 10.1063/1.112116.

[11] Y. . -F. Wu, B. P. Keller, S. Keller, D. Kapolnek, S. P. Den-Baars and U. K. Mishra, ”GaN HFETs and MODFETs with very high breakdown voltage and large transconductance,” *1996 54th Annual Device Research Conference Digest*, Jun, 1996, pp. 60-61, 10.1109/DRC.1996.546315.

[12] L. F. Eastman, ”AlGaN/GaN microwave power HEMT’s,” GaAs IC Symposium. IEEE Gallium Arsenide Integrated Circuit Symposium. 21st Annual. Technical Digest 1999 (Cat. No.99CH36369), Monterey, CA, USA, 1999, pp. 15-18, doi: 10.1109/GAAS.1999.803718.

[13] S. Karmalkar and U. K. Mishra, ”Enhancement of breakdown voltage in AlGaN/GaN high electron mobility transistors using a field plate,” in IEEE Transactions on Electron Devices, vol. 48, no. 8, pp. 1515-1521, Aug. 2001, doi: 10.1109/16.936500.

[14] W. Saito, Y. Takada, M. Kuraguchi, K. Tsuda and I. Omura, ”Recessed-gate structure approach toward normally off high-Voltage AlGaN/GaN HEMT for power electronics applications,” in IEEE Transactions on Electron Devices, vol. 53, no. 2, pp. 356-362, Feb. 2006, doi: 10.1109/TED.2005.862708.

[15] M. H. Wong et al., ”N-Face Metal–Insulator–Semiconductor High-Electron-Mobility Transistors With AlN Back-Barrier,” in IEEE Electron Device Letters, vol. 29, no. 10, pp. 1101-1104, Oct. 2008, doi: 10.1109/LED.2008.2003543.

[16] O. Hilt, F. Brunner, E. Cho, A. Knauer, E. Bahat-Treidel and J. Würfl, ”Normally-off high-voltage p-GaN gate GaN HFET with carbon-doped buffer,” 2011 IEEE 23rd International Symposium on Power Semiconductor Devices and ICs, San Diego, CA, USA, 2011, pp. 239-242, doi: 10.1109/ISPSD.2011.5890835.

[17] D. Godfrey et al., ”Investigation of AlGaN/GaN HEMT Breakdown analysis with Source field plate length for High power applications,” 2020 5th International Conference on Devices, Circuits and Systems (ICDCS), Coimbatore, India, 2020, pp. 244-246, 10.1109/ICDCS48716.2020.243589.

[18] V. Palankovski, S. Vitanov and R. Quay, ”Field-Plate Optimization of AlGaN/GaN HEMTs,” 2006 IEEE Compound Semiconductor Integrated Circuit Symposium, San Antonio, TX, USA, 2006, pp. 107-110, doi: 10.1109/CSICS.2006.319926.

[19] Fletcher, Augustine, Ph.D, D.Nirmal, J. Ajayan, and Arivazhagan, L.” Analysis of AlGaN/GaN HEMT using Discrete Field plate technique for High Power and High Frequency Applications” AEU - International Journal of Electronics and Communications, 99, 2018, doi: 10.1016/j.aeue.2018.12.006.

[20] C. Zhang et al., ”Super Field Plate Technique That Can Provide Charge Balance Effect for Lateral Power Devices Without Occupying Drift Region,” in IEEE Transactions on Electron Devices, vol. 67, no. 5, pp. 2218-2222, May 2020, doi: 10.1109/TED.2020.2981264.

[21] F. Udrea, G. Deboy, and T. Fujihira, “Superjunction power devices, history, development, and future prospects,” IEEE Trans. Electron Devices, vol. 64, no. 3, pp. 713–727, Mar. 2017, doi: 10.1109/TED.2017.2658344.

[22] B. Duan, Z. Cao, X. Yuan, S. Yuan, and Y. Yang, “New superjunction LDMOS breaking silicon limit by electric field modulation of buffered step doping,” IEEE Electron Device Lett., vol. 36, no. 1, pp. 47–49, Jan. 2015, doi: 10.1109/LED.2014.2366298.

[23] W. Zhang et al., “Non-full depletion mode and its experimental realization of the lateral superjunction,” in Proc. IEEE 30th Int. Symp. Power Semiconductor Devices ICs (ISPSD), May 2018, pp. 475–478, doi: 10.1109/ISPSD.2018.8393706.

Authorized licensed use limited to: DELHI TECHNICAL UNIV. Downloaded on November 11,2024 at 04:22:17 UTC from IEEE Xplore. Restrictions apply.
© 2024 IEEE. Personal use is permitted, but republication/redistribution requires IEEE permission. See https://www.ieee.org/publications/rights/index.html for more information.

This article has been accepted for publication in IEEE Electron Devices Reviews. This is the author's version which has not been fully edited and content may change prior to final publication. Citation information: DOI 10.1109/EDR.2024.3491716

[24] Jialin Li, Yian Yin, Fengbo Liao, Mengxiao Lian, Xichen Zhang, Keming Zhang, Yafang Xie, You Wu, Bingzhi Zou, Zhixiang Zhang, Jingbo Li," 2.57GW/cm2 normally-off composite stepped gate GaN-based HEMT with p-GaN buried layer and field plate", in Materials Science in Semiconductor Processing, vol. 153, Jan 2023, 107152, doi: 10.1016 /j.mssp.2022.107152.

[25] Huang, Huolin, Sun, Zhonghao, Zhang, Zifeng, Shen, Rensheng, Liang, YC, Liang, Hongwei, Bian, J., Du, Guotong and Zhang, Heqiu "Performance-improved normally-off AlGaN/GaN high-electron mobility transistors with a designed p-GaN area under the recessed gate",pp. 1230-1232, 2016 doi:10.1109/ICSICT.2016.7998701.

[26] J. Yang et al., "600-V p-GaN Gate HEMT With Buried Hole Spreading Channel Demonstrating Immunity Against Buffer Trapping Effects," in IEEE Electron Device Letters, vol. 44, no. 2, pp. 225-228, Feb. 2023, doi: 10.1109/LED.2022.3232474.

[27] M. Borga, M. Meneghini, S. Stoffels, X. Li, N. Posthuma, M. Van Hove, S. Decoutere, G. Meneghesso, and E. Zanoni, "Impact of substrate resistivity on the vertical leakage, breakdown, and trapping in GaN on- Si E-mode HEMTs," IEEE Trans. Electron Devices, vol. 65, no. 7, pp. 2765–2770, Jul. 2018, doi: 10.1109/TED.2018.2830107.

[28] S. Yang, C. Zhou, S. Han, J. Wei, K. Sheng, and K. J. Chen, "Impact of substrate bias polarity on buffer-related current collapse in AlGaN/GaN on-Si power devices," IEEE Trans. Electron Devices, vol. 64, no. 12, pp. 5048–5056, Dec. 2017, doi: 10.1109/TED.2017.2764527.

[29] J. A. Croon, G. A. M. Hurkx, J. J. T. M. Donkers, and J. Sonsky,"Impact of the backside potential on the current collapse of GaN SBDs and HEMTs," in Proc. IEEE 27th Int. Symp. Power Semiconductor Devices (ISPSD), Hong Kong, May 2015, pp. 365–368, doi: 10.1109/ISPSD.2015.7123465.

[30] R. Baby, K. Reshma, H. Chandrasekar, R. Muralidharan, S. Raghavan and D. N. Nath, "Study of TaN-Gated p-GaN E-Mode HEMT," in IEEE Transactions on Electron Devices, 10.1109/TED.2023.3241132.

[31] A. Stockman, E. Canato, M. Meneghini, G. Meneghesso, P. Moens and B. Bakeroot, "Schottky Gate Induced Threshold Voltage Instabilities in p-GaN Gate AlGaN/GaN HEMTs," in IEEE Transactions on Device and Materials Reliability, vol. 21, no. 2, pp. 169-175, June 2021, doi: 10.1109/TDMR.2021.3080585.

[32] J. Chen et al., "OFF-State Drain-Voltage-Stress-Induced VTH Instability in Schottky-Type p-GaN Gate HEMTs," in IEEE Journal of Emerging and Selected Topics in Power Electronics, vol. 9, no. 3, pp. 3686-3694, June 2021, doi: 10.1109/JESTPE.2020.3010408.

[33] X. Tang, B. Li, H. A. Moghadam, P. Tanner, J. Han and S. Dimitrijev, "Mechanism of Threshold Voltage Shift in p -GaN Gate AlGaN/GaN Transistors," in IEEE Electron Device Letters, vol. 39, no. 8, pp. 1145-1148, Aug. 2018, doi: 10.1109/LED.2018.2847669.

[34] T. Garg and S. Kale, "A novel p-GaN HEMT with AlInN/AlN/GaN double heterostructure and InAlGaN back-barrier," Microelectron. Reliab., vol. 145, June 2023, doi: 10.1016/j.microrel.2023.114998.

[35] Hongbo Yu, Sefer B. Lisesivdin, Basar Bolukbas, Ozgur Kelekci, Mustafa Kemal Ozturk, Suleyman Ozcelik, Deniz Caliskan, et al., Improvement of breakdown characteristics in AlGaN/GaN/AlGaN HEMT based on a grading AlGaN buffer layer, Phys. Status Solidi a 11, 207, 2593–2596, 2010, doi:10.1002/pssa.201026270.

[36] Xu Zhang, Liming Wang, Wanjie Li, Luqi Tao, Xianping Chen, Gallium nitride dual two-dimensional electron gas HEMT with a good performance: Based on TCAD simulations, in: 2020 21st International Conference on Electronic Packaging Technology, ICEPT, IEEE, pp. 1–4,2020, doi: 10.1109/ICEPT50128.2020.9202882.

[37] Sarosij Adak, Arghyadeep Sarkar, Sanjit Swain, Hemant Pardeshi, Sudhansu Kumar Pati, Chandan Kumar Sarkar, High performance AlInN/AlN/GaN p-GaN back barrier gate-recessed enhancement-mode HEMT, Superlattices Microstruct. 75,347–357, 2014, doi:10.1016/j.spmi.2014.07.036.

[38] N. Wu et al., "Enhanced Performance of Low-Leakage-Current Normally off p-GaN Gate HEMTs Using NH3 Plasma Pretreatment," in IEEE Transactions on Electron Devices, vol. 70, no. 9, pp. 4560-4564, Sept. 2023, doi: 10.1109/TED.2023.3294894.

[39] K. Shiojima, T. Takahashi, N. Kaneda, T. Mishima, and K. Nomoto, "Effect of inductively coupled plasma etching in p-type GaN Schottky contacts," Jpn. J. Appl. Phys., vol. 52, no. 8S, May 2013, Art. no. 08JJ08, doi: 10.7567/JJAP.52.08JJ08.

[40] K. J. Choi, H. W. Jang, and J.-L. Lee, "Observation of inductively coupled-plasma-induced damage on n-type GaN using deep-level transient spectroscopy," Appl. Phys. Lett., vol. 82, no. 8, pp. 1233–1235, Feb. 2003, doi: 10.1063/1.1557316.

[41] S. G. Bao et al., "Effects of low-damage plasma treatment on the channel 2DEG and device characteristics of AlGaN/GaN HEMTs," Chin. Phys. Lett., vol. 37, no. 2, Feb. 2020, Art. no. 027301, doi: 10.1088/0256-307X/37/2/027301.

[42] J. -X. Yang, D. -J. Lin, Y. -R. Wu and J. -J. Huang, "Deep Source Metal Trenches in GaN-On-Si HEMTs for Relieving Current Collapse," in IEEE Journal of the Electron Devices Society, vol. 9, pp. 557-563, 2021, 10.1109/JEDS.2021.3078522.

[43] C. Wang, S. Ho, and J. J. Huang, "Suppression of current collapse in enhancement-mode AlGaN/GaN high electron mobility transistors," IEEE Electron Device Lett., vol. 37, no. 1, pp. 74–76, Jan. 2016, doi: 10.1109/LED.2015.2498623.

[44] C. Liu, E. F. Chor, and L. S. Tan, "Enhanced device performance of AlGaN/GaN HEMTs using HfO2 high-k dielectric for surface passivation and gate oxide," Semicond. Sci. Technol., vol. 22, no. 5, pp. 522–527, Mar. 2007, doi: 10.1088/0268-1242/22/5/011.

[45] S. Ho, C. Lee, A. Tzou, H. Kuo, Y. Wu, and J. Huang, "Suppression of current collapse in enhancement mode GaN-based HEMTs using an AlGaN/GaN/AlGaN double heterostructure," IEEE Trans. Electron Devices, vol. 64, no. 4, pp. 1505–1510, Apr. 2017, doi: 10.1109/TED.2017.2657683.

[46] Li Y, Xu L, Guo Z, Sun H. "Study of High-Performance GaN-Based Trench CAVET with Stepped Doping Microstructure", Micromachines (Basel), vol.13, no.8, Aug 2022. doi: 10.3390/mi13081273.

[47] P. Bai et al., "A Novel Trench-Gated Vertical GaN Transistor With Dual-Current-Aperture by Electric-Field Engineering for High Breakdown Voltage," in IEEE Transactions on Electron Devices, vol. 69, no. 3, pp. 1219-1225, March 2022, doi: 10.1109/TED.2022.3146110.

[48] Y. Wang, M. -t. Bao, F. Cao, J. -x. Tang and X. Luo, "Technology Computer Aided Design Study of GaN MISFET With Double P-Buried Layers," in IEEE Access, vol. 7, pp. 87574-87581, 2019, doi: 10.1109/ACCESS.2019.2924999.

[49] P. Doring et al., "A Study on the Performance of AlGaN/GaN HEMTs Regrown on Mg-Implanted GaN Layers With Low Channel Thickness," in IEEE Transactions on Electron Devices, vol. 70, no. 3, pp. 947-952, March 2023, doi: 10.1109/TED.2023.3237803.

[50] K.Kohler, R.Gutt, j.Weigert, and L. Kirste, "Diffusion of Mg dopant in metal-organic vapor-phase epitaxy grown GaN and AlxGa1-xN," J. Appl. Phys., vol. 113, no. 7, Feb. 2013, Art. no. 073514, doi:10.1063/1.4792662.

[51] A. Agarwal, M. Tahhan, T. Mates, S. Keller, and U. Mishra, "Suppression of Mg propagation into subsequent layers grown by MOCVD," J. Appl. Phys., vol. 121, no. 2, Jan. 2017, Art. no. 025106, doi:10.1063/1.4972031.

[52] I. Mahaboob, S. W. Novak, E. Rocco, K. Hogan, and F. Shahedipour-Sandvik, "Investigation of the electrical behavior of AlGaN/GaN high electron mobility transistors grown with underlying GaN:Mg layer," J. Vac. Sci. Technol. B, Microelectron., vol. 38, no. 6, 2020, Art. no. 62204, doi: 10.1116/6.0000255.

[53] H. Lu et al., "Improved RF Power Performance of AlGaN/GaN HEMT Using by Ti/Au/Al/Ni/Au Shallow Trench Etching Ohmic Contact," in IEEE Transactions on Electron Devices, vol. 68, no. 10, pp. 4842-4846, Oct. 2021, 10.1109/TED.2021.3101462.

[54] Y. K. Yadav, B. B. Upadhyay, M. Meer, N. Bhardwaj, S. Ganguly, and D. Saha, "Ti/Au/Al/Ni/Au low contact resistance and sharp edge acuity for highly scalable AlGaN/GaN HEMTs," IEEE Electron Device Lett., vol. 40, no. 1, pp. 67–70, Jan. 2019, doi: 10.1109/LED.2018.2884155.

[55] Y.-S. Chiu et al., "Ti/Al/Ti/Ni/Au ohmic contacts on AlGaN/GaN high electron mobility transistors with improved surface morphology and low contact resistance," J. Vac. Sci. Technol. B, Nanotechnol. Microelectron., Mater., Process., Meas., Phenomena, vol. 32, no. 1, Jan. 2014, Art. no. 011216, doi: 10.1116/1.4862165.

[56] Y. He et al., "Scaled InAlN/GaN HEMT on Sapphire With fT/fmax of 190/301 GHz," in IEEE Transactions on Electron Devices, vol. 70, no. 6, pp. 3001-3004, June 2023, doi: 10.1109/TED.2023.3269728.

[57] D. Denninghoff, J. Lu, E. Ahmadi, S. Keller and U. K. Mishra, "N-polar GaN/InAlN/AlGaN MIS-HEMTs with 1.89 S/mm extrinsic transconductance, 4 A/mm drain current, 204 GHz fT and 405 GHz fmax," 71st Device Research Conference, Notre Dame, IN, USA, 2013, pp. 197-198, doi: 10.1109/DRC.2013.6633861.

[58] L. Li et al., "GaN HEMTs on Si With Regrown Contacts and Cutoff/Maximum Oscillation Frequencies of 250/204 GHz," in IEEE

Authorized licensed use limited to: DELHI TECHNICAL UNIV. Downloaded on November 11,2024 at 04:22:17 UTC from IEEE Xplore. Restrictions apply.
© 2024 IEEE. Personal use is permitted, but republication/redistribution requires IEEE permission. See https://www.ieee.org/publications/rights/index.html for more information.

This article has been accepted for publication in IEEE Electron Devices Reviews. This is the author's version which has not been fully edited and content may change prior to final publication. Citation information: DOI 10.1109/EDR.2024.3491716

Electron Device Letters, vol. 41, no. 5, pp. 689-692, May 2020, doi: 10.1109/LED.2020.2984727.

[59] J. Zhou et al., "RF p-GaN HEMT with 0.9-dB Noise Figure and 12.8-dB Associated Gain for LNA Applications," in IEEE Electron Device Letters, doi: 10.1109/LED.2023.3294696.

[60] Y. Cheng, Y. H. Ng, Z. Zheng, and K. J. Chen, "RF Enhancement-Mode p-GaN Gate HEMT on 200 mm-Si Substrates," IEEE Electron Device Lett., vol. 44, no. 1, pp. 29-31, Jan. 2023, doi:10.1109/LED.2022.3220693.

[61] C. Sanabria, A. Chakraborty, X. Hongtao, M. J. Rodwell, U. K.Mishra, and R. A. York, "The effect of gate leakage on the noise figure of AlGaN/GaN HEMTs," IEEE Electron Device Lett., vol. 27, no. 1, pp. 19-21, Jan. 2006, doi: 10.1109/led.2005.860889.

[62] K. Bansal, S. Chander and S. Gupta, "AlGaN/GaN HEMT based RF Switch Model," 2023 International Conference on Microwave, Optical, and Communication Engineering (ICMOCE), Bhubaneswar, India, 2023, pp. 1-4, doi: 10.1109/ICMOCE57812.2023.10166040.

[63] P. J. Zampardi and F. Kharabi, "Industrial view of III–V devices compact modelling for circuit design," IEEE Trans. Electron Devices, vol. 66, no. 1, pp. 28–33, Jan. 2019.

[64] Zhifu Hu , Qijun Zhang , Kaixue Ma , Ruicong He, and Feng Feng , "An Improved Compact Large-Signal GaN HEMT Model for Switch Application," IEEE Transactions on electron devices, Vol. 69, no.6, June 2022.

[65] C.Y. Hsieh et al., "GaN on Si RF performance with different AlGaN back barrier," 2023 International VLSI Symposium on Technology, Systems and Applications (VLSI-TSA/VLSI-DAT), HsinChu, Taiwan, 2023, pp. 1-2, doi: 10.1109/VLSI-TSA/VLSI-DAT57221.2023.10134089.

[66] T. Kabemura, S. Ueda, Y. Kawada and K. Horio, "Enhancement of Breakdown Voltage in AlGaN/GaN HEMTs: Field Plate Plus High-k Passivation Layer and High Acceptor Density in Buffer Layer," in IEEE Transactions on Electron Devices, vol. 65, no. 9, pp. 3848-3854, Sept. 2018, 10.1109/TED.2018.2857774.

[67] Chander, S., Ajay, Gupta, M. Enhancement-Mode High Electron Mobility Transistor on SiC Substrate with T-Gate Field Plate for High Power Applications. In: Sharma, R., Rawal, D. (eds) The Physics of Semiconductor Devices. IWPSD 2017. Springer Proceedings in Physics, vol 215. Springer, Cham, 2019, 10.1007/978-3-319-97604-4-45

[68] D. Godfrey et al., "Investigation of AlGaN/GaN HEMT Breakdown analysis with Source field plate length for High power applications," 2020 5th International Conference on Devices, Circuits and Systems (ICDCS), Coimbatore, India, 2020, pp. 244-246, 10.1109/ICDCS48716.2020.243589.

[69] G. Zhou et al., "Gate Leakage Suppression and Breakdown Voltage Enhancement in p-GaN HEMTs Using Metal/Graphene Gates," in IEEE Transactions on Electron Devices, vol. 67, no. 3, pp. 875-880, March 2020, 10.1109/TED.2020.2968596.

[70] V. Sandeep, J. C. Pravin, A. Ramesh Babu and P. Prajoon, "Impact of AlInN Back-Barrier Over AlGaN/GaN MOS-HEMT With HfO2 Dielectric Using Cubic Spline Interpolation Technique," *IEEE Transactions on Electron Devices*, 67(9), pp. 3558-3563, Sept. 2020, 10.1109/TED.2020.3010710.

[71] X. Wei, X. Zhang, C. Sun, W. Tang, C. Zeng, F. Chen, T. He, G. Yu, L. Song, W. Lin, X. Zhang, D. Zhao, W. Huang, Y. Cai and B. Zhang, "Improvement of Breakdown Voltage and ON-Resistance in Normally-OFF AlGaN/GaN HEMTs Using Etching-Free p-GaN Stripe Array Gate," *IEEE Transactions on Electron Devices*, 68(10), pp. 5041-5047, Oct. 2021, 10.1109/TED.2021.3105088.

[72] C. -Y. Chang, C.-S. Wang, C.-Y. Wang, Y.-L. Shen, T.-L. Wu, W.-H. Kuo, S.-F. Lin, and C.-F. Huang, "Demonstration of p-GaN/AlGaN/GaN High Electron Mobility Transistors With an Indium–Tin–Oxide Gate Electrode," *IEEE Journal of the Electron Devices Society*, 9, pp. 2-5, Oct. 2021, 10.1109/JEDS.2020.3030911.

[73] H. Du, J. Zhang, H. Zhou, Z. Liu, T. Zhang, K. Dang, Y. Zhang, W. Zhang, Y. Zhang, and Y. Hao, "GaN High-Electron-Mobility-Transistor on Free- Standing GaN Substrate With Low Contact Resistance and State-of-the-Art fT × LG Value," *IEEE Transactions on Electron Devices*, 69(3), pp. 968-972, March 2022, 10.1109/TED.2021.3138954.

[74] J. Liu, M. Mi, J. Zhu, S. Liu, P. Wang, Y. Zhou, Q. Zhu, M. Wu, H. Lu, B. Hou, H. Wang, X. Cai, Y. Zhang, X. Duan, L. Yang, X. Ma and Y. Hao,"Improved Power Performance and the Mechanism of AlGaN/GaN HEMTs Using Si-Rich SiN Si3N4 Bilayer Passivation," *IEEE Transactions on Electron Devices*, 69(2), pp. 631-636, Feb. 2022, 10.1109/TED.2021.3133822.

[75] N. Sun, H. Huang, Z. Sun, R. Wang, S. Li, P. Tao, Y. Ren, S. Song, H. Wang, S. Li, W. Cheng and H. Liang, "Improving Gate Reliability of 6-In E-Mode GaN-Based MIS-HEMTs by Employing Mixed Oxygen and Fluorine Plasma Treatment," *IEEE Transactions on Electron Devices*, 69(1), pp. 82-87, Jan. 2022, 10.1109/TED.2021.3131118.

[76] T.Garg and Sumit Kale, "A Novel Stepped AlGaN Hybrid Buffer GaN HEMT for Power Electronics Applications", Microelectronics Reliability, (2023).

[77] T. Garg and S. Kale, "A Novel Enhancement Mode GaN HEMT with MIS and p-GaN structure," 2024 IEEE 9th International Conference for Convergence in Technology (I2CT), Pune, India, 2024, pp. 1-3, doi: 10.1109/I2CT61223.2024.10543334.

[78] N. . -Q. Zhang, S. Keller, G. Parish, S. Heikman, S. P. DenBaars and U. K. Mishra, "High breakdown GaN HEMT with overlapping gate structure," in IEEE Electron Device Letters, vol. 21, no. 9, pp. 421-423, Sept. 2000, doi: 10.1109/55.863096.

[79] Shen, L., Mishra, U. K., and Kazior, T. E. (2013). "GaN-Based RF Power Devices and Amplifiers". Academic Press.

[80] Matteo Meneghini, Carlo De Santi, Idriss Abid, Matteo Buffolo, Marcello Cioni, Riyaz Abdul Khadar, Luca Nela, Nicolò Zagni, Alessandro Chini, Farid Medjdoub, Gaudenzio Meneghesso, Giovanni Verzellesi, Enrico Zanoni, Elison Matioli; GaN-based power devices: Physics, reliability, and perspectives. J. Appl. Phys. 14 Nov, 130, 18, 181101, 2021.

[81] Xin Yajie, Chen Wanjun, Sun Ruize, Yijun Shi, Liu Chao, Xia Yun, Wang Fangzhou, Xu Xiaorui, Shi Qi, Wang Yuan, Deng Xiaochuan, Zhou qi, Li Zhaoji and Zhang Bo, "Electrostatic Discharge (ESD) Behavior of p-GaN HEMTs" 317-320, 2020 10.1109/ISPSD46842.2020.9170063.

[82] G. Meneghesso et al., "Reliability of GaN High-Electron-Mobility Transistors: State of the Art and Perspectives," in IEEE Transactions on Device and Materials Reliability, vol. 8, no. 2, pp. 332-343, June 2008, doi: 10.1109/TDMR.2008.923743.

[83] Franke Jorg, Zeng Guang, Winkler Tom and Lutz J, (2018), "Power cycling reliability results of GaN HEMT devices" 467-470, 2020, 10.1109/ISPSD.2018.8393704.

[84] Kuzmik Jan, Carlin Jean-François, Gonschorek M., Kostopoulos A., Konstantinidis Giorgos, Pozzovivo G., Golka S., Georgakilas A., Grandjean Nicolas, Strasser Gottfried and Pogany Dionyz, "Gate-lag and drain-lag effects in (GaN)/InAlN/GaN and InAlN/AlN/GaN HEMTs", physica status solidi (a), 204, 2007 10.1002/pssa.200674707.

[85] del Alamo, J.A., Guo, A.and Warnock, S., "Gate dielectric reliability and instability in GaN metal insulator semiconductor high electron mobility transistors for power electronics", Journal of Materials Research vol. 32, pp. 3458–3468, 2017. doi: 10.1557/jmr.2017.363

[86] T. Ohki et al., "Reliability of GaN HEMTs: current status and future technology," 2009 IEEE International Reliability Physics Symposium, Montreal, QC, Canada, 2009, pp. 61-70, doi: 10.1109/IRPS.2009.5173225.

[87] M. Meneghini et al., "Reliability and failure analysis in power GaN-HEMTs: An overview," 2017 IEEE International Reliability Physics Symposium (IRPS), Monterey, CA, USA, 2017, pp. 3B-2.1-3B-2.8, doi: 10.1109/IRPS.2017.7936282.

[88] Zanoni, E., Rampazzo, F., De Santi, C., Gao, Z., Sharma, C., Modolo, N., Verzellesi, G., Chini, A., Meneghesso, G. and Meneghini, M., "Failure Physics and Reliability of GaN-Based HEMTs for Microwave and Millimeter-Wave Applications: A Review of Consolidated Data and Recent Results", Phys. Status Solidi A, 219, 2100722, 2022, doi:10.1002/pssa.202100722.

[89] M. A. Khan, "Challenges and opportunities for GaN high-electron-mobility transistors," IEEE Trans. Electron Devices, vol. 61, no. 10, pp. 3320-3328, Oct. 2014, 10.1109/TED.2014.2340523.

[90] A. T. Ping, Y. K. Chin, and S. P. McAlister, "Challenges in GaN HEMT technology for power conversion applications," IEEE Trans. Power Electron., vol. 30, no. 5, pp. 2425-2434, May 2015, 10.1109/TPEL.2014.2328862

[91] J. Zhang, C. K. Ong, and J. K. Fidler, "Challenges and opportunities for GaN HEMT device design," IEEE J. Emerg. Sel. Topics Circuits Syst., vol. 8, no. 2, pp. 307-316, Jun. 2018, 10.1109/JETCAS.2018.2820579

Authorized licensed use limited to: DELHI TECHNICAL UNIV. Downloaded on November 11,2024 at 04:22:17 UTC from IEEE Xplore. Restrictions apply.
© 2024 IEEE. Personal use is permitted, but republication/redistribution requires IEEE permission. See https://www.ieee.org/publications/rights/index.html for more information.

This article has been accepted for publication in IEEE Electron Devices Reviews. This is the author's version which has not been fully edited and content may change prior to final publication. Citation information: DOI 10.1109/EDR.2024.3491716

[92] J. Kuzmik, P. Poloczek, and K. Rzazewski, "Challenges in GaN HEMT technology: Materials, device design, reliability," IEEE Trans. Electron Devices, vol. 62, no. 1, pp. 38-42, Jan. 2015, 10.1109/TED.2014.2362836

[93] A. I. Emon, Mustafeez-ul-Hassan, A. B. Mirza, J. Kaplun, S. S. Vala and F. Luo, "A Review of High-Speed GaN Power Modules: State of the Art, Challenges, and Solutions," in IEEE Journal of Emerging and Selected Topics in Power Electronics, vol. 11, no. 3, pp. 2707-2729, June 2023, doi: 10.1109/JESTPE.2022.3232265.

[94] Haziq, Muhaimin, Shaili Falina, Asrulnizam Abd Manaf, Hiroshi Kawarada, and Mohd Syamsul, "Challenges and Opportunities for High-Power and High-Frequency AlGaN/GaN High-Electron-Mobility Transistor (HEMT) Applications: A Review" Micromachines 13, no. 12: 2133, 2022, doi:10.3390/mi13122133

[95] J. Ajayan, D. Nirmal, P. Mohankumar, B. Mounika, Sandip Bhattacharya, Shubham Tayal, A.S. Augustine Fletcher, Challenges in material processing and reliability issues in AlGaN/GaN HEMTs on silicon wafers for future RF power electronics and switching applications: A critical review, Materials Science in Semiconductor Processing, vol. 151, 2022, doi: 10.1016/j.mssp.2022.106982.

[96] A. Udabe, I. Baraia-Etxaburu and D. G. Diez, "Gallium Nitride Power Devices: A State of the Art Review," in IEEE Access, vol. 11, pp. 48628-48650, 2023, doi: 10.1109/ACCESS.2023.3277200.

[97] S. Yoshida, K. Makiyama, A. Hayasaka, I. Makabe and K. Nakata, "Challenges and Potential of N-polar GaN HEMT for beyond 5G Wireless Network," 2022 IEEE BiCMOS and Compound Semiconductor Integrated Circuits and Technology Symposium (BCICTS), Phoenix, AZ, USA, 2022, pp. 104-107, doi: 10.1109/BCICTS53451.2022.10051701.

[98] F. Sadeque, A. Y. Fard, A. Adib, M. B. Shadmand and B. Mirafza, "Experimental Challenges in Using a 1.2 kV GaN HEMT for High Power Density Converters," 2019 IEEE Texas Power and Energy Conference (TPEC), College Station, TX, USA, 2019, pp. 1-5, doi: 10.1109/TPEC.2019.8662190.

[99] N. Wolff, W. Heinrich and O. Bengtsson, "Challenges in the design of wideband GaN-HEMT based class-G RF-power amplifiers," 2016 German Microwave Conference (GeMiC), Bochum, Germany, 2016, pp. 189-192, doi: 10.1109/GEMIC.2016.7461587.

[100] K. Murukesan, L. Efthymiou and F. Udrea, "On the Challenges of Reliable Threshold Voltage Measurement in Ohmic and Schottky Gate p-GaN HEMTs," in IEEE Journal of the Electron Devices Society, vol. 9, pp. 831-838, 2021, doi: 10.1109/JEDS.2021.3111809.

[101] K. Murukesan, L. Efthymiou and F. Udrea, "On the Challenges of Reliable Threshold Voltage Measurement in Ohmic and Schottky Gate p-GaN HEMTs," in IEEE Journal of the Electron Devices Society, vol. 9, pp. 831-838, 2021, doi: 10.1109/JEDS.2021.3111809.

[102] K. Rawat, "Design Challenges In Continuous Mode Power Amplifiers," 2019 IEEE MTT-S International Wireless Symposium (IWS), Guangzhou, China, 2019, pp. 1-3, doi: 10.1109/IEEE-IWS.2019.8804047.

[103] H. J. Lin, P. L. Chen, G. T. Fan, Y. P. Wang and B. H. Ma, "Assembly Challenge and Solution for GaN on Si substrate," 2019 14th International Microsystems, Packaging, Assembly and Circuits Technology Conference (IMPACT), Taipei, Taiwan, 2019, pp. 128-130, doi: 10.1109/IMPACT47228.2019.9024969.

[104] Musumeci, Salvatore, and Vincenzo Barba "Gallium Nitride Power Devices in Power Electronics Applications: State of Art and Perspectives" Energies 16, no. 9, 3894,2023, 10.3390/en16093894

[105] T. Garg and S. Kale, "A Novel Enhancement Mode GaN HEMT with MIS and p-GaN structure," 2024 IEEE 9th International Conference for Convergence in Technology (I2CT), Pune, India, 2024, pp. 1-3, doi: 10.1109/I2CT61223.2024.10543334.

[106] Z. Xiang et al., "Accurate Modeling for GaN HEMTs and MMICs for C ryogenic Electronics Applications Utilizing Artificial Neural Network," in IEEE Journal of Emerging and Selected Topics in Power Electronics, doi: 10.1109/JESTPE.2024.3455999.

[107] Roccaforte, Fabrizio, Giuseppe Greco and Patrick Fiorenza. "Processing Issues in SiC and GaN Power Devices Technology: The Cases of 4H-SiC Planar MOSFET and Recessed Hybrid GaN MISHEMT." 2018 International Semiconductor Conference (CAS),7-16,2018.

[108] Drozdovski Nikolai and Caverly Robert, "GaN-based high electron-mobility transistors for microwave and RF control applications", Microwave Theory and Techniques, 50. 4 - 8, 2002, 10.1109/22.981235.

[109] S. Rahavu, B. Syihabuddin and A. Munir, "Development of Parallel RF Power Amplifier Using GaN HEMT with Independent Biasing Circuits for Wireless Communication," 2024 IEEE International Black Sea Conference on Communications and Networking (BlackSeaCom), Tbilisi, Georgia, 2024, pp. 227-230, doi: 10.1109/BlackSeaCom61746.2024.10646262.

[110] Boutros Karim, Chu Rongming and Hughes," GaN power electronics for automotive application", 1-4, 2012, 10.1109/EnergyTech.2012.6304646.

[111] Keshmiri Niloufar , Wang Deqiang, Agrawal Bharat, Hou Ruoyu, Emadi Ali, "Current Status and Future Trends of GaN HEMTs in Electrified Transportation", IEEE Access, 2020, 10.1109/ACCESS.2020.2986972.

[112] K. Varadarajan et al., "Reaching Beyond 1200 V: Lateral GaN HEMTs for High-Reliability EV and Industrial Applications," PCIM Europe 2024; International Exhibition and Conference for Power Electronics, Intelligent Motion, Renewable Energy and Energy Management, Nürnberg, Germany, 2024, pp. 1593-1598, doi: 10.30420/566262217.

Tanvika Garg received the B.Tech degree in Information and Communication Technology from Dhirubhai Ambani Institute of Information and Communication Technology, India and M.Tech degree in Electronics and Communication Engineering from National Institute of Technology, Delhi, India. She is currently pursuing Ph.D. degree from Delhi Technological University, India. Her research interests include simulation and modeling of gallium nitride high electron mobility transistor for power electronics applications.

Sumit Kale received a Ph.D. degree from the PDPM Indian Institute of Information Technology, Design, and Manufacturing, Jabalpur, India, in 2017. He is currently working as an Assistant Professor in the Department of Electronics and Communication Engineering, DTU Delhi. His current research interests include the design, simulation, and modeling of high-performance nanoscale devices for analog/RF, mixed signal, and biosensor applications.

Authorized licensed use limited to: DELHI TECHNICAL UNIV. Downloaded on November 11,2024 at 04:22:17 UTC from IEEE Xplore. Restrictions apply.

© 2024 IEEE. Personal use is permitted, but republication/redistribution requires IEEE permission. See https://www.ieee.org/publications/rights/index.html for more information.

Check for updates

RESEARCH

includes research articles that focus on the analysis and resolution of managerial and academic issues based on analytical and empirical or case research

Rethinking Security Paradigms in the Face of External Backlash: A Case Study in Private Security

VIKALPA
The Journal for Decision Makers
1–14
© The Author(s) 2024
Article reuse guidelines:
in.sagepub.com/journals-permissions-india
DOI: 10.1177/02560909241292137
journals.sagepub.com/home/vik
Sage

Soumendra Narain Bagchi and Rajeev Sharma
XLRI Xavier School of Management, Jamshedpur, Jharkhand, India

Executive Summary

Premises security is essential for organizations to function efficiently and effectively. The sanctity of space and its associated perimeter not only signals a boundary for outsiders but also serves as a second home for organizational members. These members cannot meet organizational requirements if they are constantly on guard, protecting themselves and the organization's property. However, the gradual encroachment of industrial space by squatters, while reflecting uneven economic development, presents significant security challenges, as some inhabitants of informal settlements find pilfering and other petty crimes financially rewarding. The dominant security strategy typically involves armed guards, whose presence may act as a deterrent. However, the death of an intruder or trespasser due to a guard using his firearm has far-reaching implications due to prevailing legal doctrines and stakeholder dynamics. In India, the legal system treats death as a serious matter, out of proportion to the crime of theft, and the socio-political environment echoes this perspective. Such deaths often lead to collective protests from citizens, often in the form of a *dharna* or a *gherao*, which not only disrupts the firm's operations but also poses a challenge to legal and administrative authorities and management. Dispersing the dharna and preventing it from escalating into a violent mob typically requires the management to negotiate compensation with the aggrieved family, alongside a commitment to legal authorities to impose strict restrictions on the use of firearms. The erosion of deterrence following such negotiations renders security guards ineffective. Their response to trespassing and pilfering is reduced to physical confrontation, attempting to evict individuals, which places guards at risk when faced with armed intruders. Our case study illustrates how an organization restored deterrence, and thus the sanctity of its perimeter, by incorporating attack dogs into its security strategy.

KEY WORDS

Industrial Security

Psychological Deterrence

Attack Dogs

Security Paradigm

Security forms the foundation of modern economic society by ensuring unhindered economic transactions, business processes and customers' ability to derive the benefit of ownership of assets. Private security is a necessity in many geopolitical contexts due to overwhelmed public security apparatus (Ketchell, 2017; OSACa, 2020), inefficiencies, corruption (e.g., Clark, 2018; OSAC, 2020a, 2020b)

Creative Commons Non Commercial CC BY-NC: This article is distributed under the terms of the Creative Commons Attribution-NonCommercial 4.0 License (http://www.creativecommons.org/licenses/by-nc/4.0/) which permits non-Commercial use, reproduction and distribution of the work without further permission provided the original work is attributed as specified on the SAGE and Open Access pages (https://us.sagepub.com/en-us/nam/open-access-at-sage).

or a heightened feeling of insecurity (e.g., Loader, 1997; McDowall & Loftin, 1983). Increased economic activity, often accompanied by inequitable prosperity, attracts criminal activity (Bergholt & Lujala, 2012; Hemley & McPheters, 1975; Hobbs et al., 2005; Moser, 2004; Østby, 2016), increasing demand for security. The iron and steel industry in the United States, with its violent workers' unions (Spitzer & Scull, 1977) and organized crime, is a significant example. Stagnant economies marked by income inequalities often ferment tendencies to engage in crime, often perceived by perpetrators as justified, given their deprived economic status. The increased demand for security, along with distinctive provisions for businesses and high-net-worth individuals, can hardly be met by public legal agencies (Blau & Blau, 1982; Ouimet, 2012). The proliferation of private security and the outsourcing of security, globally, as well as in Indian organizations (FICCI, 2018) is proof of organizations turning towards private security for their needs.

What strategies do private individuals and businesses adopt? The most common measures are high walls and security guards. Drones, CCTVs and remote-operated gates (Lee & Kim, 2017; Srivastava et al., 2017; Tan & Luo, 2018; Welsh et al., 2019) have brought sophistication to primarily an infrastructure-oriented-strategy aimed at preventing unauthorized access to premises or business assets. While the advent of robots in intruder-detection promises to be another evolution in technology-based security, the abilities in simulated tests reveal a long path to be travelled before the robots can substitute for human guards, especially in handling exceptions (e.g., Everett & Gage, 1999).

Despite the changes in technology, human guards have remained indispensable in the overall scheme of things. Humans bring to the security strategy their perceptual capabilities in analysing the similarities and variations in an environment and the ability to decide both the applications of general rules and the exceptions, responding to specific demands of the situation.

What are the operating procedures in most situations? Faced with typical non-violent threats, security guards' initial responses are limited to verbal warnings, physical deterrence and non-lethal physical aggression (Button, 2003). Acknowledgement of these initial mild security tactics by criminals who choose to 'delay, divert, or forgo' (Greer & Bartholomew, 1982) implies the existence of psychological deterrence. Ineffectiveness of these tactics, or increased aggression by perpetrators, necessitates severe, or in certain cases, lethal tactics (Anthony, 2004) to inflict increased 'punitiveness' (Cavadino & Dignan, 2006; Singh, 2005).

While these lethal tactics (Anthony, 2004) achieve the objective of ensuring security, the resultant fatalities bring up debates on security governance and call for security agencies to develop non-fatal responses towards transgressors (Stenson, 2005). The subject is further complicated due to varied socio-political contexts, with divergent legal and political attitudes towards the right of self-defence (Yeo, 2000).

In this article, we present a case study of an Indian that has witnessed two contrasting security paradigms with different results. The article first presents the literature on security. Though the existing literature is dominated by research in the Western context, it updates us with the relevant debates in the field and its theoretical frameworks. Then we outline the research design and our analytical approach. We structure our analysis around the concept of psychological deterrence examined from the Bourdieusian perspective, using the concepts of habitus and practice as analytical concepts (Bourdieu, 1977, 1998) to understand how security guards perceive and live their worldviews and take decisions. Finally, we integrate the findings with the previous literature and discuss implications for business leaders and researchers.

LITERATURE REVIEW

Psychological deterrence (Bodnar, 1990; Tiffany & Ketchel, 1979), signifying a criminal's sense of the situation as 'being threatening, difficult, unfavourable or not right', represents one of the important concepts in security. Shaped by the history of offensive or defensive practices as part of security strategy, psychological deterrence, we argue, forms a critical factor in defining the security guards' habitus (Bourdieu, 1977; Reay, 2004), predisposing them to either passive acquiescence of security violations or proactively challenge the perpetrators.

Contrasted with an efficient judiciary with a distinct bias towards maintaining the constitutional right of citizens towards gun ownership and the exercise of their right to self-defence in the United States, Indian organizations and citizens are faced with a judicial system where 3.7 million cases have been pending for over ten years in Indian High Courts (Krishnan, 2020).

The law of the land, including the de facto departures, influences both the practice and the habitus (Bourdieu, 1977, 1998) for the security agencies. 'Nothing is an offence which is done in the exercise of the right of private defence', as articulated in section 96 of the Indian Penal Code, might seem in alignment with the conservative ideology of the West, particularly that of the United States. For an organization, or an individual security guard employed in a non-governmental entity, the challenges of negotiating an overloaded legal system problematizes judicial ratification of the use of firearms.

Apart from being vulnerable to verbal and physical abuse (Button, 2003), guards are constrained by limits of human intelligence, staff turnover (Zedner, 2006), corruption (Sykes, 1956; Ungar, 2013) and fear of legal penalties, all of which are not overcome by an increase in numbers (e.g., Kleck & Barnes, 2014). The doctrine of reasonable force, typically defined as the use of force as necessary to protect oneself or one's property, offers no guidance to the person on the field when faced with an unknown perpetrator. Theories of rational decision-making ignore potential threats, incomplete information, and the limited window for action by security guards (Miethe, 1995). Obligated to work within the constraints of the prevailing discourse, the ethical and human-rights dilemmas (Beckley, 2018) conflict with their need for self-protection (e.g., Giblin, 2008), leading to unfortunate consequences for guards and bystanders.

Our discussion recognizes the challenges of the socio-political context and the role of government legal agencies which are constrained in their action choices yet held responsible for controlling crime. The challenges faced by private security firms are greater than those faced by government agencies, which have a modicum of legal protection by virtue of being part of the government. The dominant socio-political environment and the legal apparatus present the habitus for security guards' practices, the success of which in the form of a successful guardianship determines their motivation and self-efficacy (Reynald, 2010), in turn revising the habitus in a dynamic fashion.

In the remaining part of this article, we present our case-based research focusing on an Indian organization which transitioned from the mainstream security paradigm, that is, based on armed security guards, supported by technology, to an attack dog–based security paradigm.

RESEARCH METHOD

With its inherent ability to explore complex phenomena and underlying relationships, the case study method was the logical choice to explore this intrinsically interesting case (Stake, 1995). Guided by the proprietor of the dog agency, informants willing to discuss were contacted. The search for informants was not a publicized one in the industrial area, to avoid potential hindrances to the study, as well as to avoid any potential repercussions on the participants. The anonymity of informants was further ensured due to the existence of multiple cement plants, numbering approximately 51, in the eastern part of the country.

Data were gathered over a three-month period involving multiple discussions with informants. Each discussion ranged from 40 to 90 minutes. The discussions, carried out in a semi-structured format, were guided to obtain a chronology of the events, and decisions as taken by different stakeholders.

The informant pool for this study is detailed in Table 1. The limited informant pool signifies the limited number of people who were aware of the chronology of events, and the decisions taken by different stakeholders. We found that, given its sensitive nature, organizational security decisions hardly involved the majority of the employees. Avoiding employees who were involved peripherally and restricting our informant pool to those who were intimately involved, we avoided getting entangled in a Roshomonian conundrum. The informant pool included security staff (security-in-charge and a security guard) of a neighbouring organization located in the same industrial belt. This allowed us to understand and validate the socio-political environmental factors and challenges.

The small informant pool is an evident limitation of our study. Contrasted to a common social phenomenon, which by its very nature would engender multiple respondents, our case study is more of Yin's 'revelatory case' (2003, p. 43), providing an opportunity to study a rarely investigated topic. Given the nature of the case, we stressed on achieving data saturation (Francis et al., 2010; Guest et al., 2006) from our limited pool of informants.

ANALYTICAL APPROACH

In this article, we first present the story, as true to facts as a reconstructed story can be, with a description of

Table 1: Details of Informants.

Sl. No.	Designation	Gender	Age	Employment Details
1	Manager (administration)	Male	50	Employee of Cemcco
2	Proprietor of dog agency	Male	35	Proprietor
3	Security- in-charge	Male	55	Employee of Cemcco
4	Security guard	Male	27	Contractual employee of agency engaged by Cemcco
5	Dog handler	Male	27	Employee of dg agency
6	Dog handler	Male	25	Employee of dog agency
7	Dog handler	Male	28	Employee of dog agency
8	Security guard	Male	35	Employee of Cemcco
9	Security guard	Male	37	Employee of Cemcco
10	Security guard	Male	45	Employee of Cemcco
11	Security-in-charge of neighbouring organization	Male	58	Employee of a neighbouring organization located in the same industrial belt, e.g., CISF with experience of dog teams at Mumbai Airport.
12	Security guard	Male	46	Security guard of neighbouring organization located in the same industrial belt.

Note: The table indicates the informants who engaged with authors in this study. The names of the informants and the organizations have been anonymized. The informants were obtained using the snowballing technique to protect their confidentiality.

the context within which the events occurred (Dyer & Wilkins, 1991). The development of the story has been supported by developing a causal diagram parallel to data gathering. Widely used in organizational studies (e.g., Perlow et al., 2002; Sastry, 1997), causal diagrams allowed us to concisely capture decisions, and consequences of the same, presenting a visual picture illustrating the complex dynamics within the situation. This allowed us to visually summarize different chunks of information into a coherent whole (Miles & Huberman, 1994).

THE CASE

Cemcco (anonymized), a cement manufacturing company in the eastern part of India, has its plant situated outside the municipal limits of the city. It is surrounded by a slum comprising almost 3,000 families, which skirts the 10 km of the plant's boundary wall. These families typically comprised migrant villagers from rural areas settled over a period of time. An inventory of malfunctioning equipment and spare parts inside the boundary wall has attracted intruders on a regular basis, as copper, aluminium and other metals in these parts fetched good prices in the grey market.

With the increase in thefts, the leadership mandated an increase in the number of armed security guards. This was duly provided by the private security agency. Cemcco also invested in additional floodlights and CCTVs that were monitored in a centralized control room. Additionally, loudspeakers were operated from the control room.

Typically (traditional approach), when intruders were detected, they were warned via loudspeakers and asked to retreat. They were warned that they would be shot if they did not go back. On occasion, security guards were ordered to fire warning shots. More commonly, security guards were sent to the spot as directed by the control room, and the security guards would confront the intruders physically and force them out. In most cases, when the intruders were isolated individuals, this strategy worked. Sometimes, the intruder would pick up the nearest item he could lay his hand on, throw it across and run across the boundary wall.

However, the intruders had increased in frequency, and small groups coordinated to spread out the security guards. This changed the dynamics as the security guards were outnumbered. There were instances when the intruders had attacked the security guards with

brickbats. Forced to defend themselves, the security guards fired in self-defence, which led to the death of intruders. In another incident, the security guards fired a warning shot in the dark in the direction of the intruders which resulted in a fatal injury. The consequent collective backlash in the form of a *dharna* had led to a complete prohibition on all shooting, including that of warning shots, by Cemcco leadership.

AFTERMATH OF A FATALITY

> A procession of nearly a hundred persons headed by the bereaved family members brings the body along and places it in front of the main gate. Imagine the situation and you representing the company and asking the people to peacefully disperse so that the plant's operations are not hampered. (Manager, Admin)

The dharna became a rallying point, bringing out anger and frustration against the company. It also became an expression of collective grief and solidarity at what was considered a disproportionate reaction to a down-to-earth crime of stealing. The local politicians joined the dharna, which made it more aggressive. The crowd was unwilling to discuss or reach a settlement. It was intent on getting their hands on the 'person who fired the shot'. Faced with an emotionally charged crowd, the local police were reduced to idle bystanders. Often the senior officials preferred to wait and watch, consistent with their approach that as long as the crowd was not indulging in violence, the police did not have a *locus standi* for getting involved.

> A death in front of local elections is dreadful experience, as the politicians want to extract the maximum political mileage from the situation. They prolong the negotiation, preventing the body from being sent to post-mortem… unless adequate compensation has been paid, and management has apologised. Most of the police force are employed from the middle and lower-middle strata…. Even if they do not support the criminal activities, a death case is a highly emotional issue. (Manager, Admin)

Security Guards' Firearms: A Contested Domain

When incidents flared up, like a *gherao* that stopped all movements from the plant, officers from the administrative departments would try to resolve the situation. Often countenancing the emotional anguish expressed by the families and apologizing on behalf of the company, they would offer apologies and monetary compensation, negotiating with the family members and the crowd to resolve the issue. However, by that time, the plant would have witnessed all stoppage of movement from the gates for a couple of days.

Post such gheraos, discussions between CEO and top managers often witnessed managers expounding the cost–benefit argument and advocating a more accommodating approach.

> The cost of the item stolen was in hundreds of rupees. But the cost of one day of blockage is in lacs [Indian term 1 Lac = 100,000]. So, most managers argue that security guards are causing a loss to the company.
>
> Another relevant point is the incentive. All management personnel are incentivised on sales achieved. So, a day of lost sales is lost incentive. (Manager, Admin)

The prevalent discourse was more in terms of preventing disruptions to operations and accommodating what was considered a minor cost.

We explored the worldview of a security guard who had fired shots at the intruders, either in the line of duty or in self-defence. This elicited the following responses from the proprietor of the private security agency.

> …the slum dwellers filed a criminal case against the security guard… A police case filed under section 299 of the Indian Penal Code of culpable homicide. Luckily, the police constable had given an early warning, and the person packed his bags and absconded. There was no other way to keep himself out of jail. Neither he, nor we as a security agency, have financial resources to hire a criminal lawyer to fight his case.
>
> This incident has demotivated the security guards a lot. For them, it is a question of a paltry 12,000 rupees per month as salary plus all the risks …Even we [as agency] are forced to pay as penalty for any item stolen…It is deducted from our bill. …So, we are caught in the middle.

The security guards' position reflected an unenviable power inequity, forced to act to stop trespassing and yet constrained not to inflict any injury which could turn into a fatality. As the blame shifted towards the security guards, Bourdieu's notion of habitus as a theoretical lens cogently incorporates the security guards' concerns and the managers' anxieties illuminating the power dynamics, within the context of the Indian socio-political milieu. The guards' rationality of acquiescence, providing a modicum of meaning and well-being, emanates from the habitus structured by leadership's decisions and managers' focus on maintaining peace.

Existing Security Paradigm and Commitment Escalation

Fearful of being assaulted outside the plant, the managers collectively advocated a pacifist approach and structured the issue as a failure of the security guards. Within this discourse, the use of firearms became a confirmation of the guards' incompetence. The extant discourse hinging on increasing manpower in the field was based on increasing deterrence via increased numbers of security guards. The premise remained unchallenged despite consistent evidence of failure.

> Most management personnel argued for increasing the numbers of armed guards. … Most managers never understand the situation, since they are confined to their arm-chair thinking. An armed guard who cannot shoot is absolutely no different from a guard holding a plastic toy gun. (Security in-charge officer)

Satisficing and Consequences

The capitulation by the company's leadership to the compensation demands in cases of death, and the pressure on the security guards to not shoot, signalled the weakness of the leadership among external stakeholders.

> It was like an open invitation to come and take what-ever you wanted…. Soon the losses went up. Forget small tools and metal pieces. A 24-ft industrial ladder was carried over the boundary wall…'. (Security in-charge officer)

The same was confirmed by the security staff of the neighbouring organization. The question related to additional CCTVs elicited the following response:

> The CCTVs allow me to understand what is going on a real-time basis. I know who is coming and what is he about to steal. I can inform the security guard to stop him, or if he has picked up something and is about to cross the boundary wall, give chase. It is physical brawling with the groups of intruders.

The situation becomes threatening when we know a group of intruders come, steal in a methodical manner, and we all know that they are not afraid of us….there is a high probability that they will be armed. (Security in-charge officer of neighbouring organization)

Perpetuating the discourse centred on blame attribution disempowered the guards, creating a deleterious vicious cycle within the organization as illustrated in Figure 1. With no support from any significant stakeholder, the powerless security guards represented an unwelcome constituent of the organization, relegated to the fringes of organizational discourse.

The doctrine of reasonable force provides no functional guidelines to a security guard at night.

'The response has to be proportionate to the threat' is the legal doctrine that can get a security guard killed, or in the best case, to resign from the job and take refuge in a less arduous role. A security guard can be, and in case of death is, often reprimanded for not following a scaled response. A criminal case filed against a security guard is an effective threat by intruders, ensuring a complete standstill of the guard's career. He is faced with an imprecise situational analysis regarding the number of intruders, the possible arms the intruders might be bearing, and the chance that there are multiple groups the presence of which he may be unaware of.

> How many groups have entered the premises, which one is the diversion, and which one is armed—these are issues, which often are discussed by the arm-chair managers but are of little help to a security guard in the field. (Security in-charge officer)

Bourdieu's notion of habitus provides us with a nuanced insight into the security guards position, a complex situation bounded within the organization's concern for the security of its assets, managers desire for uninterrupted operations and protection of their bonuses and the outsiders' concerns for economic survival forcing them to trespass. The guards' acquiescence reflected their powerlessness within their habitus, an interplay of embodied asymmetric power hierarchy (Bourdieu, 1977).

LEADERSHIP CHANGE AND A BREAK FROM THE PAST

Around 2016, Cemcco was taken over by another conglomerate. Along with this change, there was also a change in CEO. To handle the problem with intruders, the CEO's initial steps involved taking stock of the situation from the security guards, and head of the departments (HODs) of the plant. The CEO also interacted with the police. The CEO disregarded the narratives put up by HODs. The HOD's view was to accommodate the pilferage and treat it as a cost of business, that is, normalize the pilferage and treat it as a cost item. The HODs wanted the CEO to accommodate the trespassing since the aftermath of strict action by

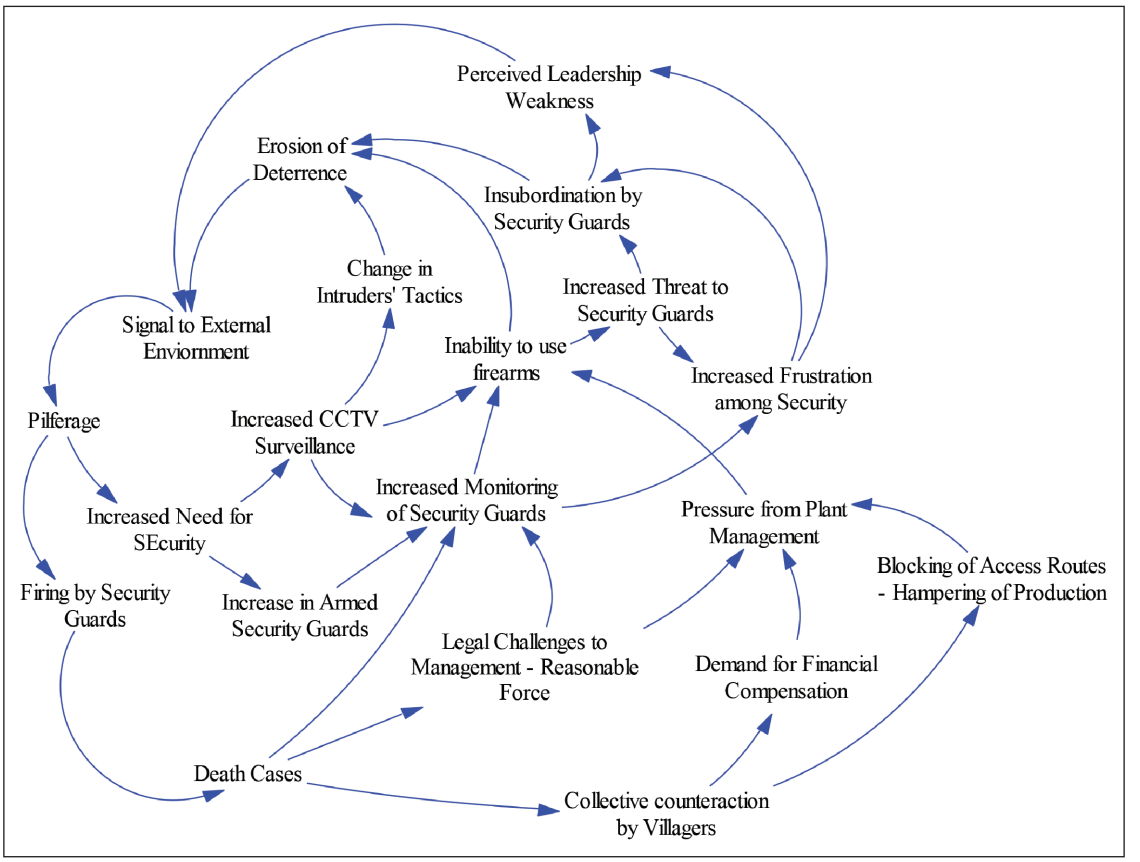

Figure 1: Situation Reflecting the Traditional Security Paradigm

Note: The diagram summarizes the previous situation when the dominant paradigm guiding the security was based on security guards supported by monitoring technology. The consequences of backlash by external stakeholders on the performance of security apparatus have been mapped.

the security led to a disruption in operations that also impacted the HOD's incentives.

> …the CEO talked to the senior officers of police. These police officers come from a variety of backgrounds and with experiences in different fields. The core issues impressed upon the CEO by the officers, it seems, was that in no case there can be firing. (Manager, Admin)

The security guards getting a preferential audience signalled a new paradigm. This simple act rendered the old discourse defunct by ignoring the legacy and the collective decision-making process that incorporated the management. The new CEO, based on his interactions, advocated a new security strategy—the introduction of attack dogs.

> After interacting with the police officers, we got to know that an attack-dog–based firm has been awarded the contract of security. The contract required the agency to provide a certain number of dogs, along with handlers. Never it was announced that these were attack dogs. It was simply informed that we now have security dogs. (Manager, Admin)

The inclusion of attack dogs in security led to an effective force—continuum for the security guard. The verbal warnings over the loudspeaker were not followed by warning shots, as was the earlier protocol. Under the new paradigm, the guards informed the intruders that they would release the dogs. After giving the intruders enough time to retreat across the wall, they would do so.

> An attack-dog is different from a guard dog/ or a security dog. It is trained not to bark. It is trained for only one thing—to attack. …When we think that the intruders are more in numbers, we release multiple dogs. (Dog handler)

To understand the behaviour of attack dogs, we requested elaboration from the proprietor of the dog agency.

> For the dog it is just a target – not a human. A single attack-dog first goes for the limbs to disable the target. Once the target is down, throats, necks or other soft muscle areas like the groin will be targeted. Specific targeting is also by training…But then, do not forget, the instinct takes over … a dog will attack the way it is driven by its instinct.

> A pack of dogs is another story altogether. If you have watched National Geographic, you would have noticed that the target is a meal. Each dog starts to tear at the target, trying to eat as much as possible, that is the instinct in group attacks. (Proprietor, dog agency)

What would happen if the person jumped over the wall?

> 'Dogs, once they have tasted blood, do not follow boundaries. Nor are they, at that time, in mood to obey the handlers. If there are multiple dogs following, there is a high chance the pack will follow beyond'.

The security system worked on the condition of complete information sharing between the organization and the dog handlers. Reminiscing about an incident that highlighted the ferocity of the dogs when employees entered the site without prior information, the proprietor laughingly recalled:

> Once a couple of officers came in a Maruti Gypsy. We were not informed, [as was the new protocol] and the dogs had been let loose. One of the dogs had climbed on the canvas roof, while the others surrounded the jeep. Once the handlers reached, it took some time to get the dogs under control…. The officers were sweating inside the jeep.

Extreme Aggression: The Essence of the New Paradigm

The new security paradigm implied a higher probability of physical injury for the trespassers. The impact of a dog attack is more than a physical injury. The rapid charge of multiple dogs, and the inability to retaliate against a pack of dogs, is a visceral experience, triggering a primordial fear reaction.

> Those who can run away safely would remember the chase for a long time. However, those who could not—they literally have nightmares. Imagine your leg caught in a pair of jaws which digs till the bone and crushes it. A person would limp for life in cases where veins and arteries are torn apart. (Proprietor, dog agency)

> 'Everyone who has survived discusses the attack, and how they survived. The fear spreads easily…(Dog handler)

Earlier, the security guards' passivity reflected the learned experience within an unsupportive socio-cultural and historical context. With the change in leadership, they found themselves in the hub of activities, with the attack dogs liberating them from their earlier reticence.

A New Level of Psychological Deterrence

Dogs' ability to cover large areas, supported by their hearing ability and exceptional olfactory function, have made them preferred companions of law enforcement agencies (Van Jaarsveld-Schalkwyk, 2015).

The adoption of attack dog–based security paradigm brought in a heightened level of psychological deterrence. With their superior sensitivity, a dog is in complete sync with the situation. The combined animal intelligence of a pack of dogs provides an exponential increase in situational awareness. Multiple attack dogs behave like a pack of wild dogs, going back to their primal instincts of attacking to protect their territory.

> It is about changing the narrative. Do we think more about the intruders' human rights or the security of organisational resources, employees and security guards'? (Manager, Admin.)

The boundary wall, which earlier had ended up as a mere symbolic barrier, now had a new meaning. The presence of attack dogs across the boundary heightened psychological deterrence replacing the earlier moribund situation.

Tacit Sanction by the Government Authority

Implementation of the new security paradigm brought its own casualties, in the form of people who had suffered dog bites (Fonseca et al., 2015). Though the dog bites were serious injuries, the police did not intervene in the entire exercise. Compared to a fatality from a gunshot, a dog bite was not a fatal injury in most cases, relieving the police of any involvement. The legal dimension of a dog bite was discussed.

> A dog bite to be traced to a particular dog, and for a police case to be filed, it requires evidence from different forensic professionals such as pathologists, odontologists, veterinarians, biologists, and police investigators. … He must prove that it was not a stray dog that bit him. And we have a lot of stray dogs in the surrounding garbage dumps, as well as in the slums.

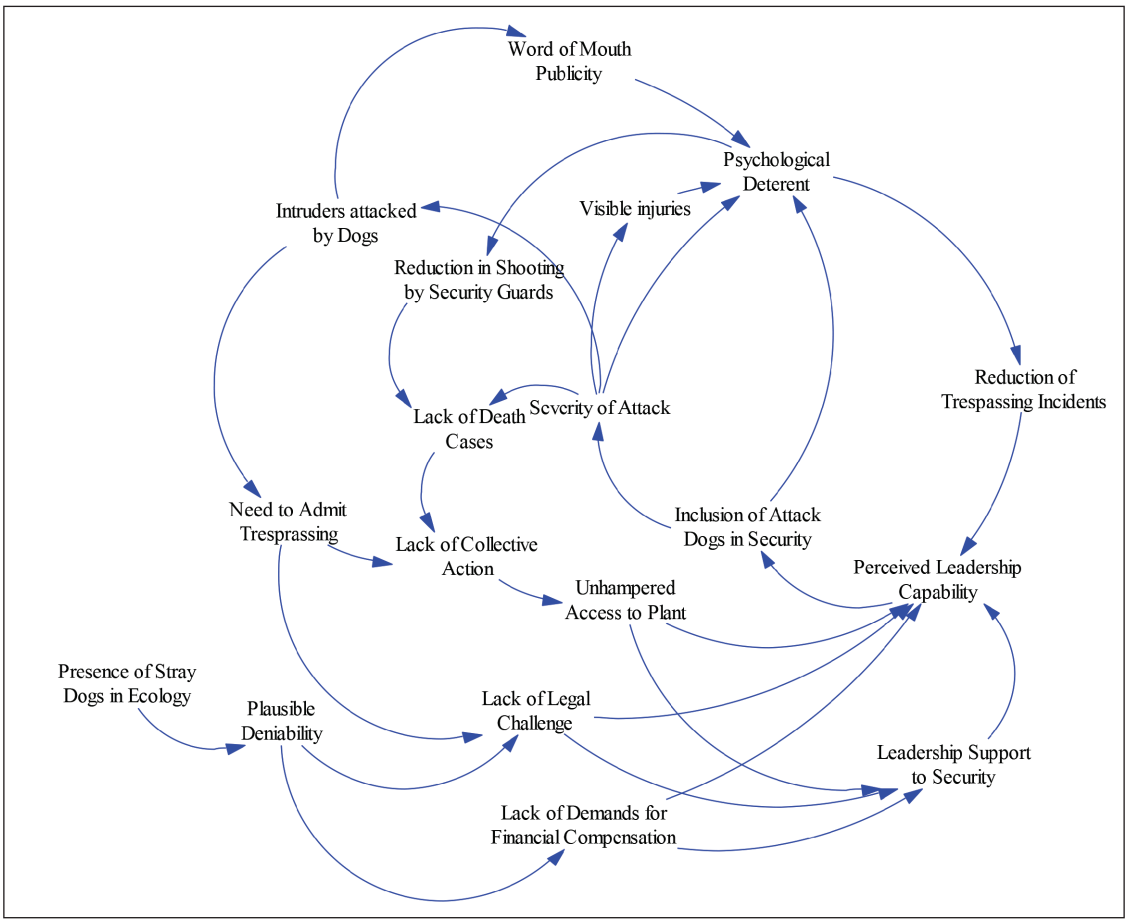

Figure 2: Situation as an Outcome of New Paradigm of Security.

Note: The diagram summarizes the new situation after the implementation of an aggressive security strategy relying on attack dogs.

> And most important of all, the person must admit that he crossed the boundary wall. If he admits, immediately the question the police ask, what business did you have across the company boundary wall? So, unless they answer, they do not file cases. (Manager, Admin.)

The success of attack dogs has boosted the morale of the security guards, which sometimes has led to certain excesses, an act of revenge for what they suffered earlier.

> Security guards have their own lives. I am their boss, but they have their own subculture, and their peer-influences…. Let us be honest. Some of the security guards had been beaten up by intruders. So, these guards influence our handlers to, you know, be easy on the dogs. It is a way to hit back at the intruders...However, we regularly instruct the handlers to reach the spot as fast as possible. (Proprietor, dog agency)

Figure 2 shows the changed scenario that prevailed after the inclusion of attack dogs in the security.

Discussion on the reaction of the police elicited an accommodative stance towards the organization's new security paradigm. Often, the territory guarded by the dogs doubled up as an informal punitive measure for the police.

> Police are happy with us. Now they know that the grey economy has reduced, and therefore the nonchalant attitude of the slum-based gangs has come down.

> For the criminal, it is like 'police can pick us and throw us across the boundary wall', a way for the police to bypass the judicial process and give a 'lesson' to some criminals. (Manager, Admin.)

CONCLUSIONS

Organizations and their members are not passive consumers of security (e.g., Goold et al., 2010; Loader, 1999), but are active architects of communal habitus

with multiple stakeholders in the security narrative. Our research establishes how different stakeholders, apart from the organizational leaders, sway the narrative. The initial dominance by managers, despite their inexperience in security and possible strategies, had escalated commitment to the technology and guards-based stratagem, despite recurring evidence of its failure as witnessed by a lack of psychological deterrence. Psychological deterrence and implementation of reasonable force by security guards, the essential facets of security strategy, depend on the fear of 'dire consequences' (Greer & Bartholomew, 1982) established by punitive consequences. The doctrine of reasonable force, an essential component of security discourse, is linked not only to subject resistance (Boivin & Lagacé, 2016), but, as our research identifies, the acceptance by different stakeholders within the habitus.

Compared to Figure 1, Figure 2 illustrates evidence of reinforcement and recalibration of psychological deterrence, provided by the primal fear and the panic aroused by the dogs (Van Jaarsveld-Schalkwyk, 2015). The attack dogs (Begeç, 2012) restored the guardianship and the authority, the essence of a security guard's worldview, as compared to the earlier disempowered existence. While the firearms had been reduced to mere artefacts, the attack dogs' savagery was crucial in the re-establishment of the security guards' authority, as evidenced by the new protocol of managers having to pre-inform the security guards before venturing out in the plant yards.

The police, by discouraging the futility of trespassers' filing cases against the company, provided a sanction to the organization in an informal exchange for its unconventional contribution towards undermining the criminal ecosystem (Dorn & Meerts, 2009). Constrained due to official compunctions and yet charged with the responsibility of ensuring public law and order, and minimizing criminal resistance (Boivin & Lagacé, 2016), police's accommodation of strong responses, that would be 'acceptable' within the current socio-political environment, by private guards indirectly implies maintaining an agency for enforcing punitiveness beyond the official purview.

DISCUSSION AND IMPLICATIONS

We consider our study to be significant to practitioners and researchers in multiple ways. For the first time, we have presented a case highlighting the failure and adaptation of security strategy, which can only be understood by considering the nuances of the context within which the entire case is embedded. Second, we have highlighted the role of leadership and leadership discourse, which inconspicuously binds leaders and managers to a failing course of action. Another significant contribution is that our research provides a rare inside view of the challenges in maintaining security in the Indian context with its myriad stakeholders.

We classify our case as critical as well as revelatory (Yin, 2003), challenging the dominant view of private security as being non-punitive and defensive in nature. Our research has highlighted how collective action by citizens in the Indian context can overwhelm the organization, and constrain the security guards, with a resulting erosion of psychological deterrence. We believe this is one of the rare research projects that highlight the possibility of external stakeholders halting the organization's security strategy.

The consequences of a lackadaisical security in a community go beyond the immediate stakeholders. The 'reputational risk' (Dupont, 2014) that goes beyond the organization, with a crime against specific private organizations morphing into a general breakdown in law and order, has significant implications for practitioners and policymakers. The spread of knowledge of failure in guardianship, despite the implementation of a technology-based and firearm-driven strategy (Luxenburg et al., 1994), among different stakeholders leads to a vicious downward spiral in criminality and crime-based economy. This insight from our study points out the potential of spill-over to society at large as emboldened criminals move from softer targets and broad base their activities.

While commitment to failing strategies has been a widely researched area (Staw, 1981), our research has illustrated how a failing paradigm can be reinforced and strengthened by the dominant discourse of internal stakeholders, like senior managers, who are not accountable for resulting consequences (e.g., Posen, 1993). Organizations tend to suffer double jeopardy—stoppage of production due to retaliatory actions, and individualization of risk borne by the security guard (Gray, 2009) leading to a security guard who absconds to protect himself and thus engendering negative morale for the remaining security guards.

The implicit accommodation and advocacy by police for strong action by their private counterparts to preserve law and order is another area where our

study makes a significant contribution. Conceptually distinctive from police brutality (e.g., Worden, 2015), or private violence to advance the objectives of certain stakeholders (e.g., Porteux & Kim, 2016), this tacit approval of borderline methods has its ramification of creating parochial security regimes (Dupont, 2014). Our study has highlighted situations when faced with politicization of law and order (McLaughlin et al., 2001), or breakdown in urban governance (MacLeod, 2011), police expect their private counterparts to act on their behalf, provided the consequences are controlled. While it does help to prevent lawlessness from spreading due to the convergence of objectives of official police and private security, as compared to strained relationships (Morley & Fong, 1995), it can establish its own political economy, with its own rules and practices.

An aggressive security apparatus raises questions regarding the legal status of private security staff as agents of property owners (Button, 2003; De Waard, 1999) and the legal rights of criminals. The legitimacy of the principal that contracts the security agency is restricted to the private domain (Phelps, 2014) and does not necessarily empower the agency to be a punishing authority. However, with police as sponsors of a new security paradigm in the community questions, further research is needed to settle the questions about accountability and control (Gill & Hart, 1999; Stenning, 2000). With economies becoming more complex, the possibilities of increased socio-political inequities triggering the evolution and adoption of unconventional security paradigms offer significant challenges for practitioners and researchers (Dupont, 2014).

The evolution of the social and cultural capital (Bourdieu, 1986), including the stakeholders' challenge to a dominant stakeholder's 'private property' (Shearing & Stenning, 1983), is another unexplored area unearthed by our research. It is not yet known what path stakeholder activism would take in the face of private coercive apparatuses and how it would modify social and cultural capital. As contrasted to a conflict-driven paradigm characterized by perpetual hostility, adopting collaborative and cooperative strategies would require organizations to invest significantly in the social and economic development of the perceived 'outsiders'. There is scant research on such approaches that can guide practitioners, including the probability of the success of such paradigms. However, the evolution of the socio-cultural capital (Dupont et al., 2003) along with the redefinition of practice by myriad stakeholders in the context of security cannot remain untouched by the security paradigm adopted. While being a relatively unexplored area, with its potential for extensive impact on broader society, we think that it would be an important area for exploration for policymakers, apart from researchers.

DECLARATION OF CONFLICTING INTERESTS

The authors declared no potential conflicts of interest with respect to the research, authorship and/or publication of this article.

FUNDING

The authors received no financial support for the research, authorship and/or publication of this article.

REFERENCES

Anthony, R. (2004). A calibrated model of the psychology of deterrence. *Bulletin on Narcotics, 56*(1–2), 49–64.

Beckley, A. (2018). Examining human rights and ethical practice in Australian policing: A New South Wales case study. PhD thesis, Western Sydney University. Australia.

Begeç, S. (2012). The use of dogs in defense and security management in Turkey. *Journal of the Faculty of Veterinary Medicine/Veteriner Fakultesi Dergisi*, *31*(2), 51–61.

Bergholt, D., & Lujala, P. (2012). Climate-related natural disasters, economic growth, and armed civil conflict. *Journal of Peace Research*, *49*(1), 147–162.

Blau, J. R., & Blau, P. M. (1982). The cost of inequality: Metropolitan structure and violent crime. *American Sociological Review*, *47*, 114–129.

Bodnar, R. J. (1990). K9 patrols: Physical and psychological deterrence. *American Jails, 2*, 35–38.

Boivin, R., & Lagacé, M. (2016). Police use-of-force situations in Canada: Analyzing the force or resistance ratio using a trichotomous dependent variable. *Police Quarterly*, *19*(2), 180–198.

Bourdieu, P. (1977). *Outline of a theory of practice*. Cambridge University Press.

Bourdieu, P. (1986). The forms of capital. In J. Richardson (Ed.), *Handbook of theory and research for the sociology of education* (pp. 241–258). Greenwood.

Bourdieu, P. (1998). *Practical reason: On the theory of action*. Stanford University Press.

Button, M. (2003). Private security and the policing of quasi-public space. *International Journal of the Sociology of Law*, *31*(3), 227–237.

Cavadino, M., & Dignan, J. (2006). Penal policy and political economy. *Criminology & Criminal Justice*, *6*(4), 435–456.

Clark, C. (2018). South Africans are taking the law into their own hands. *Foreign Policy*. https://foreignpolicy.com/2018/11/29/south-africans-are-taking-the-law-into-their-own-hands-vigilantism-extralegal-justice-police-apartheid-anc-private-security/

De Waard, J. (1999). The private security industry in international perspective. *European Journal on Criminal Policy and Research*, *7*(2), 143–174.

Dorn, N., & Meerts, C. (2009). Corporate security and private justice: Danger signs? *European Journal of Crime, Criminal Law and Criminal Justice, 17*(2), 97–111.

Dupont, B. (2014). Private security regimes: Conceptualizing the forces that shape the private delivery of security. *Theoretical Criminology*, *18*(3), 263–281.

Dupont, B., Grabosky, P., & Shearing, C. (2003). The governance of security in weak and failing states. *Criminal Justice*, *3*(4), 331–349.

Dyer, W. G. Jr, & Wilkins, A. L. (1991). Better stories, not better constructs, to generate better theory: A rejoinder to Eisenhardt. *Academy of Management Review*, *16*(3), 613–619.

Everett, H. R., & Gage, D. W. (1999). From laboratory to warehouse: Security robots meet the real world. *The International Journal of Robotics Research*, *18*(7), 760–768.

FICCI. (2018). Private security industry: Job creation and skill development. https://ficci.in/spdocument/23012/Private%20Security%20Industry%20Report.pdf

Fonseca, G., Mora, E., Lucena, J., & Cantin, M. (2015). Forensic studies of dog attacks on humans: A focus on bite mark analysis. *Research and Reports in Forensic Medical Science*, *2015*(5), 39–51.

Francis, J., Johnston, M., Robertson, C., Glidewell, L., Entwistle, V., Eccles, M., & Grimshaw, J. (2010). What is an adequate sample size? Operationalising data saturation for theory-based interview studies. *Psychology and Health*, *25*(10), 1229–1245.

Giblin, M. J. (2008). Examining personal security and avoidance measures in a 12-city sample. *Journal of Research in Crime and Delinquency*, *45*(4), 359–379.

Gill, M., & Hart, J. (1999). Private security: Enforcing corporate security policy using private investigators. *European Journal on Criminal Policy and Research, 7*(2), 245–261.

Goold, B., Loader, I., & Thumala, A. (2010). Consuming security? Tools for a sociology of security consumption. *Theoretical Criminology*, *14*(1), 3–30.

Gray, P. (2009). The political economy of risk and the new governance of youth crime. *Punishment & Society*, *11*(4), 443–458.

Greer, W., & Bartholomew, J. C. (1982). Psychological aspects of mine warfare (No. CNA-PP-365). Center For Naval Analyses. Available at https://apps.dtic.mil/dtic/tr/fulltext/u2/a128244.pdf

Guest, G., Bunce, A., & Johnson, L. (2006). How many interviews are enough? An experiment with data saturation and variability. *Field Methods, 18*(1), 59–82.

Hemley, D., & McPheters, L. (1975). Crime as an externality of economic growth: An empirical analysis. *The American Economist*, *19*(1), 45–47.

Hobbs, D., Winlow, S., Hadfield, P., & Lister, S. (2005). Violent hypocrisy: Governance and the night-time economy. *European Journal of Criminology*, *2*(2), 161–183.

Ketchell, M. (2017). South African crime stats police struggling to close cases. *The Conversation*. https://theconversation.com/south-african-crime-stats-show-police-struggling-to-close-cases-86429

Kleck, G., & Barnes, J. (2014). Do more police lead to more crime deterrence? *Crime & Delinquency*, *60*(5), 716–738.

Krishnan, M. (2020). 3.7 million cases pending in courts for over 10 years: Data. *Hindustan Times.* https://www.hindustantimes.com/india-news/3-7-million-cases-pending-in-courts-for-over-10-years-data/story-ytI7P0rm5Plwe5r8ubNVyJ.html

Lee, J., & Kim, H. (2017). Security and privacy challenges in the internet of things [security and privacy matters]. *IEEE Consumer Electronics Magazine*, *6*(3), 134–136.

Loader, I. (1997). Private security and the demand for protection in contemporary Britain. *Policing and Society: An International Journal, 7*(3), 143–162.

Loader, I. (1999). Consumer culture and the commodification of policing and security. *Sociology, 33*(2), 373–392.

Luxenburg, J., Cullen, F., Langworthy, R., & Kopache, R. (1994). Firearms and fido: Ownership of injurious means of protection. *Journal of Criminal Justice*, *22*(2), 159–170.

MacLeod, G. (2011). Urban politics reconsidered: Growth machine to post-democratic city? *Urban Studies*, *48*(12), 2629–2660.

McDowall, D., & Loftin, C. (1983). Collective security and the demand for legal handguns. *American Journal of Sociology, 88*(6), 1146–1161.

McLaughlin, E., Muncie, J., & Hughes, G. (2001). The permanent revolution: New labour, new public management and the modernization of criminal justice. *Criminal Justice*, *1*(3), 301–318.

Miethe, T. (1995). Fear and withdrawal from urban life. *The Annals of the American Academy of Political and Social Science*, *539*(1), 14–27.

Miles, M., & Huberman, A. (1994). *Qualitative data analysis: An expanded sourcebook.* Sage.

Morley, H., & Fong, R. (1995). Can we all get along? A study of why strained relations continue to exist between sworn law enforcement and private security. *Security Journal, 2*(6), 85–92.

Moser, C. (2004). Urban violence and insecurity: an introductory roadmap. *Environment and Urbanization*, *16*(2), 3–16.

OSAC. (2020a). Brazil 2020 crime and safety report: São Paulo. Overseas Security Advisory Council, U.S. Department of State. https://www.osac.gov/Country/Brazil/Content/Detail/Report/e2e8a425-32bf-45f5-aa49-18aceb1e211e

OSAC. (2020b). India 2020. India 2020 crime and safety report: New Delhi. Overseas Security Advisory Council, U.S. Department of State. https://www.osac.gov/Country/India/Content/Detail/Report/f1f28aed-1d4d-4c9f-97d3-185b66351d03

Østby, G. (2016). Rural–urban migration, inequality and urban social disorder: Evidence from African and Asian cities. *Conflict Management and Peace Science*, *33*(5), 491–515.

Ouimet, M. (2012). A world of homicides: The effect of economic development, income inequality, and excess infant mortality on the homicide rate for 165 countries in 2010. *Homicide Studies*, *16*(3), 238–258.

Perlow, L., Okhuysen, G., & Repenning, N. (2002). The speed trap: Exploring the relationship between decision making and temporal context. *Academy of Management Journal, 45*(5), 931–955.

Phelps, M. (2014). Doppelgangers of the state: Private security and transferable legitimacy. *Politics & Policy*, *42*(6), 824–849.

Porteux, J., & Kim, S. (2016). Public ordering of private coercion: Urban redevelopment and democratization in South Korea. *Journal of East Asian Studies*, *16*(3), 371–390.

Posen, B. (1993). The security dilemma and ethnic conflict. *Survival*, *35*(1), 27–47.

Reay, D. (2004). 'It's all becoming a habitus': Beyond the habitual use of habitus in educational research. *British Journal of Sociology of Education*, *25*(4), 431–444.

Reynald, D. (2010). Guardians on guardianship: Factors affecting the willingness to supervise, the ability to detect potential offenders, and the willingness to intervene. *Journal of Research in Crime and Delinquency*, *47*(3), 358–390.

Sastry, M. (1997). Problems and paradoxes in a model of punctuated and organizational change. *Administrative Science Quarterly*, *42*, 237–275.

Shearing, C., & Stenning, P. (1983). Private security: Implications for social control. *Social Problems*, *30*(5), 493–506.

Singh, A. (2005). Private security and crime control. *Theoretical Criminology*, *9*(2), 153–174.

Spitzer, S., & Scull, A. (1977). Privatization and capitalist development: The case of the private police. *Social Problems, 25*(1), 18–29.

Srivastava, S., Bisht, A., & Narayan, N. (2017). Safety and security in smart cities using artificial intelligence: A review. In *2017 7th international conference on cloud computing, data science & engineering-confluence* (pp. 130–133). IEEE.

Stake, R. E. (1995). *The art of case study research*. Sage.

Staw, B. M. (1981). The escalation of commitment to a course of action. *Academy of Management Review*, *6*(4), 577–587.

Stenning, P. C. (2000). Powers and accountability of private police. *European Journal on Criminal Policy and Research*, *8*(3), 325–352.

Stenson, K. (2005). Sovereignty, biopolitics and the local government of crime in Britain. *Theoretical Criminology*, *9*(3), 265–287.

Sykes, G. (1956). The corruption of authority and rehabilitation. *Social Forces*, 257–262.

Tan, S., & Luo, Y. (2018). Flexible security guard scheduling to satisfy defensive power by Tabu-Search algorithm. In *Proceedings of the 2nd international conference on vision, image and signal processing* (pp.1–5).

Tiffany, W. D., & Ketchel, J. M. (1979). Psychological deterrence in robberies of banks and its application to other institutions. In Joel J. Kramer (Ed.), *The role of behavioral sciences in physical security: Proceedings of the third annual symposium (May 2–4, 1978)* (pp. 81–87). National Bureau of Standards.

Ungar, M. (2013). The rot within: Security and corruption in Latin America. S*ocial Research*, *80*(4), 1187–1212.

Van Jaarsveld-Schalkwyk, L. (2015). The use of dogs in crime prevention. *Acta Criminologica: African Journal of Criminology & Victimology, 2015*(Special Edition 4), 182–192.

Welsh, B., Piza, E., Thomas, A., & Farrington, D. (2019). Private security and closed-circuit television (CCTV) surveillance: A systematic review of function and performance. *Journal of Contemporary Criminal Justice*, *36*(1), 56–69.

Worden, R. (2015). The 'causes' of police brutality: Theory and evidence on police use of force. In *Criminal Justice Theory: Explaining the Nature and Behavior of Criminal Justice*, (pp. 149–204). Routledge.

Yeo, S. (2000). Revisiting excessive self-defence. *Current Issues in Criminal Justice, 12*(1), 39–57.

Yin, R. (2003). *Case study research: Design and methods* (3rd ed.). Sage Publications.

Zedner, L. (2006). Liquid security: Managing the market for crime control. *Criminology & Criminal Justice*, *6*(3), 267–288.

Soumendra Narain Bagchi is a faculty in the HRM area at XLRI Xavier School of Management, Jamshedpur, India. He graduated as a civil engineer from the Delhi College of Engineering and is a fellow from IIM Ahmedabad. His major interest areas are organizational capability development, decision-making and organizational performance management. He has authored two books, one on performance management and the other on strategic industrial relations. E-mail: s_bagchi@xlri.ac.in

Rajeev Sharma is a faculty in the information system and strategic management area at XLRI Xavier School of Management, Jamshedpur, India. His research interests include coordinating activities in software development projects, information processing for decision-making and information systems strategy. E-mail: rsharma@xlri.ac.in

Research Square

Preprints are preliminary reports that have not undergone peer review.
They should not be considered conclusive, used to inform clinical practice,
or referenced by the media as validated information.

Secure Novel Hybrid PUF Design For Key Generation and Authentication Applications Of IoT

Bhagyalakshmi Narayanapuram

bhagyalakshminarayanapuram_2k20phdec502@dtu.

Delhi Technological University

Jeebananda Panda

Delhi Technological University

Research Article

Keywords: SRAM PUF, Data remanance attack , modelling attack, Key generation, Internet of Things, FPGA.

Posted Date: November 4th, 2024

DOI: https://doi.org/10.21203/rs.3.rs-5296629/v1

License: This work is licensed under a Creative Commons Attribution 4.0 International License.
Read Full License

Additional Declarations: No competing interests reported.

Secure Novel Hybrid PUF Design For Key Generation and Authentication Applications Of IoT

Bhagyalakshmi Narayanapuram
ECE Department
Delhi Technilogical University
Email:bhagyalakshminarayanapuram_2k20phdec502@dtu.ac.in

Dr.J.Panda
Professor,ECE Department
Delhi Technilogical University
Email:jpanda@dce.ac.in

***Abstract*—This paper presents proposed multi mode memory PUF design for high speed 5G IOT nodes. Since in conventional IOT nodes keys are used to be stored in non volatile memory, This will cause the side channel vulnerability and compromise the integrity. Silicon PUFs are used as feasible solution for this. However there is vulnerabilities in existed PUF architectures. To overcome these a new multi mode memory PUF was designed. This new PUF can be operated in two modes i.e Weak PUF(W) mode Strong(S) PUF mode. Authentication by Strong mode and weak Mode are discussed. The performance evolution metrics of proposed PUFs are close to ideal responses. The vulnerability analysis and possible side channel attacks such as data remanance attack and modeling attacks already performed in the existed memory PUFS were discussed and counter measures are used to design novel PUF of this work. The work is implemented on Artix-7 FPGA The authentication by S mode PUF and W mode PUF for IOT is implemented. The key generation by using W mode is implemented. The propose PUF has uniqueness is 49.96 %, uniformity is 49.87%, BER is 0.41**

***Index Terms*—SRAM PUF, Data remanance attack ,modelling attack, Key generation, Internet of Things,FPGA.**

I. Introduction

Now a days the Internet of things (IoT) has emerged as vital communication technology . Because it integrates various technologies such as sensor systems, advance computing and deep learning platforms. As the advent of 5G technology growing day by day because of its higher bandwidth the effective number of IOT nodes are increased drastically [1]. In present IOT covers major areas and able to process the data with different environments. For example in the applications of wearable electronic computing devices,bio implantable devices are used to monitor the check the various human body functions. In tele medicine applications the nature of data collected is extremely private and should not be disclosed to others [2]. This should require safeguards and should have integrity and security of the patient data collected. Unfortunately because of the distributed nature of nodes will provide thirdly party physical access to the vulnerable node. The high speed IOT network should require secure,high energy efficient and fast secure protocols. In the 5G fast and light weight IOT node communication conventional cryptography can not provide device authentication with out vulnerabilities. For example every protocol of IoT requires authentication and key should be stored on each node of the device. Unfortunately this storing the keys in the nodes can cause side channel vulnerabilities [3]. The attacker can steal these keys by performing side channel attacks. As a result the secure data and integrity will be compromised. Thanks to Physically un clonnable functions (PUFs) the storing of keys on the IOT nodes is eliminated by the usage of these silicon PUFs [4]. Now a days these PUFs becomes popular in IOT authentication.

Physically Unclonable Functions (PUFs) are emerging as hardware secure cryptography primitives. In the literature many kind of PUF structures were implemented. Among these PUF structures, silicon PUFs are mostly used in the hardware security applications because of its low area and cost[5], [6], [7].

The basic principle of silicon PUFs are based on intrinsic process variations. These variations are unique for each chip. This will be used as a unique signature for each Silicon PUF. These PUF signatures can be used as key generation or device authentication etc. In silicon PUFs primarily rely on manufacturing process variations . These variations occur because of the variations in the length of transistors,oxide layer thickness and doping atoms location etc[8].

Generally, The classification of silicon PUFs can be done in two ways on the basis of their sizes of challenge-response pairs (CRPS). If the large number of CRPs are available then it is called strong PUF. Similarly Less or no number of CRPS are called weak PUFS. Arbitrary PUF , Ring Oscillator (RO) based PUF are some examples of strong PUF. All kind of memory based PUFs are classified under memory PUFs such as Flip flop PUF,Latch PUF, SRAM PUF etc. Unfortunately strong PUF as it name indicates it will not give the strong PUF behaviour[9], [10]. In the literature so many side channel attacks were preformed on various PUF structures such as Arbitrary PUF, RO PUF etc. In strong PUF CRPS are available to the third person hence the modelling of the PUF design is easy. Increasing CRPS can give some resistance to the side channel attacks[11], [12]. However with advanced quantum computing even large number CRP PUF can be cloned. Similarly in RO PUF structures RO stages will emit the ELectro magntic emanations . These emissions also can be used as side channel attack called EM attack [13], [14].Fortunately weak PUFs are not having these many side channels because of its intrinsic key generation capability. The external challenges are not required hence the attacking is difficult[15]. In addition to this The key will be generated

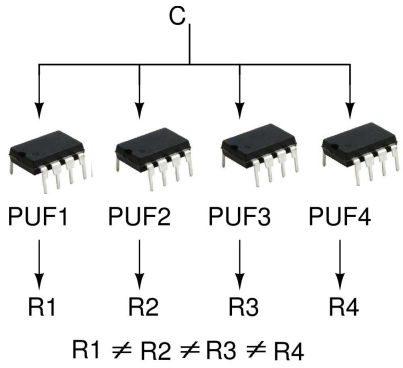

Fig. 1. Strong PUF

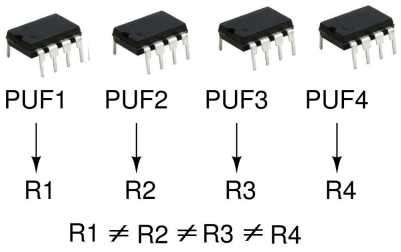

Fig. 2. Weak PUF

automatically when the PUF is switched on and we never store any key. This is the reason in current scenario lot of PUF are based On weak PUF and used in many applications such PUF key generation, secure storage and authentication etc.

As shown in the Fig.1 the weak PUF does not need any input challenges to produce responses. But in strong PUFs challenges should be required to produce responses as shown in Fig.2

II. Limitations of strong PUFs and weak PUFs

Strong PUFs need external challenges and responses also available to the third person. By some modelling attacking algorithms PUF signature can be retrieved [5], [16]. Increasing CRP size is one of the method to counter the modelling attacks, but in quantum cryptography era this is also not a feasible solution.

For this reason most of the PUF designs based on the weak PUF topology like SRAM PUF,LATCH PUF,RO PUF etc. The RO PUF implementation costs more area and power consumption. In the literature it is found that many invasive attacks were successfully performed on the RO PUF like EM attack and photon emission analysis attack [6], [17] . Hence in the security applications SRAM PUF shown in Fig.3 can give good unique signature compared to other PUFS. Now a days for cipher key generation SRAM PUF response is mostly used [18], [19]. In this paper we focused on Conventional SRAM vulnerabilities and proposed design to counter those vulnerabilities.

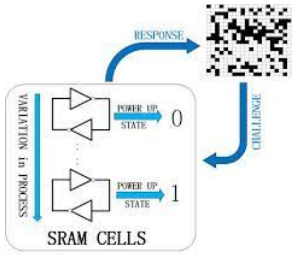

Fig. 3. Basic SRAM PUF

A. Modelling Attacks on PUF Models

Modelling attacks are based on machine learning algorithms. In this attacks the attacker will try to model the real PUF behaviour with mathematical algorithms etc. As discussed above in strong PUf based authentication number of CRPs are available to third party. BY using this various CRPs the attacker can try to model the PUF behavior using different mathematical expressions and algorithms. In the literature there are number of ML based attacks on strong PUF were performed on the existed Memory PUF [20], [21]. These are based on the predictive modelling.

The authors in the literature successfully cone the functionality of the various existed PUF structures,by various computer based algorithms such as logistic regression (LR), simple logic regression (SLR) and Multi layer Perception (MLP) etc [22], [23].

B. Basics of Conventional SRAM PUF

The SRAM PUF was proposed in 2007 by Holcomb et al. [7], [24].The SRAM cell are made with two symmentrical cross coupled invertes. Due to manufacturing and process variations the two inverters will not match completely. A small variations can cause unstability. When SRAM is powered up in transient times it may store '1' or '0' because of of the unstability of the cross coupled inverters[25], [26]. These random bits during powered up time can be used as PUF signature. The basic SRAM cell shown in the Fig.3

C. Side Channel Attacks on conventional SRAM PUF

Unfortunately from the last decade different side channel attacks are performed on the Memory PUFs such as Photon emission analysis (PEA) attack on micro controller memory, data remanance attack and fault injection attack etc. In recent years data remanace attack on SRAM puf become big challenge for good memory PUF design. Data on SRAM will be held active for some time even after power off condition. In the literature some invasive attacks by inducing voltages also performed. There are thre ways to induse voltage by decapulating front side, by decapulating rear side and by capulated which is shown in the Fig.4 from the Fig. 4 it is clear that by Decapulated front side will be induce more voltage on PUF.

Data remanence attack(DRA): is a special type of active attack and fault injection attack. The main operation of this

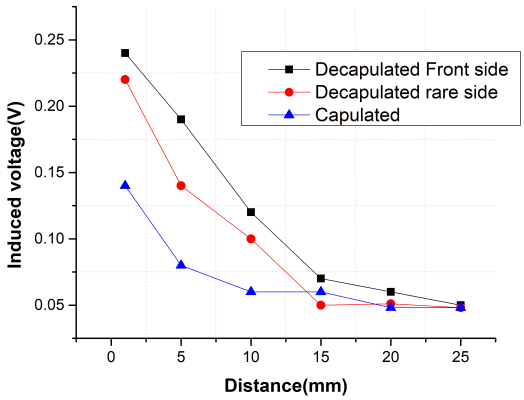

Fig. 4. SRAM PUF invasive attack

attack is injecting faults into the target and retrieving the data. In the literature, so many authors performed this DRA on various SRAM PUF topology, in which the faults are injected by changing the temperature into the SRAM PUF [8], [27]. In the work [9], [28] is using temperature along with on and off time of power to generate various responses. With these responses the attacker will match the legitimate response and by performing differential fault analysis the PUF signature will be recreated . THis can be done by reducing temperatures and inducing faults in to SRAM cells.

This attack is applicable only on memory based PUFs like SRAM and flip flop based PUFs etc.As explained in [10], [29] the stable key of SRAM PUF can be generated with data remanece based approach. In SRAM PUF stable bit response is essential for key generation. As shown in Fig.5 stable bit response can be achieved by enrolment and key generation phases. in enrolment phase first all bits are written with either 0 or 1. After that the SRAM PUF will be turned off for some time let say T seconds. After T seconds of time turn on power of SRAM and read out the data,here we can observe some of the bits will be changed from starting values and some bits will be remains stable that means no flip. Among these bits by stable bits can be identified. In the key generation phase this stable bits position can be verified again with the helper data so that stable key can be produced.

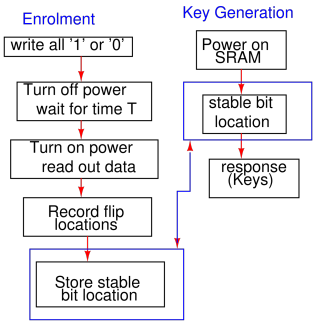

Fig. 5. Stable bit key generation by using data remanance effect

By using same data remance approach the SRAM PUF can be attacked which is explained in [8], [10], [30]. The performance of data remance attack will be increased if the operating temperature is decreased. because for the low temperature conditions the data remance duration will be high. As shown in the Fig.6 as the temperature is decreasing from

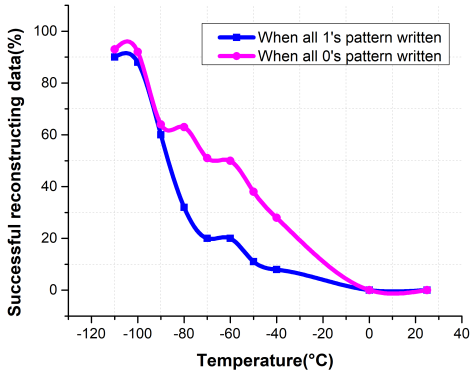

Fig. 6. Rate of Successful Reconstructing the data from SRAM PUF response after a 10ms reset time

40 degree to -120 degree centigrade the rate of reconstruction of SRAM bits is increasing. In this attack the total setup will be place din the cryogenic setup to decrease the surrounding temperature. As shown in Fig.6 the rate of reconstruction is more at low temperatures when all 1 s are written.

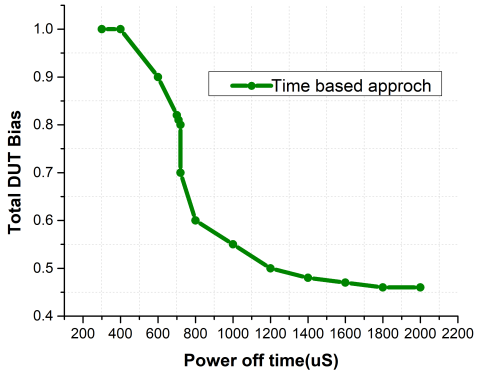

Fig. 7. Time based approach

In [14] the author explained two different approaches to perform data remance attack on SRAM PUF. one is time based approach and another one is voltage based approach. In time based approach initially all 1 s will be written and after power will be off for some time duration.Again power will be on to check the probability of storing previous data. This experiment will be repeated for several power off time duration . This time based approach result is shown for different power off times in Fig.7 Similarly the voltage based approach is shown in Fig.8

Here the bias is nothing but the probability of storing previous data.the supply voltage was set to 0 V during power off time.

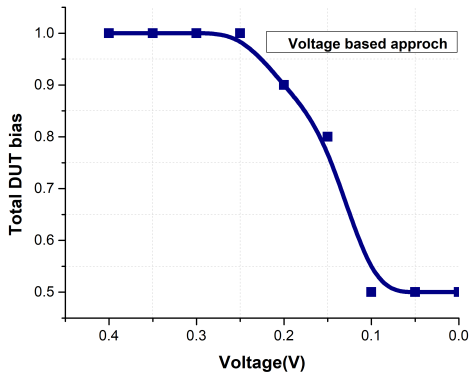

Fig. 8. Voltage based approach

Similarly in voltage based approach the supply voltage was decreased slowly and the bias of the SRAM data was recorder which is shown in the Fig.8.In this figure as the supply voltage is changing from 0.4 V to 0 V the probability of storing previous data(bias) is also decreasing. However in built SRAM cells by default will have some start up behaviour. This start up behaviour will cause vulnerability such as data remannce attack. To overcome above drawback new memory PUF is designed with same SRAM functionality and with out start up data availability.

III. Proposed Multi mode memory PUF

The proposed PUF made of re configurable delays in look up tables. As shown in the Fig 9. In the 3 input LUT inverter among 3 inputs one input is used as inverter input remaining two inputs are used as optional inputs. The proposed multi mode PUF is shown in Fig.10, these optional inputs can be fed with any bit sequence as it will not alter the operation of inverter. Hence the optional dont care inputs can be used as shown below. In the strong PUF mode PUF needs challenges hence the Controller enable the input feed to the LUT from the external peripherals. Master challenges will be given to LFSR (Linear Feedback Shift Register) through UART. The LFSR will convert master challenges into sub challenges. These sub challenges will be given to the LUT optional inputs C1 and C2 of inverter 1 and C2,C3 for inverter2. The back to back connected inverters itself can generate PUF signature in addition to this, random re configurable inverters will produce different responses this will be captured by multiplexer and counter. Finally the two memory cells out put will be compared with the comparator. The comparator output is fed to the UART and this UART will send responses us back. The proposed multi mode memory PUF operates in two modes i.e strong mode and weak mode.

In the weak PUF mode (W mode) C1C2 and C3C4 fed with boolean ”11” and C5C6,C7C8 fed with boolean ”00”. The enable control will be disabled in the controller. Hence

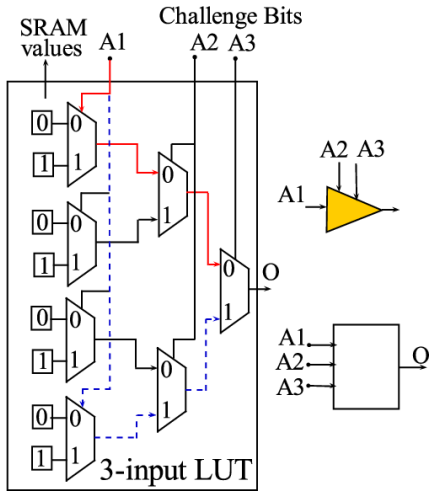

Fig. 9. Re configurable injected delay in 3 input LUT

feed from LFSR will be cut off , no challenges. Though in the absence of challenges the W mode PUF is able to produce good PUF signature(response) because of the start up unstability of the back to back connected inverters. In the strong mode (S mode), challenges will be given as inputs to the PUF and the concerned response will be generated. W mode can be used for key generation seed for PRNG and rtc. Similarly S mode can be used for Authentication devices.

Thus the proposed multi mode Memory PUF can be used in two modes. In this paper key generation , authentication using w mode PUF and authentication using S mode PUF is also explained.

IV. QUALITY METRICS FOR SILICON PUFS

A. Uniqueness

Uniqueness: Uniqueness is one of the important metric of PUF. It is the ability of a PUF to produce distinguish unique response. That means no two PUFs will have same response.. To calculate this Hamming distance (HD) is used between two PUF responses. For example If two PUF chips, i and j (i not equal to j)), have n-bit responses, Ri and Rj respectively for the same challenge C, then the avarage hamming distance of k chips is defined as below equation.

$$Uniqueness = \frac{2}{k-1}\sum_{i=1}^{k-1}\sum_{j=i+1}^{k}\frac{HD(Ri,Rj)}{n} * 100\%$$

B. Reliability

Reliability is one of the PUF evolution metrics of the PUF, it tells about reproducibility of PUF bits. This metric is measured by intra chip hamming distance of various PUF response bits. To calculate this intra Hamming distance n bit response as a reference (Ri) from the chip iat normal voltage and temperature. At different operating conditions the same n bit response is extracted. For m samples of Ri collected the avarage intra chip hamming distance as follows.

$$HD_{INTRA} = \frac{1}{m}\sum_{t=1}^{m}\frac{HD(Ri,R'i,t)}{n} * 100\%$$

$$Reliability = 100\% - HD_{INTRA}$$

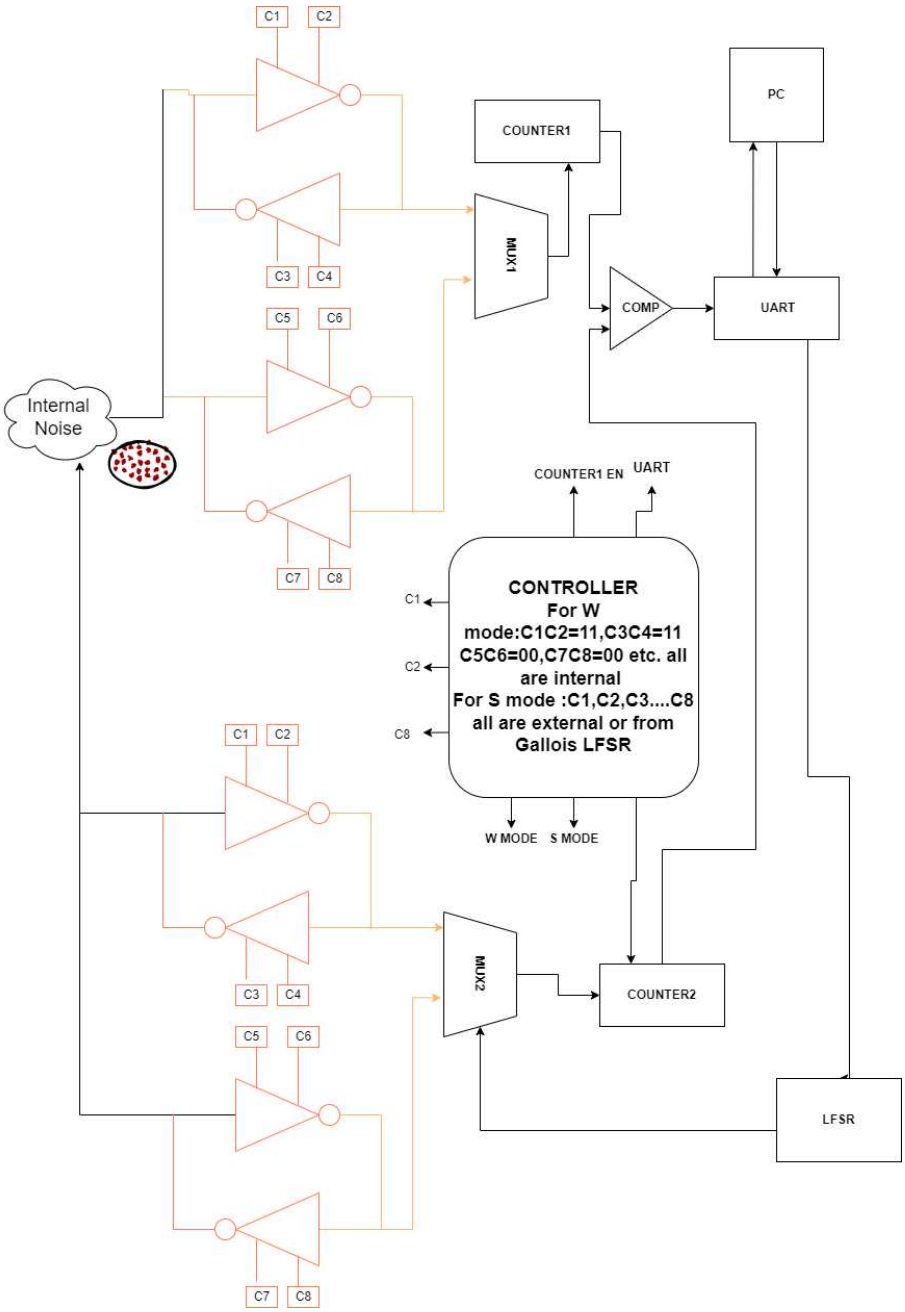

Fig. 10. Proposed Multi mode memory PUF

C. Uniformity

This is one of the important property of PUF . It estimate the proportion of '0's and '1's in the PUF response. That means '0's and '1's should distribute uniformly in the response. Ideally the PUF uniformity should be 50 percent. We define uniformity of an n-bit PUF identifier as the percentage Hamming Weight(HW) of the n-bit identifier:

$$(Uniformity)_i = \frac{1}{n}\sum_{l=1}^{n} r_{i,l} * 100\%$$

D. Bit aliasing

bit-aliasing is undesirable effect, in which different chips may produce nearly same PUF responses which is an undesirable feature in PUF. For a good PUF this value should be low To calculate this we estimate bit-aliasing of the l-th bit in the PUF identifier as the percentage Hamming Weight(HW) of the l-th bit of the identifier across k devices:

$$(Bitalising)_l = \frac{1}{n}\sum_{i=1}^{k} r_{i,l} * 100\%$$

V. Vulnerability analysis

A. Against Side Channel Attacks

In the conventional SRAM PUFs many side channel attacks were mentioned in the literature like non invasive, semi invasive and invasive methods. The invasive attack is shown in the Fig. In this method silicon PUF IC front cap or back cap will be removed and start up voltages will be sensed with photo diodes etc. or in the same way by lasers faults can also be induced It is observed that compared to back side front side decapuslated will give more favourable voltages for attacking. Fortunately in this paper FPGA based SRAM PUF is designed which is not vulnerable for this invasive attack.

The other attack mostly used is data remance attack. This is explained in the bove section. This attack can not be performed on the proposed PUF because the proposed PUF not only depends on the start up values but also on reconfigurable delay inserted. Hence cloning is not possible by this method.

B. Against ML based model building attacks

In the W mode these attacks can not be performed . However Machine learning based modelling attacks can only perform on strong PUF mode of the proposed PUF. These ML(machine learning) based attacks are based on challenge response pair. by observing challenges and responses The attacker will try to model the PUF behavior with Computer based algorithms. Among these attacks Logistic Regression (LR), simple Logistic regression (SLR), Multi layer perception (MLP) are prominent attacking models. The proposed PUF design s mode is analysed with these atatck vulnerabilities. The LR based ML attack is investigated with data mining tools(Waikato Environment Knowledge Analysis). Similarly MLP ,SLR are also tested on s mode . Performance of these attacks are based on the percentage of correctly predicting capability with given percentage of training samples which is also known as the success rate in attackers view.

By using only 8 stage proposed PUF in the success rate of attacking is only 6% which is lowest among literature survey. In the literature[11] with 8 stage PUF the success rate is around 50% but our proposed design has only 6%.BY increasing the number of stages from 8 to 16 stages its is drastically reduced to 2% with less number of stages it is possible to resist the modelling attack with proposed PUF design.

b

VI. Results And Applications

Fig.11 indicates the probability of rejection due to Bit error rate (BER) and similarly Fig.12 shows the probability of mis identification by proposed PUF design.

A. W mode Authentication

In general authentication is done by strong PUF mode comparing CRPS(challenge response pairs). For large number of users the stong PUF mode is preferred. Weak PUF mode does not have challenges hence it can not be used for authentication. Here we ve used weak PUF also as authentication that means . Based on user flexibility weak pUf mode and strong puf mode

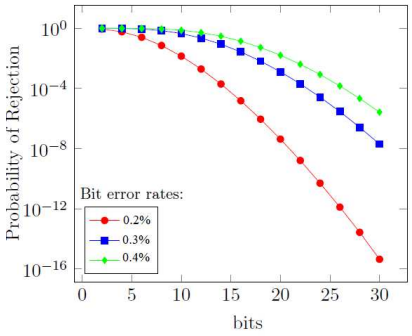

Fig. 11. Probability of rejection

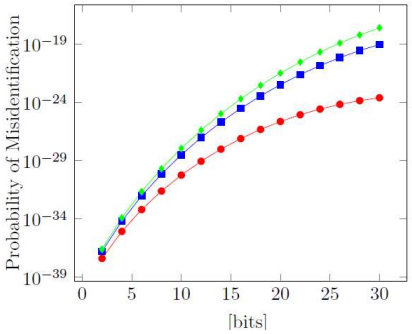

Fig. 12. Probability of mis identification

can be used with single PUF, i.e a single PUF is used for dual authentication schemes. As shown in the Fig.13 The unique PUF signature data will be encoded and it hashed response is stored in he server database. The authorised devices data will be stored in the server data base. If the same registered PUF hashed functioned decoded and compared with stored data. If both matches means both devices are authenticated. In other than PUF authentication methods there are chances for side channel attacks. But in PUF based authentication vulnerability too less compared to other designs.

B. W mode Key generation

The designed PUF in W mode can be used as intrinsic key generator. In the Key generation process there are two phases one is key enrollment shown in Fig.14 another one is key reconstruction shown in Fig.15. In the key enrollment

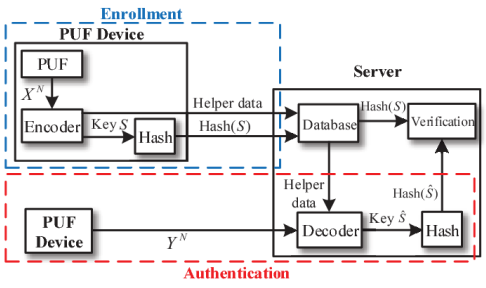

Fig. 13. Authentication using weak PUf

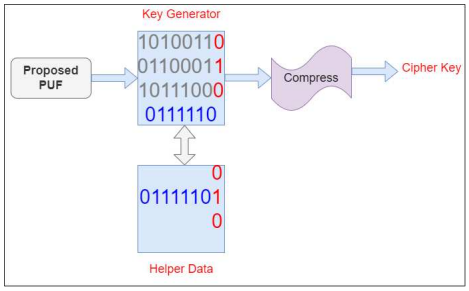

Fig. 14. key enrollement

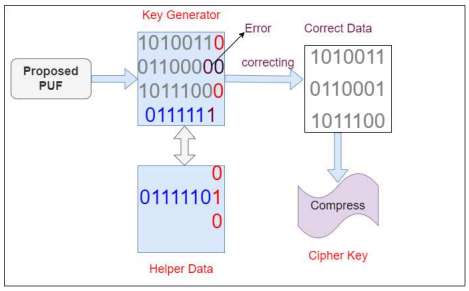

Fig. 15. key Reconstruction

phase key will be generator with PUF response , this will be appended with helper data. This helper data is useful for error detecting and correcting purposes. This helper data is generated with column hamming weight and rows hamming weight . As shown in the Fig.15 the blue and red colour bits represents helper data sequence. Because of ambient noises or vulnerabilities if there is any bit flipping that can be fixed with the helper data after compressing this data . The Cipher Key will be generated. Fig.16 shows the Proposed PUF metrics with ideal PUF behaviour. Fig.17 shows the reliability of PUF stages with varying temperatures. Similarly Fig.18 shows the bit error rate with varying temperatures.

VII. CONCLUSION

In this paper we propose novel multi mode SRAM PUF which can be used in both weak PUF mode and strong PUF mode. The design is implemented on Artix-7 FPGA .The proposed PUF in W mode has uniqueness 49.96 %, worsst case BER is0.41%, uniformity 49.87% and reliability is about

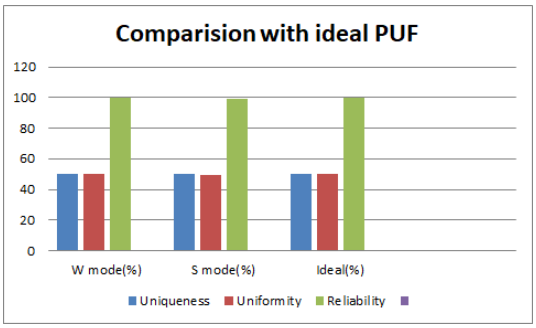

Fig. 16. Proposed Weak PUF mode and strong PUF mode comparison

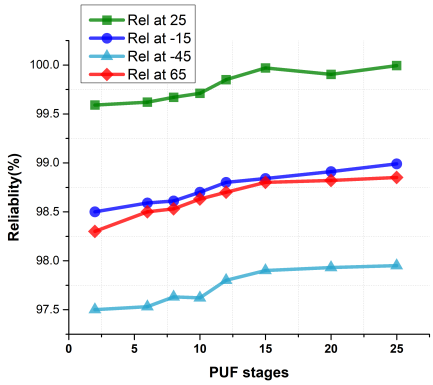

Fig. 17. Reliability with respect to temperature

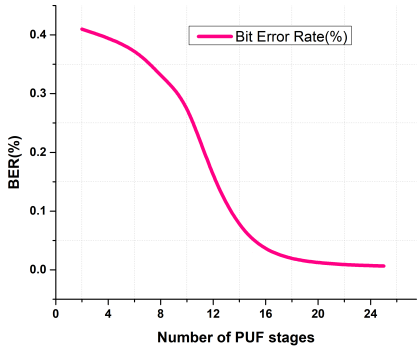

Fig. 18. Bit Error rate with respect to temperature

99.59%. The authentication schemes by both weak PUF and strong PUF are mentioned in this work.The design PUF is strong resistant to side channel attacks and modelling attacks. The proposed multi mode PUF is strong and resilient against possible side channel attacks and vulnerabilities.

REFERENCES

[1] Baek S, Yu GH, Kim J, Ngo CT, Eshraghian JK, Hong JP. A Reconfigurable SRAM Based CMOS PUF With Challenge to Response Pairs. IEEE Access. 2021 May 28.

[2] Chuang, K.H., Bury, E., Degraeve, R., Kaczer, B., Linten, D. and Verbauwhede, I., 2019. A physically unclonable function using soft oxide breakdown featuring 0 native BER and 51.8 fJ/bit in 40-nm CMOS. IEEE Journal of Solid-State Circuits, 54(10), pp.2765-2776.

[3] Tebelmann, L., Danger, J.L. and Pehl, M., 2020, April. Self-secured PUF: protecting the loop PUF by masking. In International Workshop on Constructive Side-Channel Analysis and Secure Design (pp. 293-314). Springer, Cham.

[4] Holcomb, D.E., Burleson, W.P. and Fu, K., 2008. Power-up SRAM state as an identifying fingerprint and source of true random numbers. IEEE Transactions on Computers, 58(9), pp.1198-1210.

[5] Rührmair U, Sehnke F, Sölter J, Dror G, Devadas S, Schmidhuber J. Modeling attacks on physical unclonable functions. InProceedings of the 17th ACM conference on Computer and communications security 2010 Oct 4 (pp. 237-249).

[6] Merli D, Heyszl J, Heinz B, Schuster D, Stumpf F, Sigl G. Localized electromagnetic analysis of RO PUFs. In2013 IEEE International Symposium on Hardware-Oriented Security and Trust (HOST) 2013 Jun 2 (pp. 19-24). IEEE.

PUF Class	**PUF Type**	**Nominal Condition**	**Uniquness (Ideal=50%)**	**Silicon/ FPGA**	**Worst Case BER(%) (Ideal=0%)**	**Reliability Condition**	**Uniformity (Ideal=50%)**	**Reliability (Ideal=100%)**
Memory PUF [15]2007	SRAM PUF	Tnom: 20C	49.97%	FPGA	12	Tenv: -20oC to 80oC	NA	88%
Memory PUF[16]2008	Butter y PUF	Tnom: 20oC	49.9%	FPGA	6	Tenv: -20oC to 80oC	NA	94%
Memory PUF[17]2010	D Flip op PUF	Tnom: 20oC	36%	Silicon	13	Tenv: -40oC to 80oC	75%	87%
Memory & Delay[12]2020	ECARMM	0 TO 70 Degree C	46.32%	FPGA	0.9	NA	NA	99.1%
Memory Arbitary[13]2020	Memory Arbitary	Tnom: 20oC	48%	FPGA	NA	Tenv: -40oC to 80oC	NA	NA
Memory delay[11]2018	APUF with RRAM	Tnom: 20oC	51.3%	Silicon	0.43	NA	NA	99.57%
Memory[14]2021	SRAM	Tnom: 20oC	49%	Silicon	0.96 0.1V	NA	NA	99.04%
Memory[31]2021	SRAM	Tnom: 20oC	48.93%	Silicon	0.9 0.2V	NA	NA	99.10%
Memory[32]2022	SRAM	Tnom: 25oC	37%	FPGA	7 0.1V	55%	37%	93%
Memory[33]2022	SRAM	Tnom: 20oC	48.89%	Silicon	14.8	NA	75oC	85.2%
Memory PUF (This work)	Multi mode Memory PUF	Tnom: 20oC	49.96%	FPGA	0.41	Tenv: -40oC to 80oC	49.87%	99.59%

[7] Holcomb DE, Burleson WP, Fu K. Power-up SRAM state as an identifying fingerprint and source of true random numbers. IEEE Transactions on Computers. 2008 Nov 17;58(9):1198-210.

[8] Zeitouni S, Oren Y, Wachsmann C, Koeberl P, Sadeghi AR. Remanence decay side-channel: The PUF case. IEEE Transactions on Information Forensics and Security. 2015 Dec 25;11(6):1106-16.

[9] Delvaux J, Verbauwhede I. Fault injection modeling attacks on 65 nm arbiter and RO sum PUFs via environmental changes. IEEE Transactions on Circuits and Systems I: Regular Papers. 2014 Jan 29;61(6):1701-13.

[10] Liu M, Zhou C, Tang Q, Parhi KK, Kim CH. A data remanence based approach to generate 100 stable keys from an sram physical unclonable function. In2017 IEEE/ACM International Symposium on Low Power Electronics and Design (ISLPED) 2017 Jul 24 (pp. 1-6). IEEE.

[11] Govindaraj R, Ghosh S, Katkoori S. Design, analysis and application of embedded resistive RAM based strong arbiter PUF. IEEE Transactions on Dependable and Secure Computing. 2018 Aug 21;17(6):1232-42.

[12] Goncu E, Yalcin ME. A design of cellular automata-based PUF and its implementation on FPGA. International Journal of Circuit Theory and Applications. 2020 Aug;48(8):1244-55.

[13] Idriss H, Idriss T, Williams P, Bayoumi M. Memory-based Arbiter PUF: A Novel Highly Reliable and Scalable Strong PUF Design. In2020 IEEE 6th World Forum on Internet of Things (WF-IoT) 2020 Jun 2 (pp. 1-6). IEEE.

[14] Zhang H, Wang C, Yan C, Cui Y, Gu C, O'Neill M, Liu W. A Dynamic Highly Reliable SRAM-Based PUF Retaining Memory Function. In2021 IEEE International Symposium on Circuits and Systems (ISCAS) 2021 May 22 (pp. 1-5). IEEE.

[15] Guajardo J, Kumar SS, Schrijen GJ, Tuyls P. FPGA intrinsic PUFs and their use for IP protection. InInternational workshop on cryptographic hardware and embedded systems 2007 Sep 10 (pp. 63-80). Springer, Berlin, Heidelberg.

[16] Kumar SS, Guajardo J, Maes R, Schrijen GJ, Tuyls P. The butterfly PUF protecting IP on every FPGA. In2008 IEEE International Workshop on Hardware-Oriented Security and Trust 2008 Jun 9 (pp. 67-70). IEEE.

[17] Van der Leest V, Schrijen GJ, Handschuh H, Tuyls P. Hardware intrinsic security from D flip-flops. InProceedings of the fifth ACM workshop on Scalable trusted computing 2010 Oct 4 (pp. 53-62).

[18] Bossuet, L., Ngo, X.T., Cherif, Z. and Fischer, V., 2013. A PUF based on a transient effect ring oscillator and insensitive to locking phenomenon. IEEE Transactions on Emerging Topics in Computing, 2(1), pp.30-36.

[19] An, Y., Jung, D., Ryu, K., Yim, H.S., Jung, S., Inverter-Based, P.S.U.R., Nov, T.V.L.S.I., Aridhi, H., Zaki, M.H., Tahar, S. and Arumi, D., 2016. Adil, F., see George, S., TVLSI June 2016 2253-2261 Adnan Aslam, C., Guan, YL, and Cai, K., Detector for MLC NAND Flash Memory Using Neighbor-A-Priori Information; TVLSI Sept. 2016 2827-2836 Advani, S., see Xiao, Y., TVLSI Aug. 2016 2689-2702. IEEE Transactions on Very Large Scale Integration (VLSI) Systems, 24(12), p.1.

[20] Usmani, M.A., Keshavarz, S., Matthews, E., Shannon, L., Tessier, R. and Holcomb, D.E., 2018. Efficient PUF-based key generation in FPGAs using per-device configuration. IEEE Transactions on very large scale integration (VLSI) systems, 27(2), pp.364-375.

[21] Das, J., Scott, K., Rajaram, S., Burgett, D. and Bhanja, S., 2015. MRAM PUF: A novel geometry based magnetic PUF with integrated CMOS. IEEE Transactions on Nanotechnology, 14(3), pp.436-443.

[22] Kim, M.S., Moon, D.I., Yoo, S.K., Lee, S.H. and Choi, Y.K., 2015. Investigation of physically unclonable functions using flash memory for integrated circuit authentication. IEEE Transactions on Nanotechnology, 14(2), pp.384-389.

[23] Tehranipoor, F., Karimian, N., Yan, W. and Chandy, J.A., 2016. DRAM-based intrinsic physically unclonable functions for system-level security and authentication. IEEE Transactions on Very Large Scale Integration (VLSI) Systems, 25(3), pp.1085-1097.

[24] Krishna, A.R., Narasimhan, S., Wang, X. and Bhunia, S., 2011, September. MECCA: A robust low-overhead PUF using embedded memory array. In International Workshop on Cryptographic Hardware and Embedded Systems (pp. 407-420). Springer, Berlin, Heidelberg.

[25] Chuang, K.H., Bury, E., Degraeve, R., Kaczer, B., Groeseneken, G., Verbauwhede, I. and Linten, D., 2017, April. Physically unclonable function using CMOS breakdown position. In 2017 IEEE International Reliability Physics Symposium (IRPS) (pp. 4C-1). IEEE.

[26] Sadana, S., Lele, A., Tsundus, S., Kumbhare, P. and Ganguly, U., 2018.

A highly reliable and unbiased puf based on differential otp memory. IEEE Electron Device Letters, 39(8), pp.1159-1162.

[27] Maes, R., Tuyls, P. and Verbauwhede, I., 2008, November. Intrinsic PUFs from flip-flops on reconfigurable devices. In 3rd Benelux workshop on information and system security (WISSec 2008) (Vol. 17, p. 2008).

[28] Su, Y., Holleman, J. and Otis, B., 2007, February. A 1.6 pJ/bit 96 stable chip-ID generating circuit using process variations. In 2007 IEEE International Solid-State Circuits Conference. Digest of Technical Papers (pp. 406-611). IEEE.

[29] Holcomb, D.E., Burleson, W.P. and Fu, K., 2008. Power-up SRAM state as an identifying fingerprint and source of true random numbers. IEEE Transactions on Computers, 58(9), pp.1198-1210.

[30] Bossuet, L., Ngo, X.T., Cherif, Z. and Fischer, V., 2013. A PUF based on a transient effect ring oscillator and insensitive to locking phenomenon. IEEE Transactions on Emerging Topics in Computing, 2(1), pp.30-36.

[31] S. Baek, G. -H. Yu, J. Kim, C. T. Ngo, J. K. Eshraghian and J. -P. Hong, "A Reconfigurable SRAM Based CMOS PUF With Challenge to Response Pairs," in IEEE Access, vol. 9, pp. 79947-79960, 2021, doi: 10.1109/ACCESS.2021.3084621.

[32] Cicek I, Al Khas A. A new read–write collision-based SRAM PUF implemented on Xilinx FPGAs. Journal of Cryptographic Engineering. 2022 Jan 29:1-8.

[33] J. -W. Nam, J. -H. Ahn and J. -P. Hong, "Compact SRAM-Based PUF Chip Employing Body Voltage Control Technique," in IEEE Access, vol. 10, pp. 22311-22319, 2022, doi: 10.1109/ACCESS.2022.3153359.

J. Earth Syst. Sci. (2024)133 239
https://doi.org/10.1007/s12040-024-02455-4

© Indian Academy of Sciences

Estimation of tropical cyclone's radius of maximum wind using ensemble machine learning approach

Monu Yadav[1,*], Laxminarayan Das[1] and Shashi Kant[2]

[1]*Department of Applied Mathematics, Delhi Technological University, New Delhi, India.*
[2]*India Meteorological Department, Ministry of Earth Sciences, New Delhi, India.*
[*]*Corresponding author. e-mail: yadavm012@gmail.com*

MS received 13 December 2023; revised 18 July 2024; accepted 16 August 2024

This study examines the complex behaviour of tropical cyclones, specifically focusing on accurately estimating the Radius of Maximum Wind (RMW) and its implications for climate and oceanic processes. We use RMW data provided by the India Meteorological Department (IMD) to evaluate three existing methods for estimating RMW and introduce a new method based on machine learning techniques. The findings underscore the critical role of the RMW in shaping the intensity and impact of tropical cyclones, emphasizing the need for refined estimation techniques to bolster forecasting and preparedness measures. We use four cases to test our method. The results of our method show the root square mean error is 10.63 nautical miles and the error percentage of 17.00%, which are lower than other methods. Therefore, the proposed ensemble machine learning model, designed to estimate RMW, showcases considerable promise in attaining precise RMW estimation.

Keywords. Tropical cyclone; radius of maximum wind; machine learning technique; North Indian Ocean.

1. Introduction

Tropical cyclones (TCs), disturbing atmospheric vortices, stand as focal points of scientific inquiry due to their profound impacts on global climate systems and coastal ecosystems. Emerging from the complex interplay of atmospheric and oceanic dynamics, these cyclonic systems exhibit distinctive features, with the Radius of Maximum Wind (RMW) serving as a pivotal parameter in their characterization. The RMW, representing the spatial extent of the most intense winds within a TC, holds critical significance in deciphering the storm's size, intensity, and potential for destruction (Emanuel 2003; Kossin *et al.* 2014). Understanding the complex relationship between the RMW, wind speeds, and marine heat distribution is imperative for solving the complex interdependencies within Earth's climatic and oceanic processes.

Recent advancements underscore the fundamental association between the RMW and the overall intensity of TCs. Studies have revealed a robust correlation between the RMW and maximum sustained wind speeds, indicating that changes in the RMW significantly influence the storm's wind structure and, consequently, its overall destructive potential (Emanuel 2003; Gross *et al.* 2004; Chen *et al.* 2006; Willoughby *et al.* 2006; Quiring *et al.* 2011; Yadav and Das 2024). As the

Published online: 26 November 2024

RMW contracts, wind speeds intensify, leading to a more compact and potent cyclonic system. This complex relationship necessitates precise RMW estimations to solve the underlying dynamics governing the intensity and behaviour of TCs (Kossin *et al.* 2014).

Beyond its impact on intensity and wind speeds, the RMW also plays a crucial role in the modulation of marine heat distribution (Rathore *et al.* 2022). TCs act as heat engines, extracting energy from warm ocean waters to fuel their intensification. The RMW, acting as a boundary between the TC's eyewall and the surrounding environment, influences the efficiency of this heat exchange process (Kossin *et al.* 2016). Understanding the complex connection between the RMW and marine heat distribution is pivotal, as it delineates the potential for TCs to induce marine heat waves and alter broader oceanic climate patterns (Balaguru *et al.* 2016; Rathore *et al.* 2022).

Advanced computational methodologies have become indispensable in the pursuit of refining the estimation of TC characteristics. Neural networks, a subset of machine learning techniques, have emerged as potent tools in analyzing vast and complex datasets inherent to TC dynamics. By assimilating information from historical and real-time data, neural networks facilitate a nuanced understanding of the interconnected factors influencing the behaviour and characteristics of TCs (Balaguru *et al.* 2017; Sharmila *et al.* 2019). The utilization of neural networks in TC analysis represents a paradigm shift, offering unparalleled insights into the complex and non-linear relationships governing these meteorological phenomena.

The RMW is estimated using a combination of data sources, including satellite imagery, ground-based observations, and computer models.

One common method for estimating the RMW is through the use of the Holland formula (Holland 1980), which takes into account the central pressure, the maximum sustained wind speed, and other factors such as latitude and the Coriolis parameter. This formula was developed based on observations and theoretical considerations, and it provides a good estimate of the RMW in most cases. However, the Holland formula has limitations, especially when predicting the RMW for rapidly intensifying storms or storms with unusual characteristics.

Machine learning (ML) methods can potentially improve the accuracy of RMW estimates (Lu *et al.* 2022; Wang and Li 2023; Xu *et al.* 2023) by incorporating additional data sources and learning from historical storm data. For example, ML algorithms can be trained on a large dataset of observed storms and their corresponding RMWs and then used to predict the RMW for new storms based on their characteristics. Additionally, ML methods can identify patterns in the data that may not be captured by the Holland formula, such as the influence of local topography or atmospheric conditions.

Against this backdrop, this study aims to contribute to the evolving discourse on TC dynamics by focusing on the precision enhancement of RMW estimation through neural network methodologies. By emphasizing the significance of RMW estimation in predicting the behaviour and impact of TCs, the research seeks to contribute to developing more effective forecasting models and mitigation strategies, ultimately fostering improved preparedness and resilience against the potential hazards posed by these severe weather events.

This paper is organized as follows: Section 2 presents the data and method used in the research. The proposed method is discussed in detail in section 3 and compared with other approaches: Willoughby *et al.* (2006), Tan and Fang (2018), and Yadav and Das (2024). Section 4 provides the conclusion.

2. Data and method

2.1 *Data*

This research assesses our proposed methodology utilizing the best track data of the RMW sourced from the IMD, recognized as the Regional Specialized Meteorological Center for TCs operating within the NIO region. The data collection from 2014 to June 01, 2024 encompasses pertinent information concerning TCs across the NIO. The details of the selected TCs for the training are represented in table 1 and validation in table 2.

We collect data on various parameters such as the latitude of the TC's center, estimated central pressure, and estimated pressure drop at the center related to TC formed over the NIO. This data is obtained from the best track data released by the IMD. Using this data, we find the results of three equations (equations 1, 2, and 3) in the literature to estimate the RMW.

While direct observation of RMW remains unavailable, its determination can be facilitated

Table 1. *Details of selected tropical cyclone for training of the model.*

Name of tropical cyclone	Category	Time period
Depression	Depression	04–07 January 2014
Depression	Depression	21–23 May 2014
Nanauk	Cyclonic storm	10–14 June 2014
Deep depression	Deep depression	03–07 August 2014
Hudhud	Very severe cyclonic storm	07–14 October 2014
Nilofar	Very severe cyclonic storm	25–31 October 2014
Deep depression	Deep depression	05–08 November 2014
Ashobaa	Cyclonic storm	07–12 June 2015
Komen	Cyclonic storm	26 July–02 August 2015
Deep depression	Deep depression	09–12 October 2015
Chapala	Extremely severe cyclonic storm	28 October–04 November 2015
Megh	Extremely severe cyclonic storm	05–10 November 2015
Deep depression	Deep depression	08–10 November 2015
Roanu	Cyclonic storm	17–22 May 2016
Depression	Depression	27–29 June 2016
Deep depression	Deep depression	09–12 August 2016
Deep depression	Deep depression	16–21 August 2016
Kyant	Cyclonic storm	21–28 October 2016
Depression	Depression	02–06 November 2016
Nada	Cyclonic storm	29 November–02 December 2016
Vardhah	Very severe cyclonic storm	06–13 December 2016
Marrutha	Cyclonic storm	15–17 April 2017
Mora	Severe cyclonic storm	28–31 May 2017
Deep depression	Deep depression	11–13 June 2017
Depression	Depression	18–19 July 2017
Depression	Depression	26–27 July 2017
Deep depression	Deep depression	09–10 October 2017
Depression	Depression	19–22 October 2017
Ockhi	Very severe cyclonic storm	29 November–06 December 2017
Deep depression	Deep depression	06–09 December 2017
Sagar	Cyclonic storm	16–21 May 2018
Mekunu	Extremely severe cyclonic storm	21–27 May 2018
Daye	Cyclonic storm	19–22 September 2018
Luban	Very severe cyclonic storm	06–15 October 2018
Gaja	Very severe cyclonic storm	10–19 November 2018
Pabuk	Cyclonic storm	04–08 January 2019
Fani	Extremely severe cyclonic storm	26 April–04 May 2019
Vayu	Very severe cyclonic storm	10–17 June 2019
Hikaa	Very severe cyclonic storm	22–25 September 2019
Kyarr	Super cyclonic storm	24 October–04 November 2019
Maha	Extremely severe cyclonic storm	30 October–07 November 2019
Bul Bul	Very severe cyclonic storm	05–11 November 2019
Pawan	Cyclonic storm	02–07 December 2019
Deep depression	Deep depression	03–05 December 2019
Amphan	Super cyclonic storm	16–21 May 2020
Nisarga	Severe cyclonic storm	01–04 June 2020
Gati	Very severe cyclonic storm	21–24 November 2020
Tauktae	Extremely severe cyclonic storm	14th-19th May 2021
Yaas	Very severe cyclonic storm	23–28 May 2021
Gulab	Cyclonic storm	24–28 September 2021
Shaheen	Severe cyclonic storm	30 September–4 October 2021
Depression	Depression	10–11 November 2021
Deep depression	Deep depression	03–06 March 2022

Table 1. *(Continued.)*

Name of tropical cyclone	Category	Time period
Asani	Severe cyclonic storm	07–12 May 2022
Depression	Depression	12–13 August 2022
Depression	Depression	14–16 August 2022
Deep depression	Deep depression	14-17 December 2022
Biparjoy	Extremely severe cyclonic storm	06–19 June 2023
Deep depression	Deep depression	01–03 August 2023
Michaung	Severe cyclonic storm	01–06 December 2023
Tej	Extremely severe cyclonic storm	20–24 October 2023

Table 2. *Details of selected tropical cyclones for validation.*

Name of TC	Category	Time period
Mandous	Severe cyclonic storm (SCS)	06–10 December 2022
Sitrang	Severe cyclonic storm (SCS)	22–25 October 2022
Mocha	Extremely severe cyclonic storm (ESCS)	9–15 May 2023
Remal	Severe cyclonic storm (SCS)	24–28 May 2024

through satellite and radar measurements. In the case of radar observation analysis, the radius of maximum reflectivity is acknowledged as a representative value for the RMW. Conversely, the RMW is approximated in satellite imagery using the radius of maximum reflectivity within visible imagery and the radius of the lowest cloud temperature depicted in infrared (IR) imagery, as previously expounded by reference (IMD 2021).

In conjunction with the IMD data, we employed three distinct methodologies, as described by Willoughby *et al.* (2006), Tan and Fang (2018), and Yadav and Das (2024), to determine the RMW. Each of these methodologies offers unique approaches for estimating the RMW in the context of TCs. Each of these methods is described individually below.

Willoughby *et al.* (2006) introduced an empirically derived model that describes the structure of the hurricane vortex. In their study, they provided an expression for determining the value of $r_{\max}$ for the NIO basins also.

The model's estimation equation for $r_{\max}$ (kilometer) is:

$$r_{\max} = 46.6 \times e^{(-0.015\,V_{\max}+0.0169\theta)} \quad (1)$$

where θ is latitude (degrees), $V_{\max}$ is the maximum wind speed (kt), and $r_{\max}$ is the radius of maximum wind.

Before starting the analysis, we change the $r_{\max}$ value to nautical miles.

Tan and Fang (2018) focused on simulating wind fields of historical TCs using parametric models using satellite data. In their study, they provided an expression for determining the value of $r_{\max}$ for all the seen basins (table 3 of the reference paper, Tan and Fang 2018) has the expression to determine the value of $r_{\max}$ for all seven basins).

The relation to determine the value of $r_{\max}$ (nautical miles) is:

$$r_{\max} = -26.73 \times \ln(1013.25 - P_c) + 142.41 \quad (2)$$

where P_c (hectopascals (hPa)) is the estimated central pressure of TC.

Yadav and Das (2024) introduced an empirical formula of $r_{\max}$ from the analysis of relevant variables and their impact on the RMW over the NIO, and existing studies.

The equation for determining $r_{\max}$ (nautical miles) is:

$$r_{\max} = -36640.61 \times e^{(0.00029\sqrt{P_d}+0.000029\phi)} + 36732.39 \quad (3)$$

Table 3. *Numerical result of Mandous cyclone.*

Date/time	IMD r_{max} (nautical miles)	Our method r_{max} (nautical miles)	Yadav and Das r_{max} (nautical miles)	Willoughby *et al.* r_{max} (nautical miles)	Tan and Fang r_{max} (nautical miles)	ER^{a}_{Our} (%)	ER^{b}_{YD} (%)	ER^{c}_{W} (%)	ER^{d}_{TF} (%)
07/00	64	58.59	58.86	30.36	71.39	8.45	8.03	52.56	11.54
07/06	64	54.91	58.76	31.41	69.58	14.20	8.19	50.93	8.71
07/12	64	53.64	55.95	31.53	69.58	16.18	12.58	50.73	8.71
07/18	34	36.13	53.65	29.203	67.88	6.26	51.91	14.12	76.82
08/00	34	35.58	51.39	28.97	64.78	4.64	42.32	14.79	90.52
08/06	34	29.74	47.41	27.95	60.71	12.52	39.44	17.79	78.55
08/12	22	25.84	43.67	30.15	58.309	17.45	43.95	37.045	165.04
08/18	22	23.10	29.63	31.33	58.309	5.0	34.68	34.68	165.04
09/00	22	23.96	43.25	31.509	58.309	8.90	46.59	43.22	165.04
09/06	34	30.78	42.82	28.76	60.71	9.47	25.94	15.41	78.55
09/12	34	32.13	45.39	29.32	62.002	5.5	33.50	13.76	82.35
09/18	34	36.87	46.59	30.05	64.781	8.44	37.033	11.16	90.53
10/00	64	52.87	49.93	32.95	69.58	17.39	21.98	48.51	8.71
Mean	40.46	38.01	48.26	30.26	64.30	10.33	31.24	31.13	79.23

[a] Error percentage of our method with respect to IMD.

[b] Error percentage of Yadav and Das method with respect to IMD.

[c] Error percentage of Willoughby *et al.* method with respect to IMD.

[d] Error percentage of Tan and Fang method with respect to IMD.

where P_d is the pressure drop (hPa) at the center and ϕ is the latitude (degree) of the center.

This method provides a reliable means of calculating the RMW based on the given TC characteristics. The relationship established in this study allows for accurate determination of r_{max} as long as the value of P_d is less than or equal to 12 hPa.

By elucidating the strengths and limitations of each methodology and establishing the relationship between specific TC characteristics and RMW, this study advances our understanding of TC dynamics in the NIO. These findings hold the potential to enhance the accuracy of future TC forecasts and preparedness measures, thus bolstering our ability to mitigate the potentially devastating impacts of these natural disasters on coastal regions and communities.

2.2 *Method*

The primary aim of this investigation was to develop an approach for the computation of the RMW (r_{max}) through the application of machine learning techniques, alongside the evaluation of the outcomes obtained from the three methodologies in the literature.

In our model, the input is taken as the results of the three formulas that exist in the literature, namely those by Willoughby *et al.* (2006), Tan and Fang (2018), and Yadav and Das (2024). The target variable for the model is the RMW data provided by the IMD.

Here is the whole process of our method (flow chart of the proposed method is shown in figure 1):

Data Preprocessing:

Standardization (Ioffe and Szegedy 2015) of the experimental data is performed to ensure that each feature follows a standard normal distribution. This is crucial for improving the convergence speed and performance of the models.

K-fold cross-validation:

K-fold cross-validation is a robust technique used to evaluate machine learning models by partitioning the dataset into k equal-sized folds, training the model on $k-1$ folds, and validating it on the remaining fold, repeating this process k times. This method ensures each data point is used for training and validation, providing a comprehensive performance estimate and reducing the risk of overfitting. In this model, we use the value of k equal to 5 (Pohjankukka *et al.* 2017; Nti *et al.* 2021).

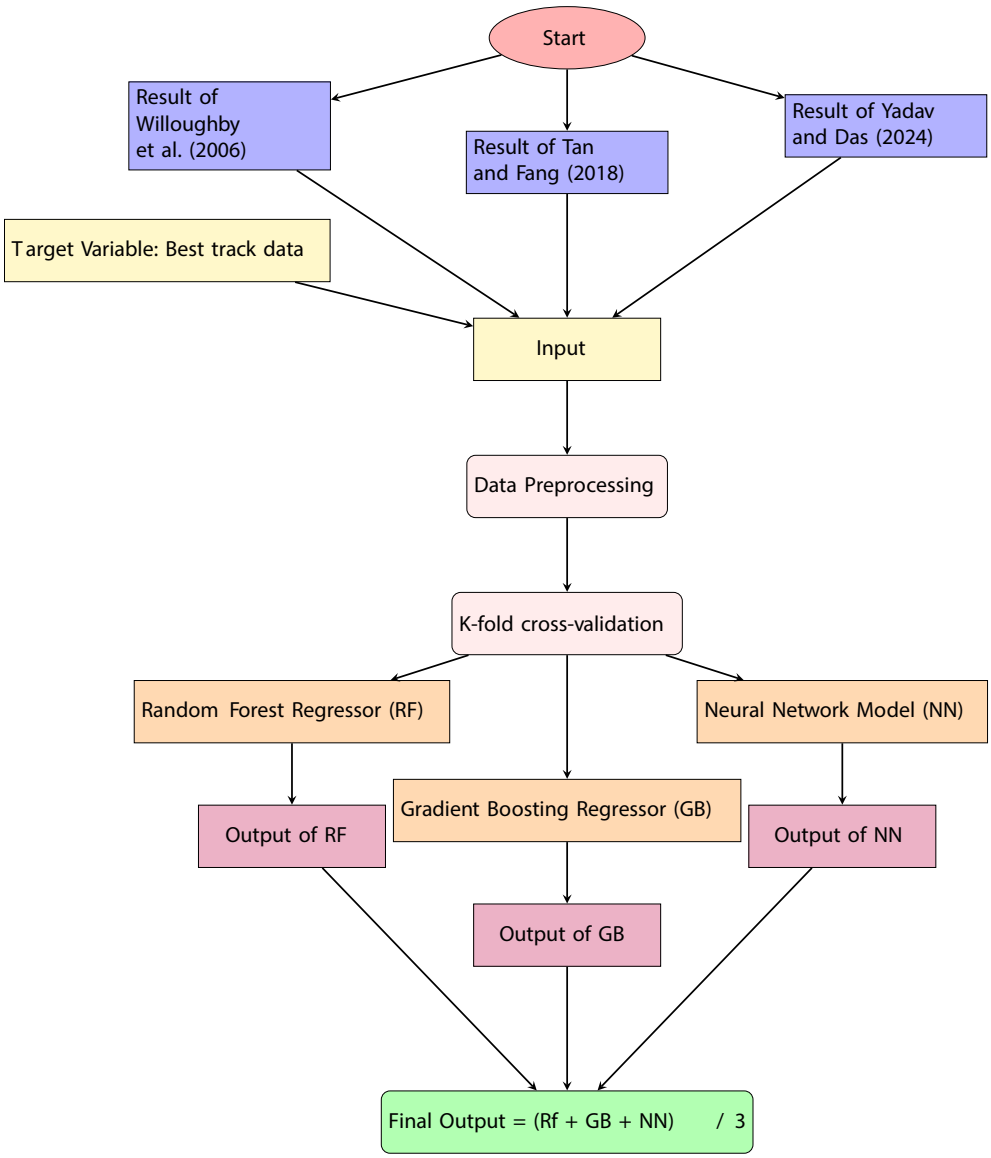

Figure 1. Flow chart of the proposed method for estimating the radius of maximum wind of the tropical cyclone.

For example, if $k = 5$, the dataset is divided into five folds. The model is trained on four folds and validated on the remaining fold. This process is repeated five times, with each fold serving as the validation set once.

- Iteration 1: Train on folds 2, 3, 4, 5; Validate on fold 1.
- Iteration 2: Train on folds 1, 3, 4, 5; Validate on fold 2.
- Iteration 3: Train on folds 1, 2, 4, 5; Validate on fold 3.
- Iteration 4: Train on folds 1, 2, 3, 5; Validate on fold 4.
- Iteration 5: Train on folds 1, 2, 3, 4; Validate on fold 5.

Model construction:

Here is a detailed explanation of our model's architecture, component by component:

(a) Random Forest Regressor (RF): This ensemble learning technique constructs multiple decision trees during training and outputs the average prediction of the individual trees. Random Forest (Breiman 2001) helps to reduce overfitting and variance in the model by averaging the results from different decision trees.

(b) Gradient Boosting Regressor (GB): Gradient Boosting (Friedman 2001) is an ensemble technique that builds a strong model by combining multiple weak models. It

sequentially adds predictors to an ensemble, and each one corrects its predecessor's errors. This method focuses on reducing bias and improving overall predictive performance.

(c) Neural Network Model (NN): The neural network is a deep learning model inspired by the structure of the human brain. It consists of interconnected layers of nodes that process and transform input data. In this model, a deep neural network is constructed using the Keras API (Chollet *et al.* 2015), consisting of multiple hidden layers with rectified linear unit (ReLU) activation functions (Agarap 2018). Dropout layers are included for regularization to prevent overfitting.
Here is a detailed explanation of the neural network's architecture (figure 2), layer by layer:

(i) **Input layer:**

- The input layer has three nodes corresponding to the three features (experimental results: the results of the three methods we mentioned above) being fed into the network.

(ii) **Dense Layer 1 (fully connected layer):**

- This layer consists of 512 neurons, each connected to all the nodes from the input layer. The ReLU activation function is applied to introduce non-linearity.
- Batch normalization is used to standardize the inputs to the next layer, which helps stabilize and accelerate the learning process.
- Dropout with a rate of 0.5 is implemented to prevent overfitting by randomly dropping half of the connections during each training step.

(iii) **Dense Layer 2:**

- The second dense layer comprises 256 neurons using the ReLU activation function and batch normalization.
- Dropout with a rate of 0.4 is applied.

(iv) **Dense Layer 3:**

- This layer consists of 128 neurons with ReLU activation and batch normalization.
- Dropout with a rate of 0.3 is applied.

(v) **Dense Layer 4:**

- The fourth dense layer has 64 neurons with ReLU activation and batch normalization.
- Dropout with a rate of 0.2 is applied.

(vi) **Dense Layer 5:**

- This layer contains 32 neurons with ReLU activation and batch normalization.
- Dropout with a rate of 0.2 is applied.

(vii) **Dense Layer 6:**

- The sixth layer has 16 neurons with ReLU activation and batch normalization.
- Dropout with a rate of 0.1 is applied.

(viii) **Dense Layer 7:**

- This layer consists of 8 neurons with ReLU activation and batch normalization.

(ii) **Output:**

- The output layer has 1 neuron, representing the predicted value.

The neural network model is trained to minimize the mean squared error (MSE) loss function using the Adam optimizer (Kingma and Ba 2014). By configuring multiple hidden layers with different activation functions and applying batch normalization and dropout, the network can learn complex patterns in the data and generalize well to unseen examples, thereby improving the overall predictive performance.

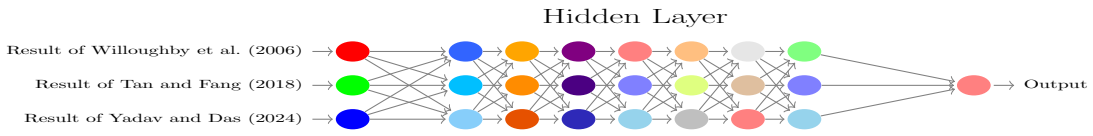

Figure 2. Architecture of proposed neural network for estimating the radius of maximum wind.

(d) Training and evaluation: The models are trained using the provided experimental data (the results of the three methods mentioned above), and the performance is evaluated based on the MSE between the predicted and actual experimental results. The training process involves optimizing the model parameters through the backpropagation algorithm, minimizing the loss function, and updating the model weights iteratively.

(e) Ensemble prediction: The final ensemble prediction is generated by combining the predictions from the Random Forest, Gradient Boosting, and Neural Network models. This ensemble method leverages the diverse predictions from different models to improve the overall predictive accuracy.

Combining these methodologies aims to enhance the predictive accuracy of experimental results by leveraging the strengths of ensemble learning and deep neural networks alongside traditional machine learning algorithms.

To check the accuracy of the designed model, we performed three statistical tests: error percentage, root square mean error, and R-squared.

Error percentage: Error percentage, also known as error rate or relative error, measures the relative difference between predicted and actual values. It quantifies how far off the model's predictions are from the ground truth. The error percentage can be calculated as follows:

$$\text{(Error percentage} = \left(\frac{|\text{ Predicted value} - \text{Actual value}|}{\text{Actual value}}\right) \times 100$$

A lower error percentage indicates a more accurate model, as it signifies that the model's predictions are closer to the actual values.

Root Mean Square Error (RMSE): RMSE is a widely used metric to assess the accuracy of regression models. It measures the average magnitude of the errors between predicted and actual values. The RMSE is calculated as follows:

$$\text{RMSE} = \sqrt{\frac{1}{n} \times \sum (\text{Predicted value} - \text{Actual value})^2}.$$

A lower RMSE indicates that the model's predictions are, on average, closer to the actual values. It represents the standard deviation of the model's errors.

In practice, the error percentage and RMSE are used to evaluate the accuracy and performance of machine learning models. While error percentage provides a relative measure of accuracy, RMSE provides an absolute measure of the model's predictive quality. Researchers and practitioners consider both metrics to assess their models' quality and make informed decisions about their performance.

R-squared (R^2): R^2, also known as the coefficient of determination, is a statistical measure that indicates the proportion of the variance in the dependent variable that is predictable from the independent variables in a regression model. It provides insight into the model's goodness-of-fit (Chicco *et al.* 2021). The value of R^2 ranges from 0 to 1, where:

- $R^2 = 1$ indicates that the model explains all the variability of the response data around its mean.
- $R^2 = 0$ indicates that the model explains none of the variability of the response data around its mean.
- Negative R^2 values can occur when the model is a poor-fit and performs worse than a horizontal line representing the mean of the dependent variable.

3. Result

We present a comprehensive analysis of the performance of various methodologies for estimating the RMW in the context of three specific TCs: Mandous, Sitrang, and Mocha. Our study evaluates these methods by comparing their error percentages and RMSE based on the data obtained from the IMD.

3.1 *Case study 1: Mandous cyclone*

The Mandous cyclone (table 2), a disturbing meteorological phenomenon known for its intense winds and significant impact on coastal regions, served as a primary case study for our analysis (Division 2022a). It followed a unique track illustrated in figure 3. Employing our proposed method, we achieved an error percentage of 10.33% (refer to table 3) compared to the RMW data obtained from the IMD. In contrast, the error percentages for the traditional methods, including Yadav and Das, Willoughby, and Tan and Fang,

were recorded at 31.24%, 31.13%, and 79.23%, respectively. Similarly, the RMSE values associated with our method were notably lower at 5.61 (refer to table 7) compared to the respective RMSE values of 14.35, 18.82, and 26.82 derived from the traditional methods.

The graphical representation in figure 4 illustrates the comparison between the IMD and all other model's results. The relative similarity or decrease in error rates between the two datasets is apparent, indicating our model's performance compared to other methods concerning the IMD data.

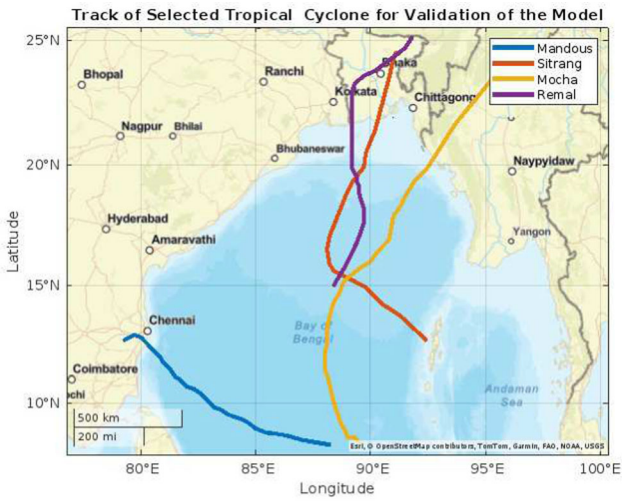

Figure 3. Track of the selected tropical cyclone for validation of the model.

The R^2 value (table 9) of 0.88 suggests that the proposed model is highly effective and explains most of the variance in the data. However, the R^2 value of 0.27 indicates a weak model that only explains a small portion of the variance, with room for significant improvement. The negative R^2 values of -0.32 and -1.68 are concerning, as they indicate that these models perform worse than a simple mean prediction.

3.2 *Case study 2: Sitrang cyclone*

The Sitrang cyclone (table 2), characterized by its complex atmospheric dynamics and profound influence on regional climate patterns, presented an equally crucial case study in our investigation (Division 2022b). The track of the TC is illustrated in figure 3. Our method demonstrated an error percentage of 10.83% (refer to table 4) when compared with the RMW data sourced from the IMD for the Sitrang cyclone. Conversely, the error percentages associated with the Yadav and Das, Willoughby, and Tan and Fang methods were determined to be 19.62%, 18.42%, and 78.34%, respectively. Correspondingly, the RMSE values for our method were computed at 7.25 (refer to table 7), highlighting its superior precision compared to the RMSE values of 9.52, 14.01, and 29.682 associated with the traditional methodologies.

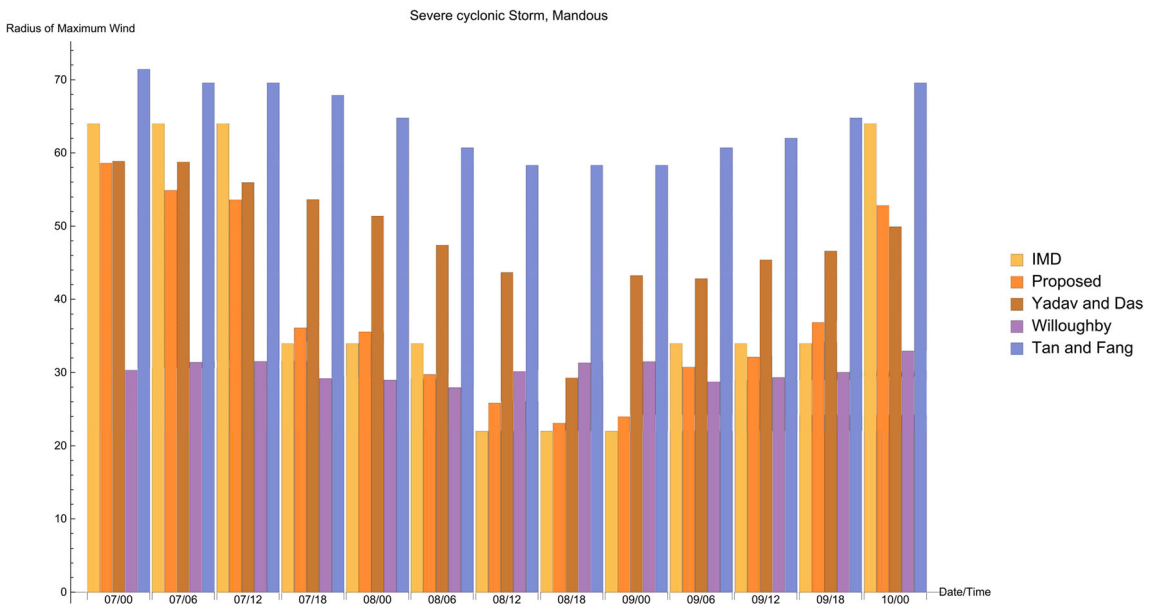

Figure 4. Graphical representation of Mandous cyclone value of RMW by our method, Yadav and Das, Willoughby *et al.*, Tan and Fang, and IMD.

Table 4. *Numerical result of Sitrang cyclone.*

Date/ time	IMD r_{max} (nautical miles)	Our Method r_{max} (nautical miles)	Yadav and Das r_{max} (nautical miles)	Willoughby *et al.* r_{max} (nautical miles)	Tan and Fang r_{max} (nautical miles)	ER^{a}_{Our} (%)	ER^{b}_{YD} (%)	ER^{c}_{W} (%)	ER^{d}_{TF} (%)
23/00	64	50.89	51.74	36.48	75.43	20.48	19.16	43	17.85
23/06	64	49.63	48.83	36.87	73.33	22.45	23.70	42.39	14.57
23/12	34	36.23	46.10	38.55	71.39	6.55	35.61	13.38	109.97
23/18	34	35.76	45.25	36.92	69.58	5.17	33.10	8.58	104.64
24/00	34	32.94	40.74	31.66	66.28	3.11	19.83	6.88	94.94
24/06	34	31.52	37.63	30.87	66.28	7.29	10.68	9.20	94.94
24/12	34	30.67	36.35	29.55	66.28	9.79	6.92	13.08	94.94
24/18	34	29.98	36.71	30.29	66.28	11.82	7.98	10.91	94.94
Mean	41.50	37.20	42.91	33.89	69.35	10.83	19.62	18.42	78.34

[a] Error percentage of our method with respect to IMD.
[b] Error percentage of Yadav and Das method with respect to IMD.
[c] Error percentage of Willoughby *et al.* method with respect to IMD.
[d] Error percentage of Tan and Fang method with respect to IMD.

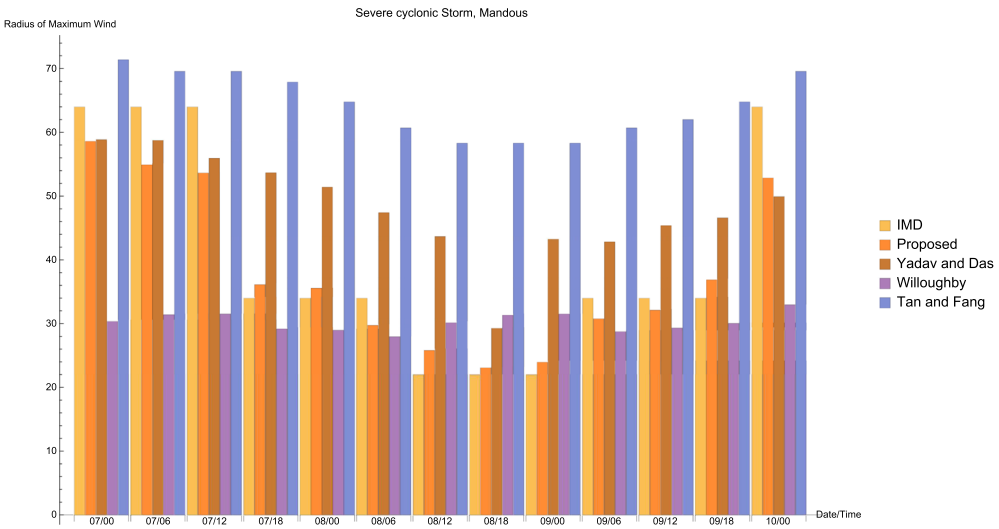

Figure 5. Graphical representation of Sitrang cyclone value of RMW by our method, Yadav and Das, Willoughby *et al.*, Tan and Fang, and IMD.

Figure 5 compares the IMD results to other models' outcomes. The relative similarity or decrease in error rates between the two datasets highlights our model's performance compared to other methods when considering IMD data.

The R^2 value (table 9) of 0.66 suggests that the proposed model is fairly effective, explaining a substantial portion of the variance in the data. The R^2 value of 0.46 indicates a moderate model that captures less than half of the variance, implying the need for improvement. The negative R^2 values of -0.16 and -4.22 are concerning, indicating that these models perform worse than a simple mean prediction. These negative values suggest that the models are not capturing the important relationships in the data and may require significant modifications or complete reevaluation.

3.3 *Case study 3: Mocha cyclone*

Mocha cyclone (table 2), the initial cyclonic storm of 2023, made landfall on Myanmar's coast (track of Mocha is shown in figure 3) with the maximum

Table 5. *Numerical result of Mocha cyclone.*

Date/time	IMD r_{max} (nautical miles)	Our Method r_{max} (nautical miles)	Yadav and Das r_{max} (nautical miles)	Willoughby *et al.* r_{max} (nautical miles)	Tan and Fang r_{max} (nautical miles)	ER^{a}_{Our} (%)	ER^{b}_{YD} (%)	ER^{c}_{W} (%)	ER^{d}_{TF} (%)
10/00	90	69.05	61.48	49.55	69.07	23.27	31.68	44.94	23.25
10/06	90	67.83	60.84	50.06	71.01	24.63	32.40	44.37	21.10
10/12	90	62.98	57.37	50.82	72.82	30.02	36.25	43.53	19.08
10/18	90	61.57	56.52	51.51	72.82	31.58	37.20	42.76	19.08
11/00	40	51.46	53.83	51.52	74.52	28.65	34.57	28.80	86.30
11/06	40	43.38	45.82	51.26	76.12	08.45	14.55	28.15	90.30
11/12	26	39.87	41.97	51.50	79.05	53.34	61.42	98.07	204.03
11/18	26	36.09	41.44	51.94	81.69	38.80	59.38	99.76	214.19
Mean	61.50	54.02	52.04	51.02	74.63	29.84	38.43	53.79	84.66

[a] Error percentage of our method with respect to IMD.

[b] Error percentage of Yadav and Das method with respect to IMD.

[c] Error percentage of Willoughby *et al.* method with respect to IMD.

[d] Error percentage of Tan and Fang method with respect to IMD

sustained wind (MSW) of 100 knots on May 14th, 2023. Analyzing the climatological data from 1965 to 2022 reveals that out of approximately 200 cyclonic storms in the BoB, 61 crossed the coasts of Bangladesh and Myanmar during this period. Comparing recent events, the last Extremely Severe Cyclonic Storm (ESCS) to impact Myanmar before Mocha was 'ESCS GIRI' in 2010. Historical records from the India Meteorological Department show that the most intense storm in the BoB was the 1999 Odisha Super Cyclone, reaching a peak MSW of 140 knots, followed by several others with peak MSWs ranging from 125 to 130 knots. Mocha cyclone was not the most intense cyclonic storm in the Bay of Bengal based on available historical data (Division 2023).

Our proposed methodology yielded an error percentage of 29.84% (refer to table 5), contrasted with the RMW data acquired from the IMD. In stark divergence, traditional approaches, namely those of Yadav and Das, Willoughby, and Tan and Fang, exhibited error percentages of 38.43%, 53.79%, and 84.66%, respectively. Likewise, the RMSE values associated with our approach were markedly lower at 19.05 (refer to table 7) compared to the corresponding RMSE values of 23.89, 31.28, and 35.00 derived from conventional methodologies.

The graph in figure 6 compares the results from the India Meteorological Department (IMD) with those from other models. Our model performs similarly or with less error than the others when considering the IMD data.

The R^2 value (table 9) of 0.56 suggests that the proposed model is moderately effective, explaining over half of the variance in the data but still leaving a substantial portion unexplained. The R^2 value of 0.31 indicates a weak model, explaining less than one-third of the variance and pointing to the need for significant improvement. The negative R values of −0.61 and −0.46 are concerning, as they indicate that these models perform worse than simply using the mean of the dependent variable, suggesting fundamental issues with the model's ability to capture the data's underlying patterns.

3.4 *Case study 4: Remal cyclone*

The Remal cyclone, characterized by its complex atmospheric dynamics and profound influence on regional climate patterns, presents a crucial case study in our investigation (table 2). The track of the TC is illustrated in figure 3.

Our method demonstrated an error percentage of 20.58% compared to the RMW data from the IMD for the Remal cyclone (table 6). In contrast, the error percentages associated with the Yadav and Das, Willoughby, and Tan and Fang methods were 28.02%, 35.73%, and 36.68%, respectively.

RMSE values for our method were computed at 20.75, underscoring its superior precision compared

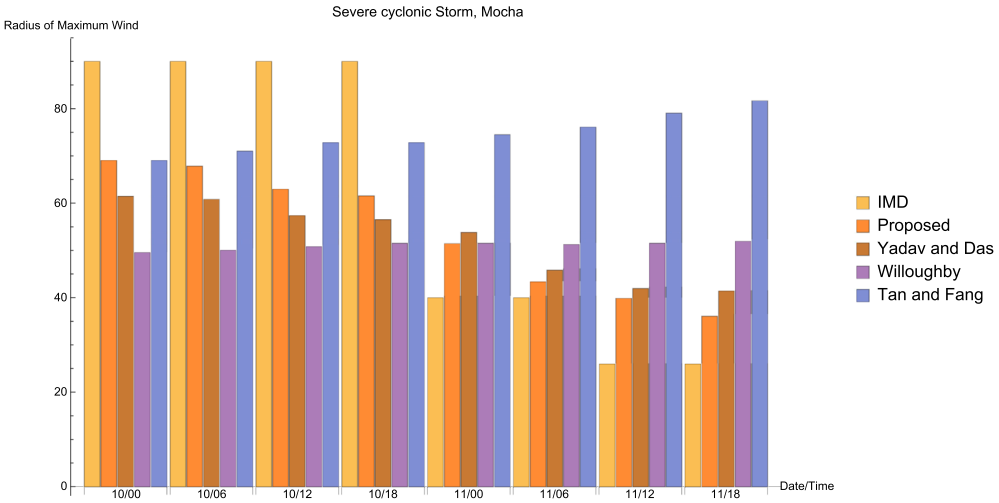

Figure 6. Graphical representation of Mocha cyclone value of RMW by our method, Yadav and Das, Willoughby *et al.*, Tan and Fang, and IMD.

Table 6. *Numerical result of Remal cyclone.*

Date/time	IMD r_{max} (nautical miles)	Our method r_{max} (nautical miles)	Yadav and Das r_{max} (nautical miles)	Willoughby *et al.* r_{max} (nautical miles)	Tan and Fang r_{max} (nautical miles)	ER^{a}_{Our} (%)	ER^{b}_{YD} (%)	ER^{c}_{W} (%)	ER^{d}_{TF} (%)
25/00	100	61.92	51.80	40.00	62.00	38.08	48.20	60.00	38.00
25/06	92	57.62	48.65	40.41	59.48	37.37	47.12	56.08	35.35
25/12	55	50.14	45.74	37.87	58.30	08.84	16.84	31.15	06.00
25/18	55	47.28	41.18	35.43	56.10	14.04	25.13	35.58	02.00
26/00	33	35.82	34.20	30.60	52.17	08.55	03.64	07.27	58.09
27/06	35	36.27	32.05	40.66	53.10	03.63	08.43	16.17	51.71
27/12	74	47.89	34.78	41.07	55.06	35.28	53.00	44.50	25.59
27/18	33	39.23	40.21	44.57	58.30	18.88	21.85	35.06	76.67
Mean	59.62	47.02	41.07	38.82	56.81	20.58	28.02	35.73	36.68

[a] Error percentage of our method with respect to IMD.
[b] Error percentage of Yadav and Das method with respect to IMD.
[c] Error percentage of Willoughby *et al.* method with respect to IMD.
[d] Error percentage of Tan and Fang method with respect to IMD.

to the RMSE values of 27.56, 32.00, and 22.93 associated with the traditional methodologies (table 7).

Figure 7 compares the IMD results to the outcomes of other models. The relative similarity or decrease in error rates between the datasets highlights our model's improved performance compared to other methods when evaluated against IMD data.

The R^2 values (table 9) provide insight into the performance of the models. The value of 0.30 indicates a weak fit, explaining only a small portion of the variance in the data. The value of 0.15 suggests an even weaker fit, with most of the variability unexplained. The negative R^2 values of -0.22 and -0.65 are particularly concerning, indicating that these models perform worse than simply using the mean of the dependent variable.

These results bear significant scientific implications. The consistent outperformance of our machine learning technique across all the case studies: Mandous, Sitrang, Mocha, and Remal cyclones underscores its robustness in estimating RMW in real-world TCs. Compared to traditional methods, the remarkable reduction in error percentages and RMSE values substantiates the efficacy of data-driven approaches in meteorological research.

Moreover, these findings emphasize the urgent need for modernizing the field of TC analysis, harnessing the potential of advanced computational techniques to enhance our understanding and predictive capabilities. Our results underscore the promise of machine learning in revolutionizing the accuracy of RMW estimation, with far-reaching implications for TC forecasting, disaster preparedness, and climate research. This study contributes to the evolving landscape of meteorological research, highlighting the potential for innovative methodologies to advance our comprehension of these dynamic and complex weather phenomena.

Upon the analysis, we observe that excluding Willoughby's formula for $R_{\max}$ from the ensemble increases the error percentage and the root square mean error. This suggests that despite the discrepancy in $R_{\max}$ value, Willoughby's formula significantly improves the accuracy of the overall model. So, we have included Willoughby's formula in the model to get a more accurate result.

The study of the RMW holds strong implications for research and operational purposes in tropical cyclone forecasting and disaster management. Accurate estimation of the RMW is integral to various applications. In the interest of research, it provides invaluable insights into the dynamics of tropical cyclones, allowing for a deeper understanding of their structure, intensity, and behaviour. By uncovering the complex relationships between the RMW and various meteorological parameters, researchers can refine existing models and develop new ones that better capture the complexity of these phenomena.

From an operational perspective, the RMW is a critical parameter for forecasting agencies and disaster response teams. It directly impacts the intensity and extent of wind and storm surge hazards associated with tropical cyclones, making it a

Table 7. *Root square mean error of all methods concerning IMD.*

Name of TC	$\text{RSMC}^{a}_{\text{Our}}$	$\text{RSMC}^{b}_{\text{YD}}$	$\text{RSMC}^{c}_{\text{W}}$	$\text{RSMC}^{d}_{\text{TF}}$
Mandous	5.61	14.35	18.82	26.82
Sitrang	7.25	9.52	14.01	29.68
Mocha	19.05	23.89	31.28	35.00
Remal	20.75	27.56	32.00	22.93
Mean	13.16	18.83	24.02	28.60

[a] RSME of our method with respect to IMD.
[b] RSME of Yadav and Das method with respect to IMD.
[c] RSME of Willoughby *et al.* method with respect to IMD.
[d] RSME of Tan and Fang method with respect to IMD.

Table 8. *Error percentage of all methods concerning IMD.*

Name of TC	$\text{Error}^{a}_{\text{Our}}$	$\text{Error}^{b}_{\text{YD}}$	$\text{Error}^{c}_{\text{W}}$	$\text{Error}^{d}_{\text{TF}}$
Mandous	10.33	31.24	31.13	79.23
Sitrang	10.83	19.62	18.42	78.34
Mocha	29.84	38.43	53.79	84.66
Remal	20.58	28.02	35.73	36.68
Mean	17.89	29.32	34.76	69.72

[a] Error percentage of our method with respect to IMD.
[b] Error percentage of Yadav and Das method to IMD.
[c] Error percentage of Willoughby *et al.* method to IMD.
[d] Error percentage of Tan and Fang method to IMD.

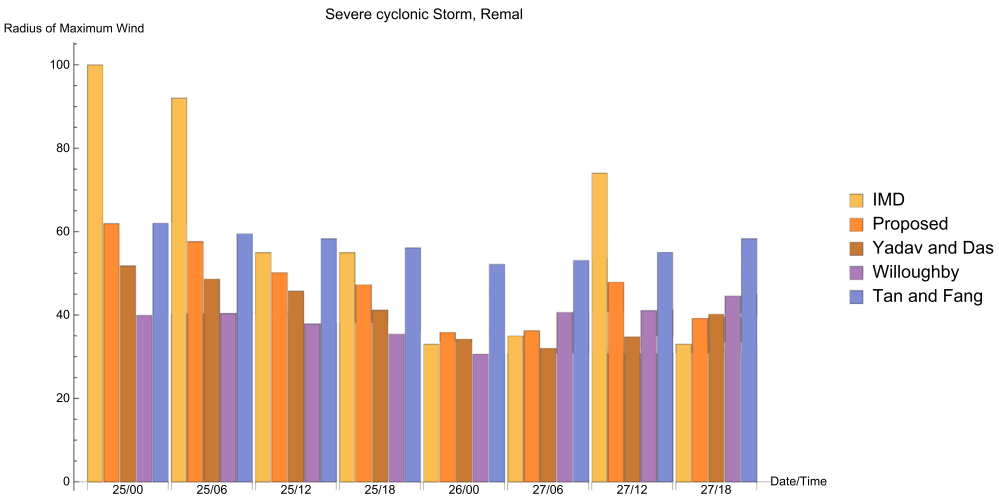

Figure 7. Graphical Representation of Remal Cyclone value of RMW by our method, Yadav and Das, Willoughby *et al.*, Tan and Fang, and IMD.

Table 9. *Details of R-squared of all cases.*

Name of TC	Our method w.r.t. best track	Yadav and Das w.r.t. best track	Willoughby *et al.* w.r.t best track	Tan and Fang w.r.t. best track
Mandous	0.88	0.27	− 0.32	− 1.68
Sitrang	0.66	0.46	− 0.16	− 4.22
Mocha	0.56	0.31	− 0.61	− 0.46
Remal	0.30	− 0.22	− 0.65	0.15

key input for operational models and forecasts. Accurate RMW estimates enable improved predictions of storm tracks, intensities, and potential impacts, enhancing the ability to issue timely warnings and advisories. This is particularly important for vulnerable coastal regions, where even minor changes in the RMW can have significant implications for preparedness and mitigation measures.

4. Conclusion

Our comprehensive analysis underscores the efficacy of the machine learning approach in accurately estimating the RMW within TCs, surpassing the limitations of traditional methodologies. The complex relationship between various meteorological parameters and the RMW, as established through advanced computational techniques, elucidates the nuanced dynamics governing cyclonic winds' intensity and spatial extent. By leveraging a diverse dataset encompassing radar and satellite measurements, we have successfully developed a robust framework that captures the complexities of the RMW and demonstrates superior predictive capabilities compared to conventional methods.

The empirical validation of our proposed model against the results obtained from the three traditional methods, as elucidated by Willoughby *et al.* (2006), Tan and Fang (2018), and Yadav and Das (2024), further solidifies the credibility and accuracy (error percentage refer to table 8, RSME refer to table 7, and *R*-squared refer to table 9) of our approach. By incorporating machine learning techniques, we have harnessed the power of data-driven algorithms to decipher complex patterns and derive more precise estimations of the RMW, thereby enhancing our ability to forecast and prepare for the impact of TCs with greater reliability and confidence.

The successful demonstration of the superior performance of our method, supported by the comprehensive analysis of the empirical data, highlights the potential of machine learning as a transformative tool in advancing the field of TC research. The implications of our findings extend beyond the realm of meteorology, providing valuable insights into the broader interplay between climate dynamics and oceanic processes. This study thus contributes to the ongoing efforts to bolster our understanding of natural disasters and foster more effective mitigation and adaptation strategies in the face of escalating climate challenges.

Acknowledgements

The best track data and metrics for TC characteristics are freely available; thanks to the India Meteorological Department for providing the information on their website. The authors thank the editor and reviewers for their valuable input.

Author statement

Monu Yadav: Research, data curation, formal analysis, investigation, and first draft preparation. Laxminarayan Das: Supervision, mentoring, reviewing, and editing. Shashi Kant: Reviewing and editing.

References

Agarap A F 2018 Deep learning using rectified linear units (RELU); *arXiv preprint* arXiv:1803.08375.

Balaguru K, Foltz G R, Leung L R and Emanuel K A 2016 Global warming-induced upper-ocean freshening and the intensification of super typhoons; *Nat. Commun.* **7(1)** 13670.

Balaguru K, Foltz G R, Leung L R and Harris L M 2017 Super typhoon Haiyan-induced cold wake observed by Argo floats and simulated by a coupled general circulation model; *J. Geophys. Res. Oceans* **122(8)** 6549–6567.

Breiman L 2001 Random forests; *Mach. Learn.* **45** 5–32.

Chen S S, Price J F and Zhao W 2006 Time-latitude distribution of tropical cyclone-induced upper-ocean

responses observed by Argo floats; *J. Phys. Oceanogr.* **36(2)** 351–363.

Chicco D, Warrens M J and Jurman G 2021 The coefficient of determination R-squared is more informative than SMAPE, MAE, MAPE, MSE and RMSE in regression analysis evaluation; *PeerJ. Comput. Sci.* **7** e623.

Chollet F *et al.* 2015 *Keras*; GitHub, https://github.com/fchollet/keras.

Division C W 2022a Severe cyclonic storm, "Mandous" (06th–10th December, 2022): A report; *India Meteorological Department.*

Division C W 2022b Severe cyclonic storm, "Sitrang" (22th–25th October, 2022): A report; *India Meteorological Department.*

Division C W 2023 Extremely severe cyclonic storm "Mocha" over the BoB (9th–15th May, 2023): A report; *India Meteorological Department.*

Emanuel K 2003 Tropical cyclones; *Ann. Rev. Earth Planet. Sci.* **31(1)** 75–104.

Friedman J H 2001 Greedy function approximation: A gradient boosting machine; *Ann. Stat.* **29(5)** 1189–1232.

Gross J M, DeMaria M, Knaff J A and Sampson C R 2004 A new method for determining tropical cyclone wind forecast probabilities; *Preprints, 26th Conf. on Hurricanes and Tropical Meteorology, Miami, FL, Amer. Meteor. Soc. A* **11**.

Holland G J 1980 An analytic model of the wind and pressure profiles in hurricanes; *Mon. Weather Rev.* **108(8)** 1212–1218.

IMD 2021 Standard operational procedure for cyclone warning in India; *India Meteorological Department.*

Ioffe S and Szegedy C 2015 Batch normalization: Accelerating deep network training by reducing internal covariate shift; *International Conference on Machine Learning,* pp. 448–456.

Kingma D P and Ba J 2014 Adam: A method for stochastic optimization; *arXiv preprint* arXiv:1412.6980.

Kossin J P, Emanuel K A and Vecchi G A 2014 The poleward migration of the location of tropical cyclone maximum intensity; *Nature* **509(7500)** 349–352.

Kossin J P, Olander T L and Knapp K R 2016 Trend analysis with a new global record of tropical cyclone intensity; *J. Clim.* **29(16)** 5817–5826.

Lu X, Kin Wong W, Yu H and Yang X 2022 Tropical cyclone size identification over the western north pacific using support vector machine and general regression neural network; *J. Meteorol. Soc. Jpn. Ser. II* **100(6)** 927–941, https://doi.org/10.2151/jmsj.2022-048.

Nti I K, Nyarko-Boateng O and Aning J *et al.* 2021 Performance of machine learning algorithms with different k values in k-fold cross-validation; *Int. J. Inf. Technol. Comput. Sci.* **13(6)** 61–71.

Pohjankukka J, Pahikkala T, Nevalainen P and Heikkonen J 2017 Estimating the prediction performance of spatial models via spatial k-fold cross validation; *Int. J. Geogr. Inf. Sci.* **31(10)** 2001–2019.

Quiring S, Schumacher A, Labosier C and Zhu L 2011 Variations in mean annual tropical cyclone size in the atlantic; *J. Geophys. Res. Atmos.* **116(D9)**, https://doi.org/10.1029/2010JD015011.

Rathore S, Goyal R, Jangir B, Ummenhofer C C, Feng M and Mishra M 2022 Interactions between a marine heatwave and tropical cyclone Amphan in the Bay of Bengal in 2020; *Front. Clim.* **4** 861477.

Sharmila S, Joseph S and Sahai A K 2019 Improving the prediction skill of Indian summer monsoon rainfall using a novel multimodel ensemble technique; *Clim. Dyn.* **52(5–6)** 3133–3153.

Tan C and Fang W 2018 Mapping the wind hazard of global tropical cyclones with parametric wind field models by considering the effects of local factors; *Int. J. Disaster Risk Science.* **9(7).**

Wang C and Li X 2023 A deep learning model for estimating tropical cyclone wind radius from geostationary satellite infrared imagery; *Mon. Weather Rev.* **151(2)** 403–417, https://doi.org/10.1175/MWR-D-22-0166.1.

Willoughby H E, Darling R W R and Rahn M E 2006 Parametric representation of the primary hurricane vortex. Part II: A new family of sectionally continuous profiles; *Mon. Weather Rev.* **134(4)** 1102–1120, https://doi.org/10.1175/MWR3106.1.

Xu J, Wang X, Wang H, Zhao C, Wang H and Zhu J 2023 Tropical cyclone size estimation based on deep learning using infrared and microwave satellite data; *Front. Mar. Sci.* **9** 1077901.

Yadav M and Das L 2024 Formulation and evaluation of the radius of maximum wind of the tropical cyclones over the North Indian Ocean basin; *Theor. Appl. Climatol.,* https://doi.org/10.1007/s00704-024-04895-w.

Springer Nature or its licensor (e.g. a society or other partner) holds exclusive rights to this article under a publishing agreement with the author(s) or other rightsholder(s); author self-archiving of the accepted manuscript version of this article is solely governed by the terms of such publishing agreement and applicable law.

Corresponding editor: P A Francis

ResearchGate

See discussions, stats, and author profiles for this publication at: https://www.researchgate.net/publication/386086813

Sustainable biodiesel from used cooking oil: a comparative life cycle, energy, and uncertainty analysis

Article *in* Environment Development and Sustainability · November 2024

DOI: 10.1007/s10668-024-05692-1

CITATIONS
0

READS
22

2 authors:

Kulvendra Patel
Delhi Technological University
12 PUBLICATIONS **55** CITATIONS

SEE PROFILE

S. K. Singh
Delhi Technological University
201 PUBLICATIONS **3,189** CITATIONS

SEE PROFILE

All content following this page was uploaded by Kulvendra Patel on 24 November 2024.

The user has requested enhancement of the downloaded file.

Environment, Development and Sustainability
https://doi.org/10.1007/s10668-024-05692-1

Sustainable biodiesel from used cooking oil: a comparative life cycle, energy, and uncertainty analysis

Kulvendra Patel[1] · **S. K. Singh**[1]

Received: 21 July 2024 / Accepted: 7 November 2024
© The Author(s), under exclusive licence to Springer Nature B.V. 2024

Abstract
This study focuses on analyzing the environmental impacts of biodiesel production from Used Cooking Oil (UCO) as a waste management strategy. Using a cradle-to-gate life cycle assessment approach, it compares UCO-derived biodiesel with the first-generation biofuel derived from palm oil. The research addresses the pressing need for sustainable energy alternatives that reduce environmental impacts while promoting waste utilization. The study analyzes multiple environmental impact categories, cumulative energy demand (CED), and includes uncertainty analysis to address variability in data and assumptions across the life cycle. Regression and scatter plot analyses are used to identify correlations between inventory inputs and environmental effects. The study shows that the total carbon and environmental footprint per kg of biodiesel produced from UCO was 0.22 kg CO_2 eq. and 0.11 mPt, compared to 9.87 kg CO_2 eq. and 1.34 mPt for palm oil biodiesel. Electricity, methanol, and steam-derived heat are the primary factors influencing this emission. The total CED for UCO biodiesel was 6.78 MJ, compared to that of palm oil at 18.5 MJ. The net energy ratio of UCO biodiesel is 5.49, outperforming palm oil biodiesel (2.01) and conventional diesel (0.83). The study also shows significant reduction in impacts when including avoided products into the system boundary. The uncertainty of the study is within 10%, which confirms the reliability and robustness of the impact results for UCO biodiesel. This study provides valuable insights for decision-makers in the biofuel industry, promoting waste-to-energy solutions to reduce environmental footprints and support the transition to greener energy systems.

Keywords Cumulative energy demand · Environmental impact assessment · Life cycle assessment · Net energy ratio · Sustainability analysis

1 Introduction

In light of escalating energy requirements, the depletion of fossil fuels and the adverse environmental consequences linked to their utilization in transportation underscores the imperative for the widespread introduction of alternative, environmentally sustainable

✉ Kulvendra Patel
kulvendrapatel_2k21phden501@dtu.ac.in

[1] Department of Environmental Engineering, Delhi Technological University, Delhi 110042, India

fuels (Aboelazayem et al., 2018; Tsoutsos et al., 2016). This urgency is further underscored by the persistent escalation in pollution and ozone depletion attributed to the consumption of non-renewable energy fuels. Over years of dependence on fossil fuel-based energy reserves, a continuous rise in global temperatures has ensued, contributing significantly to global warming through the substantial release of carbon dioxide (Zulqarnain et al., 2021). These issues emphasize the importance of transitioning towards cleaner and renewable energy sources (Abbasi et al., 2024; Garlapati et al., 2013; Patel & Singh, 2023a). Researchers propose several pivotal solutions to address these challenges. Firstly, they recommend the widespread adoption of renewable energy sources, including wind, solar, tidal, nuclear, and geothermal energy, to substantially reduce the emission of greenhouse gases (Al-Juboori et al., 2020; Vashist et al., 2024a). Another solution is emphasizing the importance of producing renewable fuels from waste materials as an innovative strategy to minimize pollution effectively. These combined measures offer a sustainable energy framework and contribute significantly to environmental preservation (IEA, 2024; Zulqarnain et al., 2021). Figure 1 shows the renewable fuel demand by various countries and sectors.

Biodiesel emerges as a promising alternative that aligns with the innovative strategy of producing renewable fuels from waste materials. In addressing the pressing need to minimize pollution, biodiesel stands out as a viable solution with the potential to replace conventional fossil fuels in various applications. As we explore biodiesel, its production, benefits, and impact on pollution mitigation will unfold as crucial components in the broader narrative of fostering a greener and more sustainable future. The use of biodiesel serves as a potent strategy to address the challenges associated with the depletion of fossil fuels and the overexploitation of traditional energy resources, a consequence of the rapid growth of the global population and industrial development (Goli & Sahu, 2018; Vashist & Singh, 2023). Biodiesel offers numerous benefits compared to conventional fossil fuels, including reduced toxicity, a high oxygen content (10–11%) leading to enhanced combustion efficiency, and inherent biodegradability (Tan et al., 2019). A challenge faced in the current biodiesel production is the comparatively higher production cost compared to conventional fossil fuels. This is primarily due to the expense associated with raw feedstock and the utilization of a homogeneous catalyst system predominantly used in the biodiesel industry. The homogeneous base-catalyzed reaction often results in a lower yield of free fatty acid, contributing to increased production costs (Singh & Verma, 2019). Lowering the production expenses of biodiesel is attainable through the utilization of more economical and readily accessible raw materials, such as used cooking oil (UCO), animal fats, palm fatty acid distillate, and Jatropha curcas oil (Mansir et al., 2018; Moreno-Peñaranda et al., 2015). Addressing the substantial capital outlay for materials, research suggests that choosing UCO as an alternative feedstock can decrease biodiesel costs. This is because UCO is more cost-effective and abundantly available compared to higher-priced alternatives like palm oil, soybean, and sunflower oil, which require additional purification expenses as pure refined vegetable oils (Gupta et al., 2016).

UCO is a waste product generated in the food industry, primarily from cooking processes in households, restaurants, and commercial kitchens. Recycling UCO for biodiesel production contributes to sustainability and waste reduction. Using UCO in biodiesel production aligns with principles of circular economy and resource efficiency (Bhonsle et al., 2022; Sanglard et al., 2023; Srikumar et al., 2024). By converting waste cooking oil into a valuable biofuel, there is a reduction in the reliance on virgin vegetable oils, which might otherwise be used for biodiesel and are associated with land use changes and potential environmental impacts. According to the FSSAI, India can convert 3–4 million metric tons of UCO into biodiesel (FSSAI, 2018). Consequently,

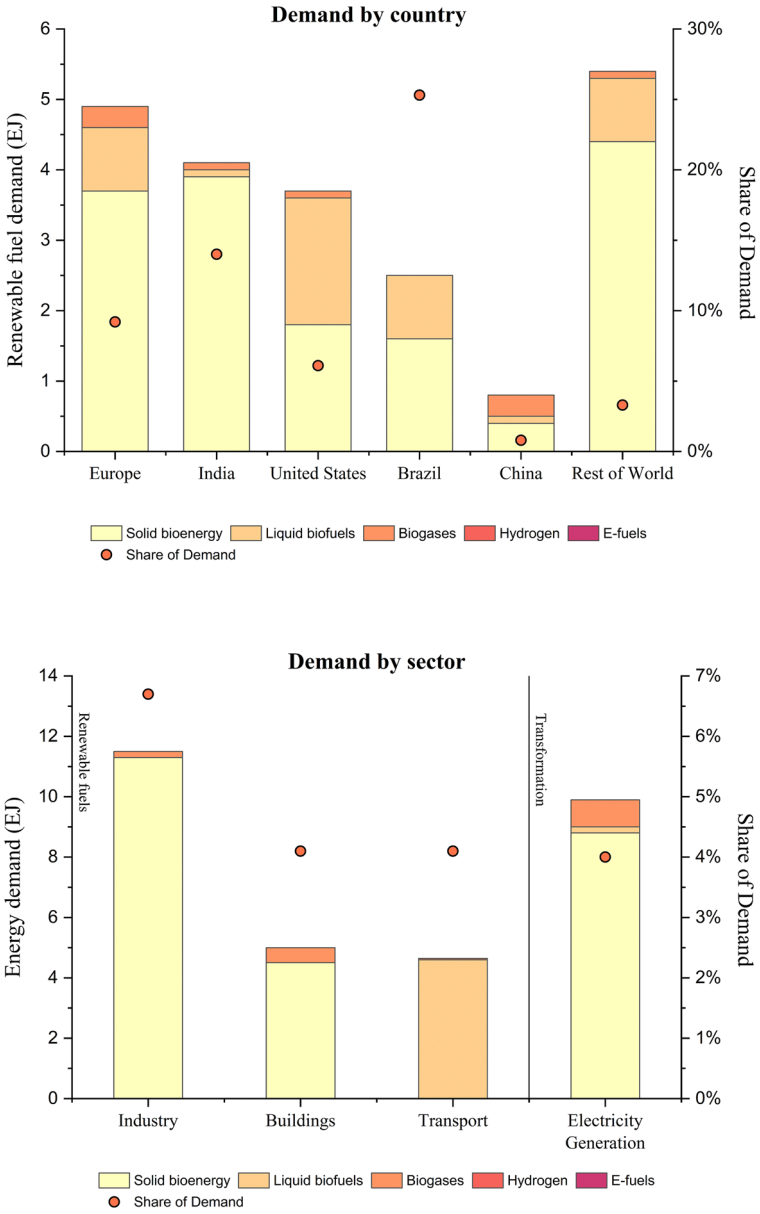

Fig. 1 Renewable fuel demand, main case, 2023 (IEA, 2024)

incorporating used cooking oil into the production of biodiesel not only redirects this waste from the food supply chain but also establishes a consistent and sustainable source of feedstock for biodiesel production. Even though biodiesel from UCO is considered a sustainable source, conducting a thorough life cycle assessment (LCA) remains crucial for a comprehensive understanding of its environmental implications and resource efficiency. The LCA process enables a detailed examination of the entire life cycle of

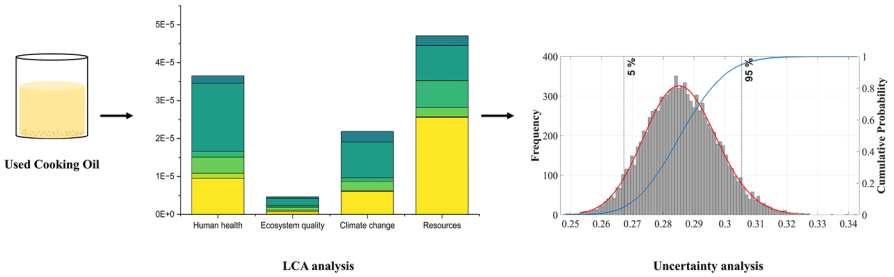

Fig. 2 Overview of LCA analysis of biodiesel production

UCO-based biodiesel production, encompassing various stages from UCO extraction to the final utilization of the biofuel. By assessing resource inputs, energy consumption, and waste generation at each stage, LCA provides insights into the efficiency of the biodiesel production process (Patel & Singh, 2022a). Additionally, the assessment helps uncover any potential environmental impacts associated with greenhouse gas emissions (Abbasi et al., 2022), water consumption, and land use.

The research gap addressed by this paper lies in the need for a comprehensive and comparative analysis of biodiesel production from UCO, specifically in the context of sustainability, energy efficiency, and uncertainty. While significant research has been conducted on biodiesel production from conventional feedstocks like soybean, palm oil, and other edible oils, more detailed studies are needed to explore the potential of UCO as an alternative, non-food-based feedstock. Current literature often focuses on the environmental benefits of biofuels but may only partially account for part of the life cycle impacts, particularly in the case of biodiesel derived from waste materials. Furthermore, the energy efficiency of converting UCO into biodiesel, including the energy inputs required for collection, processing, and refining, still needs to be explored compared to traditional biodiesel sources. In addition, existing studies frequently need to pay more attention to the uncertainties associated with the availability, quality, and processing of UCO, leading to an incomplete understanding of the risks and variability in biodiesel production outcomes. Figure 2 shows the overview of the study.

The objective of the study is to conduct a comprehensive LCA of UCO. This paper aims to fill these gaps by providing a detailed LCA and energy analysis while incorporating uncertainty modeling to offer a more holistic evaluation of the sustainability and feasibility of UCO-based biodiesel as a viable alternative fuel. This analysis is relevant to policymakers, stakeholders, and industry participants as it offers valuable insights into the ecological footprint associated with UCO-based biodiesel production. The study provides valuable managerial implications by identifying the potential use of UCO for biodiesel as a sustainable waste management solution. Policymakers could use these insights to explore alternative feedstocks, improve resource efficiency, and reduce the environmental impact of fuel production. Additionally, the analysis may help decision-makers in energy planning, supply chain optimization, and risk management by considering the variability in production inputs and environmental outcomes. The study aims to contribute to the knowledge of UCO as a feedstock for biodiesel, facilitating a more sustainable and informed approach to biofuel production and consumption.

2 Literature review

Several studies have analyzed the LCA of biodiesel, offering valuable insights into its environmental impacts in terms of midpoint and endpoint categories. Hartini et al., (2020) conducted an LCA analysis on UCO for biodiesel production to assess the eco-efficiency of the processes. The study involved the examination of two comparative scenarios. In the first scenario, UCO was transformed into biodiesel, while in the alternative scenario, UCO was disposed of in a landfill. The findings indicated increased ecotoxicity when UCO was deposited in a landfill. Conversely, the scenario involving biodiesel production demonstrated enhancements in various categories such as climate change, photochemical oxidant, oil gas depletion, and fine dust. Another study by Foteinis et al., (2020) conducted a comparative life cycle analysis of biodiesel derived from UCO in Greece, comparing it with petrodiesel and microalgae biodiesel. According to their findings, the global warming potential (GWP) per tonne of UCO-based biodiesel was 14 g CO_2 eq/MJ, and the environmental footprint single score was 58.37 Pt, demonstrating a reduction of approximately 40% compared to petrodiesel. Several studies have explored palm oil biodiesel; however, the focus has been on greenhouse gas emissions and energy needs (Castanheira et al., 2014; Hassan et al., 2011; Pleanjai & Gheewala, 2009). Only a limited number of LCA have extended their scope to encompass a broader range of environmental impacts (Castanheira & Freire, 2017; Ro et al., 2023; Silalertruksa & Gheewala, 2012; Stichnothe & Schuchardt, 2011). Table 1 presents the findings and research gaps of the studies related to the LCA of biodiesel production.

3 Methodology

The study aims to evaluate the environmental performance of second-generation biodiesel (UCO Biodiesel), identify the environmental hotspots, and compare it with first-generation biodiesel (Palm Oil Biodiesel). LCA investigations were conducted to assess biodiesel production, aligning with ISO 14040/14044 standards and enabling a comparative analysis of both feedstocks (ISO, 2006a, 2006b). The intricate methodology is elaborated in the following sections.

3.1 Scope of the study and functional unit

LCA for biodiesel production from UCO and Palm oil adopts a cradle-to-gate methodology. The system boundary for UCO encompasses the collection of UCO, followed by transport to a pre-treatment facility (Fig. 3). UCO undergoes mechanical pre-treatment at this facility to reduce solid waste content and water (Foteinis et al., 2020; Wahyono et al., 2022). Subsequently, the treated UCO is transported to a production facility where biodiesel is obtained through transesterification. Using Used Cooking Oil (UCO) as a feedstock for biodiesel production presents a promising waste management strategy due to its abundant generation from culinary activities. Improper disposal of UCO can lead to environmental issues, making repurposing for biodiesel production an environmentally responsible alternative (Pratika et al., 2024; Siregar et al., 2020). This approach addresses waste concerns and reduces reliance on virgin vegetable oils like palm oil, associated with deforestation and biodiversity loss. Choosing UCO as a feedstock aligns with circular economy

Table 1 Recent publications discussing the contribution of LCA in biodiesel production

Biomass source	System boundary	Year	Findings	Research gap	Reference
Rapeseed oil	Cradle-to-gate	2024	• Biodiesel production using methanol and dolomite resulted in the lowest global warming potential compared to other scenarios	• The study did not analyze the allocation of multi-functional resources and emissions, which could provide a more comprehensive understanding of environmental impacts	(Gaide et al., 2024)
			• The biodegradability of rapeseed oil methyl esters (RMEs) was significantly higher (78.3%) than that of rapeseed oil butyl esters (RBEs) and mineral diesel	• Further investigation is needed into the long-term sustainability and economic viability of using waste-derived catalysts in biodiesel production	
UCO	Cradle-to-gate	2024	• UCO-based biodiesel has a lower life cycle impact compared to palm oil-based biodiesel, particularly in terms of greenhouse gas (GHG) emissions, with potential savings ranging from 93 to 9254 kg CO_2-eq per ton of biodiesel	• The indirect land-use change effects associated with UCO collection and processing remain unexamined, which could significantly impact sustainability assessments	(Casas et al., 2024)
			• The economic performance of UCO-based biodiesel may be underestimated due to unaccounted benefits from avoiding mismanagement of UCO, such as reduced wastewater treatment costs and public health issues	• There is a lack of comprehensive studies on the role of UCO collection systems and their overall impacts on the sustainability of biofuel supply chains	
Microalgae	Cradle-to-gate	2023	• The system resulted in a net negative CO_2 equivalent emission of -89.42/MJ, indicating a significant reduction in greenhouse gas emissions compared to traditional biodiesel production methods	• There is a lack of comprehensive studies on the economic feasibility and market integration of microalgae biodiesel compared to conventional fuels	(Huang et al., 2023)
			• The photothermal catalyst S-NGL-600 achieved a biodiesel yield of 96.8% at room temperature, demonstrating high efficiency in the conversion process		

Table 1 (continued)

Biomass source	System boundary	Year	Findings	Research gap	Reference
UCO	Cradle-to-gate	2023	• The magnetic reactor achieved a higher biodiesel yield (96.91%) compared to the conventional reactor (93.64%), indicating improved efficiency	• There is a need for further investigation into the long-term economic viability and scalability of using magnetic reactors in industrial biodiesel production	(Lani et al., 2023)
Spent coffee grounds	Cradle-to-gate	2023	• The transesterification process results in significantly higher CO_2 emissions than pyrolysis, particularly due to the required chemical materials	• Further research is needed to assess the long-term environmental impacts of biofuel production from SCG, including the effects of land use changes and biomass sourcing	(Gu et al., 2023)
			• Pyrolysis is more economically feasible for SCG biofuel production compared to transesterification, despite the latter having lower CO_2 emissions	• There is a lack of comprehensive comparative analysis of various biofuel production technologies from SCG, which could provide deeper insights into their efficiencies and environmental impacts	
Jatropha curcas	Cradle-to-gate	2022	• The production process is hindered by high seed collection costs and limited market for by-products, necessitating technological advancements and policy support	• There is a lack of studies on the LCA and LCC of Jatropha biodiesel production using heterogeneous catalytic systems, which could provide insights into sustainability	(Liu et al., 2022)
Rapeseed	Cradle-to-gate	2022	• The integrated LCA-MCDA approach demonstrated that robust conclusions can be drawn without the need for fixed weighting vectors, addressing a common challenge in environmental assessments	• There is a need for further research on the long-term sustainability of different biomass sources and their impacts on food security and land use	(Dias et al., 2022)

Table 1 (continued)

Biomass source	System boundary	Year	Findings	Research gap	Reference
Waste palm kernel shells	Cradle-to-gate	2022	• The transesterification process is identified as the major environmental hotspot, indicating that optimizing this phase could further reduce the overall environmental burden of biodiesel production	• While the study focuses on specific impacts like acidification and global warming, there is a need for more extensive research on other potential environmental effects and the economic feasibility of using biochar in biodiesel production	(anak Erison et al., 2022)
				• There is a lack of comprehensive research evaluating the long-term sustainability and environmental impacts of biodiesel production systems using impregnated magnetic biochar catalysts derived from biomass waste	
Palm oil	Cradle-to-gate	2021	• Renewable diesel production results in a significant reduction of greenhouse gas emissions, approximately 110% lower than conventional diesel	• There is a lack of comprehensive LCA studies specifically focused on renewable diesel production from palm oil, particularly regarding its environmental impacts	(Arguelles-Arguelles et al., 2021)
			• The production process has a notable environmental impact in the human toxicity category due to high agrochemical consumption during palm cultivation	• Further research is needed to improve the cold flow properties of renewable diesel to enhance its usability in colder climates without compromising performance	
UCO	Cradle-to-gate	2020	• The environmental performance of UCO biodiesel is significantly better than that of first-generation biodiesel and petrodiesel, with a carbon footprint reduction of approximately 40% and threefold, respectively	• Future studies could explore the implications of land-use changes related to UCO collection hubs and biodiesel production facilities, which were assumed not to occur in this analysis	(Foteinis et al., 2020)

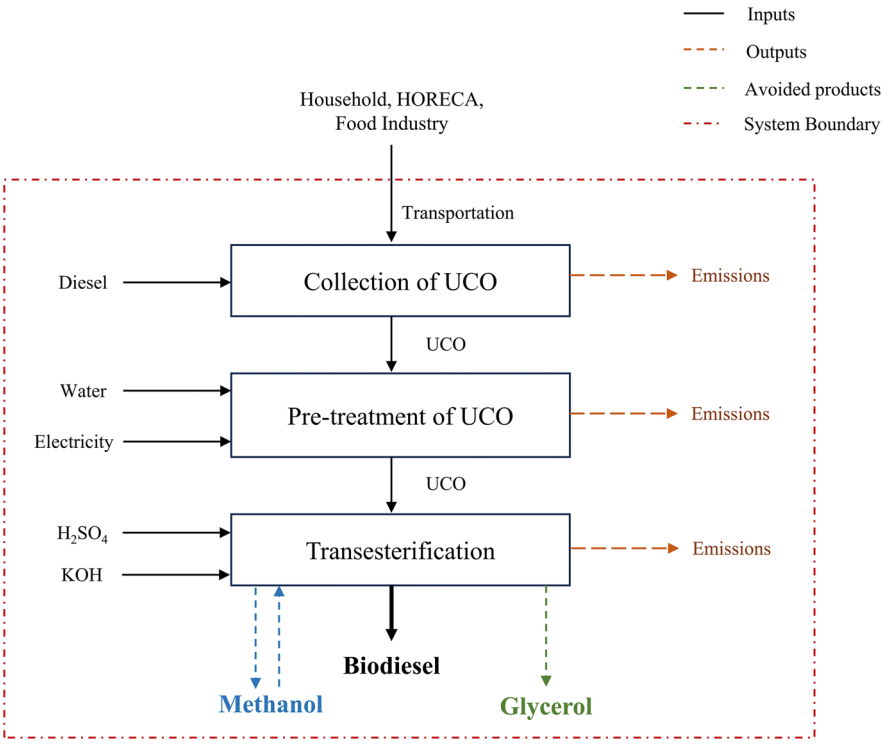

Fig. 3 System boundary of production of biodiesel from uco

principles, extending the resource lifecycle and promoting sustainability. From an economic perspective, UCO's readily available and simpler processing makes it a cost-effective option for biodiesel production. The system boundary for Palm oil biodiesel includes the cultivation stage, oil production, and biodiesel production (Haryati et al., 2022; Lee & Ofori-Boateng, 2013; Mukoro et al., 2021; Queiroz et al., 2012), as shown in Fig. 4. In each phase, the analysis takes into account the energy inputs, materials, as well as the energy production of the product and its co-products. The distribution and biodiesel consumption are not included in the goal of the study.

The functional unit (FU) in an LCA study is determined by its goal and scope, serving as a reference to normalize and express all inputs and outputs within the studied system (Foteinis et al., 2020; Kumar et al., 2024; Patel & Singh, 2022b). In this study, the per kg of biodiesel produced was considered FU. This FU was selected because (i) it establishes context within the current literature, (ii) it facilitates a direct comparison of the outcomes of this study with the existing knowledge on biodiesel, and (iii) it allows for a more accessible understanding and effective communication of results to non-specialized audiences, including policymakers.

3.2 Life cycle inventory (LCI)

In this study, the LCI was taken from several sources to obtain a complete and comprehensive picture (Foteinis et al., 2020; Lee & Ofori-Boateng, 2013; Patel & Singh, 2024a;

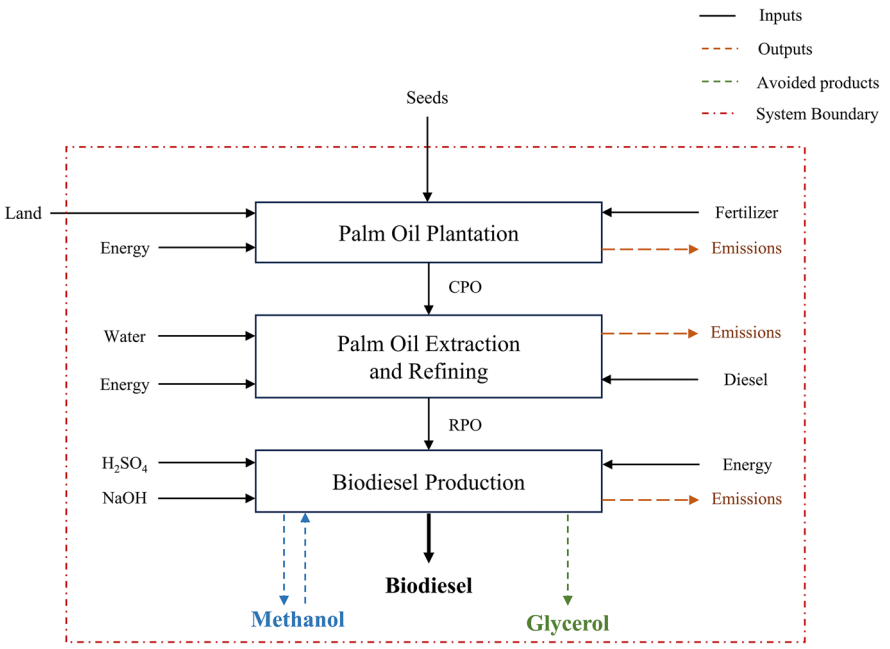

Fig. 4 System boundary of production of biodiesel from Palm Oil

Siregar et al., 2020). The Ecoinvent database provides comprehensive and up-to-date data for various environmental impacts associated with the life cycle of biodiesel production. Table 2 presents an overview of the materials and energy resources used and generated in producing 1 kg of biodiesel. Moreover, this study adopted the attributional approach instead of the consequential approach. In the attributional approach, an inventory of input and output data is conducted, which represents global averages and normative allocation norms and is scaled linearly to each functional unit (Bhonsle et al., 2022; Lopresto et al., 2024; Patel & Singh, 2023a; Wahyono et al., 2020).

3.3 Life cycle impact assessment (LCIA)

The LCIA was employed to assess the environmental impact of biodiesel production from UCO and Palm oil, focusing on carbon footprint, midpoint, and endpoint impact categories. The IMPACT 2002 + impact method was utilized for this assessment, encompassing various impact categories such as climate change, ozone depletion, acidification, eutrophication, human toxicity, and more, as outlined in (Jolliet et al., 2003). This broad coverage enables a more holistic evaluation of the environmental performance of a product, process, or system (Patel & Singh, 2023b). Additionally, this study utilizes the cumulative energy demand (CED) method, specifically focusing on quantifying cumulative energy consumption associated with the life cycle (Frischknecht et al., 2015). This dual-method approach ensures a more holistic understanding of the environmental and energy implications, contributing to a well-rounded assessment of the sustainability of biodiesel production. The

Table 2 Inventory data for the production of biodiesel from UCO and Palm oil

Materials	Unit	UCO	Palm oil
Inputs			
Used cooking oil	kg	1.18	–
Water	kg	0.092	2.19E3
Methanol	kg	0.12	0.12
Sulfuric acid	kg	0.01	–
Potassium hydroxide	kg	0.01	–
Diesel	kg	0.02	0.06
Fertilizers	kg	–	0.14
Sodium hydroxide	kg	–	0.01
Phosphoric acid	kg	–	0.01
Electricity	MJ	0.52	1.28
Steam	MJ	0.24	0.22
Outputs			
Biodiesel	kg	1.0	1.0
Glycerol	kg	0.1	0.24
Emission to air	kg	0.06	8.90
Wastewater	kg	0.16	0.05
Emission to soil	kg	–	0.005
Waste	kg	0.08	4.79

pedigree matrix determines the uncertainties related to data reliability, measurement accuracy, and temporal relevance.

4 Result and discussion

Table 3 shows the environmental impact associated with the production of 1 kg of UCO biodiesel. The system considers UCO to be a waste product. As a result, its generation does not require additional material and energy inputs or has no environmental impact. Therefore, UCO is excluded from the environmental assessment. The LCA results obtained from IMPACT 2002 + and the evaluation of CED are reported in this section.

4.1 IMPACT 2002 +

The analysis shows that for UCO biodiesel, electricity use has significant contribution in impact categories of ecotoxicity (40%), acidification (41%), global warming (43%), and eutrophication (47%), whereas methanol use in transesterification has significant contribution in carcinogens (78%) and non-carcinogens (35%), ozone layer depletion (52%), and respiratory organics (62%) impact categories. Using fertilizers during cultivation has high environmental impacts on Palm Oil biodiesel, followed by electricity and methanol.

Table 3 Environmental impacts of biodiesel production from UCO and Palm Oil (per functional unit)

Impact category	Unit	UCO	Palm oil
Carcinogens	kg C_2H_3Cl eq	0.014	0.037
Non-carcinogens	kg C_2H_3Cl eq	0.007	0.027
Respiratory inorganics	kg $PM_{2.5}$ eq	2.88E-04	0.002
Ionizing radiation	Bq C-14 eq	2.548	8.065
Ozone layer depletion	kg CFC-11 eq	4.07E-08	1.23E-07
Respiratory organics	kg C_2H_4 eq	9.61E-05	2.95E-04
Aquatic ecotoxicity	kg TEG water	35.637	126.216
Terrestrial ecotoxicity	kg TEG soil	6.975	29.415
Terrestrial acid/nutri	kg SO_2 eq	0.004	0.028
Aquatic acidification	kg SO_2 eq	1.09E-03	0.007
Aquatic eutrophication	kg PO_4 P-lim	3.62E-05	1.69E-04
Global warming	kg CO_2 eq	0.216	9.873

4.1.1 Human health potential (HHP)

HHP associated with UCO biodiesel stands at 2.6E-7 Disability Adjusted Life Years (DALY) per FU. The primary contributors to HHP are electricity consumption (49%), methanol usage (26%), and potassium hydroxide (11.6%). The midpoint categories responsible for HHP include carcinogens (14.8%), non-carcinogens (7.1%), respiratory inorganics (77.8%), and other factors (0.3%). For both carcinogens and non-carcinogens, environmental impacts were mainly due to methanol (78.7% and 35.1%, respectively), followed by electricity (9.3% and 28.9%), and heat (6.3% and 16.5%). In the case of respiratory inorganics, impacts were due to electricity (58.5%), methanol (15.1%), and the use of potassium hydroxide (13.3%). Figure 5 shows the midpoint impact categories of UCO biodiesel. Comparatively, when assessing Palm oil biodiesel, HHP accounts for 1.4E-6 DALY / FU. The significant factors influencing HHP endpoint categories are carcinogens (7.3%), non-carcinogens (5.3%), respiratory inorganics (87.1%), and other factors (0.3%). For carcinogens and non-carcinogens, impacts were majorly due to fertilizers (38.1% and 43.8%), methanol (32.4% and 9.51%), electricity (8.68% and 17.7%), and urea (15.4% and 11.5%). In the case of respiratory inorganics, emissions directly released during production cause high impacts (36.3%), followed by electricity consumption (24%) and fertilizer use (12.4%). The major emissions related to HHP are $PM_{2.5}$ (45.8%), NO_x (17.5%), SO_2 (14.3%), aromatic hydrocarbons (13.6%), arsenic (3.02%), and others (5.78%).

4.1.2 Ecosystem quality potential (EQP)

EQP for UCO biodiesel accounts for 0.064 PDF*m2*yr (potential disappeared fraction of species over a certain area during a certain time) per FU. The primary contributors to EQP are electricity use (42%), with potassium hydroxide as a transesterification catalyst contributing 16.6%, methanol at 15.8%, and heat at 9.2%. Regarding midpoint contributors to ecosystem quality, terrestrial ecotoxicity has a significant impact (87%), with aquatic ecotoxicity contributing 3% and other factors making up 10%. The notable terrestrial ecotoxicity is primarily attributed to electricity consumption throughout biodiesel production stages (42%), followed by potassium hydroxide (16.3%) and methanol use (14.6%). The major contributors to biodiesel derived from Palm oil are terrestrial and aquatic ecotoxicity (77.6% and 2%, respectively), along with other factors (20.4%). The elevated terrestrial

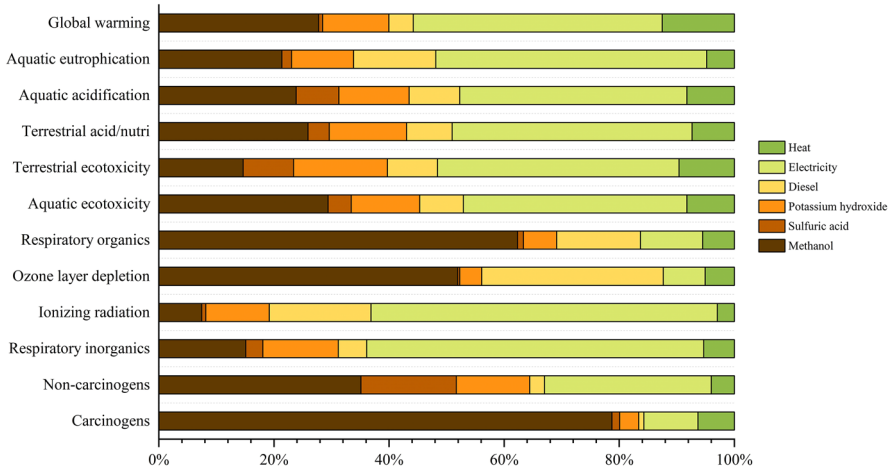

Fig. 5 Midpoint impact categories of UCO biodiesel production

ecotoxicity in palm oil biodiesel is primarily linked to fertilizers (48%) and electricity consumption (25%). The emissions causing damage to ecosystem quality are aluminium (Al_{soil}) (49.3%) which is released due to production of electricity to be used in biofuel production, followed by Al_{air} (16%), $zinc_{soil}$ (7%) from methanol, copper (4.92%) from sulfuric acid, NOx (4.58%), and other emissions contributing 18.2%.

4.1.3 Climate change potential (CCP)

Biodiesel production from UCO results in an emission of 0.216 kg CO_2 eq. / FU of CCP. The primary factors influencing this emission are electricity (43.3%), methanol (27.8%), steam-derived heat (12.5%), KOH (11.5%), and other factors (4.9%). The major emissions are CO_2 (93.6%), followed by CH_4, fossil (5.39%), dinitrogen monoxide (0.4%), and others (0.71%). Compared to Palm oil biodiesel, the CCP is 9.87 kg CO_2 eq. / FU, primarily attributed to the emissions during biodiesel production (91%), followed by fertilizers (3.8%), electricity (2.4%), and others (2.8%). The major emissions are CO2 (88.5%), CO2, fossil (8.16%), CO (2.51%), dinitrogen monoxide (0.46%), CH_4, fossil (0.29%), and others (0.08%).

4.1.4 Resources depletion potential (RDP)

The RDP for UCO biodiesel (7.15 MJ) is majorly by methanol (54.3%), electricity (19.6%), diesel (15%), and other factors (11.1%). The primary midpoint contributor is non-renewable energy, constituting 99.9%. In comparison, palm oil biodiesel has an RDP of 19.3 MJ, with methanol (22.3%), electricity (18.1%), diesel (17.2%), fertilizers (26%), and other factors (16.4%) being the major contributors, shown in Fig. 6. For UCO biodiesel, the major contributors from non-renewable energy are natural gas (62.1%) used in methanol production, crude oil (18.9%), hard coal (12.6%) and brown coal (1.95%) used in electricity production, and others (4.45%); impact of mineral extraction from copper (72.5%) used for

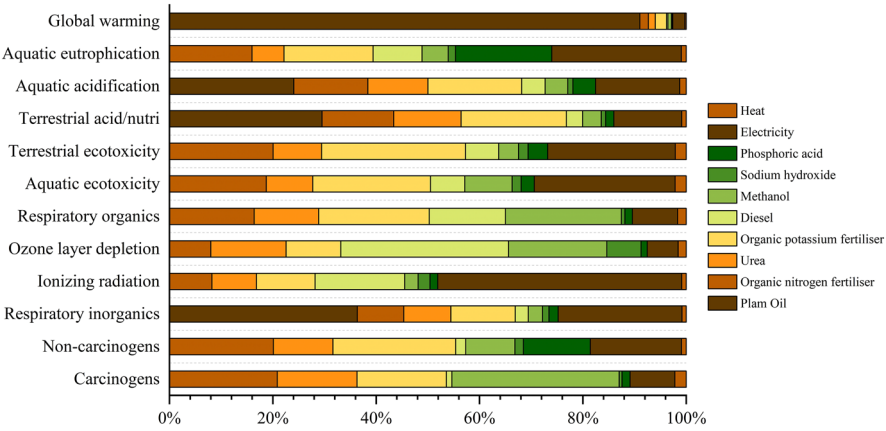

Fig. 6 Midpoint impact categories of Palm Oil biodiesel production

fertilizers, nickel (12.3%), zinc (4.88%), aluminium (2.54%), lead (1.92%), tin (1.88%), and others (3.98%). For palm oil biodiesel, the major contributors from non-renewable energy are natural gas (48%) used in methanol production, crude oil (28%), hard coal (17.1%) and brown coal (2.08%) used in electricity production, and others (4.82%); impact of mineral extraction from copper (63.6%) used for fertilizers, nickel (18.4%), zinc (6.02%), tin (3.4%), aluminium (3.16%), lead (2.34%) and others (3.08%).

4.2 Cumulative energy demand (CED)

Cumulative energy demand specifically focuses on assessing the total energy consumption associated with a product or system. It helps identify the environmental impacts associated with energy consumption. High energy demands lead to high GHG emissions, depletion of non-renewable energy resources, and other environmental burdens. In this study, CED associated with fossil fuels, including hard coal, lignite, natural gas, and crude oil, was taken into account throughout the life cycle of biodiesel production from UCO and Palm Oil. As shown in Table 4, Palm oil biodiesel has the highest consumption of fossil fuel (16.9 MJ / FU), which is mainly due to methanol (22.7%), diesel (18.4%), electricity (15.9%), fertilizer use (26.2%), and others (16.8%). As observed in Fig. 7, the energy sources required to produce biodiesel from UCO still rely on fossil fuels. The total CED for producing biodiesel from UCO was quantified as 6.78 MJ / FU, which mainly comes from fossil fuel (92.4%), followed by nuclear energy (4.4%), hydro energy (1.97%), renewable energy sources such as wind, solar and geothermal (0.6%), and others (0.63%).

4.3 Energy Balance

The energy balance in the life cycle assessment of biodiesel production involves four parameters: net energy ratio (NER), net energy value (NEV), renewability (Rn), and net renewable energy value (NRnEV). The energy input and output values correspond to the cumulative energy demand and energy content of biodiesel and its co-product, respectively (Frischknecht et al., 2015).

Table 4 Cumulative energy demand in the biodiesel production from UCO and Palm Oil (per FU)

Impact category	Unit	UCO	Palm oil
Non-renewable, fossil	MJ	6.268	16.933
Non-renewable, nuclear	MJ	0.302	0.867
Non-renewable, biomass	MJ	0.00015	0.42349
Renewable, biomass	MJ	0.040	0.122
Renewable, wind, solar, geothermal	MJ	0.041	0.192
Renewable, water	MJ	0.133	0.001

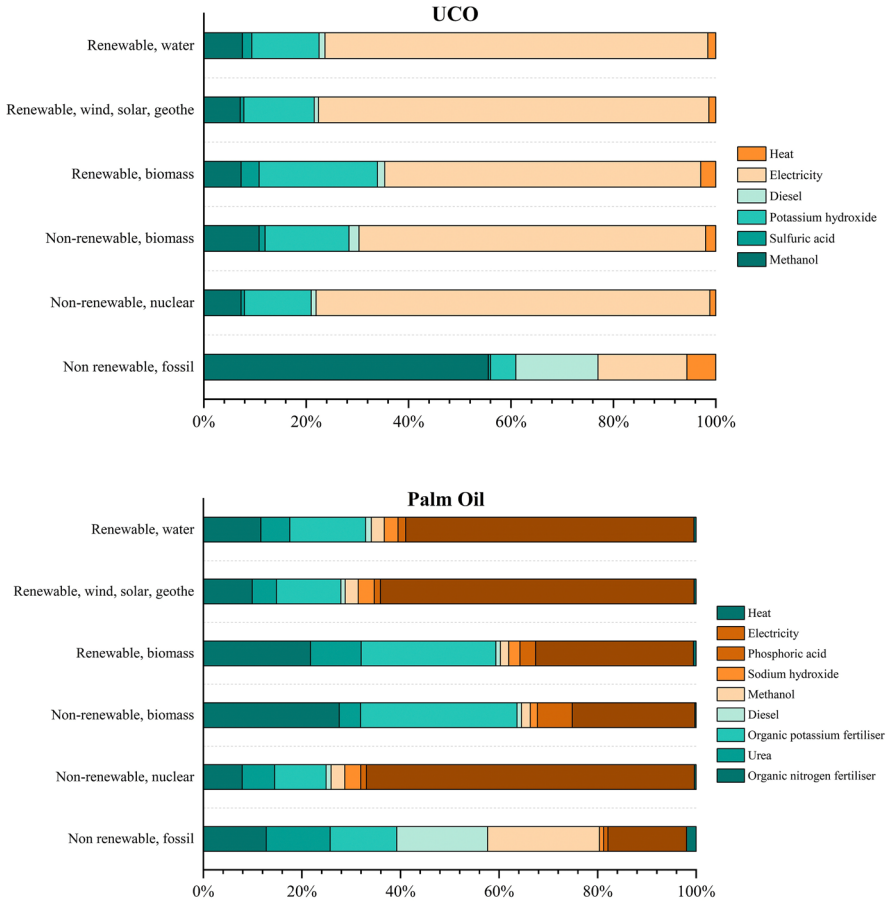

Fig. 7 Cumulative energy demand results obtained for biodiesel from UCO and Palm Oil

The study shows that both feedstocks have positive NEV; however, UCO biodiesel exhibits higher NEV and NRnEV, indicating more efficient utilization of energy resources and greater net energy gain per kg biodiesel. Similarly, NER and Rn were also high for UCO biodiesel, indicating a more efficient conversion process, generating more energy than required for production. The results are comparable to the value obtained by (Consiglio,

Table 5 Energy balance of biodiesel production from UCO, Palm Oil and Diesel

Energy balance	UCO	Palm oil	Diesel
NEV	30.5	18.73	−8.21
NRnEV	31.0	20.34	−7.96
NER	5.49	2.01	0.83
Rn	5.95	2.20	0.84

2017; Farid et al., 2020). Table 5 shows the energy balance of biodiesel production and compared with conventional diesel. The high NER of UCO (5.5) is mainly because of the reduced fossil energy required during biodiesel production.

4.4 Scenario analysis

Conducting scenario analysis through the adjustment of the system boundary, especially by incorporating the avoided products, offers valuable insights into the life cycle impacts of biodiesel production. Biodiesel production results in the generation of by-products, specifically glycerol (Talens Peiró et al., 2010). During the scenario analysis, the research considered the resources and energy inputs required for the recovery of these by-products. Table 6 shows the environmental impacts associated with the production of biodiesel per kg from UCO and palm oil per kg with the extended system boundary.

The analysis shows that the UCO biodiesel results in a 28.57% reduction in carcinogens, whereas palm oil achieves a slightly lower reduction of 24.32%. In the case of non-carcinogens, the impact reductions are significantly higher, with UCO at 228.57% and palm oil at 140.74%, indicating a substantial decrease in harmful chemical emissions. UCO shows similar trends with several environmental impact categories. However, a significant difference is observed in global warming potential and terrestrial ecotoxicity, where UCO biodiesel achieves a reduction of 138.89% and 471.83%, respectively compared to 7.43% and 272.06%, respectively for palm oil biodiesel. This shows UCO's effectiveness in reducing GHG emissions and environmental benefits over multiple impact categories. Glycerol contributes −0.3 kg CO_2 eq. to GWP for UCO biodiesel, meaning it substantially reduces CO_2 emission, making it a major factor in net negative CO_2 eq. For palm, the impact is even more substantial at −0.7 kg CO_2 eq.; however, the overall GWP remains high due to emissions during production.

4.5 Uncertainty analysis

The production of biodiesel uses secondary data and various unit processes; thus, a Monte Carlo Simulation (MCS) was undertaken to assess and quantify uncertainties linked to each unit process. As per the standard approach, the uncertainties are evaluated in each impact category by determining the ratio of standard deviation to mean (Bhonsle et al., 2022; Sharma et al., 2020; Vashist et al., 2024b). The uncertainty assessment employing an MCS involves the application of a pedigree matrix. Each input has an uncertainty score from 1 to 5, based on how reliable the source is, showing the level of confidence in the data quality for that parameter (Weidema, 1998).

Table 6 Percentage reduction due to avoided product in production of biodiesel

Impact category	Unit	UCO		Palm oil	
		Impact value	% Reduction	Impact value	% Reduction
Carcinogens	kg C_2H_3Cl eq	0.010	28.57	0.028	24.32
Non-carcinogens	kg C_2H_3Cl eq	− 0.009	228.57	− 0.011	140.74
Respiratory inorganics	kg $PM_{2.5}$ eq	− 7.6E-05	126.39	8.6E-04	57.00
Ionizing radiation	Bq C-14 eq	1.056	58.56	4.435	45.00
Ozone layer depletion	kg CFC-11 eq	5.6E-09	86.24	3.7E-08	69.84
Respiratory organics	kg C_2H_4 eq	− 5.1E-05	153.07	− 6.2E-05	121.69
Aquatic ecotoxicity	kg TEG water	3.105	91.29	47.091	62.68
Terrestrial ecotoxicity	kg TEG soil	− 25.935	471.83	− 50.628	272.06
Terrestrial acid/nutri	kg SO_2 eq	− 0.006	250.00	0.004	85.71
Aquatic acidification	kg SO_2 eq	− 5.8E-04	158.00	2.5E-03	64.29
Aquatic eutrophication	kg PO_4 P-lim	− 6.3E-05	274.03	− 7.2E-05	142.77
Global warming	kg CO_2 eq	− 0.084	138.89	9.141	7.43

In this study, 10,000 iterations of impact categories were derived for each input and output. For LCA uncertainty analysis, lognormal distribution is considered as many real-life phenomena exhibit multiplicative effects rather than additive ones, which lead to a lognormal distribution (Patel & Singh, 2024b; Sonnemann et al., 2003). The analysis also provides basic parameters such as standard deviation (SD), mean, median, coefficient of variation (CoV), and standard error of the mean (SEM). The MCS shows that the CoV, which measures the relative stability, is 7.6% and 5.1% for non-carcinogens and carcinogens, respectively, suggesting that data for non-carcinogens is slightly more consistent. The SD, representing the data spread around the mean, is 0.012 and 2.0E-4 kg C_2H_3Cl eq. for non-carcinogens and carcinogens, respectively. Higher SD indicates greater variability in the data set. Additionally, the SEM, which reflects how accurately the sample mean approximates the population mean (De Marco et al., 2018), is 1.0E-05 and 2.0E-06 for non-carcinogens and carcinogens, respectively. Altogether, this statistical measure shows that while the data for both is reliable, non-carcinogens show slightly better consistency and accuracy. Table 7 shows the uncertainty parameters for each impact category. The CoV ranges from 3.3% to 7.6%, indicating moderate variability in impact data. UCO exhibits its highest CoV in categories like carcinogens (7.6%) and aquatic eutrophication (6.5%), while palm oil shows more consistent CoV across categories, such as 4.0% for aquatic ecotoxicity and 4.1% for ozone layer depletion. Meanwhile, the SEM values suggest that both UCO and palm oil have reliable averages, however, UCO typically has smaller SEM values, which suggests that its mean impact measurements are slightly more precise compared to those of palm oil.

The frequency distribution and cumulative probabilities for midpoint impact categories for UCO and Palm Oil biodiesel are shown in Figs. 8 and 9. The uncertainties linked to non-renewable fossil, renewable, and non-renewable biomass in the context of biodiesel production from UCO and Palm Oil are shown in Figs. 10 and 11. The narrow ranges between the 5th and 95th percentiles reflect a high level of consistency in the data, suggesting that the environmental impacts of the process are quite predictable.

Table 7 Uncertainty analysis of the LCA of UCO and Palm Oil based biodiesel (using monte carlo analysis; 10,000 iterations)

Environmental Impact Categories	UCO				Palm Oil			
	Mean	SD	CoV (%)	SEM	Mean	SD	CoV (%)	SEM
IMPACT 2002 +								
Aquatic acidification	1.3E-03	6.1E-05	4.9	6.1E-07	5.7E-03	1.9E-04	3.3	1.9E-06
Aquatic ecotoxicity	20.035	0.929	4.6	9.3E-03	110.701	4.428	4.0	4.4E-02
Aquatic eutrophication	9.6E-05	6.3E-06	6.5	6.3E-08	3.2E-04	1.6E-05	5.1	1.6E-07
Carcinogens	0.012	0.001	7.6	1.0E-05	1.7E-02	9.9E-04	5.6	9.9E-06
Global warming	0.286	0.012	4.1	1.2E-04	9.608	0.715	7.4	7.2E-03
Ionizing radiation	2.513	0.114	4.5	1.1E-03	5.601	0.272	4.9	2.7E-03
Non-carcinogens	3.9E-03	2.0E-04	5.1	2.0E-06	4.5E-02	2.0E-03	4.5	2.0E-05
Ozone layer depletion	4.1E-08	2.0E-09	4.9	2.0E-11	9.6E-08	4.0E-09	4.1	4.0E-11
Respiratory inorganics	6.2E-04	4.3E-05	6.9	4.3E-07	2.3E-03	1.1E-04	4.8	1.1E-06
Respiratory organics	8.7E-05	5.0E-06	5.8	5.0E-08	1.9E-04	7.1E-06	3.7	7.1E-08
Terrestrial acid/nutri	3.4E-03	1.5E-04	4.5	1.5E-06	2.5E-02	8.8E-04	3.5	8.8E-06
Terrestrial ecotoxicity	3.382	0.126	3.7	1.3E-03	87.679	4.614	5.3	4.6E-02
Cumulative Energy Demand								
Non-renewable, fossil	6.252	0.308	4.9	3.1E-03	12.297	0.469	3.8	4.7E-03
Non-renewable, biomass	6.2E-05	2.7E-06	4.4	2.7E-08	0.052	0.003	5.7	3.0E-05
Non-renewable, nuclear	0.330	0.018	5.6	1.8E-04	0.642	0.041	6.4	4.1E-04
Renewable, biomass	3.3E-02	1.5E-03	4.4	1.5E-05	1.424	0.078	5.5	7.8E-04
Renewable, water	0.207	0.013	6.5	1.3E-04	0.521	0.033	6.3	3.3E-04
Renewable, wind, solar, geothermal	3.2E-02	1.6E-03	5.0	1.6E-05	0.061	0.003	5.3	3.0E-05

SD: Standard Deviation; CoV: Coefficient of Variation; SEM: standard error of the mean

This predictability is crucial for effective planning and optimization. The graphs serve as essential tools for illustrating the environmental consequences of biofuel production. By analyzing the frequency distribution and cumulative probability for each impact category, stakeholders can identify the most critical environmental challenges and focus their efforts on areas that need improvement. These visualizations also show how probabilities accumulate as values increase, highlighting trends in medians and variability across different ranges. This comprehensive perspective enhances statistical reasoning and supports informed decision-making by showcasing the interrelatedness of probabilities and their cumulative effects.

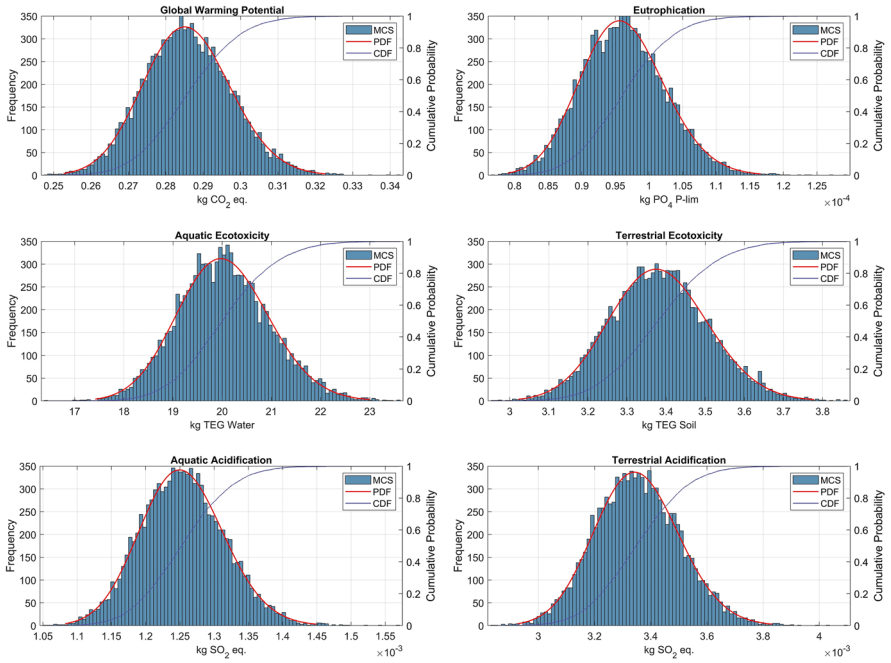

Fig. 8 Probability Density and Cumulative Probability Function of midpoint impact category for the biodiesel production from UCO

Figure 12 shows the scatter plot, showing the variability and correlation between LCI inputs and impact categories obtained by MCS. The regression line and equation measure the relationship, while R^2 indicates the proportion of variance in the impact category explained by the LCI input. This relationship is crucial for understanding how changes in inventory inputs can influence environmental outcomes, helping to identify key areas for improvement and optimization in production processes. The varying R2 values across the scatter plots highlights the differences in how effectively these inventory inputs influence the impact categories. The scatter plot as shown in Fig. 12 shows that electricity consumption has the highest correlation with global warming potential, with an R^2 value of 0.6027, indicating it is a significant contributor to global warming. In terms of carcinogens, methanol usage shows an exceptionally high correlation with an R^2 value of 0.9990. For ecotoxicity, methanol usage has an R^2 value of 0.4053, followed by potassium hydroxide with an R^2 of 0.2787. Regarding eutrophication, electricity consumption demonstrates a strong correlation with an R^2 value of 0.9834. This knowledge enables targeted strategies for reducing emissions and enhancing sustainability efforts, ultimately guiding effective decision-making and resource allocation.

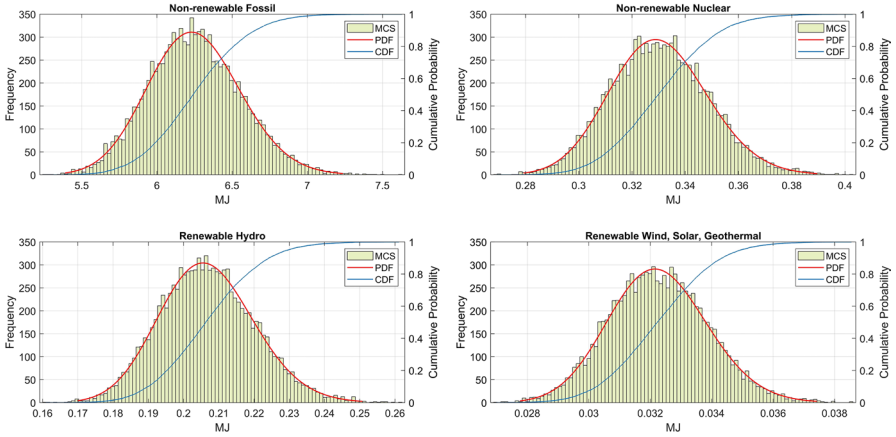

Fig. 9 Probability Density and Cumulative Probability Function of midpoint impact category for the biodiesel production from Palm Oil

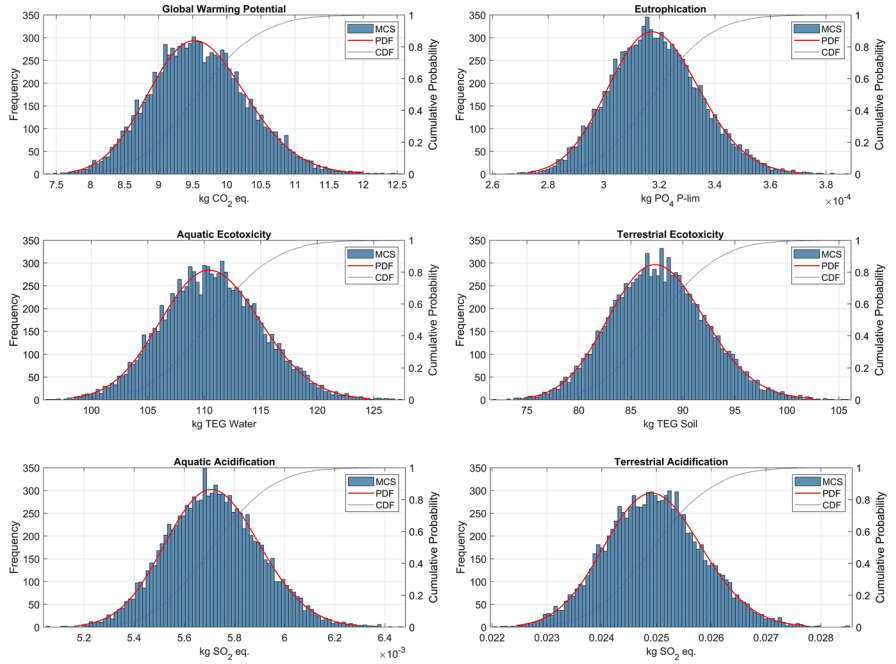

Fig. 10 Probability Density and Cumulative Probability Function of CED for the biodiesel production from UCO

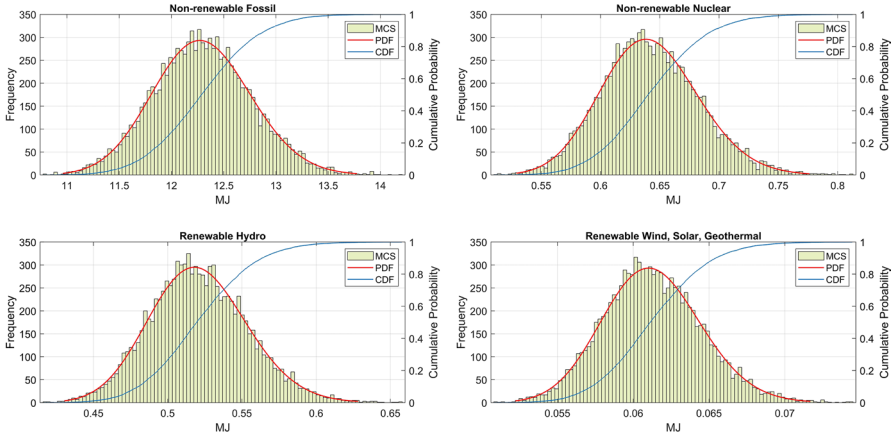

Fig. 11 Probability Density and Cumulative Probability Function of CED for the biodiesel production from Palm Oil

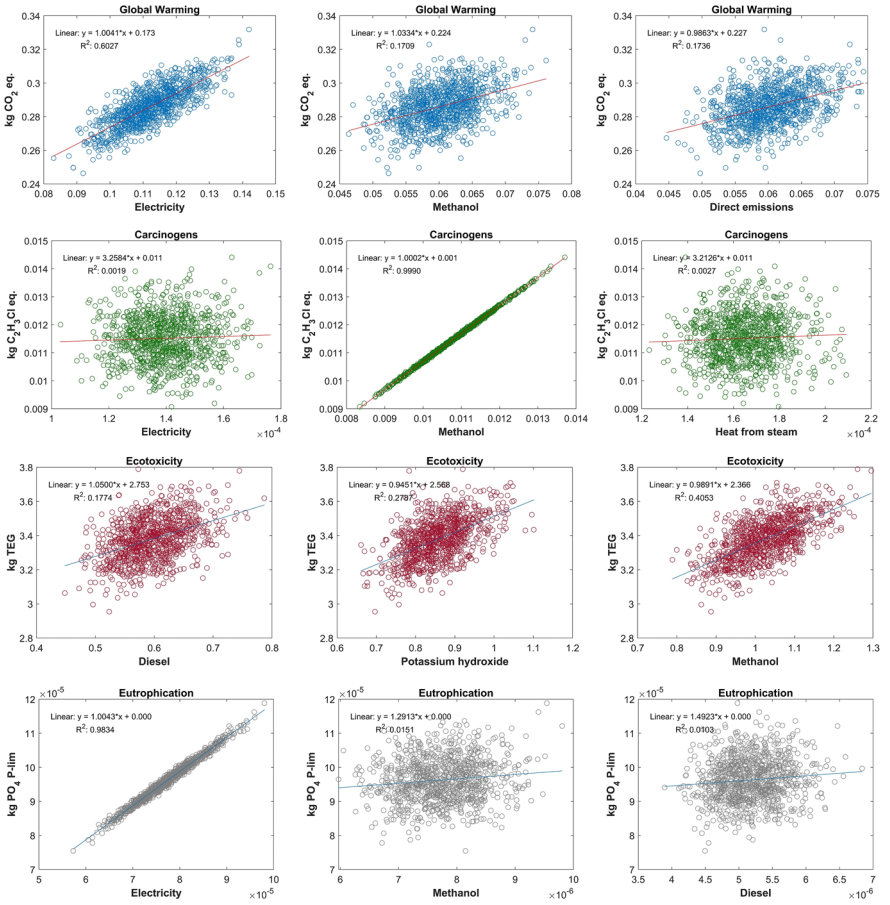

Fig. 12 Scatter plot showing relationship between inventory inputs and impact category for the biodiesel production from UCO

5 Conclusion

UCO biodiesel serves as a waste management solution and a sustainable energy source. Its multifaceted contribution to waste management and energy production underscores the imperative for conducting a comprehensive LCA for biodiesel derived from UCO. The findings show that UCO biodiesel has significantly lower environmental impacts across various categories, including human health, global warming potential, and ecosystem quality, due to reduced reliance on raw materials and energy inputs, particularly fossil fuels, contributing to lower carbon emissions and resource depletion. The GWP of UCO biodiesel was 0.216 kg CO_2 eq. compared to 9.87 kg CO_2 eq. for palm oil biodiesel. Further, the scenario analysis shows the 138.89% and 7.43% reduction in GWP when considering recovery of by-products. The study also shows that the NER of UCO biodiesel (5.49) is higher than palm oil (2.01) and petroleum diesel (0.83). This dual impact highlights the significance of the LCA in comprehensively evaluating UCO biodiesel's environmental implications, facilitating comparisons with alternative feedstocks, and guiding decisions toward a more circular and energy-efficient biofuel industry. The study emphasizes the advantages of utilizing waste materials like UCO in biodiesel production. The analysis underscores the potential of UCO in mitigating the environmental impacts associated with fossil fuels and conventional feedstock such as palm oil. The lower cumulative energy demand, positive energy balance, and scenario analysis further support the viability of UCO as a sustainable feedstock. However, the study also highlights areas for improvement, such as optimizing the use of electricity and methanol during the transesterification process to minimize environmental impacts. The uncertainty analysis, using Monte Carlo simulations, provides robust validation of the LCA results, ensuring the reliability of the conclusions drawn. Acknowledging and resolving these uncertainties is essential for making informed decisions and steering future research efforts. The study primarily focuses on the environmental impacts of biodiesel production. Addressing social or economic factors are also crucial for a holistic understanding of biodiesel's sustainability. Future research should aim to incorporate a broader range of sustainability indicators, including social and economic dimensions, to provide a comprehensive evaluation of UCO biodiesel. As a comprehensive tool, LCA bridges scientific assessments with practical decision-making, ensuring that the biofuel industry evolves in an environmentally responsible and economically viable manner.

Author contribution Kulvendra Patel: Writing—original draft, Methodology, Conceptualization, Formal analysis, Data curation. S.K. Singh: Writing—review & editing, Validation, Conceptualization, Supervision.

Data availability The authors confirm that the data supporting the findings of this study are available within the article and/or its supplementary materials.

Declarations

Conflict of interest All authors certify that they have no affiliations with, or involvement in, any organization or entity with financial or non-financial interests in the subject matter or materials discussed in this manuscript.

References

Abbasi, S., Abbaspour, S., Eskandari Nasab SiahkoohiYousefi Sorkhi, M. M., & Ghasemi, P. (2024). Supply chain network design concerning economy and environmental sustainability: Crisis perspective. *Results in Engineering, 22*, 102291. https://doi.org/10.1016/j.rineng.2024.102291

Abbasi, S., Daneshmand-Mehr, M., & Ghane Kanafi, A. (2022). Designing sustainable recovery network of end-of-life product during the COVID-19 pandemic: A real and applied case study. *Discrete Dynamics in Nature and Society*. https://doi.org/10.1155/2022/6967088

Aboelazayem, O., Gadalla, M., & Saha, B. (2018). Valorisation of high acid value waste cooking oil into biodiesel using supercritical methanolysis: Experimental assessment and statistical optimisation on typical Egyptian feedstock. *Energy, 162*, 408–420. https://doi.org/10.1016/j.energy.2018.07.194

Al-Juboori, O., Sher, F., Khalid, U., Niazi, M. B. K., & Chen, G. Z. (2020). Electrochemical production of sustainable hydrocarbon fuels from CO_2 co-electrolysis in eutectic molten melts. *ACS Sustainable Chemistry & Engineering, 8*(34), 12877–12890. https://doi.org/10.1021/acssuschemeng.0c03314

Anak Erison, A. E., Tan, Y. H., Mubarak, N. M., Kansedo, J., Khalid, M., Abdullah, M. O., & Ghasemi, M. (2022). Life cycle assessment of biodiesel production by using impregnated magnetic biochar derived from waste palm kernel shell. *Environmental Research, 214*, 114149. https://doi.org/10.1016/j.envres.2022.114149

Arguelles-Arguelles, A., Amezcua-Allieri, M. A., & Ramírez-Verduzco, L. F. (2021). Life cycle assessment of green diesel production by Hydrodeoxygenation of palm oil. *Frontiers in Energy Research, 9*, 690725. https://doi.org/10.3389/fenrg.2021.690725

Bhonsle, A. K., Singh, J., Trivedi, J., & Atray, N. (2022). Comparative LCA studies of biodiesel produced from used cooking oil using conventional and novel room temperature processes. *Bioresource Technology Reports, 18*, 101072. https://doi.org/10.1016/j.biteb.2022.101072

Casas, L. C., Orjuela, A., & Poganietz, W.-R. (2024). Sustainability assessment of the valorization scheme of used cooking oils (UCOs): The case study of Bogotá. *Colombia. Biomass Conversion and Biorefinery, 14*(14), 15317–15333. https://doi.org/10.1007/s13399-023-03800-1

Castanheira, É. G., Acevedo, H., & Freire, F. (2014). Greenhouse gas intensity of palm oil produced in Colombia addressing alternative land use change and fertilization scenarios. *Applied Energy, 114*, 958–967. https://doi.org/10.1016/j.apenergy.2013.09.010

Castanheira, É. G., & Freire, F. (2017). Environmental life cycle assessment of biodiesel produced with palm oil from Colombia. *The International Journal of Life Cycle Assessment, 22*(4), 587–600. https://doi.org/10.1007/s11367-016-1097-6

Consiglio, D. (2017). Biofuels, fossil energy ratio, and the future of energy production. *Physical Sciences Reviews*. https://doi.org/10.1515/psr-2017-0055

De Marco, I., Riemma, S., & Iannone, R. (2018). Uncertainty of input parameters and sensitivity analysis in life cycle assessment: An Italian processed tomato product. *Journal of Cleaner Production, 177*, 315–325. https://doi.org/10.1016/j.jclepro.2017.12.258

Dias, L. C., Passeira, C., Malça, J., & Freire, F. (2022). Integrating life-cycle assessment and multi-criteria decision analysis to compare alternative biodiesel chains. *Annals of Operations Research, 312*(2), 1359–1374. https://doi.org/10.1007/s10479-016-2329-7

Farid, M. A. A., Roslan, A. M., Hassan, M. A., Hasan, M. Y., Othman, M. R., & Shirai, Y. (2020). Net energy and techno-economic assessment of biodiesel production from waste cooking oil using a semi-industrial plant: A Malaysia perspective. *Sustainable Energy Technologies and Assessments, 39*, 100700. https://doi.org/10.1016/j.seta.2020.100700

Foteinis, S., Chatzisymeon, E., Litinas, A., & Tsoutsos, T. (2020). Used-cooking-oil biodiesel: Life cycle assessment and comparison with first- and third-generation biofuel. *Renewable Energy, 153*, 588–600. https://doi.org/10.1016/j.renene.2020.02.022

Frischknecht, R., Wyss, F., Büsser Knöpfel, S., Lützkendorf, T., & Balouktsi, M. (2015). Cumulative energy demand in LCA: The energy harvested approach. *International Journal of Life Cycle Assessment, 20*(7), 957–969. https://doi.org/10.1007/s11367-015-0897-4

FSSAI. (2018). Handling and disposal of used cooking oil.

Gaide, I., Grigas, A., Makareviciene, V., & Sendzikiene, E. (2024). Life cycle assessment and biodegradability of biodiesel produced using different alcohols and heterogeneous catalysts. *Green Chemistry Letters and Reviews, 17*(1), 2394503. https://doi.org/10.1080/17518253.2024.2394503

Garlapati, V. K., Kant, R., Kumari, A., Mahapatra, P., Das, P., & Banerjee, R. (2013). Lipase mediated transesterification of Simarouba glauca oil: A new feedstock for biodiesel production. *Sustainable Chemical Processes, 1*(1), 11. https://doi.org/10.1186/2043-7129-1-11

Goli, J., & Sahu, O. (2018). Development of heterogeneous alkali catalyst from waste chicken eggshell for biodiesel production. *Renewable Energy, 128*, 142–154. https://doi.org/10.1016/j.renene.2018.05.048

Gu, J., Lee, A., Choe, C., & Lim, H. (2023). Comparative study of biofuel production based on spent coffee grounds transesterification and pyrolysis: Process simulation, techno-economic, and life cycle assessment. *Journal of Cleaner Production, 428*, 139308. https://doi.org/10.1016/j.jclepro.2023.139308

Gupta, J., Agarwal, M., & Dalai, A. K. (2016). Optimization of biodiesel production from mixture of edible and nonedible vegetable oils. *Biocatalysis and Agricultural Biotechnology, 8*, 112–120. https://doi.org/10.1016/j.bcab.2016.08.014

Hartini, S., Puspitasari, D., Roudhatul Aisy, N., & Widharto, Y. (2020). Eco-efficiency Level of production process of waste cooking oil to be biodiesel with life cycle assessment. *E3S Web of Conferences, 202*, 10004. https://doi.org/10.1051/e3sconf/202020210004

Haryati, Z., Subramaniam, V., Noor, Z. Z., Hashim, Z., Loh, S. K., & Aziz, A. A. (2022). Social life cycle assessment of crude palm oil production in Malaysia. *Sustainable Production and Consumption, 29*, 90–99. https://doi.org/10.1016/j.spc.2021.10.002

Hassan, M. N. A., Jaramillo, P., & Griffin, W. M. (2011). Life cycle GHG emissions from Malaysian oil palm bioenergy development: The impact on transportation sector's energy security. *Energy Policy, 39*(5), 2615–2625. https://doi.org/10.1016/j.enpol.2011.02.030

Huang, J., Wang, J., Huang, Z., Liu, T., & Li, H. (2023). Photothermal technique-enabled ambient production of microalgae biodiesel: Mechanism and life cycle assessment. *Bioresource Technology, 369*, 128390. https://doi.org/10.1016/j.biortech.2022.128390

IEA. (2024). Renewable fuel demand by sector, main case, 2023. Paris. https://www.iea.org/data-and-statistics/charts/renewable-fuel-demand-by-sector-main-case-2023. Accessed 27 October 2024.

ISO. (2006b). ISO - ISO 14040:2006 - Environmental management — Life cycle assessment — Principles and framework. International Organization for Standardization (ISO). https://www.iso.org/standard/37456.html. Accessed 5 October 2022.

ISO. (2006a). ISO - ISO 14044:2006 - Environmental management — Life cycle assessment — Requirements and guidelines. International Organization for Standardization (ISO). https://www.iso.org/standard/38498.html. Accessed 5 October 2022.

Jolliet, O., Margni, M., Charles, R., Humbert, S., Payet, J., Rebitzer, G., & Rosenbaum, R. (2003). IMPACT 2002+: A new life cycle impact assessment methodology. *The International Journal of Life Cycle Assessment, 8*(6), 324–330. https://doi.org/10.1007/BF02978505

Kumar, R., Patel, K., & Singh, S. K. (2024). Biological wastewater treatment: A comprehensive sustainability analysis using life cycle assessment. *Environmental Monitoring and Assessment, 196*(5), 416. https://doi.org/10.1007/s10661-024-12578-2

Lani, N. S., Ngadi, N., Mohammed Inuwa, I., Anako Opotu, L., Zakaria, Z. Y., & Haron, S. (2023). A cleaner approach with magnetically assisted reactor setup over CaO-zeolite/Fe3O4 catalyst in biodiesel production: Evaluation of catalytic performance, reusability and life cycle assessment studies. *Journal of Cleaner Production, 419*, 138329. https://doi.org/10.1016/j.jclepro.2023.138329

Lee, K. T., & Ofori-Boateng, C. (2013). *Life cycle assessment of biodiesel from palm oil* (pp. 95–129). New York: Springer.

Liu, Y., Zhu, Z., Zhang, R., & Zhao, X. (2022). Life cycle assessment and life cycle cost analysis of Jatropha biodiesel production in China. *Biomass Conversion and Biorefinery*. https://doi.org/10.1007/s13399-022-03614-7

Lopresto, C. G., De Paola, M. G., & Calabrò, V. (2024). Importance of the properties, collection, and storage of waste cooking oils to produce high-quality biodiesel – An overview. *Biomass and Bioenergy, 189*, 107363. https://doi.org/10.1016/j.biombioe.2024.107363

Mansir, N., Teo, S. H., Rabiu, I., & Taufiq-Yap, Y. H. (2018). Effective biodiesel synthesis from waste cooking oil and biomass residue solid green catalyst. *Chemical Engineering Journal, 347*, 137–144. https://doi.org/10.1016/j.cej.2018.04.034

Moreno-Peñaranda, R., Gasparatos, A., Stromberg, P., Suwa, A., Pandyaswargo, A. H., & Puppim de Oliveira, J. A. (2015). Sustainable production and consumption of palm oil in Indonesia: What can stakeholder perceptions offer to the debate? *Sustainable Production and Consumption, 4*, 16–35. https://doi.org/10.1016/j.spc.2015.10.002

Mukoro, V., Gallego-Schmid, A., & Sharmina, M. (2021). Life cycle assessment of renewable energy in Africa. *Sustainable Production and Consumption, 28*, 1314–1332. https://doi.org/10.1016/j.spc.2021.08.006

Patel, K., & Singh, S. K. (2023b). Assessing the Sustainability of Jatropha and Rapeseed Biodiesel: An LCA Approach. In R. Al Khaddar, S. K. Singh, N. D. Kaushika, R. K. Tomar, & S. K. Jain (Eds.), (pp. 191–200). Singapore: Springer Nature Singapore. https://doi.org/10.1007/978-981-99-1388-6_15

Patel, K., & Singh, S. K. (2022a). A life cycle approach to environmental assessment of wastewater and sludge treatment processes. *Water and Environment Journal, 36*(3), 412–424. https://doi.org/10.1111/wej.12774

Patel, K., & Singh, S. K. (2022b). Assessing the sustainability of municipal solid waste management using life-cycle analysis. *Proceedings of the Institution of Civil Engineers - Waste and Resource Management, 175*(3), 64–74. https://doi.org/10.1680/jwarm.21.00018

Patel, K., & Singh, S. K. (2023a). Environmental sustainability analysis of biofuels: A critical review of LCA studies. *Clean Technologies and Environmental Policy*. https://doi.org/10.1007/s10098-023-02596-y

Patel, K., & Singh, S. K. (2024a). Sustainable waste management: A comprehensive life cycle assessment of bioethanol production from agricultural and municipal waste. *Environmental Science and Pollution Research*. https://doi.org/10.1007/s11356-024-34612-z

Patel, K., & Singh, S. K. (2024b). Environmental sustainability, energy efficiency and uncertainty analysis of agricultural residue-based bioethanol production: A comprehensive life cycle assessment study. *Biomass and Bioenergy, 191*, 107439. https://doi.org/10.1016/j.biombioe.2024.107439

Pleanjai, S., & Gheewala, S. H. (2009). Full chain energy analysis of biodiesel production from palm oil in Thailand. *Applied Energy, 86*, S209–S214. https://doi.org/10.1016/j.apenergy.2009.05.013

Pratika, R. A., Nafisah, Z., Yuliana, Y., Syarpin, S., Iqbal, R. M., Ysrafil, Y., & Wijaya, K. (2024). Conversion of used cooking oil into biodiesel by utilizing zirconia catalyst as acid catalyst (SO4/ZrO2) and base catalyst (ZrO2/CaO). *Arabian Journal for Science and Engineering*. https://doi.org/10.1007/s13369-024-09520-6

Queiroz, A. G., França, L., & Ponte, M. X. (2012). The life cycle assessment of biodiesel from palm oil ("dendê") in the Amazon. *Biomass and Bioenergy, 36*, 50–59. https://doi.org/10.1016/j.biombioe.2011.10.007

Ro, J. W., Zhang, Y., & Kendall, A. (2023). Developing guidelines for waste designation of biofuel feedstocks in carbon footprints and life cycle assessment. *Sustainable Production and Consumption, 37*, 320–330. https://doi.org/10.1016/j.spc.2023.03.009

Sanglard, B., Lachaize, S., Carrey, J., & Tiruta-Barna, L. (2023). Life cycle assessment of a parabolic solar cooker and comparison with conventional cooking appliances. *Sustainable Production and Consumption, 42*, 211–233. https://doi.org/10.1016/j.spc.2023.09.018

Sharma, B., Larroche, C., & Dussap, C.-G. (2020). Comprehensive assessment of 2G bioethanol production. *Bioresource Technology, 313*, 123630. https://doi.org/10.1016/j.biortech.2020.123630

Silalertruksa, T., & Gheewala, S. H. (2012). Environmental sustainability assessment of palm biodiesel production in Thailand. *Energy, 43*(1), 306–314. https://doi.org/10.1016/j.energy.2012.04.025

Singh, T. S., & Verma, T. N. (2019). An assessment study of using Turel Kongreng (river mussels) as a source of heterogeneous catalyst for biofuel production. *Biocatalysis and Agricultural Biotechnology, 20*, 101185. https://doi.org/10.1016/j.bcab.2019.101185

Siregar, K., Ichwana, N., & I. S., Sholihati, Sofiah, I., & Miharza, T. (2020). Implementation of Life Cycle Assessment (LCA) for oil palm industry in Aceh province, Indonesia. *IOP Conference Series: Earth and Environmental Science, 542*(1), 012046. https://doi.org/10.1088/1755-1315/542/1/012046

Sonnemann, G. W., Schuhmacher, M., & Castells, F. (2003). Uncertainty assessment by a Monte Carlo simulation in a life cycle inventory of electricity produced by a waste incinerator. *Journal of Cleaner Production, 11*(3), 279–292. https://doi.org/10.1016/S0959-6526(02)00028-8

Srikumar, K., Tan, Y. H., Kansedo, J., Tan, I. S., Mubarak, N. M., Ibrahim, M. L., et al. (2024). A review on the environmental life cycle assessment of biodiesel production: Selection of catalyst and oil feedstock. *Biomass and Bioenergy, 185*, 107239. https://doi.org/10.1016/j.biombioe.2024.107239

Stichnothe, H., & Schuchardt, F. (2011). Life cycle assessment of two palm oil production systems. *Biomass and Bioenergy, 35*(9), 3976–3984. https://doi.org/10.1016/j.biombioe.2011.06.001

Talens Peiró, L., Lombardi, L., Villalba Méndez, G., & Gabarrell i Durany, X. (2010). Life cycle assessment (LCA) and exergetic life cycle assessment (ELCA) of the production of biodiesel from used cooking oil (UCO). *Energy, 35*(2), 889–893. https://doi.org/10.1016/j.energy.2009.07.013

Tan, Y. H., Abdullah, M. O., Kansedo, J., Mubarak, N. M., Chan, Y. S., & Nolasco-Hipolito, C. (2019). Biodiesel production from used cooking oil using green solid catalyst derived from calcined fusion waste chicken and fish bones. *Renewable Energy, 139*, 696–706. https://doi.org/10.1016/j.renene.2019.02.110

Tsoutsos, T. D., Tournaki, S., Paraíba, O., & Kaminaris, S. D. (2016). The used cooking oil-to-biodiesel chain in Europe assessment of best practices and environmental performance. *Renewable and Sustainable Energy Reviews, 54*, 74–83. https://doi.org/10.1016/j.rser.2015.09.039

Vashist, M., & Singh, S. K. (2023). Potential of Individual Leaf Traits and Leaf-Associated Microorganisms in the Removal of Particulate Matter (pp. 201–207). https://doi.org/10.1007/978-981-99-1388-6_16

Vashist, M., Kumar, T. V., & Singh, S. K. (2024a). A comprehensive review of urban vegetation as a Nature-based Solution for sustainable management of particulate matter in ambient air. *Environmental Science and Pollution Research, 31*(18), 26480–26496. https://doi.org/10.1007/s11356-024-33089-0

Vashist, M., Kumar, T. V., & Singh, S. K. (2024b). Assessment of air quality benefits of vegetation in an urban-industrial region of India by integrating air monitoring with i-Tree Eco model. *Clean: Soil, Air, Water, 52*(7), 2300198. https://doi.org/10.1002/clen.202300198

Wahyono, Y., Hadiyanto, H., Budihardjo, M. A., & Adiansyah, J. S. (2020). Assessing the environmental performance of palm oil biodiesel production in Indonesia: A life cycle assessment approach. *Energies, 13*(12), 3248. https://doi.org/10.3390/en13123248

Wahyono, Y., Hadiyanto, H., Gheewala, S. H., Budihardjo, M. A., & Adiansyah, J. S. (2022). Evaluating the environmental impacts of the multi-feedstock biodiesel production process in Indonesia using life cycle assessment (LCA). *Energy Conversion and Management, 266*, 115832. https://doi.org/10.1016/j.enconman.2022.115832

Weidema, B. P. (1998). Multi-user test of the data quality matrix for product life cycle inventory data. *The International Journal of Life Cycle Assessment, 3*(5), 259–265. https://doi.org/10.1007/BF02979832

Zulqarnain, Yusoff, M. H. M., Ayoub, M., Hamza Nazir, M., Zahid, I., Ameen, M., et al. (2021). Comprehensive review on biodiesel production from palm oil mill effluent. *ChemBioEng Reviews, 8*(5), 439–462. https://doi.org/10.1002/cben.202100007

Publisher's Note Springer Nature remains neutral with regard to jurisdictional claims in published maps and institutional affiliations.

Springer Nature or its licensor (e.g. a society or other partner) holds exclusive rights to this article under a publishing agreement with the author(s) or other rightsholder(s); author self-archiving of the accepted manuscript version of this article is solely governed by the terms of such publishing agreement and applicable law.

View publication stats

2024 International Conference on Electrical Electronics and Computing Technologies (ICEECT) | 979-8-3503-7809-2/24/$31.00 ©2024 IEEE | DOI: 10.1109/ICEECT61758.2024.10738998

Unveiling Enhanced Model Predictive Control for Power Regulation in Single Phase AC/DC Converter

Philemon Yegon
Electrical Engineering Department
Delhi Technological University
Delhi, India
pkuruiphilemon@gmail.com

Mukhtiar Singh
Electrical Engineering Department
Delhi Technological University
Delhi, India
smukhtiar_79@yahoo.co.in

***Abstract*—This article presents enhanced MCP controller for active and reactive power regulation. Constant switching frequency is obtained through optimization of PMW. The regulation of the Dc voltage is achieved by using PI controller. The effectiveness of the adopted optimization technique is confirmed by its validation using Matlab/Simulink environment. This validation demonstrates its sturdy performance and reliability, hence confirming its practical appropriateness for real-world application. The control scheme is a multi-objective; active as well as reactive power from enhanced MCP controller precisely regulated to the required levels, resulting in little deviation and shorten restoration time. In addition, dc voltage was regulated independently.**

keywords—model predictive control (mcp), pi, active power, reactive power and dc voltage.

I. INTRODUCTION

The energy sector has seen significant transformation in recent decades. The problem of the world's growing energy consumption is one that many nations face. Furthermore, conventional power producing techniques are harmful to the environment. Greenhouse gas emissions from fossil fuels contaminate the environment and endanger local life. Consequently, recent research have proposed power converters that supply voltage with controlled source Pulse width modulation (PWM) approach have been largely applied in grid-interfaced power network systems, such as renewable energy sources (RES) [1][2][3]. Regrettably, instability, unpredictability, and randomness characterise the energy supply of the majority of renewable sources Sustainable and stable operation is unattainable for microgrids with loads and RES. As such, various control strategies have been suggested for PMW converters switching control for fixed dc-link voltage, UPF and pure sinusoidal wave [4]. Schemes like proportional-resonant, voltage-oriented control (VOC), hysteresis and proportional integral (PI) have been extensively researched on [5][6].

Phase-lock-phase (PLL) technique provide rotational frame coordinate from the grid interfaced. VOC technique is applied in PMW to regulate real and imaginary powers to tack the given references [7]. However, it is not immune to power ripples and harmonics. conventional linear PI controller has been widely adopted in PMW converters but has a drawback of complex computational burden while tuning PI parameters. The sliding mode controller is proposed by [8] as a solution to the drawbacks of conventional linear PI control. The parameters are chosen. In the sliding mode control (SMC), which is not immune to system disturbances and parameter adjustment. Nevertheless, there are sluggish dynamic response faults, hysteresis, and communication delays. As a result, high-frequency chattering is introduced, which limits the system's ability to increase frequency.

Conversely, due to its straightforward design, model predictive control (MPC) is also extensively employed [9]. To determine the ideal switching state, optimise the value function of the ESS converter [10]. MPC strengthens the system's resilience while lowering interferences and disturbances. References [9] and [11] highlight how MPC performs better and is more resilient in closed loops when compared to the conventional PI control technique. In order to reduce the cost function and have the real current track the reference current, [11] offer the model predictive current control (MPCC) technique. Nevertheless, the control of the bus voltage is not taken into account. A model predictive voltage and power method is proposed by [12][13] to regulate the bidirectional dc-dc converter of the BESS. Ac/dc interlinking converter control is obtained from power technique.

This research study introduces an innovative model predictive control (MPC) technique called Enhanced MPC, which combines MPC with PI control. The DC microgrid framework is first created, and models of the energy storage converters are created. The enhanced MPC control strategyis developed using a systematic prediction model. This paper research on single phase PMW converters. The proposed scheme is multi-objective; DC voltage control and reactive powers when load is varied. Finally, the enhanced Model Predictive Control (MPC) is verified by simulation, thus validating it. System Configuration and Modelling of AC/DC Single Phase Converter

In the Fig. 1, It shows power flow schematic of a single-phase ac/dc converter which composed of four insulated gate bipolar transistors (IGBT) switches; S_1, S_2, S_3 and S_4. Harmonic series filters inductor L and resistance R are connected in the grid side while capacitor C is integrated with the dc side.

979-8-3503-8719-3/24/$31.00 ©2024 IEEE

Authorized licensed use limited to: DELHI TECHNICAL UNIV. Downloaded on November 09,2024 at 04:49:14 UTC from IEEE Xplore. Restrictions apply.

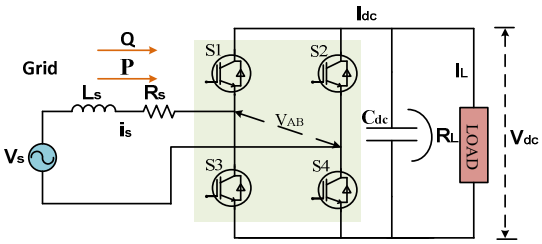

Fig. 1. Configuration of a single-phase AC/DC converter

The mathematical expression for the single-phase model is as follow;

$$\begin{bmatrix} L_s \dfrac{di_s}{dt} \\ C_{dc} \dfrac{dV_{dc}}{dt} \end{bmatrix} = \begin{bmatrix} -R_s & 0 \\ S_g & -1 \end{bmatrix} \begin{bmatrix} i_s \\ I_L \end{bmatrix} + \begin{bmatrix} V_s - V_{AB} \\ 0 \end{bmatrix} \quad (1)$$

Where V_s, i_s is a grid voltage, grid current; V_{AB} input voltages of the converter; I_L output current V_{dc} load voltage; S_g switching states which determines gate signal

$$S_g = \begin{cases} 1, & upper\ gate\ switches\ S_1 and\ S_2\ are\ ON \\ 0, & Lower\ gate\ switches\ S_3 and\ S_3\ are\ OFF \end{cases} \quad (2)$$

S_g is alternating hence ON and OFF are alternating between the upper and lower gate switches.

Both active power P and reactive power Q drawn from the grid can be calculated as follows:

$$\begin{cases} P = \dfrac{V_p I_P \cos\varphi}{2} \\ Q = \dfrac{V_p I_P \sin\varphi}{2} \end{cases} \quad (3)$$

Where V_p *and* I_p are peak voltage and current respectively; while φ displacement angle.

In three phase converters, park and Clarke transformation to achieve stationary α *and* β or $d-q$ coordinates in rotating orthogonal. In single phase, virtual two phase system is created by applying Helbert transformation formula [14]. The main components virtual transformation two-axis (α *and* β) are as follows;

$$\begin{cases} V_{s\alpha} = V_s = V_p \cos\omega t \\ V_{s\beta} = V_p \sin(\omega t) \end{cases} \quad (4)$$

$$\begin{cases} i_{s\alpha} = I_s = I_p \cos(\omega t - \varphi) \\ i_{s\beta} = I_p \sin(\omega t - \varphi) \end{cases} \quad (5)$$

From this fundamentals, active and reactive power can express as shown in $\propto$ *and* β form

$$\begin{cases} P = \dfrac{V_p I_P \cos\varphi}{2} = \dfrac{V_{s\alpha} I_{s\alpha} + V_{s\beta} I_{s\beta}}{2} \\ Q = \dfrac{V_p I_P \sin\varphi}{2} = \dfrac{V_{s\beta} I_{s\alpha} - V_{s\alpha} I_{s\beta}}{2} \end{cases} \quad (6)$$

Active power and reactive power of equation (6) is done and substituted the differential of i_s in equation one in orthogonal formation;

$$\begin{cases} \dfrac{dP}{dt} = \dfrac{1}{2L}[V_P^2 - (V_{s\alpha} V_{AB\alpha} + V_{s\beta} V_{AB\beta}) - 2RP] - \omega \\ \dfrac{dQ}{dt} = -\dfrac{1}{2L}[(V_{s\beta} V_{AB\alpha} - V_{s\alpha} V_{AB\beta}) - 2RQ] + \omega P \end{cases} \quad (7)$$

The equation (7) is very instrumental when implementing MPC controller

II. Proposed Enhanced MCP Scheme

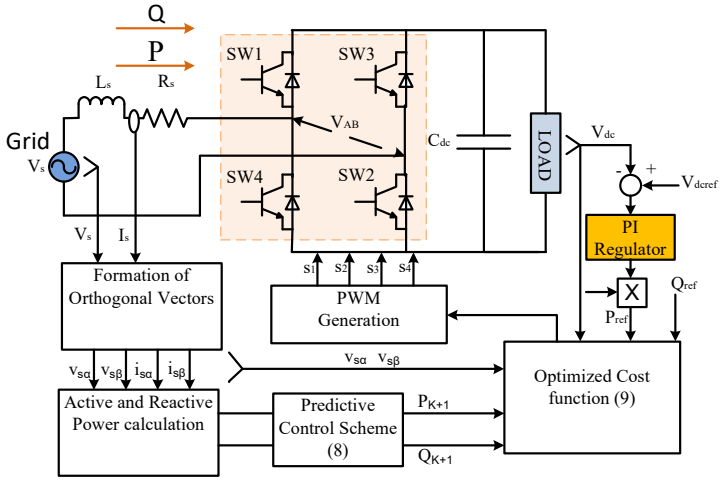

Fig. 2. Illustration of the enhanced MCP scheme

It is notable from Fig. 2 that primary goal of this controller aims to regulate active and reactive power of the system to response to any fluctuation. The MCP in this article allowed the desired power to flows. On the other hand, PI Controller regulates dc-link voltage to follow the given track. MCP is very susceptible to model discrepancies and potentially determinations of inaccurate model parameters [15].

Equation (7) can be sampled at intervals $(K+1,2,3\ldots..t)$ and ignore resistance since it is small hence ineffective.

$$\begin{cases} P(K+1) = P(K) - \omega T Q(K) + \dfrac{T}{2L}[V_P^2 - V_{g\alpha}(K) V_{AB\alpha} - V_{g\beta}(K) V_{AB\beta}(K)] \\ Q(K+1) = Q(K) + \omega T P - \dfrac{T}{2L}[(V_{g\beta}(K) V_{AB\alpha}(K) - V_{g\alpha}(K) V_{AB\beta}(K)] \end{cases} \quad (8)$$

The cost function employed for module optimization is in this system is shown in equation (9) [16].

$$J = \sqrt{(P - P_{actual})^2 + (Q - Q_{actual})^2} \quad (9)$$

Where P_{actual} *and* Q_{actual} are given desired active power and reactive power respectively.

A. DC bus voltage control

The DC bus voltage is determined by the power balance. When the grid power goes higher than the load demand, the DC voltage is high. Conversely, when the load demand power surpasses the grid power, the DC voltage is low [17]. The power absorbed by the power converter may be controlled by modifying the I_q and I_d references. To get

Authorized licensed use limited to: DELHI TECHNICAL UNIV. Downloaded on November 09,2024 at 04:49:14 UTC from IEEE Xplore. Restrictions apply.

a unity power factor, the value of I_q is set to zero, resulting in a reactive power $Q_S = 0$.

The deviation error in the actual voltage and measured voltage is used to attain the desired dc-link voltage;

$$\Delta V = V_{dc} - V_{dc,actual} \tag{10}$$

The optimized PI controller is used to reduce the error to zero

$$G_{\Delta V} = K_P + \frac{K_I}{S} \tag{11}$$

The dynamics of DC bus are:

$$\frac{C}{2}\frac{dV_{dc}(t)^2}{dt} = P_s - P_{load} \tag{12}$$

$$P_{load} = \frac{V_{dc}(t)^2}{R_{load}}, P_S = \frac{V_{sd}(t)I_{sd}(t)}{2} \tag{13}$$

$$\frac{C}{2}\frac{dV_{dc}(t)^2}{dt} + \frac{V_{dc}(t)^2}{R_{load}} = \frac{V_{sd}(t)I_{sd}(t)}{2} \tag{14}$$

The equation shown above utilizes I_q to regulate the voltage of the DC bus. Owing to the non-linear essence of the system with V_{dc}^2 , it is easiest to regulate the V_{dc}^2 in order to linearize the system under this control the V_{dc}.

$$\frac{C}{2}\frac{dV_{dc}(t)^2}{dt} + \frac{V_{dc}(t)^2}{R_{load}} = P_S(t) \quad \frac{V_{dc}(S)^2}{P_s(S)} = \frac{R_{load}}{(\frac{R_{load}C}{2}S+1)} \tag{15}$$

The analysis reveals that the dynamics of the current loop are much faster than those of the voltage loop.

$$\frac{I_d(S)}{I_{dactual}(S)} \approx 1 \tag{16}$$

The voltage loop gain is

$$G_{loop}(S) = \left(\frac{V_{dc}(S)^2}{P_s(S)}\right)\left(\frac{K_pS+K_i}{S}\right) = \left(\frac{2k_p}{Cs}\right)\left(\frac{s+\frac{k_i}{k_p}}{s+\frac{2}{R_{load}C}}\right) \tag{17}$$

$$V_{dc}(s)^2 = V_{dcactual}(s)^2 \frac{G_{loop}(s)}{1+G_{loop}(s)} \tag{18}$$

$$\frac{V_{dc}(s)^2}{V_{dcactual}(s)^2} = \frac{1}{1+\left(\frac{C}{2k_p}s\right)} \tag{19}$$

$$\frac{V_{dc}(s)^2}{V_{dcactual}(s)^2} = \frac{1}{1+(\tau_v s)} \tag{20}$$

$$s+\frac{k_i}{k_p} = s+\frac{2}{R_{load}C} \tag{21}$$

$$G_{loop}(s) = \left(\frac{2k_p}{Cs}\right) \tag{22}$$

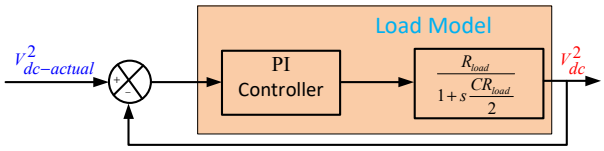

Fig. 3. Dc link voltage control

The assumption is that the voltage time constant (τ_v) should be at least 10 times greater than the current time constant (τ_i) in the current dynamics loop. However, τ_i is equal to 20 times the period of the switching frequency.

$$k_p = \frac{C}{2\tau_v}, k_i = \frac{1}{\tau_v R_{load}} \tag{23}$$

III. Simulations and Results Discussion

This section presents the simulation results produced from the Model Predictive Control (MPC) and the PI schemes. The simulations were conducted using the MATLAB/Simulink software, using a thorough ac/dc converter arrangement as shown in Figure 1. Table I displays the operational simulation and electrical parameters of the converter. It is important to mention that the intended voltage across the dc-link is 200 V. three scenarios were conducted, the first operation was done with the reference reactive power, Q_{actual}, is consistently set to 0 var to guarantee operation with a power factor of unity. The other two cases were considered with both lagging and leading power factor. It should be noted that, in the simulation, the PI values were derived from cascaded dynamic voltage loop, taking into account the overshoot and restoration time. It was simulated with $K_p = 67$ and $K_i = 0.25$.

A. Operation under increased active power consumed

Fig. 4 depicts the simulation results of active power tracking with unity power factor. At 0.5 s, abrupt load demand increase from 1.75kW to 2.5 kW. At this juncture, it is notable dc-link voltage maintained at 200V thanks to PI regulator. Reactive power Q remained 0 VAR before and after disturbances. In addition, PMW modulations enlarge to accommodate more active power. When connected, the source current I_S is in phase with the corresponding source voltage V_S simply because there is no reactive power transmitted. Fig. 4 depicts the

Authorized licensed use limited to: DELHI TECHNICAL UNIV. Downloaded on November 09,2024 at 04:49:14 UTC from IEEE Xplore. Restrictions apply.

representation of active power, reactive power, supply voltage and current, and PMW modulations. The performance of the suggested MCP controller was found to be exceptional.

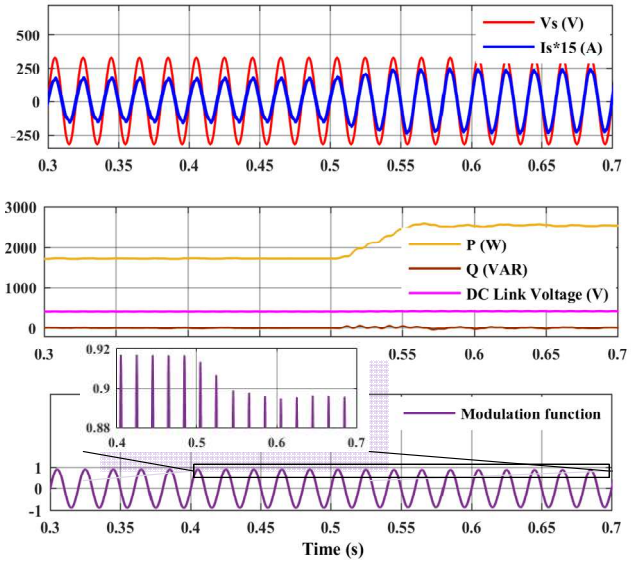

Fig. 4. The response due to increase active power consumed

B. *Operation under step down of reactive power from 0 to 0.4 kVAR*

It is observed in Fig. 5 that, active power is supplying a constant power of 1.2 kW. At 0.5 s, the source current, I_S, leads its phase voltage showing leading power factor waveform. The controller achieved its objective by maintaining dc link voltage and settling reactive power in 75 mS.

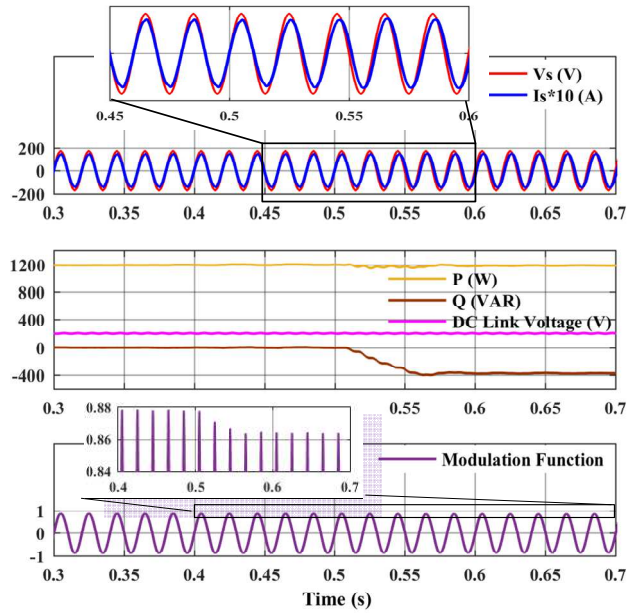

Fig. 5. The response due to Capacitive compensation (VAR)

C. *Operation under step up of reactive power from 0 to 0.4 kVAR*

In Fig. 6, it is noted that the active power remains constant at 1.2 kW. At a time of 0.5 seconds, step up change in system reactive power. The presence of a MCP controller allows the system to stabilize within 100 milliseconds, with the output voltage being regulated at 200 volts using a proportional-integral (PI) controller. The voltage and current waveforms exhibit a lagging power factor.

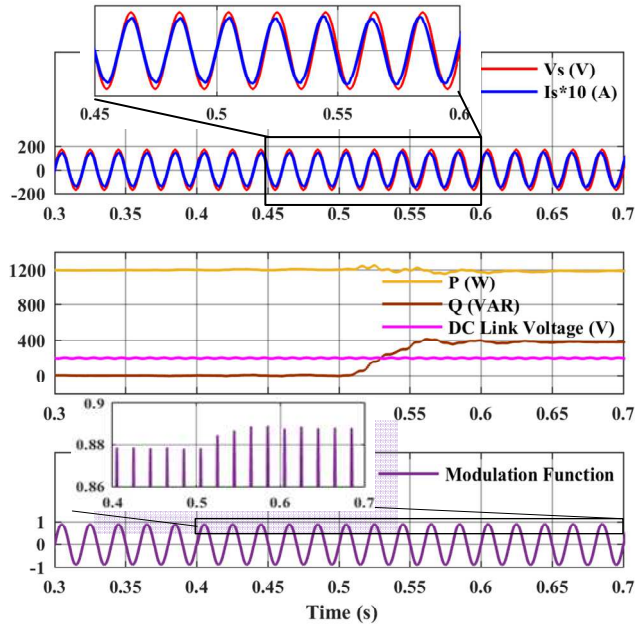

Fig. 6. The response due to Inductive compensation (VAR)

IV. Conclusion

In this article, it proposed MCP for active and reactive power control and PI controller for dc voltage control. Simulations were conducted to ascertain their effectiveness. The performance of the controllers is exceptional. The intended objectives have been successfully achieved in all three situations, with rapid dynamic and consistent steady state performance. The suggested approach prevents any overshoot or undershoot of the DC voltage. It is possible to independently regulate the DC voltage, active power, and reactive power. The proposed approach reduces the fluctuation in active power and minimizes distortion in the grid current. The use of cascaded dynamic voltage loop approach to fine-tune the Proportional-Integral (PI) parameters helps to avoid the demand of extensive computations.

References

[1] W. Wei *et al.*, "Reliability Assessment for AC/DC Hybrid Distribution Network with High Penetration of Renewable Energy," *IEEE Access*, vol. 7, pp. 153141–153150, 2019, doi: 10.1109/ACCESS.2019.2947707.

[2] D. Liang, C. Qin, S. Wang, and H. Guo, "Reliability evaluation of DC distribution power network," *China Int. Conf. Electr.*

Authorized licensed use limited to: DELHI TECHNICAL UNIV. Downloaded on November 09,2024 at 04:49:14 UTC from IEEE Xplore. Restrictions apply.

Distrib. CICED, pp. 654–658, 2018, doi: 10.1109/CICED.2018.8592284.

[3] P. Yegon and M. Singh, "Frequency Stability Enhancement of Microgrid Using Optimization Techniques-Based Adaptive Virtual Inertia Control," *Int. Trans. Electr. Energy Syst.*, vol. 2023, 2023, doi: 10.1155/2023/2121721.

[4] S. K. Kim, D. K. Choi, K. B. Lee, and Y. Il Lee, "Offset-Free Model Predictive Control for the Power Control of Three-Phase AC/DC Converters," *IEEE Trans. Ind. Electron.*, vol. 62, no. 11, pp. 7114–7126, 2015, doi: 10.1109/TIE.2015.2436353.

[5] X. Chen *et al.*, "Distributed Cooperative Control of Multiple Hybrid Energy Storage Systems in a DC Microgrid Using Consensus Protocol," *IEEE Trans. Ind. Electron.*, vol. 67, no. 3, pp. 1968–1979, 2020, doi: 10.1109/TIE.2019.2898606.

[6] S. K. Kollimalla, M. K. Mishra, A. Ukil, and H. B. Gooi, "DC Grid Voltage Regulation Using New HESS Control Strategy," *IEEE Trans. Sustain. Energy*, vol. 8, no. 2, pp. 772–781, 2017, doi: 10.1109/TSTE.2016.2619759.

[7] R. Kadri, J. P. Gaubert, and G. Champenois, "An Improved maximum power point tracking for photovoltaic grid-connected inverter based on voltage-oriented control," *IEEE Trans. Ind. Electron.*, vol. 58, no. 1, pp. 66–75, 2011, doi: 10.1109/TIE.2010.2044733.

[8] D. B. Wickramasinghe Abeywardana, B. Hredzak, and V. G. Agelidis, "A Fixed-Frequency Sliding Mode Controller for a Boost-Inverter-Based Battery-Supercapacitor Hybrid Energy Storage System," *IEEE Trans. Power Electron.*, vol. 32, no. 1, pp. 668–680, 2017, doi: 10.1109/TPEL.2016.2527051.

[9] Y. Shan, J. Hu, Z. Li, and J. M. Guerrero, "A Model Predictive Control for Renewable Energy Based AC Microgrids Without Any PID Regulators," *IEEE Trans. Power Electron.*, vol. 33, no. 11, pp. 9122–9126, 2018, doi: 10.1109/TPEL.2018.2822314.

[10] P. Yegon, "Optimization of battery / ultra-capacitor hybrid energy storage system for frequency response support in low-inertia microgrid," no. November 2023, pp. 1–15, 2024, doi: 10.1049/pel2.12723.

[11] X. Zhang, B. Wang, U. Manandhar, H. Beng Gooi, and G. Foo, "A Model Predictive Current Controlled Bidirectional Three-Level DC/DC Converter for Hybrid Energy Storage System in DC Microgrids," *IEEE Trans. Power Electron.*, vol. 34, no. 5, pp. 4025–4030, 2019, doi: 10.1109/TPEL.2018.2873765.

[12] Y. Shan, J. Hu, K. W. Chan, Q. Fu, and J. M. Guerrero, "Model Predictive Control of Bidirectional DC-DC Converters and AC/DC Interlinking Converters-A New Control Method for PV-Wind-Battery Microgrids," *IEEE Trans. Sustain. Energy*, vol. 10, no. 4, pp. 1823–1833, 2019, doi: 10.1109/TSTE.2018.2873390.

[13] M. Singh and A. Chandra, "Control of PMSG based variable speed wind-battery hybrid system in an isolated network," *2009 IEEE Power Energy Soc. Gen. Meet. PES '09*, pp. 1–6, 2009, doi: 10.1109/PES.2009.5275419.

[14] M. Saitou, N. Matsui, and T. Shimizu, "A Control Strategy of Single-phase Active Filter Using a Novel d-q Transformation," *Conf. Rec. - IAS Annu. Meet. (IEEE Ind. Appl. Soc.*, vol. 2, no. 2, pp. 1222–1227, 2003, doi: 10.1109/ias.2003.1257706.

[15] S. Kouro, P. Cortés, R. Vargas, U. Ammann, and J. Rodríguez, "Model predictive control - A simple and powerful Method to control power converters," *IEEE Trans. Ind. Electron.*, vol. 56, no. 6, pp. 1826–1838, 2009, doi: 10.1109/TIE.2008.2008349.

[16] S. Vazquez, A. Marquez, R. Aguilera, D. Quevedo, J. I. Leon, and L. G. Franquelo, "Predictive Optimal Switching Sequence Direct Power Control for Grid-Connected Power Converters," *IEEE Trans. Ind. Electron.*, vol. 62, no. 4, pp. 2010–2020, 2015, doi: 10.1109/TIE.2014.2351378.

[17] G. Yadav and M. Singh, "Robust Control Design for Grid-Tied EV System with SOGI-Based Architecture in Wide Voltage Range Scenarios," *IEEE Int. Conf. Electr. Electron. Commun. Comput. ELEXCOM 2023*, no. August 2023, pp. 1–6, 2023, doi: 10.1109/ELEXCOM58812.2023.10370088.

Authorized licensed use limited to: DELHI TECHNICAL UNIV. Downloaded on November 09,2024 at 04:49:14 UTC from IEEE Xplore. Restrictions apply.

Co-published by
Institute of Fluid-Flow Machinery
Polish Academy of Sciences
Committee on Thermodynamics and Combustion
Polish Academy of Sciences

Copyright©2024 by the Authors under licence CC BY-NC-ND 4.0

http://www.imp.gda.pl/archives-of-thermodynamics/

Use of butanol, pentanol and diesel in a compression ignition engine: A review

Deepak Kumar[a*], Naveen Kumar[b], Rajiv Chaudhary[a]

[a]Department of Mechanical Engineering, Delhi Technological University, New Delhi, India, 110042
[b]Centre for Advanced Studies and Research in Automotive Engineering, Delhi Technological University, Delhi, India, 110042
*Corresponding author, kumar.deepak2501@gmail.com

Received: 12.07.2023; revised: 07.07.2024; accepted: 16.07.2024

Abstract

Using oxygenated alternative fuels in compression ignition (CI) engines is feasible for energy security problems and climate change. Alcohols are regarded as alternative fuels for compression ignition engines because of their excellent physicochemical features, emission, and combustion characteristics. Research on alcohols and their additions has progressed significantly in recent years. Several researchers have examined the combined effect of higher alcohol with diesel and their impact and challenged that concentrations of higher alcohol reduce harmful particulate emissions in CI engines. This paper mainly focused on the performance and emissions properties of higher alcohols like butanol and pentanol. Alcohol has a low energy content, typically affecting engine brake-specific fuel consumption (BSFC). Low-temperature combustion (LTC) in compression ignition engines can lower NO_x and smoke emissions, and improve the efficiency of the engine. LTC is done by combining higher alcohol with increased exhaust gas recirculation (EGR) rate and retarded fuel injection timing. The higher alcohol, along with the oxygen in the fuel reduces exhaust fumes, improves the air/fuel mixture by providing a longer ignition delay (ID), and can replace the fossil fuel like diesel (partially or whole) to allow efficient and clean combustion in CI engines. Finally, several significant findings and comments are provided regarding potential avenues for experimental research and future development. According to thorough analysis, bio-alcohols are considered to be a substitute fuel for CI engines.

Keywords: Diesel engines, Higher alcohol, Diesel, Butanol, Pentanol

Vol. 45(2024), No. 4, 27–35; doi: 10.24425/ather.2024.151994

Cite this manuscript as: Kumar, D., Naveen Kumar, N., & Chaudharya, R. (2024). Use of butanol, pentanol and diesel in a compression ignition engine: A review. *Archives of Thermodynamics*, 45(4), 27–35.

1. Introduction

The application of alternative fuels in the transportation and power-generating industries used in compression ignition (CI) engines is becoming increasingly significant [1]. This requirement becomes necessary because of two issues: decreased oil reserves, price instability, and emission regulations for human health and environmental preservation [2].

The petroleum industry is a crucial sector of the Indian economy, accounting for about 25% of the country's total energy consumption. However, India remains heavily reliant on imports to meet its domestic demand for crude oil, with nearly 80% of its crude oil requirements being imported [3]. India's oil demand is projected to rise from the current 4.7 million barrels per day (mb/d) to 6.7 mb/d in 2030 and 8.3 mb/d in 2050 [4]. Despite the high efficiency of CI engines, the primary pollutants emitted from diesel fuel are HC, NO_x, and CO [5].

Nomenclature

ABE – acetone-*n*-butanol-ethanol
ABED – ABE/diesel blends
BSFC – brake-specific fuel consumption
BTE – brake thermal efficiency
CI – compression-ignition
CN – cetane number
CO – carbon monoxide
CO_2 – carbon dioxide
CRDI – common rail direct injection
CV – calorific value
DI – direct injection
EGR – exhaust gas recirculation
HC – hydrocarbon
HCCI – homogeneous charge compression ignition
HRR – heat-release-rate
LHE – latent heat of evaporation
LHV – lower heating value
LTC – low-temperature combustion
NO_x – nitrogen oxides
PODEn – poly-oxy methylene dimethyl ethers
PPCI – partially-premixed-compression-ignition
RCCI – reactivity-controlled-compression-ignition
RSM – response surface methodology
SCR – selective catalytic reduction
HCOOH – formic acid
HCHO – formaldehyde

In recent years, various measures have been taken to reduce these exhaust gases from diesel engines by implementing regulations such as BS (brake-specific) standards, alternative fuels, etc. Among these measures, alternative biofuels have become essential because of the rising price of retrofitting CI (compression-ignition) engines, rising oil prices, and declining oil reserves [6]. Due to their abundant sources and self-contained oxygen properties, oxygenated fuels are gaining much attention as new alternative fuels. Alcohol [7], ester [8], ether [9], and other alcohol-based fuels are currently the primary oxygenated alternative fuels. Numerous experiments have shown that blending these fuels with diesel reduces smoke opacity and increases the ambiguous interactions between NO_x and soot [10,11].

Different alcohols, like methanol and ethanol, are currently used as alternative biofuels, and higher alcohols, like butanol, pentanol, etc. can also be used as alternative fuels in CI engines. By using these alcohols with diesel in CI engines, the particulate emissions can be decreased. Moreover, a few issues exist while using lower alcohol in diesel engines. Previous researchers have found that lower alcohols, such as methanol and ethanol, have less miscibility in diesel and might cause phase separation problems at low temperatures due to their poor chemical and physical characteristics [12]. Also, low-carbon alcohols have low CN (cetane number), low viscosity, and high latent heat of evaporation (LHE), impacting engine performance and emissions [13–15]. To address these issues, various approaches can be employed, including alcohol fumigation, dual injection, blending alcohol with diesel fuel, and creating alcohol-diesel fuel emulsions [16].

A double injection system or alcohol fumigation can productively solve the miscibility problems of alcohol/diesel fuel blends. Ghadikolaei et al. [17] examined that fumigation might solve the miscibility problem in the alcohol-diesel blend. In addition, Liu et al. [18] discovered the various consequences of ethanol/PODEn/diesel fuel blends on CI engines. They found that PODEn enhanced the emission and combustion features of CI engines. Phase separation problems can be reduced by adding co-solvents or emulsifiers in lower alcohol/diesel blends [19]. Higher alcohols have drawn more attention because of their high cetane number, energy density, mixing stability, and reduced moisture absorption compared to lower alcohols. Higher alcohols contain more carbon, are less hygroscopic, and are less polar. The suitability of neat butanol for CI engines is constrained by several factors. Its lower cetane number, diminished energy density, elevated heat of vaporization, potential corrosiveness to engine components, and compatibility issues with seals and gaskets all pose challenges. Moreover, the limited availability and underdeveloped infrastructure for butanol distribution exacerbate its practicality as a transportation fuel for CI engines. These properties contribute to ignition delays, incomplete combustion, reduced efficiency, heightened emissions, and reliability concerns. Nonetheless, despite these limitations, the environmental benefits of butanol, such as lower emissions, suggest potential avenues for improvement through fuel blending or the adoption of advanced engine technologies [20]. Therefore, the combination of higher alcohols such as butanol, pentanol, etc. along with diesel without the addition of emulsifiers or co-solvents does not cause phase separation problems. Higher alcohols can be utilized as solvents for alcohols like methanol and ethanol [21]. Secondly, they are less corrosive in nature because of their lower hygroscopicity and lower water content [22]. These alcohols have longer carbon chains than lower alcohols, which increases their CV (calorific values), CN, and density. Higher alcohol concentrations can also extend the ignition delay period, improving the premixed and diffusion combustion phases and thoroughly mixing the air and fuel.

Biobutanol and biopentanol are biofuels produced via fermentation processes, but they differ in microorganisms and pathways. Biobutanol, often derived from acetone-butanol-ethanol (ABE) fermentation by Clostridium bacteria, utilizes various feedstocks like sugar cane and cellulose-rich biomass. The process involves hydrolysis to break down feedstock into fermentable sugars, fermentation by bacteria yielding butanol, acetone, and ethanol, and distillation to separate butanol. Conversely, biopentanol production may involve the genetic engineering of microorganisms for pentanol synthesis, with similar feedstock options. Challenges include optimizing microbial strains for high yields and reducing production costs to compete with traditional fuels. Both biofuels represent promising alternatives necessitating ongoing research and development [23].

Integrating an economic analysis into the assessment of higher alcohol fuels entails evaluating their cost of production, including raw materials, processing, and infrastructure, alongside feedstock availability and price fluctuations. Assessing energy content and engine efficiency relative to conventional fuels is essential, as is considering the cost of infrastructure modifications. Market demand, price sensitivity, environmental and social costs, policy support, and long-term technological advancements all play pivotal roles in determining the economic viability and potential societal benefits of adopting higher alcohol

Table 1. Physicochemical properties of fuels [16,22,48].

Properties	Diesel	Methanol	Ethanol	*n*-Butanol	*n*-Pentanol
Mol. formula	$C_{12}H_{26}$-$C_{14}H_{30}$	CH_3-OH	C_2H_5-OH	C_4H_9-OH	C_5H_{11}-OH
Mol. weight (kg/kmol)	191–210	31.84	45.88	75.12	87.85
Density (kg/m^3) at 15℃	838	790.73	790.2	810.1	815.2
Flashpoint (℃)	72	11.5–12.5	14.5	27	48
Boiling point (℃)	181–358	65.2	79.3	116.2	138.1
Cetane number (CN)	51.5	5.5	8.2	16	17.82–20
LHE (kJ/kg)	252–288	1160.73	919.37	582.24	309.15
Water solubility at 20℃ (%weight)	Immiscible	Miscible	Miscible	8.1	1.9
C (%weight)	85.83	38.18	51.84	65.22	67.83
O (%weight)	0.0	50.10	35.23	22.15	19.05
H (%weight)	14.20	13.24	12.92	13.54	14.21
C/H ratio	5.98	3.08	3.92	5.02	5.06
Self-ignition temperature (°C)	248–302	385	363	343	298
LHV (MJ/kg)	44.15	20.04	27.08	34.17	34.92
Vapour pressure (mmHg)	0.42	126.5	54.6	6.8	6.8
Saturation pressure (kPa) at 38℃	2.08	32.02	14.06	2.94	4.18
Lubricity (µm corrected wear scar)	314.8	1109.2	1056.5	592.10	677.15
Kinematic viscosity at 40℃ (mm/s^2)	3.45	0.52	0.98	2.56	2.83

fuels. Higher alcohols have lower total production costs than lower alcohols in terms of price. To control fuelling in internal combustion engines using either fossil fuel or biodiesel, various strategies are employed to optimize engine performance and emissions. Two primary approaches are commonly focused on: maintaining a constant initial injection angle or optimizing the combustion phasing, typically measured by the CA50 angle (the crank angle at which 50% of the fuel mass has burned) [24]. Research trends indicate that while maintaining a constant initial injection angle provides a useful baseline, optimizing the CA50 angle generally yields better efficiency, performance, and emissions outcomes. This optimization is especially critical for biodiesel due to its distinct combustion properties compared to fossil fuels. Consequently, modern engine control strategies often include CA50 optimization to adapt to varying fuel characteristics and operating conditions, ensuring optimal engine performance and reduced environmental impact.

Yanai et al. [25] examined the consequences of neat butanol and found that the performance and emission features of the engine are affected by the spray characteristics and advanced injection angle strategy. Gautam et al. [26] have also found that the CO emission decreased and BTE (brake thermal efficiency) increased with the advancement in injection angle. By using RSM (response surface methodology), Kumar et al. [27] observed the impact of different factors on CI engines and concluded that fuel injection pressure seriously influences the performance and emissions behaviour of CI engines. Low-temperature combustion (LTC) is a promising strategy for simultaneously reducing NO_x and smoke emissions while enhancing combustion efficiency. LTC is characterized by a well-prepared premixed fuel/air mixture that combusts at lower temperatures after an extended ignition delay. The most effective methods to achieve LTC include using exhaust gas recirculation (EGR) and delaying the injection timing. Combustion tests were conducted in an optically accessible diesel engine using a 20% butanol/diesel blend under varying injection timings and EGR rates. A partially premixed low-temperature combustion (LTC) was achieved with late injection timing combined with a high EGR rate of 50%. This resulted in significant reductions in smoke and NO_x emissions, with a minor decrease in efficiency [28].

For instance, RCCI (reactivity-controlled-compression-ignition) [29], PCCI (partially-premixed-compression-ignition) [30], and HCCI (homogeneous charge compression ignition) [31] have demonstrated the ability to achieve the most stringent emissions standards in the transportation sectors. Higher alcohol PFI (port fuel injection) and diesel DI (direct injection) can produce RCCI. The combustion phase may be more readily controlled, a more comprehensive operating range is attained, the efficiency of diesel engines is substantially improved, and extremely low NO_x and particulate matter emissions are maintained. However, because of its physicochemical characteristics, increasing alcohol consumption in compression ignition engines typically impacts the performance of the engines. While using higher alcohols in compression ignition engines, including nanoparticles [32] and polymethyl dimethyl ether [33] can also enhance the performance of the engines.

The primary goal of this study is to present a thorough analysis of higher alcohol and its impacts on CI engines' performance, combustion, and emissions. Numerous researchers and scientists have examined butanol and pentanol in various ratios with diesel to see whether or not they are suitable as fuel for the current diesel engines. The recent research and prior results about replacing (fully or partially) fossil fuel with these alcohols in compression ignition engines were usually successful since they increased the fuel's renewable fraction while reducing regulated emissions and improving efficiency.

2. Butanol as fuel in CI engine

Butanol, saturated hydrocarbon, is a straight-chain alcohol having 4-carbon atoms mainly extracted from fossil fuels and bio-derived substances. Despite this, both butanol and pentanol have similar physicochemical properties and give identical results when used in CI engines. Butanol can be added in significant proportion to diesel fuel and used; however, it is not suitable for the complete replacement of diesel directly in diesel engines due to the different properties than diesel (see Table 1). Butanol/diesel blends are one of several possibilities for making diesel engines suitable with alcohol. Due to the hydrophilic nature of methanol and ethanol, it does not form a proper mixture with

diesel as they become separated into different liquid phases over several periods, and it gives undesirable effects while using them in diesel engines. Hence, it requires an additional co-solvent to attain a better blend with diesel. Butanol exhibits better miscibility characteristics with diesel blends because of its lower polarity [34]. No emulsifying agents are required for diesel/butanol blends as they do not undergo phase separation even after many days [35].

Moreover, it acts as a solvent for methanol/diesel fuel blends [36] and ethanol/diesel fuel blends [37–39] while used in CI engines. Although blending can be completed either splash-blended in the storage reservoir right before distribution or in-line at the terminal, a specific manufacturing facility is not required to handle the stable diesel/butanol fuel blend due to its ease of attainment [40]. Another significant benefit is that butanol may be blended into diesel at larger ratios, indicating that perhaps the fuel has a more substantial share of renewable energy. According to several studies, using butanol/diesel mixes, butanol can substitute up to 40% of diesel fuel without requiring significant changes to the current engine system [41].

The low heating value (LHV) of a fuel impacts the engine's power production. Because alcohol's heating value rises as carbon atoms increase, butanol has a higher heating value compared to lower alcohols like methanol and ethanol. However, butanol has a 23% lesser LHV than diesel; therefore, it requires a higher quantity of diesel-butanol blended fuels to obtain equal power output from the engine. As the number of carbon atoms grows, alcohol's volatility and auto-ignition temperature drop. Therefore, diesel/butanol mixtures do not impact the ignition issues at various low-load settings [42]. It lowers the CN of blends with diesel, reduces auto-ignition properties and lengthens ignition delay. Direct application of these higher alcohols in unmodified CI engines is prohibited for this very reason.

2.1. Combustion, performance and emission behaviour of butanol

An exhaustive research review on the effects of blending butanol with diesel in various kinds of CI engines is shown in Table 2.

2.2. Summary

According to the above literature review, adding butanol to diesel has various effects on the CI engine performance and emissions:

1. More butanol content in diesel/butanol blends lowers the fuel's CN, increases ignition delay (ID), and increases the maximum heat release rate (HRR).
2. The peak pressure inside the engine cylinder improves the premixed phase of combustion, increases BTE, reduces indicated torque, power and IMEP (indicated mean effective pressure), and increases CO and HC emissions.
3. Combustion temperatures of diesel/butanol blends are low at medium and low loads, and which also, due to the lower calorific value and higher LHE of butanol as compared to diesel, reduce NO_x emissions. Alternatively, increased NO_x emissions are caused by an extended premixed combustion phase due to the higher combustion temperatures at high loads.
4. Butanol increases combustion by increasing the distillation and viscosity of biodiesel/butanol blends, increasing the BTE and decreasing soot particles, CO, and unburnt hydrocarbon emissions but lowering BSFC. Its higher distillation temperature, in comparison to ethanol, aids in superior fuel vaporization, thereby enhancing the combustion process.
5. When PODEn is added to diesel blend (DB), it increases the CN, which decreases the delay period while increasing HC, NO_x, and exhaust emissions while reducing soot emissions. Reducing the time intervals between the pilot and direct injections can help lower hydrocarbons and carbon monoxide emissions.

Adding butanol to biodiesel improves the BTE and increases BSFC while reducing ID period, cylinder pressure, maximum HRR, and NO_x, HC, and CO emissions. Simultaneously, the current research also suggests that ABE has a high potential for reducing butanol recovery costs and lowering soot and NO_x emissions.

Oxygen in fuel affects combustion and emissions, promoting complete oxidation and reducing CO and hydrocarbon emissions while potentially increasing NO_x. It also influences soot and particulate matter formation, favouring smaller particles in oxygen-rich environments [43]. Understanding oxygen's role is crucial for emission control strategies, offering opportunities to mitigate emissions. Balancing oxygen content is essential for efficient combustion with minimal environmental impact, enhancing sustainability in combustion-related activities for cleaner air and improved environmental health.

The mixed results observed in studies on using higher alcohols as fuel in diesel engines – where some parameters increase in some studies and decrease in others – can be attributed to factors such as variations in fuel composition, engine types, measurement techniques, environmental conditions, and data analysis methods. Addressing these factors can help researchers reach more definitive conclusions about the use of higher alcohols in diesel engines, potentially leading to optimized formulations and enhanced performance and emissions profiles. Additionally, several studies indicated that combining higher alcohols with nanoparticles might enhance engine performance by boosting combustion and reducing emissions.

3. Pentanol as fuel in CI engine

Pentanol is also a saturated higher alcohol with 5-carbon atoms having a higher CN, a higher energy density, a more stable pentanol-diesel blend, and a less moisture-absorbing tendency than other lower alcohols. Pentanol is more similar to diesel fuel in comparison to other alcohols in terms of its latent heat of vaporisation, viscosity, and density. It can be manufactured using biological processes such as biosynthesis of glucose using bacteria (Escherichia coli) and natural fermentation using engineered microorganisms [44]. Pentanol is a fantastic sustainable fuel for CI engines.

Table 2. An overview of studies of blended butanol/diesel fuels in various types of compression ignition engines.

Ref.	Engine	Fuels used	Test conditions/ variables	Blend designation	Performance BSFC	Performance BTE	NOx	Soot	HC	CO
[49]	4-cylinders, 16-valve	Diesel + *n*-butanol	2000 rpm, 4000 rpm	20% NB	↑	↑	↑		↓	↑
				30% NB	↑	↑	↑		↓	↑
				40% NB	↑	↑	↑		↑	↑
[50]	4-stroke, 1-cylinder	Diesel + butanol isomers	3000 rpm	10% NB	↑	↑				
[51]	4-stroke, 1-cylinder	Diesel + butanol isomers	2000 rpm	8%, 16%, 24% NB			↓	↓		
[52]	4-stroke, 4-cylinder, 4-valve, VGT	Diesel + butanol isomers	1400 rpm	50% NB	↑		↑	↓	↑	↑
				50% IB	↑		↑	↓	↑↑	↑
				50% SB	↑		↑	↓	↑↑	↑↑
				50% TB	↑		↑	↓	↑↑	↑
[53]	4-stroke, 4-cylinder, DI	Diesel + methanol + *n*-butanol	2000 rpm	10%, 15% NB			↓	↓	↓	↓
[54]	4-cylinder, DI	Diesel + ethanol + *n*-butanol	1600 rpm	5 %, 10 %, 13 %, and 18 %NB	↑	↑	↓ LL ↑ HL	↓		↓
[55]	4-cylinders, 16 valves	Diesel + *n*-butanol + PODEn	Injection strategy 1600 rpm	20% NB 20% PODEn			↑	↓		↓
[56]	4-stroke, 2-cylinder, CRDI engine	Diesel + butanol + DEE	1600 rpm	85% diesel 15% NB doped with 0.3% DEE	↓	↑	↓			↓
[57]	4-stroke, 4-cylinder	Diesel + butanol	1800 rpm	80% diesel, 20% NB			↓		↑	↑
[58]	4-stroke, 1-cylinder, diesel engine	Diesel, mango seed, butanol	1500 rpm	75% diesel 20% MS 0%, 5%, 10%, and 15% butanol	↓	↑	↓		↓	↓
[59]	4-stroke, 1-cylinder	Diesel +ABE	1200 rpm	80 % diesel, 20 %ABE			↓	↑	↑	↑
[60]	4-stroke, 1-cylinder, DI, diesel engine	Diesel + alcohol + Al_2O_3 nanoparticles	1200 rpm	84% diesel, 16% *n*-butanol doped with Al_2O_3 nanoparticles			↑	↑ LL ↓ HL	↓	↓

Note: ↑↑ means increased substantially by, / – not changed significantly by, ↓ – decreased by, ↑ – increased by, NB – *n*-butanol, TB – *tert*-butanol, IB – isobutanol, DEE – diethyl ether, MS – mango seed, SB – *sec*-butanol, ABE – acetone–butanol–ethanol, VGT – variable geometry turbocharger, LL – low-load, HL – high-load.

Even after long days, pentanol diesel blend fuel exhibits improved blend stability without phase separation [45]. Pentanol and diesel have comparable viscosities; however, pentanol/diesel mixtures often have a lower density than pure diesel fuel. Pentanol/diesel blends could help to achieve better atomization and combustion of fuels in CI engines. Pentanol/diesel mixes have flashpoints exceeding 37.8°C, making them inflammable from a safety perspective. The CFPP (cold filter plugging point) behaviour of pentanol/diesel blends are below the limit as per EN 116 standards [46].

3.1 Combustion, performance and emission behaviour of pentanol

An exhaustive research review on the effects of blending pentanol along with diesel in various kinds of CI engines is shown in Table 3.

Table 3. An overview of studies on using blended pentanol/diesel fuels in various types of compression ignition engines (for legend see Table 2).

Ref.	Engine	Fuels used	Test conditions/ variables	Blend designation	Performance BSFC	Performance BTE	NO_x	Soot	HC	CO
[61]	1-cylinder	Diesel + *n*-pentanol	1500 rpm,		↑	↓	↓ LL ↑ HL		↑	↑
[62]	4-cylinder	Diesel + pentanol		Diesel/n-pentanol blends				↑		↑
[63]	4-stroke, 1-cylinder, DI	Diesel + pentanol	1500 rpm	Diesel/n-pentanol blends	↑	↓			↑	↑
[64]	4-stroke, 1-cylinder, DI	Diesel + pentanol	3000 rpm	10% NP	↑	↓				
[65]	1-cylinder diesel engine	1-pentanol/diesel blend	2000 rpm	10%, 20%, and 30%	↑	↓	↓	↓	↑	↑
[66]	4-stroke engine	Diesel-Jatropha-pentanol	1500 rpm	J20 D65 P15		↓	↑	↓	↓	↑
[67]	4-stroke, 4-cylinder, diesel engine	waste oil-derived biodiesel, diesel, and pentanol	1800 rpm indirect-injection	79.09% diesel, and 12.58% 1-pentanol 8.33% WOB	↑	↓	↓		↓	↓
[68]	4-stroke, 1-cylinder, diesel engine	Diesel–mahua methyl ester–pentanol	20 MPa to 50 MPa 2000 rpm	70% diesel 10% pentanol, and 20% MME biodiesel	↓	↑		↓	↓	↓
[69]	4 stroke, 1-cylinder	Diesel + biodiesel + pentanol		BD70 P30			↑		↓	↓
[66]	4-stroke 1-cylinder diesel engine	Diesel, Jatropha, biodiesel, and pentanol	1500 rpm	10%, 15% pentanol		↑	↑	↓	↓	↑

Note: WOB – waste oil-derived biodiesel, MME – mahua methyl ester, BD – diesel +biodiesel, P – pentanol.

3.2. Summary

According to the above literature review, adding pentanol to diesel has different effects on CI engine performance and emissions:

1. Pentanol-diesel blended up to 45% v/v can be used in CI engines without any modification or damage.
2. Pentanol-diesel blended up to 45% v/v can be used in CI engines without any modification or damage.
3. Several researchers conducted chemical modelling studies and kinetic tests to examine the principles of *n*-pentanol to employ pentanol as a next-generation biofuel. Data on oxidation, laminar flame velocity, reactivity flame instability, ignition delay time, species, and concentration are all included in the combustion modelling.
4. As the content of pentanol increases, the ID period increases due to the low CN of the pentanol/diesel blend fuel. Unlike diesel, higher peak cylinder pressures and higher premix HRRs are reported for pentanol-diesel blends.
5. Because of their lower viscosity and high oxygen concentration, pentanol/diesel blends enhance the performance of atomization and combustion compared to diesel. Generally, it offers much better thermal efficiency than other alcohols. However, the pentanol/diesel mixture slightly increases the engine's BSFC, so more fuel is required for the same performance.

The increased combustion temperature and oxygen content increase the NO_x emissions at very high loads while using pentanol/diesel blends as fuel. Pentanol/diesel blends have a lower cetane number due to the higher LHV of pentanol. Due to their increasing oxidizing properties, soot emissions decrease with increasing the pentanol content in diesel/pentanol blends. In CI engines, pentanol typically exhibits superior combustion, performance and emissions characteristics. Pentanol and its additives, like cetane number modifiers and nanoparticles, can simultaneously improve efficiency and reduce emissions in advanced combustion. Using pentanol in engines minimizes fossil fuel needs and reduces environmental pollution.

First-generation biofuels are derived from edible crops such as corn and sugarcane. Second-generation biofuels use non-edible sources, including plant materials like wood, agricultural residues, and municipal solid waste. Third-generation biofuels primarily come from algae and can also utilize carbon dioxide (CO_2) as a feedstock [47]. Oxygenated fuels and paraffinic fuels each have unique benefits and drawbacks. Oxygenated fuels are effective in lowering emissions and making use of renewable resources, although they struggle with lower energy density and compatibility issues. On the other hand, paraffinic fuels offer

high energy density and clean combustion, but they are more expensive to produce and less widely available. The decision to use one type of fuel over the other depends on the specific application, existing infrastructure, and environmental objectives.

4. Conclusions

Butanol and pentanol are second/third-generation biofuels made from lignocellulosic biomass in environmentally friendly ways that do not rely heavily on food crops. They are similar to traditional biofuels in that they can address environmental degradation and energy insecurity. The following findings have been derived from this thorough study of the applications of higher alcohols in CI engines:

- Compared to diesel, higher alcohol/diesel blends have higher premixed heat release rates and peak cylinder pressures. Brake thermal efficiency of engines is improved by applying higher alcohols such as butanol due to low cetane number. It also enhances the quality of fuel atomization as the mixture becomes less viscous and denser.
- The oxygenated nature of higher alcohols typically results in a reduction in particulate emissions. The use of pentanol in diesel engines reduces brake thermal efficiency.
- Increasing the amount of butanol in the butanol/diesel blend generally decreases NO_x emissions. However, at high loads, for pentanol-containing alcohol NO_x, emissions rise linearly with their content. Generally, higher alcohol levels lead to a rise in CO and HC emissions. For engines running on higher alcohol levels, EGR is the most common technique to reduce NO_x emissions, followed by delayed injection.
- Diesel/higher alcohols blended fuel that contains PODEn, or CN modifiers, increases the CN, shortens the ID, and reduces soot particles and CO emissions. Nanoparticles enhance the combustion chamber's superior mixing capability with fine atomization; due to this, their use improves engine brake thermal efficiency and reduces brake-specific fuel consumption. It has been discovered that the application of higher alcohols as well as nanoparticles can improve engine performance and lower its emissions.

The impact of butanol and pentanol blended with diesel is more significant on CI engine performance and emissions and requires further investigation at high altitudes and under time-dependent (transient) conditions such as changes in load, acceleration, and transient or rotary drive cycles. Furthermore, the study is necessary to apply higher alcohol levels in compression ignition engines, optimize combustion characteristics, and specify optimum blend fuel ratios for the stability and long-term durability of the engines.

References

[1] Singh, P., Varun, Chauhan, S.R., & Kumar, N. (2016). A review on methodology for complete elimination of diesel from CI engines using mixed feedstock. *Renewable and Sustainable Energy Reviews*, 57, 1110–1125. doi: 10.1016/j.rser.2015.12.090

[2] Panoutsou, C., Germer, S., Karka, P., Papadokostantakis, S., Kroyan, Y., Wojcieszyk, M., Maniatis, K., Marchand, P., & Landalv, I. (2021). Advanced biofuels to decarbonise European transport by 2030: Markets, challenges, and policies that impact their successful market uptake. *Energy Strategy Reviews*, 34, 100633. doi: 10.1016/j.esr.2021.100633

[3] IEA (2021), *India Energy Outlook 2021*. IEA, Paris. https://www.iea.org/reports/india-energy-outlook-2021

[4] IEA (2023), *Oil Market Report - April 2023*, IEA, Paris https://www.iea.org/reports/oil-market-report-april-2023.

[5] Nabi, Md.N. (2010). Theoretical investigation of engine thermal efficiency, adiabatic flame temperature, NO_x emission and combustion-related parameters for different oxygenated fuels. *Applied Thermal Engineering*, 30(8-9), 839–844. doi: 10.1016/ j.applthermaleng.2009.12.015

[6] Salvi, B.L., Subramanian, K.A., & Panwar, N.L. (2013). Alternative fuels for transportation vehicles: A technical review. *Renewable and Sustainable Energy Reviews*, 25, 404–419. doi: 10.1016/ j.rser.2013.04.017

[7] Yilmaz, N., Donaldson, A.B., & Johns, A. (2005). Some Perspectives on Alcohol Utilization in a Compression Ignition Engine. *SAE Technical Paper*, 2005-01-3135. doi: 10.4271/2005-01-3135

[8] Wu, G., Wang, X., Abubakar, S., Li, Y., & Liu, Z. (2021). A realistic skeletal mechanism for the oxidation of biodiesel surrogate composed of long carbon chain and polyunsaturated compounds. *Fuel*, 289, 119934. doi: 10.1016/j.fuel.2020.119934

[9] Jeevanantham, A.K., Nanthagopal, K., Ashok, B., Al-Muhtaseb, A.H., Thiyagarajan, S., Geo, V.E., Ong, H.C., & Samuel, K.J. (2019). Impact of addition of two ether additives with high speed diesel- *Calophyllum Inophyllum* biodiesel blends on NO_x reduction in CI engine. Energy, 185, 39–54. doi: 10.1016/j.energy.2019.07.013

[10] Atmanli, A., Ileri, E., & Yilmaz, N. (2016). Optimization of diesel–butanol–vegetable oil blend ratios based on engine operating parameters. *Energy*, 96, 569–580. doi: 10.1016/j.energy.2015.12.091

[11] Atmanli, A., & Yilmaz, N. (2018). A comparative analysis of n-butanol/diesel and 1-pentanol/diesel blends in a compression ignition engine. *Fuel*, 234, 161–169. doi: 10.1016/j.fuel.2018.07.015

[12] Fayyazbakhsh, A., & Pirouzfar, V. (2017). Comprehensive overview on diesel additives to reduce emissions, enhance fuel properties and improve engine performance. *Renewable and Sustainable Energy Reviews*, 74, 891–901. doi: 10.1016/j.rser.2017.03.046

[13] Li, L., Wang, J., Wang, Z., & Liu, H. (2015). Combustion and emissions of compression ignition in a direct injection diesel engine fueled with pentanol. *Energy*, 80, 575–581. doi: 10.1016/ j.energy.2014.12.013

[14] Ma, Y., Huang, R., Fu, J., Huang, S., & Liu, J. (2018). Development of a diesel/biodiesel/alcohol (up to n-pentanol) combined mechanism based on reaction pathways analysis methodology. *Applied Energy*, 225, 835–847. doi: 10.1016/j.apenergy.2018.05.065

[15] EL-Seesy, A.I., Waly, M.S., He, Z., El-Batsh, H.M., Nasser, A., & El-Zoheiry, R.M. (2021). Influence of quaternary combinations of biodiesel/methanol/n-octanol/diethyl ether from waste cooking oil on combustion, emission, and stability aspects of a diesel engine. *Energy Conversion and Management*, 240, 114268. doi: 10.1016/j.enconman.2021.114268

[16] Agarwal, A.K. (2007). Biofuels (alcohols and biodiesel) applications as fuels for internal combustion engines. *Progress in Energy and Combustion Science*, 33(3), 233–271. doi: 10.1016/j.pecs.2006.08.003

[17] Ghadikolaei, M.A., Yung, K.-F., Cheung, C.S., Ho, S.S.H., & Wong, P.K. (2020). Non-polar organic compounds, volatility and

oxidation reactivity of particulate matter emitted from diesel engine fueled with ternary fuels in blended and fumigation modes. *Chemosphere*, 249, 126086. doi: 10.1016/j.chemosphere.2020.126086

[18] Liu, H., Wang, X., Wu, Y., Zhang, X., Jin, C., & Zheng, Z. (2019). Effect of diesel/PODE/ethanol blends on combustion and emissions of a heavy duty diesel engine. *Fuel*, 257, 116064. doi: 10.1016/j.fuel.2019.116064

[19] Gao, Z., Wu, S., Luo, J., Zhang, B., Zhang, H., & Xiao, R. (2021). Optimize the co-solvent for methanol in diesel with group of oxygen-containing reagents: Molecular structure and intermolecular forces analysis. *Fuel Processing Technology*, 222, 106980. doi: 10.1016/j.fuproc.2021.106980

[20] Thakur, A.K., Kaviti, A.K., Singh, R., & Gehlot, A. (2020). An overview of butanol as compression ignition engine fuel. *International Journal of Energy for a Clean Environment*, 21(4), 333–354. doi: 10.1615/InterJEnerCleanEnv.2020033667

[21] Jin, C., Zhang, X., Han, W., Geng, Z., Tessa Margaret Thomas, M., Dankwa Jeffrey, A., Wang, G., Ji, J., & Liu, H. (2020). Macro and micro solubility between low-carbon alcohols and rapeseed oil using different co-solvents. *Fuel*, 270, 117511. doi: 10.1016/j.fuel.2020.117511

[22] Raman, R., & Kumar, N. (2019). The utilization of n-butanol/diesel blends in Acetylene Dual Fuel Engine. *Energy Reports*, 5, 1030–1040. doi: 10.1016/j.egyr.2019.08.005

[23] Visioli, L.J., Enzweiler, H., Kuhn, R.C., Schwaab, M., & Mazutti, M.A. (2014). Recent advances on biobutanol production. *Sustainable Chemical Processes*, 2, 15. doi: 10.1186/2043-7129-2-15

[24] Heywood, J.B. (2018). *Internal Combustion Engine Fundamentals* (2nd ed.). McGraw-Hill Education, New York.

[25] Yanai, T., Han, X., Reader, G.T., Zheng, M., & Tjong, J. (2015). Preliminary investigation of direct injection neat *n*-butanol in a diesel engine. *Journal of Energy Resources Technology*, 137(1), 012205. doi: 10.1115/1.4028519

[26] Gautam, R., Chauhan, B.S., & Chang Lim, H. (2022). Influence of variation of injection angle on the combustion, performance and emissions characteristics of Jatropha Ethyl Ester. *Energy*, 254C, 124436. doi: 10.1016/j.energy.2022.124436

[27] Kumar, M., Singh, V.K., Sharma, A., Ansari, N.A., Gautam, R., & Singh, Y. (2022). Effect of fuel injection pressure and EGR techniques on various engine performance and emission characteristics on a CRDI diesel engine when run with linseed oil methyl ester. *Energy & Environment*, 33(1), 41–63. doi: 10.1177/0958305X20983477

[28] Huang, H., Zhou, C., Liu, Q., Wang, Q., & Wang, X. (2016). An experimental study on the combustion and emission characteristics of a diesel engine under low temperature combustion of diesel/gasoline/n-butanol blends. *Applied Energy*, 170, 219–231. doi: 10.1016/j.apenergy.2016.02.126

[29] Žvar Baškovič, U., Vihar, R., Rodman Oprešnik, S., Seljak, T., & Katrašnik, T. (2022). RCCI combustion with renewable fuel mix – Tailoring operating parameters to minimize exhaust emissions. *Fuel*, 311, 122590. doi: 10.1016/j.fuel.2021.122590

[30] Nachippan, N.M., Parthasarathy, M., Elumalai, P.V., Backiyaraj, A., Balasubramanian, D., & Hoang, A.T. (2022). Experimental assessment on characteristics of premixed charge compression ignition engine fueled with multi-walled carbon nanotube-included Tamanu methyl ester. *Fuel*, 323, 124415. doi: 10.1016/j.fuel.2022.124415

[31] Gainey, B., Yan, Z., & Lawler, B. (2021). Autoignition characterization of methanol, ethanol, propanol, and butanol over a wide range of operating conditions in LTC/HCCI. *Fuel*, 287, 119495. doi: 10.1016/j.fuel.2020.119495

[32] Khan, H., Soudagar, M.E.M., Kumar, R.H., Safaei, M.R., Farooq, M., Khidmatgar, A., Banapurmath, N.R., Farade, R.A., Abbas, M.M., Afzal, A., Ahmed, W., Goodarzi, M., & Taqui, S.N. (2020). Effect of nano-graphene oxide and n-butanol fuel additives blended with diesel-Nigella sativa biodiesel fuel emulsion on diesel engine characteristics. *Symmetry*, 12(6), 961. doi: 10.3390/sym12060961

[33] Liu, X., Wang, H., Zheng, Z., & Yao, M. (2021). Development of a reduced primary reference fuel-PODE$_3$-methanol-ethanol-*n*-butanol mechanism for dual-fuel engine simulations. *Energy*, 235, 121439. doi: 10.1016/j.energy.2021.121439

[34] Lapuerta, M., García-Contreras, R., Campos-Fernández, J., & Dorado, M.P. (2010). Stability, Lubricity, viscosity, and cold-flow properties of alcohol−diesel blends. *Energy & Fuels*, 24(8), 4497–4502. doi: 10.1021/ef100498u

[35] Rakopoulos, D.C., Rakopoulos, C.D., Papagiannakis, R.G., & Kyritsis, D.C. (2011). Combustion heat release analysis of ethanol or n-butanol diesel fuel blends in heavy-duty DI diesel engine. *Fuel*, 90(5), 1855–1867. doi: 10.1016/j.fuel.2010.12.003

[36] Huang, Z., Lu, H., Jiang, D., Zeng, K., Liu, B., Zhang, J., & Wang, X. (2005). Performance and emissions of a compression ignition engine fueled with diesel/oxygenate blends for various fuel delivery advance angles. *Energy & Fuels*, 19(2), 403–410. doi: 10.1021/ef049855d

[37] Huang, J., Wang, Y., Li, S., Roskilly, A.P., Yu, H., & Li, H. (2009). Experimental investigation on the performance and emissions of a diesel engine fuelled with ethanol-diesel blends. *Applied Thermal Engineering*, 29(11-12), 2484–2490. doi: 10.1016/j.applthermaleng.2008.12.016

[38] Chandra, R., & Kumar, R. (2007). Fuel properties of some stable alcohol-diesel microemulsions for their use in compression ignition engines. *Energy & Fuels*, 21(6), 3410–3414. doi: 10.1021/ef0701788

[39] Asfar, K.R., & Hamed, H. (1998). Combustion of fuel blends. *Energy Conversion and Management*, 39(10), 1081–1093. doi: 10.1016/S0196-8904(97)00034-4

[40] Ahmed, I. (2001). Oxygenated diesel: Emissions and performance characteristics of ethanol-diesel blends in CI engines. *SAE Technical Paper*, 2001-01-2475. doi: 10.4271/2001-01-2475

[41] Al-Hasan, M.I., & Al-Momany, M. (2008). The effect of iso-butanol-diesel blends on engine performance. *Transport*, 23(4), 306–310. doi: 10.3846/1648-4142.2008.23.306-310

[42] Yao, M., Wang, H., Zheng, Z., & Yue, Y. (2010). Experimental study of n-butanol additive and multi-injection on HD diesel engine performance and emissions. *Fuel*, 89(9), 2191–2201. doi: 10.1016/j.fuel.2010.04.008

[43] Kozak, M., & Merkisz, J. (2022). oxygenated diesel fuels and their effect on PM emissions. *Applied Sciences*, 12(15), 7709. doi: 10.3390/app12157709

[44] Cann, A.F., & Liao, J.C. (2010). Pentanol isomer synthesis in engineered microorganisms. *Applied Microbiology and Biotechnology*, 85, 893–899. doi: 10.1007/s00253-009-2262-7

[45] Rajesh Kumar, B., & Saravanan, S. (2015). Effect of exhaust gas recirculation (EGR) on performance and emissions of a constant speed DI diesel engine fueled with pentanol/diesel blends. *Fuel*, 160, 217–226. doi: 10.1016/j.fuel.2015.07.089

[46] Campos-Fernandez, J., Arnal, J.M., Gomez, J., Lacalle, N., & Dorado, M.P. (2013). Performance tests of a diesel engine fueled with pentanol/diesel fuel blends. *Fuel*, 107, 866–872. doi: 10.1016/j.fuel.2013.01.066

[47] Dahman, Y., Dignan, C., Fiayaz, A., & Chaudhry, A. (2019). An introduction to biofuels, foods, livestock, and the environment. In *Biomass, Biopolymer-Based Materials, and Bioenergy* (pp. 241–

276). Woodhead Publishing. doi: 10.1016/B978-0-08-102426-3.00013-8

[48] Yilmaz, N., & Atmanli, A. (2017). Experimental evaluation of a diesel engine running on the blends of diesel and pentanol as a next generation higher alcohol. *Fuel*, 210, 75–82. doi: 10.1016/j.fuel.2017.08.051

[49] Chen, Z., Liu, J., Han, Z., Du, B., Liu, Y., & Lee, C. (2013). Study on performance and emissions of a passenger-car diesel engine fueled with butanol-diesel blends. *Energy*, 55, 638–646. doi: 10.1016/j.energy.2013.03.054

[50] Zhang, Z.-H., Chua, S.-M., & Balasubramanian, R. (2016). Comparative evaluation of the effect of butanol–diesel and pentanol-diesel blends on carbonaceous particulate composition and particle number emissions from a diesel engine. *Fuel*, 176, 40–47. doi: 10.1016/j.fuel.2016.02.061

[51] Rakopoulos, D.C., Rakopoulos, C.D., Giakoumis, E.G., Dimaratos, A.M., & Kyritsis, D.C. (2010). Effects of butanol–diesel fuel blends on the performance and emissions of a high-speed DI diesel engine. *Energy Conversion and Management*, 51(10), 1989–1997. doi: 10.1016/j.enconman.2010.02.032

[52] Pan, M., Tong, C., Qian, W., Lu, F., Yin, J., & Huang, H. (2020). The effect of butanol isomers on diesel engine performance, emission and combustion characteristics under different load conditions. *Fuel*, 277, 118188. doi: 10.1016/j.fuel.2020.118188

[53] Zhang, Z., Tian, J., Xie, G., Li, J., Xu, W., Jiang, F., Huang, Y., & Tan, D. (2022). Investigation on the combustion and emission characteristics of diesel engine fueled with diesel/methanol/n-butanol blends. *Fuel*, 314, 123088. doi: 10.1016/j.fuel.2021.123088

[54] Zhang, Z., Li, J., Tian, J., Dong, R., Zou, Z., Gao, S., & Tan, D. (2022). Performance, combustion and emission characteristics investigations on a diesel engine fueled with diesel/ ethanol /n-butanol blends. *Energy*, 249, 123733. doi: 10.1016/j.energy.2022.123733

[55] Huang, H., Li, Z., Teng, W., Zhou, C., Huang, R., Liu, H., & Pan, M. (2019). Influence of n-butanol-diesel-PODE$_{3\text{-}4}$ fuels coupled pilot injection strategy on combustion and emission characteristics of diesel engine. *Fuel*, 236, 313–324. doi: 10.1016/j.fuel.2018.09.051

[56] Sahu, T.K., & Shukla, P.C. (2022). Combustion and emission characteristics of butanol-diesel blend (B15) doped with diethyl ether, diglyme and ethyl diglyme in a CRDI diesel engine. *SAE Technical Paper*, 2022-01-1073. doi: 10.4271/2022-01-1073

[57] Yilmaz, N., Vigil, F., & Donaldson, B. (2022). Effect of n-butanol addition to diesel fuel on reduction of PAH formation and regulated pollutants. *Polycyclic Aromatic Compounds*, 43(10), 8785–8799. doi: 10.1080/10406638.2022.2153881

[58] Ahmad, K., & Saini, P. (2022). Effect of butanol additive with mango seed biodiesel and diesel ternary blends on performance and emission characteristics of diesel engine. *Energy Sources, Part A: Recovery, Utilization, and Environmental Effects*, 44(4), 9988–10005. doi: 10.1080/15567036.2022.2143954

[59] Duan, X., Xu, Z., Sun, X., Deng, B., & Liu, J. (2021). Effects of injection timing and EGR on combustion and emissions characteristics of the diesel engine fuelled with acetone-butanol-ethanol/diesel blend fuels. *Energy*, 231, 121069. doi: 10.1016/j.energy.2021.121069

[60] Chen, Q., Wang, C., Shao, K., Liu, Y., Chen, X., & Qian, Y. (2022). Analyzing the combustion and emissions of a DI diesel engine powered by primary alcohol (methanol, ethanol, *n*-butanol)/diesel blend with aluminum nano-additives. *Fuel*, 328, 125222. doi: 10.1016/j.fuel.2022.125222

[61] Rajesh Kumar, B., & Saravanan, S. (2015a). Effect of exhaust gas recirculation (EGR) on performance and emissions of a constant speed DI diesel engine fueled with pentanol/diesel blends. *Fuel*, 160, 217–226. doi: 10.1016/j.fuel.2015.07.089

[62] Huang, H., Lv, D., Zhu, J., Chen, Y., Zhu, Z., Pan, M., Huang, R., & Jia, C. (2018). Development and validation of a new reduced diesel/*n*-pentanol mechanism for diesel engine applications. *Energy & Fuels*, 32(9), 9934–9948. doi: 10.1021/ acs.energyfuels.8b02083

[63] Rajesh Kumar, B., & Saravanan, S. (2016). Effects of *iso*-butanol/diesel and *n*-pentanol/diesel blends on performance and emissions of a DI diesel engine under premixed LTC (low temperature combustion) mode. *Fuel*, 170, 49–59. doi: 10.1016/j.fuel.2015.12.029

[64] Zhang, Z.-H., Chua, S.-M., & Balasubramanian, R. (2016). Comparative evaluation of the effect of butanol-diesel and pentanol-diesel blends on carbonaceous particulate composition and particle number emissions from a diesel engine. *Fuel*, 176, 40–47. doi: 10.1016/j.fuel.2016.02.061

[65] Ashok, A., Gugulothu, S.K., Venkat Reddy, R., Burra, B., & Panda, J.K. (2022). A systematic study of the influence of 1-pentanol as the renewable fuel blended with diesel on the reactivity controlled compression ignition engine characteristics and Trade-off study with variable fuel injection pressure. *Fuel*, 322, 124166. doi: 10.1016/j.fuel.2022.124166

[66] Venkatesan, S.P., Sriharihara n, P., Rohith, B., Purusothaman, M., & Venkatesh, S. (2023). Study of the performance and emissions of diesel engines operating by blends of Jatropha biodiesel, diesel and pentanol. *Materials Today: Proceedings*, 72(4), 2513–2517. doi: 10.1016/j.matpr.2022.09.532

[67] Yilmaz, N., Atmanli, A., Hall, M.J., & Vigil, F.M. (2022). Determination of the optimum blend ratio of diesel, waste oil derived biodiesel and 1-pentanol using the response surface method. *Energies*, 15(14), 5144. doi: 10.3390/en15145144

[68] Ramachander, J., Gugulothu, S.K., Sastry, G.R., & Bhsker, B. (2022). An experimental assessment on the influence of high fuel injection pressure with ternary fuel (diesel-mahua methyl ester-pentanol) on performance, combustion, and emission characteristics of common rail direct injection diesel engine. *Environmental Science and Pollution Research*, 29, 119–132. doi: 10.1007/s11356-021-13909-3

[69] Ashok, A., Gugulothu, S.K., Reddy, R.V., & Burra, B. (2023). Influence of fuel injection timing and trade-off study on the RCCI engine characteristics of Jatropha oil-diesel blend under 1-pentanol dual-fuel strategies. *Environmental Science and Pollution Research*. 30, 98848–98857. doi: 10.1007/s11356-022-22039-3

YAR-Net: Yoga Asanas Recognition Network Based on Variational Autoencoder

Roli Kushwaha
Department of Electronics & Communication Engineering, Delhi Technological University
Delhi, India
rolikushwaha.bbd@gmail.com

Manjeet Kumar
Department of Electronics & Communication Engineering, Delhi Technological University
Delhi, India
manjeetchhillar@gmail.com

Dinesh Kumar
Department of Electronics & Communication Engineering, Delhi Technological University
Delhi, India
dineshkumar@dtu.ac.in

***Abstract*— Yoga is a holistic practice aimed at rejuvenating individuals physically, mentally, and spiritually. Despite rapid technological advancements, there remains ample room for computational exploration across various social domains. Yoga image analysis is a nascent field that aims at finding the exact location of yoga postures so that they can recognize the yoga asana more reliably. Yet, yoga asanas recognition is a challenging task that is worsened due to increased dimensionality, and the problem of segmentation, leading to difficulties in recognizing asanas with high precision. To address these challenges, a variational autoencoder-based Yoga asanas recognition network ($YAR-Net$) is proposed, capable of reliably identifying numerous yoga asanas. The proposed methodology incorporates segmentation from Mask Region-based Convolutional Neural Network (mR-CNN) to identify the Region of Interest (ROI) followed by feature extraction from segmented ROI utilizing Local Binary Patterns (LBP), Histogram of Oriented Gradients (HOG), and Edge features. Finally, recognition of yoga asanas is accomplished by $YAR-Net$ which provides the recognition accuracy of 97.46%, and 99.91% using benchmark datasets Yoga107 and YogaPoses, respectively. The results underscore the $YAR-Net's$ remarkable performance as compared to the state-of-the-art techniques.**

Keywords*— *Yoga Asanas Recognition, Variational Autoencoder, Convolution Neural Network, Mask R-CNN, Human Pose Estimation.

I. Introduction

Human body-pose estimation is a challenging issue in computer vision. Lately, there has been an increasing study focus on sports, yoga, and dancing positions as means to enhance health and well-being. These human body-pose estimation are considered a fine-grained image classification task because of the intricate movements of the body parts involved [1]. Unlike sports and dance, which may not be as accessible or feasible for everyone, yoga provides a more inclusive and adaptable approach to maintaining overall health for all categories of population [2]. Through yoga practice, one can achieve a union of personal consciousness with universal consciousness, symbolizing perfect harmony between body and mind, and between humans and nature. Yoga techniques may be roughly categorised into three groups: asana-based, breathing-based, and meditation-based. The asana-based yoga practice entails the execution of several bodily postures synchronised with controlled breathing. On the contrary, a yoga practice that is centred around meditation necessitates the act of dissociating oneself from disruptive ideas. Pranayama, a kind of yoga that focuses on breathing, includes deliberate and controlled inhalation and exhalation, resulting in improved breathing [3].

Yoga asanas are classified within the broader field of computer vision known as action recognition [4]. Yoga poses, specifically, consist of intricate positions that are too difficult to be accurately shown from a singular viewpoint [5], [6]. Also, when practicing yoga independently, the practitioner must maintain the accuracy of their posture. Engaging in incorrect posture might lead to severe health complications. To address this concern, there is a requirement for an advanced system that can accurately identify yoga asanas and analyse the practitioner's postures [7]. This article employs a yoga asanas identification network that is built on a variational autoencoder (VAE). The selection of VAE is motivated for three reasons: i) it is effective when data has high dimensional properties, ii) it can simultaneously reduce dimensionality and perform classification and (iii) VAEs are able to model complex probability distributions and to generate new samples [8], [9] . This makes the model useful in building better training datasets and this way the overall performance of the model will also improve.

To enhance the effectiveness of the recognition system, Mask Region-based Convolutional Neural Network (mR-CNN) is employed to identify the Region of Interest (ROI) followed by extraction of features; Local Binary Patterns (LBP) [10], Histogram of Oriented Gradients (HOG) [11], and Edge features [12] from the segmented ROI of yoga asanas. These features capture texture, shape, and boundary information, respectively, providing a comprehensive and robust representation of yoga asanas. Due to aforementioned advantages, the proposed methodology incorporates $YAR-Net$ based on VAE and multilayer perceptron (MLP) for recognition of various asanas. The process flow of the proposed methodology is shown in Fig. 1.

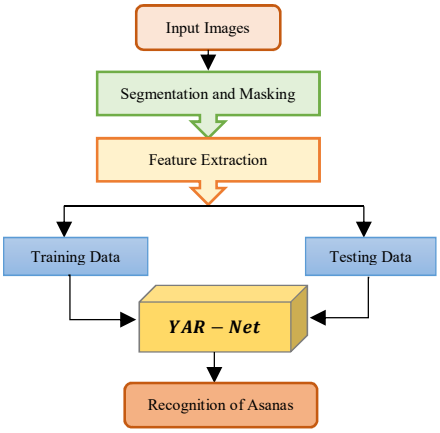

Fig. 1. The process flow of the proposed methodology for yoga asanas recognition.

2024 IEEE Region 10 Symposium (TENSYMP) | 979-8-3503-6486-6/24/$31.00 ©2024 IEEE | DOI: 10.1109/TENSYMP61132.2024.10752274

979-8-3503-6486-6/24/$31.00 ©2024 IEEE

Authorized licensed use limited to: DELHI TECHNICAL UNIV. Downloaded on November 25,2024 at 04:47:27 UTC from IEEE Xplore. Restrictions apply.

The rest of the paper is outlined as: Section II provides a concise overview of related studies. Section III discusses the proposed $YAR-Net$. The Benchmark dataset's description is in Section IV whereas, Section V shows the results and discussion of the $YAR-Net$. Lastly Section VI concludes the proposed methodology by discussing future scope.

II. Related Works

Yoga asanas recognition methodologies have been categorized based on the means of data collection: (a) wearable devices, (b) Kinect and (c) computer vision. Luo et al. [13] introduced a yoga training system that utilises a specialised outfit equipped with sixteen inertial measurement units and six tactors to identify motion characteristics using motion imitation techniques. In [14], authors presented a wearable sensor-based yoga recognition network to recognize eighteen static yoga poses by using backpropagation artificial neural networks to categorize yoga postures and fuzzy C-means to classify the yoga postures. Nevertheless, the act of donning many sensors on various body regions is impractical for the user in a real-life situation. Moreover, the intrusiveness of the device might impact the user's physical activity. To address this limitation various researchers applied vision-based approach for yoga asanas recognition. Rector et al. [15] developed eyes-free yoga, an exergame using a Kinect depth sensor for skeletal tracking and auditory feedback to teach six common postures to the blind and visually impaired. Patil et al. [16] proposed a 'yoga tutor' that uses the SURF algorithm to detect posture differences between beginners and experts, though it struggled to precisely describe and compare poses. Wu et al. [17] developed an expert system that utilizes problem-oriented study and the decision expert scheme to provide yoga training instructions through images and text, but it lacked posture analysis, so users couldn't confirm if they were performing asanas correctly.

Chen et al. [18] introduced a self-training system using a Kinect depth sensor to recognize twelve yoga asanas and assist practitioners in correcting their postures, but it required separate models for each asana and manual feature extraction, and depth-sensor cameras are not widely available. Gochoo et al. [19] devised an IoT-based yoga recognition system using deep CNNs and infrared sensors with wireless sensor network. Maddala et al. [20], developed a system that represents joint motion in 3D, tested on a dataset of 42 poses recorded with multiple cameras using single-stream CNN. Verma et al. [21], presented the Yoga-82 dataset with 28.4K images across 82 asana classes and tested with different CNN architectures for yoga asanas recognition. However, recognizing asanas from single images may lead to inaccuracies due to their sequential nature. Ashraf et al. [2] introduced a YoNet deep learning model, designed to identify five yoga poses from a subset of 82 poses in the Yoga-82 dataset, emphasizing hand-picked home-based exercises. In [22], a yoga recognition system was developed to classify six asanas, employing OpenPose to extract eighteen human body keypoints, which were then processed by a hybrid CNN and LSTM model. Similarly, Yadav et al. [23], presented a system for activity recognition and fall detection using a classification network based on pose estimation but system lacks in detecting accurate keypoints and intricate yoga poses. Yadav et al. [7] introduced YogNet, a multi-person yoga expert system utilizing a two-stream deep spatiotemporal neural network architecture for 20 asanas recognition, incorporating keypoint detection and time-distributed CNNs with LSTM networks. Pradeep et al. [24], introduced a classification method for yoga poses in a hierarchical manner by employing a three-stage transfer learning approach.

From the literature, it is evident that the subtle variations in yoga asanas are not recognized precisely. Also, vision-based yoga asanas recognition techniques are advantageous as they require no additional infrastructure, making data collection scalable and straightforward. So, this paper focuses on leveraging vision-based approach to achieve effiecient yoga asanas recognition using $YAR-Net$.

III. Proposed Methodology

The proposed methodology incorporates mR-CNN for segmentation and masking of yoga asanas ROI followed by extraction of LBP, HOG and Edge features from masked ROI. Finally, classification is executed by $YAR-Net$ which includes VAE and MLP. The detailed architecture of the proposed model $YAR-Net$ is shown in Fig. 2. Initially, images which are applied to the model are segmented using mR-CNN. The mR-CNN module exploits a two-stage procedure (i) first stage uses a region proposal network (RPN) to identify likely object regions and score their confidence and (ii) the second stage refines these proposals in parallel; classifying them (e.g., human, surroundings) and adjusting their bounding boxes for precise yoga asana localization. It utilizes a convolutional neural network for feature extraction, employs a RPN to identify yoga asana, and generates a binary mask.

This mask essentially delineates the exact pixels belonging to the human body within the image, even in poses where limbs might be overlapping or obscured. The mR-CNN's ability to differentiate the human body from the background and isolate it with a mask is crucial for accurate asana recognition. After segmentation of image, the model extracts LBP, HOG, and Edge features to capture texture, shape and boundary information. Further, the extracted features are fused to get a set of fused features as given:

$$Fused\ Features(\mathcal{F}) = (LBP; HOG; EDGE) \quad (1)$$

Building upon the rich information contained within the fused features, the proposed $YAR-Net$ now utilizes a VAE for recognition of yoga asanas. VAEs excel at learning latent representations that encode complex data, making them ideal for the yoga asanas recognition. By feeding $\mathcal{F}$ into the VAE, the model aims to extract even more compact and informative latent representations using encoder by producing mean vector μ and standard deviation vector Σ of the probability of latent variables using variational inference on the input data and reconstruct the compressed data into the original input using decoder. The encoder aims to learn a set of parameters ($\emptyset$) that enable it to compress the input data ($\mathcal{F}$) into a latent vector z.

Authorized licensed use limited to: DELHI TECHNICAL UNIV. Downloaded on November 25,2024 at 04:47:27 UTC from IEEE Xplore. Restrictions apply.

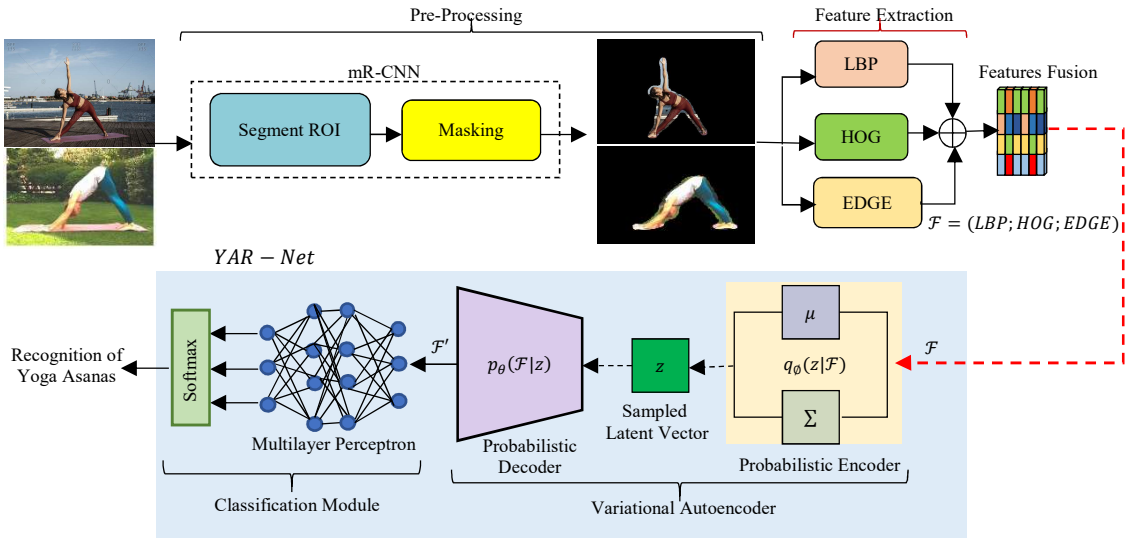

Fig. 2. The framework of the proposed methodology for recognition of yoga asanas.

This latent vector is then drawn from a Gaussian distribution with parameters $\emptyset$. Subsequently, the decoder takes the latent vector (z) as input. The decoder utilizes another set of parameters (θ) to model the reconstructed data $(\mathcal{F}')$, which reconstructs the probability distribution of the original data based on the probability distribution of the latent variable.

The encoder and decoder of VAE are probabilistic, represented by $q_\emptyset(z|\mathcal{F})$ as the approximate posterior and $p_\theta(\mathcal{F}|z)$ as the likelihood of the data $\mathcal{F}$ given the latent variable z, respectively as shown by:

$$q_\emptyset(z|\mathcal{F}) = \mathcal{N}_d(z; \mu_{z|\mathcal{F}}, {\Sigma_{z|\mathcal{F}}}^2 I_m) \quad (2)$$

$$p_\theta(\mathcal{F}|z) = \mathcal{N}_d(\mathcal{F}; \mu_{\mathcal{F}|z}, {\Sigma_{\mathcal{F}|z}}^2 I_m) \quad (3)$$

where $\mu_{z|\mathcal{F}}, \Sigma_{z|\mathcal{F}}$ and $\mu_{\mathcal{F}|z}, \Sigma_{\mathcal{F}|z}$ are derived from $\mathcal{F}$ and z, respectively with the corresponding variational parameters $\emptyset$ and θ, $\mathcal{N}_d$ is the normal distribution and I_m is the covariance or Identity matrix.

The objective of the VAE is to minimize the difference between the approximated posterior $q_\emptyset(z|\mathcal{F})$ and the true intractable posterior $p_\theta(\mathcal{F}|z)$. This difference is quantified using the Kullback–Leibler (KL) divergence $\mathcal{D}_{KL}(q_\emptyset(z|\mathcal{F})||p_\theta(\mathcal{F}|z))$.

However, since the KL divergence cannot be directly computed, it is minimized by maximizing the variational lower bound on the marginal likelihood of the individual data points $\mathcal{F}_i, i = 1, \ldots, n$. Consequently, the cost function $\mathcal{C}_{VAE}(\emptyset, \theta; \mathcal{F})$ which combines reconstruction loss $\mathbb{E}_{q_\emptyset(z|\mathcal{F}^{(i)})}[\log p_\theta(\mathcal{F}^{(i)}|z)]$ and KL divergence to achieve a balance between reconstructing the input data accurately and maintaining a well-behaved latent space of the VAE can be expressed as follows:

$$\mathcal{C}_{VAE}(\emptyset, \theta; \mathcal{F}) = \sum_{i=1}^{N} \mathbb{E}_{q_\emptyset(z|\mathcal{F}^{(i)})}[\log p_\theta(\mathcal{F}^{(i)}|z)] - \sum_{i=1}^{N} \mathcal{D}_{KL}(q_\emptyset(z|\mathcal{F}^{(i)})||p_\theta(z)) \quad (4)$$

where $\mathbb{E}$ denotes the expected value. It represents the average or mean value of a random variable over all possible outcomes, weighted by their probabilities and N is the number of training samples. The second term in eq. (4) measures the difference between the approximate posterior $q_\emptyset(z|\mathcal{F})$ and isotropic unit Gaussian $p_\theta(z) = \mathcal{N}_d(z; 0, I_m)$.

The term $\mathcal{D}_{KL}(q_\emptyset(z|\mathcal{F}^{(i)})||p_\theta(z))$ is represented as:

$$\sum_{i=1}^{N} \mathcal{D}_{KL}(q_\emptyset(z|\mathcal{F}^{(i)})||p_\theta(z)) = -\frac{1}{2}\sum_{i=1}^{N}\sum_{k=1}^{\mathcal{K}}(1 + \log\left(\left(\Sigma_k^{(i)}\right)^2\right) - \left(\mu_k^{(i)}\right)^2) \quad (5)$$

where $\mathcal{K}$ represents the dimensionality of the latent variables z and k refers to the k-th element of z.

After extracting a meaningful latent representation $(\mathcal{F}')$ from VAE, the model leverages a MLP classifier for yoga asana recognition. The MLP consists of several hidden layers that utilise activation functions, such as ReLU to facilitate the network's ability to understand complex, non-linear relationships between the latent representation and the yoga asanas classes. The last layer of the Multilayer Perceptron (MLP) has a Softmax activation function. This function converts the output vector from the last hidden layer into a probability distribution that encompasses all potential yoga asanas. Every element in the output vector indicates the likelihood of the input features corresponding to a particular yoga asana. By selecting the yoga asana with the highest probability score, the model effectively recognizes different the yoga asanas.

IV. Dataset

The datasets used for training and evaluation of the proposed $YAR - Net$, two datasets are utilized; YogaPose and Yoga107 datasets. The YogaPose [25] dataset is an open-source dataset consisting of seven yoga poses (Cobra, Chair, Dog, Shoulder stand, Triangle, Tree, and Warrior) and one no pose. The dataset contains 4400 images of

Authorized licensed use limited to: DELHI TECHNICAL UNIV. Downloaded on November 25,2024 at 04:47:27 UTC from IEEE Xplore. Restrictions apply.

different yoga postures. The Yoga107 dataset [26] is obtained from the Kaggle repository. It consists of 107 distinct categories of yoga postures, with a total of 5,900 high-resolution images. The yoga dataset is particularly complex due to the presence of over 100 classes. Some sample images of used datasets and the masked ROI is shown in Fig. 3.

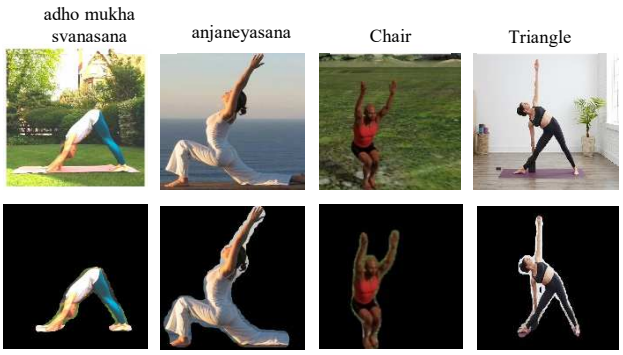

Fig. 3. Some sample images and their corresponding masked images of different yoga asanas.

V. Results and Discussions

The performance of the proposed $YAR-Net$ was gauged using metrics such as accuracy ($\mathcal{A}_c$), precision ($\mathcal{P}_r$), recall ($\mathcal{R}_l$), and F1 score ($\mathcal{F}_s$) as given in eqs. (6), (7), (8) and (9):

$$Accuracy\ (\mathcal{A}_c) = \frac{(T_p + T_n)}{(T_p + T_n + F_p + F_n)} \times 100 \quad (6)$$

$$Precison\ (\mathcal{P}_r) = \frac{T_p}{T_p + F_p} \times 100 \quad (7)$$

$$Recall\ (\mathcal{R}_l) = \frac{T_p}{T_p + F_n} \times 100 \quad (8)$$

$$F1\ Score\ (\mathcal{F}_s) = 2 * \frac{(\mathcal{P}_r * \mathcal{R}_l)}{(\mathcal{P}_r + \mathcal{R}_l)} \times 100 \quad (9)$$

where, T_p denotes true positives, T_n denotes true negatives, F_p is false positive, F_n is false negative outcomes.

The results exhibit promising performance, achieving recognition accuracies of 99.51% with the YogaPose dataset as shown by confusion matrix in Fig. 4, and 96.45% with the Yoga107 dataset. The performance metrics of the proposed model with each dataset is illustrated in Table I. Also, the recognition accuracy and loss of the $YAR-Net$, using both the datasets are shown by Fig. 5 (a) and (b), respectively. Some of the spatial and depth feature maps of the YogaPose and Yoga107 datasets from last layer of the $YAR-Net$ are shown in Fig. 6 and Fig. 7 respectively. The process of extracting edges and important features from the spatial feature mapping, together with the depth feature mapping that gives the location of the human body and depth information, helps in accurately classifying yoga asanas.

To evaluate the efficacy and efficiency of the proposed model relative to state-of-the-art techniques using similar datasets, a comprehensive comparison study is shown in Table II. The results shown in Table II highlight the exceptional performance of the $YAR-Net$ not only in terms of $\mathcal{A}_c$ but also in terms of $\mathcal{P}_r$, $\mathcal{R}_l$ and $\mathcal{F}_s$. This shows that model is able to recognize similar asanas or complex asanas accurately.

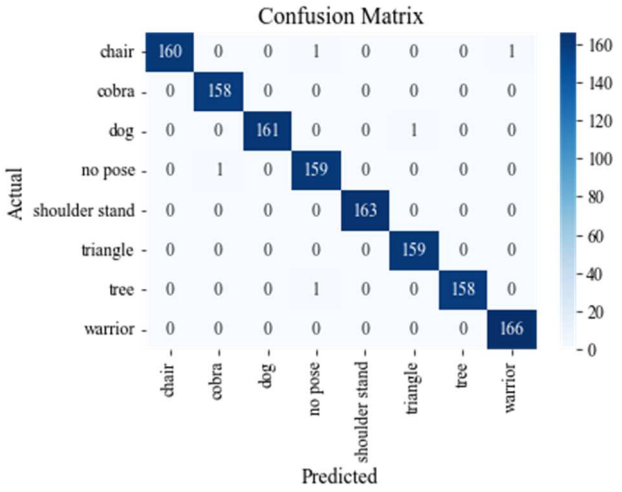

Fig. 4. Confusion matrix of proposed $YAR-Net$ using YogaPose dataset for yoga asanas recognition.

TABLE I. Performance Metrics of the Proposed $YAR-Net$ Using Both Datasets for Yoga Asanas Recognition

Dataset	A_c (%)	P_r (%)	R_l (%)	F_s (%)
YogaPose	99.91	99.68	99.34	99.51
Yoga107	97.46	96.13	96.79	96.45

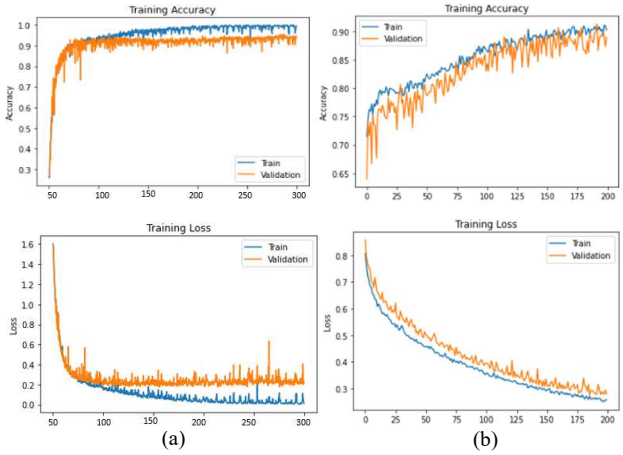

Fig. 5. Accuracy and loss curve vs epochs of the proposed $YAR-Net$ for yoga asanas recognition using (a) YogaPose dataset (b) Yoga107 dataset.

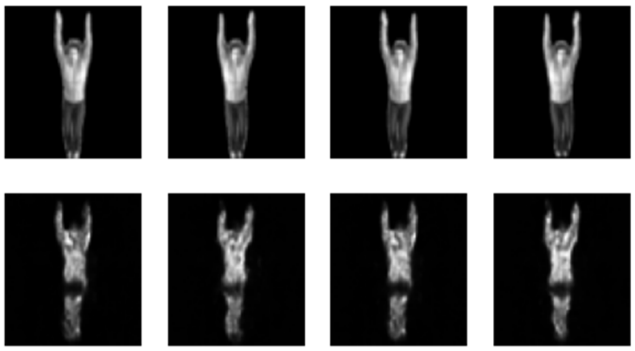

Fig. 6. Spatial feature maps from last layers of $YAR-Net$ for yoga asanas recognition using YogaPose dataset.

Authorized licensed use limited to: DELHI TECHNICAL UNIV. Downloaded on November 25,2024 at 04:47:27 UTC from IEEE Xplore. Restrictions apply.

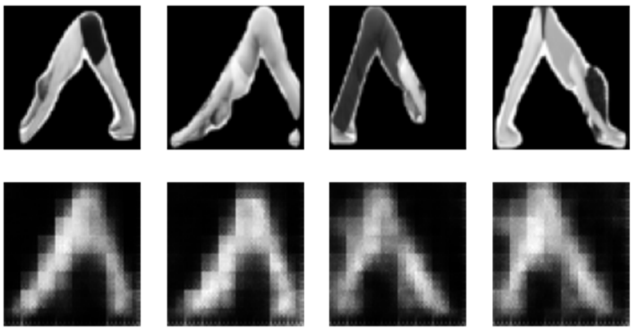

Fig. 7. Depth feature maps from last layers of $YAR-Net$ for yoga asanas recognition using Yoga107 dataset.

TABLE II. COMPARISON OF THE PROPOSED $YAR-Net$ FOR YOGA ASANAS RECOGNITION WITH STATE-OF-THE-ART TECHNIQUES

Dataset	Author	Method	A_c (%)
YogaPose	Nguyen et al. [27]	VGG-16	94.94
		VGG-19	95.70
		ResNet-101	94.54
		MobileNet	92.49
	Upadhyay et al. [25]	Y-PN-MSSD	99.88
	Proposed	$\boldsymbol{YAR-Net}$	**99.91**
Yoga107	Bera et al. [26]	SYD Net+ResNet50	85.04
		SYD Net+DenseNet201	87.17
		SYD Net+MobileNet-v2	85.14
		SYD Net+Xception	85.20
	Ashraf et al. [2]	YoNet	94.91
	Chollet [28]	Xception	89.83
	He et al. [29]	ResNet50	91.52
	Proposed	$\boldsymbol{YAR-Net}$	**97.46**

VI. CONCLUSION

Human pose estimation has long been a challenging task in computer vision. Consequently, the recognition of yoga asana is highly important due to its profound impact on human well-being. In this article, an efficient yoga asanas recognition network $YAR-Net$ based on variational autoencoder is proposed to recognize yoga asanas precisely. By integrating segmentation from mR-CNN and feature extraction techniques such as LBP, HOG, and Edge features, the $YAR-Net$ achieved noteworthy recognition accuracies. The results highlight the superiority of $YAR-Net$ over existing yoga asanas recognition methods, addressing the complexities of asanas recognition with higher precision and reliability.

In future endeavors, the focus is not only on the recognition of yoga asanas but also on developing techniques for correcting and enhancing the precision of the yoga asanas. Additionally, to address the challenges associated with multi-person yoga asana recognition, system will be developed that can provide real-time feedback for asanas correction of multiple persons.

REFERENCES

[1] C. S. Pradeep and N. Sinha, "CAM based fine-grained spatial feature supervision for hierarchical yoga pose classification using multi-stage transfer learning," *Expert Syst Appl*, vol. 249, p. 123625, Sep. 2024, doi: 10.1016/j.eswa.2024.123625.

[2] F. Bin Ashraf, M. U. Islam, M. R. Kabir, and J. Uddin, "YoNet: A Neural Network for Yoga Pose Classification," *SN Comput Sci*, vol. 4, no. 2, Mar. 2023, doi: 10.1007/s42979-022-01618-8.

[3] B. Xu, X. Shu, J. Zhang, G. Dai, and Y. Song, "Spatiotemporal Decouple-and-Squeeze Contrastive Learning for Semisupervised Skeleton-Based Action Recognition," *IEEE Trans Neural Netw Learn Syst*, 2023, doi: 10.1109/TNNLS.2023.3247103.

[4] K. Peng, A. Roitberg, K. Yang, J. Zhang, and R. Stiefelhagen, "Delving Deep Into One-Shot Skeleton-Based Action Recognition With Diverse Occlusions," *IEEE Trans Multimedia*, vol. 25, pp. 1489–1504, 2023, doi: 10.1109/TMM.2023.3235300.

[5] J. Li, D. Zhang, L. Shi, T. Ke, and C. Zhang, "An Improved High-Resolution Network-Based Method for Yoga-Pose Estimation," *Applied Sciences (Switzerland)*, vol. 13, no. 15, Aug. 2023, doi: 10.3390/app13158912.

[6] Z. Sun, Q. Ke, H. Rahmani, M. Bennamoun, G. Wang, and J. Liu, "Human Action Recognition From Various Data Modalities: A Review," Mar. 01, 2023, *IEEE Computer Society*. doi: 10.1109/TPAMI.2022.3183112.

[7] S. K. Yadav, A. Agarwal, A. Kumar, K. Tiwari, H. M. Pandey, and S. A. Akbar, "YogNet: A two-stream network for realtime multiperson yoga action recognition and posture correction," *Knowl Based Syst*, vol. 250, Aug. 2022, doi: 10.1016/j.knosys.2022.109097.

[8] J. Chen, L. Du, and L. Liao, "Discriminative Mixture Variational Autoencoder for Semisupervised Classification," *IEEE Trans Cybern*, vol. 52, no. 5, pp. 3032–3046, May 2022, doi: 10.1109/TCYB.2020.3023019.

[9] D. Sharma, C. Dhiman, and D. Kumar, "Control With Style: Style Embedding-based Variational Autoencoder for Controlled Stylized Caption Generation Framework," *IEEE Trans Cogn Dev Syst*, pp. 1–11, 2024, doi: 10.1109/TCDS.2024.3405573.

[10] M. Umer, A. A. Alarfaj, E. A. Alabdulqader, S. Alsubai, L. Cascone, and F. Narducci, "Enhancing fall prediction in the elderly people using LBP features and transfer learning model," *Image Vis Comput*, vol. 145, p. 104992, May 2024, doi: 10.1016/j.imavis.2024.104992.

[11] X. Chao, G. Ji, and X. Qi, "Multi-view key information representation and multi-modal fusion for single-subject routine action recognition," *Applied Intelligence*, vol. 54, no. 4, pp. 3222–3244, Feb. 2024, doi: 10.1007/s10489-024-05319-y.

[12] J. Zhang, P.-H. Tsai, and M.-H. Tsai, "Semantic2Graph: graph-based multi-modal feature fusion for action segmentation in videos," *Applied Intelligence*, vol. 54, no. 2, pp. 2084–2099, Jan. 2024, doi: 10.1007/s10489-023-05259-z.

[13] Z. Luo *et al.*, "'Left Arm Up!' Interactive Yoga training in virtual environment," in *2011 IEEE Virtual Reality Conference*, IEEE, Mar. 2011, pp. 261–262. doi: 10.1109/VR.2011.5759498.

[14] Z. Wu, J. Zhang, K. Chen, and C. Fu, "Yoga Posture Recognition and Quantitative Evaluation with Wearable Sensors Based on Two-Stage Classifier and Prior Bayesian Network," *Sensors*, vol. 19, no. 23, p. 5129, Nov. 2019, doi: 10.3390/s19235129.

[15] K. Rector, C. L. Bennett, and J. A. Kientz, "Eyes-free yoga," in *Proceedings of the 15th International ACM SIGACCESS Conference on Computers and Accessibility*, New York, NY, USA: ACM, Oct. 2013, pp. 1–8. doi: 10.1145/2513383.2513392.

[16] S. Patil, A. Pawar, A. Peshave, A. N. Ansari, and A. Navada, "Yoga tutor visualization and analysis using SURF algorithm," in *2011 IEEE Control and System Graduate Research Colloquium*, IEEE, Jun. 2011, pp. 43–46. doi: 10.1109/ICSGRC.2011.5991827.

[17] W. Wu, W. Yin, and F. Guo, "Learning and Self-Instruction Expert System for Yoga," in *2010 2nd International Workshop on Intelligent Systems and Applications*, IEEE, May 2010, pp. 1–4. doi: 10.1109/IWISA.2010.5473592.

[18] H.-T. Chen, Y.-Z. He, and C.-C. Hsu, "Computer-assisted yoga training system," *Multimed Tools Appl*, vol. 77, no. 18, pp. 23969–23991, Sep. 2018, doi: 10.1007/s11042-018-5721-2.

[19] M. Gochoo *et al.*, "Novel IoT-Based Privacy-Preserving Yoga Posture Recognition System Using Low-Resolution Infrared Sensors and Deep Learning," *IEEE Internet Things J*, vol. 6, no.

Authorized licensed use limited to: DELHI TECHNICAL UNIV. Downloaded on November 25,2024 at 04:47:27 UTC from IEEE Xplore. Restrictions apply.

4, pp. 7192–7200, Aug. 2019, doi: 10.1109/JIOT.2019.2915095.

[20] T. K. K. Maddala, P. V. V. Kishore, K. K. Eepuri, and A. K. Dande, "YogaNet: 3-D Yoga Asana Recognition Using Joint Angular Displacement Maps With ConvNets," *IEEE Trans Multimedia*, vol. 21, no. 10, pp. 2492–2503, Oct. 2019, doi: 10.1109/TMM.2019.2904880.

[21] M. Verma, S. Kumawat, Y. Nakashima, and S. Raman, "Yoga-82: A New Dataset for Fine-grained Classification of Human Poses," in *2020 IEEE/CVF Conference on Computer Vision and Pattern Recognition Workshops (CVPRW)*, IEEE, Jun. 2020, pp. 4472–4479. doi: 10.1109/CVPRW50498.2020.00527.

[22] S. K. Yadav, A. Singh, A. Gupta, and J. L. Raheja, "Real-time Yoga recognition using deep learning," *Neural Comput Appl*, vol. 31, no. 12, pp. 9349–9361, Dec. 2019, doi: 10.1007/s00521-019-04232-7.

[23] S. K. Yadav, A. Luthra, K. Tiwari, H. M. Pandey, and S. A. Akbar, "ARFDNet: An efficient activity recognition & fall detection system using latent feature pooling," *Knowl Based Syst*, vol. 239, p. 107948, Mar. 2022, doi: 10.1016/j.knosys.2021.107948.

[24] C. S. Pradeep and N. Sinha, "CAM based fine-grained spatial feature supervision for hierarchical yoga pose classification using multi-stage transfer learning," *Expert Syst Appl*, vol. 249, p. 123625, Sep. 2024, doi: 10.1016/j.eswa.2024.123625.

[25] A. Upadhyay, N. K. Basha, and B. Ananthakrishnan, "Deep Learning-Based Yoga Posture Recognition Using the Y_PN-MSSD Model for Yoga Practitioners," *Healthcare (Switzerland)*, vol. 11, no. 4, Feb. 2023, doi: 10.3390/healthcare11040609.

[26] A. Bera, M. Nasipuri, O. Krejcar, and D. Bhattacharjee, "Fine-Grained Sports, Yoga, and Dance Postures Recognition: A Benchmark Analysis," *IEEE Trans Instrum Meas*, vol. 72, 2023, doi: 10.1109/TIM.2023.3293564.

[27] T. N. Nguyen, T. H. Tran, and H. Vu, "An automatic tool for yoga pose grading using skeleton representation," in *Proceedings - 2022 9th NAFOSTED Conference on Information and Computer Science, NICS 2022*, Institute of Electrical and Electronics Engineers Inc., 2022, pp. 187–192. doi: 10.1109/NICS56915.2022.10013455.

[28] F. Chollet, "Xception: Deep Learning with Depthwise Separable Convolutions," in *2017 IEEE Conference on Computer Vision and Pattern Recognition (CVPR)*, IEEE, Jul. 2017, pp. 1800–1807. doi: 10.1109/CVPR.2017.195.

[29] K. He, X. Zhang, S. Ren, and J. Sun, "Deep Residual Learning for Image Recognition," in *2016 IEEE Conference on Computer Vision and Pattern Recognition (CVPR)*, IEEE, Jun. 2016, pp. 770–778. doi: 10.1109/CVPR.2016.90.

Authorized licensed use limited to: DELHI TECHNICAL UNIV. Downloaded on November 25,2024 at 04:47:27 UTC from IEEE Xplore. Restrictions apply.

Physica Scripta

INCLUSIVE PUBLISHING TRUSTED SCIENCE

PURPOSE-LED PUBLISHING™

ACCEPTED MANUSCRIPT

Zirili map-based image encryption method for healthcare, military, and personal data security

To cite this article before publication: Puneet Kumar Pal *et al* 2024 *Phys. Scr.* in press https://doi.org/10.1088/1402-4896/ad8d47

Manuscript version: Accepted Manuscript

Accepted Manuscript is "the version of the article accepted for publication including all changes made as a result of the peer review process, and which may also include the addition to the article by IOP Publishing of a header, an article ID, a cover sheet and/or an 'Accepted Manuscript' watermark, but excluding any other editing, typesetting or other changes made by IOP Publishing and/or its licensors"

This Accepted Manuscript is **© 2024 IOP Publishing Ltd. All rights, including for text and data mining, AI training, and similar technologies, are reserved.**.

During the embargo period (the 12 month period from the publication of the Version of Record of this article), the Accepted Manuscript is fully protected by copyright and cannot be reused or reposted elsewhere.

As the Version of Record of this article is going to be / has been published on a subscription basis, this Accepted Manuscript will be available for reuse under a CC BY-NC-ND 3.0 licence after the 12 month embargo period.

After the embargo period, everyone is permitted to use copy and redistribute this article for non-commercial purposes only, provided that they adhere to all the terms of the licence https://creativecommons.org/licences/by-nc-nd/3.0

Although reasonable endeavours have been taken to obtain all necessary permissions from third parties to include their copyrighted content within this article, their full citation and copyright line may not be present in this Accepted Manuscript version. Before using any content from this article, please refer to the Version of Record on IOPscience once published for full citation and copyright details, as permissions may be required. All third party content is fully copyright protected, unless specifically stated otherwise in the figure caption in the Version of Record.

View the article online for updates and enhancements.

This content was downloaded from IP address 14.139.251.98 on 08/11/2024 at 04:40

Zirili map-based image encryption method for healthcare, military, and personal data security

Puneet Kumar Pal[1] **& Dhirendra Kumar**[1*]

[1*]Department of Applied Mathematics, Delhi Technological University, Delhi, India-110042.

E-mail: dhirendrakumar@dtu.ac.in

‡

Abstract. Chaotic maps have been widely explored for encrypting information pertaining to sensitive data sources such as medical fields, military operations, satellite imagery, and personal photographs. Developing chaotic maps with a wide range of chaotic dynamics is crucial for encryption applications to safeguard information. In this work, we have proposed a novel two-dimensional hyperchaotic Zirili map that exploits the properties of the Zirili test optimization function. The proposed Zirili map demonstrates excellent chaotic behaviour compared to several chaotic maps in terms of bifurcation diagram, Lyapunov exponent, permutation entropy, correlation diagram, sample entropy and Kolmogorov entropy. The proposed Zirili map is utilised in confusion and diffusion processes to develop an efficient image encryption method. We have suggested cascading confusion transformation to reduce the correlation coefficient between adjacent pixels. Additionally, a novel modified cyclic diffusion with pixel mixing is proposed to enhance randomness in encrypted images. A thorough assessment of the proposed image encryption method is performed on a variety of image datasets by utilising multiple cryptanalysis methods, including key space analysis, information entropy, correlation coefficient evaluation, differential attack, key sensitivity testing, histogram analysis, computational time analysis, and occlusion and noise attacks. The quantitative evaluation measures obtained in terms of average information entropy with value 7.9989, number of pixel change rate with value 99.6112, and unified averaged changed intensity with value 33.4246 (averaged over several images) is better than other state-of-the-art image encryption methods, which indicate the robustness of the proposed image encryption method. Furthermore, analysis based on encryption time shows the superiority of the proposed image encryption algorithm over other related works. The experimental results confirm the method's reliability and robustness for its application in secure and practical encryption solutions for real-world applications.

Keywords: Chaotic Map, Hyperchaotic Map, Zirili Map, Image Encryption Method, Discrete Map, Information Security, Multimedia Security.

Submitted to: *Phys. Scr.*

‡ *Corresponding author: Department of Applied Mathematics, Delhi Technological University, Delhi, India-110042.
E-mail: dhirendrakumar@dtu.ac.in

Accepted Manuscript

1. Introduction

The revolution in information communication has received significant academic and professional attention. The widespread use of various forms of information media, including audio, video, and images, to share information over unprotected networks accessible to everyone has raised critical concerns about maintaining information confidentiality. Images, one of the most prevalent forms of media, often contain substantial amounts of information, characterised by high data redundancy and strong correlations between pixels. Sensitive information embedded in images from various sources, such as medical fields, military operations, satellite imagery, and personal photographs, poses a significant risk if accessed without authorisation [1]. Encryption technologies protect these valuable information assets to ensure privacy and mitigate the risk of harm.

Image encryption is a technique that converts image data into an unrecognisable form, thus protecting information confidentiality and security [2]. Image encryption methods (IEMs) typically conceal the image data using confusion and diffusion operations. Confusion involves rearranging the pixels of the image, thus obscuring its original structure and reducing the correlation among the pixels. Diffusion alters the pixel intensity values to improve the unpredictability of the encrypted image [3]. The robustness of an IEM depends on the efficiency of confusion and diffusion operations. Further, the security of the IEM may be enhanced by applying several rounds of confusion and diffusion operations [4].

Chaotic systems have become prominent in the encryption of images due to their sensitivity to initial values, ergodicity and unpredictability [5]. Chaotic maps are categorised into discrete and continuous types. Continuous maps have more complicated algebraic structures and need at least four dimensions to reach hyperchaos. In contrast, discrete chaotic maps have simpler algebraic structures and can reach hyperchaos with fewer dimensions only, which makes them computationally efficient for IEM applications [6]. Also, it is observed that the traditional encryption methods such as DES [7] and AES [8] are unsuitable for image encryption. This challenge has driven researchers to explore alternative encryption methods based on wavelet transforms [9], Deoxyribonucleic acid (DNA) coding [10], quantum operations [11], and chaotic maps [12, 13, 14]. Among the various techniques employed in IEMs, chaotic maps hold particular significance.

In the research work [15], the authors introduced a two dimensional Salomon map (2D-SM) and pixel split operations, which were implemented within an IEM. The analysis presented in the research work [15] demonstrate the robustness and security of the proposed IEM. The research work [16] proposed an IEM that uses the 2D Hènon-Sine map (2D-HSM). The IEM utilises the sequences generated from the map and performs operations in two rounds to achieve a highly secure cipher-image. The outcomes underscore the robust security measures employed in the process. In the research work [17], the authors proposed a 2D Schaffer map (2D-ScM) for high-complexity required applications. The 2D-ScM is used in the IEM to protect confidential data in images. The authors of the research work [18] proposed a novel 2D$-e\pi$ map (2D-EPM) and a bit-reversion operation utilised in the IEM. The research article [20] proposed 2D infinite collapse with logistic map (2D-ICLM).

Accepted Manuscript

The phase diagram of the map represents some pattern and is not uniformly distributed. The proposed map is utilised in the encryption of audio files. The research work [19] and [21] contrived a 2D logistic coupling cubic chaotic map (2D-LCCCM) and 2D logistic memristive hyperchaotic map (2D-LMHM), respectively, to encrypt remote-sensing images. The experimental findings emphasise the effectiveness of the IEM, demonstrating good encryption, reconstruction precision, and resilience against cropping attacks. However, the phase diagram of 2D-LCCCM and 2D-LMHM lack uniform distribution. The research work [22] based on chaotic maps and random DNA coding uses the chaotic sequences generated by the map to get two column-confused and row-confused matrices. The row and column coordinates utilised in the confusion procedure are taken from the second and row-confused matrix components. These jumble the DNA-encoded image, simultaneously confusing the rows and columns. The diffusion step uses the chaotic sequence that the chaotic map produces. To get multi-directional diffusion and improve the encryption, the DNA XOR operation is used on the image's horizontal line and centre point, and then the spread moves to the top and bottom directions of the matrix. The research work [23] established a novel 4D hyperchaotic map for IEM that exhibits excellent resistance to attack after conducting multiple-bit diffusion and confusion. In the research work [24], an IEM is proposed that joins the Sine and Tent maps with the Hill cipher to improve security. This chaotic IEM is rapid and effective in terms of security and complexity. Including the Sine map shortens the iteration time needed for a chaotic process. In the research work [25], the plain images are encrypted based on chaotic maps, cellular automata, and SHA256. The research work [26] is based on a 2D-CLSS hyperchaotic map. The map uses the features of the Sine map and the Logistic map (LM). The IEM based on the 2D-CLSS map uses simultaneous confusion and diffusion operations. The authors in the research work [27] proposed a chaotic map based on coupling map lattices. The authors mixed the LM, Sine, and Tent maps to produce a mixed coupled map. The map generates the sequences that encrypt the images based on the Z-scan method and improved diffusion scheme. The authors in the research work [28] used the fractal sorting matrix and Chen map. The IEM employs a fractal sorting matrix to scramble and the Chen map for diffusion. This approach ensures both robustness and security. In the research work [29], a 2D Cosine-Logistic-Sine map is proposed that is used in the IEM. Although the phase diagram of the map lacks uniform distribution. In the research work [30], the authors proposed a 1D-CICMIC map exhibiting periodic behaviour used to encrypt the medical images. In research work [31], authors developed a technique to create random Hamiltonian paths within digital images, equivalent to permutations in IEM. The operation shuffled the bits within a pixel by creating a Hamiltonian route over bit planes. An altered Bernoulli map is proposed to guarantee the randomness of the created Hamiltonian route. The research work [32] is based on the combined advantages of the LM, piece-wise linear chaotic map (PWLCM), and DNA rules. The PWLCM is used to obtain a secret key image. Subsequently, DNA rules are applied to encode the secret key image and the input plain image, row by row, utilising the LM for encoding. The LM is further utilised to create an intermediate image, which serves as an additional secret key to establish DNA functions row by row on the originally encoded image. Furthermore, the intermediate image is decoded in the next stage. Finally, the above steps are repeated

Accepted Manuscript

over image columns to produce a ciphered image. The research article [33] presents a new 2D iterative Gaussian Sine chaotic map (2D-IGSCM) with enhanced ergodicity and unpredictability. Furthermore, a 3D Hill Cipher model is proposed, incorporating a dynamic column vector derived from chaotic sequences to strengthen encryption. An IEM based on these models is introduced, and experimental results show that the IEM offers strong security and high efficiency. However, some chaotic maps introduced recently exhibit deficiencies like unevenly distributed trajectories and discontinuous chaotic ranges [16, 19, 21], making their prediction easy for an attacker, implying that predicting them could be relatively straightforward for an attacker [34, 35]. In addition, many IEMs have security deficiencies. Some process pixels in a specified order, which may lead to a decrease in the security of the IEMs [36, 37].

In this article, we propose a novel 2D discrete map termed as Zirili Map (ZM) that exploits the properties of the Zirili test optimization function. We have evaluated and compared the chaotic dynamics of the proposed ZM maps along with several recent chaotic maps in terms of phase diagram (PD), bifurcation diagram (BD), Lyapunov exponents (LE), permutation entropy (PE), correlation dimension (CD), sample entropy (SE), and Kolmogorov entropy (KE). Additionally, we present a new confusion technique named Cascading Confusion Transformation (CCT), designed to reduce pixel correlation in images, and a unique diffusion method called Modified Cyclic Diffusion with Pixel Mixing (MCDPM) to conceal image information effectively. Building on these innovations, we propose a novel IEM based on ZM, CCT, and MCDPM, referred to as ZM-IEM. This encryption method involves four rounds of CCT and MCDPM ensuring that the resulting cipher image is highly unpredictable with no statistical link to the original image.

The structure of the paper is as follows: The proposed 2D ZM and its analysis of chaotic behaviour are described in Sections 2 and 3, respectively. Section 4 delves into the detailed discussion of the proposed encryption and decryption methods. Section 5 encompasses the presentation of experimental results. Lastly, Section 6 summarises the study's findings and outlines potential future research directions.

2. Proposed 2D Zirili map (2D-ZM)

2.1. Zirili function

The Zirili optimisation test function [38] is a continuous, differentiable, and multi-modal function. The Zirili function is given in (1).

$$f(x, y) = 0.5x^2 + 0.5(1 - \cos(2x)) + y^2 \tag{1}$$

where $x, y \in (-500, 500)$. The function has a global minimum $f(x, y) = 0$ at $(x, y) = (0, 0)$ including several local minima.

2.2. 2D Zirili Map (2D-ZM)

Chaotic maps play a key role in constructing intricate IEMs. The level of complexity in these IEMs is directly influenced by the complexity of the chaotic maps used in their design.

Accepted Manuscript

The more complex the chaotic map, the more intricate and secure the resulting encryption method becomes. In this research, we have formulated the new map based on the Zirili function described in (1), termed as ZM. This novel map is a 2D discrete map characterised by a pair of control parameters ($p,\ q$). The map involves a Cosine function that oscillates between -1 and 1. A modular operation ensures the map's outputs fall within the $(0, 1)$ range. The map is given as in (2).

$$\begin{aligned} x_{i+1} &= (2^p x_i^2 + 2^q(1 - cos(p((\frac{\pi}{2}) + q\pi x_i))) + 2^q y_i^2) \bmod 1 \\ y_{i+1} &= (2^q x_i^2 + 2^p(1 - cos(q((\frac{\pi}{2}) + p\pi y_i))) + 2^p y_i^2) \bmod 1 \end{aligned} \tag{2}$$

where p and q are control parameters in the range $(0, \infty)$. x_{i+1} and y_{i+1} denote the future states of the states x_i and y_i, respectively. Including coefficients 2^p and 2^q assures oscillatory motion and precludes the possibility of decay or settlement. For experiment purposes, we have utilised the values of control parameters p and q in the range $[0, 10]$. The ZM exhibits a high level of chaotic behaviour owing to its incorporation of non-linear components and modular operations. The map demonstrates hyperchaotic tendencies within a broad control parameter range, displaying intricate and unpredictable dynamics for different initial conditions.

3. Analysis of the chaotic behaviour of 2D Zirili Map (2D-ZM)

The chaotic dynamics of the ZM are analysed using various parameters such as a PD, a BD, the LE, the PE, the CD, the SE, and the KE. Further, these results are also compared with the existing 2D chaotic maps shown in Table 1. The randomness test is also performed for the chaotic sequence obtained from the chaotic map. The forthcoming sections exhibit the analysis and outcomes via figures and tables.

3.1. Phase diagram (PD)

PD is plotted to analyse the distribution of the ZM in relation to the recent chaotic map. Figure 1 shows the PD of the ZM $((x_0, y_0, p, q)=(0.6, 0.07, 7.13, 5.38))$, ScM $((x_0, y_0, a, a_1)=(0.5, 0.7, 10, 10))$, HSM $((x_0, y_0, b_1, b_2, \omega)=(0.3, 0.6, 5, 1.57, 10))$, LC-CCM $((x_0, y_0, \mu, p_1)=(0.6, 0.9, 5, 8.78))$, SM $((x_0, y_0, a, b)=(0.3, 0.5, 6, 4))$, and EPM $((x_0, y_0, a)=(0.2, 0.5, 10))$, LMHM $((x_0, y_0, \beta, k_1, k_2, \rho, k)=(0.87, 0.51, 0.1, 1, 0.1, 100, 0.7))$, ICLM $((x_0, y_0, a, a_1)=(0.9, 0.6, 2, 1))$, IGSCM $((x_0, y_0, r_1, r_2)=(0.21, 0.31, 25, 23.3))$. It is concluded that PD for the proposed ZM is uniformly distributed without any pattern clustering compared to ScM, HSM, LCCCM, LMHM, ICLM, and IGSCM, except SM and EPM exhibit improved ergodic properties and unpredictability. Hence, we can say that the ZM exhibit chaotic properties.

3.2. Bifurcation diagram (BD)

A chaotic map generates a sequence concerning the control parameter and initial value. It is expected that whenever initial values and control parameters are varied, the chaotic map

Accepted Manuscript

Table 1: 2D Chaotic maps used for comparison.

Ref.	Name (year)	Chaotic Map	Cont. Para.
[15]	2D-SM (2023)	$\begin{cases} x_{i+1} = \left(10^a - \cos\left(2\pi\sqrt{x_i^2+y_i^2}\right) + 10^b\sqrt{x_i^2+y_i^2}\right) \bmod 1 \\ y_{i+1} = \left(10^b - \cos\left(2\pi\sqrt{x_{i+1}^2+y_i^2}\right) + 10^a\sqrt{x_{i+1}^2+y_i^2}\right) \bmod 1 \end{cases}$	$a \in (0,\infty)$, $b \in (1.5,\infty)$
[16]	2D-HSM (2023)	$\begin{cases} x_{i+1} = 0.5(1-\sin(1-\omega b_1 x_i^2 - \omega b_2 y_i)) \\ y_{i+1} = \sin(\omega b_2 x_i) \end{cases}$	$\omega = 10, b_1 \in [0,5], b_2 = 1.57$
[17]	2D-ScM (2023)	$\begin{cases} x_{i+1} = 0.5 + \dfrac{\sin^2\left(e^a\sqrt{x_i^2+y_i^2}\right) - 0.5}{(1+0.001(x_i^2+y_i^2))^2} \\ y_{i+1} = 0.5 + \dfrac{\sin^2\left(e^{a_1}\sqrt{x_{i+1}^2+y_i^2}\right) - 0.5}{(1+0.001(x_{i+1}^2+y_i^2))^2} \end{cases}$	$a, a_1 \in (0,\infty)$
[18]	2D-EPM (2022)	$\begin{cases} x_{i+1} = (x_i^{\pi^3}e^4 + aye^{10}) \bmod 1 \\ y_{i+1} = (y_i^{\pi^3}e^4 + ax_{i+1}\pi^9) \bmod 1 \end{cases}$	$a \in (0,\infty)$
[19]	2D-LCCCM (2022)	$\begin{cases} x_{i+1} = \cos\left(\pi^2(4\mu x_i(1-x_i) + p_1 y_i(1-y_i^2)) + \dfrac{\pi}{2}\right) \\ y_{i+1} = \cos\left(\pi^2(4\mu y_i(1-y_i) + p_1 x_i(1-x_i^2)) + \dfrac{\pi}{2}\right) \end{cases}$	$\mu \in (0,4), p_1 = 8.78$
[20]	2D-ICLM (2024)	$\begin{cases} x_{i+1} = \cos\left(\dfrac{a}{x_i}\right)\sin\left(1 + \dfrac{a}{a_1 y_i(1-y_i)}\right) \\ y_{i+1} = \cos\left(\dfrac{a}{a_1 x_i(1-x_i)}\right)\sin\left(1+\dfrac{a}{y_i}\right) \end{cases}$	$a, a_1 \in (0,\infty)$
[21]	2D-LMHM (2024)	$\begin{cases} x_{i+1} = \beta\left(2\rho - \dfrac{x_i^2}{\rho}\right) + kx_i\sin(y_i) \\ y_{i+1} = k_1 x_i + k_2 y_i \end{cases}$	$\begin{cases} \beta = 0.1, k_1 = 1, k_2 = 0.1, \\ \rho = 100, k \in [-1.32,-0.15] \\ \cup[0.15, 0.26] \cup [0.32, 1.26] \end{cases}$
[33]	2D-IGSCM (2024)	$\begin{cases} x_{i+1} = r_1\sin(e^{x_i^2} + y_i) \\ y_{i+1} = r_2\sin\left(\dfrac{y_i}{\sin(\pi x_i)^2}\right) \end{cases}$	$r_1 \in [0,25], r_2 \in [0,25]$

should show hypersensitive behaviour [39]. Thus, BD for the proposed map is drawn to analyse the effect of varying control parameters. With this, the BD of the ZM between the control parameter and variables is shown in Figure 2. When the control parameter varies, the chaotic sequences in each dimension exhibit a uniform distribution. The BD illustrates that the outputs of the ZM are widely dispersed and highly responsive across a wide range of parameter values. As a result, the ZM demonstrates robust chaotic behaviour, leading to a more randomised system output. Consequently, it is well-suited for applications in IEM.

3.3. Lyapunov exponent (LE)

The LE is a significant metric used to analyse the chaotic dynamics of a map by quantifying the exponential divergence between two infinitesimally close trajectories as a function of change in the control parameter [40]. The LE of a chaotic map can be calculated using (3).

$$LE = \lim_{n\to\infty} \frac{1}{n}\sum_{i=0}^{n-1} ln|f'(x_i)| \tag{3}$$

Where n is the maximum number of iterations and $f'(x_i)$ is the first derivative of the chaotic map at point x_i. If the LE of the 1D chaotic map is greater than zero, the map is said to be chaotic. If a nD map has LEs corresponding to each variable greater than 0, then the map is said to be hyperchaotic. Figure 3 shows the LE spectrum corresponding to the ZM and other 2D chaotic maps. LE_x and LE_y show the LEs corresponding to the

Accepted Manuscript

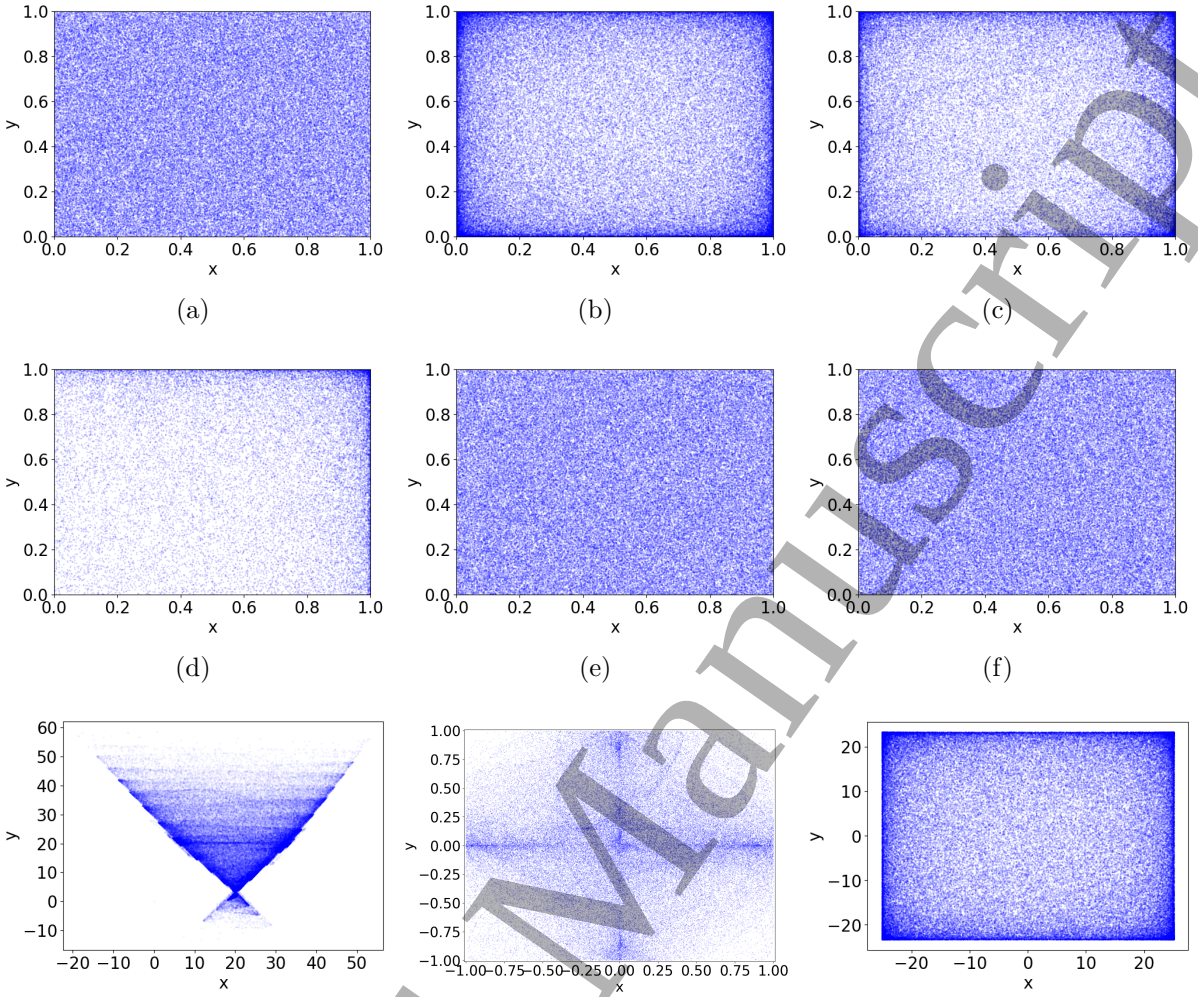

Figure 1: PD (x and y): (a) ZM, (b) ScM, (c) HSM, (d) LCCCM, (e) SM, (f) EPM, (g) LMHM, (h) ICLM,(i) IGSCM.

variables x and y, respectively. LE_x and LE_y are calculated over the parameter range q. While using one parameter, the other is fixed to the constant value $p = 25$. The mean values of LEs of ZM, i.e., $LE_x = 17.0223$ and $LE_y = 22.2769$, are shown in Table 2. It can be noted from Table 2 that the LEs corresponding to the ZM are greater than the LEs of all other relevant maps, suggesting that the ZM possesses superior hyperchaotic behaviour and is suitable for IEM.

3.4. Permutation entropy (PE)

PE is a metric to evaluate the degree of randomness within a data of dynamic map. It achieves this by analysing the connections among time series data and deriving the probability distribution of a given sequence. When the PE value of the data approaches 1, it indicates that the dynamic map exhibits chaotic behaviour [41]. The PE can be

Accepted Manuscript

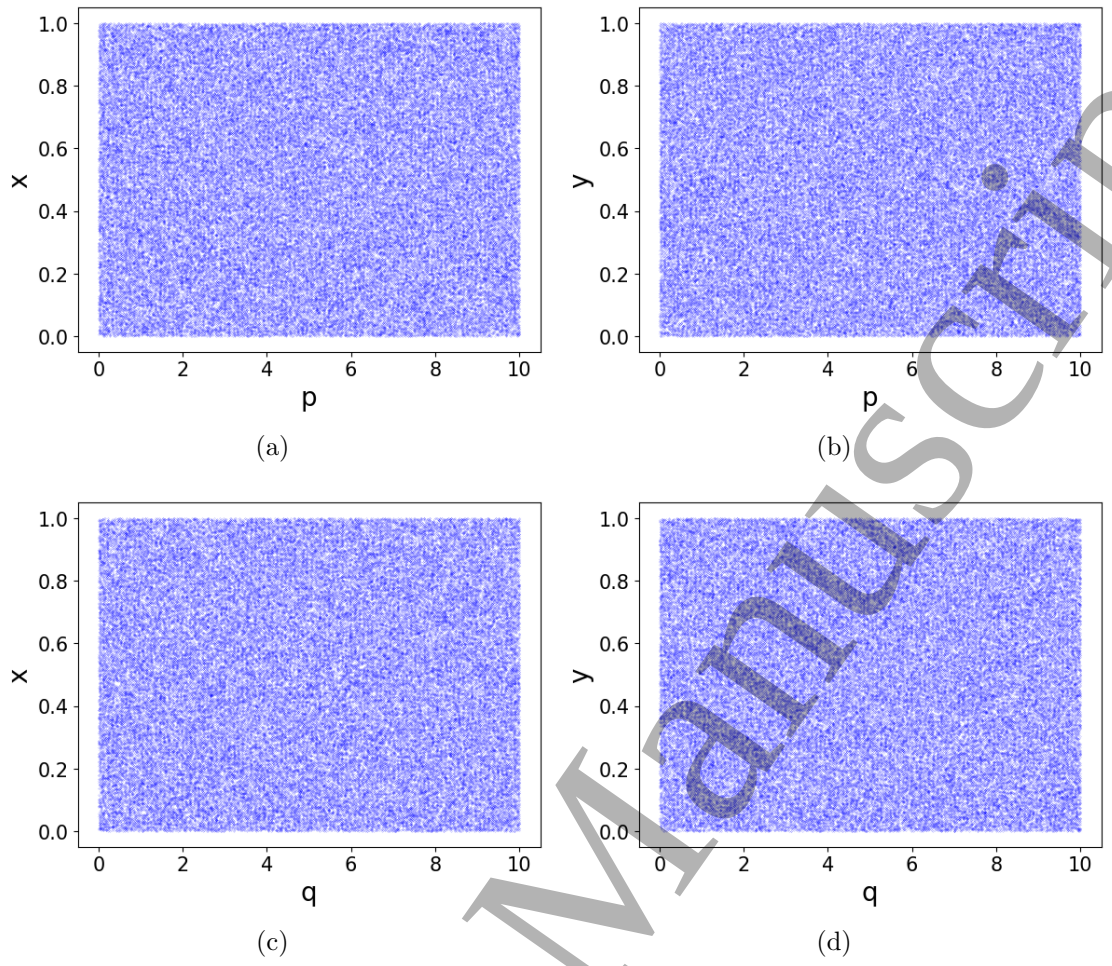

Figure 2: Bifurcation diagram of ZM: (a) plot of p and x, ($q = 5.6620$), (b) plot of p and y, ($q = 5.6620$), (c) plot of q and x, ($p = 7.4169$), (d) plot of q and y, ($p = 7.4169$).

calculated using the formula

$$PE(n) = -\sum p(\zeta) log_2(p(\zeta)) \tag{4}$$

where the sum runs over all $n!$ permutations ζ of order n. $p(\zeta)$ shows the probability of the occurrence of permutation ζ. The PE of the variable x corresponding to the ZM and control parameter q is shown in Figure 4 along with the other related chaotic maps. The mean value of PE is shown in Table 2 along with related research works. The ZM has a mean value of PE equal to 0.9990, close to 1, which shows that the ZM is hyperchaotic and generates more complex sequences than previous maps. Hence, it is a suitable method for IEM.

3.5. Correlation dimension (CD)

The CD is a measure from chaos theory and fractal geometry that helps quantify the complexity of a system. It is beneficial for analysing the behaviour of dynamical systems, especially those that exhibit chaotic behaviour [42]. In chaotic maps, the value of CD tends

Accepted Manuscript

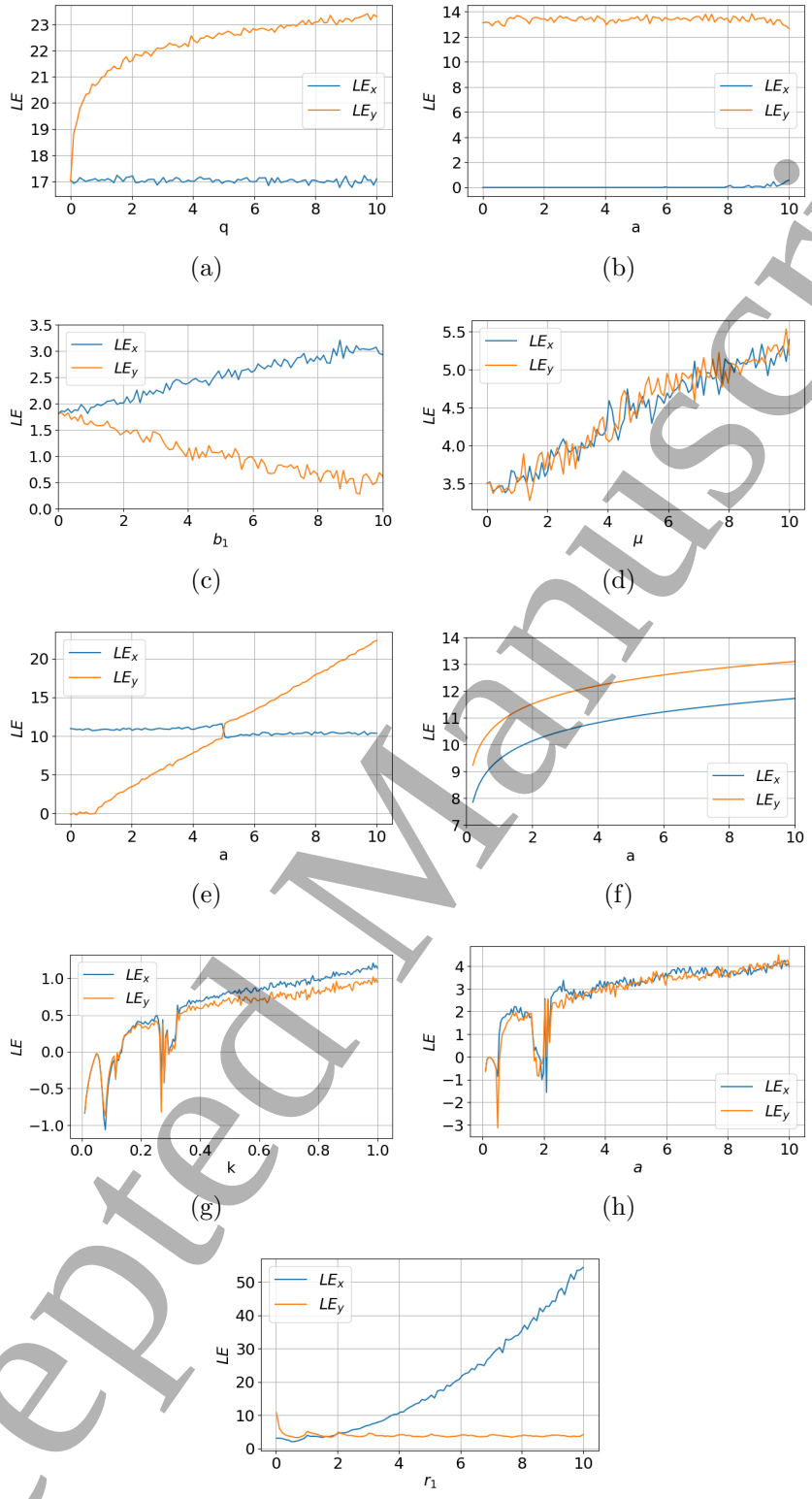

Figure 3: LE spectrum: (a) ZM, (b) ScM, (c) HSM, (d) LCCCM, (e) SM, (f) EPM, (g) LMHM, (h) ICLM, (i) IGSCM.

Accepted Manuscript

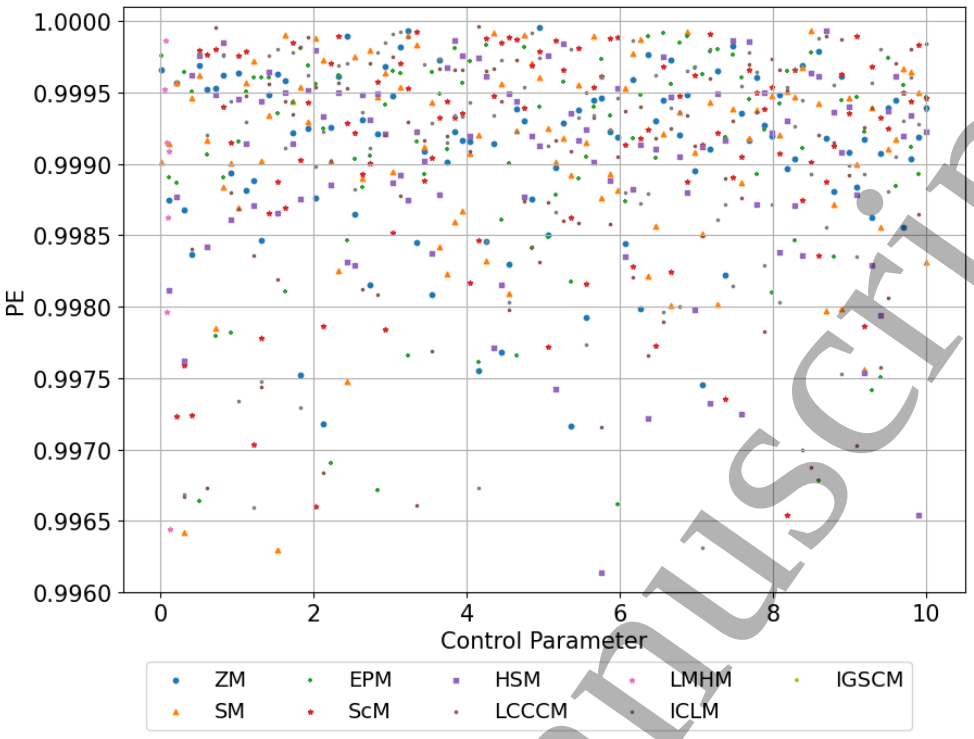

Figure 4: Plot of control parameter and PE.

to be non-integer and less than the embedding dimensions of the system. When the CD of a time series is greater than zero, it signifies chaotic behaviour. Moreover, as the series occupies more space dimensions, the CD expands. Figure 5 shows the spectrum of the CD§ of the proposed map and the maps available in the literature, and the mean values of the CD are given in Table 2. The ZM map has a mean CD value of 1.7451, exhibited in Table 2, indicating that the attractors of the robust chaotic mapping are very complex.

3.6. Sample entropy (SE)

SE is a measure of entropy employed to assess the intricacy of time series data. It quantitatively defines the complexity generated by the dynamic map. A series with higher SE implies lower regularity and, thus, higher randomness of the dynamic map. If the SE value is positive, the generated sequences are chaotic and do not follow any regular order or have a pattern that has not been seen before [43]. Figure 6 displays the SE‖ of the variable x corresponding to the ZM and the control parameter q. The map has a mean SE value of 2.1885, shown in Table 2. Based on the SE value spectrum, it is evident that the ZM is chaotic and generates complex sequences. Therefore, the ZM can be a good candidate for the IEM.

§ https://cschoel.github.io/nolds/_modules/nolds/measures.html#corr_dim
‖ https://cschoel.github.io/nolds/_modules/nolds/measures.html#sampen

Accepted Manuscript

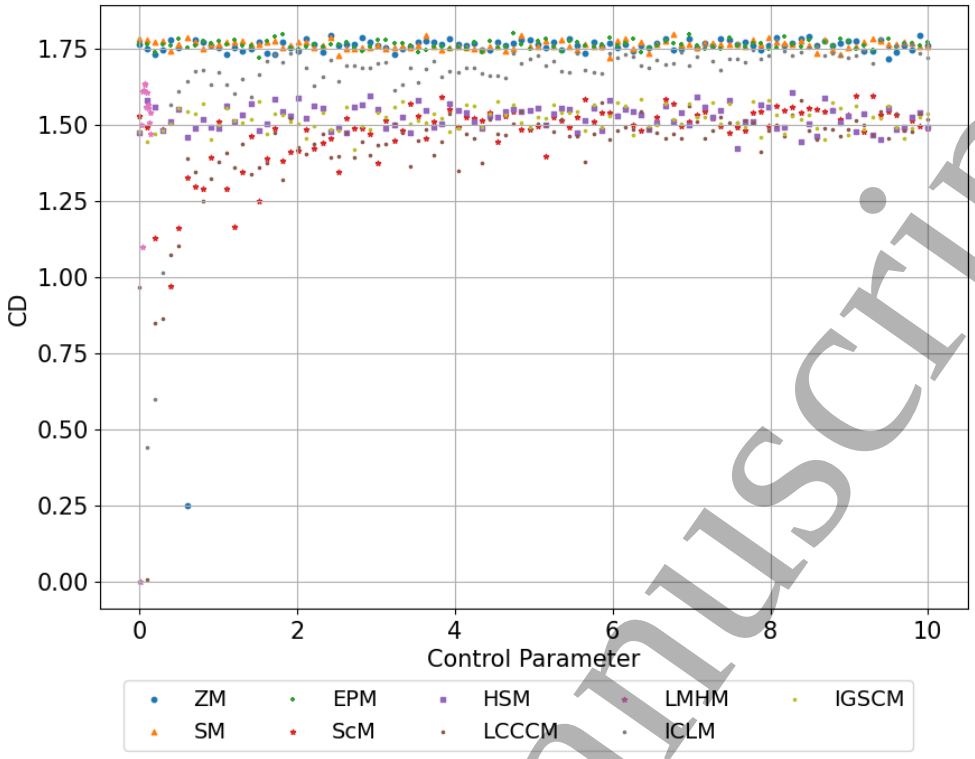

Figure 5: Plot of control parameter and CD.

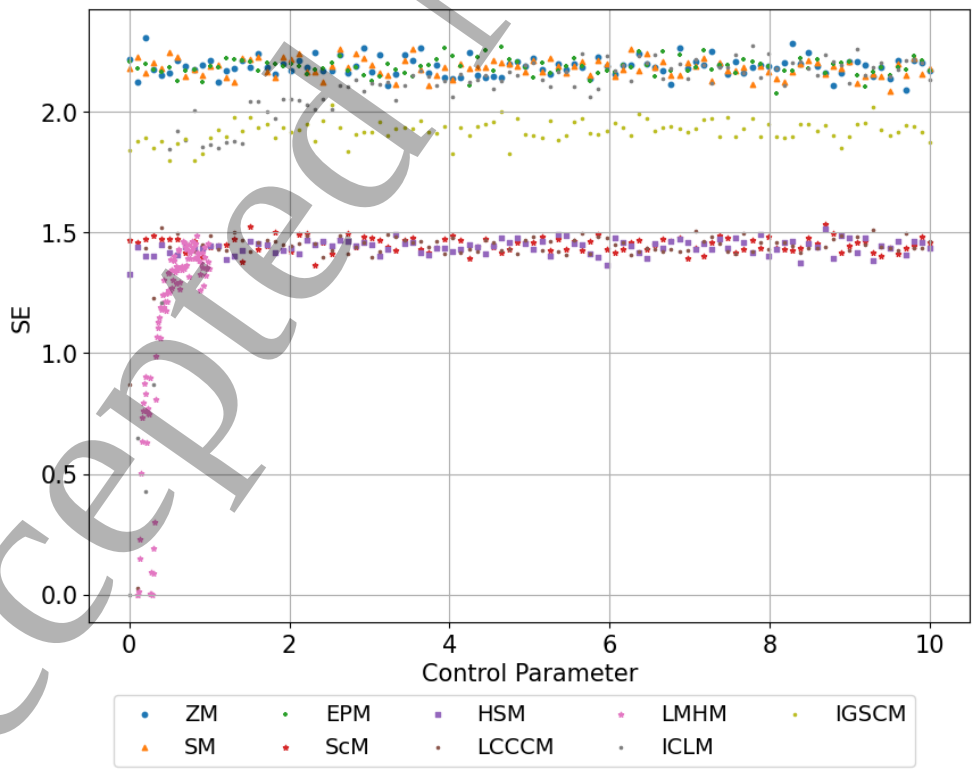

Figure 6: Plot of the control parameter and SE.

Accepted Manuscript

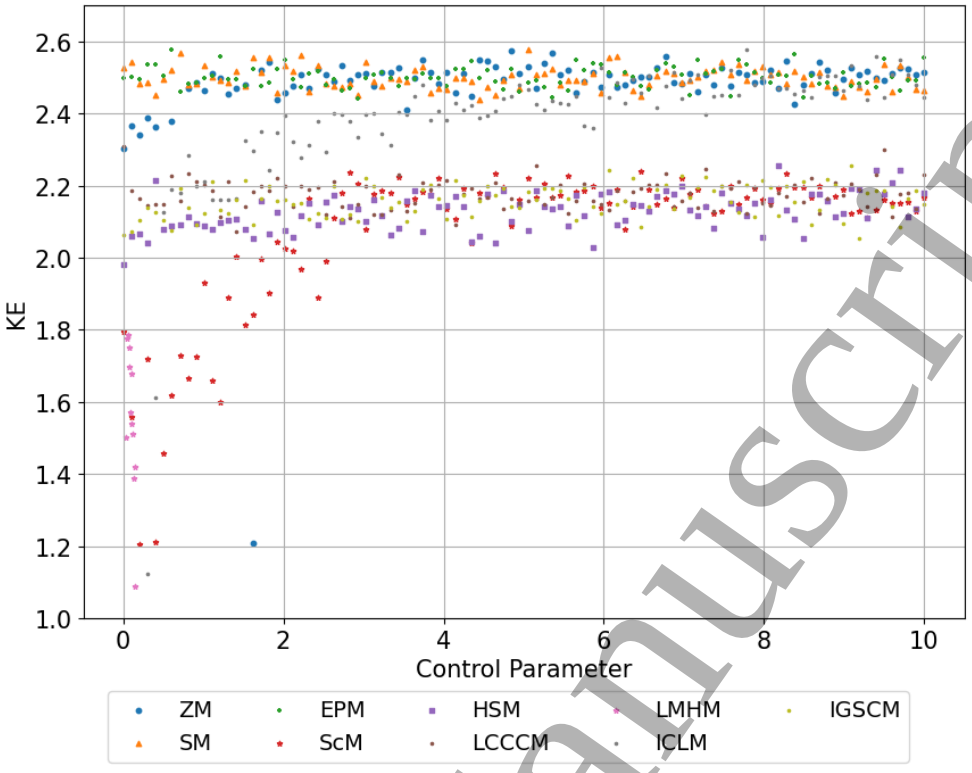

Figure 7: Plot of control parameter and Kolmogorov entropy.

3.7. Kolmogorov entropy (KE)

KE is an indicator that can be used to estimate a non-linear map's future trajectory from its current state [44]. If the KE is zero, the non-linear map behaves normally concerning the movement. Positive KE signifies that further information is required for the non-linear map to estimate a future trajectory. Consequently, non-linear maps exhibiting positive KE are considered to be unpredictable. Figure 7 illustrates the distribution of KE scores from 2D chaotic maps for comparison, while Table 2 provides an overview of the average KE values. Notably, the ZM stands out with a KE score of 2.4711, making it the optimal choice for IEM.

Table 2: Comparison of mean values of chaotic indicators.

Chaotic maps	LE_x	LE_y	PE	CD	SE	KE
ZM	17.0223	22.2769	0.9990	1.7451	2.1885	2.4711
SM [15]	10.6242	10.6279	0.9990	1.7613	2.1869	2.1278
HSM [16]	2.4832	1.0563	0.9989	1.5238	1.4350	2.1247
ScM [17]	0.0317	13.3695	0.9988	1.1558	1.4486	2.0741
EPM [18]	10.7910	12.1730	0.9990	1.7264	2.1665	2.5052
LCCCM [19]	5.3979	5.1889	0.9914	1.4198	1.4242	2.1702
ICLM [20]	2.9461	2.8162	0.9873	1.6496	2.0373	2.3287
LMHM [21]	-0.2815	-0.5573	0.2015	1.3247	1.1011	1.2969
IGSCM [33]	19.8044	3.9539	0.2133	1.5188	1.9208	2.1566

Accepted Manuscript

Table 3: NIST SP800-22 test results for the proposed ZM map.

Test name	p-value	Result
Frequency Test	0.0108	Successful
Run Test	0.2366	Successful
Run Test (Longest Run of Ones)	0.5926	Successful
Block Frequency Test	0.3435	Successful
Universal Statistical Test	0.4579	Successful
Linear Complexity Test	0.6256	Successful
Serial Test	0.3705	Successful
Binary Matrix Rank Test	0.0154	Successful
Non-overlapping Template Matching Test	0.1183	Successful
Overlapping Template Matching Test	0.5140	Successful
Approximate Entropy Test	0.3734	Successful
Random Excursion Test	0.5786	Successful
Random Excursion Variant Test	0.7618	Successful
Cumulative Sums	0.0235	Successful
Discrete Fourier Transform Test	0.1455	Successful

3.8. NIST Randomness test

The National Institute of Standards and Technology (NIST) SP800-22 is a developed tool for evaluating randomness by running fifteen distinct types of tests [45]. Each test utilizes a p-value obtained at a significance level β. The random sequence is considered to pass a given randomness test if the obtained $p-value$ is greater than β [45]. Table 3 shows the $p-value$ calculated at a significance level $\beta = 0.01$ for all fifteen tests on random sequence generated from the proposed ZM map (bit-stream size of 10^8). It is evident from the Table 3 that random sequence obtained from the proposed ZM map passes all the randomness test.

4. Image Encryption Method Based on Zirili map (ZM-IEM)

Suppose a plain image P of size $M \times N$ is to be encrypted, where M is the height, and N is the width of the image. The ZM-IEM involves the formation of sequences, diffusion and confusion steps. The steps of the ZM-IEM are displayed in Figure 8. Further, the formation of sequences, diffusion and confusion operations are described in section 4.1, 4.2 and 4.3, respectively.

4.1. Obtaining secret key and chaotic sequence

The secret key is an essential component of a cryptosystem, which ensures that messages may only be encrypted and decrypted using a particular key. If the key size is less than 2^{100}, the key can be obtained using a brute-force attack. So, to thwart such threats, the key space must have a size greater than 2^{100} [46]. In this study, we have used a key K

Accepted Manuscript

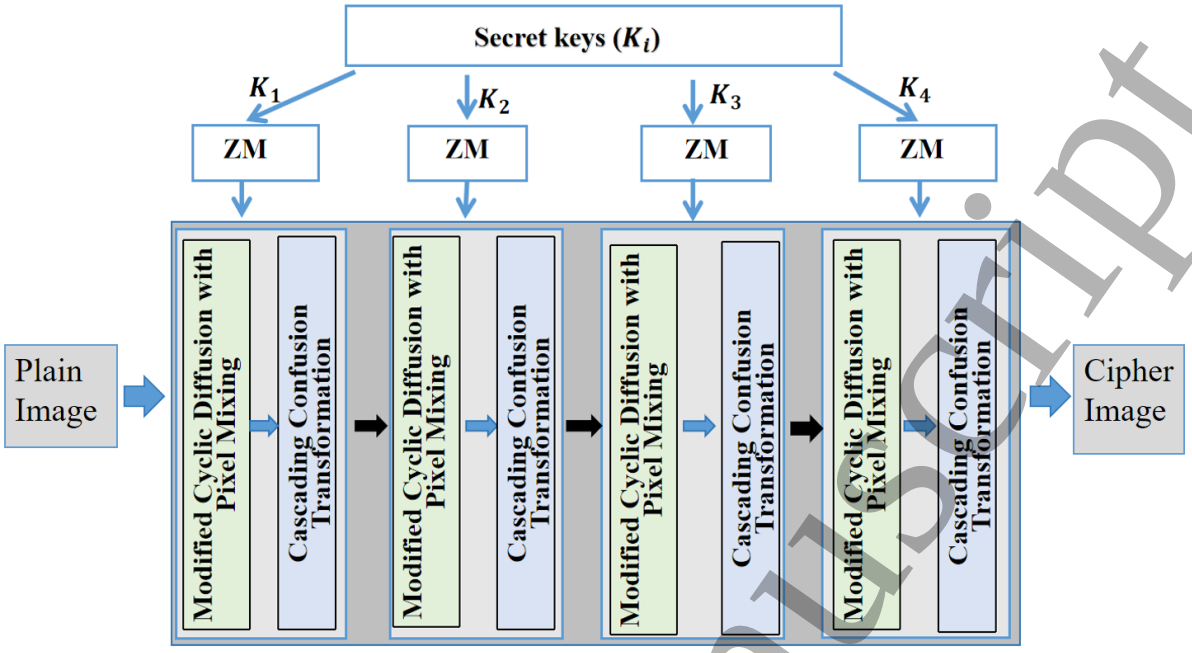

Figure 8: The image encryption method based on 2D Zirili Map (ZM-IEM).

consisting of 64 hexadecimal numbers equivalent to 256-bits. Hence, the key space size is 2^{256}, enough to prevent brute-force attacks. The hexadecimal key is partitioned into eight decimal numbers, and the corresponding integer is stored as $\{I_i : 1 \leq i \leq 8\}$ using (5):

$$I_i = Hex2Dec(K_{8(i-1)+1:8i}),\ 1 \leq i \leq 8 \tag{5}$$

The values of I_i are used to generate the ZM's initial values and control parameters. These are modified using (6) and set as x_0, y_0, p, and q.

$$\begin{cases} x_0 = \dfrac{1}{e}\left(\dfrac{I_1}{10^9} + \sin\left(\dfrac{\pi}{2} I_j\right)\right) \bmod 1 \\ y_0 = \dfrac{1}{e}\left(\dfrac{I_2}{10^9} + \sin\left(\dfrac{\pi}{2} I_j\right)\right) \bmod 1 \\ p = \dfrac{1}{e}\left(\dfrac{I_3}{10^9} + \sin\left(\dfrac{\pi}{2} I_j\right)\right) \bmod 10 \\ q = \dfrac{1}{e}\left(\dfrac{I_4}{10^9} + \sin\left(\dfrac{\pi}{2} I_j\right)\right) \bmod 10 \end{cases} \quad for\ j = 5, 6, 7, 8 \tag{6}$$

The initial values and control parameters obtained for $j = 5$ are stored as $K_1 = \{x_0, y_0, p, q\}$. Similarly, for other values of j, the values are calculated and stored as $\{K_k, k = 1, 2, 3, 4\}$. Each K_k is used to iterate the ZM for $(M + M \times N)$ times, and the output sequences x and y are modified and used in ZM-IEM. To eliminate the transitory impact, the first M values are removed. The chaotic sequence of size $M \times N$ is used in the further steps of the ZM-IEM, i.e., to disturb pixel placements and change pixel values.

Accepted Manuscript

4.2. Modified Cyclic Diffusion with Pixel Mixing (MCDPM)

The pixel values provide vital information about the image, and attackers may retrieve the image by analysing statistical features, even if the locations of the pixels are completely modified. To avoid this, a robust method for modification of the pixel values is required. In order to apply the diffusion process, firstly a matrix V of the size of $M \times N$ is obtained using chaotic sequence y using (7).

$$V = \lfloor y_i \times 10^{10} \rfloor, \ 0 \leq i < M \times N \tag{7}$$

Where $\lfloor \bullet \rfloor$ represents floor operation, array V is reshaped into a matrix of size $M \times N$.

The MCDPM is proposed to guarantee the information's security and ensure the IEM's robustness. The plain image is divided into four blocks, and then MCDPM is applied to enhance the randomness in the cipher images. The method introduces localised diffusion by dividing the image into blocks, which helps achieve high randomness and unpredictable pixel changes across the entire image. The use of neighbouring pixel values (both horizontally and vertically) in the diffusion process increases the dependency between adjacent pixels, making the relationship between the original image and the encrypted image more complex and resistant to several attacks. The multi-dimensional relationships in the Algorithm 1 help quickly propagate small changes in the plaintext throughout the encrypted image, ensuring high sensitivity to initial conditions. The method leverages multiple dependencies between neighbouring pixels and chaotic values that improve the unpredictability, making it resistant to common cryptographic attacks such as differential and brute-force attacks. Modular arithmetic operations are computationally lightweight, enabling efficient encryption and decryption processes. Hence, we have applied the mod 256 operation to keep the resultant pixel values between 0 and 255. Also, the proposed MCDPM methodology can be parallelly applied to the blocks, leveraging parallel computing to save time for high-resolution images. A bit of modification in the value of a single pixel results in a significant adjustment in the pixel values of the whole image.

Figure 9 illustrates the MCDPM and its directions, using the matrix of size (8×8) applied to the plain image block-wise. The MCDPM process to obtain the diffused image C can be described using (8).

$$C_{i,j} = \begin{cases} (P_{i,j} + V_{i,j} + P_{i+1,j} + P_{i,j+1}) \bmod 256, & i = 0, j = 0 \\ (P_{i,j} + C_{i,j-1} + V_{i,j}) \bmod 256, & i = 0, 0 < j < BN \\ (P_{i,j} + C_{i-1,j} + V_{i,j}) \bmod 256, & 0 < i < BM, j = 0 \\ (P_{i,j} + C_{i,j-1} + C_{i-1,j} + V_{i,j}) \bmod 256, & 0 < i < BM, 0 < j < BN, i \neq j \\ (P_{i,j} + C_{i-1,j-1} + V_{i,j}) \bmod 256, & 0 < i < BM, 0 < j < BN, i = j. \end{cases} \tag{8}$$

Where BM and BN represent the height and width of the block of the plain image P, respectively. V represents chaotic matrix block of size $(BM \times BN)$. C is block of the diffused array obtained after MCDPM process.

Furthermore, the MCDPM is exhibited in Algorithm 1 and Figure 9. The elements of the array C are to be permutated now using the CCT. Once the confusion and

Accepted Manuscript

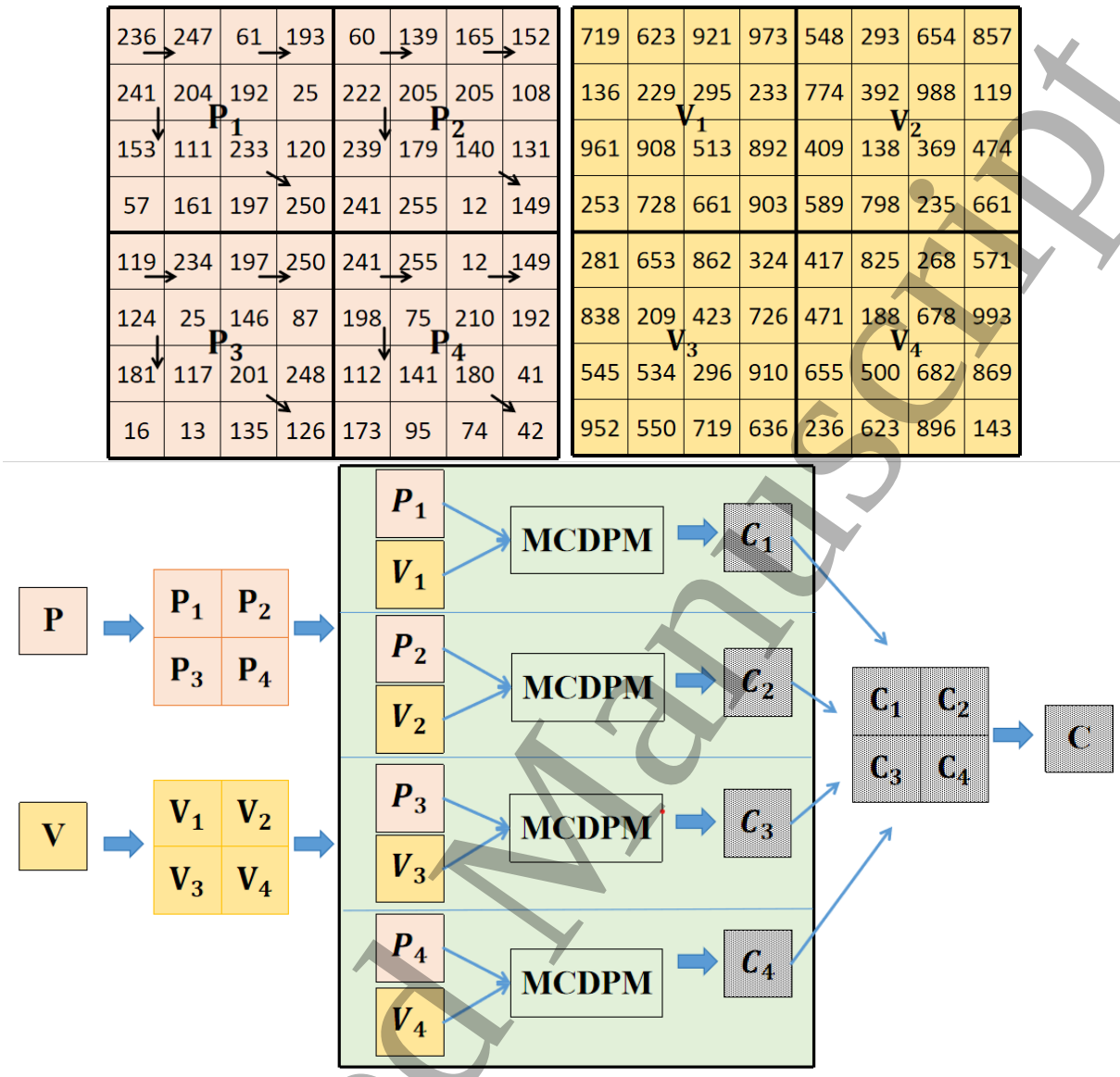

Figure 9: Illustration of Modified Cyclic Diffusion with Pixel Mixing (MCDPM).

Algorithm 1: Steps for applying Modified Cyclic Diffusion with Pixel Mixing.

Input : Plain image P, chaotic sequence V

Output: Diffused image C

1 Divide the P into four blocks i.e., P_1, P_2, P_3, P_4;
2 Divide the V into four blocks i.e., V_1, V_2, V_3, V_4;
3 Compute C_1 by substituting values of block pair (P_1, V_1) in (8) ;
4 Compute C_2 by substituting values of block pair (P_2, V_2) in (8) ;
5 Compute C_3 by substituting values of block pair (P_3, V_3) in (8) ;
6 Compute C_4 by substituting values of block pair (P_4, V_4) in (8) ;
7 Concatenate the blocks $(C_1,\ C_2,\ C_3,\ C_4)$ to obtain diffused image C.

Accepted Manuscript

diffusion stages are over, all the essential information in the image becomes permanently irretrievable.

4.3. Cascading Confusion Transformation (CCT)

This section provides the details of the CCT, a method designed to disrupt the spatial arrangement of image pixels. This process significantly reduces the correlation between adjacent pixels in the confused image, enhancing its confusion level. To initiate this process, sequences are initially generated using ZM (2), as described in Subsection 4.1. After iterating the ZM (2), the chaotic sequence, x of length $(M \times N)$, is obtained. The chaotic sequence x is sorted row-wise and column-wise in ascending order and is stored in SX_r and SX_c. The new position of the element of sequence x in the sorted sequences SX_r and SX_c is stored in the argument sequences Arg_r and Arg_c, respectively. These argument sequences Arg_r and Arg_c are used to shuffle the pixels of the plain image P as shown in Figure 10 and Algorithm 2. In the first step of the confusion process, the columns of the plain image are swapped, followed by the clockwise circular shift of the rows. The second step involves swapping the matrix rows and clockwise shifting the columns. All the pixels of the plain image are shuffled, resulting in a complex cipher image. Further, the output matrix is stored as a new permutated matrix T. The matrix T is the obtained cipher image.

Algorithm 2: Cascading Confusion Transformation (CCT).

Input : Diffused image C, chaotic sequences x.
Output: Permutated matrix T

```
x = reshape(x, M × N);
Sort x row-wise, SX_r = row_sort(x);
Sort x column-wise, SX_c = col_sort(x);
Store positions of elements of SX_r in x in Arg_r Arg_r = arg(SX_r), Arg_c =
  arg(SX_c);
Function SwapColumns(C, i, j);
    for r = 1 to M do
        Swap C[r, i] and C[r, j];
    end
Function Circular-shift-Rows(C, Arg_r);
    Circular shift each row of C in a clockwise direction using the elements of the
     row of Arg_r;
Function SwapRows(C, i, j);
    for cs = 1 to N do
        Swap C[i, cs] and C[j, cs];
    end
Function Circular-shift-Columns(C, Arg_c);
    Circular shift each column of C in a clockwise direction using the elements of
     the columns Arg_c;
Store the resulting matrix as T;
```

Accepted Manuscript

The first round of encryption uses K_1, MCDPM and CCT operations. Similarly, the MCDPM and CCT operations are performed for K_2, K_3, and K_4. The obtained cipher image after the last step is random and possesses no information about the plain image. Since the ZM-IEM uses four rounds of encryption and four different initial seeds in each round, the IEM is complex and highly sensitive.

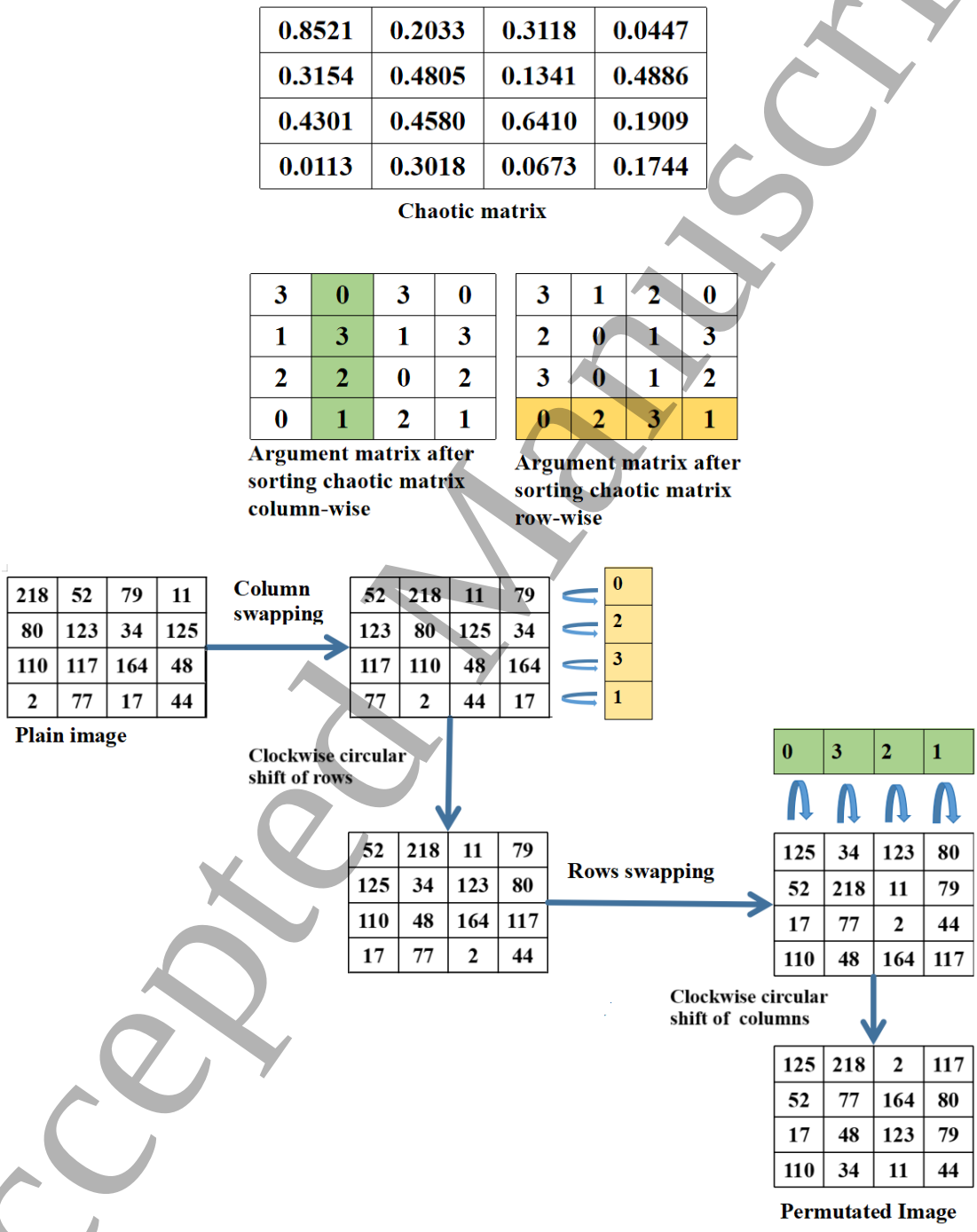

Figure 10: Cascading Confusion Transformation (CCT).

Accepted Manuscript

4.4. Image decryption method

Since the proposed ZM-IEM is symmetric, it uses the same key in the encryption and decryption operations. As encryption and decryption processes are inherently reversible, the decryption process entails executing the inverse operations of the encryption process. The initial step involves inverse CCT, shown in Algorithm 3 followed by the inverse MCDPM. The step involved in the inverse diffusion process is demonstrated using (9). The process is repeated four times, and the obtained final array is reshaped into the matrix of size $M \times N$; hence, the decrypted image is obtained.

$$P_{i,j} = \begin{cases} (C_{i,j} - C_{i-1,j-1} - V_{i,j}) \bmod 256, & 0 < i < BM, 0 < j < BN, i = j \\ (C_{i,j} - C_{i,j-1} - C_{i-1,j} - V_{i,j}) \bmod 256, & 0 < i < BM, 0 < j < BN, i \neq j \\ (C_{i,j} - C_{i-1,j} - V_{i,j}) \bmod 256, & 0 < i < BM, j = 0 \\ (C_{i,j} - C_{i,j-1} - V_{i,j}) \bmod 256, & i = 0, 0 < j < BN \\ (C_{i,j} - V_{i,j} - P_{i+1,j} - P_{i,j+1}) \bmod 256, & i = 0, j = 0. \end{cases} \tag{9}$$

Algorithm 3: Inverse Cascading Confusion Transformation (I-CCT).

Input : Cipher image matrix T, chaotic sequences x.
Output: Recovered diffused image C

x = reshape(x, $M \times N$);
Sort x row-wise, $SX_r = row_sort(x)$;
Sort x column-wise, $SX_c = col_sort(x)$;
Retrieve positions of elements of SX_r in x in Arg_r, $Arg_r = \arg(SX_r)$, $Arg_c = \arg(SX_c)$;
Function *Inverse-Circular-shift-Columns*(T, Arg_c);
    Circular shift each column of T in a counter-clockwise direction using the elements of the columns Arg_c;
Function *InverseSwapRows*(T, i, j);
    for $cs = 1$ **to** N **do**
        Swap $T[i, cs]$ and $T[j, cs]$;
    end
Function *Inverse-Circular-shift-Rows*(T, Arg_r);
    Circular shift each row of T in a counter-clockwise direction using the elements of the row of Arg_r;
Function *InverseSwapColumns*(T, i, j);
    for $r = 1$ **to** M **do**
        Swap $T[r, i]$ and $T[r, j]$;
    end
Store the resulting matrix as C;

Accepted Manuscript

5. Experimental results and performance analysis

To assess the security and efficiency of the newly introduced ZM-IEM, we performed a set of tests on images with diverse dimensions, including sizes 256×256, 512×512, and 1024×1024. Furthermore, the proposed IEM's effectiveness and resilience are compared to various contemporary methods regarding information entropy, correlation coefficient, running time, efficiency analysis, $NPCR$, and $UACI$. The ZM-IEM is executed on a computer equipped with Windows 11, featuring a CPU with a clock speed of 2.60 GHz and 8 GB of RAM. Numerical simulations are conducted using Python 3.10.

5.1. Information entropy analysis

The information entropy is calculated to determine the degree of unpredictability of the cipher image obtained using the ZM-IEM [47]. The ideal value of the information entropy for the cipher image is 8, which shows the maximum degree of randomness. The mathematical formula for information entropy is shown in (10).

$$H(x) = \sum_{i=0}^{255} P(x_i) \log_2 \left(\frac{1}{P(x_i)} \right) \tag{10}$$

where $P(x_i)$ is the probability of the occurrence of grey level x_i. Table 4 shows the information entropy values of the cipher images obtained using the ZM-IEM and other related methods. The mean information entropy value of the cipher image obtained using ZM-IEM is 7.9989, close to 8, showing the maximum degree of randomness of the cipher image. We suggest that the proposed ZM-IEM demonstrates robustness by evenly distributing pixel values, producing highly random cipher images.

5.2. Histogram analysis

The image histogram is a tool for analysing the intensity distribution of pixels inside an image. The uniformly distributed histogram indicates the strength of permutation and diffusion operations within IEM and its resistance against potential statistical attacks [48]. The histogram of a cipher image obtained from a secure IEM is uniformly distributed. Further, we have used the chi-square test to check the uniform distribution of pixels in the encrypted image [49]. The χ^2 test formula is given in (11).

$$\chi^2 = \sum_{i=0}^{255} \frac{(O_i - E)^2}{E}, \; E = \frac{M \times N}{256} \tag{11}$$

where O_i shows the observed pixel values. The histogram in Figure 11 displays the distribution of pixel intensity values corresponding to plaintext and ciphertext images. The histogram of cipher images is evenly distributed, as seen in the figure. Further, the uniformity of the cipher images is observed and is shown in Table 5. The $\chi^2(0.05, 255)$ value should be lower than the critical value of 293.2478. The examination of the cipher images reveals that their test values fall below the critical value threshold. This leads to the conclusion that the distribution of the cipher images is uniform. Consequently, it can be inferred that the ZM-IEM demonstrates resilience against statistical analysis attacks.

Accepted Manuscript

Table 4: Comparison of information entropy values of the ZM-IEM with methods available in the literature.

Image/IEM	ZM-IEM	[25]	[26]	[18]	[28]	[22]	[31]	[32]	[24]	[29]	[30]	[27]	[21]	[33]
black	7.9971	7.9765	7.9967	7.9975	7.9952	7.9973	7.9975	7.9971	7.8955	7.9973	7.6049	7.9965	7.9970	7.9971
bridge256	7.9975	7.9759	7.9969	7.9971	7.9972	7.9973	7.9970	7.9974	7.9973	7.9968	7.9975	7.9971	7.9973	7.9971
horiz	7.9973	7.9783	7.9974	7.9969	7.9958	7.9971	7.9975	7.9972	6.6513	7.9971	7.9608	7.9972	7.9973	7.9976
lena256	7.9970	7.9751	7.9971	7.9967	7.9974	7.9972	7.9973	7.9970	7.9969	7.9972	7.9973	7.9973	7.9973	7.9969
MI1256	7.9972	7.9769	7.9975	7.9972	7.9972	7.9972	7.9970	7.9971	7.9975	7.9975	7.9967	7.9974	7.9974	6.7412
MI3256	7.9973	7.9766	7.9975	7.1095	7.9976	7.9969	7.9972	7.9973	7.9972	7.9973	7.9969	7.9977	7.9970	7.9976
squares	7.9975	7.9777	7.9968	7.9968	7.9964	7.9973	7.9971	7.9971	6.8726	79970	7.9711	7.9974	7.9970	7.9970
barb512	7.9994	7.9792	7.9994	7.9992	7.9992	7.9993	7.9994	7.9993	7.9993	7.9993	7.9993	7.9993	7.9992	7.9993
boat512	7.9993	7.9785	7.9993	7.1238	7.9992	7.9993	7.9993	7.9994	7.9992	7.9994	7.9993	7.9993	7.9994	7.9993
mandrill512	7.9992	7.9793	7.9992	7.3579	7.9993	7.9993	7.9993	7.9994	7.9993	7.9994	7.9993	7.9993	7.9992	7.9993
peppers512	7.9993	7.9801	7.9992	7.9993	7.9993	7.9993	7.9992	7.9994	7.9993	7.9993	7.9993	7.9993	7.9993	6.6956
texmos1	7.9991	7.9791	7.9993	7.9992	7.9993	7.9993	7.9994	7.9993	7.9994	7.9993	7.9993	7.9993	7.9994	7.9993
texmos2	7.9993	7.9784	7.9993	7.9993	7.9991	7.9993	7.9993	7.9993	6.8236	7.9993	7.9989	7.9993	7.9993	7.9993
texmos3b	7.9992	7.9803	7.9993	7.9993	7.9994	7.9993	7.9993	7.9993	7.9993	7.9993	7.9993	7.9994	7.9993	7.9993
zelda512	7.9990	7.9798	7.9992	7.9993	7.9993	7.9993	7.9994	7.9993	7.9993	7.9992	7.9993	7.9994	7.9994	7.9993
1.3.02	7.9998	7.9800	7.9998	7.9998	7.9998	7.9998	7.9998	7.9998	7.9998	7.9998	7.9998	7.9998	7.9998	7.9996
1.3.03	7.9998	7.9799	7.9998	7.2942	7.9998	7.9998	7.9998	7.9998	7.9998	7.9994	7.9998	7.9998	7.9998	7.9998
1.3.04	7.9998	7.9796	7.9998	7.9998	7.9998	7.9998	7.9998	7.9998	7.9998	7.9998	7.9998	7.9998	7.9998	7.9998
1.3.07	7.9998	7.9799	7.9998	7.9998	7.9998	7.9998	7.9998	7.9998	7.9998	7.9998	7.9998	7.9998	7.9998	6.7496
1.3.09	7.9998	7.9795	7.9998	7.9998	7.9998	7.9998	7.9998	7.9998	7.9998	7.9998	7.9998	7.9998	7.9998	7.9998
1.3.10	7.9998	7.9802	7.9998	7.9998	7.9998	7.9998	7.9998	7.9998	7.9998	7.9998	7.9998	7.9998	7.9998	7.9998
1.4.01	7.9998	7.9798	7.9998	7.9998	7.9998	7.9998	7.9998	7.9998	7.9998	7.9998	7.9696	7.9998	7.9998	7.9998
1.4.05	7.9998	7.9799	7.9998	7.9998	7.9998	7.9998	7.9998	7.9998	7.9998	7.9998	7.9356	7.9998	7.9998	7.9998
1.4.06	7.9998	7.9797	7.9998	7.9998	7.9998	7.9998	7.9998	7.9998	7.9998	7.9998	7.9755	7.9998	7.9998	7.9998
1.4.07	7.9998	7.9798	7.9998	7.9998	7.9998	7.9998	7.9998	7.9998	7.9998	7.9998	7.9815	7.9998	7.9998	6.9990
1.4.09	7.9996	7.9797	7.9998	6.7840	7.9998	7.9999	7.9998	7.9998	7.9998	7.9998	7.9703	7.9998	7.9998	7.9998
1.4.12	7.9998	7.9797	7.9998	7.9998	7.9998	7.9998	7.9998	7.9998	7.9998	7.9998	7.9998	7.9998	7.9998	7.9998
Mean	7.9989	7.9789	7.9990	7.8387	7.9988	7.9990	7.9990	7.9990	7.8602	7.9990	7.9759	7.9990	7.9990	7.8208

5.3. Adjacent pixel correlation analysis

In general, the pixels in an image demonstrate a significant correlation; hence, correlation attacks can successfully retrieve important information from images. So, the IEM must be designed to reduce correlation among the pixels [50]. The correlation coefficient can be calculated as follows:

$$\rho(x,y) = \frac{Cov(x,y)}{\sqrt{Var(x)} \times \sqrt{Var(y)}} \tag{12}$$

where x and y represent the pixel intensities. $Cov(x,y)$ represents the covariance between x and y, while $Var(x)$ and $Var(y)$ denote the variance of x and y, respectively. The range of the correlation coefficient value is [-1, 1]. Consequently, a correlation value close to zero suggests less correlation, whereas values approaching the extremes indicate a strong degree of correlation. A diverse set of images is employed to demonstrate the efficacy of the ZM-IEM in diminishing the correlation between neighbouring pixels. Initially, 6000 pixels are randomly selected from the plain and cipher images along three directions (HD, VD, and DD).

The distribution of these adjacent pixels chosen from each plain and cipher image is shown in Figure 12. In Figure 12, it is visible that the pixels of the plain images are highly correlated and form a straight line. Still, the pixels of the cipher images are uniformly distributed over the region and show no correlation. Further, these pixel values

Accepted Manuscript

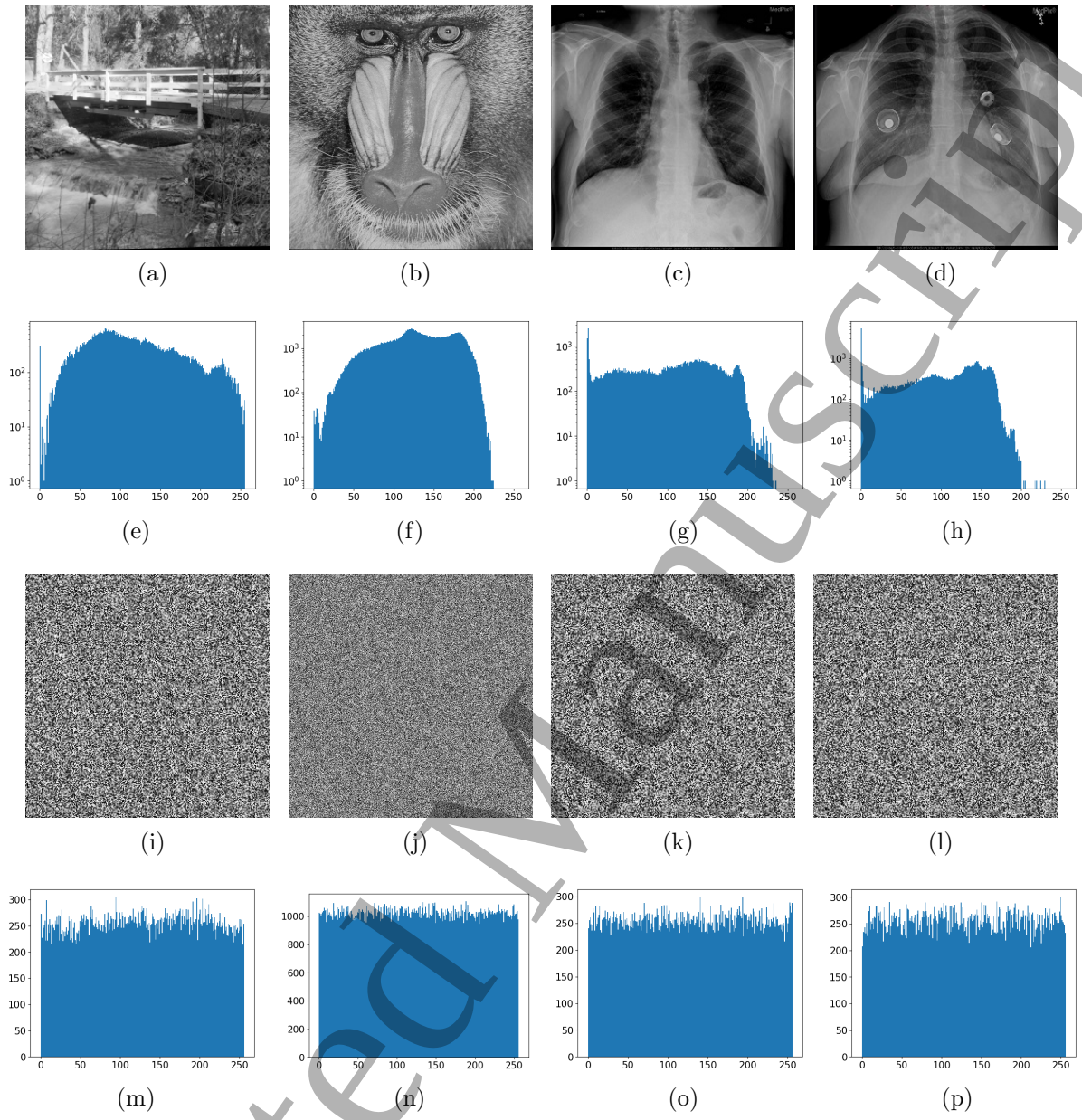

Figure 11: Histograms of plain and cipher images: (a) Plain image Bridge, (b) Plain image Mandrill, (c) Plaine image MI1256, (d) Plain image MI3256, (e-h) Histograms of corresponding plain images, (i) Cipher image bridge, (j) Cipher image mandrill, (k) Cipher image MI1256, (l) Cipher image MI3256, (m-p) Histograms of corresponding cipher images.

are used to calculate the correlation in Table 6. It can be observed that for the plain images, the correlation coefficient is close to 1. Thus, the pixel values of plain images are highly correlated. Meanwhile, in the case of cipher images, the correlation coefficient is close to 0. Hence, it is evident that the cipher images have very little correlation among adjacent pixels. Further, Table 6 compares the correlation coefficient of the ZM-IEM with available state-of-the-art methods. From Table 6, it is evident that the ZM-IEM can remove the correlation among adjacent pixel values of the plain image and provides a cipher

Accepted Manuscript

Table 5: Test of uniform distribution analysis of histogram (χ^2 test).

Image	Cipher image ($\chi^2(0.05, 255)$)	Result
black	266.3125	Pass
bridge256	188.8984	Pass
horiz	233.6172	Pass
lena256	241.8281	Pass
MI1256	284.9922	Pass
MI3256	247.1094	Pass
squares	281.4531	Pass
barb512	234.4297	Pass
boat512	284.7070	Pass
mandrill512	300.7734	Pass
peppers512	211.7871	Pass
texmos1	265.0723	Pass
texmos2	249.2129	Pass
texmos3b	234.1621	Pass
zelda512	276.0996	Pass
1.3.02	274.7539	Pass
1.3.03	246.1372	Pass
1.3.04	251.9243	Pass
1.3.07	256.8760	Pass
1.3.09	247.9438	Pass
1.3.10	244.1611	Pass
1.4.01	241.6929	Pass
1.4.05	266.2734	Pass
1.4.06	265.5781	Pass
1.4.07	235.0117	Pass
1.4.09	253.1807	Pass
1.4.12	245.1646	Pass

image having negligible adjacent pixel correlation. Therefore, deriving any meaningful information from the cipher images is a challenging task, indicating the resilience of the ZM-IEM to correlation attacks.

5.4. Cross-correlation (CC) analysis

To evaluate the efficacy of the proposed ZM-IEM, we calculated the CC between the plain and encrypted images. The CC is computed using (12), where x and y denote the pixel values of the plain and cipher images, respectively. The computed CC values are tabulated in Table 6. Given that the CC values are incredibly close to zero, we can conclude that there is a minimal correlation between the plain and cipher images.

Accepted Manuscript

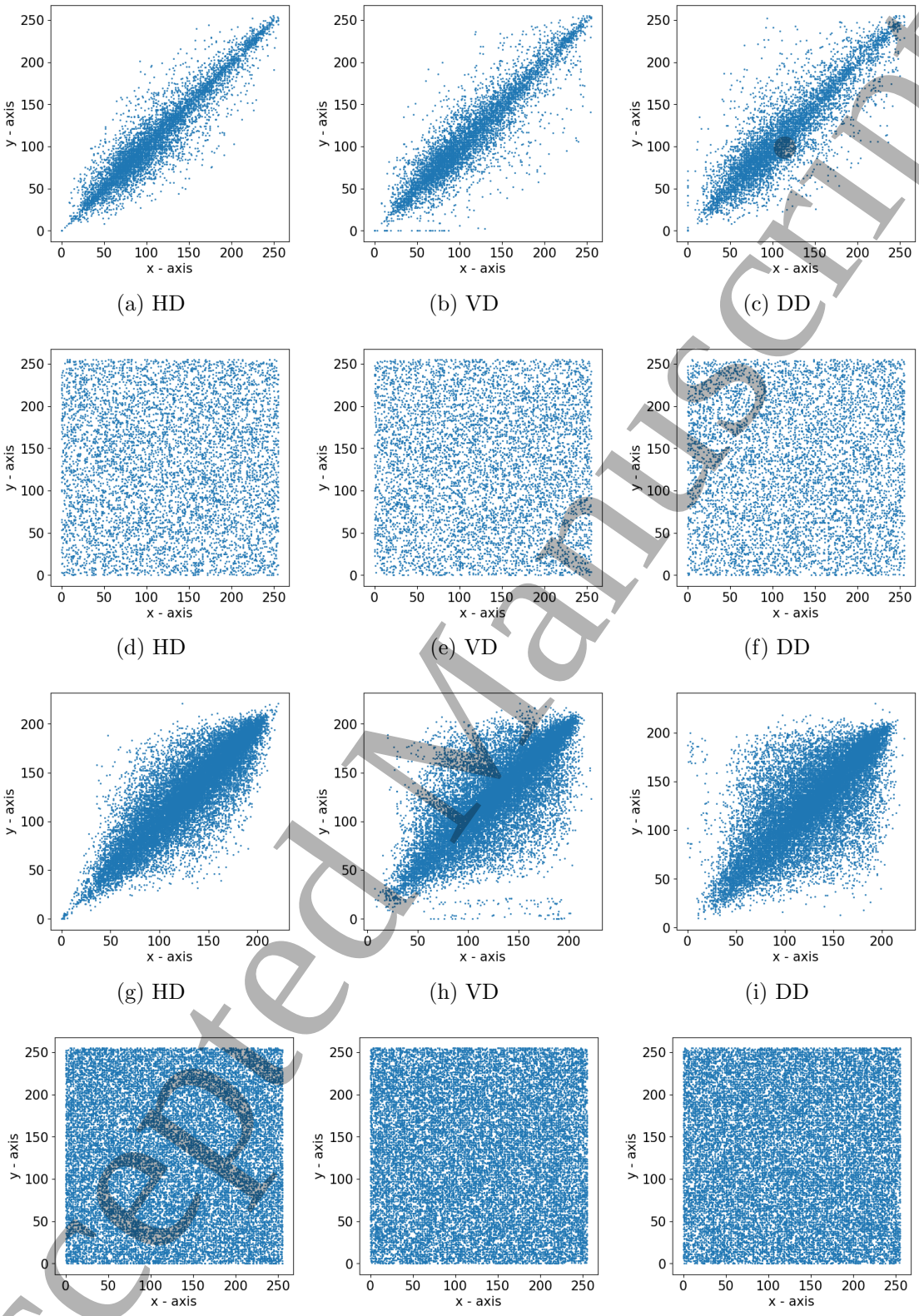

(a) HD (b) VD (c) DD

(d) HD (e) VD (f) DD

(g) HD (h) VD (i) DD

(j) HD (k) VD (l) DD

Figure 12: Adjacent pixel distribution: (a)-(c) Adjacent pixel distribution of plain image Bridge, (d)-(f) Adjacent pixel distribution of cipher image Bridge, (g)-(i) Adjacent pixel distribution of plain image mandrill512 (j)-(l) Adjacent pixel distribution of cipher image mandrill512.

Accepted Manuscript

Table 6: Comparison of Correlation Coefficient values of ZM-IEM with methods available in the literature.

Image	Direction	Plain image	ZM-IEM	[26]	[18]	[28]	[25]	[22]	[31]	[32]	[24]	[21]	[33]
MI1256	DD	0.9579	-0.0064	-0.0113	0.0041	-0.0087	0.0071	-0.0091	0.0067	-0.0210	0.0148	0.0072	-0.0120
	HD	0.9855	0.0057	0.0114	0.0097	-0.0191	0.0009	-0.0091	0.0013	0.0098	0.0009	-0.0103	0.0007
	VD	0.9651	0.0185	0.0022	0.0099	0.0014	-0.0066	-0.0070	0.0084	-0.0039	0.0048	-0.0091	0.0017
	CC		-0.0043	-0.0138	0.0099	-0.0194	0.0006	0.0067	-0.0210	0.0148	0.0008	0.0007	0.0057
mandrill512	DD	0.7220	-0.0094	-0.0079	0.0028	0.0017	-0.0008	-0.0091	-0.0070	0.0084	-0.0241	0.0023	-0.0048
	HD	0.8769	-0.0096	-0.0023	0.0059	0.0151	0.0002	0.0214	-0.0091	-0.0070	0.0084	0.0100	0.0090
	VD	0.7500	-0.0144	-0.0091	0.0013	0.0098	0.0052	-0.0215	0.0214	-0.0091	-0.0070	0.0037	-0.0018
	CC		-0.0254	-0.0091	0.0067	-0.0210	0.0148	0.0008	0.0214	-0.0091	-0.0070	-0.0017	0.0105
boat512	DD	0.9240	0.0178	-0.0027	-0.0178	0.0009	0.0140	-0.0138	0.0099	-0.0194	0.0006	0.0077	-0.0002
	HD	0.9524	0.0017	-0.0132	-0.0059	-0.0033	0.0029	0.0067	-0.0210	0.0148	0.0008	-0.0117	0.0208
	VD	0.9593	0.0000	-0.0043	-0.0029	0.0058	0.0004	-0.0091	-0.0070	0.0084	-0.0039	0.0011	0.0032
	CC		0.0178	-0.0005	-0.0044	-0.0159	-0.0090	-0.0138	0.0099	-0.0194	0.0006	0.0087	-0.0023
zelda512	DD	0.9234	-0.0083	0.0053	0.0023	0.0024	-0.0008	-0.0091	-0.0070	0.0084	-0.0039	-0.0097	-0.0008
	HD	0.9511	0.0015	-0.0019	0.0046	-0.0010	-0.0027	-0.0091	-0.0070	0.0084	-0.0039	0.0011	0.0045
	VD	0.9602	-0.0091	-0.0070	0.0084	-0.0039	0.0048	-0.0083	0.0053	0.0023	0.0024	0.0012	0.0061
	CC		0.0028	-0.0159	-0.0102	-0.0102	0.0001	0.0067	-0.0210	0.0148	0.0008	0.0001	0.0084
1.3.02	DD	0.8627	-0.0105	0.0070	0.0007	-0.0167	0.0060	-0.0039	0.0048	-0.0083	0.0053	-0.003	0.0099
	HD	0.9097	0.0036	-0.0271	0.0026	0.0000	-0.0078	-0.0091	-0.0070	0.0084	-0.0039	-0.0040	-0.0080
	VD	0.9254	-0.0007	0.0132	0.0047	0.0149	0.0196	-0.0008	0.0030	0.0084	0.0076	-0.0056	-0.0043
	CC		-0.0202	0.0056	-0.0070	0.0046	-0.0108	-0.0091	-0.0070	0.0084	-0.0039	-0.0194	-0.0008
1.4.12	DD	0.8636	-0.0069	0.0073	0.0013	-0.0001	-0.0035	0.0067	-0.0210	0.0148	0.0008	-0.0070	-0.0034
	HD	0.9114	0.0268	0.0105	-0.0008	-0.0034	-0.0033	-0.0138	0.0099	-0.0194	0.0006	-0.0138	0.0178
	VD	0.9259	0.0253	-0.0008	0.0030	0.0084	0.0076	-0.0091	-0.0070	0.0084	-0.0039	0.0105	0.0052
	CC		-0.0092	-0.0110	-0.0059	-0.0061	0.0000	-0.0091	-0.0070	0.0084	-0.0039	-0.0033	0.0070

5.5. Secret key sensitivity analysis

To design a secure and robust IEM, it is crucial to utilise a unique secret key for encryption and decryption procedures [51]. Even a minor alteration to the secret key will lead to a distinct cipher image, exhibiting the sensitivity and uniqueness of the encryption process. This emphasises the need for precision and confidentiality in managing the secret key to ensure the integrity and security of the encrypted images. The proposed ZM-IEM is based on a hexadecimal key of size 64, where changing one number prevents recovery of the content of the plain image. We used the key K to encrypt the plain image. Further, two keys, SK_1 and SK_2, are formed with only one-bit difference and are used to decrypt the cipher image.

K = *65BDA1580E6A69628FD4E61F7FBFC4719DA4A8945AB4851B0B9F572624C095D8*
SK_1 = *65BDA1580E6A69628FD4E61F7FBFC4719DA4A8945AB4851B0B9F572624C095D7*
SK_2 =*65BDA1580E6A69628FD4E61F7FBFC4719DA4A8945AB4851B0B9F572624C095D9*

Figure 13(b) exhibits the cipher image C obtained using ZM-IEM and key K. Furthermore, Figures 13(c),(d) show decrypted images with the keys $SK_1$and SK_2, respectively. It is concluded that the cipher image cannot be decrypted using the modified keys. Since decryption using modified keys is impossible, we can say that the IEM is susceptible to encryption keys.

Accepted Manuscript

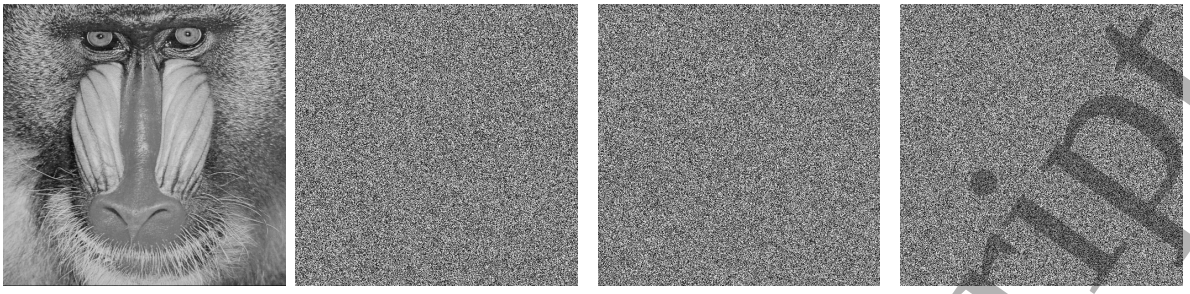

(a) (b) (c) (d)

Figure 13: (a) Plain mandrill image, (b) Cipher mandrill C encrypted with key K, (c) Cipher mandrill C decrypted with key SK_1, (d) Cipher mandrill C decrypted with key SK_2.

5.6. Resistance to potential classical attacks

Chosen-plaintext attacks, chosen-ciphertext attacks, ciphertext-only attacks, and known-plaintext attacks are well-known classical threats to encryption systems. The chosen-plaintext attacks are widely applied in the field of cryptanalysis as it is the most common form of attack [52]. It has been shown in the literature that a qualified IEM algorithm can resist chosen-plaintext attack [53, 54, 55], if (13) holds.

$$P_1(i,j) \oplus P_2(i,j) \neq T_1(i,j) \oplus T_2(i,j) \tag{13}$$

where P_1 and P_2 represent the two plain images, and T_1 and T_2 are the corresponding encrypted images, respectively. The visualisation of the operation described in (13) is shown in Figure 14. From Figure 14(c) and Figure 14(f), it can be observed that (13) holds which supports resistance against the chosen-plaintext attack. Further, quantitative evaluation was performed in terms of NPCR value for the images shown in Figure 14(c) and Figure 14(f). The quantitative NPCR value between the images is 99.5986%, which again supports the ZM-IEM against chosen-plaintext attacks. The chosen-plaintext attack is one of the strongest among the rest of classical attacks. Hence, the proposed ZM-IEM can withstand the rest of the classical attacks.

5.7. Resistance to occlusion and noise attack

The potential for data loss due to factors like noise or occlusion attacks during transmission over unsecure communication channels is a crucial concern. The robustness of an IEM can be determined by how well it withstands occlusion and noise attacks. A robust IEM ensures that the decryption process does not significantly impede the recovery of the original image, even if the cipher image is under occlusion and noise attacks.

To exhibit the strength of the ZM-IEM towards the occlusion attack, 10% portion of the cipher image occluded. Further, the occluded image shown in Figure 15(b) is decrypted and is shown in Figure 15(e). Similarly, the cipher image is corrupted with 10% salt and pepper noise for the noise attack. The noise image shown in Figure 15(c) is decrypted and shown in Figure 15(f). The Figures 15(e), and 15(f) are similar to the Figure 15(d),

Accepted Manuscript

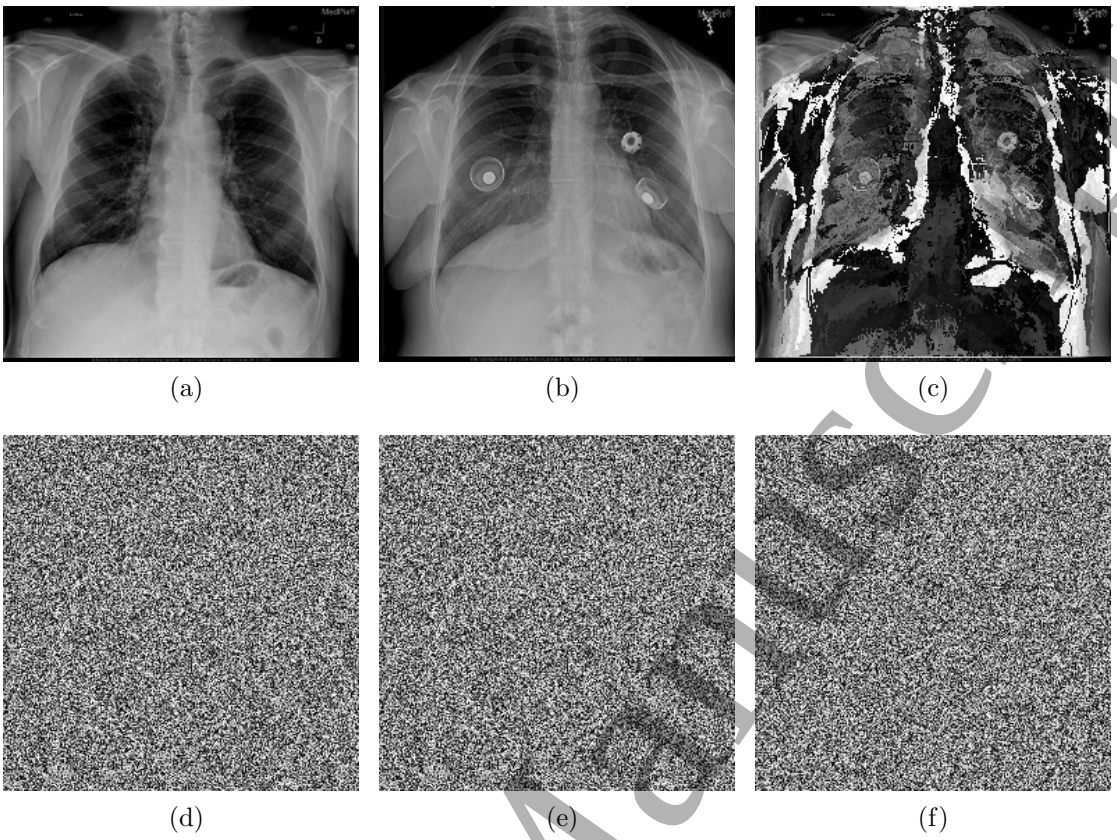

Figure 14: Demonstration on resistance chosen-plaintext attacks of ZM-IEM: (a) Plain Image MI1256, (b) Plain Image MI3256, (c) Plain Image MI1256 $\oplus$ Plain Image MI3256, (d) Encrypted Image MI1256, (e) Encrypted Image MI3256, (f) Encrypted Image MI1256 $\oplus$ Encrypted Image MI3256.

which is the decrypted image obtained from the original cipher image. It can be seen that the decryption process can recover some of the image's visual content, which is enough to understand the content of the plain image.

5.8. Resistance to differential attack

An attacker can try to analyse the encryption and decryption process for the plain images with slight modifications in some pixel values. To avoid this, it is mandatory to produce a completely different cipher image even in case of a one-bit change in the pixels of the plain image [56]. The Number of Pixels Change Rate ($NPCR$) and Unified Averaged Changed Intensity ($UACI$) metrics are computed for two encrypted images derived from the same original image with minor alterations. These metrics are used to assess and compare the effectiveness of the proposed ZM-IEM with other relevant methods available in the literature. The $NPCR$ and $UACI$ values can be calculated as follows:

$$NPCR = \frac{\sum_{i,j} D_{i,j}}{M \times N} \times 100\%, \ \textit{where } D_{i,j} = \begin{cases} 1, & \text{if } RP_{i,j} \neq RM_{i,j}; \\ 0, & \text{if } RP_{i,j} = RM_{i,j}; \end{cases} \tag{14}$$

Accepted Manuscript

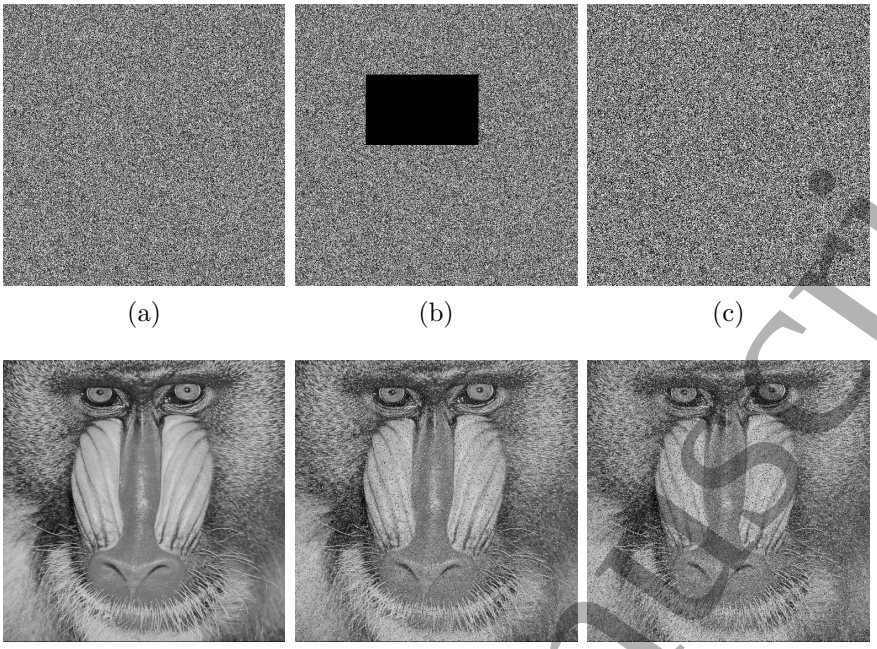

Figure 15: Resistance against occlusion and noise attack: (a) Cipher mandrill image, (b) Cipher mandrill image with 10% occluded part, (c) Cipher mandrill image with 10% salt and pepper noise, (d) The Decryption of the cipher mandrill image (shown in (a)), (e) The decryption of occluded image (shown in (b)), (f) The decryption of noise image (shown in (c)).

$$UACI = \frac{1}{M \times N}\left[\sum_{i,j}\frac{|RP_{i,j} - RM_{i,j}|}{255}\right] \times 100\% \tag{15}$$

Here, M and N represent the height and width of the original image, respectively. RP is the cipher image derived from the original plain image, while RM is the cipher image resulting from alterations made to the original plain image. For a cipher image, $NPCR$ has an ideal value of 99.6094%, and $UACI$ has an ideal value of 33.4635% [57]. Tables 7 and 8 show the comparison and analysis of the $NPCR$ and $UACI$ values obtained for different encrypted images, respectively. The average values of $NPCR$ and $UACI$ obtained by the proposed ZM-IEM are 99.6112% and 33.4246%, respectively. Tables 7 and 8 show that the ZM-IEM is passed against all images in contrast to other related methods. Hence, the ZM-IEM can resist differential attacks.

5.9. Randomness test

The cipher image should exhibit a pixel distribution characterised by randomness and uniformity. The National Institute of Standards and Technology (NIST) SP800-22 is a developed tool for evaluating randomness by running fifteen distinct types of tests [45]. The test uses a p-value at a significance level β. The random sequence is considered to

Accepted Manuscript

Table 7: Comparison of NPCR values of ZM-IEM with methods available in the literature.

Image/IEM	ZM-IEM	[25]	[26]	[18]	[28]	[22]	[31]	[32]	[24]	[29]	[30]	[27]	[21]	[33]
black	99.5819	99.6140	99.6078	99.6140	99.5956	99.5880	99.5834	99.6048	0.0000	99.6429	61.8759	99.6445	0.1877	99.6078
bridge256	99.5743	99.6277	99.6033	99.6094	99.6201	99.5911	99.6078	99.5911	99.6048	99.5941	99.4690	99.5667	99.5758	99.6155
horiz	99.6048	99.5499	99.6262	99.6674	99.6414	99.5926	99.5911	99.6475	99.5682	99.6002	99.3637	99.6124	93.6188	99.5956
lena256	99.6109	99.6307	99.5926	99.6338	99.6216	99.6033	99.6399	99.6002	99.5819	99.5728	99.3011	99.5956	99.6353	99.2065
MI1256	99.6368	99.6017	99.6124	99.6094	99.6262	99.6155	99.6033	99.6307	99.5667	99.6567	99.5422	99.6582	99.6353	99.5514
MI3256	99.6323	99.6201	99.6353	99.5544	99.6429	99.5880	99.6094	99.5834	99.6216	99.6170	99.5132	99.6338	99.6506	99.5941
squares	99.5911	99.6323	99.5941	99.5911	99.5300	99.6140	99.6002	99.5667	99.4263	99.5850	99.3225	99.6124	94.2078	99.6002
barb512	99.6288	99.5857	99.5998	99.5846	99.6140	99.6155	99.6155	99.6113	99.6143	99.5987	99.3385	99.6117	99.5964	99.6334
boat512	99.6056	99.5861	99.5930	0.0004	99.6082	99.5945	99.6048	99.6132	99.6002	99.5998	99.3412	99.6021	99.6132	99.5960
mandrill512	99.5972	99.6227	99.6025	99.5884	99.6075	99.6109	99.6181	99.5918	99.6128	99.6181	99.4576	99.6140	99.6288	99.6105
peppers512	99.6300	99.6006	99.6044	99.6040	99.6010	99.5811	99.6147	99.6063	99.6056	99.5872	99.2882	99.6075	99.6143	99.6033
texmos1	99.5983	99.6033	99.6136	99.6136	99.6006	99.6075	99.5922	99.6086	99.6040	99.6120	99.3462	99.6140	99.5899	99.6029
texmos2	99.6227	99.5781	99.5850	99.6490	99.6040	99.6243	99.6075	99.6063	99.6616	99.6040	99.4171	99.6178	99.0707	99.6101
texmos3b	99.6185	99.5850	99.6193	99.6113	99.6143	99.6304	99.6059	99.6281	99.6174	99.6189	99.4476	99.5884	99.6109	99.6052
zelda512	99.6151	99.6067	99.6078	99.6075	99.6140	99.5937	99.6147	99.6265	99.5972	99.6006	99.3542	99.6208	99.5995	99.5987
1.3.02	99.6062	99.6013	99.6016	99.6083	99.6095	99.6066	99.6063	99.5992	99.6169	99.6140	99.3408	99.6024	99.6048	99.5994
1.3.03	99.6071	99.6103	99.6208	0.0001	99.6053	99.5987	99.6119	99.6219	99.6116	99.6170	99.3355	99.6162	99.6057	99.6067
1.3.04	99.6046	99.5963	99.6001	99.6109	99.6033	99.6030	99.6065	99.6075	99.6163	99.5994	99.3197	99.6066	99.6125	99.6097
1.3.07	99.6077	99.5947	99.6199	99.6067	99.6119	99.6204	99.6075	99.6096	99.6117	99.6131	99.3128	99.6100	99.6125	99.2199
1.3.09	99.5948	99.5935	99.6174	99.6176	99.6087	99.6085	99.6177	99.6125	99.6041	99.6181	99.2979	99.6049	99.6034	99.6122
1.3.10	99.6088	99.5988	99.6113	99.6138	99.6017	99.6161	99.6096	99.6122	99.6033	99.6147	99.3386	99.6102	99.6128	99.6110
1.4.01	99.6099	99.6095	99.6092	99.6139	99.6134	99.6242	99.6118	99.5961	99.6055	99.6094	96.8081	99.6048	99.6094	99.6264
1.4.05	99.6081	99.6026	99.6096	99.6017	99.6067	99.6057	99.5989	99.6012	99.6156	99.6107	99.3300	99.6159	99.6146	99.6110
1.4.06	99.5988	99.5994	99.6058	99.6092	99.6089	99.6053	99.6093	99.6088	99.6035	99.6139	97.2220	99.6036	99.6161	99.6143
1.4.07	99.6166	99.5927	99.6195	99.6034	99.5998	99.6163	99.6190	99.6165	99.6007	99.6076	99.2927	99.6043	99.6051	99.2144
1.4.09	99.5995	99.5995	99.6121	99.6061	99.6073	99.6084	99.6088	99.6190	99.6031	99.6108	99.2812	99.6034	99.6089	99.6207
1.4.12	99.5995	99.5919	99.6115	99.5975	99.6115	99.6149	99.6190	99.5124	99.6076	99.6192	99.3416	99.6065	99.6120	99.6155
Mean	99.6112	99.6013	99.6087	92.2306	99.6085	99.6066	99.6087	99.6049	95.9105	99.6095	97.8000	99.6107	95.4872	99.5627

Table 8: Comparison of UACI values of the ZM-IEM with methods available in the literature.

Image/IEM	ZM-IEM	[25]	[26]	[18]	[28]	[22]	[31]	[32]	[24]	[29]	[30]	[27]	[21]	[33]
black	33.4844	33.0262	33.3810	33.4100	33.2010	33.4073	33.4296	33.5316	0.0000	33.5089	20.7814	33.5244	0.0007	33.4010
bridge256	33.3591	32.9774	33.4964	33.4568	33.5488	33.4519	33.5217	33.3954	33.6516	33.4427	33.4409	33.6143	33.3253	33.5909
horiz	33.1752	32.8974	33.4048	33.6355	33.5095	33.4258	33.4432	33.5139	31.4296	33.4220	33.1621	33.5369	32.3218	33.3446
lena256	33.3882	33.0881	33.4441	33.4608	33.5825	33.4711	33.5545	33.4002	33.4059	33.4652	33.3559	33.4317	33.4489	33.4187
MI1256	32.7037	33.1394	33.5875	33.3999	33.5445	33.4910	33.4120	33.3477	33.4421	33.3384	33.5015	33.2843	33.4110	33.4608
MI3256	33.2166	32.9003	33.6223	30.7786	33.4464	33.4298	33.5953	33.5486	33.4123	33.3942	33.5512	33.4517	33.4529	33.4546
squares	33.5820	33.1512	33.2901	33.5383	33.2326	33.5458	33.5666	33.6500	36.0689	33.3559	33.5024	33.4913	33.0722	33.3649
barb512	33.5716	33.0039	33.4300	33.4747	33.5034	33.4170	33.4759	33.4090	33.5578	33.4796	33.3938	33.4156	33.4309	33.4865
boat512	33.2978	33.0314	33.4724	33.2478	33.4669	33.4712	33.4386	33.4571	33.4193	33.4362	33.4319	33.4565	33.4741	33.4559
mandrill512	33.4751	33.0260	33.4251	27.8026	33.5151	33.4299	33.4578	33.4748	33.5327	33.4134	33.3980	33.4494	33.4760	33.4239
peppers512	33.0466	33.1133	33.5436	33.4378	33.5330	33.4232	33.4852	33.4918	33.4389	33.4425	33.3983	33.5322	33.4443	33.5283
texmos1	33.6028	32.9644	33.4456	33.4566	33.4268	33.4408	33.5432	33.4194	33.5381	33.4892	33.3558	33.4547	33.5237	33.4345
texmos2	33.5920	32.9963	33.3823	33.5462	33.5347	33.5026	33.4566	33.4222	33.6037	33.4769	33.4589	33.4587	33.3144	33.4355
texmos3b	33.4638	33.0773	33.3958	33.3854	33.4423	33.5272	33.4035	33.5410	33.4467	33.4399	33.4245	33.5079	33.4574	33.4900
zelda512	33.3682	33.0454	33.4979	33.5535	33.4602	33.4165	33.4729	33.4881	33.4062	33.4418	33.4409	33.4314	33.3933	33.4534
1.3.02	33.8426	32.9747	33.4182	33.4623	33.4535	33.3999	33.4349	33.5535	33.4229	33.4480	33.3937	33.4717	33.4543	33.4852
1.3.03	33.5250	33.0076	33.4528	33.5478	33.4781	33.4703	33.4684	33.4623	33.4557	33.4571	33.4274	33.4649	33.4822	33.4893
1.3.04	33.7526	33.0103	33.4849	33.4474	33.4910	33.4727	33.4842	33.5478	33.4604	33.4542	33.3940	33.4636	33.4494	33.4819
1.3.07	33.4805	33.0044	33.4770	33.4611	33.4619	33.5160	33.4773	33.4474	33.4671	33.4138	33.3828	33.4868	33.4254	33.3938
1.3.09	33.4442	32.9761	33.4698	33.4669	33.5635	33.4679	33.4656	33.4611	33.4368	33.4776	33.3581	33.4535	33.4521	33.4488
1.3.10	33.7309	33.0550	33.4487	33.4406	33.4465	33.5074	33.4378	33.4669	33.4657	33.4405	33.4338	33.4692	33.4851	33.4458
1.4.01	33.4938	32.9516	33.4450	33.5086	33.5359	33.4834	33.5065	33.4406	33.4857	33.4479	32.5283	33.4867	33.4384	33.4951
1.4.05	33.3643	33.0187	33.4390	33.4612	33.4643	33.4683	33.4516	33.5086	33.6008	33.4326	33.4422	33.4872	33.4530	33.4882
1.4.06	33.1409	33.0267	33.4383	33.4658	33.4536	33.4572	33.4369	33.4612	33.6529	33.4470	32.6876	33.4944	33.4306	33.4759
1.4.07	33.5173	33.0046	33.4857	33.4324	33.4541	33.4323	33.4795	33.4658	33.4915	33.4467	33.3684	33.4790	33.3672	33.4986
1.4.09	33.3618	33.0323	33.4734	28.9777	33.4821	33.5027	33.4316	33.4324	33.4455	33.4767	33.6221	33.4454	33.4814	33.4739
1.4.12	33.4832	32.9991	33.4663	33.5057	33.4287	33.4899	33.4600	28.9777	33.4548	33.4959	33.4029	33.4688	33.4157	33.4779
Mean	33.4246	33.0185	33.4562	32.9912	33.4689	33.4637	33.4737	33.3080	32.2664	33.4439	32.8903	33.4708	32.1438	33.4592

Accepted Manuscript

Table 9: Randomness test results (NIST SP800-22 test).

Test name	p-value	Result
Frequency Test	0.0242	Successful
Run Test	0.8390	Successful
Run Test (Longest Run of Ones)	0.4995	Successful
Block Frequency Test	0.6046	Successful
Universal Statistical Test	0.1145	Successful
Linear Complexity Test	0.5912	Successful
Serial Test	0.2851	Successful
Binary Matrix Rank Test	0.0287	Successful
Non-overlapping Template Matching Test	0.5029	Successful
Overlapping Template Matching Test	0.9334	Successful
Approximate Entropy Test	0.1074	Successful
Random Excursion Test	0.5786	Successful
Random Excursion Variant Test	0.8608	Successful
Cumulative Sums	0.0335	Successful
Discrete Fourier Transform Test	0.1355	Successful

Table 10: Comparison of computational time values (in second (s)) of ZM-IEM with methods available in the literature.

Image(size)	ZM-IEM	[25]	[26]	[18]	[28]	[22]	[31]	[32]	[24]	[29]	[30]	[27]	[21]	[33]
bridge(256×256)	2.28	3.55	0.92	0.27	0.08	11.70	20.72	198.48	0.57	0.52	1.09	2.47	0.33	31.15
zelda(512×512)	8.7	13.01	3.93	1.21	0.35	44.44	24.83	700.05	2.44	2.12	4.44	12.74	1.60	37.61
1.3.02(1024×1024)	33.35	93.93	11.81	4.61	1.23	224.51	30.54	3541.14	5.27	8.60	18.80	48.00	6.31	48.94

pass a given randomness test if the obtained $p - value$ is greater than β [45]. Table 9 shows the $p - value$ for 15 tests for the cipher image (1.3.02). The sequence tested has a bit-stream size of the cipher image and $\beta = 0.01$. All the prescribed tests have passed since the $p - value \geq 0.01$ shows that the cipher image is random.

5.10. Computation time analysis

The computation time of the IEM plays a crucial role in determining its suitability for real-world applications [58]. A comprehensive analysis of the running time of the proposed ZM-IEM method has been conducted by comparing it with related methods. For the purpose of evaluating performance in terms of execution time, three images, bridge256, zelda512, and 1.3.02, of varying dimensions are utilised. The mean execution time (mean value calculated for 30 individual runs) for encryption is quoted in Table 10. The analysis demonstrates that the ZM-IEM exhibits a significantly lower mean execution time compared to related works [25], [22], [31], [32], [27] and [33]. Although the mean execution time for the proposed ZM-IEM is slightly higher compared to some of the methods, the complex dynamics of the Zirili map provide an unbeatable security feature to the proposed IEM approach.

Accepted Manuscript

6. Conclusion

In this study, we proposed a 2D Zirili map that exploits the properties of the Zirili test optimization function. The chaotic performance of the Zirili map is analysed and compared with other recent maps in terms of various chaotic indicators. The phase diagram of the map spreads throughout the region and does not show any specific pattern. The Zirili map shows noticeable changes when the control parameter is varied. The Lyapunov exponents of the Zirili map are high compared to other recent maps. The positive Lyapunov exponents strongly indicate that the Zirili map exhibits hyperchaotic behaviour, making it a promising candidate for applications in image encryption. We have used the proposed map to develop a robust image encryption method. The image encryption uses Cascading Confusion Transformation and Modified Cyclic Diffusion with Pixel Mixing to encrypt images, followed by four encryption rounds. This method has been tested on various grey-scale images with varying dimensions to assess its security performance comprehensively. This evaluation encompassed differential attacks, statistical assessments, brute force attacks, potential vulnerabilities, information entropy and resistance to interference. The research results reveal that the proposed ZM-IEM method resists several attacks due to the unpredictability of the chaotic sequence, the key's length, and, confusion and diffusion strategy. Further, the NIST test performed on the encrypted image supports the effectiveness of the proposed ZM-IEM. In future, it will be interesting to explore multidimensional chaotic maps along with compression strategy suitable for hyper-spectral images, audio and video data encryption.

Acknowledgements

The first author received financial support from CSIR, India, with sanction order number 08/0133(13253)/2022-EMR-I for conducting research work.

Authorship contributions There are equal contributions to this research from all the authors of this article.

Data availability statements Image data utilised to analyse the proposed approach and related methods is publicly available.

Declarations

Conflict of interest The authors declare that they have no conflict of interest.

Ethical approval This article contains no studies with human participants or animals performed by authors.

Informed consent Informed consent was obtained from all individual participants included in the study.

[1] Mingjie Zhao, Lixiang Li, and Zheng Yuan. An image encryption approach based on a novel two-dimensional chaotic system. *Nonlinear Dynamics*, pages 1–27, 2024.

[2] Bowen Zhang and Lingfeng Liu. Chaos-based image encryption: Review, application, and challenges. *Mathematics*, 11(11), 2023.

[3] Honglian Shen, Xiuling Shan, and Zihong Tian. Color image encryption scheme combining a 2D hyperchaotic Sin–Henon system and the division algorithm. *Journal of Information Security and Applications*, 85:103858, 2024.

Accepted Manuscript

[4] Omar Farook Mohammad, Mohd Shafry Mohd Rahim, Subhi Rafeeq Mohammed Zeebaree, and FY Ahmed. A survey and analysis of the image encryption methods. *International Journal of Applied Engineering Research*, 12(23):13265–13280, 2017.

[5] Toshiki Habutsu, Yoshifumi Nishio, Iwao Sasase, and Shinsaku Mori. A secret key cryptosystem by iterating a chaotic map. In *Advances in Cryptology—EUROCRYPT'91: Workshop on the Theory and Application of Cryptographic Techniques Brighton, UK, April 8–11, 1991 Proceedings 10*, pages 127–140. Springer, 1991.

[6] Qiang Lai, Liang Yang, and Yuan Liu. Design and realization of discrete memristive hyperchaotic map with application in image encryption. *Chaos, Solitons I& Fractals*, 165:112781, 2022.

[7] M.E. Smid and D.K. Branstad. Data Encryption Standard: past and future. *Proceedings of the IEEE*, 76(5):550–559, 1988.

[8] Rijmen Vincent and Daemen Joan. Advanced encryption standard. In *Proceedings of Federal Information Processing Standards Publications, National Institute of Standards and Technology*, pages 19–22, 2001.

[9] Xiaoling Huang, Youxia Dong, Guodong Ye, and Yang Shi. Meaningful image encryption algorithm based on compressive sensing and integer wavelet transform. *Frontiers of Computer Science*, 17(3):173804, 2023.

[10] Huipeng Liu, Lin Teng, Yijia Zhang, Ruiying Si, and Pengbo Liu. Mutil-medical image encryption by a new spatiotemporal chaos model and DNA new computing for information security. *Expert Systems with Applications*, 235:121090, 2024.

[11] Jinwen He, Hegui Zhu, and Xv Zhou. Quantum image encryption algorithm via optimized quantum circuit and parity bit-plane permutation. *Journal of Information Security and Applications*, 81:103698, 2024.

[12] Wassim Alexan, Yen-Lin Chen, Lip Yee Por, and Mohamed Gabr. Hyperchaotic maps and the single neuron model: A novel framework for chaos-based image encryption. *Symmetry*, 15(5):1081, 2023.

[13] Yi Huang and Lili Zhou. A hyper-chaos-based image encryption scheme with double parity alternate scrambling. *Multimedia Tools and Applications*, pages 1–15, 2023.

[14] C Madan Kumar, R Vidhya, and M Brindha. An efficient chaos based image encryption algorithm using enhanced thorp shuffle and chaotic convolution function. *Applied Intelligence*, 52(3):2556–2585, 2022.

[15] Qiang Lai, Genwen Hu, Uğur Erkan, and Abdurrahim Toktas. A novel pixel-split image encryption scheme based on 2D Salomon map. *Expert Systems with Applications*, 213:118845, 2023.

[16] Madhu Sharma, Ranjeet Kumar Ranjan, and Vishal Bharti. An image encryption algorithm based on a novel hyperchaotic Hénon sine map. *Multimedia Tools and Applications*, 82(8):11949–11972, 2023.

[17] Uğur Erkan, Abdurrahim Toktas, and Qiang Lai. 2D hyperchaotic system based on Schaffer function for image encryption. *Expert Systems with Applications*, 213:119076, 2023.

[18] Uğur Erkan, Abdurrahim Toktas, Feyza Toktas, and Fayadh Alenezi. 2D eπ-map for image encryption. *Information Sciences*, 589:770–789, 2022.

[19] Shi-xian Nan, Xiu-fang Feng, Yong-fei Wu, and Hao Zhang. Remote sensing image compression and encryption based on block compressive sensing and 2D-LCCCM. *Nonlinear Dynamics*, 108(3):2705–2729, 2022.

[20] Rui Wu, Suo Gao, Herbert Ho-Ching Iu, Shuang Zhou, Uğur Erkan, Abdurrahim Toktas, and Xianglong Tang. Securing Dual-Channel Audio Communication With a 2-D Infinite Collapse and Logistic Map. *IEEE Internet of Things Journal*, 11(6):10214–10223, 2024.

[21] Qiang Lai, Yuan Liu, and Liang Yang. Remote sensing image encryption algorithm utilizing 2D Logistic memristive hyperchaotic map and SHA-512. *Science China Technological Sciences*, 67(5):1553–1566, 2024.

[22] Jiming Zheng, Zheng Luo, and Qingxia Zeng. An efficient image encryption algorithm based on multi chaotic system and random DAN coding. *Multimedia Tools and Applications*, 79(39):29901–29921, 2020.

[23] Taiyong Li and Duzhong Zhang. Hyperchaotic image encryption based on multiple bit permutation

Accepted Manuscript

and diffusion. *Entropy*, 23(5):510, 2021.

[24] Shamsa Kanwal, Saba Inam, Fahima Hajjej, Omar Cheikhrouhou, Zainab Nawaz, Ayesha Waqar, Majid Khan, et al. A New Image Encryption Technique Based on Sine Map, Chaotic Tent map, and Circulant Matrices. *Security and Communication Networks*, 2022, 2022.

[25] Lanhang Li, Yuling Luo, Senhui Qiu, Xue Ouyang, Lvchen Cao, and Shunbin Tang. Image encryption using chaotic map and cellular automata. *Multimedia Tools and Applications*, pages 1–19, 2022.

[26] Lin Teng, Xingyuan Wang, and Yongjin Xian. Image encryption algorithm based on a 2D-CLSS hyperchaotic map using simultaneous permutation and diffusion. *Information Sciences*, 605:71–85, 2022.

[27] Xingyuan Wang, Nana Guan, Hongyu Zhao, Siwei Wang, and Yingqian Zhang. A new image encryption scheme based on coupling map lattices with mixed multi-chaos. *Scientific reports*, 10(1):9784, 2020.

[28] Yongjin Xian and Xingyuan Wang. Fractal sorting matrix and its application on chaotic image encryption. *Information Sciences*, 547:1154–1169, 2021.

[29] Xiaosong Gao and Xingbin Liu. CLSM-IEA: a novel cosine-logistic-sine map and its application in a new image encryption scheme. *Signal, Image and Video Processing*, pages 1–15, 2024.

[30] Zhen Le, Quanjun Li, Huang Chen, Shuting Cai, Xiaoming Xiong, and Linqing Huang. Medical image encryption system based on a simultaneous permutation and diffusion framework utilizing a new chaotic map. *Physica Scripta*, 99(5):055249, apr 2024.

[31] Wei Zhang, Shuwen Wang, Weijie Han, Hai Yu, and Zhiliang Zhu. An Image Encryption Algorithm Based on Random Hamiltonian Path. *Entropy*, 22(1):73, 2020.

[32] Walid El-Shafai, Fatma Khallaf, El-Sayed M El-Rabaie, and Fathi E Abd El-Samie. Robust medical image encryption based on DNA-chaos cryptosystem for secure telemedicine and healthcare applications. *Journal of Ambient Intelligence and Humanized Computing*, 12(10):9007–9035, 2021.

[33] Yuxiao Zheng, Qingye Huang, Shuting Cai, Xiaoming Xiong, and Linqing Huang. Image encryption based on novel Hill Cipher variant and 2D-IGSCM hyper-chaotic map. *Nonlinear Dynamics*, pages 1–19, 2024.

[34] Zhihuan Chen, Xiaohui Yuan, Yanbin Yuan, Herbert Ho-Ching Iu, and Tyrone Fernando. Parameter Identification of Chaotic and Hyper-Chaotic Systems Using Synchronization-Based Parameter Observer. *IEEE Transactions on Circuits and Systems I: Regular Papers*, 63(9):1464–1475, 2016.

[35] Meiqin Liu, Senlin Zhang, Zhen Fan, Shiyou Zheng, and Weihua Sheng. Exponential H∞ Synchronization and State Estimation for Chaotic Systems Via a Unified Model. *IEEE Transactions on Neural Networks and Learning Systems*, 24(7):1114–1126, 2013.

[36] Majid Mollaeefar, Amir Sharif, and Mahboubeh Nazari. A novel encryption scheme for colored image based on high level chaotic maps. *Multimedia Tools and Applications*, 76:607–629, 2017.

[37] Ping Liu, Tongxun Zhang, and Xiang Li. A new color image encryption algorithm based on DNA and spatial chaotic map. *Multimedia Tools and Applications*, 78:14823–14835, 2019.

[38] F Aluffi-Pentini, V Parisi, and F Zirilli. Global optimization and stochastic differential equations. *Journal of optimization theory and applications*, 47:1–16, 1985.

[39] Zhongyun Hua, Yicong Zhou, and Hejiao Huang. Cosine-transform-based chaotic system for image encryption. *Information Sciences*, 480:403–419, 2019.

[40] Robert M May. Simple mathematical models with very complicated dynamics. In *The Theory of Chaotic Attractors*, pages 85–93. Springer, 2004.

[41] Christoph Bandt and Bernd Pompe. Permutation entropy: a natural complexity measure for time series. *Physical review letters*, 88(17):174102, 2002.

[42] James Theiler. Efficient algorithm for estimating the correlation dimension from a set of discrete points. *Physical review A*, 36(9):4456, 1987.

[43] Joshua S Richman and J Randall Moorman. Physiological time-series analysis using approximate entropy and sample entropy. *American Journal of Physiology-Heart and Circulatory Physiology*, 278(6):H2039–H2049, 2000.

[44] Peter Grassberger and Itamar Procaccia. Estimation of the Kolmogorov entropy from a chaotic signal. *Physical review A*, 28(4):2591, 1983.

Accepted Manuscript

[45] Lv-Chen Cao, Yu-Ling Luo, Sen-Hui Qiu, and Jun-Xiu Liu. A perturbation method to the tent map based on Lyapunov exponent and its application. *Chinese Physics B*, 24(10):100501, 2015.

[46] Xiuli Chai, Jianqiang Bi, Zhihua Gan, Xianxing Liu, Yushu Zhang, and Yiran Chen. Color image compression and encryption scheme based on compressive sensing and double random encryption strategy. *Signal Processing*, 176:107684, 2020.

[47] Claude E Shannon. Communication theory of secrecy systems. *The Bell system technical journal*, 28(4):656–715, 1949.

[48] Yicong Zhou, Weijia Cao, and CL Philip Chen. Image encryption using binary bitplane. *Signal processing*, 100:197–207, 2014.

[49] Abdurrahim Toktas, Uğur Erkan, and Deniz Ustun. An image encryption scheme based on an optimal chaotic map derived by multi-objective optimization using ABC algorithm. *Nonlinear Dynamics*, 105(2):1885–1909, 2021.

[50] Nestor Tsafack, Jacques Kengne, Bassem Abd-El-Atty, Abdullah M Iliyasu, Kaoru Hirota, and Ahmed A Abd EL-Latif. Design and implementation of a simple dynamical 4-D chaotic circuit with applications in image encryption. *Information Sciences*, 515:191–217, 2020.

[51] Noura Khalil, Amany Sarhan, and Mahmoud AM Alshewimy. An efficient color/grayscale image encryption scheme based on hybrid chaotic maps. *Optics & Laser Technology*, 143:107326, 2021.

[52] Sundararaman Rajagopalan, Siva Poori, Mukund Narasimhan, Sivaraman Rethinam, Chandrasekar Vallipalayam Kuppusamy, Ramalingam Balasubramanian, Vijaya Moorthi Paramasivam Annamalai, and Amirtharajan Rengarajan. Chua's diode and strange attractor: a three-layer hardware–software co-design for medical image confidentiality. *IET Image Processing*, 14(7):1354–1365, 2020.

[53] Suo Gao, Rui Wu, Xingyuan Wang, Jin Wang, Qi Li, Chunpeng Wang, and Xianglong Tang. A 3D model encryption scheme based on a cascaded chaotic system. *Signal Processing*, 202:108745, 2023.

[54] Yongjin Xian, Xingyuan Wang, Lin Teng, Xiaopeng Yan, Qi Li, and Xiaoyu Wang. Cryptographic system based on double parameters fractal sorting vector and new spatiotemporal chaotic system. *Information Sciences*, 596:304–320, 2022.

[55] C Lakshmi, Karuppusamy Thenmozhi, John Bosco Balaguru Rayappan, and Rengarajan Amirtharajan. Hopfield attractor-trusted neural network: an attack-resistant image encryption. *Neural Computing and Applications*, 32(15):11477–11489, 2020.

[56] Yu-Guang Yang, Bao-Pu Wang, Yong-Li Yang, Yi-Hua Zhou, Wei-Min Shi, and Xin Liao. Visually meaningful image encryption based on universal embedding model. *Information Sciences*, 562:304–324, 2021.

[57] Yue Wu, Joseph P Noonan, Sos Agaian, et al. NPCR and UACI randomness tests for image encryption. *Cyber journals: multidisciplinary journals in science and technology, Journal of Selected Areas in Telecommunications (JSAT)*, 1(2):31–38, 2011.

[58] Alenrex Maity and Bibhas Chandra Dhara. An Audio Encryption Scheme Based on Empirical Mode Decomposition and 2D Cosine Logistic Map. *IEEE Latin America Transactions*, 22(4):267–275, 2024.

Accepted Manuscript